14TH INTERNATIONAL CONFERENCE ON HYDROSCIENCE AND ENGINEERING

26-27 MAY, 2022
IZMIR-TURKEY

PROCEEDINGS BOOK

ICHE2022
IZMIR, TURKEY

EDITORS
Prof. Dr. Şebnem ELÇİ
Assoc. Prof. Dr. Gökçen BOMBAR

PROCEEDINGS OF THE INTERNATIONAL CONFERENCE ON HYDROSCIENCE AND ENGINEERING, URLA, IZMIR, TURKEY, MAY 26-27, 2022

ICHE 2022

EDITORS

Prof. Dr. Şebnem Elçi
Izmir Institute of Technology, TURKEY

Assoc. Prof. Dr. Gökçen Bombar
Izmir Katip Celebi University, TURKEY

COMPILED BY

Res. Asst. Binhan Arık
Izmir Institute of Technology, TURKEY

Table of Contents

PREFACE

Dear Colleagues,

It is a great honor and privilege for us to present the 'Proceedings Book' of the 14th International Conference on Hydroscience & Engineering hosted by Izmir Institute of Technology on 26-27 May 2022. The global focus on the water keeps rising due to the extreme events such as floods and droughts and due to the increasing demand for improved technologies to expand the capacity of available freshwater. ICHE conferences aim to bring together researchers and practicing engineers to share the latest scientific and technological advancements in hydroscience and engineering. We hope that you will find the proceedings book beneficial and inspiring.

The history of Hydroscience & Engineering conferences began in Washington DC in 1993, and followed by Beijing hosted ICHE in 1995, Cottbus (1998), Seoul (2000), Warsaw (2002), Brisbane (2004), Philadelphia (2006), Nagoya (2008), Chennai (2010), Orlando (2012), Hamburg (2014) Tainan (2016) and finally in 2018, Chongqing hosted ICHE 2018. After being organized in four continents, yet we had to skip year 2020 due to the global Covid-19 pandemic. After two years of delay, ICHE 2022 is organized in Izmir, with more than 100 participants from more than 15 countries. We are all delighted to present you the papers of ICHE 2022.

The conference themes 'Coastal and Maritime Hydraulics', 'Dam Hydraulics and Safety', 'Computational Hydraulics and Turbulent flows', 'Water Resources and Climate Change', 'Fluvial Hydraulics and Waterway Navigation', 'Water Quality and Ecohydraulics', 'Watershed Hydrology and Management', 'Sediment Transport and Reservoir Sedimentation', 'Groundwater Flow and Contaminant Transport', 'Hydropower and Sustainable Energy', 'Urban Flooding and Drainage', 'Advances in Laboratory Measurements and Instrumentation', 'Field Measurements and Data Collection' cover a wide range of topics related to hydro-engineering and the papers presented here focus on the central roles of these themes on the effective and sustainable management of the water resources.

We would like to thank all the participants for their contributions to the Conference Technical Program and for their contributions to the Proceedings Book. We would like to express our sincere gratitude and appreciation to our local organizing committee and to all the students who worked voluntarily during the event. We would also like to thank our sponsors, Nel Electronics, Tencate, Tekfen Engineering, Yüksel Project, IOG Engineering, and Hydrodesign companies and also to Tübitak, The Scientific and Technological Research Council of Turkey, for supporting this event.

We hope that you have a stimulating and rewarding conference and enjoy our beautiful Izmir.

Şebnem Elçi and Gökçen Bombar

Conference Co-Chairs

MEMBERS OF THE LOCAL ORGANISING COMMITTEE

Mustafa Altınakar	Argonne National Laboratory	USA
Gökçen Bombar	Izmir Katip Celebi University	Turkey
Ebru Eriş	Ege University	Turkey
Şebnem Elçi	Izmir Institute of Technology	Turkey
Muhammet Emin Emiroğlu	Fırat University	Turkey
Cevza Melek Kazezyılmaz Alhan	Istanbul University-Cerrahpasa	Turkey
Özgür Kırca	Istanbul Technical University	Turkey
Mete Köken	Middle East Technical University	Turkey
Mehmet Ali Kökpınar	TED University	Turkey
Yurdagül Kumcu	Necmettin Erbakan University	Turkey
Bergüzar Özbahçeci	Izmir Institute of Technology	Turkey
Yavuz Özeren	University of Mississippi	USA
Gökmen Tayfur	Izmir Institute of Technology	Turkey
Melih Çalamak	Middle East Technical University	Turkey

MEMBERS OF THE INTERNATIONAL SCIENTIFIC COMMITTEE

Alper Baba	Izmir Institute of Technology	Turkey
Alp Küçükosmanoğlu	Burdur Mehmet Akif Ersoy University	Turkey
Alper Elçi	Dokuz Eylul University	Turkey
Ana Quaresma	University of Lisbon	Portugal
Ana Margarida Ricardo	University of Lisbon	Portugal
Ana Maria Ferreira Da Silva	Queen's University	Canada
António Heleno Cardoso	University of Lisbon	Portugal
Aslı Numanoğlu Genç	TED University	Turkey
Asu İnan	Gazi University	Turkey
Benjamin Dewals	University of Liege	Belgium
Berna Ayat	Yildiz Technical University	Turkey
Bogumil Ulanicki	De Montfort University	UK
David R. Fuhrman	Technical University of Denmark	Denmark
Doğan Kısacık	Dokuz Eylul University	Turkey
Dilek Eren Akyüz	Istanbul University-Cerrahpasa	Turkey
Eddy Langendoen	United States Department of Agriculture (USDA)	USA
Elçin Kentel	Middle East Technical University	Turkey
Elena Volpi	University of Roma Tre	Italy

Elif Oğuz	Middle East Technical University	Turkey
Fırat Gümgüm	Dicle University	Turkey
Fotis Sotiropoulos	Stony Brook University	USA
Gülizar Özyurt	Middle East Technical University	Turkey
Hafzullah Aksoy	Istanbul Technical University	Turkey
Hajime Mase	Kyoto University	Japan
İsmail Aydın	Middle East Technical University	Turkey
İsmail Yücel	Middle East Technical University	Turkey
James Rigby	United States Department of Agriculture (USDA)	USA
Jorge Matos	University of Lisbon	Portugal
Kamal Abderrezzak El Kadi	Electricity of France	France
Karsten Rinke	Helmholtz Centre for Environmental Research	Germany
Kasım Yenigün	Kastamonu University	Turkey
Krzysztof Kochanek	Institute of Geophysics	Poland
Latif Kalın	Auburn University	USA
Lindsey Yaşarer	United States Department of Agriculture (USDA)	USA
Levent Kavvas	University of California, Davis	USA
Miguel Medina	Duke University	USA
Mohammad Ebrahim Banihabib	University of Tehran	Iran
Mohammad Hantush	United States Environmental Protection Agency	USA
Mustafa Kemal Cambazoğlu	University of Southern Mississippi	USA
Nadim Copty	Bogaziçi University	Turkey
Nobihito Mori	Kyoto University	Japan
Ömer Yüksek	Karadeniz Technical University	Turkey
Orhan Gündüz	Dokuz Eylul University	Turkey
Paul Work	United States Geological Survey (USGS)	USA
Peter Troch	The University of Arizona	USA
Ramesh S. V. Teegavarapu	Florida Atlantic University	USA
Rob Wells	United States Department of Agriculture (USDA)	USA
Salvatore Grimaldi	Tuscia University	Italy
Sameh Kantoush	Kyoto University	Japan
Sándor Baranya	Budapest University of Technology and Economics	Hungary
Sezar Gülbaz	Istanbul University	Turkey
Tamer Ayvaz	Pamukkale University	Turkey
Tommaso Moramarco	National Research Council	Italy
Tuğrul Yılmaz	Middle East Technical University	Turkey
Umut Türker	Eastern Mediterranean University	Cyprus

Vahed Nourani	Near East University	Cyprus
Valentin Heller	The University of Nottingham	UK
Vladimir Nikora	University of Aberdeen	UK
Yong Lai	United States Bureau of Reclamation (USBR)	USA
Z. Fuat Toprak	Dicle University	Turkey
Zafer Bozkuş	Middle East Technical University	Turkey
Zuhal Akyürek	Middle East Technical University	Turkey

SPONSORS

This conference is supported by TÜBİTAK

SILVER SPONSORS

ADVERTISING SPONSORSHIP

COMPUTATIONAL HYDRAULICS AND TURBULENT FLOWS

14TH INTERNATIONAL CONFERENCE
ON HYDROSCIENCE & ENGINEERING

MAY 26-27, 2022
IZMİR-TURKEY

ICHE2022
IZMIR, TURKEY

NUMERICAL SIMULATION OF LANDSLIDE GENERATED SURFACE WAVES USING OVERSET MESH METHOD

Adnan Tolga Kürümüş

Department of Civil Engineering, Eskişehir Osmangazi University, Eskişehir,Türkiye.

tolgakurumus@gmail.com

Reza Mohajer Barough

Department of Civil Engineering, Middle East Technical University, Ankara, Türkiye,

rezamohajer22@gmail.com

Erhan Tarık Karayama

Department of Civil Engineering, Middle East Technical University, Ankara, Türkiye,

tarik.karayama@metu.edu.tr

Ender Demirel

Department of Civil Engineering, Eskişehir Osmangazi University, Eskişehir, Türkiye,

edemirel@esogu.edu.tr

İsmail Aydın

Department of Civil Engineering, Middle East Technical University, Ankara, Türkiye,

ismaydin@metu.edu.tr

ABSTRACT: To study the landslide phenomena, an open source computational fluid dynamics (CFD) simulation program OpenFOAM used with the overset mesh functionality. Sliding rigid mass with six degree of freedom (6DoF) motions simulated with this dynamic mesh method. The advantage of the overset grid technique than the mesh morphing methods is being able to calculate large amplitude body motions while keeping the high mesh quality, hence forms a computational domain with non-distorted cells. Numerical results compared with the previous experimental data to validate the free surface fluctuations, which generated by a 3D rigid wedge. For the validation case, a reservoir of 6 m long, 3.7 m wide and 4.6 m deep with a sliding rigid mass on a slope (1:2) used to simulate the landslide effects. During the validation tests, above water level and fully submerged positions selected for the sliding wedge. Free surface data compared throughout all time-steps and a good agreement demonstrated. The purpose of this study is gain a better insight to landslide on a coastal area and create a numerical model to simulate on relatively larger reservoirs.

Keywords: Landslide, water entry, overset mesh method.

1. INTRODUCTION

In the computational fluid dynamic simulations, overset mesh method is a relatively new dynamic mesh solving technique and still in the development phase to have better optimized solutions. Overset mesh method is provided for open-source CFD toolbox OpenFoam (ESI version v1706, 2017). Computation of complex dynamic geometries in a fluid has always been a challenging task. Benek, 1986, developed a new method called chimera approach (overset mesh method) computational domain is divided into two regions. The first region called overset interpolation zone, which covers the surroundings of moving object and the second region called background mesh, which contains the fluid. Dynamic solid-fluid interaction is defined by interpolation algorithms between these two zones.

Different CFD programs are compared to investigate the difference in the results while using identical overset mesh cases (Chandar et al., 2018). In most of the cases, results are similar, however, for unsteady flows discrepancy occurred between results due to the interpolation methods between overset meshes. They also concluded that optimizations of the mesh and the numerical schemes were important to achieve the most efficient results.

The performance of the overset mesh method evaluated with a floating object in a numerical wave tank was presented by Chen et al., 2019. The computed data agreed with the experimental results and comparison with the dynamic mesh morphing method gave good accuracy. However, overset mesh method was less efficient than dynamic mesh method in terms of the computing time. Another disadvantage of the overset method is the lack of capability of modelling interaction between solid surfaces. In order to overcome this challenge, Alessandro et al., 2019, presented a new method to define solid boundaries by using porous zone with a very low permeability. Pre-determined movement of a 3D wedge on a slide implemented by using six degree of freedom (6DoF) method for analysis of the landslide-generated tsunamis was performed.

In the current study, landslide analysis is presented with overset mesh method in OpenFoam. To validate the CFD solutions, results are compared to the experimental studies on free surface fluctuations due to the 3D sliding wedge by Liu et al., 2005. After the validation, a relatively larger case is simulated to have a better understanding of landslides.

2. NUMERICAL MODEL

The present numerical model utilizes two-phase flow solver overInterDyMFoam from OpenFoam. In this solver, water and air phases are included in the numerical model and the volume of fluid (VOF) method is used to calculate the location of free surface. Dynamic motion of the mass is described in the sixDoFRigidBodyMotion library with overset mesh boundary conditions. Mass and momentum conservation equations, used in the solver are as follows:

$$\nabla \cdot U = 0 \tag{1}$$

$$\frac{\partial \rho U}{\partial t} + \nabla \cdot (\rho U U) - \nabla \cdot (\mu_{eff} \nabla U) = \nabla \cdot p^* - g \cdot \nabla \rho + \nabla U \cdot \nabla \mu_{eff} + \sigma k \nabla \alpha \tag{2}$$

$$\frac{\partial \alpha_1}{\partial t} + \nabla \cdot U \alpha_1 + \nabla \cdot U_c \alpha_1 (1 - \alpha_1) = 0 \tag{3}$$

where U $[m/s]$ is the velocity field, p $[m^2/s^2]$ is the pseudo-dynamic pressure, g $[m/s^2]$ is the acceleration of gravity, ρ $[kg/m^3]$ is the fluid density, X is the position vector, σ is the surface tension coefficient, k is the curvature of the interface, α is the volume fraction and μ_{eff} is the efficient dynamic viscosity, which takes into account the molecular dynamic viscosity plus the turbulent effects.

2.1. Validation of the Numerical Results

Experimental data obtained by Liu et al. (2005) is utilized to validate the solver. Landslide experiments are conducted in a water tank of 6 m long, 3.7 m wide on a 26.56° bed slope. Water depth in the tank was 2.44 m in all experiments. Water surface waves generated by a 3D wedge slide with dimensions a=45.72 cm, b=91.44 cm and width of w=65.25 cm are recorded. The mass of the moving wedge was 475.5 kg.
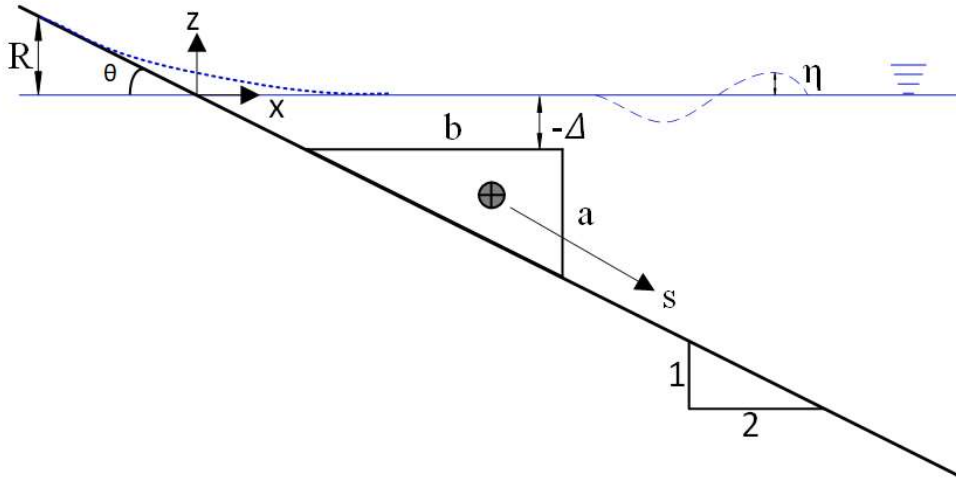
Figure 1. Definition sketch of the experimental setup

Numerical mesh of the setup was generated with the snappyHexMesh utility in OpenFoam by dividing the computation zone into 3 parts. The first part of the mesh was overset interpolation zone that covers the moving slide and calculates the interaction between solid and fluid. Second part was the background mesh where the conservation equations of the fluid are solved. Third part was the low permeability zone to define the solid boundary of the slide and Darcy-Forchheimer equations were used to define the porous zone. Since overset mesh method does not calculate the solid-solid interaction, a line constraint is defined in the 6DoF library to force the mass to move along the slide. Friction force between mass and slide is added as a constant force to the opposite direction of the movement.
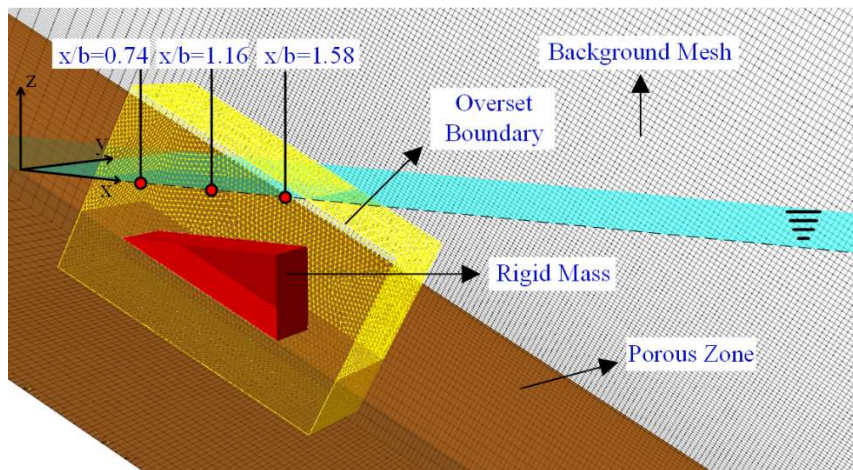
Figure 2. Illustration of the three-dimensional overset mesh method

Rigid mass velocity throughout the slide is validated with the experimental data and water surface waves are compared at three different locations along the tank (x/b=0.74, x/b=1.16, x/b=1.58). 1.2 million cells were used for the simulation. To capture better resolution on the water fluctuations finer cells were formed on the free surface. A successful agreement is observed between the numerical and experimental data. The results proved that the proposed numerical method is eligible to simulate the landslide-generated waves. Overset mesh method could also give a good performance on larger scale landslide simulations. However, for each different geometry the computational mesh should be optimized to reduce the high computation time. Besides overset mesh method's time consuming nature, using Darcy-Forchheimer equations to create low permeable zone increases computational

time. Relatively coarser cells were used at the porous zone to decrease additional computational cost. Constricting the width of the porous zone along the body movement path was also helpful on the time efficiency.
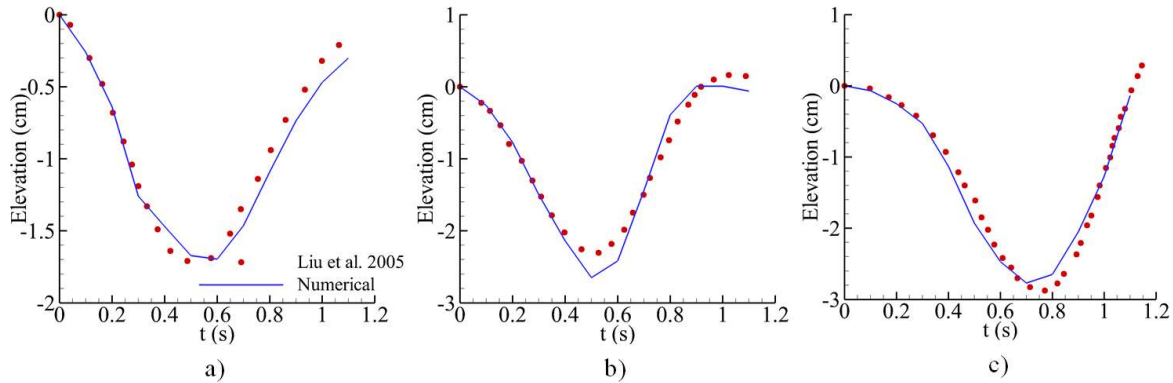
Figure 3. Comparison of water fluctuations at three locations, a) x/b=0.74, b) x/b=1.16, c) x/b=1.58

ACKNOWLEDGEMENT

REFERENCES

Alessandro, R., Javier, L., Gabriel, B., Benedetto, P., Giorgio, B., Marcello, R., Inigo, L. & Paolo, G. (2019). Numerical modelling of landslide-generated tsunamis with OpenFOAM®: a new approach. *Coastal Structures.* 486-495.

Benek, J. (1986). Chimera: A Grid-Embedding Technique. *Arnold Engineering Development Center.*

Chandar, D. & Boppana, V. (2018). A comparative study of different overset grid solvers between OpenFOAM, STAR-CCM+ and ANSYS-Fluent. *AIAA Aerospace Sciences Meeting.*

Chen, H., Qian, L., Ma, Z., Bai, W., Li, Y., Causon, D. & Mingham, C. (2019). Application of an overset mesh based numerical wave tank for modelling realistic free-surface hydrodynamic problems. *Ocean Engineering*, 97-117.

Liu, P., Wu, T., Raichlen, F., Synolakis, C. & Borrero, J. (2005). Runup and rundown generated by three-dimensional sliding masses. *Journal of Fluid Mechanics*, 107-144.

OpenFOAM, ESI. (2020) v2012 release notes: new and improved numerics. https://www.openfoam.com/releases/openfoam-v1812/numerics.php#numerics-overset

14TH INTERNATIONAL CONFERENCE
ON HYDROSCIENCE & ENGINEERING

MAY 26-27, 2022
IZMİR-TURKEY

ICHE2022
IZMIR, TURKEY

LES OF ASYMMETRIC COLLIDING GRAVITY CURRENTS

Angelos Kokkinos

Hydraulics Laboratory, Department of Civil Engineering, Aristotle University of Thessaloniki

Thessaloniki, Greece

angeloks@civil.auth.gr

Panagiotis Prinos

Hydraulics Laboratory, Department of Civil Engineering, Aristotle University of Thessaloniki

Thessaloniki, Greece

prinosp@civil.auth.gr

ABSTRACT: This paper presents results from LES simulations of two colliding gravity currents in the framework of a laboratory lock-release experiment. A partial-depth setup is used which is considered to simulate better the collision conditions of the atmosphere. The simulations are performed using three-dimensional Large-Eddy Simulation (LES) code using a dynamic Smagorinsky subgrid model. Our focus is on the examination of the dynamical features of the collision of gravity currents with different densities. The ratio of the reduced gravities (r_g) varies from 0.25 to 1.0 (symmetric collision). The maximum height and the vertical velocity of the displaced fluid are investigated. It is found that the maximum height of the displaced fluid is not affected by the ratio of the reduced gravities and is approximately equal to 1.45D. Maximum vertical velocity is detected at the time of collision with a value approximately equal to $2U_{f,1}$ ($U_{f,1}$: front velocity of the denser gravity current). The temporal evolution of energies is quantified for all the simulations. It is shown that in the asymmetric collision maximum potential energy is lower than that in the symmetric collision and that dissipation is increasing with decreasing r_g.

1. INTRODUCTION

Gravity currents are buoyancy driven flows in which hydrostatic pressure gradients due to concentration or temperature variations produce a primarily horizontal motion. They occur in a wide range of physical conditions such as thunderstorm outflows, sea breezes or katabatic flows. The gravity current collision is an important interaction between opposing gravity currents which has received attention in atmospheric studies due to the detected relation with the triggering of mesoscale convection (Intrieri et al., 1990; Lapworth, 2005). The similarities between laboratory and experimental gravity currents have motivated experimental studies on lock-exchange gravity current collision (Okon et al., 2021; van der Wiel et al., 2017; Zhong et al., 2018). This study presents a new set of numerical results of colliding gravity currents via large-eddy simulation (LES). It has been shown that LES can describe accurately most of the features of gravity currents (Meiburg et al., 2015; Ooi et al., 2009). The aim of the study is the investigation of the asymmetric collision of two counterflowing gravity currents, i.e., gravity currents with same initial lock height but different densities. The focus is on the role of the ratio of reduced gravities on maximum height and vertical velocity of the displaced fluid. The transformation between kinetic and potential energy is revealed through the quantification of energy temporal evolution.

2. SETUP AND NUMERICAL MODEL

The lock-exchange configuration is composed of two locks at the left and right corners of a horizontal tank. At t=0 the locks are released, and the dense fluids start moving one towards the other. The locks size is $D \times D \times W$, where D is the lock height and $W = D$ is the width of the tank. The size of the

tank is $L \times H \times W$, where $L = 10D$ is the length and $H = 2D$ is the height of the channel. From the dimensional analysis for any quantity A, it is:

$$A = f(\rho_1, \rho_2, \rho_0, D_1, D_2, H, \nu, g) \Rightarrow A' = f(r_g, Gr_D) \tag{1}$$

where ρ_1, ρ_2 are the densities of the fluids in locks with $\rho_1 \leq \rho_2$ and ρ_0 is the density of the ambient fluid. The ratio of the reduced gravities is $r_g = \frac{\rho_2 - \rho_0}{\rho_1 - \rho_0}$ and Grashof number is $Gr_D = (u_b D/\nu)^2$, where $u_b = \sqrt{g_1' D}$ is the buoyancy velocity and $g_1' = \frac{\rho_1 - \rho_0}{\rho_0} g$ is the reduced gravity of the denser fluid. In the simulations the ratio of reduced gravities varies from 0.25 to 1.0 while the Grashof number is equal to $5 \cdot 10^8$.

The numerical model solves the three-dimensional filtered incompressible Navier-Stokes equations. Boussinesq gravity currents are considered, so the variation of density is neglected except from the gravitational term of the momentum equations. Density is related to concentration ($\rho/\rho_0 = 1 + \beta C$, where β is the expansion coefficient and $C \in [0,1]$ is the concentration) and hence an extra transport equation for the concentration is considered. The unresolved scales of motion are considering through the SGS model in momentum and concentration equations. Using an eddy-viscosity model the SGS fluxes are modelled inserting the SGS viscosity (ν_{SGS}) and SGS diffusivity (Γ_{SGS}). SGS viscosity is calculated using a dynamic version of the classic Smagorinsky model, while SGS diffusivity is calculated explicitly considering a constant turbulent Schmidt number, $\Gamma_{SGS} = \nu_{SGS}/Sc_t$, where $Sc_t = 0.85$. The simulations are performed with a finite volume method using the open source OpenFOAM code. The pressure-velocity couping is solved using a PISO method where a 2nd order Crank-Nicolson scheme is used for the time discretization. For the spatial discretization a 2nd order central differencing scheme is used, except from the divergence term of the concentration equation in which a TVD scheme (limitedLinear) is used to keep concentration bounded at [0,1]. The momentum equations are solved with a preconditioned bi-conjugate gradient solver (PBiCG) and the pressure equation is solved with a Geometric Algebraic Multi-Grid solver (GAMG).

The space is discretized using a uniform mesh $0.01D$ along all directions. Special care is given in the vertical direction near the bottom so that the boundary layer is resolved. There the mesh is getting finer with the size of the first cell to be equal to $0.0005D$ maintaining $y_+ < 1$. The total number of cells is $22.4 \cdot 10^6$. The time step is varied so as $CFL \leq 0.15$. No slip condition is chosen for the bottom wall where the boundary layer is developed, while slip condition is employed in the left, right and top walls. Periodic condition is considered in the spanwise direction to avoid the influence of the lateral walls. The initial condition of the problem is $C = 1$ for the fluid in the left corner and $C = 0.25, 0.5, 0.75, 1.0$ for the fluid in the right corner. The reference value for the ambient fluid is $C = 0$.

3. RESULTS

After the release of the dense fluids from the locks, gravity currents start moving one towards the other with no interaction (pre-collision phase). The temporal evolution of the front displacement x_f/D calculated by tracking the iso-contour $C = 0.1$ on the line $y = 0.05D$ for $r_g = 0.5$ is shown in Figure 4a. The time has been made dimensionless dividing by $\tau = D/u_b$. It is shown that the currents insert in the slumping phase moving with constant front velocity (constant slopes), soon after the lock release. Figure 4b, presents the front velocity U_f calculated by differentiating the front displacement. During the slumping phase denser fluid moves faster with $U_{f,1}/U_{f,2} = 1.45$ setting the place of collision at $x_f = 11.5D$. After $t/\tau = 8$, the interaction of the currents takes place with reduced velocities. Despite the deceleration the denser fluid front velocity remains higher just before the collision and equal to $U_{f,1}/U_{f,2} = 4$ at $t/\tau = 9$.
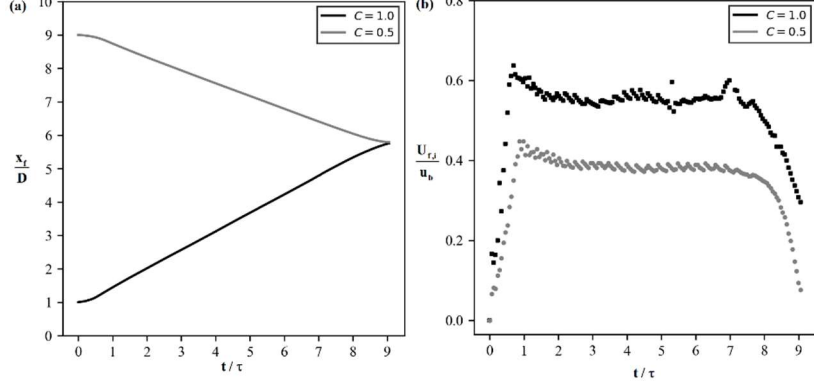
Figure 4. Temporal evolution of (a) front displacement and (b) front velocity for $r_g = 0.5$

Figure 5 shows the spanwise averaged concentration contours (Figure 5a₁-d₁) and the velocity magnitude (Figure 5a₂-d₂) for four characteristic times. In Figure 5a₁-a₂, the currents are slightly before the collision. The shape of the denser front is tilted in contrast to the shape of the lighter fluid. From the velocity field it seems that intense vertical velocity is developed pushing the ambient fluid upwards. In Figure 5b₁-b₂, the currents have collided at an angle in contrast to the symmetric case where the fluids collide vertically. At that time the maximum vertical velocity appears equal to $v/U_{f,1} \approx 2.0$. Figure 5c₁-c₂ shows the time of the maximum vertical displacement of the fluid. Vertical displacement is considered as the highest height where C=0.1 is detected and is equal to $1.44D$. This value is almost the same for all the simulations (e.g, $1.47D$ for symmetric collision) indicating no trend of vertical displacement with r_g. In Figure 5d₁-d₂, the formation of a horizontal bore moving in the same direction as the denser gravity currents is detected. It moves with considerably lower velocity and height than those of the initial gravity current.
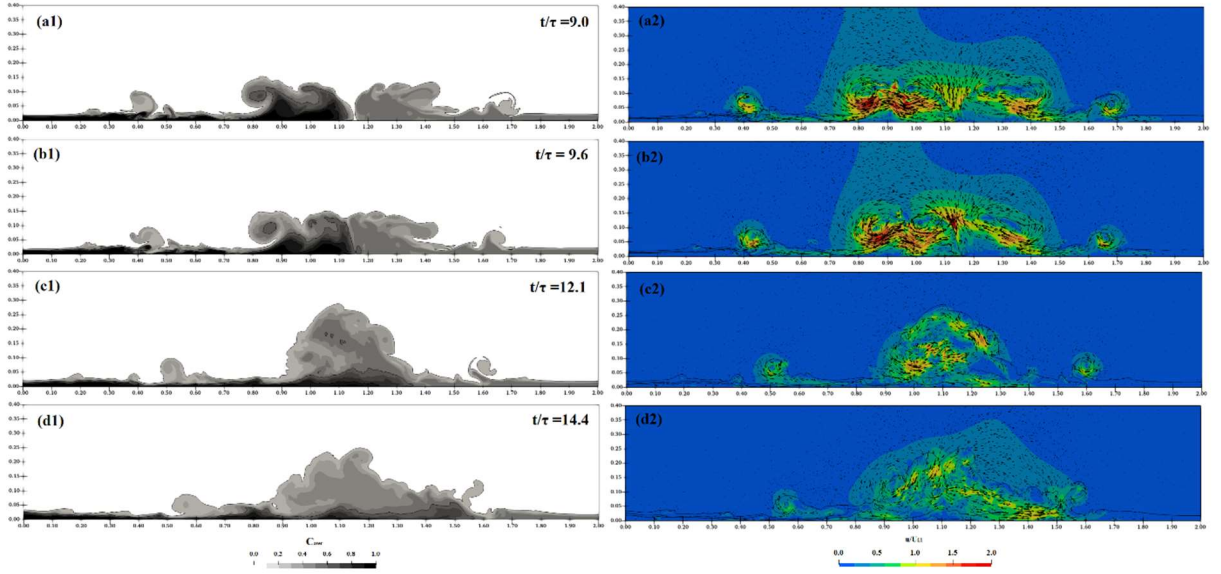
Figure 5. Spanwise averaged concentration contours (a₁-d₁) and velocity magnitude (a₂-d₂) for $r_g = 0.5$

In Figure 6, the temporal evolution of energies for $r_g = 0.5$ is presented, where E_p and E_k are the potential and the kinetic energy, respectively, and E_d is the dissipation of the fluid. $E_{p,0}$ is the initial potential energy of the system. The vertical line at $t/\tau = 9$ indicates the start of the collision. After the lock release dense fluids start moving increasing the kinetic energy of the system at the expense of the potential energy. During the slumping phase of the currents E_k and E_p are almost constant equal to $0.55E_{p,0}$ and $0.40E_{p,0}$, respectively. After collision potential energy increases with $E_{p,max} =$

9

$0.65E_{p,0}$. At the same time $E_{k,min} = 0.20E_{p,0}$. The rate of change of dissipation is increased after the collision.
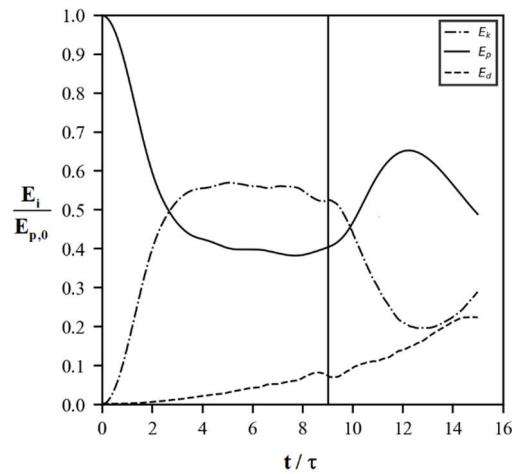
Figure 6. Temporal evolution of energies for $r_g = 0.5$ (red)

4. CONCLUSIONS

In asymmetric cases ($r_g < 1$) the collision occurs at an angle and in a position closer to the lighter fluid lock in comparison to the symmetric case ($r_g = 1$) where the currents collide vertically in the middle of the domain. The maximum height of the displaced fluid is not dependent on r_g. In colliding gravity currents the initial transformation of potential energy to kinetic, which creates the motion, is inverted as the currents converge. After collision dissipation is increased. Maximum potential energy after collision is lower in asymmetric cases ($r_g < 1$) than that of the symmetric case ($r_g = 1$). Detailed results for all r_g will be presented at the conference.

REFERENCES

Intrieri, J. M., Bedard, A. J., & Hardesty, R. M. (1990). Details of colliding thunderstorm outflows as observed by Doppler lidar. *Journal of the Atmospheric Sciences*, *47*(9). https://doi.org/10.1175/1520-0469(1990)047<1081:doctoa>2.0.co;2

Lapworth, A. (2005). Collision of two sea-breeze fronts observed in Wales. *Weather*, *60*(11). https://doi.org/10.1256/wea.92.05

Meiburg, E., Radhakrishnan, S., & Nasr-Azadani, M. (2015). Modeling gravity and turbidity currents: Computational approaches and challenges. *Applied Mechanics Reviews*, *67*(4), 1–23. https://doi.org/10.1115/1.4031040

Okon, S. U., Zhong, Q., & He, Z. (2021). Experimental study on the vertical motion of colliding gravity currents. *Physics of Fluids*. https://doi.org/10.1063/5.0031738

Ooi, S. K., Constantinescu, G., & Weber, L. (2009). Numerical simulations of lock-exchange compositional gravity current. *Journal of Fluid Mechanics*, *635*, 361–388. https://doi.org/10.1017/S0022112009007599

van der Wiel, K., Gille, S. T., Llewellyn Smith, S. G., Linden, P. F., & Cenedese, C. (2017). Characteristics of colliding sea breeze gravity current fronts: a laboratory study. *Quarterly Journal of the Royal Meteorological Society*, *143*(704), 1434–1441. https://doi.org/10.1002/qj.3015

Zhong, Q., Hussain, F., & Fernando, H. J. S. (2018). Quantification of turbulent mixing in colliding gravity currents. *Journal of Fluid Mechanics*, *851*, 125–147. https://doi.org/10.1017/jfm.2018.488

SIMULATION OF FLOW STRUCTURE IN 90° GOMATI RIVER BEND USING CCHE2D MODEL

Animesh Das

Research Scholar, Civil Engineering Department, National Institute of Technology,

Agartala, Tripura, India

animesh.nit14@gmail.com

Sushant Kumar Biswal

Assistant Professor, Civil Engineering Department, National Institute of Technology,

Agartala, Tripura, India

sushantb69@gmail.com

ABSTRACT: In this study, flow structure in a river bend has been analyzed using Center for Computational Hydroscience and Engineering (CCHE) 2D model. For this purpose, a meander bend of Gomati River was considered as study area. The CCHE2D model was calibrated using different Manning's roughness coefficients and κ-ε turbulent models. Simulation results were compared with observed field data for two different flow rates. The results showed that for the low and high discharges, lower Manning's roughness coefficients ($0.015 \geq n \geq 0.025$) are more suitable than higher Manning's roughness coefficients ($0.030 \leq n \leq 0.040$). Moreover, deviations of hydraulic parameters like flow depth, velocity, shear stress and Froude number are evaluated and reflected. The results of the numerical model showed that variation in flow structure in the river bend is strongly influenced due to the presence of centrifugal force and helical cell. Due to the effect of helical flow, the latitude gradient of the water surface and depth averaged velocities within the cross sections of a meander bend is different. The R-squared (RSQ) and linear correlation coefficient (r) factors between velocity and shear stress show that there is linear and direct relationship between these two hydraulic parameters in the entire study reach. The results of the model show that the computational model can successfully simulate the flow field within the river bend.

KEY WORDS: Gomati River; numerical simulation; CCHE2D, flow pattern

1. INTRODUCTION

Meandering rivers are one of the most common river patterns in nature and acquired plan shapes by rivers, because of their dynamic nature. Its platform is changing all times and these alterations significantly affect the hydraulic condition and morphology. Meandering rivers are single channels with a sinuous planform comprise a series of loops, depicted as regular in form and size, but in reality, often having some irregularity, asymmetry and complexity (Hooke, 2013). In meander river or river bend, flows are highly three-dimensional and very complex because of the combined effects of secondary flow, free surface variation, section geometry and flow separation along the inner bend wall that are not observed along straight paths. Distribution of flow velocity in longitudinal and lateral direction is one of the important aspects in open channel flows and it relates to number of flow features like water profile, shear stress distribution, secondary flow, channel conveyance and other flow entities. One of the significant features, which characterize flow in meander bends are secondary currents. Chang (1984) illustrated that flow resistance or energy expenditure produced by transverse flow can be very significant even for mild curves without flow separation. Damaskinidou-

Georgiadou et al. (1986) carried out an experimental and numerical investigation in a curved converging channel to compute the parameters required for the design of a curved channel sediment excluder. The author employed the Finite Difference Method (FDM) and the compared the calculated and observed values of mean longitudinal velocity approximated to a free vortex along the channel. Some researchers have carried out extensive studies on flow characteristics in channels with different bend angels by using the numerical models. In recent decades, application of Computational Fluid Dynamics (CFD) models is assumed to be an effective tool in the study of outdoor channels and river processes and have significantly increased as a result of advances in computers and numerical calculation methods. In this regards, mathematical models have been widely used in solving complex hydrodynamic topics in a wide range of scales. Ye and Mccorquodale (1998) applied a mathematical model of three-dimensional (3D) free surface flows to simulate the 270°curved channel flows and mass transport. The governing equations are solved in a collocated grid system by a fractional three-step implicit algorithm. Shino (1999) developed turbulence models and studied the behaviour of secondary flows and centrifugal forces for straight and meandering channels. Lien et al. (1999) studied the flow pattern at a 180° bend with a rigid bed using a two-dimensional (2D) numerical model, and reported the secondary flow has a significant effect on the flow structures and on the maximum velocity path along the channel. Mohanty et al. (2012) studied wide meandering compound channel to analyse the depth-averaged velocity using CCHE2D and the results were compared with the observed values for validation purpose. Elyasi and Kamandbedast (2014) examined the numerical modelling of flow in a river with 90° bend using the CCHE2D model and focused on the velocity distributions, the streamlines at different water levels, and the distribution of shear stresses. The results revealed that the flow patterns in a channel bend is heavily influenced by the secondary flow and centrifugal force. McKeogh and Kiely (1989) studied velocity distribution in meandering compound channels and stated that the maximum velocity in main channel, whether above or below the bank level, is closer towards the inner bend. Similar observation was made by Sellin and Willets (1996) showing that the velocity weakens and moves across to the outside of the bend while moving further downstream. The results of flow pattern simulation at a meandering reach with CCHE2D model in the Khoshke-rud River of Iran showed that using CFD for water flow modelling is one step closer to having a universal predictor for processes in meandering rivers (Fathi et al. 2012). Zhou et al. (2009) using the 2D depth-averaged model, simulated the flow pattern in 180° sharp bend and 270° mild bend, with and without consideration of the secondary flow, and claimed that, given the effect of the secondary flow, the simulation results in the first state have a better agreement with the experimental results. Sanjou and Nezu (2009) focused on the 3D structure of horizontal coherent motion and its advection property in the channel transition zone from the straight to meandering compound open-channel flows by using a multi-layer scanning PIV, and compared with continuous meandering channel flows. A relation between the horizontal vortices and secondary currents was obtained, resulting in a phenomenological flow model. Sui-Liang et al. (2009) applied different turbulence closure schemes i.e., the mixing-length model and the k-ε model with different pressure solution techniques to study the helical secondary flows in an experiment curved channel.

Review of the research shows that there is a lack of comprehensive reviews in 2D numerical modelling of meandering flow in the literature. Therefore, aim of this study is to analysis the earlier studies that employed numerical approaches to assess the flow characteristics of the river meandering. Current study performs flow pattern analysis of Gomati River using the latest version CCHE2D modelling software. Using the topography and measured flow data as the initial condition, Manning's roughness coefficient for Gomati River flow simulation is calibrated using CCHE2D model. In this paper, numerical model is performed to examine the flow features in a meandering channel with 90° crossover angle for channel beds. Following this, the study of flow pattern in meander reaches, determination of different hydraulic parameters such as velocity, shear stress and Froude number in the studied reach of Gomati River are the important goals of this research. Output results from the model showed that qualitative models correctly simulating the flow pattern in the study area.

2. STUDY AREA AND DATA

This study is a part of a major field project on the river bend undertaken at the Gomati River, 56 km south west of Agartala (Figure 1). The Gomati catchment about of 2492 km² (1921 km² belongs to hilly region and only 571 km² about 23% lies on the plain) is situated in the lower middle part of Tripura. It locates between latitude 23°47'N and 23°47'N and longitude 91°14'E and 91°58'E. The Gomati River is the major river in Tripura and is surrounded by Bangladesh on its east and west. It has small number of tributaries which are distributed on both sides. The total length of the river is 167.4 km and elevation is varying from 18.288 m to112.166 m above the mean sea level.
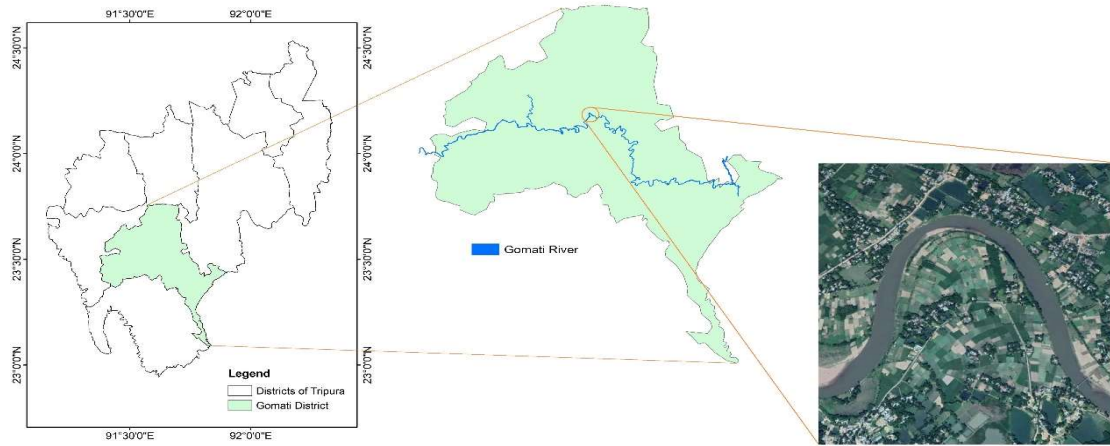
Figure 1. Location map of the considered Gomati River section

3. NUMERICAL METHOD

In the present study, the results of the CCHE2D model are based on finite volume discretization of Reynolds Averaged Navier-Stokes (RANS) equations with the second order upwind scheme. CCHE2D is an integrated package for simulation and analysis of free surface flows, sediment transport and morphological processes. The basic input data requirements to run CCHE2D model include DEM, river location, initial water surface elevation, discharge and Manning's roughness coefficient. The output of CCHE2D model consists of grids representing flow depth and flow velocity at any time increment given by the user. The depth integrated 2D continuity and momentum were solved using the CCHE2D model. The governing equations are as follows:

Continuity Equation

$$\frac{\partial Z}{\partial t} + \frac{\partial (hu)}{\partial x} + \frac{\partial (hv)}{\partial y} = 0 \tag{1}$$

Momentum Equations

$$\frac{\partial u}{\partial t} + u\frac{\partial u}{\partial x} + v\frac{\partial u}{\partial y} = -gh\frac{\partial Z}{\partial x} + \frac{1}{h}\left[\frac{\partial (h\tau_{xx})}{\partial x} + \frac{\partial (h\tau_{xy})}{\partial y}\right] - \frac{\tau_{bx}}{\rho h} + f_{Cor}v \tag{2}$$

$$\frac{\partial v}{\partial t} + u\frac{\partial v}{\partial x} + v\frac{\partial v}{\partial y} = -gh\frac{\partial Z}{\partial y} + \frac{1}{h}\left[\frac{\partial (h\tau_{yx})}{\partial x} + \frac{\partial (h\tau_{yy})}{\partial y}\right] - \frac{\tau_{by}}{\rho h} + f_{Cor}u \tag{3}$$

where u and v are depth integrated velocity components in x and y directions respectively, g is gravitational acceleration, z is the water surface elevation, ρ is water density, h is the local water

depth, f_{Cor} is the Coriolis parameter, τ_{xx}, $\tau_{xy,}$ τ_{yx} and τ_{yy} are the depth integrated Reynolds stresses and τ_{bx}, τ_{by} are shear stresses on the bed surface. The Coriolis parameter f_{Cor} has no significant effect for small area, so it was neglected in this study (Dutta et al. 2010).

4. METHODOLOGY

The development of CCHE2D mesh generator is explained, followed by the modelling in CCHE2D graphical user interface (GUI) Fig.2. Mesh Generator helps in the creation of a complex structured mesh system for CCHE2D model system. The modelling procedure involved the use of ArcGIS to make a file with topographic data that could be imported in CCHE-2D family, which constitutes mesh generator and CCHE-2D GUI. Initial flow condition, for example the initial water surface level for the inlet and outlet of the river stretch was set to some arbitrary values with minimum dry grid cells. An interpolation of the water surface level was made by using interpolation tool in set flow initial conditions toolbar. The roughness characteristics were also input with assumed values for overall topography in CCHE2D GUI . In the present study, a simulation time of one day was used with time steps 10 seconds, and flow discharge and water surface level were set with inlet boundary condition and outlet boundary condition respectively. A long term mean monthly flow of 102 cumecs obtained from the water data was used for the inlet boundary condition, while for the outlet boundary condition; the water surface level was used corresponding to the 102 cumecs discharge obtained from the gaging data.

```
          Digital Elevation Model
                   │
                   ▼
              ARC - GIS
                   │
                   ▼
          DEM in ASCII Format
                   │
                   ▼
          CCHE2D Mesh
            Generator
                   │
                   ▼
             CCHE2D GUI
                   │
                   ▼
           Model Simulation
                   │
   ┌────────┬────────┬────────┼────────┬────────┬────────┐
   ▼        ▼        ▼        ▼        ▼        ▼
 Water    Water    Water    Total Specific  Total Shear  Froude
Surface   Depth   Velocity    Discharge      Stress     Number
```
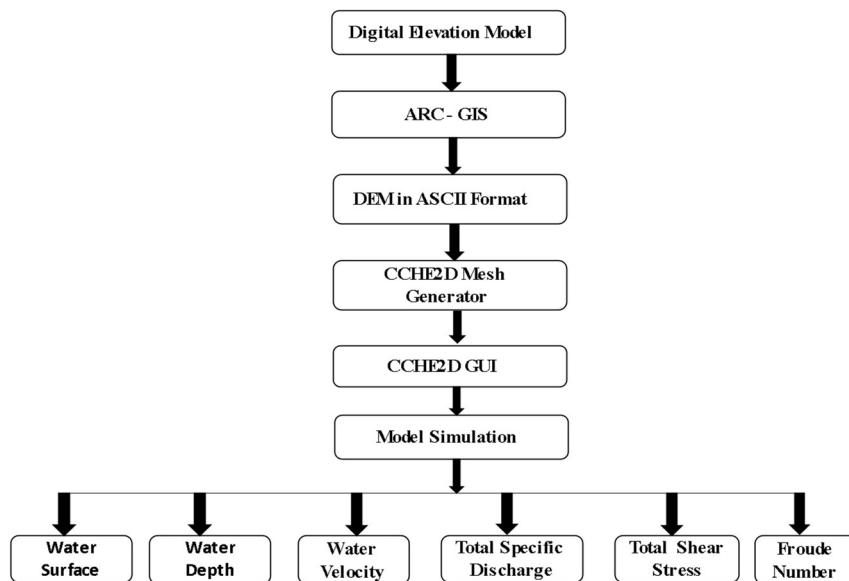
Figure 2. Flow chart shows the operations involved in the flow simulation modelling with the digital elevation model and the combination of Arc GIS and CCHE2D models

5. RESULTS AND DISCUSSION

The bed elevation was randomly interpolated CCHE2D mesh generator and the export results from the mesh editor is shown in Figure 3, that represents the bed elevation with minimum and maximum values 32.79 m and 67.24 m respectively. In this study, initial water level was taken to be more than 32.79m to prevent negative depths.
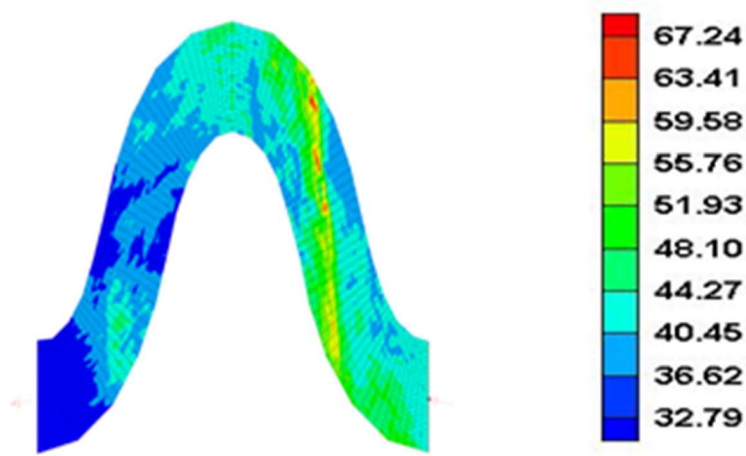
Figure 3. Initial ed elevation (m) generated by CCHE2D

The results of flow simulation from CCHE2D GUI are presented in Fig. 4, which comprises of water surface elevation in meters after the simulation period of more than a day with maximum long term monthly average. The cross-profiles of the water surface obtained from the CCHE2D numerical model in different cross sections of the 90^0 river bend from study reach are shown in Fig. 5. In the bend, the gradient of the water surface due to the presence of secondary currents increases to the outer bank of the bend (the right bank of the river). The results show the water surface level increases in upstream for discharge of $102 \text{ m}^3/\text{sec}$. The water depth at the river boundary is nearly zero while the maximum depth for the taken flow is 6.38 m. The large depth gives the idea about the size of the river conveying large volume of discharge. The depth results can be modified by taking more reliable inputs such as bathymetric data which gives more detailed information about the submerged surfaces. The water depth, velocity, specific discharge, total shear stress and Froude numbers are attained the maximum value near the centreline of the river. Based on the model result as water depth for the considered reach it can be depicted that the minimum water depth is 0.001 meter and there is no flow velocity in the corresponding regions of low depth. This depth signifies the marshy land in the boundaries of Gomati as the considered long term monthly average is most likely occurring discharge. The numerical results show the water surface finds or attains a transversal slope due to centrifugal force once the flow enters the bend. The water depth profiles derived from CCHE2D model and observed data are revealed in Fig. 6 based on six roughness coefficients of 0.015, 0.020, 0.025, 0.030, 0.035 and 0.040. It is seen that the water depth profiles of the numerical model and observational data both follow the similar trend for different roughness coefficients. To select the best roughness coefficient, the water depth profile was evaluated at the Gomati River section. For this purpose, statistical analysis was carried out between the observed and simulated data using two factors of "coefficient of determination (R^2)" and "linear correlation coefficient (r)," as defined in Eqs. (4) and (5), for all tests according to Fig. 7.

$$\text{RSQ } (R^2) = \sum_i^j (B\text{-}\overline{A})^2 / \sum_i^j (A\text{-}\overline{A})^2 \qquad (4)$$

$$\text{Correlation } (r) = N \sum AB \text{ - } (\sum A \sum B)/[(N \sum A^2)\text{-}(\sum A)^2] \, [N \sum B^2 \text{-}(\sum B)^2]^{0.5} \qquad (5)$$

15

where B is the simulated variable, A is the observed variable, $\bar{A}$ is the sample mean of A value, and N the total number of variables.
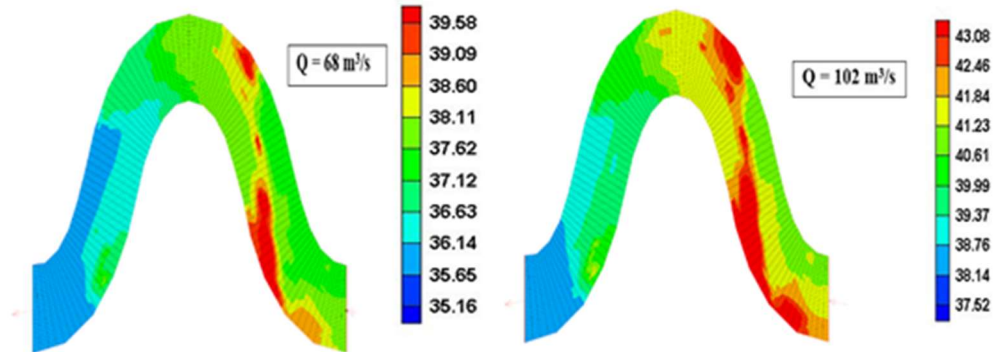
Figure 4. Water surface profile at 90⁰ meander for two different discharges
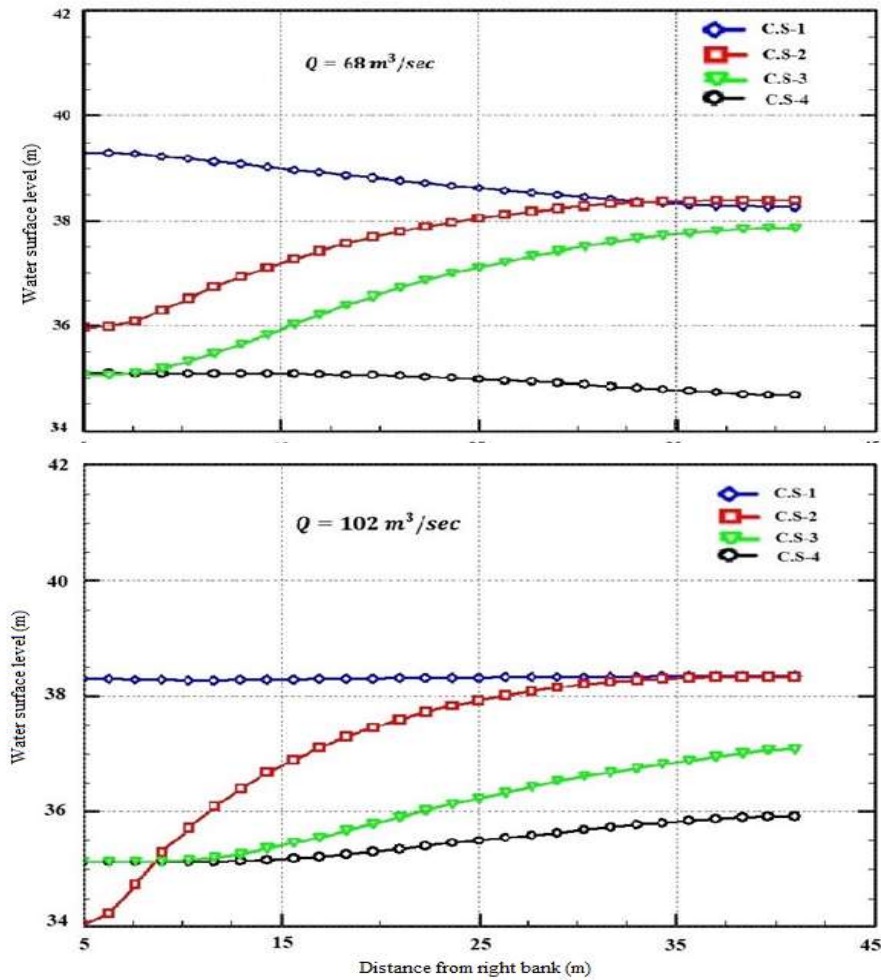
Figure 5. Cross-profiles of water surface at 90⁰ meander for two different discharges
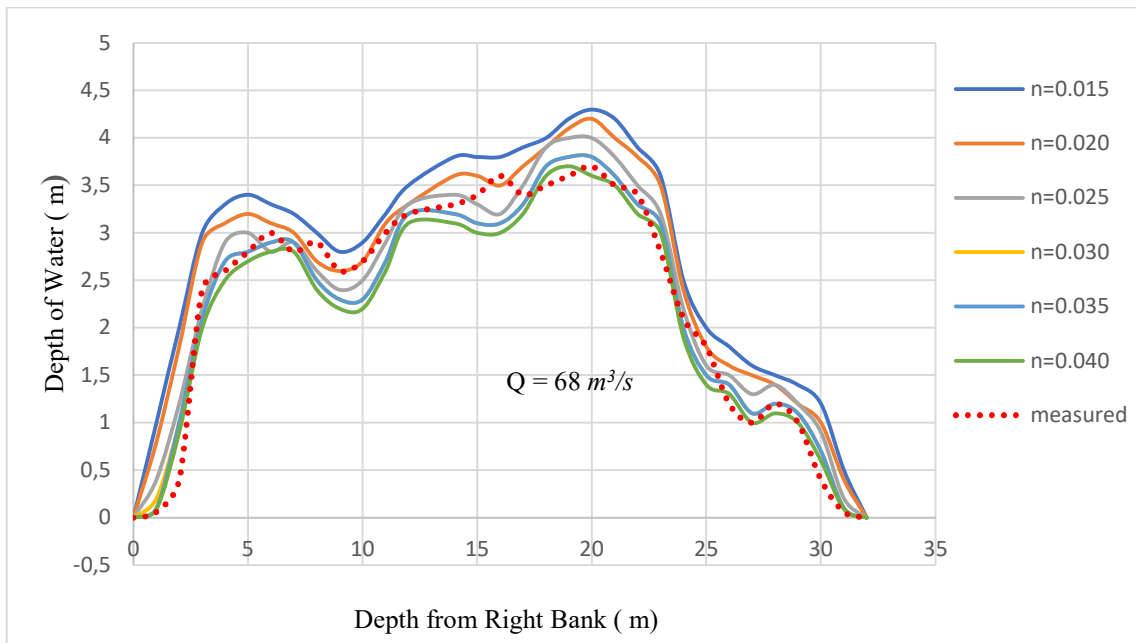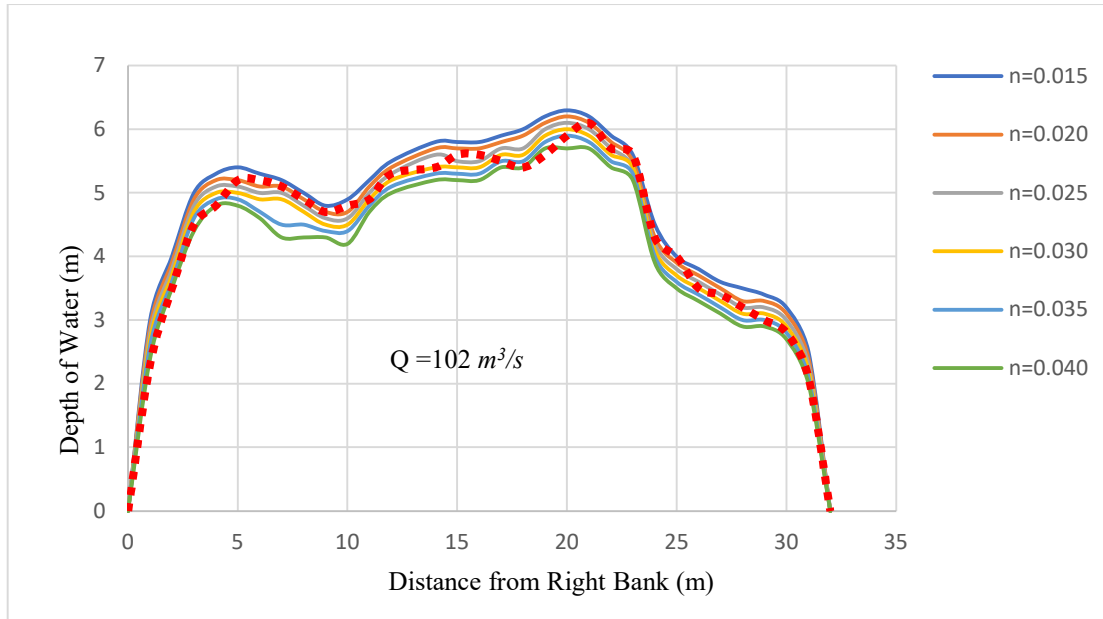
Figure 6. Water depth elevation at 90° meander for two different discharges

Fig. 7 shows that Manning's roughness coefficients in the range of $(0.015 \geq n \geq 0.025)$ for both low and high discharges (68 m³/s and 102m³/s). It can be said that for low discharge, the effect of bed roughness on the flow is greater due to its lower depth and higher roughness coefficients $(0.030 \geq n \geq 0.040)$ for modelling have better and closer results to observational data. Therefore, for low and high discharges, lower roughness coefficients are more appropriate.
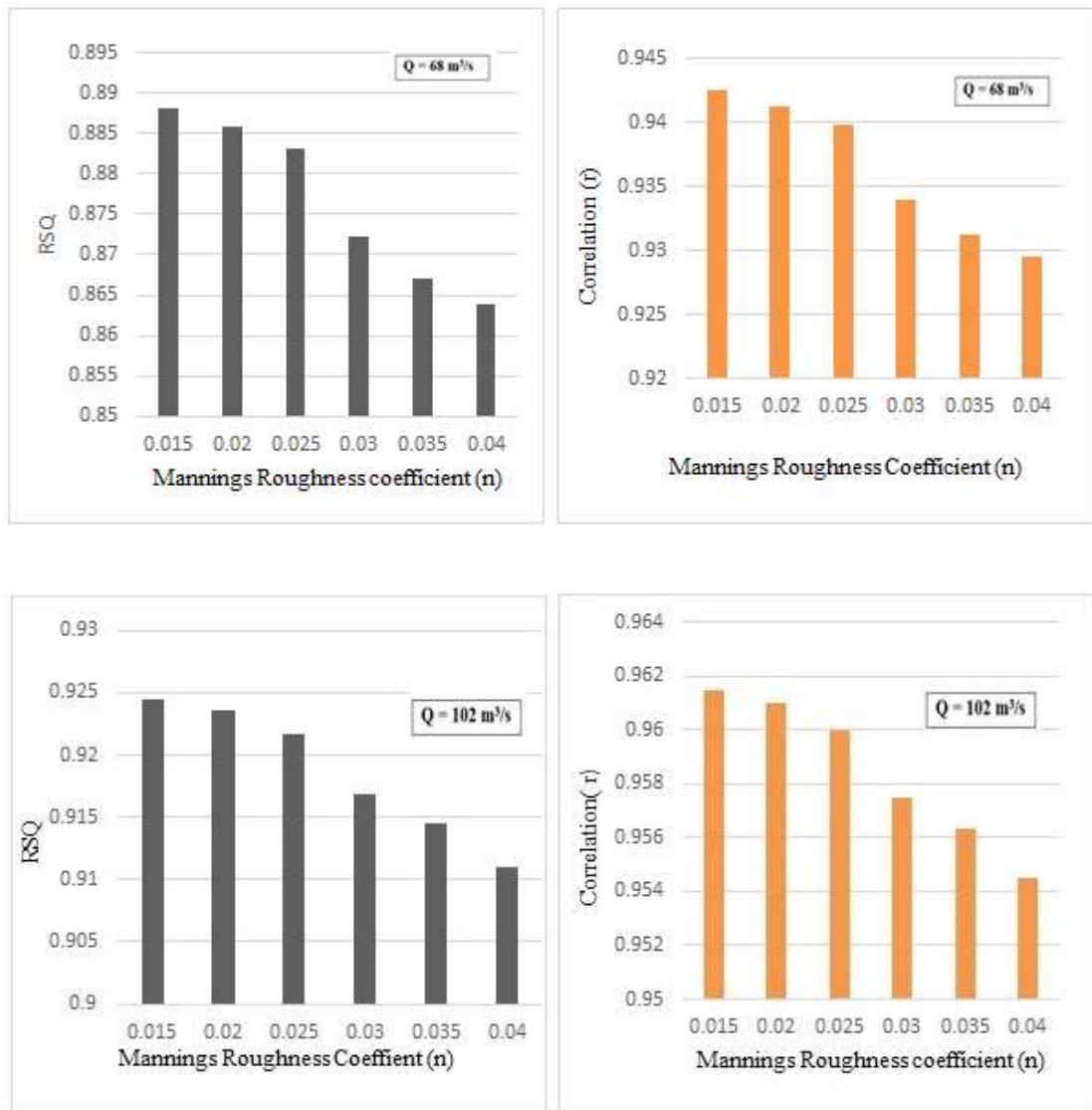
Figure 7. The performance of the CCHE2D model for different Manning's roughness coefficients for two different discharges

For a given discharge the velocity profile is taken throughout the meander path across the channel in Figure 8. The velocity remains higher towards the left of the channel section which is the inner wall in the initial sections of the meander path. At the cross-over section the higher velocity moves towards the centre of the channel, as observation usually seen in straight channels. This observation depicts that a meandering channel behaves as a straight channel at around the cross-over section. At sections subsequent to the cross-over, the higher velocity moves towards the right of the channel section, this is now the outer wall for the channel section. Moreover, the study of the cross-profiles of the velocity distribution in different cross sections of the 90^0 river bend are shown in Fig. 9 shows that, the maximum velocities are located in the middle of the cross sections of the profiles.
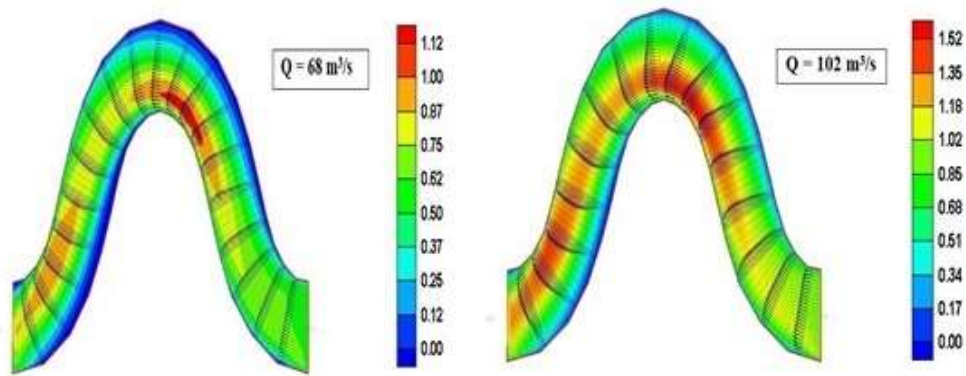
Figure 8. Velocity vector at 90°meander for two different discharges
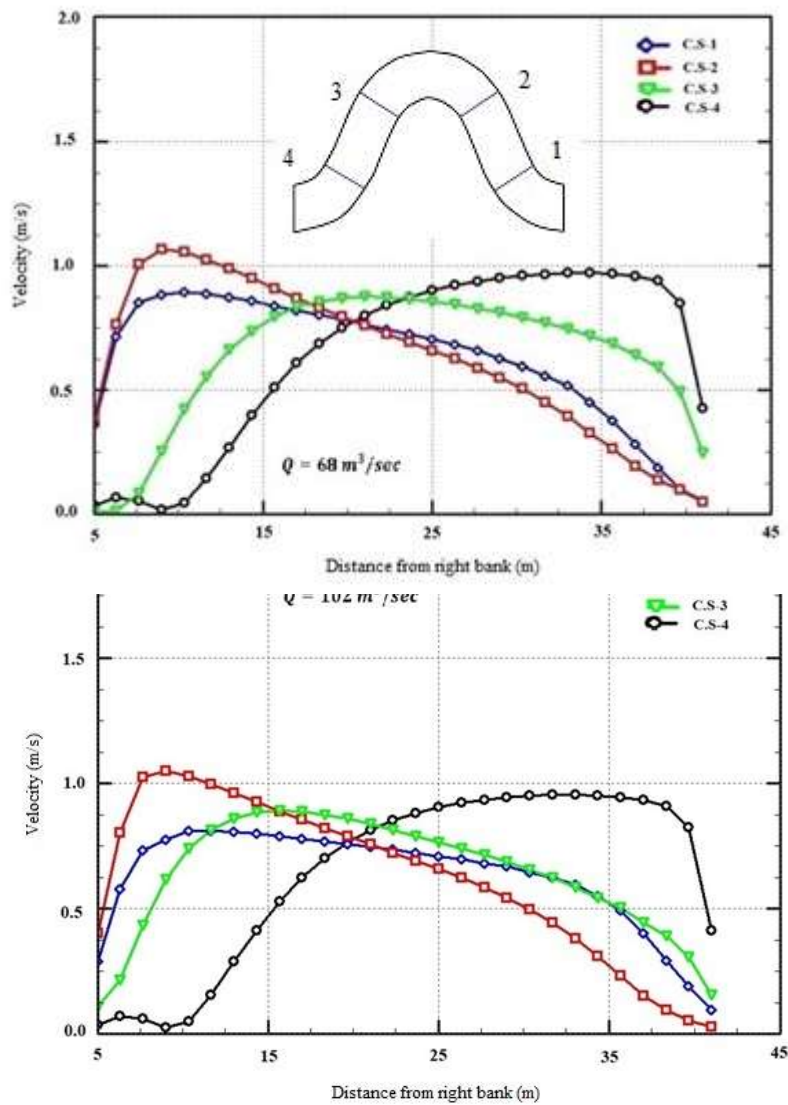
Figure 9. Cross-profiles of velocity at 90°meander for two different discharges

Flow attributes of an open channel flow are directly dependent on the boundary shear force distribution along the channel bed. The shear stress generally increases with discharge throughout the bend and reaches maximum values during the highest discharge (Figure 10).
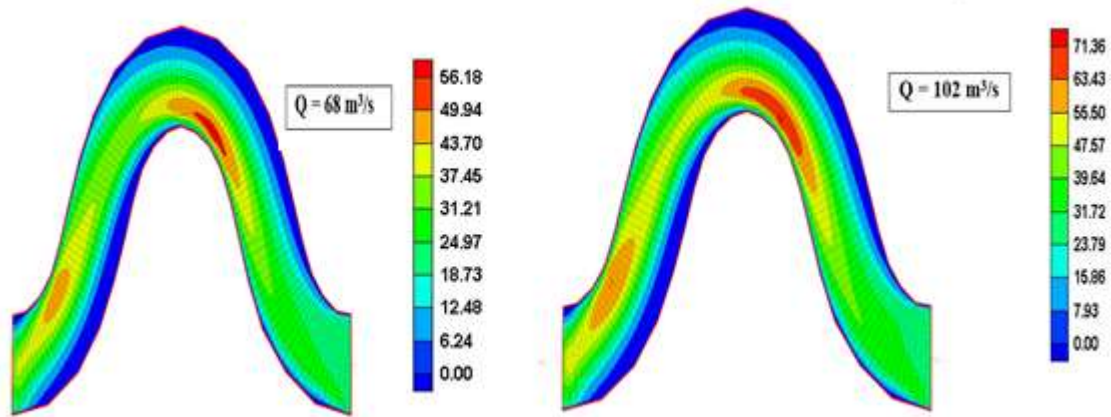
Figure 10. Shear stress at 90° meander for two different discharges

In the present work, the effects of parameters like specific discharge and Froude number on the flow dynamics are also studied, and the Fig. 11 shows that the total specific discharge (m^2/s) is the maximum near the centreline of the river. Fig. 12 reveals the mapping of Froude number which stated that the flow in the upstream reach is subcritical $(Fr < 1)$, however it attains supercritical $(Fr > 1)$ due to the blockage in the contraction area at the upstream. The present study confirmed that the flow in the channel reach is mostly subcritical.
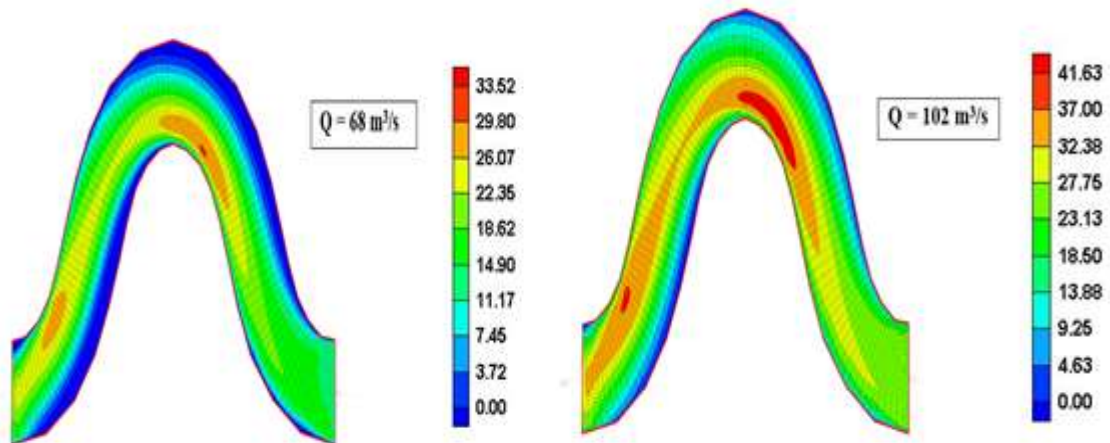
Figure 11. Total specific discharge at 90° meander for two different discharges
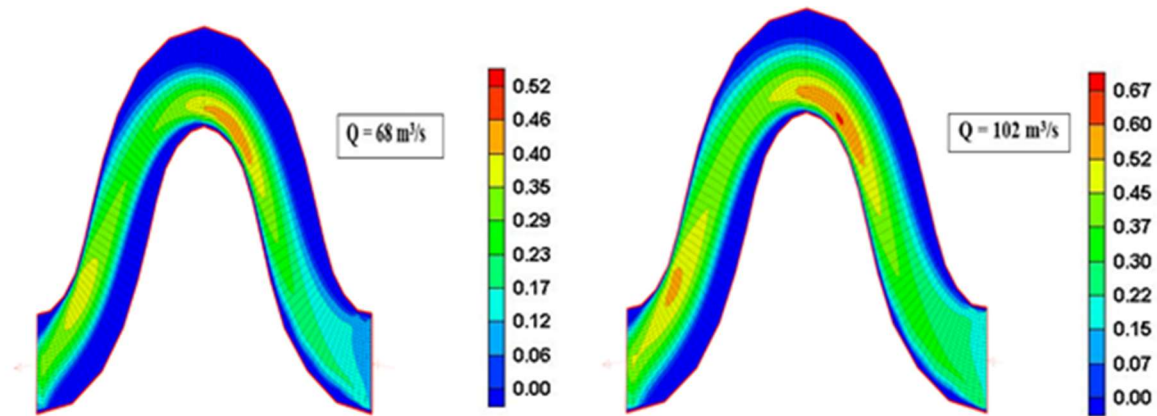
Figure 12. Froude number at 90° meander for two different discharges

6. CONCLUSION

In this paper, numerical modelling of the flow pattern at a Gomati River bend has been carried out by using CCHE2D. The numerical results are simulated with field data. The key findings of the research such as the variations of the water surface profile, velocity profile, shear stress, specific discharge and Froude number were studied numerically and are discussed. The results show that, the Manning's roughness coefficient ranges of 0.030–0.040 will have better results, and for medium and high discharges, the roughness coefficient ranges of 0.015–0.025 provide the more accurate result. The analysis suggests that the water surface and the maximum velocities in the river arch develop toward the outer bank. The simulation results indicate that the average velocity for the discharges of 68 m^3/s and 102 m^3/s in the study reach is 0.56 and 0.77 m/s, respectively. Moreover, the average shear stress for the two discharges mentioned above is 27.99 and 35.62 N/m², respectively. The results of the study show that the CCHE2D model has the ability to simulate the complex rivers with varying river morphology. Therefore, in the engineering and operational projects of the Gomati River, the results of this numerical model can be trusted and used.

REFERENCES

Chang, H.H. (1984). Variation of flow resistance through curved channels. J. Hydraul. Eng., 110(12): 1772-1782.

Damaskinidou-Georgiadou, A., and Smith, K.V.H. (1986). Flow in curved converging channel. J. Hydraul. Eng. 112:476-495.

Dutta, S., Medhi, H., Karmaker, T., Singh, Y., Prabu, I., and Dutta, U. (2010). Probabilistic flood hazard mapping for embankment breaching. ISH Journal of Hydraulic Engineering, 16(1), 15–25. https://doi.org/10.1080/09715010.2010.10515012.

Elyasi, M., & Kamandbedast, A.A. (2014).The efect of angle of intakes on diversion sediments in river bend with CCHE2D model. Adv Environ Biol J 8(22), 180–186.

Fathi, M., Honarbakhsh, A., Rostami, M., Nasri, M., andMoradi, Y. (2012). Sensitive analysis of calculated mesh for CCHE2D numerical model. World Appl Sci J 18:1037–1051.

Hooke, J. (2003). River meander behaviour and instability: a framework for analysis.Trans Inst Br Geogr, 28(2), 238–253.

Lien, H. C., Yang, J. C., Yeh, K. C., and Hsieh, T. Y. (1999). Bend-flow simulation using 2D depth-averaged model. Journal of Hydraulic Engineering, 125(10), 1097-1108.

McKeogh, E. J., & Kiely, G. K. (1989). Experimental study of the mechanisms of flood flow in meandering channels," in Proceedings of the 23rd IAHR Congress, pp. 491–498.

Mohanty, P.K., Dash, S.S., and Khatua, K.K. (2012). Flow investigations in a wide meandering compound channel. Int J Hydraul Eng 1(6), 83– 94.

Rosgen, D.L. (1994). A classification of natural rivers. Catena 22 (1994),169-199.

Sanjou, M., and Nezu, I. (2009). Turbulence structure and coherent motion in meandering compound open-channel flows. Journal of Hydraulic Research Vol. 47, No. 5 (2009), pp. 598–610.

Sellin, R. H. J. and Willets, B. B. (1996). Three-dimensional structures, memory and energy dissipation in meandering compound channel flow. Wiley, Chichester, UK. Floodplain Processes, pp. 255–298.

Shiono, K., Muto, Y., Knight, D. W., and Hyde, A. F. L. (1999). Energy losses due to secondary flow and turbulence in meandering channels with overbank flows. Journal of Hydraulic Research, 37(5), 641-664.

Sui-liang, H. JIA Ya-fei, CHAN Hsun-Chuan, Wang Sam S. Y. (2009).Tthree-dimensional numerical modeling of secondary flows in a wide curved channel. J. Hydrodynamics., 21(6):758-766.

Ye, J., and Mccorquodale, J. A. (1998). Simulation of curved open channel flows by 3d hydrodynamic model.J. Hydraul. Eng., 124(7): 687-698.

Zhou, G., Wang, H., Shao, X., and Jia, D. (2009). 2-D numerical simulation of flow in a curved open channel. Advanced in Water Resources and Hydraulic Engineering, pp. 871-876.

14TH INTERNATIONAL CONFERENCE
ON HYDROSCIENCE & ENGINEERING

MAY 26-27, 2022
IZMİR-TURKEY

ICHE2022
IZMIR, TURKEY

ASSESSMENT OF HEC-RAS TWO-DIMENSIONAL HYDRAULIC MODEL FOR AN URBANIZED REGION

Enver Taşçı

Department of Civil Engineering, Eskisehir Technical University

Eskisehir, Tepebasi, Turkey

envertasci@eskisehir.edu.tr

Gökçen Uysal

Department of Civil Engineering, Eskisehir Technical University

Eskisehir, Tepebasi, Turkey

gokcenuysal@eskisehir.edu.tr

Aynur Şensoy

Department of Civil Engineering, Eskisehir Technical University

Eskisehir, Tepebasi, Turkey

asensoy@eskisehir.edu.tr

ABSTRACT: Floods are fatal disasters that cause huge amounts of material damage and human loss, especially in developing countries. Due to reasons such as the increase in the world population, urbanization, and global climate change, the effects of floods are becoming more devastating. The preparedness of the flood risk is accomplished by an assessment of river analysis using hydraulic models. The propagation of flood wave through urbanized regions require high quality terrain data, two-dimensional modeling of flow and an improved speed computational algorithm. This ongoing study aims to test the newly released River Analysis System (HEC-RAS) 6 model that has been developed by the U.S. Army Corps of Engineers (USACE) for 2-dimensional flood analysis with some new features and to assess output flood maps (flood inundation, velocity, depth etc.) in an urbanized region using ESA WorldCover (10 m) and CORINE (100 m) land cover data. The selected study area (Imranli, Sivas) necessitates flood risk assessment since it is located in an urbanized region of Kizilirmak River branch, Turkey. Further spatial assessments are done by employing flood hazard analysis for an expected flood event having a 500-year return period using computed flood maps. The resulting hazard map reveals the potential for different areas and settlements in the region to be affected by the flood disaster.

1. INTRODUCTION

Floods can be defined as the overflow of a stream for various reasons, such as heavy rain or sudden snowmelt. They cause huge amounts of material damage and human loss. Calculation of the expected flow rates of floods within the scope of flood hydrology is one of the subjects studied to a certain extent, but river rehabilitation and flood control structures can be partially implemented in certain regions to prevent floods. Flood models are best method to analyze flood inundation, water depth, water velocity, arrival time etc., but an appropriate set up is subjected various data and model requirements. Among them, Hydrologic Engineering Center-River Analysis System (HEC-RAS) model that has been developed by the U.S. Army Corps of Engineers (USACE) is a free widespread software and highly used for flood studies. Shrestha et al. (2020) compared MIKE 21 and HEC-RAS to study the flood extent in the urbanized area. Ongdas et al. (2020) studied HEC-RAS (2-dimensional, 2D) to simulate different scenarios for different mesh sizes and flow rates. Costabile et al. (2020) performed a 2-D flood analysis for different computational methods (diffusion wave and

fully dynamic) by using HEC-RAS version 5 in their study. Dursun and Gül (2018) studied dam break analysis to optain flood maps by using HEC-RAS for Sürgü Dam.

Considering its geographical location, Turkey is among the countries that will be most affected by climate change and is faced with increasing intense rains, floods and drought disasters. In this study, HEC-RAS version 6.1 which is the newest version is used to perform 2D flood analysis model for Imranli town located upstream part of Kızılırmak River with ESA WorldCover (10 m) and CORINE (100 m) land cover maps. Flood hazard maps are expected to be produced for an expected flood event hydrograph having a 500-year return period.

2. MATERIALS AND METHOD

2.1. Study Area and Data Preparation

Imranli town is located within the boundaries of Sivas city in Turkey. Figure 1 presents an aerial view of Imranli town together with Kizilirmak River that passes through the center of the town. The area of the town center is nearly 2 km^2 and Imranli town has 2984 population. Population and flat land necessitate to perform a flood analysis in the region. There are three bridges constructed on the river. Discharge data having 500 years return period (Q_{500}) is determined using flood hydrograph analysis method of DSI (State Hydraulic Works) and the consideration of flood routing for the dam located upstream of the town.

RasMapper embedded in HEC-RAS program provides additional geospatial capabilities such as creating and refining model geometry and analyzing the computed results. High-resolution LIDAR (0.5 m) surface model is used as terrain data and a 2-dimensional mesh area is created with bridges. GeoMatica program is used to modify terrain data in order to remove trees and bridges detected in the LIDAR data. HEC-RAS version 6 provides allows users to lay out a bridge inside of a 2D flow area. Therefore, the flow is still computed as two-dimensional flow through and over top of the bridge.

Another important data is land cover for defining Manning's n values. In this study, ESA WorldCover (10 m) and CORINE (100 m) land cover data are alternatively used and ESA World map is shown in Figure 2.

Figure 1. Google Earth view of Imranli town and the creek
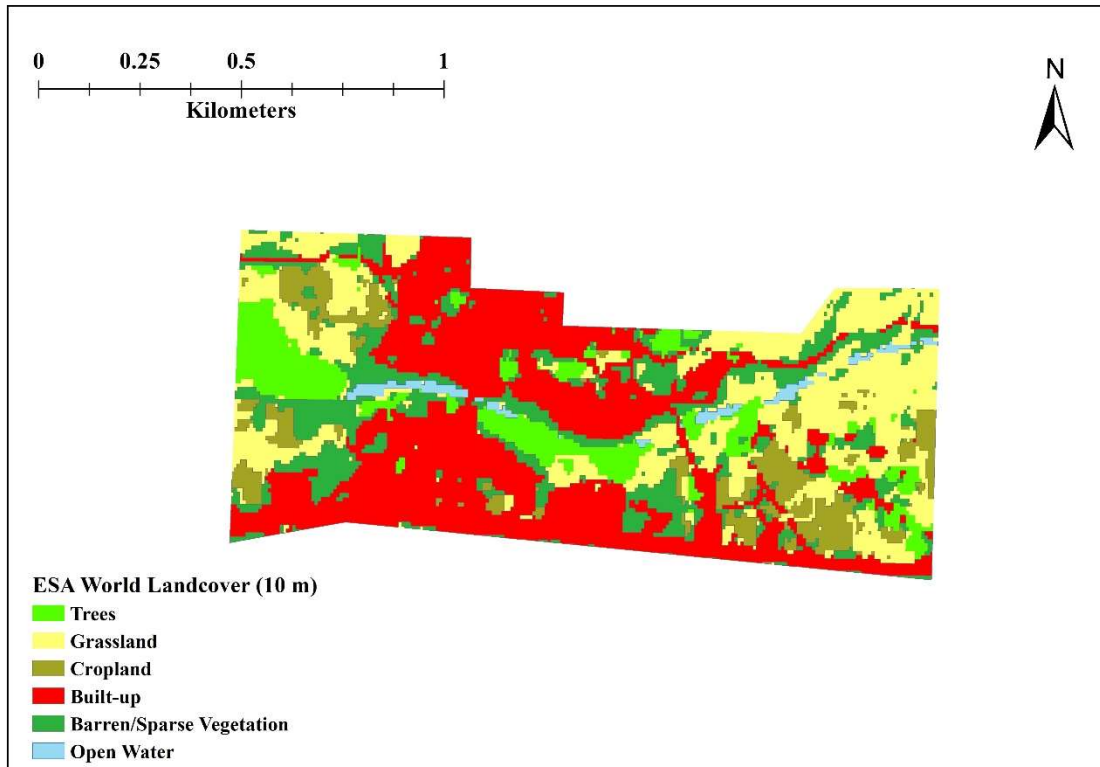
Figure 2. ESA WorldCover (10 m) Land Cover map for Imranli town

2.2. Hydraulic Modeling

The hydraulic modeling is accomplished by HEC-RAS 6.1 that is designed to perform one-dimensional (1D) and two-dimensional (2D) hydraulic calculations for a full network of natural and constructed channels, overbank/floodplain areas, levee protected areas, etc. (USACE HEC, 2021). The 2D model solves the Diffusion-Wave Equation (DWE) and Shallow-Water Equations (SWE). In this study, SWE method is selected for better representation of the hydrodynamic effect. The 2D unsteady flow equations solver uses an Implicit Finite Volume algorithm. Also, Courant number is considered to select an appropriate computational time step. The new version also provides an improved computational speed algorithm.

3. PRELIMINARY RESULTS

The preliminary result is given in Figure 3 for the flood inundation area computed using ESA WorldCover land use map. As a result, the flood event having a 500-years return period affect the urban area within 0 – 6 m varying water depths. Flood inundation area equals to 0.20 km^2 and 0.19 km^2 for CORINE and ESA WorldCover maps, respectively. Although the flood inundation is similar in terms of area, the downstream of the region is partly affected according to ESA WorldCover compared to CORINE land use map.
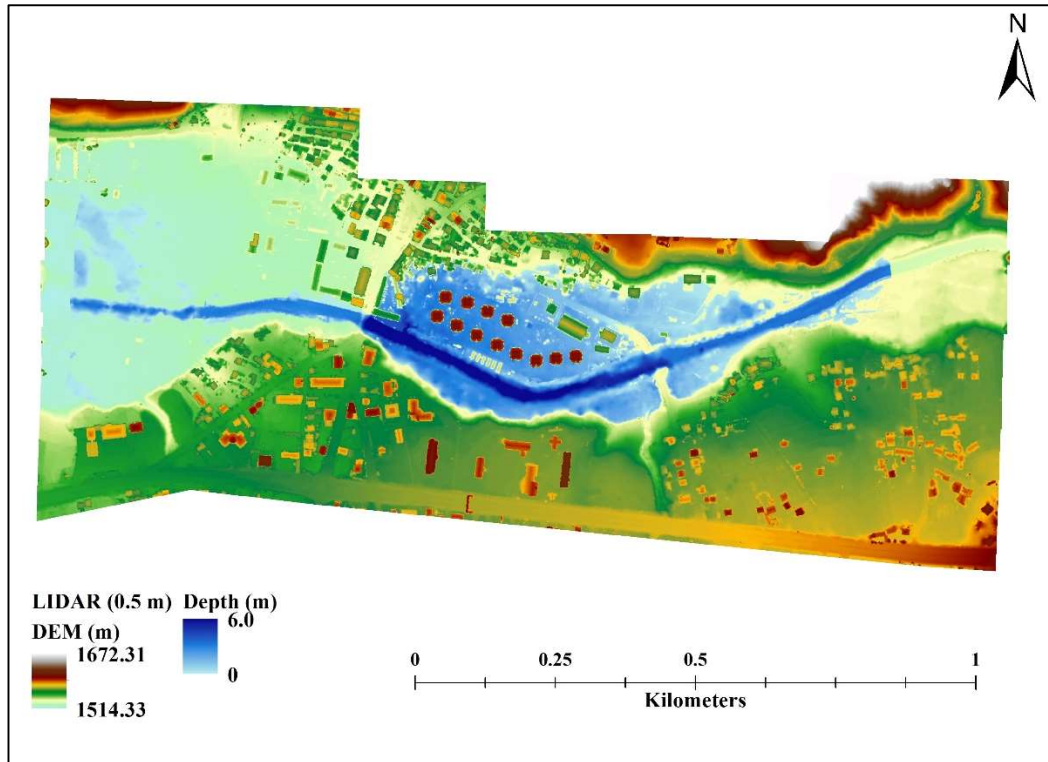
Figure 3. Preliminary model results (max. flood inundation) of 2-D flood propagation model of the Q_{500} flood event.

4. CONCLUSIONS

In this study, 2-dimensional (2D) flood analysis is performed for an urbanized town at the upstream part of Kızılırmak river, using newly released HEC-RAS 6.1 model. LIDAR based geometric data set having 0.5 m spatial resolution is used together with CORINE and ESA WorldCover land use satellite data. 2-D mesh area is created considering three bridges. According to preliminary results, flood propagation through the town is properly detected with high resolution data sets and suitable hydraulic model. Ongoing efforts will reveal the flood hazard maps using produced results.

ACKNOWLEDGEMENT

REFERENCES

Costabile, P., Costanzo, C., Ferraro, D., Macchione, F., & Petaccia, G. (2020). Performances of the New HEC-RAS Version 5 for 2-D Hydrodynamic-Based Rainfall-Runoff Simulations at Basin Scale: Comparison with a State-of-the Art Model. *Water*, 1-19.

Dursun, Ö. F., & Gül, E. (2018). Two Dimensional Dam Break Modelling; A Case Study of Sürgü Dam. *Science and Engineering Journal of Fırat University*, 97-104.

Ongdas, N., Akiyanova, F., Karakulov, Y., Muratbayeva, A., & Zinabdin, N. (2020). Application of HEC-RAS (2D) for Flood Hazard Maps Generation for Yesil (Ishim) River in Kazakhstan. *Water*, 1-20.

Shrestha, A., Bhattacharjee, L., Baral, S., Thakur, B., Joshi, N., Kalra, A., & Gupta, R. (2020). Understanding Suitability of MIKE 21 and HEC-RAS for 2D Floodplain Modeling. *World Environmental and Water Resources Congress 2020*, 237-253.

USACE, HEC. (2021). HEC-RAS River Analysis System 2D Modelling User's Manual. Version 6.

NUMERICAL STUDIES ON PREDICTING VELOCITY FIELDS OF UPSTREAM CHANNEL THAT COMBINED WITH HEAD POND USED IN MECHANICAL WASTEWATER TREATMENT PLANT

First Author: Nagihan Şahin

Gümüşhane University, Civil Engineering Department

Gümüşhane, Turkey

nagihansahin@gumushane.edu.tr

Second Author: Rahim Şibil

Gümüşhane University, Civil Engineering Department

Gümüşhane, Turkey

rahimsibil@gumushane.edu.tr

ABSTRACT: In this study, head pond, made to stabilize water level in the Wastewater Treatment Plant (WWTP) and upstream channel of screens that is maintain velocities in design criteria at mechanical treatment plant have been analyzed in terms of hydraulic and hydrodynamics by using Computational Fluid Dynamics (CFD). CFD simulations are carried out with the CFD software Ansys Fluent with the three-dimensional (3D), steady, incompressible flow based on the Reynolds-Average Navier-Stokes equations for flow field calculations in the combined intake-head pond-upstream channel system. Also, the standard K-Epsilon (ske) model was chosen as a turbulence model. The numerical studies results showed that there was no homogeneous flow field distribution in upstream channel. It can also be noted that the upstream channel does not meet the desired velocity values for screening.

1. INTRODUCTION

Water resources are rapidly exhausted in worldwide, because of population growth, global warming and increasing drought. One of the most important ways to protect water resources corresponding to increasing demand is reuse wastewater. Generally, wastewater treatment plant (WWTP) consists of three stages. These are mechanical, biological, and advanced treatment methods. Hydraulic characteristics of each stage are important to operate the facilities economically and efficiently. Screens are a physical treatment method planned to remove floating or suspended coarse materials from wastewater. The use of the screens is important to separate these substances from the water so that they do not damage the installation, thereby reducing the burden on other treatment units. Headpond is built to support flow rate continuity by retaining water. The upstream channel is built to provide the approach velocity which is essential to be limited to approximately between 0.6 m/s – 1.2 m/s and adequate screen area for accumulation of screening between raking operations. Computational fluid dynamics (CFD) is the mathematical solution of fluid flow by computer-based simulation. CFD has been successfully used various units of WWTP: grit chambers (Couture et al., 2009), (Dutta et al., 2014), (Hoiberg & Shah, 2021), (He et al., 2008), (Meroney & Sheker, 2015), (McNamara et al., 2012), settling tanks (Miklós & Katalin, 2015), (Gao & Stenstrom, 2019), (Tarpagkou & Pantokratoras, 2013), (Matko et al., 1996), (Robescu & Manea, 2015), oxidation ditches (Şibil et al., 2021), (Xie et al., 2014), etc. The importance and originality of this study are that it is the first numerical study has been done on screens, as can be clearly seen from the literature.
In the present paper the numerical and theoretical studies was carried out on predicting hydrodynamic properties of selected WWTP by CFD simulations.

2. MATERIAL AND METHOD

2.1. Full-Scale Plant and Problem Description

The mechanical treatment unit of the Gümüşhane WWTP with a treatment capacity of 8333,28 m^3 per day was chosen as a full-scale facility. The upstream channel is a width of 143 cm, length of 420 cm and, the maximum water heigh in the upstream channel is 26 cm. Headpond, which is built to support flow rate continuity is a width of 214 cm, length of 250 cm, and height of 278 cm. The diameter of the inlet pipe, placed at headpond is 60 cm (Figure 1).
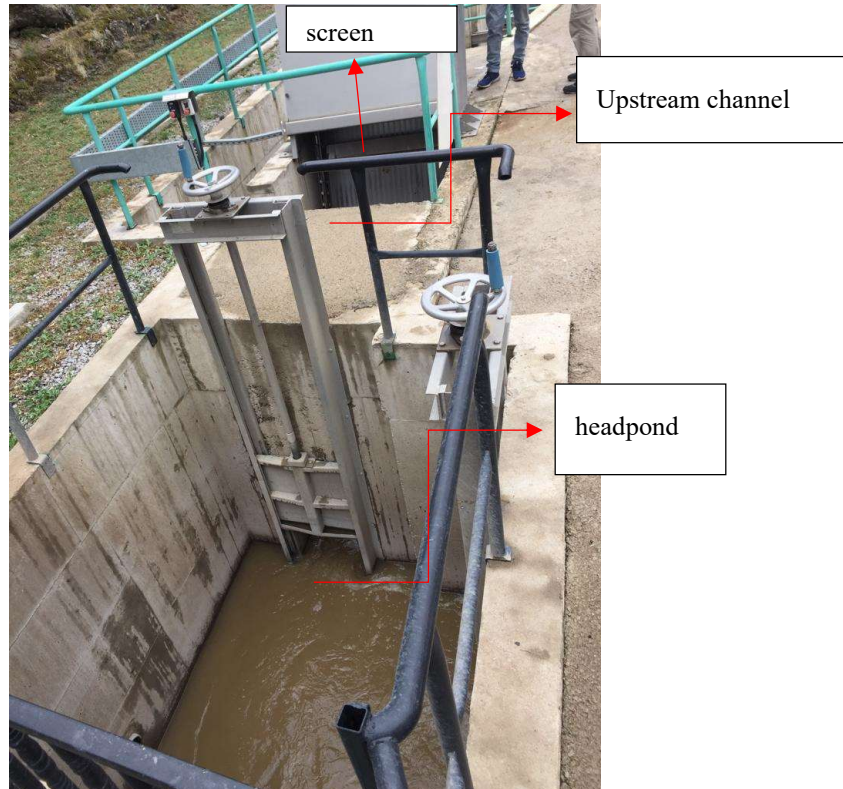
Figure 7. View of intake-head pond-upstream channel-screen

Typical design information for mechanically cleaned bar screens is provided in Table 1 (Metcalf & Eddy, 2003).

Table 1. Typical design information for mechanically cleaned screens (Metcalf & Eddy, 2003).

Parameter	SI units		
		Cleaning method	
	Unit	Manual	Mechanical
Bar size			
Width	mm	5-15	5-15
Depth	mm	25-38	25-38
Clear spacing between bars	mm	25-50	15-75
Slope from vertical	°	30-45	0-30
Approach velocity			
Maximum	m/s	0.3-0.6	0.6-1.2
Minimum	m/s		0.3-0.5
Allowable headloss	mm	150	150-600

The velocity of the upstream channel named approach velocity, one of the hydraulic design parameters of the existing screen is calculated by using the Manning equation as follows;

$$V = \frac{1}{n} R^{2/3} J^{1/2} \tag{1}$$

$$V = \frac{1}{0.013} \times (0.191m)^{2/3} \times (0.0001)^{1/2}$$
$$V = 0.255m / s$$

$$R = \frac{A \text{ (Area)}}{P \text{ (wetted perimeter)}} = \frac{0.26m \times 1.43m}{2 \times 0.26m + 1.43m}$$
$$R = 0.191m$$

Where V is approach velocity, n is Manning coefficient, R is the hydraulic radius, J is the hydraulic slope. It is clearly seen that the approach velocity calculated from equation 1 is not meet the typical design criteria given in Table 1. This problem is investigated to determine hydraulic and hydrodynamic characteristics of a selected full-scale wastewater treatment plant under real operating conditions by CFD.

2.2. Numerical Modeling

The numerical study was carried out to determine the velocity fields in upstream channel, which is feeding by head pond are determined in existing operation conditions. Although the flow rate from the Municipality change monthly according to the population mobility, the flow has been considered steady in the solutions. For the fluid flow, based on the Reynolds-average Navier-Stokes (RANS) equations, three-dimensional, steady, non-compressible flow is applied, and velocity field calculations were carried out in upstream channel for the CFD analysis by ANSYS Fluent software. Ske turbulence model that used most commonly in the literature was chosen as a turbulence model (Couture et al., 2009), (Dufresne et al., 2009), (He et al., 2008), (Matko et al., 1996), (Meroney & Sheker, 2015), (McNamara et al., 2012), (Tarpagkou & Pantokratoras, 2013). The flow is turbulence as calculated in detail follow. There is both pipe flow and channel flow in system which is seen in (Figure).
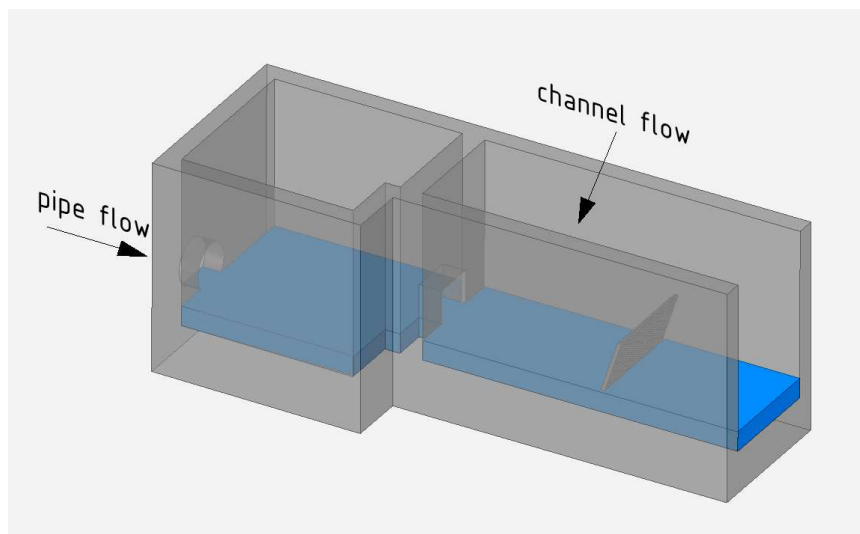
Figure 2. The pipe and channel flow

29

The Reynolds number is calculated in pipe flow as follows equation.

$$Re = \frac{V \times D}{V} \qquad (2)$$

Where ρ is the density, V is the velocity, D is diameter of the pipe, ν is the kinematic viscosity. The Reynolds number is calculated as follow in intake pipe.

$$Q = V \times A \qquad (3)$$

$$0.0492 \frac{m^3}{s} = V \times \frac{\pi \times 0.6^2}{4}$$

$$V = 0.174 \text{ m/s}$$

$$Re = \frac{0.1470 \frac{m}{sn} \times 0.60 \text{ m}}{1.003 \times 10^{-6} m^2/sn} = 104087.7 > 4000 \text{ turbulent}$$

For open-channel flow, the Reynolds number is generally defined as

$$Re = \frac{V \times R_h}{V} \qquad (4)$$

Where the hydraulic radius Rh is the characteristic length. And the Reynolds number is calculated as follow in channel.

$$R_h = \frac{A}{P} \qquad (5)$$

$$Rh = \frac{1.43 \text{ m} \times 0.26 \text{ m}}{(1.43 + 2 \times 0.26) \text{ m}} = 0.19 \text{ m}$$

$$Q = V \times A$$
$$0.0492 = V \times (1.43 \times 0.36) \text{ m}$$
$$V = 0.1323 \text{ m/sn}$$

$$Re = \frac{0.1323 \frac{m}{sn} \times 0.19 \text{ m}}{1.003 \times 10^{-6} \frac{m^2}{sn}} = 25061.8 > 1000 \text{ turbulent}$$

2.2.1. Geometry and Meshing

Fluid and solid domain was created in SpaceClaim, one of the three-dimensional (3D) Computer-Aided Design modeling software (Figure 3).
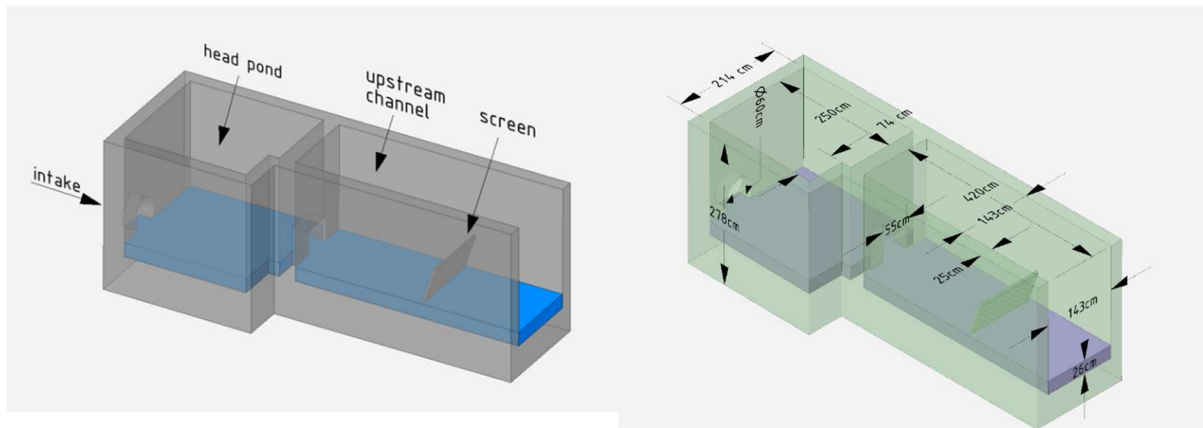
Figure 3. The designed geometry of the Model with dimensions

In addition, the intake is considered to the simulation. According to numerical studies, the hydrodynamic behaviors of the headpond and upstream channel units are evaluated in terms of the typical design criteria (Table 1).

The mesh is constructed with the tetrahedrons element structure, patch conforming method. Also, the body sizing method for screen and edge sizing method for screen bars was applied to the geometry. For body sizing, element size is 3, for edge sizing, the number of divisions is 7. Moreover, the inflation method, which including the first layer thickness option has a 0.5 cm first layer height and 5 layers, to describe the near-wall treatment was applied to the mesh study (Figure 4). After a series of grid-independent tests, the total number of elements turned out to be 1 035 204.
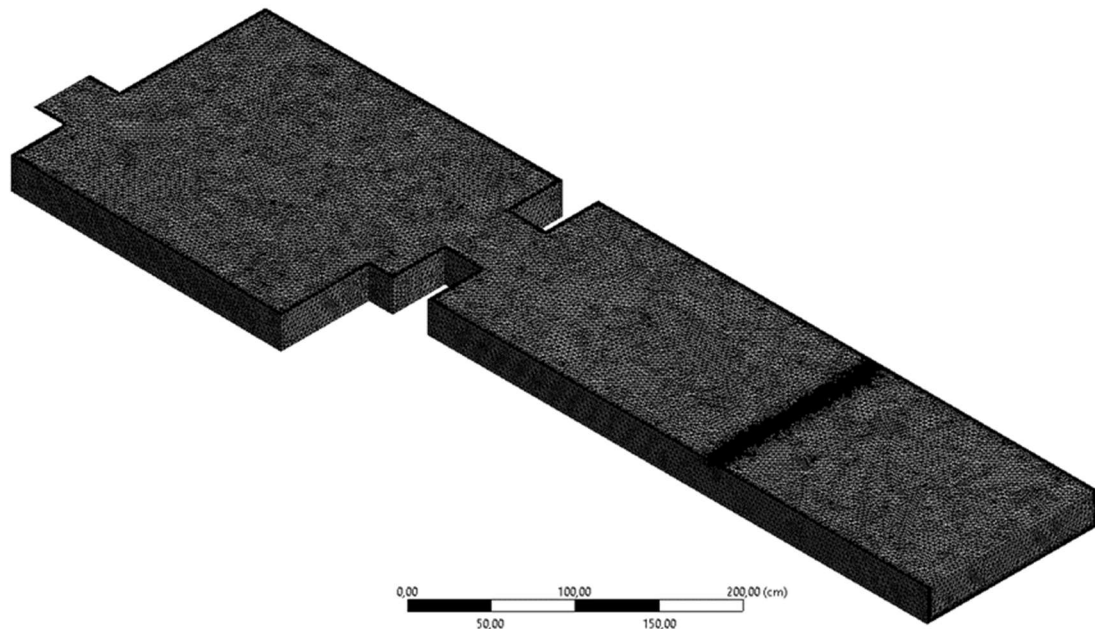
Figure 4. The mesh structure of Model

2.2.2. Boundary Conditions

Simulation is performed for WWTP with 8333,28 m^3/day flow rate and V=0.3477 m/s inlet velocity for Model. The boundary condition for inlet is "velocity-inlet", for outlet is "pressure-outlet" and for water surface is "symmetry". Solid boundaries are specified as "wall".

2.2.3. CFD Simulation of Model

3-D, steady, single-phase, non-compressible flow with the k-ε turbulence model is performed in Ansys Fluent. The criterion for convergence in the numerical model requires the scaled residuals to decrease to 10^{-6} for all equations. The calculation time was approximately 4 hours for the steady-state calculation on an Intel (R) Core ™ computer with an i7-10750H CPU @ 2.60 GHz 5.0 GHz processor, 16.00 GB RAM, and a 64-bit operating system.

3. RESULTS AND DISCUSSION

The numerical study results are visualized to evaluate the hydraulic performance of WWTP. The velocity fields of intake-headpond-upstream channel combined system are given in figure 5.
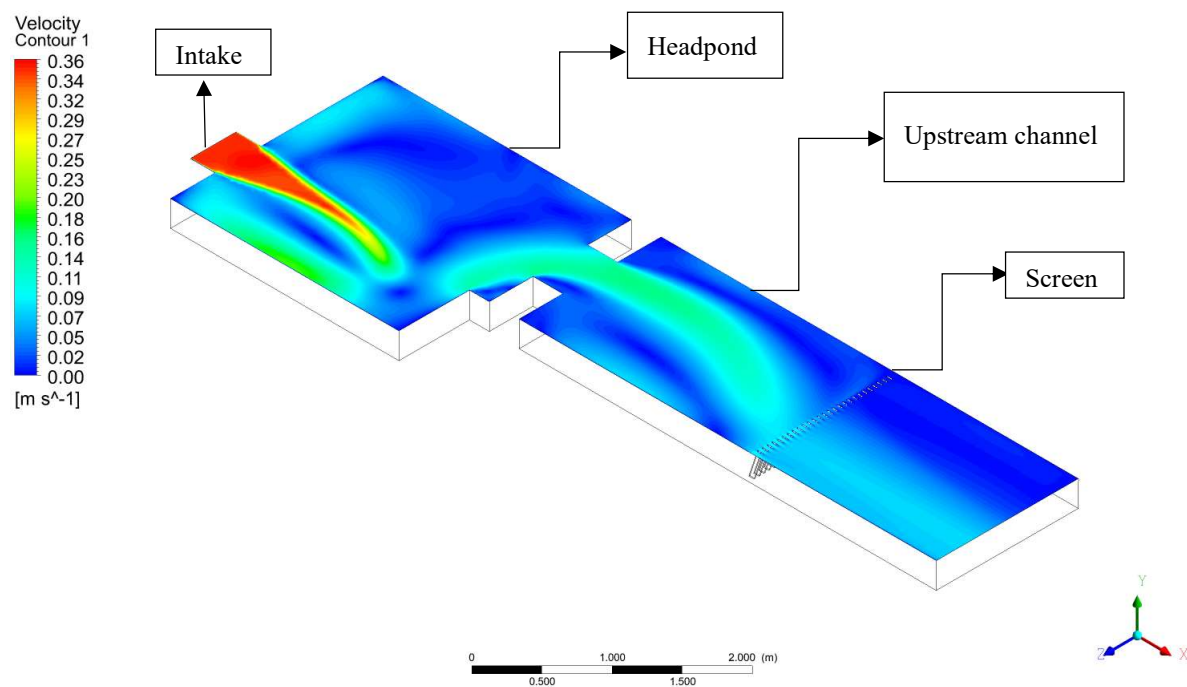
Figure 5. Velocity contour at intake-headpond-upstream channel
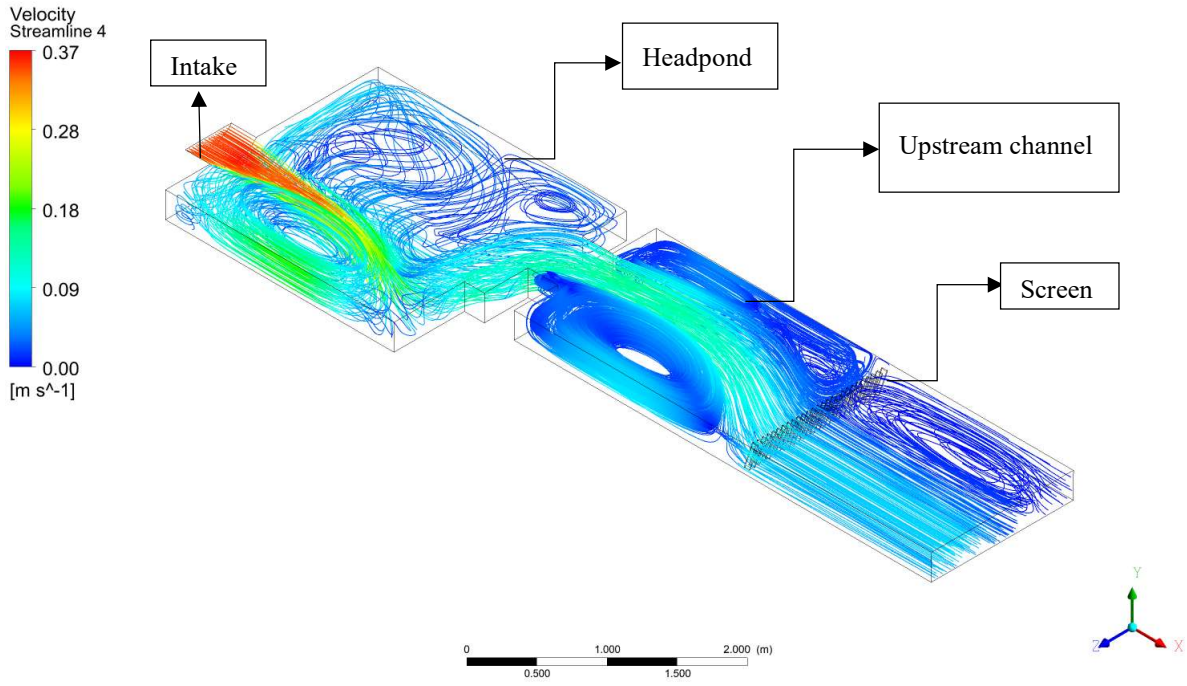
Figure 6. Velocity streamline at intake-headpond-upstream channel

As can be seen from figure 5 above, there is no homogenous velocity distribution at intake-headpond-upstream channel. The main problem is that headpond, built to provide to increase depth of water in upstream channel doesn't retain water and it operates like a channel. The figure 6 shows that the velocity streamline at unit. Since the inlet pipe is not in line with the outlet section of the headpond, the water draws a flow profile as shown in the figure 6.
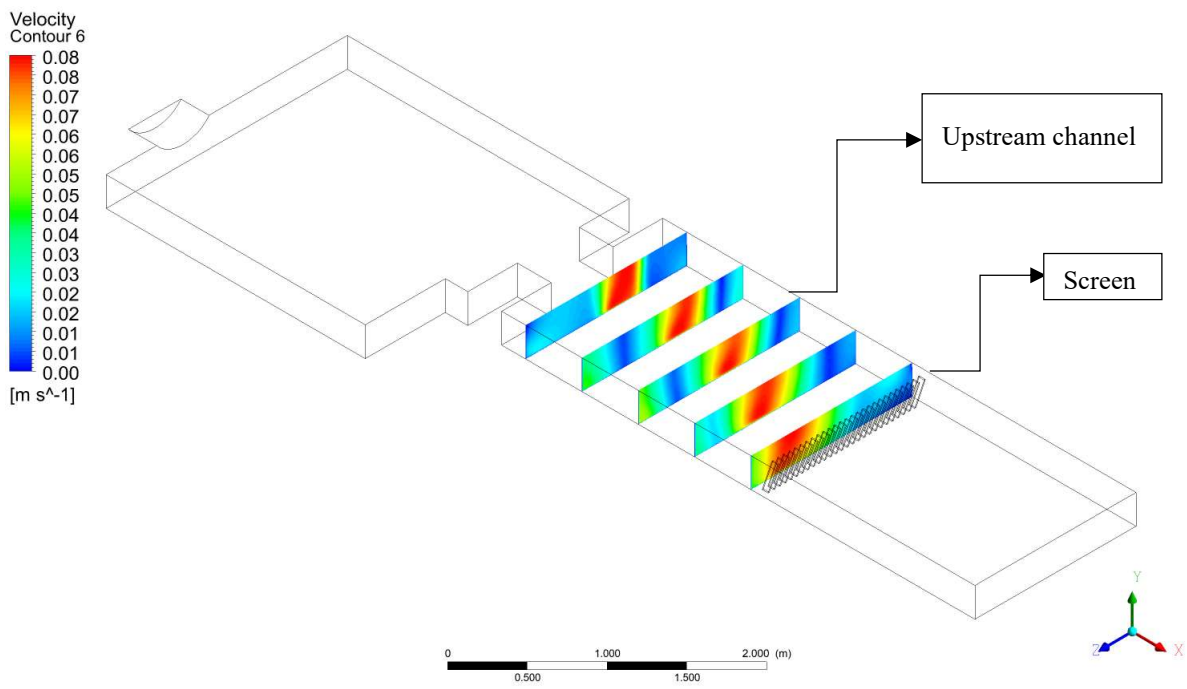
Figure 8. Velocity fields at vertical section at upstream channel

33

Figure 7 illustrates the velocity fields at vertical section at upstream channel. As seen in Figure 7 there is no homogenous velocity fields at upstream channel. Also, it clearly seems at Figure 7 that the approach velocities, which is essential be limited between 0.6 m/s – 1 m/s at upstream channel are vary between 0–0.08 m/s.

4. CONCLUSIONS

In this study, the hydrodynamic evaluation of the full-scale WWTP's intake-headpond-upstream channel was performed with the numerical simulation used by the CFD software ANSYS Fluent. The numerical studies results showed that:

- Due to the low flow rate and insufficient wrong-operated headpond, the upstream channel does not meet the desired velocity values for screening.
- The maximum wastewater velocity occurs at the inlet. The water velocity also decreases as it moves away from these points at vertical and horizontal.
- There is no homogeneous flow field distribution in upstream channel.

REFERENCES

Couture, M., Steele, A., Bruneau, M., Gadbois, A., Hohman, B., Couture, M., Steele, A., Bruneau, M., Specialist, H. P., Gadbois, A., President, T. V., & Hohman, B. (2009). *A 360°.* 773–783.

Dufresne, M., Vazquez, J., Terfous, A., Ghenaim, A., & Poulet, J. B. (2009). Experimental investigation and CFD modelling of flow, sedimentation, and solids separation in a combined sewer detention tank. *Computers and Fluids, 38*(5), 1042–1049. https://doi.org/10.1016/j.compfluid.2008.01.011

Dutta, S., Tokyay, T. E., Cataño-Lopera, Y. A., Serafino, S., & Garcia, M. H. (2014). Application of computational fluid dynamic modelling to improve flow and grit transport in Terrence J. O'Brien Water Reclamation Plant, Chicago, Illinois. *Journal of Hydraulic Research, 52*(6), 759–774. https://doi.org/10.1080/00221686.2014.949883

Gao, H., & Stenstrom, M. K. (2019). Generalizing the effects of the baffling structures on the buoyancy-induced turbulence in secondary settling tanks with eleven different geometries using CFD models. *Chemical Engineering Research and Design, 143*, 215–225. https://doi.org/10.1016/j.cherd.2019.01.015

He, C., Wood, J., Marsalek, J., & Rochfort, Q. (2008). Using CFD Modeling to Improve the Inlet Hydraulics and Performance of a Storm-Water Clarifier. *Journal of Environmental Engineering, 134*(9), 722–730. https://doi.org/10.1061/(asce)0733-9372(2008)134:9(722)

Hoiberg, B., & Shah, M. T. (2021). CFD study of multiphase flow in aerated grit tank. *Journal of Water Process Engineering, 39*(July 2020), 101698. https://doi.org/10.1016/j.jwpe.2020.101698

Matko, T., Fawcett, N., Sharp, A., & Stephenson, T. (1996). Recent progress in the numerical modelling of wastewater sedimentation tanks. *Process Safety and Environmental Protection, 74*(4), 245–258. https://doi.org/10.1205/095758296528590

McNamara, B. F., Layne, J., Hyre, M., Kinnear, D. J., & Bott, C. B. (2012). Evaluation of three full-scale grit removal processes using CFD modeling. *WEFTEC 2012 - 85th Annual Technical Exhibition and Conference, 10*(September 2014), 6008–6030. https://doi.org/10.2175/193864712811710335

Meroney, R. N., & Sheker, R. E. (2015). Removing Grit During Wastewater Treatment:CFD Analysis of HDVS Performance. *Water Environment Research, 88*(5), 438–448. https://doi.org/10.2175/106143015x14212658614478

Miklós, P., & Katalin, K. (2015). *Analysis of suspended solids transport processes in primary settling tanks Miklós Patziger and Katalin Kiss.* 1–9. https://doi.org/10.2166/wst.2015.168

Robescu, L. D., & Manea, E. E. (2015). Using CFD Techniques in Teaching Rectangular Settling Tank Hydrodynamics. *Balkan Region Conference on Engineering and Business Education, 1*(1), 41–48. https://doi.org/10.1515/cplbu-2015-0005

Şibil, R., Aras, E., & Kankal, M. (2021). *Experimental and numerical studies on predicting and improving the full- scale wastewater treatment plant hydrodynamics Experimental and numerical studies on predicting*

and improving the full-scale wastewater treatment plant hydrodynamics. December. https://doi.org/10.5004/dwt.2021.27708

Tarpagkou, R., & Pantokratoras, A. (2013). CFD methodology for sedimentation tanks: The effect of secondary phase on fluid phase using DPM coupled calculations. *Applied Mathematical Modelling*, *37*(5), 3478–3494. https://doi.org/10.1016/j.apm.2012.08.011

Xie, H., Yang, J., Hu, Y., Zhang, H., Yang, Y., Zhang, K., Zhu, X., Li, Y., & Yang, C. (2014). Simulation of flow field and sludge settling in a full-scale oxidation ditch by using a two-phase flow CFD model. *Chemical Engineering Science*, *109*, 296–305. https://doi.org/10.1016/j.ces.2014.02.002

14TH INTERNATIONAL CONFERENCE
ON HYDROSCIENCE & ENGINEERING

MAY 26-27, 2022
IZMİR-TURKEY

ICHE2022
IZMIR, TURKEY

NUMERICAL INVESTIGATION OF FLOW AROUND AN ISOLATED PIER ON AN INCLINED SURFACE

Mete Köken

Department of Civil Engineering, Middle East Technical University

Ankara, Turkey

mkoken@metu.edu.tr

Emre Hesap

Department of Civil Engineering, Middle East Technical University

Ankara, Turkey

emre.hesap@metu.edu.tr

Gökçen Bombar

Department of Civil Engineering, İzmir Katip Çelebi University

İzmir, Turkey

bombar@ikcu.edu.tr

Şebnem Elçi

Department of Civil Engineering, İzmir Institute of Technology

İzmir, Turkey

sebnemelci@iyte.edu.tr

Antonio H. Cardoso

CERIS, Instituto Superior Técnico, Universidade de Lisboa

Lisboa, Portugal

antonio.cardoso@tecnico.ulisboa.pt

ABSTRACT: Coherent structures and turbulent flow characteristics around an isolated pier which is located on an inclined surface are investigated numerically within this study. DES model (Detached Eddy Simulation) is used in the simulations which are performed at Reynolds numbers of 52480 and 262400. Although the turbulence is more amplified in the high Reynolds number case, in both cases it was observed that there is an asymmetrical horseshoe vortex forming around the pier which contributed in the amplification of the shear stress on the bed. Furthermore, pressure root mean square fluctuations which is an important parameter in the formation of the scour are amplified along the bed especially at the downstream of the pier.

1. INTRODUCTION

Pier and abutment scour in bridges are the two major sources for the bridge failure. In the literature there are many studies that investigate the pier scour phenomena (i.e. Chang et. al. 2013, Dargahi 1989, Dey and Raikar 2007 etc.). However, all these investigations are made for horizontal channel bottom. In the present study turbulent flow characteristics around a pier on a laterally inclined channel is numerically investigated.

Spalart Almaras based DES (Detached Eddy Simulation) turbulence model was used in the simulations. This model is a hybrid model where regions close to the walls are resolved in RANS (Reynolds Average Navier Stokes) mode, while regions far from the walls are resolved in LES (Large

Eddy Simulation) mode. DES simulations were performed at two different Reynolds numbers with flat bed conditions that corresponds to the initiation of scour. Of these two solutions, the lower Reynolds number case corresponds to the flume experiments whereas the higher Reynolds number case represent the situation that would actually occur in natural rivers. Simulations run at low and high Reynolds numbers are labeled as BI and BII simulations, respectively. In the simulations, all lengths are non-dimensionalized with the bridge pier diameter D. The view of the flow domain is given in Figure 1. In the calculations, the channel length was taken as 35D and the bridge pier was placed at a distance of 10D from the entrance section.
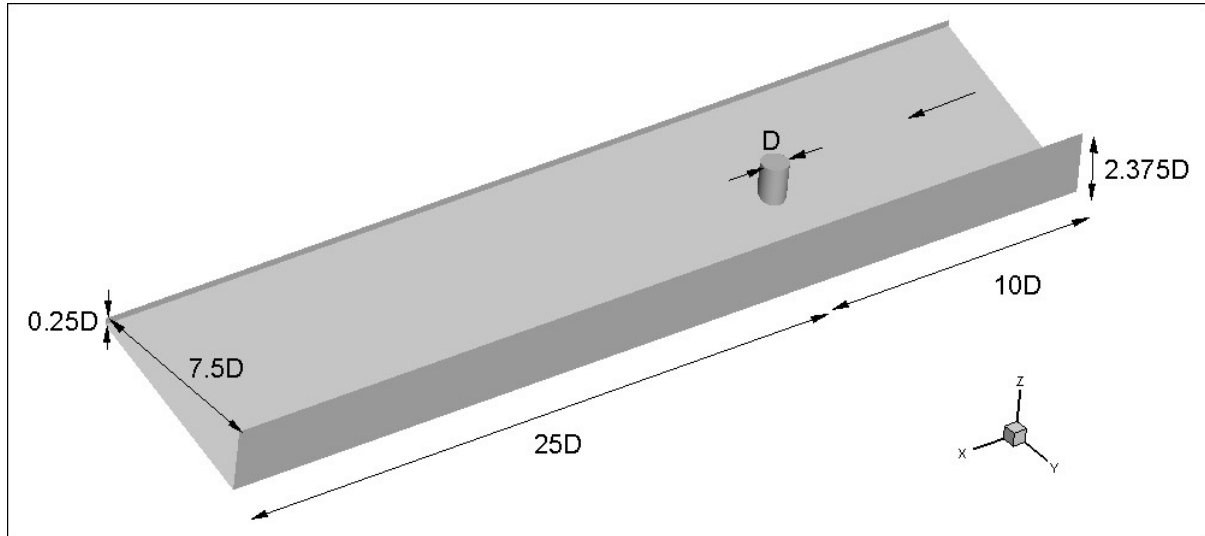
Figure 9. Flow domain

The wall functions are not used in the simulations and the viscous sublayer is directly resolved. For this purpose, the computational grid was refined in the regions close to the wall and the first point of the created mesh has been positioned as y+=1 (y+ = yu*/ν). 4.4 million grid points were used in BI simulation; whereas a total of 6.1 million grid points were used in BII. The no-slip wall boundary condition is used on all solid surfaces, and the water free surface is modeled as rigid lid. Synthetic turbulence conditions were added to the developed flow profile obtained in a periodic channel at the entrance (Demirbaş, 2021).

2. RESULTS

2.1. Average Velocity and Vorticity Distribution

Once the streamwise velocity values are investigated, in both simulations, velocity values along the deep edge of the channel are observed to be quite high compared to the narrow side of the channel. Accelerating flow conditions were observed only in a limited area near the foot of the pier on the shallow side. Behind the bridge pier, a recirculation zone is formed where negative velocities are observed. When simulation BI and BII are compared, it is observed that the maximum dimensionless velocity value observed in case BII is approximately 3% higher than the value observed in BI.

In case BI, the recirculation regions formed behind the bridge pier can be easily distinguished from the dimensionless vertical vorticity distributions at water free surface and mid-depth as given in Figure 2. The vertical vorticity values in the separated shear layers are considerably larger than the other flow regions. Here, the separated shear layer on the left hand side at the free surface (Fig. 2a) is slightly oriented towards the deep channel wall (shown by dashed lines). This orientation disappears when descending to the mid-depth in the channel (Figure 6b). A similar situation was observed in case BII.
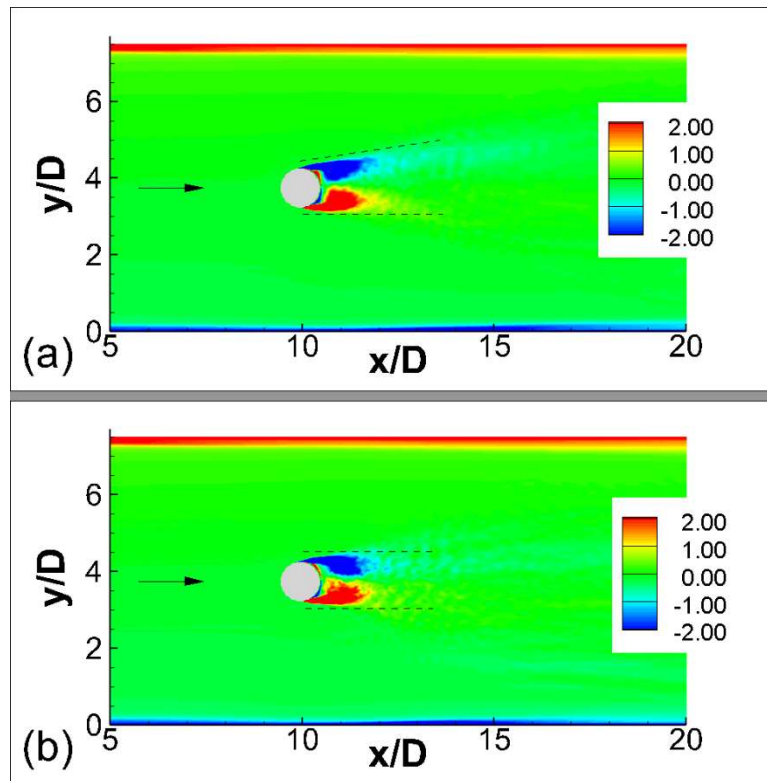
Figure 2. Vertical vorticity contours, $\omega_z D/U$, for the mean flow in case BI at: a) Water free surface; b) Mid flow depth

2.2. Bed Shear Stress Distribution

Non-dimensional bed shear stress distribution, $\tau_w/(\rho U^2)$, for the mean flow in Case BI and Case BII are given in Figures 3 and 4. In both simulations, the bed shear stress values increase along the axis of the horseshoe vortex and downstream of the pier in the regions where the flow accelerates on both sides of the bridge pier. While the maximum bed shear stress value in case BI is 0.011, this value is approximately 0.006 in case BII. In both simulations, the region where the bed shear stress values increase is effective in a slightly wider area on the shallower side of the bridge pier, and the maximum bed shear stress values occur next to the pier in this region.
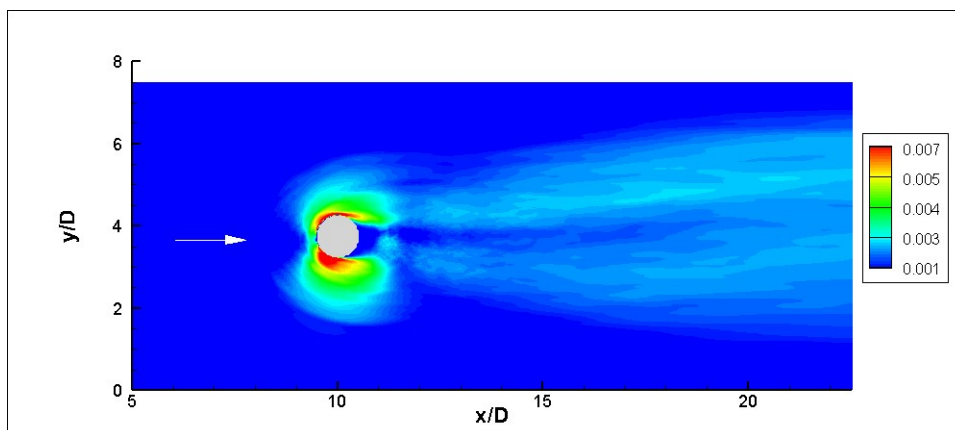
Figure 3. Non dimensional mean bed shear stress distribution $\tau_w/(\rho U^2)$ over the bed for case BI
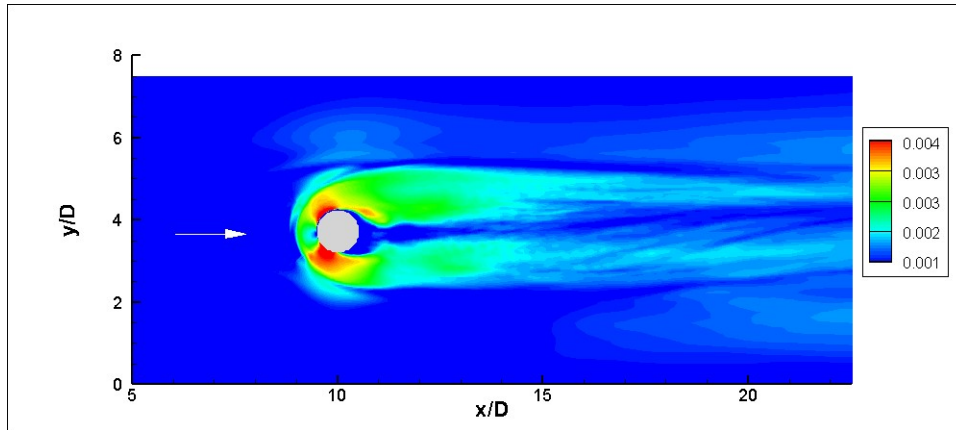
Figure 4. Non-dimensional mean bed shear stress distribution $\tau_w/(\rho U^2)$ over the bed for case BII

3. CONCLUSIONS

The turbulent flow structures and bed shear stress distribution around a bridge pier placed in a triangular channel were investigated using DES turbulence model at two Reynolds numbers.

• In both simulations, it has been observed that the velocities in the channel are higher in the deep part of the channel. However, near the bridge pier, a region where local velocities increase on the shallow side of the channel as well.

• Separated shear layers are observed on both sides of the bridge pier. Among these two separated shear layers, the one which is on the deeper side of the channel is oriented slightly towards the deeper channel wall at the free surface. This orientation disappears once the mid-flow depth is reached.

• When the bed shear stress distribution is examined, it is observed that high bed shear stress values occur in the acceleration zones on both sides of the bridge pier and along the detached shear layers. It was observed that these stresses were effective along a wider band on the shallow channel side than on the deep channel side in both simulations. Maximum bed shear stress values were also formed in this shallow side. While the maximum dimensionless bed shear stress value is 0.011 in the low Reynolds number simulation, this value is 0.006 in the high Reynolds number simulation.

REFERENCES

Chang, W-Y., Constantinescu G., Lien H-C., Tsai W-F., Lai J-S., Loh C-H. (2013). "Flow Structure around Bridge Piers of Varying Geometrical Complexity.", Jounral of Hydraulic Engineering, 139(8), 812-826.

Dargahi, B. (1989). "The turbulent flow field around a circular cylinder." Exp. Fluids, 8(1–2), 1–12.

Demirbaş, G. D. (2021). "Numerıcal investigation of wind load characteristics around an isolated tall building.", Y. Lisans tezi, Orta Doğu Teknik Üniveristesi, Ankara.

Dey, S., and Raikar, R. V. (2007). "Characteristics of horseshoe vortex in developing scour holes at piers." J. Hydraul. Eng., 133(4), 399–413.

14TH INTERNATIONAL CONFERENCE
ON HYDROSCIENCE & ENGINEERING

MAY 26-27, 2022
IZMİR-TURKEY

ICHE2022
IZMIR, TURKEY

NEW DEVELOPMENT IN CCHE1D CHANNEL NETWORK MODEL

Yaoxin Zhang

National Center for Computational Hydroscience and Engineering, University of Mississippi.

Oxford, MS, USA

yzhang@ncche.olemiss.edu

Yafei Jia

National Center for Computational Hydroscience and Engineering, University of Mississippi.

Oxford, MS, USA

jia@ncche.olemiss.edu

ABSTRACT: For large scale and long-term hydraulic and hydrological processes, when seeking the average solutions, one-dimensional model is the most suitable and efficient tool. CCHE1D model (Wu and Vieria, 2002) has been developed for long-term sediment loads and morphological changes, evaluations of the effects of erosion control and channel remediation measures on sediment yields of watersheds, and analysis of the influences of land use changes and agricultural management practices on sedimentations. It is capable of efficiently simulating unsteady 1D channel network flows including in-stream hydraulic structures, non-equilibrium and non-uniform sediment transport and channel morphological change, and transport and fate of general pollutants, nutrient dynamics and water temperatures. In this paper, some new developments of CCHE1D channel network model package are presented. The newly developed CCHE1D model is focused on 64-bit platform to satisfy users' mega data requirements. In addition, a simple and effective algorithm by using watershed-merging method is proposed to automatically identify channel networks based on the observation that the channel network identification is equivalent to the watershed identification. Distinguished from other methods on treating the flat and depression areas, the proposed algorithm is using a more intuitive but conceptually clearer way to resolve the discontinuities caused by the depression and flat areas. That is, dynamically and iteratively merge small neighboring sub-watersheds into larger watersheds. According to the demonstrations of examples and applications, the proposed algorithm is turned out to be effective in identifying channel networks and easy to implement.

1. INSTRUCTIONS

For large scale and long-term hydraulic and hydrological processes, when seeking the average solutions, one-dimensional model is the most suitable and efficient tool. CCHE1D model (Wu and Vieria, 2002; 2004) has been developed for long-term sediment loads and morphological changes, evaluations of the effects of erosion control and channel remediation measures on sediment yields of watersheds, and analysis of the influences of land use changes and agricultural management practices on sedimentations. It is capable of efficiently simulating unsteady 1D channel network flows including in-stream hydraulic structures, non-equilibrium and non-uniform sediment transport and channel morphological change, and transport and fate of general pollutants, nutrient dynamics and water temperatures.

CCHE1D model has been developed for dendritic channel networks. However, looped channel networks are more general and more complicated than the dendritic channel network. To expand its capabilities in handling looped channel networks, new developments on the numerical solver and the generation tools of looped channel networks are needed for CCHE1D model.

The junction-point water stage prediction and correction (JPWSPC) method proposed by Zhu et al. (2011) for general 1D channel networks (looped or dendritic) will be integrated in CCHE1D model to resolve the looped channel network. In JPWSPC, each branch is computed independently, which guarantees the simplicity, efficiency, and robustness of the numerical model.

For generations of looped channel networks, a simple and effective watershed-merging algorithm (Zhang and Jia, 2020) to identify and extract dendritic channel network from DEM will be adopted and further developed to enable looped channel networks generation. Alternatively, digitation tool provides more flexibilities and interactions for generating looped channel network based on any topography data.

CCHE1D version 3.0 was based on ArcView which is obsolete, while version 3.2 was based on ArcGIS that has frequent libraries updates but incompatible backward. To make CCHE1D model independent of GIS environments provided by ArcView and ArcGIS, new stand-alone version needs to be developed. To accommodate the development of the looped channel network generator and the new CCHE1D looped channel network model, the CCHE1D-GUI version 4.x has been developed.

This paper will present some preliminary results of abovementioned new developments, watershed-merging algorithm, looped channel network generator, and CCHE1D-GUI version 4.1, for CCHE1D model. With all these new developments, CCHE1D model will be more capable for watershed hydrological processes and hydrodynamic processes in channels.

2. WATERSHED-MERGING ALGORITHM

The D8 algorithm (Jenson and Domingue, 1988) has been widely used to identify channel networks from digital elevation model (DEM), but it will fail in depression areas and flat areas (DAFA). DAFA are common in DEMs. Hydrologic corrections (i.e., bed smoothing, depression filling, and depression breaching, etc.) are usually applied to those DEMs to make them workable for the D8 algorithm. For the early low-resolution DEMs with limited accuracy, DAFA are considered spurious, while for nowadays high-resolution DEMs, they are considered true terrains.

Distinguished from other algorithms, the watershed-merging algorithm (Zhang and Jia, 2020) uses the input DEM as is, and does not need hydrological corrections. The watershed-merging algorithm considers DAFA as watershed-to-watershed disconnection and assumes a merging flow path exists between two neighboring watersheds. The flow direction of the neighboring watersheds is determined by the macro-scale watershed information, such as averaged elevation. Therefore, the resulted flow routes can maintain the original topography characteristics as much as possible. Figure 1 compares the resulted channel networks from the watershed-merging and the TOPOAGNAPS (Garbercht and Martz, 1999). The results are identical, though minor differences can be observed.
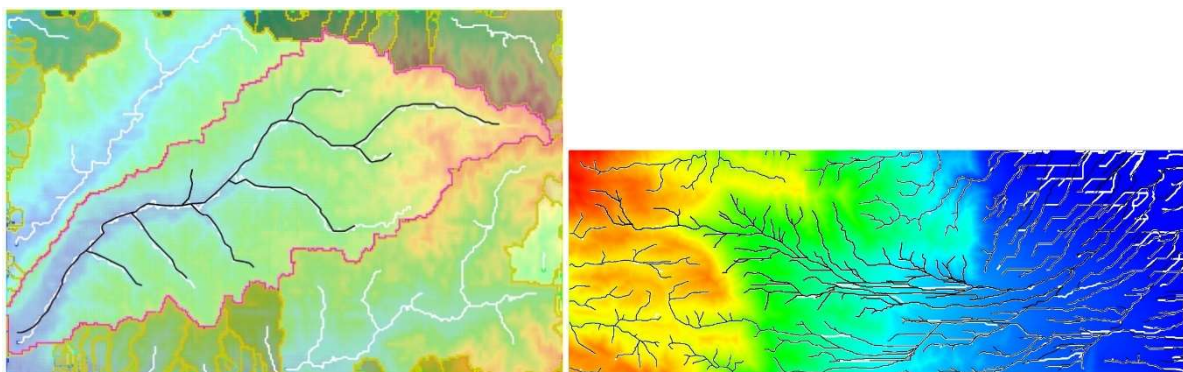
Figure 1. Comparisons of watershed-merging algorithm (black) and TOPOAGNAPS (white)

3. LOOPED CHANNEL NETWORK

CCHE1D model will adopt the junction-point water stage prediction and correction (JPWSPC) method proposed by Zhu et al. (2011) to resolve looped channel networks. At the junction, the water stage correction and the discharge are related according to the 1D characteristic curves for the subcritical flow.

$$\Delta Q_{in}^k = \Delta \eta^k \cdot [(QB/A)_{in} - \sqrt{gA_{in}B_{in}}] \tag{1a}$$

$$\Delta Q_{out}^k = \Delta \eta^k \cdot [(QB/A)_{out} + \sqrt{gA_{out}B_{out}}] \tag{1b}$$

where Q is the discharge; B is the width; A is the cross-section area; η is the water stage; the subscript "in" denotes the inflow and "out" the outflow; and the superscript "k" denotes the correction iteration step. According to mass conservation, at the junction, we have

$$\Delta \eta^k = \frac{\Delta t \sum Q^k}{A_c^k} \tag{2a}$$

$$A_c^k = \alpha \{ [\sum \sqrt{gA_{in}B_{in}} - (QB/A)_{in}] + [\sum (QB/A)_{out} + \sqrt{gA_{out}B_{out}}] \} \cdot \Delta t \tag{2b}$$

where α is in the range [1, 2].

CCHE1D model will use the watershed-merging algorithm to identify and extract dendritic channel network from DEM, based on which the looped channel network would be generated. In the looped channel network, multiple outflows from junctions are possible, compared to only one outflow in dendritic channel network. This implies that the loops only occur between junctions, which makes it possible to generate a looped channel network based on a dendritic channel network.

A digitization tool has been developed and integrated into CCHE1D-GUI to generate looped channel networks. In a looped channel network, there are four types of links, namely, source-to-end link, source-to-junction link, junction-to-junction link, and junction-to-end link.

Dendritic channel network   (b) Looped channel network
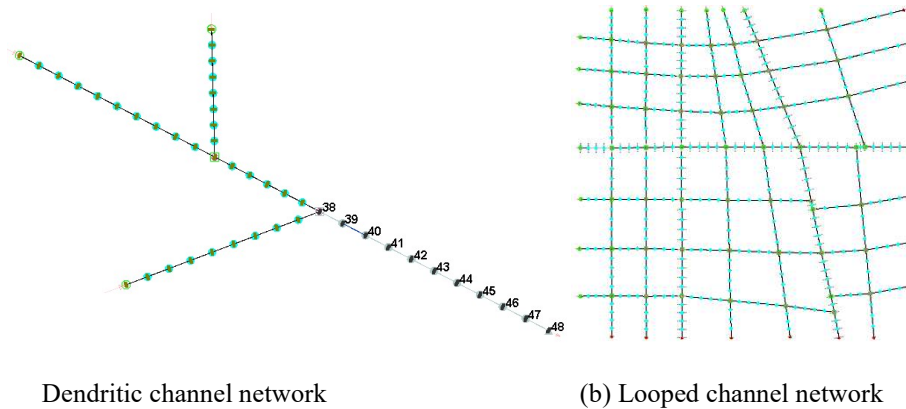
Figure 2. Digitization tools for (a) dendritic channel network and (b) looped channel network

4. CCHE1D-GUI 4.X

A 64-bit new Windows-based Graphical Users' Interface (CCHE1D-GUI) has been developed based on VC++ and OpenGL. A independent GIS module based on LibTIFF library, Shapefile C Library, and Cartographic Projection Library has been developed and integrated (Figure 3).
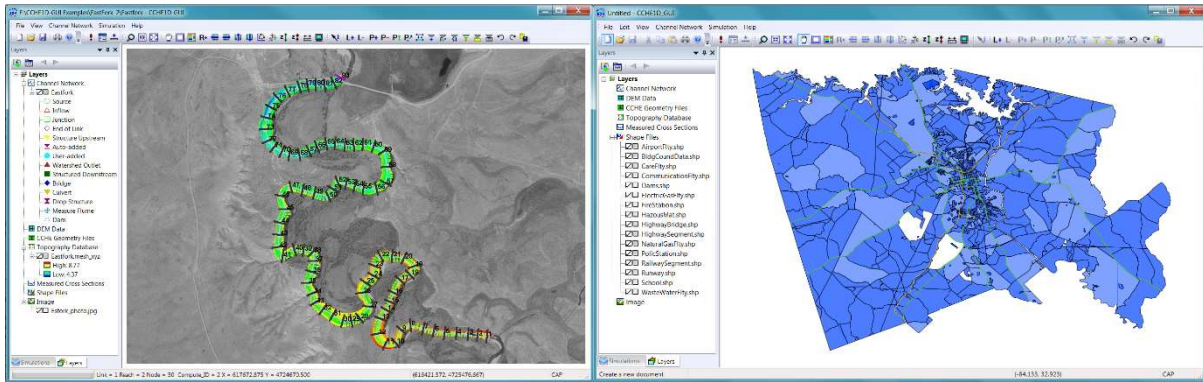
Figure 3. CCHE1D-GUI

CONCLUSIONS

Some new developments have been conducted to improve CCHE1D model. Those new developments include a new delineation tool based on the watershed-merging algorithm, a digitization tool for both dendritic and looped channel networks, and a new graphical users' interface (CCHE1D-GUI). Further developments on the numerical solver based on JPWSPC method for looped channel networks and automatic generator for looped channel networks based on the watershed-merging algorithm have been planned and will be carried out in the future.

REFERENCES

Jenson, S.K. and Domingue, J.O. (1988), Extracting topographic structure from digital elevation data for geographic information system analysis. *Photogramm. Eng. Remote Sens.* , 54 (11):1593–1600.

Garbercht, J., and Martz, L.W. (1999), "TOPAGNPS: an automated digital landscape analysis too for topographic evaluation, drainage, identification, watershed segmentation, an subwatershed parameterization for AGNPS", TOPAZ users manual, USDA-ARS, 1999

W. Wu and D. A. Vieria (2002). "One-dimensional channel network model CCHE1D 3.0 -- technical manual," Technical Report No. NCCHE-TR-2002-1, National Center for Computational Hydroscience and Engineering, The University of Mississippi.

Wu, W., Vieira, D. A., Wang, S. S. Y. (2004). A 1-D numerical model for nonuniform sediment transport under unsteady flows in channel networks. *J. Hydraulic Eng.*, ASCE, 130(9), 914-923.

Zhang, Y. and Jia, Y. (2020). "Watershed-merging: A Simple and Effective Algorithm for Channel Network Identification and Extraction", *Water Resources Research*, 56(10), 2020: https://doi-org.umiss.idm.oclc.org/10.1029/2019WR026943.

Zhu, D.J, Chen, Y.C., Wang, Z.Y., and Liu, Z.W. (2011), "Gradually varied subcritical flow simulation in general channel networks", *J. Hydraul. Eng.,* 2011, 137(7): 766-774

3D NUMERICAL SIMULATION OF FLOW, SEDIMENT AND MERCURY DISTRIBUTION IN ENID LAKE, MISSISSIPPI

Xiaobo Chao

National Center for Computational Hydroscience and Engineering, University of Mississippi

P.O. BOX 1848, University, MS 38677, USA

chao@ncche.olemiss.edu

A.K.M. Azad Hossain

Department of Biology, Geology and Environmental Science, University of Tennessee at Chattanooga

Chattanooga, TN 37403, USA

Azad-Hossain@utc.edu

Yafei Jia

National Center for Computational Hydroscience and Engineering, University of Mississippi

P.O. BOX 1848, University, MS 38677, US

jia@ncche.olemiss.edu

James Cizdziel

Department of Chemistry and Biochemistry, University of Mississippi

P.O. BOX 1848, University, MS 38677, USA

cizdziel@olemiss.edu

ABSTRACT: Enid Lake is a large reservoir located in Yazoo River Basin, the largest basin in Mississippi. It was impounded by Enid Dam on the Yocona River in Yalobusha County and covers an area of 30 square kilometers. The soil in this region is highly erodible, resulting in a large amount of sediment discharged into the lake. Sediment is normally associated with many pollutants and greatly affect water quality and aquatic lives of the lake. It has been observed that Mercury concentrations in water, sediment and fish in Enid Lake are relatively high, and a fish consumption advisory has been issued by Mississippi Department of Environmental Quality since 1995. In this study, a 3D numerical model was developed to simulate the flow, sediment and mercury distributions in Enid Lake. Flow circulations in the lake are generally determined by the wind fields and the upstream river discharge. Sediment is normally introduced from upstream river flow. The total mercury in water and sediment were simulated, and the major processes, including advection, diffusion, adsorption/desorption, bed release, atmosphere deposition and settling were considered in the model. This model was applied to simulate a storm event and the simulated results were validated using remote sensing data. This model provides useful information to analyze the processes of fate and transport of mercury in natural lakes.

1. INSTRUCTIONS

The Yazoo River Basin is the largest basin in Mississippi. Abundant streams, reservoirs and lakes are located in this region, including four large flood control reservoirs: Arkabutla Lake, Sardis Lake, Enid Lake and Grenada Lake. These lakes are significant natural and recreational resources. The soils in this region are highly erodible, resulting in a large amount of sediment discharged into water bodies. Mississippi Department of Environmental Quality (MDEQ 2012) reports that many water bodies in this region are impaired due to contaminated sediment, and nutrients, suspended sediment (SS), DDT, PCBs, pathogens, and mercury have been identified as major pollutants. Since 1995, Enid Lake has

been listed among now 14 water bodies that are under fish consumption advisories for mercury in Mississippi, reducing the recreation values of these lakes. In 2002 a Total Maximum Daily Loads (TMDLs) was developed for mercury in the Yocona River including the Enid Lake.

Numerical model is one of effective approaches to study the distribution of mercury in a large water body. The National Center for Computational Hydroscience and Engineering (NCCHE) of the University of Mississippi has developed a three-dimensional hydrodynamic and sediment transport model, CCHE3D. This model has been verified against analytical solutions and validated using experimental data and field measurements (Chao et al. 2010, Jia et al. 2009, Wang et al. 2008). In this study, a numerical model was developed based on CCHE3D for simulating the fate and transport of mercury in large lakes. The developed model was integrated into CCHE3D for simulating flow, sediment, and mercury in Enid Lake. The simulated results were compared with remote sensing imageries, and good agreements were obtained.

2. NUMERICAL MODELING OF TOTAL MERCURY

Mercury is a widely distributed and persistent pollutant in the environment. The chemical forms of mercury in air, water, and sediment include elemental mercury Hg(0), inorganic ionic mercury (HgII), and the organic form methylmercury (MeHg). When mercury enters the water and soil, microorganisms transform the mercury into MeHg, which is the most toxic form and accumulated by fish, shellfish and other aquatic organisms. When humans consume contaminated fish, they are exposed to mercury. The adverse effects of mercury in humans include neurodevelopmental, cardiovascular, and immunological deficits. Sediment plays an important role in the fate and transport processes of mercury in water bodies. Mercury may adsorb to sediment particles and also desorb from sediment to the water, and a linear approach can be applied to describe the processes of adsorption and desorption (Katsenovich et al 2010). Bed sediment associated mercury can be released gradually into the water column due to diffusion and sediment resuspension (Kuwabara et al 2003).

In the water column, the concentration of total mercury can be expressed by the following mass transport equation:

$$\frac{\partial C_m}{\partial t} + \frac{\partial (uC_m)}{\partial x} + \frac{\partial (vC_m)}{\partial y} + \frac{\partial (wC_m)}{\partial z} = \frac{\partial}{\partial x}(E_x \frac{\partial C_m}{\partial x}) + \frac{\partial}{\partial y}(E_y \frac{\partial C_m}{\partial y}) + \frac{\partial}{\partial z}(E_z \frac{\partial C_m}{\partial z}) + \sum S_m \quad (1)$$

in which u, v, w are the water velocity components in x, y and z directions, respectively; C_m is the concentration of the total mercury; E_x, E_y and E_z are the diffusion coefficients in x, y and z directions, respectively; ΣS_m is the effective source term of mercury, which can be calculated by:

$$\sum S_m = S_{load} + S_{decay} + S_{air-w} + S_{bed-w} + S_{sed} \quad (2)$$

in which S_{load} is the external loads from upstream/ tributaries, etc.; S_{decay} is the sink term due to biodegradation; S_{air-w} is the exchange term at the air-water interface; S_{bed-w} is the bed release term; S_{sed} is the source term due to sediment erosion/ deposition. Those source terms can be expressed by:

$$S_{air-w} = k_a (\frac{C_g}{H_e} - f_d C_m) \quad (3)$$

$$S_{decay} = -K_b C_m \quad (4)$$

$$S_{Bed-w} = \frac{k_f}{D}(S_d - C_d) \quad (5)$$

$$S_{sed} = J_e + J_d = \max(E_b - D_b, 0)\frac{S_T}{1-p} + \min(E_b - D_b, 0)\left(\frac{f_p}{c_v}\right)C_m \quad (6)$$

in which k_a is the overall volatilization transfer coefficient; C_g is the concentrations of total gaseous mercury in air; H_e is the Henry's constant; f_d is the fraction of total dissolved mercury; K_b is the

overall degradation rate; k_f is the mass diffusion coefficient; S_d is the dissolved mercury concentration in bed sediment; C_d is the dissolved mercury concentration in water column; S_T is the total mercury concentration at bottom; E_b and D_b are the sediment erosion and deposition rates; p' is the porosity of bed sediment; f_p is the particulate mercury fraction; and c_v is the volumetric concentration of sediment in water column.

In the numerical model, the flow dynamics, sediment transport, total mercury distributions in water and sediment were simulated. The simulations of flow and sediment were coupled, while the modeling of mercury was decoupled with flow and sediment simulations.

3. MODEL APPLICATION TO ENID LAKE

3.1. Study Site

Enid Lake is a large reservoir located in Yazoo River Basin, Mississippi (Figure 1). It is a US Army Corp of Engineers (USACE) flood control structure built in 1952. It was impounded by Enid Dam on the Yocona River in Yalobusha County and covers an area of 30 square km. The mean water depth of the lake is around 4 meters. This lake has significant natural and recreational resources. However, it is impaired by mercury, and a fish consumption advisory was issued by the MDEQ in 1995.
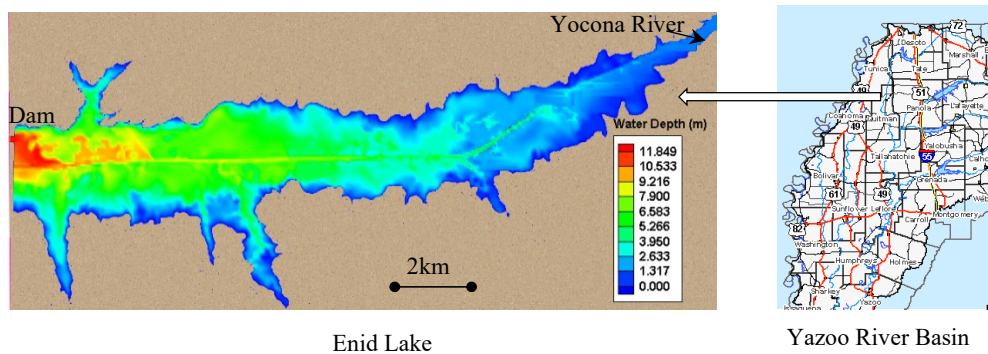
Figure 1. Study Site

3.2. Model Simulation and Discussion
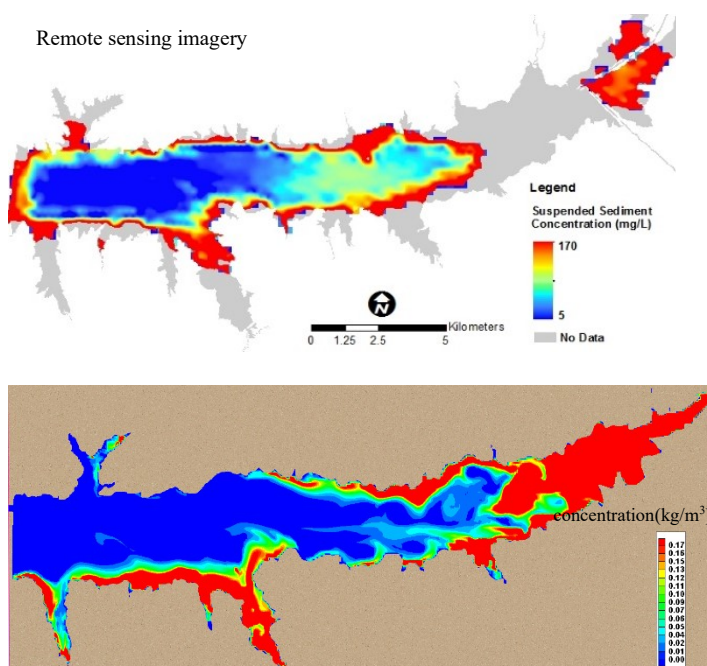
Figure 2. Concentration of SS in Enid Lake (3/12/2013)

The developed model was applied to simulate flow, suspended sediment (SS) and mercury distributions in Enid Lake during a storm event occurred in March 2013. A simulation period from March 10 to 18, 2013, was selected for model applications. Figures 2 shows the simulated SS concentration (SSC) in the lake on March 12. It is generally in agreement with the results obtained from remote sensing data. The SSC were higher near the river mouth and shoreline area, while it was much lower in the deeper water near the dam. Some differences between simulation results and remote sensing data can be observed near northwest shoreline. The numerical model underestimates the SSC concentration in this area. It may be the reason that the effect of wind induced wave on the sediment resuspension was
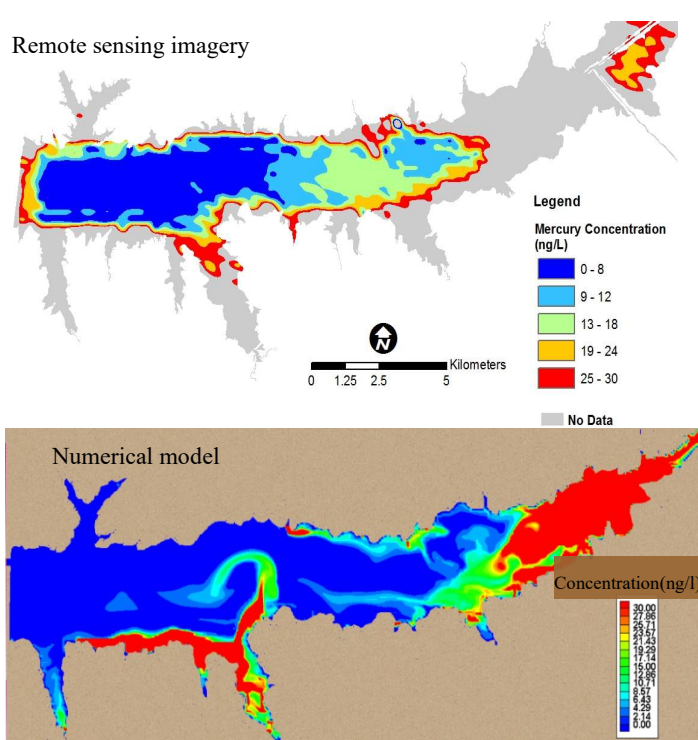
Figure 3. Total mercury concentration in Enid Lake (3/12/13)

not taken into account in the numerical model. In addition, the wind fields on the large lake, like Enid Lake may vary spatially. However, there is only one wind station near the lake for providing the wind data. In the model simulation, the wind fields were assumed to be uniformly distributed on the entire lake surface at each timestep, which may cause some errors for simulating wind driven flow.

Figure 3 shows the simulated concentration of total mercury in the lake on March 12, 2013. It is generally in agreement with the results obtained based on remote sensing technology. Some differences between numerical results and remote sensing data can be observed near northwest shoreline. It may be the reason that the numerical model underestimated the SSC in these areas. So, the concentration of absorbed mercury on the sediment was also underestimated by the numerical model.

4. CONCLUSIONS

A numerical model has been developed to predict the dynamic flow fields, and the temporal and spatial concentrations of sediment and mercury in the entire lake. Based on the upstream river flow discharge and SSC, outlet water surface elevation, and wind conditions, the flow fields, and the concentration of sediment in the lake can be solved. After obtaining flow information and SSC, the model can be applied to simulate the concentrations of total mercury in the lake (water and sediment). The developed model was used to simulate a spring storm event and the modeling results of SSC and Hg concentration were generally in agreement with satellite imagery. Model results and satellite imagery show that the concentrations of SS and Hg were higher near the river mouth and shallow shoreline area than that in the deeper water areas near the dam. The model provides a useful tool to predict the mercury distributions of the entire lake.

REFERENCES

Chao, X., Jia, Y., Shields, F. D. Jr., Wang, S.S.Y. and Charles M. Cooper (2010), Three-Dimensional Numerical Modeling of Water Quality and Sediment-Associated Processes with Application to a Mississippi Delta Lake, Journal of Environmental Management, 91(7), 1456-1466.

Jia, Y., Scott, S., Xu, Y., and Wang, S. S. Y. (2009). Numerical Study of Flow Affected by Bendway Weirs in Victoria Bendway, the Mississippi River, J. Hydraul. Eng., 135(11), 902-916.

Katsenovich, Y., Tachiev, G., Fuentes, H.R., Roelant, D. and Henao, A. (2010), A study of the mercury sorption and transport with Oak Ridge Reservation soil, 2010 Waste Management Conference, March 7-11, Phoenix, AZ.

Kuwabara, J.S. et al. (2003), Sediment-water interactions affecting dissolved-mercury distributions in Camp Far West Reservoir, California, USGS, Water Resources Investigations Report 03-4140

MDEQ (2012). State of Mississippi Water Quality Assessment 2012 Section 305(b) Report, Office of Pollution Control, Mississippi Department of Environmental, Jackson, MS.

Wang, S.S.Y., Roche, P.J., Schmalz, R.A., Jia, Y., and Smith, P.E. (ed.) 2008, Verification and Validation of 3D Free-Surface Flow Models, American Society of Civil Engineering, Reston, Virginia.

WATER RESOURCES AND CLIMATE CHANGE

CHARACTERISING THE WATER FOOTPRINT IN SEYHAN RIVER BASIN

Abdullah Muratoglu (Corresponding Author)

Civil Engineering Department, Batman University

Batman, Turkey

abdullah.muratoglu@batman.edu.tr

Erkan Erdem

Civil Engineering Department, Batman University

Batman, Turkey

erkn__erdm@hotmail.com

Muhammed Sungur Demir

Civil Engineering Department, Batman University

Batman, Turkey

muhammed.sungur@batman.edu.tr

ABSTRACT: In recent years, water scarcity problems have been encountered all over the world due to inefficient and unconscious use of water resources. To overcome this problem, an effective water management is required. Water footprint methodology provide quite comprehensive and contemporary outlook to the local and global water management. There have been very few research on water footprint analysis of hydrological basins in Turkey. In this study, the water footprint of the Seyhan basins has been analyzed and district-based agricultural production is investigated in details. The blue and green water footprint was modeled based on climate, precipitation, plant characteristics, production amount, and planted area data for the period of 2008–2018. Accordignly, the entire water footprint of the study area is calculated as 3.53 billion m^3/year. Furthermore, it has been shown that agricultural products grown in the basin is more reliant on the green water with 56% of total resources. The blue, green and total virtual water contents of agricultural products in the study area has also been evaluated. Wheat was determined as the product having the highest overall water footprint whereas chickpeas are determined as the product having the highest virtual water content. Wheat, barley, rye, oats, radish, black cabbage, broad beans, green and seed onion are of higher green water content and these products significantly reduce the rate of blue water use. The current study is projected to increase the amount and quality of fresh water resources by balancing water conservation and usage, as well as to guide watershed-based management through a rational and holistic approach.

1. INTRODUCTION

Water, the primary source of life on Earth, covers around 80% of the planet's surface. However, only 1% of the world's water is drinkable. Population growth, increased agricultural activities, industrialization, pollution, and climate change have all deteriorated the quality and quantity of water resources [1]. While around 25% of the world's population currently lacks access to clean drinking water. Studies show that 40% of the world's population will face severe water stress by 2050 [2]. According to the Falkenmark index (Table 1), countries with annual water quantities of 1000-1700 m^3 per capita are experiencing water stress. In Turkey, per capita fresh water potential has decreased from 1652 m^3 to 1346 m^3 in the last 20 years. [3]. Accordingly, statistics show that Turkey is remarkably affected by water scarcity. Furthermore, it is predicted that the amount of potable water per person in Turkey will decrease up to 1120 m^3 by 2030 [4]. On the other hand, agricultural irrigation accounts for 73% of usable water potential (Figure 1) [5]. Consequently, investigation of the utilization of agricultural irrigation is critical in terms of water management.

Table 1. Theresholds of Falkenmark index.

Water Situation	Indicator Value*
No water stress	>1700
Water stress	1000-1700
Water scarcity	500-1000
Absolute water scarcity	<500

* $(m^3/capita/yr)$
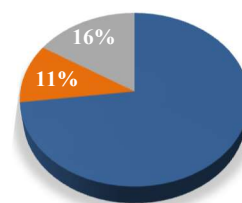
Figure 1. Water usage rates by sector [5]

Water footprint (WF) and virtual water content (VWC) approaches provides one of the most essential and comprehensive indicators of freshwater usage for sustainable water management. Virtual water refers to the water contained in products or services, that is, the amount of invisible or hidden water [6]. Water footprint, on the other hand, is a parameter that shows not only direct but also indirect water consumption of a product or service, as well as the type of water source used [7]. The water footprint not only indicates the amount of water used in production and consumption, but also expresses the components of the water used [8]. The type of water used in water footprint calculations is represented by the blue, green and gray water footprint components. In conventional water use, only the blue water footprint, which expresses the amount of surface and groundwater, is taken into account. However, unlike traditional water uses, in the water footprint method, green and gray water components are defined in addition to the blue water footprint [9]. Consequently, the surface and ground water resources constitute the blue water as a result of primary production. Access to blue water (irrigation network infrastructure, operation and maintenance costs) is usually only possible at a high cost. Green water is sources of rainwater stored in the soil as moisture. It is easier to access and less costly than blue water. Therefore, it is important to distinguish between blue and green water in terms of water conservation [10]. The main purpose of this research is to investigate the agricultural water footprint of the Seyhan basin, which contains Turkey's most important agricultural areas. The amount and context of the existing studies analyzing the WF of the study area is quite limited. Accordingly, the water footprint analysis within this study is expected to contribute to the water management of agricultural production, as the sector of the highest water use in the study area.

2. MATERIALS AND METHOD

2.1. Study Area and Data

In Seyhan river basin (Figure 2), the agricultural production is intensive and significant amount water resources are located for crop production. The basin, constitutes 2.4% of the total area of Turkey with an average drainage area of 24.000 km^2. The most important water source of the basin is Seyhan River with a length of around 560 km [11]. The basin is characterized as a water-stressed watershed according to Falkenmark Water Stress Index. The population , is 1.9 million and the amount of per capita water use is around 1475 m^3/year [12]. Mainly, melon, watermelon, cotton, citrus fruits, wheat, and corn is cultivated at the southern part of the basin. . Towards the northern parts, grain, chickpeas, potatoes, onions, beans and sugar beet are produced [13].

Climate data and reference evapotranspiration (ET_0) data were obtained from the New LocClim software, the General Directorate of Meteorology (MGM), in the current study. The obtained data was mapped into spatial values using ARCGIS software. In addition, plant characteristic data were obtained

Figure 2. Location of Seyhan basin modified from [4]

from TAGEM. Finally, vegetative evapotranspiration values were calculated using CROPWAT software [14].

2.2. Methodology

The water footprint method developed by Hoekstra [15] was employed in this study. The flow diagram of the preferred approach is illustrated in Figure 3. Reference evapotranspiration (ET_0), crop coefficients (K_c), cultivated areas (A), production amounts (P), and precipitation data are all processed as inputs, as illustrated in the flow diagram. Finally, the crop evapotranspirations (ET_c), effective precipitation (P_{eff}), crop water use (CWU), water footprints (WF), and virtual water contents (VWC) are the main outputs of the applied model.
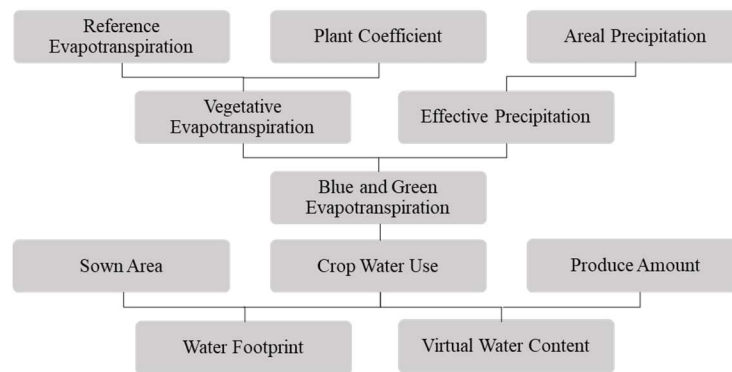
Figure 3. Flow chart of the methodology applied in this study modified from [14]

The overall water footprint is calculated as the sum of water footprint in agricultural, animal, domestic and industrial sectors (Equation 1).

$$F_{total} = WF_{agricultural} + WF_{animal} + WF_{domestic} + WF_{industrial} \qquad (1)$$

Blue and green evapotranspiration amounts are calculated using Equations 2 and 3. ET_{blue} represents the evapotranspiration from the groundwater and surface water resources (mm); ET_{green} represents the evapotranspiration from the rain water or soil moisture (mm) and P_{eff} is defined as effective precipitation [16]. Blue and green evapotranspiration of different crops vary depending on vegetative evapotranspiration and effective precipitation.

$$ET_{blue} = \max\left(0, ET_c - P_{eff}\right) \tag{2}$$

$$ET_{green} = \min\left(ET_c, P_{eff}\right) \tag{3}$$

Generally, the blue and green evapotranspiration are calculated in millimeters. Accordingly a unit conversion is used to calculate crop water consumption, which is 10 times the blue and green evapotranspiration values (Equations 4 and 5). CWU_{blue} represents the blue crop water use (m^3/ha); CWU_{green} designates the green crop water use (m^3/ha); and CWU_{total} is the total crop water use (m^3/ha) [17] (Equation 6).

$$CWU_{Blue} = 10\sum ET_{Blue} \tag{4}$$

$$CWU_{Green} = 10\sum ET_{Green} \tag{5}$$

$$CWU_{Total} = CWU_{Blue} + CWU_{Green} \tag{6}$$

The virtual water content (VWC), which expresses the amount of water contained in the products, is obtained dividing the plant water consumption by the yield. Blue virtual water content (m^3/t), green virtual water content (m^3/t) and total virtual water content (m^3/t) are noted in Equations 7, 8 and 9, respectively. The total water footprint is obtained by multiplying the production amount of the products by the total virtual water content (Equation 10).

$$VWC_{blue} = \frac{CWU_{blue}}{V} \tag{7}$$

$$VWC_{green} = \frac{CWU_{green}}{V} \tag{8}$$

$$VWC_{total} = VWC_{blue} + VWC_{green} \tag{9}$$

$$WF_{total} = \sum_{i=1}^{n} VWC_i * P_i \tag{10}$$

3. RESULTS AND DISCUSSION

3.1 Virtual Water Content

Virtual water contents of different products in Seyhan Basin is shown in Figure 4. Chickpeas (3773 m^3/ton), sesame (3575 m^3/ton), green lentils (2950 m^3/ton), safflower (2276 m^3/ton), walnuts (1795 m^3/ton), dry beans (1592 m^3/ton), peanuts (1567 m^3/ton), sunflowers (1433 m^3/ton), cotton (1149 m^3/ton), paddy (1149 m^3/ton), soybeans (1077 m^3/ton), and olives for oil (1008 m^3/ton) are products with a blue virtual water content of more than 1000 m^3/ton in the study area. Wheat (1816 m^3/ton), oats (1572 m^3/ton), durum wheat (1426 m^3/ton), chickpeas (1298 m^3/ton), barley (1285 m^3/ton), rye (1177 m^3/ton), sesame (1024 m^3/ton), and green lentils (1018 m^3/ton) are among the agricultural products grown in the basin with a green water content of more than 1000 m^3/ton (Figure 4).
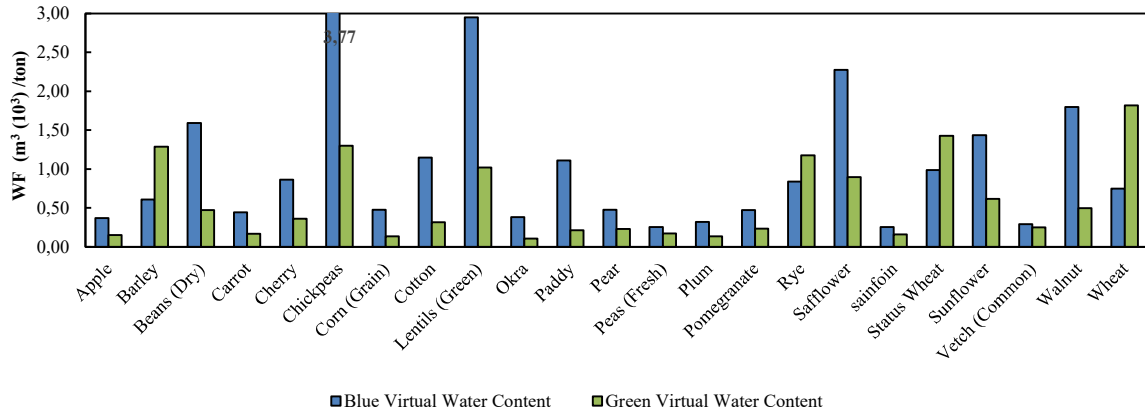
Figure.4 Virtual water contents of different products

Growing products with high green virtual water content is particularly significant in terms of water management since products with high blue virtual water content cause water scarcity. Therefore, it may be concluded that wheat, oats, durum wheat, barley, rye, seed onions, fresh broad beans, green onions, lettuce, and parsley (products with a higher green virtual water content than blue virtual water content) are particularly water-saving agricultural crops in the Seyhan basin [14].

Because of the rising global water scarcity scores in recent years, the virtual water content of products has become increasingly important. Also, virtual water content is expected to be decisive in international trade in the future. Because, by considering the virtual water content in international trade, it will be able to minimize water stress in nations who are experiencing water scarcity. Otherwise, countries with water scarcity may face even greater water stress.

3.2 Water Footprint

In the Seyhan basin, 3.76 million tons of agricultural products were produced on an area of 7.32 million decares. The basin's overall water footprint was calculated as 3.53 billion m^3, with 1.58 billion m^3 blue water and 1.95 billion m^3 green water. The world average per capita water footprint was estimated as 1240 m^3/year/person [15]. The amount of water footprint per capita in Turkey is predicted as 1392 m^3/year/person, according to the study reported by Muratoğlu and Avanoz [18]. Accordingly, our calculations show that a water use of 1709 m^3/year/. This value is 1.37 times the world average and 1.23 times the Turkey average. In addition, the average water footprint per area (Total area of Turkey) in Turkey is 140 mm according to Hoekstra's study [15]. In this study, the water footprint per area (Total area of Seyhan Basin) is calculated as slightly higher than Turkey's country average with 171 mm.Seyhan basin's per capita and per area water footprint is larger than Turkey's average because of intense agricultural production such as especially wheat and cotton. According to the study of Mekonnen and Hoesktra [19], most of the anthropogenic factors on a global scale are considered to be due to green water [14]. Similarly, in the current study, green water water dependency was found to be higher in the Seyhan basin.

The water footprint of wheat produced in Turkey was calculated as 33.52 billion m^3 for 2008-2018 [10]. The total water footprint of the wheat produced in the Seyhan basin (1.97 billion m^3) corresponds to 5.9% of this amount. In addition, it has been observed that the total water footprint of agricultural products produced in the Seyhan basin (4.45 billion m^3) corresponds to 4.2% of the total agricultural water footprint of Turkey (106.85 billion m^3) between 2008-2018. Figure 5 shows the ten products with the highest blue (BWF), green (GWF) and total (TWF) water footprints, respectively, in the Seyhan basin.
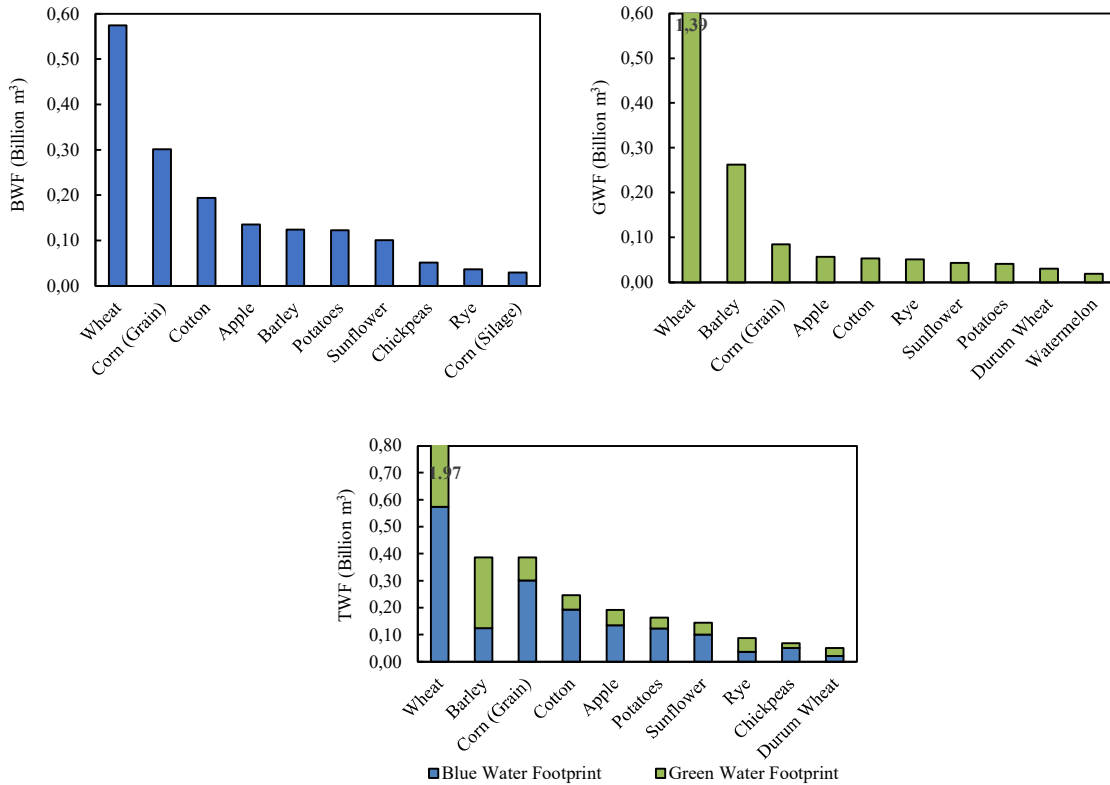
Figure.5 Ten products with the highest blue, green and total agricultural water footprints in the Seyhan Basin

The green water footprint of cereal products is obtained to be higher than the blue water footprint. Wheat, barley, rye, oats, radish, black cabbage, broad beans, green and seed onion are of higher green water content and these products significantly reduce the rate of blue water use.

This study provides information about the current water use of the region by revealing the blue and green water footprints of agricultural products. In addition, the results can be useful for an efficient agricultural production in terms of exploitation of water resources. For example, growing crops with green water footprint in the basin will have a positive contributions to diminish the water stress. However, high green water footprint may not be the only criteria for crop cultivation. In addition to the ratio of the green/blue water footprint, the product's economic value, the agricultural demands of the region or its surroundings, the country's import/export policies, and access to water resources should all be considered simultaneously.

2. CONCLUSIONS

The water footprints and virtual water contents of agricultural products produced in the Seyhan basin were analyzed and discussed for 2008–2018. It has been shown that blue water is responsible for 44 percent of agricultural products produced in the Seyhan basin, while green water is responsible for 56 percent. Wheat, barley, and corn were calculated to have the most green water footprints, whereas wheat, corn, and cotton had the highest blue water footprints. Also, the water footprint per area and per capita in the Seyhan Basin was calculated 171 mm and 1709 m³/year/ respectively.

Basin-scale water footprint studies are rare in national water footprint investigations. The Seyhan basin, which plays a significant role in Turkey's agricultural production, was analyzed in the current study. Chickpeas, sesame, green lentils, safflower, walnuts, dried beans, peanuts, sunflowers, cotton, paddy, soybeans and olives produced in the Seyhan basin have been identified as products of great importance in terms of water management due to their high blue virtual water content. Consequently, more research, policies and applications are needed to decrease blue water footprint of the study area.

REFERENCES

Yaykıran S. Sakarya Havzası'nın Yüksek Çözünürlüklü Hidrolojik Modelin Yapılandırılması. İstanbul Teknik Üniversitesi, 2016.

Tarım ve Orman Bakanlığı. Temiz Su 2021. https://www.tarimorman.gov.tr/ (accessed October 4, 2021).

SARIŞ F. Türkiye'de Evsel Su Tedarik ve Tüketim İstatistiklerinin Değerlendirilmesi. Coğrafi Bilim Derg 2021;19:195–216. https://doi.org/10.33688/aucbd.883794.

T.C. Orman ve Su İşleri Bakanlığı Su Yönetimi Genel Müdürlüğü. İklim Değişikliğinin Su Kaynaklarına Etkisi Projesi 2016.

Kalkınma Bakanlığı. Su Kaynakları Yönetimi Ve Güvenliği 2018:110.

[Williams RB, Al-Hmoud R. Virtual Water on the Southern High Plains of Texas: The Case of a Nonrenewable Blue Water Resource. Nat Resour 2015;06:27–36. https://doi.org/10.4236/nr.2015.61004.

Şahin H. Su Ayak İzi Kavramının Sürdürülebilir Su Yönetimi Çalışmalarında Kullanılması. Akdeniz Üniversitesi, 2018.

Turan ES. Türkiye'nin Su Ayak İzi Değerlendirmesi. Turk Hij Den Biyol Derg 2017;74:55–62.

Dumont A, Salmoral G, Llamas MR. The Water Footprint of a River Basin With a Special Focus On Groundwater: The Case of Guadalquivir Basin (Spain). Water Resour Ind 2013;1–2:60–76. https://doi.org/10.1016/j.wri.2013.04.001.

Avanoz Z. Türkiye'de Tarımsal Üretimin Su Ayak İzinin Hesaplanması. 2020.

Kuzucu A. Seyhan Havzası'nda Kuraklığın Zamansal ve Alansal Değişiminin İncelenmesi 2016:123.

Karşılı C. Türkiye'de Akarsu Havzalarında Kişi Başına Düşen Su Miktarının Coğrafi Bilgi Sistemleriyle Analizi 2011.

Gürkan D. Seyhan Havzasında İklim Değişimlerinin Yüzeysel Su Kaynaklarına Olan Etkilerinin Araştırılması 2005.

Erdem E. Seyhan, Ceyhan ve Asi Havzalarında Tarımsal Su Ayak İzi Analizi 2021:6.

Chapagain a K, Hoekstra a Y. Water footprint of nations. Volume 1 : Main report. Value Water Res Rep Ser 2004;1:1–80.

Muratoğlu A. Assessment of water footprint of production: A case study for Diyarbakır province. J Fac Eng Archit Gazi Univ 2020;35:845–58. https://doi.org/10.17341/gazimmfd.543933.

Muratoglu A. Assessment of wheat's water footprint and virtual water trade: a case study for Turkey. Ecol Process 2020;9:1–16. https://doi.org/10.1186/s13717-020-0217-1.

Muratoglu A, Avanoz Z. Spatial Analysis of Blue and Green Water Footprints of Agricultural Crop Patterns: Turkey. Proc Inst Civ Eng Water Manag 2021;174:291–308. https://doi.org/10.1680/jwama.20.00085.

Mekonnen MM, Hoekstra A. The Relation Between National Water Management and International Trade: A case study for Kenya 2011.

14TH INTERNATIONAL CONFERENCE
ON HYDROSCIENCE & ENGINEERING

MAY 26-27, 2022
IZMİR-TURKEY

ICHE2022
IZMIR, TURKEY

INVESTIGATING THE CHEMICAL STATUS OF GROUNDWATER FOR IRRIGATION PURPOSES: A CASE STUDY FROM A GEOTHERMALLY POLLUTED AREA (ALASEHIR, TURKEY)

Onur Gungor Sahin

Department of International Water Resources, Izmir Institute of Technology

Izmir-Turkey

onursahin@iyte.edu.tr

Serhat Tonkul

Department of International Water Resources, Izmir Institute of Technology

Izmir-Turkey

serhattonkul@iyte.edu.tr

Orhan Gunduz

Department of International Water Resources, Izmir Institute of Technology

Izmir-Turkey

orhangunduz@iyte.edu.tr

ABSTRACT: Irrigated agriculture is an indispensable part of sustainable agricultural production for arid and semi-arid regions worldwide. It is typically made with groundwater, the quality of which is a function of complex processes that involves many physical and chemical factors. Geographic Information System (GIS) based indexes have been developed to evaluate the spatial distribution irrigation water quality This study is conducted in the Gediz basin located in western Turkey where approximately 86% of groundwater is used for agricultural purposes. The irrigation water quality (IWQ) index of the Alaşehir sub-basin in Gediz basin was calculated using the physical and chemical data obtained from different wells during 2018. The spatial distribution of index values was used to assess the agricultural water quality in the basin. IWQ index values were found to be above 37 in the eastern parts of the study area where irrigation water quality status was comparably high. In the central and western parts, water quality status was moderate, and IWQ index values ranged between 29.5 and 35. Due to the increasing number of geothermal power plants in the central and western parts of the basin in recent years, the groundwater in the region is exposed to the geothermal water contamination. Consequently, quality of groundwater was found to be less suitable for irrigation when compared to eastern parts of the basin.

Keywords: Irrigation Water Quality, Geospatial Assessment, Alaşehir, Turkey

1. INTRODUCTION

About one percent of the world's water resources consist of freshwater resources and are suitable for human consumption. Groundwater resources constitute a major part of this freshwater. Therefore, groundwater resources must be managed and protected wisely (Asadi et al., 2020). Irrigated agriculture is an indispensable part of sustainable agricultural production for arid and semi-arid regions worldwide as it uses a significant amount of water and has profound impacts on soil quality (Bozdağ, 2015).

Groundwater quality assessment is a very complex process involving many physical and chemical factors. Geographic Information System (GIS) based indexes have been developed to evaluate

irrigation water quality (IWQI) (Simsek & Gunduz, 2007; Islam et al., 2018). From a managerial point of view, many relevant physical and chemical water quality parameters need to be considered as a single variable to assess irrigation water quality and related hazards to soil properties. For these reasons, Simsek and Gunduz (2007) proposed a GIS-based method that evaluates the quality of irrigation waters with regards to potential soil and crop problems. GIS-based IWQ index developed by Simsek and Gunduz (2007) has been used in many studies in the literature (Ashraf et al. 2011; Khalaf and Hassan 2013; Bozdağ 2015; Jasmin and Mallikarjuna 2015; Towfiqul Islam et al. 2017; Islam et al. 2018; Romanelli et al. 2012; Asadi et al. 2020).The method proposed in this study is an application of the method developed by Gunduz and Simsek (2007) and considers five hazard groups: a) salinity hazard, b) infiltration and permeability hazard, c) specific ion toxicity, d) trace element toxicity, and e) miscellaneous effects on sensitive crops.

The Gediz basin is located in western Turkey and has an area of about 17000 square kilometers. Approximately 86% of groundwater extracted in the basin is used for agricultural purposes (Tonkul et al., 2019). The Alaşehir sub-basin of Gediz basin lies in the southeast-northwest direction between Alaşehir and Salihli. The total drainage area of the sub-basin is 2710.5 km². There are water scarcity and socio-economic problems in the Alaşehir sub-basin due to the wells drilled for agricultural purposes without permission as well as the geothermal installations for energy production (Tonkul et al., 2021). Tonkul et al. (2021) studied the groundwater status and the recharge potential of Alaşehir sub-basin. In this study, dozens of wells were drilled in Alaşehir sub-basin, and physicochemical monitoring were conducted from these wells to determine the quality of groundwater in Alaşehir sub-basin. Research indicated that groundwater and geothermal fluids mix in Alaşehir sub-basin and boron is found to be an indicator parameter for geothermal mixing into cold groundwater. Accordingly, it was found that the mixing in the area was in the order of %17.

Based on these fundamentals, the irrigation water quality index of the Alaşehir sub-basin was analyzed by using the physicochemical quality data obtained from different wells during the dry season of 2018. The calculated indexes for different hazard groups were interpolated in the GIS environment and the agricultural water quality maps of the basin were created. These are later merged to a single index value, which is used to investigate the irrigation water quality status of the basin.

2. STUDY AREA

The study area demonstrates a typical graben structure. The topographical elevation varies between 83 and 2155 m above mean sea level, and the wide Alaşehir plain is located at the lowest elevations (Fig. 1). The plain is surrounded by Bozdağ and Seyran mountains. There is overall southeast northwest directed drainage throughout the sub-basin. The drainage networks coming from the elevations surrounding the Alaşehir Plain are connected to the Alaşehir Stream in the plain and merged with the Gediz River in the northwest of the basin. There is Avşar Dam on Avşar Stream in the southwest of the study area, and Derbent Dam on Çamköy Stream in the south. Both dams are used as storage structures for agricultural irrigation waters. The western parts of the project area constitute higher areas than the eastern parts. For this reason, more frequent and deep drainage networks have developed in the western parts. The geological structure and structural features of the area control the development of drainage networks. Important settlement areas within the study area have developed in the alluvial Alaşehir plain.

The geological map of the study area is presented in Fig. 2. Pre-Miocene metamorphic rocks of the Menderes Massif form the basement rocks. The Miocene-Quaternary sedimentary filling of the basin consists of Alaşehir formation and current alluviums. Considering the general geological structure and sediment transport mechanism, it can be seen that coarse-grained soils are dominant in high topography areas, and fine-grained soils are dominant in flat areas with low topography. Coarse material can be transported and deposited in nearby areas, whereas fine material can be transported to farther points. Due to the geological structure of the study area, Neogene units generally provide fine-grained sediment units, while schists provide the formation of coarse-grained soils (Tonkul et al., 2019; Tonkul et al., 2021).
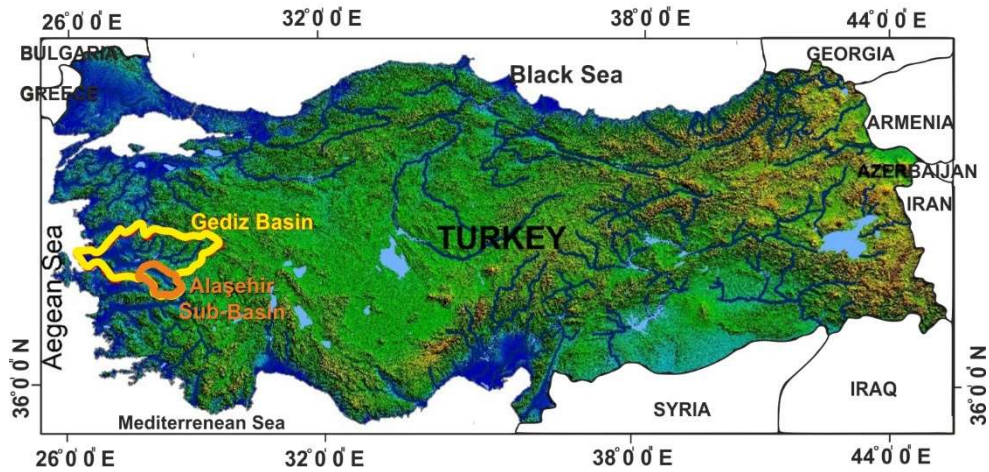
Figure 10. Location map of the study area (Tonkul et al., 2019)
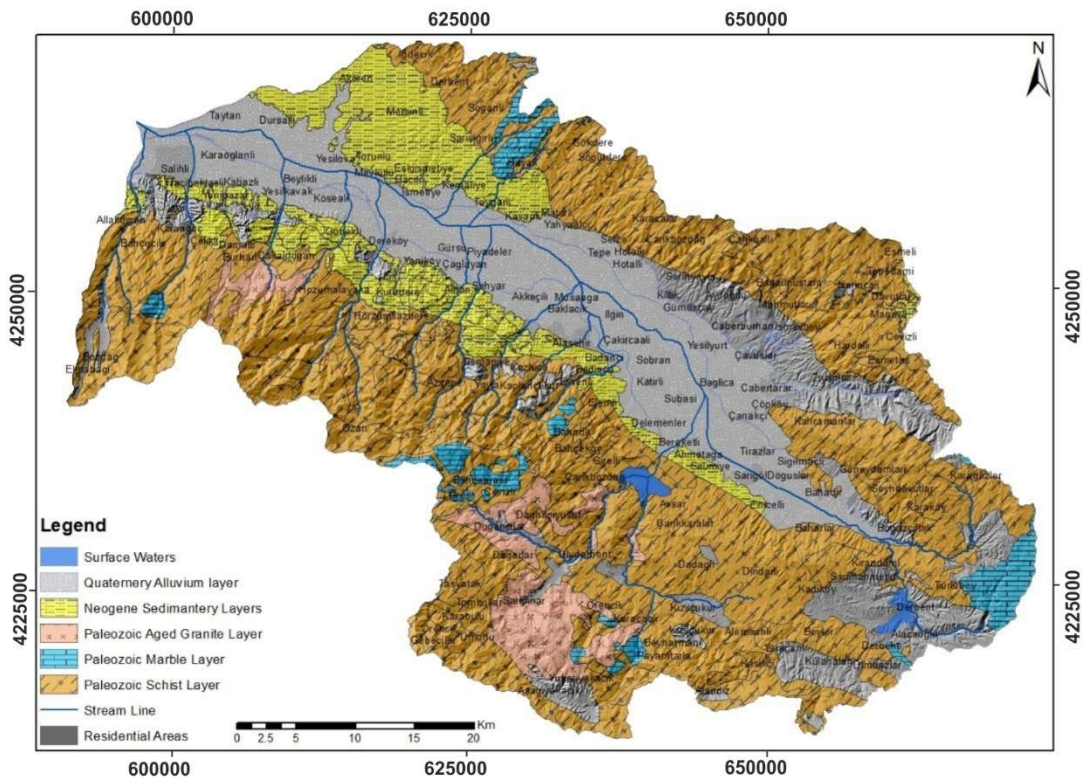
Figure 11. Geology map of the study area (Tonkul et al., 2019)

3. METHODOLOGY

The IWQ index proposed by Simsek and Gunduz (2007) is calculated by a linear combination of the five different groups of irrigation water quality parameters to assess the overall quality of waters for irrigation purposes. The IWQ index are calculated by Equation (1) where G represents hazard groups that effect water, soil, and water crop yield quality.

$$IWQ\ Index = \sum_{i=1}^{5} G_i \tag{1}$$

ArcGIS software of Environmental Systems Research Institute Inc (ESRI, 1999) was used to create the distribution maps. In this study, Inverse Distance Weighted (IDW) and Kriging interpolation methods were used to form these maps, both of which are preferred methods for generating grids by interpolation from sample point data. Before starting the analysis, the point-based water quality database is converted to grid datasets for each parameter. During this conversion, the cell size of grid datasets depends on the resolution of the point data.

3.1. Salinity Hazard

The salinity hazard is the expression of the activity of the sodium ion in the ion exchange reactions and is a general measure used in the classification of waters in terms of sodicity. The Salinity Hazard (G_1) is calculated by using the Electrical Conductivity (EC) values of the samples:

$$G_1 = w_1 \; x \; r_1 \tag{2}$$

where w is the weight factor and and r is the rating value. The weight factor of salinity hazard is 5. The value of the rating value changes with the EC value as shown in Table 1.

Table 2. Weight and ratings of first hazard group.

Weight	Parameter	Range	Rating	Suitability
5	Electrical conductivity ($\mu S/cm$)	$EC < 700$	3	High
		$700 \leq EC < 3000$	2	Medium
		$EC \geq 3000$	1	Low

3.2. Infiltration and permeability hazard

The second hazard group is the infiltration and permeability hazard, which can be calculated by using the Sodium Absorption Ratio (SAR) and EC. The weight and rating values of this group are given in Table 2.

$$G_2 = w_2 \; x \; r_2 \tag{3}$$

Table 3. Weight and ratings of second hazard group.

Weight		SAR					Rating	Suitability
		< 3	3–6	6–12	12–20	> 20		
4	EC	> 700	> 1,200	> 1,900	> 2,900	> 5,000	3	High
		700 − 200	1,200 − 300	1,900 −500	2,900 − 1,300	5,000 − 2,900	2	Medium
		< 200	< 300	< 500	< 1,300	< 2,900	1	Low

3.3. Specific Ion Toxicity

The third group represents the toxicity of specific ions. In this study, sodium (depicted by SAR value), chloride and boron values of samples are used to assess the specific ion toxicity. This group is calculated according to Equation (4) and the weight and rating values are given in Table 3.

$$G_3 = \frac{w_3}{3} \sum_{j=1}^{3} r_j \tag{4}$$

Table 4. Weight and ratings of third hazard group.

Hazard	Weight	Parameter	Range	Rating	Suitability
Specific ion toxicity	3	Sodium adsorption ratio (-)	SAR < 3.0	3	High
			3.0 ≤ SAR ≤ 9.0	2	Medium
			SAR > 9.0	1	Low
		Boron (mg/L)	B < 0.7	3	High
			0.7 ≤ B ≤ 3.0	2	Medium
			B > 3.0	1	Low
		Chloride (mg/L)	CI < 140	3	High
			140 ≤ CI ≤ 350	2	Medium
			CI > 350	1	Low

3.4. Trace Element Toxicity

Although Simsek and Gunduz (2007) used more than ten trace elements to compute trace element toxicity, only arsenic measurements were avaiable in Alaşehir basin. (Table 4). Therefore, the calculation of trace element toxicity is made according to Equation (5).

$$G_4 = w_4 \, x \, r_4 \tag{5}$$

Table 5. Weight and ratings of fourth hazard group.

Weight	Factor	Range	Rating	Suitability
2	Arsenic (mg/L)	$As < 0.1$	3	High
		$0.1 \le As \le 2$	2	Medium
		$As > 2$	1	Low

3.5. Miscellaneous Effects on Sensitive Crops

The fifth group is used to assess the impact of a variety of factors on the growth of sensitive crops. This group includes pH, bicarbonate ion, and nitrate–nitrogen and is calculated according to Equation (6). However, since nitrate-nitrogen measurements were not made in Alaşehir basin, the calculation of the fifth hazard group was modified to include only pH and bicarbonate ion. (Table 5). The weight and rating values of this group are given in Table 5.

$$G_5 = \frac{w_5}{2} \sum_{j=1}^{2} r_j \tag{6}$$

Table 6. Weight and ratings of fifth hazardous group.

Hazard	Weight	Parameter	Range	Rating	Suitability
Miscellaneous	1	Bicarbonate	$HCO_3 < 90$	3	High

effects to sensitive cops	(mg/L)		
		$90 \leq HCO_3 \leq 500$	2	Medium

		$HCO_3 > 500$	1	Low
	pH	$7.0 \leq pH \leq 8.0$	3	High
		$6.5 \leq pH < 7.0$ and $8.0 < pH \leq 8.5$	2	Medium
		$pH < 6.5$ or $pH > 8.5$	1	Low

Once the index values of all hazard groups are calculated, the IWQ index is calculated and analyzed according to the values given in Table 6.

Table 7. Suitability of water for irrigation based on IWQ index.

IWQ index	Suitability of water for irrigation
<22	Low
22-37	Medium
>37	High

3.6. Dataset

Physical and chemical data collected and used for calculation of IWQ index for Alaşehir sub-basin are presented in Table 7.

Table 8. Required Physical and Chemical Data.

Well ID	EC (μS/cm)	pH	T (°C)	Ca (mg/L)	Na (mg/L)	HCO₃ (mg/L)	Cl (mg/L)	As (mg/L)	B (mg/L)	Br (mg/L)
SK-1	2190	7.56	21.50	161.30	99.04	456.41	61.0	0.155	0.143	0.212
SK-2	2182	7.70	18.40	66.33	118.63	449.09	44.0	0.430	1.016	0.137
SK-3	1831	7.77	20.60	42.45	162.04	295.93	43.0	0.049	0.734	0.134
SK-5	2224	7.02	20.45	119.05	163.63	818.24	30.0	0.004	1.998	0.136
SK-6	8181	6.80	21.60	183.80	1287.00	4098.51	37.0	0.044	22.220	0.121
SK-7	1167	7.80	23.60	61.98	86.72	260.54	22.0	0.001	0.141	0.109
SK-8	2055	7.30	21.90	100.53	126.61	435.05	49.0	0.004	5.214	0.203
SK-9	1420	6.96	24.10	154.60	110.09	666.92	24.0	0.011	4.159	0.097
SK-10	1402	7.40	21.70	82.87	56.31	398.44	16.0	0.001	0.304	0.054
SK-11	3655	6.60	21.95	199.64	207.00	1360.68	71.0	0.002	2.020	0.293
SK-12	5451	6.80	21.80	254.00	196.00	1245.36	37.0	0.044	1.871	0.121
SK-13	1781	7.20	21.20	127.49	28.50	436.27	15.0	0.001	0.070	0.057
SK-14	1761	7.60	22.20	89.61	116.56	290.44	111.0	0.011	0.249	0.477
SK-19	1413	7.50	21.30	145.97	31.67	409.42	16.0	0.076	0.053	0.047
SK-20	1750	8.10	20.20	39.10	85.77	220.88	38.0	0.009	0.451	0.156
PM-1	1203	7.70	20.80	98.95	40.41	318.51	25.0	0.035	0.062	0.090
PM-2	1150	7.60	26.10	50.50	77.89	319.12	28.0	0.006	0.212	0.145
PM-5	1412	7.50	21.20	78.69	52.35	396.61	17.0	0.001	0.223	0.058
PM-6	2662	6.60	25.70	196.75	108.95	1156.27	17.0	0.001	2.599	0.059

MP-7	3998	6.40	22.60	326.19	72.29	1555.93	21.0	0.005	0.263	0.104
PM-8	1075	7.60	20.50	85.20	22.96	293.49	13.0	0.040	0.065	0.050
PM-9	1353	8.10	21.50	51.10	50.45	239.19	40.0	0.004	0.348	0.130
PM-10	2332	7.30	19.30	162.37	61.87	565.02	136.0	0.168	0.080	0.165
KM-1	1051	8.96	20.00	8.10	97.48	120.81	27.0	0.002	2.217	0.068
TRB	864	8.00	19.75	76.07	19.03	240.41	14.0	0.003	0.034	0.056
CPM2	2129	7.20	21.10	121.52	125.82	735.87	22.0	0.002	1.604	0.094
GURSU	435	8.70	20.00	10.76	28.58	73.22	9.0	0.044	0.369	0.034

4. RESULTS AND DISCUSSION

Ranking values were found using the necessary tables (Table 1, 2, 3, 4, and 5) for five different hazard groups, and IWQ index values were calculated by multiplying the ranking values for all wells with the weight coefficients of the hazard groups. Finally, a map containing IWQ values was created for the Alaşehir sub-basin in the 2018 dry period,

Based on the comparisons with the criteria given in Table 1, 2 of the 27 wells have high suitability, 21 have medium, and 4 have low suitability when EC values are evaluated. The electrical conductivity values are high between 2300-5000 $\mu S/cm$, exceeding the normal limits highly in the northwest region where the sixth well is located (Figure 3). The electrical conductivity values are generally at normal levels in other regions for the first hazard group. 24 of the 27 wells have high suitability for the second hazard group.

When pH values are evaluated, 24 of 27 wells have medium and high suitability. The basin waters has generally low suitability for bicarbonate ion and concentrations are not in the acceptable range for five hazard group (Figure 4).

Only arsenic values were used for the heavy toxic materials in the fourth hazard group in this study. 24 of 27 wells are suitable and arsenic concentration of the area in the acceptable ranges.

Boron is an important indicator and gives significant information about the mixing mechanism of geothermal fluid and groundwater. The boron concentration in geothermal waters can reach up to 127 mg/L and the highest concentration in the Alaşehir sub-basin. The boron concentrations in groundwater wells are between 0.04 and 22 mg/L and SK6 well has the highest value (Figure 5). Boron concentration exceeds the normal limits in the northwest region due to geothermal activities.

For the third hazard group, 23 of the 27 wells have high suitability, 3 of have medium, and 1 have low suitability when SAR values are used. Generally, it can be said that the SAR distribution of the basin is suitable for irrigation purposes. All wells have high suitability value for the chloride levels (Figure 6).

IWQ index values are above 37 in the east of the study area. Irrigation water status is qualitatively high in this region. In the central and western parts, water status is qualitatively at medium levels, and IWQ index values range between 29.5 and 35 (Figure 7).

Alaşehir basin is an important water basin with regards to not only agricultural production but also geothermal potential. Significant amounts of water are extracted from groundwater and used for irrigation purposes. Due to the increasing number of geothermal power plants in the region in recent years, the groundwater in the region is exposed to the geothermal water contamination. In fact, the SAR and EC values of groundwater are higher in the west-central part of the basin, where geothermal power plants are concentrated.
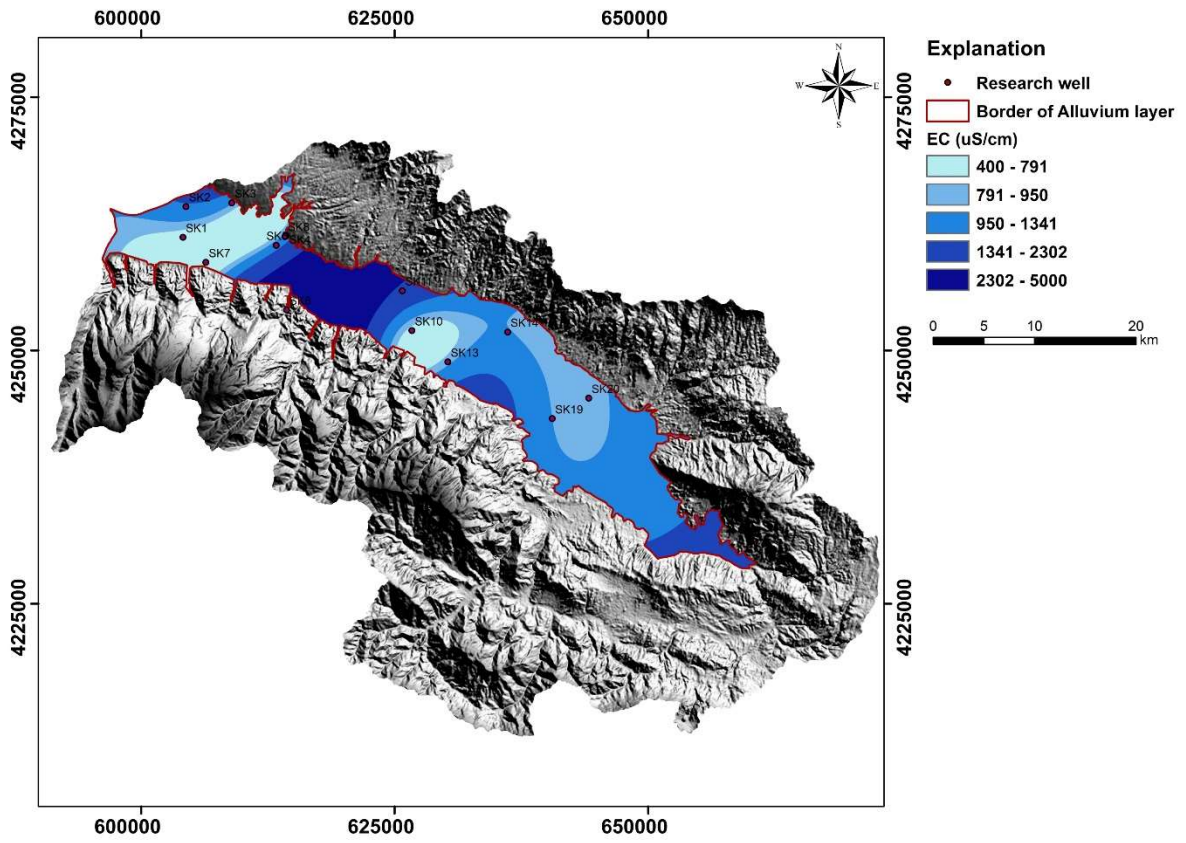
Figure 3. EC distribution map of the basin
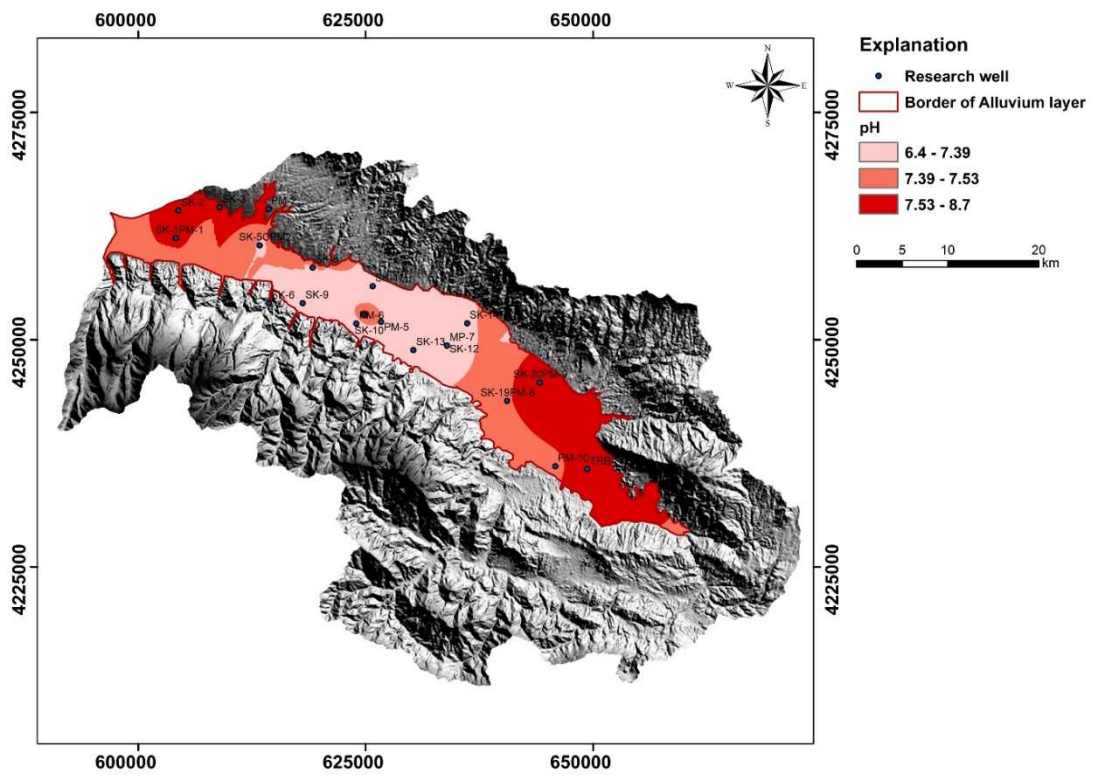
Figure 412. pH distribution of the basin
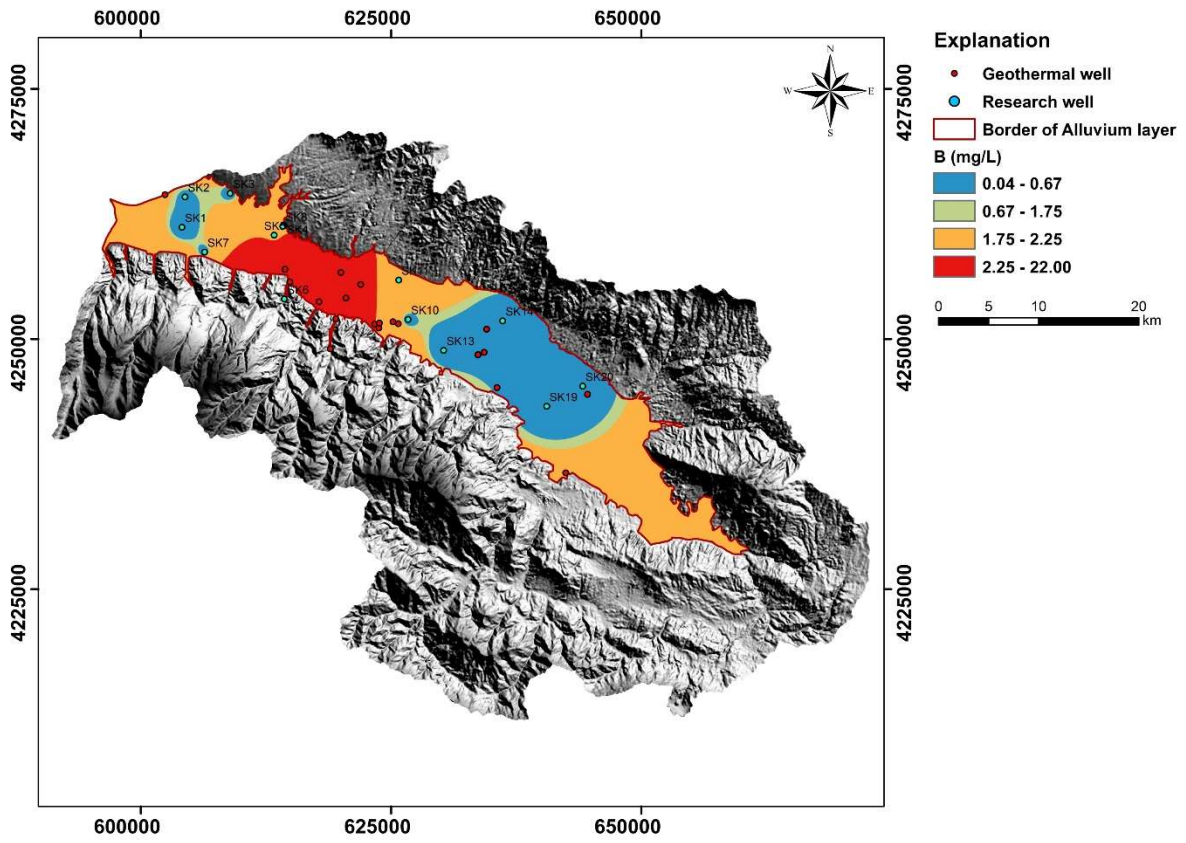
Figure 5. Boron distribution map of the basin
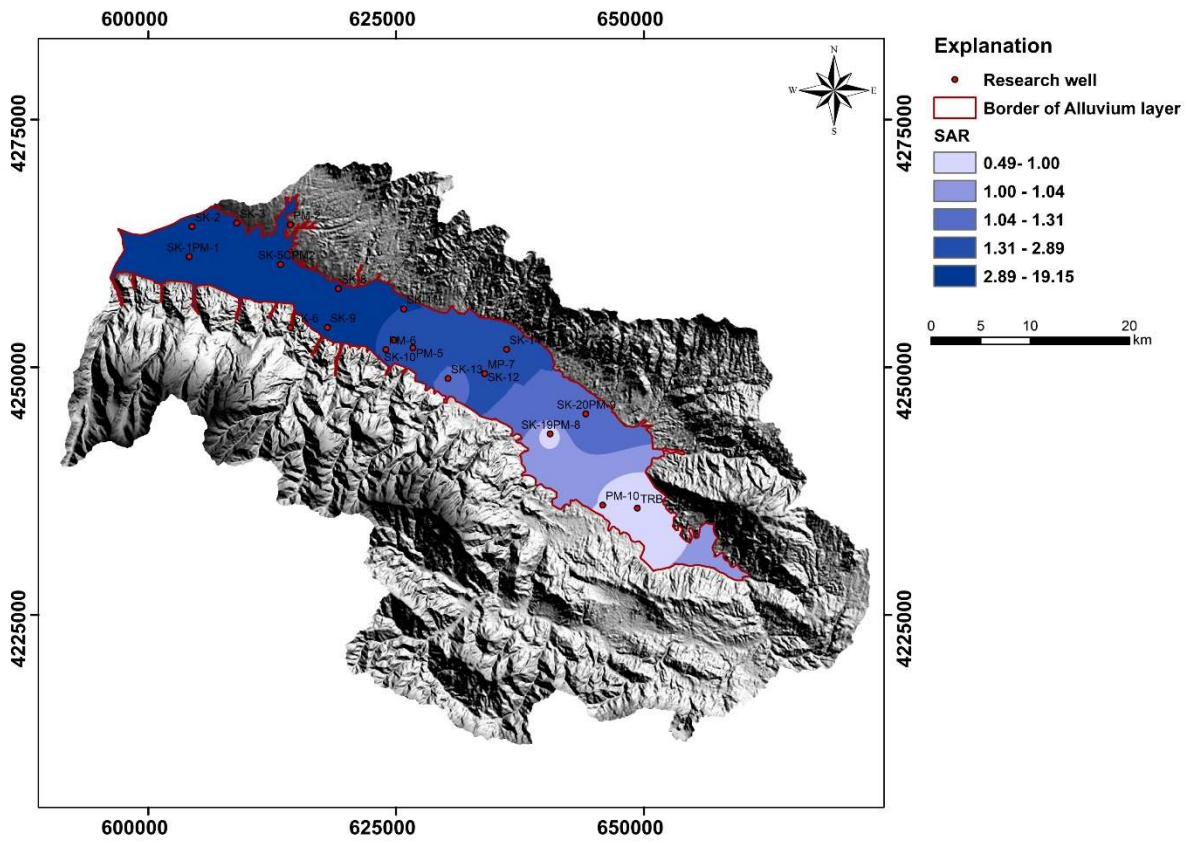
Figure 6. SAR distribution map of the basin
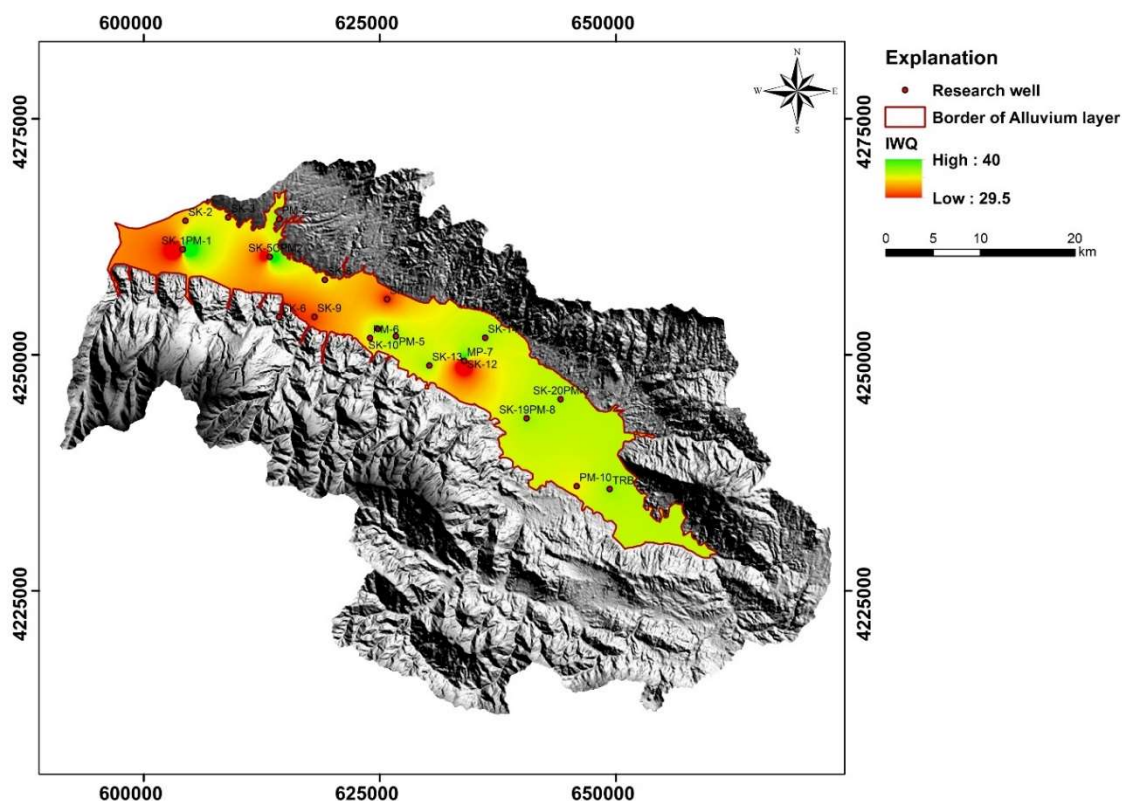
Figure 7. IWQ index values of Alaşehir sub-basin in dry period

5. CONCLUSION AND RECOMMENDATIONS

Groundwater quality assessment for irrigational purposes is a complex process involving many physical and chemical factors. Therefore, in the dry season of 2018, agricultural water quality assessment was made for the Alaşehir basin using the IWQ index.

Irrigation water status is qualitatively high in the east of the study area. In the central and western parts, water status is qualitatively at moderate levels. This situation shows that the groundwater quality is lower in the west-central part of the basin compared to other regions where geothermal waters mix with the groundwater. On the other hand, the increase in boron concentrations in groundwater in regions close to geothermal power plants is another indicator of mixing geothermal fluid with the groundwater. It can be said that the irrigation water quality will worsen with the increase in geothermal activities in the region in the future.

When the findings are evaluated, it is thought that it is necessary to carry out some studies to manage the quality of groundwater in the region. Accordingly, it is thought that preventing the mixing between hot and cold-water aquifers in the study area can significantly increase the groundwater quality. In addition, using treated wastewater for irrigation in the basin is another method that can reduce groundwater withdrawal and ensure aquifer sustainability.

REFERENCES

Asadi, E., Isazadeh, M., Samadianfard, S., Ramli, M. F., Mosavi, A., Nabipour, N., Shamshirband, S., Hajnal, E., & Chau, K. W. (2020). Groundwater quality assessment for sustainable drinking and irrigation. *Sustainability (Switzerland)*, *12*(1), 1–13. https://doi.org/10.3390/su12010177

Ashraf, M., Afzal, M., Ahmad, R., Ali, S., Shahzad, S. M., Aziz, A., & Ali, L. (2011). Growth and yield components of wheat genotypes as influenced by potassium and farm yard manure on a saline sodic soil. *Soil and Environment*, *30*(2), 115–121.

Ayers, R. S., & Westcot, D. W. (1985). Water Quality for Agriculture. FAO Irrigation and Drainage. In *FAO Irrigation and Drainage Paper: Vol. No.29*.

Bozdağ, A. (2015). Combining AHP with GIS for assessment of irrigation water quality in Çumra irrigation district (Konya), Central Anatolia, Turkey. *Environmental Earth Sciences*, *73*(12), 8217–8236. https://doi.org/10.1007/s12665-014-3972-4

ESRI. (1999). Getting to know ArcView (3th Edition)*, California, ESRI.*

Islam, M. A., Rahman, M. M., Bodrud-Doza, M., Muhib, M. I., Shammi, M., Zahid, A., Akter, Y., & Kurasaki, M. (2018). A study of groundwater irrigation water quality in south-central Bangladesh: a geo-statistical model approach using GIS and multivariate statistics. *Acta Geochimica*, *37*(2), 193–214. https://doi.org/10.1007/s11631-017-0201-3

Jasmin, I., & Mallikarjuna, P. (2015). Evaluation of Groundwater Suitability for Irrigation in the Araniar River Basin, South India-A Case Study Using Gis Approach. *Irrigation and Drainage*, *64*(5), 600–608. https://doi.org/10.1002/ird.1930

Khalaf, R. M., & Hassan, W. H. (2013). Evaluation of Irrigation Water Quality Index (Iwqi) for Al-Dammam Confined Aquifer in the West and Southwest of Karbala City, Iraq. *International Journal of Civil Engineering (IJCE)*.

Romanelli, A., Lima, M. L., Londoño, O. M. Q., Martínez, D. E., & Massone, H. E. (2012). A Gis-based assessment of groundwater suitability for irrigation purposes in flat areas of the wet pampa plain, Argentina. *Environmental Management*, *50*(3), 490–503. https://doi.org/10.1007/s00267-012-9891-9

Simsek, C., & Gunduz, O. (2007). IWQ Index: A GIS-integrated technique to assess irrigation water quality. *Environmental Monitoring and Assessment*, *128*(1–3), 277–300. https://doi.org/10.1007/s10661-006-9312-8

Tonkul, S., Baba, A., Şimşek, C., & Demirkesen, A. C. (2021). Groundwater recharge estimation in the Alaşehir sub-basin using hydro-geochemical data; Alaşehir case study. *Environmental Earth Sciences*, *80*(7), 1–19. https://doi.org/10.1007/s12665-021-09543-4

Tonkul, S., Baba, A., Şimşek, C., Durukan, S., Demirkesen, A. C., & Tayfur, G. (2019). Groundwater recharge estimation using HYDRUS 1D model in Alaşehir sub-basin of Gediz Basin in Turkey. *Environmental Monitoring and Assessment*, *191*(10), 1–19. https://doi.org/10.1007/s10661-019-7792-6

Towfiqul Islam, A. R. M., Shen, S., Bodrud-Doza, M., & Safiur Rahman, M. (2017). Assessing irrigation water quality in Faridpur district of Bangladesh using several indices and statistical approaches. *Arabian Journal of Geosciences*, *10*(19). https://doi.org/10.1007/s12517-017-3199-2

14TH INTERNATIONAL CONFERENCE
ON HYDROSCIENCE & ENGINEERING

MAY 26-27, 2022
IZMİR-TURKEY

ICHE2022
IZMIR, TURKEY

ESTIMATING THE WATER FOOTPRINT OF ELECTRICITY IN ARTIFICIAL RESERVOIRS: A CASE STUDY FOR ATATURK DAM

Abdullah Muratoglu (Corresponding Author)

Civil Engineering Department, Batman University,

Batman, Turkey

abdullah.muratoglu@batman.edu.tr

Zehra Sakinc

Civil Engineering Department, Gaziantep University

Gaziantep, Turkey

zehrasakinc@outlook.com

M. Ishak Yuce

Civil Engineering Department, Gaziantep University

Gaziantep, Turkey

yuce@gantep.edu.tr

Ali Aytek

Civil Engineering Department, Gaziantep İslam Bilim ve Teknoloji University

Gaziantep, Turkey.

ali.aytek@gmail.com

ABSTRACT: Artificial reservoirs are constructed to store water for electricity production, agricultural irrigation, flood mitigation and water supply to domestic and industrial sectors. In the last two centuries, artificial reservoirs have successfully provided water and energy to various part of the world. However, due to climate change and high rate of use and pollution of existing resources, many scientists expect critical water and energy deficiencies and disputes in the future. Accordingly, the environmental impacts and sustainability of these resources become quite important. Water footprint (WF) methodology is one of the mostly preferred and influential tools to reveal the anthropogenic effects on water resources. Its methodology has been recently developed and applied to the hydrological basins, production and consumption of nations, agricultural products, etc. However, the WF of artificial reservoirs especially for the energy production is quite less studied, especially in Turkey. In this study, the WF of the Ataturk dam has been analyzed for hydroelectric energy production. The monthly (open water surface) evaporation amounts were estimated employing widely used Penman model. The monthly and annual virtual water behind the hydroelectricity production has been analyzed for seven years between 2012–2018.The average annual WF of Ataturk reservoir has been obtained as 1538 million m^3 (2012-2018). The WF of electricity generation has been calculated as 57.1 m^3/GJ or 0.205 m^3/kWh. The surface area and thus the evaporation represented a decreasing trend. Monthly changes in the virtual water behind the electricity generation has also been detailed for the study period. Consequently, this study is expected to contribute to management of water resources by quantifying the evaporation losses in the artificial reservoirs and to reveal the environmental impacts of hydroelectricity production.

Key words: blue, water, footprint, hydropower, electricity, evaporation

1. INTRODUCTION

Water footprint (WF) is a comprehensive tool or indicator of sustainable environmental management. The basic principles of the WF methodology have been put by Hoekstra et al. (2011) and the method has been standardized by ISO 14046 (2017). There have been many literature studies on the WF of agriculture (Mekonnen & Hoekstra, 2011a), nations (Hoekstra & Chapagain, 2007; Muratoglu & Avanoz, 2021), hydrological basins (Muratoglu, 2019), cities (Feng et al., 2017) and industry (Hoekstra, 2015), etc. On the other hand, WF of energy due to bio diesel and ethanol production have been analyzed by Elena & Esther (2010), Gerbens-Leenes & Hoekstra (2009). Mekonnen & Hoekstra (2011b and 2012) conducted the initial systematic research on the WF of hydropower production. The main scope of this study is to calculate the WF of Ataturk Dam, Turkey. The virtual water behind the hydroelectric energy production has been analyzed using the WF methodology and Penman method of open surface evaporation.

2. MATERIALS AND METHOD

2.1. Study Area

Ataturk dam (Figure 1) is the largest HEPP and artificial reservoir of Turkey. It is a rock fill and earth fill dam having around 84.5 million m^3 dam volume asof the world's largest earth fill dam (Britannica, 2022). The reservoir is located at the Southeastern region of Turkey. The dam has been constructed on Euphrates River for the energy production and agricultural irrigation. The total power capacity is 2300 MW consisting of 8 turbines (AD, 2022). The dam is the most important unit of the Southeastern Anatolian Project (GAP, in Turkish acronym). In 2010, around 22 % of national electricity demand is generated by Ataturk HEPP (NASA, 2022).
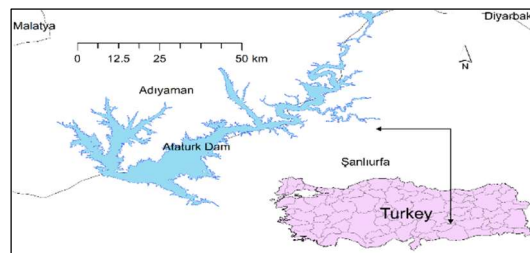
Figure 1. The location and reservoir of Ataturk dam

2.2. Data

The monthly reservoir surface area (km^2) value has been obtained from the GRSAD, Global Reservoir Surface Area Dataset (Gao & Zhao, 2019). The monthly meteorological data have been received from Turkish State Meteorological Service (TSMS, 2021). Due to the missing data of nearby stations, the meteorological station of Bozova has been used. The monthly average energy production capacity of the Ataturk dam has been derived from the Lower Euphrates Basin Master Plan (MAF & TSHW, 2017). The energy production of various months across different years were reported to be quite close where the imbalances were smaller than 1 %. Also, no data were reported for the years after 2014. Therefore, the average monthly energy production capacity has been assumed to be constant for each year and the average data of 2012 and 2013 is employed. On the other hand, the albedo coefficient of the open water surface and shortwave radiation coefficients have been obtained from Allen et al. (1998) and McMahon et al.(2013).

2.3. Method

In this study the evaporation from the open water surface has been estimated using the Penman methodology. The equations have been basically followed from the supplementary file that is provided by McMahon et al. (2013). If the equations do not fit the specifications of the data within the scope of this study, the specific equations have been preferred which are reported by FAO (Food and

Agriculture Organization of the United Nations), Guidelines for computing crop water requirements (Allen et al., 1998). Accordingly, the Penman method estimates, the evaporation is written as radiative and aerodynamic components (Equation 1).

$$E_0 = \underbrace{\frac{\gamma}{\Delta + \gamma}(E_a)}_{\text{Aerodynamic component}} + \underbrace{\frac{\Delta}{\Delta + \gamma}(R_{nw}/\lambda)}_{\text{Radiative component}} \qquad (1)$$

where, E_0 (mmday^{-1}) is the daily evaporation, R_{nw} (MJm^{-2}day^{-1}) is the net radiation at the water surface, E_a (mmday^{-1}) is a function of wind speed, saturation vapour pressure and average vapour pressure, Δ (kPaC^{-1}) is the slope of the vapour pressure curve, γ (kPaC^{-1}) is the psychrometric constant, λ (MJkg-1) is the latent heat of vaporization. The E_a term is modeled using the wind function and vapour pressure deficit in Equation 2. The WF of hydropower is calculated as the ratio of total evaporative water loss to the amount of energy generated as in Equation 2.

$$WF = \frac{V}{E} \qquad (2)$$

where, the WF (m^3/kWh=277.78 m^3/GJ) is the water footprint, V (m^3) is the evaporated water volume and E (kWh of GJ) is the produced energy.

3. RESULTS and DISCUSSION

The monthly, annual and average water footprint of electricity generation of Ataturk HEPP has been listed in Table 1. The annual WF of the hydroelectricity in Karakaya dam which is located on the very upstream side of the Ataturk dam is reported as 21.8 m^3/GJ (Mekonnen & Hoekstra, 2012). To the authors, the larger evaporation rates are associated to the differences in climatic conditions and reservoir area characteristics. Accordingly, the average WF of energy production in Ataturk dam is obtained around 2.6 times than that of Karakaya dam. In this study, the average annual evaporation height of the Ataturk Dam is estimated around 2042 mm which is reported as 1920 mm for Karakaya reservoir (Mekonnen & Hoekstra, 2012).

Table 1. WF of electricity generation in Ataturk Dam in m^3/GJ. Please divide by 277.8 to convert into m^3/kWh.

Year/Month	Jan	Feb	Mar	Apr	May	Jun	Jul	Aug	Sept	Oct	Nov	Dec	Annual
2012	13.1	25.5	38.9	64.7	85.6	93.1	92.0	93.7	84.1	48.7	22.0	14.3	59.3
2013	15.8	21.8	43.8	60.3	80.6	93.8	97.3	92.6	80.4	58.3	26.5	17.1	60.4
2014	17.2	30.6	43.3	61.0	90.6	89.0	92.3	87.2	74.7	44.8	23.3	12.3	58.3
2015	13.5	17.4	34.4	51.2	86.7	84.7	92.3	87.4	79.7	47.0	29.9	21.9	56.6
2016	15.1	26.6	47.4	68.7	87.9	88.3	90.4	85.8	73.6	51.9	24.6	14.6	58.9
2017	15.8	27.1	36.6	52.0	79.1	84.0	86.0	77.3	75.7	50.8	23.8	17.5	54.6
2018	17.1	19.5	40.9	57.4	67.7	72.6	77.6	85.1	74.6	46.7	18.5	10.7	51.5
Average	15.3	24.1	40.8	59.3	82.6	86.5	89.7	87.0	77.6	49.7	24.1	15.5	57.1

The evaporation volume and reservoir surface area for each month through 2012-2018 (seven years) is illustrated in Figure 2. A decreasing trend in the surface area is exhibited which directly effects the evaporation rates. The limitations of this study can be illustrated as below: Dam reservoirs usually used for multi purposes such as hydroelectric power production, agricultural irrigation, domestic & industrial water supply, flood control, recreation and other minor purposes. In this study, only the hydroelectric energy production of the study area is considered. Water allocation for other sectors is neglected. On the other hand, the WF of construction materials and construction process is not included. Finally, due to lack of data, we relied on the meteorological data of single station. Continuous spatial maps of meteorological data would deliver more accurate results.
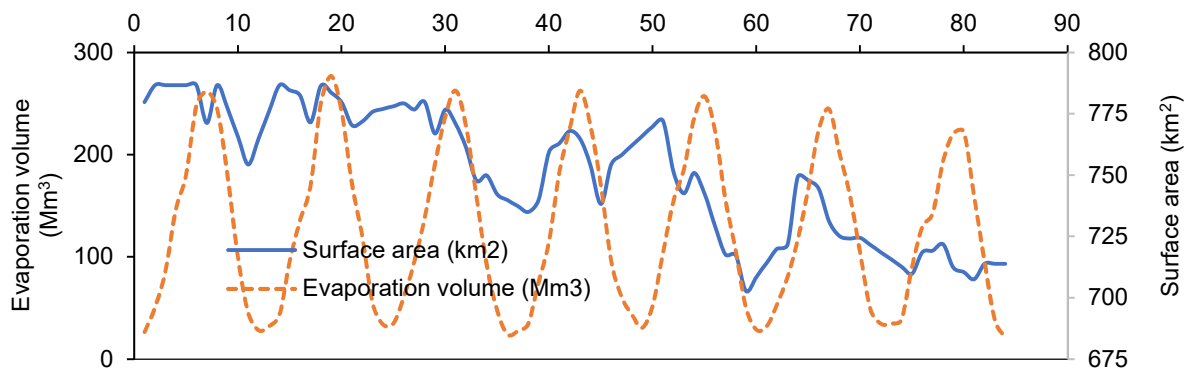
Figure 2. Monthly total evaporation volume and surface area of the Ataturk Dam for 2012-2018

4. CONCLUSION

The virtual water concept has gained more importance in the last decades due to the water scarcity problems. Artificial reservoirs are considered one of the most important engineering structures having direct impacts on the water and energy resources. However, there have been insufficient number of studies using the virtual water approach or WF analyses on traditional HEPPs or artificial reservoirs. In this study, the virtual water behind the hydropower production of Ataturk dam has been analyzed using the WF methodology and Penman equation for open surface evaporation. The monthly variations in the evaporation rates and WF outputs have been illustrated. Further studies may include the comparison of impacts of artificial reservoirs on the water resources and discussing possible solutions to decrease the WF of energy generation.

ACKNOWLEDGMENTS

REFERENCES

AD. (2022). *Ataturk Dam*. http://www.ataturkbaraji.com/tr

Allen, R. G., Pereira, L. S., Raes, D., & Smith, M. (1998). Crop evapotranspiration: Guidelines for computing crop water requirements (FAO Irrigation and Drainage paper No: 56). In *FAO*. https://doi.org/10.1016/j.eja.2010.12.001

Britannica. (2022). *Ataturk Dam*. https://www.britannica.com/topic/Ataturk-Dam

Elena, G.-C., & Esther, V. (2010). From water to energy: The virtual water content and water footprint of biofuel consumption in Spain. *Energy Policy*, *38*(3), 1345–1352. https://doi.org/10.1016/J.ENPOL.2009.11.015

Feng, L., Hayat, T., Alsaedi, A., & Ahmad, B. (2017). The driving force of water footprint under the rapid urbanization process: a structural decomposition analysis for Zhangye city in China. *Journal of Cleaner Production*, *163*, S322–S328. https://doi.org/10.1016/J.JCLEPRO.2015.09.047

Gao, H., & Zhao, G. (2019). *Global Reservoir Surface Area Dataset (GRSAD) - Huilin Gao Dataverse*. https://doi.org/10.18738/T8/DF80WG

Gerbens-Leenes, P. W., & Hoekstra, Arjen. Y. (2009). *The water footprint of sweeteners and bio-ethanol from sugar cane, sugar beet and maize*. https://waterfootprint.org/media/downloads/Report38-WaterFootprint-sweeteners-ethanol_1.pdf

Hoekstra, A. Y. (2015). Chapter 7 - The water footprint of industry. In J. J. Klemeš (Ed.), *Assessing and Measuring Environmental Impact and Sustainability* (pp. 221–254). Butterworth-Heinemann. https://doi.org/https://doi.org/10.1016/B978-0-12-799968-5.00007-5

Hoekstra, A. Y., & Chapagain, A. K. (2007). Water footprints of nations: Water use by people as a function of their consumption pattern. *Water Resources Management*, *21*(1), 35–48. https://doi.org/10.1007/s11269-006-9039-x

Hoekstra, A. Y., Chapagain, A. K., Aldaya, M. M., & Mekonnen, M. M. (2011). The Water Footprint Assessment Manual. In *Water Footprint Network*. https://doi.org/978-1-84971-279-8

ISO 14046. (2017). *Environmental Management, Water Footprint, A practical Guide for SMEs*. https://www.iso.org/obp/ui/#iso:std:iso:14046:ed-1:v1:en

MAF, & TSHW. (2017). *Lower Euphrates Basin Master Plan*.

McMahon, T. A., Peel, M. C., Lowe, L., Srikanthan, R., & McVicar, T. R. (2013). Estimating actual, potential, reference crop and pan evaporation using standard meteorological data: a pragmatic synthesis. *Hydrology and Earth System Sciences*, *17*(4), 1331–1363. https://doi.org/10.5194/hess-17-1331-2013

Mekonnen, M. M., & Hoekstra, A. Y. (2011a). The green, blue and grey water footprint of crops and derived crop products. *Hydrology and Earth System Sciences*, *15*(5), 1577–1600. https://doi.org/10.5194/hess-15-1577-2011

Mekonnen, M. M., & Hoekstra, A. Y. (2011b). *The water footprint of electricity from hydropower*. UNESCO-IHE Institute for Water Education. Value of Water Research Report Series No.51.

Mekonnen, M. M., & Hoekstra, A. Y. (2012). The blue water footprint of electricity from hydropower. *Hydrology and Earth System Sciences*, *16*(1), 179–187. https://doi.org/10.5194/hess-16-179-2012

Muratoglu, A. (2019). Water footprint assessment within a catchment: A case study for Upper Tigris River Basin. *Ecological Indicators*, *106*, 105467. https://doi.org/https://doi.org/10.1016/j.ecolind.2019.105467

Muratoglu, A., & Avanoz, Z. (2021). Spatial analysis of blue and green water footprint of agricultural crop pattern in Turkey. *Proceedings of the Institution of Civil Engineers - Water Management*, *174*(6), 291–308. https://doi.org/https://doi.org/10.1680/jwama.20.00085

NASA. (2022). *Ataturk Dam*. https://earthobservatory.nasa.gov/images/3796/ataturk-dam

TSMS. (2021). *Turkish State Meteorological Service*. https://www.mgm.gov.tr/genel/hidrometeoroloji.aspx?s=5

14TH INTERNATIONAL CONFERENCE
ON HYDROSCIENCE & ENGINEERING
MAY 26-27, 2022
IZMİR-TURKEY

ICHE2022
IZMIR, TURKEY

EVALUATION OF GREEN ROOF MODELING PERFORMANCE OF EPA SWMM AND AN IMPROVED EQUATION FOR GREEN ROOF DRAINAGE FLOW

First Author: Kavsar Bako

Civil Engineering Department, Istanbul University-Cerrahpaşa

Avcılar, Istanbul, 34320, Turkey

kavsar.bako@ogr.iuc.edu.tr

Second Author: Cevza Melek Kazezyılmaz-Alhan

Civil Engineering Department, Istanbul University-Cerrahpaşa

Avcılar, Istanbul, 34320, Turkey

meleka@istanbul.edu.tr

ABSTRACT: Green roofs are among important green infrastructures which decrease negative impacts of urbanization. In this study, first, sensitivity analyses are performed using the EPA Storm Water Management Model (SWMM) to identify the design parameters which influence the green roof hydrological performance. Next, the methodology used in EPA SWMM Green Roof Module for green roof modeling is evaluated, and thereby, the issues, which need improvements, are determined. Then, an improved equation for the drainage mat model is developed which calculates the drainage flow. Finally, the SWMM model results and results of the improved equation are compared with experimental data. Based on the comparisons, the results of improved equation are in better agreement with the experimental data than the results of EPA SWMM.

Keywords: Green Roof, Low Impact Development, EPA SWMM, Hydrologic Model, Drainage Mat

1. INTRODUCTION

The increase in impervious surfaces and the decrease in green spaces due to the urbanization have negative effects on the ecological system and the natural hydrological cycle. In urban areas, storm water runoff peak increases on impervious surface, which may result in flooding events. To reduce the negative impacts of urbanization and preserve the natural hydrological cycle, "Low Impact Development (LID)" practices also known as "Green Infrastructure" are introduced for storm water management. Green roofs, which are evaluated within the scope of this study, are a popular type of LID practices. Green roofs typically consist of three main layers: Drainage layer, soil layer for growing plants and surface layer for vegetation. Based on the properties of these layers, green roofs are able to store rainwater, decelerate the drainage flow, and reduce the peak flow. Based on the thickness of the soil layer, there are two types of green roofs: intensive and extensive. Intensive green roofs have deep soil layer and variety of plantings whereas extensive green roofs typically have shallower soil layer, require less maintenance (Oberndorfer et al. 2007).

Green roof performance has been evaluated in various experimental and modeling studies. Computer models can be used to make quick assessments for green roofs to evaluate environmental impacts at various scales (Li & Babcock 2014). The United States Environmental Protection Agency (EPA) Stormwater Management Model (SWMM), one of the most widely used software, is used for green roof hydrology simulations (Li and Babcock 2014). In recent years, different studies have evaluated the hydrological performance of green roofs using SWMM's green roof module. Peng et al. (2017)

used data from a previously monitored extensive green roof test bed to evaluate the accuracy of the SWMM green roof module for modeling an extensive green roof for both long-term and short- term simulations. According to the results of this study, the green roof modeling capacity of SWMM is significantly limited. Abualfaraj et al. (2018) simulated a green roof with the potential evapotranspiration adjusted according to the moisture content of the soil during continuous rainfall with SWMM green roof module. Palla et al. (2018) presented a methodological approach to estimate the actual evapotranspiration as climate input data in continuous simulation with SWMM.

For accurate simulations of green roofs, the programs used should be continuously developed and their accuracy should be tested. In this study, the green roof modeling capacity of SWMM is investigated. Improvement is suggested by developing a drainage flow equation for green roofs.

2. MATERIALS AND METHODS

2.1. SWMM Green Roof Module

SWMM is a dynamic rainfall-runoff simulation model that models processes such as evaporation, infiltration, groundwater movements, and LID applications, and provides performance estimates on water quantity and quality (Rossman 2015). In SWMM green roof module, the infiltration of surface water into the soil layer, f_1, is modeled with the Green-Ampt equation. The rate of percolation of water through the soil layer into the drainage layer f_2 is modeled using Darcy's Law. The runoff rate over the soil layer surface q_1 and the drainage mat flow rate q_3 are computed using the Manning equation.

2.2. Sensitivity Analysis

Sensitivity analysis is performed for the parameters of the equations used by SWMM in green roof modeling. First, ranges for each parameter are determined based on the former studies. The average value of each parameter is used in the reference green roof. The green roof runoff and drainage flow are calculated with EPA SWMM using the reference, minimum and maximum values for each parameter and results are compared in order to determine the effective parameters.

2.3. Drainage Flow Equation Development

In SWMM, the drainage mat flow is modeled by the Manning equation. However, (Peng et al. 2017) emphasized that this model does not accurately simulate the hydrological behavior of the drainage mat. Therefore, in this study, the drainage mat flow equation is improved.

After drainage mat receives water from the top layer, first, some water is stored in its voids. When the storage capacity is full, the drainage flow starts. Finally, when the flow is over, the stored water is evaporated. However, SWMM does not take the storage capacity of the drainage mat into account. Therefore, in this study, an additional variable Ds_3, which represents the storage capacity of the drainage mat, is proposed for the Manning equation (Equation 1). Then, the improved drainage flow equation is tested using the results of former experimental studies.

$$W_1/A_1 = \frac{1}{L} \rightarrow q_3 = \frac{c}{n_3} s^{\frac{1}{2}} \frac{1}{L} \emptyset_3 (d_3 - Ds_3)^{5/3} \tag{1}$$

Where q_3 is the drainage flow rate, L is the drainage length of the layers, c coefficient depends on the units, s is surface slope (m/m), ϕ_3 is void fraction of the drainage mat, d_3 is depth of water in the drainage mat (m), W_1 is the total length along edge of the roof where runoff is collected (m), A_1 is the roof surface area (m^2), n_3 is a roughness coefficient for the mat. Vesuviano (2014) tested different types of drainage mat for different drainage length and surface slope conditions. Using precipitation data, the drainage flow calculated with different depth exponent values are compared with the measured flow values, and an improved value for a is determined.

$$q_3 = \frac{c}{n_3} s^{\frac{1}{2}} \frac{1}{L} \emptyset_3 (d_3 - Ds_3)^{a} \tag{2}$$

2.4. SWMM Green Roof Model Calibration

In this part of study studies the data of the experiments from Sims et al. (2019) and Peng et al. (2019) are compared with the results of SWMM and improved equation. For this purpose, the green roof, which was used in both experimental studies, is modeled with SWMM; the design parameters provided in these studies are used in the SWMM model and the ones, which are not provided, are calibrated. Percolation and drainage flow rates are obtained with SWMM, and the percolation rate obtained from SWMM is used as input for the improved equation and the drainage flow is calculated with the improved equation. Finally, the drainage flow calculated with SWMM, the drainage flow calculated with the improved equation and the measured drainage flow are compared.

3. RESULTS

3.1. Sensitivity Analysis

After sensitivity analyses, the effective parameters on the stormwater retention performance are determined as field capacity, wilting point and soil thickness. The detention performance shows better results with small hydraulic conductivity, large porosity, large conductivity slope, large drainage mat roughness, large drainage mat void ratio and small slope values. In the low permeable soil condition, green roof shows higher performance with the large storage depth of the surface layer, small vegetation volume ratio, large surface roughness and small slope values.

3.2. Improved Drainage Flow Equation

The depth exponent a is determined as 2. The unit of the new c coefficient of the equation becomes (1/s). Thus, the Manning equation, which was written in a different form by giving different values to the coefficient c for the SI unit system and the English unit system, can be given with a more general expression as follows:

$$q_3 = \frac{1}{n_3} s^{\frac{1}{2}} \frac{1}{L} \emptyset_3 (d_3 - Ds_3)^2 \qquad (3)$$

The comparison of the results show that the drainage flow calculated with the improved equation is in better agreement with the measured data than the one calculated with the Manning's equation (Figure 3.1).
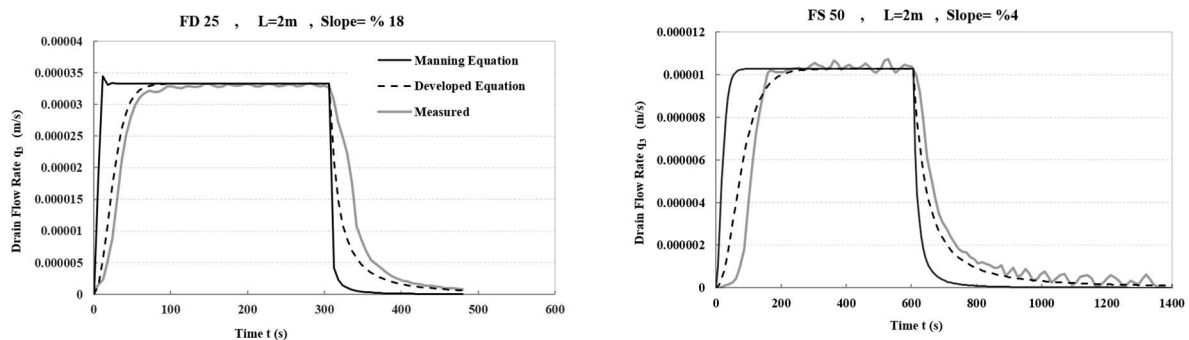
Figure 1. Comparison of the measured drainage flow for different drainage mat types and the calculated drainage flows using Manning and the improved equation.

Linear regression was performed using eight Experiments data and the mean correlation coefficient was calculated as $R^2 = 0.69$ for Manning's equation and $R^2 = 0.95$ for the improved equation.

3.3. SWMM green roof model calibration

When the drainage flow calculated with the improved equation, the drainage flow calculated with the SWMM and the measured drainage flow are compared, the results with both calculation methods are in good agreement with the measured data. However, but the drainage flow calculated with the improved equation is in better agreement with the measured data (Figure 3.2).
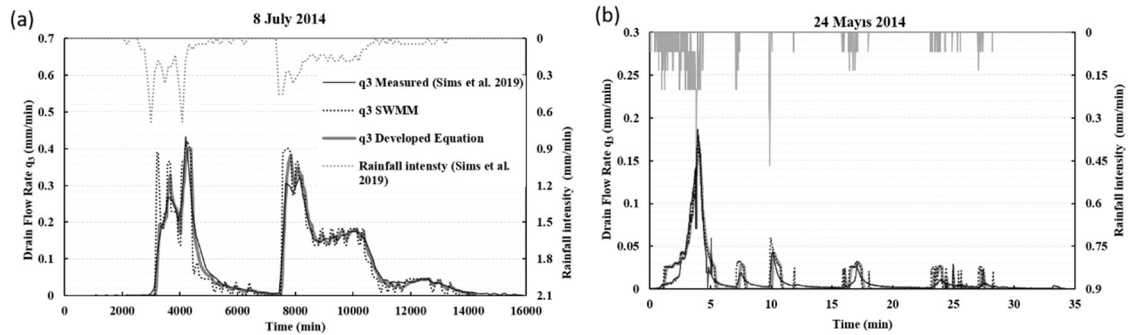
Figure 2. Time-series rainfall, drainage flow for events (a) from (Sims et al. 2019), (b) from (Peng et al. 2019)

Linear regression is performed using seven experiments data and the mean correlation coefficient was calculated as $R^2= 0.73$ for SWMM and $R^2= 0.8$ for the improved equation.

4. CONCLUSIONS

In this study, SWMM performance capacity on green roof modeling is evaluated. The effective green roof parameters are determined via sensitivity analyses. Then, an equation, which represents the drainage mat flow more accurately, is developed. Comparison of the results show that the drainage flow obtained with the improved equation give closer results to the experimental findings than the drainage flow obtained with the Manning equation.

REFERENCES

Abualfaraj, N., Cataldo, J., Elborolosy, Y., Fagan, D., Woerdeman, S., Carson, T., ve Montalto, F., 2018, Monitoring and Modeling the Long-Term Rainfall-Runoff Response of the Jacob K. Javits Center Green Roof, *Water*, 10 (11), 1494.

Li, Y. ve Babcock, R.W., 2014, Green roof hydrologic performance and modeling: a review, *Water Science and Technology*, 69 (4), 727–738.

Oberndorfer, E., Lundholm, J., Bass, B., Coffman, R.R., Doshi, H., Dunnett, N., Gaffin, S., Köhler, M., Liu, K.K.Y., ve Rowe, B., 2007, Green roofs as urban ecosystems: Ecological structures, functions, and services, *BioScience*, 57 (10), 823–833.

Palla, A., Gnecco, I., ve La Barbera, P., 2018, Assessing the Hydrologic Performance of a Green Roof Retrofitting Scenario for a Small Urban Catchment, *Water*, 10 (8), 1052.

Peng, Z., Smith, C., ve Stovin, V., 2019, Internal fluctuations in green roof substrate moisture content during storm events: Monitored data and model simulations, *Journal of Hydrology*, 573 (April), 872–884.

Peng, Z., Stovin, V., Unless, R., Act, P., Rose, W., If, T., ve Rose, W., 2017, Independent validation of the SWMM green roof module, *Journal of Hydrologic Engineering*, 22 (9), 1–12.

Rossman, L.A., 2015, *Storm Water Management Model User ' s Manual Version 5 . 1 Storm Water Management Model*, United States Environmental Protection Agency.

Sims, A.W., Robinson, C.E., Smart, C.C., ve O'Carroll, D.M., 2019, Mechanisms controlling green roof peak flow rate attenuation, *Journal of Hydrology*, 577 (May), 123972.

Vesuviano, G.M., 2014, *A Two-Stage Runoff Detention Model for a Green Roof*. Doctoral dissertation, University of Sheffield.

14TH INTERNATIONAL CONFERENCE
ON HYDROSCIENCE & ENGINEERING

MAY 26-27, 2022
IZMİR-TURKEY

ICHE2022
IZMIR, TURKEY

A SUSTAINABLE CLEAN ENERGY SOURCE FOR MITIGATING CO2 EMISSIONS IN WEST ANATOLIAN-AEGEAN EXTENSIONAL REGION

Tolga Ayzit

International Water Resources, Izmir Institute of Technology

İzmir, Urla, Turkey

tolgaayzit@iyte.edu.tr

Dornadula Chandrasekharam

International Water Resources, Izmir Institute of Technology

İzmir, Urla, Turkey

dornadulachandra@iyte.edu.tr

Alper Baba

International Water Resources, Izmir Institute of Technology

İzmir, Urla, Turkey

alperbaba@iyte.edu.tr

EXTENDED ABSTRACT: For countries to achieve sustainable economic growth, efficient and diversified energy sources, especially renewable energy sources (RES), are essential. The cost of RES should also be affordable for economic growth. In this context, Turkey has great opportunity to promote renewable energy, especially geothermal energy from high heat-generating granitoids, using EGS (Enhanced Geothermal Systems) technology. This energy source will help Turkey to mitigate CO_2 emissions and sustain a sound Gross Domestic Product (GDP) growth. According to Turkey Energy Outlook, Turkey´s energy demand will increase by 93%, 2040. Turkey needs a sustainable energy source to meet all future energy demands and achieve the desired target of the 2 D scenario recommended by IEA. The exploitation of the energy from the radiogenic granitoids will help the country to save about 32211 million kg of CO_2 from gas-based electricity power plants. Currently, Turkey utilizes 3488 MWt of geothermal energy from its hydrothermal sources for direct applications like space heating and cooling and greenhouse cultivation. These two applications use about 1453 MWt annually. In addition to the hydrothermal energy sources, energy from EGS will make the country free from energy deficit and provide sustainable power, water, and food. The scope of this study to assess the suitability of western Anatolian granitoids as a EGS source. The west part of southern margin of Eurasian Plate is covered by Alpine Mountain belt that extending from Anatolian Plate to the north Atlantic Ocean and includes radiogenic granitoids. Plutons of variable age and composition crop out extensively in Western and Northwestern Anatolia. The Anatolian Plateau is known for extension tectonics and is explained by the west-southwestward tectonic escape and subduction rollback processes. This is controlled by the right-lateral North Anatolian fault and the left-lateral East Anatolian fault. The most prominent structures of western Anatolia are E-W and ENE-WSW trending grabens and horsts controlled by low and high-angle oblique to dip-slip normal faults. Plutonic rocks with high radioactive element content, which are directly related to alkaline magmatism, are present along to the İzmir-Ankara-Erzincan suture zone (IAESZ) dominantly in northern part of the west Anatolian-Aegean extensional region. These granitoid rocks result from slab

melting of a series of northward-dipping subduction zones of the Hercynian to Hellenic arcs since the Late Carboniferous age. Extensional active tectonic regime has still forming and result in high heat flow and high geothermal gradient in this region. Moreover, the high heat flow values as 120 mW/m^2 overlap the regions where the Curie depth is shallow as 6 km. The high heat flow values are associated with deep-seated normal or strike-slip faults and volcanic centers. The plutonic rocks are largely represented by I type granitoids, and medium to high potassium calc-alkaline rocks. Heat generated by predominantly Oligo-Miocene age granites spread over an area of 4221 sq. km, varies from 5.3 to 16.34 $\mu W/m^3$. Additionally, the temperature of the granitoids in the western Anatolian region range from 170 to 270 °C at 4 km depth which is similar to the Soultz-sous-Forets (France) EGS area. This plant is generating 3 MWe by extracting heat from granites at 200°C from a depth of 5 km. Based on the electricity generation capacity of granites from Cooper Basin (Australia) EGS site, one km^3 of such granite can generate 79 x 10^6 kWh of electricity for 30 years. Considering this information and the probable volume of the granitoids it is estimated that the power can be generated is of the order of 4 x 10^9 MWh of electricity. Even 2% of energy extracted from these granites can provide base-load electricity and heat to the country, thereby highly mitigating dependency on imported gas/oil and, CO_2 emissions. The west Anatolian-Aegean extensional region has a huge potential for implementing "Enhanced Geothermal System" (EGS) technology and realize future clean energy.

Keywords

Geothermal exploration, Enhanced geothermal systems (EGS), Radiogenic granitoid, Renewable energy, Western Anatolia

REFERENCES

Akin, U., Ulugergerli, E., Kutlu, S. (2014). The assessment of the geothermal potential of Turkey by means of heat flow estimation. *Bulletin Mineral Resources Exploration 149*: 201- 210.

Aldanmaz, E., Pearce, J., Thirlwall, MF., Mitchell, J. (2000). Petrogenetic evolution of late Cenozoic, post-collision volcanism in western Anatolia, Turkey. *Journal of Volcanology and Geothermal Research 102*: 67-95.

Aldanmaz, E. (2006). Mineral-chemical constraints on the Miocene calc-alkaline and shoshonitic volcanic rocks of Western Turkey: disequilibrium phenocryst assemblages as indicators of magma storage and mixing conditions. *Turkish Journal of Earth Science 15*: 47–73.

Altunkaynak, Ş., Dilek, Y. (2006). Timing and nature of post-collisional volcanism in Western Anatolia and geodynamic implications. In: Dilek Y, Pavlides S, editors. Post-Collisional Tectonics and Magmatism of the Eastern Mediterranean Region. Boulder, CO, USA: *Geological Society of America Special Papers*, pp. 321-351.

Altunkaynak, Ş., Dilek, Y. (2013). Eocene mafic volcanism in northern Anatolia: its causes and mantle sources in the absence of active subduction. *International Geological Reviews 55*: 1641-1659.

Altunkaynak, S., Dilek, Y., Genc S. C., Sunal, G., Gertisser, R. (2012a). Spatial, temporal and geochemical evolution of Oligo–Miocene granitoid magmatism in western Anatolia, Turkey. *Gondwana Research 21*: 961-986.

Baba, A., Bozkurt, C., Gokcen Akkurt, G., Gudmarrson, T., Uzelli, T., Yakut, A. O., and Döğerlioğlu, M. O. (2021). Turkey – Assessment of Opportunities and Interest in Direct Uses of Geothermal Energy. *World Bank, Report*. 132.

Bozkurt, E. (2001). Neotectonics of Turkey - a synthesis. *Geodinmica Acta 14*: 3–30.

Chandrasekharam, D., Baba, A. (2021). High heat generating granites of Kestanbol: Future Enhanced Geothermal System (EGS) province in Western Anatolia. *Turkish Journal of Earth Science*, Special Issue

Chandrasekharam, D., Baba, A. (2021). Carbon dioxide emissions mitigation strategy through Enhanced Geothermal systems: western Anatolia, Turkey. DOI: 10.21203/rs.3.rs-876036/v1.

Cooper, G. T., Beardsmore, G. R., Waining, B. S., Pollington, N. and Driscoll. J. P. (2010). The Relative Costs of Engineered Geothermal System Exploration and Development in Australia. Proceedings. *World Geothermal Congress, 2010*, Bali, Indonesia, April 2010, 17 p.

Delaloye, M., Bingöl, E. (2000). Granitoids from western and Northwestern Anatolia: geochemistry and modeling of geodynamic evolution. *International Geology Review 42*: 241– 268.

Diddglio, C., Guray, B. S., Merdan, E. (2020). Turkey Energy Outlook 2020. International Centre for Energy and Climate, *Sabanci University Pub.* 452p. https://iicec.sabanciuniv.edu/.

Dilek, Y., Altunkaynak, Ş. (2007). Cenozoic crustal evolution and mantle dynamics of post-collisional magmatism in western Anatolia. *International Geological Reviews 49*: 431-453.

Dilek, Y., Altunkaynak, Ş. (2010). Geochemistry of Neogene-Quaternary alkaline volcanism in western Anatolia, Turkey, and implications for the Aegean mantle. *International Geolological Reviews 52*: 631-655.

Dilek, Y., Altunkaynak, Ş. (2009). Geochemical and temporal evolution of Cenozoic magmatism in western Turkey: Mantle response to collision, slab breakoff, and lithospheric tearing in an orogenic belt., In Geodynamics of collision and collapse at the Africa– Arabia–Eurasia Subduction Zone., Londra: *The Geological Society of London*, Special Publication, 311, pp. 213-233.

Dilek, Y., Altunkaynak, Ş., Öner, Z. (2009). Syn-extensional granitoids in the Menderes core complex and the late Cenozoic extensional tectonics of the Aegean province. *Geological Society, London*. Special Publications 321: 197–223.

Eckstein, Y. (1978). Review of heat flow data from the eastern Mediterranean region. *Pure and Applied Geophysics 117*: 150– 159.

Erkul, S. T., Erkul, F. (2012). Magma interaction processes in synextensional granitoids: The Tertiary Menderes Metamorphic Core Complex, western Turkey. *Lithos 142*-143: 16-33.

Ersoy, Y.E., Helvacı, C., Palmer, M. R. (2009). Petrogenesis of the Neogene volcanic units in the NE-SW-trending basins in western Anatolia, Turkey. *Contributions to Mineralogy and Petrology 163*: 379-401.

Erkan, K. (2015). Geothermal investigations in western Anatolia using equilibrium temperatures from shallow boreholes. *Solid Earth, 6, 103*–113, 2015.

Harris, N. B. W., Kelley, S., Okay, A. I. (1994). Post-collisional magmatism and tectonics in northwest Anatolia. *Contributions to Mineralogy and Petrology 117*: 241-252.

Hasozbek, A., Satır, M., Erdoğan, B., Akay, E., Siebel, W. (2010). Early Miocene post-collisional magmatism in NW Turkey: geochemical and geochronological constraints. *International Geological Reviews 53*: 1098-1119.

Jolivet L, Menant A, Sternai P, Rabillard A, Arbaret L et al. (2015). The geological signature of a slab tear below the Aegean. Tectonophysics 659: 166-182. doi: 110.1016/j. tecto.2015.1008.100

IEA, (2014). World Energy Outlook 2014, *International Energy Agency*, ISBN: 978-92-64- 20805-6, p.727, Paris, France,www.iea.org.

IEA, (2021c). Turkey 2021: Energy Policy Review. *International Energy Agency*, 2021, 191 p.

IPCC, (2018). Global Warming of 1.5°C. An IPCC Special Report on the impacts of global warming of 1.5°C above pre-industrial levels, *Intergovernmental Panel on Climate Change (IPCC)*, https://www.ipcc.ch/sr15/.

Karat, H. I., Aydın, I. (2004). Report on Preparation of the Curie Isotherm Depth Map of Turkey, *Unpublished Report no. 10638,* MTA, Ankara (in Turkish).

Koelbel, T., Genter, A. (2017). Enhanced Geothermal Systems: The Soultz- sous- Forêts Project in TS Uyar (ed.), Towards 100% Renewable Energy, *Springer Proceedings in Energy*, DOI 10.1007/978-3-319-45659-1_25, 243-270.

Köprübaşı, N., Aldanmaz, E. (2004). Geochemical constraints on the petrogenesis of Cenozoic I-type granitoids in Northwest Anatolia, Turkey: evidence for magma generation by lithospheric delamination in a post-collisional setting. *International Geological Reviews 46*: 705-729.

Lachenbruch AH (1968). Preliminary geothermal model of the Sierra Nevada. Journal of Geophysical Research 73: 6977-6989.

Letcher, T. M. (2020). Future Energy Improved, Sustainable and Clean Options for our Planet. *Springer*, 776p.

Lund, J., Toth, A. N. (2020). Direct utilization of geothermal energy 2020 worldwide review. *Geothermics, 90*:101915. 10.1016/j.geothermics.2020.101915.

Mertoğlu, O., Şimşek, S., Başarir, N., (2020). Geothermal energy use: projections and country update for Turkey. In: Proceedings, *World Geothermal Congress 2020*. Reykjavik, Iceland. 11 p.

Okay, A.I., Satır, M. (2006). Geochronology of Eocene plutonism and metamorphism in northwest Turkey: evidence for a possible magmatic arc. *Geodinamica Acta 19*: 251-266.

Papadopoulos, A., Altunkaynak, S., Koroneos, A., Ünal, A., Kamacı, O. (2016). Distribution of natural radioactivity and assessment of radioactive dose of the western Anatolian pluton, Turkey. *Turkish Journal of Earth Sciences 25*: 434-455.

Rybach, L. (1976). Radioactive Heat Production: A Physical Property Determined by the Chemistry. In: R.G.I. Strens (Editor), The Physical and Chemistry of Minerals and Rocks. *Wiley- Interscience Publication*, New York, USA, pp. 245-276.

Somerville, M., Wyborn, D., Chopra, P., Rahman, S., Don Estrella, Theo Van der Meulen, (1994). Hot Dry Rock Feasibility Study. *Energy Research and Development Corporation, unpublished report.* 214 p.

Şengor, A. M. C., Yılmaz, Y. (1981). Tethyan evolution of Turkey: a plate tectonic approach. *Tectonophysics 75*: 181-241.

Tezel, T., Shibutani, T., Kaypak, B. (2013). Crustal thickness of Turkey determined by receiver function. *Journal of Asian Earth Sciences 75*: 36-45.

Uzel, B., Sozbilir, H., Özkaymak, C. (2012). Neotectonic Evolution of an Actively Growing Superimposed Basin in Western Anatolia: The Inner Bay of İzmir, Turkey. *Turkish Journal of Earth Sciences 4*: 439 – 471.

Yilmaz, Y. (1997). Geology of Western Anatolia: active tectonics of northwestern Anatolia. The Marmara Poly Project. VDF, *Hochschulverlag Ag An Der ETH*, Zurich 1–20.

EXPERIMENTAL INVESTIGATION OF LANDSLIDE GENERATED WAVES IN A LABORATORY TEST SET-UP

Reza Mohajer Barough

Department of Civil Engineering, Middle East Technical University

Ankara, Turkey

reza.barough@metu.edu.tr

Erhan Tarık Karayama

Department of Civil Engineering, Middle East Technical University

Ankara, Turkey

tarik.karayama@metu.edu.tr

Adnan Tolga Kürümüş

Department of Civil Engineering, Eskişehir Osmangazi University

Eskişehir, Turkey

tolgakurumus@gmail.com

Ender Demirel

Department of Civil Engineering, Eskişehir Osmangazi University

Eskişehir, Turkey

edemirel@ogu.edu.tr

İsmail Aydın

Department of Civil Engineering, Middle East Technical University

Ankara, Turkey

ismaydin@metu.edu.tr

ABSTRACT: Dam reservoirs are manmade lakes that may be subjected to extraordinary hydrodynamic pressures and water waves due to landslides, earthquakes or both simultaneously when an earthquake triggers a landslide. There are many examples of dam failure due to landslide that cause water overtopping the dam body. Landslides on the other hand become more frequent due to soil erosion and floods. In this study, the wave behavior due to landslides in dam reservoirs in three important regions: generation zone, propagation and overtopping area is investigated experimentally. Experiments are conducted in a laboratory test set-up to understand the effects of variables such as water depth and slide runout distance in generating impulse waves and resulting overtopping volume. In the experiments, a solid slide with prescribed shape and density is released from different initial positions on a ramp into the water reservoir. Larger slide runout distances and higher water depths are the novelties of this study in generating waves. Water wave data recorded by ultrasonic sensors is analyzed to find the relations between the slide variables and water surface waves that will be utilized in the development of a Computational Fluid Dynamics (CFD) code.

1. INTRODUCTION

Mass movements such as landslides, rock falls, or meteorite impacts in oceans or dam reservoirs can generate impulse waves which can cause a disaster. In 1963 in Vajont a landslide into a dam reservoir led to impulse waves which overtopped the dam crest by 70 meters that caused a disaster in the downstream village and approximately 2000 people died (Schnitter 1964). Landslide generated impulse waves occur frequently all over the world at least in small cases and they are the reason of nearly 10% of all dam breaches according to Singh (1996). Landslide generated waves, regarding the initial position of the slide are classified as subaerial landslides, partially submerged landslides and underwater landslides. In this study, waves generated by subaerial landslides will be investigated. Subaerial landslides include three phases of solid, water and air. Heller et al. (2008) discussed perfectly the scale effects in landslide generated impulse waves and offered the water depths higher than 0.2 m to reduce the scale effects. Heller and Spinneken (2015) conducted a total of 177 three dimensional tests dealing with subaerial landslides. In their experiments, the blocked shaped landslides were modeled in the wave tank and the test results were compared with the previous 2D experimental data which led to empirical equations for predicting wave properties due to landslides for 3D and 2D configurations. They discussed the existing 2D-3D transformation formula. Evers et al. (2019) generated 3D impulse waves in a hydraulic laboratory basin and recorded the water surface deformation using a video metric measurement system. They derived some equations for predicting the impulse wave magnitudes.

2. EXPERIMENTAL SETUP

Experiments are conducted with a physical model constructed in the Hydraulics Laboratory of the Civil Engineering Department at Middle East Technical University. A rectangular concrete reservoir of horizontal dimensions 6 m ×13 m is used (Figure 1). The setup is designed to study landslide sliding into the reservoir from ramps on the boundaries. The dam crest is simulated on one side where overflow due to waves will be measured. Two ramps are considered to generate impulse waves; Ramp 1 on the side wall and Ramp 2 on the upstream end, opposite of the dam crest. Ramp 1 is 4 m high and 5.2 m long, 1 m wide and fixed at an angle of 60^0 from the horizontal (Figure 2). A circular transition section is inserted between the constant slope ramp and the horizontal. A wheeled rigid block of 0.235 m^3 volume is used to simulate the slide. There are guide rails on the ramp to keep the block moving along a prescribed path. The block can be fixed on the ramp at variable distances to the water surface to obtain different impact velocities on the water reservoir. The dimensions of the ramp 1 makes it possible to reach higher impact velocities comparing previous studies. A cable potentiometer is used to record the position of the sliding block. The potentiometer's output voltage after the calibration process indicates the exact location of the slide along the path in function of time. The slide velocity and acceleration are computed from the slide position recorded. Six boxes are installed on the downstream side of the dam crest to collect the overtopping water volumes from the crest. Seven acoustic wave probes are placed above the basin, allowing the wave measurements at points arranged along the generation zone, propagation zone and overtopping crest. The sensors are calibrated in the basin by changing the water level. Wave probes 1, 2 and 3 are located along the ramp 1 axis with equal spacing of 1.5 m and wave probes 4, 5, 6 and 7 are located in the space between the dam crest and wave probe 2 with equal spacing of 2.2 m along the wave propagation axis towards the dam crest as shown in Figure 1.
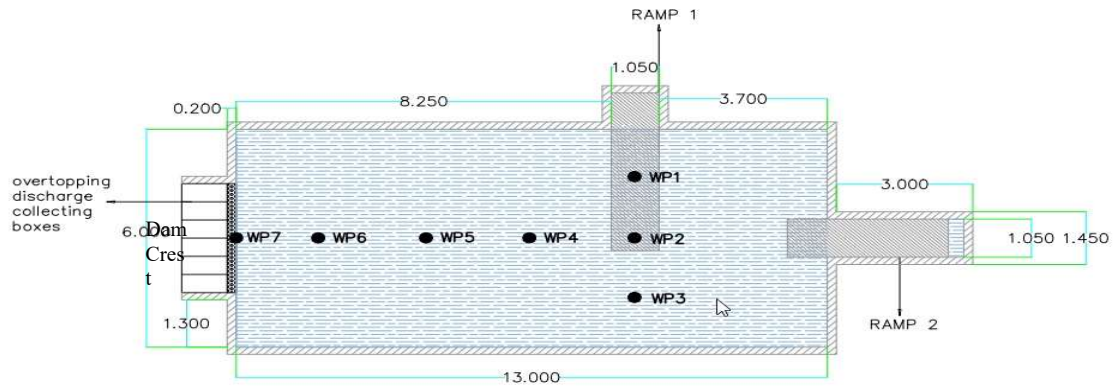
Figure 1. Plan view of experimental setup
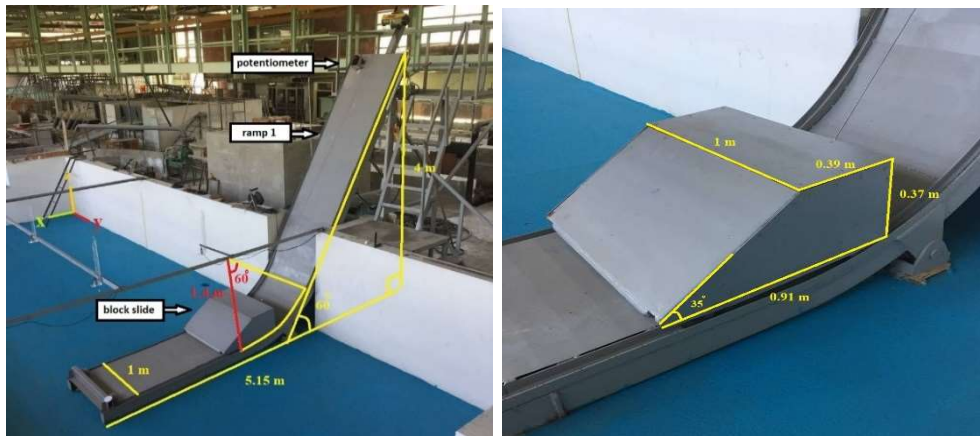
Figure 2. Ramp 1 and rigid block

3. EXPERIMENTS

In the first series of experiments, the block is sliding over Ramp1 (Figure 3). The density of the block is fixed as 1200 kg/m^3. The water depth in the reservoir and the runout distance between the initial position of the block and the water surface are the variables. The runout distance affects the impact velocity of the block at the moment of hitting the water surface. 30 different runs are conducted to observe water waves and overtopping the dam crest.

Figure 3. A photograph taken after impact of the slide block

The data recorded from the potentiometer included too much electronically noise to calculate the velocity and acceleration of the block. The existing data smoothing methods weren't efficient enough for the data recorded by the potentiometer and they led to unacceptable results, therefore, a FORTRAN code is developed to smooth the noisy oscillations without losing the unsteady characteristics. The block acceleration and velocity are obtained by differentiating the block position record. An example record of block position, computed velocity and acceleration are shown in Figure 4(a). The block reaches about 4.4 *m/s* velocity before the impact and then decreases as it moves into the water. As can be seen from the acceleration record, the first momentum of the block causes water waves, later, these waves move the block back and forth on the guide rails.

Figure 4(b) to (f) shows the water surface waves recorded by the acoustic wave probes for the same test case. Probe 1 is the closest probe to the impact point and thus the maximum wave heights are observed at that point (Figure 4(b)). Similar wave records are seen at Probes 3 and 4. Probe 6 is close to the dam crest where wave heights are reduced due to the distance traveled. Probe 7 is located just on the crest from which one can observe that overtopping occurred twice due to two wave peaks.

According to the experimental results, for the fixed water depth of 0.983 m, when the runout distance varies from 0.695 *m* to 1.881 *m*, the impact velocity rises from 3.18 *m/s* to 4.73 *m/s* and the overtopping water increases from 0.05477 m^3 to 0.10430 m^3.

Experiments are repeated for variable ranges of water levels and runout distances. Repeatability of the experiments is examined by comparing 10 repeated tests with identical initial and boundary conditions. It was found that the difference in terms of the block position is less than 5 %.

In the following tests, the slide block density will be changed and all experiments for variable runout distances and reservoir water levels will be repeated. After collection of sufficient data for the rigid block, different forms of slide material will be considered. The ramp 2 will be used to investigate the effect of ramp angle on wave generation. The experimental data collected from the available physical model will be utilized to develop a computer code for numerical analysis of landslide generated waves in dam reservoirs.
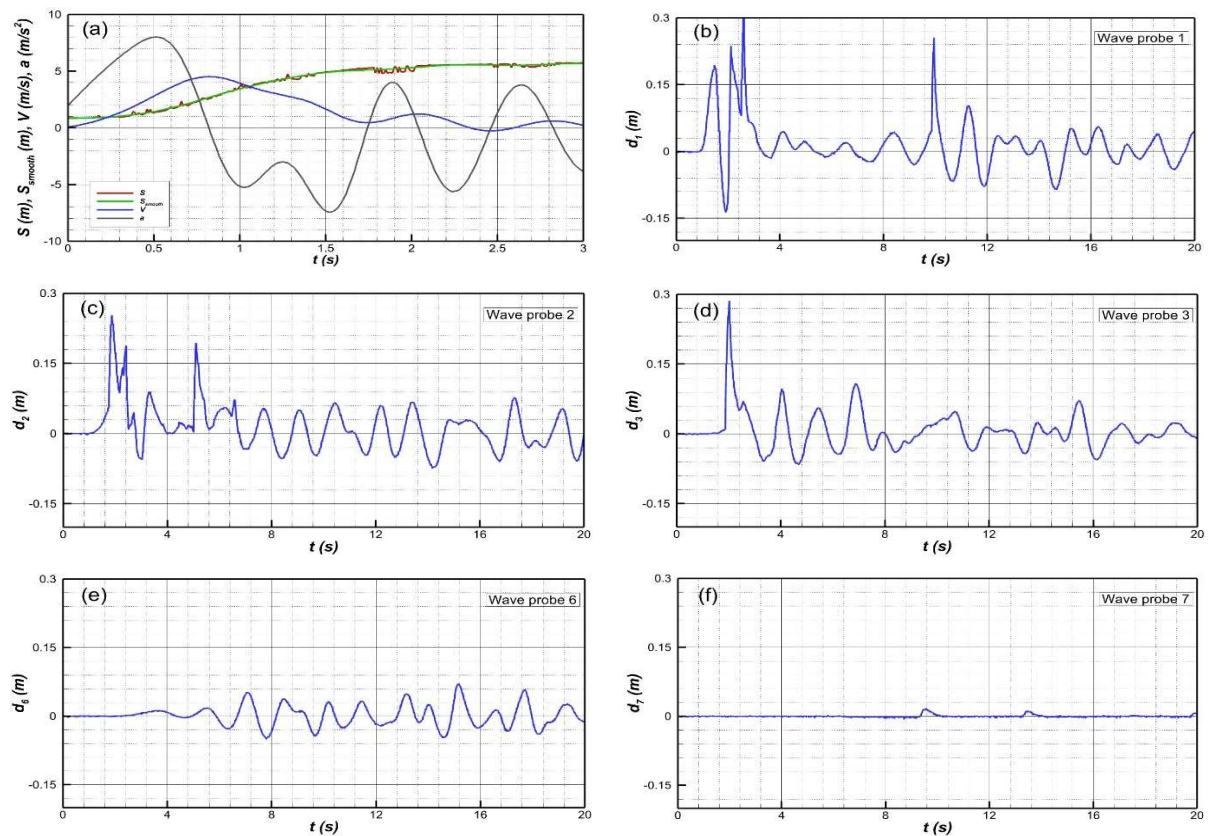
Figure 4. Block position, velocity, acceleration and wave probe records

4. CONCLUSIONS

In the present study, 30 different experimental cases were conducted to understand the effects of parameters such as the still water depth and the slide runout distance on the generation and propagation of impulse waves due to landslides. The possibility and amount of overtopping in such situations is observed. Increasing in runout distance increases the impact velocity and larger impact velocities results in much more overtopping water.

REFERENCES

Evers, F.M., Hager, W.H., Boes, R.M. (2019). Spatial impulse wave generation and propagation. Journal of Waterway, Port Coastal and Ocean Engineering 145(3):0401901-1-15.

Heller, V., Hager, W.H., Minor, H.-E. (2008). Scale effects in subaerial landslide generated impulse waves. Experiments in Fluids 44(5):691-703.

Heller, V., Spinneken, J. (2015). On the effect of the water body geometry on landslide-tsunamis: Physical insight from laboratory tests and 2D to 3D wave parameter transformation. Coastal Engineering 104(10):113-134.

Schnitter, G. (1964). Die Katastrophe von Vaiont in Oberitalien. Wasser- und Energiewirtschaft 56(2/3):61-69

Singh, V.P. (1996). Dam break modelling technology (pp. 27-34). Kluwer Academic Publishers, Dordrecht.

14TH INTERNATIONAL CONFERENCE
ON HYDROSCIENCE & ENGINEERING

MAY 26-27, 2022
IZMİR-TURKEY

ICHE2022
IZMIR, TURKEY

PHYSICAL AND NUMERICAL MODELING OF ENERGY DISSIPATION RATIOS OF T_SHAPED OF ENERGY DISSIPATING BLOCKS IN STILLING BASIN

Kamil Ispır

State Hydraulic Works

Konya, Turkey

kamilispir@gmail.com

Serife Yurdagul Kumcu

Civil Engineering Department, Necmettin Erbakan University,

Konya, Turkey

yurdagulkumcu@gmail.com

Ozgur Yılmaz

Istanbul Technical University

Konya, Turkey

yozgur1997@gmail.com

ABSTRACT: Energy dissipating structures are constructions that transfer the water from upstream to downstream safely by reducing the energy of the flow. They are generally used in irrigation channels, discharging from a dam bottom outlet, at the foot of the spillway structures and in dissipating the energy of water in a similar situations. The main principle of stilling basin is to keep the hydraulic jump in the channel while flow regime is changing from super critical to sub critical. In this study, the channel was set to investigate the performance of various types of energy dissipating blocks which were placed in different layouts in plan at the downstream of the ogee spillway in the stilling basin. The aim of this study is to investigate the energy dissipating ratios of T shape of energy dissipators by physical and numerical modelling methods.

Keywords: Open channel flows, Energy dissipating, Energy dissipating blocks, FLOW-3D, Hydraulic jump, Spillway design, Stilling basin, Shute blocks.

1. INTRODUCTION

In the spillway structures, energy dissipaters play an important role in terms of the safety and cost of the structure. During the transfer of water from the dam approach channel to the downstream, the water has a high energy due to the hydraulic jump that occurs at the downstream, as the flow regime changes from super critical to sub critical. This energy can create very high velocities in the current; it leads to scour, erosion and cavitation, causing damage to the downstream structures and the stream bed. Energy-dissipating structures are, facilities that safely transfer the energy of the water from upstream to the downstream, designed in conjunction with intake structures, canal structures, outlet works and spillways.

The basic principle of energy-dissipating pools, which is one of the energy-dissipating structure types, is to reduce the energy by breaking within a certain distance with the help of the hydraulic jump that occurs during the transition of the flow from the flood regime to the river regime. A series of experiments on dissipating blocks and outlet end sills have been carried out by USBR III and standard pools. Type of energy dissipating pool is classified according to the Froude number (Chow,

V.T, 1959). The energy dissipating blocks are placed in the energy dissipating pool in order to ensure breaking the energy. Energy breaking blocks shorten the pool length needed to break energy. Energy dissipating blocks can be used in a single row or in more than one row. It has been suggested by the USBR that the blocks in the second and subsequent rows should be placed in a staggered manner, the first block should be placed half the width of the block from the wall, and the width of the blocks in the same row and the distance between the blocks should be equal (Peterka, 1984).

Bestawy (2013) conducted a study on the use of different shaped energy dissipation blocks as energy dissipaters. In this study, 14 different models of energy dissipation blocks were designed and placed in a single row in the energy dissipation pool. It has been stated that a vertically placed, semicircular cross-section gives the best results.

Kuttiammu (1951) designed a different head pool by examining the performance of energy breaking blocks in energy breaking pools, showing that the performance is increased with T-shaped blocks.

Bradley et al. (1957) conducted experimental research on the hydraulic design of energy dissipating pools at low Froude numbers, USBR IV. They suggested the use of a type reduction pool.

Morris (1968) tried to optimize the distance between the dissipating blocks. In his study, dimensionless parameters were found depending on the spacing and height ratios of the energy dissipation blocks.

Pillai et al. (1989) investigated the hydraulic splash phenomenon in energy dissipation pools under flow conditions with low Froude numbers. In this study, a new type of abatement pool is proposed against the existing abatement pools. It has been stated that the type obtained by placing pentagonal energy dissipating blocks in the middle of this reduction pool gives better results.

Kaya examined the energy absorption rates of different types of energy scattering blocks in energy scattering pools in his study in 2003 and stated that the T-shaped and pentagonal type blocks studied on the breaking of the current energy passing through the bottom weirs in this study gave the best results.

In his study in 2007, Varol examined the energy dissipation ratios, velocity changes and dynamic forces acting on the blocks of different types of energy dissipating blocks placed in the reduction pools by numerical analysis and stated that the blocks with triangular geometry gave the best results in this study.

Özbay (2008) examined different types of energy dissipation blocks placed in chute channels. In this study, it was stated that the energy dissipation ratios of the different shaped blocks, which were studied with 4 different energy dissipation blocks, were close, but the stepped type energy dissipation block had a slightly higher energy dissipation rate than the other blocks.

Bestawy (2013) conducted a study on the use of different shaped energy breaker blocks as energy breaker. In this study, 14 different models of energy breaker blocks were designed and placed in a single row in the energy breaker pool. It has been stated that a vertically placed, semicircular cross-section gives the best results.

In this study, the contribution of the baffle blocks in stilling basins located downstream of the ogee spillway to energy dissipation ratios were investigated by physical and numerical modeling methods. T shape of baffle block geometries were used. The stilling basin is sized as USBR III type according to the Froude number and flow rate. As a result, the energy dissipation ratios of the baffle blocks and the results obtained by numerical modeling methods are given.

2. ENERGY DISSIPATION POOL

A hydraulic jump is an event that occurs where the flow passes from the flood regime to the river regime and creates a sudden rise in the water surface. Since a significant amount of energy is lost in a short distance during the event, the hydraulic jump is provided to break the energy. Rectangular cross-section pools are generally preferred because it is recommended that the side walls be vertical or close to vertical for a good hydraulic jump (DSI, 2012). The schematic view of the energy dissipation pools is given in Figure 1.

3. ENERGY DISSIPATING STILLING BASINS (TYPE III)

It is used when the Froude number is greater than 4.5 and the flow velocity is less than 18.3 m/s (60 ft/s). Dimensioning of the pool and chute blocks in Figure 1.
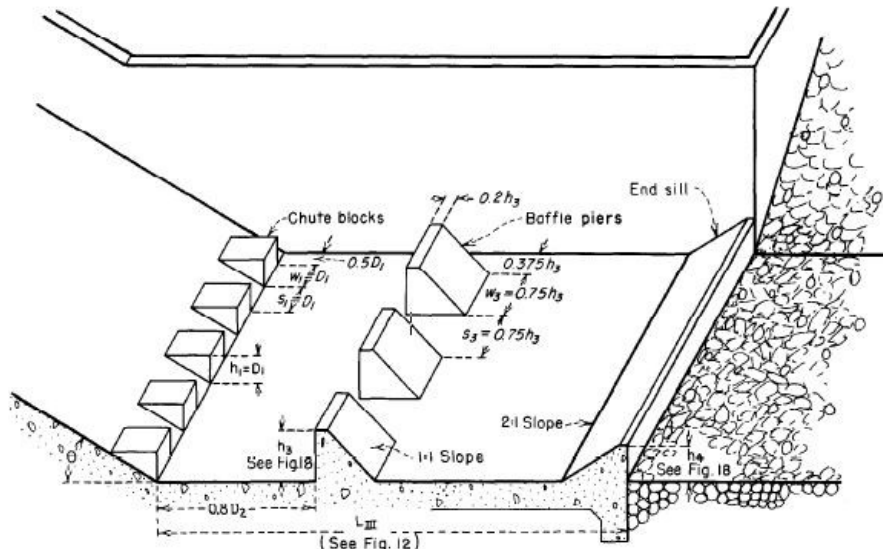
Figure 1. Type III Pool (Peterka, 1984)

4. MATERIALS AND METHOD

4.1. Physical Model

Experimental studies were carried out in Konya Technical University, Hydraulics Laboratory. on the energy dissipation ratios of the energy dissipating blocks placed in the USBR Type III energy dissipation pool with experimental methods. In this study, a total of 3 experimental setups with T shapes of energy dissipating blocks and single row, two rows and two rows without end sill were used. In the experimental setup, the height and the width of the chute blocks and energy dissipation blocks were kept constant and different flow rates were studied. In the experiments, the data obtained by measuring the conjugate water depths for 7 different flow rates. The measurements were analyzed and the energy breaking amounts were computed.

4.1.1. The Experimental Setup

A rectangular glass-walled horizontal laboratory flume of 6.7 m length, 0.30 m width and 0.5 depth was used in the experiments at the Hydraulic Labaratory of the Konya Technical University. The models were manufactured from plexiglass and gypsum at the labaratory workshop and placed the labaratory flume. By means of bricks and sheet-iron strainer, which paced between brick-walls,placed at he entrance of the channel as a filter, turbulence ofthe flow was reduced and the uniform flow conditions were maintained which were required for uprstream head measurements. The scour depthswere also measured with a pointgage to an accuracy of ±1 mm.In the experimental setup, the water is circulated by pumps to the open channel placed between the two tanks. By means of bricks placed at the entrance of the channel, turbulence of the flow was reducing and uniform flow condition were maintained which required for upstream head measurements. The discharge of the flow is measured with the flow meter placed in the circulation pipe. In order to regulate the flow conditions, the flow depth obtained by passing through the flow regulator was measured with a limnimeter with ±1 mm accuracy. The open channel is made of 1.2 cm thick laminated glass, which is obtained by combining two 0.6 cm thick tempered glass sheets with a plastic layer placed between them. The purpose of using thick laminated glass is to prevent the glass from breaking in small impacts and to

enable it to carry excessive loads. In the experiments, chute legs made of fiberglass were used. The water flowing in the open channel system is supplied from two reservoirs. The pumps take the water from the 1st chamber and press it into the 2nd chamber. The water that comes to the 2nd chamber and overflows passes through the open channel and is poured back into the 1st chamber from there (Figure 2).
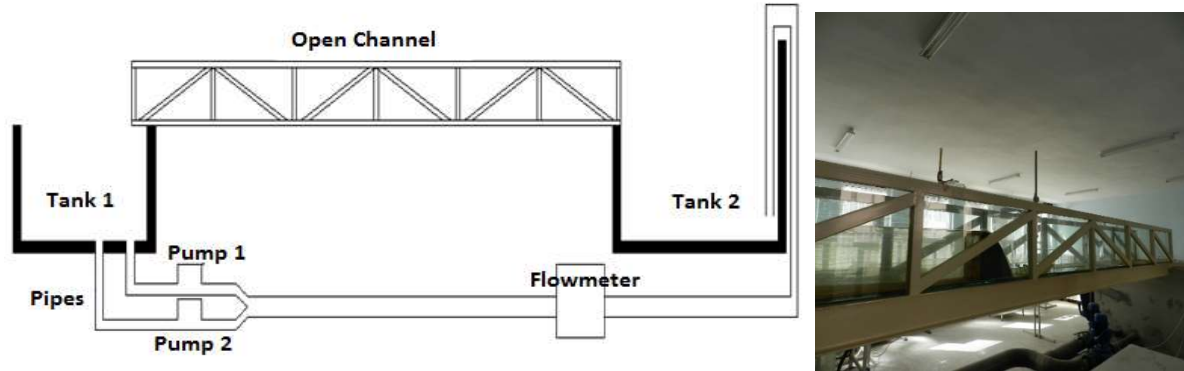
Figure 2. Schematic and laboratory view of the open channel assembly

Rating curve of the weir enabling the water from the tank is given in Figure 3.
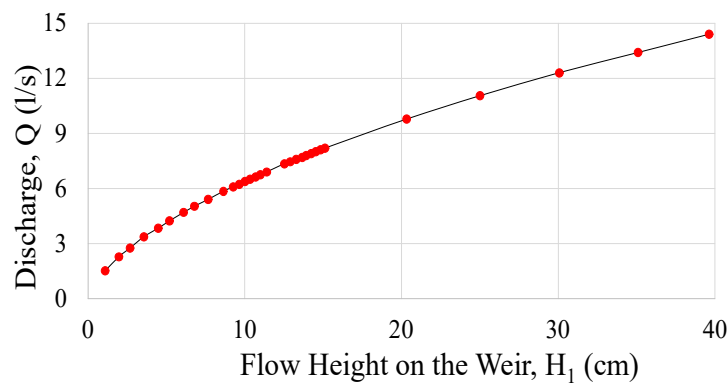
Figure 3. Weir Discharge Rating Curve

For each downstream water height, the velocity and Froude were computed. The computed highest flow velocity and Fr number was recorded as 2.75 m/s and 8.83, respectively.

As stated previously, USBR type III was chosen, which is suitable for the design in flow conditions where the computed Froude number is greater than 4.5 and the maximum computed flow velocity is less than 18.3 m/s (60 ft/s). It has been sized according to the chart based on the sizing given in Table 1.

Experimental study specifications are given in Table 1.

Table1. Design computations.

Q (l/s)	H (cm)	h_1 (cm)	Channel Width, B (cm)	V=Q/A (m/s)	$F_r = V/\sqrt{gh_1}$	$\dfrac{h_2}{h_1} = \dfrac{\sqrt{1+8Fr^2}-1}{2}$
1.10	1.52	0.26	30.00	1.41	8.83	3.12
39.62	14.40	4.80	30.00	2.75	4.01	24.92

In the experiments, T shape energy dissipation block types, were used. The energy block types used were placed in the energy dissipating pool first in a single row, then 2 rows and then 2 rows without end sill, and the flow conditions were examined. Plan and profile views of energy dissipation block types are given in Figure 4.
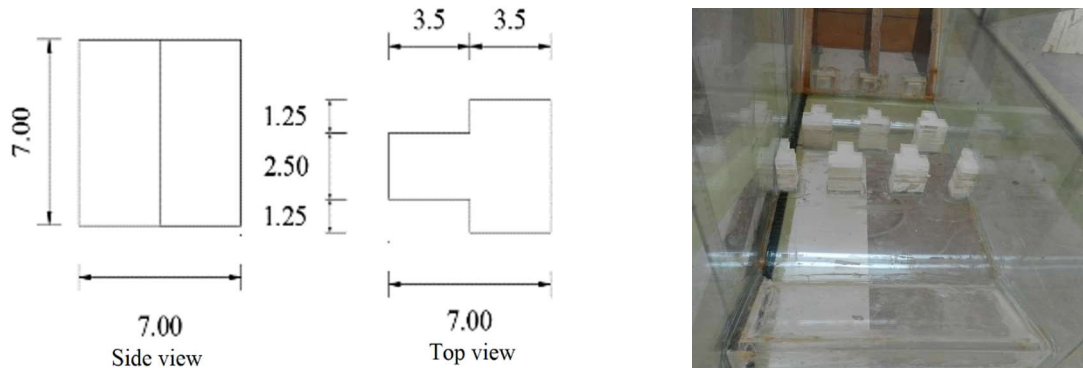
Figure 4. T section block

Single and 2-row layouts of energy-dissipating block types, and 2-row non-end sill layout and sections and block details are given in Figure 5.
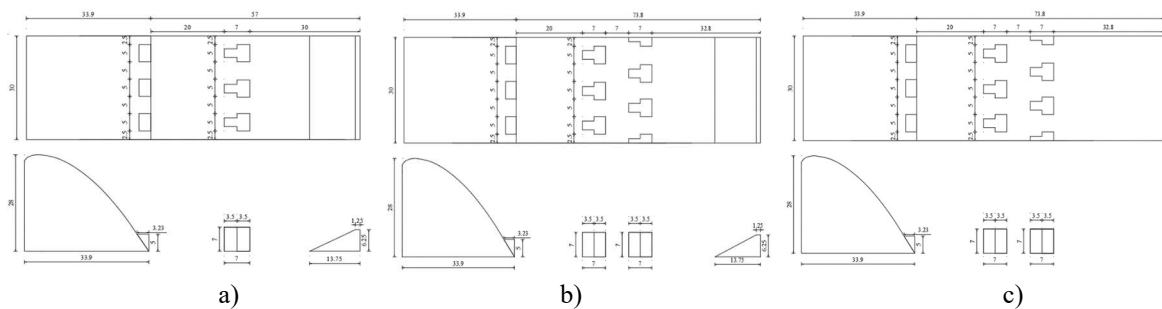
a) Layout of single row energy dissipation blocks with T section
b) Layout of T-shaped double row energy dissipation blocks
c) Layout of T-shaped double row energy dissipation blocks without end sill
Figure 5. Layout and sections of blocks

Energy dissipation ratios versus belonging discharges observed from the experiments are given in Figure 8. This figüre shows that, if the buffle blocs are designed in a line, its energy dissipation performance for a given discharge is less than the 2 lined layouts. T-shape two lines with end sill gives lower energy dissipation ratio up to Q=0,035 m^3/s. T-shape two lines without end sill generally gives the highest energy dissipation ratios for a given discharge.
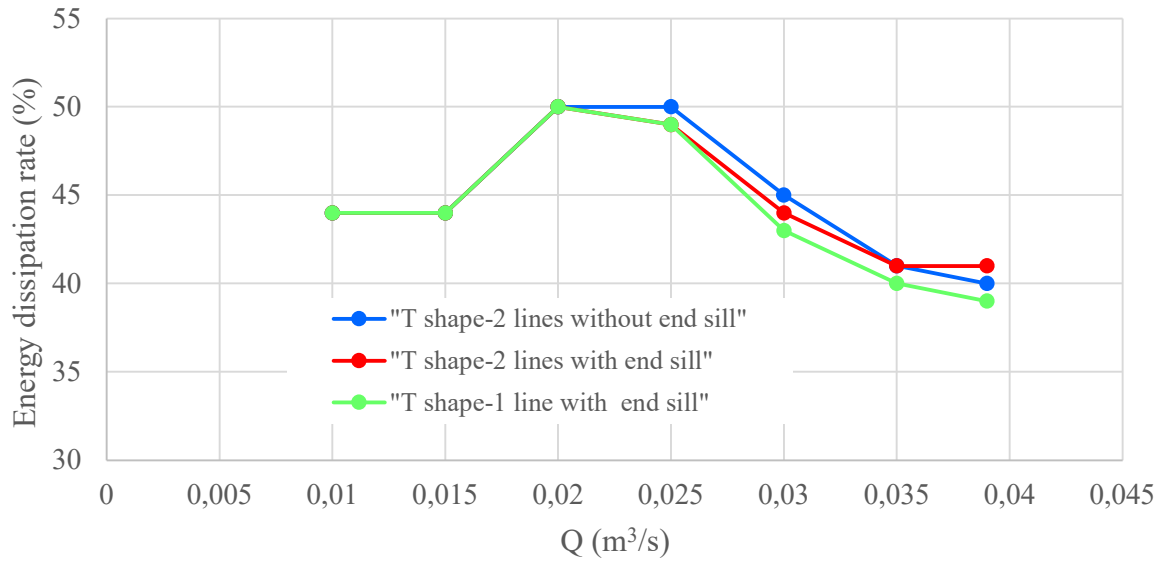
Figure 6. Comparison of experimental observations

4.2. Numerical Modelling (FLOW 3D)

FLOW-3D is a computational fluid dynamics solver, a commercial mathematical computation program that can solve multiple fluid mixtures using the finite difference method. A single fluid-free surface flow solution was used in the analyses. For the VOF (Volume of fluid) method, it is provided to define the fill or void ratio of each mesh cell and to perform pre-debugging by using pre-process. Mesh cells of 5 mm size were used in the analyses, and the mesh block contains a total of 1,536.000 cells. The part where water enters the system (-X side) is defined as the pressure (static water level). Depending on the desired weir load on the weir, the height of this static water level was adjusted and water was allowed to enter at the desired height. The side surfaces and the bottom of the pool were chosen as walls, the downstream part as outflow and the upper part as pressure to represent the atmospheric pressure. To obtain the desired analysis results, Fluid Fraction (filling ratio) and hydraulic data options are marked in the "output" section. The solid model and layer conditions used in the analysis are shown in the Figure 9.
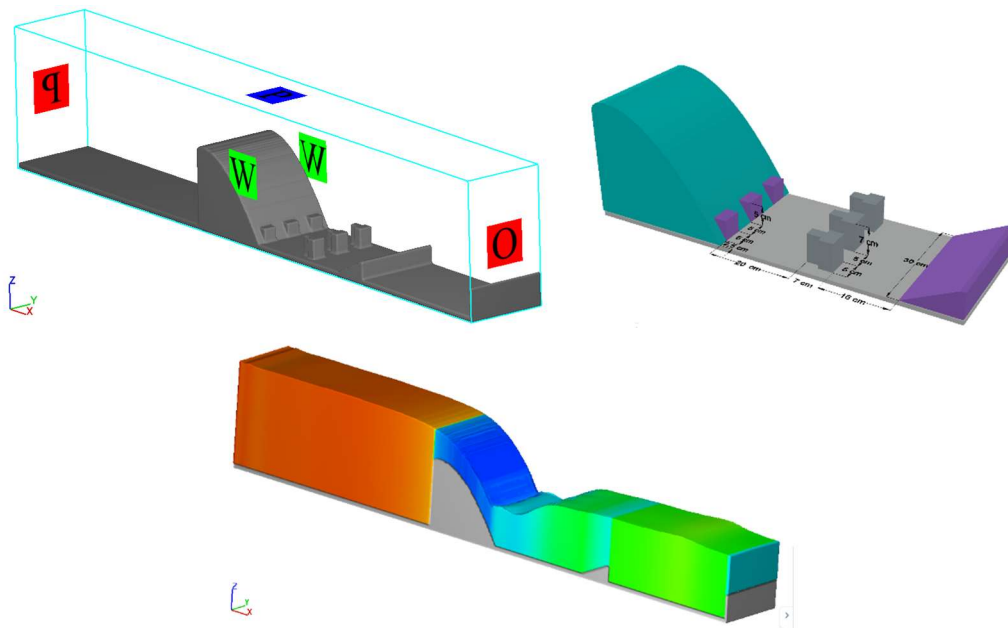
Figure 7. Single row T-shaped layout energy dissipation blocks

5. RESULTS

Experimental setups of single row energy breaker blocks were tested physically at seven different flow rates and with the FLOW-3D mathematical method at the design flow value. When the energy dissipation rates of the single-row energy breaker blocks are examined in Table 2, the experimental study results and the FLOW-3D results have almost the same values. When Table 2 is examined, it is seen that the h3 values are very close to each other, and the energy breaking percentages are the same, both in the physical modeling and in the numerical model study, under the same flow conditions.

ıt is seen that the highest energy dissipating rate is reduced by 41% with 20 l/s, which corresponds to almost 50% of the design flow.

Table 2. Single row T-shaped layout energy dissipation blocks.

Block	Phsical Modelling			Numerical Modelling		
	h_3 (m)	V_3 (m/s)	$(E_1\text{-}E_3)/E_1$	h_3 (m)	V_3 (m/s)	$(E_1\text{-}E_3)/E_1$
T-shaped	0.2425	0.54	0.41	0.2410	0.54	0.41

6. CONCLUSIONS

A series of experiments were carried out to investigate the similarities and differences of the damping ratios of the different geometric shaped energy dissipating blocks placed in the USBR Type III Energy breaker pool, the experimental study and the results of the FLOW-3D mathematical calculations, and the same test conditions were studied with the mathematical model. The results were compared with each other. The results obtained according to the studies carried out are as follows: The block heights and widths of the energy-dissipating blocks were chosen equally, and the total energy-dissipating block length was designed to be 50% of the energy-dissipating pool width, and it was observed that the energy-breaking rates were different. Hydraulic jump occurred in all experimental setups. The energy absorption ratios were close to each other in all the apparatus and energy breaker block types used in the experiment. In all experimental setups, the highest dissipation rate was obtained at 20 l/s flow rate and the lowest dissipation rate was obtained at design flow rate. Energy breaker blocks shorten the spawning distance and shorten the length of the pool. Experimental study results and FLOW-3D results had almost the same values. Although experimental studies are thought to give more reliable results, it should be kept in mind that experimental studies cannot always be carried out, considering laboratory facilities, time, labor and construction costs. Although the assumptions made during the calculations of the mathematical studies, the initial investment cost and the training difficulties are considered, the ease of use and the duration of the program results and the similarity of the results to the experimental studies and real results should be considered. In the continuation of this study, it is planned to continue experimental and mathematical studies by changing the heights and distances of different types of energy blocks under different flow conditions. It is important to carry out studies in different spillway shapes and different flow conditions in terms of generalizing the design.

REFERENCES

Anonim (2012). Baraj Hidrolik Yapılar Tasarım Rehberi, Devlet Su İşleri Genel Müdürlüğü (DSİ), 1. *Barajlar Kongresi*, Ankara.

Bestawy, A. (2013). New shapes of baffle piers used in stilling basins as energy dissipator, *ATE*, 03 (1), 1-7.

Bradley, J. N., & Peterka, A. J. (1957) The hydraulic design of sitiling basins, Journal *Hydraulic Div., ASCE*, 82 (5), 1401.

Chow, V.T. (1959). *Open Channel Hydraulics*, Mc Graw-Hıll Book, New York

Erkek, C. & Ağıralioğlu, N. (1993). *Su Kaynakları Mühendisliği*, Beta Basım A.S., İstanbul, 395s.

Kaya, N. (2003). Enerji kırıcı havuzlarda farklı tip enerji kırıcı blokların enerji sönümleme oranlarının incelenmesi, PhD Thesis, *Fırat University,* Turkey, 101 pages.

Kuttiammu, T. P. & Rao, J. V. (1951). Bhavani type stilling basin for spillways of large dams, Q 12, R 44; 4th *ICOLD*, New Delhi,

Mohamed Ali, H. S. (1991). Effect of roughened-bed stilling basin on lenght of rectangular hydraulic jump, *Journal of Hydraulic Engineering, ASCE*, 117 (1), 83- 93.

Morris, H. M., Hydraulics of energy dissipation in steep, rough channels, *Research division*; Bulletin 19, Virginia Polytechnic Institute, USA, Nov 1968.

Nakato, T. (2000). Model tests of hydraulic performance of Pit 6 Dam stilling basin", *Journal of Hydraulic Engineering, ASCE*, 126 (9), 638-652.

Özbay, Ö. (2008). Şüt Kanallarına Yerleştirilen Farklı Tip Enerji Kırıcı Blokların İncelenmesi, Master Thesis, *Fırat University*, 50 pages, Turkey.

Peterka, A. J. (1984). Hydraulic design of stilling basins and energy dissipators, *United States Department of the Interior Bureau of Reclamation*, A Water Resources Technical Publication, Engineering Monograph No. 25.

Pillai, N. N., Goel, A., & Dubey, A.K. (1989). Hydraulic jump type stiling basin for low Froude numbers, *Journal of Hydraulic Engineering, ASCE*, 115 (7), 989-994.

Rajaratnam, N. & Hurting, K. I. (2000). Screen-type energy dissipator for hydraulic structures, *Journal of Hydraulic Engineering, ASCE*, 126 (4), 310-312.

Varol, S. (2007). Düşüm Havuzlarına Yerleştirilen Farklı Tip Enerji Kırıcı Blokların Enerji Sönümleme Oranlarının Sayısal Analizi, PhD Thesis, Turkey.

Verma, D. V.S. & Arun, G. (2000). Sitiling basins for pipe outlets using Wedge-Shaped Splitter Block, *Journal of Irrigation and Drainage Engineering, ASCE*, 126 (3), 179-184.

EXPERIMENTAL STUDY OF BREACH EVOLUTION AND DISCHARGE THROUGH BREACH RESULTING FROM PIPING DUE TO SEEPAGE AT THE UPPER CORNER OF IN AN EARTH-FILL DAM

M. Sukru Guney

Department of Civil Engineering, Izmir University of Economics

Izmir, Turkey

sukru.guney@ieu.edu.tr

Emre Dumlu

Department of Civil Engineering, Izmir Institute of Technology

Izmir, Turkey

emredumlu@iyte.edu.tr

Merve Okan

Department of Civil Engineering, Izmir University of Economics

Izmir, Turkey

merve.okan@ieu.edu.tr

Gokmen Tayfur

Department of Civil Engineering, Izmir Institute of Technology

Izmir, Turkey

gokmentayfur@iyte.edu.tr

ABSTRACT: Piping is one of the main problems which threatens stability of earth-fill dams. Realistic approaches are needed for breach mechanism as well as breach geometry and flow. The aim of this study is to realize experiments to provide data needed to perform numerical analyses by making more realistic assumptions. Dam having a height of 0.6 m, a bottom width of 2 m and a crest width of 0.20 m is built in a channel of 1 m wide, 0.81 m high and 6.14 m long. Evolution of dam failure resulting from seepage at upper corner of the dam is recorded by six cameras located at different locations. The time-varied of breach areas at upstream and downstream sides are determined by applying the Gauss Area functions. Discharge of water through the breach and average outflow velocity are determined by using the continuity equation.

Keywords: Earth-fill dam, Piping, Breach geometry, Breach development, Discharge through breach

1. INTRODUCTION

Piping is one of the main problems which threatens the stability of earth-fill dams. Soil erosion can be experienced in earth structures, especially in earth dams and levees, through embankment, foundation or from embankment to foundation. This kind of erosion can occur in three stages: a) initiation and continuation of erosion, b) progression to form a pipe, and c) formation of a breach (Fell, Wan & Foster, 2003). The FP5 IMPACT (Investigation of Extreme Flood Process and Uncertainty) European project (2001-2004) reveals the assessment and reduction of risks from extreme flooding caused by natural events or failure of dams and water defense structures (Zech & Soares-Frazão ,2007). Chen,

Zhong, & Shen (2019) show that between 1954 and 2018, 3541 dam breach accidents had occurred and more than 30% of them were due to piping. Sparmos homogenous dam in Greece is one of the recent examples (Dounias & Bardanis, 2019).

The ICOLD Bulletin B164 (2013) had analyzed the internal erosion of existing dams, levees and dikes, and their foundations. Greco, Pontillo, Iervolino , & Leopardi (2008) used a two-dimensional depth-averaged (2DH) numerical model to simulate the evolution of a breach in an earth-fill dam. Sharif, Elkholy, Hanif Chaudhry, & Imran (2015) constructed a dam in a laboratory flume by using a mixture of sand, silt, and clay with different compaction rates and examined the changes in the depth, area, and volume of erosion during the piping evaluation by utilizing an image processing technique. Most of the researchers realizing numerical analyses make some simplified assumptions concerning shape of a breach and discharge of water flowing through the breach. Morris, Hassan, Kortenhaus, Geisenhainer, Visser & Zhu (2008) reveals that instead of simplified approaches, more realistic approaches are required about the breach mechanism as well as the breach geometry and flow through the breach.

The aim of this study is to realize experiments to study the evolution of dam failure resulting from piping at the upper corner of a dam. For this purpose, the temporal water depths in the channel and discharge through the breach, the temporal variations of the breach area at downstream, upstream and right side, the time dependent wetted area and velocity values were investigated.

2. EXPERIMENTAL PROCEDURE

The dam was built in a rectangular flume of 1 m width, 0.81 m height and 6.14 m length (Figure 1). A homogeneous dam with a height of 0.6 m, a bottom width of 2 m and a crest width of 0.20 m was built in the upper channel. The slope of the upstream and downstream sides was 1:1.5. A pump was utilized to circulate water between the lower reservoir and the upper channel.
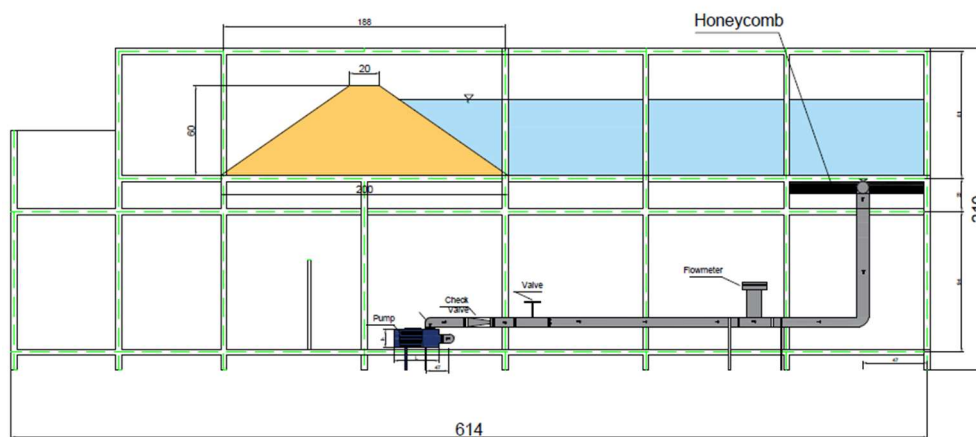
Figure 1. Experimental Flume

Some common soil mechanics tests were performed before the construction of the dam. The dam soil mixture consists of 85 % sand and 15 % clay. The grain- size distribution of the mixture obtained from the wet sieve and hydrometer analyses is given in Figure 2.
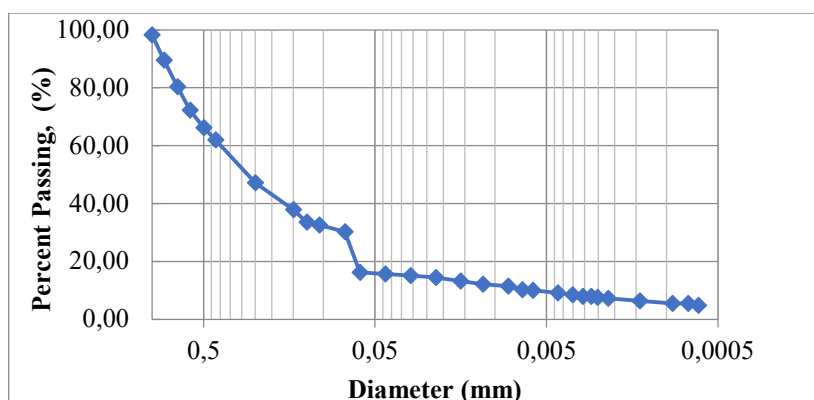
Figure 2. Grain Size Distribution of the dam material

Some characteristic diameters are D_{10}= 0.006 mm, D_{30}= 0.057 mm, D_{50}= 0.099 mm, and D_{60}= 0.3 mm. The uniformity coefficient C_u equals 54.5 and the curvature coefficient C_c is equal to 1.969.

The specific weight of the given soil mixture was determined according to ASTM D854 – 14 and was found to be as G_s =2.63.

The permeability of the mixture was obtained as k= $4.66 \cdot 10^{-4}$ cm/s from the falling head permeability test.

From the direct shear test, it was found that the soil has a cohesion value of 15.33 kPa and an internal friction angle of 33.93^0.

According to the consolidation test results, the compression index (C_c), recompression index (C_r) -and swelling index (C_s) were found to be as 0.100, 0.009 and 0.007, respectively. The oedometric modulus of deformation (E_{oed}) was obtained as 35714 kN/m².

In order to increase the probability of the piping occurrence, the standard proctor test (ASTM-698) was conducted by reducing the applied energy by 50% (13 blows instead of 25) and so obtained the relationship between the maximum dry density and optimum water content was determined as Υ_{drymax}= 1.794 g/cm³ and w_{opt} = 12.5 % (Fig.3). The void ratio (e) was calculated as 0.469.

During the soil compaction, the bulk density of 1.997 g/cm³ was satisfied for each layer according to the proctor test results. Each layer has the same weight in the same volume. The dam consisted of 6 layers and each 10 cm layer was created in four parts by reducing 3.5 cm-height to 2.5 cm with 22 hammer blows on 46x92 cm² plate.
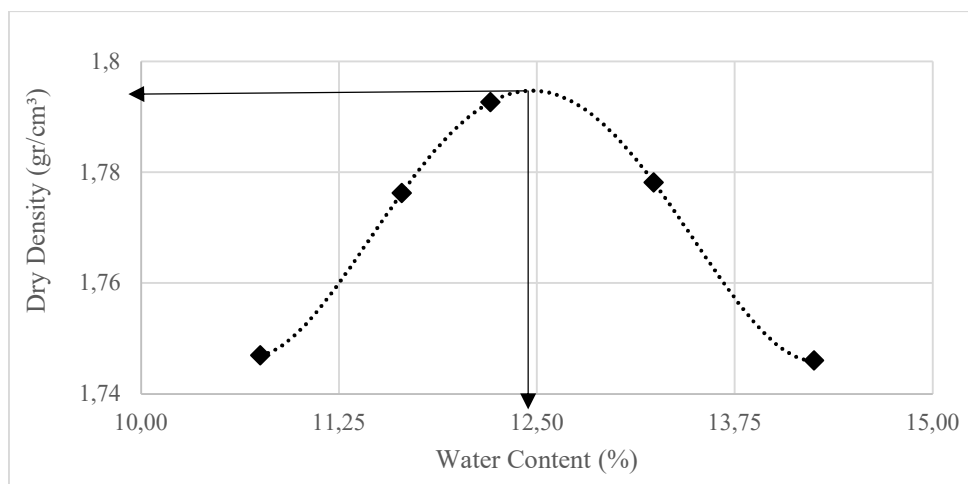
Figure 3. Dry density - water content relationship

Some construction stages and completed shape of the dam body are given in Figure 4. The mixture has distributed homogenously and then it was compacted by using a smooth plate and proctor hammer (Figure 4a). At the end of the compaction stage, the molds were removed, and then the sides of the dam were trimmed by means of a trowel.

(a)   (b)

Figure 4. Some construction stages: a) Compacting by proctor hammer, b) After compaction of the first layer

(c)   (d)

Figure 4. Some construction stages (continued): c) After compaction of the last layer, d) final shape

The flow rate was measured by a magnetic flowmeter. Six cameras located at different locations recorded the evolution of the dam failure. In order to regulate the water level, an electromagnetic sensor was mounted which starts and stops the pump when water depth in the channel was 0.540 m and 0.555 m, respectively.

In order to initiate the breach formation, a circular hole of 2 cm diameter extending from upstream to downstream was created at 54 cm from the upper right side of the dam body. The experiment was started when the water in the flume reached this level and passed through the hole.

3. EXPERIMENTAL FINDINGS

The temporal developments of the breach recorded by the cameras located at downstream, upstream and lateral side of the dam are shown in Figure 5, Figure 6 and Figure 7, respectively. The time t=0 indicates the beginning of the seepage.

(c)   (d)

Figure 5. The temporal development of the breach at downstream a) t=0 s, b) t=220 s, c) t=340 s, d) t=680 s

(e)   (f)

Figure 5. The temporal development of the breach at downstream (continued) e) t=1020 s, f) t=1360 s

(a)   (b)

(c)   (d)
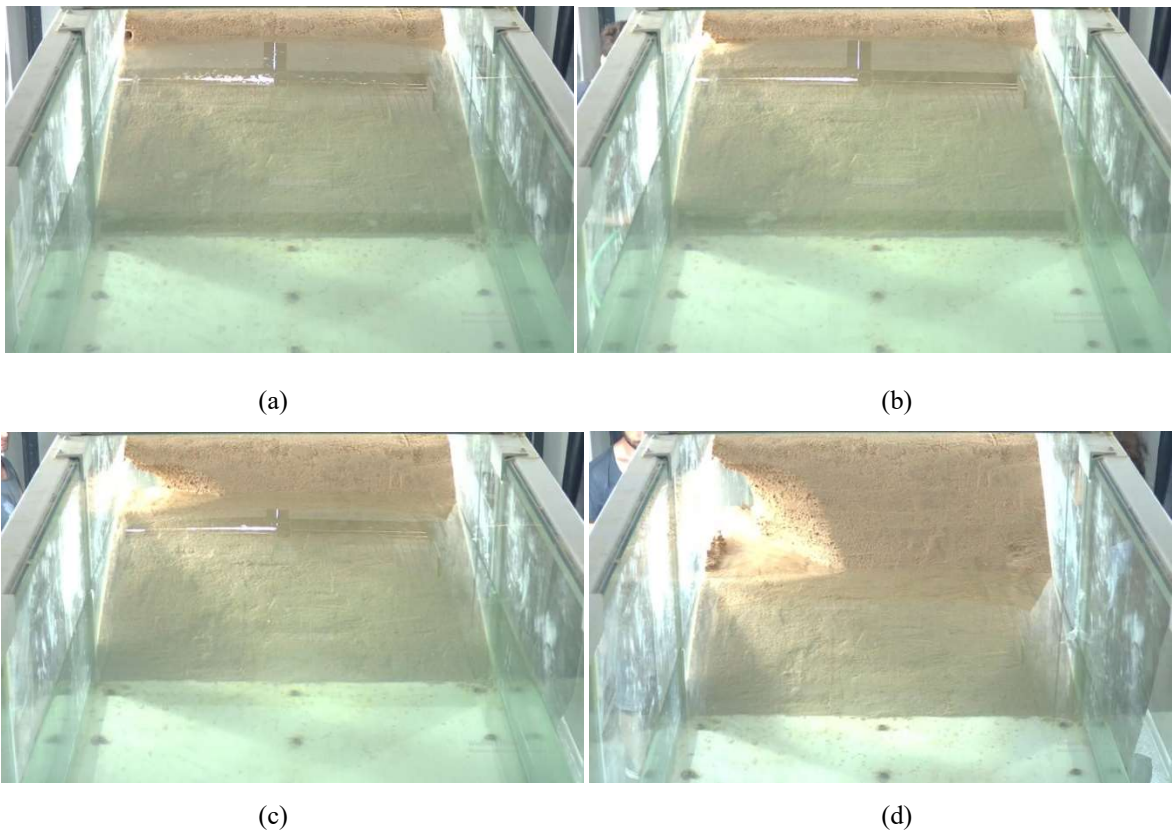
(e)   (f)

Figure 6. The temporal development of the breach at upstream a) t=0 s, b) t=220 s, c) t=340 s, d) t=680 s, e) t=1020 s, f) t=1360 s

(g)   (h)

Figure 7. The temporal development of the breach at upstream (continued) g) t=1700 s, h) t=2040 s

(a)

(b)

(c)

Figure 7. The temporal development of the breach at lateral side a) t=0 s, b) t=220 s, c) t=340s

(d)

(e)

(f)

(g)

Figure 7. The temporal development of the breach at lateral side (continued) d) t=680 s, e) t=1020 s, f) t=1360 s, g) t=1700s

The water depths in the channel were obtained from the camera recordings. In order to obtain the shape of the breach and calculate the changes in its geometry, the upstream, downstream and lateral side cameras images were examined. In order not to work with fisheye images, the videos acquired from lateral camera recording were edited and straightened using Hit-film-Express version 2021.1. Besides, extra sensitive solutions have been applied to ensure that the images are completely flat. The images obtained from the records corresponding to a certain time were scaled and the boundary coordinates of the breaches in downstream and upstream sides were determined in Get-data Graph Digitizer 2.26 environment. The surface areas of the breach evolved at different instants were calculated by using the Gauss Area method.

The discharge of water through the breach was determined by using the continuity equation:

$$\Delta S = (Q_{pump} - Q_{breac}\ ) \cdot \Delta t \tag{1}$$

where Q_{pump} is the flow rate delivered by the pump, Q_{brea} is the discharge through the breach, ΔS is the storage in the channel during the time interval Δt.

The average velocity V of the flow through the breach was approximately calculated by using

$$V = \frac{Q_{breach}}{A} \tag{2}$$

where A represents wetted area.

The temporal water depths in the channel and discharge through the breach calculated by Equation 1 are shown in Figure 8 and Figure 9, respectively.
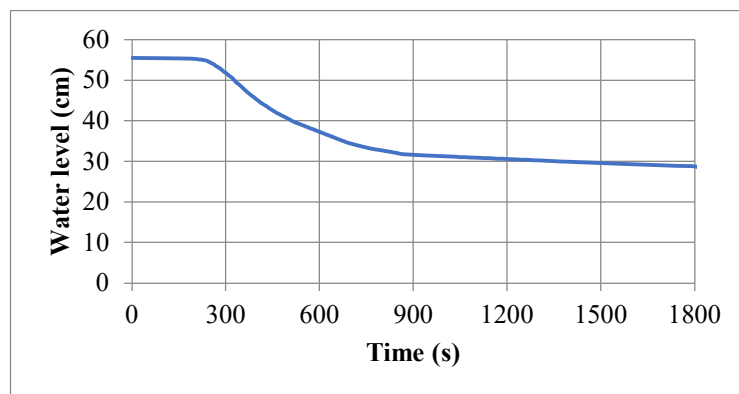
Figure 8. Time-varied water depths in channel
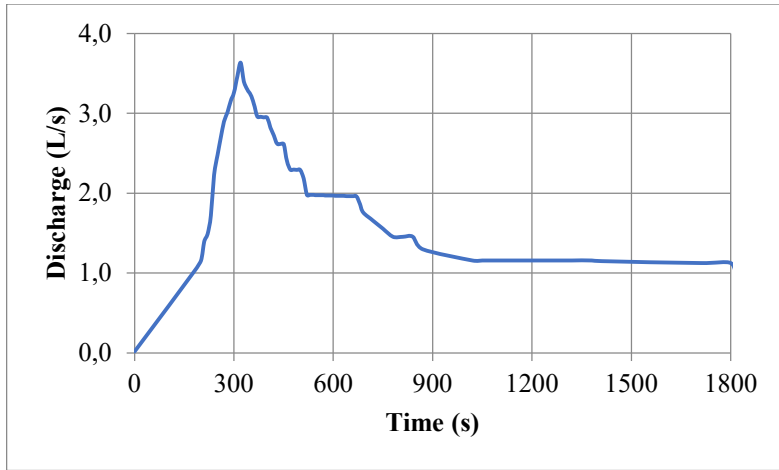
Figure 9. Time-varied average discharge through the breach

The temporal variations of the breach area at downstream, upstream and lateral side are given in Figure 10.
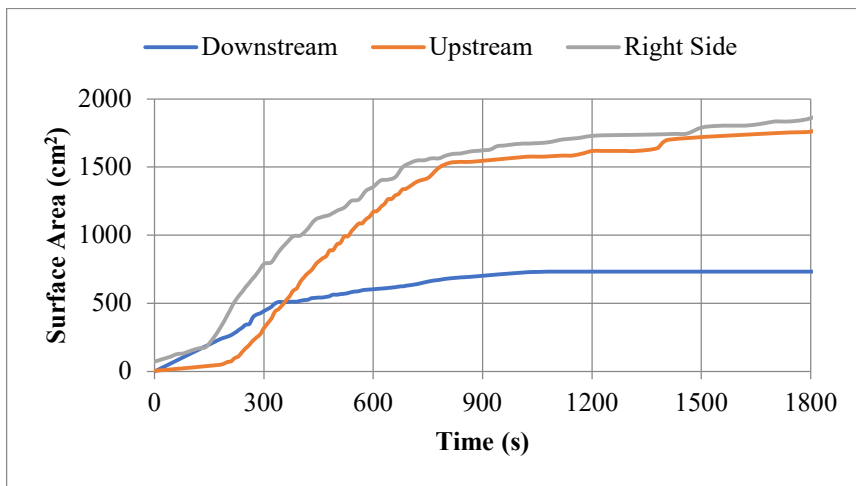
Figure 10. Temporal variations of the breach area at downstream, upstream and lateral side

Besides, the time dependent wetted area and velocity values obtained by using Equation 2 at upstream and downstream are presented in Figure 11 and Figure 12, respectively.

(a)	(b)
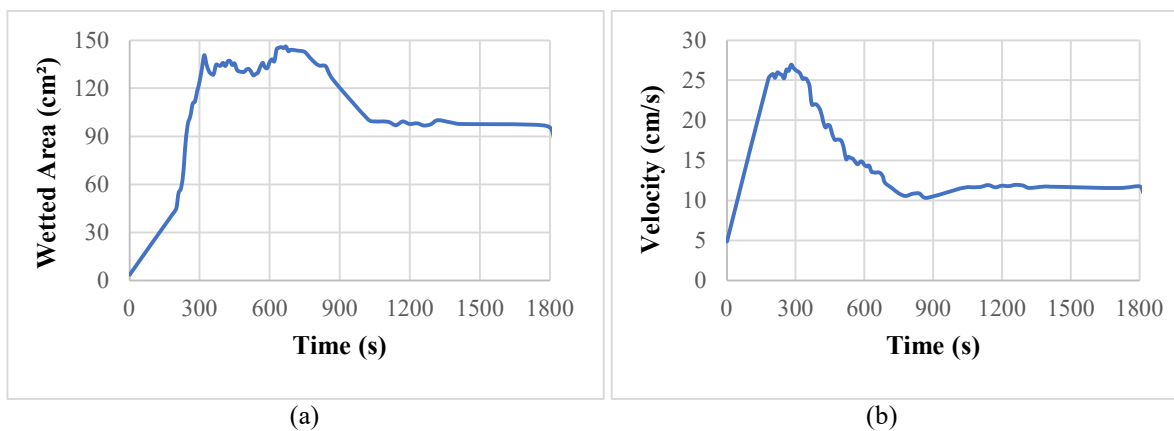
Figure 11. (a) Wetted area and (b) velocity values at upstream
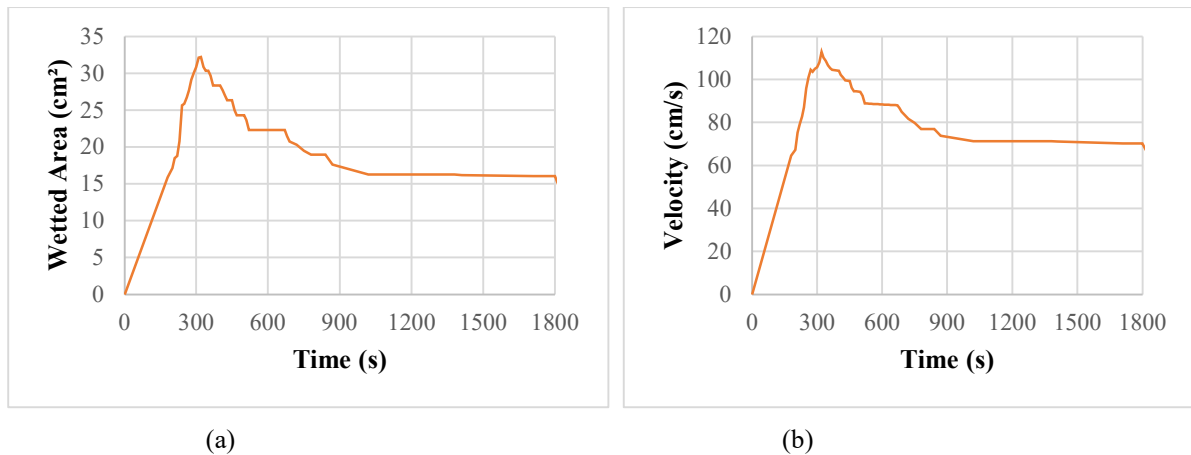
Figure 12. (a) Wetted area and (b) velocity values at downstream

4. RESULTS AND CONCLUSIONS

In this study, time-varied evolution of breach resulting from piping at the upper corner earth-fill dam was experimentally investigated. Camera recordings taken in high resolution were flattened using the Hit-film Express 2021.1. The discharges through the breach corresponding to different instants were calculated using the continuity equation. The boundary coordinates of the breach surface areas and wet areas of the breach were obtained by using the Get-Data Graph Digitizer, and the areas at each time were calculated by applying the Gauss-area function of these obtained coordinates. The time dependent velocity values through the breach areas were also calculated. During the experiment, it was observed that the breach started on the downstream side and then developed towards to upstream side. The maximum discharge through the breach was calculated as Q_{breach}=3.64 L/s at t=320 s. The breach surface area of the upstream was recorded a maximum level of A_{ups}=1760 cm^2 at t =1800 s, while downstream A_{down}= 732 cm^2 at t=1080 s and remained unchanged, also $A_{lateral}$= 1875 cm^2 at t=1800 s. Reached maximum wetted area was found to be $A_{wetted-ups}$=146 cm^2 at t=670 s, $A_{wetted-downs}$=32 cm^2 at t=320 s. The maximum velocity values through the breach were calculated as V_{ups}=27 cm/s at t=280 s and V_{down}=113 cm/s at t=320 s. The pump was turned off and the experiment was terminated at t=1800 s.

In addition to the experimental studies, numerical analysis is also being continued by using the software PLAXIS-3D. It is aimed to give some comments of these experimental findings, in the light of the numerical analysis results, during the oral presentation.

REFERENCES

Chen S., Zhong Q., & Shen G. (2019). Numerical modeling of earthen dam breach due to piping failure. *Water Sci. Eng*., *12*(3) 169–178.

Dounias, G.& Bardanis, M. (2019). The failure of homogeneous dams by internal erosion -The case of Sparmos Dam, Greece. *Sustainable and Safe Dams Around the World* – Tournier, Bennett & Bibeau (Eds) © 2019 Canadian Dam Association, ISBN 978-0-367-33422-2

Fell R., Wan C. H. & Foster M. (2003). Progress report on methods for estimating the probability of failure of embankment dams by internal erosion and piping. *University of New South Wales*, Sydney, Australia.

Greco, M., Pontillo, M., Iervolino, M., & Leopardi, A. (2008). 2DH numerical simulation of breach evolution in an earth dam. *River-flow2008*, Vol. 1, (M. S. Altinakar, M. A. Kökpınar, I. Aydın, S. Çokgör, and S. Kırkgöz, eds., Kubaba, Ankara, Turkey, pp. 661–667).

ICOLD Bulletin No.164. (2013). Internal erosion of existing dams, levees and dikes, and their foundations. Vol 1 & 2

Morris M. W., Hassan M. , Kortenhaus A., Geisenhainer P., Visser P. & Zhu Y. (2008). Modeling breach initiation and growth. *Floodrisk*, Oxford, UK, 30 September-2 October.

Sharif Y. A., Elkholy M., Hanif Chaudhry M., & Imran J. (2015) .Experimental Study on the Piping Erosion Process in Earthen Embankments. *J. Hydraul. Eng*., *141*(7), 04015012.

Zech, Y. & Soares-Frazão, S. (2007). Dam-break flow experiments and real-case data. A database from the European IMPACT research. *Journal of Hydraulic Research*, *45*(1), 5-7, DOI: 10.1080/00221686.2007.9521827

IRRIGATION WATER CONSERVATION PRACTICES IN THE MISSISSIPPI RIVER ALLUVIAL PLAIN: ON-FARM RESERVOIRS

Yavuz Ozeren, Ph.D., P.E.

Research Assistant Professor, National Center for Computational Hydroscience and Engineering, University of Mississippi,

University, MS, USA

yozeren@ncche.olemiss.edu

Daniel Wren, Ph.D.

Research Hydraulic Engineer, USDA-ARS National Sedimentation Laboratory

Oxford, MS, USA

William Rossell

Research Assistant, National Center for Computational Hydroscience and Engineering, University of Mississippi,

University, MS, USA

ABSTRACT: The Lower Mississippi River Basin (the Delta) is one of the major agricultural regions in the United States. Irrigation water in the Delta relies mainly on the Mississippi River alluvial aquifer, which ranks third in the United States for total groundwater withdrawals. Excessive groundwater pumping in the area has resulted in significant groundwater decline in the past 30 years. A number of measures to provide a sustainable source for irrigation water in the region are under investigation. A widely adapted method to reduce the dependence on groundwater resources is the use on-farm reservoirs and tailwater recovery systems. The embankments of the on-farm reservoirs are constructed using locally available soils and typically remain unprotected, which makes them susceptible to erosion due to wind generated waves and surface runoff. Protection and maintenance of the reservoir embankments create additional economic burden on the producers. A series of field studies were carried out by the authors at various on-farm reservoirs in the states of Mississippi and Arkansas to assess the level of embankment impairment in relation to measured wind and wave properties. Laboratory experiments were carried out to identify processes that occurred during wave induced embankment erosion. This paper summarizes the key findings of the laboratory and field measurements.

1. INTRODUCTION

The Lower Mississippi River Basin (locally referred to as the Delta) is the third most irrigated agricultural region in the United States, primarily for the production of rice, corn, soybeans, cotton, sugarcane, and catfish. Despite more than 1 m of average annual rainfall, the majority of the rainfall occurs during winter and spring months and often does not coincide with growing seasons. Thus, producers rely heavily on the shallow Mississippi River Valley Alluvial Aquifer (MRVAA) for irrigation and aquaculture to avoid the risk of drought and to maximize yields (Vories and Evett, 2010). The MRVAA is the second most pumped aquifer in the United States, providing 55 million m³/day irrigation water to approximately 8 million acres (3.2 million hectares) (Lovelace et. al 2020; Alhassan t al 2019). The exact number of irrigation wells in Arkansas and Mississippi is not known; nonetheless, Reba and Massey (2020) reported as many as 14,000 irrigation wells in Mississippi and 40,000 in Arkansas. Due to the intensive pumping, groundwater levels declined more than 30 m in Arkansas and 15 m in Mississippi from predevelopment conditions to 2007 (Clark 2011). Barlow and Clark (2011) reported 186 million m³ average yearly groundwater deficit in the Delta. Groundwater declines have also resulted in decreases in baseflow in numerous streams in the area (Barlow and Clark 2011).

A number of measures to provide sustainable sources for irrigation water in the region are under investigation, including the use of better irrigation management practices to conserve water. One solution is the use of on-farm reservoirs and tailwater recovery systems for irrigation water management and storage Mississippi. Tailwater recovery systems are used to capture excess runoff from production fields in nearby ditches. The collected water is then either re-distributed back to the crops or pumped into an on-farm reservoir. On-farm reservoirs store water during the wet season to be used for irrigation during the dry season to reduce dependence on groundwater resources. In addition to their function as water storage, on-farm reservoirs provide additional benefits by capturing sediment and nutrient rich runoff from the fields.

The embankments of the on-farm reservoirs are built above ground following a cut-and-fill method using the surrounding soil. The inner slopes of the earthen embankments range between 1:5 to 1:3 and typically are not protected against erosion (USDA-NRCS, Wren et al. 2016). The average surface area of on-farm reservoirs range between 5 ha and 20 ha (Yaeger et al. 2017) with a storage depth typically ranging between 2 - 4 m (Wren et al. 2018). The reservoirs are filled to capacity during winter and spring months which coincides with the highest winds observed in the area. Sustained winds up to 50 km/h are common during spring months (Wren et al. 2016). Due to the size of the reservoirs and the open terrain surrounding them, winds can generate waves as high as 30 cm along the down-wind embankments.

Protection of the embankments against wind-generated waves is rarely practiced during construction because of its cost (Wren et al. 2016). The USDA-Natural Resources Conservation Service (NRCS) recommends using vegetation for erosion protection, but high-water levels in spring and dry conditions in the summer make it difficult to maintain vegetation cover on the inner slopes of the embankments. Other protection methods, such as rock armoring, concrete, and geotextiles, are not widely practiced due to their high cost and large amounts of material required.

In the past decade, we have carried out field studies in a number of reservoirs to measured wind and wave conditions, and embankment profiles in several reservoirs in an effort to understand the primary mechanisms of embankment erosion. The goal of this effort has been to establish predictive relationships between embankment erosion and wind and wave characteristics (Wren et al. 2016 and 2018). We conducted laboratory experiments using a model earthen embankment to quantify erosion and retreat rates as a function of incident wave height (Ozeren et al. 2020). We have tested a model floating pipe breakwater design that can be used as a cost-effective erosion protection method for reservoir embankments (Ozeren et al., 2011. We have also investigated mooring arrangements for float breakwaters, since mooring is a key parameter that determines the effectiveness of the breakwaters (Rossell et al., 2021). The construction of a prototype-scale floating pipe breakwater for deployment in a working irrigation reservoir is underway. The following sections summarize the key findings of these studies.

Figure 1. The northeast embankment of Johnson Farm reservoir near Shelby, MS

2. FIELD MEASUREMENTS

2.1. Wind and Wave Conditions

Field studies were carried out in on-farm reservoirs in the states of Arkansas and Mississippi. In March 2005, a temporary wind and wave monitoring station was deployed in an irrigation reservoir east of Carlisle, Arkansas, USA (Ozeren et al. 2008). The reservoir depth was approximately 2.5 m. The rectangular shaped reservoir was 370 m along the north-south direction,770 m along the east-west direction, and approximately 2.5 m deep at the measurement site on the south-west corner of the reservoir. The measurement station consisted of two ultrasonic distance sensors and a wind anemometer. Up to 48 km/h sustained winds were recorded, which generated 0.25 m high significant waves over a fetch length of 586 m during a 1.5 hour data collection period. Additional wind and wave measurements were carried out in the same reservoir in 2007 and 2008 (Ozeren and Wren, 2009). Wave heights reached up to 0.2 m under winds up to 43 km/h over a 300 m long fetch. In June 2012, a wind and wave monitoring station were installed in an on-farm reservoir near Fisher, Arkansas. The rectangular reservoir was 500 m in the north-south direction and 280 m in the east-west direction. Wind and wave data was collected between June and September 2012 using three wave staffs and a wind anemometer at the wave measurement station near the northeast corner of the reservoir. Winds as high as 43 km/h were observed, generating waves with significant heights of up to 0.25 m at a 560 m fetch and at water depths around 1.5 m (Wren et al., 2016).

More recently, a field campaign was carried out in an on-farm reservoir near Shelby, Mississippi (Johnson Farm reservoir). The reservoir was 300 m (east-west) by 390 m (north-south). Two self-logging wave staffs near the north and south embankments and a wind measurement station on the northeast corner of the reservoir were deployed. Winds exceeding 55 km/h and significant wave heights over 0.25 m were recorded between March-September 2021 (Figures 2 and 3). In all of these studies, the strongest winds were observed from the south and north, especially during the winter months.
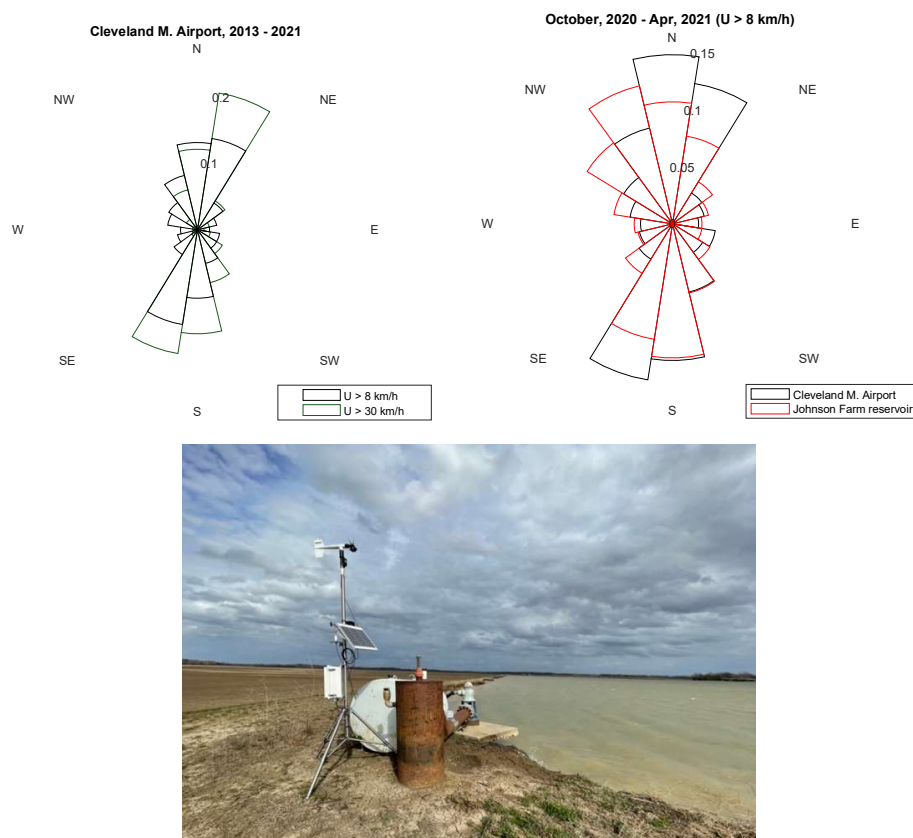
Figure 13. Comparison of wind measurements at the Johnson Farm reservoir and Cleveland Mississippi Municipal Airport between October, 2020 and April, 2021 (top), and a picture of the wind station (bottom)
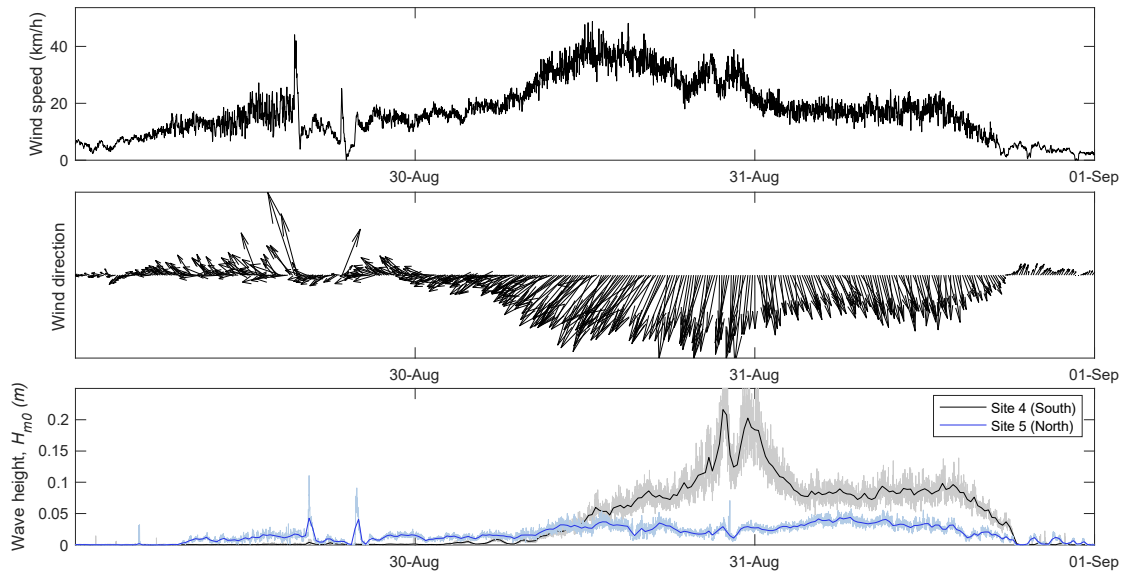
Figure 3. A sample wind and wave dataset recorded at the Johnson Farm reservoir (Shelby, Mississippi, USA)

2.2. Embankment Erosion

Erosion measurements were made with a ground-based LIDAR system and erosion pins at the reservoir near Fisher, Arkansas. Approximately 1350 m³ of soil loss was measured from a 1530 m long levee during a seven-month period between December 2012 and July 2013 (Figure 4a). Strong southerly winds aligned with the longest fetch length resulted in 3 m embankment retreat on the northeast corner of reservoir. The 5-year maintenance cost of the embankments was estimated to be approximately 16% of the initial construction cost of the reservoir (Wren et al., 2016).

Two comprehensive surveys along the embankments of a reservoir at the University of Arkansas Pine Bluff (UAPB) Lonoke Demonstration Farm was carried out in 2015 and 2017. The reservoir was built in 2007, using 17 different slope configurations and 5 different mechanical treatment techniques (geotextile, concrete, etc.) distributed along the embankments to compare their effectiveness against wave erosion. The surveyed transects were compared with as-built embankment transects to quantify the effectiveness of these treatment methods. Almost all of the slope configurations were significantly eroded over the 10 year period (Figure 4b). Mechanical treatment methods were superior compared to slope treatment methods. In general, milder slopes and berms delayed embankment recession.
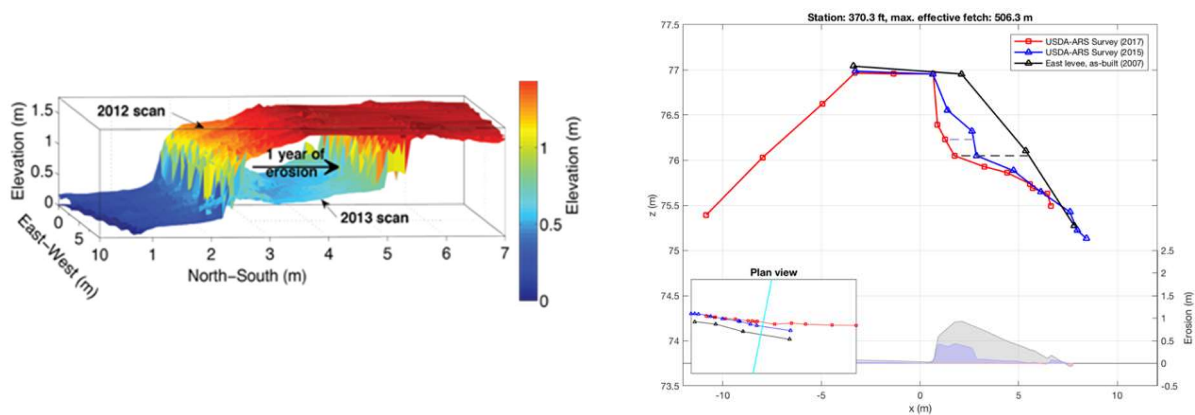
Figure 4. (a) LIDAR data showing 2012 and 2013 scans on a 10 m section of the north levee of an irrigation reservoir near Fisher, Arkansas, USA (Wren et al 2016), and Shelby, Mississippi 2021 in the photo; (a) a typical transects from the 2007, 2015, and 2017 surveys of UAPB Demonstration Farm reservoir (Ozeren et al. 2018)

Embankment profiles for Johnson Farm reservoir were surveyed between December 2020 and September 2021. The embankments were significantly deteriorated due to wave erosion. The survey results showed noticeable erosion along the inner slopes of north and south embankments. The largest change in the embankment geometry was observed between the December 2020 and April 2021 surveys.

3. LABORATORY MEASUREMENTS

Laboratory efforts focused on the recession of model embankments constructed using an artificial granular material, sand and natural soils. Experiments were carried out in a 20.6 m long, 0.7 m wide, and 1.2 m deep laboratory wave tank at the USDA-ARS, National Sedimentation Laboratory in Oxford, Mississippi. A standardized packing procedure was developed to establish the steep model embankment in the wave tank. Particle size distribution, critical shear stress and the packed density of the model embankments were measured for the experiments. The model embankment was exposed to wave action for up to 48 hours, and the evolution of the embankment profile was monitored using photogrammetric methods. The embankment profiles were digitized manually or using automated edge detection algorithms. Figure 5 shows the envelope of digitized profiles of a model earthen embankment. The embankment profiles progressed from blue to red under the action of regular waves for 24 hours. Discrete bank top retreat progression in Figure 5 indicates block failures, which is the primary mode of embankment retreat observed in the field. Although the recession rates of both sand and earthen embankments were similar, the sand embankment reached an equilibrium profile much quicker and at a steeper beach slope then the earthen embankment. The collected data was used to establish semi-empirical relationships between erosion, retreat rate, and incident wave characteristics (Ozeren et al. 2021).
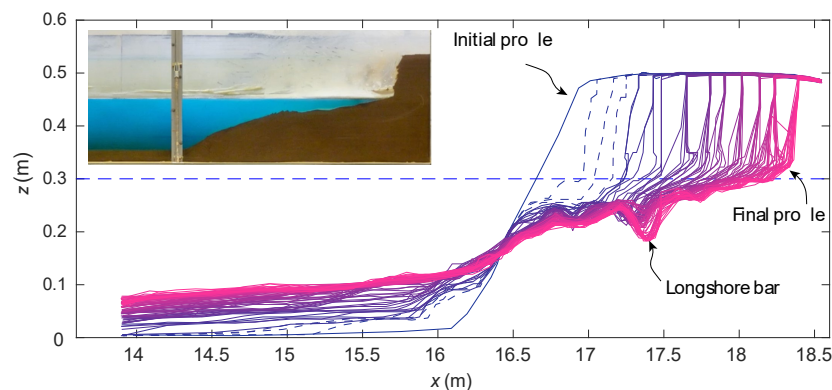
Figure 514. Erosion and retreat progression by wave action in the laboratory wave tank at NSL.

4. CONCLUSIONS

Irrigation reservoirs have been used effectively in the Lower Mississippi River Basin in the United States for water storage to reduce demand on declining groundwater resources. Earthen embankments of the irrigation reservoirs are subjected to wave erosion when left unprotected, which creates additional maintenance costs for producers. A series of field and laboratory studies were carried out over the past decade to understand the relationships between wind generated wave characteristics and embankment impairment. The studies also aimed to generate datasets that can be used to provide an economic basis for selecting a protection method for vulnerable embankments. The key findings of these studies were summarized. A pilot study to test the performance of a prototype scale floating wave barrier is underway in an irrigation reservoir near Shelby, Mississippi, USA. A numerical study to simulate long-term embankment recession is also ongoing. The model will be used to improve the estimated embankment recession rates at the laboratory and test a simpler theoretical model that relates incident wave properties and time-evolution of the erosion and retreat of reservoir embankments.

REFERENCES

Alhassan, M., Lawrence, C. B., Richardson, S., & Pindilli, E. J. (2019). *The Mississippi Alluvial Plain aquifers—An engine for economic activity* (No. 2019-3003). US Geological Survey.

Barlow, J.R.B., and Clark, B.R. (2011), *Simulation of water-use conservation scenarios for the Mississippi Delta using an existing regional groundwater flow model:* U.S. Geological Survey Scientific Investigations Report 2011–5019, 14 p.

Clark, B.R., Hart, R.M., and Gurdak, J.J. (2011), *Groundwater availability of the Mississippi embayment:* U.S. Geological Survey Professional Paper 1785, 62 p.

Lovelace, J. K., Nielsen, M. G., Read, A. L., Murphy, C.J., and Maupin, M. A. (2020). "Estimated groundwater withdrawals from principal aquifers in the United States." *US Geological Survey.*

Ozeren, Y., and D. G. Wren. (2009). Predicting wind-driven waves in small reservoirs. *Transactions of the ASABE* 52 (4): 1213–1221.

Ozeren, Y., D. G. Wren, and C. V. Alonso. (2008). Development of floating wave barriers for cost-effective protection of irrigation pond levees. *Transactions of the ASABE* 51 (5): 1599–1612.

Ozeren, Y., D. G. Wren, and H. Yasarer. (2018). Assessment of levee treatments for an irrigation reservoir in Arkansas. *Transactions of the ASABE* 61 (5): 1677–1689

Ozeren, Y., Wren, D. G., Altinakar, M. and Work, P. A. (2011). Experimental Investigation of Cylindrical Floating Breakwater Performance with Different Mooring Configurations, *J. Waterway, Port, Coastal, Ocean Eng.*, *ASCE*, 137(6), 300-309

Reba, M. L., & Massey, J. H. (2020). Surface irrigation in the lower Mississippi river basin: Trends and innovations. *Transactions of the ASABE*, *63*(5), 1305-1314.

Rossell, W., Ozeren, Y., and Wren, D.(2021). Experimental Investigation of a Moored, Circular Pipe Breakwater. *Journal of Waterway, Port, Coastal, and Ocean Engineering*. 147(5), p.04021019

Vories, E. D., & Evett, S. R. (2010). Irrigation research needs in the USA mid-south and southeast, humid and sub-humid regions. In M. Dukes (Ed.), *Proc. 5th National Decennial Irrigation Conf.* St. Joseph, MI: ASABE.

Wren, D. G., Y. Ozeren, and M. L. Reba. 2016. Measuring the erosion of an irrigation reservoir levee. *Transactions of the ASABE* 59 (1): 41–48.

Wren, D. G., Y. Ozeren, J. M. Taylor, M. L. Reba, and C. Bowie. (2018). Assessment of irrigation reservoir levee impairment in Arkansas, United States. *J. Soil Water Conserv.* 73 (5): 533–540.

Yaeger, M. A., M. L. Reba, J. H. Massey, and M. A. A. Adviento-Borbe. (2017). On-farm irrigation reservoirs in two Arkansas critical ground- water regions: A comparative inventory. *Appl. Eng. Agric.* 33 (6): 869–878

WATER QUALITY AND ECOHYDRAULICS

MATHEMATICAL MODELING OF WATER QUALITY MODELING IN A POLLUTED RIVER UNDER POINT AND NON-POINT SOURCES: CASE STUDY, BAKIRÇAY RIVER

Yiğithan Kazancı

Environmental Engineering Department, Izmir Institute of Technology

Izmir, Turkey

yigithankazanci@iyte.edu.tr

Yakup Karaaslan

General Directorate of Water Management, Republic of Turkey Ministry of Agriculture and Forestry

Ankara, Turkey

yakup.karaaslan@tarimorman.gov.tr

Taner Kimençe

General Directorate of Water Management, Republic of Turkey Ministry of Agriculture and Forestry

Ankara, Turkey

taner.kimence@tarimorman.gov.tr

Burhan Fuat Çankaya

General Directorate of Water Management, Republic of Turkey Ministry of Agriculture and Forestry

Ankara, Turkey

burhanfuat.cankaya@tarimorman.gov.tr

Aylin Okuldaş Çetin

General Directorate of Water Management, Republic of Turkey Ministry of Agriculture and Forestry

Ankara, Turkey

aylin.okuldascetin@tarimorman.gov.tr

Selcan Batuk

Cinar Engineering Consulting Company

Ankara, Turkey

s.batuk@cinarmuhendislik.com

Okan Fıstıkoğlu

Civil Engineering Department, Dokuz Eylül University

Izmir, Turkey

okan.fistikoglu@deu.edu.tr

Alper Baba

Civil Engineering Department, Izmir Institute of Technology

Izmir, Turkey

alperbaba@iyte.edu.tr

Orhan Gündüz

Environmental Engineering Department, Izmir Institute of Technology

Izmir, Turkey

orhangunduz@iyte.edu.tr

ABSTRACT: Mathematical models are useful tools to estimate the impact of point and non-point sources of pollution in basins on surface water quality. Therefore, it is an integral part of decision-making mechanism in river basin management. These models allow us to understand how the natural system behaves under current anthropogenic stresses and also enable us to make predictions for future conditions under various administrative scenarios. For this reason, mathematical modeling is considered as an important component of river basin management and planning. Based on this premise, a water quality modeling study was implemented for the Bakırçay River, one of the most polluted streams of Western Anatolia. For this purpose, the AQUATOOL model developed by the Polytechnic University of Valencia Water and Environmental Engineering Research Institute was used and the effects of point and non-point pollution sources on the surface water quality of Bakırçay River were examined. In this application, Dissolved Oxygen (DO) state variable is evaluated in order to show the improvement in the total status of water quality with Biological Oxygen Demand (BOD_5), Organic Phosphorus (Organic P) and Ammonium (NH_4), which were found to be above legal limits. Unit load assumptions were used to identify pollution loads from the point and non-point sources and the performances of domestic and industrial wastewater treatment plants were also taken into account to reveal the total loads of the parameters in the basin. Model calibration was performed on hydraulic parameters and biochemical decay constants. The calibrated model was then run in conjunction with 9 different basin management scenarios to assess the impact of precautions taken to improve water quality in the river system and the cumulative impact was assessed. The results revealed that a reduction of 31% in BOD_5, 16% in Organic P and 23% in NH_4 was observed thanks to the cumulative precautions applied. However, 1% improvement in DO parameter suggested that background pollution was already high in Bakırçay River Basin.

1. INTRODUCTION

In the last several decades, surface and ground waters are polluted due to anthropogenic sources. Discharge of wastewaters originating from increased population density and associated unplanned urbanization and industrialization, agricultural runoffs containing high levels of chemical fertilizers and pesticide residues and uncontrolled leakages from solid waste dump sites and landfills can be counted as the major sources of anthropogenic sources of pollution. These sources are responsible from carbon compounds and nutrients such as nitrogen and phosphorus that are found in elevated levels in surface waters. Carbonaceous compounds lead to a decrease in the amount of dissolved oxygen levels, and substances containing nitrogen and phosphorus cause eutrophication in surface waters. These degradations in water quality often hinder the use of surface waters for drinking purposes as well as for recreation and fishing.

The Bakırçay River, which is the subject of this study, is located in the Kuzey Ege Basin in Western Anatolia and is born from the foothills of Kocadağ. It has a total length of about 120 km and flows through the provinces of Manisa and İzmir before it finally reaches the Aegean Sea. The drainage area of Bakırçay Riveris approximately 3400 km^2 (SYGM, 2020). Bakırçay Riveris the most important river of the Kuzey Ege Basin and is under pressure from domestic and industrial pollution. As of 2017, the total population of the basin is 275,786. The most important settlements in the basin are Soma and Kırkağaç district centers of Manisa and Kınık and Bergama district centers of İzmir. According to 2017 data, there are approximately 104,000 cattle, 254,000 sheep and 7,918,000 poultry in the Bakırçay Basin. There are 17 urban wastewater treatment plants in the basin, 8 of which are operational, 9 of which are at the tender and/or planning stages. In addition, wastewater disposal of smaller settlements throughout the basin is carried out by means of septic tanks or wastewater is discharged to the surface water resources directly without any treatment. According to 2019 data, the number of active septic tanks in the basin is 205 and the number of urban raw wastewater discharges is 38. According to CORINE data, about 1500 km^2 of the basin's total area is agricultural lands. The basin also contains intense energy production and mining activities. A total of 19 individual industrial wastewater treatment plants are present in the Bakırçay basin, and 15 of which are currently operative. These facilities are mainly located in the energy and mining sectors. In addition, Kınık,

Soma and Bergama Organized Industrial Zones are also located within the borders of the basin (SYGM, 2020).

Discharge of wastewater containing biodegradable organic substances into rivers leads to a decrease in dissolved oxygen concentrations. This reduction in oxygen level results from the metabolic degradation and chemical oxidation of organic pollutants by microorganisms (Paliwal et al., 2007). Dissolved oxygen level is an indicator parameter in determining the biological and chemical quality of surface water ecosystems. For this reason, oxygen levels and organic matter concentrations in rivers should be followed spatially and temporally at certain intervals. In addition, elevated presence of nitrogen and phosphorus-containing compounds in water triggers excessive biological production and cause quality deterioration of the general condition of the water. In particular, eutrophication process begins, especially in the case of excessive nitrogen and phosphorus inflow into stagnant lake water bodies, and the overall quality of the water body is often irreversibly impaired. In the light of this information, control of both organic and nutrient inflows into surface waters is of great importance in terms of sustainability of water quality. In order to minimize the loads of organic matter and nutrients, it is necessary to determine the point and non-point precautions that need to be taken and to decide on administrative issues such as planning and resource use, in order to predict how the quality situation in the water bodies will improve following these precautions. The most basic tool used for this purpose is water quality modeling.

In this study, AQUATOOL model was used to mathematically model the water quality in Bakırçay River. AQUATOOL model was preferred due to its ease of use in basin systems. The model was first calibrated and verified and was later used as a simulation tool to test the effectiveness of 8 precautionary best management scenarios. With these scenarios, the fate of carbon, nitrogen and phosphorus loads that are coming to the river stream as point or non-point sources are analyzed and the fate of dissolved oxygen that is indirectly effected by these loads are evaluated.

2. METHODOLOGY

2.1. Study Area (Bakırçay River)

Bakırçay River is located in the north of the Aegean region, generally between the latitudes of 39°-40° North and longitudes of 27°- 28° East, within the borders of İzmir and Manisa provinces (Figure 1). The average flow of the river is 14.26 cubic meters per second, while the total annual water potential is around 450 million cubic meters. The main pollutant sources in Bakırçay River Basin are urban and industrial point discharges and non-point pollution originating from agriculture, animal husbandry and land use. A few of the important facilities in the basin are the Soma Thermal Power Plant in Soma district and the coal mining carried out accordingly, milk and dairy products factories in Bergama and tomato paste production facilities (ÇŞB, 2015). In addition, olive-growing activities are an important economic activity in the Bakırçay basin.

Approximately 1140 tons/year COD, 160 tons/year Total Nitrogen and 26 tons/year Total Phosphorus load are formed from 8 active urban wastewater treatment plants in the basin. In addition, there are 2250 tons/year COD, 110 tons/year Total Nitrogen and 50 tons/year Total Phosphorus load originating from 9 individual industrial facilities in the basin and 3 organized industrial zones. Furthermore, 33 olive and olive oil production facilities process about 38 million olives per year, and create an approximate pollution load of 325 tons of COD, 3.25 tons of Total Nitrogen and 0.218 tons of total phosphorus per year. In addition, there are approximately 220 tons of Total Nitrogen and 8 tons of Total Phosphorus load annually, which results from about 90,000 cattle, 262,000 ovine and 7,820,000 poultry. The annual Total Nitrogen and Total Phosphorus loads that originate from land use are 990 and 47 tons, respectively. Additional Total Nitrogen and Total Phosphorus loads enter the basin from the atmosphere and these loads are is estimated to be approximately 77 tons and 7 tons, respectively. Two additional anthropogenic and non-point pollutant sources are septic tanks and solid waste landfills. It is expected that 70 tons per year Total Nitrogen and 11 tons per year Total Phosphorus load occur in the basin from these sources. Finally, it is calculated that the loads expected to be formed from the uncontrolled solid waste disposal areas are 850 tons per year COD, 68 tons per year Total Nitrogen and 2 tons per year Total Phosphorus (SYGM, 2020).

Figure 1. Bakırçay river basin
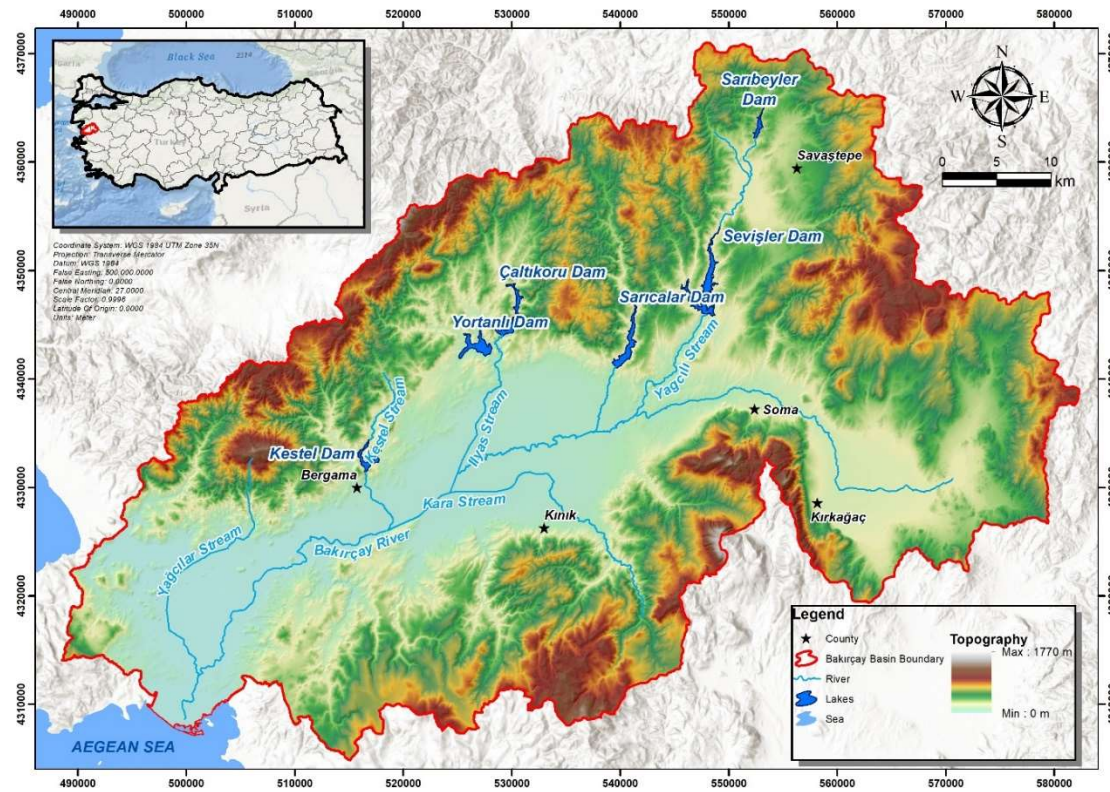
2.2. Model and Dataset

AQUATOOL, the modeling platform used in this study, is a user-friendly modeling and decision support system developed by Polytechnic University of Valencia. The system consists of several modules and allows the analysis of different approaches in water resources studies (Andreu et al., 1996; Pedro-Monzonís et al., 2016). EVALHID is one of the modules that make up AQUATOOL and is used to evaluate the amount of water quantity in the system. It also enables the establishment of precipitation-flow models in the basins. Another module, SIMGES, is a general simulation model where the drainage network is created to perform the flow accumulation in accordance with the defined restrictions. SIMGES executes a simple flow balance on the monthly scale. GESCAL module on the other hand is a module developed to estimate water quality. In addition to these modules, OPTIGES module is sometimes used to solve the problem of monthly water allocation with the help of optimization tools of different water demands and reservoir operating conditions in river basins and SIMRISK module is used to assess administrative risks under different hydrological scenarios to be used in river basin management plans in the medium term.

The model prepared for Bakırçay is a platform consisting of EVALHID, SIMGES and GESCAL modules and used to simulate the hydrological and water quality situation in the stream. The first stage of the model establishment process is to introduce the main reach and side tributaries of the Bakırçay River to the model interface. Meanwhile, while the reservoirs in the basin are introduced as a node, the branches forming the drainage network are defined as channel type. Bakırçay and its tributaries are divided into segments for this purpose. This segmentation process is seen as the process elements where the mathematical analysis of the model is made, and the surface water bodies determined by the Ministry of Agriculture and Forestry are taken into consideration. The river parts that make up the drainage network are divided into 2 equal parts and 3 sub-watershed areas are created for each part. These sub-basins are important for more precise identification of pollutant loads to the model. The natural flow input of the river system are calculated based on the precipitation-flow relationship and the hydrodynamic connection are established and introduced to the model. The interaction of surface water with groundwater are determined and entered into the system by using the relative hydraulic heads and interface conductivities. In addition to natural flow rates, the flow rate values of the point pollution sources entering the river system are input from relevant node points of

the segments where they are located. The flow simulation of the Bakırçay river system, along with the given natural flow rates, point source flow rates and water intakes, was calculated with EVALHID and SIMGES modules. With the completion of this phase, the process of introducing the necessary datasets to the model was initiated in order to operate the GESCAL water quality module. At this stage, the concentrations of all pollution sources of the system were calculated and entered to the model. In addition, the hydraulic parameters, biochemical reaction constants and transport characteristics required for water quality modeling were defined and input on a segment basis. In the meantime, channel hydraulic parameters such as section type, length, width, Manning roughness coefficient and slope of channel segments were created based on the information provided by field studies, geographic information system analysis and remote sensing methods. Temporal and spatial step sizes and dispersion constants are also entered. In addition, chemical parameters such as re-aeration constant, organic substance degradation constant, nitrification constant, denitrification constant, organic phosphorus degradation constant for each segment and reservoir were also entered to the model. All the data layers that are necessary to run the model have been revealed by defining related information that represent the basin in general besides such spatial model parameters. Finally, the water quality measurement results obtained from the monitoring activities in the basin were also entered to the model for use in the model calibration and verification stages. The kinetic parameters and constants used in the calibration process were determined based on the values in the literature (Bowie, 2004; Metcalf et al., 2002; Te Chow, 1959). These parameters are given in Table 1.

Table 1. Biochemical constants recommended and used in the model.

Parameter	Unit	Recommended range	The calibrated value
Organic matter degradation constant	1/day	0.02 - 3.4	0.4
Organic nitrogen degradation constant	1/day	0.02 - 0.4	0.1
Ammonium nitrification constant	1/day	0.01 - 1	0.1
Organic phosphorus degradation constant	1/day	0.01 - 0.7	0.2
Light saturation intensity	-	-	250

During the operation of the model, it is assumed that all diffuse source pollutants enter the system with natural flow rates, and the concentration values that occur for each pollutant from each flow input are calculated and entered to the model. All hydrological data and water quality monitoring results used in the model were obtained from the Kuzey Ege River Basin Management Draft Plan prepared for the General Directorate of Water Management of the Ministry of Agriculture and Forestry (SYGM, 2020). The model topology, whose segmentation is completed and whose pollution sources and natural flow inputs are specified, is shown in Figure 2.
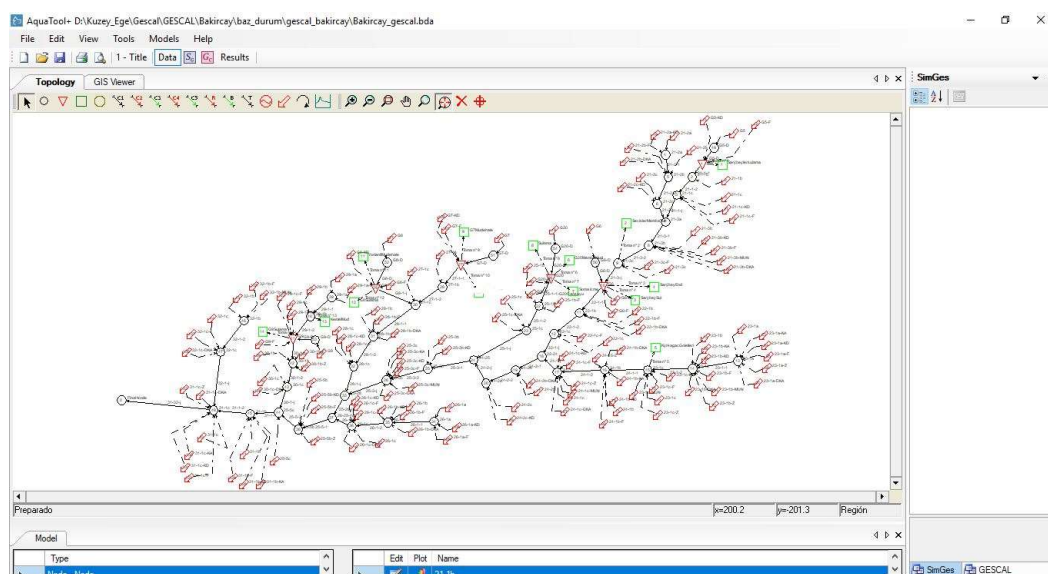
Figure 2. Bakırçay model topology

It is important to complete the calibration and verification of the hydrological model in order to run the quality model. In this context, GR2M, a monthly precipitation-flow model developed by Mouelhi et al. (2006) and included in the EVALHID module, was used. The calibration range of the hydrological model covers between 01/10/1973 and 01/05/1990, and the verification range between 01/05/1990 and 01/09/2014. The water quality model was calibrated using the GESCAL module. In the modeling study, dissolved oxygen (DO), biological oxygen demand (BOD_5), organic phosphorus (Organic P) and ammonium (NH_4) constituents are modeled. The calibration of the quality model was carried out in a 7-month period from February 2018 to August 2018. February data were used as the initial values of the model. The model was run in one dimension using monthly variable load values.

2.3 Scenarios to Improve Pollution Status

After model calibration and verification, the measures that can be taken to improve water quality have been analyzed. Different precautionary measures that can be applied to different pollution sources have been evaluated and formulated to reduce point and non-point organic pollutants and nutrient loads. Accordingly, the following scenarios have been created and tested in the model:

- Scenario 1: Combined Basic Precautions
- Scenario 2: Application of Advanced Treatment Technologies for Industrial WWTPs
- Scenario 3: Nutrient Control
- Scenario 4: Terracing
- Scenario 5: Green Belt
- Scenario 6: Pesticide Control
- Scenario 7: Crop Rotation
- Scenario 8: Application of 1-meter wide herbal barrier to the boundaries of the lands with slope to the water body

Within the scope of the combined basic measures called Scenario 1, precaution to establish septic tanks for urban direct discharges originating from the population of 1000 and below, the rehabilitation of irregular solid waste disposal areas and the precaution to ensure zero discharge with leak-proof evaporation tanks for olive and olive oil production facility wastewaters are all implemented together. In Scenario 2, the scenario of applying advanced treatment technologies to industrial wastewater treatment plants without advanced treatment is considered. In Scenario 3, the effects of nutrient control measures are modeled by increasing the use of animal fertilizers instead of chemical fertilizers used in agricultural areas. In Scenario 4, the reduction of non-point nutrient loads is investigated by terracing high (12-20%) and very high (> 20%) sloping agricultural areas. In Scenario 5, the effects of applying forest buffer zones along the rivers and lakes (also known as green belts), are examined in order to reduce the penetration of non-point nutrient loads into water bodies. In Scenario 6, the results of the precaution of controlling pesticides applied to agricultural areas through biological control, active substance exchange and reduction of use are examined. In Scenario 7, the effects of planting different crops with a planned order, either yearly or periodically (also known as crop rotation), are examined. Finally, in Scenario 8, the effects of applying a 1-meter wide herbal barrier to the boundaries of the lands sloping directly towards the water body are evaluated. The load reduction rates expected to occur as a result of the implementation of the above mentioned water quality improvement measures are given in Table 2 and Table 3.

Table 2. Removal efficiencies according to treatment type.

Treatment Type	COD Removal Efficiency (%)	TN Removal Efficiency (%)	TP Removal Efficiency (%)
Physical	10	0	0
Biological	80	25	10
Advanced Biological (N and P removal)	80	70	70
Natural treatment	55	20	35
Septic Tank	50	20	30
Package Treatment	90	40	30
Other (Unknown)	80	20	30

Table 3. Load reduction rates used in scenarios.

Scenario Definition	COD/BOD Removal Efficiency (%)	TN Removal Efficiency (%)	TP Removal Efficiency (%)
WWTP to direct discharges (N> 1000)	Varies according to facility type	Varies according to facility type	Varies according to facility type
Septic Tanks to direct discharges (N< 1000)	Varies according to facility type	Varies according to facility type	Varies according to facility type
Rehabilitation of uncontrolled solid waste storage (with the acceptance of point input)	35	35	35
Zero discharge from olive growing facilities	100	100	100
Advanced treatment to industrial WWTPs	90	90	90
Nutrient Control (Using animal fertilizer instead of chemical fertilizer)	0	Reduces by area	Reduces by area
Terracing	50	50	50
Green Belt (Forest buffer by the river and lake)	50	80	50
Pesticide Control (Biological control, Active substance change, Reducing use)	0	0	0
Crop Rotation	50	50	30
Herbal Barrier	50	70	70

In addition, in order to use the chemical processes internally in the model's GESCAL module, the total nitrogen parameter was entered to the model as its own components, ammonium, nitrate and organic nitrogen, and the total phosphorus parameter as its own components, organic phosphorus and inorganic phosphorus. The percent distributions of the components of total nitrogen and total phosphorus for different pollutant sources are given in Table 4 (Metcalf et al., 2002).

Table 4. Conversion rates used to express calculated nutrient loads in terms of model parameters.

Source	Total N Fractions			Total P Fractions	
	Organic N	Ammonium	Nitrate	Organic P	Inorganic P
Raw wastewater	0.4	0.6	0	0.3	0.7
Biologically treated wastewater	0.1	0.1	0.8	0.4	0.6
Solid waste storage leachate	0.47	0.47	0.06	0.33	0.67
Land use	0.1	0.2	0.7	0.2	0.8
Fertilizer	0.1	0.2	0.7	0.3	0.7
Farming	0.1	0.2	0.7	0.2	0.8
Atmosphere	0	0.5	0.5	0	1

3. FINDINGS AND DISCUSSION

3.1. Model Calibration and Verification

The results of the model are given in the analysis element that corresponds to the water body number 32, which is the closest monitoring location to the point where the Bakırçay River flows into the sea. The calibration and verification results of the hydrological model at this point are given in Figure 3.
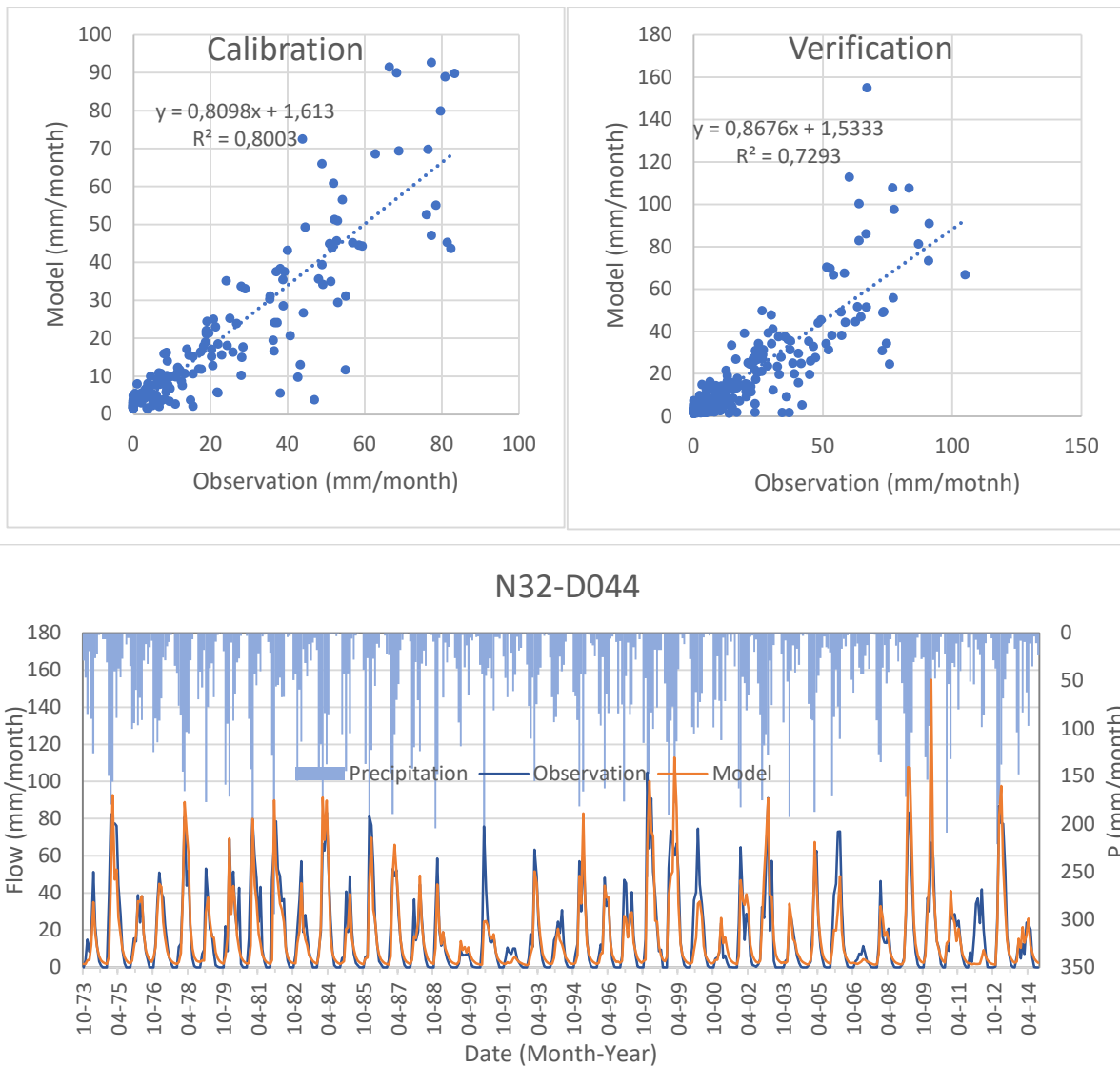
Figure 3. GR2M model results and observed flow graph for KEN32 water body

While the average of the flow values observed during the calibration period is 19.53 mm/month and the standard deviation is 23.04 mm/month, the average of the model results is 17.43 mm/month and the standard deviation is 20.85 mm/month. The performance parameters of the hydrological model are calculated as Nash 0.792, LnNash 0.637, %Bias -10.77 and R^2 0.8. While the average of the flow values observed during the verification period was 16.73 mm/month and the standard deviation was 22.07 mm/month, the average of the model results was 16.05 mm/month and the standard deviation was 22.42 mm/month. Performance parameters for this period are calculated as Nash 0.702; LnNash 0,537; %Bias -4.08 and R^2 0.729. As can be seen from the statistical values, the natural flow estimates of the hydrological model are sufficient, and the model can represent the real situation in a satisfactory manner.

The observed values with the calibration results of the water quality model are given in Figure 4 for BOD_5, DO, Organic P and NH_4. According to these results given in the water body number 32 near the point where the Bakırçay River flows into the sea, a very good similarity is obtained between the model estimates and the observed values. Rather than determining the numerical error value between observation and model estimates, the correlation between observation and estimation results is examined using the correlation coefficient. For this purpose, monthly model results of BOD_5, DO, Organic P and NH_4 parameters are compared with the measurement results that are accepted to represent that month. As a result of the correlation analysis for BOD_5, DO, Organic P and NH_4

parameters, the correlation coefficient values were calculated as 0.80, 0.21, 0.35 and 0.41, respectively. The model whose calibration has been completed has been verified for a different date range. The range of September 2018 to January 2019 is selected for the verification. Model results obtained as a result of verification and observation results are given in Figure 5 for BOD_5, DO, Organic P and NH_4 parameters. It is seen that the location used for calibration and verification in the model are very close to each other. It is considered that the proximity obtained is at an acceptable level since the mentioned location is located just before the Bakırçay River flows into the sea.
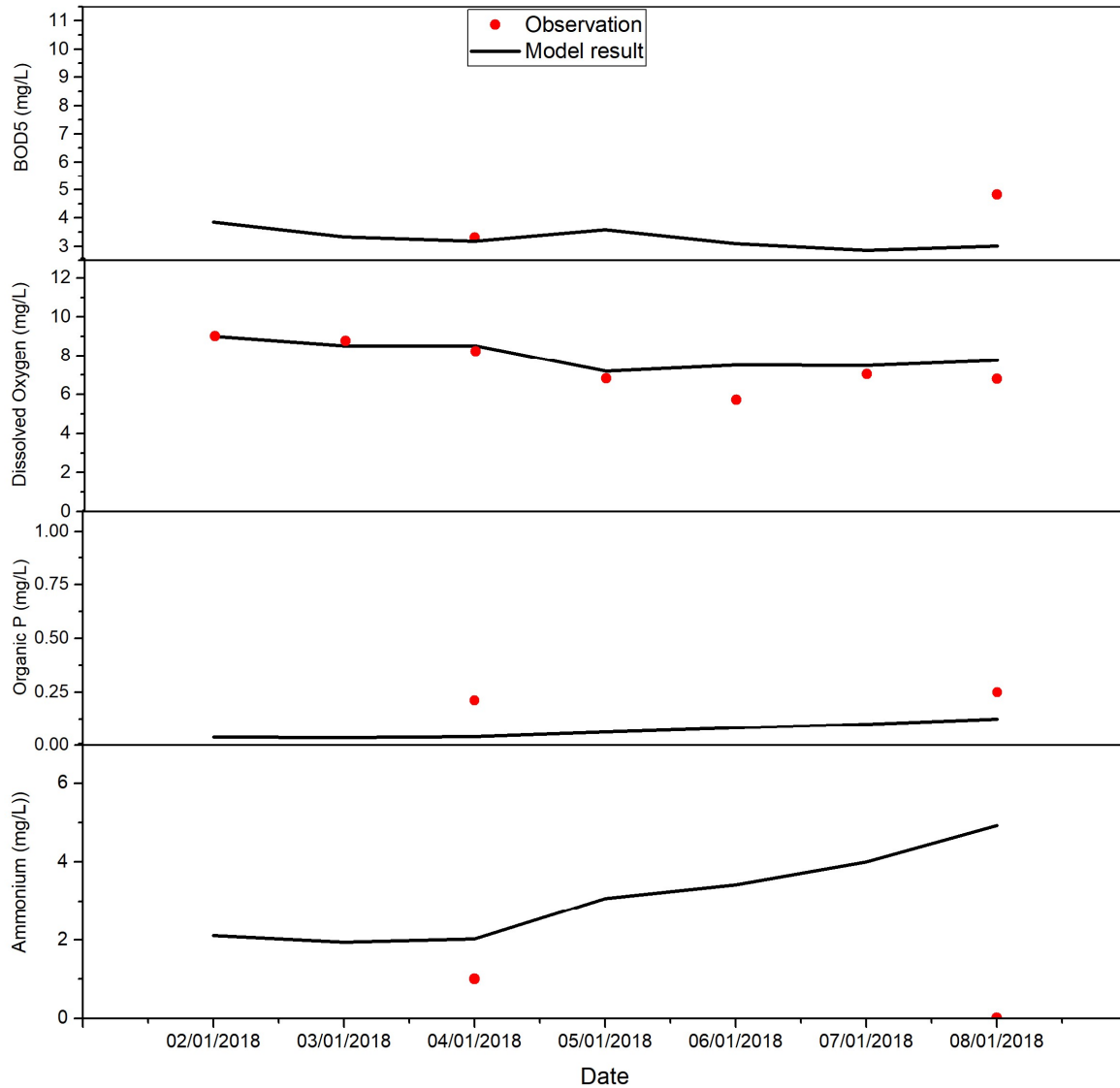
Figure 4. Comparison of observations and model results of various water quality parameters during the calibration period (Bakırçay main branch, near Bergama)
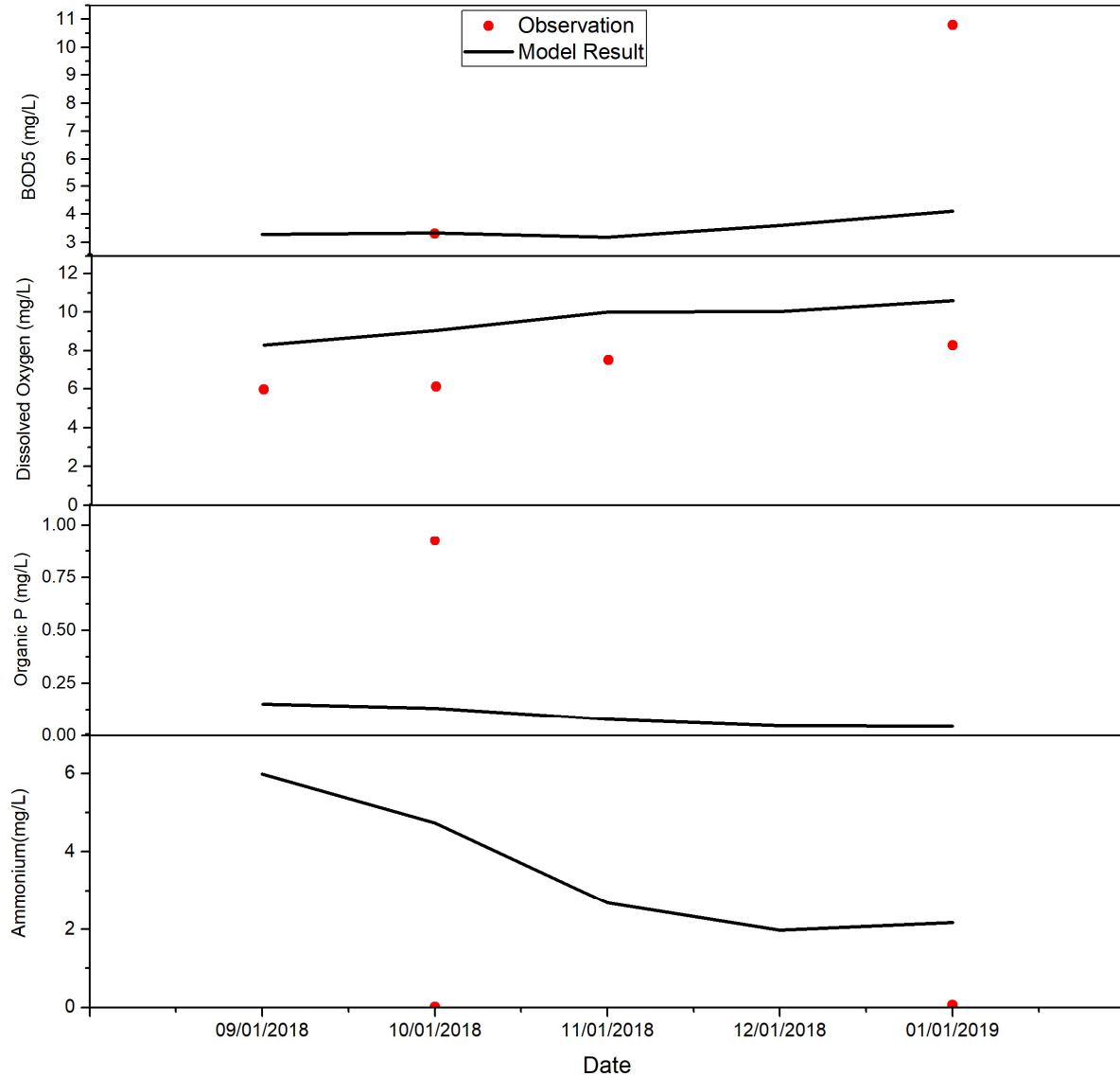
Figure 5. Comparison of observations and model results of various water quality parameters during the verification period (Bakırçay main branch, near Bergama)

3.2. Scenario Analysis

As a result of scenario analysis, the effect of each precaution is examined. The changes that will occur in the water quality as a result of the cumulative implementation of all scenarios are presented in Figure 6. Accordingly, as a result of applying all the precautions within the scope of the scenarios together, an improvement in the water quality of Bakırçay river is achieved. Thanks to the precautions taken for organic matter and nutrient load control as a result of the scenarios, it can be seen that the concentrations of ammonium and BOD_5 in the 32-31-J segment of Bakırçay River are significantly reduced. If all scenarios are applied cumulatively during the simulation period, the BOD_5 concentration appears to decrease by about 31%. It is seen that this ratio is 23% for ammonium and 16% for Organic P. Due to these reductions in organic and nutrient load, there is a slight increase in Dissolved Oxygen results which is about 1% on average.
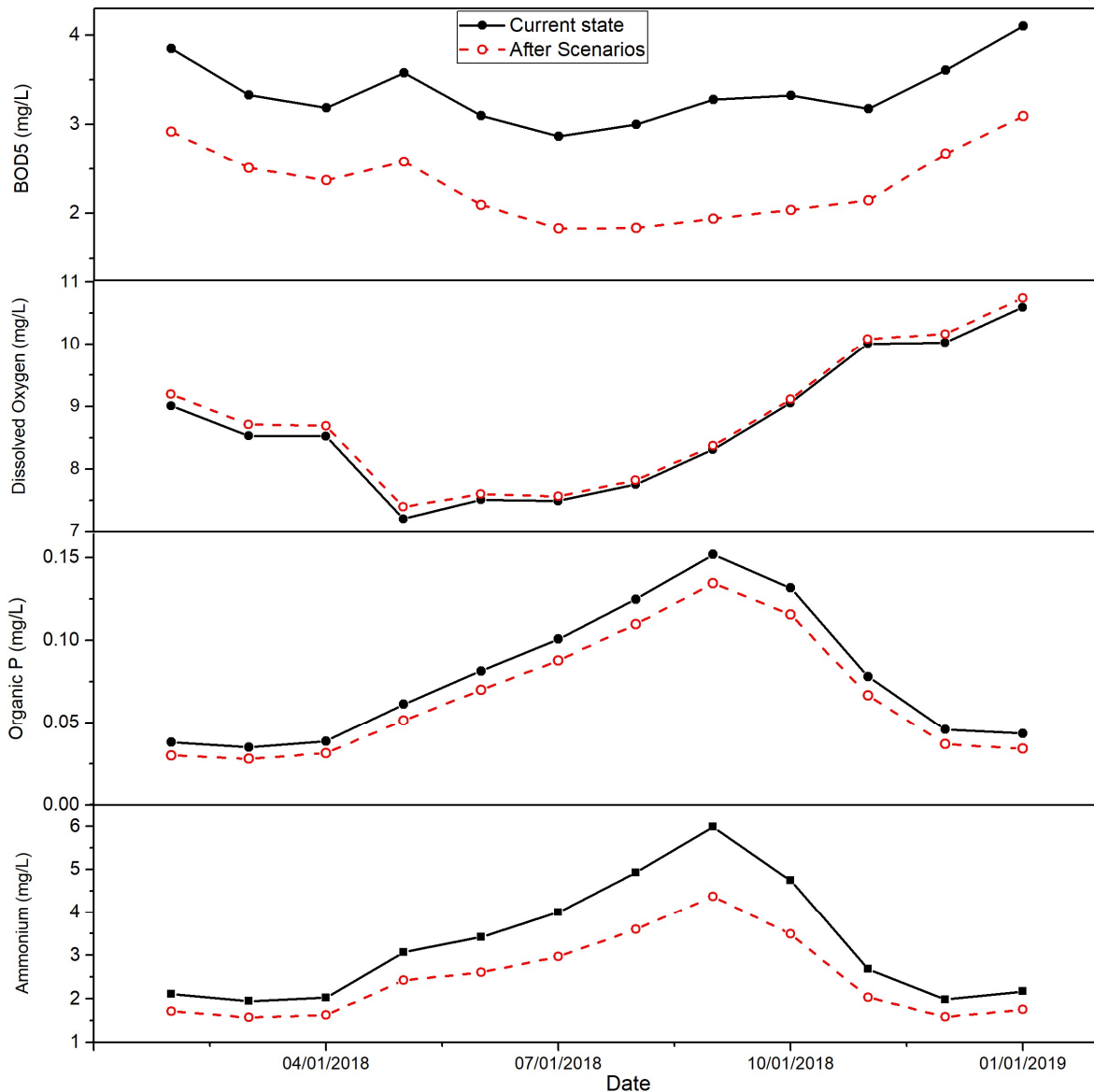
Figure 6. Cumulative effect of 8 different scenarios applied in the study on various water quality parameters (segment 32-31-J)

4. CONCLUSIONS

In this study, AQUATOOL model is used to model the water quality of Bakırçay River. The general consistency observed between simulation and observation data in the calibration and verification processes shows that the AQUATOOL model can be used for the Bakırçay River for testing the effectiveness of a number of measures to improve river's water quality. It is observed that if all the scenarios described in the study are applied together, the organic matter and nutrient load in the river can be reduced effectively to a better level. In addition to these parameters, it is thought that the background pollutant level may be the reason for the relatively low level of improvement in the dissolved oxygen level. As future work, the ratio of the background pollutant loads to the existing pollutant loads should be determined and the selection of the precautionary measures could be made accordingly. It is further thought that an additional monitoring study can be carried out to take more observations extending beyond one water year to model the effect of oscillations in natural flow rates more effectively. Such modeling studies are of great importance for the water quality management of Bakırçay River. By the help of models, it is possible to predict what level of improvement can be achieved by the proposed theoretically appropriate precautions without physically implementing the

precautions. Furthermore, a comparative analysis of precautions can also be used to prioritize measures within themselves.

ACKNOWLEDGEMENTS

REFERENCES

Andreu, J., Capilla, J., & Sanchís, E. (1996). AQUATOOL, a generalized decision-support system for water-resources planning and operational management. *Journal of Hydrology*, *177*(3–4), 269–291. https://doi.org/10.1016/0022-1694(95)02963-X

Bowie, G., Mills, W., Porcella, D., Campbell, C., & Chamberlin, C. (2004). *Rates, constants, and kinetics formulations in surface water quality modeling* (2nd ed.). Washington, D.C.: Environmental Protection Agency. Retrieved from https://books.google.com.tr/books?id=-0d42CDRygcC

Çevre ve Şehircilik Bakanlığı ÇED İzin ve Denetim Genel Müdürlüğü Laboratuvar Ölçüm ve İzleme Dairesi Başkanlığı. (2015). *Bakırçay Havzası Su Kalitesi İzleme Raporu İlkbahar ve Yaz Dönemi 2015*.

Metcalf & Eddy, I., Tchobanoglous, G., Burton, F., & Stensel, H. D. (2002). *Wastewater Engineering: Treatment and Reuse*. McGraw-Hill Education. Retrieved from https://books.google.com.tr/books?id=-eoeAQAAIAAJ

Mouelhi, S., Michel, C., Perrin, C., & Andréassian, V. (2006). Stepwise development of a two-parameter monthly water balance model. *Journal of Hydrology*, *318*(1–4), 200–214. https://doi.org/10.1016/j.jhydrol.2005.06.014

Paliwal, R., Sharma, P., & Kansal, A. (2007). Water quality modelling of the river Yamuna (India) using QUAL2E-UNCAS. *Journal of Environmental Management*, *83*(2), 131–144. https://doi.org/10.1016/j.jenvman.2006.02.003

T.C. Tarım ve Orman Bakanlığı Su Yönetimi Genel Müdürlüğü. (2020). *Kuzey Ege Havzası Havza Yönetim Planı Taslak Nihai Rapor*.

Te Chow, V. (1959). *Open-channel hydraulics*. McGraw-Hill. Retrieved from https://books.google.com.tr/books?id=OwZSAAAAMAAJ

14TH INTERNATIONAL CONFERENCE
ON HYDROSCIENCE & ENGINEERING

MAY 26-27, 2022
IZMİR-TURKEY

ICHE2022
IZMIR, TURKEY

A SIMULATION-OPTIMIZATION APPROACH FOR SOLVING THE WASTEWATER LOAD ALLOCATION PROBLEMS IN RIVER BASIN SYSTEMS

Derya Sadak

Department of Civil Engineering, Sakarya University

Sakarya, Turkey

deryasadak@sakarya.edu.tr

M. Tamer Ayvaz

Department of Civil Engineering, Pamukkale University

Denizli, Turkey

tayvaz@pau.edu.tr

Alper Elçi

Department of Environmental Engineering, Dokuz Eylül University

İzmir, Turkey

alper.elci@deu.edu.tr

Mehmet Dilaver

Environment and Cleaner Production Institute, TUBITAK Marmara Research Center

Kocaeli, Turkey

mehmet.dilaver@tubitak.gov.tr

Selma Ayaz

Environment and Cleaner Production Institute, TUBITAK Marmara Research Center

Kocaeli, Turkey

selma.ayaz@tubitak.gov.tr

ABSTRACT: A linked simulation-optimization approach is proposed to determine the receiving body-based discharge limits by considering the discharge standards used by the water authorities. By using the proposed simulation-optimization approach, wastewater loads of point sources can be determined in such a way that the parameters exceeding the water quality targets (WQT) in receiving water environment meet the relevant WQT values. In the simulation part of the proposed approach, pollution concentrations are determined by modeling the given system using the AQUATOX water quality simulation model. Since AQUATOX is an independent simulation model, it is not possible to execute it from the optimization model for the generated load combinations. Therefore, as a surrogate simulation model, a concentration-response-matrix approach is developed by using the results of AQUATOX model. After this process, the developed concentration-response-matrix is integrated into an optimization model where the heuristic differential evolution (DE) optimization approach is used. The performance of the proposed simulation-optimization approach is evaluated on a sub-watershed of the Küçük Menderes River Basin by considering different waste load allocation scenarios. Identified results indicated that the proposed simulation-optimization approach can effectively allocate the wastewater loads among different point sources by considering the WQT values for the modeled water quality parameter.

1. INTRODUCTION

Wastewater load allocation is an essential part of water quality management along with the river systems. Uncontrolled and unconscious wastewater discharge causes decreased water quality and negatively affects aquatic life systems. From past to present, studies on this subject suggest different solutions to reduce the harmful effects of wastewater discharge and increase water quality by water resources planning and management. The vast majority of these studies aim to reduce the pollution loads resulting from the point or non-point sources to obtain satisfactory water quality. This approach is one of the best options for the conservation of water quality. Still, it is quite difficult to determine the amount of pollution reduction in sources to meet the relevant WQS limit values. Generally, simulation-optimization models use to determine the quantity of reducing pollution levels in sources to provide satisfactory water quality and economic efficiency. According to the European Union Water Framework Directive (2000/60/EC), the concentration of conventional, priority, and specific pollutants should meet the Environmental Quality Standards (EQS) to obtain good quality water status. The optimization model allocates wastewater loads at sources, and the water quality simulation model represents water quality changes along the river system, which optimization model continues to reduce pollution levels at point sources until obtaining satisfactory water quality.

There are many water quality studies using different simulation-optimization models. In these studies, various simulation models such QUAL2E, QUAL2K, CE-QUAL, WASP4, etc., which are used to represent the water quality change throughout the river system. (Burn and Yulianti, 2001; Jia and Culver, 2006; Saadatpour and Afshar, 2007; Parmar and Keshari, 2014; Afshar et al., 2018). This defined water quality simulation model is combined with heuristic or deterministic optimization approaches. It is known that Deiniger (1965) solved a similar problem by linear programming based on deterministic optimization to improve the water quality by taking into account the dissolved oxygen concentration in the river system. Similarly, Revelle et al. (1968) used linear programming to obtain satisfactory water quality in the river system. Unlike this method, Liebman and Lynn (1966) and Klemetson and Grenny (1985) used dynamic programming to minimize wastewater management costs. Initially, deterministic optimization approaches were used in waste load management. But with the emergence of heuristic optimization approaches, different algorithms were applied in water quality management. For instance, Burn and Yulianti (2001) developed the simulation optimization algorithm based on a genetic algorithm (GA) to minimize wastewater treatment costs. It is known that the basic idea of previous studies was to reach the water quality targets, to minimize the cost of wastewater treatment, and to allocate the maximum wastewater load which, was given importance to equally load allocation and or equally pollutant level reduction among sources. (Burn and Yulianti, 2001; Cho et al., 2004; Afshar and Masaumi, 2016; Afshar et al., 2018; Saadatpour et al., 2019). Although this equal load allocation approach seems quite reasonable, it may not provide economic results for river systems considering the magnitude of the sources. It would not be reasonable to accept the same wastewater body discharge of two point sources, such as a industrial wastewater treatment and a domestic wastewater treatment plant.

In this study, a new simulation-optimization approach is proposed that allocates wastewater discharge loads to meet the WQTs. In contrast to previous studies, waste loads are allocated among the source locations by considering different allocation weights. In the simulation part of the proposed approach, carbonaceous biochemical oxygen demand ($CBOD_5$) is considered as the main water quality parameter, and the AQUATOX (Park et al., 2008) model is used to simulate it. It should be noted that the water quality model should be run separately for each scenario created by the optimization model. However, AQUATOX is an independent simulation model and cannot be operated directly within the optimization model. Therefore, a concentration-response-matrix approach (CRM) is developed based on the concentration of the discharged substance in the receiving environment. CRM is a surrogate water quality model that is based on expressing the change in pollutant concentration in the receiving environment for the unit load discharged in terms of coefficients. The surrogate water quality model based on CRM was originally developed to solve groundwater problems by Gorelick (1982a, 1982b), but Su et al. (2019) and Sadak et al. (2020) have used it to solve surface water quality problems. The surrogate water quality model is developed in this study for $CBOD_5$ pollutant parameter; it will be integrated into an optimization model where the DE optimization approach is used. The performance

of the proposed simulation-optimization approach is evaluated on a sub-watershed of the Küçük Menderes River Basin by considering different waste load allocation scenarios. The proposed simulation-optimization approach is described in detail in the problem definition.

2. PROBLEM DEFINITION

As described in the previous section, pollutant discharge loads are reduced at the sources by usually applying the equity approach. Although it can be easily implemented to point sources at upstream locations, it may be difficult to do so for downstream locations since the flowing water is already polluted, and it is not always economical and acceptable This problem is described in detail below.
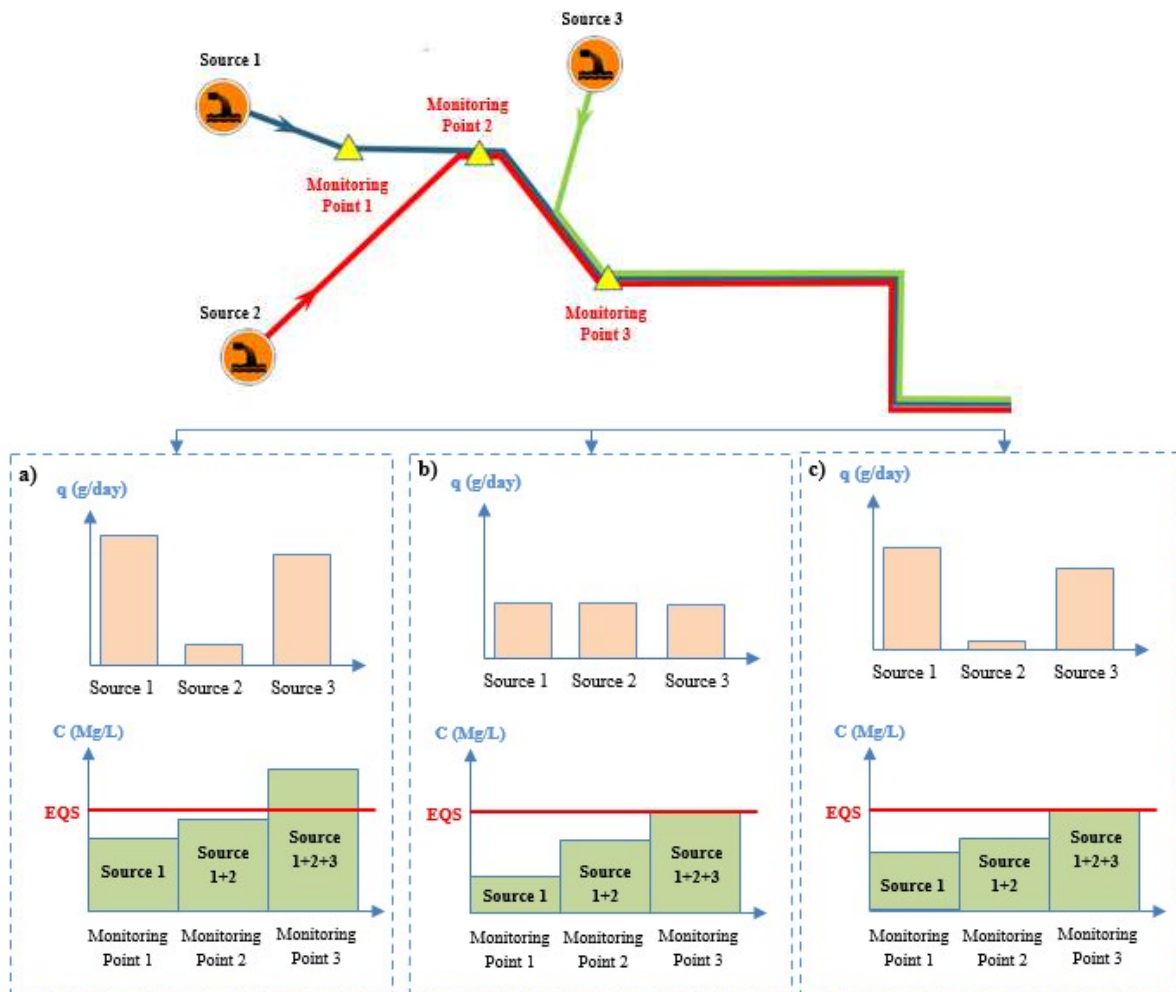
Figure 15. A conceptual model of wastewater load allocation a) Before allocation b) Equal allocation approach c) Proposed allocation approach

As shown in Figure 1.a., there are three-point pollution sources throughout river systems, and initially, wastewater loads are discharged without measures. As a result of discharge without treatment and management, the water upstream is contaminated, and the WQT is not met at downstream locations. In Figure 1.b., with the equal load allocation approach, as proposed in many previous studies, wastewater load is allocated to these point sources, and EQS is met at all three monitoring points. Considering the initial case shown in Figure 1.a., while the wastewater load was allocated to sources 1 and 3 less than its capacity, it was allocated more than the discharge load capacity of source 2. Using this approach is inappropriate if the sources have different magnitudes. Suppose an equally more significant discharge load is allocated to the sources to provide approximately their initial load capacities. In that case, the EQS value will not be met at monitoring point 3 located downstream. Therefore, it is required to apply a systematic solution approach for

allocating pollutant loads among different source locations and magnitudes based on the given EQS. Figure 1.c. shows the multiple approaches proposed within the scope of this study. As can be seen, the discharge load has been allocated in all sources depending on the initial discharge load capacities until EQS values were met at monitoring points. The suggested weighted load allocation approach is described with a determined load allocation coefficient considering the magnitude of each source. With this approach, while EQS are met in the receiving environment, it is aimed to pollutants provide maximum benefit from this load allocation, which loads allocated by considering the initial capacity of sources. The following section explains how this suggested load allocation considering the magnitude of the source is made.

2.1. Proposed Simulation-Optimization Approach

In this section, the proposed simulation-optimization approach to solve the waste load allocation (WLA) problem is mathematically formulated. The objective function of the optimization model is to maximize the total wastewater load allocation at the sources when the receiving water body met EQS, considering different magnitudes of the pollutant sources. The formulation is given below ($i = 1, 2, 3, \ldots, n_d$; $j = 1, 2, 3, \ldots, n_m$; $t = 1, 2, 3, \ldots, n_t$):

$$Z = \max\left\{\sum_{i=1}^{n_d} (q_i - \lambda_1 \times (q_i - \omega_i \times q^*)^2) - \lambda_2 \times \sum_{j=1}^{n_m} \sum_{t=1}^{n_t} (C_j(t) - \widetilde{C})^2\right\} \tag{1}$$

subject to

$$q_i = \mathcal{C}_i \times Q_i \tag{2}$$

$$q^* = \frac{\sum_{i=1}^{n_d} q_i}{\sum_{i=1}^{n_d} \omega_i} \tag{3}$$

$$C_j(t) = \sum_{i=1}^{n_d} \alpha_{i,j}(t) \times q_i + C_j^0(t) \tag{4}$$

$$\mathcal{C}_{\min} \leq \mathcal{C}_i \leq \mathcal{C}_{\max} \tag{5}$$

$$\alpha_{i,j}(t) = \frac{\partial \left(\hat{c}_j(t) - c_j^0(t)\right)}{\partial q_i} \tag{6}$$

where n_d is the number of point sources, n_m is the number of monitoring points, n_t is the time step and q_i is the load of the ith point sources, Z is the objective function value to be maximized, λ_1 is the first penalty function, which maintains an equal or weighted load allocation among pollution sources, λ_2 is the second penalty function that provides maximum load discharges from the point sources, ω_i is the load allocation coefficient at point sources, q^* is the allocation load, which ensures that the load of the pollutant is allocated among the source locations at desired levels (q^* equals to mean of q_i if ω_i values are all equal to 1), $C_j(t)$ is the concentration of the jth pollutant calculated by the response-matrix and $\widetilde{C}$ is the WQT value of CBOD$_5$ parameter, $\mathcal{C}_{\min}$ and $\mathcal{C}_{\max}$ are the minimum and maximum CBOD$_5$ concentrations.

The first term of problem formulation is used to allocate the maximum waste load among sources based on the provided load allocation coefficients representing. The second term is used to ensure that the EQS value is minimized. In the first part, the optimization model allocates the waste loads among point sources and then the corresponding CBOD$_5$ concentrations in the receiving water environment are calculated by using the CRM, the surrogate water quality model. Note that the elements of the CRM are calculated by running separate AQUATOX model simulations, and by considering the unit

waste load discharges from the source locations. After this process, the output concentrations provided by the AQUATOX model are further processed by considering the background concentrations observed in the field to develop a surrogate simulation model of the AQUATOX. After this process, the obtained CRM is linked to an optimization model, where a Differential Evolution algorithm is used.

2.2. Differential Evolution Algorithm

In this study, the Differential Evolution (DE) algorithm was selected as the optimization method. DE is a heuristic optimization method that was firstly proposed by Storn and Price (1997). It is based on similar computational techniques as genetic algorithms (GA) in terms of mutation, natural selection, crossover processes. The difference between the two methods, while the binary system is mostly used in GA, the decimal system is used in DE. Furthermore, each candidate solution in GA is subjected to the genetic evolution process if the associated probability of that process is satisfied whereas each candidate solution in DE is subjected to those processes without considering any probability. Compared to other heuristic optimization algorithms, DE is easy to program and is less prone to becoming stuck in local optimums. Therefore, in this study, the DE optimization algorithm was used to allocate wastewater discharge in the river system taking the water quality restrictions into account. The solution algorithms to an optimization problem with DE are mathematically performed according to the following steps:

Np is the number of population, Nd is the number of decision variables, x is the decision variables ($x = [Np, Nd]$), i is the population index ($i = 1, 2, 3, ..., Np$) and j is the decision variables index ($j = 1, 2, 3, ..., Nd$), $x_{\max}$ and $x_{\min}$ respectively, shows the upper and lower limits of decision variables. Using these definitions, the initial value of the jth decision variable in the ith candidate solution at the generation $G = 0$ can be generated as follows.

$$x_{i,j}^0 = x_{\min_i} + r(0, 1) \times (x_{\max_i} - x_{\min_i}) \tag{7}$$

where $r(0,1)$ represents a uniform random number within the range of (0,1). After this stage, the following is repeated until a termination criterion is met. The mutation process is performed, and a new solution vector is obtained as in the step below.

$$\mathcal{V}_j^G = x_{r_{1,j}} + F(x_{r_{2,j}} - x_{r_{2,j}}) \tag{8}$$

where F is the scale coefficient of mutation process is controlled, r_1, r_2, r_3 are the random integers produced in $[1, Np]$ as different from each other. Then the new solution vector is produced as a result of the crossover as follows.

$$u_{i,j}^G = \begin{cases} V_{i,j}^G & \text{if } r(0, 1) \leq C_r \text{ or } j = j_{rand} \\ x_{i,j}^G & \text{otherwise} \end{cases} \tag{9}$$

where C_r is crossing rate, j_{rand} is randomly generated in the closed range $[1, Nd]$ shows.

$$x_{i,j}^{G+1} = \begin{cases} u_i^G & \text{if } f(u_i^G) \leq f(x_i^G) \\ x_i^G & \text{otherwise} \end{cases} \tag{10}$$

It can be seen that the final value of the objective function is changed based on the condition given in Equation 10. Note that this form of Equation 10 is valid for the minimization problems and should be revised when the objective is to solve a maximization problem. In this study, the objective of the DE-based optimization problem is to maximize the total discharge load from the point sources.

3. STUDY AREA

The proposed simulation-optimization model is applied on the sub-watershed of the Kucuk Menderes River Basin (KMRB) in Turkey. KMRB is located in the western part of Turkey (Figure 2), which lies between 38° 41' 05'' and 37° 24' 08'' N latitudes and 28° 24' 36'' and 26° 11' 48'' E longitudes. The flow of the basin is discharged to the Aegean Sea through the Kucuk Menderes River and its tributaries. As can be seen in Figure 2, basin boundaries are located in the province of Izmir, where industrial and agricultural activities are highly developed; therefore, the Kucuk Menderes river is under significant environmental stress. To conduct the wastewater management studies in KMRB, a research project titled "Identification of Receiving Water Body-Based Discharge Limits Kucuk Menderes River Basin (Turkey) Case Study" was completed. This study is one of the outputs of the project, and data related to the study area were obtained due to detailed field studies.
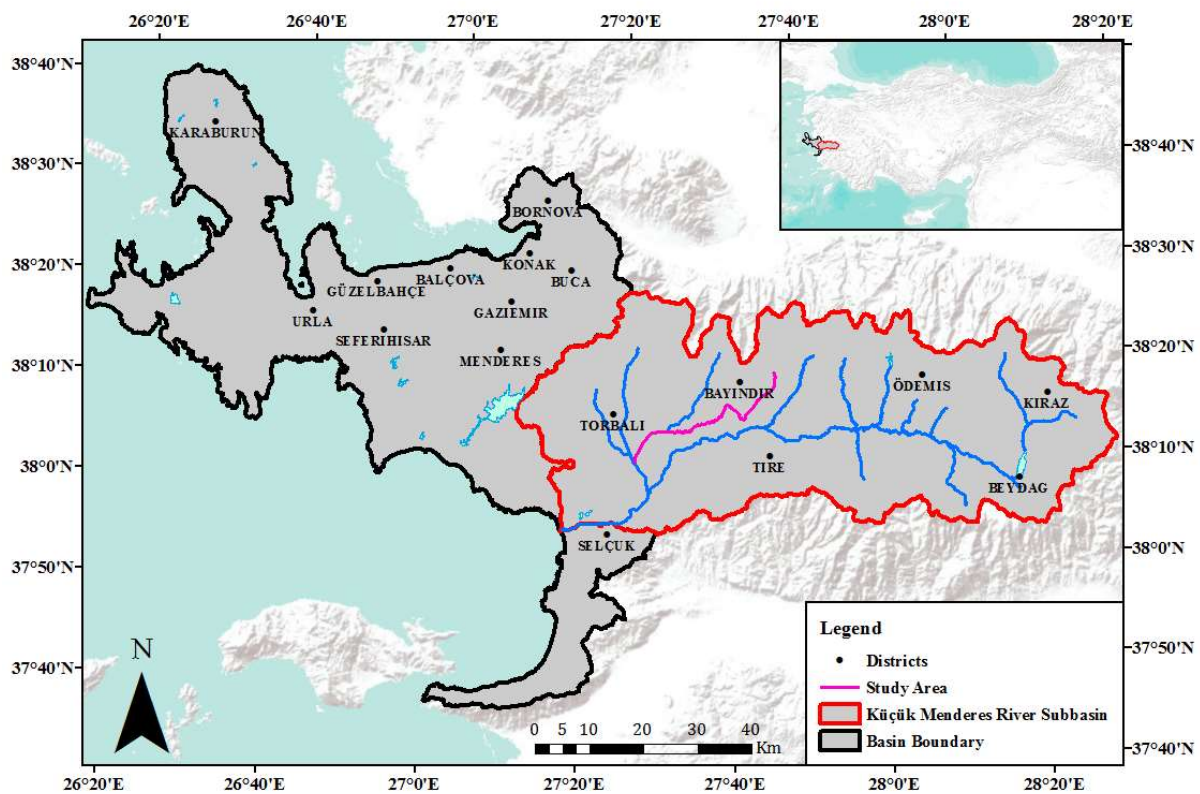
Figure 16. The Kucuk Menderes River and its basin boundary

As a result of the field studies, the point sources discharging wastewater to the Kucuk Menderes river were identified. A tributary of the Kucuk Menderes river was considered within the scope of this study. The studied tributary and identified pollutant sources are shown in Figure 3.

The tributary to be modeled is the Ilica Stream (pink-colored reach in Figure 3), where there are five pollutant sources. S_1 represents a domestic wastewater treatment, S_2 is considered as a point source representing the mass influx from the connecting tributary (Uladi Stream). The remaining three sources (S_{3-5}) represent the discharge locations of wastewater caused by industrial activities in the region. After determining the pollutant sources, the AQUATOX-based water quality model is used to simulate the fate and transport of the pollution for the entire stream and its monitoring points (KM-19, KM-20, KM-22).
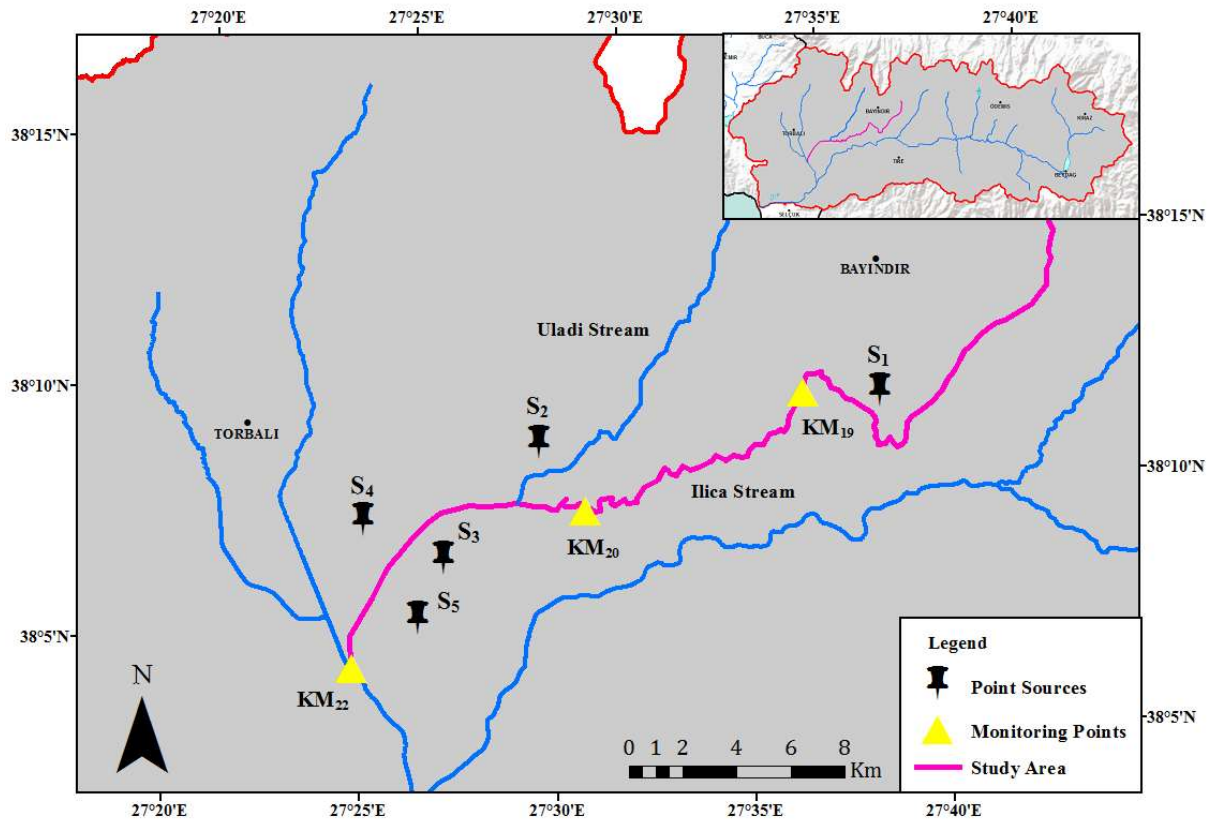
Figure 17. Application study area on the Kucuk Menderes river sub-basin

This study is within the scope of a research project, the samples collected in field studies were analyzed in the laboratory, and the AQUATOX model was set up based on the information obtained from these field studies. $CBOD_5$ is selected to determine the water quality in the river. This parameter directly affects the amount of dissolved oxygen that is crucial in river systems. In the setup of the AQUATOX simulations, it is assumed that $CBOD_5$ is discharged from the point sources, and this affects the water quality at the monitoring locations shown in Figure 3. The AQUATOX is an independent model, , for this reason a surrogate of the AQUATOX water quality simulation model is used in conjunction with the optimization model. With this purpose, a CRM is developed by considering the input-output relationships of the pollutant parameter. The CRM is based on the principle of linear superposition and can be used to simulate water quality processes in a river. Detailed information regarding the development of the CRM approach is provided in Sadak et al. (2020).

3.2. Model Application

In this section, the applicability of the proposed approach was evaluated for different load allocation weights by considering four different scenarios (Table 1). In the first scenario, the load allocation weights are taken as 1 for all the sources. In the other scenarios, different load allocations weights are considered for the point sources to evaluate if the pollutant loads are proportionally allocated among the source locations with the provided load allocation weights. Application of the simulation-optimization approach for the studied tributary, problem definition is given as $n_d = 5$ (S_1, S_2, S_3, S_4, S_5), $n_c = 1$ (Susp. and dissolved detritus), $n_m = 3$ (KM-19, KM-20, KM-22) and $n_t = 30$ days. The penalty parameters of λ_1 and λ_2 are selected as 1 and 10^9 , respectively, in the optimization model based on previous trials. Note that the optimization process is conducted by considering an EQS limit of $\tilde{C} = 8$ mg/L for $CBOD_5$.

Table 9. The load allocation coefficients (ω_i) for each scenario.

Sources	Scenario 1	Scenario 2	Scenario 3	Scenario 4
S_1	1	2	1	2
S_2 (Tributary)	1	1	1	1
S_3	1	1	1.5	1
S_4	1	1	1	2
S_5	1	1	2.5	3

4. RESULTS

Application results of the simulation-optimization approach for Scenario 1 – 4 are presented in Table 2. As indicated previously, the waste load is allocated among point sources to be proportional to the provided load allocation weights. This situation can be seen in Table 2 such that all the sources have the same pollutant loads in Scenario 1 since all the load allocation coefficients are set the same value. For the other scenarios, it is evident that all the waste loads are allocated proportionally with the load allocation weights given in Table 1.

Table 210. Simulation-optimization model results for each scenario.

	Scenario 1		Scenario 2		Scenario 3		Scenario 4	
	ω_i	q_i (kg/day)	ω_i	q_i (kg/day)	ω_i	q_i (kg/day)	ω_i	q_i (kg/day)
S_1	1	462.13	2	796.58	1	325.94	2	516.51
S_2 (Tributary)	1	462.13	1	398.29	1	325.94	1	258.25
S_3	1	462.13	1	398.29	1.5	488.91	1	258.25
S_4	1	462.13	1	398.29	1	325.94	2	516.51
S_5	1	462.13	1	398.29	2.5	814.85	3	774.77

Table 3 shows the calculated $CBOD_5$ concentrations for the allocated waste loads among the source locations. It can observe that the resulting $CBOD_5$ concentrations are all lower than the EQS values at the monitoring points of KM-19 and KM-20. For monitoring point KM-20, the concentration turns out to be equal to the EQS value which is an expected result since KM-20 is located in the most downstream reach of the tributary.

Table 3. Resulting $CBOD_5$ concentrations for the obtained load allocations of each scenario.

	$CBOD_5$ concentrations in the stream after load allocation			
EQS $\tilde{C}$ (mg/L)	$C_j(30)$ (mg/L)			
	Scenario 1	Scenario 2	Scenario 3	Scenario 4

KM-19		2.33	4.01	1.64	2.60
KM-20	8	5.82	6.51	4.80	5.40
KM-22		8.00	8.00	8.00	8.00

5. CONCLUSIONS

In this study, a linked simulation-optimization approach is proposed to determine the receiving body-based discharge limits by considering different source magnitudes and the discharge standards used in European Union Water Framework Directive. In the proposed model, wastewater discharge loads are allocated among point sources by considering the WQTvalues in the receiving water body. To simulate the water quality process on a river system, AQUATOX water quality simulation model is used. Since, AQUATOX is an independent model that is not possible to link with an optimization algorithm, a concentration-response-matrix (CRM) is developed by using the results of AQUATOX model. This developed CRM is then linked to an optimization model where DE algorithm is used. The main objective of the DE based optimization model is to allocate the total waste loads by using a new optimization formulation that can allocate the loads by using according to the provided load allocation coefficients. The performance of the proposed simulation-optimization approach is evaluated on a sub-watershed of the Kucuk Menderes river basin in Turkey by considering different waste load allocation scenarios. According to the identification results, it can be concluded that the proposed simulation-optimization approach can successfully allocate pollutant loads by considering the provided load allocation weights and by satisfying the EQS for all the monitoring points. Therefore, the proposed simulation-optimization approach can be used as an effective tool to solve the waste load allocation problems in river basins.

ACKLOWLEDGMENTS

REFERENCES

Afshar, A., & Masoumi, F. (2016). Waste load reallocation in river–reservoir systems: simulation–optimization approach. *Environmental Earth Science,* 75(1), 53. https://doi.org/10.1007/s12665-015-4812-x

Afshar, A., Masoumi, F., Solis, S. S. (2018). Developing a Reliability-Based Waste Load Allocation Strategy for River-Reservoir Systems. *Journal of Water Resources Planning and Management,* 144(9). https://doi.org/10.1061/(ASCE)WR.1943-5452.0000973

Burn, D. H., & Yulianti, J. S. (2001). Waste-load allocation using genetic algorithms. *Journal of Water Resources Planning and Management,* 127(2), 121-129. https://doi.org/10.1061/(ASCE)0733-9496(2001)127:2(121)

Cho, J. H., Ki, S. S., Sung, R. H., (2004). A river water quality management model for optimising regional wastewater treatment using a genetic algorithm. *Journal of. Environmental Management,* 73(3), 229-242. https://doi.org/10.1016/j.jenvman.2004.07.004

Deininger, R. A. (1965). Water Quality Management: The Planning of Economically Opti- mal Pollution Control Systems. *Ph.D. Thesis*, Northwestern University.

Directive 2000/60/EC of the European Parliament and of the Council of 23 October 2000 on Establishing a Framework for Community Action in the Field of Water Policy

Gorelick, S. M. (1982a.) Optimal Dynamic Management of Groudwater Polluant Sources. *Water Resources Research,* 18(1),71-76. https://doi.org/10.1029/WR018i001p00071

Gorelick, S. M. (1982b.) A model for managing sources of groundwater pollution, *Water Resources Research*, 18(4), 773– 781. https://doi.org/10.1029/WR018i004p00773

Jia, Y. B., & Culver, T.B., 2006. Robust optimization for total maximum daily load allocations. *Water Resources Resources,* 42(2). https://doi.org/10.1029/2005WR004079

Klemetson, S.L., & Grenny, W.J. (1985). Dynamic optimization of regional wastewater treatment systems. *Journal of Water Pollution Control Federation,* 57(2), 128–134. https://www.jstor.org/stable/25042543

Liebman, J. C., & Lynn, W. R. (1966). The Optimal Allocation of Stream Dissolved Oxygen. *Water Resources Research*, 2(3). https://doi.org/10.1029/WR002i003p00581

Park, R. A., Clough, J. S., Wellman, M. C., (2008). AQUATOX: modeling environmental fate and ecological effects in aquatic ecosystems. *Ecological Modelling,* 213(1), 1-15. https://doi.org/10.1016/j.ecolmodel.2008.01.015

Parmar, D. L., & Keshari, A. K. (2014). Wasteload Allocation Using Wastewater Treatment and Flow

Augmentation. *Environmental Model Assessment*, 19, 35-44. https://doi.org/10.1007/s10666-013-9378-y

Revelle, C.S., Loucks, D.P., Lynn, W.R. (1968). Linear programming applied to water quality management. *Water Resour. Res*. 4(1), 1–9. https://doi.org/10.1029/WR004i001p00001

Sadak, D., Ayvaz, M. T., Elçi, A. (2020). Allocation of unequally-weighted wastewater discharge loads using a simulation-optimization approach. *Journal of Hydrology*, 588. https://doi.org/10.1016/j.jhydrol.2020.125158.

Saadatpour, M., & Afshar, A. (2007). Waste load allocation modeling fuzzy goals; simulation-optimization approach. *Water Resources Management,* 21, 1207-1224. https://doi.org/10.1007/s11269-006-9077-4

Saadatpour, M. Afshar, A., Khoshkam, H. (2019). Multi-objective multi-pollutant waste allocation model for rivers using coupled archived simulated annealing algorithm with QUAL2Kw. *Journal of Hydroinformatics,* 21(3), 397-410. https://doi.org/10.2166/hydro.2019.056

Su, Y., Li, K.Q., Yang, B., Liang, S.K.,Wang, X.L., Bao, X.W., Jiang,W.S., Li, Y.B. (2018). Improving land-based total nitrogen load allocation using a variable response matrix-based simulation–optimization approach: a case study. *Ecological Indicators*, 91, 575–588.

Su, Y., Li, K., Liang, S., Lu, S., Wang, Y., Dai, A., Li, Y. B., Ding, D., Wang, X. (2019). Improved simulation–optimization approach for identifying critical and developable pollution source regions and critical migration processes for pollutant load allocation. *Science of Total Environment,* 646, 1336-1348. https://doi.org/10.1016/j.scitotenv.2018.07.326

Storn. R., & Kenneth, P. (1997). Differential evolution–a simple and efficient heuristic for global optimization over continuous spaces. *Journal of global optimization,* 11.4: 341-359.

14TH INTERNATIONAL CONFERENCE
ON HYDROSCIENCE & ENGINEERING

MAY 26-27, 2022
IZMİR-TURKEY

ICHE2022
IZMIR, TURKEY

EVALUATING THE EFFECT OF LOW IMPACT DEVELOPMENTS ON WATER QUALITY IMPROVEMENT: A CASE STUDY IN BANDAR SUNWAY

Andreas Aditya Hermawan

Department of Civil Engineering, Monash University Malaysia

Bandar Sunway, Selangor, Malaysia

andreas.aditya1@monash.edu

Jing Pang Haw

Department of Civil Engineering, Monash University Malaysia

Bandar Sunway, Selangor, Malaysia

jphaw3@student.monash.edu

Amin Talei*

Department of Civil Engineering, Monash University Malaysia

Bandar Sunway, Selangor, Malaysia

amin.talei@monash.edu

ABSTRACT: Bandar Sunway is one of the highest urbanized areas in Malaysia with multiple waterways connected to the Klang River. Both point and non-point sources pollutants have contributed to the deterioration of water quality in the waterways, which may contaminate the Klang River. An assessment was conducted to study the pollutant transport within two sampling points located 1.3 km apart in the waterway. Five water quality parameters were selected, including pH, dissolved oxygen, nitrate, ammonia, and total suspended solid. Water quality analysis simulation program (WASP) was used to simulate the water quality downstream by introducing the input of upstream data. An excellent correlation was obtained between simulated and collected data with overall CE values higher than 0.9 for DO, NO_3, NH_3-N, and TSS, while the pH had a CE value of 0.853. An additional assessment was conducted by simulating two water quality improvement scenarios (swale and biofiltration system) available in the stormwater management model (SWMM) to the upstream data in WASP. Based on the predicted downstream water quality in WASP, the biofiltration system showed a better performance of pollutant reduction than swale by 5-35% differences.

1. INTRODUCTION

The rapid population growth, urbanization, and industrialization in Malaysia have led to a deterioration of quality in many of the water bodies. According to the department of statistics Malaysia (2017), the percentage of clean rivers has decreased from 58% to 46% from 2012 to 2017. Over the same period, the number of polluted rivers has grown from 8% to 11%. Several sources are contributing to the rivers' pollution, which can be categorized into point sources (PS) and non-point sources (NPS). The PS are referred to the specific sources of pollutions such as ineffective effluent treatment from various commercial and industrial sites that are directed towards water bodies. On the other hand, NPS refer to a mix of non-specific pollutants that enter the water bodies from a wide range of areas, such as road and residential area (Lai, Yang, Hsieh, Wu, & Kao, 2011). Most of the water management strategies have been focused on PS, neglecting the importance of NPS pollution treatment due to its irregular and varied nature (Dzikiewicz, 2000). In addition, irresponsible human activities such as littering further aggravate the effect of the pollution.

The high content of pollutants in the water bodies can normally be observed in the first flush, which is highly correlated to the rainfall-runoff process in the study site. Since rainfall is the primary source of runoff, it is quite important to have reliable rainfall-runoff (R-R) models, especially for urban stormwater management. To date, R-R models have provided significant support to decision-making in hydrological problems such as flood forecasting and stormwater management. Stormwater management model (SWMM) is one of the modelling software developed by the U.S. Environmental Protection Agency (USEPA) that has been widely used by consultants in analyzing hydrological processes in different types of catchments under various management scenarios (Rossman, 2010).

Other than SWMM, there are several modelling tools to relate the streams' water quality with land use. Examples of such models are Streeter-Phelps (S-P model), MIKE, enhanced stream water quality model (QUALs), and water quality analysis simulation program (WASP) as reviewed by Wang, Li, Jia, Qi, and Ding (2013). WASP model is well-known for its surface water quality modelling, which was also developed by USEPA. In the past decade, WASP has been improved to cover various features such as water bodies response prediction, interpretation from PS and NPS pollution (Wool, Ambrose, Martin, Comer, & Tech, 2006), and providing flexibility in simulating the pollutants transport in water bodies (up to 3-D simulation). For example, Lin, Chen, Kao, Hong, and Wu (2011) used WASP for an evaluation of water quality and proposed some remedial watershed management strategies for the Salt-water River.

Bandar Sunway is one of the heavily urbanized areas in Malaysia, which comprises residential, commercial, and industrial areas. Many water channels pass through this highly active region, resulting in increased water pollution in the water bodies. All channels in this site eventually reach Klang River, which has been flagged as the most polluted river in Malaysia (Mohamed, Othman, Ibrahim, Alaa-Eldin, & Yunus, 2015; Sharif, Kusin, Asha'ari, & Aris, 2015). It is believed that the Bandar Sunway canal is one of the PS and NPS pollution contributors to the Klang River. This paper aims to develop and calibrate a water quality model for the Bandar Sunway canal and use it to simulate the pollutant transport in this canal and also predict the effectiveness of any proposed water quality management measure in reducing pollutant concentration in the canal.

2. METHODOLOGY

2.1. Study Site

Bandar Sunway canal is located in Selangor, Malaysia, and connects Kelana Lake (3.094323 N, 101.597208 E) to Klang River. In this study, 2 water sampling stations are considered downstream of Kelana Lake as shown in Figure 1 (denoted as W1 and W2). The distance between the two sampling points is 1.3 km while the surrounding land use in this canal stretch is mainly residential and industrial. The width of the channel at W1 and W2 is 9.2 m and 17.8 m, respectively.

2.2. Water Sampling and Testing

For each sampling point, the rating curve was developed by measuring water depth (stage) and velocity. The stage was measured by using a standard meter while the velocity was measured by applying the floating object method (Hafsi, Ouerdachi, Kriker, & Boutaghane, 2016). For both W1 and W2, the stage and velocity measurements were distributed over 3 segments due to the channel topography as shown in Figure 2. The rating curve was then used to relate the measured canal stage to discharge during the water quality sampling at certain rainfall-runoff events.

Water sampling was made during two rainfall-runoff events on 16 April 2019 and 26 April 2019 to develop the water quality model. For each event, 7 water samples were collected with 5-min intervals by using the counter-current method before being transported to the laboratory for analysis. In this study, 5 water quality parameters pH, total suspended solid (TSS), dissolved oxygen (DO), nitrate (NO_3), and ammoniacal nitrogen (NH_3-N) are considered. All parameters were measured by using water quality multi-parameter instrument Xylem YSI ProDSS with a detection limit of 0.01 mg/L (unitless for pH).

Figure 1. Aerial view of the two sampling points in Bandar Sunway waterway, Malaysia
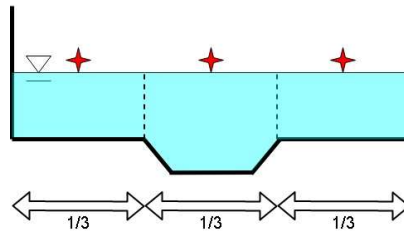
Figure 2. Location of 3 different points spread evenly in the width of the channel

2.3. Model Description and Application

In this study, WASP/EUTRO model is used to simulate the pollutant transport between stations W1 and W2 for all given parameters. In this model, the conservation of mass and momentum equations are used as shown in Eqs. (1) and (2), respectively.

$$\frac{\partial Q}{\partial t} + \frac{1}{B}\frac{\partial Q}{\partial x} = q_s \tag{1}$$

$$\frac{\partial Q}{\partial t} + \frac{\partial}{\partial x}\left(\frac{Q^w}{A}\right) + gA\left(\frac{\partial z}{\partial x} + \frac{Q|Q|}{K^2}\right) = 0 \tag{2}$$

where t is the time, Q is the flow rate, x is the distance along the channel, B is the wetted cross-sectional width, z is the water surface elevation, A is the wetted cross-sectional area, K is the conveyance of the channel, g is the gravitational acceleration, and q is the side discharge per unit channel length (Ambrose, Wool, & Martin, 1993). The water system in the WASP model was segmented into numerous mixed water cells by inputting hydraulic geometry parameters such as width, depth, and cross-sectional area. Additionally, WASP/EUTRO model applied key kinetic coefficients such as nitrification rate, reaeration coefficient, and denitrification rate. To determine the reaeration coefficient in the stream, Eq. (3) was used in this study (Tsivoglou & Neal, 1976).

$$K_2 = 0.054 \left(\frac{\Delta h}{t}\right) \ at \ 25°C \tag{3}$$

where Δh is the change in water elevation in feet and t is time in days.

Moreover, SWMM rainfall-runoff model was also developed to predict the discharge at W1 and W2 by inputting rainfall data and physical characteristics of the site. Rainfall data were obtained from the nearby rain gauge in Monash University Malaysia while the measured discharges at W1 and W2 were used for calibration of the model. There were 6 parameters adjusted for SWMM modelling including catchment width, catchment area, base flow, slope, imperviousness, and Manning's coefficient. However, infiltration-based parameters were set to the default value given by the SWMM.

Furthermore, a built-in function in SWMM for water quality improvement strategies was utilized to predict the changes to the water quality parameters at W2. The configuration of the built-in function was then incorporated with the WASP model to produce the treated water quality at W2. Based on the available and related functions of low impact development (LID) strategies, swale and biofiltration systems were chosen as the two scenarios modelled in this study due to their well-known performance as on-site stormwater management techniques (Hermawan et al., 2019; Kachchu Mohamed, Lucke, & Boogaard, 2013). Although the two systems are similar, swales focus more on directing the water to another area, while biofilters focus on the infiltration of water. The configuration of swale comprised of 8000 m^2 area with 4 m width, while the biofiltration system total area was put to be 10% of the total impervious area. It is noted that only the second rainfall-runoff event was modelled for the management scenarios.

2.4. Model Performance Criteria

Evaluation of the model performance was conducted by comparing the observed data with simulated data. Four performance criteria were applied including Nash-Sutcliffe coefficient of efficiency (CE), coefficient of determination (R^2), mean absolute error (MAE), and root mean square error (RMSE). The equation, units, and range for each criteria are tabulated in Table 1.

Table 1. Summary of formula for model performance evaluators (Chang, Talei, Chua, & Alaghmand, 2019).

Performance Criteria	Formula	Unit	Range
Nash-Sutcliffe Coefficient of Efficiency	$CE = 1 - \dfrac{\sum_{i=1}^{n}(X_{Obs,i} - X_{Sim,i})^2}{\sum_{i=1}^{n}(X_{Obs,i} - \overline{X}_{Obs})^2}$	Dimensionless	$(-\infty, 1]$
Coefficient of Determination	$R^2 = \left[\dfrac{\sum_{i=1}^{n}(X_{Obs,i} - \overline{X}_{Obs})(X_{Sim,i} - \overline{X}_{Sim})}{\sqrt{\sum_{i=1}^{n}(X_{Obs,i} - \overline{X}_{Obs})^2} \times \sqrt{\sum_{i=1}^{n}(X_{Sim,i} - \overline{X}_{Sim})^2}}\right]^2$	Dimensionless	$[0, 1]$
Mean Absolute Error	$MAE = \dfrac{\sum_{i=1}^{n}|X_{Sim,i} - X_{Obs,i}|}{n}$	mg/L for WASP m^3/s for SWMM	$[0, +\infty)$
Root Mean Square Error	$RMSE = \sqrt{\dfrac{\sum_{i=1}^{n}(X_{Sim,i} - X_{Obs,i})^2}{n}}$	mg/L for WASP m^3/s for SWMM	$[0, +\infty)$

* Note: X refers to pollutant concentration or discharge, $X_{Obs,i}$ = The ith observed data, $\overline{X}_{Obs}$ = The average value of observed data, n = total number of data points, $X_{Sim,i}$ = The ith simulated data, $\overline{X}_{Sim}$ = The average value of simulated data.

3. RESULTS AND DISCUSSION

3.1. Correlation Between Stage and Discharge

Figure 3 shows the rating curve developed for both W1 and W2. The curve-fitting on collected data points favors power functions for both stations W1 and W2, with an excellent R^2 value of 0.9959 and 0.9916, respectively. Using the rating curves, the mathematical relationships between the stage and discharge are shown for stations W1 and W2 in Eqs. (4) and (5), respectively.

$$Q = 9.528 \times 10^{-3} (x + 1.678)^{5.939} \tag{4}$$

$$Q = 1.065 \times 10^{-7} (x + 4.031)^{11.13} \tag{5}$$

where Q = flow rate (m3/s) and x = stage (m).
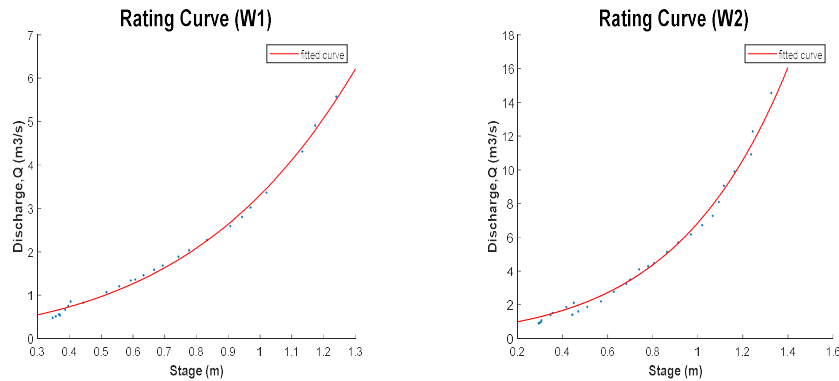
Figure 3. Rating curve for stations W1 and W2 in the canal

3.2. WASP Model Results in W2 Station

Table 2 presents the data collected from the site for both events at W1 and W2. In general, the concentration of the pollutants at W2 was higher than W1. This was expected as W1 is mainly surrounded by residential areas while W2 is downstream of industrial areas. However, the water quality data at W2 satisfied standard B by Malaysia industrial effluents regulation (DOE, 2009).

The data obtained from W1 was used as input in the WASP model. After calibrating the model, the targeted output was predicting the concentration of the pollutants in W2. Figure 4 provides the comparison between observed and simulated data at W2 for both events. DO shows an increasing trend in event 1, while it decreases during event 2. However, other pollutants (TSS, NO_3, NH_3-N) show opposite trends, i.e., decreasing during event 1 and increasing in event 2. The difference between the trends in events 1 and 2 is hypothesized to be due to the effect of the first flush. During the initial period of the first flush, pollutants tend to accumulate in the waterway, resulting in the increasing trend as observed in event 2. However, the data captured during event 1 has passed the first flush thus decreasing pattern is observed. Naturally, DO behave the other way around as it tends to enter the recovery stage once the first flush is concluded.

Table 2. The average concentration of water quality indicators for both rainfall events.

Parameter	April 16, 2019		April 26, 2019	
	W1	W2	W1	W2
Flow rate (m^3/s)	0.77 ± 0.04*	1.78 ± 0.33	0.76 ± 0.06	1.46 ± 0.25
DO (mg/L)	0.86 ± 0.23	0.84 ± 0.21	1.00 ± 0.29	0.98 ± 0.27
NO$_3$ (mg/L)	3.07 ± 0.48	2.55 ± 0.23	2.93 ± 0.61	2.48 ± 0.31
NH$_3$-N (mg/L)	3.22 ± 0.48	2.64 ± 0.24	3.13 ± 0.61	2.58 ± 0.31
pH	7.06 ± 0.11	6.96 ± 0.02	7.13 ± 0.15	6.93 ± 0.01
TSS (mg/L)	91.29 ± 18.35	69.57 ± 21.06	90.71 ± 20.31	69.29 ± 16.78

* mean ± standard deviation

W2 (DO)

W2 (DO)

W2 (NO3)

W2 (NO3)

W2 (NH3-N)

W2 (NH3-N)

W2 (pH)

W2 (pH)

(a)   (b)
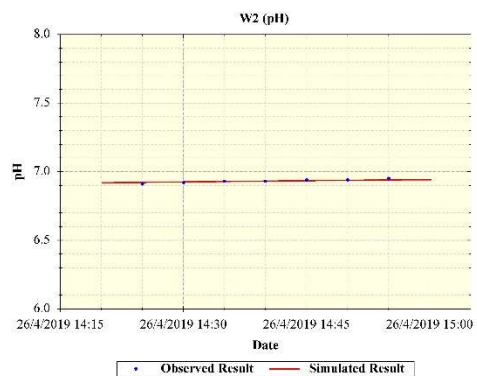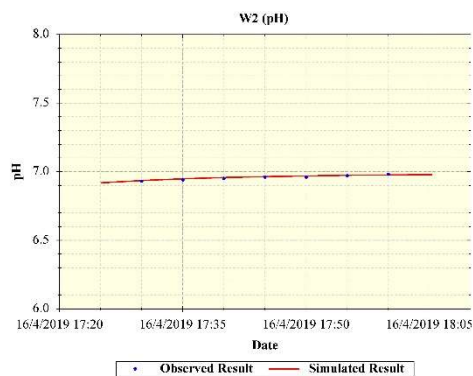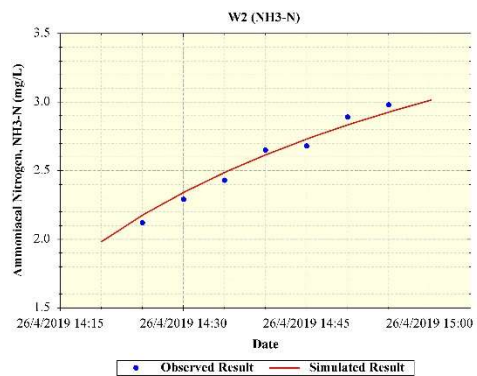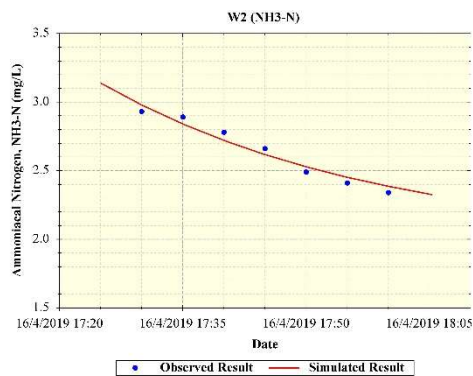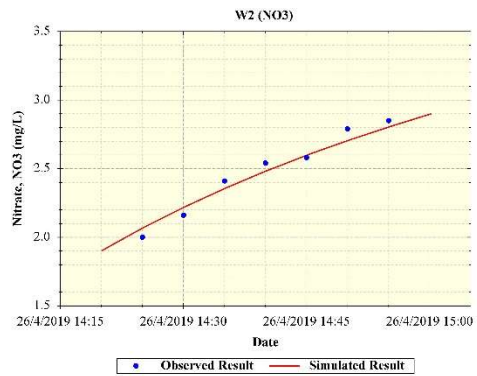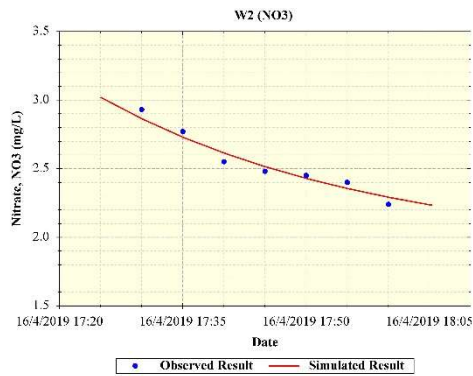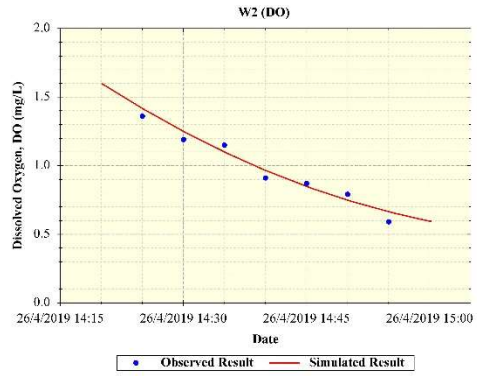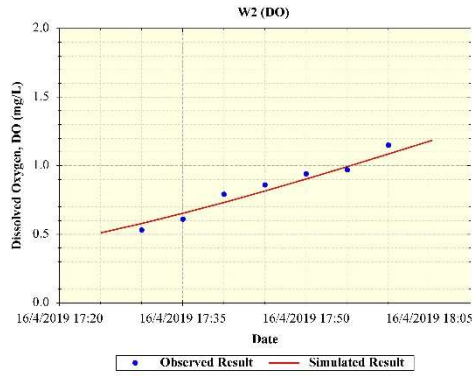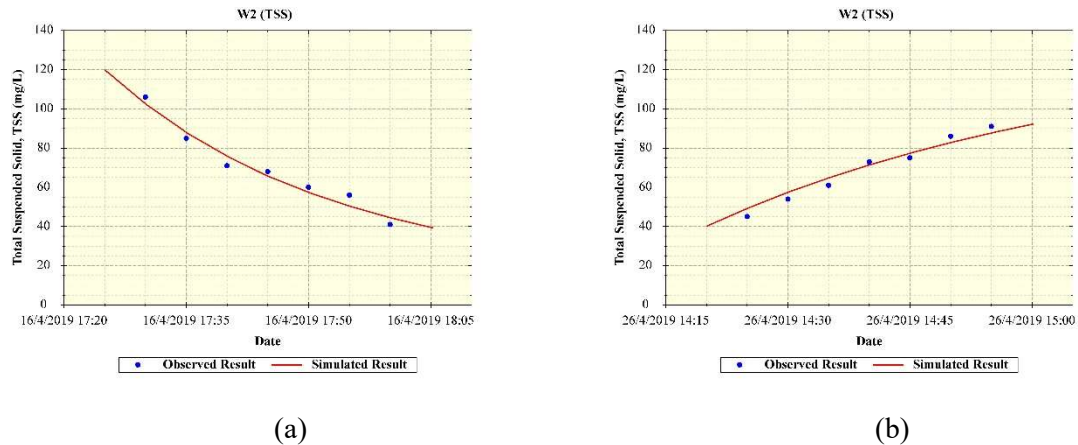
Figure 4. Water quality model results for Bandar Sunway River on (a) 16 April 2019 and (b) 26 April 2019

Table 3 summarizes the performance of the WASP model in simulating the downstream (W2) water quality in comparison with the observed data on-site. It can be observed that the simulated data have a very high correlation and almost excellent matching with overall CE and R^2 value >0.95 (except for pH). This shows that the model can predict the transport of the pollutants given the initial concentration, geometry, and few characteristics as inputs value. Looking into the performance criteria based on error (MAE and RMSE), it was found that the overall MAE and RMSE were at <0.05 mg/L, except for TSS at approximately 3.50 mg/L. However, the overall performance of the WASP model is quite promising.

Table 3. Summary of WASP model performance results for Event 1 at W2.

Performance Criteria	DO	NO$_3$	NH$_3$-N	pH	TSS
CE	0.945	0.948	0.952	0.853	0.964
R^2	0.964	0.959	0.958	0.950	0.966
MAE (mg/L)	0.045	0.048	0.047	0.006	3.509
RMSE (mg/L)	0.047	0.049	0.048	0.006	3.690

3.3. Discharge Prediction by SWMM

Figure 5 shows the comparison between observed and simulated discharge by the SWMM model at W1 and W2. As it can be seen, the simulated flow time series follows the same patterns available in the observed data; however, the model generally overestimates the flows. This could be attributed to the limited number of data points available to calibrate the model (<40 data points for both W1 and W2). The performance criteria in simulating discharge are tabulated in Table 4. As it can be seen, model performance in terms of R^2 in stations W1 and W2 are 0.761 and 0.702, respectively. In general, the errors in W2 are larger due to the fact that W2 has been the validation station.
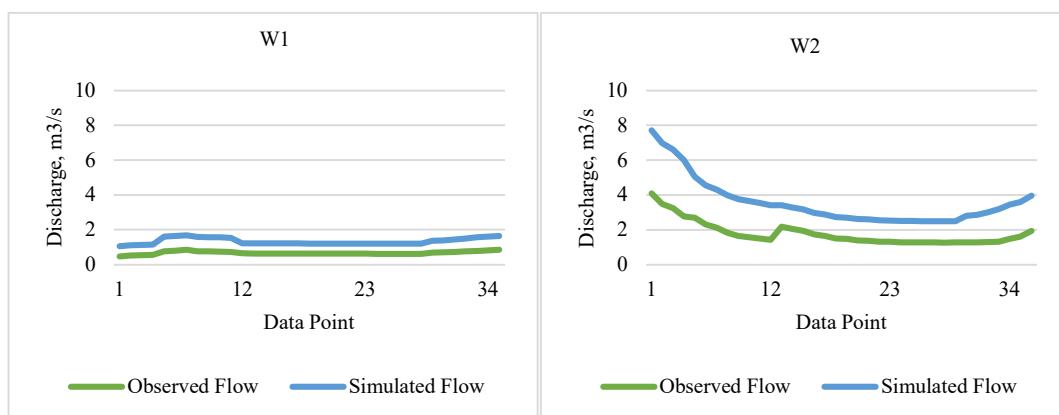
Figure 5. Predicted runoff from the R-R model generated by SWMM for the two sampling points (W1 and W2)

Table 4. Summary of SWMM model performance results for W1 and W2.

Performance Criteria	W1	W2
CE	0.662	0.667
R^2	0.761	0.702
MAE (m^3/s)	0.047	0.311
RMSE (m^3/s)	0.053	0.393

3.4. Predicted Performance of the Proposed Management Scenarios

In the next stage of this study, swales and biofiltration systems were implemented in the model as two separate scenarios where their impact on water quality improvement at W2 was evaluated. Water quality measures at W2 for these two scenarios are presented in Fig. 6. As it can be seen, improvement in water quality has occurred for both scenarios. Although both scenarios did not show any impact on pH value, the other 4 parameters have been significantly reduced. The overall comparison of the two scenarios is presented in Table 5. It can be seen that swales showed less efficiency in removing nitrogen-based pollutants compared to the biofiltration systems. This finding is in agreement with a study conducted by Kachchu Mohamed et al. (2013). Overall, biofiltration systems offer a better improvement towards water quality than swales. This is due to the flexibility of the biofiltration system, which can be designed for various land use and ground condition (Hermawan & Talei, 2018). In addition, swales allow less retention time in comparison with biofilters. A study by Tang, Huang, Huang, and Lin (2011) concluded that the hydrological impacts of high imperviousness in urban areas can be significantly mitigated by implementing biofiltration systems. This can be done by considering a small portion of the land to biofiltration system in places such as public parks, parking lots, or roadside. Therefore, for this study site, the biofiltration system was found to be a suitable low impact development for enhancing the water quality in the river.
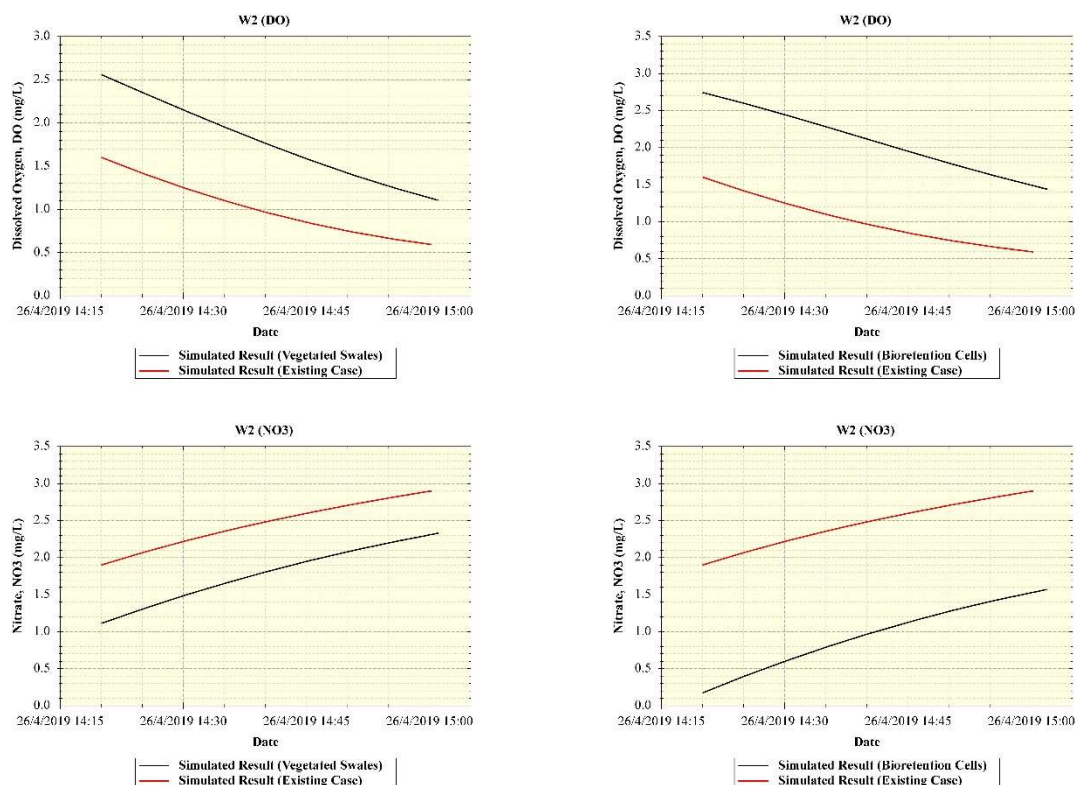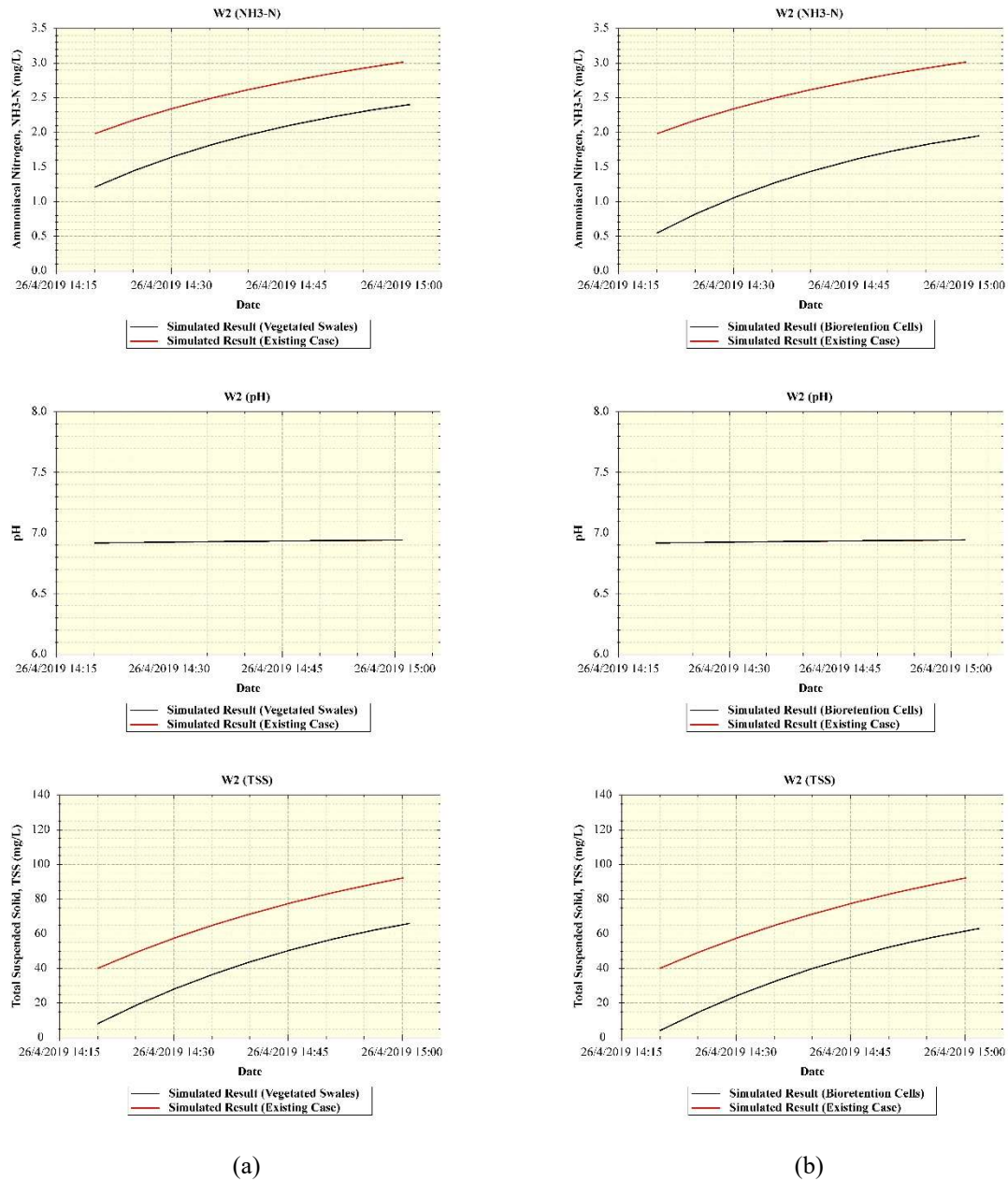
Figure 6. Two scenarios for improving water quality in Bandar Sunway river (a) Scenario 1 (Swales) and (b) Scenario 2 (Bioretention Cells)

Table 5. The average concentration of water quality indicators for both scenarios.

Parameter	Observed Value	Scenario 1 (Swales)		Scenario 2 (Bioretention Cells)	
	W2	W2	Reduction (%)	W2	Reduction (%)
DO (mg/L)	0.98	1.77	(80.66)	2.10	(114.62)
NO$_3$ (mg/L)	2.48	1.79	27.64	0.95	61.68
NH$_3$-N (mg/L)	2.58	1.93	25.04	1.40	45.80
pH	6.93	6.93	0.00	6.93	0.00
TSS (mg/L)	69.29	42.39	38.82	38.59	44.30

4. CONCLUSION

The major findings of this research include:

(1) WASP model was calibrated with the collected data during the first rainfall event and validated using the second rainfall event. Simulated results indicated that the WASP model was well calibrated and had excellent matching with the observed data (CE and $R^2 > 0.95$) for water quality parameters of DO, NO_3, NH_3-N, pH, and TSS.

(2) The efficiency of two LID solutions (swales and biofiltration systems) in water quality improvement was evaluated through modelling. Both scenarios showed improvement in overall water quality parameters. However, the biofiltration system performed better in improving water quality than swales. Therefore, the biofiltration system was recommended for water quality management strategies in Bandar Sunway River.

REFERENCES

Ambrose, R. B., Wool, T. A., & Martin, J. L. (1993). The water quality analysis simulation program, WASP5, Part A: Model documentation. *Environmental Research Laboratory, US Environmental Protection Agency, Athens, GA.*

Chang, T. K., Talei, A., Chua, L. H., & Alaghmand, S. (2019). The impact of training data sequence on the performance of neuro-fuzzy rainfall-runoff models with online learning. *Water, 11*(1), 52.

DOE. (2009). *Environmental Quality (Industrial Effluent) Regulation.* Malaysia

Dzikiewicz, M. (2000). Activities in nonpoint pollution control in rural areas of Poland. *Ecological Engineering, 14*(4), 429-434.

Hafsi, R., Ouerdachi, L., Kriker, A., & Boutaghane, H. (2016). Assessment of urbanization/impervious effects on water quality in the urban river Annaba (Eastern Algeria) using physicochemical parameters. *Water Science and Technology, 74*(9), 2051-2059.

Hermawan, A. A., & Talei, A. (2018). *Removal process of nutrients and heavy metals in tropical biofilters.* Paper presented at the E3S web of conferences.

Hermawan, A. A., Talei, A., Leong, J. Y. C., Jayatharan, M., Goh, H. W., & Alaghmand, S. (2019). Performance assessment of a laboratory scale prototype biofiltration system in tropical region. *Sustainability, 11*(7), 1947.

Kachchu Mohamed, M., Lucke, T., & Boogaard, F. (2013). Preliminary investigation into the pollution reduction performance of swales used in a stormwater treatment train. *Water Science and Technology, 69*(5), 1014-1020.

Lai, Y., Yang, C., Hsieh, C., Wu, C., & Kao, C. (2011). Evaluation of non-point source pollution and river water quality using a multimedia two-model system. *Journal of Hydrology, 409*(3-4), 583-595.

Lin, C., Chen, C., Kao, C., Hong, A., & Wu, C. (2011). Development of the sediment and water quality management strategies for the Salt-water River, Taiwan. *Marine pollution bulletin, 63*(5-12), 528-534.

Mohamed, I., Othman, F., Ibrahim, A. I., Alaa-Eldin, M., & Yunus, R. M. (2015). Assessment of water quality parameters using multivariate analysis for Klang River basin, Malaysia. *Environmental monitoring and assessment, 187*(1), 1-12.

Rossman, L. A. (2010). *Storm water management model user's manual, version 5.0*: National Risk Management Research Laboratory, Office of Research and ….

Sharif, S. M., Kusin, F. M., Asha'ari, Z. H., & Aris, A. Z. (2015). Characterization of water quality conditions in the Klang River Basin, Malaysia using self organizing map and K-means algorithm. *Procedia Environmental Sciences, 30*, 73-78.

Tang, P. K., Huang, Y. C., Huang, J. S., & Lin, Y. J. (2011). *Water quality management strategies for various river flows with QUAL2K model.* Paper presented at the Applied Mechanics and Materials.

Tsivoglou, E., & Neal, L. (1976). Tracer measurement of reaeration: III. Predicting the reaeration capacity of inland streams. *Journal (Water Pollution Control Federation)*, 2669-2689.

Wang, Q., Li, S., Jia, P., Qi, C., & Ding, F. (2013). A review of surface water quality models. *The Scientific World Journal, 2013*.

Wool, T. A., Ambrose, R. B., Martin, J. L., Comer, E. A., & Tech, T. (2006). Water quality analysis simulation program (WASP). *User's Manual, Version, 6.*

14TH INTERNATIONAL CONFERENCE
ON HYDROSCIENCE & ENGINEERING

MAY 26-27, 2022
IZMİR-TURKEY

ICHE2022
IZMIR, TURKEY

JELLYFISH TRANSPORT MODEL DEVELOPMENT IN AN IRISH FJORD

Md Ashkar Bin Sayeed

Civil Engineering, School of Engineering, National University of Ireland

Galway, Ireland

m.sayeed1@nuigalway.ie

Fearghal O'Donncha

IBM Research

Dublin, Ireland

feardonn@ie.ibm.com

Tom Doyle

School of Biological, Earth and Environmental Sciences, University College Cork

Ireland

t.doyle@ucc.ie

Reduan Atan

Mott MacDonald Engineering Consultancy

London, UK

reduan.atan@gmail.com

Michael Hartnett

Civil Engineering, School of Engineering, National University of Ireland

Galway, Ireland

michael.hartnett@nuigalway.ie

Stephen Nash

Civil Engineering, School of Engineering, National University of Ireland

Galway, Ireland

stephen.nash@nuigalway.ie

ABSTRACT: Jellyfish pose a significant threat to marine-farmed fish with many records of fish kills and economic losses reported globally. This is associated with the transportation of jellyfish, which is directly linked to their swarm or bloom formation. To simulate their transport, here, we developed and use a particle-track coupled hydrodynamic model and made comparisons with the measured data. Due to recent fish fatalities by jelly swarms, Killary Harbour, a fjord on the west coast of Ireland, was chosen as a case study site. A 3D baroclinic hydrodynamic model of Killary was developed using the Environmental Fluid Dynamics Code (EFDC) and a particle-track module was integrated with it. Jellyfish were modelled as passive drifters within this model and the outputs were compared with some recorded movements of tagged jellyfish within the harbour. Jellyfish movements in Killary were detected by 8 GPS receivers placed along the banks of the harbour. At each detection instance, the number of modelled particles within each detector's range and the centroid of the corresponding particle distribution were determined and compared with the GPS observations. Movements and spatiotemporal detections of the modelled particles agreed relatively well with the observed jellyfish in the short term after their release. Longer-term, the results were mixed. Although the analyses reveal the concurrence of jellyfish and particles even at times separated by long time intervals and distances (e.g., both

detected at a time 133 hrs after their release at a 5 km distance from the release point), the levels of agreement shown are small. There was a difference between the short-term and long-term transport of particles released at mid-depth in the water column compared to those released at the surface. In the short term, wind-induced surface currents result in many surface particles being transported west of the release point towards the sea, whereas many sub-surface particles are transported eastward of the release point. Ultimately, the simulations have shown that tidal and wind-driven currents can indeed cause particles to be transported in a similar manner to the tagged jellyfish; thus, corroborating the literature. However, the limited agreements in long-term transport suggest that the horizontal and vertical motility of the jellyfish might play an important role in their net transport.

1. INTRODUCTION

The mass killing of marine-farmed fish due to sting toxins by the swarms of jellyfish has been

Figure 1. Map of the study site at Killary Harbour, Co. Mayo, Ireland (courtesy: Google Maps)

reported all over the world and identified as a global problem (Rodger et al., 2011; Purcell et al., 2007). The economic consequences are significant with annual losses of 68–205 million USD and 10 million USD previously estimated for Korea (Kim et al., 2012) and the Gulf of Mexico (Graham et al., 2003), respectively. In Ireland, in 2017, swarms of jellyfish wiped out about 80 % of the salmon stock from several farms in Killary Harbour (Figure 1) and some 10,000 fish from adjacent waters along the west coast (O'Sullivan, 2017). The present research aims to develop a particle-track coupled hydrodynamic model to simulate the transport and fate of jellyfish to get a better understanding and insights into their swarm/bloom formation. The research results can be useful in predicting any potential adverse interactions of jellyfish with fish farms. Due to its recent problems, Killary Harbour, a fjord on the Irish west coast, was chosen as the case study site for the research.

2. METHODOLOGY

2.1. Hydrodynamic and Jellyfish Observations in Killary

Current speeds and directions in Killary were recorded using a bed-mounted ADCP deployed from Aug to Oct 2015 at 446.7 km E and 5939.7 km N. The vertical profile of the ADCP data is 8.5 m in height and divided into 17 bins up to the surface. As a quality control measure, the ADCP current speed data was passed through the Butterworth lowpass filter for noise filtering and smoothing. Ten jellyfish in Killary were captured, tagged, and released to track their movements in the same period of hydrodynamic observation. Eight geostationary recorders (500 m signal transmission coverage radius of each) along the harbour were used for this monitoring (Figure 2). Among those, five jellyfish provided useful information for analysis. The records were analyzed to investigate the tidal influences on jellyfish net transport. This was finally used to compare with particle tracking results to facilitate the development of the jellyfish transport model.
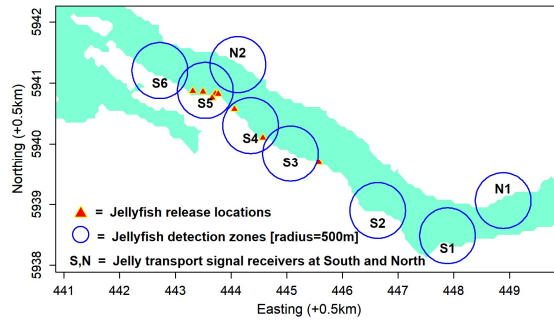
Figure 2. Map showing jellyfish release and detection locations

2.2. Model Setup and Calibration

Environmental Fluid Dynamics Code (EFDC), a 3D coastal model (Hamrick, 1992), has been used as a numerical tool to simulate the hydrodynamics of the Killary harbour. EFDC's hydrodynamic module is mainly based on the Navier-Stokes equation. Its physics and many numerical aspects are like the Blumberg-Mellor model (Blumberg and Mellor, 1987) and US Army Corps of Engineers' Chesapeake Bay model (Park et al., 2005). The model domain is approximately 20 km East-West (435.4 km to 455.8 km Easting) and 6.4 km North-South (5938.5 km to 5944.9 km Northing) within UTM zone 29. It is gridded at 64×64 m^2 spatial resolution with 20 sigma layers in the vertical direction, thereby yielding $320 \times 100 \times 20$ cells. A timestep of 0.25 s was used in the model through a process of optimization. Bathymetry of Killary was developed by depth interpolation. The sea surface elevation by the local tide was mainly used as the open boundary (west) condition. Discharges from two eastern rivers Bundorragha and Errif were used as the freshwater inflow. The model was forced with a constant salinity of 35 psu and a temperature of 15°C. The ERA-Interim model wind was used as the main atmospheric input. These settings were assigned in the parallel computing version of the model developed by O'Donncha, one of the fellows of this research, along with his team (details available in O'Donncha et al. (2014)). The simulated surface elevation and current speeds were compared with the observed hydrodynamics in Killary; the results have had a fair degree of agreement (Figure 3).
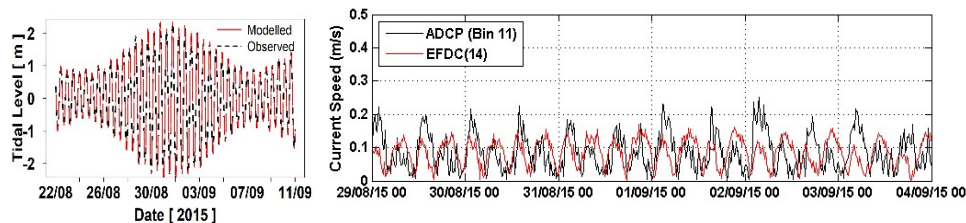
Figure 3. Comparison of modelled (red) with measured (black) hydrodynamics in Killary

2.3. Transport Module Setup and Particle Tracking

The Lagrangian particle tracking (LPT) module was prepared for the Killary harbour and integrated with the main hydrodynamic model to simulate the passive transportation of jellyfish. For preliminary investigation of this, it was hypothesized that the jellyfish were passive drifters. Both the advection and diffusion transport processes were activated in the integrated model. A second-order Explicit-Euler numerical solver was used for discretizing the differential equations of the above processes to allow the calculation of Lagrangian trajectories of the particles or drifters. The solver was used for its relative simplicity in operational procedure, numerical calculation, computational economy, and functional adaptation to any potential modification of codes. Instead of EFDC's original drifter module, a modified version of it enhanced by Chung & Craig (2009) and later parallelized by O'Donncha et al. (2014) was used in this study. For scenario modelling, batches of one hundred particles were released at the water surface and mid-depth layers at the same horizontal locations and times that the tagged jellyfish were released (Figure 2). The particles were tracked batch-wise for the

duration of the corresponding jellyfish to help compare the agreement of modelled particle transportations with observed jellyfish movements.

3. RESULTS

The hydrodynamic modelling results show that the modelled hydrodynamics agree with the measured hydrodynamics (Figure 3). This ensured the model's readiness to couple the particle-track model with it. Basically, the jellyfish transportation results have been the focus of the presentation here. So, the part of the results specific to the sensitivity modelling to assess and evaluate the model development does not cover in this paper. Figure 4 shows the tidal influence of an example jellyfish movements observed in Killary. Coloured and white rings indicate jellyfish detections and non-detections within a detector's range respectively with ring thickness being representative of the time duration of an

individual incidence. Each sequential detection has been numbered to help track the inter-zone movements of jellyfish, which in conjunction with the inset time-series plot of the surface elevation marked by the same set of numbers further helps to read the tidal influences of jellyfish movements. In the figure, a westward/seaward movement from detection 1 at S4 to 2 at S5 during ebbing indicates an example of tidally influenced transportation, while an eastward movement

Figure 4. Jellyfish (J-18495) transportation observed in Killary on 20~27 Aug 2015

from detection 4 at S1 to 5 at N1 during ebbing is an example of an opposite case. Thus, the observation in Killary confirms that a share of jellyfish movements is tidally influenced, which complies with the literature. For an initial modelling investigation of jellyfish transport, the choice of tidally influenced passive movement is thereby justified as the scientific basis of the present modelling.

The jellyfish transport model developed here through the development and integration of hydrodynamic and particle-track models using the EFDC can simulate jellyfish movements as passive drifters in Killary. Figure 5 shows a graphical representation of transport based on the spatiotemporal occurrence of the observed jellyfish and the corresponding modelled particles. This is presented as a primary and qualitative approach to analyzing the transport agreements over time and across detection zones. The figure also exhibits the sensitivity of the model to the particle release depth. Unlike the mid-depth released particles (hereinafter MRP), the transport of the surface water released particles (hereinafter SRP) agreed with the jellyfish movements at all the time instances, which are represented by the golden cells in the figure. All particles were ultimately distributed over the Killary in the long run though, in short term, the detections of MRP were relatively skewed eastward towards the harbour than that of the SRP, which are represented by the green cells in the figure. Thus, a differential tendency in the net transport is seen in the short-term transport of particles released in the middle of the water column compared to those released at the surface. Wind-induced surface currents result in many surface particles being transported west of the release point towards the sea, whereas many sub-surface particles are transported eastward of the release point. This might give rise to differential agreements with jellyfish movements in the long term.
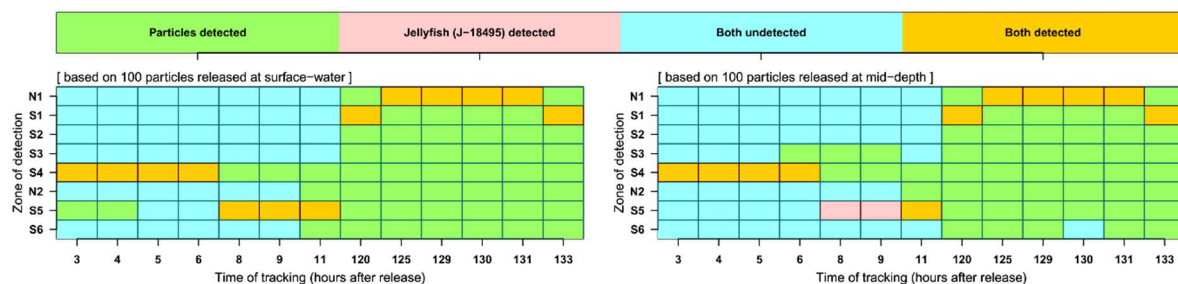
Figure 5. Tracking of the modelled particle and observed jellyfish transportation in Killary

Since the above manifestation was only qualitative, an estimation of quantitative agreement of the modelled transport with the observation was made, which is presented in Table 1, to help explore the level of drifts in jellyfish transportation. The table shows the overall detection of particles as well as the percentage of their agreement at each detection instance of the jellyfish at the two release depth scenarios. The short-term transport agreement was near about 100%, which shows a gradual decrease over the period of the simulation. The percentage agreement in the long term confirms that some particles were discoverable on the travel route of the example jellyfish even at a distance from the release location (e.g., 9.68 % agreement at 5 km away from the release point 133 hr after release). Further calibration in the model and the transport process is necessary to improve the level of this agreement, which is ongoing.

Table 1. Comparison of particle-jellyfish transport agreements within and between the surface water and mid-depth release scenarios.

Deciphering column headings: jel_hrs = jellyfish detected at hours after release; npd_av_dom = total number of particles available in the domain; S6~N1 = detection locations; npd_dt = cumulative particles detected by the individual detectors; npd_exclsv = total number of particles detected by all detectors without overlapping; prcnt_agr = percentage of agreement; jocr_stn = location of jellyfish detection; dis_cen = distance (m) of the particle centroid from the corresponding detector; dir_cen = direction (angle in deg) of the particle centroid with respect to the corresponding detector

A: Analysis based on the transportation of the surface water released particles

	jel_hrs	npd_av_dom	S6	S5	N2	S4	S3	S2	S1	N1	npd_dt	npd_exclsv	prcnt_agr	jocr_stn	dis_cen	dir_cen
1	3	100	0	1	0	99	0	0	0	0	100	100	99.00	S4	−110	131
2	4	100	0	0	0	100	0	0	0	0	100	100	100.00	S4	−253	131
3	5	100	0	0	0	100	0	0	0	0	100	100	100.00	S4	−398	142
4	6	100	0	0	0	100	0	0	0	0	100	100	100.00	S4	−391	171
5	8	100	0	27	0	69	0	0	0	0	96	96	27.00	S5	110	296
6	9	100	0	86	23	8	0	0	0	0	117	98	86.00	S5	−203	278
7	11	100	47	57	1	8	0	0	0	0	113	94	57.00	S5	−115	125
8	120	77	4	2	2	2	3	4	6	1	24	21	7.79	S1	3048	124
9	125	68	4	3	3	1	3	6	6	2	28	25	2.94	N1	3847	110
10	129	65	4	5	4	3	3	6	4	3	32	29	4.62	N1	3384	110
11	130	65	2	5	5	1	5	6	4	3	31	29	4.62	N1	3110	110
12	131	65	2	4	6	1	4	5	6	3	31	29	4.62	N1	2948	111
13	133	63	2	6	4	1	4	4	6	2	29	26	9.52	S1	2367	129

B: Analysis based on the transportation of the mid-depth released particles

	jel_hrs	npd_av_dom	S6	S5	N2	S4	S3	S2	S1	N1	npd_dt	npd_exclsv	prcnt_agr	jocr_stn	dis_cen	dir_cen
1	3	100	0	1	0	99	0	0	0	0	100	100	99.00	S4	−389	192
2	4	100	0	0	0	100	0	0	0	0	100	99	100.00	S4	−240	281
3	5	100	0	0	0	100	0	0	0	0	100	98	100.00	S4	−47	284
4	6	100	0	0	0	100	0	0	0	0	100	92	100.00	S4	73	283
5	8	100	0	27	0	69	0	0	0	0	96	62	27.00	S5	800	291
6	9	100	0	86	23	8	0	0	0	0	117	68	86.00	S5	489	285
7	11	100	47	57	1	8	0	0	0	0	113	97	57.00	S5	−17	226
8	120	76	4	2	2	2	3	4	6	1	24	28	7.89	S1	2433	127
9	125	69	4	3	3	1	3	6	6	2	28	31	2.90	N1	3070	110
10	129	65	4	5	4	3	3	6	4	3	32	27	4.62	N1	2272	105
11	130	66	2	5	5	1	5	6	4	3	31	27	4.55	N1	2185	103
12	131	66	2	4	6	1	4	5	6	3	31	28	4.55	N1	2126	104
13	133	62	2	6	4	1	4	4	6	2	29	23	9.68	S1	1165	128

As per the percentage agreement analysis strategy, a similar level of agreement is seen between the two release depth scenarios (Table 1). Instead of relying only on this strategy, the analysis has been extended forward to determining the distance of the particle centroid from the corresponding detectors (Figure 6), which is regarded as another measure of agreement. Figure 6 shows the areas between the detectors and the particle centroids over the period of tracking, the grey polygon representing the SRP

and the golden polygon representing the MRP. The size comparison of the polygon areas determines the tendency of the particles to agree with the jellyfish movement. The smaller the area, the higher the possibility of agreement. Thus, the particles released at mid-depth in the water column are likely to agree more compared to those released at the surface in the long-term period.
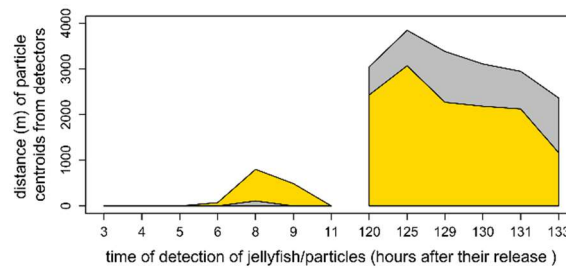
Figure 6. Centroid-based agreement analysis.

4. CONCLUSIONS

The model development and coupling were successful. The developed hydrodynamic model could simulate the current flows in Killary. Analysis of both the observed and modelled jellyfish tracking data has indicated a tidal influence on their movements. This agrees with the literature (e.g. Berline et al. (2013) and Yin et al. (2019)), which reports ocean and wind-driven currents to be the main drivers of jellyfish transportation. The developed particle-track model could replicate the tidally influenced passive transportation of jellyfish as observed in Killary. Simulating the jellyfish in Killary as a passive drifter has shown that the tidal and wind-driven currents can cause particles to be transported in a similar manner to the tagged jellyfish, which further corroborates the literature. However, the limited agreements in the long-term transport suggest that there might be some behavioural movements involved in their net transportation. The model is slightly sensitive to the particle release depth. Overall, the surface water releasing particles agree better at the beginning of the simulation, whereas the mid-depth releasing particles agree better in the later period of the simulation. The model would predict better with an optimized combination of parameters and forcings. Further statistical analysis of model results must be conducted. The next phase of the research involves including jellyfish behaviour in their transport modelling.

ACKNOWLEDGEMENT

REFERENCES

Berline, L., Zakardjian, B., Molcard, A., Ourmieres, Y., & Guihou, K. (2013). Modeling jellyfish Pelagia noctiluca transport and stranding in the Ligurian Sea. Mar. Pol. Bul., 70(1-2): 90-99.

Blumberg, A. F., & Mellor, G. L., (1987). A description of a three-dimensional coastal ocean circulation model. In: HEAPS, N.S. (ed.), Three-dimensional Coastal Ocean Models. Coastal and Estuarine Science, vol 4, (pp. 1-19). American Geophysical Union.

Chung, D. H., & Craig, P. M. (2009). Implementation of a Lagrangian particle tracking sub-model for the Environmental Fluid Dynamics Code. Dynamic Solutions-International, LLC Knoxville, TN and Hanoi Vietnam, 1–21. WWW.DS-INTL.BIZ

Graham, W., Martin, D., Felder, D., Asper, V, & Perry, H. (2003). Ecological and economic implications of a tropical jellyfish invader in the Gulf of Mexico. Biological Invasions, 5: 53-69.

Hamrick, J. M. (1992). A Three-Dimensional Environmental Fluid Dynamics Computer Code: Theoretical and Computational Aspects. In: Special report in applied marine science and ocean engineering, Issue 317. Virginia Institute of Marine Science, College of William and Mary. https://doi.org/10.21220/V5TT6C

Kim, D. H., Seo, J. N., Yoon, W. D., & Suh, Y. S. (2012). Estimating the economic damage caused by jellyfish to fisheries in Korea. Fisheries Science, 78: 1147-1152.

O'Donncha, F., Ragnoli, E., & Suits, F. (2014). Parallelisation study of a three-dimensional environmental flow model. Computers and Geosciences, 64, 96–103. https://doi.org/10.1016/j.cageo.2013.12.006

O'Sullivan, K. (2017, Oct 6). Stinger jellyfish swarms wipe out farmed salmon in west of Ireland. The Irish Times. Retrieved from http://www.irishtimes.com

Park, K., Jung, H., Kim, H., & Ahn, S. (2005). Three-dimensional hydrodynamic-eutrophication model (HEM-3D): Application to Kwang-Yang Bay, Korea. Mar. Environ. Res., 60(2), 171–193.

Purcell, J. E., Uye, S., & Lo, W. T. (2007). Anthropogenic causes of jellyfish blooms and their direct consequences for humans: a review. Marine Ecology Progress Series, 350: 153-174.

Rodger, H. D., Henry, L., & Mitchell, S. O. (2011). Non-infectious gill disorders of marine salmonid fish. Rev Fish Biol Fisheries, 21: 423-440.

Yin, L., Shan, X., Zhao, C., Jin, X., Wang, G., & Qiao, F. (2019). A model for the transportation and distribution of jellyfish Rhopilema esculentum for stock enhancement in the Liaodong Bay, China. Acta Oceanol. Sin., 38(1): 90–101.

KITCHEN GREY WATER TREATMENT USING A RAIN GARDEN

Amira Atiqah Mustafa

Department of Civil Engineering, Faculty of Engineering, Universiti Putra Malaysia

Serdang, Selangor, Malaysia

amiraatiqah04@gmail.com

Badronnisa Yusuf

Department of Civil Engineering, Faculty of Engineering, Universiti Putra Malaysia

Serdang, Selangor, Malaysia

nisa@upm.edu.my

ABSTRACT: A rain garden is widely used for treating storm water but its application in treating grey water is still limited. A rain garden is a type of bio-retention system normally used to reduce the runoff peak flow, treat, and filter the pollutants present in the stormwater. A typical rain garden consists of several layers where it consists of a filter media, soil suitable for planting and a garden of plants. To optimize the performance of the rain garden, type of filter media, soil, and plants to be used should be carefully selected. This paper presents the laboratory study on the effectiveness of rain gardens with different filter media and plants in treating kitchen greywater. The filter media of wood chips and peanut shells with varying thickness of 100 mm and 300 mm and two types of plants, namely Lemongrass and Pandan were tested. Seven water quality parameters were analyzed for both influent and effluent of the raingarden. The results show that a combination of wood chips and peanut shells as filter media is effective in lowering the pollutants content in the kitchen greywater. The materials have good adsorbent properties and provide adequate environmental conditions for the rain garden system. Results showed that the rain garden with 300 mm filter media depth has a higher percentage of pollutants removal compared to 100 mm. Pandan showed better performance in treating kitchen wastewater than the Lemongrass. Overall, the designed rain garden has been proved effective in treating the kitchen wastewater with an average percentage removal of pollutants of more than 90%.

1. INTRODUCTION

Grey water discharge management is one of the challenges faced by many developed countries especially in rural areas where there is lack of a proper system for grey water discharge. According to the World Health Organization (2006), grey water is described as wastewater from the laundry, bath and kitchen, excluding toilet wastewater. Grey water is categorized into two types: dark grey water and light grey water (Albalawneh & Chang, 2015). Light grey water is wastewater from the bathroom, the tub, clothes washing machines, and the bathroom, while dark grey water is water from kitchen sinks, laundry facilities, and dishwashers. Grey water represents more than half of the total domestic wastewater volume and kitchen grey water is makes up 10% of the total grey water produced (Edwin, et al., 2013) and it is considered as the most polluted grey water. Kitchen grey water has a relatively high amount of suspended solid compared to the other source of grey water and contributes up to 50% of COD to the total COD in the grey water (Katukiza, et al., 2013). Kitchen grey water composition varies depending on climatic conditions, fixtures, and lifestyle. It contains a high level of pathogenic microorganisms, including bacteria, protozoa and protein and viruses. Besides, it also consists of detergents, oils, soaps, fats, and others which may cause an adverse effect on the environment and human health.

In some of the rural and early development residential areas the greywater is directly discharged into the tertiary drain system. Stagnation and sedimentation in the drain may happen especially during dry weather. A stagnant grey water in the drain poses a serious health risk to the public due to the high pollutant loads (Katukiza, 2013). Thus, grey water should be treated and achieved a certain standard before being discharged. Treated grey water may also be reused for a non-potable application. To address public concerns and acceptance, safety, hygiene, environmental tolerance, and aesthetics are four criteria that the reclaimed grey water must fulfil (Albalawneh and Chang, 2015).

A rain garden is a kind of bioretention system that may remove pollutants in grey water by slowing the flow of water via adsorption and entrapment. In addition, plants may absorb some pollutants such as nutrients and metals through a process called phytoremediation. Additionally, oxygen supplied into the soil by the plants may aid microorganisms in transforming and degrading contaminants. A rain garden can be built in ground or above ground in a planter box. There are two vital components of the rain garden that must be carefully selected to ensure effective pollutant removal that are plants and filter media. This paper presents laboratory investigation on the impact of various plants and filter media depths on rain garden performance in removing pollutants in kitchen greywater.

2. MATERIAL AND METHODS

A planter box type of rain garden of 1.2 m length, 0.4 m width and 0.56 m height was fabricated in the laboratory. For the plants, Lemongrass (*Cymbopogon Citratus*) and Pandan (*Pandanus Amaryllifolius*) were selected. Lemongrass is one of the best vegetation for the rain garden as it has the capability of nitrate removal around 95% (Hunt et al., 2015) and Adonadaga et al. (2020) reported that Lemongrass gave high pollutant removal efficiency. Pandan was shown to grow effectively in hydrophytic conditions and be very efficient at removing high nutrient levels (Han, et. al. 2014). Both plants are widely available and commonly used for cooking especially in tropical South-East Asia countries. Wood chips and peanut shells mixture was chosen as a supporting filter media material beside sand and gravel. This filter media combination has strong adsorbent properties and provides ideal growing conditions for plants as it contains lignin, cellulose, and hemicellulose (Tejedor et al., 2020). The proportion of the wood chips and peanut shells mixture of 25% of peanut shells and 75% of wood chips was used as recommended. Figure 1 shows the pictures of plants and filter media used in this study,
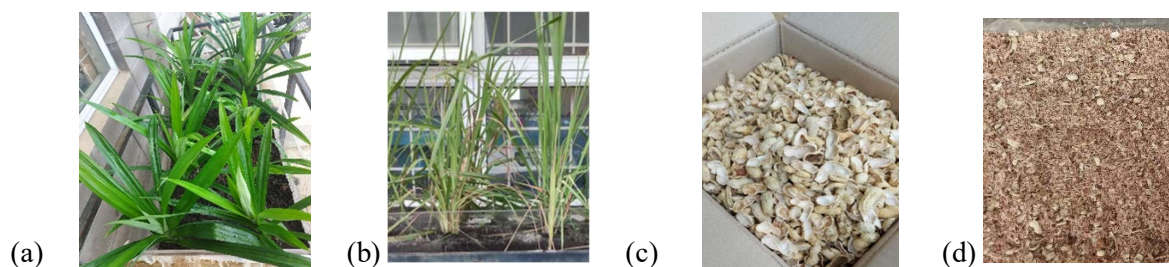
Figure 1. Rain garden plants and filter media (a) Pandan, (b) Lemon grass (c) Uncrushed peanut shell (d) Crushed peanut shell and wood chips mixture

Figure 2 (a) and (b) shows the rain garden experimental setup and filter media layers, respectively. A pump was used to flow the kitchen grey water from the influent tank into the rain garden. The discharge value was set based on the typical mean discharge of the kitchen grey water in a cafeteria per day. The flow of water entering the system is regulated by a valve. The treated kitchen grey water or the effluent that comes out from the rain garden was collected every minute for 15 minutes. The kitchen grey water samples were collected from cafeterias and underwent an aeration process for at least one day before the grey water is tested to ensure that the sample in its natural state in terms of dissolved oxygen concentration. The influent and effluent of the rain garden were tested for pH, turbidity, total suspended solid (TSS), total nitrogen (TN), oil and grease, chemical oxygen demand (COD) and biochemical oxygen demand (BOD_5) and the percentage removal were calculated to indicate the performance of the rain garden.

(a)   (b)
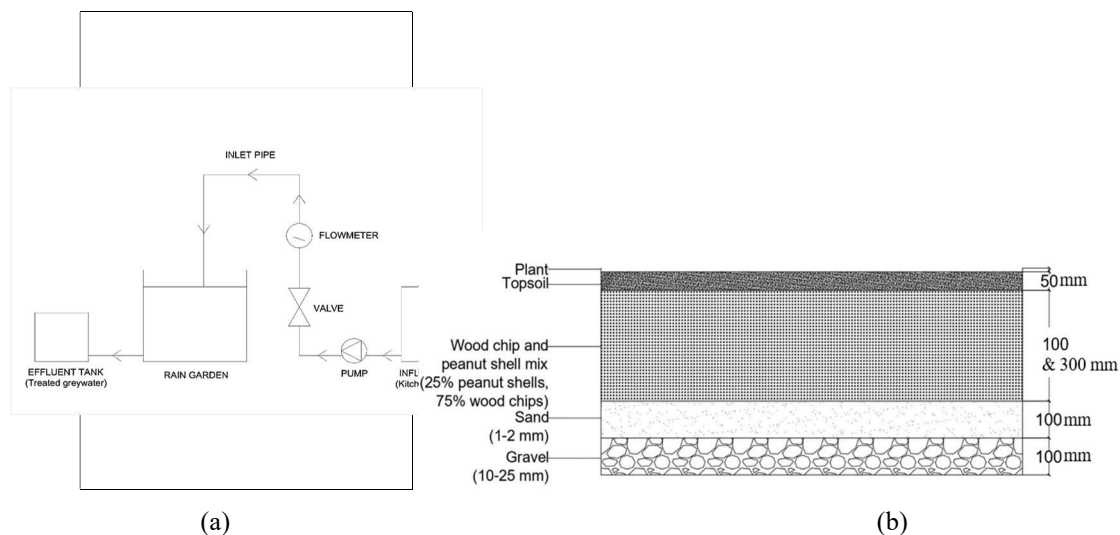
Figure 2. (a) Rain garden experimental setup (b) Filter media layers

3. RESULTS AND DISCUSSION

The performance of the rain garden with different planting mixtures in treating kitchen grey water was determined by comparing the grey water quality parameters of the influent and effluent of the rain garden. The test results were then compared with the Effluent Standard of Malaysia Water Quality Standard (Sewage and Industrial Effluents) Regulations. The range of the quality parameters measured for all cases are as presented in Table 1.

Table 11. Characteristics of raw (influent) and treated (effluent) kitchen grey water.

Quality Parameters Tested	Unit	Effluent Standard A	Effluent Standard B	Influent	Effluent
pH	-	6.0 - 9.0	5.5 - 9.0	4.90 - 5.49	6.0 - 6.5
Turbidity	NTU	-	-	133 - 211	7.87 - 22.40
Total Suspended Solid (TSS)	mg/L	Max 50	Max 100	1180 - 10985	16 - 67
Total Nitrogen (TN)	mg/L	-	-	22.8 - 49.7	15.8 - 23.7
Oil and Grease	mg/L	Not detectable	Max 10.0	645.1 - 15610.6	7.0 - 8.2
Chemical Oxygen Demand (COD)	mg/L	Max 50	Max 100	2027 - 2224	152.00 - 186.37
Biological Oxygen Demand (BOD$_5$)	mg/L	Max 20	Max 50	682 - 776	35 - 43

Overall, the results clearly show that the proposed rain gardens have great capabilities in removing the pollutants in the greywater There is a huge difference in quality parameter values between raw and treated grey water. All parameters satisfied the Effluent Standard B except for the COD. The performance of the rain garden with different plants and filter media depths were also investigated. Figure 3 shows the comparison of percentage or pollutant removal for Pandan and Lemongrass. Pandan gave a slightly higher percentage of removal for most pollutant parameters and significant higher percentage removal of about 5 % are observed for turbidity, TSS and TN. This might be due to Pandanus roots that are more fibrous and thicker compared to Lemongrass. Further investigation on the impacts of root structures is necessary in the future. Figure 4 presents the performance of the rain garden with difference depths of peanut shells and wood chips mixture layer. It is obvious that the higher depth of filter media gave better performance in pollutant removal especially for TN removal,

4. CONCLUSIONS

It is found that the pollutant removal efficiency of the rain garden exceeds 90% for most measured parameters. The Pandanus plant and filter media of peanut shell and wood chips mixture is discovered to be a good combination for the rain garden system. Furthermore, the system is low in cost as Pandanus are plants that can be easily grown and commonly used for cooking, and peanut shells and wood chips are waste material. The system can be easily installed in any household where the kitchen greywater can be first treated before discharge to the drain or for non-potable reuse.
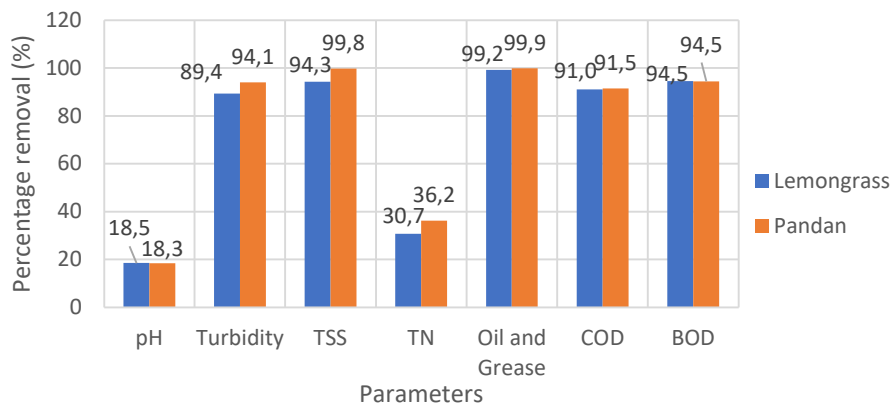
Figure 3. Comparison of pollutant removal percentage of rain garden with Pandan and Lemon grass
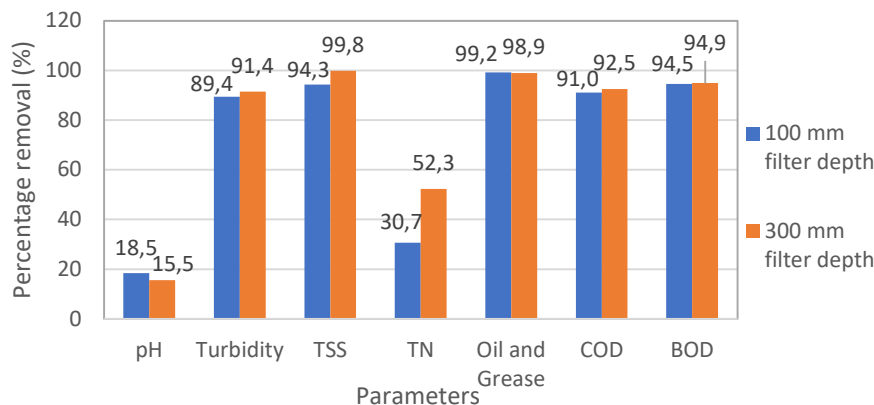
Figure 4. Comparison of pollutant removal percentage of rain garden with Lemongrass and 100mm and 300 mm filter media depths

REFERENCES

Adonadaga, M. G., Takramah, B. K. S., Ampadu, B., & Sackey, I. (2020). Performance evaluation of three different grasses for use as willows in greywater treatment in semi-arid Ghana. Journal of Applied Sciences and Environmental Management, 24(1), 179. DOI:10.4314/jasem.v24i1.26.

Albalawneh, A., & Chang, T.-K. (2015). Review of the Greywater and Proposed Greywater Recycling Scheme for Agricultural Irrigation Reuses. International Journal of Research 3(12), 16–35.

Edwin, G. A., Gopalsamy, P., & Muthu, N. (2014). Characterization of domestic grey water from point source to determine the potential for urban residential reuse: a short review. Applied Water Science, 4(1), 39–49.

Han, P., Kumar, P., & Ong, B. L. (2014). Remediation of nutrient-rich waters using the terrestrial plant, Pandanus amaryllifolius Roxb. *Journal of Environmental Sciences (China)*, *26*(2), 404–414.

Hunt, W. F., Lord, B., Loh, B., & Sia, A. (2015). Springer Briefs in Water Science and Technology Plant Selection for Bioretention Systems and Stormwater Treatment Practices.

Katukiza, A.Y., Temanu, H., Chung, J.W., Foppen, J.W.A., Lens, P.N.L., 2013. Genomic copy concentrations of selected waterborne viruses in a slum environment in Kampala, Uganda. Journal of Water and Health 11(2), 358-369.

Tejedor J, Cóndor V, Almeida-Naranjo CE, Guerrero VH, Villamar CA. Performance of wood chips/peanut shells biofilters used to remove organic matter from domestic wastewater. Sci Total Environ. 2020 Oct 10;738:139589. doi: 10.1016/j.scitotenv.2020.139589. Epub 2020 May 21. PMID: 32531583.

WHO (2006). Guidelines for the safe use of wastewater, excreta and greywater. In: Wastewater in Agriculture, Vol. 2. WHO, Geneva, 177–182.

14TH INTERNATIONAL CONFERENCE
ON HYDROSCIENCE & ENGINEERING

MAY 26-27, 2022
IZMİR-TURKEY

ICHE2022
IZMIR, TURKEY

AN EXPERIMENTAL STUDY ON ARTIFICIAL DESTRATIFICATION OF THERMALLY STRATIFIED RESERVOIRS

Oğuz Hazar

Department of Civil Engineering, Izmir Institute of Technology

Izmir, Turkey

oguzhazar@iyte.edu.tr

Nisa Bahadıroğlu

Department of Civil Engineering, Izmir Institute of Technology

Izmir, Turkey

nisabahadiroglu@iyte.edu.tr

Derya Karakaya

Department of Civil Engineering, Izmir Institute of Technology

Izmir, Turkey

deryakarakaya@iyte.edu.tr

Şebnem Elçi

Department of Civil Engineering, Izmir Institute of Technology

Izmir, Turkey

sebnemelci@iyte.edu.tr

ABSTRACT: Reservoirs are essential instruments in water management with the multiple uses of irrigation, hydropower, water supply, flood protection and recreation. Beyond these multiple purposes, also ecological aspects and legal aspects have to be considered, both being heavily depending on water quality characteristics. Reservoirs are subjected to complicated, time-dependent forcing, and respond nonlinearly. Water managers worldwide are facing the serious problem of dense blooms of cyanobacteria in reservoirs. In the quest for the optimal method to combat cyanobacterial dominance, many questions and many possible solutions arise. Control measures (including mitigation) have a direct impact on cyanobacterial blooms by biomass removal, flushing, or mixing; however, the number of proven technologies is limited. Two main approaches to avoid cyanobacterial proliferation and their unwanted effects are, taking preventive measures and taking control measures. Preventive measures are aimed at achieving long-term improvement of a lake's aquatic ecosystem. This study aims at designing an autonomous system for artificial destratification to control cyanobacteria growth in the reservoirs. Previous applications for artificial destratification in reservoirs were based on trial and error on site, where neither the effect of air bubble size and configuration nor the effect of air density in the bubble plume could be investigated. This study will lead to design of an optimized system. We will tackle this task at two steps. Firstly, we will setup an experimental system that mimics a thermally stratified reservoir experiencing hypoxia and will oxygenate/mix the water column. A stable stratification will be obtained by a novel setup designed for this study enabling to form consistent and desired stratified layers along the water column. Next, we will investigate the effects of bubble size, bubble slip velocity and other parameters on destratification efficiency. Nondimensional numbers involving bubble diameter, bubble diffusing area, air rate and stratification rates will be used to quantify destratification efficiency for the best design of aeration systems.

KEYWORDS: artificial destratification, aeration, water quality

1. INTRODUCTION

Water resources are under increasing pressure throughout the world due to climate change, increase of human populations, human health demands, and recognition of environmental impacts of water use and transfers. Reservoirs are key elements of water management in many regions and are constructed for multiple purposes including irrigation and municipal water supply, hydropower, flood protection and recreation. Beyond these multiple purposes, ecological and legal aspects must be considered, both being heavily depending on water quality characteristics. Reservoirs are subjected to complicated, time-dependent forcing, and respond nonlinearly. Numerical models thus play an important role in optimizing reservoir operations. But many reservoirs are operated via strategies designed to meet water quantity objectives, with water quality given much less weight. Given the importance of water quality, we urgently need new approaches that include also water quality – including water temperature - aspects into operation and management of the reservoirs. This project aims at bridging this gap and provides innovations in reservoir modelling that leads to integrated water quantity and quality management.

In a lake/reservoir, the wind induced currents and the structure of the temperature profile in the vertical water column mainly control the vertical distribution of heat, dissolved substances and nutrients in the water column. Thermal stratification in the water column, where warm and cold water form layers, results in poor mixing of the water column during the summer. The warm water in the epilimnion is unable to drive through the cold, dense water of the hypolimnion since the thermocline between these layers behaves as a barrier. As a result of the incomplete mixing of the water column and lack of light for the photosynthesis in the hypolimnion, water column can become anoxic. Figure 1 shows the temperature and dissolved oxygen profiles observed during field measurements conducted once a month at the buoy located in the main pool of the Tahtali Reservoir in Izmir providing 40% of its fresh water to the drinking water supply of Izmir, Turkey (Elci, 2008). As can be seen from the figure, observed DO values dropped well below the standard limit of 5 mg/l even reaching to 0 mg/l at the thermocline in August. As oxygen depletion progresses to anoxia, ammonia, sulphides, and oxidized metals such as iron and manganese of bottom sediments are released to water. Iron and manganese are reduced to soluble forms which are toxic to aquatic life and problematic for the water supply. Phosphorus increase associated with iron reduction leads to eutrophication of lakes in combination with release of hydrogen sulphide. As a result of nutrient inflow from the catchments, coupled with tropical ambient temperatures, the reservoir is most times infested with blue-green algae. Algal blooms lead to water quality deterioration, including foul odours and tastes, deoxygenation of bottom waters, toxicity, fish kills, and food web alterations. Control and management of cyanobacterial and other phytoplankton blooms necessitates nutrient input constraints. The types and amount of nutrient input constraints depend on hydrologic, climatic, geographic, and geologic factors, which interact with anthropogenic and natural nutrient input regimes. In most cases both nitrogen and phosphorus input reductions are required for effective long-term control and management of harmful blooms. In some cases nutrient reduction might not be sufficient and other measures such as enhanced flushing and artificial mixing can be used as alternatives.

Many reservoirs worldwide experience cyanobacterial blooms that have negative impacts on ecosystem resulting in a loss of aquatic biodiversity. Cyanobacteria can negatively affect human health since they have the potential to produce toxins and numerous animal and human intoxications by cyanobacterial toxins have been reported (e.g., Kuiper- Goodman et al. 1999; Cox et al. 2003; Griffiths and Saker 2003; Hilborn et al. 2007). Cyanobacteria may also lead to other problems in drinking water supply reservoirs. Recently Turkey is experiencing problems associated with overgrowth of microscopic algae called phytoplankton-Mucilage observed in the Marmara Sea. This thick, mucus-like slimy layer contains a variety of microorganisms and is caused by an increase in seawater temperature with excessive nutrients induced by pollution and this formation pointed out the severity of situation if water resources are exposed to eutrophication. Alternative methods to control the cyanobacterial blooms will help to overcome existing and future nutrient load related problems in reservoirs. This study was motivated by the degradation of water quality in summer due to thermal stratification and high oxygen demand as observed in many reservoirs and lakes around the world.

The objective of this study is to investigate the methods of artificial destratification on the structure of the thermal stratification, and its effect on dissolved oxygen concentrations.
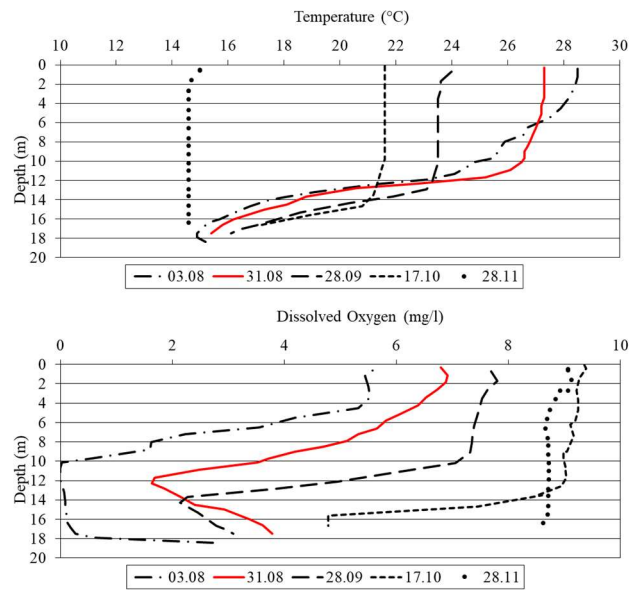
Figure 1. The temperature (a), dissolved oxygen (b) profiles observed during field measurements conducted once a month at the buoy (Elci, 2008)

Artificial destratification has been widely used to improve water quality associated with eutrophic conditions in thermally stratified lakes and reservoirs. Various forms of hypolimnetic aeration/oxygenation systems have been installed with varying degrees of success in the past (Holland and Tate, 1984; Gallagher, 1984; Meyer et al., 1992; Burns, 1981; Croome, 1981; Chipofya and Matapa, 2003, Horne, 2019, Horne and Beutel, 2019). A successful application of hypolimnetic oxygenation system was utilized in a hatchery on the Mokelumne River, California, following death of 300,000 salmonid hatchery fish, suspectively by Hydrogen sulphide (H2S). Following the oxygenation operation, Chinook salmon returns rose significantly (Horne, 2019). In another application, long term improvement in water quality was achieved by hypolimnetic oxygenation system in Camanche Reservoir, California, a eutrophic reservoir, experiencing blooms of cyanobacteria. Within days of the application water quality improved and hypolimnion phosphate and ammonium concentrations declined as stated in Horne and Beutel (2019). Previous design of artificial destratification systems were based on trial and error in site, where neither the effect of air bubble size nor the effect of air density in the bubble plume could be investigated. Through artificial destratification, the stratified water column is mixed developing isothermal conditions and thus reducing density gradients within the vertical water column. Methods of destratification commonly employed include hydraulic or pneumatic pumping and hypolimnetic aeration/oxygenation. Destratification processes involve control of multiphase flows since they are strongly affected by phase change. Another key objective is to parametrize how turbulent motions in a stratified fluid irreversibly mix the fluid contribute to transport of heat vertically. This study will attempt to parametrize such turbulent diapycnal transport via high-resolution numerical simulations validated with experimental observations.

The most basic parametrization of mixing in stratified flows is the construction of a model for the (vertical) eddy diffusivity of density, a closure relating an appropriately defined vertical buoyancy flux to buoyancy frequency. Previous research on effects of artificial mixing on temperature showed that the primary effect of artificial mixing is to increase the mixed layer depth. where as a result of mixing, the temperature of the total (mixed) water body generally decreases. As for the dissolved oxygen, by artificial mixing, high oxygen concentrations in the top layers are observed from atmospheric exchange. Also oxygen increases if the artificial mixing is generated by aeration with compressed air. In many studies, the pH in the top layer was lowered with 0.5–1 units as a result of mixing of carbon dioxide-rich hypolimnetic waters. Researchers had different findings on the affects

of mixing on nutrients. Artificial mixing is generally regarded as a good solution to prevent blooms of cyanobacteria because it reduces light availability (Beutel and Horne 1999). In fact in the application described by Horne (2019), cyanobacteria blooms stopped in the reservoir and cell concentrations fell by 95% following the oxygenation process. Following the literature, rate of mixing will be characterized by Richardson number and buoyancy fluxes (Elçi and Ekmekçi, 2016). Since these formulations involve the fluctuations of the vertical (w') and horizontal velocities (u') and the fluctuations of the density (ρ') by definition, these quantities will be calculated by subtracting 1 minute averaged values from the instantaneous 3D velocity measurements. The relative strengths of stratification and shear are assessed by the Richardson number, Ri, which is a measure of the interaction of Reynolds stresses with the shear and the stratification and its formulation is given below.

$$Ri = -\frac{g}{\rho}\frac{\partial \rho}{\partial z}\frac{1}{\left(\frac{\partial w}{\partial z}\right)^2} \tag{1}$$

where (g) is the gravity, (ρ) is the density, (z) is the depth and (w) is the vertical velocity.

Two phase flow involves modelling of air bubbles in water. Rising of the air bubbles is driven by surface tension, buoyancy, viscous and inertial forces. An air bubble adopts a shape where surface tension, hydrostatic and hydrodynamics forces are at balance at the bubble surface. The most important nondimensional number controlling the movement of the air bubbles is the Weber number. It is a measure of the relative importance of the dynamic pressure force compared to the surface tension force and given as:

$$We = \frac{\rho u_b d_b}{\sigma} \tag{2}$$

where ρ is the fluid density, d_b is the bubble diameter, u_b is the velocity of the bubble and σ is the surface tension. Another parameter that is commonly used to characterize the physical properties of air bubbly flow is Morton numbers and given as:

$$Mo = \frac{We^3}{Fr^2\,Re^4} = \frac{g\mu^4(\rho - \rho_a)}{\rho^2\sigma^3} = \frac{(viscous\ force)^4(buoyancy\ force)}{(inertia\ force)^3(surface\ tension\ force)^2} \tag{3}$$

where ρ is the fluid density, ρa is the air density, μ is the fluid viscosity, and σ is the surface tension. One of the pioneering works on plume behaviour was presented by McDougall (1978). Two nondimensional variables were presented

$$M = \frac{Q_0 p_a}{4\pi\alpha^2 \rho_r H_T u_s{}^3} \tag{4}$$

$$C = \frac{N^2 H_T{}^2}{u_s{}^2 M^{\frac{2}{3}}} \tag{5}$$

where Q_0=flow gas rate at the free surface; p_a=pressure at the surface; ρ_r=reference liquid density; H_T=total pressure head at the diffuser position; u_S=bubble slip velocity; α=entrainment coefficient; and N=buoyancy frequency given by the following equation.

$$N = \sqrt{\left(-\frac{g}{\rho}\right)(d\rho(z)/dz)} \tag{6}$$

Asaeda and Imberger (1993) introduced similar variables, called plume number, P_N and M_H, which are given as follows:

$$P_N = \frac{N^3}{Q_B g} \qquad (7)$$

$$M_H = \frac{Q_B g}{4\pi\alpha^2 H u_s^3} \qquad (8)$$

Socolofsky and Adams (2003,2005) introduced another nondimensional variable, U_N and demonstrated how to use this variable as a single parameter in predicting the behaviour of stratified multiphase plumes at a laboratory level.

$$U_N = \frac{u_s}{(Q_B g N)^{1/4}} \qquad (9)$$

The destratification number (D_N) is also utilized in the literature and is given as (Kim et al. 2010):

$$D_N = \frac{N^6 H^7}{4\pi\alpha^2 Q_0 g u_s^3} \qquad (10)$$

where N is the buoyancy, H is the depth in the tank, α is the entrainment coefficient and function of air flow rate, and Q_0 is the air flow rate and u_s is the slip velocity of the bubbles.

A final nondimensional parameter that will be discussed here is the destratification efficiency, η introduced by Asaeda and Imberger (1993). It is defined as a ratio showing how much of the energy supplied by the bubbles is converted to potential energy, PE, of the density distribution and defined as follows:

$$\eta = \frac{\Delta PE}{\overline{\rho} g Q_0 H_A \ln(1 + \frac{H}{H_A}) \Delta t} \qquad (11)$$

Where $\overline{\rho}$ is the reference density and H_A is the atmospheric pressure head.

2. METHODOLOGY

2.1. Experiments

The experimental setup utilized in this study is composed of a water tank designed and built for the purposes of this study. The main tank with dimensions of 1 m x 1 m x 1 m is made of steel panels and it has an observation window located on the front side of the tank made of 10 mm thick glass (Figure 2). The water tank is covered with insulating material to minimize the heat transfer in and out through the walls. An observation window at the front wall is used to observe the progress of the test and some of the measurements. The water is provided to the main tank through tiny holes on the side wall for providing low rates of influx and to minimize turbulence, and the excess flow will be discharged using a weir. If desired, water can be withdrawn from three outlets with different levels on the other side wall of the tank, enabling the investigation of the withdrawal effect on the stratification structure. To generate thermal stratification, a cooling system is integrated to the bottom section of the tank. The cooling system is composed of a compressor, condenser, filter, capillary tube, copper pipes as an evaporator, a thermostat, and a monitor. The copper pipe which is approximately 20 meters is placed at a spiral shape at the bottom of the water tank enabling the passage of the cooling gas during operation which is controlled via a thermostat attached to the system. The cooling system is shown in Figure 3.

The heating of the top layers is maintained by strip heaters placed on top of the tank to heat the top layer as desired. A typical temperature profile achieved prior to the experiments are shown in Figure 4. Custom made air diffusers are used in all experiments. A set of replaceable plates are designed and a total of 20 plates are custom made those having one hole, two holes, five holes and twelve holes, with diameters of d=1, 2, 3, 4 and 5 mm. The Plane views of diffuser configuration and diffusers in operation are given in Figure 5. The air to the diffusers is provided by air pumps providing Q=100l/h, 200l/h and 400l/h of air (Tetra-Tec Aps 400).
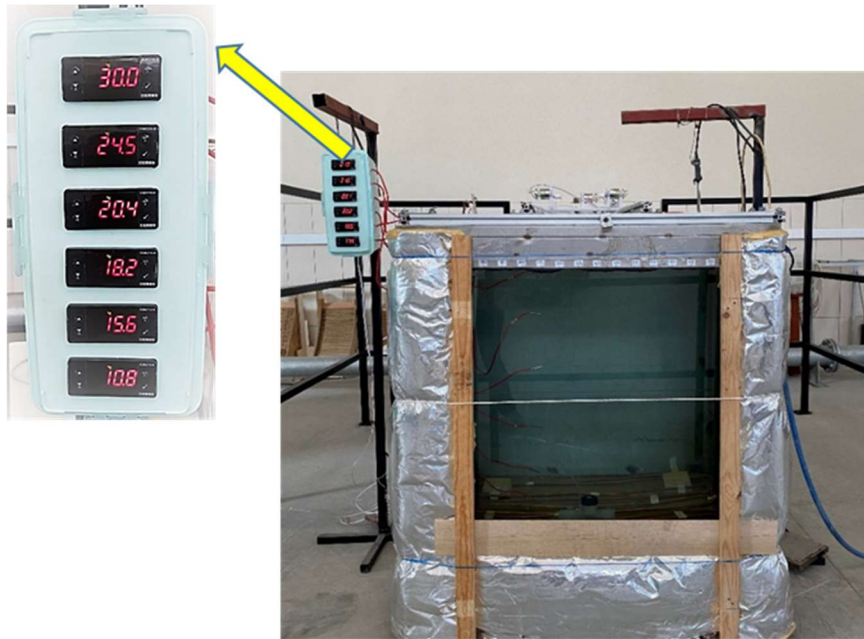
Figure 2. Experimental setup modified for this study. Monitor on the left shows the measured water temperatures at 5, 15, 30, 50, 70, 90 cm (measured from the bottom) after stratification of the water column
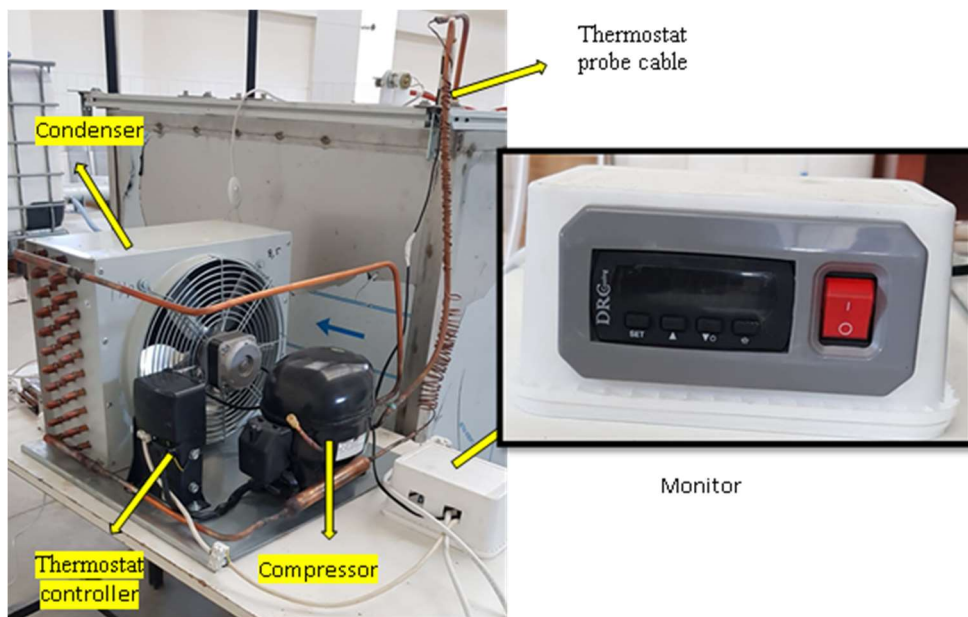
Figure 3. Parts of the cooling system attached to the experimental setup

The final temperature profile of the water column obtained prior to the experiments is shown in Figure 4. This stratified profile mimics a typical reservoir experiencing thermal stratification in summer (please refer to Figure 1).
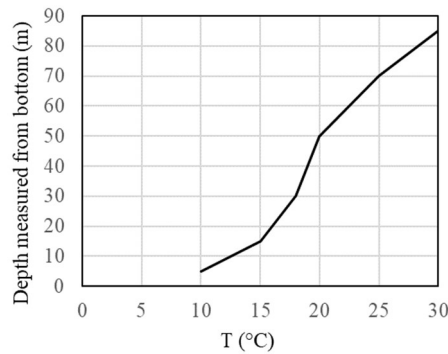
Figure 4. Variation of the water temperature along the depth profile prior to the experiments

(a)   (b)
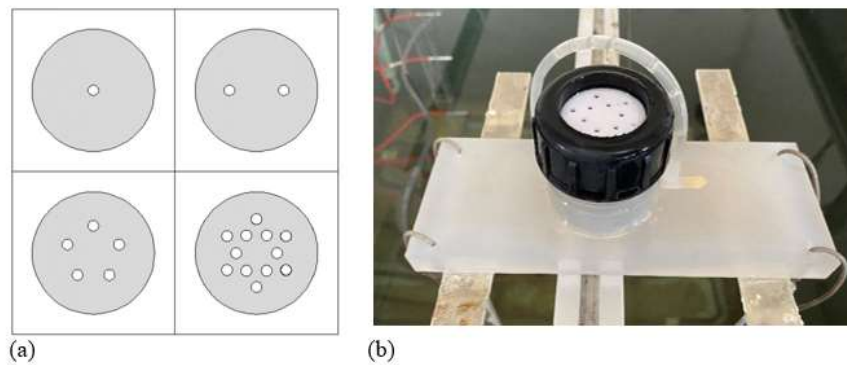
Figure 5. Plane views of single hole, two holes, five holes and twelve holes diffusers (a) and diffusers in operation (b)

A total of 12 experiments are conducted to study the effects of diffuser size, diffuser configuration, and rate of air flow on the destratification efficiency. Summary of the observed experimental data and the parameters used in the calculation of various nondimensional parameters are listed in Table 1. In the literature (reference) bubble diameters are then derived using an equation reported by Wűest et al. (1992) that is giving a constant value for a wide range bubble diameters utilized. Instead of using this constant value (given as 0.23 m/s for bubble diameters between 1.4 mm and 10 mm), we measured bubble slip velocities during the experiments. Variation of the bubble slip velocities and bubble diameters with the hole diameters is provided in Figure 6. A relationship is then fitted with an R^2 value of 0.99 between bubble slip velocity nondimensionalized by the reference velocity of the air flow and bubble diameter nondimensionalized with hole diameter (Figure 7) as in the following:

$$\frac{u_s}{u_r} = 8.6864(\frac{d_b}{d_h})^{-3.282}$$

(12)
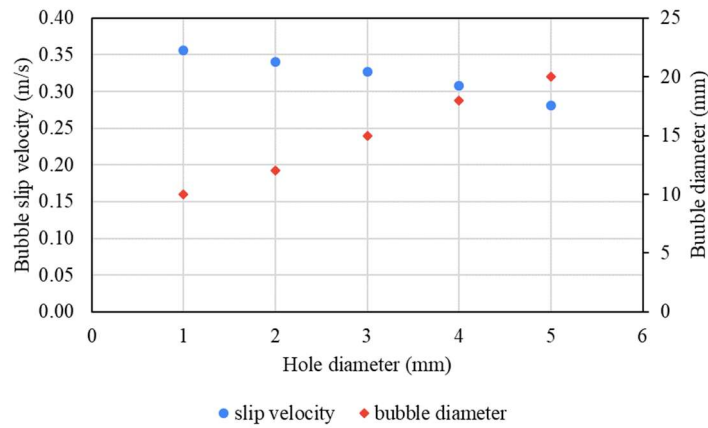
Figure 6. Variation of the bubble slip velocity and diameter with the hole diameter (single hole diffusser)

$$y = 8.6864x^{-3.282}$$
$$R^2 = 0.9846$$
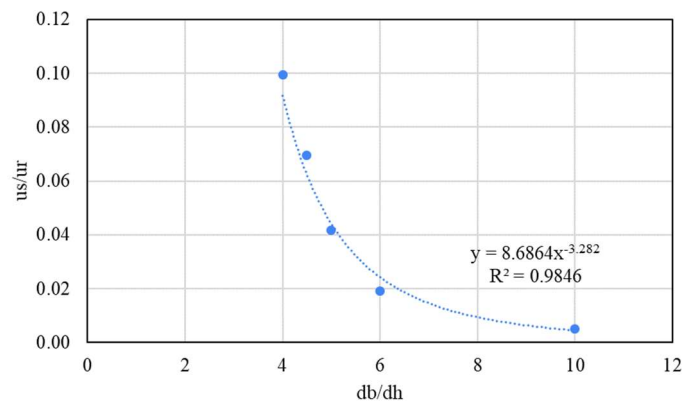
Figure 7. Variation of the nondimensionalized bubble slip with the nondimensionalized bubble diameter (single hole diffusser)

Figure 8 presents comparison of the temperature variations at 15 cm and 85 cm measured from the bottom for both air flow rates of 200 l/h and 400 l/h. As expected, mixing with 400 l/h air flow rate was observed at almost half the time it took for 200l/h. The temperature profiles measured at time=0, 5, 10 and 20 minutes after the destratification activated are presented for three different hole diameters (2,3 and 4 mm) and two different air flow rates (200l/h and 400l/h) in Figure 9. To study the effect of different diffuser configurations, we used 1, 2, 5 and 12 hole diffusers. Although destratification times followed the same trends in all experiments at the same measurements levels, we observed that 12 hole diffuser configuration is slightly more effective in mixing of the stratified water column. We also investigated the effect of increasing air flow rate on destratification times.

Case	H (m)	A_t (m²)	Q_{air} (m³/s) x10⁻⁵	n	D (mm)	d_b (mm)	u_s (m/s)	u_{ref} (m/s)	D_a (m²) x10⁻⁴	h (m)	T (°C)	ρ(kg/m³)	N	α	M	C	D_l	U_N	η (%)
1	0.85	1	5.6	1	2	12	0.34	17.68	15	0.3	20.1	998.15	0.220	0.029	0.107	230.913	1.293	3.251	10.58
										0.1	14.2	999.13							
2	0.85	1	5.6	2	2	12	0.34	17.68	15	0.3	18.3	998.48	0.193	0.029	0.107	178.303	1.293	3.358	10.04
										0.1	13.35	999.24							
3	0.85	1	5.6	5	2	12	0.34	17.68	15	0.3	18.4	998.47	0.207	0.029	0.107	204.362	1.293	3.301	10.32
										0.1	12.6	999.33							
4	0.85	1	5.6	12	2	12	0.34	17.68	15	0.3	17.8	998.57	0.185	0.029	0.107	163.630	1.293	3.394	9.87
										0.1	13.15	999.27							
5	0.85	1	5.6	1	3	15	0.33	7.86	15	0.3	18.4	998.47	0.198	0.029	0.121	188.465	1.453	3.207	13.02
										0.1	13.15	999.27							
6	0.85	1	5.6	1	4	18	0.31	4.42	15	0.3	18.2	998.5	0.199	0.029	0.144	190.297	1.739	3.017	15.93
										0.1	12.8	999.31							
7	0.85	1	11	1	2	12	0.37	35.37	15	0.3	18.6	998.43	0.209	0.034	0.124	158.062	1.496	3.029	9.34
										0.1	12.75	999.32							
8	0.85	1	11	1	3	15	0.36	15.72	15	0.3	19.2	998.32	0.217	0.034	0.132	171.136	1.597	2.935	12.07
										0.1	13.05	999.28							
9	0.85	1	11	1	4	18	0.32	8.84	15	0.3	17.9	998.55	0.185	0.034	0.195	123.718	2.351	2.687	14.30
										0.1	13.3	999.25							
10	0.85	1	11	5	2	12	0.34	35.37	15	0.3	18.2	998.5	0.194	0.034	0.162	136.486	1.960	2.820	9.49
										0.1	13.15	999.27							
11	0.85	1	11	2	2	12	0.34	35.37	15	0.3	16.9	998.72	0.177	0.034	0.162	113.256	1.960	2.886	9.14
										0.1	12.4	999.36							
12	0.85	1	11	12	2	12	0.34	35.37	15	0.3	17.3	998.66	0.189	0.034	0.162	129.263	1.960	2.839	9.38
										0.1	12.2	999.38							
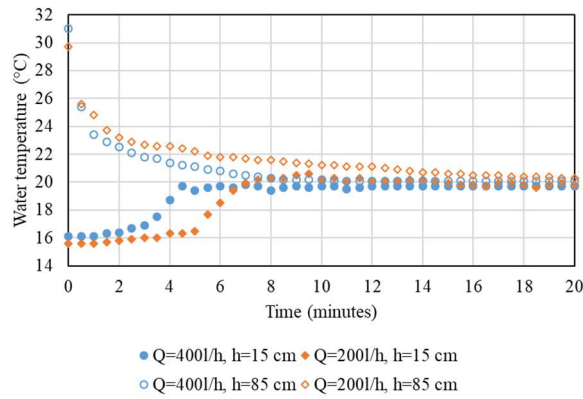
Figure 8. Variation of the monitored temperature values for different air flow rates at two locations
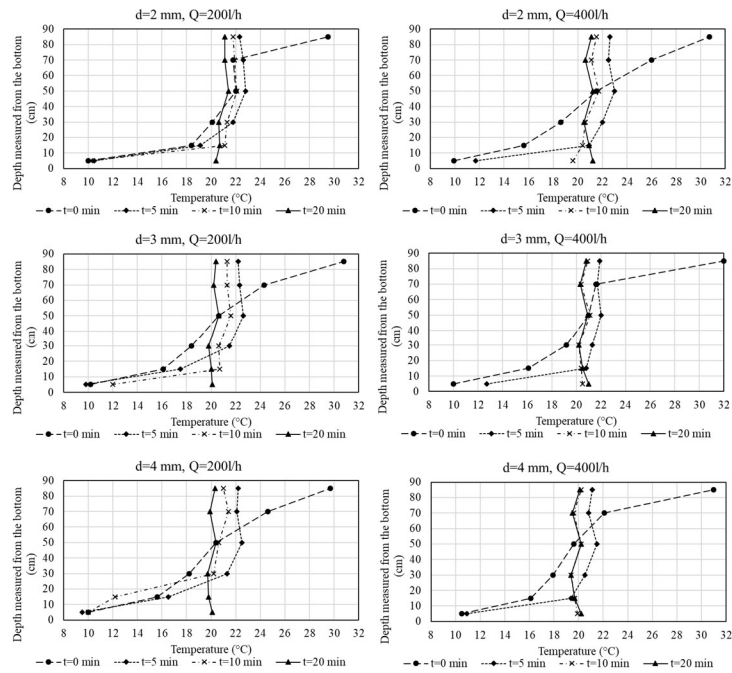
Figure 9. Time variation of the monitored temperature profiles for different cases

We also observed that when all other parameters kept the same, the destratification efficiency is linearly dependent on the diffuser hole diameter (Figure 10). Increasing number of holes in the diffuser did not have a significant effect on the destratification efficiency. When two, five and twelve hole diffusers compared, using five holes improved the destratification efficiency only slightly (Figure 11). We utilized multiple linear regression analysis to relate the destratification efficiency with the nondimensionalized bubble slip velocity, nondimensionalized bubble diameter and buoyancy frequency. Several assumptions with the analysis include: the relationship between the independent and dependent variables to be linear and the errors between observed and predicted should be normally distributed. The adjusted variance value, R^2 is 0.98 for the analysis indicating that the destratification efficiency is predicted well based on the independent parameters.

$$\eta(\%) = 18.98 - 1.94\frac{d_b}{d_h} + 59.55\frac{u_s}{u_r} + 7.85N \tag{13}$$
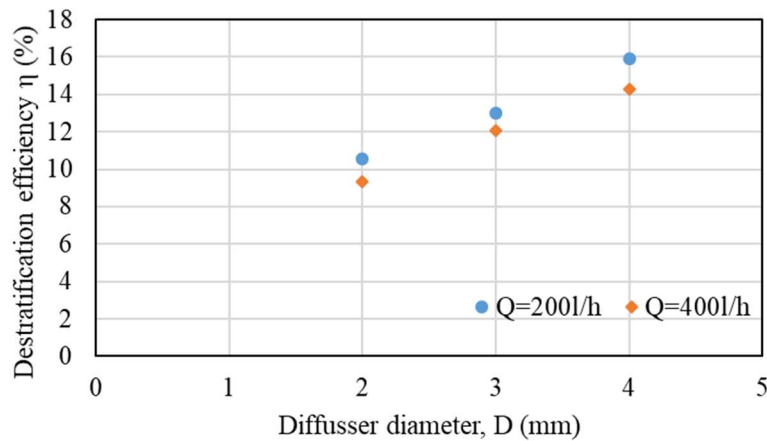
Figure 10. Variation of the destratification efficiency with the diffuser hole diameter for two different air flow rates
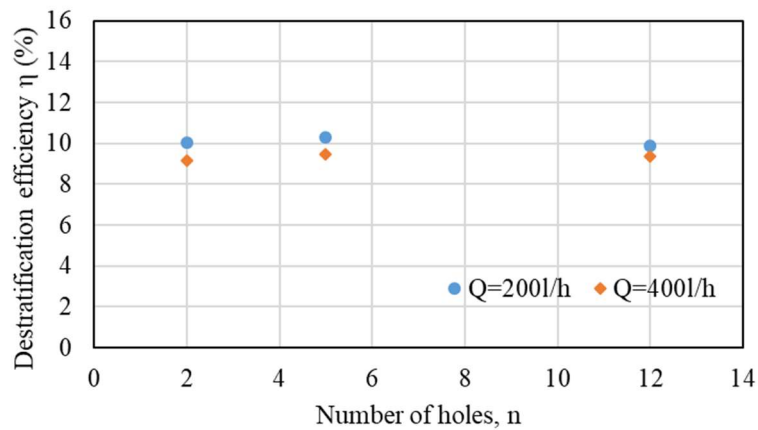
Figure 11. Variation of the destratification efficiency with the number of holes in the diffuser (d=2 mm) for two different air flow rates

3. DISCUSSION OF EXPERIMENTAL RESULTS

This study investigated destratification of an artificially stratified water column via air diffusers. Effects of hole diameter, number of holes in a diffuser, rate of air flow, and stratification ratio on destratification efficiency are studied. Experimental observations showed that:

1.Nondimensional numbers previously derived by other researchers M and Dl has also proved to be that they are linearly depending on destratification efficiency. As the values of these two nondimensional parameters increased so did the destratification efficiency.

2.Bubble slip velocities measured in experiments showed that previously accepted constant values in the literature for a range of bubble diameters are not correct and a new equation based on nondimensionalized bubble slip velocity and nondimensionalized hole diameter are suggested in this study.

3.Increasing number of holes, while keeping the flow rate as the same did not have a significant effect on the destratification efficiency and destratification time.

4.The destratification efficiency is related with the nondimensionalized bubble slip velocity, nondimensionalized bubble diameter and buoyancy frequency via multiple linear regression analysis as given in Equation 13.

REFERENCES

Burns, F.L. and Powling, I.J. , 1981. Destratification of Lakes and Reservoirs to Improve. Water Quality. Proceedings of a joint United States/Australia seminar and workshop. Melbourne, Australia, February 19–24, 1979. Australian Government Publishing Service,Canberra. 915 pp.

Calıskan, A., and Elçi, Ş. "Investigation of the hydrodynamics and withdrawal effects in a stratified lake," *Water Resources Management*, (23) 1257-1273, 2009.

Chipofya, V.H. and Matapa, E.J., 2003. Destratification of an impounding reservoir using compressed air—case of Mudi reservoir, Blantyre, Malawi. *Physics and chemistry of the earth* [1474-7065] vol.:28,20-27 pg.1161.

Cox, P. A., Banack, S. A., & Murch, S. J. (2003). Biomagnification of cyanobacterial neurotoxins and neurodegenerative disease among the Chamorro people of Guam. *Proceedings of the National Academy of Sciences,* 100(23), 13380-13383.

Croome, R.L., 1981. Artificial destratification of two South Australian Reservoirs. Proceedings of the *International Symposium on Artificial Destratification*. Melbourne, 1979, AGPS.

Elçi, Ş., 2008. Effects of thermal stratification and mixing on reservoir water quality. *Limnology*, 9(2) : 111-123.

Elçi, Ş. and Ekmekçi, B. 'Observational and Numerical Methods for Quantifying and Modelling of Turbulence in a Stratified Reservoir' *Journal of Applied Fluid Mechanics*, 9(4),1603-1614, 2016.

Gallagher, J. W., Jr., 1984. *Richard B. Russell Dam and lake oxygen injection system*, Proceedings of a seminar on applications in water quality control, US Army Corps of Engineers, Committee on Water Quality, Washington, DC.

Griffiths, D. J., & Saker, M. L. (2003). The Palm Island mystery disease 20 years on: a review of research on the cyanotoxin cylindrospermopsin. *Environmental Toxicology: An International Journal,* 18(2), 78-93.

Hilborn ED, Carmichael WW, Soares RM, Yuan M, Servait esJC, Barton HA et al (2007) Serologic evaluation of human microcystin exposure. *Environmental Toxicology An International Journal*, 22(5), 459-463.

Holland, J. P., and Tate, C. H., Jr., 1984. Investigation and Discussion of Techniques for Hypolimnion Aeration/Oxygenation, Technical Report E-84-10, US Army Engineer Waterways Experiment Station, Vicksburg.

Horne AJ, 2019 Hypolimnetic oxygenation 1: win–win solution for massive salmonid mortalities in a reservoir tailwater hatchery on the Mokelumne River, California. *Lake Reservoir Manage*. 35(3):308–322.

Horne AJ, Beutel M. 2019. Hypolimnetic oxygenation 3: an engineered switch from eutrophic to a meso/oligo-trophic state in a California reservoir. *Lake Reservoir Manage*. 35(3):338–353.

Kim, H.S., Kim J., Park, H, Park, N., 2010. Effects of Bubble Size and Diffusing Area on Destratification Efficiency in Bubble Plumes of Two-Layer Stratification, *Journal of Hydraulic Engineering* 136(2) 106-115.

Kuiper-Goodman T, Falconer I, Fitzgerald J (1999) Human health aspects. In: Chorus I, Bartram J (eds) Toxic cyanobacteria in water: a guide to their public health consequences, monitoring and management. London, UK, E & FN Spon, pp 113–153.

Menter, F. R. (1992). "Improved two-equation k-omega turbulence models for aerodynamic flows." NASA Ames Research Center, Moffett Field, CA.

Meyer, E.B., Price, R.E., Wilhelms, S.C., 1992. Destratification System Design for East Sidney Lake, New York. Final report for USACE, Miscallenous paper, W-92-2.

USACE. 1992. "Authorized and operating purposes of Corps of Engineers' reservoirs," Washington, DC.

APPLICATION OF WASP MODEL FOR ASSESSMENT OF WATER QUALITY OF THE PORSUK RIVER, TURKEY

Emre Dumlu

Department of Civil Engineering, Izmir Institute of Technology, Izmir, Turkey

emredumlu@iyte.edu.tr

Sebnem Elçi

Department of Civil Engineering, Izmir Institute of Technology, Izmir, Turkey

sebnemelci@iyte.edu.tr

ABSTRACT:Porsuk Stream is the longest branch of the Sakarya Basin which originates from Murat Mountain bypasses through the provinces of Kutahya and Eskisehir. Based on recent increasing pollution concentrations as reported in the literature, main river is experiencing lower water quality. In this study, hydrodynamics and water quality parameters are simulated in the Porsuk River via application of Water Quality Analysis Simulation Program (WASP). The main river is divided into 25 segments and physical properties of each segment is defined respectively. Next, the model is calibrated considering the observed flows at Beskaris, Porsuk Ciftligi, Calca, Esenkara, Parsibey and Kiranharmani stations. After validation of the hydrodynamics along the river, water quality parameters are simulated using the eutrophication module. Special attention is given to the simulated dissolved oxygen parameters. The results are then visualized using QGIS 3.16 and discussed.

1. INTRODUCTION

Eutrophication plays an important role in water quality in terms of excessive richness of nutrients in a lake or other water body, which may cause a dense growth of contaminants and death of animal life due to the threatened of water quality. Since freshwater systems are vital in transporting domestic and industrial wastewater constitutes or irrigation, seasonal changes of water quality largely affect not only in the watershed area, also ecosystem in region of interest. It can also result in drastically deteriorations in its physical, chemical, ecological and hydrogeological properties.

In recent years, excessive population growth and migration events, rapid increase in industry, wrong urbanization processes, unconscious use of natural resources and agricultural activities cause streams to lose their natural characteristics and become polluted (Singh et al., 2005; Strobl and Robillard, 2008; Tanyolaç)., 2009; Tokatli et al., 2014a; Tokatli, 2015). The efficient transport and pollution processes in water management for a river or lake such as meteorological and water quality must be sufficient to determine the pollution and their source and contributions. For this reason, water quality models have become an important tool for identifying water pollution and the final fate and behaviors of pollutants in a water environment (Wang, Dai, Zhao, Li, & Zhao, 2009).

There are numerous studies for water quality analysis. A water quality analysis simulation program (WASP8) was used to assess the eutrophication process by dividing El Pañe Reservoir into 11 segments and simulated water quality parameters (Larico et. al,2019). A hydrodynamic model was validated with the discharge measurements conducted by **Electrical** Power Resources Survey and Development Administration (EIEI) and State Hydraulic Works (DSI) in five different stations within the modeled segment of Kizildere Geothermal Power Plant on water quality of the Great Menderes River (Elçi et.al, 2010). Samples were collected from 18 stations located on the Porsuk Stream and some important physicochemical parameters were investigated to determine the water quality of Porsuk Stream (Kose et. al,2016). The expected responses of the whole Porsuk river and reservoir

system under different pollution control scenarios were estimated to develop plausible water quality management strategies (Muhammetoglu et. al, 2004).

In this study, water quality analyses are implemented for the water year of 2015 (10/1/2014 - 9/30/2015) by using WASP 8. The Porsuk main river is divided into 31 segments in total, based on the monitoring stations of water quality parameters as reported by Kose et. al, (2016). While dividing the main river into the segments, segment length is set to 20 km at most, and the segments are named considering the starting and the ending locations. The average width and length of each segment are then calculated. For calibration of the model, all the available stations; Beskaris, Porsuk Ciftligi, Calca, Esenkara, Parsibey and Kiranharmani are considered, and the flow rates are obtained from the State Hydraulic Works (DSI) and Electrical Power Resources Survey and Development Administration (EIEI). Once the numerical model is calibration based on flow rates, observed dissolved oxygen parameters are used to validate the model. Meteorological data are obtained from Giovanni, NASA. The results are visualized by using QGIS and discussed.

2. MATERIALS & METHODS

2.1. Study Site

Porsuk Stream Basin, a branch of Sakarya river extends 201 km in the East-West direction in Northwest Anatolia and reaches 135 km long in the south direction and covers precipitation area of 10,869 km² (Tekkanat and Sariş, 2015). It originates from Murat Mountain and after passes through province of Kutahya and Eskisehir, it spills to the Sakarya River. The study area, segmentation of the river and available stations along the river are given in Figure 1. In the figure, the blue dot represents stations where water quality parameters are monitored by Köse et al. 2016, are presented by blue dots, monitoring stations for flow rates are shown by brown dots. Additional stations added for the segmentation are shown by green dots. The reference coordinate system is arranged to WGS 84/Pseudo-Mercator (EPSG:3857)
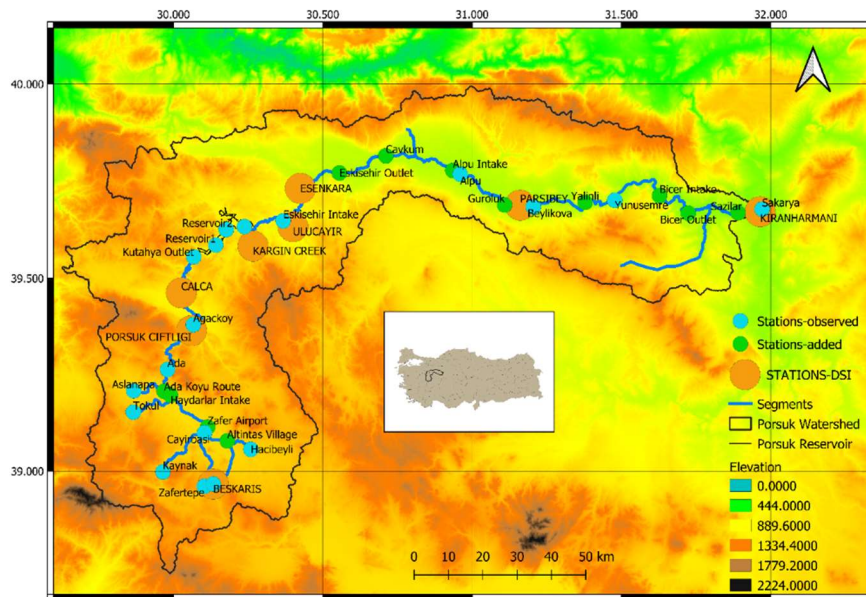
Figure 1. Porsuk Watershed and Locations of stations

2.2. Data Sources

The observed air temperature, wind speed and solar radiation data for the water year of 2015 are obtained and presented in Figures 2,3 and 4.
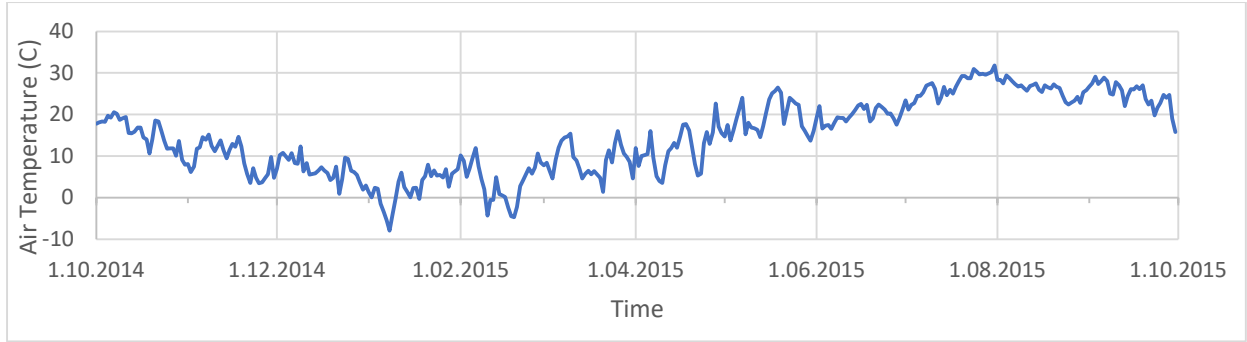
Figure 2. Observed Air Temperature Time Series
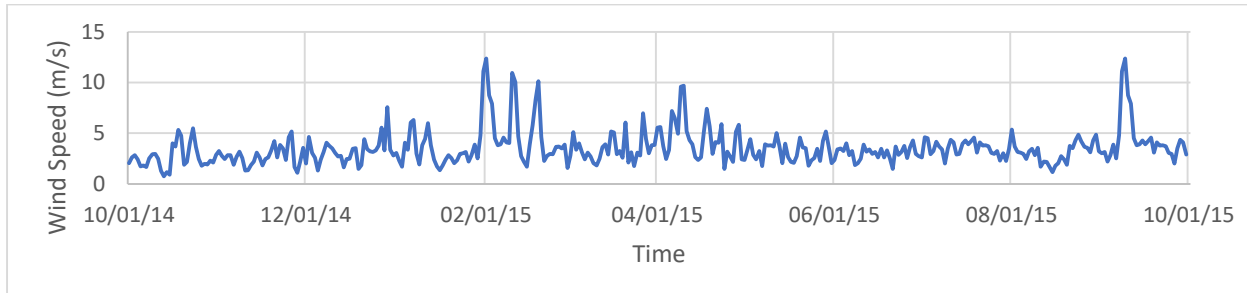
Figure 3. Observed Wind Speed Time Series
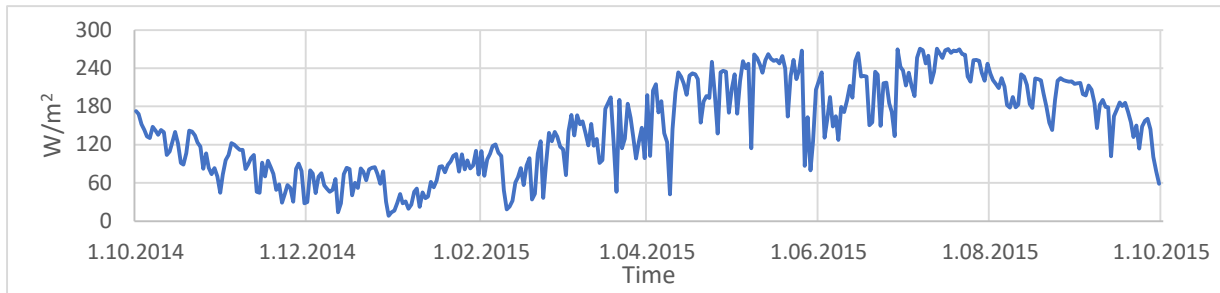
Figure 4: Observed Solar Radiation Time Series

Water temperatures monitored once a month at the suspended sediment monitoring station of Besdegirmen are obtained for the period of 2006-2012 and are used to issue a relation between measured water temperature values and air temperatures for the same dates. The equation relating air temperatures to the water temperatures is derived as follows:

$$T_w = 0.487 * T_a + 8.6027 \tag{1}$$

Comparison of monitored water temperatures at Besdegirmen station with the values predicted by the equation are given in Figure 5. Error analysis is conducted to evaluate the errors between the predicted and observed water temperature values. The Root Mean Square Error (RMSE) and Mean Absolute Error (MAE) used to examine the difference between the observed and measured temperature time series are given as follows:

$$RMSE = \sqrt{\sum_{i=1}^{n} \frac{(T_{observed} - T_{predicted})^2}{n}} \tag{2}$$

$$MAE = \frac{1}{n} \sum_{i=1}^{n} |T_{observed} - T_{predicted}| \tag{3}$$

The RMSE and MAE values are calculated as 2.57˚C (11% of the maximum temperature) and 1.89 ˚C (8% of the maximum temperature) indicating that water temperatures are predicted reasonably for the purposes of the study.

Equation 1 is then used to predict daily water temperature input data to the model for the water year of 2015 (Figure 6). The data presented in Figure 6 are input as water temperature time series to the model for the simulation period.
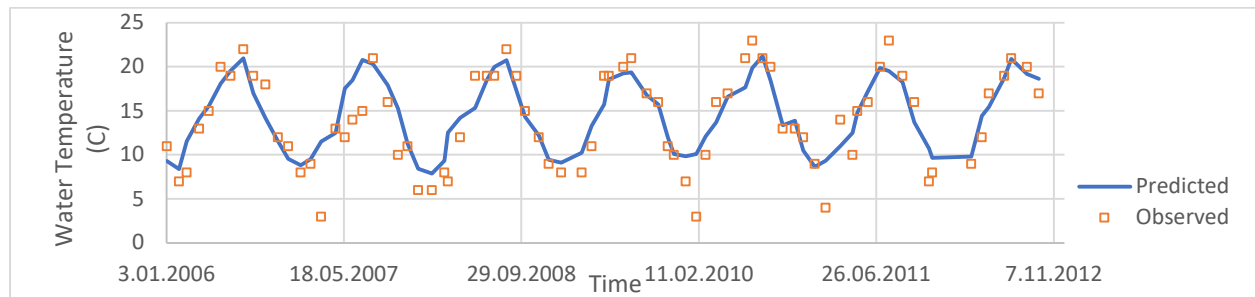
Figure 5. Comparison of observed water temperatures at Besdegirmen station with the values predicted by the Equation 1
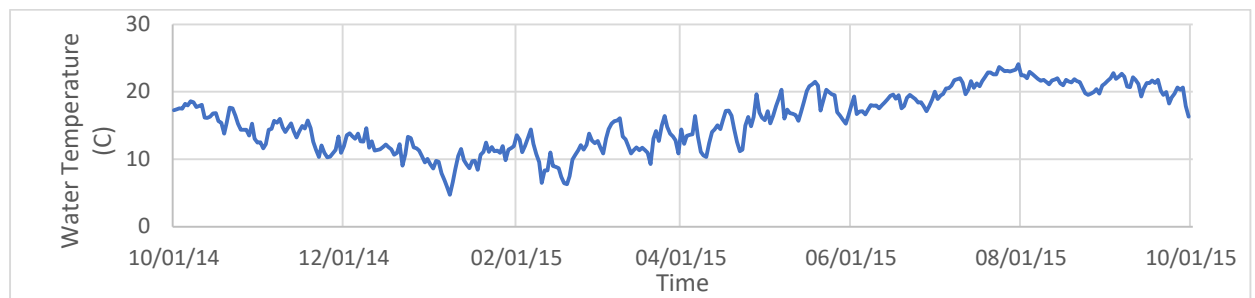
Figure 6. Water Temperature Time Series used in the simulations

2.3. WASP 8 Application

The water quality analysis simulation program (WASP), supported and developed by the US Environmental Protection Agency (USEPA), is the multi-dimensional and dynamic water quality modeling program. The model can be used to analyze a variety of water quality problems in ponds, streams, lakes, reservoirs, rivers, estuaries, and coastal waters. The time-varying processes of advection, dispersion, point and diffuse mass loading and boundary exchange are represented in the model. WASP also can be linked with hydrodynamic and sediment transport models that can provide flows, depths, velocities, temperature, salinity and sediment fluxes. WASP contains four layers representing different parts of water ecosystems. These layers are defined as 1) The water column in contact with atmosphere, 2) The water column non-contact with atmosphere, 3) The underlying benthos in contact with water, 4) The sediment bed non-contact with water. When the conservation of mass and momentum are solved for both water and solids between the layers, flow and transport in the water column, transport in the porous media of the bed sediment, transport in the water column via settling/re-suspension and transport with rainfall/evaporation are considered. Although the model cannot execute hydrologic computations, it can be linked to hydrologic models such as HSPF and SWIMM, and can be linked to hydrodynamic models through input files. When WASP is used alone, it solves the hydrodynamics using the kinematic wave equation. It can also transfer data to the central database system developed by the EPA (Ambrose et al., 1993).

Water quality processes are represented in special kinetic subroutines that are either chosen from a library or written by the user. WASP is structured to permit easy substitution of kinetic subroutines into the overall package to form problem-specific models. WASP7 comes with four modules: TOXI for simulation of toxicants and EUTRO for simulation of conventional water quality including

ammonia, nitrate, dissolved oxygen, salinity, organic/inorganic phosphorus, MERCURY for simulation of mercury and HEAT for simulation of temperatures in water bodies.

In this study, for the application of WASP model to predict water quality parameters, Porsuk river is divided into 25 segments and location and physical properties of each segment are defined respectively in Table 1.

Table 1. Location and physical properties of the main river segments used in the model.

Segment No	X coordinate	Y coordinate	Segment Name	Length(m)	Width(m)	Slope(Θ)
1	38.96667	30.13333	Beskaris-Altintas Village	12403.4	8.8	0.00274
2	39.07876	30.1808	Altintas Village- Zafer Airport	8569.3	6.9	0.00082
3	39.11447	30.11463	Zafer Airport-Haydarlar Intake	15405.5	25.7	0.00045
4	39.19748	29.99047	Haydarlar-Adakoyu Route	3091.5	14.8	0.00032
5	39.20738	29.9687	Adakoyu Route-Ada	7647.4	13.7	0.00026
6	39.26397	29.98031	Ada-Agackoy	20000.0	15.2	0.00260
7	39.38014	30.06653	Agackoy- Calca	20000	22.95	0.00105
8	39.46242	30.02649	Calca-Kutahya Intake	15210.4	24.8	0.00092
9	39.55533	30.06802	Kutahya Outlet-Reservoir1	12468.5	77.3	0.00128
10	39.586	30.14198	Reservoir1-Reservoir2	6046.0	1363.2	0.00000
11	39.62566	30.17688	Reservoir2-Reservoir3	5845.7	1724.1	0.00000
12	39.63312	30.23757	Reservoir3-Eskisehir Intake	20000.0	54	0.00260
13	39.64833	30.36753	Eskisehir Intake-Esenkara	20000	21.42	0.00120
14	39.72944	30.4248	Esenkara-Eskisehir Outlet	20000	23.78	0.00120
15	39.77156	30.55555	Eskisehir Outlet-Cavkum	20000	24.5	0.00060
16	39.81572	30.71093	Cavkum-Alpu Intake	20000	18.7	0.00050
17	39.77813	30.93529	Alpu Intake-Alpu	2693.8	18.4	0.00037
18	39.76836	30.96016	Alpu-Guroluk	20000.0	20.1	0.00015
19	39.68892	31.10943	Guroluk-Beylikova	12229.3	15.3	0.00049
20	39.68423	31.20469	Beylikova-Yalinli	20000	22.4	0.00055
21	39.69572	31.37774	Yalinli-Yunusemre	12404.1	18.9	0.00048
22	39.70131	31.47751	Yunusemre-Bicer Intake	20000.0	17.4	0.00090
23	39.71313	31.62732	Bicer Intake-Outlet	20000	13.1	0.00110
24	39.66823	31.72424	Bicer Outlet-Sazilar	20000	12.7	0.00075
25	39.67838	31.9709	Sazilar-Sakarya	2370.1	13.4	0.00338

As mentioned above, monitored water quality parameters are obtained from the literature (Kose et al 2016). The segmentation of the river is conducted based on monitoring stations where water quality data are available and flow stations where flow rates are monitored regularly (Figure 1). Prior to the simulation of water quality parameters, simulation results of the hydrodynamics along the river are validated with the available observations. For these simulations, eutrophication module (EUTRO) is selected, and 1-D kinematic wave approach is utilized. Maximum time step is set to 2.46 minute in the simulations. The flow rates are output at all stations daily for the simulation period (10/1/2014-9/30/2015). For the model domain, the segments are specified as input based on the properties summarized in Table 1. The parameters measured at the stations at the beginning of the simulation period are specified in the model as initial conditions. The daily values of air temperature, wind speed, solar radiation, and water temperature are provided as input data for the simulation period.

3. RESULTS

In flows section, the flow functions showing flow time series at the boundaries of the model are specified using daily flow measurements recorded at the river monitoring stations. As shown previously in Figure 1, eight different flow functions are defined. Figure 7 presents comparison of simulated flow rates with the observations for six different stations: Beskaris, Porsuk Ciftligi, Calca, Esenkara, Parsibey and Kiranharmani stations. To evaluate the errors between the simulated and observed discharge time series, again RMSE and MAE calculated. The RMSE and MAE values for each station are given in Table 2.
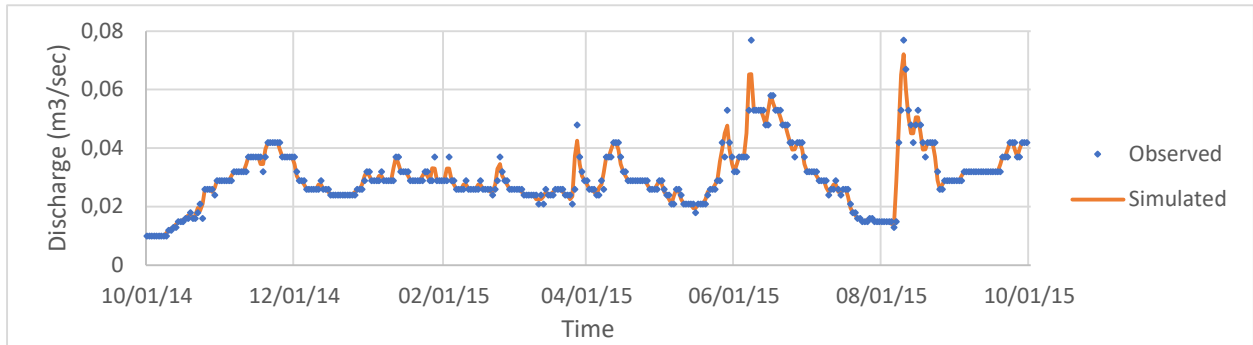
(a)
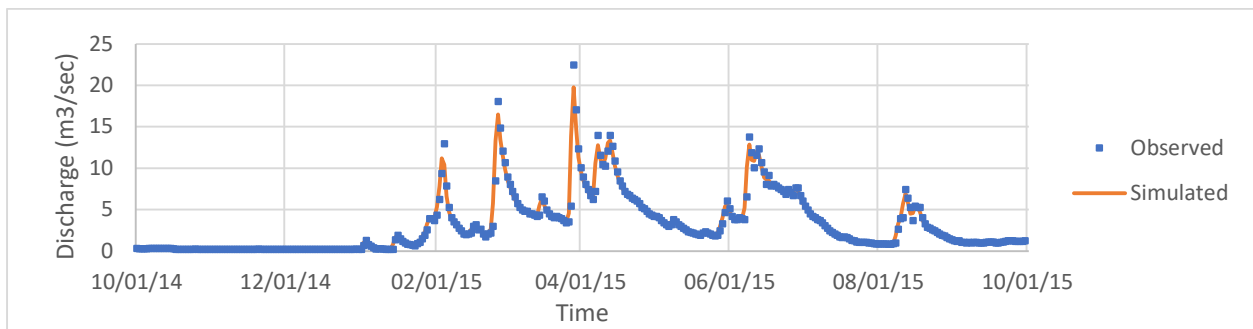
(b)
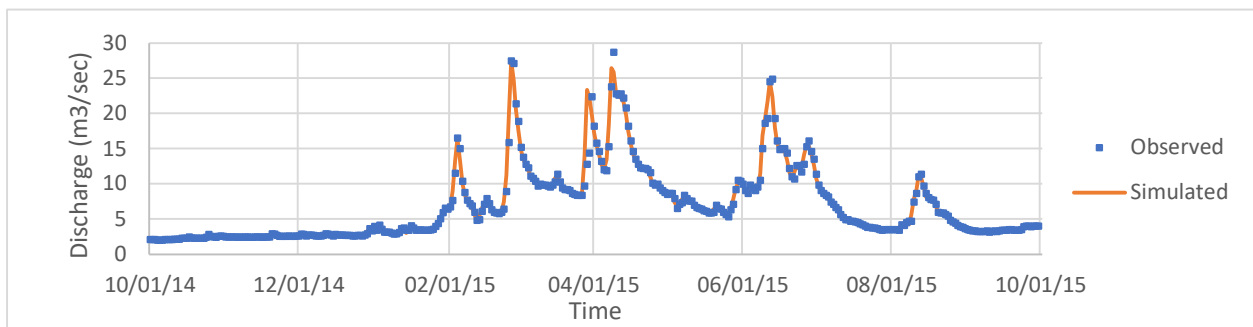
(c)
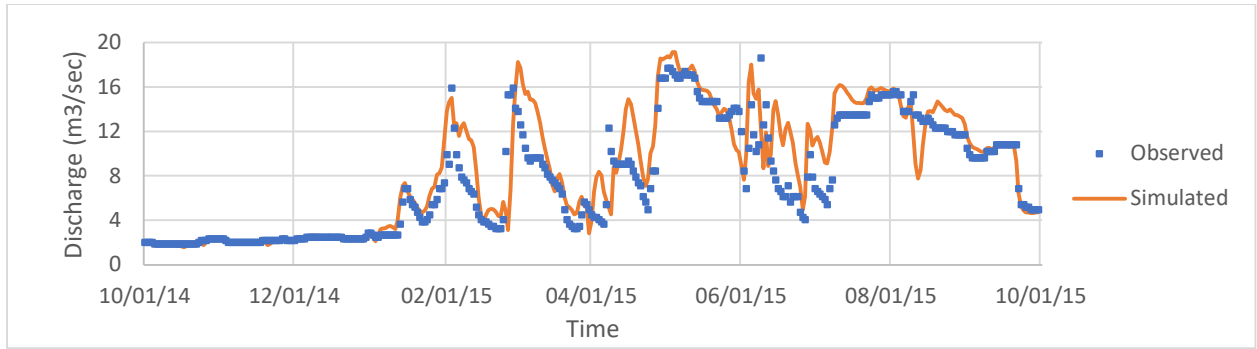
(d)
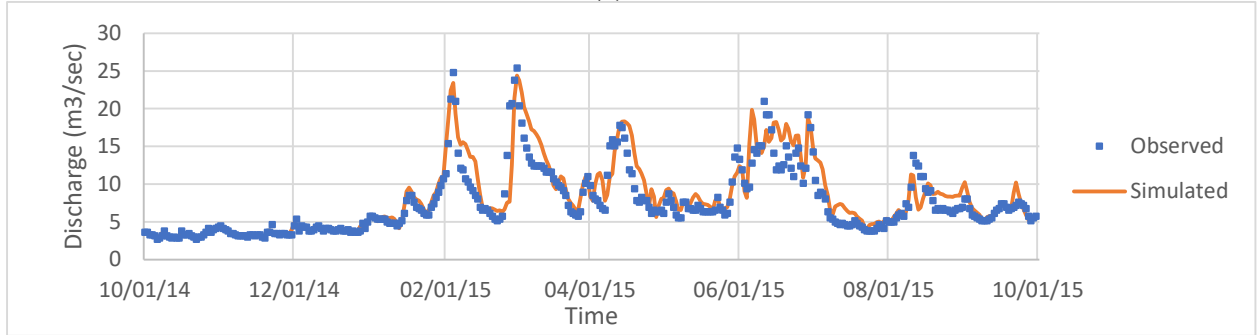
(e)
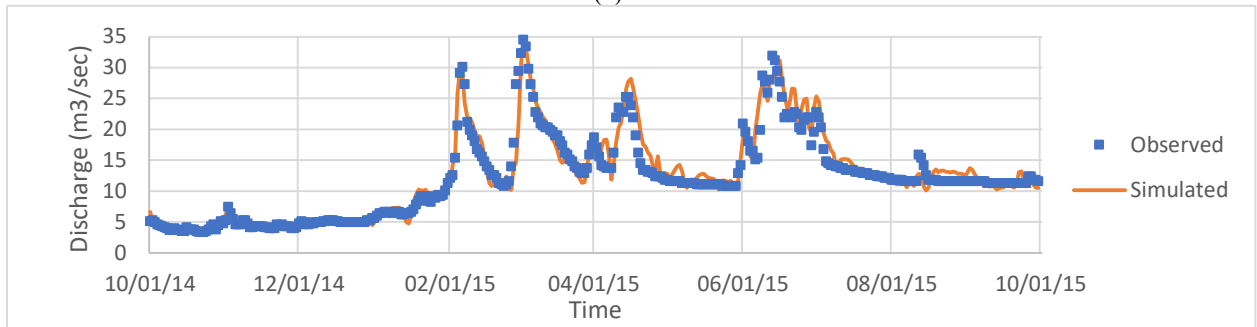
(f)

Figure 7. Comparison of flow rates at six stations; a) Beskaris, b) Porsuk Ciftligi, c) Calca, d) Esenkara, e) Parsibey, f) Kiranharmani stations

Table 2. RMSE and MAE values for discharge stations.

Stations	Root Mean Square Error (RMSE)	Mean Absolute Error (MAE)
Beskaris	0.002	0.001
Porsuk Ciftligi	0.718	0.260
Calca	0.918	0.313
Esenkara	2.415	1.555
Parsibey	2.088	1.324
Kiranharmani	1.823	1.172

The RMSE and MAE values are calculated as 0.002 m³/s (2.8% of the maximum discharge) and 0.001 m³/s (1.3% of the maximum discharge), 0.718 m³/s (3.2% of the average temperature) and 0.260 m³/s (1.2% of the maximum discharge) , 0.918 m³/s (3.2% of the maximum discharge) and 0.313 m³/s (1.1% of the maximum discharge), 2.415 m³/s (13% of the maximum discharge) and 1.555 m³/s (8.4% of the maximum discharge), 2.088 m³/s (8.2% of the maximum discharge) and 1.324 m³/s (5.2% of the maximum discharge), 1.823 m³/s (5.28% of the maximum discharge) and 1.172 m³/s

(3.4% of the maximum discharge) for Beskaris, Porsuk Ciftligi, Calca, Esenkara, Parsibey and Kiranharmani stations respectively.

3.1. Simulation of Results

Following the simulation of discharges at monitoring stations accurately, water quality parameters are modeled. In the loads section, water quality parameters are specified as input data for the model segments according to sampling locations. The model is run for the water year of 2015 by the euthrophication module and the simulated dissolved oxygen concentrations are compared with the observed values reported by Kose et al, 2016 (Table 5).

Table 3: Comparison of simulated and observed Dissolved Oxygen (Kose et. al,2016).

Segment	Segment Name	Simulated DO-July (mg/L)	Observed DO (mg/L)
1	Beskaris-Altintas Village	7.89	7.86
5	Adakoyu Route -Ada	8.09	7.97
6	Ada-Agackoy	7.36	7.56
8	Calca-Kutahya Intake	3.67	3.3
9	Kutahya Outlet-Reservoir1	15.35	14.14
10	Reservoir1-Reservoir2	13.09	13.24
11	Reservoir2-Reservoir3	12.78	13.08
12	Reservoir3-Eskisehir Intake	6.74	7.29
17	Alpu Intake-Alpu	4.34	4.33
18	Alpu-Guroluk	6.67	6.61
21	Yalinli-Yunusemre	5.43	5.66
25	Sazilar-Sakarya	7.67	7.97

Following this analysis simulation results are also compared for two different months of the year having very different flow regimes: June and January (Figure 8). These periods are selected since the rivers is expected to have the lowest (July) and the highest (January) dissolved oxygen concentrations throughout the year. Comparison of the simulation results indicated that in both months, lowest dissolved oxygen values are observed at specific locations: Agackoy-Calca segment and Calca-Kutahya segment as 3.48 and 3.67 mg/L (Red dot) respectively, and at Alpu intake- Alpu segment as 4.34 mg/L. At these stations dissolved oxygen falls below 5 mg/L throughout the year. Therefore, immediate measures are found to be necessary for the study site.
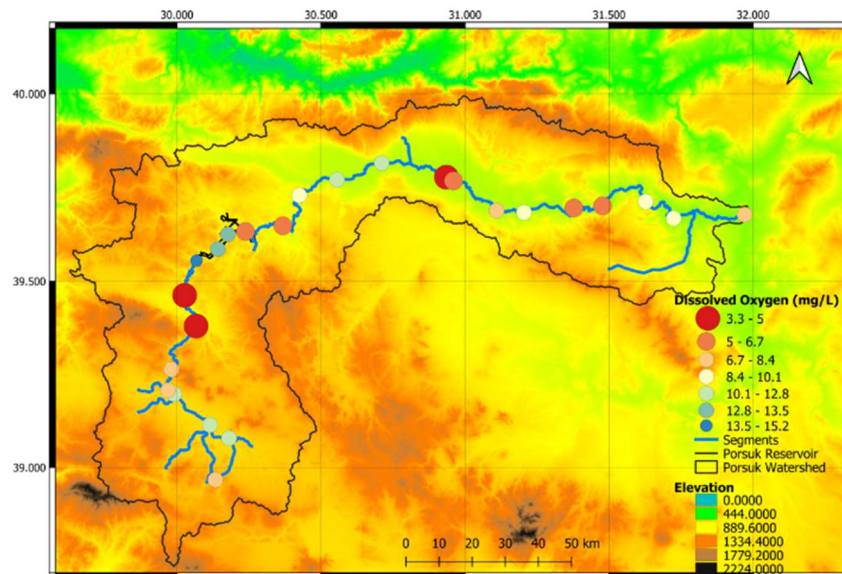
(a)
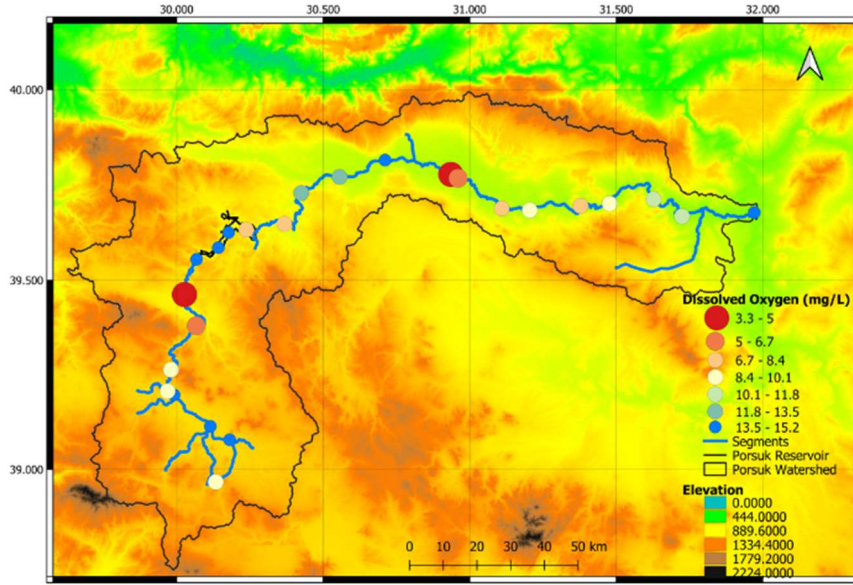
(b)

Figure 8: Comparison of the simulated dissolved oxygen concentrations along the river for two different months; a) June, b) January

4. CONCLUSIONS

In this study, hydrodynamics and water quality parameters are simulated in the Porsuk River via application of Water Quality Analysis Simulation Program (WASP) for the water year of 2015. The Porsuk main river is divided into 25 segments in total, considering available water quality and flow monitoring stations. For calibration of the model, the flow rates monitored at Beskaris, Porsuk Ciftligi, Calca, Esenkara, Parsibey and Kiranharmani stations are used. Following the simulation of discharges at monitoring stations accurately, water quality parameters are modeled. Comparison of the simulation results for dissolved oxygen indicated that in both January and July having very different flow regimes, lowest dissolved oxygen values are observed at specific locations: Agackoy-Calca segment and Calca-Kutahya segment as 3.48 and 3.67 mg/L (Red dot) respectively, and at Alpu intake- Alpu segment as 4.34 mg/L. At these stations dissolved oxygen falls below 5 mg/L throughout the year. Therefore, immediate measures are found to be necessary for the study site.

REFERENCES

Köse, Esengül & Çiçek, Arzu & emiroğlu, Özgür & Tokatli, Cem & Uğurluoğlu, Alper & Başkurt, Sercan & Aksu, Sadi & Uylaş, Merve. (2016). Water quality assessment of Porsuk stream basin. Biological Diversity and Conservation

Kunwar P. Singh, Amrita Malik, Sarita Sinha, Water quality assessment and apportionment of pollution sources of Gomti river (India) using multivariate statistical techniques—a case study, Analytica Chimica Acta, Volume 538, Issues 1–2,2005, Pages 355-374

Mamani Larico, AJ, Zúñiga Medina, SA. Application of WASP model for assessment of water quality for eutrophication control for a reservoir in the Peruvian Andes. Lakes & Reserv. 2019; 24: 37– 47.

Tekkanat, İ. S., & Sarış, F. (2015). Porsuk Çayı Havzasında Akarsu Akımlarında Gözlenen Uzun Dönemli Eğilimler. Türk Coğrafya Dergisi, 64,69-83.

Akımlarında Gözlenen Uzun Dönemli Eğilimler. Türk Coğrafya Dergisi, 64,69-83.

Wang, Q., Dai, W., Zhao, X., Li, S., & Zhao, Y. (2009). Numerical model
of thermal discharge from Laibin power plant based on Mike 21FM.China Environmental Science, 22, 332–336.
Muhammetoglu, Ayse & Muhammetoglu, Habib & Oktas, Sedat & Ozgokcen, Levent & Soyupak, Selçuk. (2005). Impact Assessment of Different Management Scenarios on Water Quality of Porsuk River and Dam System – Turkey. Water Resources Management. 19. 199-210. 10.1007/s11269-005-3473-z.

Ambrose, R.B., Wool, T., Martin, J.L.: WASP User's Manual, US Environmental Protection Agency, Environmental Research Laboratory, Athens, Georgia (1993).

COASTAL AND MARITIME HYDRAULICS

MODELING OF WIND AND WAVE CLIMATE OF BOZCAADA COASTAL REGION

Asu Inan

Sea and Aquatic Sciences Application and Research Center, Gazi University

Ankara, Turkey

asuinan@gazi.edu.tr

Kagan Cebe

Department of Civil Engineering, Engineering Faculty, Nevsehir Hacı Bektas Veli University

Nevsehir, Turkey

kagan.cebe@gmail.com

Yunus Yilmaz

Department of Civil Engineering, Engineering Faculty, Gazi University

Ankara, Turkey

yunusylmaz2013@gmail.com

ABSTRACT: Numerical modeling of wind and wave climate is basic tool for the solutions of the coastal engineering problems such as understanding of hydrodynamics of coastal waters, design of coastal structures, discharge problems, modeling of sediment movement and determination of wind and wave energy in the coastal zone. The HYDROTAM 3D, which is geographic information system (GIS) and cloud computing based, three dimensional hydrodynamic, turbulence and transport model, has been applied to Bozcaada coastal waters. Bozcaada is the second biggest island of Turkey that is located in the Aegean Sea. Wind data of the meteorological station in Bozcaada and ECMWF (European Center for Medium-Range Weather Forecasts) wind data have been used for the wind climate modeling in the HYDROTAM 3D. The predictions of the wind climate based on two different wind data have been compared. For the prediction of the wave climate, ECMWF wind data has been used. WAM model as a numerical method and CEM model as an empirical method have been applied based on long term statistics and the predictions have been compared. Predictions with six hours interval of ECMWF operational archive at the coordinates of 39.800N-26.100E have been used in the wave model.

1. INTRODUCTION

Determination of the wind and wave climate of a coastal region is the basic study to understand the hydrodynamics of the coastal region, design of the coastal structures and coastal zone management and planning. Data sets, that will be used, should be long term and reliable to obtain reliable wind and wave climates. Otherwise the studies and design based on the wind and wave climate do not have effective solutions.

In Turkey, the waves are generally wind induced waves. There are two measurement methods for the wind prediction data: Measurements using wind measurement instruments in the sea and land and measurements based on wind pressure differences. The measurements in the sea are safer than the measurements in the land. If there is any sea measurement, land measurement can be used as calibrated (Buyruk, 2019). After the analyzing of wind data and building wind climate, wind induced waves can be modeled. Wave models can be empirical or numerical. The most used empirical models are SMP, JONSWAP, SPM and CEM.

Wave prediction studies begun in 1940's with the empirical models. The first classification was made 1947 by Sverdrup and Munk, and then Bretschneider developed this model in 1952. The basic of the empirical approaches is the law with the fetch length and wave growth. The growth of the waves induced by the wind with a constant direction and speed in fetch length is limited with effective fetch length (Sverdrup and Munk, 1947; Bretschneider, 1952; Al-Sammarraie, 2019). In 1950's, spectral methods were used and observed that their results are more accurately. Spectral methods are based on the wave frequencies, kinetic and potential energies of the waves. Philips said that the waves grow linearly (Philips, 1957). Pierson and Moskowitz defined the parameters of Philips and developed Pierson-Moskowitz spectra (Pierson and Moskowitz, 1964). They are first generation wave models. Hasselmann et al. (1980) developed the second generation wave models using wave interaction after 1964 (Al-Sammarraie, 2019). Hasselmann et al. proposed the third order generation model in 1980. (Hasselmann et al., 1980). The difference between the second and third generation wave models is the difference of the solution methods. The third generation models simulate the wave growth using nonlinear wave-wave interaction, minimizing the restrictions of the spectral shape. WAM model is one of the examples of the third generation wave models (Buyruk, 2019).

2. METHOD

2.1. Study Area

Bozcaada is a small island, which is located in the northeast of the Aegean Sea and southwest of Dardanelles. Its area is 36.03km^2. It is a popular touristic area and holiday destination. The location of Bozcaada is seen in Figure 1. A wind farm in Bozcaada which has a capacity of 10.2 MW was established in 2000 and 17 wind turbines which have a power of 600 kW. Wave can be also thought as a renewable energy source in this region besides the wind.
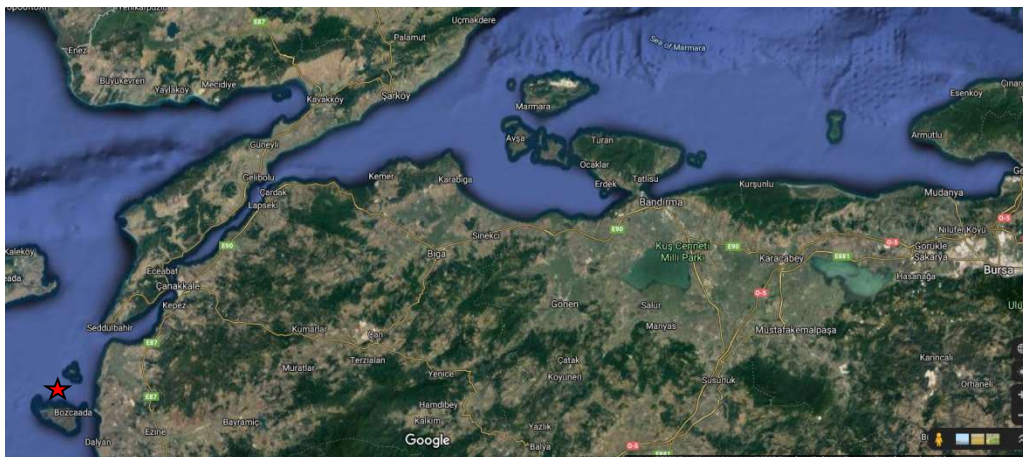
Figure 1. The location of Bozcaada (Googlemaps, 2020)

In this study, HYDROTAM-3D is used for the determination of the wind and wave climates. HYDROTAM-3D is validated with the analytical and experimental results in the literature and comparisons with the field measurements. It is a three dimensional hydrodynamic and transport model. It uses a GIS based cloud computing architecture (HYDROTAM-3D, 2019; Yılmaz, 2018; Fidanoğlu Yıldırım vd., 2017; Cebe ve Balas, 2016). The submodules of HYDROTAM-3D are: wind climate module, wave climate module (long-term wave statistics and extreme wave statistics), wave propagation module (wave transformation using mild-slope equations), longshore sediment transport module (sediment transportation from breaking waves), hydrodynamic module (3D modeling of wind, tidal or density stratification-induced currents, changes in water surface elevation and, storm surge), turbulence module, pollutant transport module. Inputs of the simulation setup are the bathymetry of the study area, the time series of the wind speeds and directions, currents at the initial time, salinity and temperature of the sea water, the tide level and period (Inan, 2019). In this study, wind and wave climate submodules are used. The database of the wind climate submodule includes 46 y of hourly

wind data from the meteorological stations on Turkish coasts and 16 y (2000-2016) of 6 hourly wind data of ECMWF (Buyruk, 2019; HYDROTAM-3D, 2019).

Wave climate is obtained from the wind data, because there is not long-term wave data in Turkey. In this study, CEM method as an empirical method and WAM model as a numerical method are used for the wave climate. The wave growth is simulated by the effective fetch length in CEM method empirically (Buyruk, 2019).

In the CEM method, the length of fetch in a given direction is obtained from plotting through 30 radii (with intervals of 1 Degree) on both sides of the wind direction of blowing from the certain point to the first point of intersection with the coastline. The mean value of these radii is called the fetch length. The wave height and period are determined with wind speed, fetch length and wind duration. (Abbasi, 2019).

The WAM model is the first model that solves the complete action density equation, including non-linear wave–wave interactions. The WAM model is a 3rd generation model which integrates the basic transport equation. It describes the evolution of a two-dimensional ocean wave spectrum without additional unplanned assumptions considering the spectral shape. There are three explicit source functions which describe the wind input, non-linear transfer and whitecapping dissipation (BODC, 2022). In the WAM model, the significant wave height is obtained by the mean wave direction, frequency and directional wave spectrum (Buyruk, 2019).

The wind data of the Meteorological Station of Bozcaada and ECMWF are used for obtaining the wind climate of Bozcaada. For the wave climate, the study is continued with the wind data of ECMWF and CEM method and WAM model is applied.

2.2. Wind Climate

The hourly wind data of Bozcaada Meteorological Station, which is a land station, is compared with the six hourly wind data of ECMWF. The coordinate of ECMWF is shown in the Figure 2. The comparison of these two data sets is given in Figure 3.
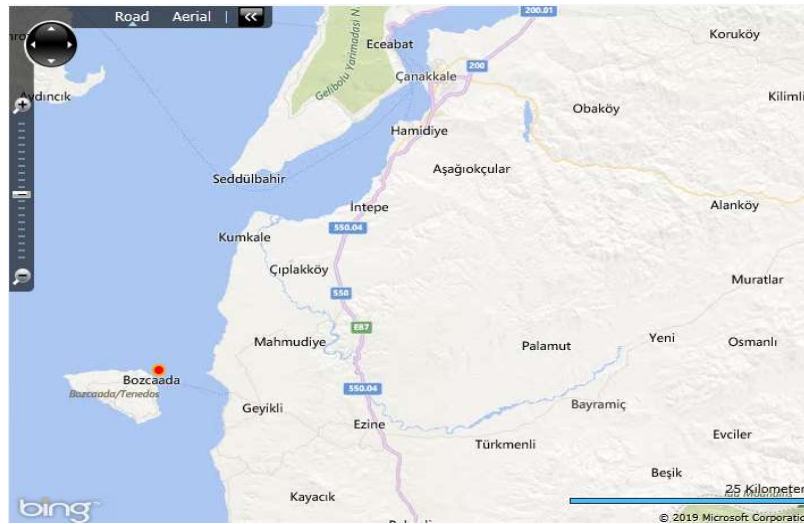
Figure 2. The coordinate of wind data of ECMWF (39.8N, 26.1E) for Bozcaada (HYDROTAM-3D, 2019)
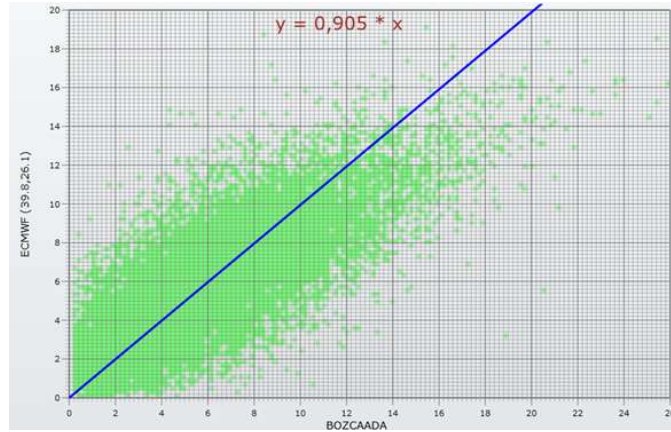
Figure 3. The relationship of the wind data sets of ECMWF and Bozcaada Meteorological Station
(HYDROTAM-3D, 2019)

In Figure 3, the predictions of the wind data sets of land based Bozcaada Meteorological Station and ECMWF for the coordinate (39.8N, 26.1E). The wind data set of Bozcaada Meteorological Station covers the six hourly wind data between the years 1972-2016 and ECMWF's includes the hourly wind data from 2000-2016. In Figure 3, it is seen that the prediction of ECMWF wind data is 0.905 times of the prediction of the wind data of the land based Bozcaada Meteorological Station. In the literature, the sea wind data is generally 1.5-2.0 times of the land base wind data (Buyruk, 2019).

The difference for Bozcaada predictions is caused by the orographic features of the region and low high buildings in the settlement, which do not block the wind.

In Figure 4, the wind roses of the Bozcaada Meteorological Station and ECMWF (39.8N, 26.1E) are presented. The dominant wind direction based on the Bozcaada Meteorological Station is NNE. The predictions of the data set of ECMWF (39.8N, 26.1E) result NE as the dominant wind direction.
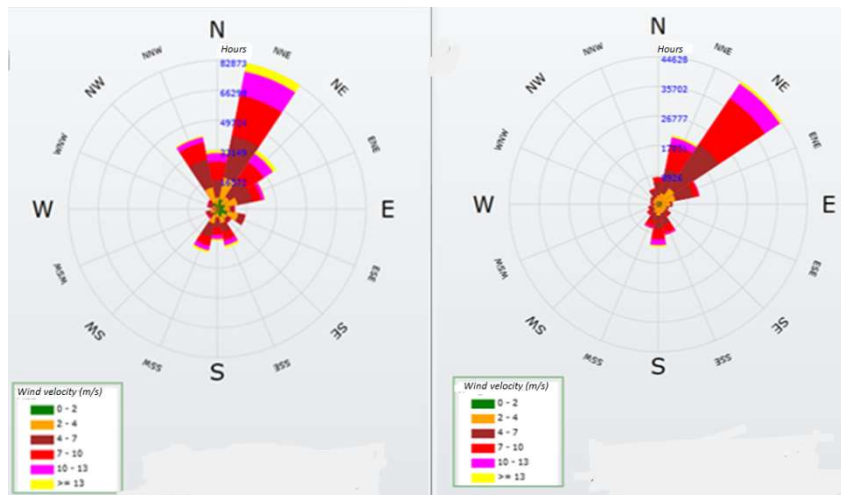
Figure 4. Wind roses of a) Bozcaada Meteorological Station b) ECMWF (39.8N, 26.1E)
(HYDROTAM-3D, 2019)

The annual and directional wind velocities are shown in Figure 5 and monthly average and extreme wind velocities are presented in Figure 6.
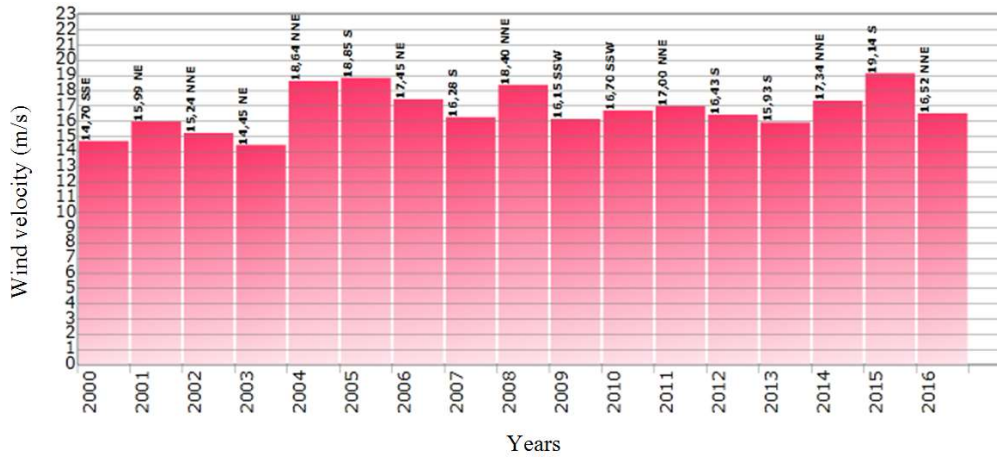
Figure 5. The annual and directional wind velocities (HYDROTAM-3D, 2019)
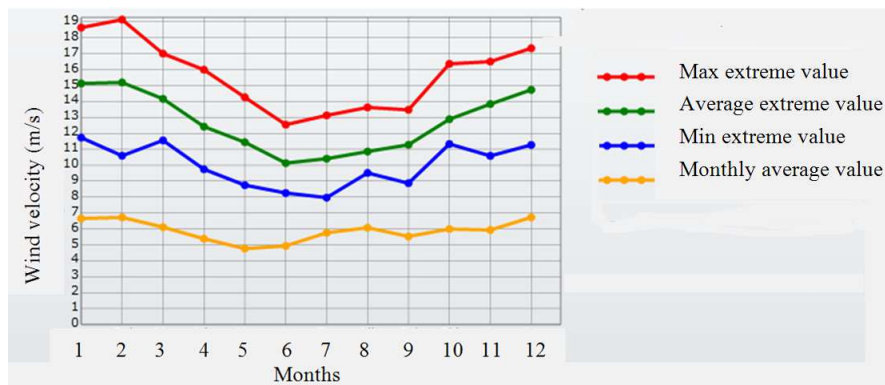
Figure 6. Monthly average and extreme wind velocities (HYDROTAM-3D, 2019)

2.3. Wave Climate

Empirical and numerical approaches are applied in modeling of the wave climate. The predictions of the wind data of the ECMWF are used for the analyses of the wave climate. Empirical approach is CEM method, numerical approach is the WAM model. In Figure 7, the fetch distances of Bozcaada coastal region are shown. The longest fetch length corresponds to WNW.
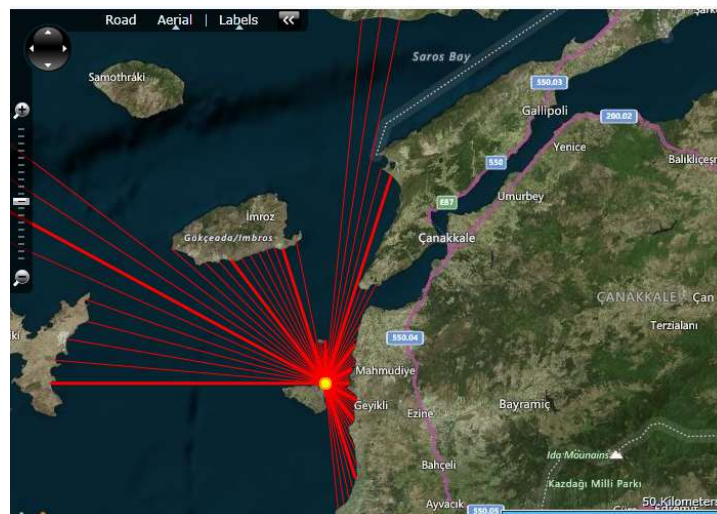
Figure 7. Bozcaada fetch lengths (HYDROTAM-3D, 2019)

2.3.1. Application of CEM Method

The wind data set of the coordinate 39.8N, 26.1E of the ECMWF is used for the wave modeling by CEM method. Long term wave statistics is applied for the modeling. The scatter diagram for the significant wave height (H_s) and wave period (T) and the relationship between H_s and T are given in Figure 8 and Figure 9, respectively.
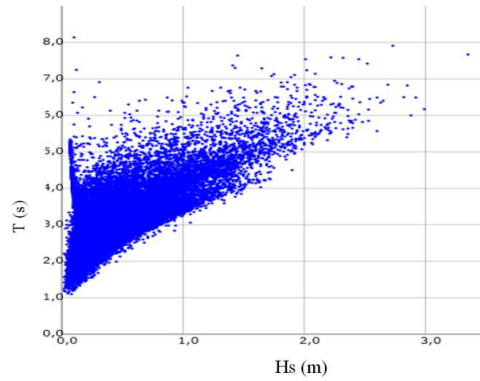
Figure 8. Scatter diagram of H_s vs. T (CEM method) (HYDROTAM-3D, 2019)
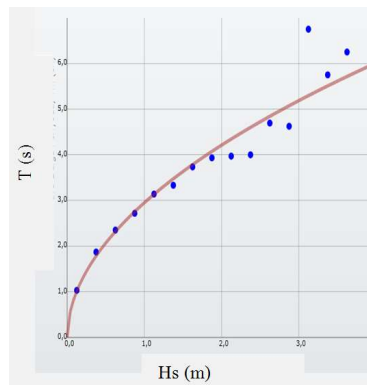
Figure 9. The relationship between Hs and T (CEM method) (HYDROTAM-3D, 2019)

In Figure 10, monthly average and extreme values of significant wave height computed by CEM method is presented.
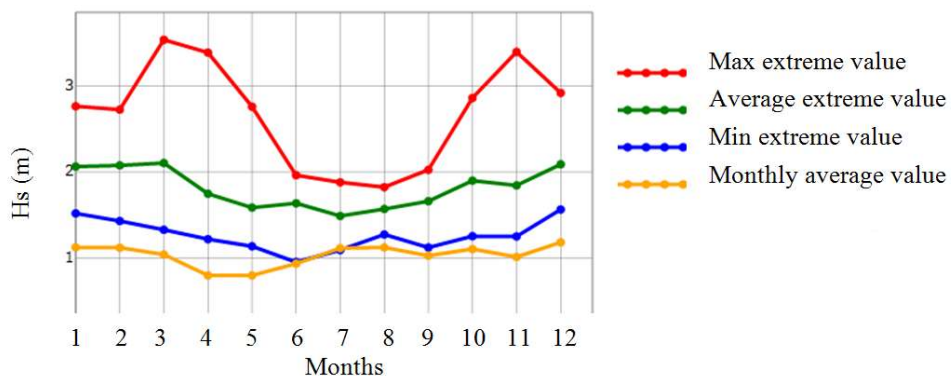
Figure 10. Monthly average and extreme values of significant wave height by CEM method

(HYDROTAM-3D, 2019)
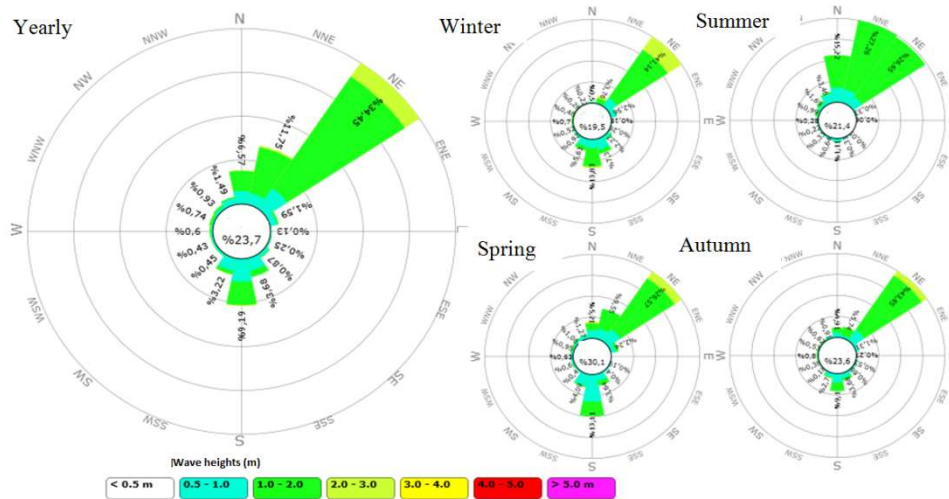
Figure 11. Yearly and seasonal wave roses by CEM method (HYDROTAM-3D, 2019)

The wave roses show the occurrence possibility of the significant wave heights, which propagate from different directions in a year. If the wave height is smaller than 0.5m then the sea is assumed calm. In that condition, they are shown in the middle of the wave rose without direction sign. Yearly and seasonal wave roses are given in Figure 11.

2.3.2. Application of WAM Model

The scatter diagram for the significant wave height (H_s) and wave period (T) and the relationship between H_s and T based on the numerical WAM model are given in Figure 12 and Figure 13, respectively. The used coordinate of ECMWF is 39.8N, 26.1E. In Figure 14, monthly average and extreme values of significant wave height computed by WAM model is presented. In Figure 15, monthly average and extreme values of significant wave height computed by WAM model is presented.
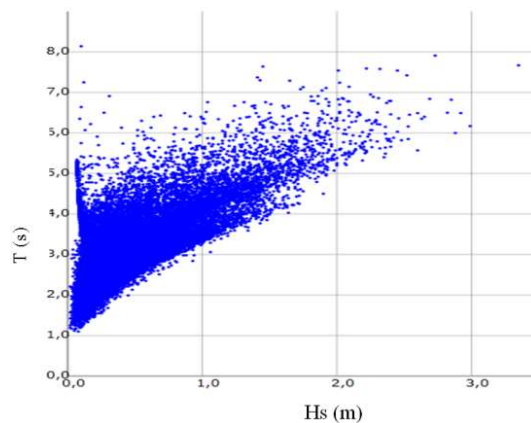
Figure 12. Scatter diagram of H_s vs. T (WAM model) (HYDROTAM-3D, 2019)
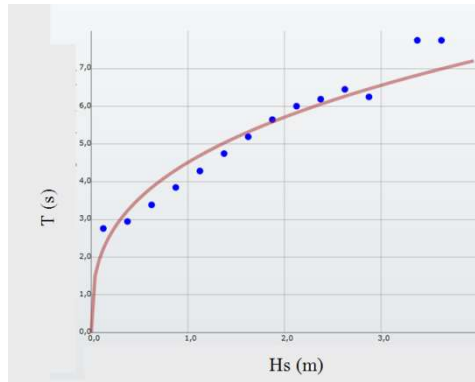
Figure 13. The relationship between Hs and T (WAM model) (HYDROTAM-3D, 2019)
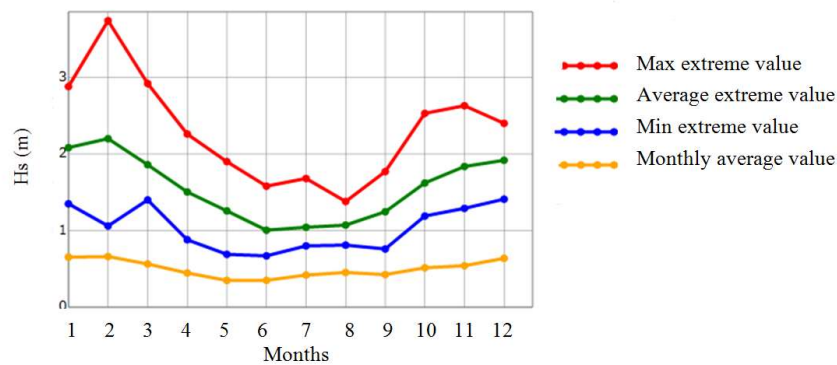
Figure 14. Monthly average and extreme values of significant wave height by WAM model
(HYDROTAM-3D, 2019)
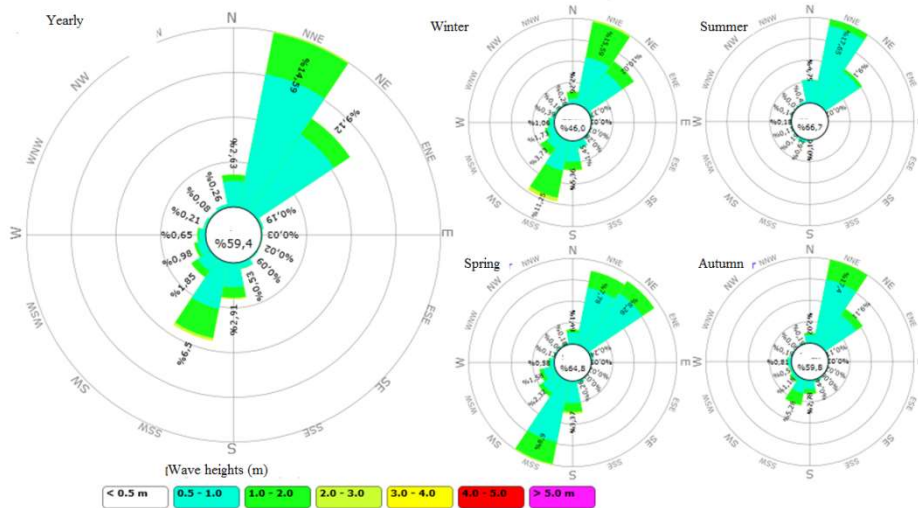
Figure 15. Yearly and seasonal wave roses by WAM model (HYDROTAM-3D, 2019)

3. CONCLUSIONS

In this study, wind and wave climates of Bozcaada coastal region are presented using HYDROTAM-3D. In Turkey, there are any long-term wave measurements, therefore the wind data sets are used for the wave modeling. HYDROTAM-3D is a complex coastal engineering model, which has different submodules depending on the type of the problem. Here, the wind and wave climate submodules are applied only. The model covers the wind data of the Turkish Coasts measured by Meteorological Stations approximately for 50 years and also the wind data sets of the ECMWF from 2000 to 2016.

As the measurements of the meteorological stations are land based, the wind predictions of the ECMWF are sea based. Therefore the data sets of ECMWF are used for the modeling of the wave climate in the point of view of reliability.

The dominant wind direction is determined as NE with the data set of the Bozcaada Meteorological Station and NNE with data set of the ECMWF.

In wave modeling, two approaches are applied. The first one is CEM method. It is an empirical model. The second one is the numerical WAM model. The dominant wave direction obtained by CEM method is NE, and obtained by WAM model is NNE. %23.7 and %59.4 of waves correspond to a calm sea by CEM method and WAM model, respectively. The predictions of CEM method have higher values of wave heights for the same coordinate.

Determination of the wind and wave climate is essential for the coastal engineering problems. It is the basic step of the design of the coastal structures, understanding of the hydrodynamics of a coastal region, determining wind and wave energy potentials of a coastal region, coastal zone management and planning.

ACKNOWLEDGEMENT

REFERENCES

Abbasi, M.R., (2019), Evaluating semi -empirical wave forecasting method CEM in the Strait of Hormuz, *International Journal of Coastal and Offshore Engineering,* 3(3), 43 -46 .

Al-Sammarraie K., .(2019), *A Comparative Study on the Wave Climate of Southern Aegean Coastline of Turkey.,* MSc Thesis, Atılım University, Institute of Science and Technology, Ankara, Turkey.

BODC, (2022), Available: https://www.bodc.ac.uk/data/documents/nodb/254628/

Bretschneider, C. L. (1952), The generation and decay of wind waves in deep water, *Trans. A.G.U.,* 33(3), 381–389.

Buyruk, T., (2019), *GIS based Electronic Atlas of Wind and Wave Climate and Energy Potential on Turkish Coasts*, Ph.D. Thesis, Graduate School of Natural and Applied Sciences, Gazi University, Ankara, Turkey.

Cebe, K., Balas, L., (2016), Water quality modelling in Kaş Bay, *Applied Mathematical Modelling*, 40 (3), 1887-1913.

Fidanoğlu Yıldırım, P. Inan, A., Balas, L., Yılmaz, N., Cebe, K., (2017), The need for the integration of land use planning and water quality modelling in the case of Fethiye Bay, *Journal of Polytechnic*, 20 (2), 427-435.

Googlemaps, (2020), Available: https://www.google.com/maps/place/G%C3%B6k%C3%A7eada%2F%C3%87anakkale/@39.7669856,25.9396144,8.77z/data=!4m5!3m4!1s0x14b02d44bc69c92b:0xd4fbaaf8fe8a67f7!8m2!3d40.1621148!4d25.8285153

Hasselmann, D. E., M. Dunkel and J. A. Ewing (1980), Directional wave spectra observed during JONSWAP 1973., *J. Phys. Oceanogr.*, 10, 1264–1280.

HYDROTAM-3D, (2019), 3-D Hydrodynamic Transport Model website, Available: http://hydrotam.com

Inan, A., (2019), Modeling of Hydrodynamics and Dilution in CoastalWaters, *WATER*, 11 (83), 1-17.

Phillips, O. M. (1957). On the generation of waves by turbulent wind, *J. Fluid Mech*., 2, 417–445.

Pierson, W. J. and L. Moskowitz (1964): A proposed spectral form for fully developed wind seas based on the similarity theory of S. A. Kitaigorodskii., *J. Geophys. Res.*, 69, 5181–5190.

Sverdrup, H. U. and W. H. Munk (1947): Wind, sea and swell. Theory of relations for forecasting. *U.S. Navy Hydrographic Office,* Washington, Pub. No. 601, 44 pp.

Yılmaz, N., (2018), Modeling of wind climate, wave climate and current pattern in Samsun Bay coastal waters, *Journal of the Faculty of Engineering and Architecture of Gazi University,* 33(1), 279-297.

MODELING OF POLLUTION LOADS CARRIED BY SURFACE STREAMS TO KAVAKLARBOĞAZI SALT MARSH

First Author: Kağan Cebe

Department of Civil Engineering, Nevşehir Hacı Bektaş Veli University

Nevşehir, Turkey

kcebe@nevsehir.edu.tr

Second Author: Asu İnan

Sea and Aquatic Sciences Application and Research Center, Gazi University

Ankara, Turkey

asuinan@gazi.edu.tr

ABSTRACT: Various land use practices have varying adverse effects on the water quality of surrounding coastal areas. Land use plans, which do not take into consideration direct and indirect impacts of human activities on nearby water body have outcomes such as land and water pollution, hence degradation of the ecological balance. Alternatively, proper land use planning, which employs pollution prevention methods that address the sources of pollution can be an effective tool to reduce the flow of pollutants into the water body, and reverse the previous environmental degradation. Achieving this requires a holistic approach to the relationship between land use planning and water quality. In this respect, this study analyzes the effect of land use practices on the pollution loads carried by surface steams at the basins surrounding the Kavaklarboğazı Salt Marsh by using Environmental Protection Agency's Storm Water Management Model (SWMM). Kavaklarboğazı, which has a narrow contact to Güllük Bay in the Aegean Sea, has been, for decades, a target of nitrogen loading from upstream agricultural activities and urban development, practices which recently amounted to an environmental crisis. The study divides the coastal area into sub-basins considering the elevations extracted from the topography data provided by Global Digital Elevation Model and the land-use types according to CORINE data. It models the pollutants buildup in the basin and their washoff with the surface runoff by using SWMM. The model shows the land-based pollutant levels on a long term simulation for the recent status. As a result, the study suggests a model that integrates land use data into runoff and pollution, which provides reliable results and offers better solutions ecological problems.

1. INTRODUCTION

Various anthropogenic activities affect the quality of water in the Mediterrenean coasts of Turkey in a negative way. The complex interaction between chemical and physical environments sustains the ecosystems in coastal waters, in particular closed or semi-closed waters. Various forms of land use have considerable detrimental impacts on quality of semi-closed water bodies. Water quality models, which can be integrated into land use planning, provides a comprehensive tool with better solutions for the sustainability of water quality.

This study focuses on Kavaklarboğazı Salt Marsh as the coastal area to identify the pollution loads washed off from its basin with different landuse types. Kavaklarboğazı Salt Marsh is located in the southeast of Güllük Bay on the Aegean coast of Turkey (Figure 1). The inlet of the marsh is located 3.5km away from the Güllük harbor. The Güllük center covers 1.78km^2 with an estimated population of 6021 in 2019, also making it the most populous city on the coast of Güllük Bay. As previous studies point out, local industries are mainly based on fish farming for sea bass and bream, and the export of bauxite from the Güllük harbor. Public port and nearby private piers in Güllük Bay have a capacity of handling over 5 million tons of cargo per year (Acar, 2015). The pollution caused by the

freighter ships anchoring offshore at the commercial port, which leave their ballast waters to the bay has been often brought to the local agenda. Tourism is also an important source of income for the local population. Increasing number of the residential housing around the bay lead to dramatic landscape modification and also put a remarkable pressure on the natural areas nearby.
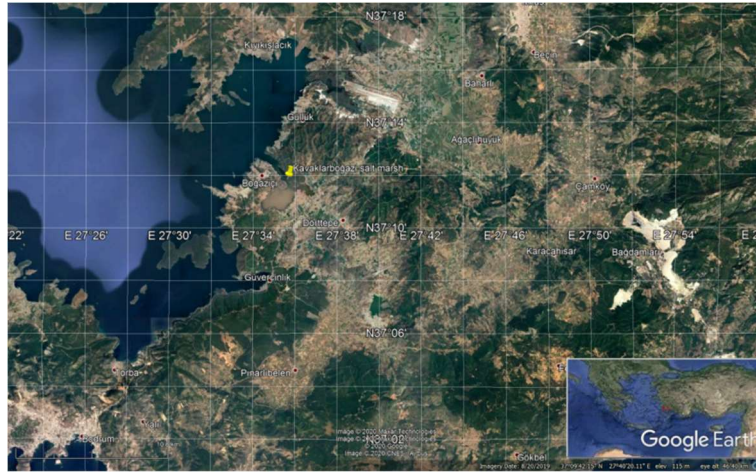
Figure 118. Kavaklarboğazı Salt Marsh (Google Earth, 2020)

Sarıçay and Değirmendere streams end up at Dalyan estuary, which is the biggest wetland around the bay with a critically high pollution carried from both streams. Although basins of both streams have wide zones of natural vegetation, irrigation and over fertilization are used intensively in agricultural regions close to the river, which leads to a deterioration in water quality. The residential areas, especially Milas district with a population of 141107 in 2019, heavily pollute Sarıçay due to their domestic wastewater. The Yatağan thermal power plant located in the Değirmendere basin causes sulfur dioxide (SO_2) pollution through its atmospheric discharge with an effective radius of 25km to the region. In addition, 238U, 232Th, 226Ra radioisotopes detected in lignite deposits, which spread over the region together with the flue gas. They reach Dalyan with surface streams and float from there to the waters of the Güllük Bay (Büke & Köne, 2009).

Milas Bodrum Airport is located on the northeastern plains, 6km away from the Güllük city center. The construction of Milas Bodrum Airport was completed in 1997. 470ha of wetland around Dalyan estuary was dried for the construction. In order to dry the wetland, Sarıçay and Değirmendere streams adjacent to the airport were taken into an artificial canal and directed to the bay, which also greatly reduced the pollution absorption capacity of the wetland. Since 2000s, the bay has been exposed to water pollution due to high number of fish farming and aquaculture facilities. Most of these farms have expelled since 2007, when the farm wastes caused an environmental crisis in the bay. Since there is very low water current at the bay, the residue originated from the fish farms is still visible at the bottom of the sea.

In addition to those mentioned above, another factor that increases the level of pollution in Güllük Bay is the pollutants drained to the Kavaklarboğazı Salt Marsh. The aim of this study is to develop a basin model to calculate the pollution loads carried by surface streams to Kavaklarboğazı Salt Marsh.

2. TERRAIN ANALYSIS

In order to draw the boundaries of the basin surrounding the Kavaklarboğazı Salt Marsh, ASTER Global Digital Elevation Model V003 is used to derive topographic information. The spatial resolution of the model is 1 arc second, approximately 30-meter horizontal posting at the equator (NASA / METI / AIST / Japan Spacesystems and U.S. / Japan ASTER Science Team, 2019). TauDEM v5.3 Hydrologic Terrain Analysis Tool in ArcGIS is used to analyse the digital elevation data retrieved from ASTER GDEM. TauDEM is an open source software written in C++ programming language and includes a suite of functions for deriving hydrological terrain analysis products (Tarboton, 1997). By using TauDEM v5.3 the digital topographic map is created for the

basin in ArcMap for Desktop v10.2.2, which is a component of Esri's ArcGIS suite of geospatial processing programs.

The basin surrounding the Kavaklarboğazı Salt Marsh covers an area of 349.71km². The basin of Kavaklarboğazı is bordered by the Yaran Mountains in the south and the Batı Menteşe Mountains in the east. The average height at the basin is 193 meters and the height of the mountains in the southeast reaches up to 873 meters. The average slope of the basin is 17.4% and its dominant exposure is towards the north. The altitude map, streams and the borders of the surrounding basin are shown in Figure .

Figure 2. The altitude map, streams and the borders of the basin (embedded) (OpenTopoMap, 2020)

The basin is divided into 5 sub-basins. Drainage routes are determined on the digital topographic map (Figure 19). Main streams draining to the marsh are the Kavaklarboğazı stream and the Kemikler brook, which have subbasin areas of 286.48km² (Sub-basin-4) and 41.06km² (Sub-basin-3) respectively. Sub-basins 1, 2 and 5 have a total area of 13km². There are no persistent water bodies in these small sub-basins; they only drain the surface runoff from the northern side into the salt marsh in rainy seasons.
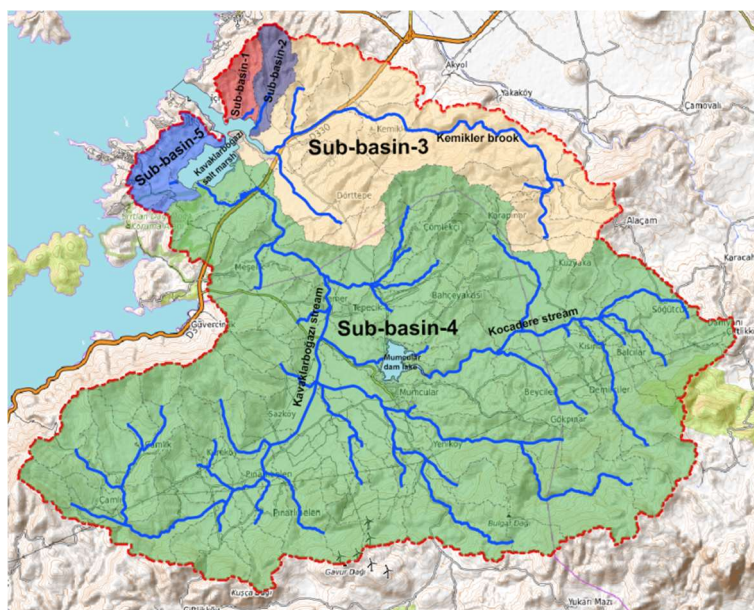
Figure 19. Sub-basins

The main stream of Kavaklarboğazı has a 26.5km length and a lot of tributaries, most of them dry in summer. Biggest tributary of the Kavaklarboğazı stream is the Kocadere stream with a 19km main channel length. The basin surrounding the Kavaklarboğazı Salt Marsh has dense agricultural areas of 12500ha amid Yeniköy, Pınarlıbelen, Çiftlikköy and Dörttepe villages. To provide water for irrigation from the Kocadere stream, the Mumcular dam is built in 1989. It serves an irrigation area of 1365ha (DSI, 2020a). The dam has an earth fill body and 32m height from the stream bed. The volume of the dam lake at normal water level is 19.04 hm³, and the lake area is 1.42km² (DSI, 2020b).

The distribution of land slopes for each raster cell in sub-basins is calculated by using ArcMap tools on the digital terrain model (Figure). The stream network delineation for main and tributary channels is derived by using TauDEM. According to the digital model, the average slope of the main channel of Kavaklarboğazı stream is calculated as 0.76%, the average slope of the main channel of Kemikler brook is calculated as 0.88%, and the average slope of the Kocadere tributary stream is calculated as 1.16%.
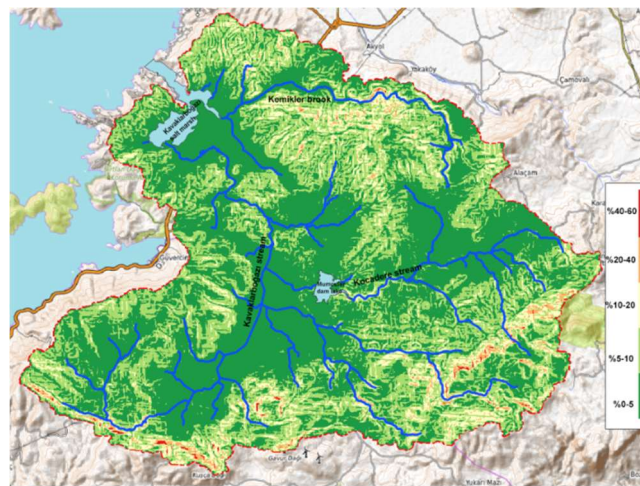
Figure 4. Aerial distribution of slopes

3. LAND USE TYPES

The CORINE Land Cover (CLC) inventory was initiated in 1985 (reference year 1990). It has been updated in 2000, 2006, 2012, and 2018. It consists of an inventory of land cover in 44 classes based on data from two satelites, Sentinel-2 and Landsat-8, for gap filling. CLC uses a minimum mapping unit of 25ha for areal phenomena and a minimum width of 100m for linear phenomena (Büttner et al., 2000). The land use types in the basin are acquired from CORINE Land Cover Project as raster data and used for defining the subcatchments in the sub-basins. The subcatchments are assigned according to the CORINE classifications and are shown in Figure . The distrubition of land classes in the basin is listed in Table 12.
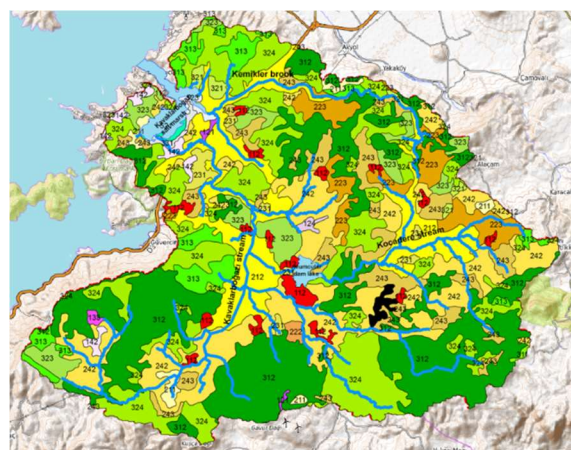
Figure 5. Corine 2018

Table 12. Corine landuse types (Corine, 2018).

Level-3 CORINE landuse classes	Code	Symbol	Sub-basin-1 Area (ha)	Sub-basin-2 Area (ha)	Sub-basin-3 Area (ha)	Sub-basin-4 Area (ha)	Sub-basin-5 Area (ha)	Total Area (ha)	Percentage (%)
Discontinuous urban fabric	112		-	-	63.43	623.60	1.66	688.69	1.99%
Industrial or commercial units	121		-	-	12.34	42.40	-	54.74	0.16%
Airports	124		-	-	-	65.09	-	65.09	0.19%
Construction sites	133		-	-	-	45.94	-	45.94	0.13%
Sport and leisure facilities	142		-	-	-	189.88	112.15	302.03	0.87%
Non-irrigated arable land	211		-	-	64.65	206.54	69.29	340.48	0.98%
Permanently irrigated land	212		1.25	56.54	914.36	2805.01	-	3777.16	10.90%
Fruit trees and berry plantations	222		-	-	-	92.91	-	92.91	0.27%
Olive groves	223		-	-	684.36	900.43	-	1584.79	4.57%
Pastures	231		-	-	27.95	355.28	-	383.23	1.11%
Complex cultivation patterns	242		-	-	224.48	5232.49	38.14	5495.11	15.86%
Land principally occupied by agriculture, with significant areas of natural vegetation	243		-	-	338.16	2012.82	59.45	2410.43	6.96%
Broad-leaved forest	311		-	-	-	24.57	-	24.57	0.07%
Coniferous forest	312		-	-	1098.04	8200.85	61.33	9360.22	27.01%
Mixed forest	313		189.18	62.33	295.93	799.84	-	1347.28	3.89%
Natural grasslands	321		43.90	28.74	101.51	57.19	-	231.35	0.67%
Sclerophyllous vegetation	323		18.94	35.14	433.93	761.23	157.92	1407.15	4.06%
Transitional woodland-shrub	324		102.81	230.26	1669.05	4424.96	170.63	6597.70	19.04%
Beaches, dunes, sands	331		-	-	24.10	61.05	7.57	92.72	0.27%
Burnt areas	334		-	-	-	133.79	-	133.79	0.39%
Water bodies	512		-	-	-	100.67	-	100.67	0.29%
Coastal lagoons	521		-	-	0.11	39.51	3.80	43.42	0.13%
Sea and ocean	523		-	8.80	63.71	1.31	2.03	75.85	0.22%
	Total		356.08	421.81	6016.12	27177.36	683.97	34655.35	100%

According to the CORINE data, 27.01% of the total basin area consists of coniferous forests, 19.04% of transitional woodlands or shrubs, 15.86% of complex cultivation patterns, 10.90% of permanently irrigated lands and 3.34% of urban, industrial, commercial, sport or leisure units, airports and construction sites. Most of the irrigation lands are accumulated in Sub-basin-4, which is drained by Kocadere and Kavaklarboğazı stream. 11.6km^2 of Sub-basin-4 consist of irrigated and nonirrigated agricultural areas, 14.46km^2 of seminatural areas, mainly coniferous forests. 2.25km^2 of Sub-basin-3 is agricultural zones and 3.62km^2 forests and seminatural areas.

4. HYDROGEOLOGICAL CONDITION

The basin is examined in terms of geological and lithological formation according to the geospatial data of the General Directorate of Mineral Research and Exploration (Figure). The Menderes massif rocks with autochthonous character, the Lycian nappes settled as allochthonous rocks and the young sediments covering these two rock groups determine the stratigraphic structure of the region. The

units forming the lithologies in the Menderes Massif from older to younger are metamorphic basement, Milas formation and Kalınağıl formation (Barut et al., 2001).
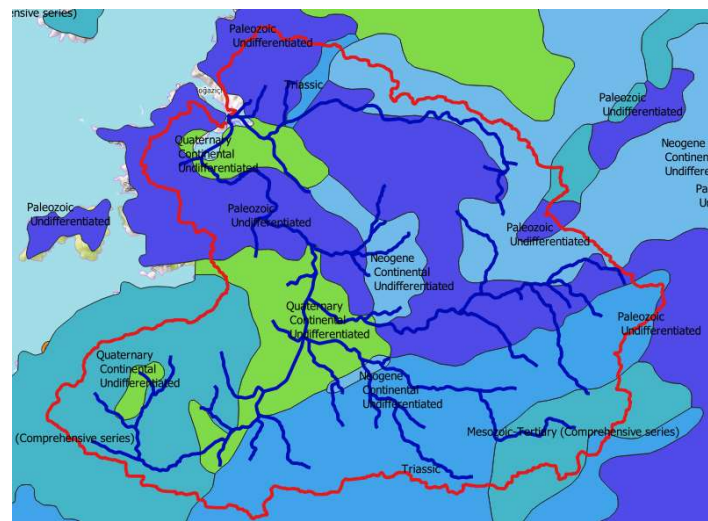
Figure 6. Geological formations (MTA, 2002)

The Precambrian metamorphic basements consist of gneisses, schists, quartzites and marbles (Akat, 1975). The areas where marbles are transitional with schists form local karstic aquifers. Milas formation on the schists consists of dolomitized limestone. This layer is permeable and karstic. The Paleocene Kalınağıl formation, overlying the Milas formation is the uppermost rock scale of the autochthonous layer (Eroskay et al., 1992). Brecciated red limestones, cherty, micritic limestones levels of this formation are karstic and permeable. The upper shale, marl, siltstone levels of the formation is impermeable. The region, where the limestones in the lower levels are exposed, are karstic areas and can be considered as locally permeable in terms of hydrogeology (Barut et al., 2001). The Lycian nappes overlie tectonically the Eocene flysch of the Menderes massif. The emplacement age of the Lycian nappes over the Menderes massif is regarded as Mid-Eocene (Okay, 1985).

The Güllük formation is the lowest rock of the allochthonous Lycian nappes. It is mainly composed of conglomerate, sandstone, shale layered and lens-shaped limestone rock formations (Barut et al., 2001). The age of the Güllük formation is Late Permian-Early Triassic (Çağlayan, 1980). Due to its lithological properties it is impermeable and it creates a barrier in terms of groundwater movement in the region (Eroskay et al., 1992). The sandstone near the base of the formation and the limestones under the shales are karstic in character.

5. METEOROLOGICAL DATA

Average precipitation amounts, average humidity and temperatures are calculated by using the 5-year data between 2011 and 2016 obtained from the Milas-Bodrum Airport Meteorological Observation Station no. 17291, located 8.5km northeast of Kavaklarboğazı Salt Marsh. According to the data, the yearly averaged temperature of the basin is 17.6ºC and the yearly averaged total rainfall is 819mm. Monthly averaged precipitation is about 138mm in winter, 6mm in summer, and 65mm in spring and autumn. According to the data, there is no snowfall in the region. Monthly mean, minimum, maximum temperature (°C), mean precipitation (mm) and mean humidity (%) are listed in Table . Daily total and monthly averaged daily precipitation is shown in Figure 720.

Table 2. Monthly mean, min., max. temperature (°C), precipitation (mm) and humidity (%).

	Jan	Feb	Mar	Apr	May	Jun	Jul	Agu	Sep	Oct	Nov	Dec
Mean Temp.(°C)	7.8	8.7	11.2	14.8	19.8	25.2	29	28.9	24.1	18.7	13.6	9.4
Min. Temp. (°C)	4.1	4.6	6.3	9.5	14	18.7	22.2	22.5	18.4	13.8	9.3	5.7
Max. Temp (°C)	11.8	12.9	15.9	19.8	25.1	30.9	35.2	35.1	30	24	18.3	13.4

	Jan	Feb	Mar	Apr	May	Jun	Jul	Agu	Sep	Oct	Nov	Dec
Precipitation (mm)	148	121	90	66	40	10	3	4	18	61	113	145
Evoporation (mm)	18.36	18.97	30.02	52.58	87.3	114.38	145.54	130.91	87.25	57.46	33.42	22.32
Humidity (%)	78%	74%	70%	67%	60%	47%	39%	42%	50%	62%	72%	78%
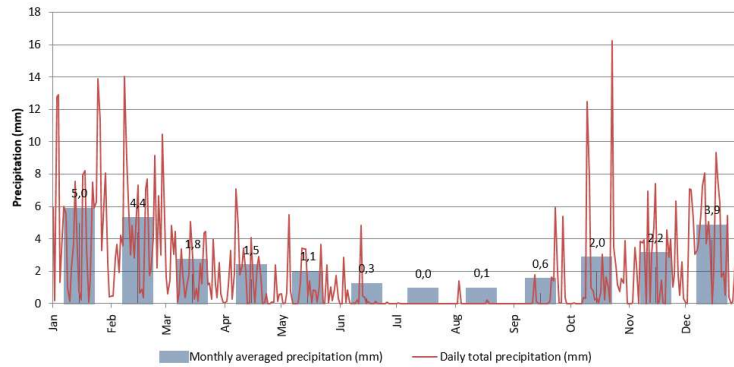
Figure 720. Daily total and monthly averaged daily precipitation (mm)

6. SWMM APPLICATION

SWMM (Storm Water Management Model) v5.1 is used to model the surface runoffs to the salt marsh and distributed loads carried by them. SWMM is a dynamic rainfall-runoff simulation model first developed in 1969 and used for simulation of quantity and quality of surface runoff. "SWMM tracks the quantity and the quality of runoff generated within each subcatchment, and the flow rate, the flow depth, and the quality of water in each pipe and channel, during a simulation period comprised of multiple time steps" (Rossmann & Huber, 2016a).

The simulation is performed as a series of water and contaminent flows between the compartments of the model. The atmospheric compartment calculates the precipitation and the pollutants in the precipitation. The land surface compartment calculates the surface contaminants and the surface flows in the land. The groundwater compartment calculates the infiltrations from land surface. A portion of this is transferred to the transport compartment, which makes hydraulic calculations for surface flow drainage. These compartments can also run individually (Rossmann & Huber, 2016a).

The model simulates the surface runoff by rendering the subcatchment as an ideal rectangular surface area with a uniform slope (S) and a uniform width (W) that drains to a single outlet channel. The modeled subcatchment receives inflow from precipitation and loses from evoporation and infiltration. The surplus is accumulated on the surface upto the depth (d). Ponded water above the depression limit becomes the runoff flow (q). The change in the depth above the surface can be expressed as in Equation 1 (Rossmann & Huber, 2016a).

$$\frac{\partial d}{\partial t} = i - e - f - q \tag{1}$$

Here, i is the rate of rainfall + snowmelt (mm/s), e is the surface evaporation rate (mm/s), f is the infiltration rate (mm/s) and q is the runoff rate (mm/s). Model uses Mannings equation (Equation 2) to simulate the flow across the subcatchment's surface assuming a uniform flow.

$$Q = \frac{1}{n} S^{1/2} \cdot R_x^{2/3} \cdot A_x \tag{2}$$

Here, n is surface roughness coefficient, S is the average slope of the subcatchment, A_x is the area across the subcatchment's width (m^2) through which the runoff flows, and R_x is the hydraulic radius (m) associated with this area. If A_x is assumed as a rectangular area with a width of W and height of $(d-d_s)$, then $A_x = W(d-d_s)$ and $R_x = (d-d_s)$. Substituting these into Equation 2 gives Equation 3 (Rossmann & Huber, 2016a).

$$q = \frac{W \cdot S^{1/2}}{A \cdot n} (d - d_s)^{5/3} \tag{3}$$

SWMM uses equations to generate surface runoff on the basis of an idealized rectangular subcatchment area with uniform properties. In order to apply this model to urban and natural areas, the percent imperviousness parameter is implied to the original mass balance equations (Equation 1 and 3). The subcatchment is divided into 3 sub-areas, namely, pervious subarea, impervious subarea with depression storage, and impervious subarea without depression storage. These subareas are assumed to discharge their runoff independently to the same outlet location (Rossmann & Huber, 2016a).

Channels/conduits that drain the flow are defined as a network of links connected at nodes. The surface runoffs enter to the nodes on the network and are transported along the channels/conduits defined as links between nodes. SWMM solves the equations of one-dimensional, gradually varied, unsteady flow, namely St. Venant equations (Equation 4 and 5), throughout the node and the link network. It determines the water level at each node and the flow rate and flow depth within each link at each time step during a simulation period (Rossmann, 2017).

$$\frac{\partial A}{\partial t} + \frac{\partial Q}{\partial x} = 0 \tag{4}$$

$$\frac{\partial Q}{\partial t} + \frac{\partial (Q^2/A)}{\partial x} + gA\frac{\partial H}{\partial x} + gAS_f = 0 \tag{5}$$

Here, x is distance (m), t is time (s), A is cross sectional area of the flow (m^2), Q is flow rate (m^3/s), H is the hydraulic head in the channel (m), Z is invert elevation (m), S_f is friction slope (head loss per unit length), gravitational acceleration (m/s^2).

In order to simulate the surface flow, the sub-basins are split into subcatchments according to regions geological formation and its CORINE land cover definition. According to their topography, average slope and characteristic width of the subcatchments are calculated by using GIS tools. The nodes and links are defined on drainage routes derived by TauDEM. The subcatchments, drainage routes and outfalls of the model are shown in Figure.
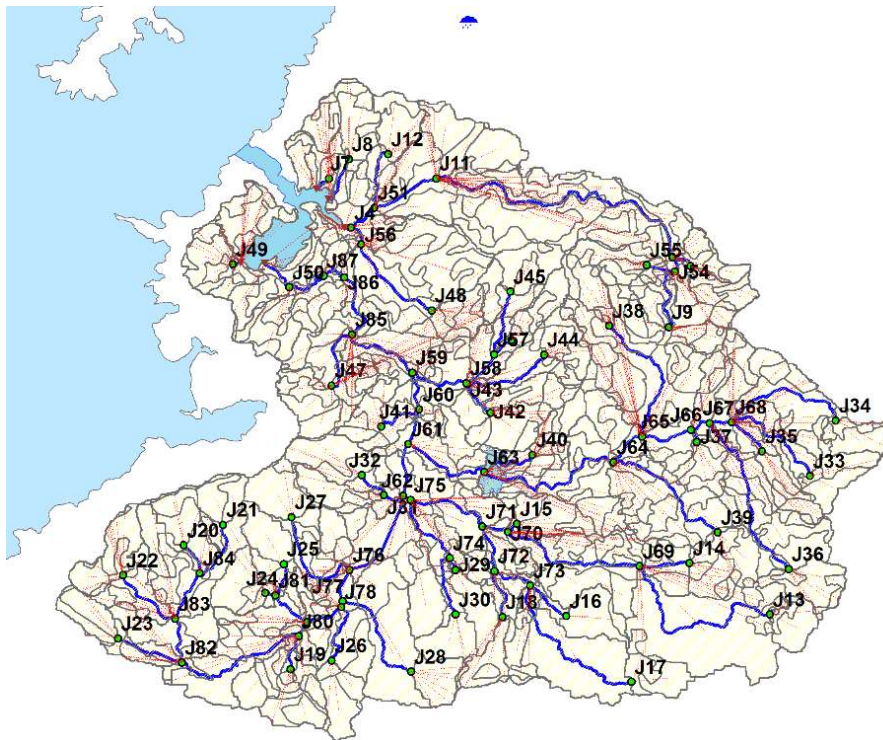
Figure 8. Subcatchments, drainage routes and outfalls

The precipitation data, defined as 5 year averaged daily time series are applied to all subcatchments in the model. Temperature and humidity are defined as monthly averaged time series during the

simulation period. Subcatchments in the basin are set as permeable or impermeable. The imperviousness percent, the surface roughness coefficient, the depression storage and other hydraulic parameters of the subcatchments in the model classified according to its landuse and geological formation are shown in Table 3.

Table 313. Hydrological variables of subcatchments defined by its landuse.

Type of land use	Impermeable areas (%) [*]	Manning coef. impermeable areas [**]	Manning coef. permeable areas [**]	Storage height impermeable areas [***] (mm)	Storage height permeable areas [***] (mm)	Impermeable areas without storage (%)
Industrial or Commercial Units	76	0.015	0.035	1.27	2.54	40
Discontinuous Urban Fabric, Sport and Leisure Facilities	51	0.030	0.075	1.27	2.54	25
Airports	56	0.015	0.12	1.27	5.08	50
Construction Sites and Sands	10	0.030	0.032	1.27	5.08	25
Urban Green Areas, Olive Groves, Pastures Cultivated Areas with Natural Vegetation	2	0.030	0.055	1.27	5.08	10
Coniferous Forests, Mixed Forests, Natural Meadows, Sclerophyll Vegetation, Transitional Woodland-Shrub, Areas with Sparse Vegetation	1.9	0.030	0.35	1.27	7.62	10
Non-irrigated Agriculture- Non-irrigated Fruits	2	0.030	0.12	1.27	7.62	10
Irrigated Agriculture-Irrigated Fruits	2	0.030	0.12	1.27	5.08	10

[*]USEPA(2011), [**]Yen (2001), [***]ASCE (1992)

Accumulation and drainage of the pollutants by surface flow are calculated in SWMM by buildup and washoff processes. "The buildup process calculates the accumulated mass of pollutant loads in the field defined on the model depending on the land use type. This process is expressed in SWMM by a semi- saturation curve. The buildup amount is da function depending on the number of consecutive days without precipitation" (Rossman & Huber, 2016b).

As reference values for the pollutant load buildup values, the average values of annual pollutant loads according to land use types presented in the report of the national surface flow program results (USEPA, 1983; Cebe and Balas, 2018) are used as shown in Table 414.

Table 414. Maximum pollutant build-up values defined by landuse (C1, kg/ha).

TYPE OF LAND USE	TSS	BOD	COD	Total P	Dissolved P	Total N	NO_2-NO_3
Industrial and Commercial Units*	1460	98	666	3.40	1.20	15.40	7.0
Discontinuous Urban Fabric, Sport and Leisure Facilities*	550	36	250	1.30	0.50	5.80	2.60
Discontinuous Rural Areas **	550	36	250	1.30	0.50	5.80	2.60
Airports **	1460	98	666	3.40	1.20	15.40	7.0
Construction Sites **	1460	98	666	3.40	1.20	15.40	7.0
Urban Green Areas - Olive Groves	550	36	250	1.30	0.50	5.80	2.60

- Pastures - Cultivated Areas with Natural Vegetation**							
Coniferous Forests - Mixed Forests - Natural Meadows - Sclerophyll Vegetation - Transitional Woodland-Shrub Areas - Areas with Sparse Vegetation**	250	18	-	0.75	0.25	2.90	1.30
Non-irrigated Agriculture - Non-irrigated Fruits**	550	36	250	15	7.5	85	43
Irrigated Agriculture - Irrigated Fruits**	550	36	250	15	7.5	85	43

*,**USEPA, 1983; ***Cebe & Balas, 2018

The wash-off process is expressed by a constant average wash-off coefficient (C1). It refers to the average concentration of pollutant in the surface flow and does not change during the simulation period (Gironás et al., 2009). Although the quality of stormwater runoff can be calculated by using the measured data from runoff events, there is a lack of data on water quality especially from various land use types. The collected measurements are mostly from urban stormwater events with a large variability in the pollutant concentration data (Müller et al. 2020).

The U.S. Nationwide Urban Runoff Program (USEPA, 1983) provides a larger scale stormwater quality data as presented in Table .

Table 5. Average concentration of surface water quality parameters by landuse (USEPA, 1983).

POLLUTANT	Residential Area	Mixed	Commercial	Open Space
TSS (mg/L)	101	67	69	70
BOD (mg/L)	10	7.8	9.3	-
COD (mg/L)	73	65	57	40
Total N (μg/L)	1900	1288	1179	965
$NO_2 - NO_3 - N$ (μg/L)	736	558	572	543
Total P (μg/L)	383	263	201	121
Dissolved P (μg/L)	143	56	80	26

7. RESULTS

The surface runoff and pollution transport model application on Kavaklarboğazı Salt Marsh basin is run in SWMM. As a result of one-year simulation of the model, the amount of average flow and total annual pollution loads drained from the basin to the Kavaklarboğazı Salt Marsh is estimated. The calculated daily distribution of total inflow from Sub-basin-3 and 4 drained into the Kavaklarboğazı Salt Marsh are shown in Figure .
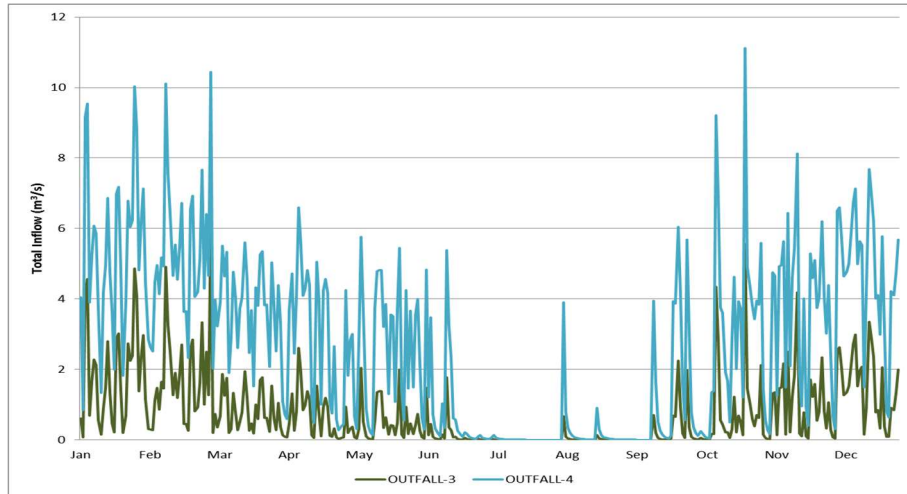
Figure 9. Daily distribution of total inflow from Sub-basin 3 and 4 to salt marsh (m³/s)

The average inflow drained in Kemikler brook from Sub-basin-3 to the salt marsh is 1.69m³/s in winter, 0.67-0.69 m³/s in spring and autumn, and 0.10m³/s in summer. The annual average of the flow rate drained in Kemikler brook is 0.77m³/s. The flow drained in Kavaklarboğazı stream from Sub-basin-4 is 5.05m³/s in winter, 3.11-2.56 m³/s in spring and autumn, and 0.40m³/s in summer. Sub-basin 1, 2 and 5 have a smaller drainage area and are dry in summer, but produce flows in other seasons. Daily distribution of total inflow from Sub-basin 1, 2 and 5 are shown in Figure .
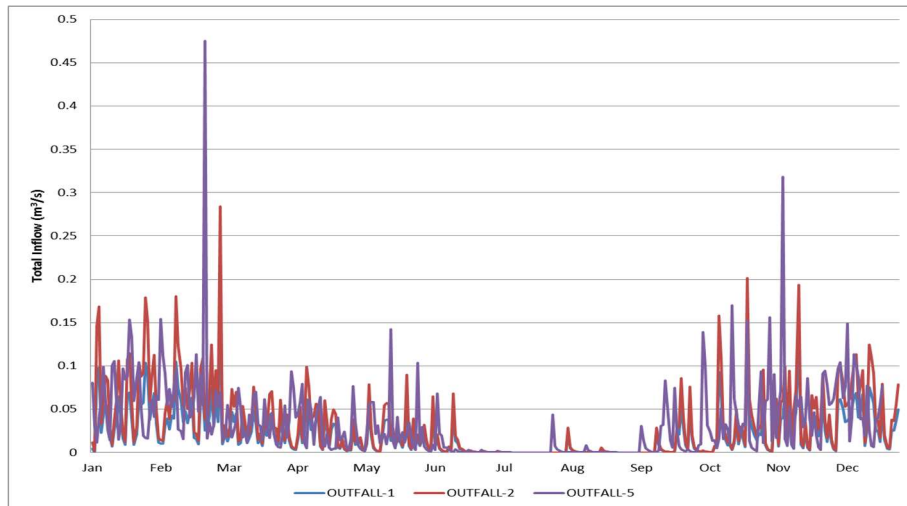
Figure 10. Daily distribution of total inflow from Sub-basin 1, 2 and 5 to salt marsh (m³/s)

The annual averages of runoff calculated from Sub-basin 1, 2 and 5 are around 0.03m³/s. Average run-off flows in these basins, which are 0.05m³/s during the winter, spring and autumn, dry up completely in the summer. The monthly average of the total runoff inflow drained from all sub-basins into Kavaklarboğazı Salt Marsh is given in Table 615.

Table 615. Monthly averaged total inflow to Kavaklarboğazı Salt Marsh (m³/s).

Jan	Feb	Mar	Apr	May	Jun	Jul	Agu	Sep	Oct	Nov	Dec
7.31	7.37	4.73	3.53	3.33	1.17	0.02	0.27	1.53	3.82	4.63	6.07

According to the table, total flow rate from the surface runoff into the salt marsh has the highest value of 7.37m³/s in February and the lowest in July when the surface flow become almost dry. The total annual pollution loads transported to the salt marsh are given in Table .

Table 7. Total annual pollution load drained to Kavaklarboğazı by surface streams (tons).

TSS	BOD	COD	NT	NO$_2$+NO$_3$	PT	PC
6,29	796.18	3665.76	54.05	28.96	7.42	1.87

8. CONCLUSIONS

As the study have demonstrated, integrating land use data into a model of surface runoff and pollution transport provides a better understanding of environmental pollution. It can reliably calculate pollution originating from various landuse types. Consequently, it offers a more efficient tool for land use planning and management.

The particular simulation on Kavaklarboğazı Salt Marsh demonstrates the use of SWMM model to calculate the pollution loads carried by surface runoff by buildup and washoff processes by using average values of pollutant loads according to land use types, presented in the report of the national surface flow program results. In order to calibrate and validate the model, monitoring studies in the region can be carried out on the pollutant concentrations in Salt March and in surface runoffs towards it.

The model has shown that the pollution loads from surface runoff are majorly caused by agricultural fertilizers. Therefore, the annual pollution can be reduced by good agricultural practices in the basin. Planning and limiting the use of fertilizers can be another solution to the pollution load in the salt marsh. It may also be possible to confine the pollution loads by terracing the agricultural lands and creating green zones at the borders and along the route of streams carrying surface waters. As a result, integrating runoff and pollution models into land use planning provides better solutions to the conflicts between the economic and the ecological interests, hence the sustainability of natural areas.

REFERENCES

Acar, S. (2015). *Tsunami Hazard Analysis for Güllük Bay*. (Unpublished master's thesis in Civil Engineering). Graduate School of Natural and Applied Sciences, Middle East Technical University, Ankara, Turkey.

Aksu, A., Balkis, N. & Altuğ, G. (2020). Güllük Körfezi (Muğla-Türkiye) Yüzey Sedimentlerinde Toksik Metal Kirliliği. *Geological Bulletin of Turkey, 63,* 117-124. http://doi.org/10.25288/tjb.585304

Akat, U. (1975). *Menderes Masifi Güneyi GB Toros Kuşağı İlişkisi, (Ön Rapor)*, Maden Tetkik ve Arama Raporu, Rep., 5488, Ankara.

ASCE. (1992). *Design & Construction of Urban Stormwater Management Systems*, Water Environment Federation and American Society of Civil Engineers, New York, USA. https://doi.org/10.1061/9780872628557

Barut, İ., Eroskay, O. & Özer, N. (2001). *Milas-Ekinambarı ve Savran Tuzlu Karst Kaynaklarının Hidrojeokimyasal Araştırılması*. Tübitak Araştırma Projesi. Proje No: YDABÇAĞ-588/A.

Büke, T. & Köne, A.Ç. (2009). Yatağan Termik Santrali Çevresindeki Radyasyon ve SO2 Kaynakli Risklerin Değerlendirilmesi. Türkiye 11. Enerji Kongresi Bildirileri, 16-18.

Büttner, G., Feranec, J., Jaffrain, G. (2002). *Corine land cover update 2000, Technical Guidelines*. Eurpean Environment Agency, Technical Report 89, Copenhagen, Denmark.

Cebe, K. & Balas, L. (2018). Monitoring and modeling land-based marine pollution. Regional Studies in Marine Science, 24, 23-39. https://doi.org/10.1016/j.rsma.2018.06.010

Çağlayan, M.A. (1980). Menderes Masifi Güneyine Ait Bulgular ve Yapısal Yorum. *Jeoloji Mühendisliği Dergisi* 10: 9-17.

Demirak, A., Balcı, A. & Tüfekçi, M. (2006). Environmental Impact of the Marine Aquaculture in Güllük Bay, Turkey. *Environmental Monitoring and Assessment, 123*, 1–12. https://doi.org/10.1007/s10661-005-9063-y

DSI. (2020a). "DSİ 2019 Yılı Resmi Su Kaynakları İstatistikleri". Retrieved from: https://dsi.gov.tr/Sayfa/Detay/1344 [Accessed 03.04.2020].

DSI. (2020b). "Mumcular Barajı". Retrieved from: https://www2.dsi.gov.tr/baraj/detay.cfm?BarajID=129 [Accessed 03.04.2020].

Eroskay, S.O, Gürpınar, O., Gözübol, A.M. & Şenyuva, T. (1992). *Muğla-Gökova ile Milas-Savran ve Ekinambarı Karst Kaynaklarının Jeolojik ve Hidrojeolojik İncelemesi, Sonuç Raporu*, DSİ Genel Müdürlüğü, Ankara.

Gironás, J., L.A. Roesner and Davis, J. (2009). Storm Water Management Model Applications Manual. National Risk Management Research Laboratory, Office of Research and Development, USEPA, EPA/600/R-09/000, Ohio, USA.

Google Earth. (2020). Kavaklarboğazı salt marsh, 37°11'50.00"N, 27°35'37.16"E. Primary data layer, https://earth.google.com [Accessed 20 April 2020].

MTA. (2002). *Türkiye Jeoloji Haritası – Denizli Paftası*. Maden Tektik ve Arama Genel Müdürlüğü, Jeoloji Etütleri Dairesi, Ankara.

Müller, A., Österlund, H., Marsalek, J. and Viklander, M. (2020). The pollution conveyed by urban runoff: A review of sources. *Science of the total environment*, 709. https://doi.org/10.1016/j.scitotenv.2019.136125.

NASA/METI/AIST/Japan Spacesystems and U.S./Japan ASTER Science Team. (2019). ASTER Global Digital Elevation Model V003 [Data set]. NASA EOSDIS Land Processes DAAC. Accessed 2021-02-18 from https://doi.org/10.5067/ASTER/ASTGTM.003

Okay, A.İ. (1985), *Bafa Gölü-Muğla-Uşak arasında Menderes Masifi ve allokton birimlerin ilişkisi ve metamorfizması*: TPAO, Arama Grubu. Rep., 2030.

OpenTopoMap. (2020). Kavaklarboğazı salt marsh. Retrieved from https://opentopomap.org [Accessed 03 April 2020].

Rossmann, L.A. & Huber, W.C. (2016a). *Storm Water Management Model Reference Manual Volume I – Hydrology (Revised)*. EPA/600/R-15/162A Revised January 2016, Office of Research and Development, Water Supply and Water Resources Division, U.S. Environmental Protection Agency, Cincinnati, USA.

Rossmann, L.A. & Huber, W.C. (2016b). *Storm Water Management Model Reference Manual Volume II – Water Quality*. EPA/600/R-16/093, Office of Research and Development, Water Supply and Water Resources Division, U.S. Environmental Protection Agency, Cincinnati, USA.

Rossman, L.A. (2017) *Storm Water Management Model Reference Manual Volume II – Hydraulics*. EPA/600/R-17/111, Office of Research and Development, Water Supply and Water Resources Division, U.S. Environmental Protection Agency, Cincinnati, USA.

Somay, M.A. (2017). Investigation of Güllük (Muğla) Wetland Using Stable Isotopes (δ^{18}O, δD). *Bulletin of the Mineral Research and Exploration, 154*, 181-191.

Tarboton, D. (1997). A new method for the determination of flow directions and upslope areas in grid digital elevation models. *Water Resources Research*, 33 (2), 309–319.

USEPA. (2011). Estimating Change in Impervious Area (IA) and Directly Connected Impervious Areas (DCIA) for New Hampshire Small MS4 Permit, USEPA Region I, Boston, MA, USA. Retrieved February 22, 2021, from https://nepis.epa.gov/Exe/ZyPDF.cgi/P100ALMQ.PDF?Dockey=P100ALMQ.PDF

USEPA. (1983). *Results of the Nationwide Urban Runoff Program (NURP)*, Vol. 1, NTIS PB 84-185552, Water Planning Division, Washington DC, USA.

Yen, B.C. (2001). Hydraulics of Sewer Systems. Chapter 6 in *Stormwater Collection Systems Design Handbook*, L.M. Mays, ed., McGraw-Hill, New York, USA.

Yücel-Gier, G., Pazı, İ., & Küçüksezgin, F. (2013). Spatial Analysis of Fish Farming in the Gulluk Bay (Eastern Aegean). *Turkish Journal of Fisheries and Aquatic Sciences, 13*, 737-744. http://doi.org/10.4194/1303-2712-v13_4_19

14TH INTERNATIONAL CONFERENCE
ON HYDROSCIENCE & ENGINEERING

MAY 26-27, 2022
IZMİR-TURKEY

ICHE2022
IZMIR, TURKEY

FLOW PATTERNS AROUND SINGLE AND DOUBLE PERMEABLE AND IMPERMEABLE GROYNES

Obaidullah Safie

Department of Civil and Environmental Engineering, Nagoya Institute of Technology

Nagoya, Aichi, Japan

obaidullah.safie1@gmail.com

Akihiro Tominaga

Department of Civil and Environmental Engineering, Nagoya Institute of Technology

Nagoya, Aichi, Japan

a.tominaga@nitech.jp

ABSTRACT: Smooth deceleration of flow from mainstream to the bank with less turbulence around the structure is a desirable attempt for riverbank protection. It can be achieved by applying modifications to groyne permeability or layout. In this study, the flow in groyne fields of single and double groynes with various aspect ratios were investigated experimentally. Permeable pile-group groynes with two types of pile arrangements and a typical impermeable groyne were considered to identify an efficient design of pile arrangement within a pile-group groyne for obtaining a smooth flow deceleration. The results demonstrated significant effects of pile arrangement on the flow structure and turbulence in the channel. A gradual deceleration of the flow from the mainstream toward the bank with suppressed turbulence can be obtained by changing the pile arrangement. This study also revealed that the overall flow structure in the impermeable groyne field was strongly influenced by a downstream groyne. However, the flow structure in the pile-group groyne fields was mainly controlled by the pile arrangement of the upstream groyne.

1. INTRODUCTION

One of the effective methods of protecting a riverbank is construction of a series of groynes or spur-dikes to guide the flow, thus avoiding strong currents along the bank (Jansen et al, 1979). A groyne or spur dike is a hydraulic structure that extends from a bank into the river to control the flow direction and velocity.

Modifications in permeability and shape of groynes have been applied in the literature to reduce the velocity gradient, turbulence, or local scour near the groyne tip (Zhang et al, 2013; Uijttewaal, 2005).

Pile groynes are one of the common types of permeable groynes (Abam, 1993). For permeable pile groynes, gradual reduction of velocity from mainstream to the bank (Teraguchi et al, 2011), reducing local scour around structure (Alauddin et al, 2011), enhancement of sediment deposition for further stabilization and reclamation of the eroded bank (Teraguchi et al, 2008; Nakagawa et al, 2011), and reduction of the shear and turbulence intensities around the structure (Uijttewaal, 2005) are the main advantages that are reported in the literature.

Applications of pile-group groynes exist in rivers but are less common than impermeable types. Many pile-group groynes have been used along the Kiso and Yahagi Rivers in Japan for bank protection purposes. An example from the Kiso River is shown in Figure 1. However, few studies have been conducted to explain the effects of pile arrangement on the flow characteristics around a pile-group groyne. Ikeda et al (1991) reported flow retardation and sediment deposition along the bank behind a pile-group groyne. However, the study considered only one type of pile arrangement and a single pile-

group groyne. The pile-arrangement type is expected to affect the flow in the groyne field. Additionally, groynes are commonly used in series in river training works for bank protection, navigation or environment aims (Przedwojski, 1995). As a practical example, a series of 16 pile-group groynes with face to face spacing varying from 3 to 7 times the length of the groyne have been used for bank protection along a reach of the Yahagi River in Okazaki, Japan. Nevertheless, no detailed explanation of the flow characteristics in the groyne fields of multiple pile-group groynes with different pile arrangements has been found in the literature. It requires further investigations.

Figure 1. A series of pile-group groynes along the Kiso River, Japan

This study investigated the flow structure and turbulence around single and double groynes with various aspect ratios between the groynes. Experiments are conducted on different pile-group groynes and a typical impermeable groyne. The purpose of this research is to find a suitable pile-arrangement type to smoothly reduce the velocity from mainstream to the bank with suppressed turbulence around the structure. Additionally, to identify the effects of a downstream groyne on the flow structure in the groyne fields while using different aspect ratios in both of the permeable and impermeable groynes.

2. MATERIAL AND METHODS

The experiments were conducted in a 7.5m long, 0.3m wide, and 0.4m deep rectangular flume. The slope of the flume S was set to 0.001. The pile-groups were made of acrylic cylinders with diameter d of 0.5 cm and height h_d of 5.0 cm. Two types of pile-group groynes and a typical impermeable groyne were considered. Same pile density (number of piles), but different pile arrangements were used for both types of the pile-group groynes. Each groyne contained 7×7 piles on each side with two different pile arrangements, namely in-line and staggered arrays, as shown in Figure 2. The length L and width W of the pile-groups were 7.5 cm in both of the pile-groups, as shown in Figure 2. The spacing between the piles in both the longitudinal and transverse directions was $S_x = S_y = 0.67$ cm.

The groynes were attached to one side of the channel. Figure 3 shows the schematic view of the groynes in the flume. The origin was selected to be the downstream edge of the pile-group attached to the side wall, as shown in Figure 3a. First, the flow velocities were measured around a single groyne and then double groynes were considered. The face-to-face distance between the double groynes, aspect ratio a/L as shown in Figure 3a, was changing as 2, 3 and 4. The experimental conditions are noted in Table 1. The water depth h was set to 0.04 m before the installation of the groyne model in the flume.

Table 2 shows the cases nomenclature. Each case name begins with number 7 that indicates the number of rows and columns (7×7) combined with the letter L or S for in-line or staggered type, respectively, followed by the aspect ratio inside a bracket. Exceptionally, the aspect ratio of 0 is chosen for the single groynes. One experiment when no structure was installed in the channel, Case NoS, was also conducted. Case NoS was considered to capture and compare the changes in the flow that occurred after the installation of a groyne in the channel.

Table 1. Flow conditions.

Parameter	Value
Discharge Q (m³/s)	0.00187
Initial water depth h (m)	0.040
Mean velocity U_m (m/s)	0.156
Froude number F	0.25
Reynolds number Re	6216

Table 2. Cases nomenclature.

Aspect ratio	In-line	Staggered	Impermeable
Single groyne	7L(0)	7S(0)	Imp(0)
$a/L = 2$	7L(2)	7S(2)	Imp(2)
$a/L = 3$	7L(3)	7S(3)	Imp(3)
$a/L = 4$	7L(4)	7S(4)	Imp(4)
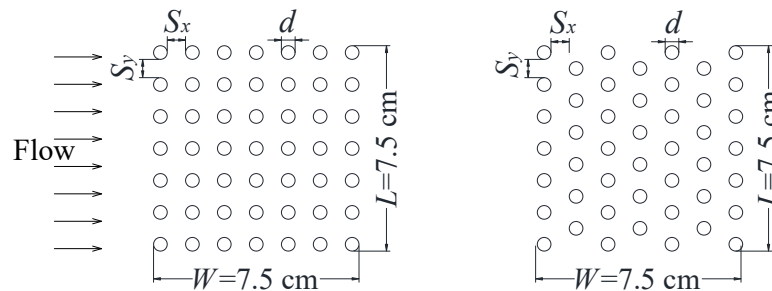
Figure 2. Pile-group groyne layouts, left: in-line, right: staggered

(a) Plan view   (b) Cross-section
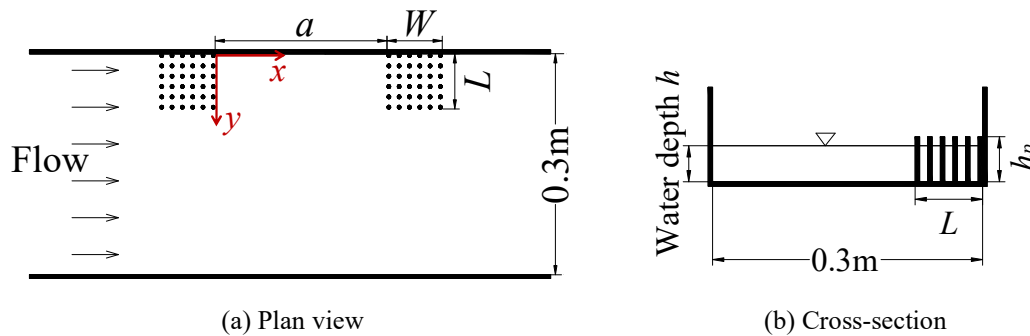
Figure 3. Pile-group placement in the channel

Velocity vectors were measured by the particle image velocimetry (PIV) method in horizontal ($x - y$) planes. A commercial PIV software (FlowExpert by Katokoken) was used for analyses. Nylon resin particles with 80 microns in diameter and 1.02 in specific weight were used for visualization of the flow. A 3 mm green laser light sheet was projected on horizontal ($x - y$) planes. For each case. Seven layers were recorded from the bed to the surface with 5 mm increments. The visual images were taken by a high-speed video camera with 200 frames in a second, and they were recorded as AVI files with 1024×1024 pixels. Time-averaged velocity vectors were obtained by processing 3200 successive images in 16 seconds. The averaging time of 16 s was confirmed to be sufficient to obtain steady time-average values by comparing with 50 s data.

3. RESULTS AND DISCUSSION

3.1. Vertical Profiles of Longitudinal Velocity

Flow characteristics are studied from bed to the water surface. Figure 4 shows the normalized vertical profiles of averaged longitudinal velocity U_w/U_m. The velocity U_w is averaged behind the length L of the groyne at section $x/L = 1.0$ and defined by Equation 1.

$$U_w(x,z) = \frac{1}{L}\int_0^L U(x,y,z)dy \tag{1}$$

Where, U is the time-averaged longitudinal velocity and z indicates the vertical direction.
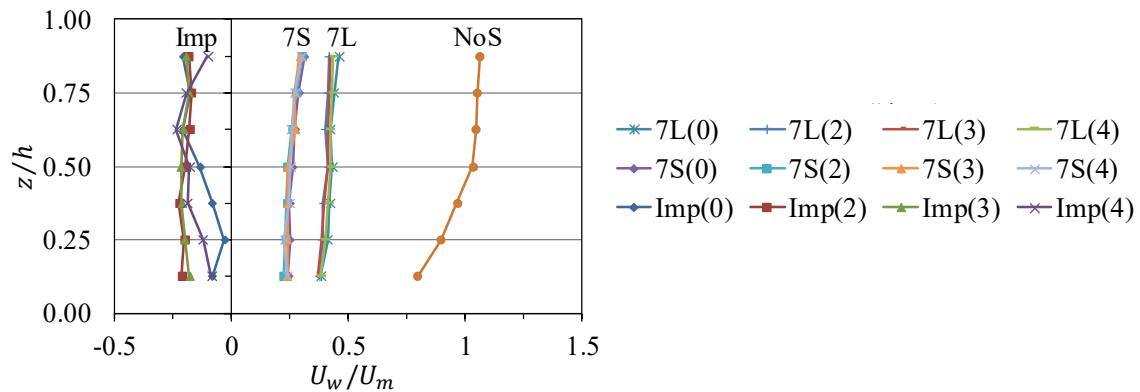
Figure 4. Vertical profiles of longitudinal velocities at $x/L = 1.0$

Figure 4 shows negative velocities with varying velocity gradients over the vertical for the impermeable groynes, Case Imp, which represents a return flow behind the structure. For the pile-group groynes, a milder velocity gradient over the vertical direction in comparison with the no structure condition (Case NoS) is noticed from Figure 4. The pile-group groynes contained small changes of the flow velocity and planar flow structures in the vertical direction downstream of the structure. As a typical planar flow structure, mid-layer data $z/h = 0.5$ are selected to show the results in the next sections of the present study.

3.2. Longitudinal Velocity Distribution

Figure 5 shows the contours of time-averaged longitudinal velocity distribution normalized by the mean velocity (U/U_m). In contrast with the impermeable groyne, the momentum transfer by the water flowing through the permeable groynes resulted in a unidirectional flow in the downstream, as shown in Figure 5. In all the permeable groynes in Figure 5, the in-line pile-groups show larger velocities behind the groyne compared to the staggered type.

The presence of a downstream groyne is a further resistance against the flow that discharges from the upstream pile-group. Therefore, from a comparison of the flow in the downstream of single pile-group groynes Cases 7L(0) and 7S(0) and double groynes Cases 7L(2) and 7S(2), respectively, it is clear that the downstream groyne caused further deceleration of the flow behind the second groyne, as shown in Figure 5. However, regardless of the aspect ratio between the groynes, the overall flow structure behind the upstream pile-group in the single and double pile-group groynes shows a rather similar pattern in each pile arrangement type. On the other hand, the single and double impermeable groynes show a remarkable difference in the length and intensity of vortex in the groyne fields.

Not only the flow magnitudes, but also the flow pattern significantly influenced by the pile arrangement type. Figure 6 shows the lateral distribution of longitudinal velocity behind groynes at section $x/L = 1.0$. The horizontal axis shows the normalized width of the channel and the pile-group length covered from 0 to 1, as it is shaded with blue color in the Figure 6. In all the staggered cases, the flow velocities are minimized near the bank and gradually increases toward the mainstream, as shown in Figure 6a and contours of Figure 5. In contrast, the in-line cases show high velocities near

the bank which drops to a minimum value behind the tip of the structure, at $y/L = 1.0$. Then it shows a sudden jump from the minimum to maximum velocity after this point, as shown in Figure 6a and contours of Figure 5.
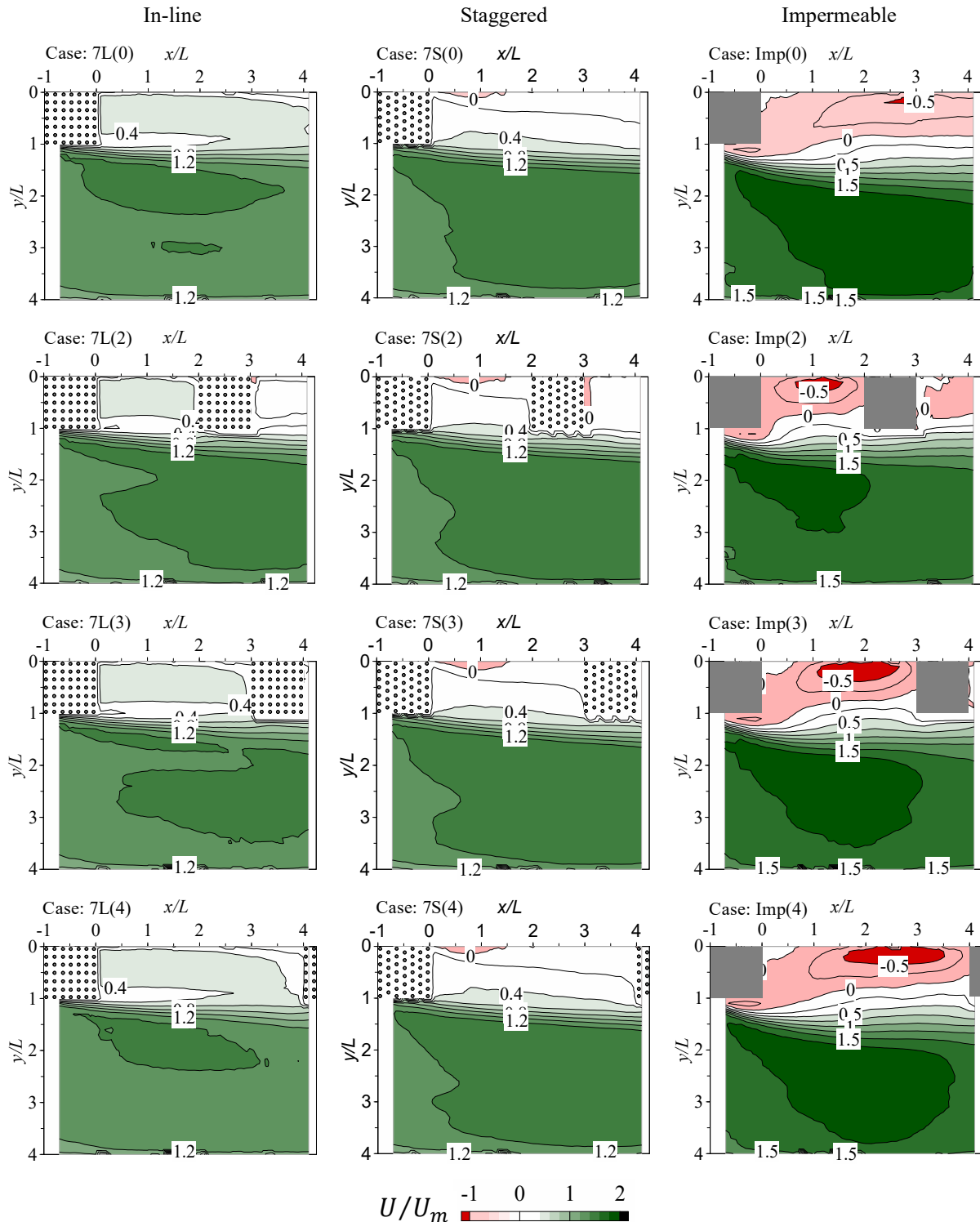
Figure 5. Contours of longitudinal velocity

The return flow near the bank in the impermeable groynes becomes faster by decreasing the aspect ratio, as shown in Figure 6b. It remarks the intensity of the primary gyre in the groyne field of the impermeable groynes.

Furthermore, the impermeable groynes show the peak velocities located around $y/L = 2$ in Figure 6b and the permeable groynes at almost $y/L = 1.5$ in Figure 6a, which shows that the permeability of pile-group groynes suppressed the width of the shear layer compared to the impermeable groyne and can provide wider navigational width.

3.3. Velocity Vector Fields

(a) Pile-group groynes   (b) Impermeable groynes
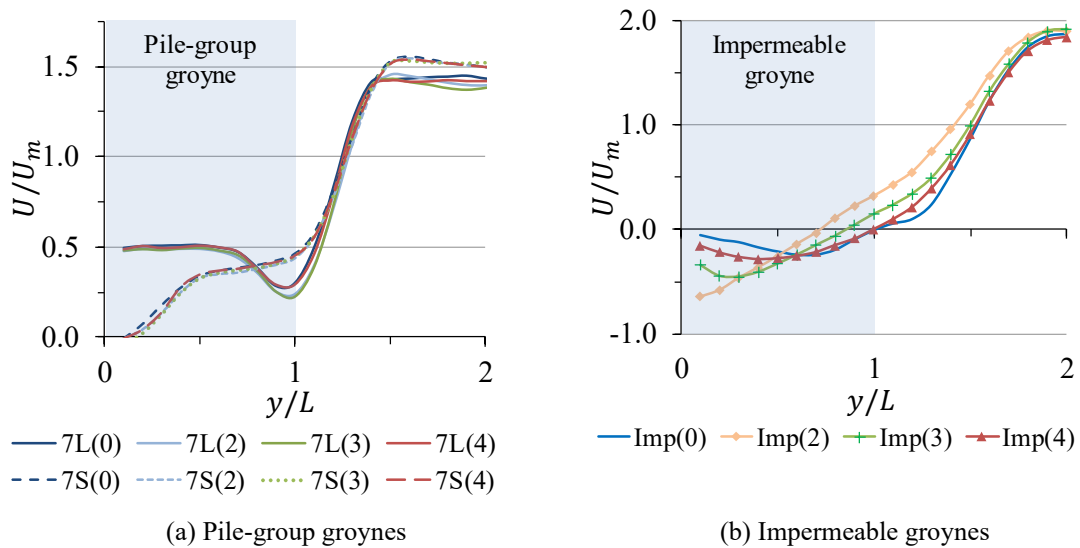
Figure 6. Longitudinal velocity profiles in the lateral direction at section $x/L = 1.0$
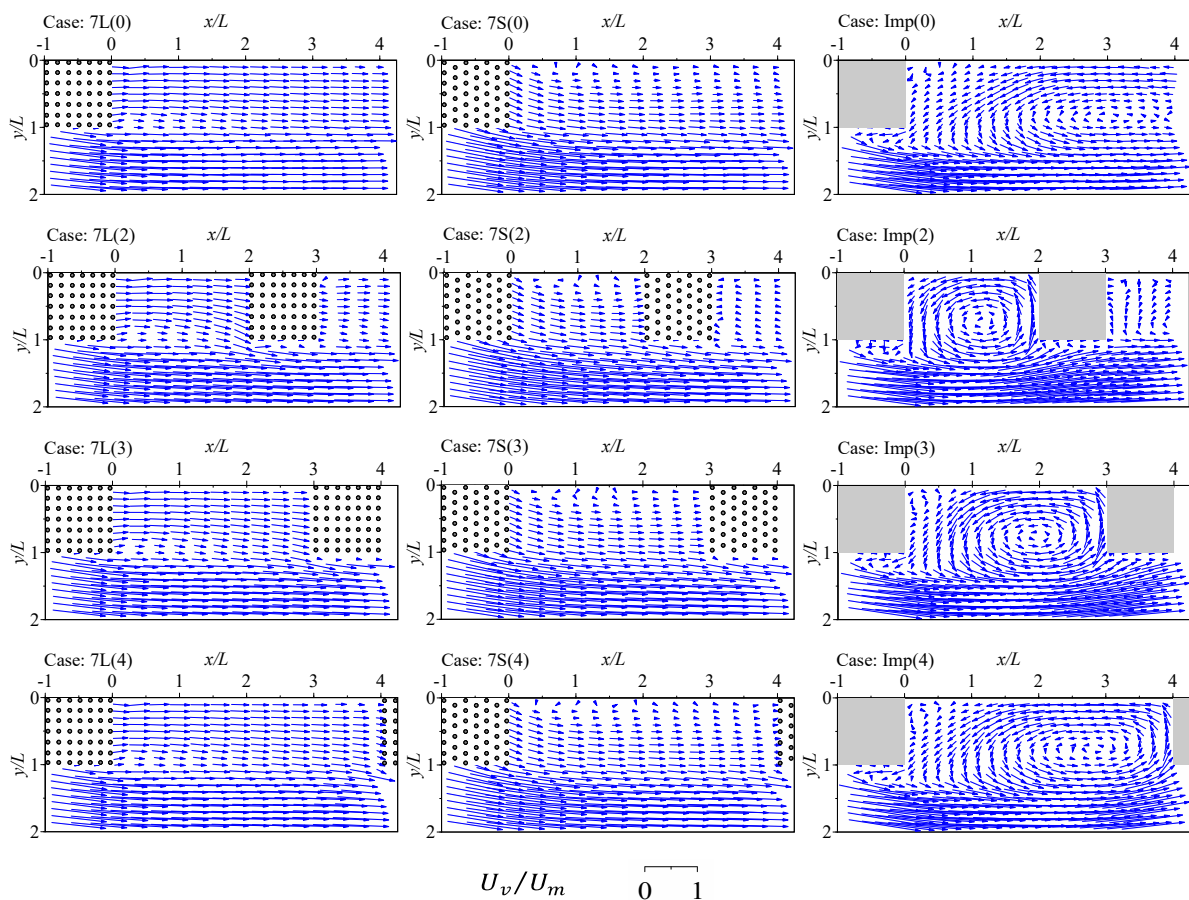
Figure 7. Velocity vector fields

The flow direction behind the groynes was also affected by the pile arrangement type. Figure 7 shows the velocity vectors U_v/U_m normalized by the mean velocity. U_v is the resultant velocity in the horizontal $(x - y)$ plane. The staggered pile arrangement guided the flow away from the bank to the mainstream. However, the flow direction behind the in-line arrangement cases show small difference from the x-direction.

Additionally, the velocity vector fields shown in Figure 7 best reveal the similarities and differences between the flow fields of single and double groynes. From Figure 7, it is clear that the effect of pile arrangement on the flow structure is maintained even in the presence of another downstream pile-group groyne. However, flow deviation takes place in the upstream of the second pile-group, and the deviation becomes weaker by increasing the aspect ratio, as shown by the vectors directions attached to the upstream tip of the second pile-group in Figure 7.
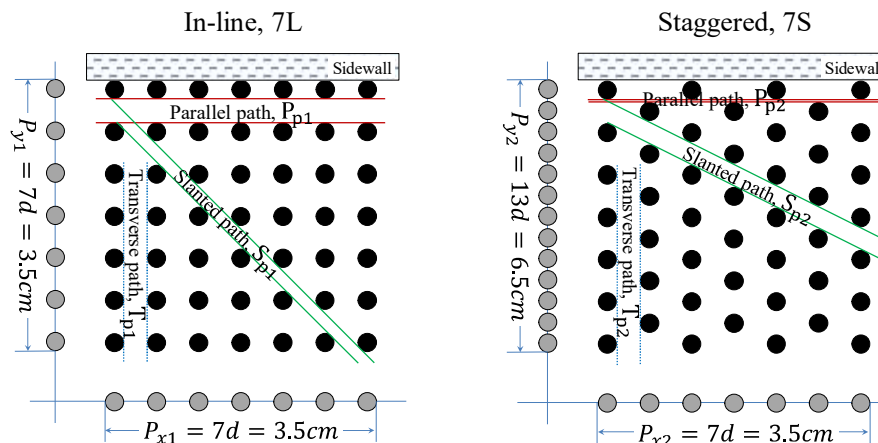
Figure 8. Projection of pile-groups on the x- and y-axes

The aspect ratio between the groynes governs the primary gyre size in the impermeable groyne field. Additionally, the generation of a secondary counter-rotating gyre just downstream of the first impermeable groyne depended on the aspect ratio. The smaller aspect ratio between the groynes in the Case Imp(2) resulted in the formation of a single primary gyre only. When the distance between the groynes increased to an aspect ratio of 3 or 4, the primary gyre elongated and also provided room for the formation of a small secondary gyre attached to the groyne and sidewall.

At the mainstream face of the impermeable groyne, a return flow is noticed from the vectors in Figure 7 and contours of Figure 5. It indicates that the flow separation started from the upstream edge of the impermeable groyne, while the permeability of pile-group groynes suppressed a sudden separation of the flow from the upstream edge of the groynes.

3.4. Mechanism of the Flow Change by Different Pile Arrangements

It deems worthy of clarifying how the arrangement of piles affects the flow structure in the downstream. Figure 8 shows the projection of the pile-groups on the x- and y-axes using gray circles. The projection area of the in-line arrangement 7L is smaller on the y-axis and the same on the x-axis compared to the staggered arrangement 7S. This controls the width of Parallel and Transverse paths inside the pile-groups, which are the normal distance between each pair of related lines in Figure 8, resulted in $P_{p1}>P_{p2}$ and $T_{p1}=T_{p2}$. Therefore, the in-line pile-group 7L allows larger flow in the longitudinal direction and higher velocity behind the pile-group compared to the staggered arrangement 7S, as shown in Figures 5-6a.

Regarding the flow pattern, Pile-group 7S created a completely different flow pattern than the 7L, which is a smooth gradual deceleration of the flow, as compared in Figure 6a. It can be related to the inclination angle of the Slanted path Sp. The Slanted path S_{p2} reached out behind the pile group in Case 7S, however, it ended to the mainstream side of the pile-group in the 7L arrangement, as shown in Figure 8. Additionally, the width S_{p2} is larger than S_{p1}. It means that the relatively larger width of the Slanted path with mild slope in type 7S better guided the flow from upstream to the downstream

of the pile-group compared to the type 7L. The discharged flow only behind the all 7S cases show a guided direction inclined from the bank to the mainstream, however, it remains almost in the same direction as the mainstream flow in the 7L cases, as shown in the velocity vectors of Figure 8.

The differences in the flow magnitudes and directions of the in-line and staggered arrangements revealed that the discharge flow is mainly influenced by the Parallel path P_{p1} in the in-line arrangement, however, it is controlled by both the Parallel path P_{p2} and Slanted path S_{p2} in the staggered cases.

3.5. Reynolds Stress Distribution
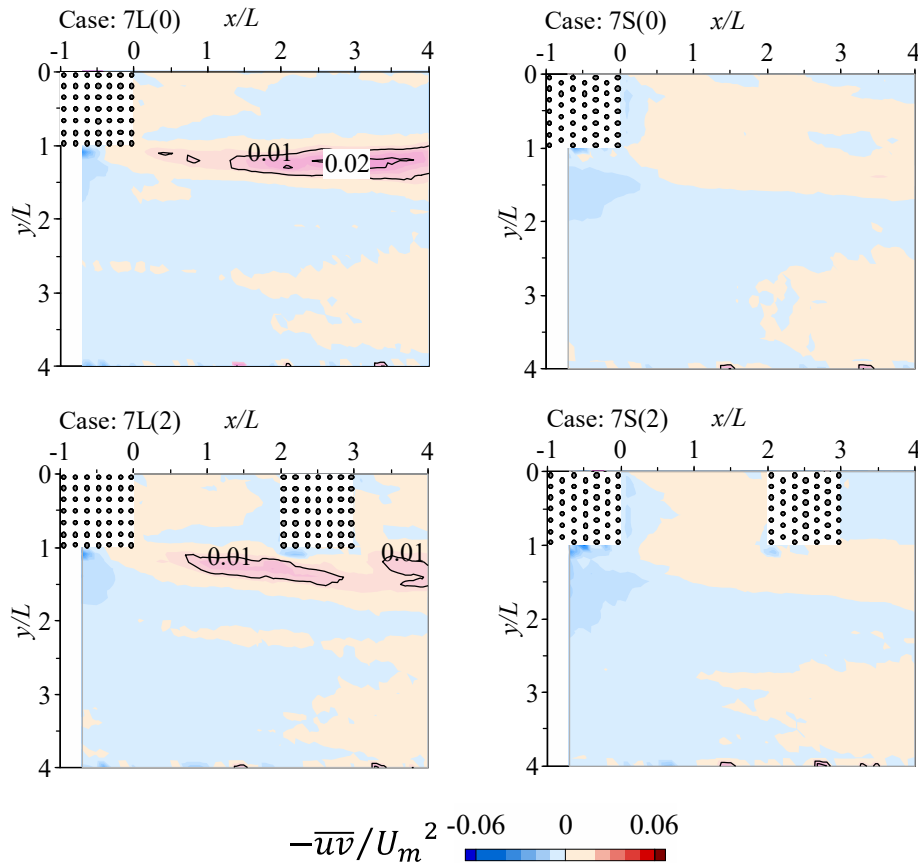
Figure 9. Contours of Reynolds stress

Figure 9 shows the contours of Reynolds stress $-\overline{uv}/U_m{}^2$. A dramatic difference is noticed in turbulence of the both types of pile arrangements. A region of intense turbulence appeared in the downstream of the in-line type 7L(0), whereas the staggered type 7S(0) did not generate such strong turbulence.

With reference to the velocity profiles in Figure 6a, the in-line cases 7L have a minimum velocity at the downstream behind the structure tip at $y/L = 1$, then there is a sudden jump to the maximum velocity in the mainstream. Therefore, abrupt change of velocity from a minimum to a maximum value created steep velocity-gradient and contributed to the generation of high turbulence along the shear layer in the in-line cases. On the other hand, staggered cases have minimum velocity near the bank and increasing gradually to the mainstream. As a result, the velocity increased smoothly from the bank to the mainstream and created a milder velocity-gradient than the in-line cases. Therefore, it suppressed the generation of such a high turbulence region in the channel.

Comparing the turbulence in single and double groynes, a sufficient distance is provided in the downstream of Case 7L(0) for turbulence intensification. However, the presence of another downstream groyne in the Case 7L(2) prevented turbulence intensification and disturbed the upstream

turbulence. A new turbulence region initiated from the downstream of the second groyne, as shown in Figure 9.

4. CONCLUSIONS

Flow in groyne fields of single and double groynes with various aspect ratios were investigated experimentally. Permeable pile-group groynes with two types of pile arrangements and a typical impermeable groyne were considered. This research was aimed at finding an efficient design of pile arrangement in a single or double pile-group groynes in order to produce a smooth flow reduction with low turbulence around the structure.

It was found that the type of pile arrangement within a group significantly affected the flow magnitude, pattern, and turbulence parameters. The staggered arrangement represented improvements compared to the in-line type. The gradual reduction of velocity from the mainstream to the bank and the substantial decrease in turbulence around the structure were the main favorable features of the staggered type.

Flow magnitude behind the pile-group was mainly controlled by the row spacing in the lateral direction. However, the flow pattern was significantly influenced by the width and inclination angle of the slanted path inside the pile-groups.

From a comparison of single and double groynes, it was revealed that the overall flow structure in the impermeable groyne field was strongly influenced by downstream groyne. On the other hand, the flow structure in single and double pile-group groyne fields was mainly controlled by the pile arrangement type of the upstream groyne. However, the second pile-group groyne induced changes in the flow deviation at the upstream tip of the second groyne and the turbulence in the channel.

Although the in-line pile arrangement is the most common type in practice, however, the results of this study suggested that the staggered arrangement creates a desirable flow change for bank protection behind the pile group. This study revealed some unknown perspectives of the flow induced by single and double pile-group groynes having different aspect ratios and pile arrangements. However, the detailed mechanism of the turbulence generation around the structure requires further investigations to be conducted in the future.

REFERENCES

Abam, T. K. S. (1993). Control of channel bank erosion using permeable groins. *Environmental Geology*, 22(1), 21-25.

Alauddin, M., Tashiro, T., & Tsujimoto, T. (2011). Design of groynes modified with both alignment and permeability for lowland river problems. *Journal of Japan Society of Civil Engineers, Series A2 (Applied Mechanics)*, 67(2), I_645-I_652.

Ikeda, S., Izumi, N., & Ito, R. (1991). Effects of pile dikes on flow retardation and sediment transport. *Journal of Hydraulic Engineering*, 117(11), 1459-1478.

Jansen, P. P., van Bendegom, L., van den Berg, J., de Vries, M., & Zanen, A. (1979). Principles of river engineering-The non-tidal alluvial rivers. *Delftse Uitgevers Maatschappij, Delft, The Netherlands*.

Nakagawa, H., Teraguchi, H., Kawaike, K., Baba, Y., & Zhang, H. (2011). Analysis of bed variation around bandal-like structures. *Annuals of Disaster Prevention Research Institute, Kyoto University*, 54(B), 497-510.

Przedwojski, B. (1995). Bed topography and local scour in rivers with banks protected by groynes. *Journal of Hydraulic Research*, 33(2), 257-273.

Teraguchi, H., Nakagawa, H., Muto, Y., Baba, Y., & Zhang, H. (2008). Flow and sediment transport around impermea-ble or permeable groins. *Journal of Japan Society of Civil Engineers, Annual Journal of Hydraulic Engineering*, 52, 175-180.

Teraguchi, H., Nakagawa, H., Kawaike, K., Baba, Y., & Zhang, H. (2011). Alternative method for river training works: bandal-like structures, *Journal of Japan Society of Civil Engineers, Series B1 (Hydraulic Engineering)*, 67(4), I_151-I_156.

Uijttewaal, W. S. J. (2005). Effects of groyne layout on the flow in groyne field: laboratory experiments. *Journal of Hydraulic Engineering*, 131(9), 782-791.

Zhang, H., Nakagawa, H., Ogura, M., & Mizutani, H. (2013). Experiment study on channel bed characteristics around spur dykes of different shapes. *Journal of Japan Society of Civil Engineers, Series A2 (Applied Mechanics)*, 69(2), I_489-I_499.

EXPERIMENTAL INVESTIGATION OF LOCAL SCOUR AROUND THE HEAD SECTION OF THE RUBBLE MOUND BREAKWATER IN CASE OF BROKEN WAVES

Yusuf Yasir

The Graduate School of Natural and Applied Sciences,

Dokuz Eylul University

Buca, Izmir, Turkey

yusuf.yasir@ogr.deu.edu.tr

Muhammed Ikbal Tortumluoglu

The Graduate School of Natural and Applied Sciences,

Dokuz Eylul University

Buca, Izmir, Turkey

muhammedikbal.tortumluoglu@ogr.deu.edu.tr

Mustafa Dogan

Civil Engineering Department, Dokuz Eylul University

Buca, Izmir, Turkey

mustafa.dogan@deu.edu.tr

ABSTRACT: Coastal structures and anchored vessels can be damaged by the effect of waves. In order to minimize these damages, long embankments called breakwaters are built to create a calm water level. The breakwaters absorb the energy of the wave before it reaches the shore, therefore reduce the wave height in the basin. However, in the trunk and head sections of these structures, scour and deposition occur with the effect of waves and currents. As a result of the scour, stability problems and damages can be occurred. For this reason, it is crucial to examine the scour that occurs around the breakwaters. Although there are existing studies on the head section of the rubble mound breakwater for unbroken waves, no experimental study examines the local scour under the effect of broken waves. Therefore, this paper aims to eliminate this deficiency in the literature and to examine the local scour that may cause stability losses in the breakwater for the broken wave case. In this study, the local scour in the head section of a rubble mound breakwater under the effect of the broken waves was experimentally investigated. The experiments were planned to be carried out by changing three different median grain diameter sand materials (0.23 mm, 0.55 mm, 1.85 mm), two different breakwater surface slopes (1:1.5 and 1:1.75), and five different regular waves (1.7 s, 2.0 s, 2.3 s, 2.7 s, 3.0 s) to find the critical parameters causing scours. The experiments showed that no significant local scour was observed in the case of 1:1.5 slope and 0.23 mm and 0.55 mm median grain diameter conditions. Therefore, less critical test cases with a coarser grain diameter of 1.85 mm and breakwater surface slope of 1:1.75 for seabed material were not needed to test.

Keywords: *Rubble mound breakwater, head section, broken waves, local scour, experimental study.*

1. INTRODUCTION

Stability losses caused by the scour can lead to significant repairing cost increases in coastal structures. Sumer and Fredsøe (2002) describe the situation caused by the scour in the coastal structures as " Scour is a threat to the stability of coastal structures " (p. 6). These structures may be pipelines, bridges breakwaters, group piles, offshore platforms, etc. The risk of the scour causing

stability losses around coastal structures makes the scour a phenomenon worth examining. For instance, there are extensive scour studies on bridge structures where any loss of stability can cost human life (Breusers and Raudkivi, 1991: Melville and Coleman, 2000). It is noticed that one of the important reasons for the collapse of bridges is the scour. Since the scour can destroy the other coastal structures, it makes the scour an important phenomenon. Similarly, breakwaters are also subjected to scour. In this sense, this paper is planning to investigate the scour process in the head section of the rubble-mound breakwater for broken wave case experimentally and fill the gap in the literature.

Breakwaters can be divided into many classes according to their shapes, the materials they are made of, their purpose of use, and their appearance in the plan. Foremost among them, the rubble mound breakwater is the most built in our country and the world. One of the important factors that make these breakwaters to be preferred is that the stone material to be used in the construction of the rubble mound breakwater is close to the construction site which means lower construction costs. Examining the stability losses that may occur due to local scours in these structures, which were built to create a calm water level, is of great importance in reducing the repair costs. In literature, only a limited number of studies on the scour of breakwaters can be found. Those studies especially examined the trunk section. Sumer and Fredsøe (1997, 2000) investigated the scour in the head section of the vertical and rubble mound breakwaters. As a result, they concluded that the scour in the head section of the breakwater can be of great value as a result of these studies. Sumer and Fredsøe confirmed the results reported by Lillycrop and Hughes (1993). Therefore, the investigation of the local scour in the head section of the breakwaters has great importance.

Myrhaug, Rue, and Tørum (2004) revealed the difference between their study and the study of Sumer and Fredsøe (1997). It was observed that the results of scour depth and protection layer thickness seen in the round head of the rubble-mound breakwater were slightly smaller than the results from waves with the highest one-third wave height (H_s) according to Sumer and Fredsøe. On the other hand, there are also studies in which scour formation is investigated both experimentally and numerically. In their study, Temel and Dogan (2021) compared the experimental and numerical results of the scour being formed at the trunk section of a rubble-mound breakwater. It is understood that the numerical model was found to be compatible with experiments. Gislason, Fredsøe, and Sumer (2009) who investigated the scour experimentally and numerically stated that the results were compatible in the case of the vertical-wall breakwater, but they could not reach a satisfactory result for the case of the sloping-wall breakwater.

In the present study, the experiments were carried out in seabed materials with median grain diameters of $d_{50} = 0.55$ mm and $d_{50} = 0.23$ mm, wave periods of 1.7 s, 2.0 s, 2.3 s, 2.7 s, 3.0 s, and a slope of 1:1.5. No significant scour depth has been observed as a result of the experiments. All experiments were carried out in regular and broken wave effect.

2. THEORETICAL BACKGROUND

In their study, Sumer and Fredsøe (1997) experimentally examined the local scour in the head section of a rubble-mound breakwater for regular and irregular wave conditions. They showed that two main mechanisms are causing the local scour in the head section of the rubble-mound breakwater. The first mechanism is the local scour induced by steady streaming. This mechanism leads to a scour hole on the side where the waves approach the breakwater (Area M in Figure 1). The other is the local scour caused by plunging breaker (Area P in Figure 1). This occurs when waves are sufficiently large, and plunging breaker may occur on the lee-side of the breakwater. It forms as a result of waves which has a sufficient height, climbing over the breakwater. The scour areas caused by the mechanisms mentioned above can be seen in Figure 1.
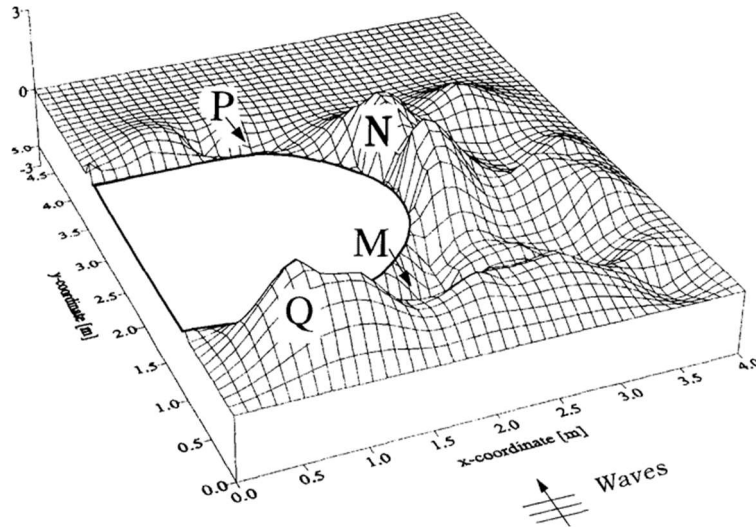
Figure 1. 3-D plot of the measured bed topograph. M: Scour induced by steady streaming. P: Scour induced by plunging breaker. N, Q: Deposition induced by steady streaming. Sumer and Fredsøe (1997)

According to their study, the main mechanism that causes scour induced by steady streaming in the head section of the breakwater is lee-wake vortices. Sediment particles exposed to these vortices eventually pile up away from the breakwater head section, causing a clear scour in the breakwater head section. In addition to that, they stated that the main parameter that causes lee-wake vortices is *Keulagen Karpenter number*, *KC*. It means that the scour in the head section is controlled by this number. The higher the number *KC*, the greater is the scour. As a physical expression, *KC* number is expressed as the ratio of the length of the movement area of the moving fluid particles to the base diameter of the breakwater. *KC* number is defined as below in their study:

$$KC = \frac{U_m T_w}{B} \tag{1}$$

where

U_m: the maximum value of the undisturbed orbital velocity at the bed

T_w: wave period

B: the base diameter of the breakwater

For the case of scour induced by steady streaming, the scour depends on the following quantities: U_m, T_w, *B*, the bed roughness, *d*, the kinematic viscosity, *v*, and the side slope of the breakwater, *m*. It means the relative maximum scour depth is the function of the quantities below:

$$\frac{S}{B} = f(KC, \theta, m, a/d, RE) \tag{2}$$

However, in the live-bed conditions ($\theta > \theta_{cr}$), the scour and deposition characteristics only vary with *KC* number in the study of Sumer and Fredsøe (1997). Sumer and Fredsøe obtained the relative maximum scour depth caused by steady streaming as a result of the experiment as follows:

$$\frac{S}{B} = 0.04C_1[1 - \exp(-4(KC - 0.05))] \tag{3}$$

where C_1 is the uncertainty factor with a mean value of 1 and its standard deviation is 0.2.

Equation (3) is valid for streaming-induced scour, and plunging-breaker-induced scour depends on different parameters. The scour can be found to depend on the following non-dimensional parameters as below:

$$\frac{S}{H_s} = f\left(\frac{T_p\sqrt{gH_s}}{h}, \theta, m\right) \tag{4}$$

where

H_S: significant wave height

T_p: peak wave period

g: acceleration due to gravity

In the live-bed conditions when $\theta > \theta_{cr}$, the plunging-breaker-induced scour will depend only the non-dimensional parameter of $T_p\sqrt{gH_s}$ / h. The numerator, $T_p\sqrt{gH_s}$, physically represents the amount of water entering into the main body of the water as a result of plunging breaker. In addition, the data points from two field studies of Lillycrop and Hughes (1993) can be seen in Figure 2. It demonstrates that there is a significant relation between the studies of Sumer and Fredsøe (1997) and Lillycrop and Hughes (1993).

Symbol	Experiments	Reference
▲	Laboratory; Tests 1-5	Present work
■	Field; Cattaraugue NY,U.S.A	Lillycrop & Hughes (1993) (see Table 2)
⊢—⊣	Field; Morro Bay CA, U.S.A.	
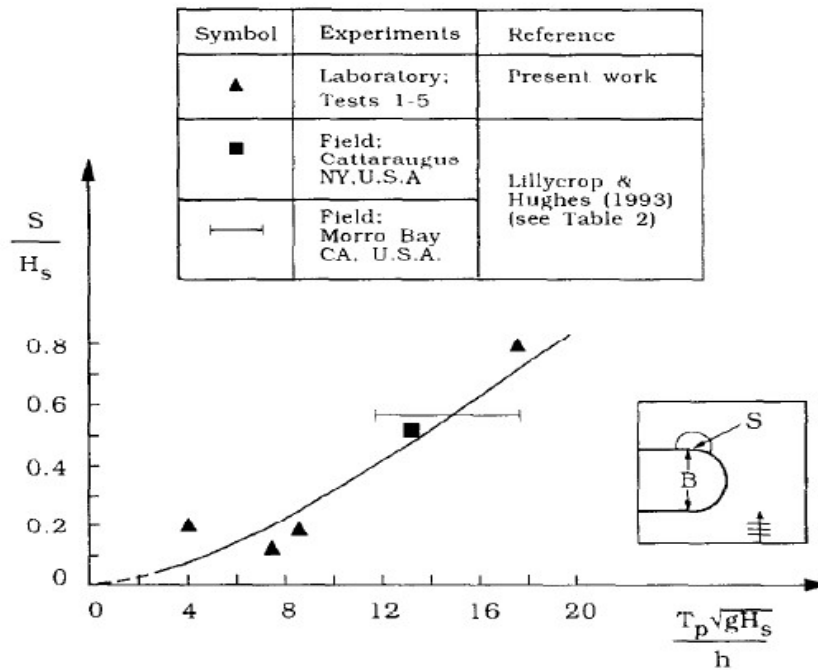
Figure 2. Maximum depth of scour hole at the lee side of the rubble-mound breakwater. Scour induced by the plunging breaker. Live bed. Sumer and Fredsøe (2002)

As a result, Sumer and Fredsøe concluded that the scour depth caused by plunging breaker can be obtained as a result of the experiment as follows:

$$\frac{S}{H_s} = 0.01 C_2 \left(\frac{T_p\sqrt{gH_s}}{h}\right)^{1.5}$$

(5)

where C_2 is an uncertainty factor with a mean value of 1 and its standard deviation is 0.34.

3. EXPERIMENTAL SET-UP AND PROCEDURE

The experimental study was carried out in an existing open-wave channel with a length of 33 m, a width of 3.6 m, and a depth of 1.2 m. The experimental studies were carried out in the channel of Dokuz Eylul University, Hydraulics Laboratory. In the open sea part of the open channel, a plunger-type wave generator was used to form regular waves with different heights and periods. Furthermore, the trunk section of the breakwater which was used in previous experiments and located on the onshore side was used to avoid the reflection of waves produced by the wave generator. A schematic view of the channel in which the experiments were carried out, is shown in Figure 3. It can be seen that regular waves created by the wave generator are broken on the ramp and then affect the breakwater.

Before each experiment, some seabed materials with the thickness of $d_{50} = 0.23$ mm and $d_{50} = 0.55$ mm were located in the surroundings of the breakwater without any compaction process. After each experiment, the surface of the disturbed bed was arranged to create a horizontal surface. The seabed materials used in the experimental studies are quartz sand and have a uniform distribution. The median grain diameters of the sands used in the experiments are as follows: $d_{50} = 1.85$ mm, $d_{50} = 0.55$ mm, and $d_{50} = 0.23$ mm for large, medium and small grain sizes, respectively. Tests with a grain diameter of $d_{50} = 1.85$ mm were not performed as significant scour did not occur in the cases of $d_{50} = 0.23$ mm and $d_{50} = 0.55$ mm.
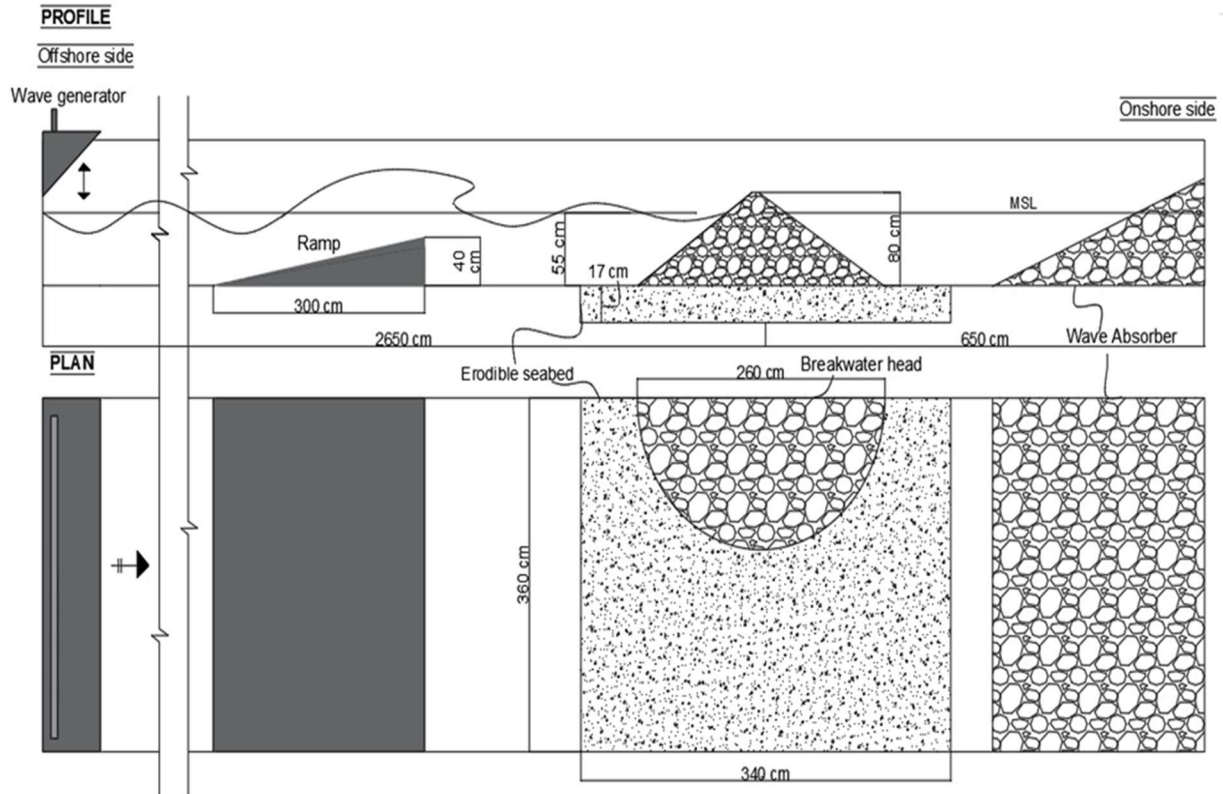
Figure 3. Profile and plan view of the head section of the breakwater with a slope of 1:1.5

The list of experiments performed is given in Table 1. It should be noted that all experiment cases are valid for the broken wave case. A wave breaker ramp was placed in the test channel to create the broken wave condition in the experiments. On the other hand, as can be seen in Table 1, four of the nine experiments were performed for sediment particles with a median grain diameter of $d_{50} = 0.55$ mm, while the remaining five were carried out for sediment particles with a median grain diameter of $d_{50} = 0.23$ mm.

Table 1. Experiments for the head section of the breakwater under the effect of broken waves.

Test Number	Wave Period 'T$_W$' (s)	Wave Height 'H' (cm)	d_{50} (mm)
1	1.7	28	0.55
2	2.7	20	0.55
3	2.3	22	0.55
4	3.1	17	0.55

5	1.7	28	0.23
6	2.0	25	0.23
7	2.3	22	0.23
8	2.7	20	0.23
9	3.1	17	0.23

As measuring instruments, UVP (Ultrasonic Velocity Profiling) and ULS (Ultrasonic Level Sensor) were used. UVP is used to measure time-dependent scour/deposition depth. The validation of this UVP device was already carried out and published in Guney et al. (2013). For measuring water levels, ULS is used. In the study, scour and deposition depth measurements are made under the effect of broken waves for different wave periods and seabed materials. During each experiment, scour/deposition measurements were made with the help of UVP at two different points. The positioning of UVP devices is shown in Figure 4. One of the UVP devices was placed in the region under the influence of steady streaming where waves approach the breakwater, and the other was placed at the lee-side of the breakwater on which the scour occurs due to plunging breaker. In Table 2, UVP_1 represents the relative maximum scour depths measured as a result of the experiment under steady streaming effect, while UVP_2 represents the relative maximum depths measured at the lee-side of the breakwater under plunging breaker effect.
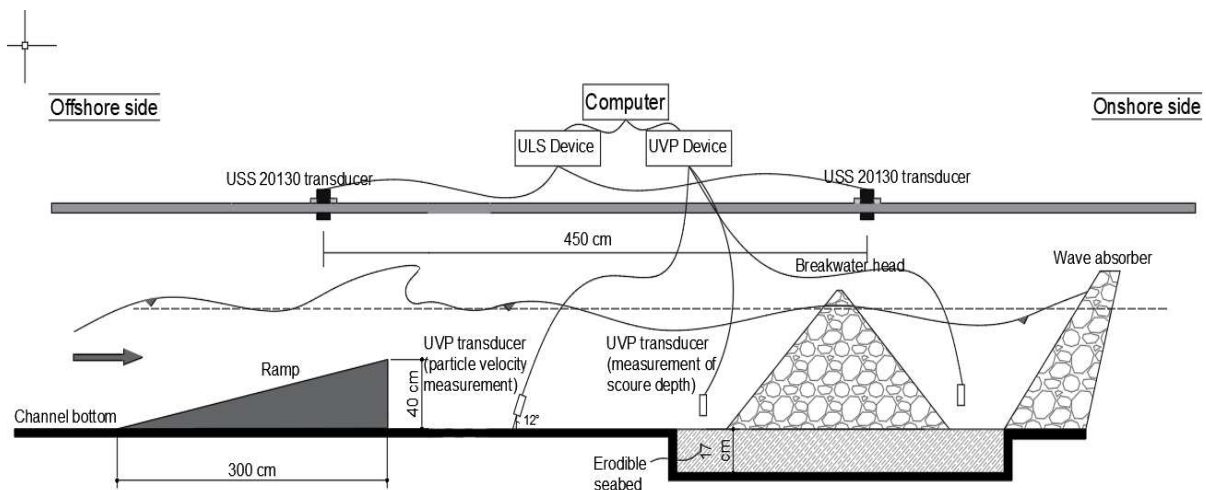
Figure 4. Profile and plan view of the head section of the breakwater with a slope of 1:1.5

The images of Ultrasonic measurement instruments used can be seen in Figure 5. ULS 80D device and USS 20130 transducers are shown in Figure 5-A, while the UVP device and transducers are shown in Figure 5-B. The positioning of all measurement devices is demonstrated in Figure 4.
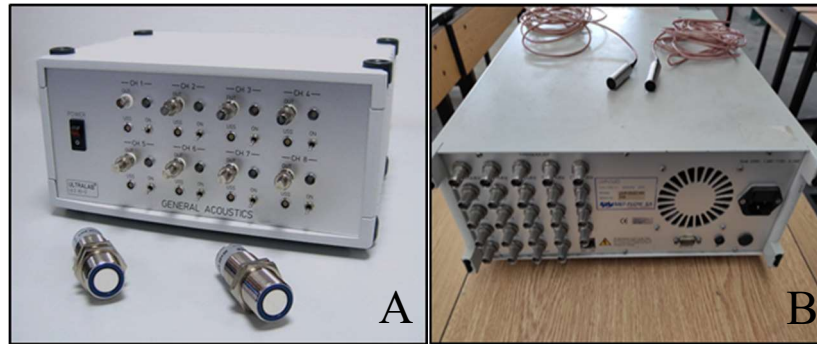
Figure 5. Images of ULS 80D device, USS 20130 transducers (A), UVP device, and transducers (B)

4. DISCUSSION

As a result of the experiments, the ground form was preserved in the head section of the rubble-mound breakwater under the effect of the broken waves, and a significant scour did not occur. As can be seen in Table 2, the maximum scour depth does not even exceed 15.52 mm. No significant scour occurred in the test results. Although the relative maximum scour depth exceeds 0.03 mm in Sumer and Fredsøe's experimental study for the unbroken wave state, the relative maximum scour depth remains maximum of 0.006 mm in our test. This was an expected result because Sumer and Fredsøe did their study for unbroken wave state whereas this study investigates the broken wave state.

Table 2. The relative maximum scour depths in the experiments.

Test Number	Smax (mm) for UVP_1	Smax (mm) for UVP_2	Smax/B for UVP_1	Smax/B for UVP_2
1	2.07	6.21	0.0008	0.0024
2	7.24	11.38	0.0028	0.0044
3	0.00	11.38	0.0000	0.0044
4	4.14	1.03	0.0016	0.0004
5	9.31	14.49	0.0036	0.0056
6	7.24	7.24	0.0028	0.0028
7	15.52	7.24	0.0060	0.0028
8	0.00	14.49	0.0000	0.0056
9	4.14	6.21	0.0016	0.0024

The time-dependent scour depths obtained from the UVP devices in the case of the broken and unbroken wave case, are given in between Figure 6 and Figure 9. The unbroken wave data in those figures belong to the experimental studies performed in the same channel previously. This means the time-dependent variation of the scour for both cases were obtained by the same method. There is a significant reduction in scour depths in the case of the broken wave case compared to the unbroken wave case as can be seen from Figure 6 to Figure 9. Since the broken of waves causes a significant reduction in scour depth, it will be beneficial to pay attention to this situation in the construction process of breakwaters. In addition, the numbers greater than zero represent "scour", while the numbers less than zero represent "deposition" in those figures. As can be seen in those figures, experimental measurements took approximately one hour. Since the waves were broken by the help of the ramp, the measurement of the wave reflection could not be performed.
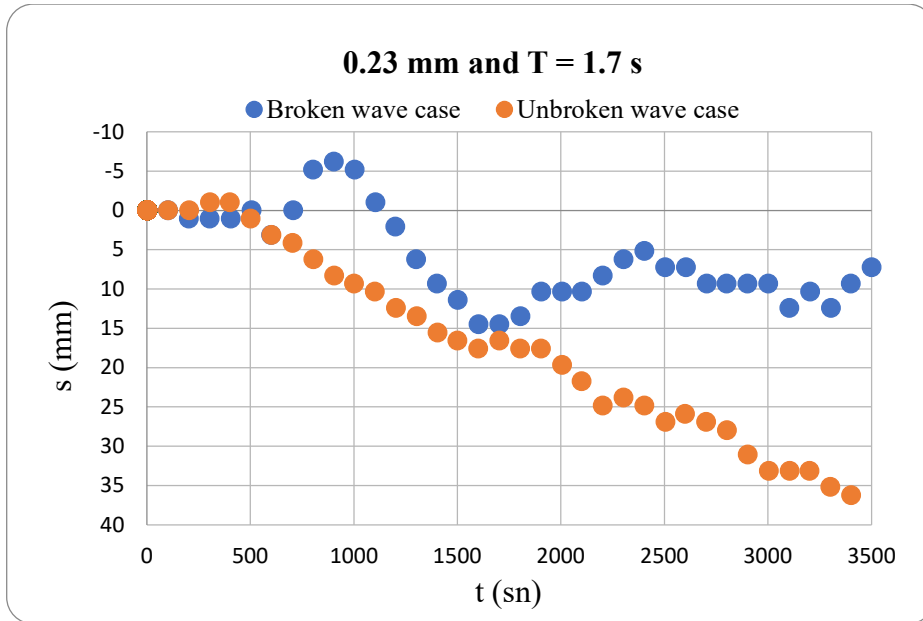
Figure 6. Time-dependent scour depths in broken and unbroken wave cases

(All measurements were taken from UVP_2 device)
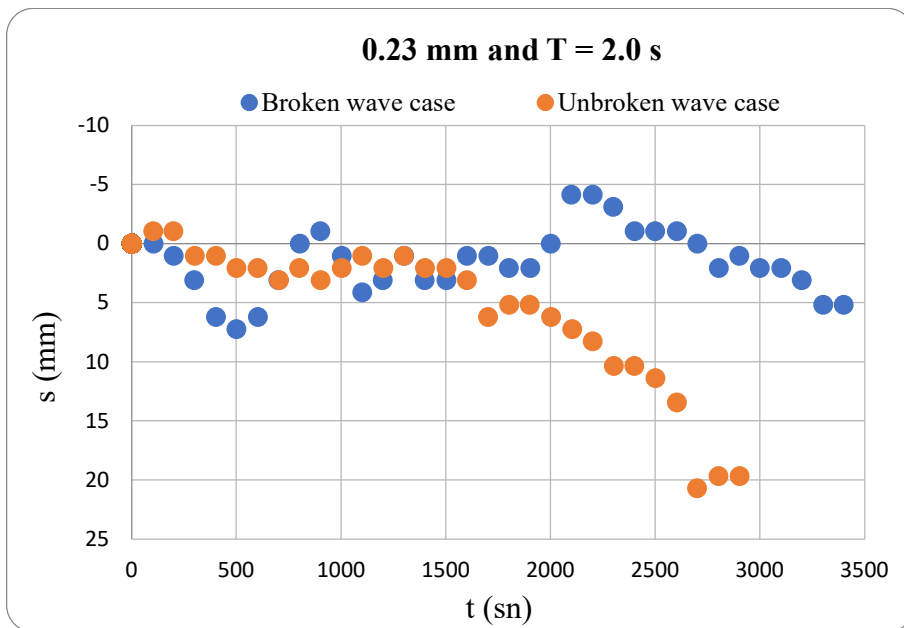
Figure 7. Time-dependent scour depths in broken and unbroken wave cases

(All measurements were taken from UVP_2 device)
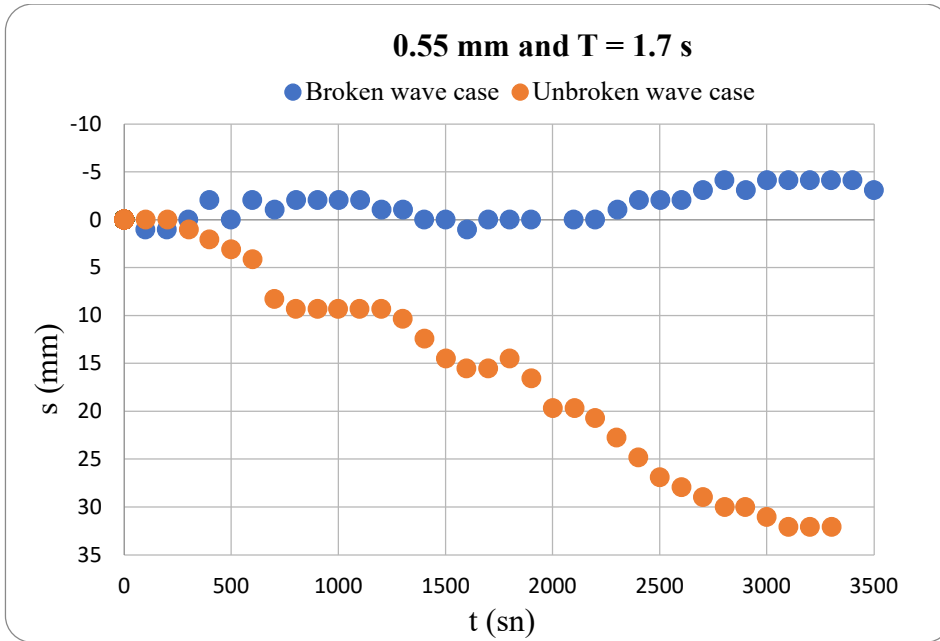
Figure 8. Time-dependent scour depths in broken and unbroken wave cases
(All measurements were taken from UVP$_1$ device)
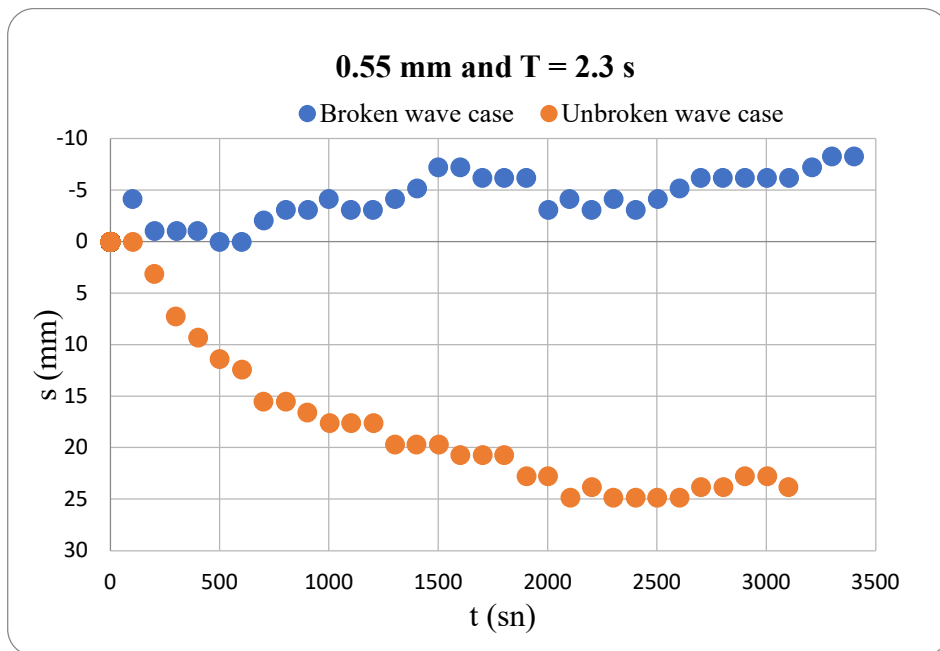
Figure 9. Time-dependent scour depths in broken and unbroken wave cases
(All measurements were taken from UVP$_1$ device)

The final state of the breakwater surrounding as a result of experiment 1 and 5 can be seen in Figure 10 and 11. As can be seen, no significant scour is observed and the ground form is preserved around the breakwater. The successive scour/deposition pattern that occurs in the head section of the breakwater as a result of the broken wave effect can be seen in those figures.

Figure 10. The final state of the breakwater surrounding as a result of experiment 1

Figure 11. The final state of the breakwater surrounding as a result of experiment 5

5. CONCLUSION

In this experimental study, the deficiency in the literature was eliminated by examining the local scour around the head section of the rubble-mound breakwater for the broken wave case. In this paper, local ground movements were examined as a result of the broken wave effect around the head section of a rubble-mound breakwater experimentally. The experiments were carried out for a specific surface slope with two different sand materials, and five different wave periods. The waves produced by the wave generator were broken with the help of the ramp. Consequently, it was observed that scour reduced significantly in the case of the wave broken case compared to the unbroken case. The scour

effect of grain diameter, wave period, and surface inclination could not be investigated properly since no significant scour did not occur in the case of the broken wave case.

ACKNOWLEDGEMENTS

REFERENCES

Breusers, H.N.C. and Raudkivi, A.J. (1991): *Scouring. A.A. Blkema, Rotterdam, viii + 143 p.*

Gislason, K., Fredsøe, J., & Sumer, B. M. (2009). Flow under standing waves: Part 2. Scour and deposition in front of breakwaters. *Coastal engineering*, *56*(3), 363-370.

Guney, M.S., Bombar, G., Ozgenc Aksoy, A., Dogan, M., 2013. *Use of UVP to investigate the evolution of bed configuration.*

Lillycrop and Hughes (1993). *Scour hole problems experienced by the Corps of Engineers; Data presentation and summary.*

Melville, B.W. and Coleman, S.E. (2000): *Bridge Scour. Water Resources Publications, LLC, CO, USA, xxii + 550 p.*

Myrhaug, Rue and Tørum (2004): *Tentative engineering approach to scour around breakwaters in random waves.*

Sumer, B.M., J. Fredsøe, 1997. *Scour at the round head of a rubble-mound breakwater.*

Sumer, B.M., J. Fredsøe, 2000. *Experimental study of 2D scour and its protection at a rubble-mound breakwater.*

Sumer, B.M., Fredsoe, J., 2002. *The Mechanics of Scour in the Marine Environment, vol. 17. World Scientific Publishing, Singapore. Advanced Series on Ocean Engineering.*

Temel, A., & Dogan, M. (2021). Time dependent investigation of the wave induced scour at the trunk section of a rubble mound breakwater. *Ocean Engineering*, *221*, 108564.

14TH INTERNATIONAL CONFERENCE
ON HYDROSCIENCE & ENGINEERING

MAY 26-27, 2022
IZMİR-TURKEY

ICHE2022
IZMIR, TURKEY

EXPERIMENTAL AND NUMERICAL INVESTIGATION OF THE SCOUR CAUSED BY SHIP PROPELLER WASH IN CASE OF FINE SAND

First Author: Cansu Özyaman

Ege University, Civil Engineering Department

İzmir, Turkey

cansuozyaman@gmail.com

Second Author: Mustafa Doğan

Dokuz Eylül University, Civil Engineering Department

İzmir, Turkey

mustafa.dogan@deu.edu.tr

Third Author: Selim Altun

Ege University, Civil Engineering Department

İzmir, Turkey

selim.altun@ege.edu.tr

Fourth Author: Vahid Abdi

Dokuz Eylül University, Civil Engineering Department

İzmir, Turkey

Vahid.aabdi@gmail.com

ABSTRACT: Investigation of the scour caused by ship propeller is important since it causes several problems such as instability of dock foundations or pollution because of resuspension. To gain a better understanding of the ship propeller jet and minimize propeller-jet-induced scour and pollution, the water jet formed by ship propellers and time-dependent scouring on seabed were investigated numerically and experimentally. Within the scope of this paper, the water jet formed by ship propeller and time dependent scouring on seabed was investigated. Efflux velocity was redefined considering three-dimensional components of the velocity measured by the means of Acoustic Doppler Velocimeter (ADV). Time dependent scour depths and bathymetry graphs were given. Experiment results have shown that scour depth increases with time and then it remains almost constant after 150 minutes. The scour depths also increased with the propeller speed. Observations show that scour acceleration is greater when the propeller is close to the seabed. In addition to experimental results, numerical model was carried out for highest propeller speed condition. The experimental results are in good agreement with numerical results.

1. INTRODUCTION

The water jet formed by ship propellers during berthing and departure to the quays and piers initiates the sediment motion on erodible seabed and can lead to local scour at the port structure. Ships that have berthed conventionally without using their propellers and with the help of tugboats can maneuver by themselves with today's developing technology with the movement of bow thruster and azipods. However, this situation emerges as a scouring/deposition problem at seabed and at the front of the quays and piers.

There are many factors that affect seabed scour. These factors are propeller characteristics such as propeller diameter, propeller speed, thrust coefficient, pitch, bar, as well as propeller height from the

bed or gradation or size of the base material. Efflux velocity equation which includes three propeller characteristics such as propeller diameter, propeller speed, thrust coefficient, is the most important parameter of the jet flow intensity as it is generally used for scour depth computations. Therefore, the estimation of the efflux velocity is important for prediction of scour. Efflux velocity is the velocity, U_o, defined as the maximum velocity measured just downstream of the propeller (Hong et al., 2013). The efflux velocity U_o is calculated using the empirical equation proposed by many researchers (Hamill, 1987, Tan, 2019, PIANC 2015, Fuehrer and Römisch 1977) in the general form below,

$$U_0 = \alpha n D_p \sqrt{c_T}$$

Where n is propeller rotational speed, C_t is thrust coefficient of the ship propeller and D_p is propeller diameter. Different coefficients are defined by many researchers according to the experimental conditions.

Within the scope of this study, the water jet velocity formed by ship propellers and time dependent scour depth will be investigated by experimental and numerical methods. Fine sand was chosen as a bed material since mostly medium sand was used in the literature studies. A new efflux velocity equation was proposed with the velocity measurements made with ADV.

2. EXPERIMENTAL STUDY

Experiments were conducted in a rectangular 5 m long, 2 m wide, and 1 m deep pool, located at the Ege University Civil Engineering Department (Figure 1). All the experiments were performed at 0.5 m water depth.
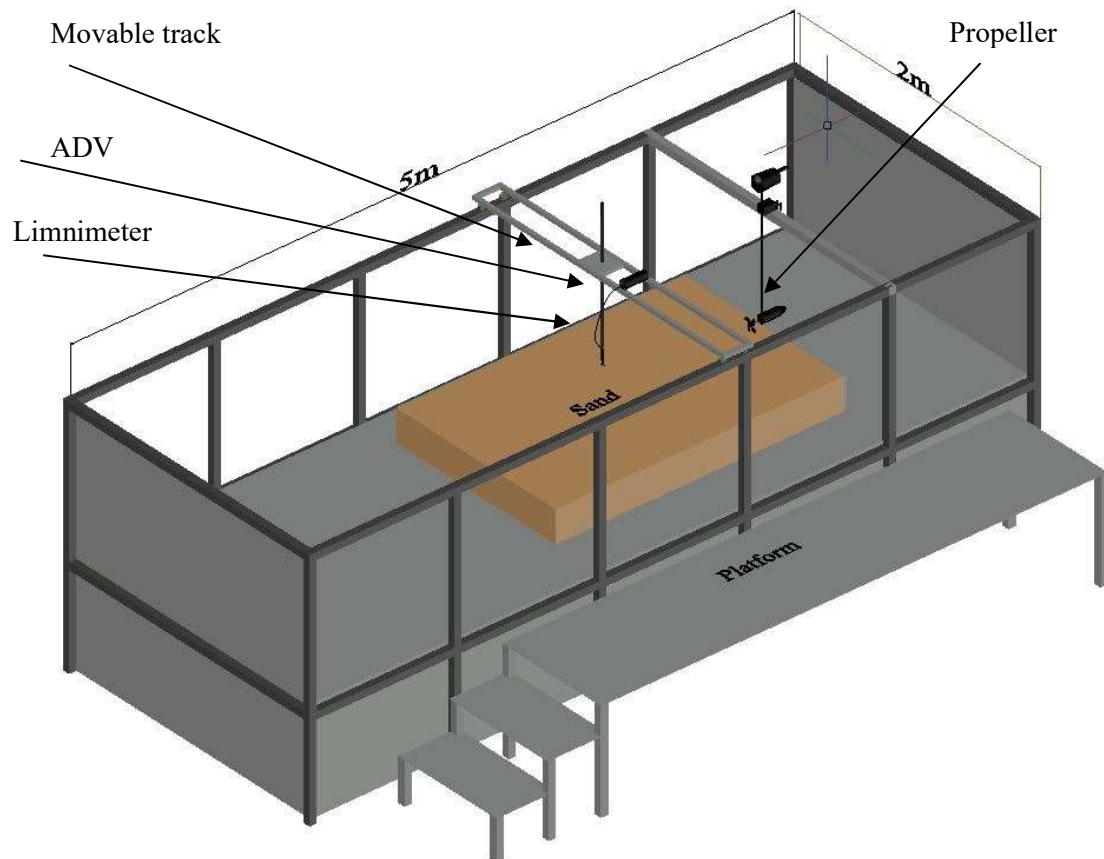
Figure 1. Schematic view of the experimental set-up

Propeller was first drawn in a 3D program and then printed with a 3D printer having hard plastic filament. Model propeller diameter was 6 cm corresponding to 1.2 m propeller in prototype. Propeller

characteristics are given in Table 1. Experiments were done at three different propeller speed (500 rpm, 750 rpm, 1000 rpm). Propeller height from the hub of propeller to sand (G) was 5 cm and 7.5 cm.

Table 1. Test Propeller Characteristics.

Propeller type	Diameter (D, mm)	Hub Diameter (D_h, mm)	Blade Nr	BAR (A_e/A_0)	P/d	Pitch (mm)
Wageningen B	60	5-15	4	0.67	1.4	84

The three-dimensional velocity components were measured by Nortek Acoustic Doppler Velocimetry (ADV). ADV was installed on movable track above the pool. The frequency rate of 25 Hz was used in ADV measurements. The sampling duration was 60 seconds in each measuring location. The output ADV data were filtered using a WinADV software developed by Tony L. Wahl. Goring and Nikora's Phase Space Thresholding method was used to filter the ADV measurements by using this software.

Fine sand having 0.25 mm median diameter was chosen as a seabed material. Sediment properties are given in Figure 2.
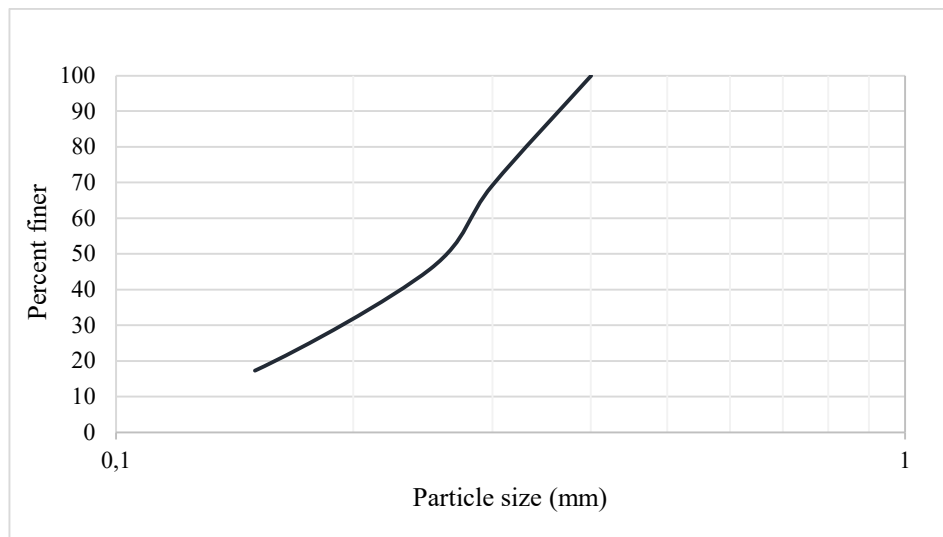
Figure 2. Sediment Characteristics

A digital laser meter was used to measure the scour depths. To determine the scour volumes, 2.5 × 2.5 cm axes were constructed on the scouring area. Scour depth coordinates were measured at more than 500 points after completely draining the water in the pool. A 3D scour map was plotted, and the scour volume was calculated from the measurements via a computer program.

3. EXPERIMENTAL RESULTS

The experiment results were presented in three sections: propeller efflux velocity, time dependent scour depths and bathymetry graphs.

3.1. Propeller Efflux Velocities

Velocity measurements were made to determine the efflux velocity for each experiment. The measurements were performed in the Cartesian coordinate system (x,y,z) in unconfined propeller jet conditions (no propeller-base-structure interaction) with a duration of 60 seconds. Velocity measurements were made in three different sections 5 cm, 10 cm, and 15 cm ahead the propeller hub (Figure 3). Efflux velocity equation was derived with the highest velocities observed in the 5 cm sections.
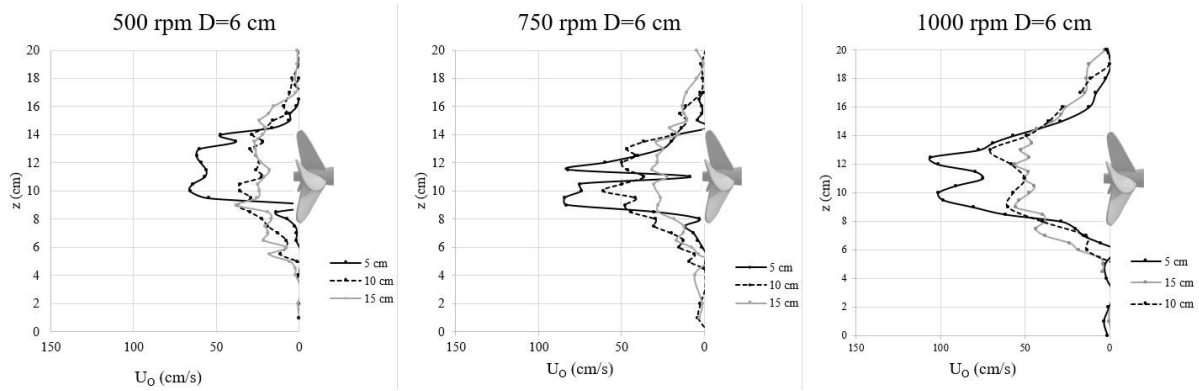
Figure 3. Efflux Velocities for 500, 750 and 1000 rpm propeller velocities for unconfined propeller jet

Equation (2) was suggested considering the geometrical characteristics of the propellers used in this study;

$$U_0 = 1.49 \, nD_p\sqrt{c_T}$$

Proposed equation is for Wageningen B series propellers with a c_T coefficient of 0.61.

3.2. Time Dependent Scour Depths

Scour depths were measured to determine the time-dependent scour depths. Experiments were carried out at rotational speeds of 1000 rpm, 750 rpm and 500 rpm. The experiment with 1000 rpm propeller speed was repeated with a long duration (up to 300 min) to determine experiment duration. Considering that 96% of the scouring occurred at the 120th minute and 98.4% at the 135th minute, the test duration was determined as 150 minutes. When considering all propeller speeds, 94% of the scour is completed in the first 60 minutes in the experiments where G=5 cm, while 86% of the scour is completed in the experiments where G=7.5 cm.

Time-dependent scour depth measurements for sand material are given in Figure 4 and Figure 5. In all experiments, the scour depth increases with time but remains constant after a certain time corresponding to 150 minutes. When we compare Figure 4 with Figure 5, for a condition with same propeller speed, the scour depth decreases with an increase in propeller height. In all experiments, scour depths were increasing with propeller speed as expected.
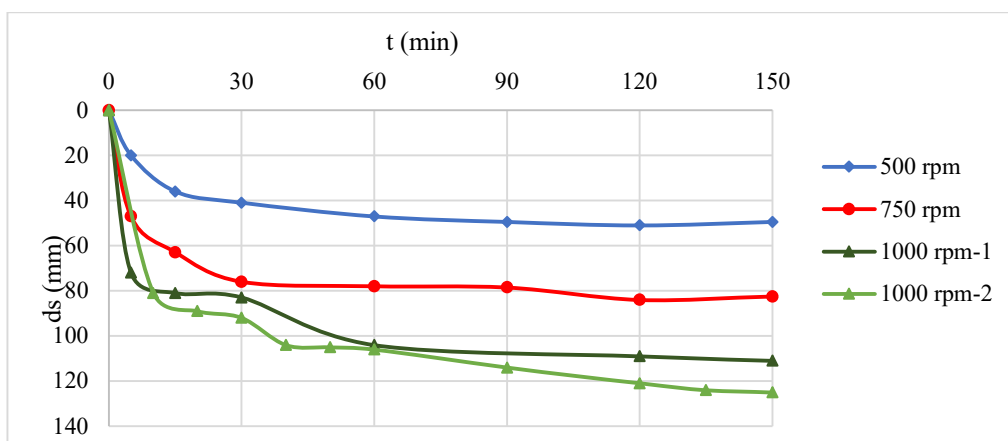
Figure 4. Time dependent scour depths for G=5 cm
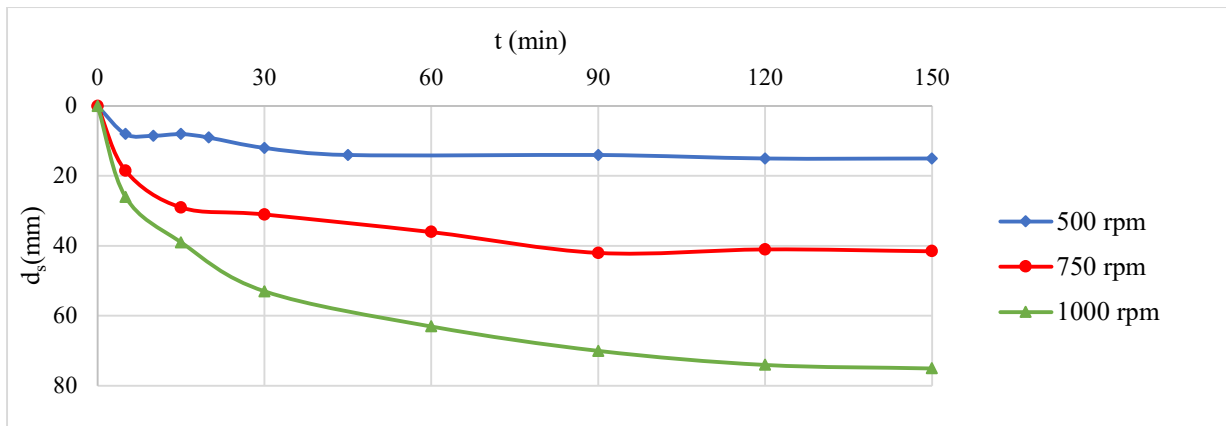
Figure 5. Time dependent scour depths for G=7.5 cm

Figure 6 shows the scouring and deposition profiles at the section of symmetry axis of the propeller. It is seen from the figure that most of the scouring occurred in the first hour of the experiments.
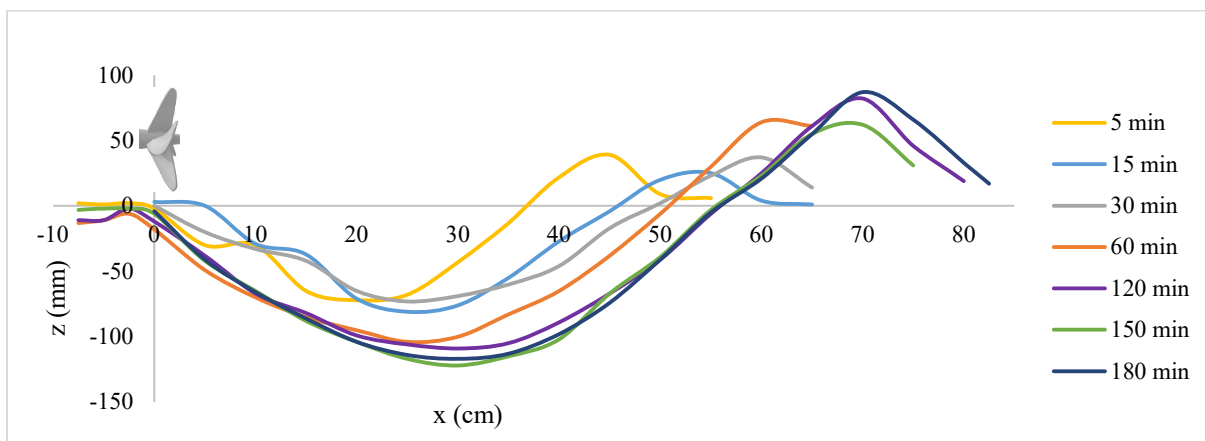
Figure 6. Time dependent scour depths at y=0, for G=5 cm, 1000 rpm

3.3. Bathymetry Graphs

Laser meter data was imported to a 3D drawing program to draw scour hole contour maps. The maximum scour depths and deposition mound heights are presented at the contour line maps in Figure 7. In general, as the propeller velocity increased, scour holes generally got deeper (Fig 6, 7) . Contour lines are in mm. Maximum scour depths were observed approximately 5 cm left side of the propeller's symmetry axis depending on propeller rotation direction. The distance between propeller and sand had important effects on the scouring geometry, depth and volume. The scour depths were higher when G=5cm. Additionally small scour holes are not formed when G=7.5 cm.
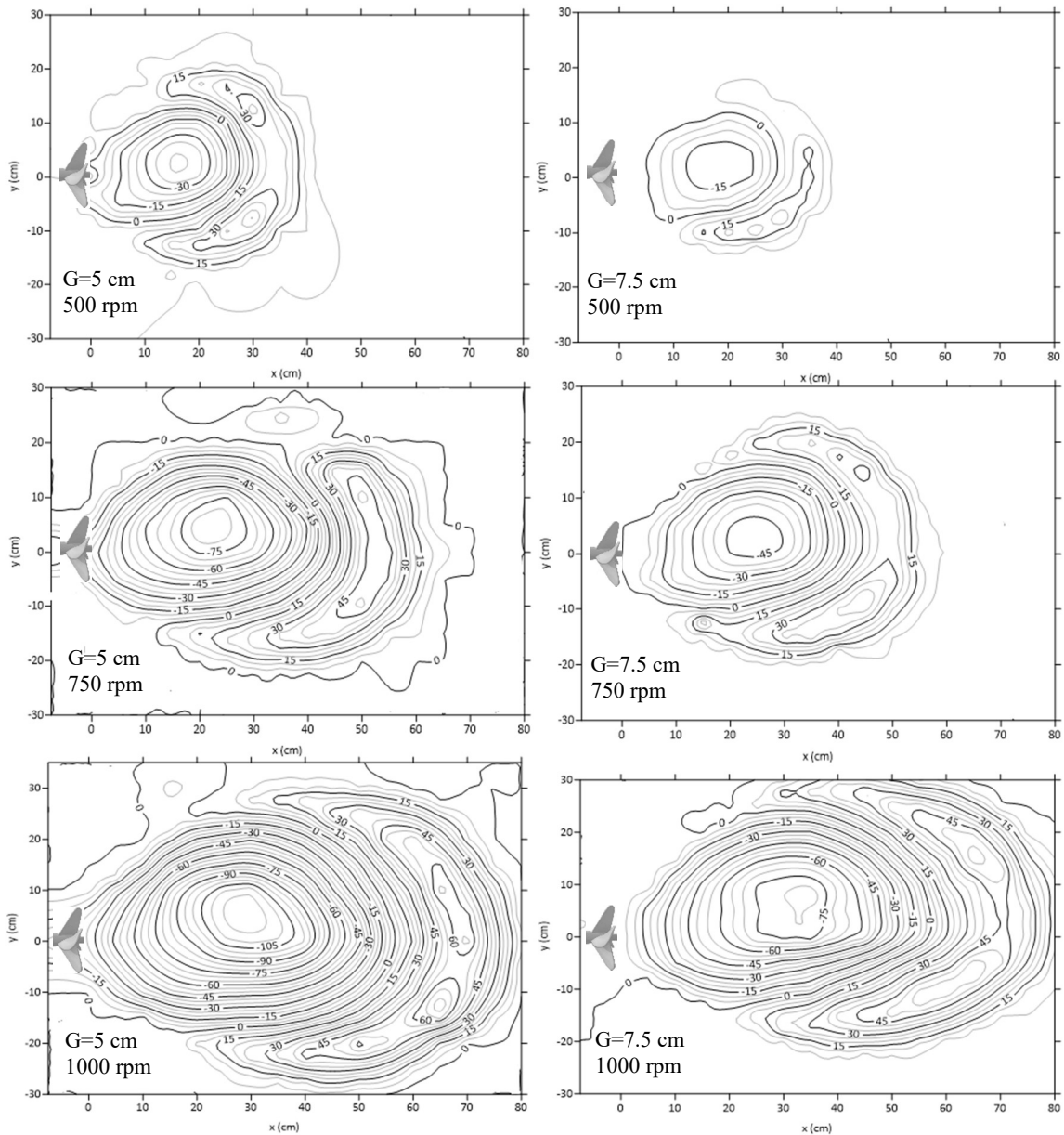
Figure 7. Contour line maps for all experiments

4. NUMERICAL STUDY

Numerical model was performed by using the Flow 3D software. Flow3D is a highly accurate computational fluid dynamic software, uses finite volume approximations in the numerical simulation for sediment transportation with solving the Reynolds Averaged Navier Stokes equations given in cartesian coordinates. In turbulent flow calculation, various turbulence model options are available in Flow 3D such as renormalized group model (RNG), two equations k-e, two-equation k-w, and Large eddy simulation (LES) model (Flow-3D User's Manual). Since the results of RNG model simulations have better agreement with experimental results, RNG turbulence model was chosen for the simulations of this study.

After choosing turbulence model, sediment scour model was activated. The sediment scour model assumes multiple non-cohesive sediment species with different properties including grain size, mass density, critical shear stress, angle of repose and parameters for entrainment and transport. The model estimates the motion of sediment by predicting the erosion, advection, and deposition of sediment. These predictions are done by computing the suspended sediment transport, settling of sediment, the

entrainment of the sediment, the bed-load transport (Flow 3-d User's manual). Sediment properties are provided to sediment scour model as suggested in user's manual. Diameter of the sediment was 0.00025 m as in the experiments. Critical shear stress calculated from velocity measurements and was taken as 0.05. Boundary conditions were chosen to model the experiment pool. Five surfaces of the experiment pool are defined as wall boundary condition and upper surface is defined as pressure boundary condition. 20 cm deep sediment was defined at the bottom of the pool.

Impeller model was chosen to simulate the propeller. This model induces both rotational and axial velocity components. The definition of an impeller is done in terms of a "phantom" obstacle that defines a region but does not have any real obstacle blockage effects. These obstacles are assumed to be circular cylinders of outer radius R, inner radius r and thickness L. Aside from the geometry, the remaining parameters that determine the performance of an impeller are its rotation rate Sd, an accommodation coefficient for rotational velocity A_d that controls how effective the blades are in setting fluid into motion, and an axial velocity coefficient B_d that controls the amount of axial flow induced (Flow 3D-User Manual).

Numerical study is conducted to compare the results of the experiment having 1000 rpm propeller speed with 5 cm propeller height. Simulation duration was 5460 second with running time of 78 days. Mesh number was 402400. Simulation variables for impeller were, 1000 rpm (104.72 rad/s) for rotation rate Sd, 1.4 is defined as A_d and 1 is defined for B_d. These numbers are determined by comparing the velocity measurements taking by ADV with the simulation impeller's efflux velocities (Figure 8).
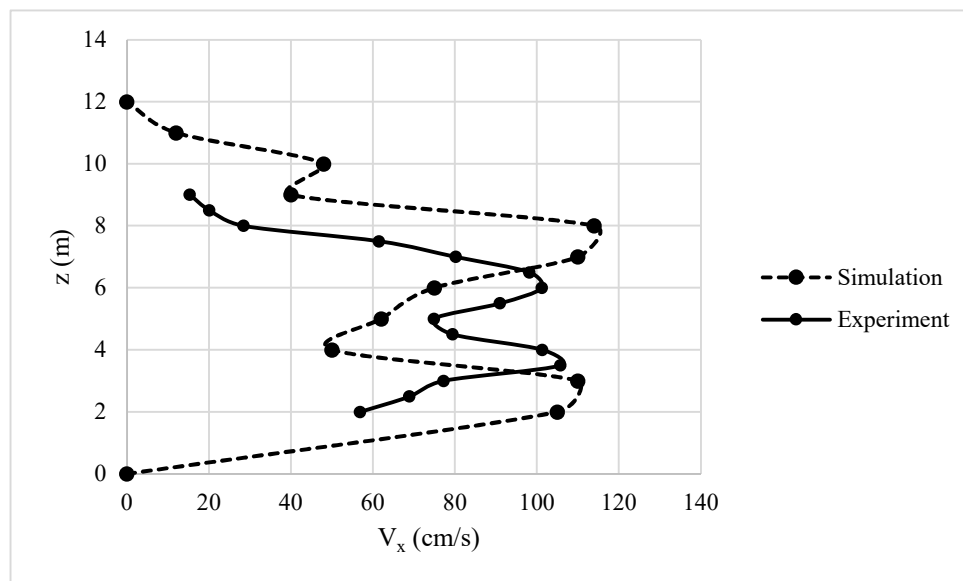
Figure 8. Velocities of experiments and simulation for 1000 rpm, G=5 cm

Comparison of time dependent scour depth for experiment and simulation is given in Figure 9. It is seen from the Figure that for the first 10 minutes experiment and simulation results are same. After 10 minutes there is a slight difference between simulation and experiments. This difference can be due to the low efflux velocity compared to experiments.
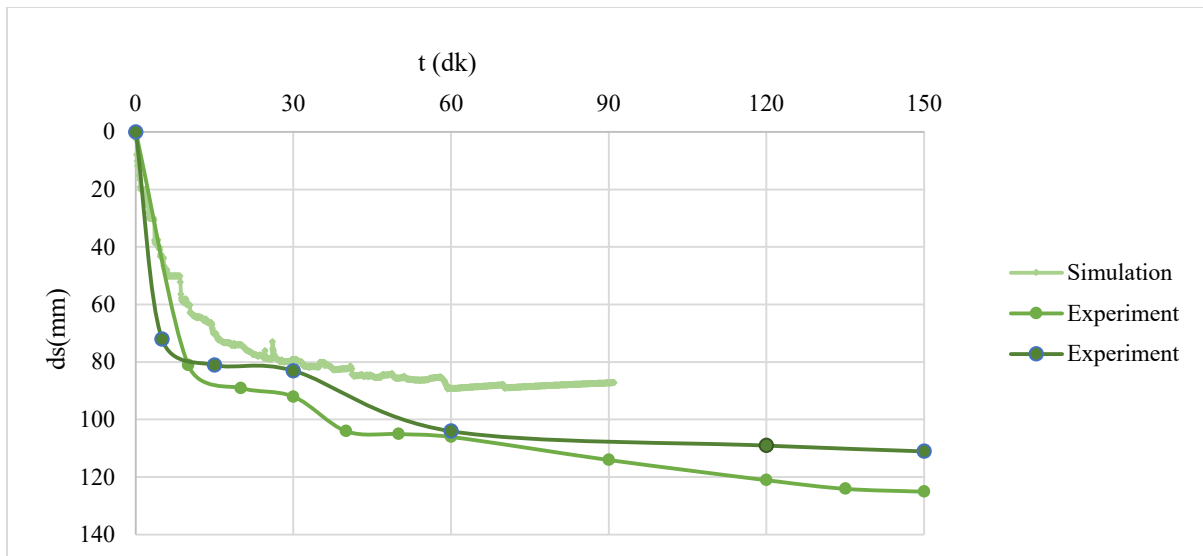
Figure 9. Time dependent scour depths for experiment and simulation, for G=5 cm, 1000 rpm

5. CONCLUSIONS

In this study, a series of experiments were conducted using propeller jet to investigate the effect of jet formed by ship propeller and time dependent scouring on seabed. The effect was described by measured propeller speeds and time dependent scour depths. Observations showed that after 150 minutes there was no significant increase in scour depths so 150 minutes was chosen as an experiment duration. The scour depths increased with the propeller speed and time, considering all the experimental results. When considering all propeller speeds, 94% of the scour is completed in the first 60 minutes in the experiments where G=5 cm, while 86% of the scour is completed in the experiments where G=7.5 cm. This indicates that the scour acceleration is greater in the first 60 minutes when the propeller is close to the seabed. The efflux velocity could be predicted by the equation below considering the geometrical characteristics of the propellers used in this study.

$$U_0 = 1.49 \, nD_p\sqrt{c_T}$$

The experimental results are in good agreement with numerical results however there is a slight difference between simulation and experiments. This difference can be due to the low efflux velocity compared to experiments. The number of simulations will be varied by using different rotational and axial velocity coefficients to achieve similar results.

In the future experiments, utilizing another feature of the ADV device, the concentration of suspended sediment will be measured, and new relations and diagrams will be associated to the scouring/deposition depths for different flow structure and base material cases.

REFERENCES

Flow 3D v11.2 User's manual. Flow Science Inc

Goring, D. G., & Nikora, V. I., (2002). "Despiking acoustic Doppler velocimeter data. Journal of hydraulic engineering" 128(1), 117-126.

Hamill, G.A., (1987). Characteristics of the Screw Wash of Manoeuvring Ship and the Resulting Bed Scour, Ph.D. Thesis, Queen's University of Belfast, Northern Ireland, UK.

Hong, J. H., Chiew, Y. M., & Cheng, N. S., 2013. Scour caused by a propeller jet. *Journal of Hydraulic Engineering*, *139*(9), 1003-1012.

Fuehrer, M., & Römisch, K., (1977). "Propeller Jet Erosion and Stability Criteria for Bottom Protection of Various Constructions", In Proceedings of PIANC, Bulletin No.58.

Permanent International Association of Navigation Congresses (PIANC), (2015). The World Association for Waterborne Transport Infrastructure, Guidelines for Protecting Berthing Structures from Scour Caused by Ships, Report No.180, Belgium.

Tan, R. İ. (2019). Propeller jet ınduced erosıon around pıle supported berth structures. Ph.D. Thesis, Yıldız Technical *University, İstanbul, Turkey*

Wei, M., Chiew, Y. M., & Guan, D. (2018). Temporal development of propeller scour around a sloping bank. *Journal of Waterway, Port, Coastal, and Ocean Engineering*, *144*(5), 06018005.

Wahl, T. L. (2000). Analyzing ADV data using WinADV. In *Building partnerships* (pp. 1-10).

EFFECT OF SEA LEVEL FLUCTUATIONS ON COASTAL FLOOD HAZARDS IN IZMIR BAY

Salih Ak

Civil Engineering Department, İzmir Institute of Technology

Urla, Izmir, Turkey

salihak@iyte.edu.tr

Bergüzar Oztunali Ozbahceci

Civil Engineering Department, İzmir Institute of Technology

Urla, Izmir, Turkey

berguzarozbahceci@iyte.edu.tr

Dogan Kisacik

Civil Engineering Department, İzmir Institute of Technology

Urla, Izmir, Turkey

dogankisacik@iyte.edu.tr

ABSTRACT: The coastline of Izmir, which draws attention due to its natural, cultural, and historical resources, has a very intensive use. Restaurants, cafes, and entertainment venues are located on the shoreline and are highly-populated places with high mobility, serving domestic and foreign guests around the inner bay. Moreover, the inner bay of Izmir is surrounded by an uninterrupted coastal road. Due to rapid urbanization, industrialization, and an increase in population density, Izmir's shoreline and coastal area have been continuously expanded, by filling in the water area. This expansion by in-filling has deformed the natural stability of the sea bottom topography and has increased the vulnerability of the coastline against coastal flood effects. Moreover, the frequency of coastal flood events is increasing. Sea-level rise and extremeness of atmospheric and oceanic conditions due to climate change have become noticeable in recent years. Coastal external forces acting against coastal defense structures and affected by climate change are rising sea levels, storm surges, and high waves. Damage to coastal structures, coastal erosion, morphological change, and coastal flood disasters are expected to increase due to sea-level rise and stormy wind and wave climates. For this reason, research on coastal hazard evaluation, accompanied by a change in atmosphere and ocean conditions has become important and should be carried out. In this study effect of sea-level fluctuations on the coastal flood hazard in Izmir Bay is investigated by considering different generation mechanisms. It can be concluded that the water level can increase up to 1.0 m during storms, considering the tide, storm surge, barometric surge, sea-level rise, and climate change effects.

1. INTRODUCTION

The city of Izmir is located around the sheltered Izmir Bay on the deeply-indented coast of the Aegean Sea. Izmir is the second largest seaport and the third-largest city in Turkey. Izmir, with its long coastline, is one of the leading tourism and trade cities in the country. The coastline of Izmir, which draws attention due to its natural, cultural, and historical resources, has a very intensive use. The coastal area between the old Dalyan in Cigli to the North and Balcova to the South is called the Izmir Inner Bay as shown in Fig.1. Restaurants, cafes, and entertainment venues are located on the shoreline and are highly-populated places with high mobility, serving domestic and foreign guests around the inner bay. Moreover, the inner bay of Izmir is surrounded by an uninterrupted coastal road.

Due to rapid urbanization, industrialization, and an increase in population density, the balance between structural areas and green areas has deteriorated. The two images in Fig. 1, captured in 1984 and in 2015, show changes in the urban area and along the coast during this window of time.

Figure 1. Two images of Inner Izmir Bay captured in 1984 (top) and in 2015 (bottom)

Fig.1 shows that Izmir's shoreline and coastal area have been continuously expanded, by filling in the water area. This expansion by in-filling has deformed the natural stability of the sea bottom topography and has increased the vulnerability of the coastline against coastal flood effects.

Izmir resonates with the water and the wind. The cooling sea breeze in summer takes away the burning heat of the sun. However, when the wind is strong it generates waves, together with storm surge, wind, and wave set-up, which increase the water level of the Bay. The combination of waves and increased water level causes coastal flooding, which results in waves overtopping the coastal protection structures. Along the shore, there are traditional coastal protection structures, like sloping-type coastal revetments and vertical walls built parallel to the coast to protect the surrounding roads, buildings, and recreation areas from coastal floods and destructive effects of the sea. During a recent coastal flood, it was observed that a huge amount of seawater floods the infilled land and causes traffic problems and damage to buildings and recreational facilities. Fig. 2 shows photos taken during a recent coastal flood disaster in Izmir's city center.

Figure 2. Example photos showing the consequences of coastal flood hazard events in the Izmir city center

The coastal flood events of the last 10 years, together with dates and the affected regions, are tabulated in Table 1.

Table 1. Coastal flood events of the last 10 years together with dates and affected areas.

Date	Affected Areas
04.12.2012	KORDON-ALSANCAK
21.09.2015	CUMHURIYET SQUARES, KONAK
18.01.2018	ALSANCAK, KORDON
23.12.2019	KARSIYAKA
05.02.2020	KARSIYAKA,1. KORDON, GUNDOGDUAND CUMHURIYET SQUARES
14.12.2020	MAVISEHIR
08.02.2021	KARSIYAKA
29-30.11.2021	KARSIYAKA

Table 2 shows that the frequency of coastal flood events is increasing. The reason for this increase in Izmir Bay is climate change due to global warming. Sea-level rise and extremeness of atmospheric and oceanic conditions due to climate change have become noticeable in recent years. Coastal external forces acting against coastal defense structures and affected by climate change are rising sea levels, storm surges, and high waves. Damage to coastal structures, coastal erosion, morphological change, and coastal flood disasters are expected to increase due to sea-level rise and stormy wind and wave climates. For this reason, research on coastal hazard evaluation, accompanied by a change of atmosphere and ocean conditions due to climate change, has become important and should be carried out.

In this paper effect of sea-level fluctuations on the coastal flood hazard problem in Izmir's inner bay is investigated in detail. In Section 2, wind climate studies are explained. Calculation of the change in seawater level considering various generation mechanisms is given in Section 3. Finally, conclusions are provided in Section 4.

2. WIND CLIMATE STUDIES

The wind is one of the sources of water level increases with the wind set-up. Therefore, determination of wind characteristics like wind speed and direction, as well as yearly distribution of the characteristics are very important.

Wind data can be obtained through in-situ measurements or widely-used model results. In-situ measurement campaigns have been carried out by the Izmir Municipality since 2017. Wind speed and direction are measured at 10-minute intervals in four locations:1)Foca 2)Guzelbahce 3)Pasaport 4)Bostanli

For the current project almost 5 years of wind data were supplied by Izmir Municipality, to be used in the analysis. However, longer data are necessary to determine the wind climate. Longer data can be obtained from re-analysis models. One of the global suppliers of long-term re-analysis wind data is ECMWF (European Centre for Medium-Range Weather Forecasts). ECMWF recently released the latest model re-analysis dataset, called ERA5, which was produced as part of the European Commission Copernicus Climate Change Service (C3S). ERA5 provides hourly estimates of a large number of atmospheric, land, and oceanic climate variables. The atmospheric data cover the Earth on a 30-km grid, while ocean wind and waves are available on a 40-km grid (Hersbach et al., 2020). The ERA5 dataset, which spans the period from 1979 to 5 days of real-time, is now available for public use. Therefore, for this study, it was decided to use ERA5 wind data to determine the wind climate for Izmir Bay. A point that is close to the entrance of the Izmir Bay(38.8N 26.5 E) was chosen, and the ERA5 hourly wind data were downloaded from the ECMWF website.

Although it is known that the ERA5 represents one of the best available open datasets for climate computations in terms of consistency and resolution (Ozbahceci, 2020, Ozbahceci et al.,2020), the data should be verified before using them in the wind climate analysis. A verification study is performed by comparing ER5 wind data with the in-situ measurements made by the Izmir Municipality in Foca, which is the closest measurement location to the ERA5 point. Fig. 3 shows the location of the ERA5 data and Foca measurement points. A time-series comparison of ERA5 and Foca for an example storm is given in Fig.4.

Figure 3. ERA5data and Foca wind measurement locations

A Time-series comparison is given for November 2018 as an example in Fig.4. Fig.4 shows that there is a good agreement between ERA5 and Foca wind speed data. As can be seen in Fig.2.4 the higher winds can be caught by ERA5 model data. However, if the time series is checked in detail, it is seen that there may be a time gap between the peaks of ERA5 and Foca data. The time gap is presented in Fig.5 as an example. The time gap may be an expected result due to the distance between the two locations. To prevent the time gap, ERA5 data were shifted 3 hours and the peaks almost coincided. The comparison after shifting 3 hours is also shown in Fig.5.
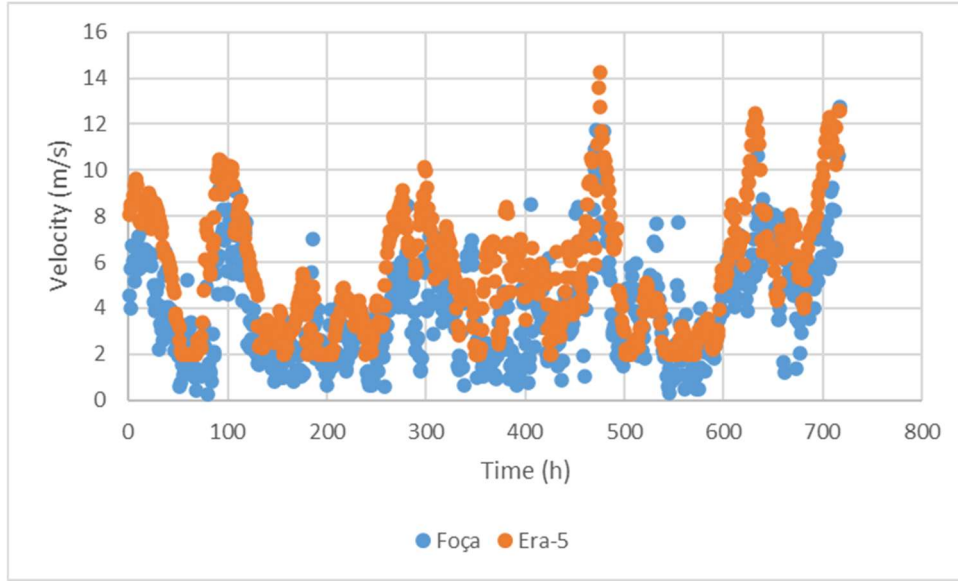
Figure 4. Time-series comparison of ERA5 and Foca wind speeds
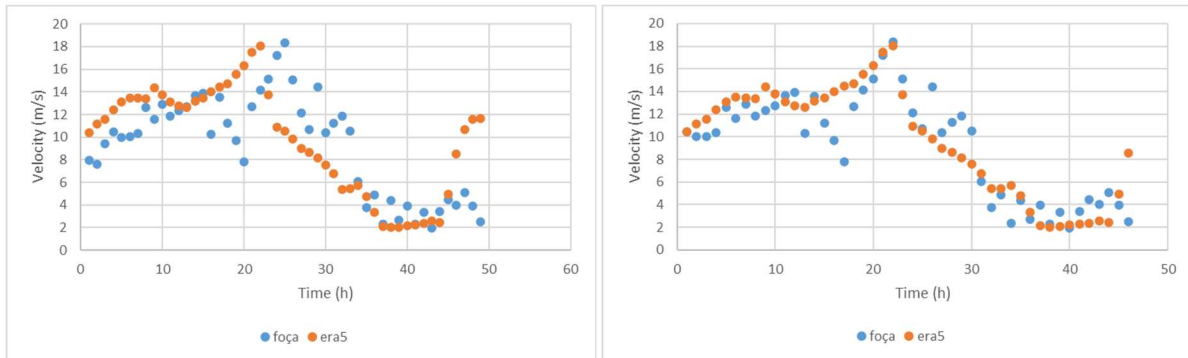
Figure 5. Time-series comparison with existing time gap (left) and after shifting (right)

Fig.5 shows that there is a good agreement between ERA5 and Foca in-situ measurement data. Therefore, it is concluded that ERA5 data can be used in the wind climate study. Almost 42 years of hourly wind data are used to obtain extreme values of the wind speed.

2.1. Extreme Value Statistics for Wind Speed

The purpose of the extreme value computation is to estimate an expected value of an extreme event that may occur once in a long period. This long period is named the return period (Rp). Extreme value analysis starts with the computation of the cumulative distribution of data which is to be fitted to a distribution function. Fitting to a distribution function is necessary to extrapolate the data set to extreme values corresponding to longer return periods with lower probabilities (Kamphius, 2020). Afterwards the best fitting distribution is examined, since the parent distribution is mostly unknown.

Ordered data are used specifically for the analysis of extreme values. The maximum annual data or the data chosen by peak over threshold (POT) method are used. In this study annual maxima of 42 years of data are used. They are arranged in descending order and non-exceedance probabilities are calculated from ordered samples by using the plotting position formula. The best-known formula to calculate the non-exceedance probability is the modified Weibull formula given in Eq. (1) (Goda, 2010).

$$P(x)=(m-\alpha)/(N+\beta) \tag{1}$$

where; $P(x)$ = probability of non-exceedance, m= order number, N=data number, a and b are coefficients changing according to the used theoretical distribution function.

The cumulative distribution functions of the commonly used distributions are given below (Goda, 2010):

Fisher Tippet I (Gumbel)

$$P(x)=\exp[-\exp(-(x-B)/A)] \quad :-\infty<x<\infty \tag{2}$$

Fisher Tippet II

$$P(x)=\exp[-(1+(x-B)/kA)^{-k}] \quad :B-kA<x<\infty \tag{3}$$

Weibull

$$P(x)=1-\exp[-((x-B)/A)^k] \quad :B\ll x<\infty \tag{4}$$

Log-normal

$$P(x)=\int p(t)dt \quad :0<x<\infty$$

$$p(x)=1/(\sqrt{2\pi}\,Ax)\exp[-(\ln x-B)^2/(2A^2)] \tag{5}$$

where; A, B, and k are scale, location, and shape parameters, respectively.

Fitting a distribution function to the calculated non-exceedance probabilities of the sample data is performed by obtaining the A, B, and k parameters. There are different methods to obtain those parameters, such as the least-squares method, the method of moments, and the maximum likelihood method. In this study, the least-squares method was used. Gumbel, Log-normal, Fisher Tippet II (k = 2.5, 3.33, 5.0 and 10.0) and Weibull (k = 0.75, 1.0, 1.4, and 2.0) distributions were used as the candidate distributions to examine the best fitting distribution function. Then the goodness of fit was tested by using the square of the correlation coefficient, MIR Criterion (Minimum Ratio of residual cor.coeff.), DOL criterion (Deviation of OutLier), and REC criterion (rejection of the candidate). Details of these tests can be found in Goda(2010).

After the best fitting distribution was determined, the extreme value corresponding to any return period Rp (in years) was calculated with the inverse function of cumulative distribution as:

$$x_{Rp}=F^{-1}(1-1/\lambda R_p \tag{6}$$

where; l is the mean rate or the number of sample data per year

The result of extreme wind speed analysis is given by plotting the non-exceedance probability, P(<u10) versus the wind speed for the Gumbel distribution, which is the best fitting one. This is demonstrated in Fig.6, together with the return periods of 50,100,200, and 500 years on the upper x-axis.95% confidence interval curves are also plotted. As can be seen in Fig.6, the speed of wind blowing from the North is equal to 20.3±2.0 m/s for Rp= 100 years.
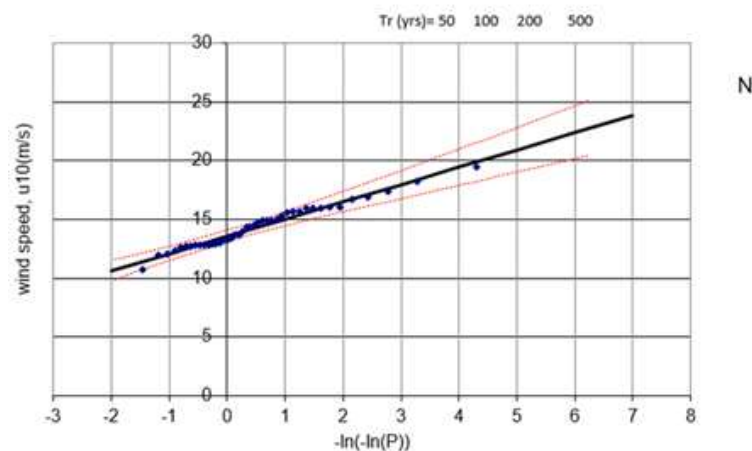
Figure 6. Extreme wind speed analysis by Gumbel distribution for the North direction

Table 2. Wind speeds (m/s) with 100 yrs return period.

Direction	Upper Limit	TR=100 yrs	Lower Limit
N	22.08	20.33	18.58
NNW	18.60	17.09	15.58
NW	18.60	16.93	15.26
WNW	19.44	17.64	15.84
W	20.28	18.31	16.34
WSW	20.13	18.33	16.53
SW	20.22	18.61	16.99
SSW	20.25	19.01	17.77
S	21.63	20.52	19.41
SSE	22.62	21.17	19.72
SE	19.54	17.96	16.39

3. FLUCTUATIONS IN SEAWATER LEVEL

Coastal design is primarily a function of water levels. Water levels control both flooding and wave exposure. When the water level rises, coastal structures will be exposed to larger waves, because water depth determines where waves break and lose most of their energy. When the water level rises this results in increased forces on the structure and overtopping of water that will damage the structure and areas behind it. Thus, most damage occurs when the water levels are high (Kamphius, 2020). There are several types of water level fluctuations, and they can be classified according to their return period or frequency of occurrence as:

—Short Term: Tides, Storm Surge, and the Barometric Surge

—Seasonal

—Long Term: Climatic Fluctuations, Sea Level Rise due to Climate Change

—Rare and Extreme: Cyclone-generated water levels and Tsunamis

Short-term and seasonal fluctuations are normally taken into account in design because they have clearly-defined statistical properties. Climatic fluctuations are taken into account in the design, but more as a basic parameter (highest/lowest water levels). The other long-term water level changes have traditionally been ignored, but are now generally recognized as necessary for design. Rare and extreme water level changes are normally not taken into account in design because they occur at very long and irregular intervals (centuries), and protection based on their extreme magnitude would be too costly to build.

In this project, to determine the fluctuations in seawater level, in-situ seawater level data measured by Izmir Municipality in Bostanli and Pasaport (Konak) locations are analyzed. The data measurement interval is 10 min and the maximum, mean, and minimum water levels are each given at 10 min intervals. Water levels due to the astronomical tide, storm surge, barometric surge, and seasonal variations are determined.

3.1. Tides

Astronomical tides are often the defining water motion in coastal areas. They cause the water level to rise and fall and may cause large-scale current patterns, sometimes with large velocities. Tides directly affect coastal morphology, navigation, fisheries, habitat, and recreational activity and they are the result of a combination of forces acting on individual water particles. These are (Kamphius, 2020):

— gravitational attraction of the earth,

— centrifugal force generated by rotation of the earth-moon combination,

— gravitational attraction of the moon,

— gravitational attraction of the sun.

If the mean water level is checked when there is no wind it is seen that the water level is increasing twice a day due to astronomical tide. This is called a semi-diurnal tide, with a tide period of almost 12 hrs. Fig.7 shows the semi-diurnal characteristics of daily tide measured in Bostanli station.
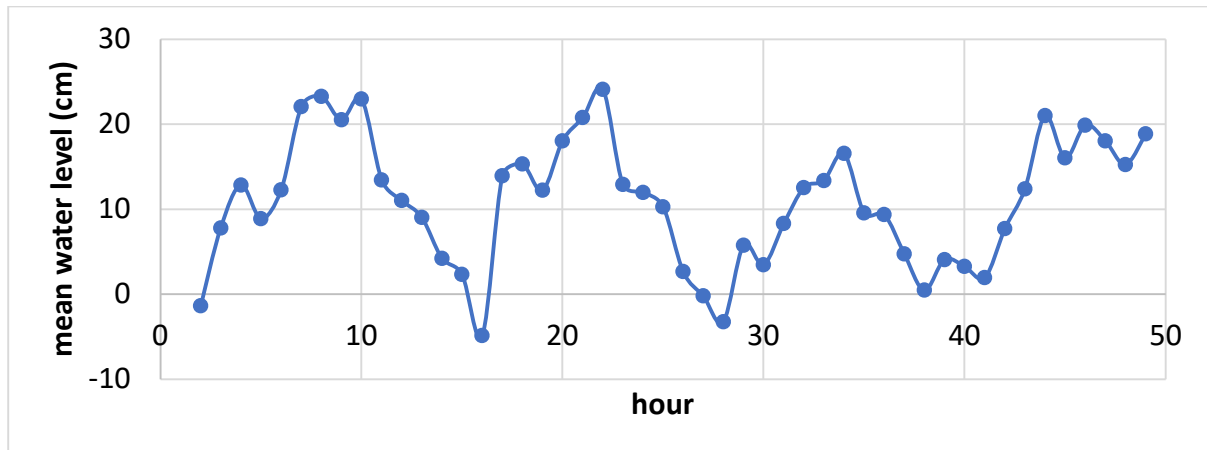
Figure 7. Semi-diurnal characteristics of daily tide measured in Bostanli measurement

Fig. 8 represents the calculated maximum daily variations in sea level for Bostanli and Pasaport measurement points in 2019. As can be seen in Fig.8, sea-level change due to astronomical tide is generally between 10-40 cm. When the water level change is higher than 40 cm., it seems that there is a storm. Fig. 8 also shows that there is a very good agreement between the Pasaport and Bostanli measurement results.
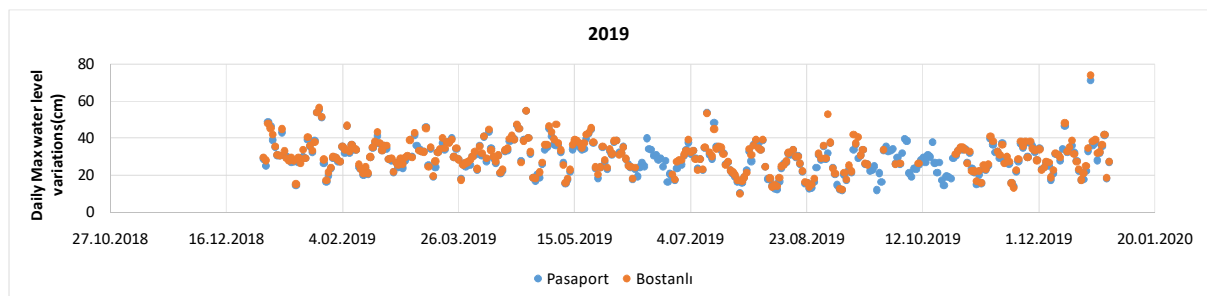
Figure 8. Calculated maximum daily variations in sea level for Bostanli and Pasaport measurement points in 2019

3.2. Storm Surge

Storm surge is a water level fluctuation of great concern in design. It is a temporary increase in water level resulting from shear stress by onshore wind. Since the same wind may also generate large waves, the combination of waves and high waterlevels is dangerous, and it is the cause of most of the world's flooding and coastal damage.

In order to determine the storm surge, the data with high wind storms are investigated. Fig.2.9 shows the change of wind speed and water level during a storm on 18.02.2018 in Bostanli.
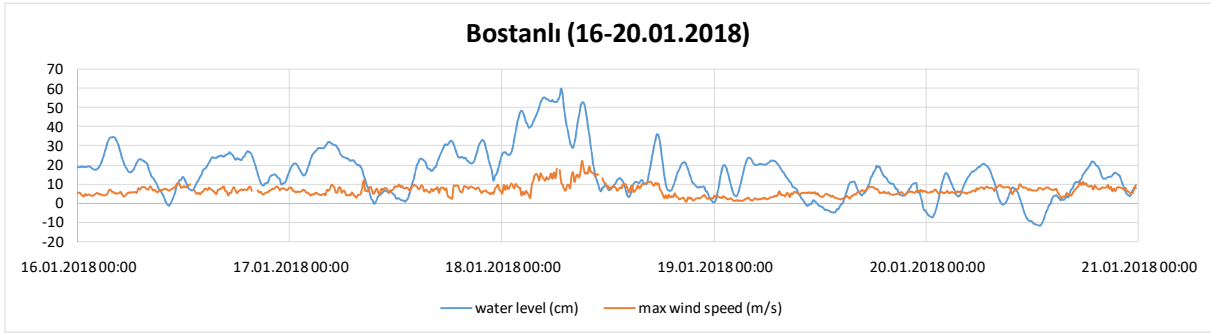
Figure 9. Change of wind speed and water level during a storm in Bostanli

Fig.9 shows that the mean water level is between 0-30cm before the storm, and as wind becomes stronger the water level is increasing until it reaches 60cm. The water level is low again during the low wind condition.

When the 5 years data are analyzed, it results that the maximum mean water level was reachedin Bostanlion 23.12.2019(76 cm). Fig.10 demonstrates the maximum increase in the mean water level in 5 years of data.
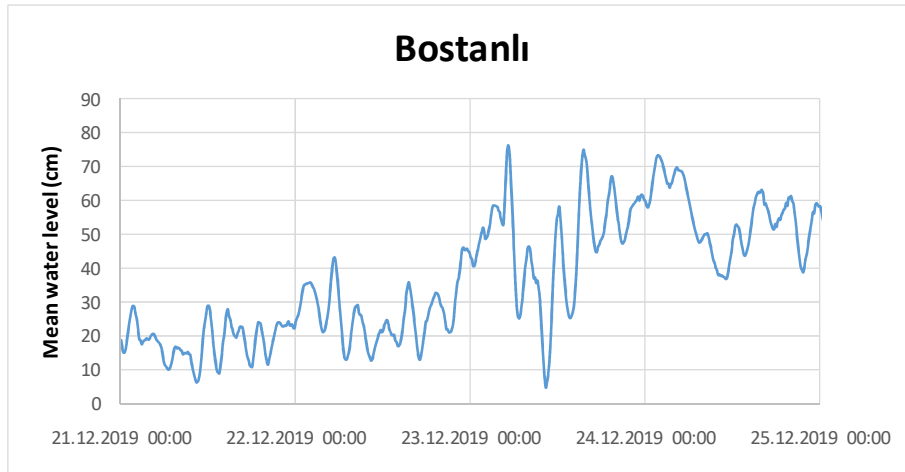
Figure 10. The maximum increase in the mean water level in 5 years data

As can be seen in Fig.10, while the mean water level was almost 20 cm on average before the storm, it increased to 76cm during the storm.

In addition to storm surge, another component that makes an increase in the mean water level is the barometric surge.

3.3. Barometric Surge

Since strong winds are the result of large pressure fluctuations, a barometric surge usually accompanies a storm surge and needs to be taken into account in storm surge calculations. The pressure over the sea surface is also measured in Bostanli and Pasaport locations. The relation between the pressure and seawater level is also investigated using measured data. An example result is presented in Fig.11. As can be seen in Fig.11, as the pressure decreases the water level increases, although there is scatter.
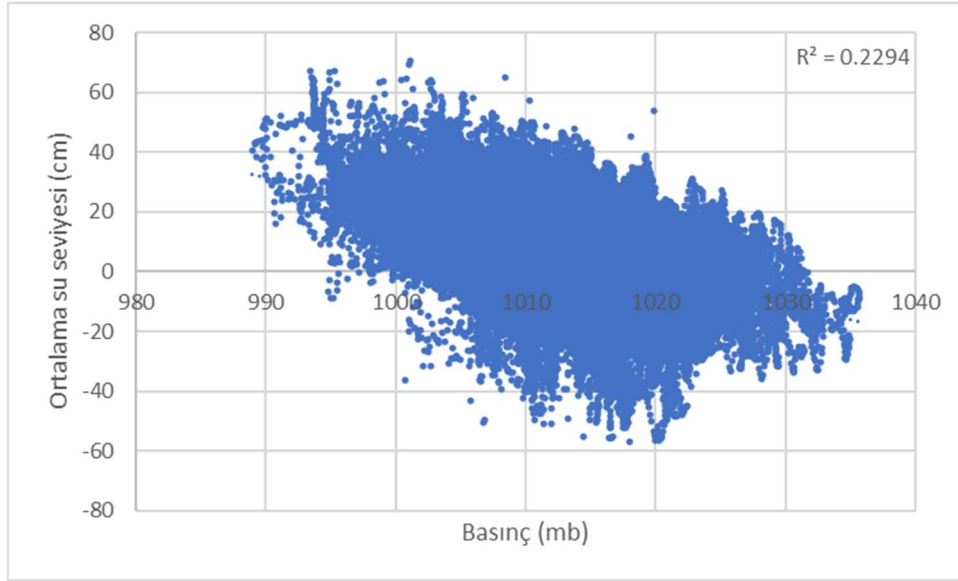
Figure 11. The relation between the pressure and sea water level

The relation between pressure and mean water level is also checked for the case of a high storm that occurred on23.12.2019 and results are shown in Fig.12.
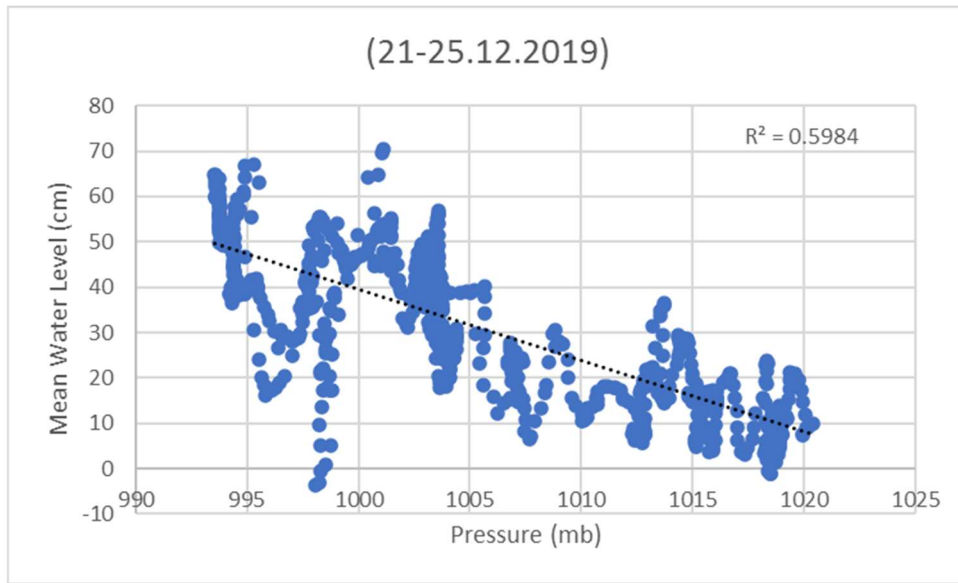
Figure 12. The relation between pressure and mean sea water level during a high storm in Bostanli

As shown in Fig.2.14, the mean water level is inversely proportional to the pressure, and there is a strong correlation between the two.

Analysis of the measured sea level data in Bostanli and Pasaport shows that the tide level is between 10-40 cm in Izmir Bay. Moreover, the mean water level increases to 80 cm due to storm and barometric surges.

3.4. Eustatic (Sea)Level Change

The term eustatic refers to a global change in ocean water levels, mainly resulting from melting or freezing of land-supported ice, such as the polar ice caps, continental ice sheets, orglaciers, and from thermal expansion or contraction of the ocean water mass with temperature change (Kamphius, 2020). At the end of the latest glaciation 20,000 years ago sea levels were 120 m below the present level. This low water level is directly related to the coverage of large landmasses, such as Canada and Northern Europe, by a continental ice sheet up to 4 km thick. The present average rate of eustatic rise

is small and therefore difficult to measure. A combination of tide gauges and satellite observations yields an estimate of 1.7 mm/yr or 0.17 m over the 20th century (IPCC, 2008). There are short-term, temporary variations in this rate, but the overall trend is quite clear. In this project sea-level measurements cover almost five years of data, from 2017 to 2021. 5 years of data are not enough to make a trend analysis and predict the future sea-level rise amounts. Therefore, another data source called TUDES data is used.

Sea level monitoring in Turkey is carried out by the General Command of Mapping within the Turkish National Sea Level Monitoring System (TUDES) program. The Monitoring network consists of 20 digital and automatic tide gauge stations positioned along the coasts of Turkey and the Turkish Republic of Northern Cyprus These tide gauge stations are in accordance with GLOSS standards. Sea level and ancillary meteorological parameters are observed at each TUDES station. 30 seconds, 15 minutes, and hourly averaged observed data are transmitted automatically to the data center in Ankara in near-real-time through GPRS, internet, and satellite telecommunication systems. Real-time and delayed mode quality controls, data analysis, database management, and data distribution activities are carried out at the data center.

One of the 20 tide gauge stations of TUDES is in Mentes, Urla. It is not in Izmir Bay but its long-term data can be used to get an idea about making a trend analysis. Hourly sea level data between 2007 and 2017 are downloaded. Yearly mean water levels are calculated and plotted. As shown in Fig.13, regression analysis reveals a trend of increasing water level between 2007 and 2017. The increase can be predicted roughly as 3mm/year.
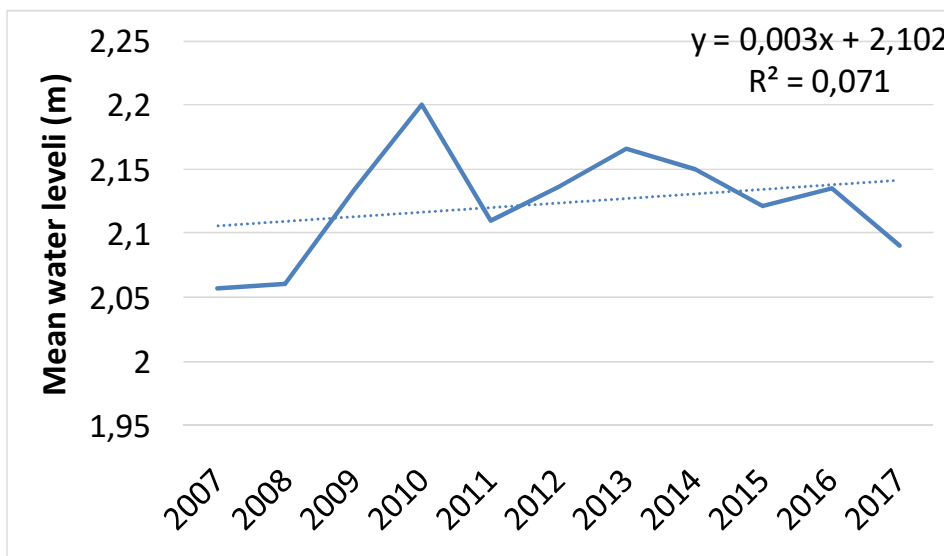
Figure 13. The increase in the water level between 2007 and 2017

In this way it may be predicted that in the next 50 years the sea will rise 15cm. As a result of analysis of fluctuations in water level, it can be concluded that in the same period the water level can increase up to 1.0 m during storms, due to tide, storm surge, barometric surge, sea-level rise, and climate change effects.

4. CONCLUSIONS

In this study, effect of sea level fluctuations on the coastal flood hazard in Izmir Bay are investigated considering different generation mechanisms.

The newest hourly re-analysis wind dataset of ECMWF (ERA5), for the years1979 -2021 is verified using in-situ wind measurements provided by the Izmir Municipality. After verification, these data are used to obtain extreme wind speeds with 100 years return period for various wind directions.

Fluctuations in water level are investigated in terms of tides, storm surges, barometric surges and the sea level rise due to possible climate change. It can be concluded that the water level can increase up

to 1.0 m during storms, considering the tide, storm surge, barometric surge, sea-level rise, and climate change effects.

REFERENCES

Bilyay, E; Ozbahceci, BO and Yalciner, AC,2011, "Extreme waves at Filyos, southern Black Sea", Natural Hazards And Earth System Sciences, 11 (3) , pp.659-666, 10.5194/nhess-11-659-2011

ECMWF. ERA 5. Retrieved from https://www.ecmwf.int/en/forecasts/datasets/reanalysis-datasets/era5.

Goda, Y., 2010. Random seas and design of maritime structures.Advanced series on ocean engineering: Vol. 33, 3rd ed. World Scientific Publishing Co. Pte. Ltd., Singapore

https://earth.esa.int/web/earth-watching/image-of-the-week/content/-/article/izmir-turkey/index.html

https://www.britannica.com/biography/Saint-Polycarp

Kamphius, J.W. (2020) Introduction to Coastal Engineering and Management. Advanced Series on Ocean Engineering: Volume 48, World Scientific,3rd Edition

Ozbahceci B.O., Turgut A.R., Bozoklu A., Abdalla, S. (2020) Calibration and Verification of Century Based Wave Climate Data Record Using Satellite Altimeter Data. Adv. Space Res. 66 (10), 2319-2339

Ozbahceci, B.O., 2020. Extreme value statistics of wind speed and wave height of the Marmara Sea based on combined radar altimeter data.Adv. Space Res. 66 (10), 2302–2318. https://doi.org/10.1016/j.asr.2019.08.025.

14TH INTERNATIONAL CONFERENCE
ON HYDROSCIENCE & ENGINEERING

MAY 26-27, 2022
IZMİR-TURKEY

ICHE2022
IZMIR, TURKEY

A FOUR-DECADE ANALYSIS OF DELTAIC SHORELINE CHANGES IN THE BLACK SEA

Tahsin Görmüş

Department of Civil Engineering, Gebze Technical University

Kocaeli, Turkey

tgormus@gtu.edu.tr

Berna Ayat

Department of Civil Engineering, Yildiz Technical University

Istanbul, Turkey

ayat@inm.yildiz.edu.tr

Burak Aydoğan

Department of Civil Engineering, Gebze Technical University

Kocaeli, Turkey

baydogan@gtu.edu.tr

ABSTRACT: River deltas are among the most fragile coastal features worldwide. The physical process active on deltas can be too complex, and one of the most important environmental indicators for a delta is how much its shoreline changed. In this study, we aimed to quantify both spatially and temporally how much the three most important deltas of Black Sea are changed their shorelines. These three deltas are Danube, Yeşilırmak and Kızılırmak. The spatiotemporal analysis reaches over 40 years. Landsat satellite image archive is used for this purpose, including Landsat 1, 5, 7 and 8. Normalized Difference Water Index (NDWI) method is used to extract the shorelines. Six to eight different satellite images are used for each delta. The results are evaluated both with the differences between the oldest and the newest date, and by considering linear regression between the data points acquired from the considered satellite images. Danube, with being the greatest discharge supplier into the Black Sea, has the biggest shoreline change occurred. Northern part of the Delta accreted greatly, where the Southern part is eroded. Both river mouths of Kızılırmak and Yeşilırmak are eroded nearly 20 m/year, same as the Danube's eroded part. It is seen that the erosion is more dominant along the Yeşilırmak shoreline, where partly accreted spots exist in Kızılırmak. Also, in the study we quantify the correlation values of linear regression rates, to justify how well aligned the points in the reported trends are. It is seen that the erosional trends are mostly coupled with relatively high correlation coefficients.

1. INTRODUCTION

The driving factors behind the shoreline change can be complex. The factors effective on the short-term could be seasonal storms and tidal characteristics of the coasts, while the long-term change may be the results of several phenomenon which redistribute the sediment along the coast. Various factors, both natural and anthropogenic, such as sea-level rise, the spatial gradients in longshore drift, change in the river sediment load, or the construction of man-made structures along the shore could result in a change in the shoreline dynamics on the long-term and cause the erosion or accretion. Sandy environments, and especially deltas are much more prone to the shoreline change because of many reasons such that they locate an intersection between the waters of different oceanographic properties, and they disrupt the longshore drifts and the sediment supply (Görmüş et al., 2021).

The quantification of shoreline change may be carried out with several approaches including in-situ beach profiling, LIDAR surveys, aerial photography; but these methods are mostly time-consuming and expensive (Do et al., 2018). Especially when the study area is vast such as Black Sea, the satellite image based mapping of shoreline change is favored (i.e. Garcia-Rubio et al., 2015). The use of satellite images is advantageous on many aspects, including the free access to several images from different dates through the date interval.

This study aims to depict the shoreline change behavior in the three most important deltas in the Black Sea, -Danube, Kızılırmak, and Yeşilırmak- through a spatial shoreline change detection algorithm based on Landsat satellite imagery along the last 40 years.

2. METHODOLOGY

The initial stages of the analysis include the selection of the satellite images to be used in the analysis. Landsat satellite images (USGS, 2018) is used as the data source in this study. The archive has been widely used in the spatial mapping of shoreline change worldwide, with several sensors used in Landsat 1/3/5 (60 m resolution), Landsat 7/8 (30 m spatial resolution) from 1972 to this day (Wulder et al., 2019). A comprehensive search is made within the archive, also considering obtaining the data in the same season and having no cloud cover near the shoreline. A selection of images for each delta is made consisting of up to 8 images in each section. To be able to make the interpretations more clearly, the study area is divided into 8 sections.

The acquired images have been radiometrically calibrated before processing. In this part, the raw pixel values are converted to spectral reflectance values. The calibrated images are then subjected to a series of analysis to acquire the exact position of the shoreline. To this aim, binary images are acquired for each satellite images dividing the study area into two zones of land and sea. The binary images are acquired using an index-based method, namely NDWI (McFeeters, 1996). The main formulation of raster calculation in the method is as follows:

$$NDWI = \frac{Green - NIR}{Green + NIR} \tag{1}$$

in where Green and NIR corresponds to the green and near-infrared band of the image set. The acquired NDWI images are yet not binary, but the binary images are acquired using a threshold value over the image which becomes more suitable for thresholding in its NDWI form. The threshold value is determined by inspecting the RGB image of the dataset together with the NDWI image.

The binary images are used to automatically extract the border between two classes of land and water, which defines the coastline position in the date of the satellite image. The differences between different dates are analyzed using two statistical parameters of End-Point Rate (EPR), and Linear Regression Rate (LRR). EPR is acquired by dividing the spatial difference between the oldest and the newest data points by the time between the two shorelines. LRR is defined by using the 1st degree polynomial fits to all available data points between the oldest and the newest shorelines. Both EPR and LRR values are given in m/year where positive values indicate accretion and negative values indicate erosion. The distance between the transects of the shoreline change computation is set to 50 m.

The natural sources of uncertainty over acquired shoreline positions is considered to be minimum, since Black Sea has very low tide levels to affect the sea levels, and the seasonal differences set to be minimum with selecting satellite image within the same season. No additional georeferencing is done to the images which are already referenced by WGS84 geographic coordinate system. Uncertainty related to the satellite geometric errors is neglected as also done by Aladwani (2022).

3. RESULTS AND DISCUSSION

The results of the analysis together with the information of the analysis sections are given in Table 1.

Table 16. Properties and the statistical averages of the shoreline change analysis for sections.

Section no	Section name	Considered year interval	Number of transects	Number of images	Average EPR (m/year)	Average LRR (m/year)
1	Danube 1	1972-2017	542	4	+4.93	+3.94
2	Danube 2	1976-2018	761	8	-4.99	-5.22
3	Danube 3	1976-2018	1882	8	-1.31	-1.55
4	Kizilırmak 1	1974-2017	512	8	-1.58	-1.10
5	Kizilırmak 2	1974-2017	227	8	-6.57	-5.99
6	Kizilırmak 3	1974-2017	501	8	+0.54	+1.42
7	Yeşilırmak 1	1975-2016	390	6	-2.05	-1.72
8	Yeşilırmak 2	1975-2016	810	6	-1.60	-1.33

The results show that the severe erosion rates are seen in some parts of the Black Sea deltas, up to 6.6 m/year for Kızılırmak. The higher accretion is seen in Danube Delta with nearly 4 m/year in the Northern part of the river mouth, in means of average values. The spatial distribution of the LRR for the Danube Delta is given in Figure 1 for three sub-sections.
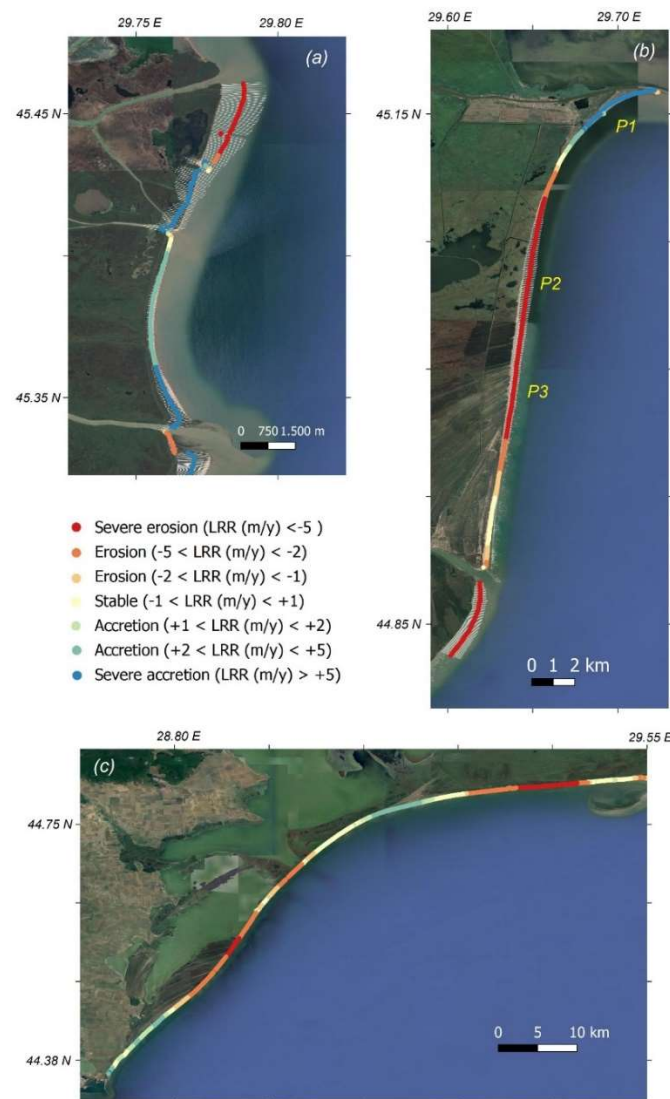
Figure 1. Spatial distribution of shoreline change in Danube Delta.

The change of shoreline change along the coastline is typically follows each other as erosion and accretion zones. The Northern part of the Danube (Figure 1a) is clearly an accretion zone, where the following Southern part (Figure 1b) is an erosion hotspot. The far Southern part (Figure 1c) is mixed with erosion and accretion hotspots, but the magnitude of shoreline change is smaller than other subsections (Table 1). According to the four transects located in the critical points of the Danube Delta; the LRR in the accreted part is +6.7 m/year with ±1.4 m/year uncertainty (R^2=0.98) for the representative transect (P1 in Figure 1). For the eroded part, the rates are -10.9 m/year with ±2.5 m/year uncertainty (R^2=0.95) and -5.3 m/year with ±1.7 m/year uncertainty (R^2=0.90) for two representative transects (P2 and P3 in Figure 1, respectively).

The spatial distribution of the LRR for Kızılırmak Delta in Figure 2 for three sub-sections, and for Yeşilırmak Delta in Figure 3 for two sub-sections.
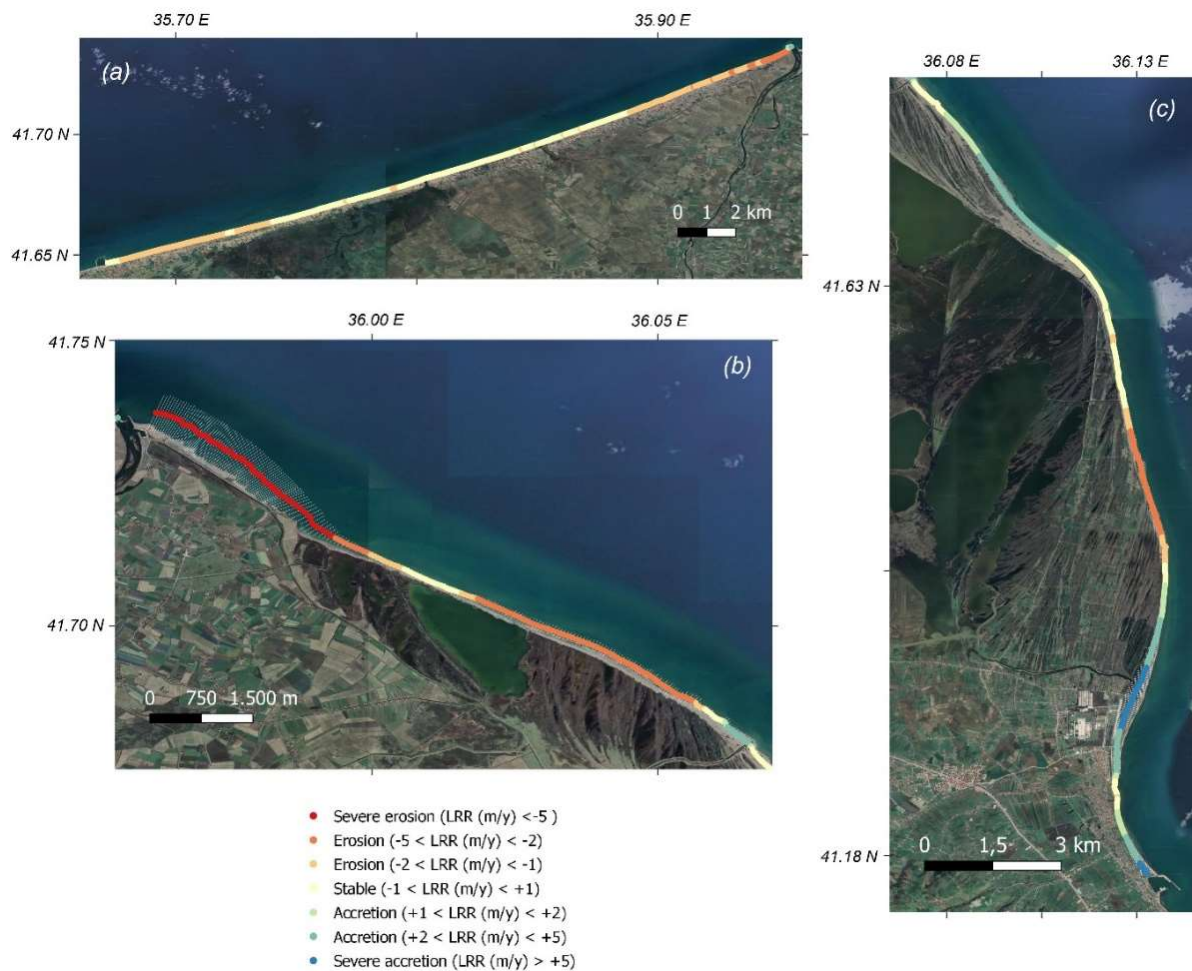
Figure 2. Spatial distribution of shoreline change in Kızılırmak Delta.
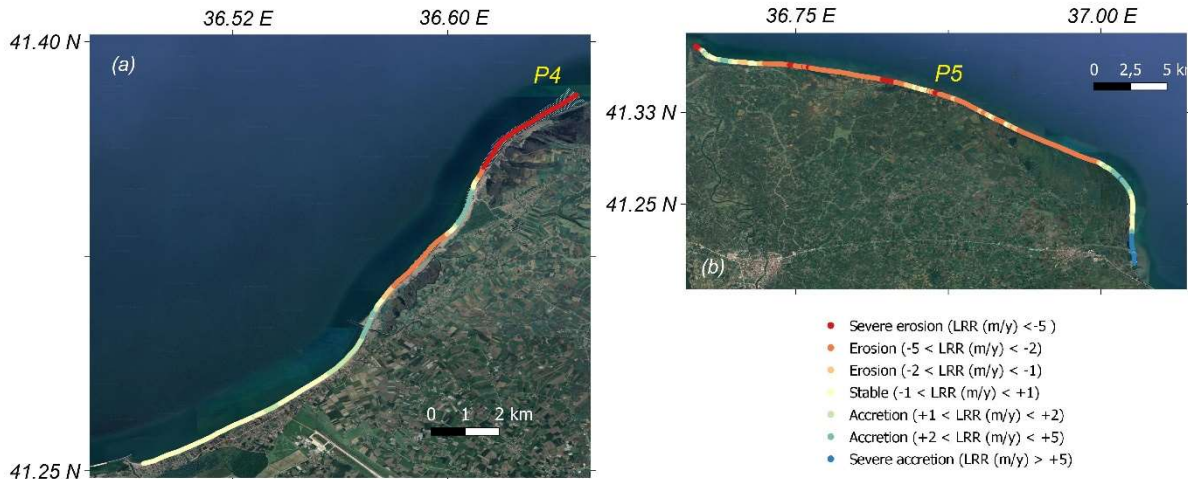
Figure 3. Spatial distribution of shoreline change in Yeşilırmak Delta.

The Kızılırmak River Delta has been divided into three sub-sections, where the Western part of the river mouth (Figure 2a) has severely eroded locations near the river mouth, but also has relatively stable (-1 < LRR (m/year) < +1) locations through the Western direction. The severe erosion (up to -6.6 m/year) near the river mouth is evident (Figure 2b), but the coastline located in the Eastern Delta has neighboring erosion and accretion spots which makes the average value positive with LRR=+1.4 m/year. The consistent erosion patterns are seen in Yeşilırmak Delta, considering both Eastern (Figure 3a) and Western (Figure 3b) part of the river mouth. Average LRR for the delta is -1.5 m/year, but near the mouth consistent erosion patterns are seen with LRR < -5 m/year. According to the two transects located in the critical points of the Yeşilırmak Delta; the LRR near the mouth has an erosion trend with -15.6 m/year with ±5.4 m/year uncertainty (R^2=0.94), where following Eastern part has a trend with -6.1 m/year with ±2.2 m/year uncertainty (R^2=0.94) (P4 and P5 in Figure 3, respectively).

Reduction in the sediment discharge from the rivers is one of the main effects over the shoreline change in the basin. It is stated that the Danube River presently supplying less than one-third of the sediment comparing to the last century because of the anthropogenic effects (Vespremeanu-Stroe et al., 2017). The shoreline dynamics in the Kızılırmak Delta is also being affected by the nine dams being constructed along the river during the last 50 years (Ataol et al., 2019). Although it is needed a closer look to all the factors effective; a rough conclusion can be made that anthropogenic forcings are the most important factors over the shoreline change in the delta basins in the long-term analysis (40 years).

4. CONCLUSIONS

This study evaluates the shoreline change along the three most important deltas of the Black Sea; Danube, Kızılırmak and Yeşilırmak. The analysis has been carried out in means of a spatial analysis over the last 40-years based on the extraction of shorelines from the Landsat satellite image archives. Severe erosion patters are reported all three deltas with relatively long coastlines having a linear rate of shoreline change greater than 5 m/year. The main driver of the shoreline change for the considered timeframe is evaluated as the anthropogenic influences.

REFERENCES

Aladwani, N.S., (2022). Shoreline change rate dynamics analysis and prediction of future positions using satellite imagery for the southern coast of Kuwait: A case study, Oceanologia. https://doi.org/10.1016/J.OCEANO.2022.02.002.

Ataol, M., Kale, M.M., Tekkanat, İ.S., (2019). Assessment of the changes in shoreline using digital shoreline analysis system: a case study of Kızılırmak Delta in northern Turkey from 1951 to 2017, Environmental Earth Sciences, 78, 579. https://doi.org/10.1007/s12665-019-8591-7.

Do, A.T.K., Vries, S. de, Stive, M.J.F., (2018). The Estimation and Evaluation of Shoreline Locations, Shoreline-Change Rates, and Coastal Volume Changes Derived from Landsat Images, Journal of Coastal Research, 35 (1), 56-71. https://doi.org/10.2112/jcoastres-d-18-00021.1.

Garcia-Rubio, G., Huntley, D., Russell, P., (2015). Evaluating shoreline identification using optical satellite images, Marine Geology, 359, 96-105. http://dx.doi.org/10.1016/j.margeo.2014.11.002.

Görmüş, T., Ayat, B., Aydoğan, B., and Tatui F., 2021. Basin Scale Spatiotemporal Analysis of Shoreline Change in the Black Sea, Estuarine, Coastal and Shelf Science, 252, 107247, https://doi.org/10.1016/j.ecss.2021.107247.

McFeeters, S.K., (1996). The use of the Normalized Difference Water Index (NDWI) in the delineation of open water features, International Journal of Remote Sensing, 17 (7), 1425-1432. https://doi.org/10.1080/01431169608948714.

USGS, 2018. LANDSAT Satellite Images, http://earthexplorer.usgs.gov. All images are courtesy of the U.S. Geological Survey. Accessed on 31/12/2018.

Vespremeanu-Stroe, A., Zăinescu, F., Preoteasa, L., Tătui, F., Rotaru, S., Morhange, C., Stoica, M., Hanganu, J., Gabor-Timar, A., Cârdan, I., Piotrowska, N., (2017). Holocene evolution of the Danube delta: an integral reconstruction and a revised chronology. Marine Geology, 388, 38-61.

Wulder, M.A., Loveland, T.R., Roy, D.P., Crawford, C.J., Masek, J.G., Woodcock, C.E., Allen, R.G., Anderson, M.C., Belward, A.S., Cohen, W.B., Dwyer, J., Erb, A., Gao, F., Griffiths, P., Helder, D., Hermosilla, T., Hipple, J.D., Hostert, P., Hughes, M.J., Huntington, J., Johnson, D.M., Kennedy, R., Kilic, A., Li, Z., Lymburner, L., McCorkel, J., Pahlevan, N., Scambos, T.A., Schaaf, C., Schott, J.R., Sheng, Y., Storey, J., Vermote, E., Vogelmann, J., White, J.C., Wynne, R.H., Zhu, Z., (2019). Current status of Landsat program, science, and applications, Remote Sensing of Environment, 225, 127-147. https://doi.org/10.1016/j.rse.2019.02.015.

EXPERIMENTAL STUDY ON A SPAR TYPE FLOATING PLATFORM WITH MODIFIED MOORING LINES IN THE WAVE CHANNEL

Kadir Aktas, Yüksel Alkarem, Elif Girgin, Bergüzar Oztunali Ozbahceci

Civil Engineering Department, İzmir Institute of Technology

Urla, Izmir, Turkey

kaktas@iyte.edu.tr, elifgirin@iyte.edu.tr, berguzarozbahceci@iyte.edu.tr

Ali Aridici

Siemens Gamesa Renewable Enerji A.Ş.

Izmir, Turkey

ali.aridici@siemensgamesa.com

Ünver Özkol

Mechanical Engineering Department, İzmir Institute of Technology

Urla, Izmir, Turkey

aliaridici@iyte.edu.tr, unverozkol@iyte.edu.tr

1. INTRODUCTION

The offshore wind industry is foreseen to be highly potent to decarbonize the energy industry. A wind farm situated offshore encounters 90% greater wind on average than an onshore wind farm (Archer & Jacobson, 2005). Walsh (2019) shows that offshore wind farms have moved gradually from the coastline in Europe since the beginning of the 21st century, and their average water depth has increased to 60 meters. As water depth increases, the shift of wind turbine foundations from being fixed to floating is gradually gaining pace in the wind industry. Therefore, the demand to capture the accurate responses of the floating offshore wind turbines (FOWT) is high (Alkarem and Ozbahceci, 2021).

There are several platform types for FOWTs, and each one adopts a different approach to achieve stability. By adding weight at high drafts, a platform type delivers better rotational restorability through gravity. Spar-buoy primarily uses this method (Jonkman, 2010). Restorations can also be produced by distributed buoyancy force by increasing the water-plane area. The barge platform is a typical example of this method(Jonkman, 2007). Another concept to produce the restoration is by using mooring lines. Any deviation from the platform's original position creates an unbalanced sum of forces on the platform. Mooring lines must be highly tensioned at the equilibrium position for the restorations to be sufficient, requiring the platform to have an excess buoyancy bank to create that tension. The tension leg platform (TLP) principally adopts this approach (Jonkman and Matha, 2013) and illustrates those three well-known platforms supporting a horizontal axis wind turbine.

One of the tools to capture the accurate responses of FOWT is an experimental study. Several experimental studies have investigated the hydrodynamic behavior of the various floating platforms of FOWT. Experiments have been conducted in different sizes of wave basins all around the world, with the scale factor varying from 1/105 at the smallest to 1/22.5 at the largest (Stewart and Muskulus, 2016)
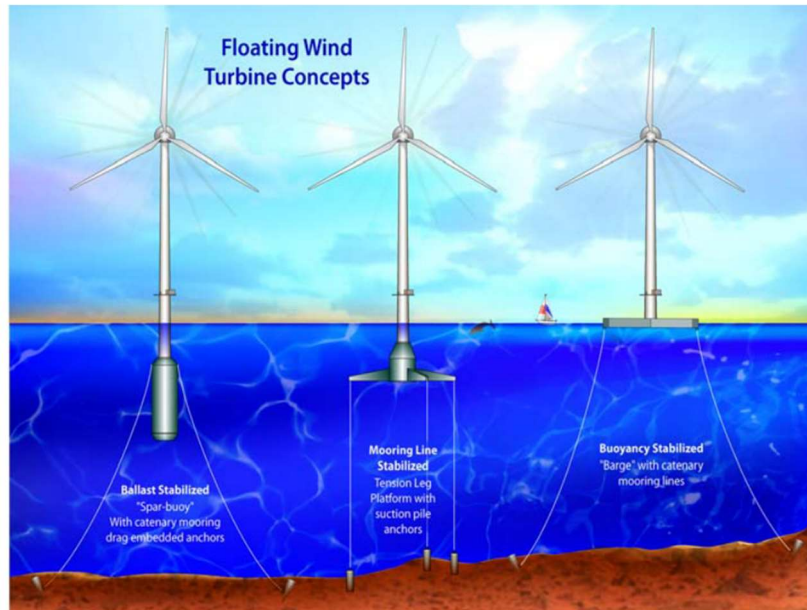
Figure 1. Three different FOWT concepts(source: Butterfield et al. 2005)

In this study, hydrodynamic responses and the forces in the mooring lines for a spar platform are experimentally investigated through a small-scale physical model in a1.0m width, 1.4m height and 40 m length wave channel. Running experiments in a wave channel instead of a basin imposes restrictions on the experimental setup. These are: 1) wind turbine, 2) spar model with a long draft to be modeled, and 3) mooring lines configuration. To overcome those restrictions: 1) A smaller wind turbine (300 KW) was modeled instead of a 5MW reference turbine, 2) A distorted spar platform was designed to be installed at 40m depth in prototype scale, and 3) the downwind mooring cables are modified. However, to preserve the angle between the mooring lines and their geometrical and elastic compliances an original vertical pulley-based system is introduced where the cable direction is deviated and kept inside the wave flume, as delineated in Fig. 2. The main advantage of this modified system is that it keeps mooring-induced stiffness relatively similar for a wide range of excursions.

Firstly, a parametric study was carried out to design a floating spar platform supporting a 300-kW wind turbine (Alkarem, 2020). Then, the model was tested numerically, and a 1/40 scaled model was manufactured and tested in the hydraulics lab of the Civil Engineering Department at Izmir Institute of Technology.

2. EXPERIMENTAL SETUP

The laboratory experiments are conducted in a wave channel of 40 m in length, 1 m in width, and 1.40 m in depth. The channel was constructed from steel, but some part of 8m length was covered by thick glass to make visual observations during the experiment. At the beginning of the wave channel, a homemade piston-type wave generator was built to generate waves (Fig.2). The wave generator runs on a 5-kW, 2000rpm AC servo motor. The servo motor is connected to a ball screw shaft which holds a vertical plane called the wave board. The revolutions of the servo motor are converted to the linear motion that drives the wave paddle back and forth in the wave channel. The wave generator can produce regular and irregular waves observed in nature.

For wind turbine modeling, the POYRA-P36 model turbine of the NORTHEL company was used. The prototype turbine has a nominal power of 300kW and a blade length of 18m. A scaled model of this turbine used in the experiments was produced by a 3D printer to ensure that it was light and had blades with a high lift to drag ratio at low Reynolds numbers. The model scale was determined as 1/40, considering wave channel and production capabilities constraints.
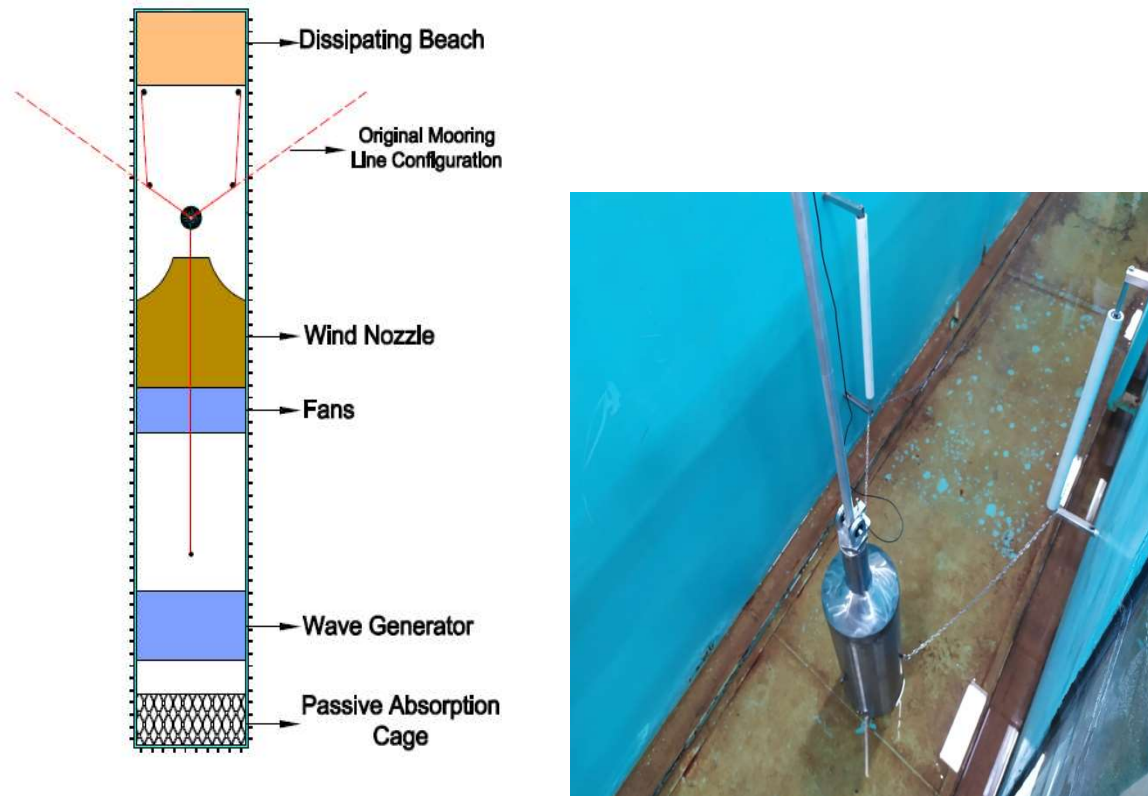
Figure 2. Top-view of the wave flume and the original and modified configuration of the mooring system. (left) and Spar model, modified cables and pulleys in the wave channel (right) (Aktas, 2021)

To generate wind on the wave channel, a wooden wind nozzle was produced. Four axial industrial speed-adjusted fans were used to control the airflow. A perforated and honeycomb plates were used to distribute the airflow coming out of the fans homogeneously and without a swirl.

The shell of the spar platform model is made of stainless steel, and studless steel chains were used for mooring lines. For the ballast, a mix of various stones was used inside the spar model and a steel ballast was used at the bottom of the model. It was ensured that the draft and center of gravity of the whole system (Platform+wind turbine+ mooring lines) were the same in the prototype design and the experimental model.

The spar platform was equipped with sensors to determine the responses in 3 DOF (surge, heave, and pitch) and the loads on the mooring chains. Since the water-proof load sensors that can operate underwater are very expensive, standard types were used after sealing the load sensors.

An extensive test series were conducted in the experiments. Various load conditions were applied during the free decay tests, test series of only waves, only wind, and waves+wind conditions. Test results were compared with the hydrodynamic numerical model. ANSYS™ AQWA® package is used in the numerical simulation. The software can model the coupled motions of all six degrees of freedom (DOF) of floating structures under the influence of gravitational, hydrostatic, hydrodynamic, wind, mooring, and current loads either in the frequency-domain (FD) for rapid evaluation (valid for the initial stages of a new design) or in the more rigorous time-domain (TD) analysis (ANSYS Inc., 2013). The global equation of motions for one structure in FD and TD, respectively, are written as:

$$[-\omega^2 M - i\omega C + K]X(\omega) = F(\omega) \tag{1}$$

$$M\ddot{X}(t) + C\dot{X}(t) + KX(t) = F(t) \tag{2}$$

where; M is the assembled structural mass and added mass matrix, C is the damping matrix and K is the total stiffness of the system including the linear hydrostatic stiffness coupled with the additional stiffness from the mooring lines, and F is the 6×1 matrix containing the combination of all external forces as a function of frequency ω or time t. In TD, AQWA uses a semi-implicit two-stage predictor-corrector scheme by integrating in time displacement X and velocity X˙ matrices to solve for the acceleration X¨ matrix. The hydrodynamic model employs a three-dimensional radiation/diffraction panel theory and Morison's equation. The details of the model can be found in Alkarem and Ozbahceci (2021).

RESULTS AND CONCLUSIONS

The maximum response and tension values under different wave conditions in the tests are compared with the corresponding valuesin the numerical model. Comparison results are given in Fig.3. Since the wave attack is perpendicular to the model, no other responses are excited in the tests as expected.Tension results are given for the modified landward cables: cable 2 and cable 3.
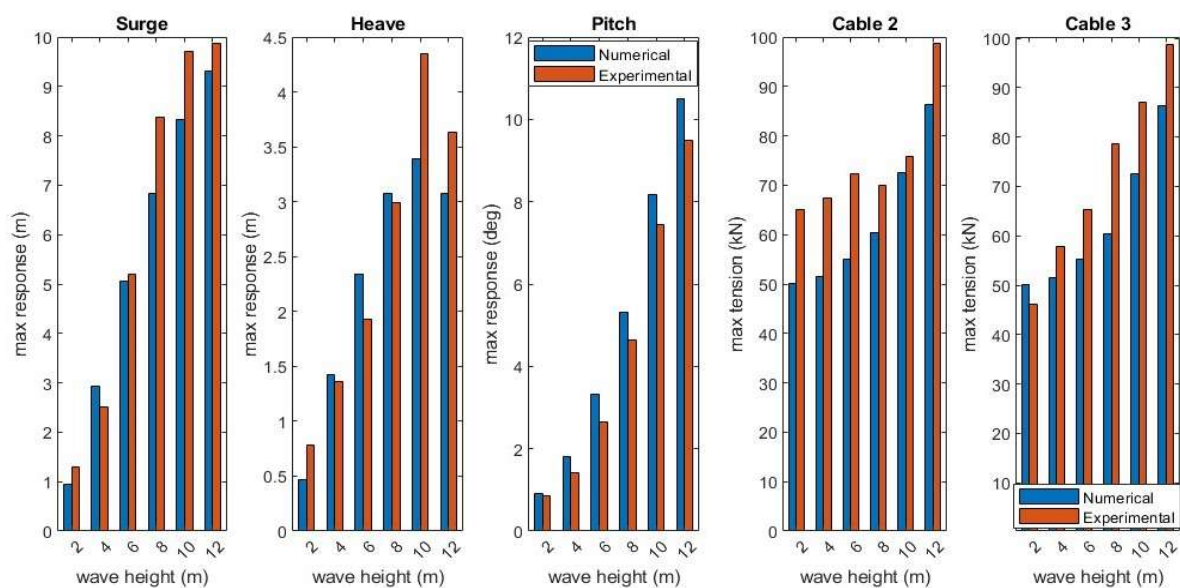
Figure 3. Comparison of the maximum response and tension values under different wave conditions in the experiments and numerical model

Fig 3 shows that the experimental and the numerical model results on the responses and tensions agree well. It is concluded that the modified cables can model the behavior of the cables in the original configuration.

REFERENCES

Aktas, Kadir (2021)." Wave Generation And Analysis In The Laboratory Wave Channel To Conduct Experiments On The Numerically Modeled Spar Type Floating Wind Turbine".Master Thesis. Izmir Institute of Technology

Alkarem, Y. (2020). "Numerical Examination of Floating Offshore Wind Turbine and Development of an Innovative Floating Platform Design." Master Thesis. Izmir Institute of Technology

Alkarem, Y.R., Ozbahceci B.O. (2021) "A complemental analysis of wave irregularity effect on the hydrodynamic responses of offshore wind turbines with the semi-submersible platform", Applied Ocean Research, 113. https://doi.org/10.1016/j.apor.2021.102757

ANSYS Inc. (2013). Aqwa Theory Manual. 174.

Archer, C. L., and Mark Z. J. (2005). "Evaluation of Global Wind Power." Journal of Geophysical Research D: Atmospheres 110 (12): 1–20. https://doi.org/10.1029/2004JD005462.

Butterfield, Sandy, Walter Musial, Jason M. Jonkman, and Paul D. Sclavounos. 2005. "Engineering Challenges for Floating Offshore Wind Turbines." Journal of Applied Physics, no. December 1989 (October):13.

Jonkman, Jason M. 2007. "Dynamics Modeling and Loads Analysis of an Offshore Floating Wind Turbine" 8 (11): 1595–1606. https://doi.org/10.4161/hv.21225.

———. 2010. "Definition of the Floating System for Phase IV of OC3." Contract 1 (May): 31. https://doi.org/10.2172/979456.

Jonkman, Jason M., and Denis Matha. 2013. "Dynamics of Offshore Floating Wind Turbines— Analysis of Three Concepts†." Wind Energy, no. January: 1–20. https://doi.org/10.1002/we.

Stewart G., Muskulus M. (2016) "A Review and Comparison of Floating Offshore Wind Turbine

Model Experiments" Energy Procedia 94 (2016) 227 – 231

Walsh, Colin. 2019a. "Offshore Wind in Europe." Refocus 3 (2): 14–17.

.

THE USE OF GEOTEXTILE SAND FILLED ELEMENTS (GEOTUBE® UNITS) FOR EROSION PROTECTION OF BEACHES AND DUNES

Mink ter Harmsel/Edwin Zengerink

TenCate Geosynthetics Netherlands bv

Hengelo, Overijssel, The Netherlands

ABSTRACT: Due to the climate change sea level is rising and extreme weather conditions become even more tougher. The result of this change in the conditions is that more and more beaches are eroding and sand dune structures are in danger. The measurements to protect the beaches and dunes is to install submerged or emerged breakwaters. These breakwaters can be created by using rock, concrete blocks or sand filled geotextile elements called Geotube® units. This paper outlines two projects where Geotextile tubes have successfully been installed as submerged breakwaters and two projects where Geotextile tubes have been installed as emerged breakwater and have proved their effect. Submerged breakwater projects are located at the Mediterranean coast in the South of France (Sete) and in the Gulf of Mexico/Caribbean Ocean (Cancun). Two emerged projects are situated at the Atlantic Ocean coast in Portugal (Ofir) and The Channel in France (Gouville-sur-mer). This paper will show you how Geotextile tubes are installed and what their effect. It will also show you the status of the submerged breakwaters after approx. 10 years after installation. Finally, a comparison for CO_2 emission between the Geotextile tubes filled with locally available sand versus a rock breakwater will be presented for one of the projects.

KEY WORDS: erosion protection; emerged breakwaters; submerged breakwaters; geotextile tube; Carbon Footprint; Geotube®

1. INTRODUCTION

1.1 Geotextile sand filled elements: What are they?

In general Geotextile sand filled elements are known as GeoBag, Geocontainer® and Geotube® units.

1.1.1. GeoBag units (Picture 1 and 2) have a capacity between 0,5 and 10 m3 and are filled mostly mechanical.

Figure 1 & 2. Installation of Geobags

1.1.2. Geotextile conatiners are installed with a split barge (figure 3 and 4) and have a volume between 150- 600 m3 depending to the split barge. Geotextile containers are filled mechanicly.

Figure 3 & 4. Deployment and installation of Geocontainer systems.

1.1.3. Geotextile tubes are filled hydraulically and are designed depending to the needs.

Figure 5. Installed Geotube system as perimeter bund

Geotextile tube is defined as "a large tube [greater than 7.5 feet (2.3 m) in circumference] fabricated from high, strength, woven geotextile, in lengths greater than 20 linear feet (6.1 m)", according to GRI Test Method GT11: Standard Practice for "Installation of Geotextile Tubes used as Coastal and Riverine Structures". Geotextile tubes used in coastal and riverine applications are most often filled hydraulically with slurry of sand and water, although other fill materials have been used. Tubes can also be filled by a combination of mechanical/hydraulic method.

Geotextile tube is typically supplied with closure seams at both ends of the tube. Also associated are "fill ports" which are geotextile sleeves sewn into the top of the geotextile tube into which the pump discharge pipe is inserted (see Fig. 3). Initially, the filling ports at the extreme ends of the geotextile tube are utilised while those in-between are temporarily closed. One end is pumping slurry in, while the other end is for water pressure relief and discharge. In this way, the slurry will flow from one end to the other in the geotextile tube gradually depositing sand along the way as pressure drops. It may be necessary to move the filling point in order to achieve more even filling of the geotextile tube. After filling the geotextile tube, the port sleeves are closed and attached to the geotextile tube in a manner sufficient to prevent movement of the sleeve by wave action. Geotextile tube may be used to

replace rock as conventional building blocks in marine and hydraulic engineering dyke structures. Geotextile tube is often more economical when compared with the use of rock and its application can also reduce construction time.
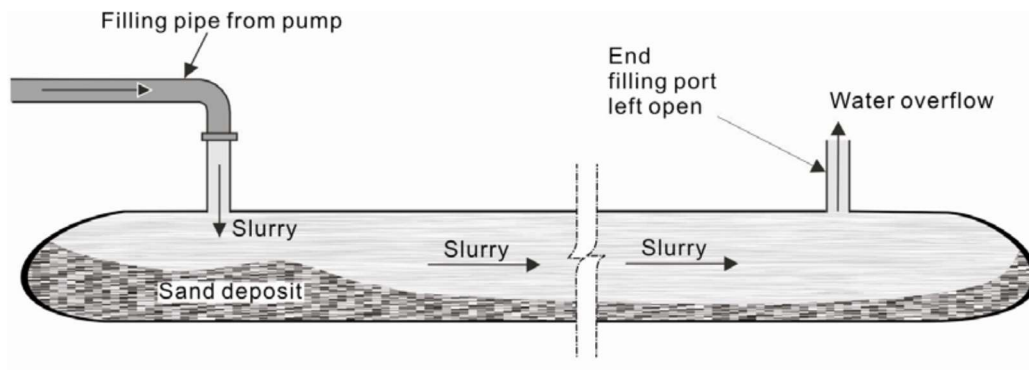
Figure 6. Schematic filling of geotextile tube with sand slurry

2. DESIGN METHODOLGY FOR GEOTEXTILE TUBES

From a technical standpoint the geotextile tube needs to fulfil the following (Yee, 2002, Yee & all 2006):
• Internal stability

> ➢ The geotextile used to fabricate the tube, including seams and closure, need to withstand the stresses that may be encountered during placement and filling process
> ➢ The geotextile should prevent excessive loss of fines but be sufficiently permeable to prevent excessive build up of pressures during installation

• External stability

> ➢ The geotextile tube should be hydraulically stable against waves and currents
> ➢ The geotextile tube should be geotechnically stable against sliding, overturning, bearing and global slip failures (see Fig. 2)

• Durability

> ➢ The geotextile should endure and perform the engineering functions over the lifespan of the design
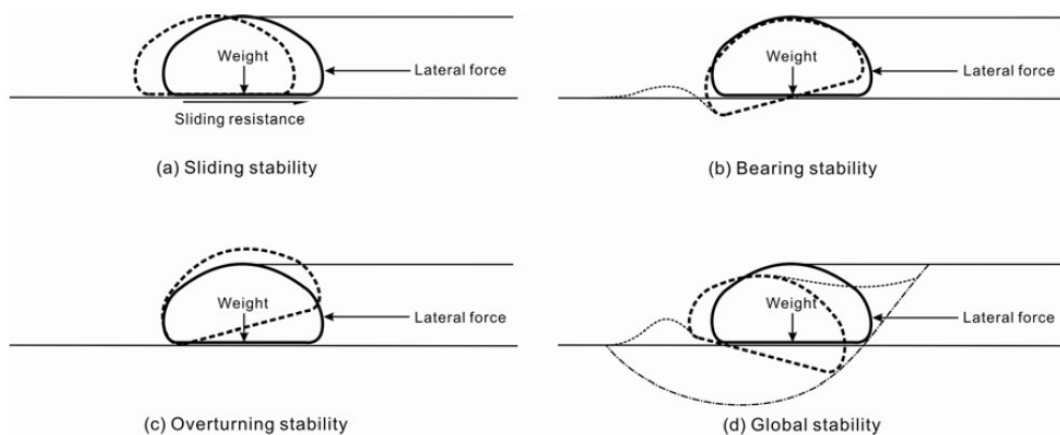
Figure 7. Geotechnical stability checks

Critical stressing period for a geotextile tube is during the pumping of slurry into the geotextile tube. Hydraulic pressure will put the geotextile tube in circumferential as well as longitudinal tension. Design software such as GeoCoPS, SOFFTWIN are available to determine tensions and geometry of geotextile tubes. Numerical analysis is based on the equilibrium of an encapsulating flexible shell filled with pressurized slurry.

Conditions that influence the properties of geotextile over time should be considered. The polymers used to manufacture geotextiles today are generally durable in biological and chemical environment of commonly found soils. Ultra-violet light exposure will degenerate polymeric materials including geotextiles. This can be significant in Asia where a large part of the continent receives high radiation intensities throughout the year. Geotextile used to fabricate the geotextile tube may be stabilized through the addition of inhibitors during manufacture to enhance durability against ultra-violet degradation. Submerged portions of the geotextile tube attract relatively reduced radiation intensities and biological growths or other depositions on the tube surface will offer additional shielding from exposure. It is necessary to apply factors of safety for creep, construction damage, environmental damage, seam efficiency, etc. to arrive at the ultimate tensile strength of the geotextile to be used for fabrication. Typically, a global factor of safety of 4 to 5 is not unusual.

There are two fundamental geotextile properties that govern how it behaves hydraulically, namely AOS (apparent opening size) and permeability. The AOS of a geotextile is a measurement of its effective pore channel diameter. Since it is not possible to manufacture geotextiles with a uniform pore channel diameter the AOS is normally expressed as some percentage of the distribution of pore sizes. Permeability of a geotextile is a measurement of its capability to allow water to pass through and is expressed either as a Darcy's 'permeability' coefficient, by a 'permittivity' value or by a volume 'flow rate'. These two geotextile hydraulic requirements are determined by applying geotextile filtration design rules.

There are many filter rules available. Generally, all the available design rules are conceptually similar; an effective filter needs to prevent the uncontrolled loss of fines over time while at the same time allow sufficient water to flow to prevent build up of excess pore water pressures. The two may be competing in the selection of an ideal geotextile filter as smaller AOS is more effective in preventing fines from passing through, but larger AOS directionally means a more permeable geotextile that would be beneficial for preventing build up of excess pore water pressures. The design and selection of the geotextile filter is often a case of compromise, depending on which of the two properties may be more critical to a structure.

3. GEOTEXTILE TUBE APPLICATIONS

3.1. Coastal Applications

Groins, submerged and emerged breakwater, dune foot protection, submerged revetments, channel

repair, land reclamation, artificial reef sill structures

3.2. River applications

Submerged breakwater, groins, sediment management, river training, bank protection

3.3. Other

Nature development areas, dewatering of dredged material, temporary structures

4. PROJECTS

4.1. LIDO, Sete France (Zengerink, 2018)

4.1.1 Introduction of the project

The Mediterranean coast in the south of France is regularly battered by heavy and storms and waves measuring over 5 m high and wind speeds of over 100 km/hour. This leads to significant erosion of

the natural beach areas. The beaches of France near the coast are famous for their appearance – long, gently sloping, sandy beaches. These are very popular with tourists from all over Europe. But nature is claiming sand back from the beaches and this is now threatening the infrastructure near the beaches.

To the south of Sete, in the Roussillon region, there is a large Lido, a small peninsula trapped between the sea on the one side and Lake Thau on the other. This peninsula carries the important road between Sete and Cap Agde and the rail connection from Montpellier to Spain, these connections between Spain and the rest of Europe are important for the countries' economies. Due to erosion, this connection was endangered and since 1999 several options had been studied with the aim of improving the situation.
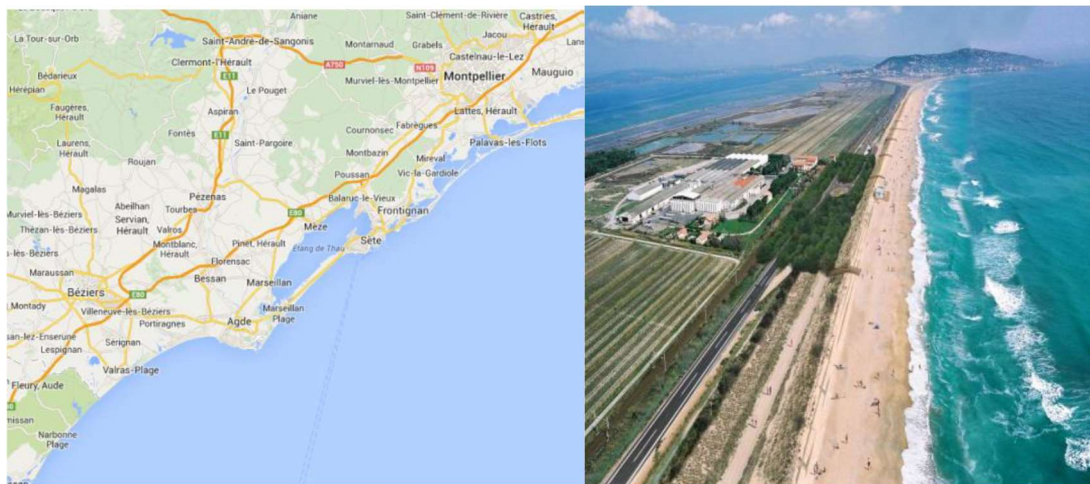
Figure 8 & 9. Location Lido and aerial view on the beach

4.1.2. Background
Submerged breakwaters in front of beaches have often been designed as detached breakwaters. Increasingly, however, circumstances on these beaches require softer solutions, and here the sand-encapsulated systems are still being regarded as a hard solution, as the particle retention by the geotextile tube prevents migration of the sand particles.
It is important to understand the performance of this type of breakwaters in comparison with conventional rock breakwaters. In making this comparison, we first calculated the coefficient of transmission of the breakwater already designed with encapsulated sand elements. This wave transmission value was used to make the optimal geometrical design of the conventional rock breakwater.

4.1.3. Geometry of the designed breakwater
The existing designed breakwater was designed with two large encapsulated sand elements with a circumference of 15 m. See below a cross section of the breakwater. This was also specified in the tender documents for construction.
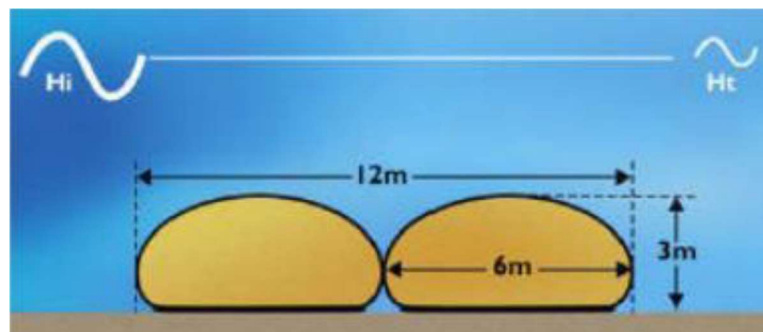
Figure 10. Cross section of the breakwater

4.1.4. Final situation after installation of the geotextile tubes
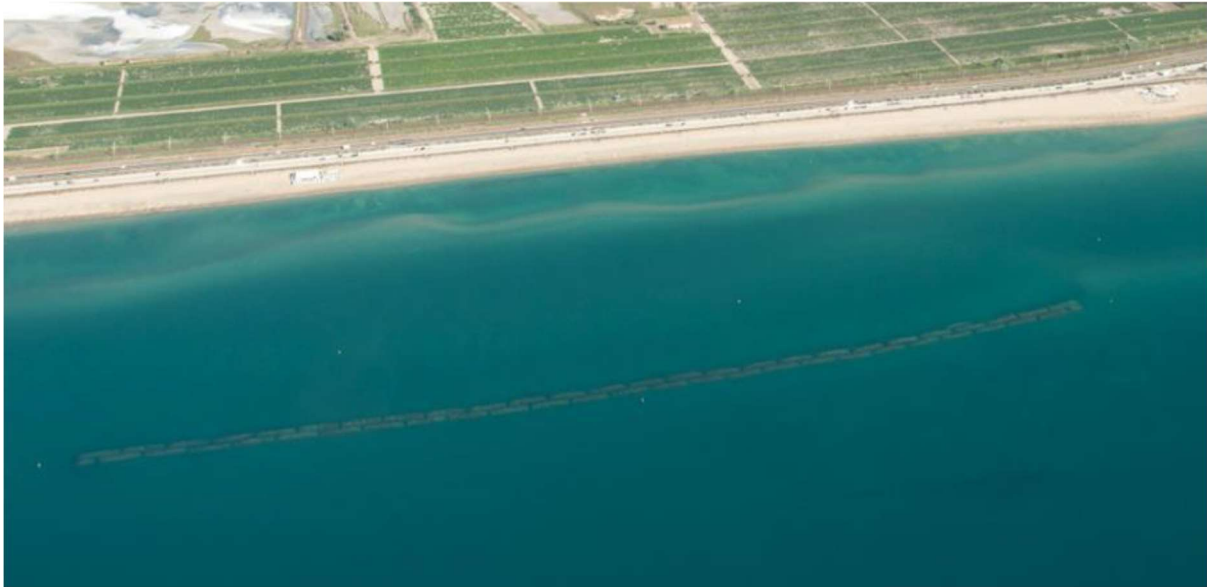
Figure 11. Aerial view of the installed submerged breakwater with encapsulated sand-filled elements at the beach of Lido, Sete, France

4.2. QUINTANA ROO, Mexico (Stephens, 2018)

In 2014, the 1.6 km long beach front MayaKoba Resort hired Tecnoceano, the same marine engineering company in Cancun that designed the protection for Gran Vela project in 2009, to develop beach development and protection plans for both properties. Using the collected data and lessons learned from observing Gran Vela for the past 9 years, Tecnoceano applied this knowledge to develop the master plans for each property.

In 2015, MayaKoba started a four-stage construction sequence following the master plan for beach development and protection. See Figure 9. First, in 2015 they installed stage one of property protection that consisted of a 1.8m high geotextile tube core for what would become the sand dune protection. See Fig. 10. Second, in 2016, MayaKoba installed five geotextile tube breakwaters protection the entire 1.6 km shoreline of the property (see Fig. 11 and 12). This was followed by completing the geotextile tube sand dune core for the same length. In June 2017, with the first two stages comprising the protection structures in place, MayaKoba has carried out the beach renourishment dredging program which included dredging from an offshore bank +500,000 m3 of sand onto the beach. The final stage was completed in late 2017.
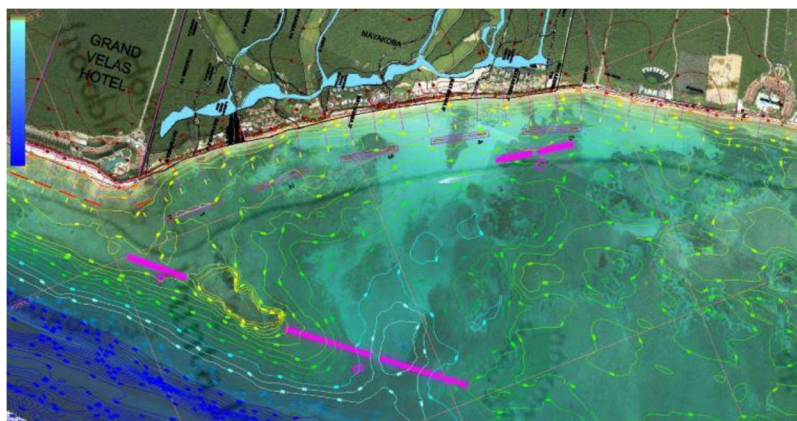
Figure 12. Masterplan

Figures 13. On shore breakwater   Figure 14. Installation 2016   Figure 15. Situation 2017

4.3. OFIR, Portugal (ter Harmsel, 2018)

4.3.1 Background

The beaches of Portugal that are located at the Atlantic Ocean erode during the storms of the fall and winter. The eroded sand moves offshore then during the spring and summer the sand is pushed back onto the beaches with the gentle waves of summer. Periodically, the fall and winter storms will erode some of the dunes and this sand replenishes the beaches. This is a common cycle that occurs in all coastline communities. When a series of storms occurs in quick succession, the shape of the barrier island changes as Mother Nature moves the sands. This would not be a problem if the coastline was left in its natural state but, human desire to enjoy the beach and ocean has led to the development and construction of infrastructure on the barrier islands that must be protected.

In Ofir all the dunes are eroded to a critical situation that the urban development came into the danger zone.

4.3.2 Attempts to solve the problem

Different attempts have been made to protect the dune area but failed until now. Heavy sandbags, rocks and wooden piles as shown in figures 13-16 have been used without any success.

Figures 16-19. Situation before installation of geotextile tubes

4.3.3. Solution using sand filled Geotextile tubes

As all solutions failed the University of Porto-FEUP-IHRH was asked to come up with a suitable solution for two critical areas in Ofir (figure 20) based on the local conditions and available sand.

Figure 20. Location of project site
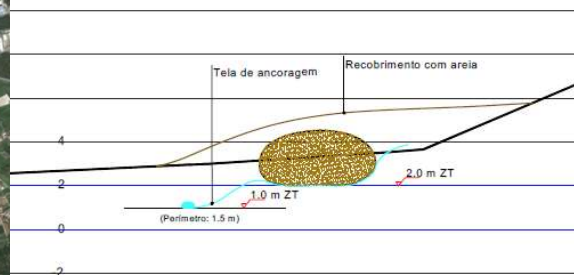
Figure 21. design of solution with geotextile tubes

The design (pic 21) included the use of a scour apron with a single anchor tube on the ocean side to avoid sinking of the geotextile tube due to erosion underneath the geotextile tube. Based on the wave conditions that were expected the geotextile tubes were designed for a filled height of 2,4 meter. With a designed width of 5,4 meter the structure was designed to be stable for significant wave height up to 5 meters.

4.3.4. Installation of the structure (figures 18-22)

The installation of the scour apron and the geotextile tubes was carried out with a submergible pump that was pumping a sand/water mixture directly from the coastline into the anchor tube of the scour apron and the geotextile tube.

Figure 22 & 23. Installation scour apron and filling anchor tube
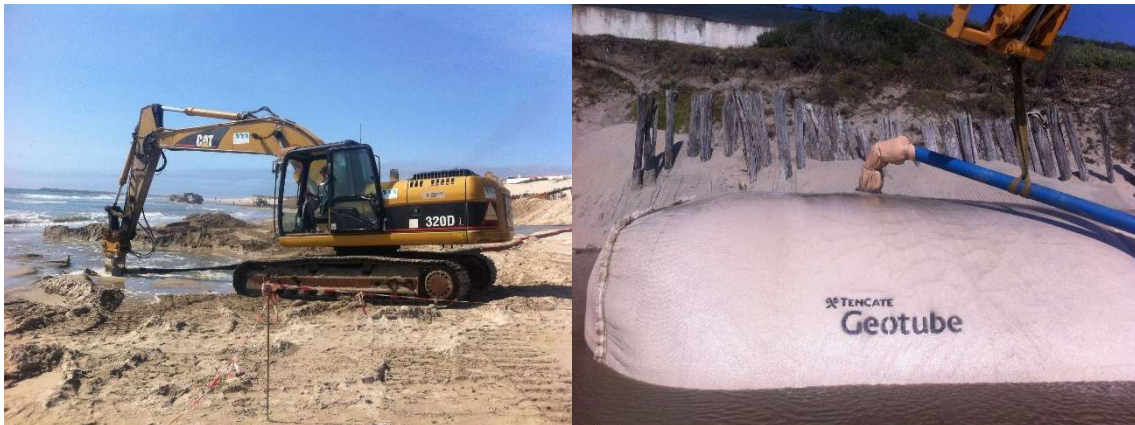
Figure 24 & 25. Submergible pump direct filling of geotextile tube

Figure 26 & 27. Installed geotextile tubes before covering with sand

4.3.4. Effect of the structure

Two months after the project was completed a severe storm hit the Atlantic Ocean shore in the North of Portugal. The structure was tested directly and proved its functionality. Figure 26 and 27 show that the beach in front of the structure was washed away but that the toe of the dunes was protected by the

geotextile tubes and was not affected by the storm. The structure itself was not affected at all and proved its value. After the storm season the beach was restored Figure 25

Figures 28.   Figure 29.   Figure 30.

4.4. GOUVILLE, France

Near the town of Gouville sur Mer there is a camping site located just behind the natural dunes. Figure 26. Due to erosion, protection on the dunes needed improvement, the solution installed a year before was not durable enough. Therefore, a new solution had to be developed by the University of Caen-Normandie. Protection of the north side, near the camping was in immediately necessity due to the presence of the campsite and severe state of former protection works. The solution was found in installation of a T-shaped groin at the north side in combination with some beach nourishment. This groin had to be capable of creating calmer water so that collection of sediments from the sea could take place. The sediment transport in the sea at this location has been proven already. Therefore, the idea of the T-shape. The T will have two orientations, each for the waves of the direction South West and North West. Waves from both directions and the bar of the T will help collection of the sediments from the sea. See of the configuration of the proposed T-head in Figure 5. It will have a length of around 75 meters, the south west part a length of 50 meter and north part 25 meter.
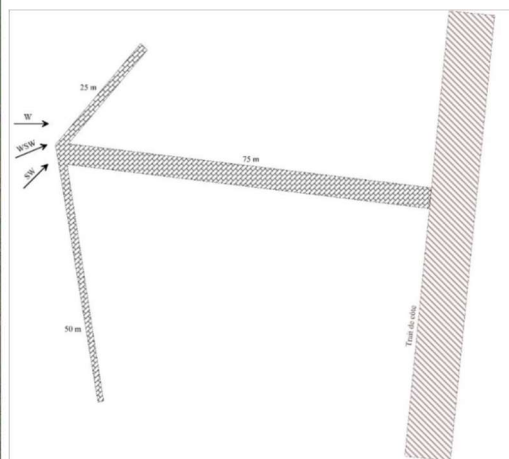
Figure 31.   Figure 32.

The height of the structure should be around 1 meter above the beach level and for the trunk length around 2 meter. Total area that will be covered with the T-head is around 300 m2, in that area calmer water will be created to allow sediments to settle.

For the construction of the T-head and protection of the sand dunes, sand encapsulated elements have been applied. At the head 1,6 diameter systems are applied with a fill height of 1 meter (Figure 32) and for the trunk of the T a 3,25-meter diameter system with a fill height of 2 meter. The elements have been designed according to the booklet "Geosystems Design Rules and applications", a state-of-the-art book with design guidelines for this kind of systems.
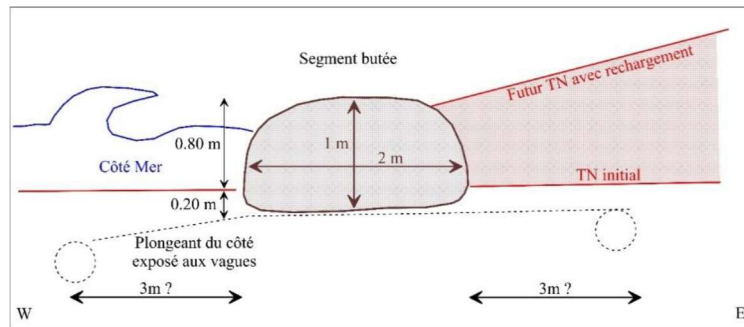
Figure 33.

The application of geotextile tubes fits in the working environment, the elements are easy to fill on site with a mixture of sand and water. Water will being squeeze through the pores of the textiles and sand will be retained in the system. Due to the local circumstances, settlements of the bottom can be followed by the elements without loss of the functionality. The fill material is sand, and the wrap is a textile with high UV resistance which allows deformation of the underground. For scour protection underneath the head, scour aprons are applied to protect the beach against erosion through breaking waves.

The project has been executed from September 2017 till around March 2018. Winter storms have been going over the structure without any loss of materials till date (figure 27). The structure is under full control of the university and will be checked regularly.

Figure 34.

5. CARBON FOOTPRINT

In several cases the Carbon Footprint from structures are based on the use of rock material have a higher Carbon Footprint impact as structures made with geotextile sand filled tubes. Especially when sand is locally available the impact is large. Based on the use of materials for both the conventional breakwater and the breakwater made of encapsulated sand elements, we determined the impact on the environment for the Lido project. We did this with a carbon footprint calculator developed by Sustain Ltd. The result of this calculation is shown in figure 35.
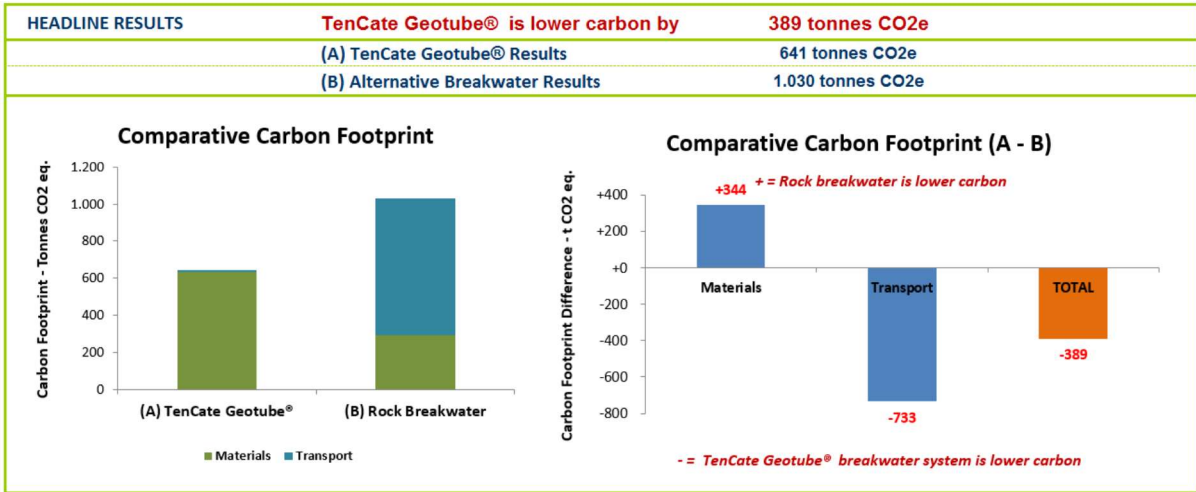
Figure 35.

6. RECENT INSTALLATIONS IN TURKEY

In the past years some projects to protect the shoreline have been installed in Turkey. An example is the installation of geotextile tubes at D Resort in Gocek (Figure 36)
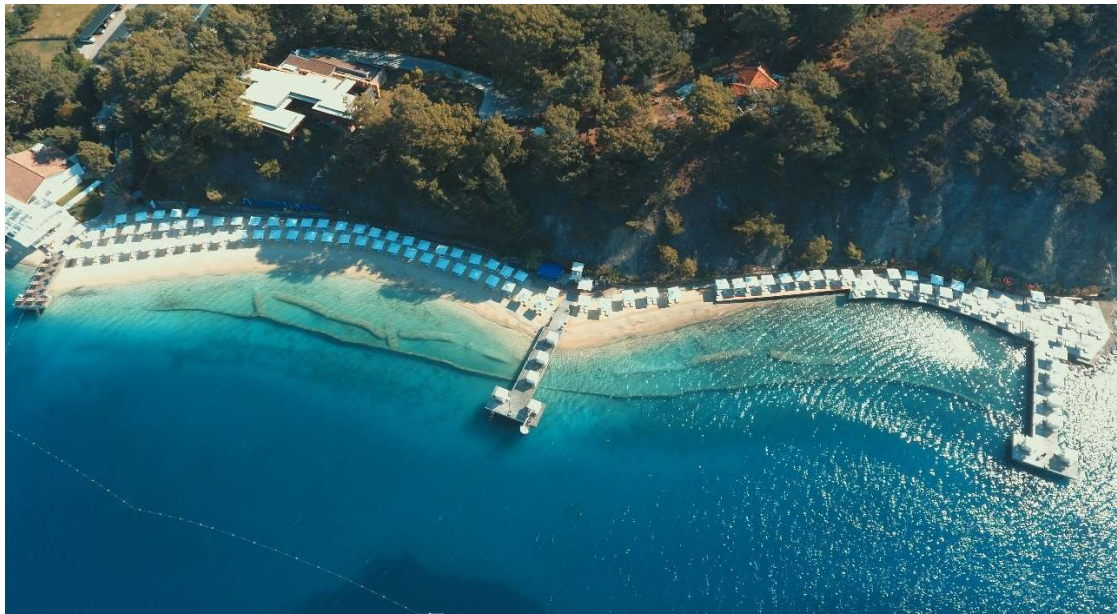
Figure 36.

7. CONCLUSIONS

Geotextile tubes are successfully used as:

- reclamation dykes to construct artificial islands,
- sub-merged and emerged breakwaters
- groins

During the use of the geotextile tubes, it has been shown that the installation can be done in a fast and efficient way using locally available sand which gives you the ability to save cost against building materials that need to be transported over a longer distance. Geotextile tubes are available in several dimensions and will be designed in close cooperation with the project designer to fit the needs of the project.

REFERENCES

Yee, T.W. (2002). Construction of underwater dykes using geotextile containment systems, *in Proceedings of the Seventh International Conference on Geosynthetics, Nice, France, Vol. 3, pp. 1161-1164.*

Yee, T.W., Zengerink E., & Choi J.C. Geotextile tube application for Incheon bridge project, Korea. *CEDA Conference Rotterdam 2006*

Zengerink E, The Use of Sand Encapsulated Elements for Beach Protection, *ICE conference Liverpool UK 2018*

Stephens T, Beach development and protection of resort coastline using geotextile tubes, *WEDA Conference USA 2018*

Ter Harmsel M., Dune and residential buildings protection using geotextile tubes, Atlantic Ocean Portugal, *ICE conference Liverpool UK 2018*

Geocontainer® and Geotube® are registered tradenames from TenCate Geosynthetics

14ᵀᴴ INTERNATIONAL CONFERENCE
ON HYDROSCIENCE & ENGINEERING

MAY 26-27, 2022
IZMİR-TURKEY

ICHE2022
IZMIR, TURKEY

HYDRODYNAMICAL COMPARISON OF NAMI DANCE AND XBEACH NON-HYDROSTATIC ON A BENCHMARK STUDY

First Author: Yagiz Arda Cicek

Middle East Technical University, Department of Civil Engineering, Ocean Engineering Research Center

Ankara, Turkey

ciceka@metu.edu.tr

Second Author: Gozde Guney Dogan Bingol

Middle East Technical University, Department of Civil Engineering, Ocean Engineering Research Center

Ankara, Turkey

gguneydogan@gmail.com

Third Author: Isikhan Guler

Middle East Technical University, Department of Civil Engineering, Ocean Engineering Research Center

Ankara, Turkey

isikhan@metu.edu.tr

Fourth Author: Cuneyt Baykal

Middle East Technical University, Department of Civil Engineering, Ocean Engineering Research Center

Ankara, Turkey

cbaykal@metu.edu.tr

Fifth Author: Ahmet Cevdet Yalciner

Middle East Technical University, Department of Civil Engineering, Ocean Engineering Research Center

Ankara, Turkey

yalciner@metu.edu.tr

ABSTRACT: Tsunamis are destructive long waves generated by a sudden displacement of a water column. Their modeling (numerical or physical) holds great importance while developing mitigation strategies. Although the methods followed during numerical and physical modeling studies differ, they feed off each other. Numerical models should be verified and validated on experimental data to get more accurate results. Within this framework, benchmark study results provide valuable data to ensure the numerical model works properly. Therefore, two different numerical models, NAMI DANCE (a non-linear shallow water equation solver with hydrostatic pressure assumption) and XBeach Non-hydrostatic (an NLSWE solver with a non-hydrostatic pressure term in the governing equations) are applied on a benchmark experiment (Park et al., 2013) during this study. This benchmark study investigates the effect of macro-roughness elements on inundation flow depth, cross-shore velocity, and momentum flux. A solitary wave having 0.2 m wave height is generated by a piston-type wavemaker. Grid and time resolutions are kept equal in both NAMI DANCE and XBeach simulations. Simulation results of the two models are compared, and the effects of non-hydrostatic pressure correction on flow parameters are presented with discussions.

DETAILED ABSTRACT

Physical and numerical modeling of tsunami flows holds great importance on assessing and understanding the tsunami effects and the development of mitigation strategies. As physical modeling requires more time compared to numerical ones, numerical modeling becomes important when fast modeling is required after extreme events. The reliability of the numerical models should be verified and validated using the existing physical data (field or laboratory measurements) to be used as a reference. Therefore, both numerical and physical models are highly dependent on each other.

In this context, two numerical models, NAMI DANCE and XBeach Non-hydrostatic are compared hydrodynamically based on a laboratory benchmark test (Park et al., 2013). In this experiment, the impact of tsunami inundation in a constructed environment is evaluated on a 1:50 scale idealized version of the coastal region Seaside, Oregon (Figure 1a).

Locations of the four fixed wave gauges are as follows: WG1 (2.086 m, −0.515 m), WG2 (2.068 m, 4.065 m), WG3 (18.618 m, 0.000 m), and WG4 (18.618, 2.860 m). In addition to these gauges, 31 more gages are employed along the streets, which collect free surface elevation and flow velocity (Figure 1b). A piston-type wavemaker placed at x = 0 m generates a solitary wave with approximately 0.2 m height, traveling along the slope and then among the streets.
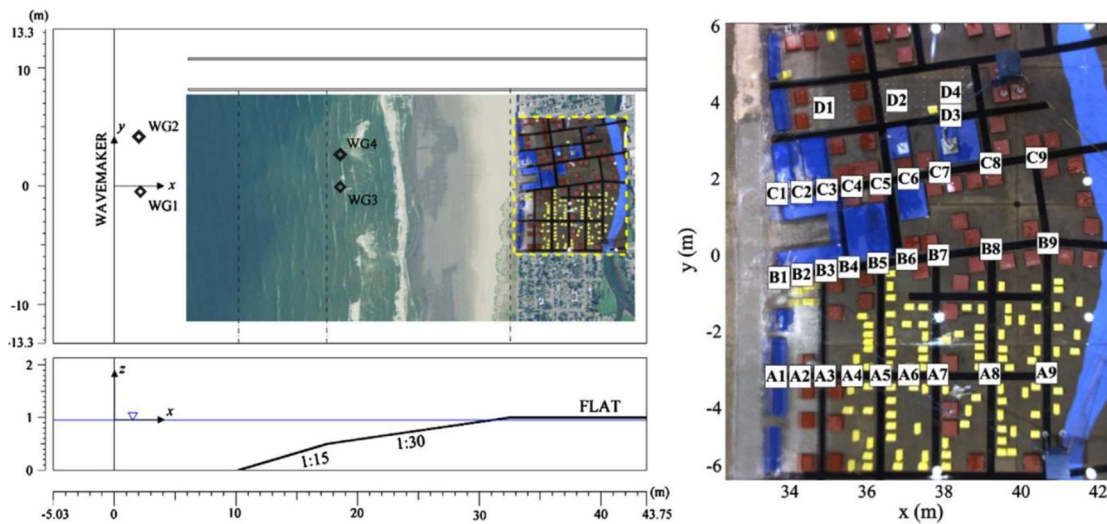
Figure 1. (a) Experimental setup. (b) Gauges along streets (adopted from Park et al., 2013)

NAMI DANCE is a tsunami numerical model which solves non-linear shallow water equations (NLSWE) for wave propagation (Velioglu Sogut & Yalciner, 2019). Also, the hydrostatic pressure distribution is employed in the model. Continuity and 2D momentum equations that NAMI DANCE solves are as follows (Dogan et al., 2021):

$$\frac{\partial \eta}{\partial t} + \frac{\partial M}{\partial x} + \frac{\partial N}{\partial y} = 0 \tag{1}$$

$$\frac{\partial M}{\partial t} + \frac{\partial}{\partial x}\left(\frac{M^2}{D}\right) + \frac{\partial}{\partial y}\left(\frac{MN}{D}\right) + gD\frac{\partial \eta}{\partial x} + \frac{\tau_x}{\rho_w} = fN \tag{2}$$

$$\frac{\partial N}{\partial t} + \frac{\partial}{\partial x}\left(\frac{MN}{D}\right) + \frac{\partial}{\partial y}\left(\frac{N^2}{D}\right) + gD\frac{\partial \eta}{\partial y} + \frac{\tau_y}{\rho_w} = -fM \tag{3}$$

In Equations (1), (2) and (3), η is the free surface elevation, t is time, x and y are horizontal geographic coordinates, M and N are the horizontal discharge fluxes along x and y coordinates respectively, D is the total water depth which is equal to $h(x,y)+\eta$, $h(x,y)$ is undisturbed basin depth, g is the gravitational constant, ρ_w is seawater density, τ_x and τ_y are the bottom shear stresses, which

are calculated by Manning law, in the horizontal plane along x and y directions and f is the Coriolis parameter with $f = 2\omega\, sin\phi/R$ where R is the radius of the earth, ω is the angular velocity of the earth, and ϕ is the y-coordinate in degrees.

On the other hand, XBeach Non-hydrostatic uses NLSWE for wave propagation too. The main difference between the equations is that XBeach Non-hydrostatic applies a non-hydrostatic correction to the momentum equations. These equations are listed as (Smit et al., 2009):

$$\partial\eta\partial t + \partial UD\partial x + \partial VD\partial y = 0 \tag{4}$$

$$\partial\partial t(DU) + \partial\partial x(DU2 + 12gD2 + D\bar{p} - 1\rho D\bar{\tau}xx) + \partial\partial y(DUV - 1\rho D\bar{\tau}yx) = gD\partial h(x,y)\partial x - p\partial h(x,y)\partial x + Sx \tag{5}$$

$$\partial\partial t(DV) + \partial\partial x(DUV - 1\rho D\bar{\tau}xy) + \partial\partial y(DV2 + 12gD2 + D\bar{p} - 1\rho D\bar{\tau}yy) = gD\partial h(x,y)\partial y - p\partial h(x,y)\partial y + Sy \tag{6}$$

In Equations (4), (5) and (6), U and V are x and y components of depth averaged velocity vectors, $\bar{p}$ is the depth averaged dynamic pressure, τ_{ij} is the turbulent stress tensor, p is the dynamic pressure normalized with the reference density ρ and the atmospheric pressure p_0 and S_x and S_y are the total of source and sink terms due to the stresses at the free surface and bottom along x and y directions.

Both NAMI DANCE and XBeach models have been executed with the same grid size and time-step values of 0.05 m and 0.001 s. All the other related parameters are set as default in both models. Free surface elevation results for WG1, flow depth, and depth-averaged velocity results for B4 are shown in Figure 2a, b, and c, respectively. The figure shows that both models work well for giving the correct boundary conditions to the domain (Figure 2a). Also, both models are able to capture arrival time and maximum flow depth along the streets, as shown in Figure 2b, although NAMI DANCE seems better in terms of arrival time and magnitude of flow depth. Finally, the maximum depth-averaged velocity calculated for B4 by XBeach Non-hydrostatic is larger than that of NAMI DANCE (Figure 2a. The reason behind it might be non-hydrostatic pressure correction employed in XBeach, as non-hydrostatic pressure contribution is more significant in shallower regions. However, as there is no flow velocity measurement before t = 27 s, which model calculates the depth-averaged velocity better is an unanswered question.
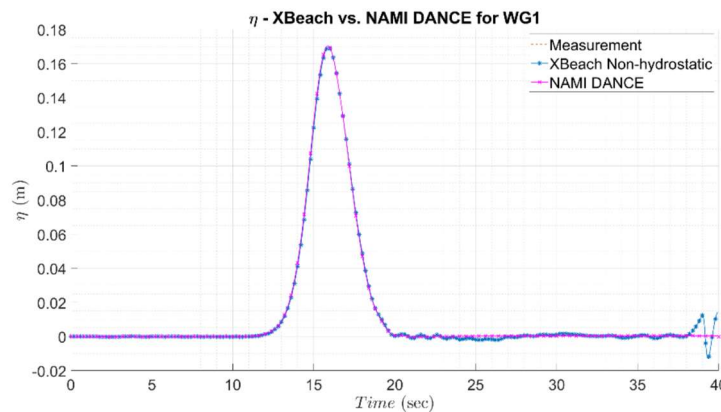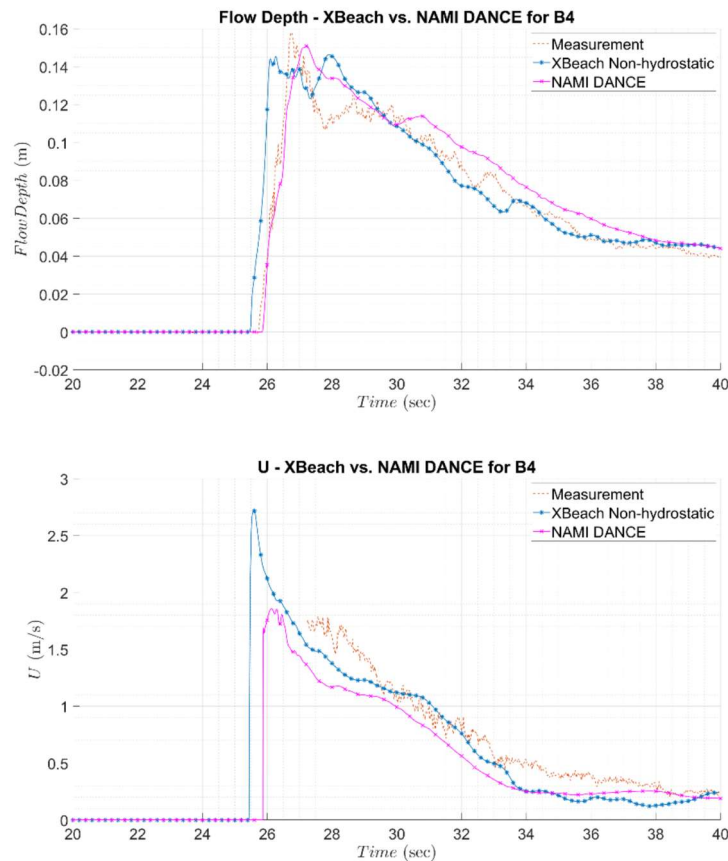
Figure 2. Time-series plots for (a) Free surface elevation of WG1 measurement (orange dashed line), XBeach Non-hydrostatic computation (blue starred line), and NAMI DANCE computation (magenta crossed line). (b) Flow depth of B4 measurement (orange dashed line), XBeach Non-hydrostatic computation (blue starred line), and NAMI DANCE computation (magenta crossed line). (c) Depth averaged velocity of B4 measurement (orange dashed line), XBeach Non-hydrostatic computation (blue starred line), and NAMI DANCE computation (magenta crossed line).

ACKNOWLEDGMENTS

REFERENCES

Dogan, G. G., Yalciner, A. C., Yuksel, Y., Ulutaş, E., Polat, O., Güler, I., Şahin, C., Tarih, A., & Kânoğlu, U. (2021). The 30 October 2020 Aegean Sea Tsunami: Post-Event Field Survey Along Turkish Coast. *Pure and Applied Geophysics*, *178*(3), 785–812. https://doi.org/10.1007/s00024-021-02693-3

Park, H., Cox, D. T., Lynett, P. J., Wiebe, D. M., & Shin, S. (2013). Tsunami inundation modeling in constructed environments: A physical and numerical comparison of free-surface elevation, velocity, and momentum flux. *Coastal Engineering*, *79*, 9–21. https://doi.org/10.1016/j.coastaleng.2013.04.002

Smit, P. ., Stelling, G. ., Roelvink, D., van Thiel de Vries, J., McCall, R., Van Dongeren, A., Zwinkels, C., & Jacobs, R. (2009). *XBeach : Non-hydrostatic model*. 1–69.

Velioglu Sogut, D., & Yalciner, A. C. (2019). Performance Comparison of NAMI DANCE and FLOW-3D® Models in Tsunami Propagation, Inundation and Currents using NTHMP Benchmark Problems. In *Pure and Applied Geophysics* (Vol. 176, Issue 7). https://doi.org/10.1007/s00024-018-1907-9

NUMERICAL MODELING OF THE 30 OCTOBER 2020 SEFERIHISAR-IZMIR (AEGEAN SEA) TSUNAMI AND ITS COASTAL EFFECTS

Gozde Guney Dogan Bingol

Department of Civil Engineering, Middle East Technical University

Ankara, Turkey

gguneydogan@gmail.com

Ahmet Cevdet Yalciner

Department of Civil Engineering, Middle East Technical University

Ankara, Turkey

yalciner@metu.edu.tr

Duygu Tufekci-Enginar

Department of Geological Engineering, Middle East Technical University

Ankara, Turkey

dtufekci@metu.edu.tr

Mehmet Lutfi Suzem

Department of Geological Engineering, Middle East Technical University

Ankara, Turkey

suzen@metu.edu.tr

ABSTRACT: On 30 October 2020, at 14:51 local time, a moment magnitude of Mw 6.6 according to Disaster and Emergency Management Presidency of Turkey (AFAD) and Mw 6.9 according to Kandilli Observatory and Earthquake Research Institute (KOERI) occurred in the central Aegean. The 30 October earthquake and the vertical seafloor deformation caused a tsunami that affected the northern coast of Samos Island in Greece and the coastline of Kusadasi Bay from Cesme Alacati to Menderes Gumuldur in Turkey. The strong currents and the high wave amplitudes in the shallow areas, marinas and small boat shelters and fishery ports significantly damaged the boats, properties, residences and coastal facilities in the area. Considering the impact of this most recent tsunami event in the Aegean Sea, the numerical modeling and appropriate reproducing of this event are important to understand the event in detail and shed light on the dynamics of the tsunami impact. In this study, we present the numerical modeling of the far-field propagation, coastal amplification and inundation of the 30 October 2020 tsunami in Kusadasi Bay and the most impacted areas, Sigacik and Akarca based on a uniform slip earthquake model. Our simulation results match fairly well with the post-event field observations.

1. INTRODUCTION

The Aegean Sea experienced many tsunami events throughout history. The researches and tsunami catalog studies that shed light on the historical tsunami events affecting Turkish coasts and surrounding regions report 53 of the total 134 tsunami events occurred in the Eastern Mediterranean and the Aegean as a result of strong earthquakes, volcanic events and landslide activities (Altinok et al. 2011; Papadopoulos et al. 2007). Some important events can be listed as 11 May 1222 Paphos-Cyprus, 8 August 1303 Crete-Dodecanese Islands, 6 October 1944 Edremit Bay-Ayvacik, 9 February 1948 Karpathos Island-Dodecanese Islands, 23 July 1949 Chios-Karaburun, 10 September 1953 Cyprus, 9 July 1956 Amorgos and 23 May 1961 Rhodes-Marmaris. The studies show that the 365

Crete Earthquake caused waves reaching 6 meters moving inland, dragged boats and caused many casualties. The eruption of the Santorini Volcano and the consequent tsunami, which is accepted to have taken place in the 16th century BC, is another important historical tsunami event that affected the entire Eastern Mediterranean coast. In recent years, the earthquakes of Midilli-Karaburun (Mw 6.3) on 12 June 2017, and off Gokceada (Mw 6.8) in May 2014 caused tsunami events with coastal waves less than 50 cm. After these events, a tsunami occurred on 31 July 2017 and impacted the coast of Bodrum and Kos Island, causing significant damage to boats and seafront facilities. Those successive events were important reminders to the coastal communities in the Aegean (Dogan et al. 2019).

On 30 October 2020, at 14:51 local time, a moment magnitude of Mw 6.6 according to Disaster and Emergency Management Presidency of Turkey (AFAD, www.afad.gov.tr), and Mw 6.9 according to Kandilli Observatory and Earthquake Research Institute (http://www.koeri.boun.edu.tr/sismo/2/30-ekim-2020-mw6-9-ege-denizi-izmir-depremi/) occurred in the central Aegean. The epicenter of the earthquake was approximately 10 km north of Avlakia town of Samos Island and 23 km south of Doganbey town of Izmir. The earthquake caused 115 deaths and caused significant structural damage in Izmir Bayrakli district, which is 70 km away from the epicenter.

The 30 October earthquake and the vertical seafloor deformation caused a tsunami which affected the northern coast of Samos Island in Greece and the coastline of Kusadasi Bay from Cesme Alacati to Menderes Gumuldur in Turkey. The strong currents and the high wave amplitudes in the shallow areas, marinas and small boat shelters and fishery ports significantly damaged the boats, properties, residences and coastal facilities in the area. The post-tsunami field survey investigations indicate a maximum tsunami height of 2.3 m was observed at the Kaleici region of Sigacik, where the most severe tsunami damage was observed and one person lost their life. In the Akarca region, the largest tsunami runup was measured as 3.8 m at a distance of 91 m from the shoreline (Dogan et al. 2021a). Considering the impact of this most recent tsunami event in the Aegean Sea, the numerical modeling and appropriate reproducing of this event are important to understand the event in detail and shed light on the dynamics of the tsunami impact.

2. METHODOLOGY

In this study, we present the numerical modeling of the far-field propagation, coastal amplification and inundation of the 30 October 2020 tsunami in Kusadasi Bay and the most impacted areas, Sigacik and Akarca. Our simulations are based on the co-seismic surface vertical deformations produced by the Ganas et al. (2020) uniform slip model. The initial sea state (Figure 1) is calculated using the Okada (1985) relations with the fault parameters given in Table 1. The tsunami simulations are performed using the NAMI DANCE model, which solves the nonlinear shallow water equations with a friction term (Lynett et al. 2017; Dogan et al. 2021b; Dogan et al. 2021c). The nonlinear forms of long-wave equations are solved using a staggering leapfrog scheme numerical solution procedure in nested domains with rectangular structured mesh.

Table 17. Fault input parameters used as source input in the simulations (Ganas et al. 2020).

Longitude	Latitude	Depth	Strike Angle	Dip Angle	Rake Angle	Length	Width	Vertical Deformation
degree	degree	km	degree	degree	degree	km	km	m
26.725	37.890	11.5	276	37.00	-88	36	18	1.80
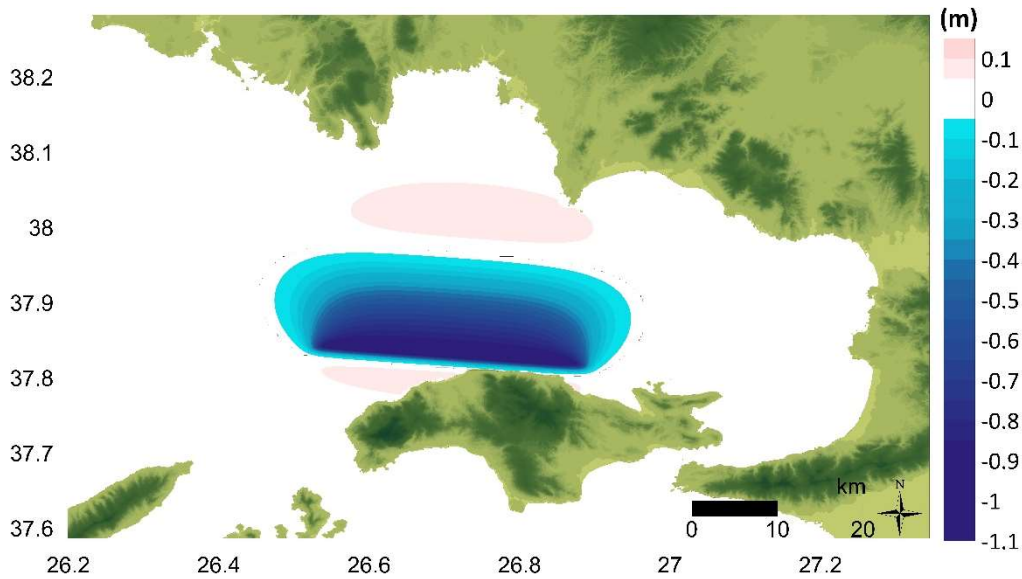
Figure 1. The initial sea state obtained from the fault parameters given in Table 1

A nested grid approach is employed in the simulations, with two nested domains of 25 m (parent grid B) and 5 m (child grid C) grid sizes. The bathy/topo data source of these two grids is the EMODnet Bathymetric grid (2018) and the national navigation charts.

3. SIMULATION RESULTS

The computed maximum water surface elevations in Kusadasi Bay (Domain B) and Sigacik and Akarca regions (Domain C) are given in Figure 2. In Figure 3, the calculated time histories of water level calculated for the 30 October tsunami at different coastal observation points (Alacati, Zeytineli, Sigacik and Akarca) are also presented.
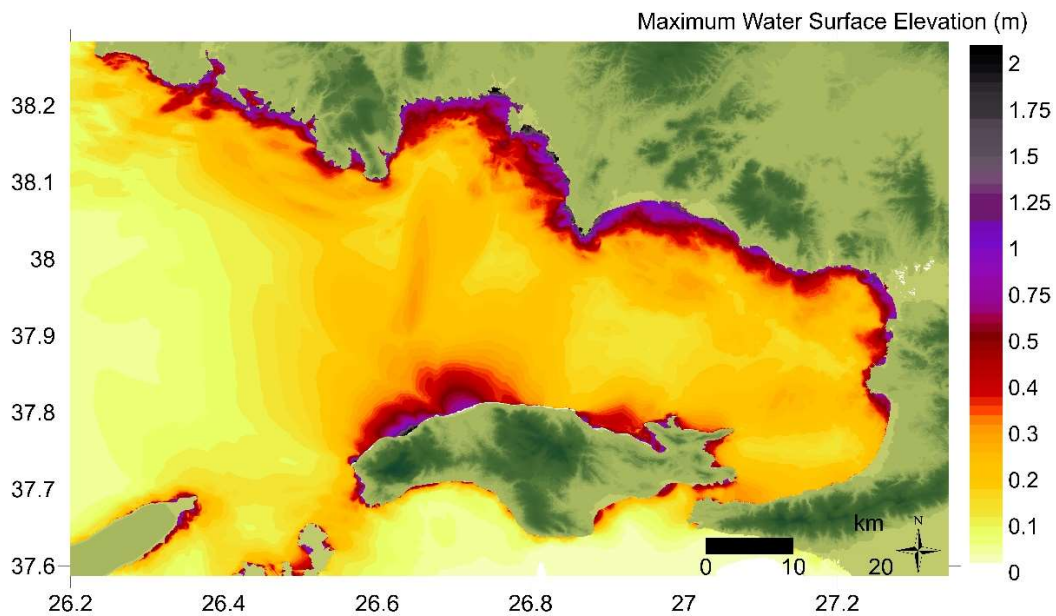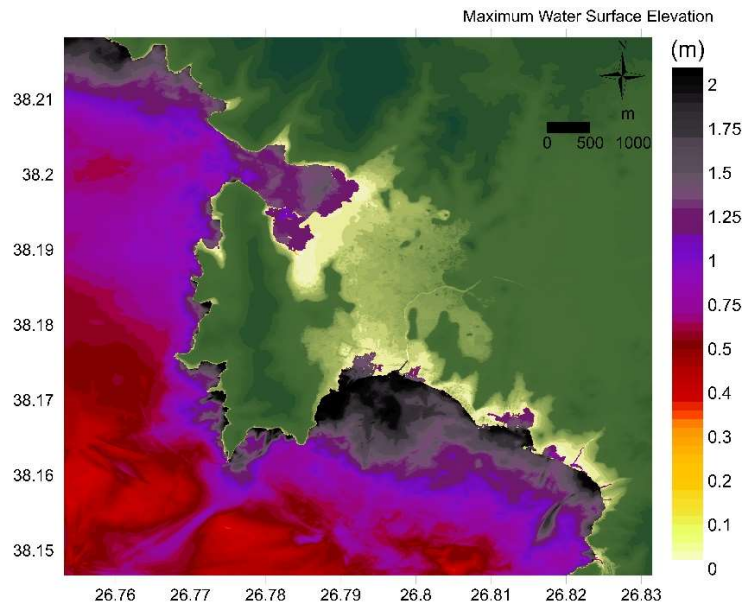
Figure 2. Distribution of maximum water surface elevations in Domains B (top) and C of near-field simulations NAMI DANCE for Sigacik and Akarca localities (bottom)
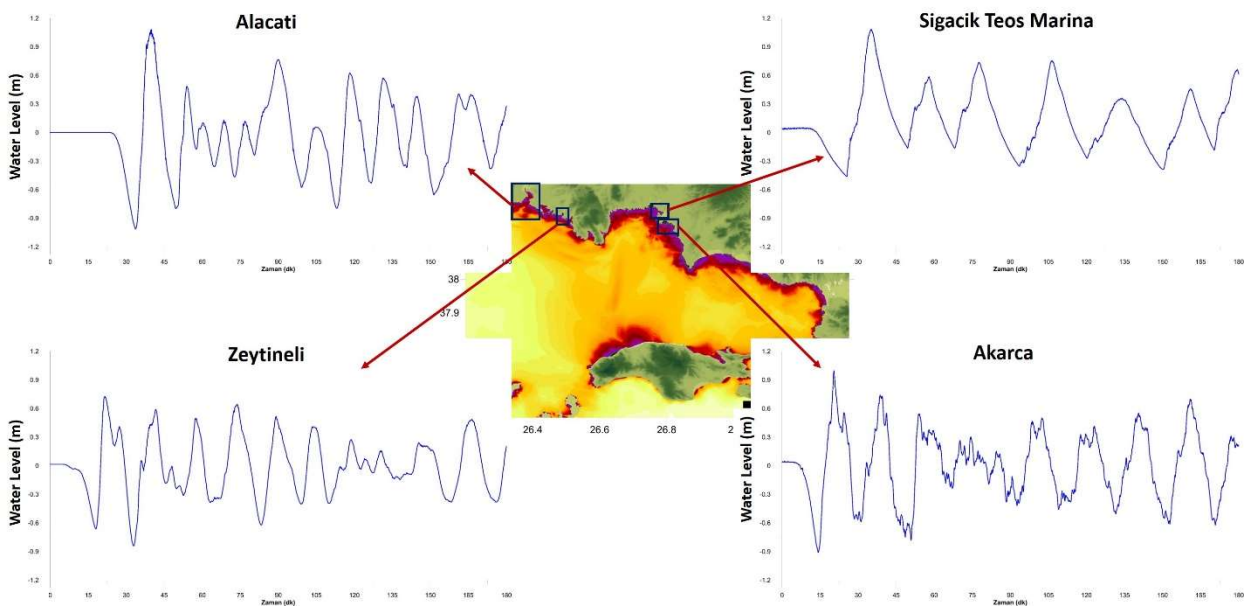
Figure 3. Time histories of computed water levels at different observation points in Kusadasi Bay

4. CONCLUSIONS

The simulation results show that the higher coastal amplitudes are computed at the most impacted regions where the observed waves reach the highest levels, along the Seferihisar coast. The maximum water level distribution computed in the finest grid shows that the water levels reach the order of 1.8 – 2.0 m in Sigacik and Akarca regions. In this regard, the modeling results match fairly well with the post-event field observations.

ACKNOWLEDGEMENT

REFERENCES

Altinok, Y., Alpar, B., Özer, N., & Aykurt, H. (2011). Revision of the tsunami catalogue affecting Turkish coasts and surrounding regions. *Natural Hazards and Earth System Sciences*, 11(2), 273-291.

Dogan, G. G., Annunziato, A., Papadopoulos, G. A., Guler, H. G., Yalciner, A. C., Cakir, T. E., ... & Synolakis, C. (2019). The 20th July 2017 Bodrum–Kos Tsunami Field Survey. Pure and Applied Geophysics, 176(7), 2925-2949.

Dogan, G. G., Yalciner, A. C., Yuksel, Y., Ulutaş, E., Polat, O., Güler, I., Şahin, C., Tarih, A., & Kânoğlu, U. (2021a). The 30 October 2020 Aegean Sea Tsunami: Post-Event Field Survey Along Turkish Coast. *Pure and Applied Geophysics*, 178(3), 785–812. https://doi.org/10.1007/s00024-021-02693-3

Dogan, G. G., Annunziato, A., Hidayat, R., Husrin, S., Prasetya, G., Kongko, W., Zaytsev, A., Pelinovsky, E., Imamura, F., & Yalciner, A. C. (2021b). Numerical Simulations of December 22, 2018 Anak Krakatau Tsunami and Examination of Possible Submarine Landslide Scenarios. *Pure and Applied Geophysics*, 178(1), 1–20. https://doi.org/10.1007/s00024-020-02641-7

Dogan, G. G., Pelinovsky, E., Zaytsev, A., Metin, A. D., Tarakcioglu, G. O., Yalciner, A. C., Yalciner B. & Didenkulova, I. (2021c). Long wave generation and coastal amplification due to propagating atmospheric pressure disturbances. *Natural Hazards*, 106(2), 1195-1221.

Earthquake Engineering Research Institute (USA), Hellenic Association of Earthquake Engineering: Report 2020/02, Earthquake Engineering Association of Turkey, Earthquake Foundation of Turkey Geotechnical Extreme Events Reconnaissance Association: Report GEER-069, "Seismological and Engineering Effects of the M 7.0 Samos Island (Aegean Sea) Earthquake", https://doi.10.18118/G6H088, December 31, 2020

Ganas, A, Elias, P, Briole, P, Tsironi, V, Valkaniotis, S, Escartin, J, Karasante, I, and Efstathiou, E, 2020. Fault responsible for Samos earthquake identified, Temblor, http://doi.org/10.32858/temblor.134.

Lynett, PJ, Gately, K, Wilson, R, Montoya, L, Arcas, D, Aytore, B, Bai, Y, Bricker, JD, Castro, MJ, Cheung, KF, David, GC, Dogan, GG, Escalante, C, González-Vida, JM, Grilli, ST, Heitmann, TW, Horrillo, J, Kânoglu, U, Kian, R, Kirby, JT, Li, W, Macías, J, Nicolsky, DJ, Ortega, S, Pampell-Manis, A, Park, YS, Roeber, V, Sharghivand, N, Shelby, M, Shi, F, Tehranirad, B, Tolkova, E, Thio, HK, Velioglu, D, Yalciner, AC, Yamazaki, Y, Zaytsev, A, and Zhang, YJ, 2017. Inter-model analysis of tsunami-induced coastal currents. *Ocean Modelling*, 114, 14–32, http://dx.doi.org/10.1016/j.ocemod.2017.04.003

Papadopoulos G. A., Daskalaki E., Fokaefs A., Giraleas N. (2007). Tsunami Hazards in the Eastern Mediterranean: Strong Earthquakes and Tsunamis in the East Hellenic Arc and Trench System. *Natural Hazards and Earth System Sciences*, Copernicus Publ. / European Geosciences Union, 7 (1), Pp.57-64. Hal-00299403

14TH INTERNATIONAL CONFERENCE
ON HYDROSCIENCE & ENGINEERING

MAY 26-27, 2022
IZMİR-TURKEY

ICHE2022
IZMIR, TURKEY

SEABED SCOUR INDUCED BY PROPELLER JET

First Author: Ali Doğu

Research Assistant, Civil Engineering Department, Kırıkkale University.

Kırıkkale, Turkey

alidogu@kku.edu.tr

Second Author: Damla Yılmaz

Research Assistant, Civil Engineering Department, Bursa Technical University.

Bursa, Turkey

damla.yilmaz@btu.edu.tr

Third Author: Kubilay Cihan

Prof. Dr, Civil Engineering Department, Kırıkkale University.

Kırıkkale, Turkey

kcihan@kku.edu.tr

Fourth Author: Ayşe Yüksel Ozan

Assoc. Prof. Dr, Civil Engineering Department, Adnan Menderes University.

Aydın, Turkey

ayse.yuksel@adu.edu.tr

Fifth Author: Osman Yıldız

Prof. Dr, Civil Engineering Department, Kırıkkale University.

Kırıkkale, Turkey

osmanyildiz2000@hotmail.com

ABSTRACT: Scour caused by the strong flows induced by ship propeller jet has been assigned as an important problem for stability of port structures and port operations in harbors. The main reason for this scour is the increase in engine power and the use of side propellers that facilitate maneuverability as the transportation volume of ships has increased in recent years. As a result, sediment motion starts on the seabed due to the jet flow caused by the propeller and this movement becomes one of the most important problems for berthing and marine structures. Since the estimation of scour depth in ports is extremely important, underestimating scour formation results in a shallow foundation design, which makes the ports unsafe. Overestimating the depth of scour leads to uneconomical design. Therefore, necessary information about the maximum depth of scour is required for the proper design of the harbor structure. The objective of this paper is to examine the unconfined scour hole caused by propeller jet experimentally. The scour experiments performed until the equilibrium conditions were satisfied. According to the results, it is obtained that relative offset height (y_o/D_P) has a significant effect on the maximum scour depth. The maximum scour depths obtained in each experiment condition were compared with semiempirical formulas proposed in literature.

Key words: propeller jet, seabed scour, unconfined scour hole

1. INTRODUCTION

With the increasing trade volume in the world, the importance of sea trade is increasing day by day. Due to the increasing needs, more powerful engines were used to enable ships to achieve their

cruising speeds faster, and side propellers that facilitate maneuverability were developed. These cause some negative effects on harbor structures. Propeller water jet may cause washing effects on seabed, and this can lead to development of a scour profile. The scour around quay walls may have a shortening effect on the life of the structure. Thus, port operations may be partially interrupted due to such problems. Bergh and Cederwall (1981) reported that 25 berthing structures in Swedish ports were damaged by propeller water flow. Qurrain (1994) declared that 42% of ports in United Kingdom had scour problems caused by propeller jets. Hamill et al. (1999) studied on scour for unconfined and confined propeller jets experimentally. They proposed equations estimating the maximum depth of erosion under confined and unconfined water jet conditions. Hong et al. (2013) investigated the evolution of a scour profile on the cohesionless bed. They also worked the time-dependent maximum scour depth under effect of an unconfined propeller jet. Tan and Yuksel (2018) carried out an experimental study by considering different sand median sizes, and different propeller offset heights and diameters. They also revised the equation proposed by Hong et.al (2013) by using their experimental results. Penna et al. (2019) performed a study on scour profiles due to propeller jet under different experimental conditions (propeller offset height, propeller rotation speed, etc.). Contrary to the general assuming, they found that erosion is asymmetric according to the propeller axis.

In the present study, the unconfined scour hole resulted from propeller jet at different propeller offset heights is investigated experimentally. The measured scour depths are compared with those obtained by previous works proposed in the literature.

2. EXPERIMENTAL SETUP

Tests were conducted in a tank in Hydraulics Laboratory at Kırıkkale University, Turkey. The dimensions of the tank are 3.2 m x 1.5m x 1m. To simulate the seabed, a sand layer was used in the part of the tank with dimensions of 2 m x 1.5 m x 0.2 m. Tank is depicted in Figure 1.
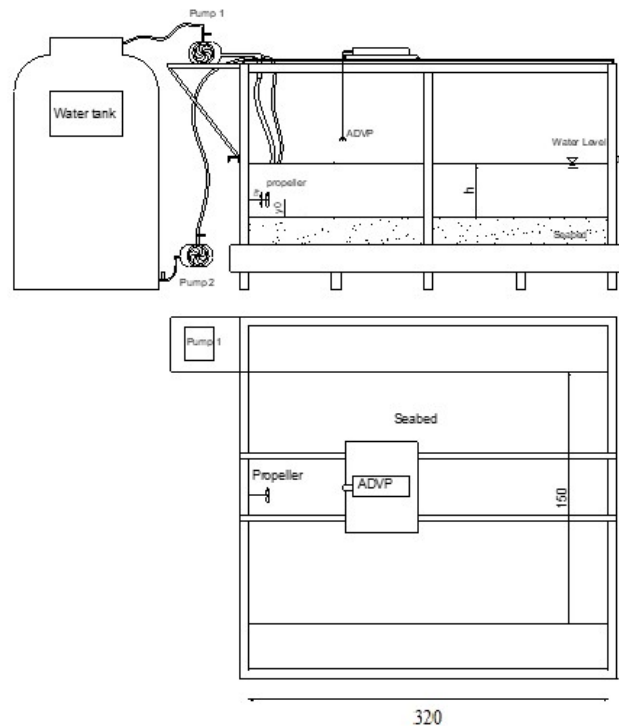
Figure 1. Experimental Set-up (units in cm)

A propeller with a diameter of 0.06 m was used to simulate the propeller water jet. Propeller offset heights (y_o) were chosen in tests as 0.06 m and 0.1 m. Characteristics of the propeller are given in Table 1.

Table 1. Propeller characteristics.

Diameter (m)	0.06
Blade number (N)	4
Blade Area Ratio (β)	0.60
Pitch Ratio	1.025
Trust Coefficient (C$_t$)	0.35
Material	Brass

The features of the sediment are given as follows, d_{50}=0.24 mm and 2650 kg/m³. The geometric standard deviations ($\sigma_g = \sqrt{\frac{d_{84}}{d_{16}}}$) was calculated as 1.50 which corresponds to moderately well sorted. d_{16} and d_{84} are entitled the sand diameter corresponds 16% and 84% are finer by weight, respectively.

Acoustic Doppler Velocimeter Profiler (ADVP) was utilized to obtain the bed elevation. Bed elevations was measured and recorded before and during tests until equilibrium conditions occurred. The scour profile was obtained by measuring the bed elevations at 2 cm intervals along the bed. When the bed elevations were measured, propeller was stopped. Hamill (1987) and Hong et al. (2013) declared that starting or stopping of the propeller has no effect on developing of the scour profile.

Efflux velocities were calculated with formula proposed by Fuehrer and Römisch (1977). Propeller rotations were considered as 500 (U_0=0.47 m/s), 750 (U_0=0.70 m/s) and 1000 (U_0=0.94 m/s) rpm (rotations per minute) where U_0 is efflux velocity in the experiments.

In order to neglect the viscosity effect, the propeller and flow Reynolds numbers must be greater than 7×10^4 and 3×10^3, respectively (Verhey (1983)). The propeller Reynolds number (Re$_{prop}$) and flow Reynolds number (Re$_{flow}$) are calculated as follows.

$$Re_{prop} = \frac{nD_pL_m}{\nu} \tag{1}$$

$$Re_{flow} = \frac{U_0D_p}{\nu} \tag{2}$$

where ν defines kinematic viscosity of the fluid, n is frequency of propeller and L_m is a term which is determined by Equation 3 given by Blaauw and van de Kaa (1978).

$$L_m = \beta D_p \pi \left(2N \left(1 - \frac{D_h}{D_p} \right) \right)^{-1} \tag{3}$$

D_h is called as the diameter of hub.

In this study, Re$_{flow}$ were between 2.8×10^4 and 5.6×10^4 and Re$_{prop}$ were between 0.86×10^4 and 1.7×10^4 which were lower than 7×10^4 and. Blaauw and van de Kaa (1978) and Verhey (1983) declared that although the Re$_{prop}$ were lower than 7×10^4, the scale effects can be neglected. Test details are given in Table 2.

Table 2. Test details.

Tests	Sediment Bed Size D_{n50} (mm)	Offset Height y_0 (cm)	Propeller Diameter D_p (cm)	Propeller Speed (rpm)	Efflux Velocity (m/s)	Densimetric Froude Number F_0
Case 1	0.24	6	6	500/750/1000	0.47/0.70/0.94	7.55/11.32/15.09
Case 2	0.24	10	6	500/750/1000	0.47/0.70/0.94	7.55/11.32/15.09

F_0 is densimetric Froude number ($F_0 = \dfrac{U_0}{\sqrt{d_{50}\left(\frac{\rho_s - \rho_w}{\rho_w}\right)g}}$)   where ρ_s and ρ_w define density of sand and water, respectively.

3. RESULTS AND DISCUSSION

Hong et al. (2013) stated that there is a general pattern of the scour profile formed in the equilibrium conditions on the sand bed under the effect of the propeller. (Figure 2). Hong et al (2013), mentioned that the scour profile at the equilibrium conditions consists of three components: the main scour hole, the secondary hole formed beneath the propeller, and the deposition zone. In tests, propeller offset heights (y_0) were chosen as 0.1(Case 1) and 0.06 m (Case 2). The equilibrium scour profiles obtained in tests for Case 1 were not compatible with the equilibrium scour profile suggested by Hong et al. (2013), except for the test for 1000 rpm. On the other hand, the small scour hole, main scour hole and deposition zone formed in all tests in Case 2. In Figure 3a., x indicates the distance of any point from the propeller along the flow, and z is elevation of the seabed. z is equal to the difference between the bed elevation (z_t) measured at any time and the reference bed elevation (z_{ref}) measured before the tests.
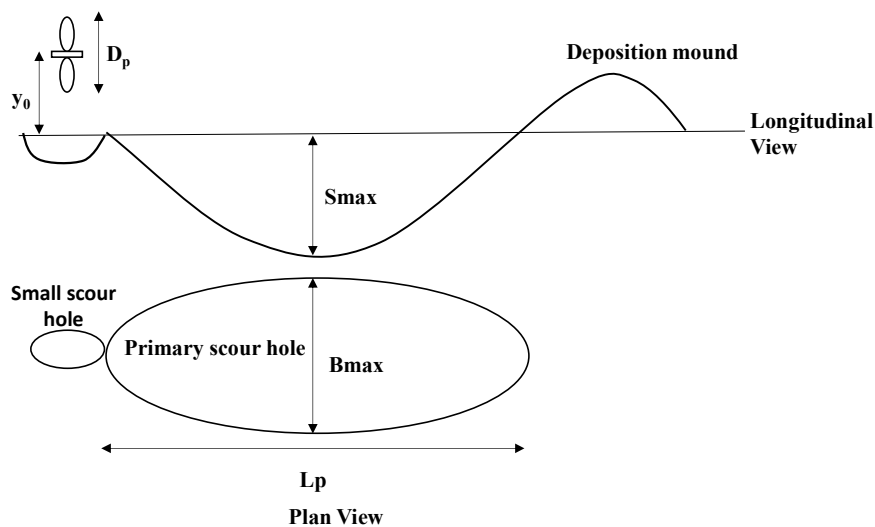
Figure 2. Erosion geometry along the bed caused by propeller jet

Figure 3a depicts the scour profile during time in Case 2 for 750 rpm. It is seen that the small scour hole, primary scour hole and deposition mound was formed at the equilibrium conditions. Time-dependent maximum scour (S_{max}) was shown in Figure 3b.

In this study, equilibrium conditions have been reached when the difference between the maximum scour depths of the profiles taken temporally is 1 mm.
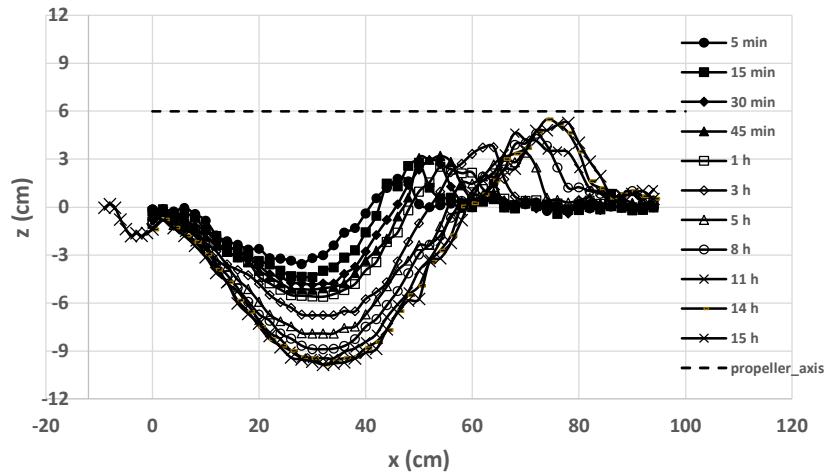
a)   Variation of the seabed profile (y_0=0.06m, 750 rpm)
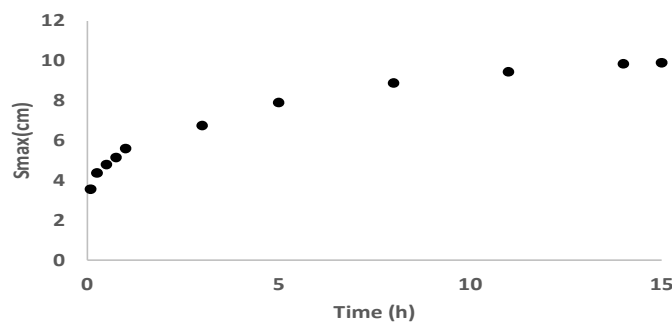
b)   Time-dependent the maximum scour depth (S_{max}) for 750 Rpm

Figure 3. Scour profile

3.1 Scour Formation

Hong et al. (2013) defined a curve for initiation of scour induced propeller water jet. Tan and Yuksel (2018) modified this curve considering their own test results. In Figure 4, curves given by Hong et al. (2013), Tan and Yuksel (2018) and present study are displayed together. Lines separates figures into two parts. The left side of the lines corresponds to no scour condition, where the other side corresponds to the scour condition. It was found that there was a good agreement between results of this study and results of Hong et al. (2013).

Hong et al. (2013) stated that small scour hole formed at the equilibrium condition. However, Tan and Yuksel (2018) and Penna et al. (2019) found that formation of small scour hole depended on test conditions such as y_0, rpm and D_p. Test result of this study were supported that small scour did not form all equilibrium conditions. Tan and Yuksel (2018) presented the critical curve depends on F_0 and y_0/D_p to define one or two scour holes conditions. In Figure 5, the critical curves given by Tan and Yuksel (2018) and present study are shown together. As seen in Figure 5, agreement between these curves was not high. Differences between the experimental conditions of previous studies and present study, especially using different d_{50}, caused the disagreement of test results. The sand considered in our experiments finer than sand in Tan and Yuksel's experiments. The present test results are used to modify the equation of critical curve for prediction of small scour hole. According to new equation, if F_0 is higher than $7.5y_0/D_p$, formation of small scour hole is observed.

In Figure 6, considering results of Penna et al. (2019), Tan and Yuksel (2018) and present study, variation of dimensionless scour hole length (L_p/D_p) and F_0 was displayed together. It is seen that equations given by Penna et al. (2019) and Tan and Yuksel (2018) are not compatible with results of present study. The equation that represents results of present study is as follows.

$$\frac{L_p}{D_p} = 0.78 F_0^{1.04} \tag{4}$$
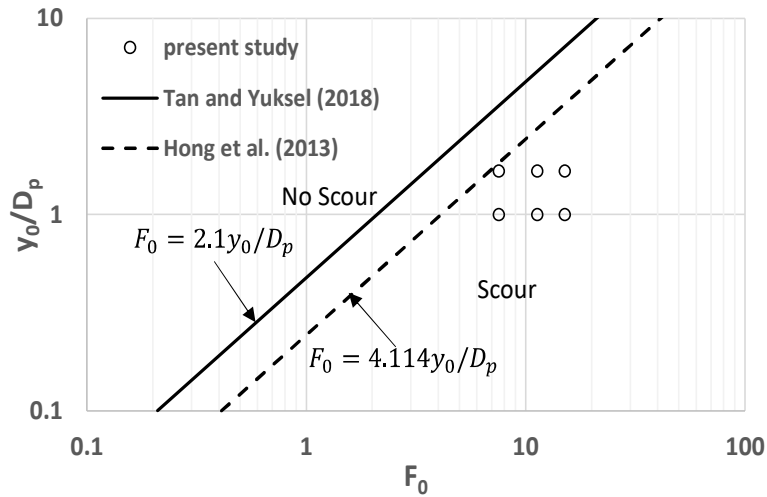
Figure 4. The critical curves for the initiation of scouring
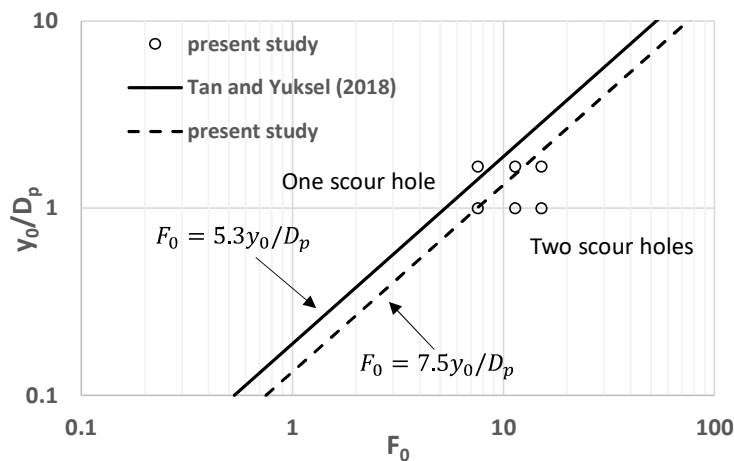
Figure 5. One or two scour hole conditions
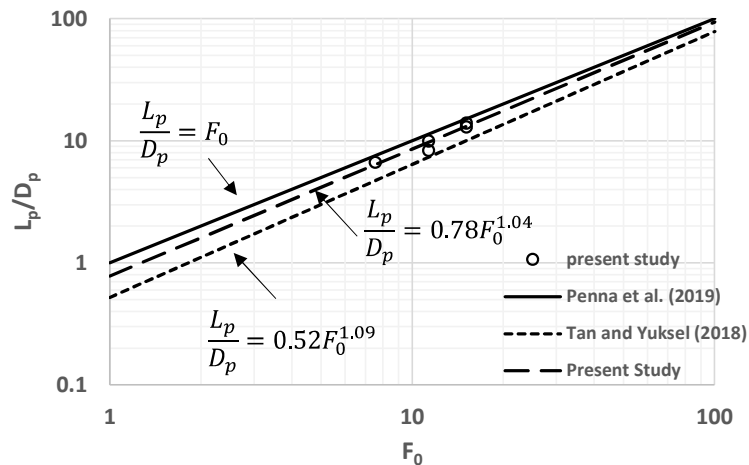
Figure 6. Relationship between (L_p/D_p) and F_0

3.2 Discussion of Maximum Scour Depth

Predicting the maximum value of the scour depth is important for the design of coastal structures. For this reason, various formulas have been proposed to obtain the maximum scour depth in previous studies (Hamill, 1987, Hong et al. (2013)). Some of these formulas for time-dependent maximum scour depth, where some of them for maximum scour depth at equilibrium conditions (Table 3). Figure 7 shows the scour depth calculated with the equations proposed in previous studies and measured during tests together. The Root-mean-square error (RMSE) were determined to determine the maximum scour depths predicted by which formula is compatible with the measured scour depths (Table 4). Hong et al. (2013) has lower RMSE since they use similar test conditions ($d_{50}=0.24$ mm) with the presented study.
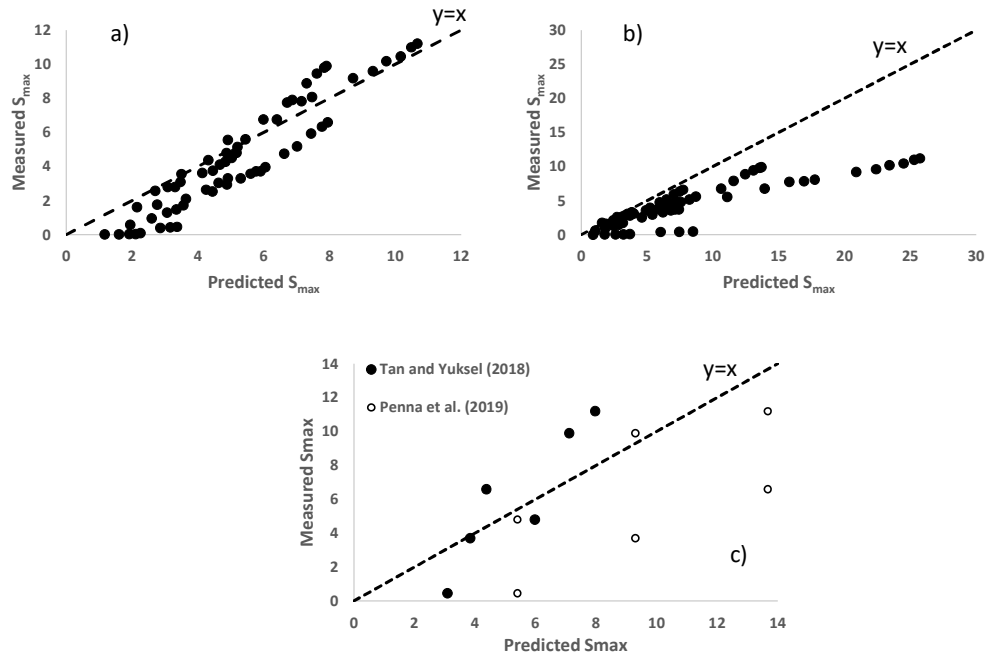
Figure 7. Evaluation of the measured and predicted data with the equations given by a) Hong et al. (2013) b) Hamill (1988), c) Tan and Yuksel (2018) and Penna et al. (2019)

Table 3. The formulas given for estimating S_{max}.

Study	Formulas	
Hamill (1988)	$S_{max} = \Omega[ln(t)]^{\Gamma}$	(5)
	$\Omega = 6.9 \times 10^{-4} \times \left(\dfrac{C}{d_{50}}\right)^{-4.63} \left(\dfrac{D_p}{d_{50}}\right)^{3.58} F_{rd}^{4.535}$	(6)
	$\Gamma = 4.113 \times \left(\dfrac{C}{d_{50}}\right)^{0.742} \left(\dfrac{D_p}{d_{50}}\right)^{-0.522} F_{rd}^{-0.682}$	(7)
	Ω : propeller coefficient;	
	Γ : propeller coefficient;	
	C: height of the propeller tip from bed	
Hong et al. (2013)	$\dfrac{S_{max,t}}{D_p} = k_1 \left[\log_{10} \dfrac{U_0 t}{D_p} - k_2\right]^{k_3}$	(8)

$$k_1 = 0.014 F_0^{1.12} \left(\frac{y_0}{D_p}\right)^{-1.74} \left(\frac{y_0}{d_{50}}\right)^{-0.17} \tag{9}$$

$$k_2 = 1.882 F_0^{-0.009} \left(\frac{y_0}{D_p}\right)^{2.302} \left(\frac{y_0}{d_{50}}\right)^{-0.441} \tag{10}$$

$$k_3 = 2.477 F_0^{-0.073} \left(\frac{y_0}{D_p}\right)^{0.53} \left(\frac{y_0}{d_{50}}\right)^{-0.045} \tag{11}$$

k_1, k_2, k_3: coefficients

y_0 : the gap between the center of propeller and bed.

Tan and Yuksel (2018)
$$\frac{S_{max}}{D_p} = 0.57(Fr_0 - Fr_{0c})^{0.33} \left(\frac{y_0}{D_p}\right)^{-1.1} \tag{12}$$

$$Fr_{0c} = 2.1 \frac{y_0}{D_p} \tag{13}$$

Penna et al. (2019)
$$\frac{S_{max}}{D_p} = 0.06 Fr_0^{1.34} \tag{14}$$

Table 4. RMSE considering previous studies.

Equation	RMSE
Hamill (1988)	5.325
Hong et al. (2013)	1.411
Tan and Yuksel (2018)	2.287
Penna et al. (2019)	4.332

In Figure 8, variation of ratio between S_{max} and D_p with F_0 is shown for Case 1 and Case 2. It is seen that lower propeller height causes increasing in scour depths. The difference between the scour depths is greater at low F_0 considering Case 1 and Case 2.
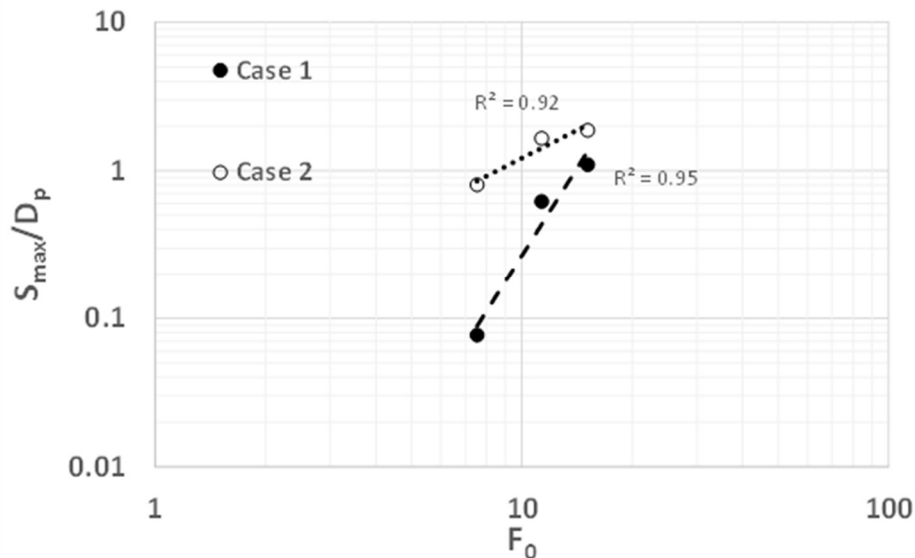
Figure 8. S_{max}/D_p versus F_0

4. CONCLUSIONS

In this experimental study, the unconfined scour hole caused by a rotating propeller jet was examined for different rotation speeds (rpm) and propeller offset heights (y_0). The study results were then compared with those obtained by the similar studies in the literature. Here, the propeller offset heights were found to have significant effects on scouring depth. It was observed that reducing the distance between the propeller and the seabed causes an increase in scour depth. Our test results were found generally compatible with those obtained by some of similar previous studies in the literature. It is suggested that practitioners and engineers must be careful to predict scour depths due to propeller jet by using formulas in practice.

ACKNOWLEDGMENTS

REFERENCES

Bergh, H. and Cederwall, K., Propeller Erosion in Harbours (1981), Hydraulics Laboratory, Royal Institute of Technology (1981), Stockholm, Sweden, Bulletin no. TRITA-VBI-107.

Blaauw, H.G., van de, Kaa E.J., 1978. Erosion of Bottom and Sloping Banks Caused by the Screw Race of Maneuvering Ships. Delft Hydraulics Laboratory, Delft, Netherlands. Report No.202.

Fuehrer, M., Romisch, K., 1977. Propeller jet erosion and stability criteria for bottom protection of various constructions. In: Proceedings of P.I.A.N.C, Bulletin No.58.

Hamill, G. A., Characteristics of the Screw Wash of a Manoeuvring Ship and the Resulting Bed Scour. Ph.D. Thesis, Queen's University of Belfast, Belfast, Northern Ireland, 1987.

Hamill, G.A. The Scouring Action of the Propeller jet Produced by a Slowly Manoeuvring Ship; PIANC: Brussels, Belgium, 1988.

Hamill, G. A., Johnston, H. T., Stewart, D. P., Propeller Wash Scour Near Quay Walls (1999) J. Waterw. Port, Coast. Ocean Eng. 125, 170–175.

Hong, J. H., Chiew, Y. M., Cheng, N.S., Scour Caused by a Propeller Jet (2013), J. Hydraulic Eng. (2013) ASCE 139, 1003–1012.

Penna, N., D'Alessandro, F., Gaudio, R., Tomasicchio, G.R., (2019), Three-dimensional manalysis of local scouring induced by a rotating ship propeller (2019), Ocean Eng. 188 (2019) 106294.

Qurrain, R., (1994), Influence of the Sea Bed Geometry and Berth Geometry on the Hydrodynamics of the Wash from a Ship's Propeller. PhD thesis, Queen's University Belfast, Belfast, UK.

Tan, R.I., Yüksel, Y., Seabed scour induced by a propeller jet (2018), Ocean. Eng. (2018),160, 132–142.

Verhey, H.J., The Stability of Bottom and Banks Subjected to the Velocities in the Propeller Jet Behind Ships. Proceedings of the 8th International Harbour Congress (1983), Antwerp, Belgium, 13–17 June. Delft Hydraulics, Delft, the Netherlands, publication no. 303.

IMPROVING WRF-HYDRO EXTREME RUNOFF SIMULATIONS THROUGH THE SEA SURFACE TEMPERATURE FIELDS WITH HIGHER SPATIO-TEMPORAL RESOLUTION

First Author: Berina M. Kilicarslan

Civil Engineering Department, Middle East Technical University

Ankara, Turkey

berinakilicarslan@gmail.com

Ismail Yucel

Civil Engineering Department, Middle East Technical University

Ankara, Turkey

iyucel@metu.edu.tr

Tugrul Yilmaz

Civil Engineering Department, Middle East Technical University

Ankara, Turkey

tuyilmaz@metu.edu.tr

ABSTRACT: This study investigates the impact of the spatio-temporal accuracy of four different sea surface temperature (SST) datasets on the accuracy of the Weather Research and Forecasting (WRF)-Hydro system to simulate hydrological response during two catastrophic flood events over the Eastern Black Sea (EBS) and the Mediterranean (MED) regions of Turkey. Three daily-updated and high spatial resolution external SST products (GHRSST, Medspiration, and NCEP-SST) and one coarse-resolution and time-invariant SST product (ERA5- and GFS-SST for EBS and MED regions, respectively) already embedded in the initial and the boundary conditions datasets of WRF model are used in deriving near-surface atmospheric variables through WRF. Event-based calibration is performed to the WRF-Hydro system using hourly and daily streamflow data in both regions. The uncoupled model simulations for independent SST events are conducted to assess the impact of SST-triggered precipitation on simulated extreme runoff. Some localized and temporal differences in the occurrence of the flood events with respect to observations depending on the SST representation are noticeable. SST products represented with higher cross-correlations (GHRSST and Medspiration) revealed significant improvement in flood hydrographs for both regions. The GHRSST dataset shows a substantial improvement in NSE (~70%) and KGE (from 0.06 to 0.3) with respect to the invariable SST (ERA5) in simulated runoffs over the EBS region. Reduction in RMSE up to 20% and an increase in correlation from 0.3 to 0.8 is observed for the same region. The use of both GHRSST and Medspiration SST data characterized with high spatio-temporal correlation resulted in runoff simulations exactly matching the observed runoff peak of 300 m3/s by reducing the overestimation seen in invariable SST (GFS) in the MED region.

1. INTRODUCTION

Extreme weather events result in devastating flood catastrophes with casualties in today's world. As the climate warms, more water vapor is pumped into the atmosphere, increasing the severity of rainfall events. With the changing climate, the impact of flood disasters may be worsened over time (Allen & Ingram, 2002).

As a result, reliable flood forecasting is critical for various operational purposes. One of the most crucial components of an accurate flood forecasting system is accurate estimates of the spatial distribution and the intensity of heavy rainfall events and their associated hydrologic responses (Yucel & Onen, 2014). Flood forecasting applications based on a hydro-meteorological modeling framework

that integrates the atmosphere-hydrology are becoming more prevalent in this regard (Kunstmann & Stadler, 2005). More accurate flood forecasts essentially necessitate enhanced Numerical Weather Prediction (NWP) forecasts. Thus, the accuracy of short-term predictions is strongly influenced by the choice of the NWP model and the inputs that drive the initial & boundary conditions (Done et al., 2004).

The ocean/sea-atmosphere interaction is the starting point that determines the climate distribution of the entire Earth. With this interaction, every change in the atmosphere determines the regional climate types and the distribution of these climates on the planet by moving vertically and horizontally with the effect of the Earth's daily and annual movement, ocean currents, winds, and topography (Bigg et al., 2003). SST is one of the most influential variables in this mentioned ocean-atmosphere interaction. Studies conducted particularly over the coastline with steeply varying topography address the fact that an accurate parameterization of the linkage between the land and atmosphere systems is required to demonstrate changes in water and energy fluxes and states for a more realistic flood prediction. To improve the reliability of such modeling systems, it is necessary to consider factors affecting this linkage. Therefore, the SST representation in the modeling system is regarded as one of the factors having a pronounced effect on water and energy fluxes in the lower-level atmosphere. Therefore, the condition of the SST has a substantial impact on the state of meteorological forcing variables in such NWP models, as the sea acts as a water and energy source for both the atmosphere and the land surface (Lebeaupin et al., 2006). Accordingly, providing high accuracy SST input to the lower boundary is crucial for accurate precipitation modelling, hencefor better flood forecasts through hydrological models.

The WRF-Hydro is a distributed, multi-physics hydrometeorological model system created by the United States National Center for Atmospheric Research (NCAR) to address major water challenges, including operational flash flood monitoring. Many studies have utilized this modeling system to examine the model's performance and applicability, including flood predictions, water balance, and water management studies across the globe (Kerandi et al., 2018; Li et al., 2017). Despite the studies compare the impact of different sources of precipitation input (i.e., comparing observed and simulated) on runoff simulation and agree that further improvement in the precipitation simulation skills is still needed (Givati et al., 2016; Senatoreet al., 2015), not many studies have investigated the impact of the spatio-temporal resolution of various SST sources over the runoff predictions of WRF-Hydro modelling system via the improvements in the simulated precipitation. In this study, to expand on the argument, different SST products are utilized in the WRF/WRF-Hydro modeling frameworks to see the impact of the temporal and spatial resolution-wise improved representation of the SST on the simulations of extreme precipitation causing significant floods over the catchments of regions in Turkey. In this context, basins and events from different geographic regions as EBS and MED represented with humid and semi-arid climates, respectively are chosen to see the SST impact on the hydrological response.

2. DATA AND METHOD

2.1. Study Area and Events

Flood events caused by heavy rainfall events that took place in the EBS and MED regions, which have different climatic characteristics are simulated. Figure 1 depicts 3-km domains (d02) the of WRF model encompassing both regions, as well as chosen basins and the associated channel networks and the locations of rain and stream gauge stations.

In this study, two significant flood events occurred in the past are selected for the following modeling practices. On August 24th, 2015, it was reported 32.4 millimeters of hourly precipitation, a total of 135 mm of rain fell during 24 hours over Artvin-Arhavi province in the EBS region. As an alternative event, on December 16th, 2018, the Antalya-Ovacik station reported an hourly precipitation of 53.1 mm, while receiving a total of 651.7 millimeters on the same day. This was the heaviest rainstorm ever recorded over the entire Turkey (Kaya et al., 2019). This recorded value was around three times greater than the Antalya city's monthly average rainfall in December (265.3 mm). A typical mesoscale

convective signal was observed for the event that occurred over the EBS area in the summer, whereas a frontal system was dominating for the event that occurred over the MED region in the winter.

For the evaluation of the model performance, streamflow data from the Arhavi provincial stations D22A049, D22A079, D22A089, and D22A147 (Hopa province), as well as the MED stations D08A071, D09A095, and E08A008 (Figure 1 and Table 1). Each calibration event in Table 1 is run for 10 days to allow the model to warm up. Average streamflow observations (m3/s) collected by the State Hydraulic Works (SHW) of Turkey are provided at daily timesteps at five of the stream gauge stations (D22A079, D22A089, and D22A147 over EBS region; D09A095 and E08A008 over MED region) and hourly timesteps at two of the stations (D22A049 over EBS and D08A071 over MED). However, the hourly streamflow data at these two stations are limited and only available after 2016.
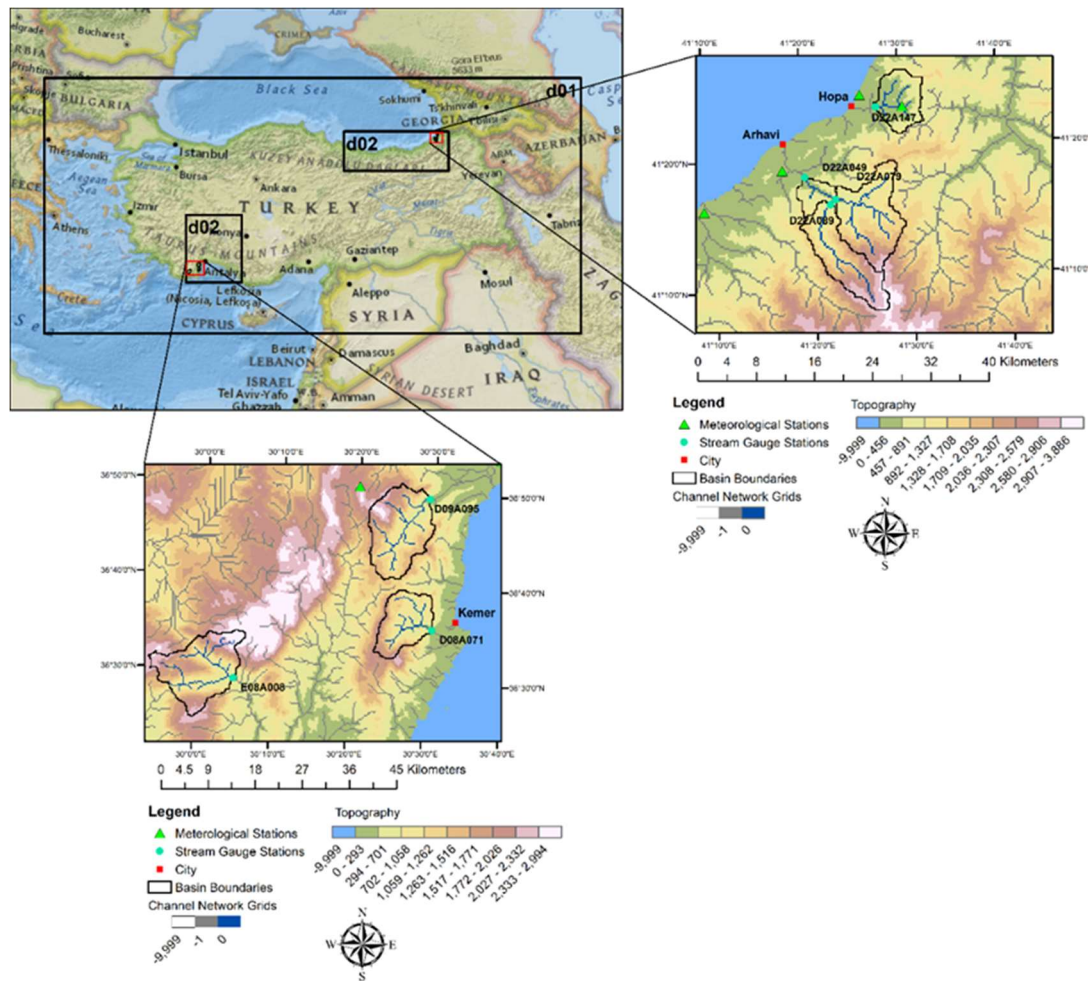
Figure 1 The outer and nested domains (d01 and d02) of the WRF model for the EBS and MED regions are displayed in the top-left. The boundaries of the selected basin, their outlet points (stream gauge stations denoted as blue dots), channel network grids in the WRF-Hydro model, and the meteorological station (denoted as a green triangle) are shown in the zoomed maps with the high-resolution topography layer in the background for the EBS region (top-right) and the MED region (bottom).

Table 1. Drainage areas and calibrated event periods of each selected basin over EBS and MED regions.

Region	Station	Drainage Area (km^2)	Calibration Event Period	
			Start	End
EBS	D22A049	175.8	08/27/2016	09/06/2016

			09/20/2017	09/30/2017
			10/19/2016	10/29/2016
			10/19/2016	10/29/2016
	D22A079	85.8	10/01/2018	01/11/2018
			06/24/2019	07/04/2019
			08/27/2016	09/06/2016
	D22A089	71.5	09/20/2017	09/30/2017
			10/19/2016	10/29/2016
			08/27/2016	09/06/2016
	D22A147	41.9	09/20/2017	09/30/2017
			10/19/2016	10/29/2016
			01/09/2015	01/19/2015
	D08A071	98.3	03/07/2017	03/17/2017
			03/23/2015	04/02/2015
			01/09/2015	01/19/2015
MED	E08A008	164.5	03/07/2017	03/17/2017
			03/23/2015	04/02/2015
			01/21/2014	01/31/2014
	D09A095	164.6	01/09/2015	01/19/2015
			03/23/2015	04/02/2015

2.2. Sea Surface Temperature Field Update in WRF Model

Along with the time-invariant SSTs (ERA5 and GFS), three additional daily-updated SST datasets are employed in this sensitivity analysis: 1) Medspiration Ultra-High-Resolution Foundation Sea Surface Temperature (CERSAT, 2012); 2) The Group for High-Resolution Sea Surface Temperature Level 4 Ultra-High Resolution (GHRSST) (Team GHRSST, 2010a, 2010b); 3) Real-Time, Global, Sea Surface Temperature (RTG_SST_HR) represented by the National Centers for Environmental Prediction (NCEP), National Oceanic and Atmospheric Administration (NOAA) (NCEP & NOAA, 2014). Medspiration, GHRSST, and NCEP SST datasets are available in daily time step and have high spatial resolutions of 0.022°, 0.01°, and 0.083°, respectively. Medspiration, GHRSST, NCEP, ERA5, and GFS will be used to refer to the simulations performed with different SST products utilized in this work henceforth. Table 2 depicts the simulation dates for the WRF model utilizing these SST products for each area of study.

Table 2. Forcings used in the SST simulations and their run periods.

| Region | Forcings | | Run Periods | |
	SST Products	Initial and Boundary Conditions	Start	End
EBS	ERA5 GHR Medspiration NCEP	ERA5 Reanalysis	08/17/2015	08/27/2015
MED	GFS GHR Medspiration NCEP	GFS Forecast	12/10/2018	12/20/2018

2.3. WRF-Hydro Model

The integrated hydrological model system named WRF-Hydro (version 5.1.1) is operated in this study (Gochis et al., 2020). The WRF-Hydro hydrological modeling system is an enhanced version of the traditional 1-dimensional Noah-MP LSM that incorporates overland, saturated subsurface, channel, and groundwater flow into a modeling structure. The LSM in the WRF-Hydro model is the same as the one-dimensional LSM (Noah-MP) operated in the WRF model. Accordingly, the hydrological modeling system is operated over the nested domain of WRF (d02) with a 3 km resolution. There are two options available in the modeling system configuration for the feedback mechanisms between WRF and WRF-Hydro model as uncoupled and coupled modes. In uncoupled mode, there is only one-way feedback from atmosphere to land. The meteorological inputs for this mode can be created by WRF model or other sourced such as radar and satellite precipitation can be used.

WRF-Hydro model disaggregates the LSM grids into high-resolution routing grids after the moisture states are computed for the land surface column. In this study LSM grid resolution is defined as 3 km (same as the WRF) and disaggregated into routing grids with a 250 m grid size in both regions.

2.4. Calibration of the WRF-Hydro Model

WRF-Hydro calibration runs are performed with the WRF meteorological forcings updated with the observed precipitation. Calibration of the WRF-Hydro is carried out for three events in each basin (seven basins, Table 1) at hourly or daily time steps depending on the availability of streamflow data. The validation of the calibrated parameters sets is performed with the SST simulations. In the D22A049 basin of the EBS region and D08A071 basin of the MED region, hourly streamflow data for two heavy precipitation events in the 2016 and 2017 hydrologic years are used to calibrate the model while other events are calibrated on a daily basis (Table 1). For the validation process (with SST events), hourly streamflow data is only available for the MED region, whereas the daily streamflow is used for the EBS region. The calibrated parameter set of the WRF-Hydro model is then validated for SST simulations over both regions. WRF-Hydro model is forced by meteorological forcings constructed using the ERA5 and GFS SSTs, as well as three additional daily-updated SST

datasets namely Medspiration, GHRSST, and NCEP. Additionally, similar SST events are modeled by substituting observed precipitation in WRF precipitation. The model is calibrated manually using a step-wise approach allowing the model to first simulate the water balance in the basin and then distribute the amount of water accurately over time ((Yucel et al., 2015)). At each step, a common parameter value was determined for all three events, and the calibration of the next parameter was started. This was done based on the visual scanning of hydrographs and the calculated statistics.

3. RESULTS

3.1. Evaluation of Precipitation Simulations for SST Events

Time series of the basin averaged simulated and observed precipitation for the SST events over D22A147 and D08A071 basins are given in Figure 2 (a) and (b), respectively. Figure 2 (a) shows the precipitation time series from 08/17/2015 00:00:00 UTC to 08/27/2015 00:00:00 UTC, for 241-hours. The highest precipitation at D22A147 is recorded at the 178th hour, or 08/24/2015 09:00:00 UTC as 26.3 mm of rain. However, the highest precipitation quantity over the whole EBS region is reported as 32.4 millimeters at 08/24/2015 00:00:00 UTC within the boundary of D22A049. In spite of this, as shown in Figure 2 (a), the D22A147 basin-average precipitation is calculated as 16.1 mm during the 169th hour, which coincides with the event peak timing over the EBS region. Although simulations with alternative SST datasets are able to approximate the broad pattern, except the primary peak is generated a few hours sooner than observed. In addition, it is seen that the GHRSST simulation underestimates the recorded peak precipitation. A substantial overestimation of the peak value for the GHRSST simulation corresponds to the observed peak, while the other simulations recreate peak values to the observed one.

The time series of the basin-averaged precipitation for the event between 12/10/2018 00:00:00 UTC-12/20/2018 00:00:00 UTC (241-hours) are shown in Figure 2 (b). Peak precipitation is recorded as 53.1 mm during the 162nd hour, corresponding to 12/10/2018 at 17:00:00 UTC. At the same time step, the peak basin-average precipitation for D08A071 is recorded as 15.7 mm. On the whole, all simulated precipitations reveal an almost exact match to the observed patterns, with modest overestimations. On the other hand, high-resolution SST simulations seem to be able to enhance the volume with decreased bias in line with the observation. Simulations performed with GFS SST, GHRSST, and NCEP SST all have slight delays in their peak timing (about 1-2 hours).
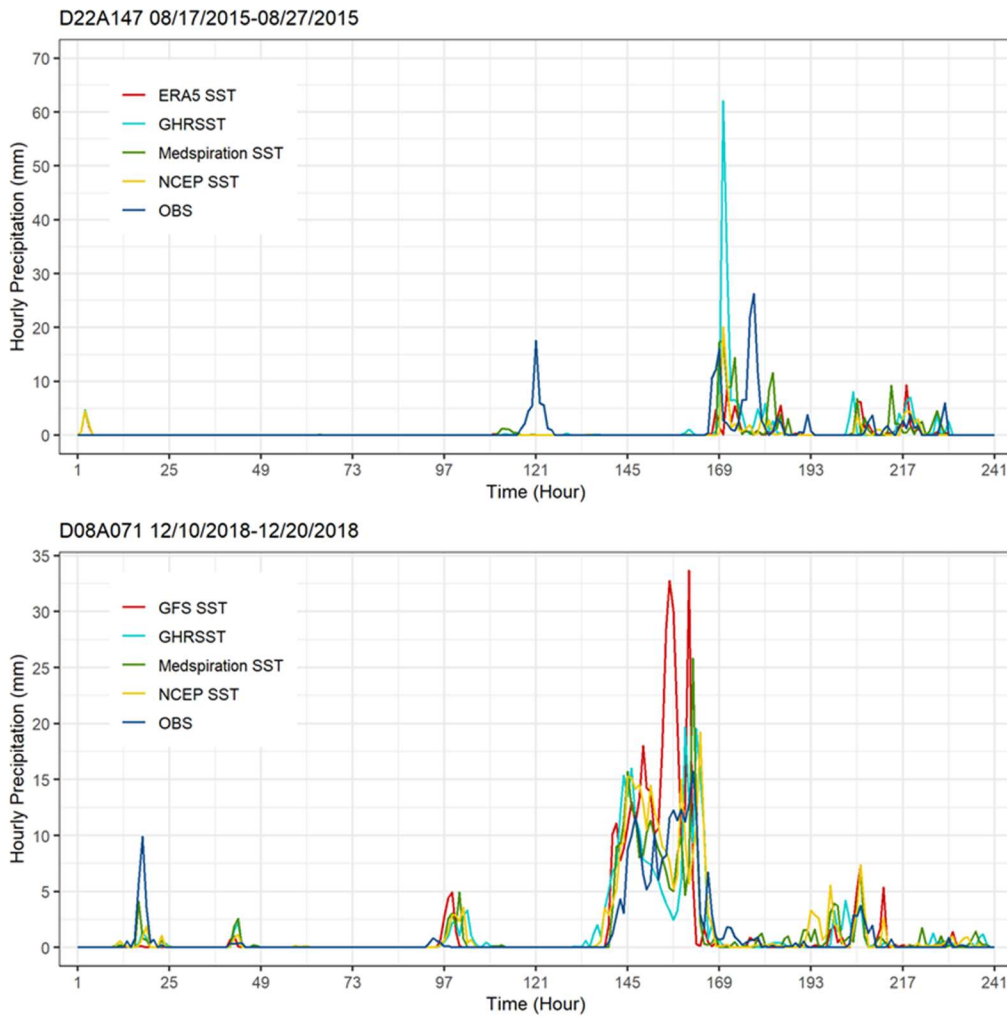
Figure 2. Time series of hourly precipitation that a) D22A147 basin over EBS region receives during the event occurred in 08/17/2015-08/27/2015 and b) D08A071 basin over MED region receives during the event occurred in 12/10/2018-12/20/2018 for ten days. Outputs are generated from the WRF model with the native SST field from ERA5 Reanalysis data (ERA5-SST) for the EBS region and GFS Forecast data (GFS-SST) for the MED region different SST products: GHRSST, Medspiration, and NCEP

3.2. Evaluation of SST Events for WRF-Hydro Model

WRF-Hydro model performances of the simulations forced by the WRF meteorological data generated with different SST datasets are examined in this section. The calibrated parameter set with the manual stepwise calibration method is utilized for Hopa (D22A147) and Kemer (D08A071) basins. The simulated hydrograph based on the observation precipitation forcing is also compared with the hydrographs forced by the WRF model to be able to see the errors caused by the interpolation process and the model itself.

Hydrological response to selected SST events over Hopa and Kemer basins is simulated, and the hydrographs derived by various SST simulations and observed precipitation are demonstrated in Figure 3. Based on the simulated hydrograph of the Hopa basin, it is observed that the ERA5 and NCEP simulations are underestimated compared to the observed hydrograph (Figure 3 (a)). The negative bias found for the WRF precipitation simulations in Figure 3 (a) may explain this underestimation issue for ERA5 and NCEP (datasets showing the highest bias error). The hydrograph volumes produced by the Medspiration simulation and the simulation using observed precipitation are marginally better than those produced by the ERA5 and NCEP simulations. Despite the fact that the GHRSST simulation overestimates precipitation and skips the peak time for Hopa, the daily mean discharge of the GHRSST is the most accurate simulation in predicting discharges. In line with the

results of cross-correlation calculations, it is determined that GHRSST is the best SST product that represents the Arhavi basin and the corresponding event.

In the Kemer basin, it is seen that the GFS simulation overestimated the peak value and missed the timing trend of the observation hydrograph (812.9 m3/s) (Figure 3 (b)). The simulations derived using high-resolution SST and observation precipitation shows that although the hydrographs follow a similar trend with the observation in the falling limb part, they decrease abruptly in the rising limb part. Minor delays are observed in the primary peak time for the high-resolution SST simulations. In particular, the simulation forced with the observed precipitation correctly identifies the time and magnitude of the first peak but produces a negative bias in the value of the second peak. High-resolution SST simulations improve the ERA5 results by ~550 m3/s volume reduction and successfully capture the peak timing.
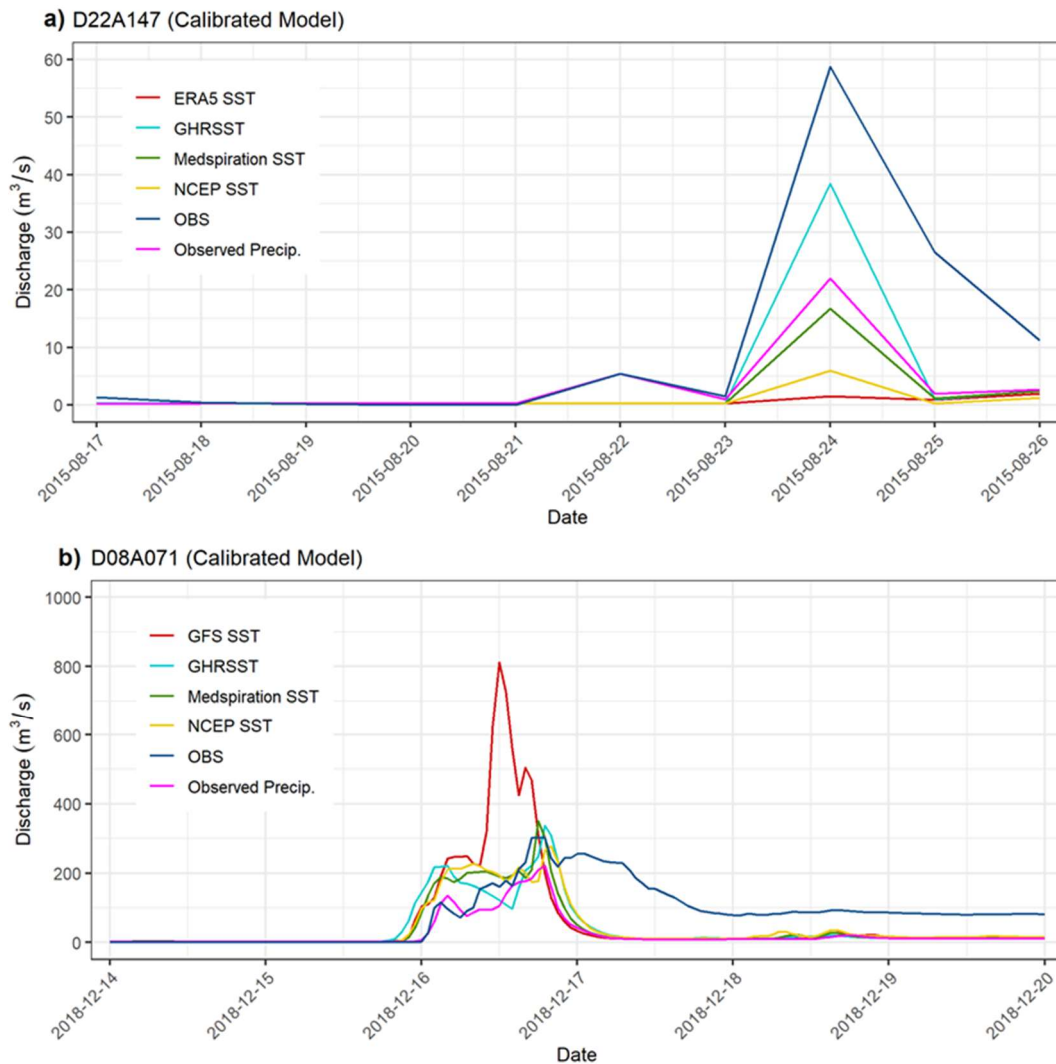
Figure 3 a) 17/08/2015-27/08/2015 event and D22A049 basin b) 03/07/2017-03/17/2017 (last six days) event and D08A071 basin observation hydrograph, modeled hydrographs with the precipitation data generated using ERA5/GFS GHRSST, Medspiration, NCEP SST products, and the modeled hydrograph with the precipitation data based on the interpolation of the observation points

4. CONCLUSIONS

Investigation of hydrologic response for extreme precipitation events simulated by different SST datasets integrated into the WRF model with coarse, high, and time-variant and -invariant resolutions in small catchments with a complex topography and experiencing coastal orography was carried out in this study. According to the results of precipitation and hydrograph simulations, high-resolution

SST products may be used as initial and lower boundary conditions for operational forecast purposes for heavy precipitation events. Extreme weather event analyses over coastal regions with complex topography must take atypical SST fluctuations caused by climate change into account using temporally and spatially changing SST characteristics defined by high-resolution datasets. Further improvement of the interflow representation in WRF-Hydro modeling structure may enhance the streamflow simulations and the hydrograph results, particularly at the falling limb stage.

REFERENCES

Allen, M. R., & Ingram, W. J. (2002). Constraints on future changes in climate and the hydrologic cycle. *Nature.Com,* 419(September), 225–232. https://www.nature.com/articles/nature01092 .

Bigg, G. R., Jickells, T. D., Liss, P. S., & Osborn, T. J. (2003). The role of the oceans in climate. *International Journal of Climatology*, *23*(10), 1127–1159. https://doi.org/10.1002/joc.926.

Done, J., Davis, C. A., & Weisman, M. (2004). The next generation of NWP: Explicit forecasts of convection using the weather research and forecasting (WRF) model. *Atmospheric Science Letters*, 5(6), 110–117. https://doi.org/10.1002/asl.72.

Givati, A., Gochis, D., Rummler, T., & Kunstmann, H. (2016). Comparing One-Way and Two-Way Coupled Hydrometeorological Forecasting Systems for Flood Forecasting in the Mediterranean Region. *Hydrology*, *3*(2), 19.

Gochis, D. J., Barlage, M., Cabell, R., Casali, M., Dugger, A., FitzGerald, K., McAllister, M., McCreight, J., RafieeiNasab, A., Read, L., Sampson, K., Yates, D., & Zhang, Y. (2020). The WRF-Hydro modeling system technical description, (Version 5.1.1). *NCAR Technical Note*, 107.

Kaya, O. F., Guler, M., Altan, A., & Yorganci, I. (2019). 15-16-17 Aralık 2018 Tarihlerinde Antalya İli Kemer/Ovacık Mevkiinde Görülen Aşırı Yağış Hadisesinin Aktüel Hava Haritaları, Uzaktan Algılama ve Sayısal Hava Tahmin Ürünleri ile Sinoptik ve Hidrolojik Analizi. *10. Ulusal Hidroloji Kongresi 9-12*, *November*.

Kerandi, N., Arnault, J., Laux, P., Wagner, S., Kitheka, J., & Kunstmann, H. (2018). Joint atmospheric-terrestrial water balances for East Africa: a WRF-Hydro case study for the upper Tana River basin. *Theoretical and Applied Climatology*, *131*(3–4), 1337–1355. https://doi.org/10.1007/s00704-017-2050-8.

Kunstmann, H., & Stadler, C. (2005). High resolution distributed atmospheric-hydrological modelling for Alpine catchments. Journal of Hydrology, 314(1–4), 105–124. https://doi.org/10.1016/j.jhydrol.2005.03.033.

Lebeaupin, C., Ducrocq, V., & Giordani, H. (2006). Sensitivity of torrential rain events to the sea surface temperature based on high-resolution numerical forecasts. *Journal of Geophysical Research Atmospheres*, *111*(12), 1–19. https://doi.org/10.1029/2005JD006541.

Li, L., Gochis, D. J., Sobolowski, S., & Mesquita, M. D. S. (2017). Evaluating the present annual water budget of a Himalayan headwater river basin using a high-resolution atmosphere-hydrology model. *Journal of Geophysical Research*, *122*(9), 4786–4807. https://doi.org/10.1002/2016JD026279.

Senatore, A., Mendicino, G., Gochis, D. J., Yu, W., Yates, D. N., & Kunstmann, H. (2015). Fully coupled atmosphere-hydrology simulations for the central Mediterranean: Impact of enhanced hydrological parameterization for short and long time scales. *Journal of Advances in Modeling Earth Systems*, *7*(4), 1693–1715. https://doi.org/10.1002/2015MS000510.

Yucel, I., & Onen, A. (2014). Evaluating a mesoscale atmosphere model and a satellite-based algorithm in estimating extreme rainfall events in northwestern Turkey. *Natural Hazards and Earth System Sciences*, 14(3), 611–624. https://doi.org/10.5194/nhess-14-611-2014

Yucel, I., Onen, A., Yilmaz, K. K., & Gochis, D. J. (2015). Calibration and evaluation of a flood forecasting system: Utility of numerical weather prediction model, data assimilation and satellite-based rainfall. *Journal of Hydrology*, 523, 49–66. https://doi.org/10.1016/j.jhydrol.2015.01.042.

APPLICATION OF GIS-BASED GALDIT METHOD TO ASSESS THE SEAWATER INTRUSION OF THE KARAREIS COASTAL AQUIFER (IZMIR, TURKEY)

Khalilullah ZULAL

International Water Resources, Izmir Institute of Technology

Urla, Izmir, Turkey

khalilullahzulal@iyte.edu.tr

Prof. Dr. Alper BABA

International Water Resources, Izmir Institute of Technology

Urla, Izmir, Turkey

alperbaba@iyte.edu.tr

Prof. Dr. Orhan GÜNDÜZ

International Water Resources, Izmir Institute of Technology

Urla, Izmir, Turkey

orhangunduz@iyte.edu.tr

ABSTRACT: Groundwater overexploitation in coastal aquifers is frequently accompanied with seawater intrusion, which is exacerbated by rising global sea levels. For several coastal locations, ensuring long-term water quality safety and hence determining sensitive zones to seawater intrusion has become a substantial hydrogeological issue. The evaluation of groundwater resources led in the creation of models that aid in the identification of sensitive zones. This study introduces the GALDIT approach, a GIS-based hydrogeological index designed to assess aquifer susceptibility to seawater intrusion in the Karareis coastal aquifer in Turkey's Karaburun Peninsula. In this model, groundwater occurrence (aquifer type) (G), aquifer hydraulic conductivity (A), depth to groundwater level above the sea (L), distance from the shore (D), impact of seawater intrusion (I), and aquifer thickness (T) are selected as important factors controlling seawater intrusion. These parameters contain the fundamental prerequisites for determining any hydrogeological setting's overall salinization capacity. Furthermore, ArcGIS geographical information systems platform was used to construct hydrogeological data, and relevant thematic maps were created. Using overlaying approaches, the final vulnerability map was created by combining the thematic maps. According to the result of the analysis, almost half of the total surface of the southern region of the Karareis coastal aquifer can be classified as highly vulnerable. However, as the area get distanced from the shore, the salinization vulnerability decreases to moderate and low levels. In this study, distance from the shore (D) and hydraulic conductivity (A) were found to be the most essential parameters in the GALDIT model. Overall, the result of this study provided a good approach for providing smart management decisions on Karareis aquifer including but not limited to covering multiple viewpoints such as locating optimal locations for potential groundwater extraction wells.

Keywords: Seawater Intrusion, Vulnerability, Groundwater, GALDIT, Geographic System Information (GIS)

1. INTRODUCTION

Coastal aquifers are frequently a major supply of freshwater for the coastal communities in the Mediterranean region. Due to the sluggish flow that impacts them, their resource has a high level of inertia, and their unsustainability has an impact on the quality and availability of groundwater (MED-EUWI 2007). This results in a decrease in piezometric values and, as a result, seawater intrusion

(Niazi 2007). Groundwater level decline is mostly caused by overexploitation of coastal aquifers for domestic, agricultural, and tourism purposes, and as a result, groundwater flow is reversed, draining from the sea to the mainland (Vrba, J, 2002). This situation has accelerated in the previous two decades, and it is most severe in European and Middle Eastern Mediterranean nations with semiarid climates, such as Portugal and Greece. (Chachadi and Lobo-Ferreira 2005).

The alluvial plain of Karareis, in Turkey's Izmir province's far west, on the Mediterranean Sea's shore, has been one of those coastal places where expanding agricultural activity in recent decades has boosted groundwater usage. Overexploitation and diversification of land use have negative consequences for the aquifer. Agricultural pollution hazards, lower piezometric levels, and seawater intrusion all seem to support this theory. Mapping the susceptibility of groundwater in relation to various risks is a critical undertaking in terms of territorial development and groundwater protection.

The word vulnerability, in general, refers to the possible degree of harm that may be predicted based on the features of an item at risk in relation to a certain danger. Different methodologies may be employed effectively on different scales depending on the unique study objective and data availability (Vironika and Judit 2017; Trabelsi et al., 2016; Kallioras et al., 2012).

Some vulnerability models that are based on overlaying methods include AVI (Stempvoort et al., 1993), SINTACS (Civita 1994), GOD (Foster 1987), EPIK (Doerfliger and Zwahlen 1997), the ISIS (Civita and Regibus 1995), DRASTIC (Aller et al., 1987), and the GALDIT model (Chachadi and Lobo-Ferreira 2005; Lobo-Ferreira et al., 2005). The study of Luoma et al. (2017) comparably assessed the performances of the AVI, SINTACS, and GALDIT models whereas Kura et al. (2015) compared the applications of DRASTIC and GALDIT models in Kapas Island of Malaysia.

The GALDIT model (Chachadi and Lobo-Ferreira 2001, 2005a) was chosen for the assessment of groundwater vulnerability to sea water intrusion in the Karareis aquifer due to its common use for coastal aquifers and aligned issues as a well-established approximation technique. GALDIT is a combination of the first letters of six parameters (Groundwater occurrence (G), aquifer hydraulic conductivity (A), height of groundwater level above sea level (H), distance from the shore (D), impact of seawater intrusion (I), and thickness of the aquifer (T). Since its development, the GALDIT model along with some of its modifications has been used in many pieces of research in coastal regions (Bouderbala et al., 2016; Mahesha et al., 2012; Recinos et al., 2015; Louma et al., 2017; Kazakis et al., 2018).

The GALDIT method's implementation is typically associated with thematic maps, which are created using geographic information systems (GIS) (Chachadi and Lobo-Ferreira 2001). GIS assists in the study of groundwater systems and can help with the development of groundwater conceptual models (Singhal and Goyal 2011).

The GALDIT approach was used in conjunction with ArcGIS in this investigation in the Karareis aquifer of Izmir, where groundwater is the primary and single source of fresh water for domestic and agricultural uses. As a result, aquifer conservation is critical to sustaining economic activities like tourism as well as ensuring the safety of water supplies for agricultural production.

2. MATERIALS AND METHODS

2.1. Study Area

Geographically, Karareis is on the westernmost tip of the Karaburun Peninsula, about 50 kilometers west of Izmir. The research area is approximately 2.34 km^2 and is located between the longitudes of 26°24′46″ and 26°26′22″ and the latitudes of 38°28′32″ and 38°29′56″. The area's elevation ranges from sea level to 40 meters. The position and domain of Karareis' model are depicted in (Figure 2). The research region's surface is defined by a plain with typical regression, and the area is divided into unequal two sections by a seasonal stream. The research area is flanked on three sides by mountains, while the fourth side is bordered by the sea. Agricultural fields, grassland, and habitation areas (summerhouses) make up the land cover of the study region, which has been significantly rising since 1980. People were driven to construct their communities along the shore due to topographic factors and commercial routes. The number of summerhouses in the area is thought to be (750). Groundwater

is the only source of freshwater for many homes. For the purpose of research and water quality, there are nine authorized observation pumping wells in the Karareis region.
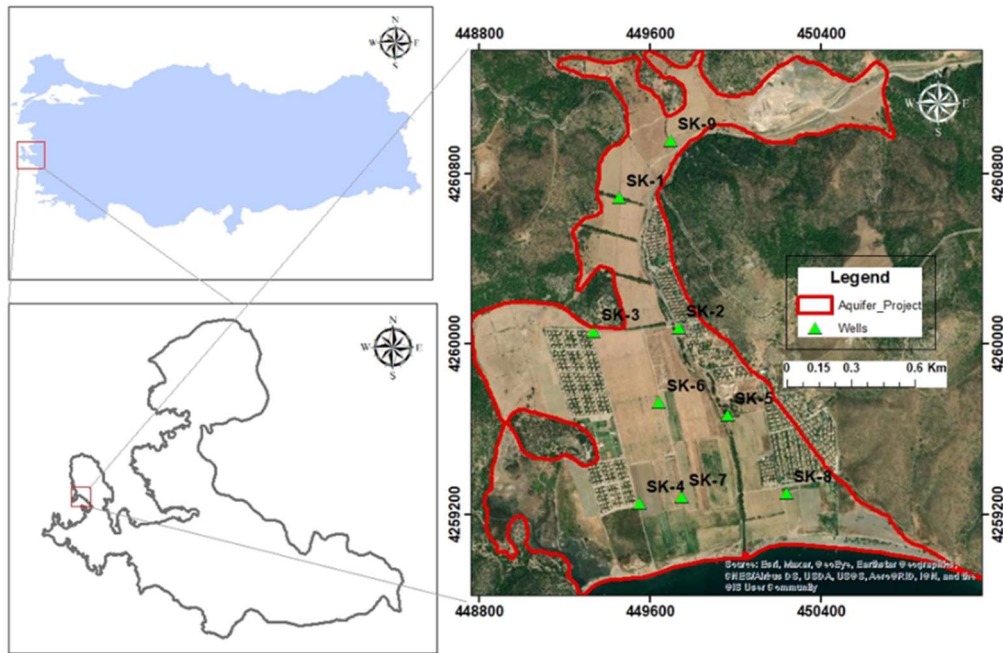
Figure 2. Location map of the study area and observation wells

2.2. Topography

The topography of the research region is derived using OpenTopography's digital elevation model (Farr et al., 2009). The research area's land surface elevation spans from mean sea level (MSL) to around 40 meters above MSL. The pattern of ground surface elevations in the Karareis region is depicted in (Figure 3), which was created using hillside layering to create a three-dimensional picture.
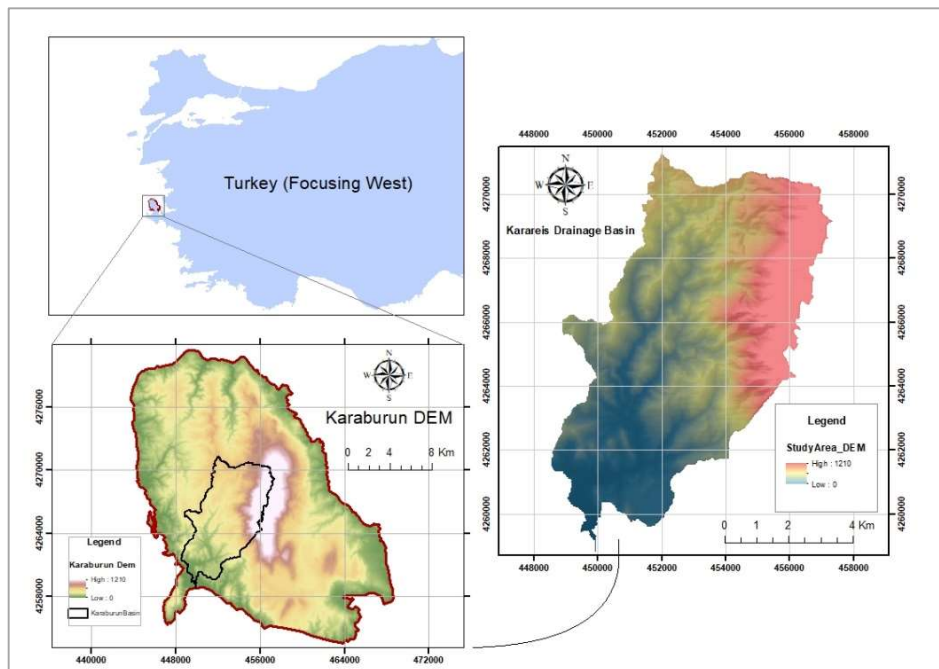
Figure 3. Topography of the study area

2.3. Climate

The Karareis and its surrounding region have a typical Mediterranean climate, in which the summers are hot and dry and have warm and rainy winters. The peninsula's average yearly temperature ranges between 15°C and 20°C. In the summer and winter, average daily maximum temperatures range from 19°C to 32°C, while minimum temperatures range from 8°C to 20°C, as shown in (Figure 4).
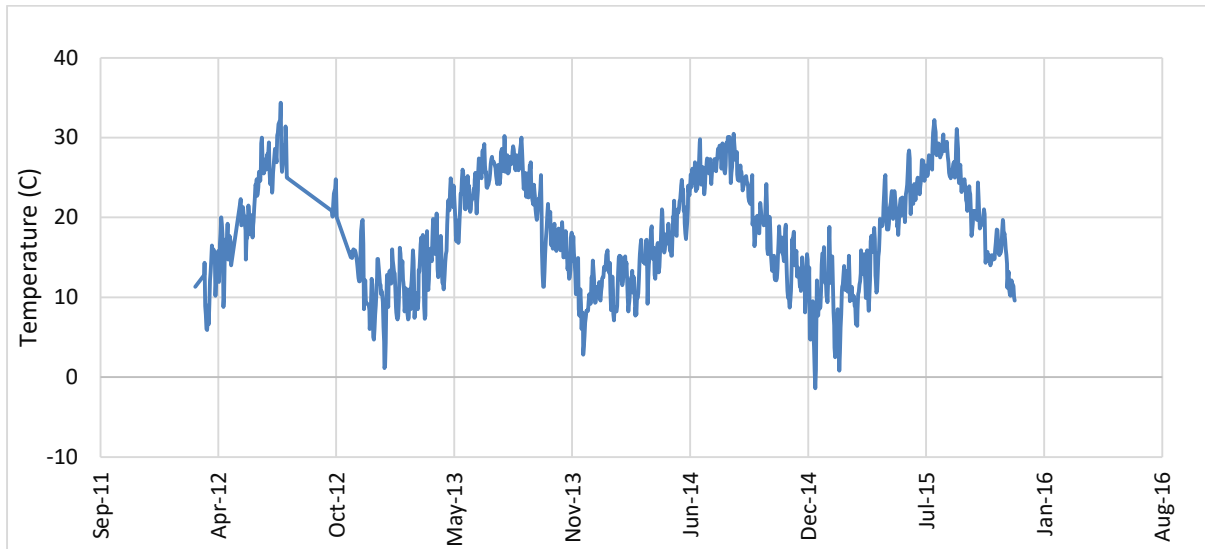
Figure 4. Time series of daily temperature values of Karaburun Region

The rainfall data of Karareis is based on data gathered from Karaburun 18032 station. From 2012 to 2015, (Figure 5) depicts the cumulative daily prepetition (mm). In 2012 and 2013, annual rainfall ranges from 1200 mm/year to 1900 mm/year, and from 450 mm/year to 1200 mm/year in 2014 and 2015. The majority of rain falls between November and March, with the rest of the year being completely or moderately dry.
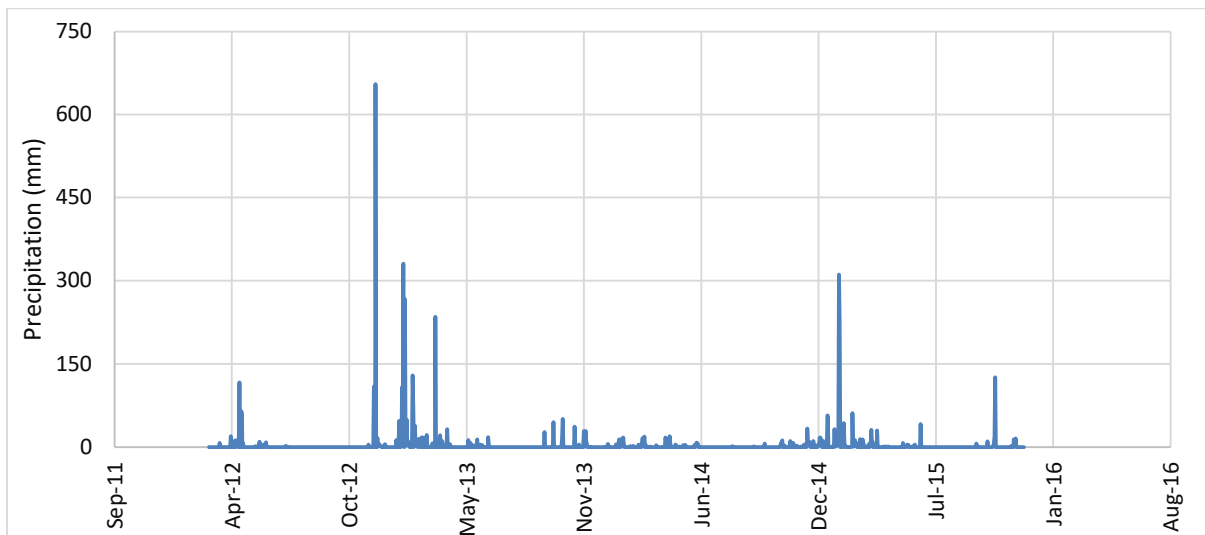
Figure 5. Time series for daily precipitation (mm) values of Karaburun region

2.4. GALDIT Method Review

In this study, the GALDIT approach is used to assess the susceptibility of the Karareis aquifer to seawater intrusion. GALDIT is a method of index mapping. In terms of applicable ratings, weightings, and vulnerability index assignment, the GALDIT approach is a simple method (Figure 6). It is mentioned expressly that the index is intended to be a first approximation tool rather than a source of definitive answers. The groundwater vulnerability index in relation to seawater intrusion is thus calculated using a combination of six main criteria that are thought to be the most critical regulating elements for seawater intrusion.

- Groundwater occurrence (G) (aquifer type; unconfined)

- Aquifer hydraulic conductivity (A)

- Depth to groundwater above sea Level (L)

- Distance from the shore (D)

- Impact on existing status of seawater intrusion in the area (I)

- Thickness of the aquifer (T)
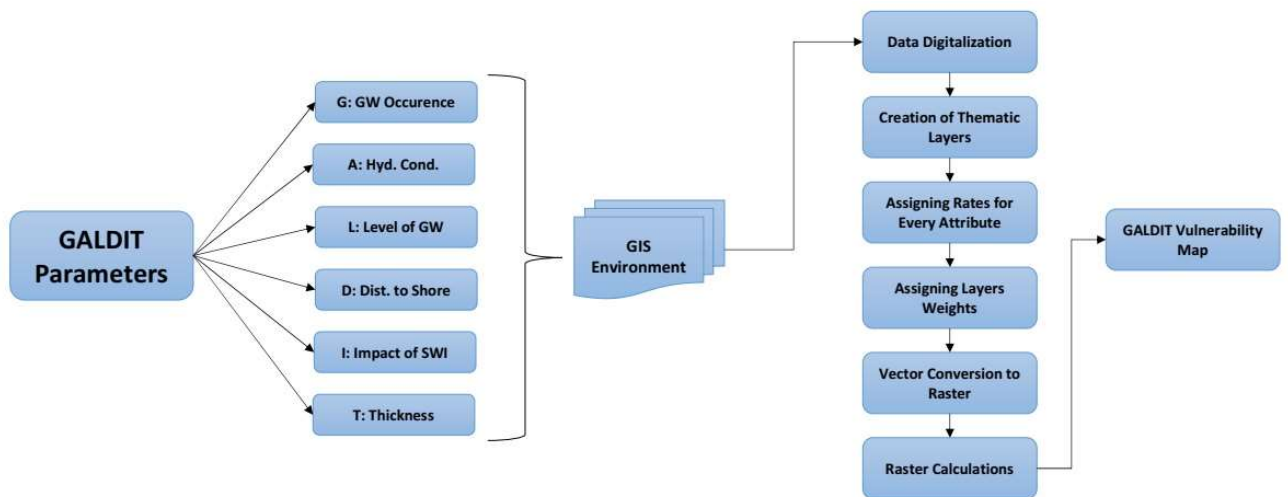
Figure 6. Flowchart of the main process of the Study

The three components that make up the GALDIT vulnerability class assignment (Lobo-Ferreira et al. 2007) are:

Indicator weights (W): A weight from 1 (low influence) to 4 (high influence) is proposed.

Rating (rank) (R): Each parameter is given a number between 2.5 and 10 based on its characteristics (a higher importance rating indicates high vulnerability to seawater intrusion).

Decision criterion: It's the entire sum of the individual indicator scores calculated by multiplying the importance rating values by the indicator weights.

Of all, a high score implies a high risk of seawater intrusion. The following equation (1) is used to calculate GALDIT's final index:

$$GI = \frac{\sum_{i=1}^{6} w_i r_i}{\sum_{i=1}^{6} w_i} = \frac{(G_W G_R + A_W A_R + L_w L_r + D_w D_r + I_w I_r + T_w T_r)}{\sum_{i=1}^{6} W_i} \tag{1}$$

$$GI = \frac{(1 * G_r + 3 * A_r + 4 * L_r + 4 * D_r + 1 * I_r + 2 * T)}{15} \tag{2}$$

where w_i is the weight and r_i is the rating of the ith parameter.

Each parameter has been given a specific weight (1–4) depending on its relative importance to seawater intrusion. Furthermore, the parameter's value is divided into four different categories and have attained scores on a scale of 2.5, 5, 7.5, and 10. (Table 18). The higher the score gets; the more vulnerable the aquifer gets to seawater intrusion.

Table 18. GALDIT Parameters Rating.

Parameters	Weights	Classifications		Ratings
Groundwater Occurrence (G)	1	Confined Aquifer		10
		Unconfined Aquifer		7-9
		Leaky Aquifer		5
		Bounded Aquifer	Range	2.5
Aquifer Hydraulic Conductivity (A) [m/day]	3	High	>40	10
		Medium	40-10	7.5
		Low	10-5	5
		Very Low	<5	2.5
Groundwater Level Height above the sea level (L) [m]	4	High	<1.0	10
		Medium	1.0-1.5	7.5
		Low	1.5-2.0	5
		Very Low	>2	2.5
Distance from the Shore (D) [m]	4	Very small	<500	10
		Small	500-750	7.5
		Medium	750-1000	5
		Far	>1000	2.5
Impact on existing status of sea water intrusion (I) (Cl/HCO3) [ppm]	1	High	>2.0	10
		Medium	1.5-2.0	7.5
		Low	1.0-1.5	5
		Very Low	<1.0	2.5
Thickness of the aquifer (T) [m]	2	Large	>40	10
		Medium	40-10	7.5
		Small	10-5	5
		Very small	<5	2.5

3. RESULTS AND DISCUSSION

3.1. Groundwater Occurrence (G)

Unconfined aquifers are consequently more influenced than confined aquifers from seawater intrusion. The occurrence of groundwater is characterized in terms of aquifer pressure circumstances. This measure was derived from the records of water wells and research done in the Karareis plain (Mansour et al., 2017). Karareis's hydrogeological system is all unconfined and the 7.5 rank vulnerability rating part is assigned. The groundwater occurrence map which is shown in (Figure 7) indicates the entire alluvial deposit in the Karareis region.

3.2. Aquifer Hydraulic Conductivity (A)

The capacity of aquifer materials to transfer water is characterized as hydraulic conductivity, which governs the pace at which groundwater flows under a particular hydraulic gradient. One of the most effective ways to determine the hydraulic conductivity values is the pumping test. In this study, the pumping test method was successfully used to find the average hydraulic conductivity values by setting a constant water withdrawal rate from each well.
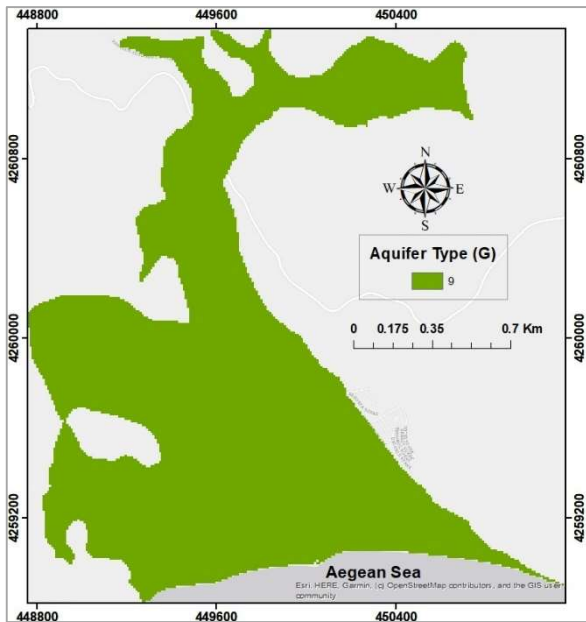
Figure 7. Map of groundwater occurrence (G)
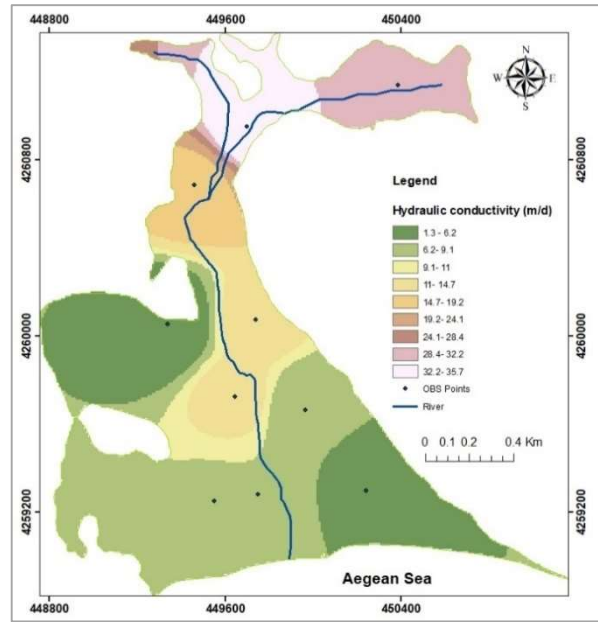
Figure 8. Map of aquifer hydraulic conductivity (A)
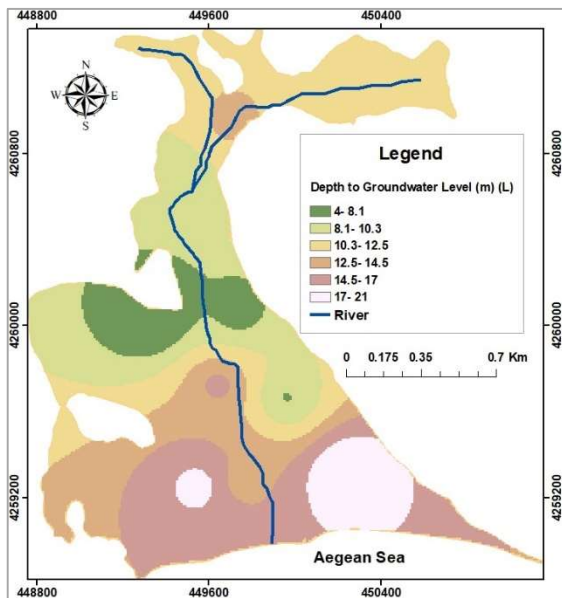
Figure 9. Depth to groundwater above sea level (L)
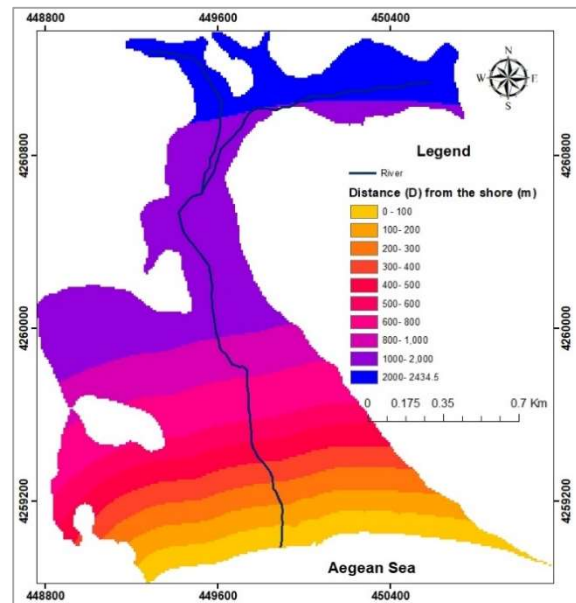
Figure 10. Distance from the shore (D)
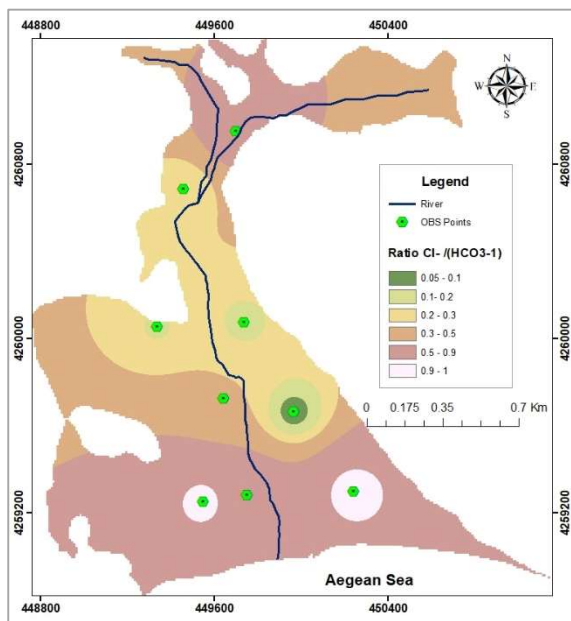
Figure 11. Impact on existing status of seawater intrusion in the area (I)
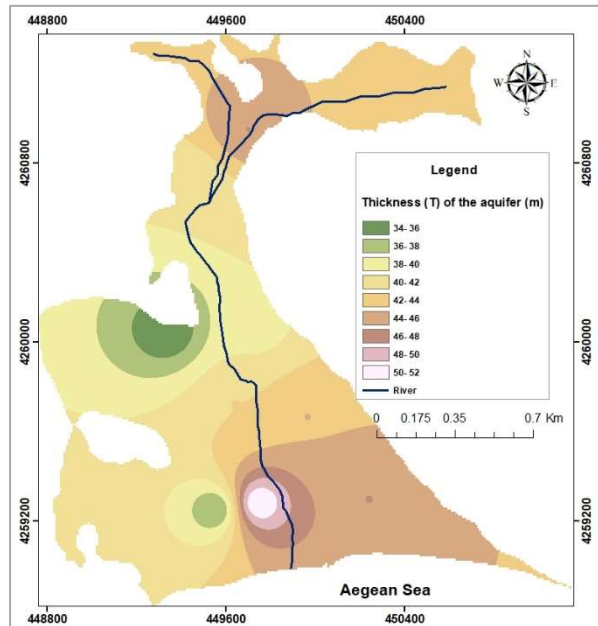
Figure 12. Thickness of the aquifer (T)

Hydraulic conductivity readings above a certain threshold imply a coastal aquifer system's susceptibility. The higher the hydraulic conductivity values, the more vulnerable is the aquifer (Figure 8). In the study project, transmissivity values were determined from pumping tests from prior investigations (Mansour et al., 2017).

3.3. Depth to Groundwater Above Sea Level (L)

Because it is a measure of the hydraulic pressure that contributes to limiting the entrance of seawater, this parameter is critical for analyzing seawater intrusion. To produce the depth to groundwater level map, the IDW interpolation is performed with a power of 2 and a variable of 12. The entire area of the Karareis aquifer was divided into main four classes of susceptibility based on the groundwater level's height above mean sea level (L) and is ranked between 2.5 and 10. A maximum rating value of 10 was given to the areas located close to the coast and low rating values as the areas get further from the coast (Figure 9).

3.4. Distance from the Shore (D)

This parameter denotes the inland perpendicular distance from the beach (Figure 10). It is common knowledge that the more one gets away from the beach, the less influence from the sea. As a result, the closer a location is to the water's edge, the more vulnerable it is to seawater intrusion.

3.5. Impact on Existing Status of Seawater Intrusion in The Area (I)

The GALDIT approach recommends using the ratio of $C_l/(HCO_3 + CO_3^2)$ to determine the degree of seawater intrusion into coastal aquifers. However, only the ratio of $Cl-/(HCO_3^2)$ has been used in this study as the values of CO_3^2 were very small and can be ignored. Based on this combination map (Figure 11), the high vulnerability areas are assigned a rating of 10 where most of the areas are in the southern part of the study area.

3.6. Thickness of the Aquifer (T)

This component has an essential value to seawater intrusion determination where it plays a role in magnifying the extent of seawater intrusion in coastal locations. Chachadi and Lobo Ferreira (2005) demonstrated that the thicker an aquifer is, the more susceptible it is to seawater intrusion. The

estimated thickness of the aquifer (T) layers in the Karareis aquifer, based on current lithological profiles, is greater than 10 m, and so it is rated with a rating of 10. Where the aquifer thickness is high, the vulnerability of the aquifer is reduced. (Figure 12) depicts the final groundwater vulnerability map.

The generated vulnerability map (Figure 13), which corresponds to data collected in March 2015, identifies three different types of vulnerability zones:

1. Very high vulnerability zone: the place very close to the sea and represents only a small amount of the area which is displayed in (Figure 13) final analysis map with red color and rated between 6-9 in GALDIT Index.

2. High vulnerability zones: the peripheral coastal regions and places near seas, which are rated between 5-6 based on GALDIT Index and are shown in yellow color in the final analysis map.

3. Moderate vulnerability area: The very central areas of the Kararies region have got moderate vulnerability to seawater intrusion and rated between 4-5 based on the GALDIT Index and displayed in light blue color in final analysis map.

4. Low vulnerability region: Far top part and some central parts of the Kararies region have a low vulnerability to seawater intrusion which is rated between 3-4 based on the GALDIT Index and displayed in green color in the final analysis map.
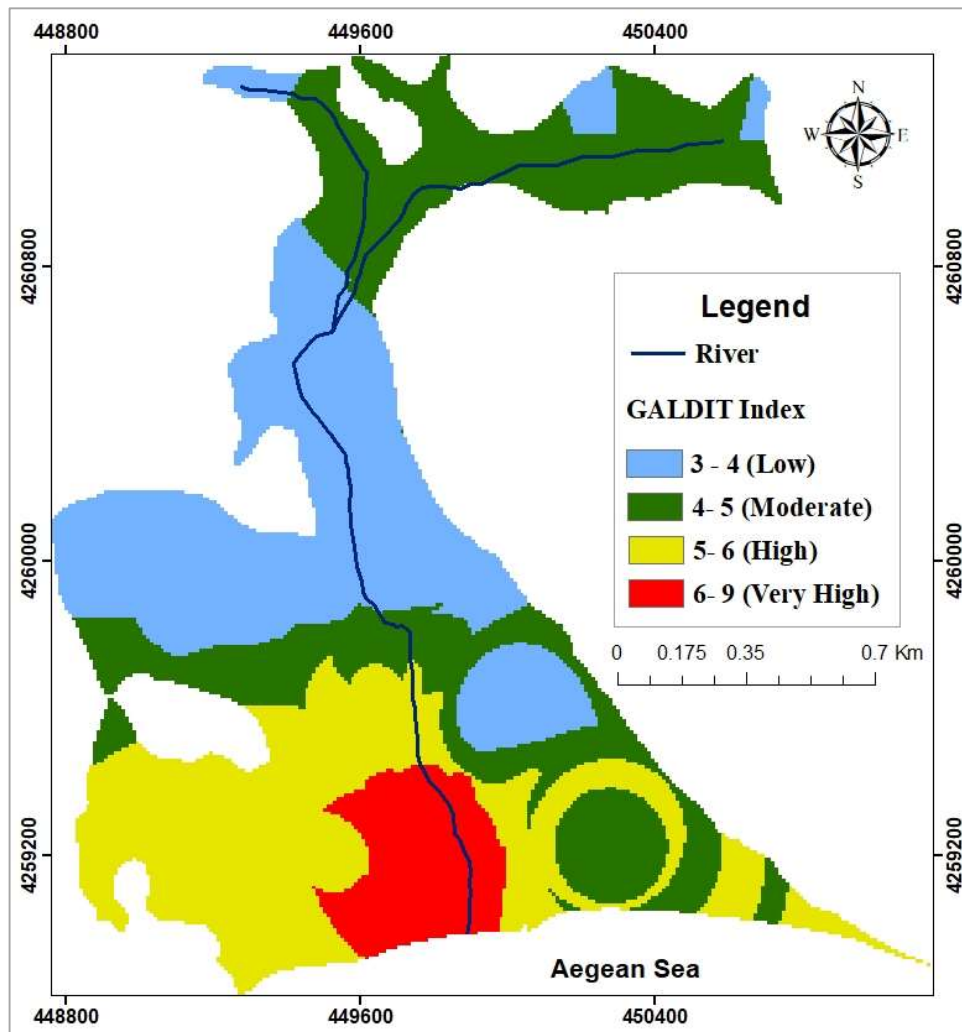
Figure 13. Study area GALDIT vulnerability map

4. CONCLUSION

In this study, the GALDIT method was used in an ArcGIS 10.8 environment to assess the groundwater vulnerability to seawater intrusion in the Kararies aquifer. The GALDIT method's final map revealed that coastal portions of the Karaburun district, particularly the Kararies region, are vulnerable to seawater intrusion, with low to very high susceptibility. After preparing all the required parameters, the assessment/vulnerability map was produced by placing the six layers of hydrogeological data in ArcGIS 10.8 setting to run the model (Figure 11). Considering the total results overall, most of the areas of the Kararies fall in moderate to highly vulnerable zones based on the GALDIT Index rating. The highest susceptible zone is around well SK-4 which is very close to the coastline. Based on the study area's characteristics, two parameters hydraulic conductivity (A) and the distance from the shore (D) through the model analysis and the results, are found to be of key importance. For better and more precise results, sensitivity analysis can be conducted with some of the parameters for future research studies. Overall, the model's final vulnerability to seawater intrusion map results gives significant information regarding the future management of aquifers.

REFERENCES

Aller, L., Lehr, J.H., Petty, R.J., & Bennett, T. (1987). Drastic: A Standardized system to evaluate groundwater pollution potential using hydrogeologic setting. Journal of The Geological Society of India, 29, 23-37.

Bouderbala, A., Remini, B., Saaed Hamoudi, A., & Pulido-Bosch, A. (2016). Assessment of groundwater vulnerability and quality in coastal aquifers: a case study (Tipaza, North Algeria). Arabian Journal of Geosciences, 9, 1-12.

Çakmakoğlu, A. & Bilgin, Z. R. (2006). Pre-neogene stratigraphy of the karaburun Peninsula (W of İzmir Turkey) . Bulletin of the Mineral Research and Exploration, 132 (132) , 33-61 . Retrieved from https://dergipark.org.tr/en/pub/bulletinofmre/issue/3951/52396?publisher=mta%3B

Civita M (1994) La carte della vulnerbilita 'deli aquifer all' inquinamento: teoria & pratica (Aquifer vulnerability maps to pollution). Pitagora Ed Bol.

Civita M, Regibus DC (1995) Sperimentazione di alcune metodologie per la valutazione della vulnerabilità degli aquiferi. Q Geol Appl Pitagora, Bol 3.

Chachadi AG, Lobo-Ferreira JP (2001) Sea water intrusion vulnerability mapping of aquifers using GALDIT method. Coastin–A Coastal Policy Res Newslett 4:7–9

Chachadi, A.G., & Ferreira, J.P. (2007). Assessing aquifer vulnerability to seawater intrusion using GALDIT method. Part 2-GALDIT indicators description. IAHS-AISH publication, 172-180.

Doerfliger, N. and Zwahlen, F. (1997) EPIK: A new method for outlining of protection areas in karstic Environment. IntSymp on karst water and environmental impacts, Antalya, Turkey. Balkema, Rotterdam, 117-123.

Farr, T.G., Rosen, P.A., Caro, E.R., Crippen, R., Duren, R.M., Hensley, S., Kobrick, M., Paller, M., Rodríguez, E., Roth, L., Seal, D.A., Shaffer, S.J., Shimada, J., Umland, J.W., Werner, M., Oskin, M.E., Burbank, D.W., & Alsdorf, D.E. (2000). The shuttle radar topography mission. Reviews of Geophysics, 45.

Foster, S (1987) Fundamental concepts in aquifer vulnerability, pollution risk and protection strategy. In: Van Duijvenbooden, W. and Van Waegeningh, H.G., Eds., Vulnerability of Soil and Groundwater to Pollutants, Committee on Hydrological Research, The Hague, 69-86.

Kallioras A., Pliakas F-K., Schuth Ch. And Rausch R. (2012). Methods to countermeasure the intrusion of seawater into coastal aquifer systems. In book: Wastewater Reuse and Management (eds. Sharma S.K and Sanghi R.) 479-490.

Kazakis, N., Spiliotis, M., Voudouris, K., Pliakas, F., & Papadopoulos, B.K. (2018). A fuzzy multicriteria categorization of the GALDIT method to assess seawater intrusion vulnerability of coastal aquifers. The Science of the total environment, 621, 524-534.

Kura, N.U., Ramli, M.F., Ibrahim, S.B., Sulaiman, W.N., Aris, A.Z., Tanko, A.I., & Zaudi, M.A. (2014). Assessment of groundwater vulnerability to anthropogenic pollution and seawater intrusion in a small tropical island using index-based methods. Environmental Science and Pollution Research, 22, 1512-1533.

Luoma, S., Okkonen, J., & Korkka-niemi, K. (2016). Comparison of the AVI, modified SINTACS and GALDIT vulnerability methods under future climate-change scenarios for a shallow low-lying coastal aquifer in southern Finland. Hydrogeology Journal, 25, 203-222.

Mahesha, A., Vyshali, Lathashri, U.A., & Ramesh, H. (2012). Parameter Estimation and Vulnerability Assessment of Coastal Unconfined Aquifer to Saltwater Intrusion. Journal of Hydrologic Engineering, 17, 933-943.

MED-EUWI (2007) Technical report on groundwater management in the Mediterranean and the WaterFramework Directive Mediterranean groundwater working group (med-euwi wg on groundwater). http://www.semide.net/initiatives/medeuwi/JP/GroundWater.

Mansour, A., Baba, A., Gunduz, O., Şimşek, C., Elçi, A., Murathan, A., & Sözbilir, H. (2017). Modeling of seawater intrusion in a coastal aquifer of Karaburun Peninsula, western Turkey. Environmental Earth Sciences, 76, 1-14.

Niazi S (2007) Assessment of the impacts of climate change and rising of the sea level on the coast of Tetouan (Western Mediterranean of morocco), vulnerability and adaptation. PhD thesis, Mohamed V University, Sciences faculty, Rabat, Morocco, 298p.

Recinos, N., Kallioras, A., Pliakas, F., & Schuth, C. (2014). Application of GALDIT index to assess the intrinsic vulnerability to seawater intrusion of coastal granular aquifers. Environmental Earth Sciences, 73, 1017-1032.

Stempvoort, D.R., Ewert, L., & Wassenaar, L.I. (1993). Aquifer vulnerability index: A GIS - compatible method for groundwater vulnerability mapping. Canadian Water Resources Journal, 18, 25-37.

Singhal, V., & Goyal, R. (2011). Development of conceptual groundwater flow model for Pali Area, India. African Journal of Environmental Science and Technology, 5, 1085-1092.

Trabelsi, N., Triki, I., Hentati, I., & Zairi, M. (2016). Aquifer vulnerability and seawater intrusion risk using GALDIT, GQISWI and GIS: case of a coastal aquifer in Tunisia. Environmental Earth Sciences, 75, 1-19.

Iván, V., & Mádl-Szőnyi, J. (2017). State of the art of karst vulnerability assessment: overview, evaluation and outlook. Environmental Earth Sciences, 76, 1-25.

Vrba, J. (2002) Chapter 5: The Impact of Aquifer Intensive Use on Groundwater Quality; Commission on Groundwater Protection of the International Association of Hydrogeologists (IAH): Prague, Czech Republic.

SEDIMENT TRANSPORT AND RESERVOIR SEDIMENTATION

SEDIMENTATION OF HASANLAR DAM RESERVOIR USING BATHYMETRIC FIELD STUDIES AND GIS

Yakup Darama

Department of Civil Engineering, Atilim University

Ankara, Turkey

yakup.darama@atilim.edu.tr

Mehmet Ali Akgül

State Hydraulic Works (DSI) 6th Regional Directorate

Adana, Turkey

mali.akgul@dsi.gov.tr

ABSTRACT: Hasanlar Dam and Hydroelectric Power Plant is located on Küçük Melen Creek in the Western Black Sea Basin of Turkey. The dam was constructed in 1974 to provide domestic water needs of the Düzce Province, to supply irrigation water need, to control and mitigate floods and to produce hydroelectric power. This dam has been subjected to severe sedimentation since its construction in 1974. Therefore, bathymetric field survey studies were conducted to determine storage loss in the Hasanlar dam reservoir by sedimentation. Bathymetric survey data from the reservoir site of the Hasanlar dam were obtained in 1979, 1999 and 2014. Analysis of the bathymetric data obtained from the Hasanlar dam reservoir showed that dead volume of the reservoir is 1.43 hm^3 which is completely filled by sediment accumulation. Furthermore, the active volume of the reservoir in 1974 was 49.2 hm^3, and this volume in 2014 was reduced to 37.41 hm^3. Thus, the loss in the reservoir volume between 1974 and 2014 was 24%. Analysis of the bathymetric maps also showed that sediment accumulation is severe near and around the dam body and the spillway discharge capacity is decreased by sediment accumulation. This is extremely critical due to reduction of spillway capacity causes increase in flood level in the reservoir which causes risk of dam failure.

1. INTRODUCTION

Sedimentation is the most important problem for the dam's reservoirs. The geology of the river basin, slope, climate, drainage density and drainage pattern, expansion in urbanization, decrease in vegetal cover, all increase basin sediment yield which settles and accumulates in the reservoir area of the dams built on rivers, causing the reduction in storage capacity. Although long term sediment and flow measurements have been used for decades to calculate the dead volumes of dams and the economic life span of dams, calculations for dead volumes of reservoirs have been inaccurate due to the variable nature of the meteorological, hydrological, and human impact parameters and the reservoirs of the dams based on these calculations have shortly filled by accumulation of sediment. Especially most sediment is exported from the catchment during short and effective flash floods and excessive amount of sediments carried during flood period accumulates in the storage of the reservoir causing it to fill in a shorter period than the calculated time. Reduced storage capacities of dams which provide domestic and agricultural water demand and producing hydroelectric energy before the calculated economic lifespan have been an important issue for many researchers (Kökpınar et al, 2015; Patil and Shetkar, 2016; Dadoria et al, 2017).

Since accumulation of sediment transported by rivers reduce the storage capacity of the reservoirs, it is crucial to determine watershed sediment yield. It is pointed out by Walling (1994) that sediment yield data can be obtained in three ways: (1) using continuously measured discharge data and applying them to the sediment rating curve obtained previously; (2) using continuously measured

discharge and sediment data together; and (3) using reservoir survey data. Among these if the reservoir survey data are obtained periodically, they represent a more reliable measure of the long term basin sediment yield (Morris and Fan 1997; Verstraeten and Poensen 2002; Kokpinar et al, 2015). Using Geographic Information System (GIS) and Pan-European Soil Erosion Risk Assessment model, Munthali et al, (2011) conducted a study for determining the hydrological sediment potential, determining critical sediment generating areas of Songwe River watershed and quantifying possibilities of sedimentation of reservoir proposed.

In addition to determining basin sediment yield, it is also important to determine the amount of the sediment transported by the river which is accumulated in the dam reservoir. Several methodologies and techniques have been used to determine the amount of sediment accumulated in dam's reservoirs. Using proxy approaches with spatiotemporal resolution of flow data including river cross sections and sediment data Bilal et al, (2017) qualitatively simulated bathymetric changes in Sakuma Dam in Japan and they concluded that their study is valuable only aiming to conceptually understand the future trends in bathymetric changes. Dadoria et al, (2017) used GIS and Remote sensing technique to compute the loss of storage capacity and sedimentation in Murrumsilli reservoir situated in Chhattisgarh State, India. Bhavsar and Gohil (2015) reviewed studies related to reservoir sedimentation by using remote sensing techniques, and stated that remote sensing technique is applicable and most useful especially in the case of lack of ground data. Patil and Shetkar, (2016) carried out a study to assess sediment deposition in Koyna reservoir in the Western Maharashtra, India, by using analytical methods and they found that the error between the result of the analytical method and the integrated bathymetric survey (Patil and Shetkar, 2015) measurements was 8.82% and suggested that the analytical method gives better results.

Wulandari et al, (2015) studied deposition pattern of Wonogiri Reservoir sedimentation by monitoring reservoir bottom elevation change in years 1980, 1993, 2004, 2005, and 2011 measurements. They found out that 73 % of the sediment was deposited in the effective storage zone and only 27 % of the sediment was settled in the dead storage zone of the Wonogiri Reservoir. Issa et al, (2015) studied sediment trapping efficiency of Mosul Dam Reservoir sedimentation. They used six different empirical methods depending on the residence time principle to determine Trapping Efficiency of Mosul Dam Reservoir for period of 1986 to 2011, and the results obtained were evaluated using observed bathymetric survey of 2011 and found that the percentage of error is very small (0.368%).

Rao et al, (2014) pointed out that the dams in India are very important in terms of water supply, and based on surveys in 122 dam reservoirs in 2012 determined that annually 0.44% volume loss occurred as a result of sedimentation. Rao et al, (2014) also suggested that for sustainable development of water resources major shall come together and formulate solutions to the problem of sedimentation. Sedimentation in reservoirs and showing how to control sedimentation, and sediment entering to the reservoir of Siazakh Dam in Iran is discussed by Gharehkhani (2011). Impact of land use on reservoir sedimentation in Zimbabwe was pointed out by Godwin et al, (2011). During the rainfall seasons using hydrographic surveys and grab sampling methods, Godwin et al, (2011) determined that Chesa Causeway Dam in Zimbabwe lost more than half (66%) of its storage capacity in its 19 years of operation. Huffaker et al, (2010) conducted a study for structurally sustainable reservoir management system which includes bifurcation threshold showing when the maximum allowable consumption rate is equal to 48.3% of the maximum storage capacity, then sustainable reservoir management can be achieved, and sediment from the storage can be removed by HD sediment removal pipeline named as "hydro suction-dredging" sediment removal technology. Beyond the bifurcation threshold (48.8%), sustainable management is no longer possible because of loss of storage capacity to sedimentation. Sediment deposition in Aswan high dam was investigated by El-Sersawy (2005) incorporating bathymetric surveys, aerial photographs and satellite images into GIS.

The aim of this study is determine the amount of storage loss by sedimentation of the Hasanlar dam and Hydroelectric Power Plant (HEPP) by using successive bathymetric surveys obtained in 1979, 1999 and 2014. The Hasanlar dam and HEPP is a multi-purpose dam which provide potable and irrigation water for the province of Duzce in the western Black Sea region of Turkey. Since this dam also produces hydroelectric energy and is the only major water source for the area, it is necessary to

determine new management scheme to allocate water for domestic use, irrigation use and hydropower production.

2. STUDY AREA

Turkey is hydrologically divided into 25 river basins and the Hasanlar Dam and Hydroelectric Power Plant was constructed on the Küçük Melen Creek in the Western Black Sea Basin as shown in Figure1. The drainage area of the Küçük Melen Creek is 696.7 km^2 (Figure 2) and the Hasanlar dam was constructed in 1974 to provide domestic water needs of the Düzce Province, provide irrigation water need, flood control and produce hydroelectric power.
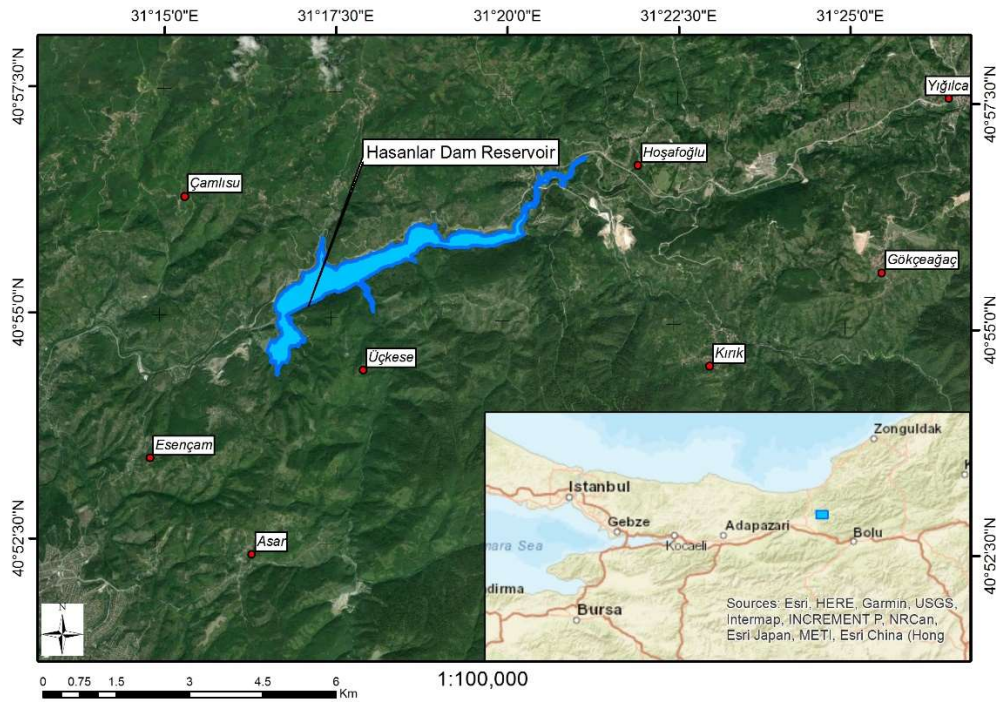
Figure 14. Location of Hasanlar Dam in Western Black Sea Basin

2.1. Hydrology and water resources

From the distribution of mean annual rainfall depth (in mm) of Turkey (Altınbilek et al., 1995; DSI, 1995; Usul, 2013) the annual average precipitation depth in the basin varies between 800 mm and 1000 mm from the inland to coastal areas. In order to determine water resources, the precipitation stations within and near by the drainage area of the Küçük Melen Creek (Figure 2) were considered and the average precipitation of the basin producing surface runoff is calculated by the Thiessen Polygons method. The precipitation values for those stations with various return periods were obtained from the State Hydraulic Works publication (DSI, 1988) and they were converted into average areal rainfall values for return period of 2 years to probable maximum precipitation by the Thiessen Polygons method for three main stations namely Hasanlar, Yığılca and Bolu stations in the drainage basin which is given in the Table 1.
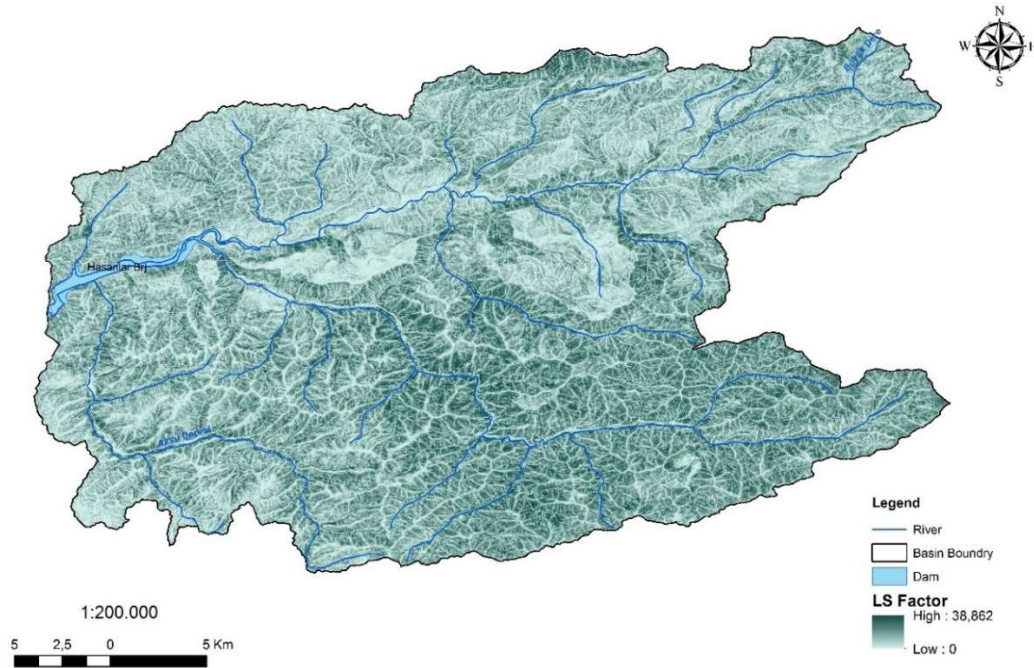
Figure 2. Basin of the Küçük Melen Creek and the Hasanlar Dam

The values of average precipitation obtained by the Thiessen Polygons method were distributed to the stations as the ratio of the area of the station to the total basin area and the results are given in Table 2. These rainfall values were used to determine surface runoff for various frequencies.

Table 1. Average precipitation values in mm for various return periods.

Station Name	P_2	P_5	P_{10}	P_{25}	P_{50}	P_{100}	P_{PMP}
Hasanlar	58.57	77.84	89.55	103.55	113.02	122.18	234.66
Yığılca	61.53	96.01	122.41	159.84	190.61	221.05	394.77
Bolu	32.09	43.03	50.70	60.81	68.61	76.64	164.55

Table 2. Precipitation values in mm distributed by ratio of areas of stations.

Station Name	Ratio of Area	P_2	P_5	P_{10}	P_{25}	P_{50}	P_{100}	P_{PMP}
Hasanlar	0.214	12.54	16.66	19.17	22.17	24.19	26.16	50.24
Yığılca	0.624	38.36	59.86	76.32	99.66	118.85	137.83	246.14
Bolu	0.162	5.21	6.99	8.23	9.88	11.14	12.45	26.73
Total	1.00	56.11	83.52	103.73	131.71	154.18	176.43	323.10

In Tables 1 and 2 P is the precipitation and subscripts 2, 5, 10, 25, 50 and 100 indicates the return period of those precipitations, and subscript PMP indicates the probable maximum precipitation. To determine the surface runoff produced by the precipitation values given in Table 2, 2-hours unit hydrograph (UH_2) of the basin was derived by using the DSI Synthetic Unit Hydrograph Method (Figure 3), and this unit hydrograph was compared by the unit hydrographs obtained by using the Mockus method and the Point frequency analysis and found that unit hydrographs obtained from those methods compared well (Table 3). Thus, unit hydrograph obtained by the DSI Method was used to calculate surface runoff for various frequencies (Table 3) at the Hasanlar Dam location. There are two stream gauging stations numbered D13A033 and D13A038 (Figure 4) measuring the flows entering the Hasanlar Dam reservoir. The long term flow data obtained from those two gauging

stations were averaged monthly and plotted as shown in Figure 5. This figure shows the long term average monthly flow rates in one calendar year. It can be seen from this figure that the lowest average monthly flow rates entering the Hasanlar Dam reservoir between July to October is ≤2 m³/s.
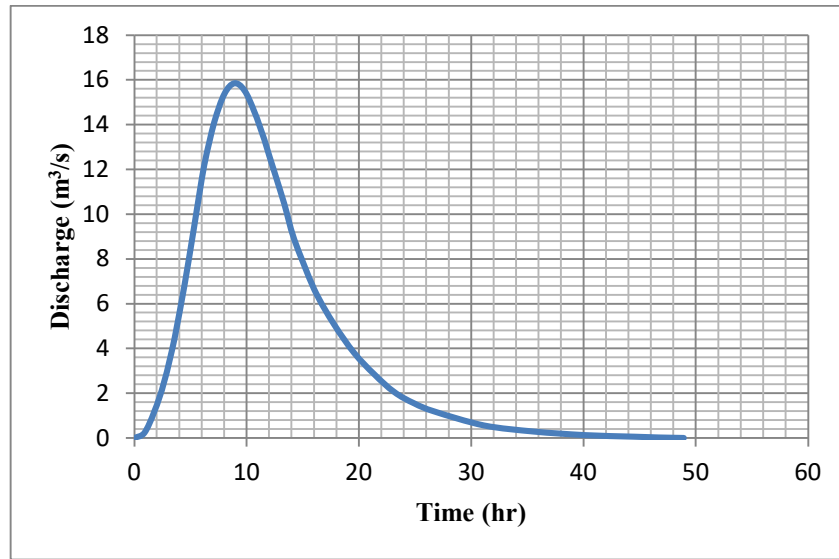
Figure 3. 2-hr Unit Hydrograph of the Küçük Melen Basin (DSI, 1988)

Table 319. Comparison of various return periods of surface runoff values computed by the DSI, the Mockus and the Point Rainfall Unit hydrographs methods (values in m³/s).

Method	Q_2	Q_5	Q_{10}	Q_{25}	Q_{50}	Q_{100}	Q_{PMF}
Point	89.38	184.55	288.92	481.62	678.28	928.19	-
Mockus	72.82	170.02	273.59	449.12	610.67	784.38	3010.39
DSI	151.21	298.23	429.24	630.90	807.77	991.07	2940.0
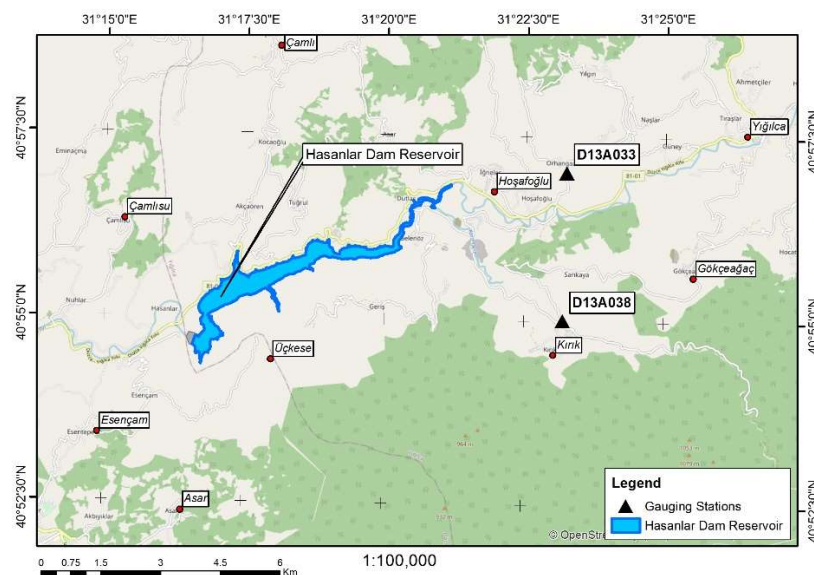
Figure 415. Location of Stream Gauging Stations
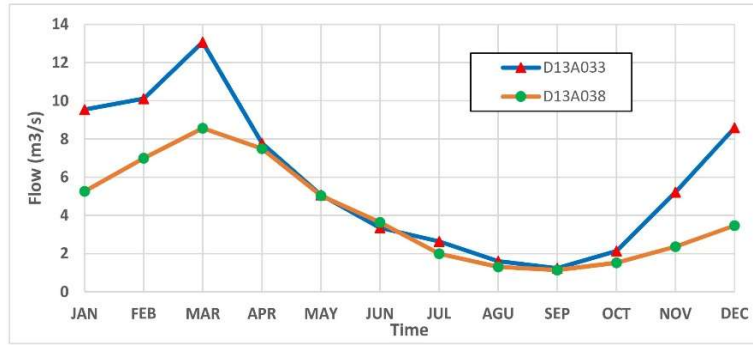
Figure 5. Monthly average flow rates of gauging stations D13A033 and D13A038

3. METHODOLOGY

3.1. Field Studies

Reservoir survey data of the Hasanlar dam reservoir located in the west of the Black Sea Region of Turkey obtained in 1979, 1999 and 2014 and the results are presented in Figure 6 for those years. These bathymetric maps in 1979, 1999 and 2014 were produced by using echo-sounder device on a floating boat. The measurements were made by every 5 m interval on a cross section. The interval between the cross sections of the measurement along the longitudinal direction of the reservoir was taken as 5 m. The data obtained from the bathymetric surveys used in arc map visualization in those years. It can be seen from this figure that considerable sedimentation problem existed in the Hasanlar Dam reservoir from 1979 to 2014. In order to show the reduction of reservoir volume in 1999 and 2014, bathymetric arc map images shown in Figure 6 was evaluated in detail as shown in Figure 7, and based on this figure and data of 1999 change in elevation-volume of the reservoir for those measurement periods was calculated and shown in Table 4 and Figure 8.
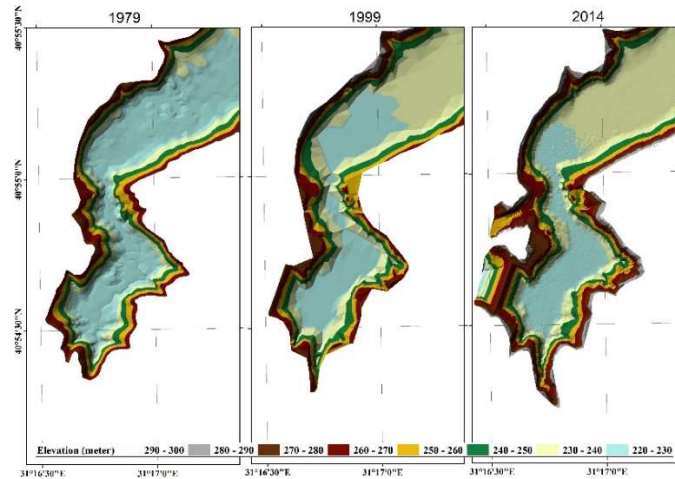
Figure 6. Hasanlar dam reservoir sedimentation ArcMap image from 1979 to 2014
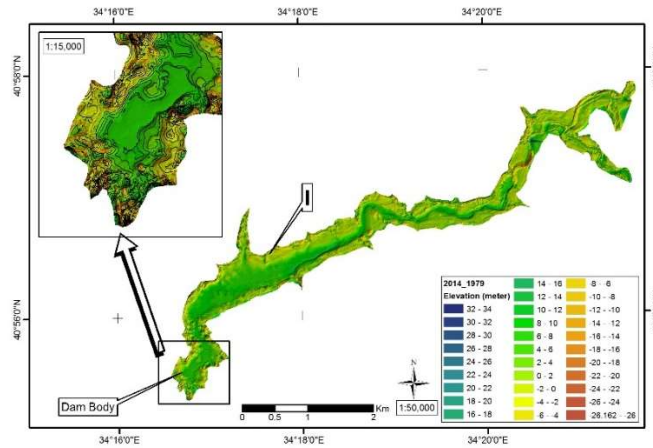
Figure 7. ArcMap image of the Hasanlar reservoir sedimentation profile in 2014

Table 4. Hasanlar Dam Reservoir elevation volume values.

Elevation (m)	Volume (hm³)		
	1974	1999	2014
228	3.20	0.05	0.02
230	4.85	0.43	0.31
235	10.30	3.49	2.91
240	17.45	8.85	7.74
245	26.15	16.02	14.94
250	36.62	25.49	24.40
255.5	*50.63*	*38.49*	*37.41*
260	64.04	51.50	50.30
265	81.15	67.93	66.84
270	100.81	86.53	85.45
271.3	106.27	91.64	90.66
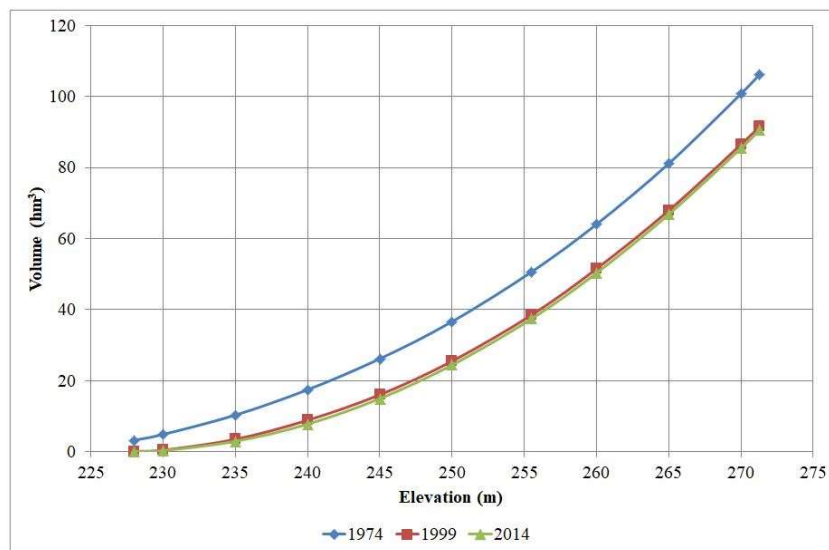
Figure 816. Hasanlar dam reservoir elevation volume change from 1974 to 2014

3.2. Calculation of Sediment Yield (SY) from Reservoir Bathymetric Maps

Sediment yield can be described as the amount of sediment eroded from a basin area by a surface runoff resulting from rainfall events, and it is continuously eroded and transported by a river over a period of time. This eroded sediment transported by the river can be assumed as the amount that will enter to the reservoir located at the downstream end of the basin and will be deposited in the reservoir. The deposited sediment can be computed by reservoir surveys and fluvial sediment monitoring program. Even though both methods potentially can give significant sources of error, reservoir survey data generally yields more reliable measure of long term basin Sediment Yield (Morris and Fan, 1977). In this study, Sediment Yield (SY) data of the Hasanlar dam reservoir drainage area was calculated by using the following general equation (Kokpinar et al., 2015)

$$SY_{RS} = \frac{SV\gamma_s}{TE \times A} \times 100 \qquad (1)$$

Where SY_{RS} is the sediment yield from reservoir surveys (ton/year/km²), SV is the annual sedimentation rate which is equal to the ratio of the net volume of sediment deposited to the time in years (m³/year), γ_s is the specific weight of the deposited sediment (t/m³), TE is the sediment trap efficiency of the reservoir (%) and A is the area of the basin (km²). γ_s was determined as 1.12 t/m³ from the laboratory analysis of sediment samples obtained from the Hasanlar dam reservoir. It is stated that (Kokpinar et al., 2015) the most widely method used to determine the trap efficiency of reservoirs was developed by Brune (1953) by assuming that TE depends on the capacity of reservoir to mean annual runoff ratio:

$$TE = f(V_{res}/Q_{inflow}) \qquad (2)$$

Where V_{res} is the initial reservoir storage capacity and Q_{inflow} is the mean annual inflow. In Equation 2 when $V_{res}/Q_{inflow}<1$, median Brune's curve can be approximated as a series of logarithmic equations whereas when $V_{res}/Q_{inflow}\geq1$, TE=97.5%. In the case of Hasanlar Dam TE was calculated by using Equation 2 such that the mean annual inflow was determined from the hydrological data of gauging station D13A033 obtained from DSI Flow Data between 1990 and 2015. The analysis of those 25 annual average flow data obtained from DSI, yield the value of mean annual inflow to the Hasanlar Dam reservoir as $100.2x10^6 m^3$ and the initial reservoir volume of the Hasanlar dam is $V_{res}=106.27$ $hm^3=106.27x10^6 m^3$. Since $V_{res}/Q_{inflow}=106.27x10^6/100.2x10^6 >1$, thus, the trap efficiency for this study is determines as TE=0.975. Using this value of TE, and reservoir bathymetric survey data in Equation 1, SY_{RS} was calculated between 1974 and 1999 and 1999 and 2014 and given Table 5.

Table 5. Sediment yield calculations based on reservoir surveys, $SY_{RS.}$

Reservoir	Basin Area (km²)	Deposition starting year	Reservoir survey year	Time period (years)	Cumulative volume of sediment (10⁶m³)	Net volume sediment deposited (10⁶m³)	Specific weight of sediment (t/m³)	SY_{RS} (t/y/km²)
Hasanlar	695.7	1974	1999	25	12.14	12.14	1.12	801.8
			2014	15	13.22	1.08	1.12	118.9

Sediment yield based on stream gauging stations could not be calculated because there is not any measurement of sediment from the stream gauging stations. However, in 1979, 1990 and 1999 average amount of eroded sediment by rainfall and transported by the rivers and creeks in Turkey was 300, 237 and 226 million tons respectively (CEM, 2018). When these value are divided by the surface area of Turkey which is equal to 780000 km², the yearly average sediment yield for Turkey in 1979, 1990 and 1999 are 384.6 t/yr/km², 303.8 t/yr/km² and 289t/yr/km². Taking the average value of these eroded sediment in three years, the average erosion of sediment between 1979 and 1999 was computed as SY_{TR} = 325.8 t/y/km². Dividing the 1974-1999 value of Hasanlar Dam Sediment yield computed by reservoir survey SY_{RS}= 801.8 t/y/km² to the Turkey average sediment erosion between 1979 and 1999 SY_{RS}/SY_{TR}=801.8/325.8=2.46. Here sediment yield for Turkey does not account for

the bed load especially during the flooding period. Since reservoir surveys accounts for both suspended sediment and bed load accumulation, it is considered to be more reliable. The results of Kokpinar et al. (2015) showed that the ratio of sediment yield by reservoir surveys and gauging station for three basins in Turkey varied between 0.99 and 3.54. The value of this ratio for this study is computed as 2.46 which is comparable with the study of Kokpinar et al. (2015)

3.3. Analysis of Field Data and Application of GIS Techniques

Analysis of the bathymetric field data of 2014 coupled with an arc map view image and field observation of the Hasanlar dam reservoir (Figure 7) show that sedimentation causing the storage loss mostly occurred between the point I shown in Figure 7, and the upstream location of the reservoir where the reservoir water level is equal to the Kuçuk Melen creek water level, and the downstream location close to the dam body, where the spillway, the penstock and the bottom outlets are located. Thus, sedimentation close to dam body is extremely critical because it reduces the spillway capacity for flood discharge, reduces penstock capacity for hydroelectric power production and reduces discharge capacity of the bottom outlet providing domestic and irrigation water.

At the normal reservoir water level which is 255.5 m, the total volume of the reservoir when the dam was completed in 1974 was 50.63 hm^3 as shown in Table 4 and Figure 8. This storage was reduced to 38.39 hm^3 (24% volume loss) in 1999 and 37.41 hm^3 (26% volume loss) in 2014 by sedimentation. From this analysis, it is clear that approximately 26% of the reservoir volume was lost due to sedimentation within 40 years' period. As pointed out (Dadoria et al. 2017; Bhavsar and Gohil, 2015) that remote sensing techniques are very useful tools for determination of storage loss of reservoirs by sedimentation. GIS techniques were also used in this study to determine the storage loss of the Hasanlar Dam reservoir. This analysis showed that dead volume of the reservoir is 1.43 hm^3 which is completely filled by sediment accumulation. Furthermore, the active volume of the reservoir in 1974 was 49.2 hm^3, and this volume in 2014 was reduced to 37.41 hm^3. Thus, the loss in the active reservoir volume between 1974 and 2014 was 24%. This analysis and the analysis from bathymetric data for determination of reservoir volume loss of the Hasanlar Dam yield same results.

4. RESULTS AND DISCUSSION

Sedimentation of Hasanlar dam reservoir was determined by using Bathymetric field surveys in 1979, 1999 and 2014 and GIS and Remote sensing techniques. Analysis of bathymetric maps in those years indicated that at the normal reservoir water level which is 255.5 m, 24% volume loss occurred between 1974 and 1999 and 26% volume loss occurred between 1974 and 2014 by sedimentation. This analysis showed that sedimentation between 1974 and 1999 was severe, and most of the reduction in reservoir volume occurred during 25 year period and 2.8 % reservoir volume loss occurred between 1999 and 2014. This results can also be seen from the sediment yield analysis based on reservoir survey SY_{RS}. The value of SY_{RS}= 801.8 $t/yr/km^2$ between 1974 and 1999, between 1999 and 2014 the value of SY_{RS} decreased to 118.9 $t/yr/km^2$. The reasons for this might be because (1) afforestation works at the upper basin started after 1999, and (2) severe deposition of sediment at the active volume and at the reservoir entrance causing almost horizontal bed slope for the river at the dam site and (3) decrease of frequency of flooding events after 1999 (DSI, 2017).

Comparison of the sediment yield of 1970-1999 SY_{RS} and average sediment erosion between 1979 and 1999, indicates that SY_{TR} seems to be less reliable than SY_{RS} due to underestimation of total sediment. The main reason for this underestimation is because it does not account the erosion during the flooding period.

Sedimentation problem of the dam reservoir is at the critical level because severe sediment was also deposited close to the spillway reduced the spillway discharge capacity. Due to the decrease in spillway capacity by sedimentation, during the flood that occurred in 21st of May 1998, Q_{500}=2406 m^3/s flood discharge entered to the reservoir. This flood value increased the lake level almost very close to crest elevation of dam body and caused the high risk of collapse of the dam. In order to eliminate this risk structural measures (dredging of sedimentation and constructing sediment retaining wall near the spillway) have been applied to increase the spillway capacity of the dam.

5. CONCLUSIONS

A study was made to determine the storage loss caused by sedimentation of the Hasanlar dam reservoir by using bathymetric surveys obtained in 1979, 1999 and 2014, and by using GIS and remote sensing techniques. Following conclusions can be reached from the results of this study:

(1) Analysis of the bathymetric data obtained from the Hasanlar dam reservoir showed that storage loss in reservoir volume from 1974 to 1999 was 24% and from 1974 to 2014 storage loss was 26%. GIS and Remote Sensing techniques were also used to determine the storage loss of the Hasanlar Dam reservoir. This analysis showed that dead volume of the reservoir is 1.43 hm^3 which was completely filled by sediment accumulation. Furthermore, the active volume of the reservoir in 1974 was 49.2 hm^3, and this volume in 2014 was reduced to 37.41 hm^3. Thus, the loss in the reservoir volume between 1974 and 2014 was 24%, which is consistent with the result of bathymetric data analysis. Analysis of the bathymetric maps also showed that sediment accumulation is severe near and around the dam body and the spillway. This is extremely critical since one of the purposes of the dam is to control and mitigate floods.

(2) Sediment yield analysis based on reservoir survey (SY_{RS}) was calculated between the periods of 1974 and 1999, and 1999 and 2014. The value of SY_{RS}= 801.8 t/yr/km^2 between 1974 and 1999. The value of SY_{RS} decreased to 118.9 t/yr/km^2 between 1999 and 2014. This situation can also be seen from bathymetric maps of 1999 and 2014 indicates that sediment yield from 1974 to 1999 was very severe. The reason for this is because the frequent flooding events occurred in the basin until 1998. After 1998, decrease in the number of flooding events in the watershed yielded less severe sediment transport and accumulation in the reservoir.

REFERENCES

Altınbilek, D., Kutoğlu Y and Akyürek Z., (1995) Rainfall Climatology of Turkey, EU AVICENCE Project No AVI-80/ACROSS, METU Civil Eng. Dept., Ankara, Turkey

Bhavsar M. V., and Gohil K. B., (2015) Review on study of reservoir sedimentation by remote sensing techniques, International Journal for Innovative Research in Science and Technology, Vol. 1, Issue: 12, pp. 251-254, ISSN: 2349-6010

Bilal A., Dai W, Larson M, Beebo Q. N., Xie Q. (2017) Qualitative simulation of bathymetric changes due to reservoir sedimentation: A Japaneese case study. PloS ONE 12(4): e0174921 doi.org/10.1371/journal.pone.0174931

Brune, G.M., (1953) Trap efficiency of reservoirs . Transactions, American Geophysical Union, 34 (3), 407-418. doi:10.1029/TR034i003p00407

CEM, (2018), http://www.cem.gov.tr/erozyon/Libraries/ cemDocument/EROZYON_CALISMA_TR.sflb.ashx

Dadoria D, H L Tiwari and R K Jaiswal, (2017) Assessment of reservoir sedimentation in Chhattisgarh State using Remote Sensing and GIS, International Journal of Civil Engineering and Technology, 8(4), pp. 526-534.

DSI, 1988: Flow Observation Annual Report, 1988 Water Year, DSI Publication, Ankara, Turkey (in Turkish)

DSI, 1995: State Hydraulic Works (DSI), Haritalı İstatistik Bulteni, DSI Publication, Ankara, Turkey (in Turkish)

DSI, 2017: State Hydraulic Works (DSI), Hasanlar Dam and HEPP Hydrology Report, prepared by ASD Engineering Consulting Co. Ankara, Turkey (in Turkish)

El-Sersawy H., (2005), Sediment deposition mapping in Aswan high dam reservoir using Geopraphic Information System (GIS), Ninth International Water Technology Conference, IWTC9, Sharm El-Sheikh, Egypt, pp. 239-247.

Gharehkhani R., (2011) Issues problems of sedimentation in reservoir Siazak dam case study, International Journal of Environmental, Chemical, Ecological, Geological and Geophysical Engineering Vol. 5, No:12, pp:829-831, World Academy of Science, Engineering and Technology

Godwin M.A., S. Gabriel, M. Hodson, D. Wellington, (2011), Sedimentation impacts on reservoir as a result of land use on a selected catchment in Zimbabwe, International Journal of Engineering Science and technology, Vol. 3, No:8, pp.6599-6608

Huffaker R., D. Rider and R. H. Hotchkiss, (2010) Stability and bifurcation analysis of reservoir sedimentation management, The Open Hydrology Journal, 4, pp.102-112.

Issa I.E., N. Al-Ansari, S. Knutsson, G. Sherwany (2015) Monitoring and Evaluating the sedimentation process in Mosul dam resorvoir using trap efficiency approach, Engineering, Scientific Researh Publishing, 190-202, dx.doi.org/10.4236/eng.2015.74015

Kokpinar M. A., A. B. Altan-Sakarya, S. Y. Kumcu and M. Gogus, (2015) Essassment of sediment yield estimation for large watershed areas: a case study for the Sethan, Demirköprü, and Hirfanlı reservoirs in Turkey, Hydrological Sciences Journal, dx.doi.org/10.1080/02626667.2014.959954

Morris, G.L. and Fan, J., (1997), Reservoir sedimentation handbook, New York: McGraw Hill.

Munthali K.G, B. J. Irvine, Y. Murayama, (2011) Reservoir sedimentation and flood control: Using Geographical Information System to estimate sediment yield of the Songwe river watershed in Malawi, Sustainibility, 3, pp.254-269, doi:10.3390/su3010254

Patil R. and R. Shetkar (2016) Prediction of sediment deposition using analytical method, American Journal of Civil Engineering, Vol.4, No. 6, pp.290-297. doi: 10.11648/j.ajce.20160406.14

Patil R. and R. Shetkar (2015) Sediment deopsition in Koyna reservoir by integrated bathymetric survey, International Journal of Research in Engineering and Technology, Vol. 04, Issue: 11, pp. 114-118, eISSN:2319-1163

Rao S.V, Satry P.G, and Ghorpade V.G. (2014) Reservoir sedimentation and concerns of stakeholders, Research Journal of Engineering Sciences, Vol. 3(2), pp.29-32, ISSN 2278-9472

Usul, N., (2013), Engineering Hydrology, METU Press, ISBN:978-975-7064-43-5, Ankara, Turkey

Verstraeten, G. And Poensen, J., (2002), Using sediment deposits in small ponds to quantify sediment yield from small catchments: possibilities and limitations, Earth Surface Processes and Landforms, 27, pp. 1425-1439, doi:10.1002/esp.439

Walling, D.E., (1994), Measuring sediment yield from river basins, In R. Lal, ed. Soil Erosion research methods, 2nd ed. Ankeny, IA: Soil and Water Conservation Society, 39-80.

Wulandari D.A., D. Legono and S. Darsono, (2015) Evaluation of deposition pattern of Wonogiri reservoir sedimentation, International Journal of Civil and Environmental Engineering, IJCEE-IJENS, Vol. 15, No:02, pp. 15-20.

14TH INTERNATIONAL CONFERENCE
ON HYDROSCIENCE & ENGINEERING

MAY 26-27, 2022
IZMİR-TURKEY

ICHE2022
IZMIR, TURKEY

NUMERICAL MODELLING OF RESERVOIR FLUSHING: A REVIEW

Gregor Petkovšek

Floods and Water Group, HR Wallingford

Wallingford, Oxfordshire, United Kingdom

g.petkovsek@hrwallingford.com

Yuichi Kitamura

Chigasaki Research Institute, J-Power

Chigasaki, Kanagawa, Japan

yuichi_k@jpower.co.jp

ABSTRACT: Reservoir storage loss due to sedimentation is a major issue affecting sustainable use of water resources. Sediment deposits can be removed by hydraulic flushing. During the flushing operation, bottom outlets are open and water and sediment released. The efficiency of the operation is improved if the reservoir water level is drawn down and free flow reestablished throughout the reservoir. Successfulness of flushing depends on a number of factors, such as bottom outlets capacity, reservoir shape and water availability. Modelling can be used to assess whether flushing is a viable solution for the management of sediment in the reservoir, as well as to design the flushing operations and optimize its scheduling. This paper reviews and analyses various modelling approaches described in the relevant literature. One, two and three dimensional numerical models have been used, as well as particle methods, such as smoothed particle hydrodynamics (SPH), more recently. One-dimensional models are useful for long term simulations, assessments on of a large number of scenarios, and optimization studies. Two- and three-dimensional models can be used to understand local scouring near the gates and other details of operation, as well as to study reservoirs of more complex shapes. Particle methods are particularly suitable for applications where the area occupied by water and sediment changes rapidly, as is the case with flushing, however they are also computationally more demanding, which limits their application to study of details.

1. INTRODUCTION

Dams with their potential to store water are important water infrastructure assets. Their history goes back several millennia and some have served not only many generations but also several civilizations. As with other projects aimed at exploitation of natural resources, their sustainable design and operation is of utmost importance for their continual service. One of the main challenges to sustainability of dams is sedimentation (Schleiss et al. 2016). Traditionally the main issue has been the loss of reservoir storage volume. Today many dams serve hydropower production, where abrasion of hydroelectric equipment by sediment passing through is another concern, as well as blockage of intakes or low level outlets that might compromise dam safety (Morris and Fan 1997). Sediment deposits can extend long distances upstream, even beyond the nominal reservoir pool, raising bed levels and impacting on flood safety and navigation. Downstream from the dam, impacts of interrupted sediment continuity may be shown as eco-morphological impacts (channel erosion, change in bed substrate composition) in rivers and even coasts. Sustainable reservoir management therefore aims to tackle sedimentation and its adverse impacts by achieving an equilibrium between sediment inflow and outflow while sustaining storage capacity (Morris 2015).

Hydraulic flushing is one of the options for removal of deposited sediment from reservoirs. This method uses hydraulic forces to remove sediment, by opening bottom outlets and thus releasing water and sediment eroded by water flow from the reservoir.

There are two types of flushing. The first type is pressure flushing, where water level in the reservoir is maintained at its normal levels. With the bottom outlets open, flow velocity increase locally and scour some sediment. Pressure flushing is efficient in keeping bottom outlets operational. However, the overall extent and amount of sediment removal is small and not sufficient to prevent the loss of reservoir storage volume nor to reestablish sediment continuity towards the downstream river reaches.

Draw down flushing is the other type of flushing where water level is fully drawn down to reestablish free flow in the impoundment. Freely flowing water scours a channel throughout the length of the reservoir, resulting in removal of a considerable amount of sediment. This type of flushing is more effective than the pressure flushing, however it does require emptying and refilling of the reservoir, which is not always feasible. Also the width of the flushing channel is limited, which in a wide reservoir may result in removal of only a small proportion of sediment deposits. A review of potential issues and their remedies is presented in Petkovsek et al. (2020).

In summary, efficiency of flushing depends on a number of factors, such as bottom outlets position and capacity, reservoir shape and water availability. To assess whether flushing is a viable solution for management of sediment in the reservoir, modelling has been used, with earliest examples several decades ago, e.g. White & Bettes (1984). Although sediment flushing is a centuries old technique (Brown 1944), a renewed interest in sustainability combined with ready access to instrumentation for physical models and especially computational power for numerical models has sparked a considerable interest in flushing modelling. Use of physical and numerical models to assess feasibility of flushing, design flushing operations and optimize its scheduling in an effective and efficient manner is recommended by many authors, e.g. Hartmann (2009), White (2001) etc. This paper reviews and analyses various modelling approaches that have been proposed and described by engineers and academics in the published literature.
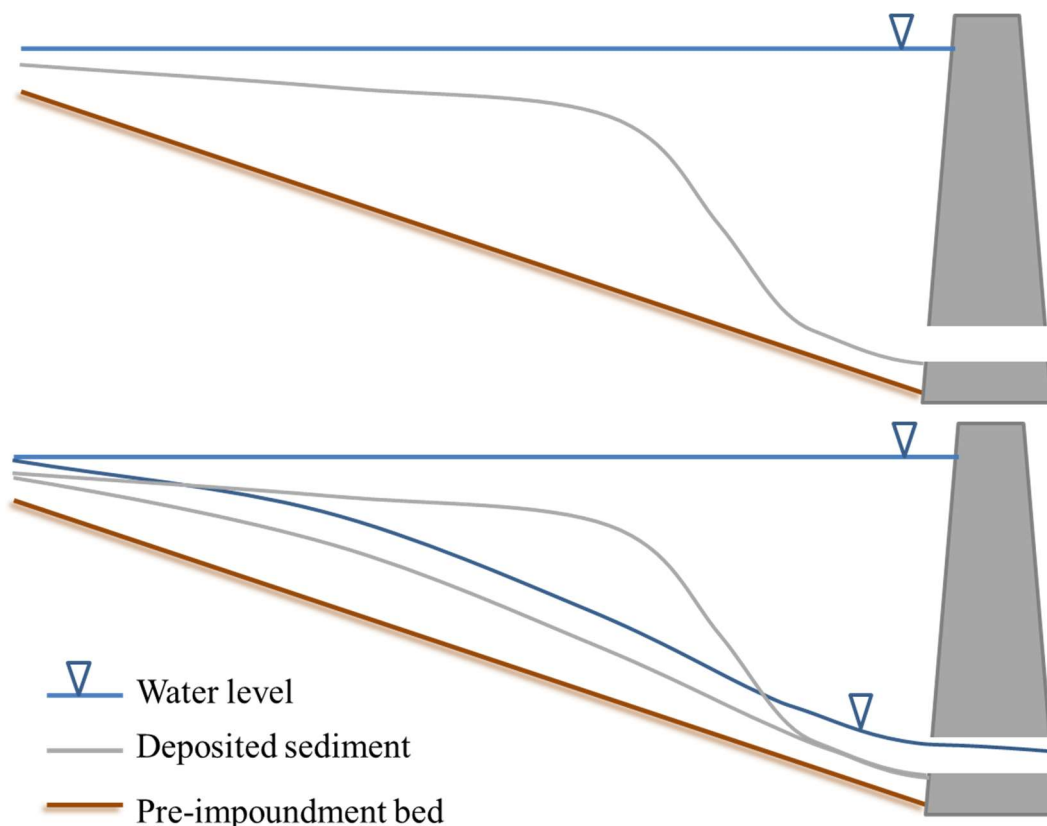
Figure 1. Reservoir before drawdown flushing (top) and at the end of the operation (bottom)

2. NUMERICAL MODELLING

2.1. Overview

Numerical models are mathematical representations of ideas about natural phenomena and their relationships that have been proposed by scientists. As such they are necessarily the idealizations and simplifications of these phenomena. Although the ideas and models may not correspond to the reality, they are still empirically known to be useful, provided that their numerical output has been satisfactorily tested against observations in circumstances similar to those of their intended application. This is often the case for simple and readily observable phenomena, however the more complex, more difficult to measure or less common the occurrence of a phenomenon is, the degree of agreement between the model predictions and observations tends to decrease. Some of the phenomena related to the reservoir sedimentation and flushing modelling fall into the latter category, for example bed load transport, sediment entrainment from bed, impact of sediment on turbulence of water flow etc. On the positive side, numerical models are relatively fast and less expensive to execute than physical models, can cover large areas (e.g. suitable for simulation of coordinated flushing of chains of reservoirs), can be used in optimization and trade-off analyses, coupled with habitat models for evaluation of environmental impact over a downstream reach, etc.

2.2. Use of Models

To study feasibility of flushing, White (2001) suggested the use of the least complex and fastest 1D models, while for the assessment of the local impacts (such as near the low level outlets), more resource demanding 2D or 3D models should be used.

This approach found confirmation in many practical studies. Castillo et al. (2013) studied sedimentation and its management by flushing in an Andean reservoir impounded by a 135 m tall dam on the Paute River, Ecuador. The authors used complementary methods to study sedimentation and flushing with respect to different temporal and spatial scales (Figure 17). A one dimensional model HEC-RAS (USACE 2016) was used to study the overall sedimentation pattern in the reservoir, including the volume of deposited sediment and the time it would take for sediment to approach the bottom outlets. To get a more detailed insight into the progress of the selected flushing operation, a two dimensional model Iber (Iberaula 2013) was used. To model the initial stages of flushing, with particular interest in assessing the possibility of whether bottom outlets could be blocked at this stage, a 3D model FLOW-3D model (Flow Sciences 2011) was used.
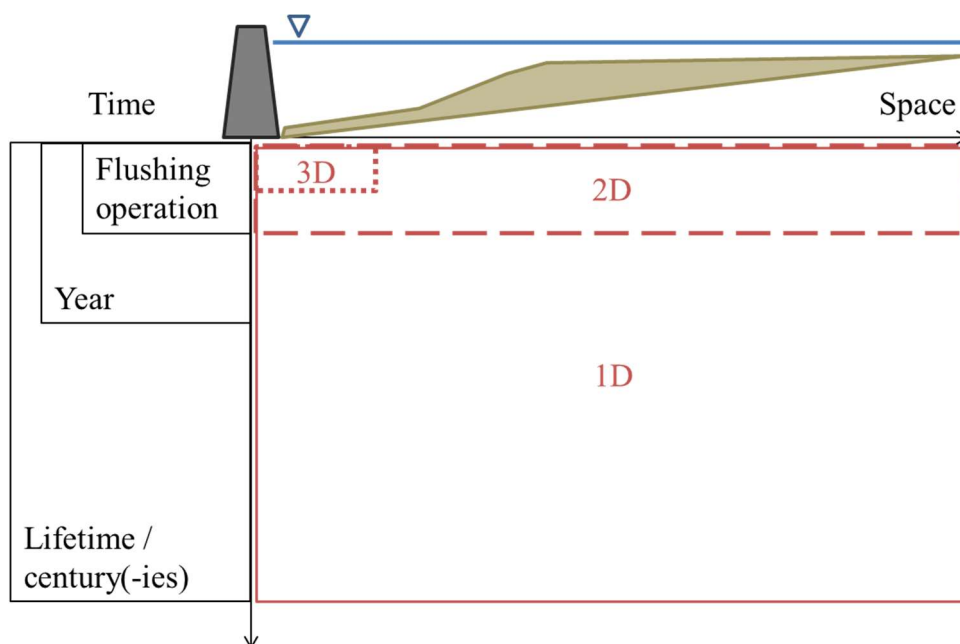
Figure 17. An example of the use of different models at different temporal and spatial scale for the same

Two dimensional models should also be used for wide reservoirs and reservoirs with complex geometries. For these shapes of reservoirs, direction and contribution of flow in different parts of the reservoir varies during the drawdown, which cannot be described by a one-dimensional model. Sometimes this applies to a part of reservoir only. Patrind reservoir in Pakistan is located in a river bend, which makes it possible to flush the main reservoir through a bypass tunnel with inlet located behind the upstream cofferdam and the outlet below the main dam (Figure). The main part of the reservoir is relatively narrow and long, suitable for simulation with a 1D model RESSASS (Petkovsek & Roca 2014), while the pond between the cofferdam and the main dam is wider and more complex. This pond serves as a sedimentation basin for finer sediment that deposits there during the normal operation and also has to be flushed through the main dam, which was modelled by a 2D model TELEMAC-SISYPHE (EDF 2014).

An interesting comparison of the model performance for simulating flushing in a long narrow reservoir with a 1D, 2D and 3D model is reported by Valette et al. (2013). Two well monitored flushing events in the St. Egrève reservoir in France were used to calibrate and validate the models that all come from the same modelling suite TELEMAC-MASCARET. They found that all three models were able to accurately predict the mass of sediment flushed during a typical flushing event and confirmed that for a simple linearly shaped reservoir, 1D modelling is sufficient for most practical purposes.
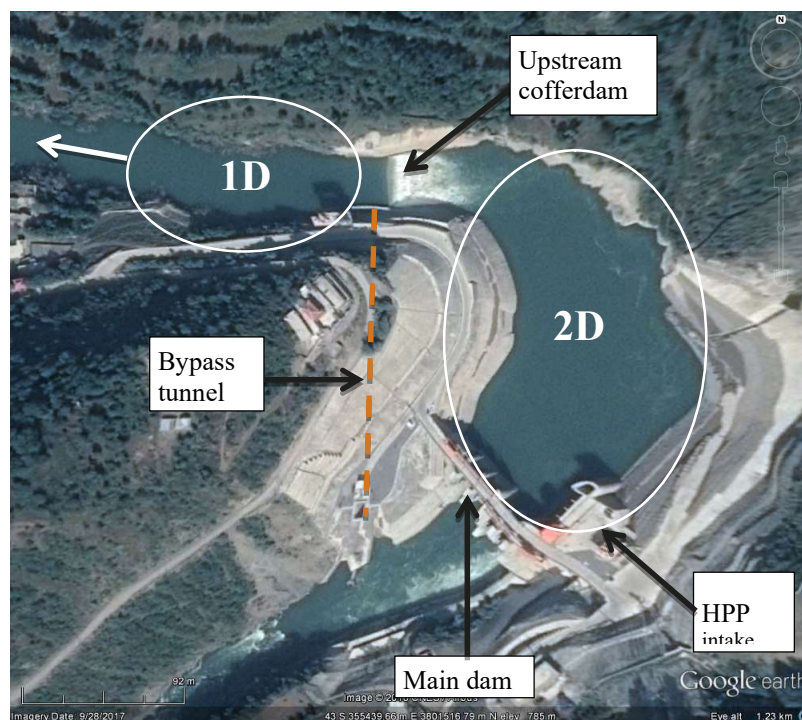
Figure 3. Use of different models for a reservoir with a wide (2D model) and narrow section (1D model)

Nevertheless, there are some specific non-1D phenomena related to reservoir sedimentation and flushing and specific solutions for modelling these phenomena should be incorporated in 1D models to make them fit for specific tasks. For example, Boyd and Gibson (2016) reported that some discrepancies between observation and HEC-RAS model results were due to the model lacking the capability to simulate lateral widening. Some vertical processes are also important. Vertical sediment concentration profile is important where intakes and outlets are positioned at different heights. An example of this is environmentally friendly flushing, where water is discharged from outlets at different levels to ensure that as much sediment is removed but at the same time the maximum

sediment concentration (downstream ecosystem constraint) is not exceeded. Typically, a mid-height outlet, which during flushing is close to the water surface, discharges water with lower sediment concentration than low near-bed outlet. To simulate environmentally friendly flushing Fruchard & Camenen (2012) used the RubarBE 1D model developed at IRSTEA. The model simulates vertical concentration profile at dam, which is otherwise not normally taken into account in 1D models. Furthermore, some slope stability concept is incorporated in the same model to model slope instability during development of flushing channel. Another purpose-developed 1D model for reservoir flushing is RESSASS (Petkovsek & Roca 2014), with functionality to simulate the vertical gradient at dam with multiple outlets, widening of flushing channel, slope stability, sediment compaction and turbid density currents. A long term simulation of the latter phenomenon was successfully tested on one of the deepest reservoirs in the world, Nurek in Tajikistan with the dam height of 300 m (Petkovsek 2017). The mentioned model can also simulate reservoirs in chains, as can the GSTARS model (Yang & Anh 2011) that has been applied e.g. for modelling flushing of the chain of reservoirs on the Dez river in Iran (Tagavifar & Adib 2010). For flushing, the most important property of a model is the ability to model channel widening resp. slope instability, which these two models as well as the Courlis model (Valette et al. 2013) can do.

While 1D and 2D models remain popular, the use of 3D models is increasing in spite of their long runtime limitation. Hoven (2010) applied the SSIIM model to study flushing of a reservoir in Costa Rica, while Harb (2013) modelled sediment flushing from two reservoirs in Austria, one using SSIIM and another using TELEMAC-3D. The latter was also used by Aliau et al. (2016) to model eco-friendly flushing in a reservoir in France. Omer et al. (2016) used Delft3D for a reservoir in Japan. Other examples of 3D modelling of flushing in Japan include the study of Esmaeili et al (2015). A special 3D model for pressure flushing was developed by Sawadogo et al. (2019). Olsen & Haun (2014) suggested that 3D models are better suited for flushing flows for reservoirs with training works or flushing channel with bends, because they can simulate secondary currents, which is naturally a 3D phenomenon. As an alternative to the use of 3D models to overcome these issues, some 2D models that can simulate secondary currents indirectly have been developed (Begnudelli et al. 2010, Petkovsek 2015), although not tested for flushing channels with bends specifically.

2.3. Specific Modelling Approaches

2.3.1. Meshless Models

Numerical models usually discretise the modelled domain to a particular set of model nodes linked into a numerical mesh. However meshless models, whereby the computational points are not ordered in a particular system but follow the movement of fluid, have also made a start in sediment transport and flushing modelling in the last decade. Two examples of using the Smoothed Particle Hydrodynamics (SPH) numerical method to simulate a flushing experiment in a laboratory are presented in Maneti et al. (2012) and Zubeldia et al. (2018). The main advantage of this method is its good handling of cases where the area occupied by fluid(s) changes rapidly. During flushing, this occurs because of the rapid erosion of sediment from the reservoir bed. Furthermore, the approach to sediment transport is in some respect more natural, by using "particles" (moving numerical nodes) of different properties: water particles and sediment particles. Nevertheless, at the moment the use of these models for simulation of reservoir flushing is in the research and academic domain only.
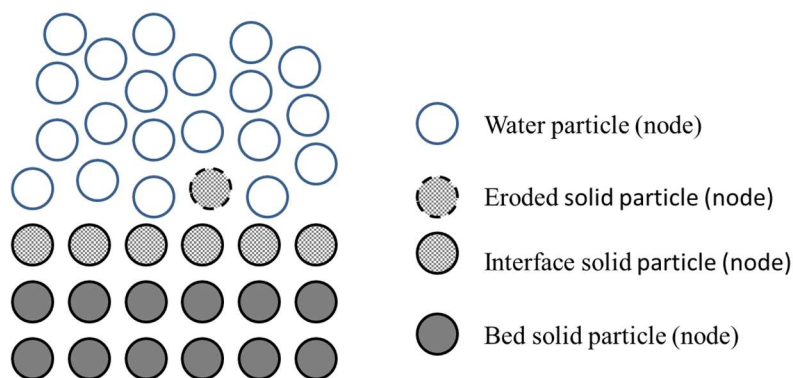
Figure 4. Computational elements of a meshless SPH model for simulation of bed erosion

2.3.2. Temporal Variations

In addition to the model dimensions there are also two approaches towards modelling the temporal variations. These can be modelled either by a quasi-steady approach or a fully unsteady approach. The former is numerically more stable and permits longer time steps, however it does not take into account local acceleration term and thus cannot simulate infill or drawdown wave propagation through a reservoir. This has some impact on the results, depending on the rate of drawdown and filling as well as the speed of the wave propagation. Gibson & Crain (2019) compared both approaches in their study of flushing from the Fall Creek Dam, USA. They observed that in terms of released sediment concentrations, both approaches predicted similar peaks that also reasonably matched observations, but the unsteady approach predicted higher values than quasi-steady approach overall. In terms of bed change predictions, Ahn (2011) compared predicted and observed cross sections and longitudinal sections at the Xiaolangdi reservoir and found that the unsteady approach performed better in the case of predicting changes in cross sections. In the case of the change of the longitudinal bed levels they found the quasi-steady approach matched the observations better.

2.3.3. One-Point Models and Optimization Studies

To analyze and predict overall flushing performance, at a specific site, simpler modelling approaches may be suitable. If relevant training and validation data is available, machine learning tools can be used for this purpose. Li et al. (2016) used artificial neural networks, ANN, to predict efficiency of flushing operations at Three Gorges Dam in China.

One point models are, due to their computational speed, also suitable for optimization studies. Hajiabadi & Zarghami (2014) performed a study of a multi-objective reservoir operation for the Sefidrud Reservoir in Iran. The objectives were water supply, sediment flushing and hydropower production with some environmental constraints on flushing. The authors used a non-dominant sorting genetic algorithm, NSGA-II, to obtain a set of optimal points (Pareto frontier). Chou & Wu (2016) analyzed operation of two jointly operated reservoirs. They constructed a simple model where flushing is triggered and halted when each reservoir achieves a defined state. The model was linked to a nonlinear optimization algorithm to calibrate the parameters that govern the process for maximum flushing efficiency while controlling the water supply function of the two-reservoir system within the acceptable threshold. The authors demonstrated that with optimization the water shortage concerns could be minimized and flushing was feasible.

Optimization studies do not need to be restricted to one-point models. An example of a Pareto frontier for a long term optimization study of a large reservoir is shown in Figure 5. The input parameters are the start date and duration of flushing and the drawdown level. The objectives are the amount of sand passing through turbines (to be minimized in order to prevent damage to the hydropower equipment), the preserved active storage volume (to be maximized for other benefits such as irrigation storage and flood control) and the hydropower production.

It can be concluded that the present operation is near optimal with respect to the analyzed objectives, although some variation in operation can be considered, depending on the relative importance of each objective:

- At the same amount of sand passing through turbines, both the preserved storage and the power production can be slightly increased;
- At the same amount of the preserved active storage, the power production can be slightly increased with increasing sand passing through turbines;
- At the same amount of the power production, either storage can be increased or the amount of sand decreased, but one will be at the expense of the other.
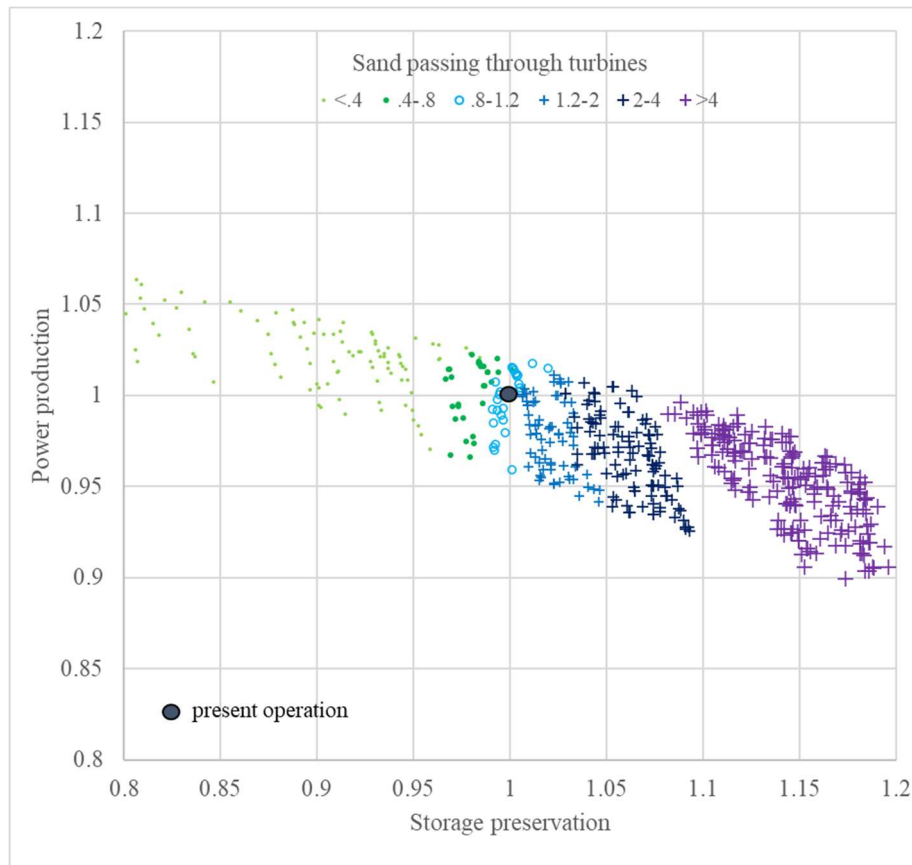
Figure 18. An example of a Pareto frontier for three objectives: the amount of sand passing through turbines; preserved active storage; and hydropower production (values relative to those corresponding to the present operation schedule)

2.3.4. Coupling with Other Models

Hydrodynamic and sediment models can be coupled with an environmental assessment to determine the flushing operation parameters. Moridi & Yazidi (2017) modelled suspended sediment concentrations during the flushing operations for Dez Dam in Iran and used the results to consider the social, environmental and water resources impacts in the study area that covered three reaches of the Dez River in the total length of 300 km.

Impacts of flushing can be also evaluated by habitat models, for example CASiMiR (Jorde 1996, Schneider et al. 2001).

3. PHYSICAL MODELS

3.1. Overview

Physical models are governed by "true" natural processes, which is their main advantage over the numerical models. Therefore the physical models provide more trustworthy results than the numerical models, provided that the problems resulted from scaling as well as others mentioned later can be overcome. Firstly, interpretation of scaling introduces some of the uncertainties related to the human

understanding of the phenomena, as mentioned in the numerical models section. Furthermore, different processes have different scaling laws which may result in difficulties in selecting an overarching scaling approach. Finally, Olsen & Haun (2014) point out that as reservoirs are large, scale must therefore be small, and to model all relevant processes (initiation of motion, bedload, suspended load, secondary currents and bedforms) in a physical model is difficult.

Physical models continue to be implemented for both theoretical investigations of the phenomena related to reservoir flushing as well as for the case-specific studies.

3.2. Theoretical Investigations

Theoretical investigations include investigation of the effects of the reservoir geometry on sediment deposition and flushing performed by Kantoush and Schleiss (2014) with a series of systematic laboratory experiments. The authors proposed a new geometry shape factor that was found to best described both deposition and flushing rates. Meshkati et al. (2010) performed experimental investigation of local half-cone scouring Based on the results, the authors concluded that the amount of flushed sediment strongly depends on the size of the outlet. With a larger bottom outlet, more sediment can be eroded, including from further distance. Sindelar et al. (2017) investigated the effect of the weir height and the reservoir widening at the dam on sediment continuity for a run-of-river hydropower project on small and medium sized gravel bed rivers.

Tarekegn (2015) performed laboratory studies of the dynamics of fine sediment (most abundant in flushing release) over a coarse bed (common in mountain areas, especially downstream of dams that cut sediment transport). Bed roughness parameters and porosity were extracted exclusively from the surface measurements using a laser scanner with a 1 mm horizontal resolution and a 0.1 mm vertical accuracy. A novel non-intrusive laser line approach for the direct measurement of sand erosion rates was developed to characterize the spatial variability of the erosion rates. The outcomes of the laboratory experiments were used to derive a new non-equilibrium erosion rate relation. The experiments of the author as well as two other sources show the increase in the effective shear stress for fine sediment entrainment below the gravel crest level due to increasing drag force, although the fluid shear stress τ decreases with increasing local-level porosity. The new relation for the entrainment rates was then applied to a 1D numerical model and applied to analyze the dynamics of the sediment wave released by a reservoir flushing operation. It was possible to obtain some qualitative responses regarding the influence of the peak-to-base flow and the intermittence of flushing release on the length and volume of the deposited material in the reach downstream of the dam.

3.3. Case Studies

Many case specific studies have been reported over the past ten years. Ratnayesuraj et al. (2016) used a scaled model (1:250) of the Rantambe Reservoir, Sri Lanka to study the flushing parameters. A physical modelling at 1:70 scale for Stage-II of the run-of-the-river Chamera Hydro-Electric Project across River Ravi in India was performed along with a 1D mathematical model to assist the design and layout of various project components and flushing operations for sustaining the reservoir capacity (Isaac et al. 2014). For the Cerro del Aguila dam in Peru, a physical model covering the dam, the first 1000 m of the reservoir and 350 m downstream from the dam, was constructed to study flushing (Sayah et al. 2014). Harb (2013) reported on a physical model of the Schönau reservoir on the river Enns in Austria at a 1:40 scale and using lightweight material to represent fine deposits, alongside a 3D numerical model, to study flushing.

3.4. Hybrid Modelling

In the hybrid (sometimes also called composite) modelling approach, both physical and numerical modelling is used, to take advantage of their respective strengths and avoid their respective weaknesses. The numerical model is usually used to model the whole domain of interest at a 1:1 scale, while the physical model supports this in some way by feeding specific information into the process. For example, the physical model component could be used:

- For cross-validation or calibration of the numerical model at the physical model scale for its application to the full scale;

- As a local model of a particular area of the domain, while the whole domain is modelled by the numerical model;
- For baseline flushing analysis for particular flows, pre-flushing bed configuration and sediment properties; while long term modelling and sensitivity analyses are conducted using the less expensive numerical modelling;
- For partial calibration/validation of the numerical model, e.g. flow/turbulence parameters at high velocities and sediment concentrations that occur in the flushing channel and through the structure.
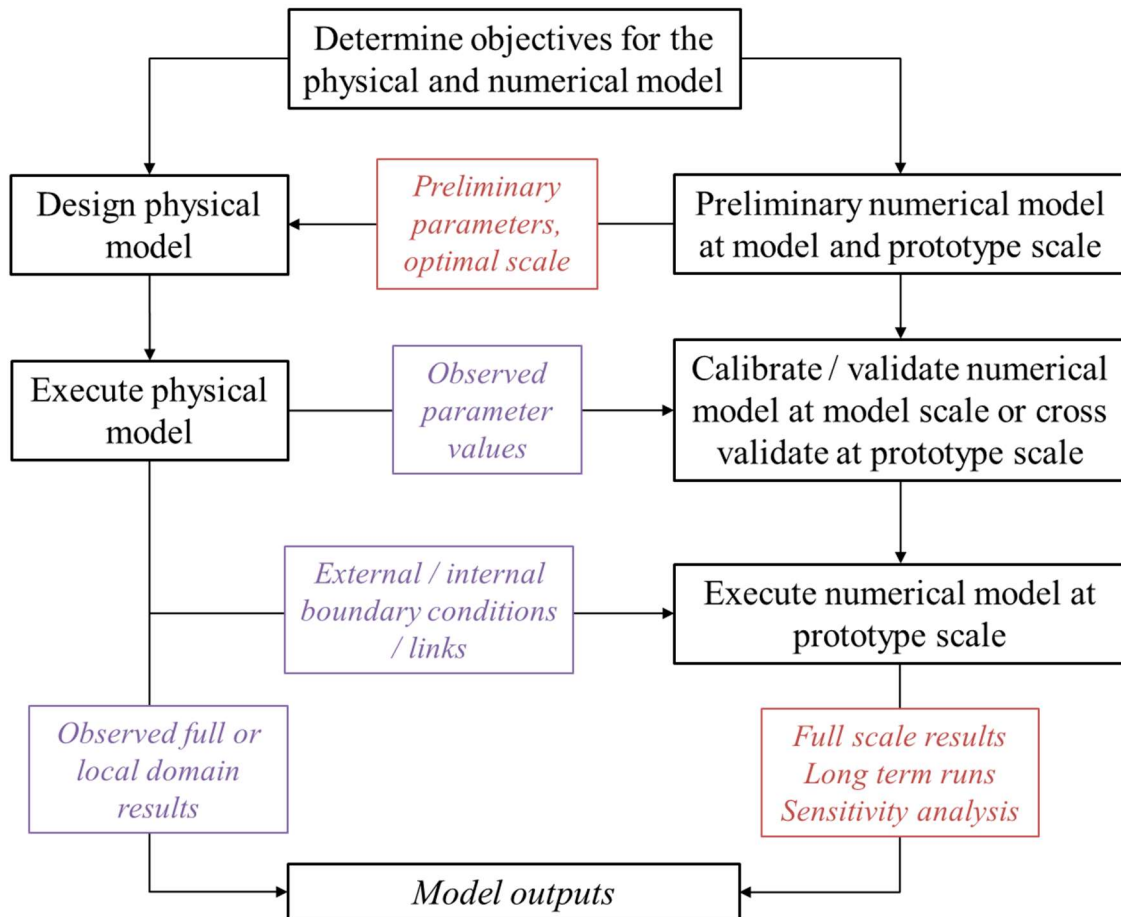
Figure 6. Possible links between a physical and numerical model in the hybrid modelling approach

On the other hand, numerical model studies can also support the design of the physical model (Gerritsen & Sutherland 2011), such as to obtain the preliminary values of flushing parameters and to determine the optimal scale of the physical model with respect to scaling problems.

Hybrid modelling has been proposed for flushing studies (Reisenbüchler et al. 2020) and implemented by some authors (e.g., Harb (2013), Sayah et al. (2014)). Schleiss et al. (2011) report on a hybrid model of pressure flushing operation at Räterichsboden reservoir in Switzerland. A 1:35 scale physical model was constructed and numerical modelling was performed by the FLOW-3D software. Both models were intercompared for various scenarios (instantaneous and gradual gate opening) as well tested against one field observations during an annual bottom gate functional testing. The authors concluded that, within the expected uncertainties, the results were of sufficient similitude to make the cross-checked models suitable for prediction of sediment flushing. The solution provides the sediment flux during pressure flushing and time and space variable sediment concentration downstream, as well as the influence of outlet gate opening height and the outflow velocity on sediment concentration. Peteuil et al. (2017) presented a hybrid model of the Champagneux reservoir water and sediment dynamics including flushing composed of a numerical model TELEMAC-3D for the whole reservoir, a physical model at a 1:35 scale near dam and a CFD numerical model of spillway section at both

scales. The main aim of modelling was to accurately represent bottom shear stress, which is the main factor in assessment of sediment erosion.

Finally, some authors use the term hybrid modelling to refer to combinations of numerical models, for example 1D and 2D models or other hybrid meshing, or to combine mesh and meshless numerical models.

4. CONCLUSIONS

Reservoir sedimentation is an important challenge to the sustainable use of water resources. Sediment management approaches that can prevent or limit storage loss can be put in place. One of them is sediment flushing which is very efficient, although not suitable for all reservoirs. Modelling can help determining flushing parameters, optimize flushing schedule as well as assess upstream and downstream impacts and support management of flushing operations. Different modelling methods can be used for assessment of different aspects of flushing operations.

For the detailed studies of water and sediment flow near outlets, in particular where vertical component of flow is important, 3D numerical models are most suitable. Examples include pressure flushing and the initial phase of drawdown flushing. Further assurance can be obtained by the hybrid approach where numerical modelling is combined with physical modelling in order to benefit from the advantages of each approach: real processes on a physical model and a prototype scale on a numerical model. These methods are well tested and suitable for practical problems. In the case of irregular, unpredictable or rapidly changing water-sediment and water-air interface, a less tested but nevertheless promising meshless particle methods can be tried, an example of which is SPH.

To model the whole reservoir, the use of 3D models might still be justified for specific applications where vertical processes have to be described in detail. Usually, modelling of the whole reservoir is of interest for full duration for drawdown flushing, but in this case the depths of flow and vertical flow magnitude are small and can be described sufficiently with a 2D model. Nevertheless some authors suggest that 3D modelling might be justified where bends or training works are present in the reservoir. Some 2D models can also capture the effect of helical flow in bends on sediment transport with a simplified secondary flow model.

If a reservoir is long compared to its width, then a 1D model can also produce satisfactory results. The advantage of these type of models is their shorter run time and less input parameters. These parameters relate well tested quantities and processes, which is not always the case with the parameters required for the more complex 3D models. One-dimensional models are also preferable for modelling flushing operations over a long time period (e.g. tens or hundreds of years), as well as for the optimization studies, which often require modelling of the downstream and upstream reaches of the impounded river as well. The downstream impacts of flushing that typically require assessment include deposition of the flushed sediment and impacts on the environment and infrastructure. The assessment of the upstream impacts includes in particular the effectiveness of flushing on removing sediment from the upper end of the reservoir to prevent rising of the bed and flood levels upstream of the reservoir.

Physical models have been used for flushing studies. The obvious advantage of these is that they are governed by the natural process, however they suffer from the scaling problem, which becomes more complex when both liquid and solid phase are modelled. The opposite is the case with the numerical models. Hybrid modelling, where physical models are combined with numerical models, has been undertaken on some occasions, to benefit from the advantages of each modelling approach, and to improve confidence in the results of modelling.

REFERENCES

Ahn, J. (2011). *Numerical modelling of reservoir sedimentation and flushing processes*. PhD Thesis, Colorado State University, Fort Collins, USA.

Aliau, D., Peteuil, Ch., & Huybrechts, N. (2016). Using an eco-friendly flushing event to calibrate 3D sediment transport model through a reservoir: the case study of Champagneux run-of-river dam on the Rhone River, France. In *Proceedings of the XXIII TELEMAC-MASCARET User Conference 2016*, (pp. 49-53).

Begnudelli, L., Valiani, A., & Sanders, B. F. (2010). A balanced treatment of secondary currents, turbulence and dispersion in a depth-integrated hydrodynamic and bed deformation model for channel bends. *Advances in Water Resources 33*, 17–33.

Bettes, R., & White, R. (1984). The feasibility of flushing sediments through reservoirs. Challenges in African Hydrology and Water Resources. In *Proceedings of the Harare Symposium, July 1984, IAHS Publ. no. 144*, (pp. 577-587).

Boyd, P., & Gibson, S. (2016). *Applying 1D sediment models to reservoir flushing studies: Measuring, monitoring, and modeling the Spencer Dam sediment flush with HEC-RAS*. ERDC/CHL CHETN-XIV-52. Vicksburg, MS: U.S. Army Engineer Research and Development Center, 12pp.

Brown, C. B. (1944). *The Control of Reservoir Silting*. United Stated Department of agriculture, Miscellaneous Publication No 521. US government Printing Office, Washington, 166 pp.

Castillo, L. G., Carillo, J. M., Álvarez, M. A. (2013). Complementary Methods for Determining the Sedimentation and Flushing in a Reservoir. *Journal of Hydraulic Engineering 141(11)*, https://doi.org/10.1061/(ASCE)HY.1943-7900.0001050

Chou, F.N.F., & Wu, C.W. (2016). Assessment of optimal empty flushing strategies in a multi-reservoir system. *Hydrol. Earth Syst. Sci. Discuss.*, doi:10.5194/hess-2016-61

EDF (2014). *TELEMAC modelling system: TELEMAC-2D User manual*, Release 7.0 (pp 1-134). Paris : Électricité de France-R&D.

Esmaeili, T., Sumi, T., Kantoush, S.A., Kubota, Y., Haun, S. (2015). Three-dimensional Numerical Modelling of Sediment flushing: Case study of Dashidara Reservoir, Japan. In *E-proceedings of the 36th IAHR World Congress*, The Hague, the Netherlands, 9 pp.

Flow Sciences (2011). *FLOW-3D users' manual version 10.0*, Santa Fe, USA.

Fruchard, F., Camenen, B. (2012). Different Type of Flushing - Friendly Flushing; Example of Genissiat Dam Flushing. *Int. Symposium Dams for a Changing World*. Kyoto, Japan.

Gerritsen, H., Sutherland, J. (2011). Composite modelling. Chapter 6 in *Users guide to physical modelling and experimentation*, CRC Press, https://doi.org/10.1201/b11335.

Gibson. S., Crain. J. (2019). *Modeling Sediment Concentrations during a Drawdown Reservoir Flush: Simulating the Fall Creek Operations with HEC-RAS*. ERDC/TN RSM-19-7. Vicksburg, MS: U.S. Army Engineer Research and Development Center. http://dx.doi.org/10.21079/11681/33884

Hajiabadi, R., & Zarghami, M. (2014). Multi-Objective Reservoir Operation with Sediment Flushing; Case Study of Sefidrud Reservoir. *Water Resour. Management 28*, 5257-5376.

Harb. G. (2013). *Numerical Modeling of Sediment Transport Processes in Alpine Reservoirs*. PhD Dissertation, Graz University of Technology, Graz, Austria.

Hartmann, S. (2009). *Sustainable Sediment Management in Alpine Reservoirs considering ecological and economical aspects*. Volume 7: Sediment Management in Alpine Reservoirs – Recommendation and best practice. ALPRESERV project, http://www.alpine-space.org/2000-2006/temp-results16.html.

Hoven LE (2010) *Three-dimensional numerical modelling of sediments in water reservoirs*. Master's thesis, Norwegian University of Science and Technology, Trondheim, Norway.

Iberaula (2013*) Iber: Hydraulic reference manual*. www.iberaula.es

Jorde, K. (1996). Ecological Evaluation of Instream Flow Regulations based on Temporal and Spatial Variability of Bottom Shear Stress and Hydraulic Habitat Quality. In *Proceedings of the second International Symposium on Habitat Hydraulics, Ecohydraulics 2000*, Quebec City, Canada (Volume B, pp. 163-174).

Kantoush, S.A., Schleiss, A.J. (2014). Influence of geometry shape factor on trapping and flushing efficiencies. In *Proceedings of River Flow 2014*, Lausanne, Switzerland (pp. 129-137)

Li, X., Qiu, J., Shang, Q., & Li, F. (2016). Simulation of Reservoir Sediment Flushing of the Three Gorges Reservoir Using an Artificial Neural Network. *Applied Sciences 6(148)*; doi:10.3390/app6050148

Manenti S, Sibilla S, Gallati M, Agate G, Guandalini R (2012) SPH Simulation of Sediment Flushing Induced by a Rapid Water Flow. *Journal Hydraulic Engineering 138*, 272–284.

Meshkati, Sh. M. E., Dehghani, A. A., Sumi, T., Naser, Gh., Ahadpour, A. (2010). Experimental investigation of local half-cone scouring against dam. In: *Proceedings of River Flow 2010*. Karlsruhe: Bundesanstalt für Wasserbau (BAW), (pp. 1267-1276).

Morris, G. L. (2015). Management Alternatives to Combat Reservoir Sedimentation. In *Proceedings of Int Workshop on Sediment Bypass Tunnels*, Zurich, Switzerland.

Morris, G. L., Fan, J. (1997). *Reservoir Sedimentation Handbook*. New York: McGraw-Hill.

Olsen, N. R. B., Haun, S. (2014). Free surface algorithms for 3D numerical modelling of reservoir flushing. In: *Proceedings of River Flow 2010*. Karlsruhe: Bundesanstalt für Wasserbau (BAW), (pp. 1105-1110).

Peteuli, Ch., Alliau, D., Wirz, C., Fretaud, Th., Decachard, M., Roux, S., Reynaud, S., Boisson, N., Vollant, A., Baux, Y. (2017). Evaluating favorable conditions for sediment transport in reservoirs: Champagneux dam case study, France. In: *Proceedings of 85th Annual Meeting of International Commission on Large Dams*, Prague, Czech Republic.

Petkovšek, G., & Roca, M. (2014). Impact of reservoir operation on sediment deposition. *Proc. Inst. Civ. Eng., Water management 167*(10), 577-584.

Petkovšek, G. (2015). Modelling suspended sediment transport due to helical flow in TELEMAC-2D. In: *Proceedings of 22nd Telemac & Mascaret User Club*, Manchester, UK.

Petkovšek, G. (2017). Long-term modelling of reservoir sedimentation with turbid underflows. *Journal of Soils and Sediments*, doi: 10.1007/s11368-017-1814-1

Petkovšek, G., Roca, M. and Kitamura, Y. (2020) Sediment flushing from reservoirs: a review. *Dams and Reservoirs 30*(1), 12-21, DOI 10.1680/jdare.20.00005

Reisenbüchler, M., Bui, M. D., Skublics, D., Rutschmann, P. (2020). Sediment Management at Run-of-River Reservoirs Using Numerical Modelling. *Water 12*(1), 249, doi:10.3390/w12010249

Sayah, S. M., Bonanni, S., Fenelli, A. (2014). Physical and Numerical Modelling of Cerro del Águila Dam: Hydraulic and Sedimentation. In *Proceedings of Hydro 2014 conference (Hydropower and Dams)*, Como, Italy.

Ratnayesuraj, C. R., Rifas, K. M., Risly, S., Weerakoon, S. B. (2015). Model Study of Sediment Flushing in Rantambe Reservoir. In *Proceedings 3rd International Symposium on Advances in Civil and Environmental Engineering Practices for Sustainable Development*, Galle, Sri Lanka (pp. 300-306).

Sawadogo, O., Basson, G. R., & Shneiderbauer, S. (2019). Physical and coupled fully three-dimensional numerical modeling of pressurized bottom outlet flushing processes in reservoirs. *International Journal of Sediment Research 34* (pp. 461–474)

Schleiss, A. J., Boes, R. M., Daneshvari, M., De Cesare, G. (2011). Hybrid modeling of sediment management during drawdown of Räterichsboden reservoir. In *Proc. of International Symposium on Dams and Reservoirs under Changing Challenges, (79th Annual Meeting of ICOLD)* (pp. 421-428)

Schleiss, A. J., Franca, M. J., Juez, C., De Cesare, G. (2016). Reservoir sedimentation. *Journal of Hydraulic Research 54*(6), 595–614

Schneider M, Jorde K, Zollner F, Kerle F (2001). Development of a user-friendly software for ecological investigations on river systems, integration of a fuzzy rule-based approach. In *Proceedings of 15th International Symposium on Environmental Informatics*, ETH Zurich, Switzerland.

Sindelar, C., Schobesberger, J., Habersack, H. (2016). Effects of weir height and reservoir widening on sediment continuity at run-of-river hydropower plants in gravel bed rivers. *Geomorphology 291* (pp. 106–115).

Tarekegn, H. T. (2015) *Downstream suspended sediment dynamics of reservoir sediment flushing*. PhD thesis, University of Trento, Italy and Queen Mary University of London, UK.

USACE (2016). *HEC-RAS River analysis System*. Hydraulic Manual Version 5.0. USACE-HEC, Davis, USA.

Zubeldia, E. H., Fourtakas, G., Rogers, B. D., Farias, M. M. (2018) Multi-phase SPH model for simulation of erosion and scouring by means of the shields and Drucker–Prager criteria. Advances in Water Resources 117, 98-114. https://doi.org/10.1016/j.advwatres.2018.04.011

A GENERALIZED FORMULA FOR SEDIMENT INCIPIENT MOTION IN RIGID BOUNDARY OPEN CHANNEL FLOW

Mir Jafar Sadegh Safari

Department of Civil Engineering, Yaşar University,

Izmir, Turkey

jafar.safari@yasar.edu.tr

ABSTRACT: Sediment incipient motion is one of the main aspects of the sediment transport hydraulics. Determination of the flow condition where sediment particles start to move from the channel bottom is of importance for channel design practice to prevent continues deposition of the sediment in drainage channels. Sediment incipient motion relationships existing in the literature for rigid boundary open channels are established considering particle Froude number and relative particle size dimensionless parameters incorporating flow, fluid and sediment characteristics. It is already reported that the channel cross-section shape effects flow resistance and incipient motion models behave differently depending on the channel cross-section shape. In this study, through a simple analyzing of hydrodynamic forces acting on the sediment particle at the channel bottom, the methodology of developing dimensionless parameters of particle Froude number and relative particle size is explained. Regarding the flow resistance and channel cross-section geometry factors, a practical cross-section shape factor is suggested and then incorporated into the incipient motion relationship structure to develop a generalized incipient motion model valid for any arbitrary channel cross-section shape. Accordingly, channel characteristic is considered in this study together with flow, fluid and sediment features. Incipient motion experimental data collected from different cross-section channels are used in this study. The outperformance of generalized incipient motion model is demonstrated in comparison to cross-section specific models available in the literature.

1. INTRODUCTION

Linked to the sediment transport process entrainment, conveyance and deposition of sediment particles are considered in rigid boundary channels for the aim of channel design. Regarding the self-cleansing definition as a well-known criteria for channel design, flow must remove the deposited sediment at the channel bottom (Safari et al., 2018). Therefore, it is an important task to determine the velocity required for the incipient motion of sediment in rigid boundary open channels (Bong et al., 2021; Wan Mohtar et al., 2022). The impact of the channel cross-section shape on sediment transport were studied by Paul and Sakhuja (1990), Safari et al. (2017) and Safari and Aksoy (2021). Determination of sediment incipient motion based on visual observation is a subjective hydraulic problem that causes variety of results because of different definitions adopted for identification of sediment incipient motion. Therefore, conducting several sets of experiments under the same laboratory conditions for different cross-section channels with almost equal size of cross-section area for minimizing the scale effect would be helpful to provide more conclusive results in terms of the effect of channel cross-section shape on incipient motion. On the other hand, existing formulae for incipient motion in rigid boundary channels were developed for specific cross-section channels and there is no a general sediment incipient motion formula valid for any channel cross-section shape.

This study aimed to establish a general incipient motion formula for rigid boundary channels using data collected from five different cross-sections namely; trapezoidal, rectangular, circular, U-shape and V-bottom. Experimental data are analyzed based on velocity approach, a cross-section shape factor is introduced and a general formula is developed and compared to the models available in the literature.

351

2. EXPERIMENTAL DATA

Experimental data of Safari (2016) are used in this study. Experiments performed in five smooth channels made of Plexiglass, 12 m length with different cross-section shapes, namely; trapezoidal, rectangular, circular, U-shape and V-bottom (Figure 1). The trapezoidal, rectangular, U-shape and V-bottom cross-sections have a width of 300 mm, while the circular cross-section has an inner diameter of 290 mm. The U-shape and V-bottom cross-sections have equal cross-falls of 50 mm at their longitudinal axis. The trapezoidal cross-section has the outer angle of 60 degree, and 30 cm-long inclines slopes. Experiments were repeated for nine channel bed slopes changing from 0.00147 to 0.01106. For each experiment, discharge was measured by an ultrasonic flow-meter, and observations were made for sediment motion. As sediment, four different size uniform non–cohesive sands were used in this study. Observations were made in a section, 4 m long and located 4 m from the upstream and 4 m from the downstream sections of the channel under uniform flow conditions adjusted with the tailgate of the channel. The uniform flow condition was controlled by measuring the flow depth at three points along the observation section. Hydraulic characteristics were also recorded through the experiments.

At the first step sediment size was selected and channel bed slope was adjusted and then observations made for identifying sediment motion conditions. Experiments start with such a flow condition that velocity is high enough to prevent the deposition of sediment particles poured into the channel using a vibrant sediment feeder. Through a gradual decrease in the discharge allows flow to switch from the non-deposition mode to the deposition in which sediment particles clustered in certain areas of the channel bottom without making a deposited bed layer. In order to achieve the incipient motion mode by increasing flow discharge up to a certain value, a random motion of the individual particles of given characteristics on the bed was observed. The flow velocity increases by gradually opening the valve until sediment particles begin to move on the bed corresponding to the incipient motion mode of sediment transport (Figure 2).
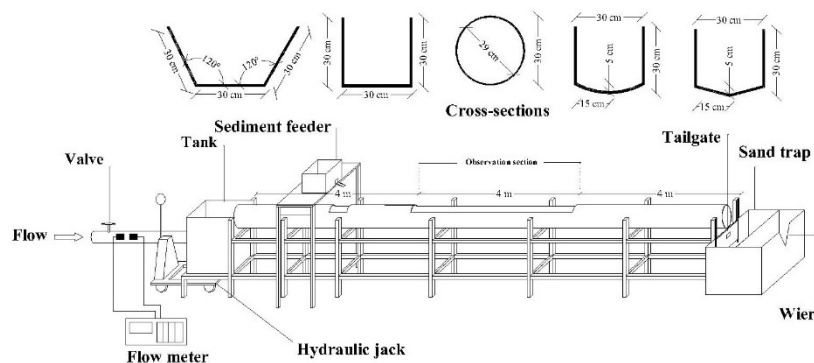
Figure 1. Experimental apparatus and channel cross-sections
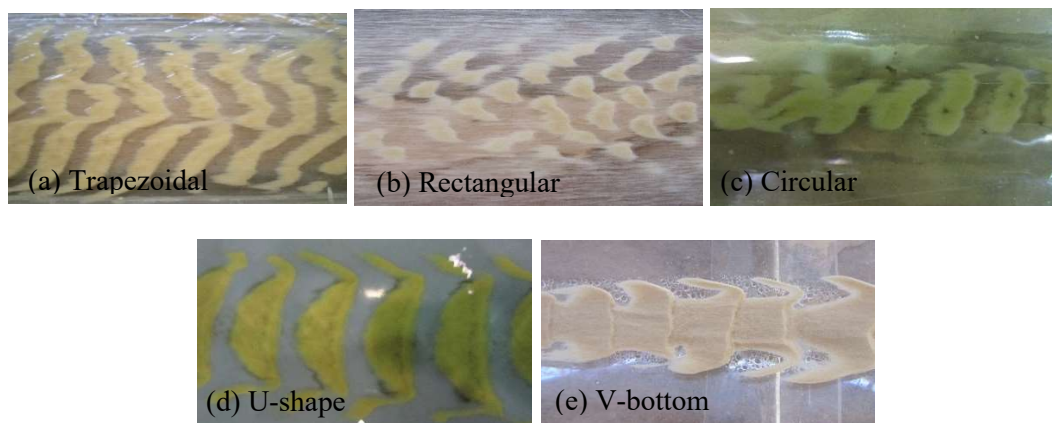
Figure 2. Sediment incipient motion for different cross-sections

3. RESULTS

3.1. Theoretical Consideration

Theoretical consideration of incipient motion of sediment in the flow is due to hydrodynamic forces which are exerted on sediment particles at the bottom of the channel. Incipient motion models were developed by using analytical solution of equilibrium between hydrodynamic forces acting on sediment particles and calibrated with experimental data (Safari et al., 2017). Sediment particles in the flow move under the influence of two types of hydrodynamic forces; the first type has a positive impact by the drag force (F_d) and the lift force (F_l), while the second discourages motion by the buoyed weight of sediment (F_g). The resisting force (F_r) against motion can be expressed as net effect of F_d and F_l. Aforementioned forces are formulated respectively, as

$$F_d = \frac{\pi}{8} c_d \rho d^2 u_b{}^2 \tag{1}$$

$$F_l = \frac{\pi}{8} c_l \rho d^2 u_b{}^2 \tag{2}$$

$$F_g = \frac{\pi}{6} d^3 (\rho_s - \rho) g \tag{3}$$

$$F_r = k(F_g - F_l) \tag{4}$$

where c_d and c_l are drag and lift coefficients, respectively; ρ and ρ_s are fluid and sediment specific masses, respectively; d sediment median diameter, u_b near bed flow velocity, g gravitational acceleration, and k the Coulomb friction coefficient. The drag force should be equal to the resistance force in the sediment threshold condition (Figure 3). Therefore,

$$F_d = k(F_g - F_l). \tag{5}$$
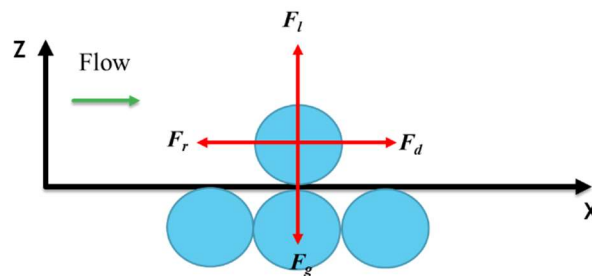
Figure 3. Hydrodynamic forces acting on sediment particle at incipient motion condition

The balance between forces acting on sediment particles is utilized for the determination of the incipient motion velocity. Substituting Eqs. (1-4) into Eq. (5) gives

$$\frac{u_b}{\sqrt{gd(s-1)}} = \sqrt{\frac{4}{3} \frac{k}{c_d + k c_l}}. \tag{6}$$

where s is relative specific mass. The right hand side of Eq. (6) depends on the channel and particle geometry. Novak and Nalluri (1984) used the relative particle size (d/R where R is hydraulic radius) as a geometrical parameter of the channel and sediment particle; also used flow mean velocity (V) instead of the near bed flow velocity to propose

$$Fr_p = \frac{V}{\sqrt{gd(s-1)}} = a\left(\frac{d}{R}\right)^b \tag{7}$$

in which Fr_p is the incipient motion particle Froude number, a and b are constant values. The incipient motion models proposed for rigid boundary channels are developed as a function between particle Froude number (Fr_p) and relative particle size (d/R) as shown in Table 1 and Figure 4. It is seen in Figure 4 that required incipient motion velocity is depended on channel cross-section shape

where rectangular channel needs lower while U-shape and V-bottom channels need higher incipient motion flow velocity.

Table 1. Incipient motion formulae in rigid boundary channels.

Fr_p	Expression in terms of d/R	Channel cross-section	Reference	Eq. No.
$\dfrac{V}{\sqrt{gd(s-1)}} =$	$0.61(d/R)^{-0.27}$	Rectangular, Circular	Novak and Nalluri (1975)	(8)
	$0.50(d/R)^{-0.40}$	Rectangular, Circular	Novak and Nalluri (1984)	(9)
	$0.75(d/R)^{-0.34}$	Circular	El-Zaemey (1991)	(10)
	$0.68(d/R)^{-0.41}$	V-bottom	Safari et al. (2011)	(11)
	$0.49(d/R)^{-0.50}$	Trapezoidal		(12)
	$0.48(d/R)^{-0.47}$	Rectangular		(13)
	$0.48(d/R)^{-0.50}$	Circular	Safari et al. (2017)	(14)
	$0.68(d/R)^{-0.44}$	U-shape		(15)
	$0.83(d/R)^{-0.39}$	V-bottom		(16)
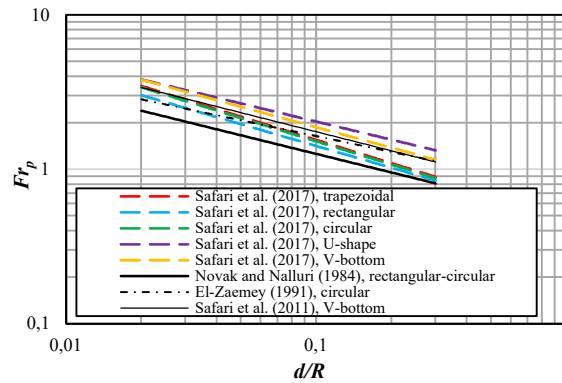
Figure 4. Comparison of incipient motion formulae in rigid boundary channels

3.2. General Incipient Motion Formula

Sediment transport formulae behave differently depending on the channel cross-section shape (Paul and Sakhuja, 1990; Nalluri and Ab Ghani, 1993; Safari et al., 2017; Safari and Aksoy, 2021). To this end, this study aims to develop a general incipient motion formula for different cross-section channels; trapezoidal, rectangular, circular, U-shape and V-bottom channels. Therefore, it is an essential issue to consider a channel cross-section shape factor. As a primary study, Jayaraman (1970) reported that the parameter of P/B could express the impact of the non-uniform shear stress distribution on the channel boundary. It illustrates the effect of channel cross-section shape on flow resistance (P is the wetted perimeter and B is water surface width). Thereafter, the importance of P/B on the flow resistance and the channel cross-section shape was demonstrated by Kazemipour and Apelt (1979, 1982), Nalluri and Adepoju (1985) and Safari and Aksoy (2021). Therefore P/B can be considered as the channel cross-section shape factor and added to the Eq. (7). Experimental data collected from the five different cross-section channels namely; trapezoidal, rectangular, circular, U-shape and V-bottom are used to develop the general incipient motion formula as follows

$$Fr_p = \frac{V}{\sqrt{gd(s-1)}} = 0.68 \left(\frac{d}{R}\right)^{-0.47} \left(\frac{P}{B}\right)^{-4.33}. \tag{8}$$

3.3. Evaluation of the General Incipient Motion Formula

Performance of the general incipient motion formula is examined in contrast to the existing incipient motion formulae in Table 2 in terms of two statistical performance criteria of the root mean square error ($RMSE$) and determination coefficient (R^2) defined as follows

$$RMSE = \sqrt{\frac{\sum_{i=1}^{n}(Fr_p^m - Fr_p^c)^2}{n}} \qquad (9)$$

$$R^2 = 1 - \frac{\sum_{i=1}^{n}(Fr_p^c - Fr_p^m)^2}{\sum_{i=1}^{n}(Fr_p^c - \overline{Fr_p^c})^2} \qquad (10)$$

where, Fr_p^c and $\overline{Fr_p^c}$ are measured, calculated and mean of calculated Fr_p, respectively, and n the data number.

The accuracy of the general incipient motion formula Eq. (8) is compared to the selected counterparts taken form the literature; Novak and Nalluri (1984), El-Zaemey (1991) and Safari et al. (2017) in terms of statistical performance criteria in Table 2. Novak and Nalluri (1984) formula was for circular and rectangular channels while, El-Zaemey (1991) model is valid for circular channel. Safari et al. (2017) introduced formulae for trapezoidal, rectangular, circular, U-shape and V-bottom channels. Comparison of formulae in terms of $RMSE$ and R^2 is given in Table 2. It is seen that the general incipient motion formula Eq. (8) provides much better performance than its alternatives with $RMSE$ of 0.309 and R^2 of 0.918. Results show that the general formula developed in this study (Eq. 8) outperforms cross-section specific models. Among cross-section specific models, Novak and Nalluri (1984) formula gives poor results. Superior performances of the general formula Eq. (8) can be attributed to the channel cross-shape factor used in its models' structure. In this study, experiments performed in five different cross-section channels having almost equal dimensions. Therefore, it can be said that the general incipient motion formula can be used as a reliable practical tool for determination of the required flow velocity at sediment incipient motion for different channel cross-section shapes.

Table 2. Comparison of general incipient motion formula to existing formulae in terms of $RMSE$ and R^2.

Model	$RMSE$	R^2
General formula	0.309	0.918
Trapezoidal	0.404	0.878
Rectangular	0.538	0.880
Circular	0.420	0.878
U-shape	0.408	0.881
V-bottom	0.475	0.883
Novak and Nalluri (1984)	0.833	0.882
El-Zaemey (1991)	0.575	0.882

4. CONSLUCSIONS

This study investigates the incipient motion mode of sediment transport in rigid boundary channels. Utilizing data collected from different cross-section channels namely; trapezoidal, rectangular, circular, U-shape and V-bottom a general incipient motion formula is recommended. The incipient motion formulae in the literature have mostly been developed for specific cross-section channels. A channel cross-section shape factor is introduced and then incorporated into the model structure. Through the development of the general incipient motion formula hydrodynamic forces acting on sediment particles are considered together with a simplification based on the velocity approach where particle Froude number and relative particle size are embedded into the model. To this end, flow, sediment, channel and fluid characteristics are considered for the model development. Comparison of general incipient motion formula to the corresponding formulae available in the literature on

experimental data of this study shows that the proposed formula has an acceptable ability to compute the incipient motion velocity for different channel cross-section shapes.

ACKNOWLEDGMENTS

REFERENCES

Bong, C. H. J., Liew, S. C., Teo, F. Y., Lau, T. L., & Ab Ghani, A. (2021). Critical shear stress approach for self-cleansing design of a rectangular channel. *International Journal of Sediment Research*, *36*(5), 678-685.

El-Zaemey, A. K. S. (1991). *Sediment transport over deposited beds in sewers*. Ph.D. thesis, Dept. of Civil Engineering, Univ. of Newcastle upon Tyne.

Jayaraman, V.V. (1970). Resistance studies on smooth open channels. *Journal of Hydraulic Division 96*(5), 1129-1142.

Kazemipour, A. K. & Apelt, C. J. (1979). Shape effects on resistance to uniform flow in open channels. *Journal of Hydraulic Research*, *17*(2), 129-147.

Kazemipour, A. K. & Apelt, C. J. (1982). New data on shape effects in smooth rectangular channels. *Journal of Hydraulic Research*, *20*(3), 225-233.

Nalluri, C., & Ab Ghani, A. (1993). Shape effect on bed load sediment transport in pipes. *Proc., Int. Con. on Hydraulic Engineering, ASCE*, San Francisco, California, July 25-30. 1200-1205.

Nalluri, C. & Adepoju, B. A. (1985). Shape effects on resistance to flow in smooth channels of circular cross-section. *Journal of Hydraulic Research*, *23*(1), 37-46.

Novak, P., & Nalluri, C. (1975). Sediment transport in smooth fixed bed channels. *Journal of the Hydraulics Division, ASCE 101*(HY9):1139-1154

Novak, P., & Nalluri. C. (1984). Incipient motion of sediment particles over fixed beds. *Journal of Hydraulic Research*, 22(3), 181–197.

Paul, T. C., & Sakhuja, V. S. (1990). Why sediment deposit in lined channels. *Journal of Irrigation and Drainage Engineering*. 116(5), 589-602.

Safari, M. J. S. (2016). *Self-cleansing drainage system design by incipient motion and incipient deposition-based models*. Ph.D. thesis, Dept. of Civil Engineering, Istanbul Technical Univ.

Safari, M. J. S., & Aksoy, H. (2021). Experimental analysis for self-cleansing open channel design. *Journal of Hydraulic Research*, *59*(3), 500-511.

Safari, M. J. S., Aksoy, H., Unal, N. E., & Mohammadi, M. (2017). Experimental analysis of sediment incipient motion in rigid boundary open channels. *Environmental Fluid Mechanics*, *17*(6), 1281–1298.

Safari, M. J. S., Mohammadi, M., & Ab Ghani, A. (2018). Experimental studies of self-cleansing drainage system design: A review. *Journal of Pipeline Systems Engineering and Practice*, *9*(4), 04018017.

Safari, M. J. S., Mohammadi, M., & Manafpour, M. (2011). Incipient motion and deposition of sediment in rigid boundary channels. *Proceedings 15th International Conference on Transport & Sedimentation of Solid Particles*, 6-9 September, Wroclaw, Poland, 63-75

Wan Mohtar, W. H. M. W., Ab Ghani, A., Safari, M. J. S., Taib, A. M., Haitham, A. F. A. N., & Ahmed, E. S. (2022). Sediment Incipient Motion in Sewer with a Bed Deposit. *Teknik Dergi*, *33*(1).

14TH INTERNATIONAL CONFERENCE
ON HYDROSCIENCE & ENGINEERING

MAY 26-27, 2022
IZMİR-TURKEY

ICHE2022
IZMIR, TURKEY

STOCHASTIC SUSPENDED SEDIMENT TRANSPORT WITH CCIES

Serena Y.Hung

PhD Candidate, Department of Civil Engineering, National Taiwan University, Taipei, Taiwan

d05521007@ntu.edu.tw

Christina W. Tsai

Professor, Department of Civil Engineering, National Taiwan University, Taipei, Taiwan

cwstsai@ntu.edu.tw

ABSTRACT: In essence, stochastic diffusion particle tracking models (SD-PTMs) are powerful Lagrangian models for simulating random particle behaviors in turbulent flows. The random term in SD-PTM simulates influences of turbulent effect on particle motions. Using the Wiener process, the particle positions' increments are independent. However, in reality, instead of statistical independence, flow events or phenomena are time persistent and might cause a statistical dependency of sediment movements. This study introduces the fractional Brownian motion(fBm) to model these distinctive behaviors. The fBm is a transformed form of the Wiener process with the most well-known property: the dependent and correlated increments. The mathematical property of correlated increments makes fBm a potential method to model the random behaviors subject to long-range memory events. In order to model the random particle trajectories subject to the long time-persistent flow events, the study proposes the fractional SD-PTM (fSD-PTM). In the study, the proposed fSD-PTM is applied to the suspended sediment transport simulation during a typhoon event in a reservoir. The simulation results reveal that the proposed model accounting for memory effect performed better than the original SD-PTM in a time-persistent flow event.

1. INSTRUCTIONS

The study focuses on suspended sediment particles whose motions are deeply coupled with surrounding turbulent flow environments cite (Chien & Wan, 1999; Hunt, 1954). Since the random motions of suspended particles are driven by turbulence, the diffusion term in suspended sediment transport often links to turbulence diffusion theories (Absi et al., 2011; Tsujimoto, 2010). The high irregularity and isotropic property of turbulence generally lead to the usage of Brownian diffusion as the suspended diffusion, which results in the independency of particle motions (Argall et al., 2004; Dimou & Adams, 1993; Heemink, 1990; Man & Tsai, 2007).

However, ever since the hydrologist Hurst examined the Nile River discharge variations and found the statistical dependency from the time-series water discharge data (Hurst, 1957), lots of research confirmed the non-Gaussian properties in geophysical records, such as stream-flow, rainfall, and floods, (Mandelbrot & Wallis, 1969a, 1969b). It, therefore, appears to be necessary to consider the impact of this dependency property of flows on suspended sediment transport. For instance, turbulent coherent structures near the wall regions are intermittent and persistent in time (Dennis, 2015; Jiménez, 2018; Martin et al., 2012). These irregular and time-persistent turbulent flow structures interact with sediments particles on the channel bed resulting in the random entrainment of deposited particles (Ninto & Garcia, 1996; Salim et al., 2017; Salim & Pattiaratchi, 2020; Sun et al., 2017). Lager time-persistent flow events in the scale of seasonal, annual, or even the decadal-scale of the El Niño oscillation cycles could result in longer-term variations in suspended sediment behaviors (Beven, 2015; Gray et al., 2015).

In order to model the random suspended sediment behaviors with dependencies, the fraction concept is introduced. Anomalous properties such as long-range spatial or temporal correlation can be described by fractional dynamics (Metzler & Klafter, 2004). The study proposes a fractional SD-PTM (fSD-PTM) aiming to describe random suspended sediment behaviors within the time-persistent flow events. By replacing the Wiener process with fractional Brownian motion process (fBm), the fSD-PTM can describe the supper-diffusive movement caused by the time-persistent turbulent flows. Defined as a transformation of the ordinary Brownian motion (BM), the fBm is still a Gaussian process but has long time dependencies on the increments. In other words, the increments need not be independent, and thus an fBm possesses the *non-memoryless* property. Accordingly, the proposed fSD-PTM is a robust model to simulate random suspended sediment trajectories with memory accounting for flow events with time-persistent properties.

2. METHODLOGY

2.1. Stochastic Diffusion Particle Tracking Model (SD-PTM)

The SD-PTM addresses positions of individual suspended sediment particle in turbulent flows (Man & Tsai, 2007). By treating sediment particle position $X_t = \{X(t), Y(t), Z(t)\}_T$ as a stochastic process, a stochastic diffusion equation (SDE) based on Ito stochastic calculus is the governing equation of SD-PTM witch is shown as

$$dX_t = u(t, X_t)dt + \sigma(t, X_t)dB_t, \tag{1}$$

where $u(t, X_t)$ is the mean drift deterministic term consisting of mean drift flow velocity U and turbulence diffusivity D (Eq.2.),

$$u(t, X_t) = U + \Delta D. \tag{2}$$

$\sigma(t, X_t)$ is the diffusion coefficient; and B_t stands for the standard Brownian motion simulated by the Wiener process at time t. By linking Eq.1 with the advection diffusion equation and applying the Euler–Maruyama scheme in the streamwise, transverse, and vertical direction, Eq.1. becomes

$$dX_t = (U + \partial \varepsilon_x \partial x)dt + \sqrt{2\varepsilon_x}dB_t$$

$$dY_t = (V + \partial \varepsilon_y \partial y)dt + \sqrt{2\varepsilon_y}dB_t \tag{4}$$

$$dZ_t = (W - w_s + \partial \varepsilon_z \partial z)dt + \sqrt{2\varepsilon_z}dB_t.$$

U, V, and W are the mean flow velocities of direction x, y, and z, respectively; w_s is the particle settling velocity; and $\varepsilon_x, \varepsilon_y, \varepsilon_z$ are the sediment diffusivities in their respective directions.

The basic assumptions of the SD-PTM are that particles are independent of each other, and particle trajectories are random processes with memoryless Markovian properties due to the independent increment of the Winer process. However, the SD-PTMs built upon the memoryless assumption may fail to describe the random path of a particle carried by time-persistent turbulent flows (Tsai et al., 2020, 2021; Tsai & Huang, 2019).

2.2. Fractional Stochastic Diffusion Particle Tracking Model (fSD-PTM)

2.2.1. Governing Equation of fSD-PTM

In order to model the random suspended particle trajectories in the long time-persistent flows, the study proposed a fractional Lagrangian model, the fractional SD-PTM (fSD-PTM). The fBm is introduced to replace the Wiener process in Eq.1. The governing equation is a SDE driven by the fBm, shown as Eq.5,

$$dX_t = \underbrace{\overline{u}(t, X_t)dt}_{deterministic\ term} + \underbrace{\sigma(t, X_t)dB_t^H}_{random\ term},$$

(5)

where B_t^H denotes the fBm with a Hurst index $H \in (0,1)$.

2.2.2. Fractional Brownian motion (fBm)

A fBm is a centered Gaussian process with mean value zero, $E[B^H]=0$, and the covariance function,

$$E(B_t^H B_s^H) = \frac{1}{2}(|t|^{2H} + |s|^{2H} - |t - s|^{2H}).$$

(7)

It can easily be found that when $H=1/2$, then Eq.7 becomes $E[B_H(t)B_H(s)]=\min(t,s)$ which represents a standard Brownian motion, i.e., the Wiener process. The covariance of the B_{tH} increments defines as the covariance $\rho(n)$ between $(B_{t+n}^H - B_t^H)$ and $(B_{s+n}^H - B_s^H)$ with $s+n \leq t$ and $t-s=nh$,

$$\rho(n) = \frac{1}{2}h^{2H}[(n + 1)^{2H} + (n - 1)^{2H} - 2n^{2H}] \sim H(2H)n^{2H-2}.$$

(8)

According to Eq.8, the increments has a power law decay when $H \neq 1/2\$$. With $H<1/2$, the increments are negatively correlated and it is called anti-persistent. Conversely, when $H>1/2$ the increments are positively correlated, and the process is known as the persistent process. The autocorrelation is zero when $H=1/2$, indicating increments are independent. Thus the collection of the incremental process, i.e., the fBm, would correspond to the standard Brownian motion. Figure 1 shows the sample paths with $H=0.5$ (standard Brownian motion/ the Wiener process) and $H=0.9$ (long-persistent path). With correlated increments, sample path of the fBm is smoother than that of the Wiener process.

Figure 1. Sample path of fractional Brownian motion

2.2.3. Definition of Memories

The main objective of the research is to propose a Lagrangian model aiming to describe individual particle trajectories with *memories* caused by the persistent flow environment. In this research, *memory* or *long time persistence* or so called the *long-range dependence,* is associated with the dependence of a stochastic process, $(X_n)_{n\in\aleph}$. A stationary sequence exhibits long-range dependence if the auto-covariance function $\rho(n):=\text{cov}(X_k,X_{k+n})$ satisfy,

$$\lim_{n\to\infty} \frac{\rho(n)}{cn^{-\alpha}} = 1$$

(9)

for some constant c and α (Brandt & de Lange, 2008). Eq.8 shows that the dependence between X_k and X_{k+n} decays slowly as n tends to infinity $\sum_{n=1}^{\infty} \rho(n) = +\infty$.

By this definition, consider Eq.8. Let $c = H(2H-1)$ and $\alpha=2-2H$. When n goes to infinity, one can get,

$$\lim_{n \to \infty} \frac{\rho(n)}{H(2H)n^{2H-2}} = 1. \tag{10}$$

By Eq. 10, for $H<1/2, \sum_{n=1}^{\infty}\rho(n) = < \infty$; for $H > 1/2, \sum_{n=1}^{\infty}\rho(n) = +\infty$ which prove the long-range temporal memory of the fBm increments.

For a modeling perspective, the modified Euler scheme (Hu et al., 2016; Y. Liu & Tindel, 2019) is used for the numerical approximation of equation Eq.5:

$$X_{n+1} = X_n + \bar{u}(X_n)\Delta t + \sigma(X_n)\left(B_{t_{n+1}}^H - B_{t_n}^H\right) + \frac{1}{2}\sigma(X_n)\sigma'(X_n)\Delta t^{2H}. \tag{6}$$
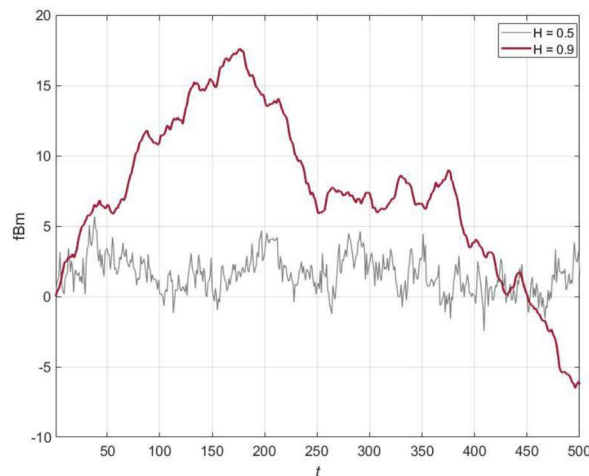
The study's underlying hypothesis is that when a time-persistent flow event carries suspended sediment particles, particles' movements are not memoryless. Thus the value of Hurst index is determined by the flow events. In the study, the Hurst value is estimated based on the second-order wavelet analysis in the wavelet domain (Flandrin, 1992; Pipiras & Taqqu, 2017).

3. APPLICATION OT SUSPENDED SEDIMENT TRANSPORT

For the present study, we attempt to apply the proposed fSD-PTM to suspended sediment transport in a more realistic yet simplified situation: the suspended sediment transport during a typhoon event in a reservoir. In the simulation, the typhoon event is the Typhoon MEGI stroked Taiwan in September 2016. The study area is in the Shihmen reservoir as shown in Fig. 2. With only two-thirds of the design capacity left, Shihmen reservoir suffers from sedimentation. Large flooding events make matters worse and exacerbate accumulation sedimentation problems. Therefore, modeling suspended sediment transport during a typhoon event can provide relevant information for the Shihmen reservoir management.

Figure 2. Study area: Shihmen Reservoir. Hydrograph was measured at Luofu station, shown at the bright yellow spot on the map at the right corner. The upstream station is station S12 and downstream Station is S07

3.1. Simulation Assumptions

With regard to the availability of the in-situ data, some simplifications and assumptions have been made for the simulation. The first simplification is the constant Hurst value. Herein, the Hurst index is determined based on the recessional limb of the hydrograph as shown in Fig.3(a). For the purpose of showing the long-range dependent flow property during the typhoon event, the autocorrelation function of the hydrograph after the peak discharge is examined in Fig.3(b). The value of autocorrelation is always greater than zero, proving the relevance of considering the time-persistence property of flow event. Using the wavelet estimation, the time series discharge data after the peak has a Hurst value of 0.64.
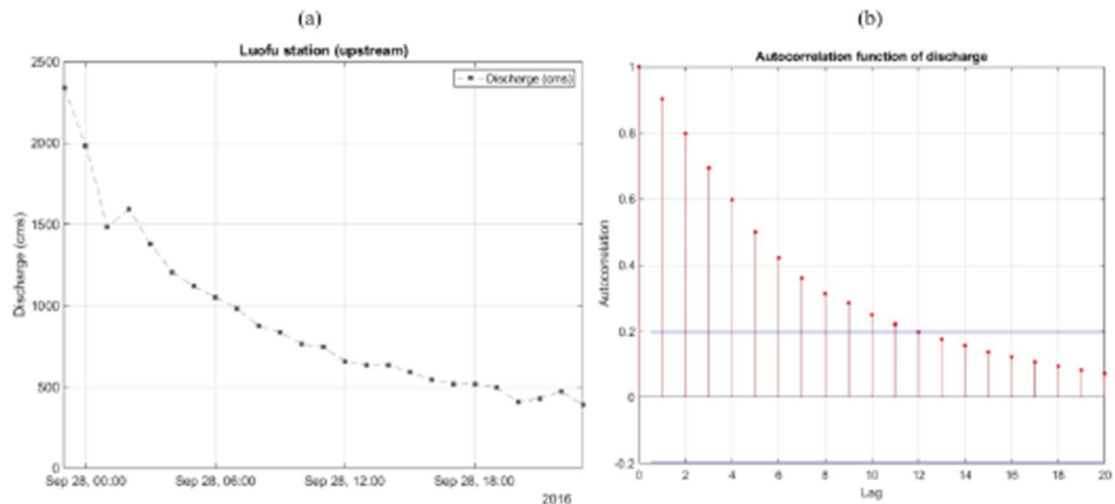
Figure 3. (a). The autocorrelation function of hydrograph with the upper and lower confidence bounds
(b). Hydrograph at Luofu station, the inlet station of the Shihmen reservoir

The second simplification is zero drift flow velocity. In the simulation, the suspended sediment transport is simulated between station S12 and S07, where time-series concentration data during typhoon MEGI at different elevations is available. The simulation area is away from the inlet station, Luofu station, the entrance station of the Shihmen reservoir, represented by a bright yellow dot in Fig.2. Consequently, the zero mean drift velocity assumption is made in the simulation.

The last simplifications are constant water level and constant diffusion coefficients. In the simulation, the initial position is at station S12, and the model results are validated with in-site concentration data at station S07. The distance between the two stations is 2.35 km, demonstrated as the yellow path in Fig.2. Compared with the whole reservoir, the simulation domain between the two stations is relatively small; hence with roughly the same bed elevation ≈190.0m, the water level is assumed to be a constant elevation ≈243.16m. Similarly, the diffusion coefficients in streamwise and vertical directions are set as time-averaged constants, $\varepsilon_x=5.0\ m2/s$ and $\varepsilon_z=1.0\ \times10-5\ m2/s$. The diffusion coefficients are determined by the Hydrodynamics module of the Environmental Fluid Dynamics Code (W.-J. Liu, 2021). The simulation uses the same particle properties and flow environmental parameters listed in Table 1.

Table 1. Modeling parameters.

Parameter	Value (unit)
Sediment diameter	50 μm
Specific gravity	2.65
Settling velocity	0.0236 m/s
Bed roughness	0.0294
Critical shear stress	0.00015 m2/s2
Total simulation time	24 hr
Time step	5 s
Monte Carlo simulation	1000

3.2. Simulation Results

In the simulation, the proposed fSD-PTM is used to simulate suspended sediment transport between stations S12 and S07. The time-series in-site concentration data measured at different elevations at the upstream station S12 are the continuous sediment inputs. According to in-situ concentration data, every 30 minutes, different particle units would be released in the domain. Then the sediment concentrations are calculated every 30 minutes along with simulation time at Station S07.

Calculations of sediment concentration are based on the particle number at the 2.35 km downstream to compare with the in-situ concentration data at station S07. The Concentration results of one

simulation at different elevations are shown in Fig4. The black dots represent the in-site concentration data at downstream station S07, and the red circles are the concentration results from only one simulation. The in-suit measured concentrations data decreased along with the time since the simulation started when the discharge decreased after the peak discharge. On the other hand, as can be seen, the concentration results are close to zero at the beginning and increase along with time. The zero values result from zero particles arriving at the downstream station S07 at such an early stage. With zero particles at the beginning, the concentration is zero in the simulation. Concentration increases when more and more particle units are released and transport downstream. Although the results of one simulation are only one plausible outcome, the purpose of demonstrating is to roughly make a comparison with the in-situ concentrations data, which are also the one plausible results that did happen in reality. The rough concentration comparison between simulation results and in-site data reveals that without any particles in the domain initially, it would take some time for simulation results to be relevant. In this situation, it takes about 18 hours. A quick glance at Fig.4 might suggest that the last 6 hours simulation results and the filed data points are from the same cluster. To further examine the simulation results, ensemble statistics should be calculated.
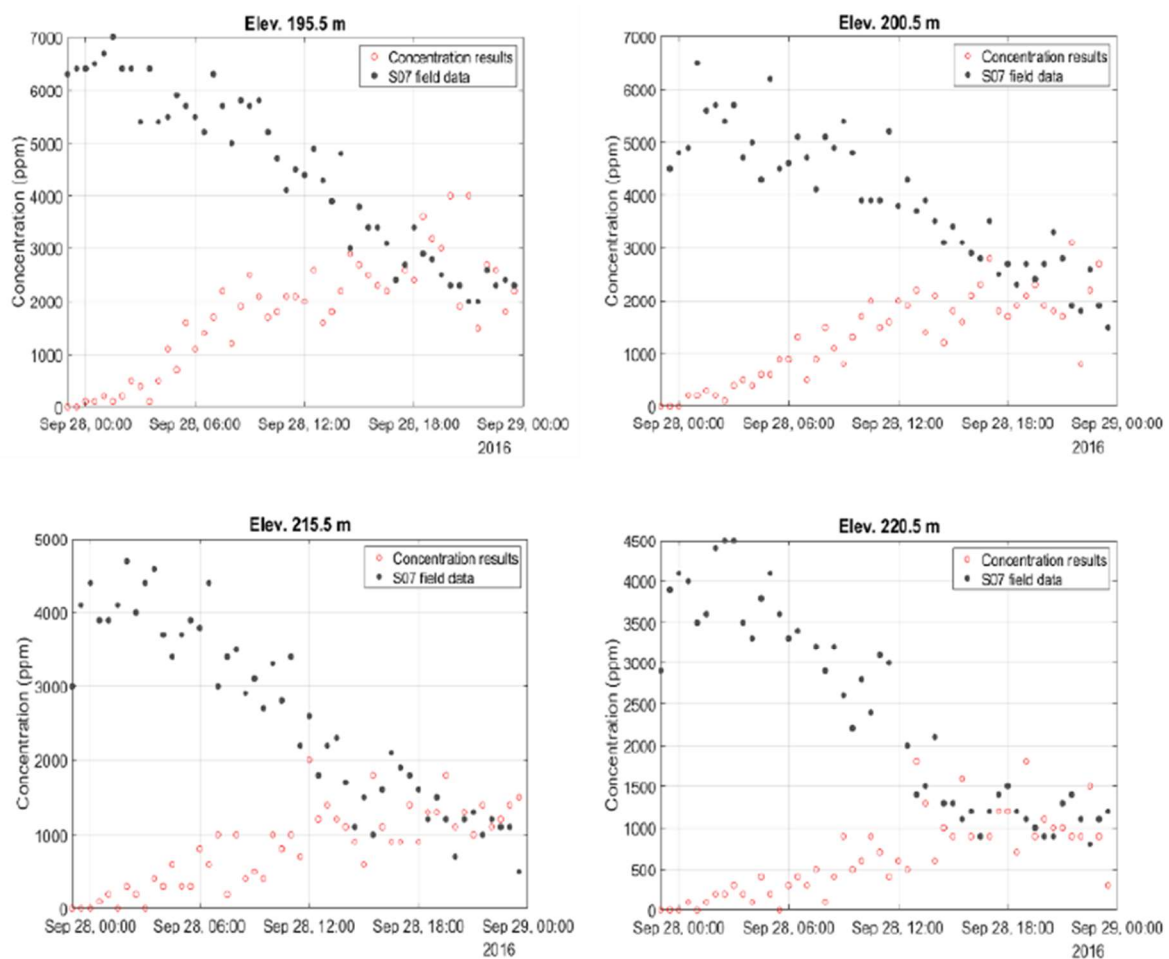
Figure 4. Concentration results at different elevations based on one simulation

Via the Monte Carlo method, ensemble concentrations are calculated based on 1000 simulations and are shown in Fig.5. Ensemble results plus or minus one standard deviation are drawn for the last 6 hours. Most in-situ data points fall within the range covered by the ensemble mean plus and minus one standard deviation. With zero mean velocity and constant diffusivity assumptions, the mean drift terms, except for the settling velocity, are equal to zero, and only the turbulence terms are left in the governing equation. We have also used SD-PTM to model the suspended sediment transport to make a comparison in Fig.6. However, concentrations from the SD-PTM show that most particles cannot arrive downstream station S07 before the end of the simulation. Ensemble concentration results of the SD-PTM depicted as the square points in Fig.6 are almost always zero along with time.
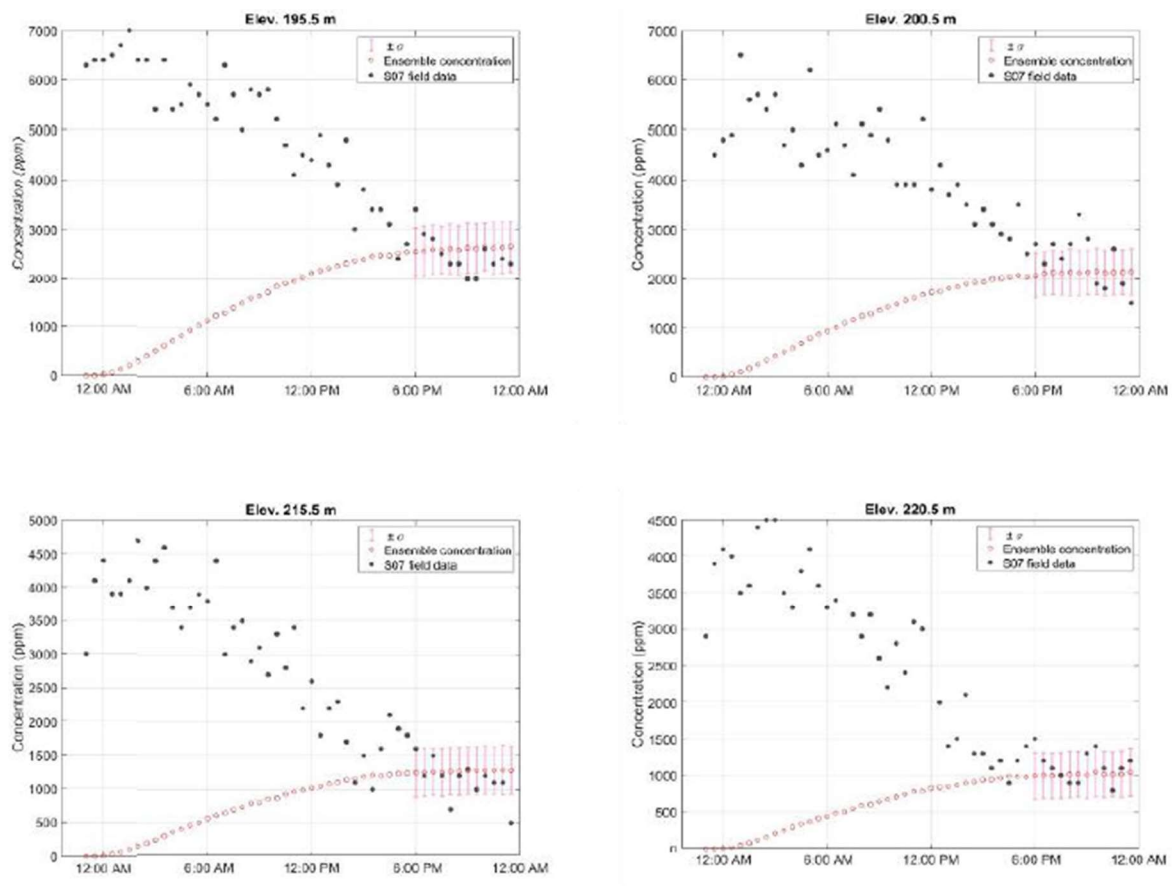
Figure 5. Ensemble concentration results based on 1000 realizations
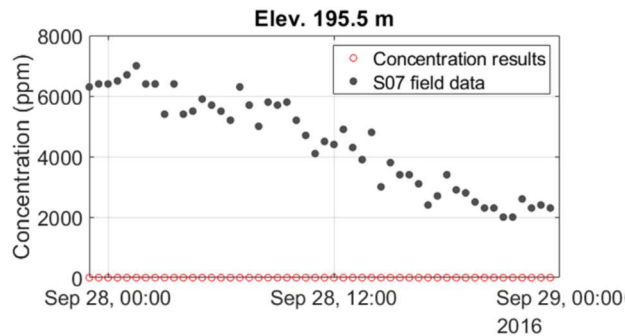
Figure 6. Ensemble concentration results based on 1000 realizations of SD-PTM

The tremendous difference between ensemble concentration results of the proposed fSD-PTM and the SD-PTM shows the necessity of considering the memory effect in suspended particles' movement. With the Hurst index capturing the time-persistent property of carrying flow, the proposed fSD-PTM can then describe the non-Gaussian turbulent fluctuations by the fractional process with the specified Hurst value.

4.   CONCLUSIONS

In this research, the underlying assumption is that when suspended sediments transport within the time-persistent flows, the spread of sediments will not follow the Fickian law. In order to describe the non-Fickian diffusive behaviors of sediments, this embryonic research introduces the fractional

concept to PTMs. The research proposes a fractional particle tracking model, the fSD-PTM, to simulate the suspended sediment transport with memories. Herein, "memory" is mathematically defined as the long-range dependency of a stochastic process. The governing equation of the proposed fSD-PTM is a SDE driven by the fBm. With Hurst index value larger than 1/2, the auto-correlation value of the fBm increments are positive and therefore indicate the increments are dependent, not memoryless. The correlated increments of the fBm make fSD-PTM a robust stochastic model to describe the random sediment movements with memories in time-persistent flow events. The simulation of suspended sediment transport during a typhoon event in a reservoir is demonstrated. The positive auto-correlation values of the flow discharges confirm the time-persistent flow property and show the relevance of considering fractional fluctuations in suspended particle movements. Results of sediment concentrations reveal that the proposed fSD-PTM has a better prediction than the SD-PTM.

The availability of this stochastic model can quantify the uncertainty of suspended sediment transport in time-persistent flow environments. Such stochastic descriptions via Monte Carlo simulations could better describe the randomness of sediment movements in a non-stationary turbulent flow. Notably, applications such as a risk assessment and safety factors required for hydraulic structure design, sedimentation, and water quality control, can thus be calculated. In practice, such information would provide a valuable reference for evaluating the operation risk of hydraulic structures, such as reservoirs, dams, and bridges in an highly uncertain future environment.

REFERENCES

Absi, R., Marchandon, S., & Lavarde, M. (2011). Turbulent diffusion of suspended particles: analysis of the turbulent Schmidt number. *Defect and Diffusion Forum*, *312*, 794–799.

Argall, R., Sanders, B. F., & Poon, Y.-K. (2004). Random-walk suspended sediment transport and settling model. In *Estuarine and Coastal Modeling (2003)* (pp. 713–730).

Beven, K. (2015). What we see now: Event-persistence and the predictability of hydro-eco-geomorphological systems. *Ecological Modelling*, *298*, 4–15.

Brandt, L., & de Lange, H. C. (2008). Streak interactions and breakdown in boundary layer flows. *Physics of Fluids*, *20*(2), 24107.

Chien, N., & Wan, Z. (1999). *Mechanics of sediment transport*.

Dennis, D. J. C. (2015). Coherent structures in wall-bounded turbulence. *Anais Da Academia Brasileira de Ciências*, *87*, 1161–1193.

Dimou, K. N., & Adams, E. E. (1993). A random-walk, particle tracking model for well-mixed estuaries and coastal waters. *Estuarine, Coastal and Shelf Science*, *37*(1), 99–110.

Flandrin, P. (1992). Wavelet analysis and synthesis of fractional Brownian motion. *IEEE Transactions on Information Theory*, *38*(2), 910–917.

Gray, A. B., Pasternack, G. B., Watson, E. B., Warrick, J. A., & Goñi, M. A. (2015). The effect of El Niño Southern Oscillation cycles on the decadal scale suspended sediment behavior of a coastal dry-summer subtropical catchment. *Earth Surface Processes and Landforms*, *40*(2), 272–284.

Heemink, A. W. (1990). Stochastic modelling of dispersion in shallow water. *Stochastic Hydrology and Hydraulics*, *4*(2), 161–174.

Hunt, J. N. (1954). The turbulent transport of suspended sediment in open channels. *Proceedings of the Royal Society of London. Series A. Mathematical and Physical Sciences*, *224*(1158), 322–335.

Hurst, H. E. (1957). A suggested statistical model of some time series which occur in nature. *Nature*, *180*(4584), 494.

Hu, Y., Liu, Y., & Nualart, D. (2016). Rate of convergence and asymptotic error distribution of Euler approximation schemes for fractional diffusions. *The Annals of Applied Probability*, *26*(2), 1147–1207.

Jiménez, J. (2018). Coherent structures in wall-bounded turbulence. *Journal of Fluid Mechanics*, *842*.

Liu, W.-J. (2021). Incorporating Backward-forward Stochastic Particle Tracking Model into the EFDC model for Probable Sedimentation Source identification in Typhoon event. In *Master Thesis, Department of Civil Engineering, College of Engineering,National Taiwan University* (Issue 2021). https://doi.org/10.6342/NTU202104126

Liu, Y., & Tindel, S. (2019). First-order Euler scheme for SDEs driven by fractional Brownian motions: the rough case. *The Annals of Applied Probability*, *29*(2), 758–826.

Man, C., & Tsai, C. W. (2007). Stochastic partial differential equation-based model for suspended sediment transport in surface water flows. *Journal of Engineering Mechanics*, *133*(4), 422–430.

Mandelbrot, B. B., & Wallis, J. R. (1969a). Computer experiments with fractional Gaussian noises: Part 1, averages and variances. *Water Resources Research*, *5*(1), 228–241.

Mandelbrot, B. B., & Wallis, J. R. (1969b). -run properties of geophysical records. *Water Resources Research*, *5*(2), 321–340.

Martin, R. L., Jerolmack, D. J., & Schumer, R. (2012). The physical basis for anomalous diffusion in bed load transport. *Journal of Geophysical Research: Earth Surface*, *117*(F1).

Metzler, R., & Klafter, J. (2004). The restaurant at the end of the random walk: recent developments in the description of anomalous transport by fractional dynamics. *Journal of Physics A: Mathematical and General*, *37*(31), R161.

Ninto, Y., & Garcia, M. H. (1996). Experiments on particle—turbulence interactions in the near–wall region of an open channel flow: implications for sediment transport. *Journal of Fluid Mechanics*, *326*, 285–319.

Pipiras, V., & Taqqu, M. S. (2017). Basics of Long-Range Dependence and Self-Similarity. In *Long-Range Dependence and Self-Similarity* (pp. 15–112). Cambridge University Press. https://doi.org/10.1017/CBO9781139600347.004

Salim, S., & Pattiaratchi, C. (2020). Sediment resuspension due to near-bed turbulent coherent structures in the nearshore. *Continental Shelf Research*, *194*, 104048.

Salim, S., Pattiaratchi, C., Tinoco, R., Coco, G., Hetzel, Y., Wijeratne, S., & Jayaratne, R. (2017). The influence of turbulent bursting on sediment resuspension under unidirectional currents. *Earth Surface Dynamics*, *5*(3), 399–415.

Sun, H., Li, Z., Zhang, Y., & Chen, W. (2017). Fractional and fractal derivative models for transient anomalous diffusion: Model comparison. *Chaos, Solitons & Fractals*, *102*, 346–353.

Tsai, C. W., & Huang, S. (2019). Modeling suspended sediment transport under influence of turbulence ejection and sweep events. *Water Resources Research*, *55*(7), 5379–5393.

Tsai, C. W., Huang, S.-H., & Hung, S. Y. (2021). Incorporating the Memory Effect of Turbulence Structures Into Suspended Sediment Transport Modeling. *Water Resources Research*, *57*(3), e2020WR028475. https://doi.org/https://doi.org/10.1029/2020WR028475

Tsai, C. W., Hung, S. Y., & Wu, T.-H. (2020). Stochastic sediment transport: anomalous diffusions and random movement. *Stochastic Environmental Research and Risk Assessment*, *34*(2), 397–413.

Tsujimoto, T. (2010). Diffusion coefficient of suspended sediment and kinematic eddy viscosity of flow containing suspended load. *River Flow 2010*, 801–806.

14TH INTERNATIONAL CONFERENCE
ON HYDROSCIENCE & ENGINEERING

MAY 26-27, 2022
IZMİR-TURKEY

ICHE2022
IZMIR, TURKEY

EXPERIMENTAL INVESTIGATION OF FLOW FEATURE AT WAKE REGION OF CIRCULAR AND SQUARE BRIDGE PIER

Cansu Özyaman

Ege University, Civil Engineering Department

İzmir, Turkey

cansuozyaman@gmail.com

Sandor Baranya

Budapest University of Technology and Economics, Faculty of Civil Engineering

Budapest, Hungary

baranya.sandor@emk.bme.hu

ABSTRACT: Understanding of flow behavior around bridge piers is important to prevent bridge failure inside rivers. The present study provides the experimental results of the flow pattern at the wake region of the bridge piers on a rigid bed at two different flowrates and correspondingly two different flow velocities. The experiments were performed in a rectangular straight open channel at Budapest University of Technology and Economics, under steady flow conditions. Three-dimensional velocity components were measured by Acoustic Doppler Velocimetry (ADV). Velocity profiles at wake region were drawn for cylindrical and square bridge piers. Velocity vectors obtained from velocity fields were drawn at the wake region to show flow features. Contour plots of longitudinal and vertical velocity components and shear stresses near the channel bed were drawn. The reversed velocities were observed at longitudinal velocity profiles next to the pier. The results indicate that, the reversed velocity just behind the bridge pier is more apparent, when the Fr is equal to 0.33. Flow disturbance is observed up to 5 pier diameters at the wake region of the pier. Higher vertical velocity components are experienced closest to the pier.

Keywords: Bridge pier, turbulent flow, wake vortices, ADV

1. INTRODUCTION

Three-dimensional flow field around bridge piers plays fundamental role in determining the factors effecting the pier safety. Understanding of this turbulent complex flow field is important to prevent destruction of bridges in rivers. For a better understanding of the flow field and turbulent flow around piers, researchers have done several studies. In these studies, different shaped and positioned bridge pier or pier groups (Das and Mazumdar, 2015; Beheshti and Ashtiani,2016) are used with or without a scour hole. Although there are so many pier shapes in practice, these studies mostly focused on the circular piers (Dargahi, 1989; Sarker, 1998; Nagueira et al., 2010; Baranya et al., 2012; Debnath et al., 2012; Ataie and Aslani, 2012,2013; Das et al., 2013; Das and Mazumdar, 2013; Ismael et al., 2015; Chavan et al., 2017; Pandey et al., 2018). The studies with different pier cross-section such as square are in the minority (Yen et al. 2008; Das et. al., 2013; Thanh et. al., 2014; Qi et al., 2014). Due to esthetical and financial reasons, different shaped piers have become popular in bridge design. However, the direct application of the results derived from only circular pier may be problematic. Despite a large number of investigations around circular piers, a comprehensive understanding of flow around square piers is still lacking.

Wake vortices are the result of flow separation at the sides of the pier. One vortex develops on one side, sheds away, and is convected downstream. Immediately, another forms on the other side, finally shedding also. The wake vortices dissipate as they move downstream (Stevens et al. 1991). The

horseshoe vortex has been investigated quite extensively in both theoretical and practical aspects (Shen et al.; 1966,1969, Breusers et al. 1977, Baker, 1980, Raudkivi, 1986; Dargahi, 1989; Sumer and Jorgen, 1997; Kirkil et al., 2005; Dey and Raikar 2007; Sahin et al., 2007; Duan et al., 2009; Das et al., 2013; Das and Mazumdar, 2015). Information on wake vortex scour at bridge piers is particularly deficient (Bearman 1984, Akıllı 2002, Kahraman et al. 2002, Ataie and Aslani, 2013).

This study aims to investigate the wake region of the bridge piers and compare the effect of square and circular pier on velocity profiles and wake vortices.

2. EXPERIMENTAL SET-UP AND PROCEDURE

The experiments were conducted in a rectangular 12 m long, 0.5 m wide, and 0.5 m deep straight tilting open channel, located at the Budapest University of Technology and Economics. All the experiments were performed in steady flow conditions. The experiments were done at two different discharges (Q=30 l/s ,40 l/s) and two different flow depths (h=15 cm, 25 cm). The gate at the end of the channel was adjusted and fixed at a level to provide the pre-determined flow depths.

The experiments were carried out by placing square and circular sectioned pier models on the centerline of the channel. The diameter and the edge length of the circular and square piers were chosen both 5 cm. Both piers were located 6 m from the channel entrance (Figure 1).
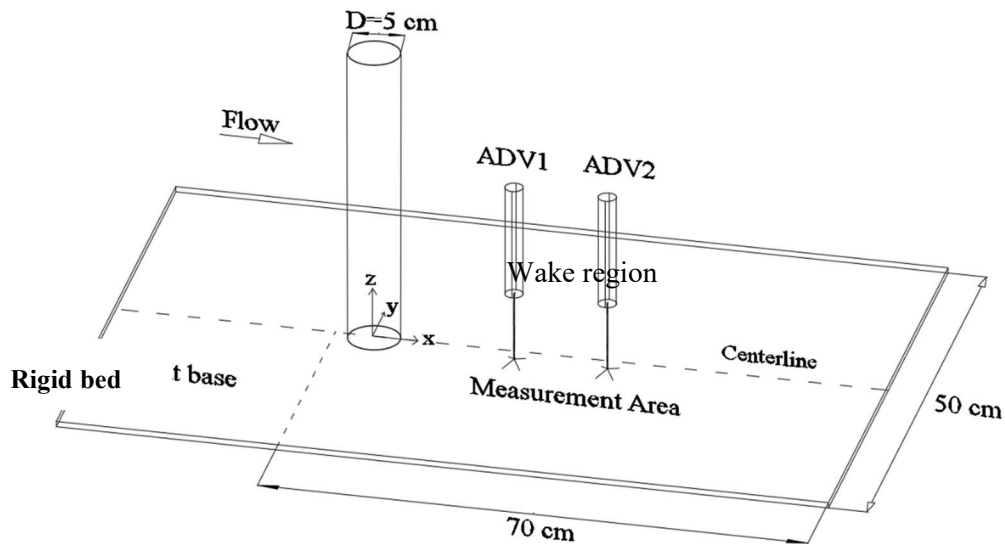
Figure 19. 3-D view of test section

The three-dimensional velocity components were measured by Nortek Acoustic Doppler Velocimetry (ADV). More than three hundred-point measurements were taken with two ADVs for each flowrate.

The measurements were taken in the Cartesian coordinate system (x,y,z). The measurements were carried out at 5 (z=0.1, 2.5, 5, 7.5, 10 cm) and 9 (z=0.1, 2.5, 5, 7.5, 10, 12.5, 15, 17.5, 20 cm) horizontal planes for 15 cm and 25 cm flow depths respectively. ADV data was taken in vertical direction at an interval of 2.5 cm. Experimental conditions are listed in Table 1.

Table 1. Experiment Conditions.

Exp. Nr	Q (l/s)	h (m)	V (m/s)	Fr
1	30	0.25	0.24	0.15
2	40	0.25	0.32	0.2
3	30	0.15	0.4	0.33
4	40	0.15	0.53	0.44

3. EXPERIMENTAL RESULTS

3.1. Velocity profiles

Velocity profiles at the centerline of the channel for different longitudinal distances are shown in Figures 2-9. Location of the pier is 0 in x coordinate for the next figures. The furthest longitudinal measurement distance to bridge pier is 65 cm while the nearest is 10 cm.

The presence of bridge pier causes a change in the longitudinal velocity profiles. The results indicate that the velocity profiles seemed to regain its original logarithmic nature at approximately 5 pier diameters (or 5 edge length) distant from the pier for all experiments (Figs 2- 9).

Approach flow velocity profile exposed to abrupt change, due to the four-cornered geometry of square piers. Accordingly, it was observed that mean velocity values at the section just behind the square pier are less than that of the circular pier. Near-bed velocity just behind the square pier was less then 0.1 m/s, while it was between 0.1 and 0.15 m/s for circular piers.

Additionally, it was observed from the Figures 2-9 that, as the distance from the pier increase, the near-bed velocities increase with a decreasing rate.

As seen from Figure 2 and 3 reversed flow was observed in the section just behind the bridge pier. The reversed flow is more pronounced for experiment having 30 l/s flowrate. The reversed flow is also apparent in circular pier (Fig. 6). Higher extension of the reversed flow area is observed at square bridge piers (Fig 2).
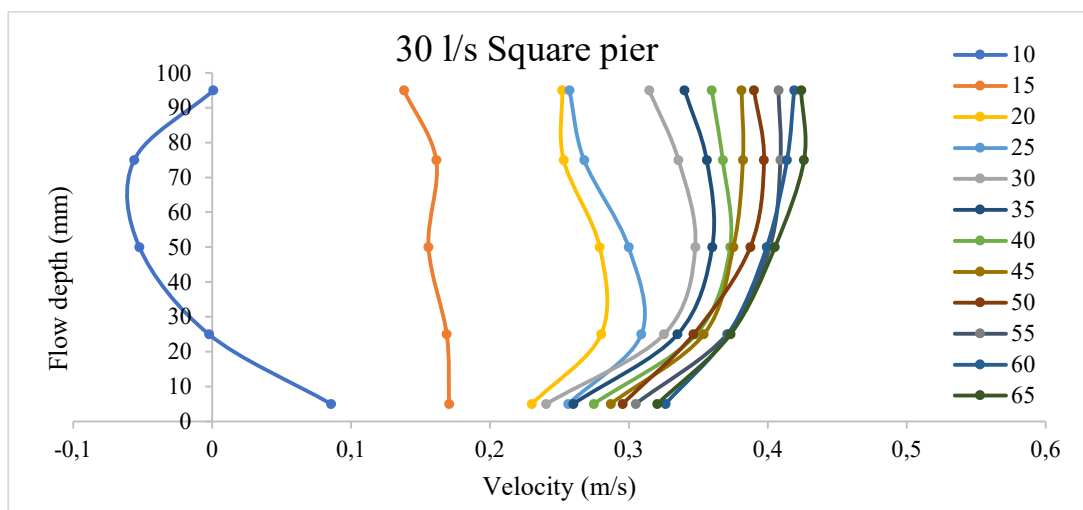
Figure 2. Velocity profiles at the centerline for different longitudinal distances (Q=30 l/s, y= 150 mm)
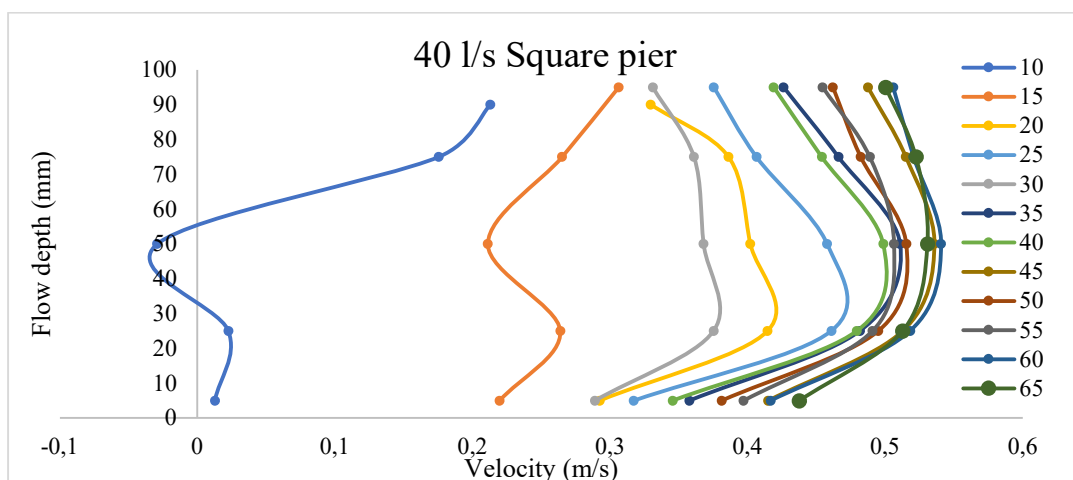
Figure 3. Velocity profiles at the centerline for different longitudinal distances (Q=40 l/s, y= 150 mm)
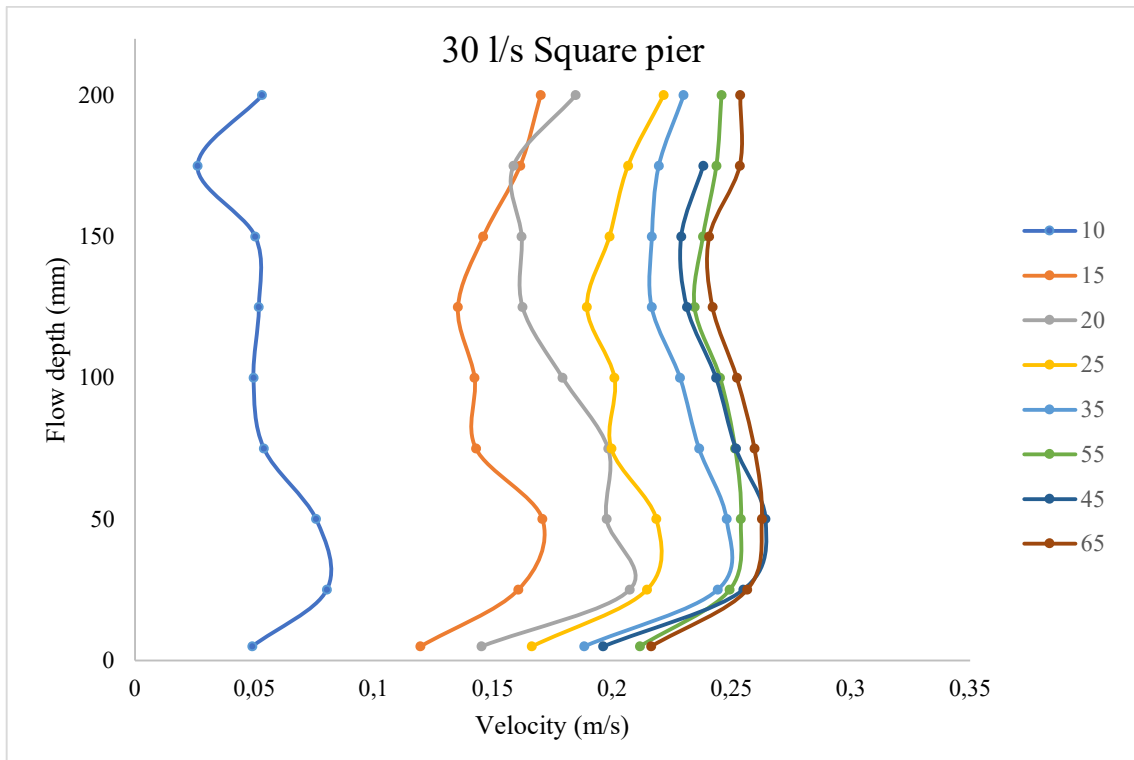
Figure 4. Velocity profiles at the centerline for different longitudinal distances (Q=30 l/s, y= 250 mm)
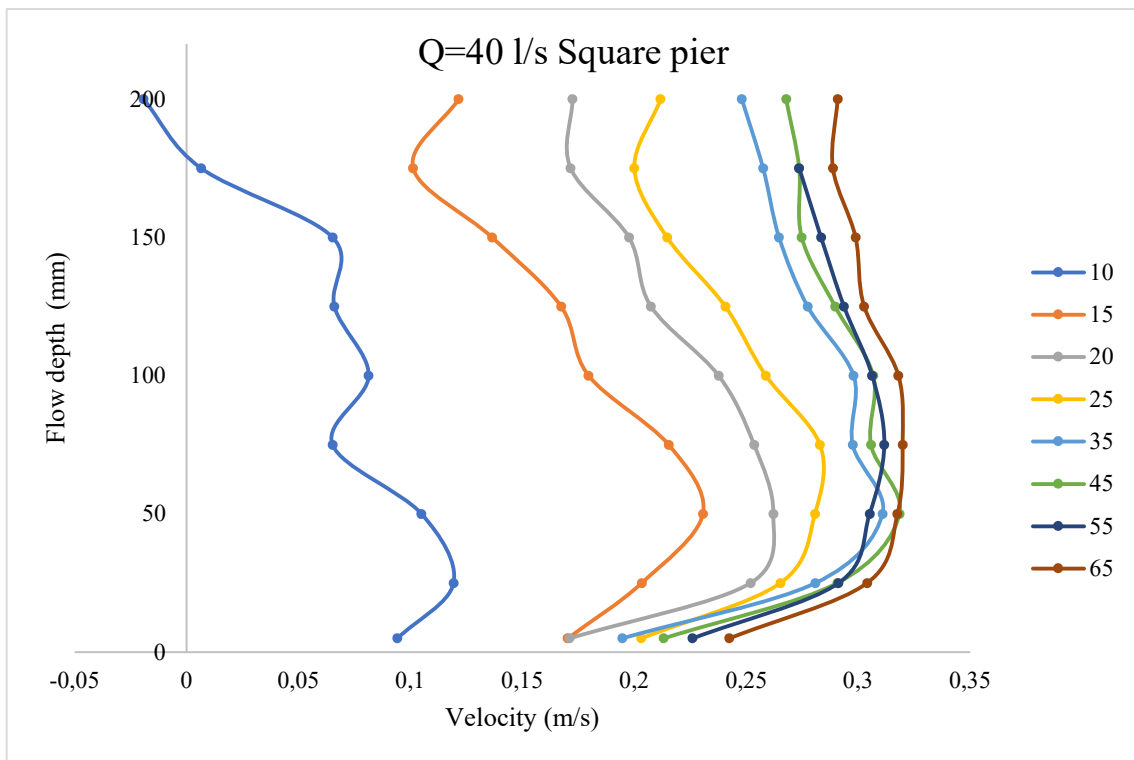
Figure 5. Velocity profiles at the centerline for different longitudinal distances (Q=40 l/s, y= 250 mm)
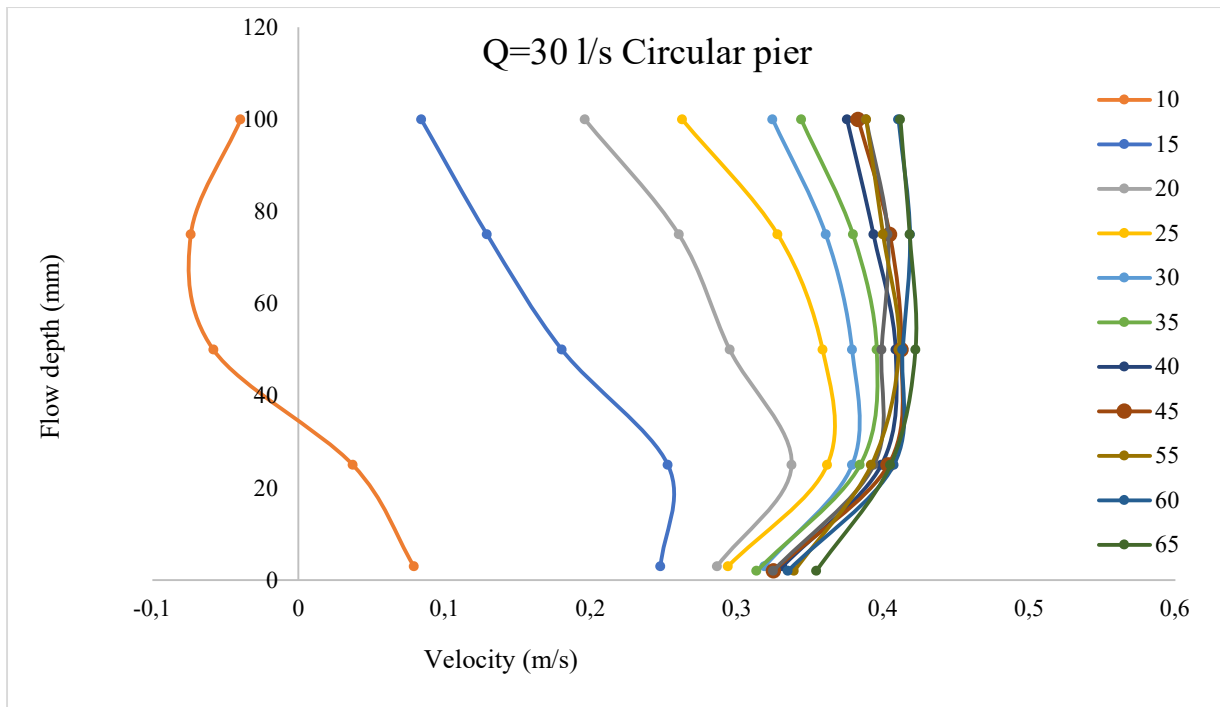
Figure 6. Velocity profiles at the centerline for different longitudinal distances (Q=30 l/s, y= 150 mm)
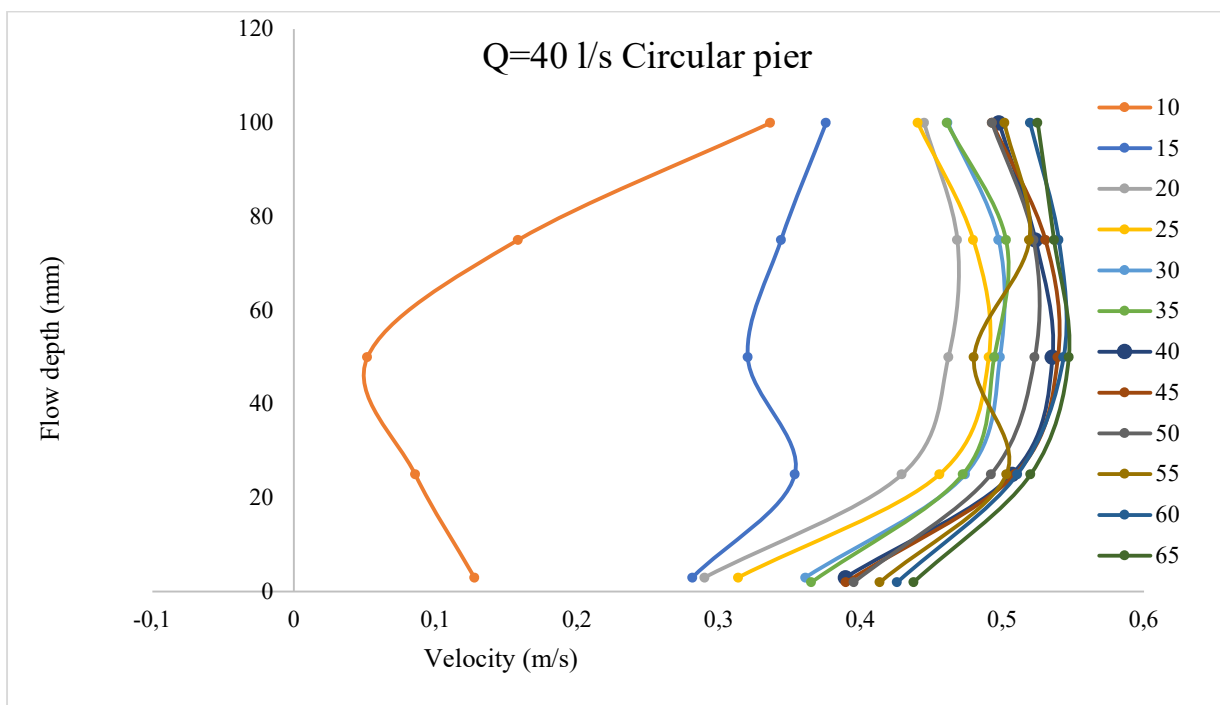
Figure 7. Velocity profiles at the centerline for different longitudinal distances (Q=40 l/s, y= 150 mm)
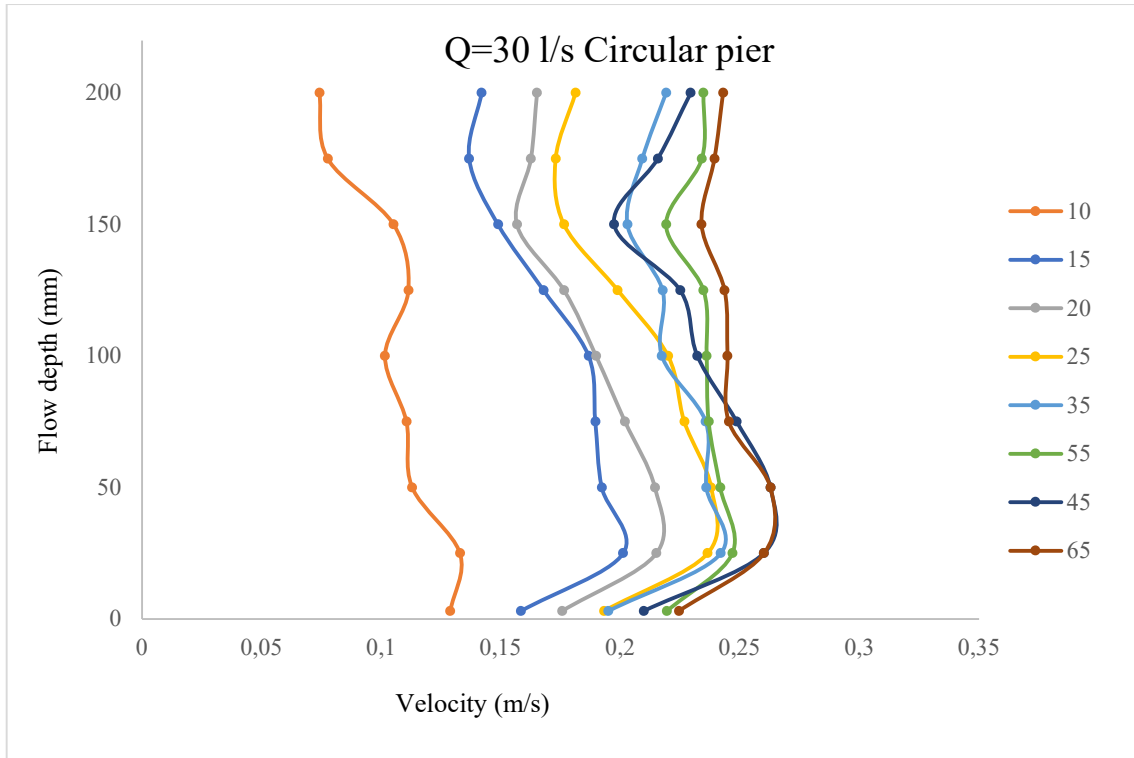
Figure 8. Velocity profiles at the centerline for different longitudinal distances (Q=30 l/s, y= 250 mm)
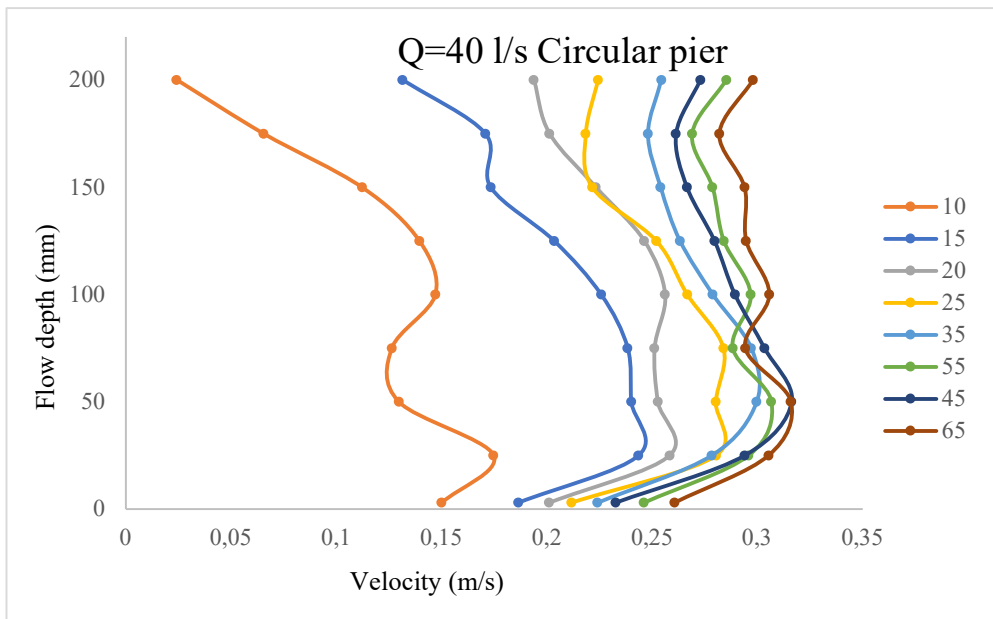
Figure 9. Velocity profiles at the centerline for different longitudinal distances (Q=40 l/s, y= 250 mm)

3.2. Velocity Vectors

The inclination of velocity vectors is a major determinant of erosion at the channel bed. The velocity vectors were drawn, in order to observe the inclination of the flow pattern. The velocity vectors at the centerline (y=250 mm) of the channel are given in Fig 10 and Fig 11 for square and circular bridge piers respectively.
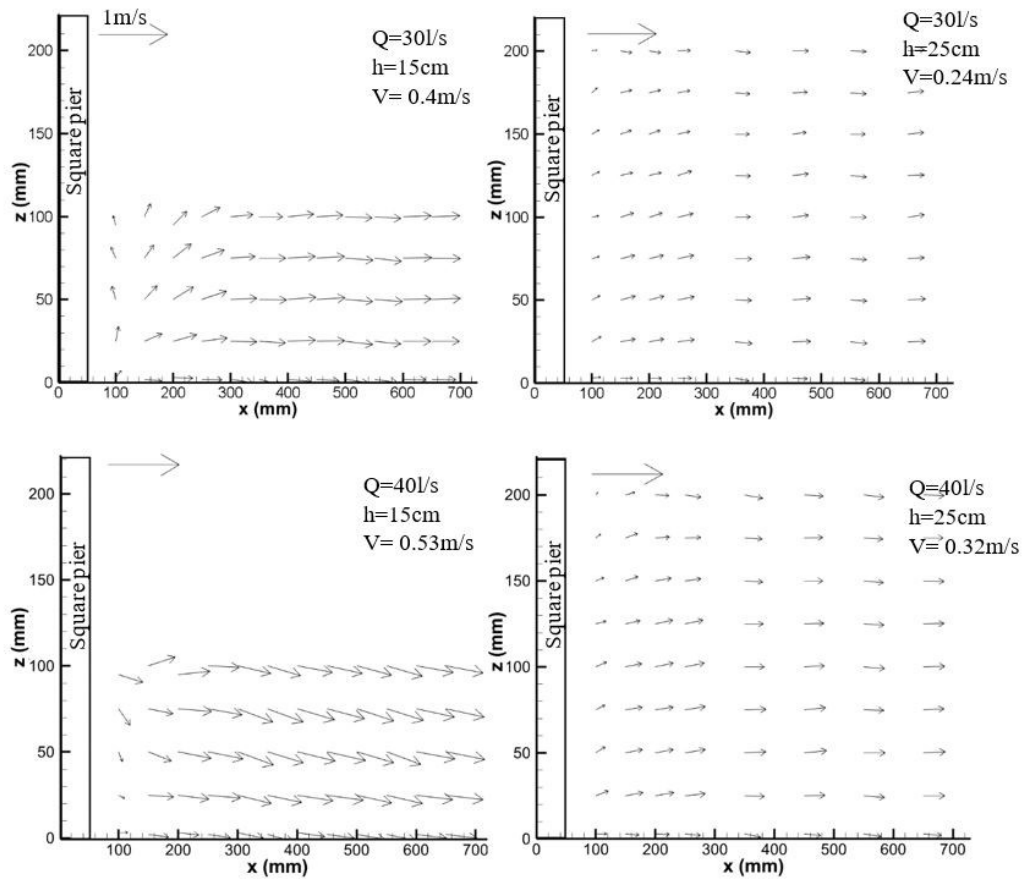
Figure 10. Velocity vectors at the centerline of the channel for square pier

It was observed from the Figure 10 and 11 that as the flow velocity increases, the magnitude of velocity vectors increases. The velocity vectors just behind the pier are inclined upward for all experiments except the ones having highest velocity (Q=40 l/s, h=15cm). In experiments with 15 cm flow depth and 40 l/s flow rate, the inclination of velocity vectors changed from top to down. Moreover, for 40 l/s experiments, velocity vectors at sections further from the pier generally inclined slightly downward.
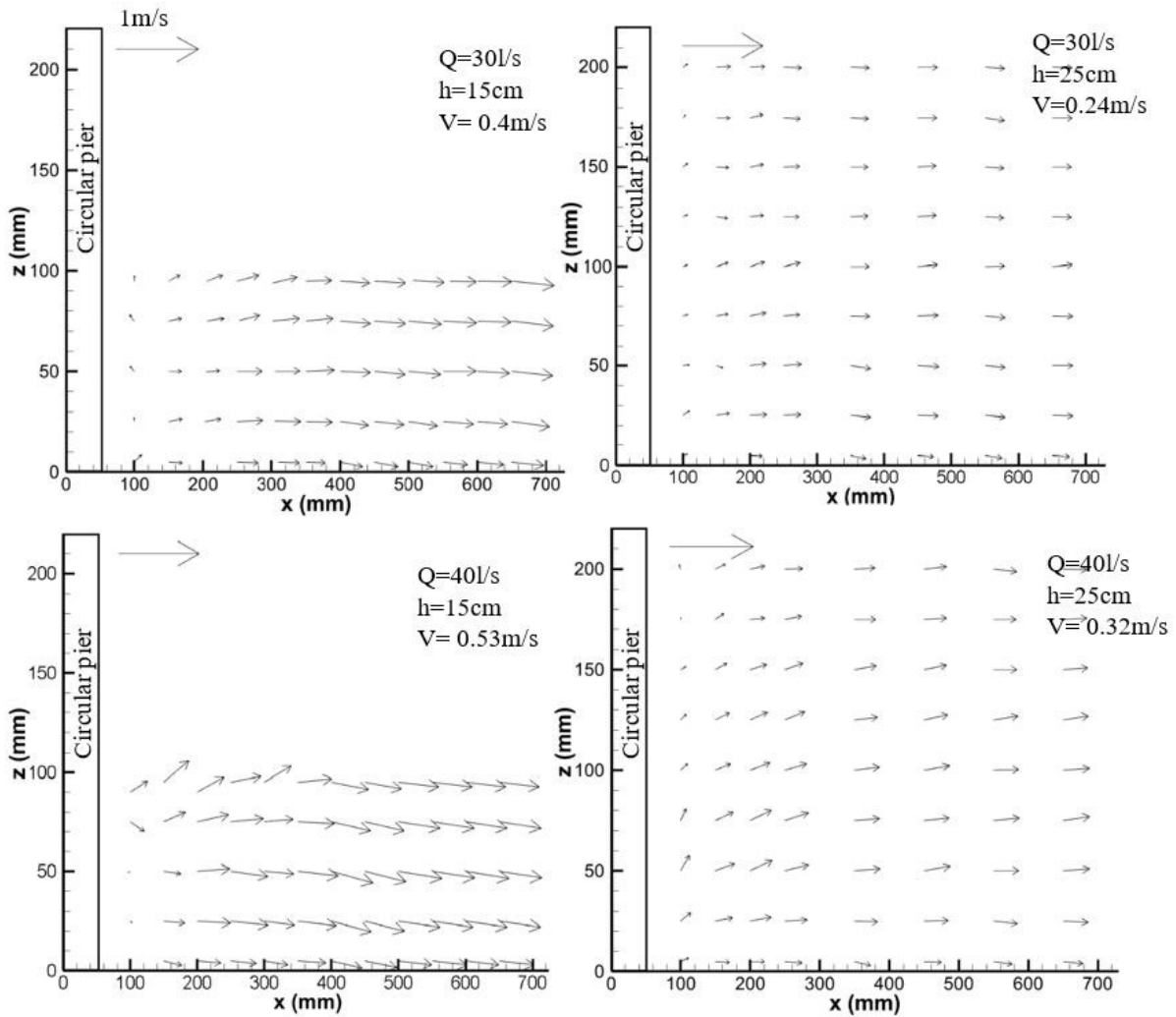
Figure 11. Velocity vectors at the centerline or the channel for Circular pier

3.3. Contour Plots

The contours plots of time averaged longitudinal velocity (u) and vertical velocity (w) for circular and square piers 3 mm above the channel bed are shown in Figure 12. The magnitude of u for the two side of square pier is greater than that of circular pier at the corresponding locations. The reversed flow observed in velocity profile figures are not apparent in contour plots since only near bed velocities is used in contour drawings. The magnitude of velocity that occurred near the base of the pier is approximately 0.1 m/s for experiments having 30 l/s flowrate and 15cm flow depth.
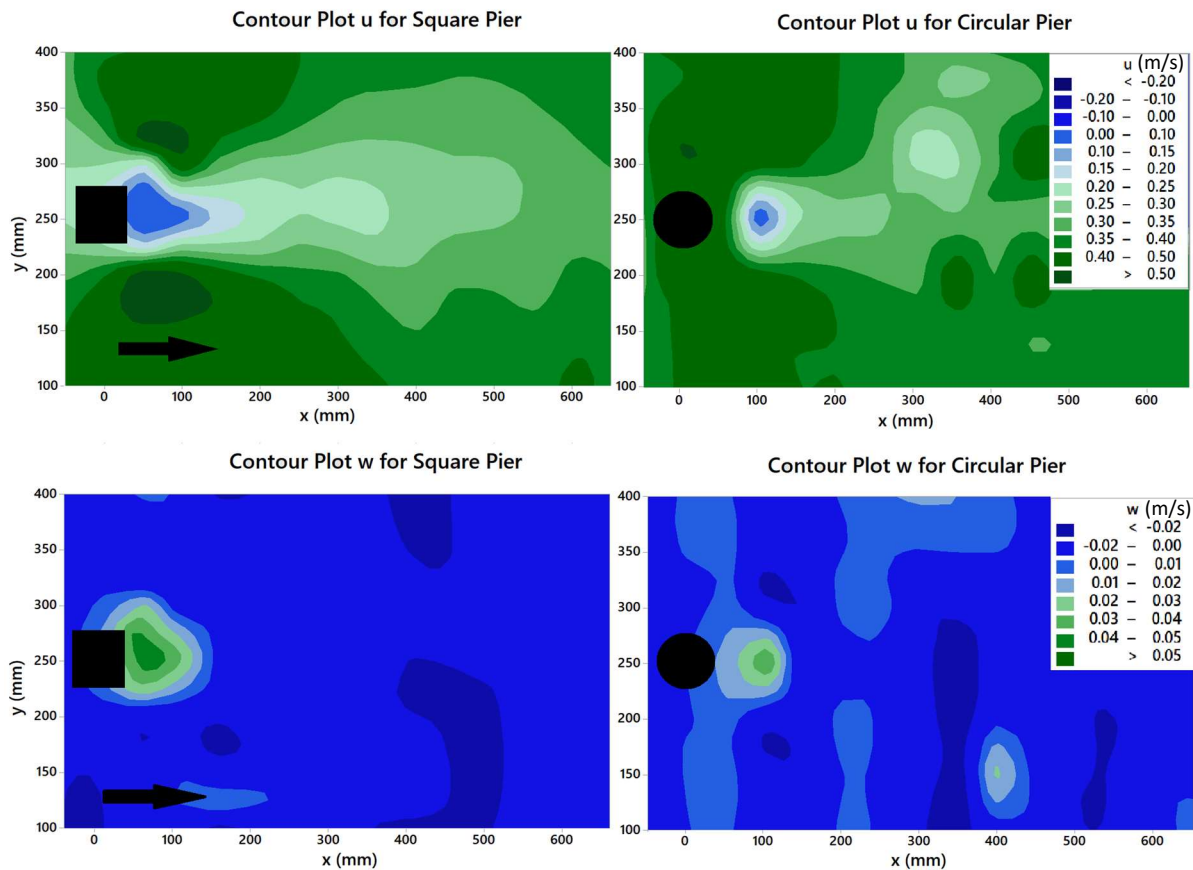
Figure 12. Contour plots of u and w 3 mm above the bed for Q=30l/s, y=15cm

Vertical velocity component (*w*) is the most important velocity component while examining the scouring process. The magnitude of vertical velocity is greater in square piers (Figure 12). In the square bridge pier, maximum vertical velocity occurs closer to the bridge pier than the circular one. Therefore, it might be implicated that scour hole formed in the wake region of the circular pier may be beyond the hole in the wake region of the square pier.

Reynolds stress method were used to calculate the bed shear stresses. Bed shear stresses determined from Reynolds stress method with $\tau_0 = -\rho <u'w'>$ formula, where *u'* and *w'* are velocity fluctuations at x and z directions. Bed shear stresses 3 mm above the channel bed were given in Figure 13. It was seen from the figure that the contour plots of vertical velocity component and the shear stresses are almost similar in geometry with a peak at the downstream side of the pier. The maximum value of the shear stress is 0.96 N/m² at 5 cm downstream of the pier.
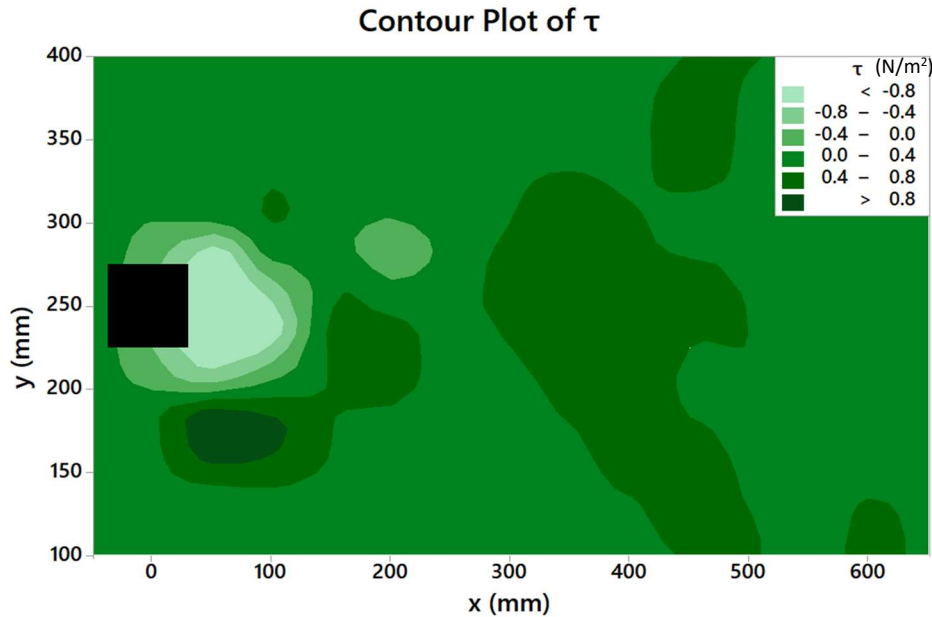
Figure 13. Contour plot of τ 3 mm above the bed for Q=30l/s, y=15cm

4. CONCLUSIONS

An experimental campaign has been devised by using circular and square bridge pier to investigate the effect of pier shape and wake area under steady flow conditions. In this study, an analysis of the 3D flow velocities was presented. The data have been analyzed with different computer programs. Velocity profiles and velocity vectors were drawn. The conclusions of this study are as follows:

-Mean velocities and bed velocities just behind the circular pier is greater than those at the square pier.

-The disturbance due to the presence of pier is approximately 5D for all experiments.

-The reversed velocities were observed at longitudinal velocity profiles next to the pier.

-Maximum bed shear stresses are observed 5 cm upstream of the pier where the w component of velocity is also maximum.

In future research, additional experiments are necessary to verify the present observations. Further experiments may be performed in a channel with sediment in order to investigate the flow behavior inside scour hole.

REFERENCES

Akilli, H., & Rockwell, D. (2002). Vortex formation from a cylinder in shallow water. Physics of Fluids, 14(9), 2957-2967.

Ataie-Ashtiani, B., & Aslani-Kordkandi, A. (2012). Flow field around side-by-side piers with and without a scour hole. European Journal of Mechanics-B/Fluids, 36, 152-166.

Ataie-Ashtiani, B., & Aslani-Kordkandi, A. (2013). Flow field around single and tandem piers. Flow, turbulence and combustion, 90(3), 471-490.

Baker, C. J. (1980). Theoretical approach to prediction of local scour around bridge piers. Journal of Hydraulic Research, 18(1), 1-12.

Baranya, S., Olsen, N. R. B., Stoesser, T., & Sturm, T. (2012). Three-dimensional RANS modeling of flow around circular piers using nested grids. Engineering Applications of Computational Fluid Mechanics, 6(4), 648-662.

Bearman, P. W. (1984). Vortex shedding from oscillating bluff bodies. Annual review of fluid mechanics, 16(1), 195-222.

Beheshti, A. A., & Ataie-Ashtiani, B. (2016). Scour hole influence on turbulent flow field around complex bridge piers. Flow, Turbulence and Combustion, 97(2), 451-474.

Breusers, H. N. C., Nicollet, G., & Shen, H. W. (1977). Local scour around cylindrical piers. Journal of Hydraulic Research, 15(3), 211-252.

Chavan, R., Sharma, A., & Kumar, B. (2017). Effect of downward seepage on turbulent flow characteristics and bed morphology around bridge piers. Journal of Marine Science and Application, 16(1), 60-72.

Dargahi, B. (1989). The turbulent flow field around a circular cylinder. Experiments in Fluids, 8(1-2), 1-12.

Debnath, K., Manik, M. K., & Mazumder, B. S. (2012). Turbulence statistics of flow over scoured cohesive sediment bed around circular cylinder. Advances in water resources, 41, 18-28.

Das, S., Das, R., & Mazumdar, A. (2013). Comparison of characteristics of horseshoe vortex at circular and square piers. Research Journal of Applied Sciences, Engineering and Technology, 5(17), 4373-4387.

Das, S., & Mazumdar, A. (2015). Turbulence flow field around two eccentric circular piers in scour hole. International Journal of River Basin Management, 13(3), 343-361.

Dey, S., & Raikar, R. V. (2007). Characteristics of horseshoe vortex in developing scour holes at piers. Journal of Hydraulic Engineering, 133(4), 399-413.

Duan, J. G., He, L., Fu, X., & Wang, Q. (2009). Mean flow and turbulence around experimental spur dike. Advances in Water Resources, 32(12), 1717-1725.

Ismael, A., Gunal, M., & Hussein, H. (2015). Effect of bridge pier position on scour reduction according to flow direction. Arabian Journal for Science and Engineering, 40(6), 1579-1590.

Kahraman, A., Sahin, B., & Rockwell, D. (2002). Control of vortex formation from a vertical cylinder in shallow water: Effect of localized roughness elements. Experiments in Fluids, 33(1), 54-65.

Kirkil, G., Constantinescu, G., & Ettema, R. (2005). The horseshoe vortex system around a circular bridge pier on equilibrium scoured bed. In Impacts of Global Climate Change (pp. 1-12).

Nogueira, H. I., Franca, M. J., & Ferreira, R. M. (2010). Bridge Piers In Mobile Beds: Visualization And Characterization Of The Flow In The Scour Hole. School Of Civil Engineering, 117.

Pandey, M., Sharma, P. K., Ahmad, Z., Singh, U. K., & Karna, N. (2018). Three-dimensional velocity measurements around bridge piers in gravel bed. Marine Georesources & Geotechnology, 36(6), 663-676.

Qi, Z. X., Eames, I., & Johnson, E. R. (2014). Force acting on a square cylinder fixed in a free-surface channel flow. Journal of Fluid Mechanics, 756, 716-727.

Raudkivi, A. J. (1986). Functional trends of scour at bridge piers. Journal of hydraulic engineering, 112(1), 1-13.

Sahin, B., Ozturk, N. A., & Akilli, H. (2007). Horseshoe vortex system in the vicinity of the vertical cylinder mounted on a flat plate. Flow Measurement and Instrumentation, 18(2), 57-68.

Sarker, M. A. (1998). Flow measurement around scoured bridge piers using Acoustic-Doppler Velocimeter (ADV). Flow measurement and instrumentation, 9(4), 217-227.

Shen, H. W., Schneider, V. R., & Karaki, S. (1966). Mechanics of local scour: supplement, methods of reducing scour. CER; 66-36.

Sumer, B. M., Christiansen, N., & Fredsøe, J. (1997). The horseshoe vortex and vortex shedding around a vertical wall-mounted cylinder exposed to waves. Journal of Fluid Mechanics, 332, 41-70.

Stevens, M. A., Gasser, M. M., & Saad, M. B. (1991). Wake vortex scour at bridge piers. Journal of Hydraulic Engineering, 117(7), 891-904.

Thanh, N. V., Chung, D. H., & Nghien, T. D. (2014). Prediction of the local scour at the bridge square pier using a 3D numerical model. Open Journal of Applied Sciences, 4(02), 34.

Yen, S. C., San, K. C., & Chuang, T. H. (2008). Interactions of tandem square cylinders at low Reynolds numbers. Experimental Thermal and Fluid Science, 32(4), 927-938.

14TH INTERNATIONAL CONFERENCE
ON HYDROSCIENCE & ENGINEERING

MAY 26-27, 2022
IZMİR-TURKEY

ICHE2022
IZMIR, TURKEY

COMPARISON OF LEVENBERG-MARQUART AND BAYESIAN LEARNING ALGORITHMS FOR SUSPENDED SEDIMENT LOAD PREDICTION

Merve Okan

Civil Engineering Department, İzmir University of Economics

İzmir, Turkey

merve.okan@ieu.edu.tr

Aslı Bor

Civil Engineering Department, İzmir University of Economics

İzmir, Turkey

asli.turkben@ieu.edu.tr

ABSTRACT: It is important to predict sediment load in advance for effective management of the reservoirs and river, including determination of the capacity of the dam reservoirs, design of flood protection structures, drought and watershed management, and conservation of natural life. This research presents alternative approaches, in particular, Multilayer Perceptron (MLP) with Levenberg-Marquardt (LM) and Bayesian Regularization (BR) algorithms to estimate the sediment concentration at Aydin Bridge gaging station, using flow discharge, water temperature and rainfall data set obtained from Büyük Menderes Basin in Turkey. The scenarios were assessed using the coefficient of determination (R^2), the mean square error (MSE), and the mean absolute error (RMSE) values. Using trial and error, 4 scenarios were developed during the studies. Our results show that the Levenberg-Marquardt algorithm has the advantages of requiring less iteration and time. However, comparison of the results of the best ANNs of the two different training algorithms shows that the values are generally close, even though the Bayesian Regularization algorithm runs longer with more iterations. This study can guide future studies in flood and water storage capacity for B. Menderes Basin.

KEY WORDS: sediment concentration; artificial neural networks; Levenberg-Marquart; Bayesian Regularization; sediment load prediction

1. INTRODUCTION

Currently, sedimentation is a key environmental issue. It is necessary to accurately estimate the amount of sediment load while determining the reservoir active volumes, as these play an important role in a country's economy, affecting water supply, flood control, irrigation, and energy production. Rivers' sediment load is usually determined by measurements or calculated using sediment transport formulas. Although direct measurement of sediment transport rate is much more reliable, it is neither possible nor economical to set up measurement stations at all desired points to collect long-term data. In addition, the measurement of the bed load is more expensive and complex than the measurement of the suspended load sediment.

There are three main approaches for estimating sediment discharges. The first is based on transport functions in which the total sediment load can be obtained through the sum of bedload and suspended load functions, which is the basis of the procedures of Einstein (1950), Colby & Hembree, (1955), Simons & Şentürk (1977) and Toffaleti (1969). The theoretical application of these formulas is quite complex. The second approach is based on the power concept, in which there is a relationship between the rate of energy available to an alluvial system and the rate of work done by the system in transporting sediment. Examples of this approach include Bagnold (1966), Engelund & Hansen (1967), and Ackers & White (1973). Chang, Simons, & Richardson (1965) computed the total load as

the sum of the bed load and suspended load. While most of these formulas are obtained in laboratory studies, some are developed with actual site data or theoretical methods. However, these have drawbacks, both experimental flume studies and field observations have limitations in predicting sediment transport capacity. Also, most sediment transport equations require extensive knowledge of river topography, flow, and sediment properties. Such formulas may give more or fewer results than expected due to changing conditions in current and other aspects, as a result, none are universally accepted (Yang, 1996). For this reason, many researchers have been involved in efforts to establish the relationship between flowrate, temperature, and sediment discharge in studies on water resources. In the final approach, in recent years, rather than solving the complex differential equations, alternatives such as regression methods, artificial neural networks (ANNs), and genetic algorithm (GA) methods have been proposed to estimate sediment discharge with numerous reliable data bases, which have become valuable in modeling problems in which the relationship between dependent and independent variables is poorly understood.

ANNs models have been widely used in hydraulics and water resources problems, and the results show successful estimation the future flow and sediment discharges, with a greater accuracy than existing empirical equations and traditional regression methods over a wider range of conditions (Bayram, Kankal, Tayfur, & Önsoy, 2014; Bhattacharya, Price, & Solomatine, 2007; Bouzeria, Ghenim, & Khanchoul, 2017; Cigizoglu, 2002; Ciğizoğlu, 2002; Danandeh Mehr & Şorman, 2018; Gao, Mu, Wang, & Li, 2011; Jain, 2001; Kisi, Dailr, Cimen, & Shiri, 2012; Nagy, Watanabe, & Hirano, 2002; Oehler, Coco, Green, & Bryan, 2012; Pektaş & Doğan, 2015; Raghuwanshi, Singh, & Reddy, 2006; Tayfur, 2002; Yitian & Gu, 2003).

The main objective of this study is to compare the accuracy of the artificial intelligence methods, feed-forward backpropagation ANNs techniques (Levenberg-Marquardt (LM) and Bayesian Regularization algorithms (BR)). Thus, for this case study, it was decided to select Aydin Bridge gauging station on the B. Menderes River, one of the major water resources of Turkey. Data used in this research is from the Aydin Bridge gauging station between 09.02.2006 and 17.09.2019. The optimal scenario was identified from among 4 different scenarios developed for the forecasts. For general performance evaluation, BR displayed the best performance when discharge, Q, and water temperature, T, are used inputs and the network is created with 3 hidden neurons.

2. METHODOLOGY

2.1. Artificial Neural Networks

Artificial neural networks (ANNs) are a modeling technique generally used for the solution of problems that cannot be created with mathematical models or are very difficult to define. Water resources studies exhibit physically non-linear behavior, resulting in complex solutions to problems. In the solution of such nonlinear problems, ANNs give good results, and need only numerical information. In engineering, real-time observations provide better understanding of complex real-life systems but it is difficult if not impossible to obtain real-time data in the field. ANNs are therefore especially helpful in the field of prediction and forecasting in complex settings. These powerful mathematical models operate as a black-box, and are flexible, and adaptive tools able to capture and identify significant structures in the data. Their computing abilities have been proven in the fields of forecast and estimation, pattern recognition, and optimization (Adeli, 2001). ANNs can solve most real-world problems considered to be non-linear.

ANNs determine the output data corresponding to the input data encountered. The input and output data do not need to be linear. ANNs parameters can be repeatedly trained to provide appropriate solutions to changing problem. ANNs identify patterns between input and output data sets and can estimate output values according to the training and learning processes. This method allows the identification of complex non-linear relationships. Multi-layer neural network architecture is the most commonly used, and is effective in dealing with non-linear relationships. A feed-forward multi-layer neural network consists of an input layer, hidden layer, and an output layer, with a certain number of inputs, hidden and output neurons. There are one or more hidden layers in between the input and the

output layers. Here, each incoming input value is added by multiplying by its own weight. The artificial neuron receives can be shown by the equation;

$$net_j = \sum_{i=1}^{n} w_{ij} x_i + b_j \tag{1}$$

where; net_j is the summation of the weighted input for the jth neuron; x_i is the input from the ith neuron to the jth neuron; w_{ij} is the weight from the ith neuron in the previous layer to the jth neuron in the current layer; and b_j is the threshold value, also called the bias, associated with node j (Figure 1). In ANNs, the bias of the node must be exceeded before it can be activated. The multi-layer neural network architecture can be seen in Figure 1 below. There are connections which include weights between the input layer and the middle or hidden layer, and weights are usually determined through training the system. The hidden layer sums the weighted inputs and uses the transfer function to create an output value. The transfer function is a relationship between the internal activation level of the neuron (called activation function) and the outputs. Because ANNs aim to minimize the difference between the network output and the observed data, training is the process of weight adjustment until a desirable outcome is obtained with least squares residuals.
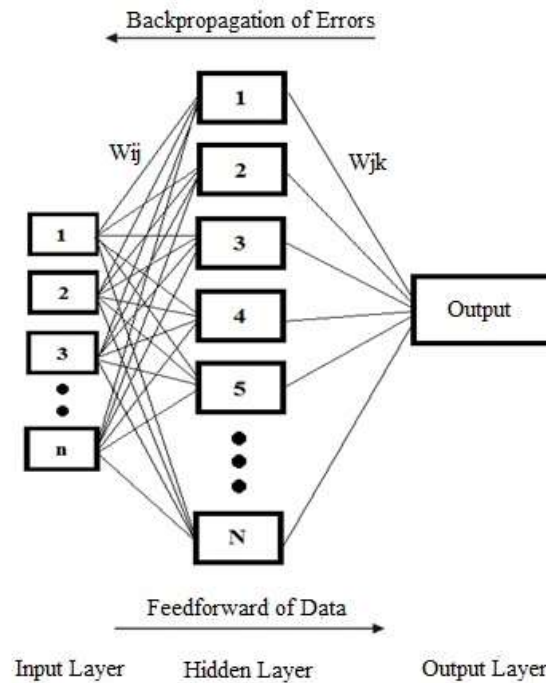
Figure 1. Architecture for Multi-Layer Perceptions (MLP).

2.1.1. Levenberg-Marquardt Algorithm

The Levenberg-Marquardt (LM) algorithm is a least squares calculation method and is a simplified version of the classical Newton method used in training the multilayer ANN model. The Jacobian matrix is obtained from the first derivatives of the network errors according to the weights and is denoted by J in the equation. At the backpropagation stage of the network error, firstly, the gradient of the network, $\nabla E(w)$ is calculated by using the transposition of the Jacobian matrix and the network errors.

$$\nabla E(w) = J^T(w)\,(T_i - Y_i) \tag{2}$$

where; T_i is the expected value, Y_i is the output, $e = T_i - Y_i$ is the error. After calculating the gradient of the network, the vector change in the network weights is determined by multiplying the inverse of the Hessian matrix by the gradient of the network. The network is trained with the LM

algorithm, but the weight change of the network is calculated as in Equation (3) and the weight of the network is updated as shown in Equation (4).

$$\Delta w = -\,[\,J^T(w)\,J(w)\,+\,\mu\,I\,]^{-1}\nabla E(w) \tag{3}$$

where; μ is the Marquardt parameter and I is the Unit matrix.

$$w_{new} = w_{old} + \Delta w \tag{4}$$

In the LM algorithm, μ parameter is defined numerically. If μ approaches zero, the method continues to function as in Newton's algorithm; if μ is a large number, the method becomes the gradient reduction method (Chen, Han, Au, & Tham, 2003; Hagan & Menhaj, 1994).

2.1.2. Bayesian Regularization Algorithm

The Bayesian regularization algorithm is based on the probability distribution of predictions made by the network and was developed by MacKay (1992). It involves modifying the commonly used performance function, such as the mean sum of squared errors (MSE). The BR algorithm aims to improve the generalization ability of the model. In the training phase, the term E_d, which is the objective function in Equation (5), is expanded to improve the generalization ability of the network (Xu et al., 2006);

$$E_d = \sum_{i=1}^{n}(T_i - Y_i)^2 \tag{5}$$

$$F = \beta E_d + \alpha E_w \tag{6}$$

where; n is the number of data set, T_i is the target value, Y_i is the output value created by model, E_d is the sum of squares of the network error, E_w is the sum of squares of the network weights and F is the regularized objective function. The α and β parameters should be estimated and adjusted according to the BR algorithm. If $\alpha \ll \beta$, the BR training algorithm shrinks errors further. If $\alpha \gg \beta$, it will emphasize the reduction of training weight size, thus producing a more accurate network response. According to the BR rule, the posterior distribution of the weights of ANN can be updated using Equation (7):

$$P(w|D,\alpha,\beta,M) = \frac{P(D|w,\beta,M)\times P(w|\alpha,M)}{P(D|\alpha,\beta,M)} \tag{7}$$

where; M is the specific ANN architecture used and D is the training set consisting of input and target data. In the implementation of the BR algorithm, optimum weights should maximize the posterior probability, $\boldsymbol{P}(w|D,\alpha,\boldsymbol{P},M)$, because maximizing the posterior probability of the weights corresponds to minimizing the regularized objective function ($F = \beta E_d + \alpha E_w$) (Foresee & Hagan, 1997; Kayri, 2016). Eventually, α, β, and the weights are initialized, then, one step of LM algorithm is performed in an attempt to minimize the regularized objective function. This is followed by the calculation of the effective number of parameters reducing the error function, and accordingly, new predictions for α and β. Finally, iterations continue until convergence (Foresee & Hagan, 1997; Xu et al., 2006).

3. APPLICATION

There are different approaches in the literature evaluating the performance of empirical formulas or soft computing methods. A basic method is finding the root mean squared error (RMSE), which is sensitive to outliers simply by taking the square root, and this is expressed as follows.

The coefficient of determination R^2 is another common metric utilized to evaluate the performance of formulas. It is defined as the square of the correlation coefficient.

$$\text{RMSE} = \sqrt{\frac{\sum_{i=1}^{n}\left(X_{obs,i} - X_{model,i}\right)^2}{n}} \tag{8}$$

$$\text{R}^2 = 1 - \frac{\sum_{i=1}^{n} X_{obs,i} - X_{model,i}{}^2}{\sum_{i=1}^{n}(X_{obs,i} - \overline{X_{model,i}})^2} \tag{9}$$

where; $X_{obs,i}$ and $X_{model,i}$ are the observed and modeled i values (at time t), $\overline{X_{model,i}}$ is the average of model values and n is the number of data.

This study aims to estimate the suspended sediment concentration (C) data obtained from B. Menderes River on E07A006 Aydin Bridge gauging station based on discharge (Q), water temperature (^{0}C), and precipitation data (P). A well-known artificial intelligence method is used, i.e., multi-layer feed-forward artificial neural network trained with two backpropagation algorithms, LM and BR. This approach involved 100 data points for each parameter taken at specific times between 09.02.2006 and 17.09.2019. The maximum, minimum, mean, standard deviation, skewness and the coefficient of variation of the data are given in Table 1, where Q is discharge (m³/s), T, water temperature (^{0}C), P, precipitation (mm/day) and C, sediment concentration (ppm).

Table 1. Statistic parameters of data utilized for ANN models distributed according to training algorithms (a) Levenberg Marquardt (b) Bayesian Regularization.

(a) Levenberg-Marquardt

Dataset		Data	Min	Max	Mean	Standard Deviation	Skewness	The coefficient of variation
Validation Training	Inputs	Q	0.373	163	31.22	30.55	2.3639	0.9784
		T	8	27	17.99	5.37	-0.1155	0.2986
		P	0	29.92	1.90	5.14	3.6985	2.7089
	Output	C	35.4	13334.8	541.70	1553.67	7.7886	2.8681
	Inputs	Q	19.7	47.2	33.92	10.18	-0.1907	0.3000
		T	17	26	21.00	4.18	0.5122	0.1992
		P	0	2.5	0.96	1.32	0.6192	1.3709
	Output	C	118.73	365.31	236.99	113.41	0.3132	0.4785
Testing	Inputs	Q	1.474	76.9	22.16	20.75	1.5744	0.9362
		T	7	29	18.10	6.55	-0.1664	0.3620
		P	0	17.96	1.13	4.00	4.3245	3.5344
	Output	C	66.99	1036.03	289.75	282.05	1.8432	0.9734

(b) Bayesian Regularization

Dataset		Data	Min	Max	Mean	Standard Deviation	Skewness	The coefficient of variation
Training	Inputs	Q	0.373	163	31.39	29.66	2.3987	0.9449
		T	8	27	18.18	4.99	-0.1455	0.2935
		P	0	29.92	1.84	5.33	3.8166	2.7126
	Output	C	35.4	13334.8	522.66	1505.75	8.0391	2.8809
Testing	Inputs	Q	1.474	76.9	22.16	20.75	1.5744	0.9362
		T	7	29	18.10	6.55	-0.1664	0.3620
		P	0	17.96	1.13	4.00	4.3245	3.5344
	Output	C	66.99	1036.03	289.75	282.05	1.8432	0.9734

ANNs were created by updating the advanced script file produced by Neural Network Fitting App (nftool) in the MATLAB environment. For training with LM algorithm, the data was divided into

three sets: training, validation, and testing, and for training with BR algorithm, divided into two sets. The first 75% of the data series were selected as the training set, the next 5% were taken as the validation set, and the remaining 20% were used for testing for the LM algorithm. For the BR algorithm, the first 80% of the data series were selected as the training set, and the next 20% were taken as the test. The data was sequentially ordered from the first to last date to be able to forecast the suspended sediment concentration. The model scenarios are represented in the Table 2, in which inputs and output can be observed.

Table 2. Scenarios.

Scenario	Inputs	Output
1	Q	C
2	Q,P	C
3	Q,T	C
4	Q,P,T	C

Training was conducted according to the training parameters. The μ was increased by increase factor for μ until the change in performance led to a reduced performance value. Then, the change was performed in the network, and μ was decreased by the decrease factor for μ. Training finished when one of the following occurred: the maximum number of epochs was reached, performance was minimized to the goal, the performance gradient decreased below minimum performance gradient, or μ exceeded maximum value for μ. In addition, while training was conducted with LM algorithm, training finished when validation performance increased more than maximum validation failure times since the last time it decreased while using validation. However, validation stops were not utilized, and this was made possible by arranging maximum validation failures as infinite for BR algorithm, allowing training to proceed until an optimal combination of errors and weights were obtained. Maximum number of epochs to train was taken as 5000, performance goal which is the mean squared error, MSE, for all the data as 0. For LM training algorithm, the number of maximum validation failures was taken as 6, and for BR training algorithm as infinite. Maximum time to train in seconds was taken as infinite, minimum performance gradient as 10^{-7}. For LM algorithm, initial μ was taken as 0.001, and for BR algorithm, the Marquardt adjustment parameter, as 0.005. The decrease factor for μ was as 0.1, increase factor for μ as 10, maximum value for μ as 10^{10}.

For activation function, tangent-sigmoid was used, and performance function was taken as mean squared error, MSE, function during the process. Gradient descent with momentum weight and bias learning function was used with a learning rate of 0.01 and momentum constant 0.9. During the process of creating ANNs, the input and target data were normalized from its original range to the range [-1 1].

While training the networks, Levenberg-Marquardt (LM) and Bayesian Regularization (BR) algorithms were used. For both, the number of hidden neurons was chosen as the odd numbers from 3 to 21, respectively, and 1000 artificial neural networks (ANNs) for LM, and 50 ANNs for BR were created for each selected hidden number of neurons. The root mean squared error (RMSE) and determination coefficient (R^2) results of both the 1000 ANNs for LM and the 50 ANNs for BR calculated were averaged for each selected number of hidden neurons, and the optimal hidden neuron number was selected, considering the test results of the smallest mean RMSE and largest mean R^2 values. This process was repeated for each scenario. Lower scores are better in case of RMSE and MAE, while scores closer to 1 are better for R^2.

4. RESULTS

1000 networks for LM and 50 networks for BR were created for each hidden number of neurons and the optimal number of hidden neurons was chosen according to their average performance values. This step was followed because all networks are different, despite all being created with the same number of hidden neurons. During the creation of each network, changes occur in the weight and threshold values given to the network, therefore, networks vary in number of hidden neurons, and thus, performance. However, when the average performance values of 1000 networks for LM and 50

networks for BR were investigated, it was observed that error values and performance values of the ANNs created according to each number of hidden neurons were very similar, but not identical, and therefore, evaluation was conducted on the general performance according to the number of hidden neurons, and the optimal number was selected for each scenario. Eventually, 1000 networks for LM and 50 networks for BR were created, their performance was averaged, and the results of the overall performance were determined. Table 3 and Table 4 give the mean RMSE and R^2 values of LM and BR algorithms for the selected best number of hidden neurons for each scenario. The closer the root mean square error values to 0 and the closer the R^2 values to 1, the closer the predicted values converge to the actual results.

The average performance values of the ANNs with the best number of hidden neurons for LM and BR were examined according to the test results of the smallest RMSE and largest R^2 values for each scenario. It can be seen that the best performance is 1st scenario with 5 hidden neurons for LM and the best performance is 3th scenario with 3 hidden neurons for BR.

Table 3. Average performance statistics of the Levenberg-Marquardt algorithm according to the best hidden neuron number.

Levenberg-Marquardt

Scenario	Scenario Input	Best # of hidden neurons	Training		Testing	
			RMSE (ppm)	R^2	RMSE (ppm)	R^2
1	**Q**	**5**	**406.7**	**0.91**	**141.7**	**0.87**
2	Q,P	5	634.2	0.81	266.9	0.69
3	Q,T	3	711.8	0.79	307.1	0.73
4	Q,P,T	3	655.0	0.78	262.7	0.71

Table 4. Average performance statistics of the Bayesian Regularization algorithm according to the best hidden neuron number.

Bayesian Regularization

Scenario	Scenario Input	Best # of hidden neurons	Training		Testing	
			RMSE (ppm)	R^2	RMSE (ppm)	R^2
1	Q	5	143.2	0.99	86.5	0.90
2	Q,P	5	132.9	0.99	86.8	0.90
3	**Q,T**	**3**	**136.0**	**0.99**	**68.1**	**0.94**
4	Q,P,T	5	116.1	0.99	74.6	0.94

Better performance has been generally observed for networks created with smaller hidden neuron numbers, with decreasing performance as the number of hidden neurons increases. Networks created with a hidden neuron number greater than 21 were not preferred because the average performance was observed to decrease when trained with both training algorithms. Therefore, the number of hidden neurons between 3 and 21 was determined in the application actualized for both of two algorithms.

It is also noteworthy that ANNs did not give successful results when the discharge is excluded as input, therefore, no scenario without discharge input is presented in this study.

1000 networks with LM and 50 networks with BR, created according to the best number of hidden neurons, were individually examined and one each was selected from the 1000 networks for LM the 50 networks for BR. These had, according to the test results, the smallest RMSE and largest R^2 values

for each scenario. The performance values of these selected best ANNs with the best number of hidden neurons for LM and BR for each scenario are shown in Table 5 and Table 6, respectively.

Figures 1 and 2 display the observed and predicted sediment concentration (ppm) values, which are target and output, respectively, with the best ANN created by the LM and the BR algorithms during both training and test periods; these are shown both as scatter plots and as continuous graphs. These best ANN models for both the LM and the BR algorithms have R^2 values of 0.99 for training, and 0.94 for testing, respectively. It is seen that these values are very close. In Figure 1, the diagonal blue line for training and green line for testing that runs between the predicted and observed values represents the case where there is a slight difference between these values.

Table 5. Statistics of the Levenberg-Marquardt algorithm according to best ANNs with the best hidden neuron.

Scenario	Scenario Inputs	Best # of hidden neurons	Training		Testing	
			RMSE (ppm)	R²	RMSE (ppm)	R²
1	Q	**5**	145.6	0.99	77.5	0.92
2	Q,P	5	147.3	0.99	78.6	0.92
3	Q,T	3	139.6	0.99	69.8	0.94
4	**Q,P,T**	**3**	**136.5**	**0.99**	**69.6**	**0.94**

Table 6. Statistics of the Bayesian Regularization algorithm according to best ANNs with the best hidden neuron.

Scenario	Scenario Inputs	Best # of hidden neurons	Training		Testing	
			RMSE (ppm)	R²	RMSE (ppm)	R²
1	Q	5	143.0	0.99	86.3	0.90
2	Q,P	5	138.2	0.99	83.5	0.91
3	**Q,T**	**3**	**136.0**	**0.99**	**68.1**	**0.94**
4	Q,P,T	5	114.6	0.99	68.3	0.94

(a)
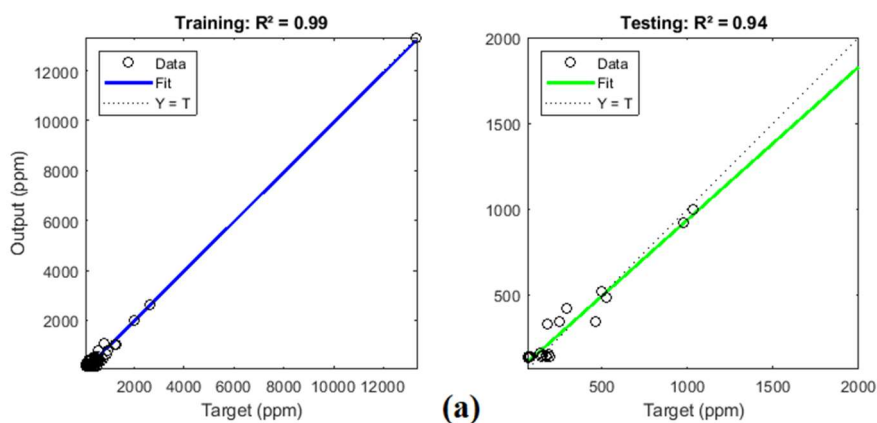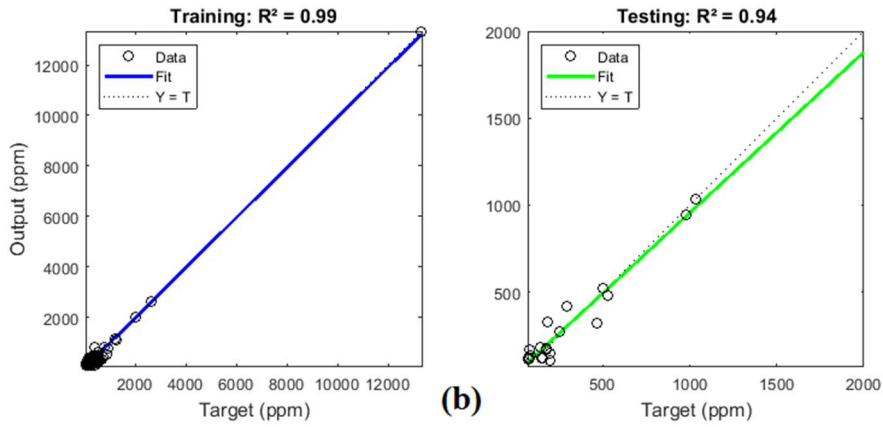
Figure 2. Regression of Target and Output Data for (a) Levenberg-Marquardt Algorithm and (b) Bayesian Regularization
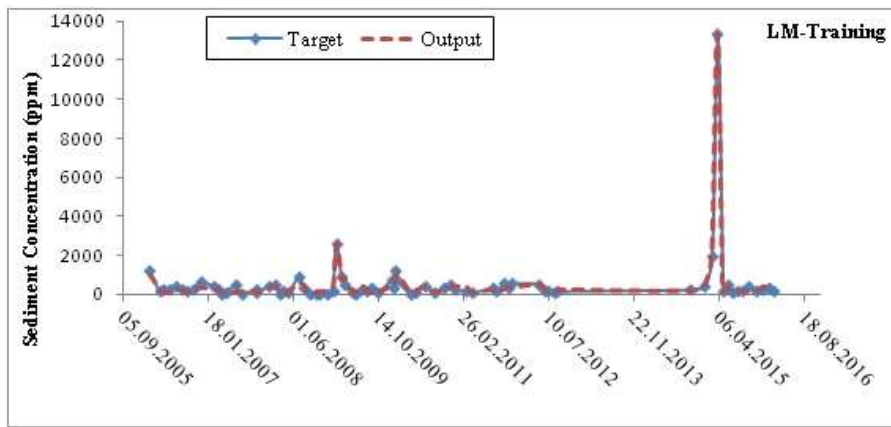
(a)
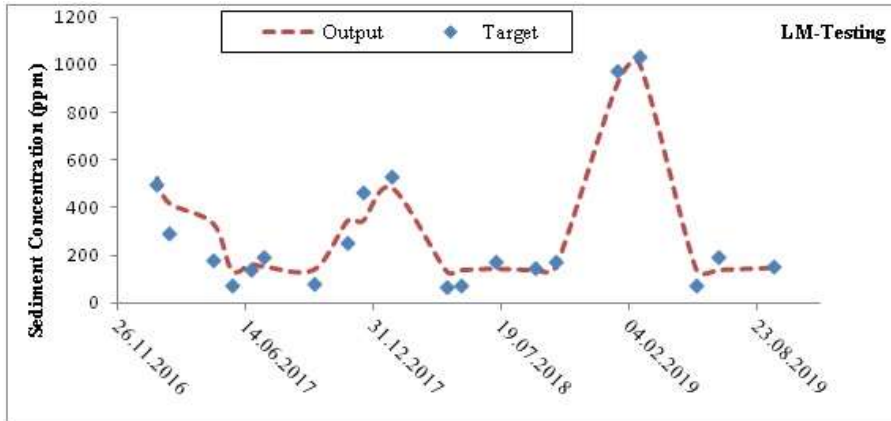
(b)
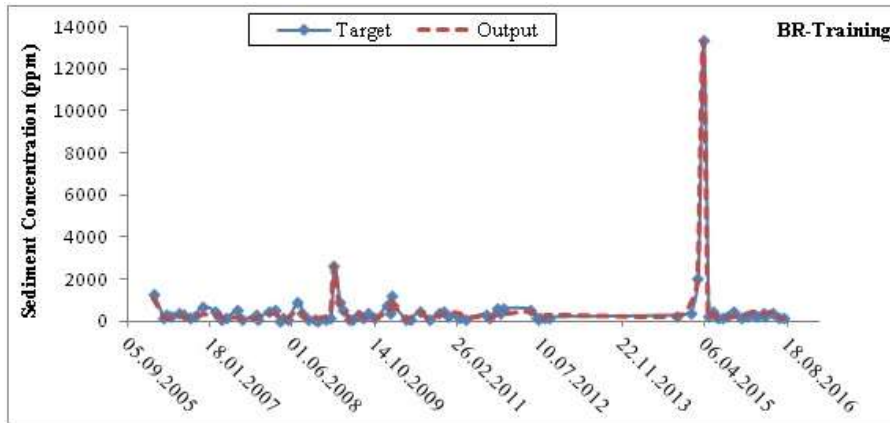
(c)
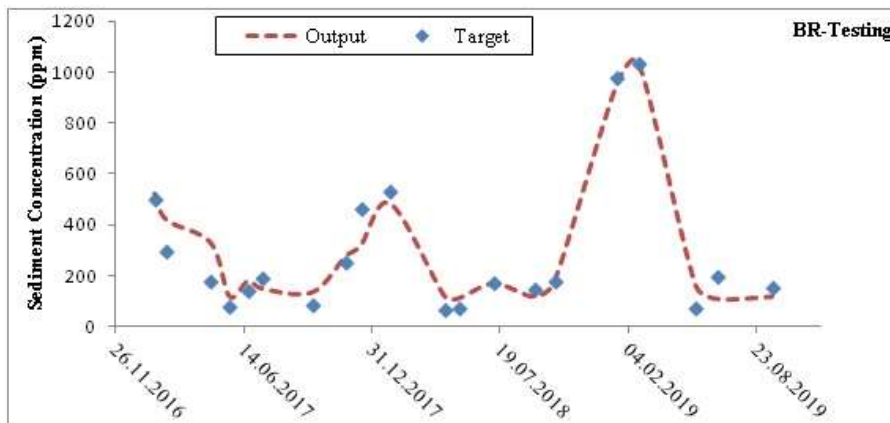
(d)

Figure 3. Comparison of Target and Output Data for (a) Levenberg-Marquardt-Training Algorithm and (b) Levenberg-Marquard- Testing (c) Bayesian Regularization-Training (d) Bayesian Regularization- Testing

According to the test results of the smallest RMSE and largest R^2 values for each scenario, it can be seen that, for LM, the best performance is 4th scenario with 3 hidden neurons, and for BR, the best is 3rd scenario with 3 hidden neurons.

The results in Table 5 and Table 6 for the best ANNs for each scenario show that performance of ANNs can be improved by including precipitation and water temperature data as inputs for predicting sediment concentration. However, the average performance values of ANNs in Table 3 reveal that including these additional data can cause a decrease in general performance while training with LM algorithm.

Table 7. The average performance comparison of best scenarios created by the Levenberg-Marquart (LM) and the Bayesian Regularization (BR) algorithms with best number of hidden neurons.

Training Algorithm	Scenario Inputs	Best # of hidden neurons	Training		Testing	
			RMSE (ppm)	R^2	RMSE (ppm)	R^2
LM	Q	5	406.7	0.91	141.7	0.87
BR	**Q,T**	**3**	**136.0**	**0.99**	**68.1**	**0.94**

A comparison of average RMSE and R^2 values for the selected best scenarios shows that BR produced more accurate results. For general performance evaluation, BR displayed the best performance when discharge, Q, and water temperature, T, are used inputs and the network is created with 3 hidden neurons.

Table 8. The performance comparison of best scenarios created by the Levenberg-Marquart (LM) and the Bayesian Regularization (BR) algorithms with best number of hidden neurons.

Training Algorithm	Scenario Inputs	Best # of hidden neurons	Training RMSE (ppm)	Training R²	Testing RMSE (ppm)	Testing R²
LM	Q,P,T	3	136.5	0.99	69.6	0.94
BR	Q,T	3	136.0	0.99	68.1	0.94

5. CONCLUSIONS

The comparison for the results of the best scenarios for different algorithms and the best ANNs with the best number of neuron number presented in Table 8 reveals that LM and BR training algorithms had very similar performances.

LM algorithm has advantages, such as needing less iteration, and less time. However, although the BR algorithm took longer with more iteration, the results of the best ANNs for each training algorithm show similar values. Nevertheless, in general performance, given in Table 3 and Table 4, reveal that training ANNs with BR algorithm generated much better performance. For BR algorithm, 50 networks were sufficient to make a generalization in order to compare performance of ANNs, but for the LM algorithm, 1000 networks were needed. The reason for this large number of networks was that the individual performance of each ANNs fluctuated when less than 1000 iterations were conducted, making it difficult generalize and select the best number of hidden neurons. During training with BR algorithm, there was much less fluctuation; in fact, for the selected best scenario with the best number of hidden neurons, training and testing achieved the same performance values, both RMSE and R², for each individual ANN of 50 networks. For general performance evaluation, BR displayed the best performance when discharge, Q, and water temperature, T, are used inputs and the network is created with 3 hidden neurons.

REFERENCES

Ackers, P., & White, W. R. (1973). Sediment transport: New approach and analysis. *ASCE Journal of the Hydraulics Division*, *99*(HY11).

Adeli, H. (2001). Neural networks in civil engineering: 1989-2000. *Computer-Aided Civil and Infrastructure Engineering*, *16*(2), 126–142. https://doi.org/10.1111/0885-9507.00219

Bagnold, R. A. (1966). *An Approach to the Sediment Transport Problem From General Physics*. Washington: PHYSIOGRAPHIC AND HYDRAULIC STUDIES OF RIVERS GEOLOGICAL SURVEY PROFESSIONAL PAPER 422-I UNITED STATES GOVERNMENT PRINTING OFFICE.

Bayram, A., Kankal, M., Tayfur, G., & Önsoy, H. (2014). Prediction of suspended sediment concentration from water quality variables. *Neural Computing and Applications*, *24*(5), 1079–1087. https://doi.org/10.1007/s00521-012-1333-3

Bhattacharya, B., Price, R., & Solomatine, D. (2007). A Machine Learning Approach to Modeling Sediment Transport. *Journal of Hydraulic Engineering*, *133*(4), 440–450. https://doi.org/10.1061/(ASCE)0733-9429(2007)133:4(440)

Bouzeria, H., Ghenim, A. N., & Khanchoul, K. (2017). Using artificial neural network (ANN) for prediction of sediment loads, application to the Mellah catchment, northeast Algeria. *Journal of Water and Land Development*, *33*(IV–VI), 47–55. https://doi.org/10.1515/jwld-2017-0018

Chang, F. M., Simons, D. B., & Richardson, E. V. (1965). *Total Bed-Material Discharge in alluvial Channels: Studies of Flow in Alluvial Channels*. (Geological Survey Water-Supply Paper 1498-I).

Chen, T. C., Han, D. J., Au, F. T. K., & Tham, L. G. (2003). Acceleration of Levenberg-Marquardt Training of Neural Networks with Variable Decay Rate. *Proceedings of the International Joint Conference on Neural Networks*, *3*(6), 1873–1878. https://doi.org/10.1109/ijcnn.2003.1223693

Cigizoglu, H. K. (2002). Suspended Sediment Estimation for Rivers using Artificial Neural. *Turkish Journal of*

Engineering and Environmental Sciences, *26*, 27–36.

Ciğizoğlu, H. K. (2002). Suspended sediment estimation and forecasting using artificial neural networks. *Turkish Journal of Engineering and Environmental Sciences*, *26*(1), 15–25.

Colby, B. R., & Hembree, C. H. (1955). *Computations of Total Sediment Discharge Niobrara River Near Cody, Nebraska*. Washington: GEOLOGICAL SURVEY WATER-SUPPLY PAPER 1357 UNITED STATES GOVERNMENT PRINTING OFFICE.

Danandeh Mehr, A., & Şorman, A. Ü. (2018). STREAMFLOW AND SEDIMENT LOAD PREDICTION USING LINEAR GENETIC PROGRAMMING. *Uludağ University Journal of The Faculty of Engineering*, *23*(2), 323–332. https://doi.org/10.17482/uumfd.352833

Einstein, H. A. (1950). *The bed-load function for sediment transportation in open channel flows*. Washington, D.C.: Tech. Bulletin No. 1026, U.S. Dept of Agriculture, Soil Conservation Service.

Engelund, F., & Hansen, E. (1967). *A monograph on sediment transport in alluvial streams*. Copenhagen: Tekniks Forlag.

Foresee, F. D., & Hagan, M. T. (1997). Gauss-Newton approximation to bayesian learning. *IEEE International Conference on Neural Networks - Conference Proceedings*, 1930–1935. https://doi.org/10.1109/ICNN.1997.614194

Gao, P., Mu, X. M., Wang, F., & Li, R. (2011). Changes in streamflow and sediment discharge and the response to human activities in the middle reaches of the Yellow River. *Hydrology and Earth System Sciences*, *15*(1), 1–10. https://doi.org/10.5194/hess-15-1-2011

Hagan, M. T., & Menhaj, M. B. (1994). Training Feedforward Networks with the Marquardt Algorithm. *IEEE Transactions on Neural Networks*, *5*(6), 989–993. https://doi.org/10.1109/72.329697

Jain, S. K. (2001). Development of integrated sediment rating curves using ANN. *Journal of Hydraulic Engineering*, *127*(1), 30–37.

Kayri, M. (2016). Predictive abilities of Bayesian Regularization and Levenberg-Marquardt Algorithms in Artificial Neural Networks: A Comparative Empirical Study on Social Data. *Mathematical and Computational Applications*, *21*(2). https://doi.org/10.3390/mca21020020

Kisi, Ö., Dailr, A. H., Cimen, M., & Shiri, J. (2012). Suspended sediment modeling using genetic programming and soft computing techniques. *Journal of Hydrology*, *450–451*, 48–58. https://doi.org/10.1016/j.jhydrol.2012.05.031

MacKay, D. J. C. (1992). Bayesian Interpolation. *Neural Computation*, *4*(3), 415–447. https://doi.org/10.1162/neco.1992.4.3.415

Nagy, H. M., Watanabe, K., & Hirano, M. (2002). Prediction of Sediment Load Concentration in Rivers using Artificial Neural Network Model. *Journal of Hydraulic Engineering*, *128*(6), 588–595. https://doi.org/10.1061/(asce)0733-9429(2002)128:6(588)

Oehler, F., Coco, G., Green, M. O., & Bryan, K. R. (2012). A data-driven approach to predict suspended-sediment reference concentration under non-breaking waves. *Continental Shelf Research*, *46*, 96–106. https://doi.org/10.1016/j.csr.2011.01.015

Pektaş, A. O., & Doğan, E. (2015). Prediction of bed load via suspended sediment load using soft computing methods. *Geofizika*, *32*(1), 27–46. https://doi.org/10.15233/gfz.2015.32.2

Raghuwanshi, N. S., Singh, R., & Reddy, L. S. (2006). Runoff and Sediment Yield Modeling Using Artificial Neural Networks: Upper Siwane River, India. *Journal of Hydrologic Engineering*, *11*(1), 71–79. https://doi.org/10.1061/(asce)1084-0699(2006)11:1(71)

Simons, D. B., & Şentürk, F. (1977). *Sediment Transport Technology*. Water Resources Publication.

Tayfur, G. (2002). Artificial neural networks for sheet sediment transport. *Hydrological Sciences Journal*, *47*(6), 879–892. https://doi.org/10.1080/02626660209492997

Toffaleti, F. B. (1969). Definitive Computations of Sand Discharge in Rivers. *Journal of the Hydraulics Division, ASCE*, *95*(HY1), 225–246.

Xu, M., Zeng, G., Xu, X., Huang, G., Jiang, R., & Sun, W. (2006). Application of Bayesian regularized BP

neural network model for trend analysis, acidity and chemical composition of precipitation in North Carolina. *Water, Air, and Soil Pollution*, *172*(1–4), 167–184. https://doi.org/10.1007/s11270-005-9068-8

Yang, C. T. (1996). *Sediment Transport: Theory and Practice*. New York: McGraw-Hill.

Yitian, L., & Gu, R. (2003). Modeling Flow and Sediment Transport in a River System Using an Artificial Neural Network. *Environmental Management*, *31*(1), 122–134. https://doi.org/10.1007/s00267-002-2862-9

A RELIABILITY-BASED INVESTIGATION OF INCEPTION OF MOTION FOR BED SEDIMENT

Omer Sari

Hydraulic Division, Department of Civil Engineering, Istanbul Technical University.

Istanbul, Turkey

sari18@itu.edu.tr

Veysel Sadan Ozgur Kirca

Hydraulic Division, Department of Civil Engineering, Istanbul Technical University.

Istanbul, Turkey

kircave@itu.edu.tr

ABSTRACT: The initiation of sediment motion is a complex process with many uncertainties involved. Shields criterion has been the most adopted method to estimate the initiation of motion among the vast amount of research devoted to the subject ever since. The present study presents the first results of a reliability-based analysis of Shields criterion based on the theory and equations developed by Zanke (2003), where turbulence and angle of repose are introduced as random parameters by means of Monte Carlo simulations using different probabilistic distributions and statistical moments. Critical shear stresses of thousands of particles are calculated for different grain Reynolds number values ranging between 0.1 and 2000. As such, probabilistic curves for the initiation of motion are obtained. Comparisons of model results with the empirical data show that the model is capable of capturing the uncertainty involved in the physical process.

1. INTRODUCTION

The initiation of sediment motion is a complex process with lots of uncertainties. Hence, many researchers approached this problem with deterministic and probabilistic models. Shields' study (1936) is known to be the first which expressed a dimensionless critical shear stress (or critical Shields parameter, θ_c) for initiation of motion for sediment particles on the bed, as a function of the grain Reynolds number, Re^*:

$$\theta_c = \frac{u_*^2}{g(s-1)d} \tag{1}$$

$$Re_* = \frac{d\,u_*}{\nu} \tag{2}$$

Here, $u_* = \sqrt{\tau_0/\rho}$ is friction velocity, τ_0 is the bed shear stress, d is the grain diameter (usually the median diameter d_{50}), g is the gravitational acceleration, ν is the kinematic viscosity of water, $s = \rho_s/\rho$ is the specific gravity, ρ_s and ρ are sediment and fluid densities, respectively. The subscript c indicates the critical conditions. Shields obtained a diagram between θ_c and Re_* (the Shields curve) by utilizing the empirical data from his experiments as well as those of Casey (1935), Kramer (1932), and Gilbert and Murphy (1914).

Shields original diagram has played a major role for sediment incipient motion. However, further studies showed that Shields diagram may not be the ultimate critical curve, and different revisions or modifications were proposed. For the fully-rough bed conditions, Meyer-Peter and Müller (1948) adopted the value of 0.047 for θ_c as a reference value in their bed load transport formula for well-

sorted fine gravel. Yalin and Karahan (1979) used a much larger data set (including their own), and obtained for $\theta_c \rightarrow 0.045$ for increasing values of $Re_* > 500$ (i.e. fully-rough region), which was also suggested by Miller et al. (1977) later. Gessler (1971) reanalysed Shields data and concluded a value of $\theta_c = 0.046$ for a %50 probability of motion on the bed. Compiling a large dataset, Buffington and Montgomery (1997) suggested that there was no definitive value for θ_c for the fully-rough region, but it ranged ranges between 0.03 and 0.07.

The effort for modifying Shields criterion continued in the recent work within the past two decades. Luckner and Zanke (2007) presented an analytical solution for the sediment incipient motion, and risk of river bed movement. Miedema (2010) constructed the Shields curve again based on a new model based on several studies about sediment incipient motion, and obtained the Shields curve for various scenarios. Simões (2014) used a movability number to develop new incipient motion equation by experimental data from many works. Yang et al. (2019) re-examined Shields curve in accordance with grain Reynolds number, grain size distributions, sediment characteristics, and turbulence.

Although many researches have offered a threshold for sediment motion, uncertainties such as grain positioning, turbulence, and other random parameters such as sediment characteristics and relative roughness make it difficult to tackle with deterministic methods. Hence, there has also been studies with probabilistic approaches. Einstein (1942, 1950) is referred to as being the first works to approach the problem in probabilistic terms. Einstein (1950) determined bed load function by using lift probability. Afterwards, probabilistic approaches were used in prediction of bed load transport by Paintal (1971) and Sun and Donahue (2000). There have been many other studies that included entrainment, rolling and lifting probabilities of sediment particles (Cheng and Chiew, 1998; Papanicolaou et al., 2002; Dancey et al., 2002; Wu and Chou, 2003; Fredsoe and Deigaard, 1992).

On the other hand, however, there are only a few studies in the literature that have dealt with the problem in terms of uncertainty and reliability. Spiliotis et al. (2018) suggested an approach in which θ_c was considered to be a fuzzy set to express partial sediment entrainment. Based on Zanke (2003) formulation, they incorporated the fuzziness of the individual angle of grain contact and the turbulence intensity, which yielded a lower and upper bound of the Shields curve signifying the uncertainty. The present paper presents the first results of a study which aimed at investigating the uncertainty involved in the initiation of motion of bed sediment in terms of exceedance probability, based on the semi-empirical formulation suggested by Zanke (2003). Since the deterministic values given by original Shields curve, or critical state curves suggested by other studies does not provide a reliability-based analysis of this motion for bed sediment, the suggested probabilistic curves that are capable of quantifying uncertainty provide more accurate estimates of the initiation of motion of bed sediment. Initial results show that the suggested method is promising, and can capture the uncertainty involved in the physical process of sediment motion.

2. METHODOLOGY

2.1. Zanke Formulation

Zanke (2003) developed a theory and derived a force balance equation of a single grain resting on the bed (Fig. 1). According to his theory, in laminar flow, randomness in the sediment incipient motion only stems from the local contact angle of individual grains ϕ, mean value of which is expected to be closely related to angle of repose, φ. However, in turbulent flow, instantaneous streamwise velocity u is defined with its mean and fluctuating parts, such as $u = \bar{u} + u'$. Same remains valid for the bed shear stress, as well. By this token, one can suggest that effective critical shear stress acting on a grain is larger than the average critical shear stress. Additionally, pocket geometry of any given sediment grain on the bed will be unique. The local contact angle ϕ is not necessarily equal to the angle of repose, but can be attributed as a random variable. As a result, the complexity and uncertainties of the initiation of motion occurs due to (1) the random positioning of the grain on the bed, and (2) the turbulence of the near-bed flow. Although other parameters related to flow and sediment are likely to pose uncertainty, the aforementioned two random effects will be considered in this study, and the rest of the parameters will be treated as deterministic values, for the sake of reducing the complexity. We

note that a similar approach was adopted in Spiliotis et al. [31], which formulated the problem on fuzziness rather than probability.
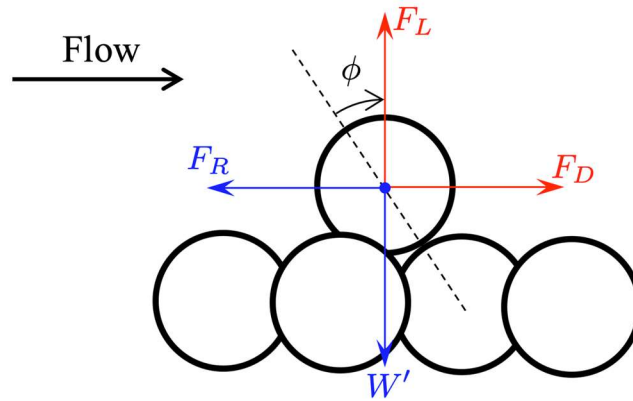
Figure 20. Definition sketch of the force balance on a single sediment grain on the bed. F_D is the drag force, F_R is the friction force, F_L is the lift force, and W' is the submerged weight of the grain

Zanke (2003) developed the following analytical/semi-empirical equation for the critical Shields parameter:

$$\theta_c = \frac{0.7 \, \tan \varphi}{\left(1 + n \dfrac{u'_{rms,b}}{u_b}\right)^2 \left(1 + \dfrac{1}{2.5}\left(\dfrac{u'_{rms,b}}{u_*}\right)^2 \tan \varphi\right)} \tag{3}$$

Here u_b is the characteristic near-bed velocity, whereas $u'_{rms,b}$ is the standard deviation of this parameter. Both values are given in normalized form with respect to u_* as follows:

$$\frac{u'_{rms,b}}{u_*} = 0.31 \, Re_* \, e^{-0.1R_*} + 1.8 \, e^{d_{50}/h} \, (1 - e^{-0.1Re_*}) \tag{4}$$

$$\frac{u_b}{u_*} = 0.8 + 0.9 \left(\frac{e^{-0.08Re_*}}{Re_*^2} + \frac{1 - e^{-0.08Re_*}}{B^2}\right) \tag{5}$$

$$B = e^{-0.08Re_*}[2.5 \ln(Re_*) + 5.25] + 8.5(1 - e^{-0.08Re_*}) \tag{6}$$

Here n is a non-dimensional coefficient which is equal to the ratio of a random turbulent fluctuation of characteristic bed velocity (at the instant of critical state of motion) to its standard deviation, $n = u'_c/u'_{rms,b}$. Zanke (2003) reasoned n to be between 0 and 3, and indicated a mean value of 1.8, which also gave the best fit with the overall empirical data. It should be further noted that the grain size to depth ratio (d_{50}/h) becomes an effective parameter only when the relative roughness is high (as described by Bayazıt, 1982). For flow conditions with a high depth value, the grain size to depth ratio becomes ineffective due to $e^{d_{50}/h} \to 1$.

2.2. Procedure for Monte Carlo Simulations

In the present study, the following procedure is applied for achieving the probabilistic description of the Shields criterion with the Monte Carlo simulations:

1. Select a distribution type for the probability density function (PDF) of n in Eq. (3) (such as normal, log-normal, uniform, triangular, etc.) with a mean and standard deviation value
2. Select a distribution type for the probability density function of ϕ in Eq. (3) (such as normal, log-normal, triangular, etc.) with a mean and standard deviation value
3. Choose a grain Reynolds number (Re_*) for the simulation
4. Numerically generate N number of n and ϕ value pairs, both of which satisfies the selected PDF's with the designated mean and standard deviation values

5. Solve Eqs. (3)-(6) for each of the N pairs of n and ϕ, and calculate N values of θ_c for the chosen Re_*. Store the calculated N values of θ_c, and assess the reliability of initiation of motion for the chosen Re_* value.
6. Go to step 3 above, and repeat the procedure to calculate θ_c for the new Re_* until simulations are completed for a range of Re_* values.

The preliminary runs showed that $N > 1500$ simulations yielded consistent results, and further increase of N did not improve the achieved accuracy significantly (Sari, 2019). As such $N = 10000$ simulations were conducted for 100 different grain Reynolds number values ranging between $0.1 \leq Re_* \leq 2000$.

3. RESULTS

Three different distributions are considered for representation of the randomness of n and ϕ parameters. These are triangular distribution, normal distribution, and truncated normal distribution (Fig. 2). Although many different combinations of probabilistic distributions and mean and standard deviation values for the two parameters are tested, the results of only four of these Monte Carlo simulation models are presented in this paper, as given in Table 1 (Sari, 2019). As can be seen, the first two model only considered the turbulence fluctuation parameter n as a random variable, whereas the third and fourth models additionally take ϕ as also a random variable.
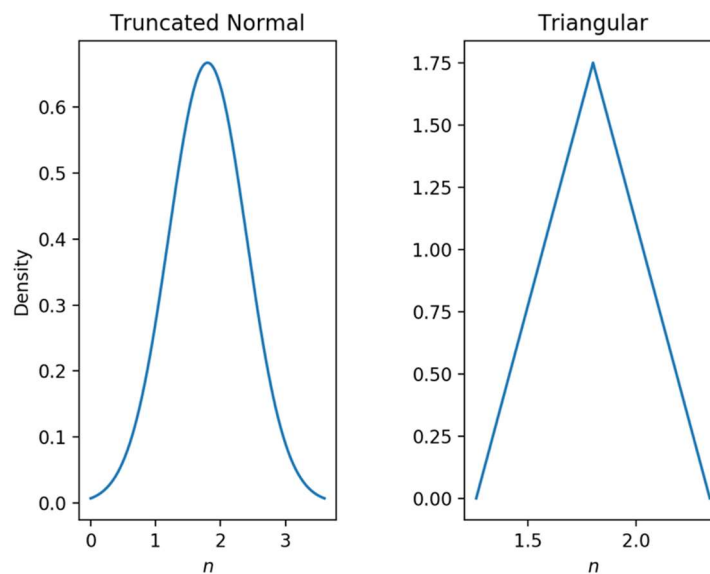
Figure 21. The truncated normal and triangular distribution of n

Table 20. The characteristics of Monte Carlo simulation model.

Model No	Mean of n	Std. dev. of n	Min. & max. of n	Distribution of n	Mean of ϕ	Std. dev. of ϕ	Min. & max. of ϕ	Distribution of ϕ
1	1.8	--	1.26 - 2.34	Triangular	32º	--	--	--
2	1.8	0.6	0 - 3.6	Truncated normal	32º	--	--	--
3	1.8	0.6	0 - 3.6	Truncated normal	32º	--	10º - 80º	Triangular
4	1.8	0.6	0 - 3.6	Truncated normal	32º	10º	10º - 80º	Truncated normal

The results of the first two models in comparison with the experimental data are presented in Figs. 3 and 4, in both of which n is the only parameter taken as random. On both figures, original function suggested by Zanke (2003) is given as the 50% probability of motion curve. Additionally, the 10% and 90% probability curves for initiation of motion are presented. In other words, these three curves signify the calculated values of the equal-probability critical Shields parameter as a function of Re_*. As seen in Fig. 3, the triangular distribution yielded a narrowing trend (in terms of uncertainty) toward low Re_* values on the double logarithmic paper, while the opposite is true for increasing Re_*. Yet, many of the data points seem to remain outside the envelop marked by the 10% and 90% probability of motion curves, which seems to be inconsistent. The results of Model 2 are apparently improved in terms of including the data points between 10% and 90% probability curves, but the same problem continues for low Re_* numbers. The range of uncertainty seem to be large for the high Re_* range, such that the values of θ_c corresponding to 50% probability and 90% probability of motion are 0.045 and 0.15, respectively. This is somewhat expected since larger bed roughness involves stronger turbulence which in turn can increase uncertainty.
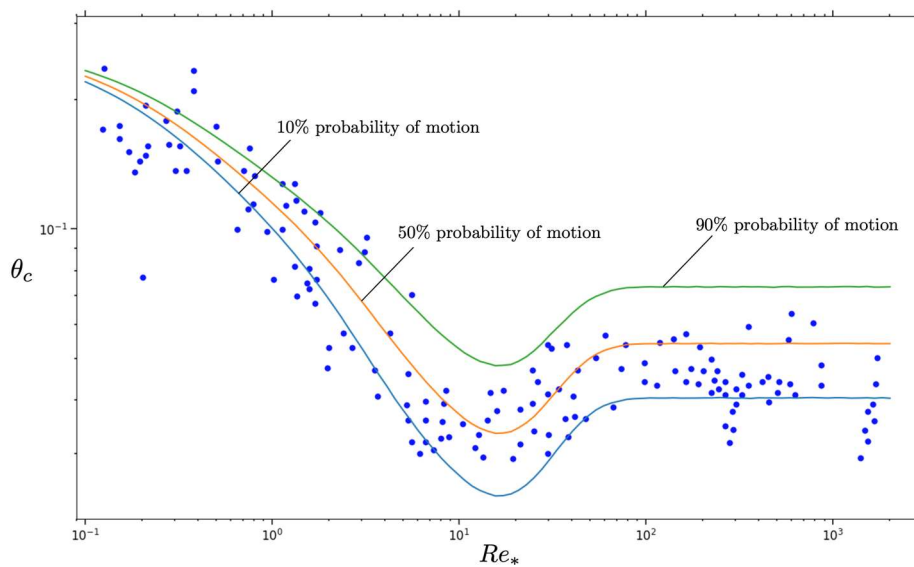
Figure 22. Comparison of Model 1 results with the empirical data (data compiled by Zanke, 2003)
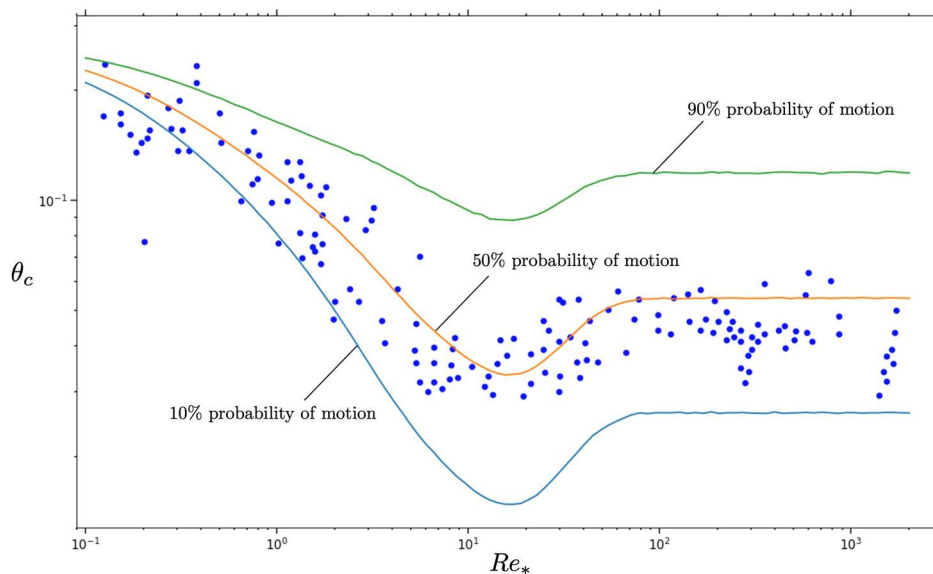
Figure 23. Comparison of Model 2 results with the empirical data (data compiled by Zanke, 2003)

The results of Model 3 and 4, where n and ϕ are considered as random variables is presented in Figs. 5 and 6, respectively. In Fig. 4, the location of the 50% probability of motion curve is shifted upwards, meaning that most of the data points are located under this mean curve. This shows that triangular distribution for ϕ is not appropriate for capturing the overall behavior. Furthermore, the uncertainty quantified by the difference between 90% and 10% exceedence probability values is increasing for low values of Re_*. This can be attributed as another inconsistency of the Model 3 results there is no reasonable physical basis for such a behavior. On the other hand, the results of Model 4 indicate a much better fit with the empirical data. The mean (50% probability) curve for motion identically fits with the original function suggested by Zanke (3).
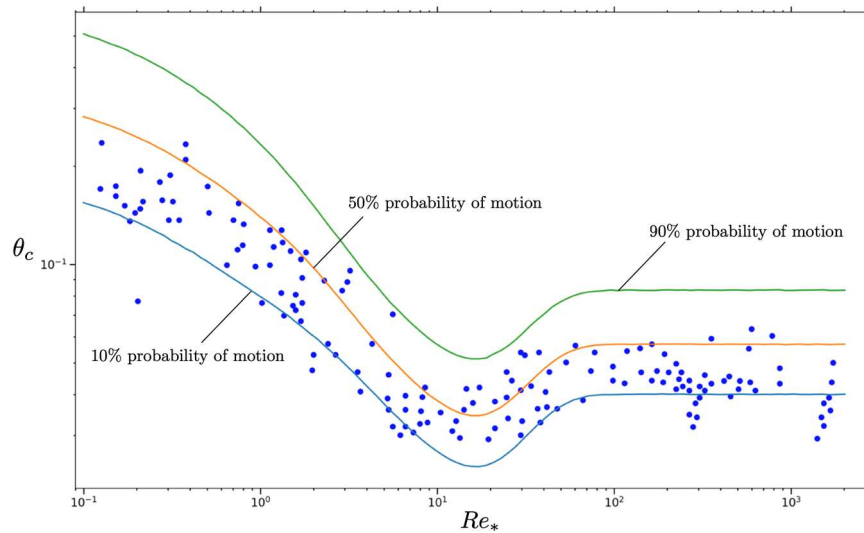
Figure 24. Comparison of Model 3 results with the empirical data (data compiled by Zanke, 2003)
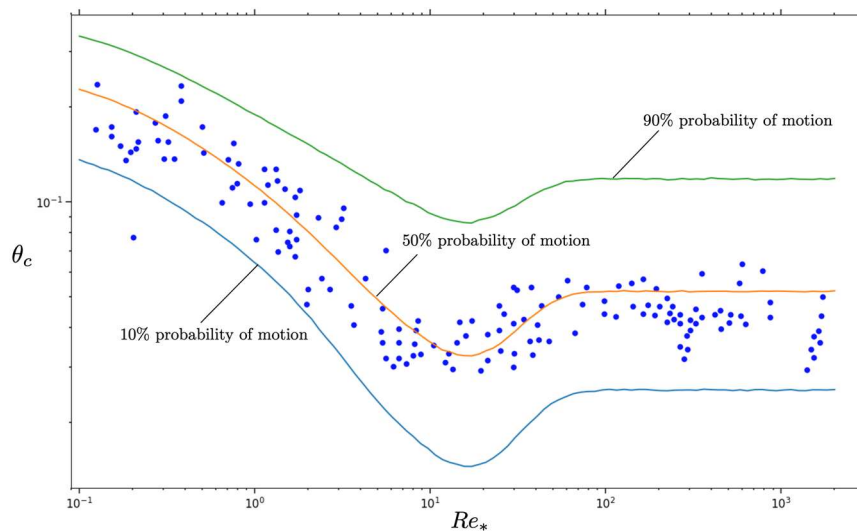
Figure 25. Comparison of Model 4 results with the empirical data (data compiled by Zanke, 2003)

Looking at Fig. 6, it is seen that 10% and 90% probability curves provide a good envelop for the empirical data (except one outstanding point). A more detailed analysis of the Model 4 results is shown in Fig. 7 in terms of plus/minus one standard deviation. It is seen that the plus/minus one standard deviation (i.e. 84% and 16% probability of motion curves) sharply encapsulates the empirical data, showing a good fit with the values at the edges. This result indicates that the present analysis is very promising in terms of capturing the uncertainty involved in the physical processes related to the initiation of motion of bed particles.
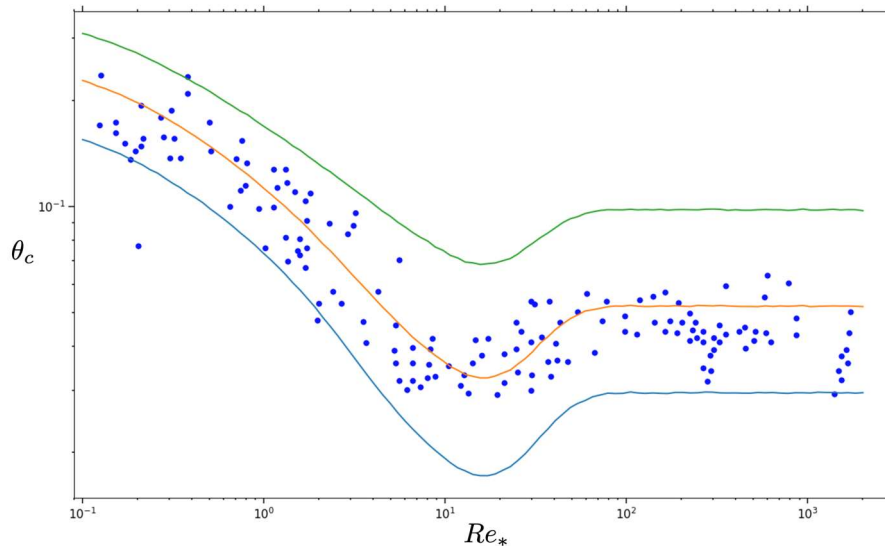
Figure 26. Plus/minus one standard deviation of Model 4 results compared with the empirical data

4. CONCLUSIONS

In this paper, the first results of an uncertainty-oriented analysis on initiation of motion of bed sediment is presented. By using the Zanke (2003) formulation, Monte Carlo simulations are utilized to obtained reliability-based curves of probabilistic Shields criterion. Uncertainty stemming from the pocket geometry of individual grains as well as turbulence is accounted for in the analysis. A wide range of grain Reynolds number values are included, and 10000 simulations are conducted for each of these values. The following conclusions are drawn from the study:

- Instead of considering only turbulence fluctuations (n in Zanke formulation) as a random parameter, taking the local contact angle of individual grains (ϕ) as a second random variable significantly improved the results.
- Triangular distribution was found not to be an appropriate choice for the present purpose since the overall behavior was not well represented.
- Truncated normal distribution for both of the random variables gave the best results. In fact, truncated normal distribution reflects the real-life conditions better than normal distribution, because physical limits (minima and maxima) are inevitable aspects of considered parameters.
- Findings of the study showed that the adopted approach can represent the overall uncertainty of the empirical data, such that the plus/minus one standard deviation curves very sharply match with the data points at the edges.
- The reliability-based Shields curves achieved by the proposed method is believed to have a merit not only in terms of theoretical studies, but also in practical applications. The lower probability curves can provide a factor of safety for the designer of hydraulic structures, whereas the higher probability curves can be used, for instance, for the design of self-cleansing
- Future studies can involve different distributions and different parameters for determination of the reliability-based Shields curves. A thorough validation of the proposed method is yet to be done in future studies.

REFERENCES

Bayazit, M. (1982). Flow structure and sediment transport mechanics in steep channels. Mechanics of Sediment Transport, *In Proc. of EUROMECH 156*, Istanbul.

Buffington, J. M. and Montgomery, D. R. (1997). A systematic analysis of eight decades of incipient motion studies, with special reference to gravel- bedded rivers. *Water Resources Research*, 33 (8), 1993–2029.

Casey, H. J. (1935). Über geschiebebewegung, Vol. 19, Preussische Druckerei- und Verlags-Aktiengesellschaft.

Cheng, N.-S. and Chiew, Y.-M. (1998). Pickup probability for sediment entrainment. *Journal of Hydraulic Engineering*, 124(2), 232–235.

Dancey, C. L., Diplas, P., Papanicolaou, A., Bala, M. (2002). Probability of individual grain movement and threshold condition. *Journal of Hydraulic Engineering*, 128(12), 1069–1075.

Einstein, H. A. (1942). Formulas for the transportation of bed load. *Transactions of ASCE*, 561–597.

Einstein, H. A. (1950). The bed-load function for sediment transportation in open channel flows, no. 1026, US Government Printing Office.

Fredsøe, J. and Deigaard, R. (1992). Mechanics of coastal sediment transport, Vol. 3, World Scientific.

Gessler, J. (1971). Beginning and ceasing of sediment motion. *River Mechanics*, 1(1), 7–1.

Gilbert, G. K. and Murphy E. C. (1914). The transportation of debris by running water, no. 86, US Government Printing Office.

H. Kramer, H. (1932). Modellgeschiebe und schleppkraft, Preussische Versuch-sanstalt für Wasserbau und Schiffbau.

Luckner, T. and Zanke, U. (2007). An analytical solution for calculating the initi- ation of sediment motion, *International Journal of Sediment Research*, 22 (2) (2007) 87–102.

Meyer-Peter, E. and Müller, R. (1948). Formulas for bed-load transport. In *Proceedings of the IAHSR 2nd meeting*, Stockholm, appendix 2, IAHR, 1948.

Miedema, S. (2010). Constructing the shields curve, a new theoretical approach and its applications, *WODCON XIX*, Beijing China.

Miller, M., McCave, I. and Komar, P. (1977). Threshold of sediment motion under unidirectional currents, *Sedimentology*, 24(4), 507–527.

Paintal, A. (1971). A stochastic model of bed load transport. *Journal of Hydraulic Research*, 9(4), 527–554.

Papanicolaou, A., Diplas, P., Evaggelopoulos, N., Fotopoulos, S. (2002). Stochastic incipient motion criterion for spheres under various bed packing conditions. *Journal of Hydraulic Engineering*, 128(4), 369–380.

Sari, O. (2019). Reliability Based Analysis of Inception of Motion of Bed Sediment, MSc. Thesis, Istanbul Technical University, Hydraulics and Water Resources Program.

Shields, A. (1936). Anwendung der aehnlichkeitsmechanik und der turbulenz- forschung auf die geschiebebewegung, PhD Thesis Technical University Berlin.

Simões, F. J. (2014). Shear velocity criterion for incipient motion of sediment, *Water Science and Engineering*, 7(2) 183–193.

Spiliotis, M., Kitsikoudis, V., Kirca, V. S. O., Hrissanthou, V. (2018). Fuzzy threshold for the initiation of sediment motion. *Applied Soft Computing*, 72, 312–320.

Sun, Z. and Donahue, J. (2000). Statistically derived bedload formula for any fraction of nonuniform sediment. Journal of Hydraulic Engineering, 126(2), 105–111.

Wu, F.-C. and Chou, Y.-J. (2003). Rolling and lifting probabilities for sediment entrainment. *Journal of Hydraulic Engineering*, 129(2), 110–119.

Yalin, M. S. and Karahan, E. (1979). Inception of sediment transport, *Journal of the Hydraulics Division*, 105 (11) 1433–1443.

Yang, Y., Gao, S., Wang, Y. P., Jia, J. Xiong, J. and Zhou, L. (2019). Revisiting the problem of sediment motion threshold, *Continental Shelf Research*, 103960.

Zanke, U.C.E. (2003). On the Influence of Turbulence on the Initiation of Sediment Motion, *International Journal of Sediment Research*, 18 (1) (2003) 17–31.

EXPERIMENTAL INVESTIGATION ON THE GEOMETRY OF SCOUR HOLES AROUND A CYLINDER PIER

Ebru Taşkaya

Civil Engineering Department, İzmir Kâtip Çelebi University

İzmir, Turkey

ebruutsky@gmail.com

Zehra Büyüker

Civil Engineering Department, İzmir Kâtip Çelebi University

İzmir, Turkey

zehra.buyuker@ikcu.edu.tr

Gökçen Bombar

Civil Engineering Department, İzmir Kâtip Çelebi University

İzmir, Turkey

gokcen.bombar@ikcu.edu.tr

António Heleno Cardoso

Ceris, Instituto Superior Tecnico, Universidade de Lisboa

Lisbon, Portugal

antonio.cardoso@tecnico.ulisboa.pt

ABSTRACT: Calculation of the amount of scour around the bridge piers is very important for the design of the bridge piers. In this study, the clear-water scouring around the circular bridge piers on the flat bed was investigated experimentally. Experiments were carried out at 17 cm water depth, on the bottom with 30 cm sediment thickness, using sediment with a median grain diameter of 1.044 mm, with a 7 cm diameter cylindrical bridge pier at two different flow intensities. At the end of each experiment, bathymetry around the scour hole is obtained. The scour hole depth, scour length, and the scour width of the scour hole was found. and compared with the equations proposed in the literature.

Keywords: clear-water scour, scour length, scour width

1. INTRODUCTION

Bridges are necessary structures to ensure the continuity of transportation. As bridge failures can cause losses of life and property, the stability and strength of bridges are of great importance. Statistical studies carried out for river bridges that have been heavily damaged or destroyed in recent years have revealed that most of the damage is caused by hydraulic phenomena, one of them being scouring. Bridge pier diameter and shape, velocity, flow depth, size and type of bed material can be listed as examples of variables influencing the scour depth (d_s). Not only the scour depth but also the geometry, i.e., the width (W_s) and length (L_s) of the scour hole are the parameters that should be estimated to predict the extension of the scour volume, as a requisite to access, for instance, the stability of the channel cross-section, including its banks, and to determine the safe location of the piers of multi-pier bridges.

Khwairakpam et al.(2012), Das et al.(2014) Eski and Aksoy (2022) experimentally investigated local scour around circular bridge piers and proposed empirical equations to estimate the scour hole length, L_S, and the scour hole width, W_S. For this purpose, they compared their experimental results with the existing literature. The equations proposed by Khwairakpam et al. (2012) are as follows;

$$L_S = \left\{3.958\left(\frac{h}{D}\right) - 2.371\right\}d_S - \left\{2.649\left(\frac{h}{D}\right) + 5.082\right\} \tag{1}$$

$$W_S = \left\{6.204\left(\frac{h}{D}\right) - 5.412\right\}d_S - \left\{-4.435\left(\frac{h}{D}\right) + 7.597\right\} \tag{2}$$

where h is the flow depth and D is the bridge pier diameter. Two years later, Das et al. (2014) proposed another set of equations for the same purpose:

$$\frac{L_s}{D} = 5.065\left(\frac{d_s}{D}\right) \tag{3}$$

$$\frac{W_s}{D} = 5.576\left(\frac{d_s}{D}\right) \tag{4}$$

Recently, Eski and Aksoy (2022) investigated the scour hole dimensions around circular bridge piers and proposed the following equations for scour length and width which only apply for clear-water flow conditions:

$$\frac{L_s}{D} = 3.39\left(\frac{d_s}{D}\right)^{0.54} F_d^{\,0.32} \tag{5}$$

$$\frac{W_s}{D} = 2.1\left(\frac{d_s}{D}\right)^{0.33} F_d^{\,0.91} \tag{6}$$

Here, F_d is the densimetric Froude number,

$$F_d = \frac{U}{\sqrt{g\Delta d_{50}}} \tag{7}$$

U is the cross-sectional average velocity, g is the gravitational acceleration, $\Delta = (\rho_s - \rho)/\rho$, and ρ and ρ_s are the mass density of water and sediment, respectively.

The aim of this exploratory study is to investigate the dimensions of a scour hole under clear-water conditions and compare the experimental results with calculated values, as given by the above equations found in literature.

2. EXPERIMENTAL SET-UP AND METHOD

Experiments were carried out in Izmir Katip Çelebi University, Civil Engineering Hydraulics Laboratory. The experiments were carried out in a rectangular open channel with a width of 74 cm, a length of 15 m and a depth of 1 m. The plan view of the channel is given in Figure 1, and the cross-section A-A defined at $x = 10.20$ m, where the pier was located, is shown in Figure 2. The thickness of the sand bed layer was 30 cm. The sand mixture was characterized by $d_{50} = 1.044$ mm and $\sqrt{d_{84}/d_{16}} = 1.13$.
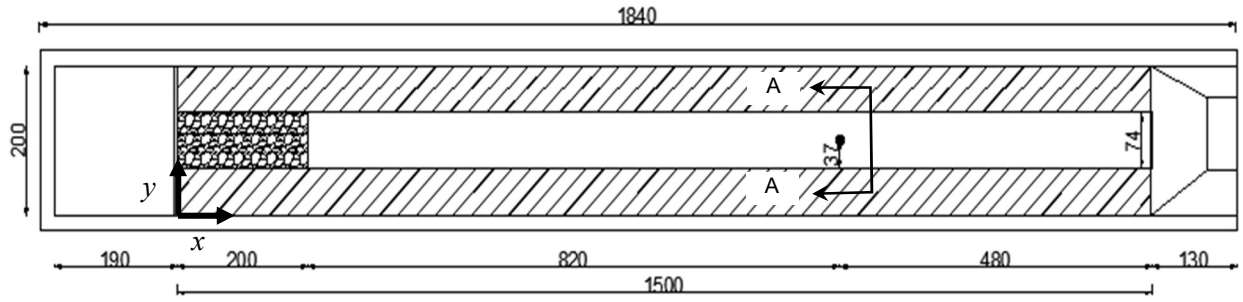
Figure 1. Plan view (dimensions are in cm)
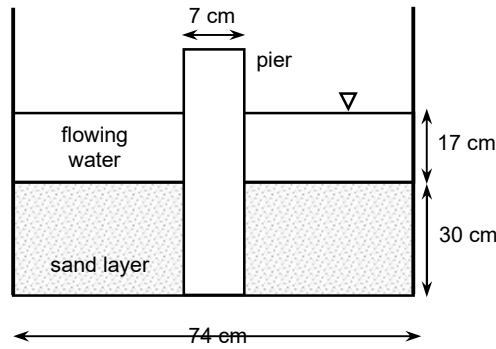
Figure 2. Cross section A-A at $x = 10.20$ m

In this experimental study, a $D = 7$ cm diameter transparent cylinder was used to simulate a bridge pier. Two different flow rates, $Q = \{31.9; 41.6\}$ L/s, were imposed. The flow depth was 17 cm in both cases, which rendered $h/D = 2.4$. The critical velocity of the beginning of motion of the sand-bed grains, U_c, was obtained by visual inspection as 40.0 cm/s.

Two experiments were run for about 4 days. The flow intensity, U/U_c, the Reynolds number, Re, the Froude number, Fr, the densimetric Froude number, F_d, and the duration, t_{dur}, of the experiments are given in Table 1, where,

$$Re = \frac{4UR_h}{v} \tag{8}$$

$$Fr = \frac{U}{\sqrt{gh}} \tag{9}$$

Table 1. The features of the experiments.

	Q (L/s)	U (cm/s)	U/U_c	Re (x10^5)	F_d	Fr	t_{dur} (hr)
A	31.9	25.4	0.63	1.18	1.95	0.20	96
B	41.6	33.0	0.83	1.54	2.54	0.26	91

The scour depths observed at the end of the experiments were measured on rulers placed inside the bridge pier at verticals 0˚, 45˚, 90˚, 135˚, 180˚, 225˚, 270˚ and 315˚, as shown in Figure 3.
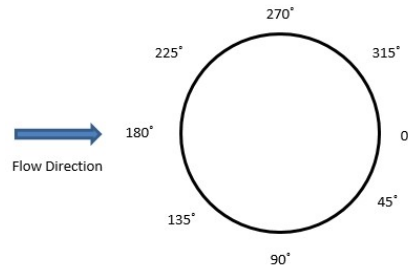
Figure 3. The angles of the points from which the scour depth is obtained around the bridge pier

At the end of the experiment, the flowrate was decreased, and the flow depth was increased by operating a tailgate located at the downstream end of the channel such that the sediments did not move under those circumstances and the bed topography was measured by a down-looking Vectrino probe. The measurement of the distance between the down tip of this probe and the sand bed surface is one of its functionalities. The measurements were taken between $x = 9.8$ m and $x = 11.35$ m of the channel at 5 cm intervals along the streamwise direction, x, and the transversal direction, y. With the results obtained thru the rulers around the cylinder and the Vectrino, the bathymetry of the scour holes was defined. For both experiments, the scour depth, scour length, and scour width at the end of the experiment were determined.

3. EXPERIMENTAL RESULTS AND DISCUSSION

The initial bed level at the beginning of the experiment, z_{int}, the bed level at the end of the experiment, z_s, and the end scour depth, d_s, are given in in Table 2 for all eight measuring verticals defined in the piers' perimeter.

Table 2. Bed levels and final scour depths (all values are in cm).

	Exp	0°	45°	90°	135°	180°	225°	270°	315°
z_{int}	A,B	30	30	30	30	30	30	30	30
z_s	A	24.3	22.7	21.1	20.3	20.2	20.6	21.7	22.7
	B	17.8	16.9	15.9	15.2	15.0	15.2	15.8	16.8
d_s	A	5.7	7.3	8.9	9.7	9.8	9.4	8.3	7.3
	B	12.2	13.1	14.1	14.8	15.0	14.8	14.2	13.2

Two photos' taken at the end of the experiments, when all the water was drained, are shown in Figure 4. The final bed bathymetry for experiment A and B is given in Figure 5 and 6, respectively. The final cross-sections at $x = 10.20$ m, containing the piers' axes, are plotted in Figure 7.a, whereas Figure 7.b displays the central longitudinal bed profiles ($y = 37$ cm). The angles of the scour holes side slopes, θ_s, at alignments 180°, 90° and 270° are also illustrated in these figures. In average, $\theta_s \approx 33°$, which means that the side slopes are slightly steeper than the natural stable slope, defined from the friction

angle, θ_r, this angle being $\theta_r \approx 29^\circ$ for the uniform sand used in the study (Chang, 1988). This increase of θ_S is due to the action of the horseshoe vortices incised in the scour holes.
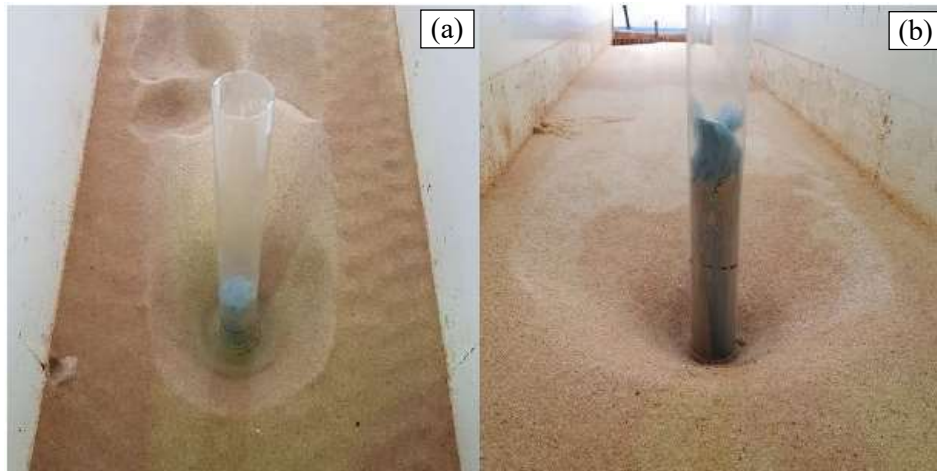
Figure 4. Photos taken after the experiments (a) A and (b) B
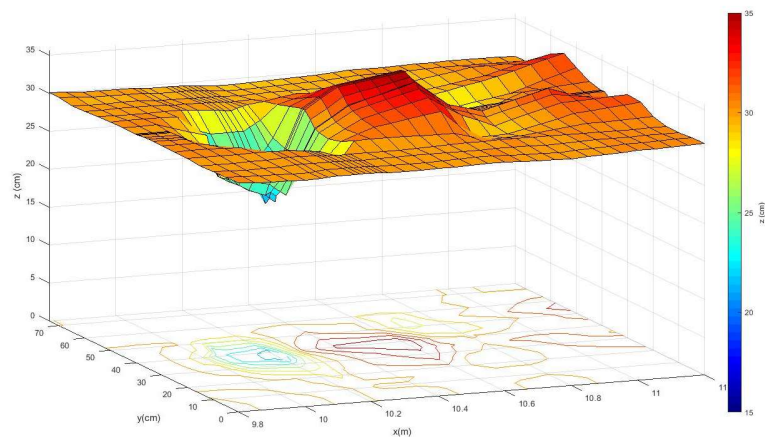
Figure 5. Bathymetry of experiment A
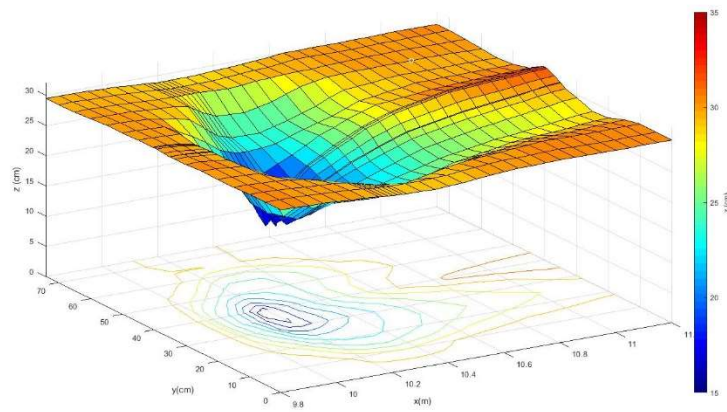
Figure 6. Bathymetry of experiment B
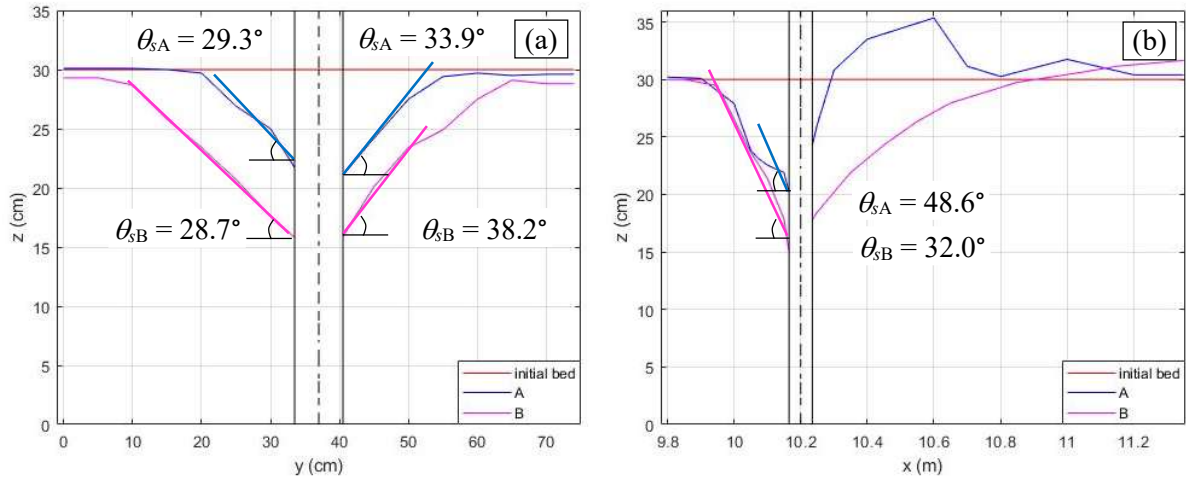
Figure 7 (a) *y-z* cross-section view for *x* = 10.20 m (b) *x-z* cross-section view for *y* = 37 cm

The final scour depths obtained at 180˚ were used to calculate the scour width and length by using equations (1) to (6) presented in the Introduction. These variables are given in Table 3 and Table 4 for L_s and W_s, respectively, together with the measured equivalents. Table 4, referring the W_s, also includes the values calculated by assuming that, around the upstream half of the piers, the scour holes can be idealized as truncated inverted cones whose side surface is determined by the friction angle. From this idealization, it can be concluded that W_s is given as

$$\frac{W_s}{D} = 2\left(\frac{d_s}{D\,tan\theta_r}\right) + 1 \tag{10}$$

Table 3. The calculated and measured values of L_s.

Exp	L_s (cm)			
	Khwairakpam et al. (2012)	Das et al. (2014)	Eski and Aksoy (2022)	Present study
A	59.4	49.6	35.2	39.0
B	97.1	76.0	48.3	110

Table 4. The calculated and measured values of W_s.

Exp	W_s (cm)				
	Khwairakpam et al. (2012)	Das et al. (2014)	Eski and Aksoy (2022)	Eq. (10)	Present study
A	97.8	54.6	30.2	42.4	45.0
B	148.0	83.6	44.2	61.1	60

The measured values of L_s and W_s were larger for experiment B than for experiment A, since the flow intensity was higher, leading to a deeper scour hole. This trend is reproduced by the predictors presented in the Introduction. The percent differences corresponding to each predictor are included in Table 5. It is revealed that the proposal of Eski and Aksoy (2022) under-predicts whereas those of Khwairakpam et al. (2012) and Das et al. (2014) overpredict, particularly, W_s. It is remarkable that W_s calculated through Eq. (10) displayed the smallest error deviation to the measured values.

Table 5. The percent differences of the calculated values from the experimental values of L_s and W_s.

Exp	L_s (cm)			W_s (cm)			
	Khwairakpam et al. (2012)	Das et al. (2014)	Eski and Aksoy (2022)	Khwairakpam et al. (2012)	Das et al. (2014)	Eski and Aksoy (2022)	Eq. (10)
A	52.4	27.3	-9.6	117.3	21.4	-33.0	-5.9
B	-11.73	-30.91	-56.09	146.7	39.4	-26.4	1.9

The values of calculated and measured values of L_s and W_s are also compared in Figure 8, which confirms the conclusions highlighted above.
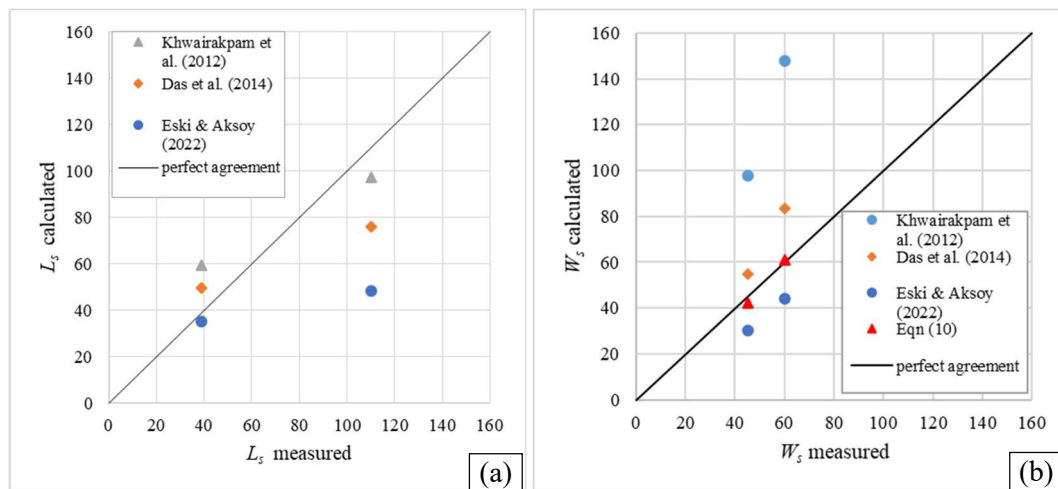
Figure 8. Comparison of calculated and measured values for (a) L_s, (b) W_s

4. CONCLUSIONS

Considering the stability assessment of river cross-sections, not only the depth, d_s, of scour holes, but also their width, W_s, and length, L_s, may need to be estimated. In this study two experiments were performed in an open rectangular channel by using only one cylindrical pier inserted in a single sand bed, imposing a constant pier diameter and flow depth, and two different flow intensities. The available predictors found in literature were applied to obtain the most important scour-hole plan dimensions. It was verified that the greater the flow intensity, the wider the scour dimensions. The predictor proposed by Eski and Aksoy (2022) under-predicts whereas those of Khwairakpam et al. (2012) and Das et al. (2014) over-predict, mostly W_s. The width calculated through Eq. (10) was the most precise.

ACKNOWLEDGE

REFERENCES

Chang, H. H., (1988). *Fluvial Processes in River Engineering*, John Wiley & Sons, February 1988, 432 pp.

Das S., Das, R., Mazumdar, A., (2014). Variations in clear water scour geometry at piers of different effective widths, *Turkish J Eng Env Sci*., *38*:97-111, https://doi:10.3906/muh-1308-11

Eski, Ö. Y., & Aksoy, A. Ö., (2022). Investigation of local scour hole dimensions around circular bridge piers under steady state conditions, Teknik Dergi, 33(2), https://doi.org/10.18400/tekderg.704352

Khwairakpam, P., Ray, S. S., Das, S., Das R., and Mazumdar, A., (2012). Scour hole characteristics around a vertical pier under clearwater scour conditions, *ARPN Journal of Engineering and Applied Sciences*, *(7)*6

APPLICATION OF GENETIC ALGORITHM METHOD TO DEVELOP EQUATIONS FOR WATER CAPTURING PERFORMANCE (WCP) AND SEDIMENT RELEASE EFFICIENCY (SRE) OF COANDA TYPE INTAKES

Oguz Hazar

Ph.D. student, Dept. of Civil Engineering, Izmir Institute of Technology

Izmir, Turkey

oguzhazar@iyte.edu.tr

Gokmen Tayfur

Professor, Dept. of Civil Engineering, Izmir Institute of Technology

Izmir, Turkey

gokmentayfur@iyte.edu.tr

Sebnem Elci

Professor, Dept. of Civil Engineering, Izmir Institute of Technology

Izmir, Turkey

sebnemelci@iyte.edu.tr

ABSTRACT: This study develops empirical equations to predict Water Capturing Performance (WCP) and Sediment Release Efficiency (SRE) for Coanda type intakes. These equations are developed using experimental data obtained from sediment-laden flows in the Hydraulics Laboratory of Izmir Institute of Technology. Taking into account the behavior of variables, nonlinear equations are proposed whose exponents and coefficients are obtained using the Genetic Algorithm (GA) method. The equations are calibrated and validated by using 70% and 30% of the data, respectively. The successful validation of the equations implies that the developed empirical equations can be employed for predictive purposes.

Keywords: Coanda intake; Dimensionless parameters; Genetic Algorithm; Empirical equations; Calibration; Validation; WCP; SRE

1. INTRODUCTION

Intake structures are mostly used for diverting the design amount of water from rivers and reservoirs for various purposes (Lauterjung and Schmidt 1989). Coanda and Tyrolean type intake structures are the most widely preferred bottom type water intake structures around the world. Besides the type of intake structure, the expectancy from any intake structure is to supply required water while filtering most of the sediments and other unwanted particles as much as possible. Due to the energy production stages being carried out with different types of high-value machinery they are sensitive to sediment particles within water. In addition, sediment particles can become a shelter for various types of microorganisms and reduce sanitation efficiency (LeChevallier and Norton 1995).

Withdrawal water and filtered sediment amounts depend on both structural design parameters such as bar spacing of an intake, screen length, screen slope inclination, etc., and also incoming flow conditions such as discharge rate and sediment concentration of incoming flow. Therefore, estimation and determination of withdrawal water and excluded sediment amounts are highly important to obtain maximum efficiency from an intake structure.

There is a structural difference between Tyrolean and Coanda intakes. Tyrolean-type water intakes have straight screen bars which are oriented parallel to flow direction. On the other hand, Coanda-type water intakes have concave screen geometry where screen bars are placed perpendicular to the flow direction. Due to these structural design differences, Coanda intakes gain the self-cleaning ability and high water withdrawal capacity which makes Coanda type water intakes more preferable than Tyrolean ones. Additionally, Coanda-type water intakes are environmentally friendly structures since they can allow fish and invertebrates to pass downstream of a river (James and Ronald 1988).

Wahl (2001) proposed empirical equations for offset height of screen bar and orifice effect. He comments that wire tilt angle, which is directly related to offset height, affects the screen capacity. Although it increases the shear mechanism and withdrawal water amount, it also increases the possibility of clogging and sediment retention on the screen. This situation negatively affects the water capturing performance. Wahl (2003) investigates the effect of changes in screen parameters, such as wire tilt angle, screen curvature (arc) radius, and screen length on the withdrawal of water discharge. The studies of Wahl (2001, 2003) are important for investigating the effect of various screen parameters on the unit withdrawal discharge under clear water conditions.

Intakes structures are mostly faced with sediment-laden flow conditions in real-life applications. It is possible to see some studies that have considered sediment-laden flow for Coanda-type intakes. For example, a series of experimental studies are performed by Howarth (2001) to investigate Coanda screens. Huber (2005) has indicated that the sediment exclusion efficiency is increasing with decreasing sloth width, on the other hand, smaller sloth width increases the risk of clogging. May (2015) is another researcher who considers both clear and sediment-laden flow conditions in studies. Similar to the recommendations of Huber (2005), May (2015) summarizes that screens having smaller wire openings show good performance for sediment exclusion but are more susceptible to clogging. Both studies, Huber (2005) and May (2015) have investigated the effect of different discharge rates and sloth widths. However, constant screen slope and curvature radius are used in their studies. On the other hand, a series of experiments in the Hydraulic Laboratory of Izmir Institute of Technology are performed by Hazar and Elci (2021) by using sediment-laden flows using Coanda intakes which have different screen design geometries. Parameters of Water Capturing Performance (WCP) and Sediment Release Efficiency (SRE) are defined to explain screen performances under different conditions. The multilinear equations for both WCP and SRE of Coanda screens are developed using linear regression as a statistical analysis method. However, these equations are not validated since all the data are employed in their construction.

The relations between WCP and related parameters of water flow, sediment, and intake characteristics are not linear, rather highly nonlinear which is also true for SRE. This implies that nonlinear empirical equations can represent the actual physical processes. The Genetic Algorithm (GA) is one of the non-linear search method where its applications in the field of water resources engineering starts from early 1990 (Tayfur, 2017). One of the earliest studies related with application of GA on water resources engineering is the study of Wang (1991) who studied on calibration of rainfall-runoff model parameters. Another study was performed by McKinney and Lin (1994) where they successfully applied GA method for simulation of maximum pumping rate and cost optimization of water supply. The GA method was also used for determining the effective cropping pattern in India by Raju and Kumar (2004). Tayfur et. al. (2009) performed a study to predict hydrographs using the rating curve formulation. They determined the optimal values of the coefficients in the formula by employing GA. The results showed good performance on predicting the hydrographs of Tiber River at different dates. The studies on the literature show that GA method can be used different areas and complex applications of the water resource engineering including proposing non-linear empirical equations. The advantage of developing such empirical equations can be beneficial for designing optimal intakes and for predicting diverted water amount and corresponding sediment concentration in the diverted water. Hence, there is a need for developing nonlinear empirical equations to predict WCP and SRE as a function of Coanda intake structural characteristics, water, and sediment parameters. This study would be the first one, to the knowledge of the authors, in the literature to develop such empirical equations. To develop the equations, it would propose empirical nonlinear equations whose coefficients and exponents would be determined by employing the genetic algorithm (GA) method.

The construction of the empirical equations would be carried out by using 70% of the data for the calibration and 30% for the validation. So developed empirical equations can be used for predictive purposes.

2. METHODS AND METHODOLOGY

2.1. Experimental Setup and Data

Experiments are performed in the Hydraulics Laboratory of Izmir Institute of Technology in Izmir, Turkey. Figure 1 shows the experimental setup. Six different Coanda screens which are constructed from acrylic material and have different properties are designed and constructed specifically for the study (Table 1).
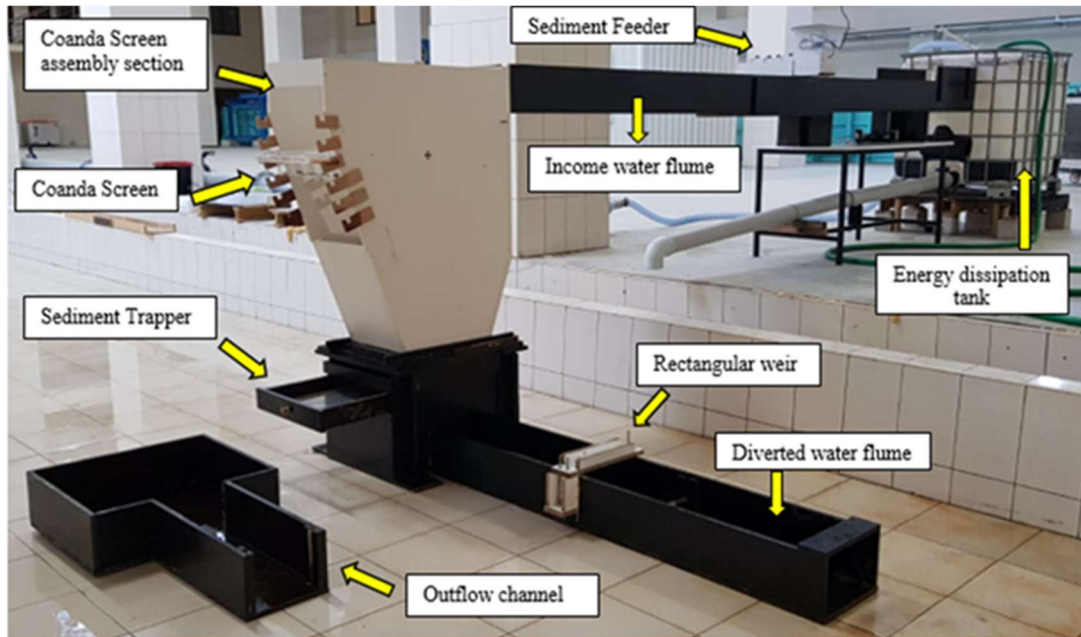
Figure 1. General View of Experimental Setup

Table 1. Screen Characteristics and Details.

Screen Type	Sloth Width (mm)	Curvature Radius (mm)	Net Screen Length (cm)	Total Screen Length (cm)	Screen Width (cm)	Void ratio "m"
Coanda R800(1)	1	800	60	100	40	0.046
Coanda R800(2)	2	800	60	100	40	0.092
Coanda R800(3)	3	800	60	100	40	0.138
Coanda R1200(1)	1	1200	60	100	40	0.046
Coanda R1200 (2)	2	1200	60	100	40	0.092
Coanda R1600 (1)	1	1600	60	100	40	0.046

Where the void ratio (m) is defined as ratio of total bar opening area to total screen area.

The T-shape bars have been constructed specifically for this study and the plan drawings of three different Coanda screens are shown in Figures 2a and 2b respectively. Their manufacturing steps are shown in Figure 3.
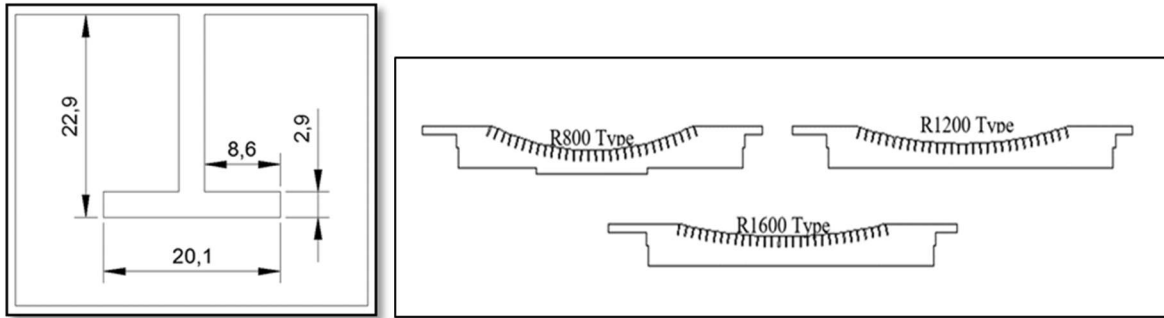
Figure 2. Formwork of T-shape bars (a), Skeletons of Coanda screens (b), where dimensions are shown in mm
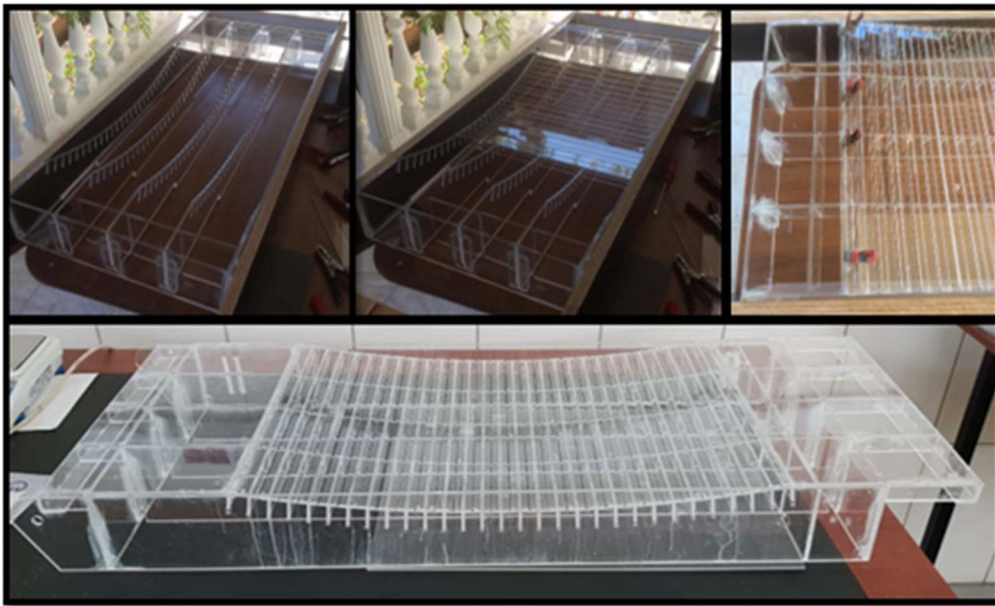
Figure 3. Manufacture steps of a Coanda intake

To observe the screen inclination effect on the screen performance, wooden sockets which allow the user to adjust a screen inclination in the range of 0 and 30 degrees are mounted on the intake body section walls (Figure 4). During the experiments, three different water discharges, 2.4 l/s, 5.56 l/s, and 7.96 l/s, are used to observe the effect of different incoming flow rates on both WCP and SRE. The incoming flow is directly pumped through a one-ton tank to dissipate its excessive energy and then it is poured into the main flume with the help of a rectangular weir. The incoming flow rate and diverted water discharges are controlled and measured by a head over a sharp-crested weir and the measured head was converted to flow discharge via the weir equation (Equation 1).

$$Q = \frac{2}{3} C_w W \sqrt{2g} h^{1.5} \tag{1}$$

Where h is the measured head, W is the channel width, and C_w is the weir coefficient (C_w=0.635).

Figure 4. Wooden sockets assembled on intake walls

In the case of sediment-laden flow, a novel sediment feeder device was designed which offers options to users to adjust the sediment concentration during experiments (Figure 5). The rotation of the sediment feeder is controlled via a transistor that is connected to an electrical circuit. Uniform sediment particles that had 0.8 mm diameter are used during the sediment-laden flow experiments.

Figure 5. Sediment Feeder Device

A total of 216 data sets are obtained after experiments: 108 for the WCP and 108 for the SRE. The statistics of the measured WCP and SRE from all the experiments are summarized in Table 2. All of the Coanda-type intakes, whose features are given in Table 1 are tested for both WCP and SRE under six different slope angles and three different water discharges. In the case of SRE experiments, 300 g, 695 g, and 995 g sediment amounts are fed into the main channel corresponding to 2.4 l/s, 5.56 l/s, and 7.96 l/s, respectively, to obtain the same sediment concentration for each discharge case. For developing the empirical equations, dimensionless parameters are developed, as presented in Table 3.

Table 2. Statistical Summary of data sets.

Data Sets	WCP (Q_{in} / Q_{div})	SRE (S_{in} / S_{re})
Maximum	100	90.4
Minimum	38.7	0.3
Range	61.3	90.0
Mean	70.3	52.7
St. Deviation	16.8	26.0

Table 3. Dimensionless parameters used in analysis.

DIMENSIONLESS PARAMETERS	DESCRIPTION
Θ	Screen Slope (degree)
L / R	The ratio of net screen length to the screen curvature radius
m = e / a	The ratio of total bar opening areas to the total screen area (void ratio)
e / R	The ratio of bar opening to curvature radius
$Fr_{(R)} = \dfrac{V}{\sqrt{g.R}}$	Froude number based on screen curvature radius
$We_{(R)} = \dfrac{\rho V^2 R}{\sigma}$	Weber number based on screen curvature radius
D_{50} / R	The ratio of the median of the sediment diameter to screen curvature radius.
D_{50} / e	The ratio of the median of the sediment diameter to the bar opening
WCP (Q_{in} / Q_{div})	Water capture performance
SRE (S_{in} / S_{re})	Sediment release efficiency

Definition of parameters: Θ is the screen slope, L is the net screen length, R is the screen curvature radius, a is the distance between mid-points of two consecutive screen bars, e is the net opening between two consecutive bars, V is the velocity of water, g is the gravitational acceleration, ρ is the density of the water, σ is the surface tension, d50 median of the sediment diameter, Q_{in} is the incoming discharge through the intake, Q_{div} is the diverted water discharge by the intake, S_{in} is the total sediment amount which was fed into the main flume, S_{re} is the released sediment amount by the intake.

2.2. Genetic Algorithm (GA)

The Genetic Algorithm (GA) is a nonlinear search and optimization method. It is inspired by a biological process of natural selection and survival of the fittest. GA has two main units as gene and chromosome. A gene consists of bits and a chromosome consists of genes. The gene represents a model parameter to be optimized. Each chromosome is a candidate for a solution. In GA, the search process is initiated with many chromosomes. In each iteration, search space is scanned by the chromosomes, while the fitness evaluation, selection, pairing, crossover, and mutation operations are performed. Figure 6 shows the flowchart summarizing the GA operations. There are innumerous studies (papers and books) available in the literature, including Tayfur (2012), on the details of the GAs and their operations, and GA applications in water resources engineering.
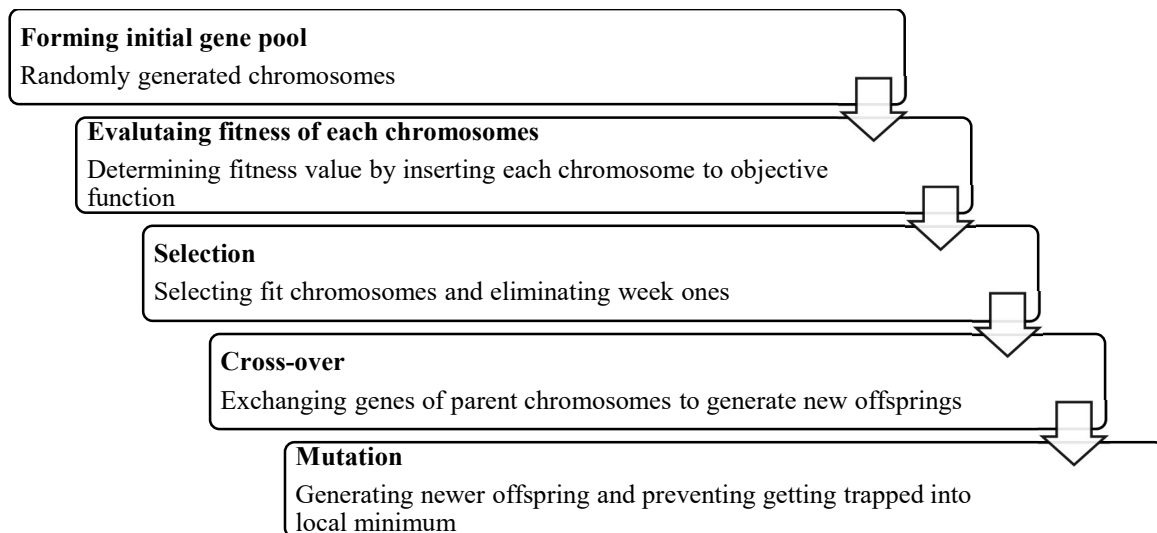
Figure 6. Genetic Algorithm flow chart

2.3. Proposing Empirical Equations

This study proposes nonlinear empirical equations for predicting WCP and SRE, based on the related dimensionless parameters. The parameters (e/R, m, Weber, Ө) are considered in the empirical equation for WCP. However, an important issue is to decide the form of the equation, i.e.; how to place each parameter (as numerator or denominator) with a positive exponent in the equation. To do so, the behavior (direct or inverse variation) between each parameter and the output variable, WCP, is analyzed (Figure 7). According to Figure 7; WCP varies directly with e/R and the void ratio (m) while it varies inversely with Weber number and the screen slope (Ө). Therefore, the following nonlinear equation is proposed for WCP:

$$WCP = c_1 \left[\frac{(m)^{a_2} \left(\frac{e}{R} \right)^{a_3}}{(\theta)^{a_1} (Weber)^{a_4}} \right] \tag{2}$$

Where c_1 is a coefficient and a_1, a_2, a_3, and a_4 are exponents whose optimal values are obtained by the GA, searching for values within the positive range, as more details are given in the next section.
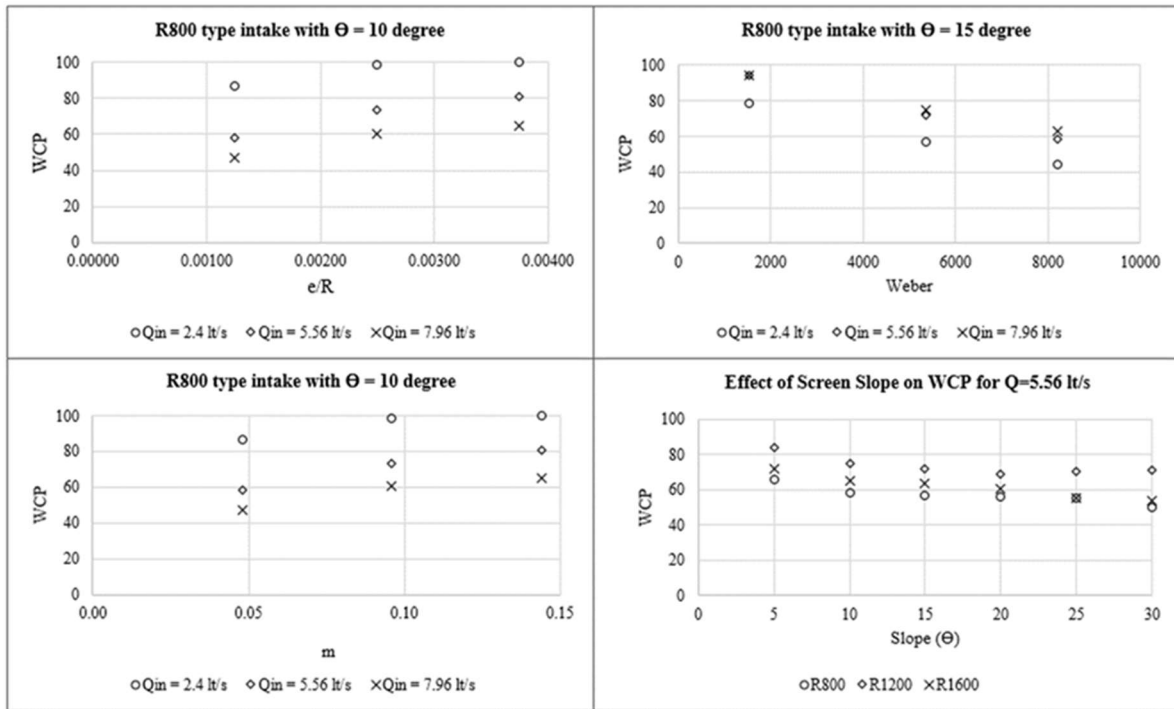
Figure 7. Variation of e/R, Weber number, m, and slope parameters with WCP

The parameters (Ө, Weber, m, e/R, L/R, D50/R) need to be considered in the empirical equation for the SRE. To decide the form of the equation, as it is presented above for the WCP, the behavior (direct or inverse variation) between each parameter and the output variable, SRE, is first analyzed. According to Figure 8; SRE varies directly with Weber number and the screen slope (Ө) while it inversely varies with e/R and the void ratio (m). There is no clear variation behavior is observed for L/R and D50/R parameters.
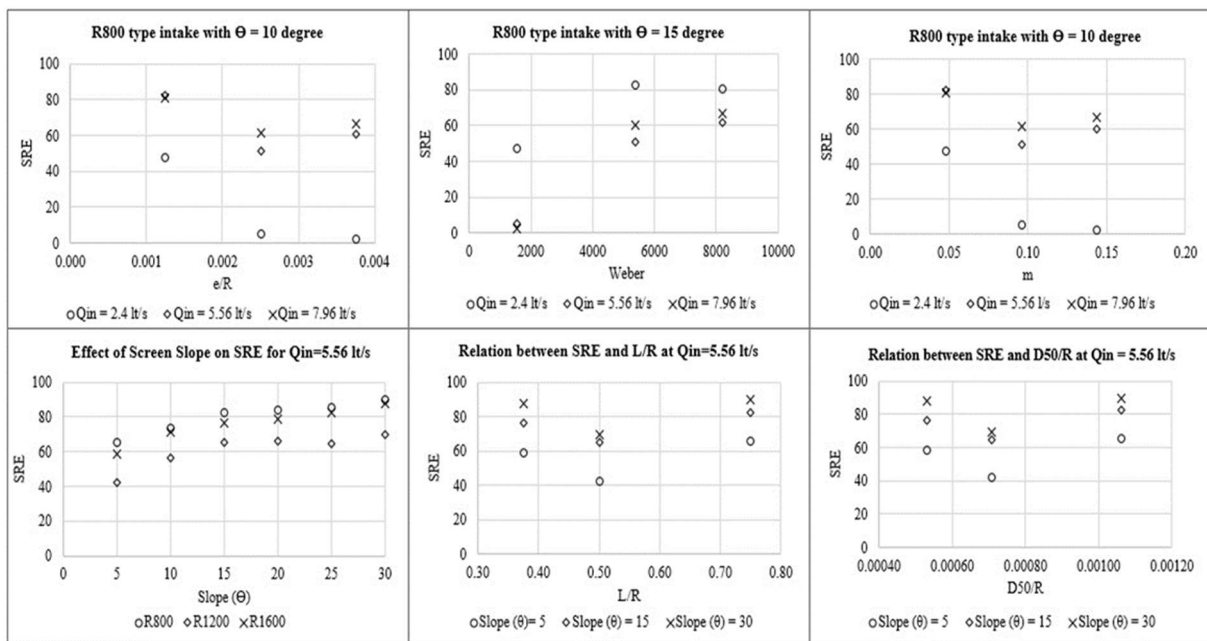
Figure 8. Variation of e/R, Weber, m, Slope, L/R, and D50/R parameters with SRE

Hence, the following nonlinear empirical equation is proposed for the SRE:

$$SRE = c_2 \left[\frac{(\theta)^{b_1} (Weber)^{b_5}}{(m)^{b_2} \left(\frac{e}{R}\right)^{b_3} \left(\frac{L}{R}\right)^{b_4} \left(\frac{D50}{R}\right)^{b_6}} \right] \tag{3}$$

Where c_2 is a coefficient and b_1, b_2, b_3, b_4, b_5, and b_6 are exponents. The optimal values of c_2, b_1, b_2, b_3, b_5 are obtained by the GA, searching values within the positive range while the search space covered a wide range (positive to negative) for b_4 and b_6 since there is no clear variation pattern between L/R and SRE and D50/R and SRE, as more details are given in the next section.

3. RESULTS

The optimal values of coefficients for both WCP and SRE were obtained by employing the GA. Totally 216 data were gathered from the experimental study, 108 for WCP and 108 for SRE. Of the 108 sets for WCP, 70 are selected for calibration, while the rest are for validation. The same is done for SRE. The mean absolute error functions are minimized while finding the optimal values of the coefficients and exponents of Equations (2) and (3). The respected error functions can be expressed as follows:

$$MAE = \frac{1}{N} \sum_{i=1}^{N} | \, WCP \text{ model } -WCP \text{ predicted} \, | \tag{4}$$

$$MAE = \frac{1}{N} \sum_{i=1}^{N} | \, SRE \text{ model } -SRE \text{ predicted} \, | \tag{5}$$

During iterations, 80% crossover rate, 4% mutation rate, and 6000 epochs are employed. The search space for c_1 and c_2 is set to 1-500 and for exponents b_5 and b_6 the search space is set to -3 and +3 while it is set to 0-3 for the other exponents. The obtained optimal values of the coefficients are presented in Table 4. Figures 9 and 10 present the validation and calibration stages for WCP and SRE, respectively. As seen, predictions are satisfactory for both cases, for which the related error measures are summarized in Table 5.

Table 4. Optimal values of the coefficients for GA based equations.

Parameter	c_1	c_2	a_1	a_2	a_3	a_4	b_1	b_2	b_3	b_4	b_5	b_6
WCP	308.41	-	0.08	0.02	0.01	0.13	-	-	-	-	-	-
SRE	-	57.75	-	-	-	-	0.24	0.23	0.01	0.50	0.47	- 0.81
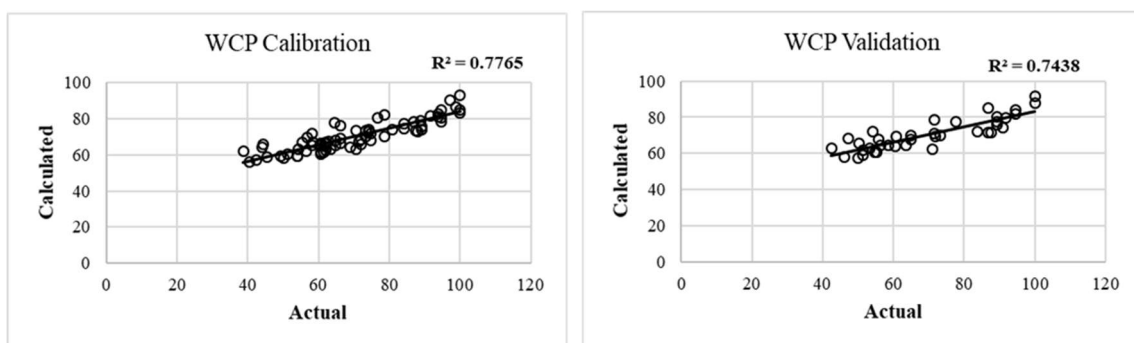
Figure 9. Calibration and validation stages for WCP
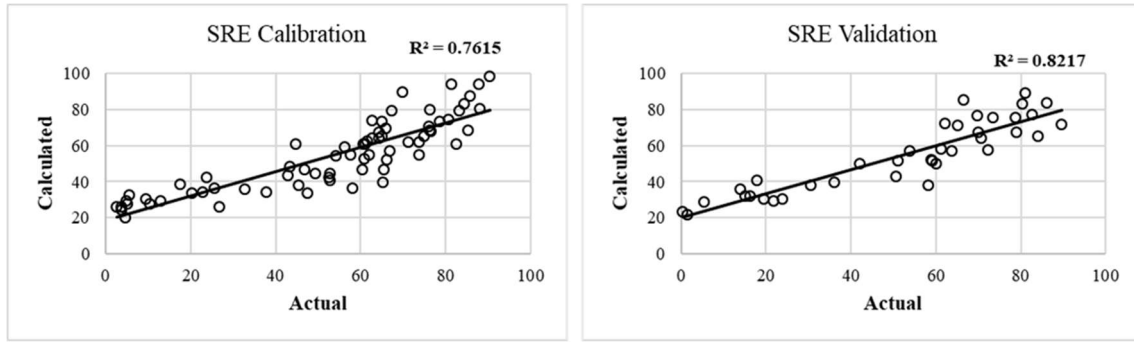
Figure 10. Calibration and validation stages for SRE

Table 5. Measured errors for WCP and SRE.

GA	Calibration (Training)		Validation (Testing)	
	WCP	SRE	WCP	SRE
MAE	8.08	10.4	9.29	10.3
RMSE	9.81	12.9	10.7	12.4
R^2	0.78	0.76	0.74	0.82

The resulting empirical equations can be presented as follows:

$$WCP = 308.41 \left[\frac{(m)^{0.02} \left(\frac{e}{R}\right)^{0.01}}{(\Theta)^{0.08} (Weber)^{0.13}} \right] \quad (6)$$

$$SRE = 57.75 \left[\frac{(\theta)^{0.24}(Weber)^{0.47}}{(m)^{0.23} \left(\frac{e}{R}\right)^{0.01} \left(\frac{L}{R}\right)^{0.50} \left(\frac{D_{50}}{R}\right)^{-0.81}} \right] \quad (7)$$

4. DISCUSSION

The calibration and validation of the GA-based Equation 6 successfully predict WCP values as a function of intake geometry and flow characteristics variables with low errors (MAE=8.08, RMSE=9.81, R^2=0.78 for the calibration stage and MAE=9.29, RMSE=10.7, R^2=0.74 for validation stage). The calibration and validation of Equation 7, the GA-based empirical equation predicting SRE as a function of the intake geometric, sediment, and flow characteristics variables, was accomplished with low errors (MAE = 10.4, RMSE= 12.9 for calibration, and MAE = 10.3, RMSE = 12.4 for validation).

It is important to note that this study is the first one developing empirical equations for the SRE and the WCP as functions of water, sediment, and flow parameters and Coanda intake physical characteristics. Based on the results of the experiments, an optimum design, based on curvature radius, is proposed with the maximum SRE to prevent clogging during the operation of the intakes. As pointed out in the Introduction section, there is a limited number of studies on Coanda intakes, especially subjected to the sediment-laden flows. These studies have involved mostly experimental works that lack any equation development. Therefore, discussing the developed empirical equations within the framework of existing literature becomes quite limited. Hazar and Elci (2021) have, only, attempted to propose multilinear regression (MLR) equations for the variables of SRE and WCP. Apart from the fact that the process is nonlinear rather than linear, they have employed all the data for the calibration stage and they have not verified their equations. In this study, however, the nonlinear

empirical equations are calibrated with about 70% of the data and validated using the rest (about 30%).

Note that when Equation 6 and Equation 7 are developed, about 76 sets of data are used in its calibration, i.e., finding the optimal values of the exponents and the coefficient of the equation. The developed equation is employed for the remaining 32 data to predict the WCP values, that are not presented to the model at all during its calibration stage.

5. SUMMARY AND CONCLUSION

The main objective of this study is to develop nonlinear empirical equations for WCP and SRE, as functions of fluid, sediment, flow, and intake structure parameters for Coanda type intakes. This study has employed 216 sets of experimental data: 108 for the SRE and 108 for the WCP. As a result, related 4 dimensionless parameters for the WCP and 6 for the SRE are considered in the equations. Next, the form of the equations is decided by investigating direct or inverse variation between each parameter and the respected output variable of SRE and WCP. The optimal values of the exponents and coefficients of the proposed equations are obtained using the GA. The proposed equations are successfully calibrated with 70% of the data and validated with the rest. This study concludes that the developed empirical equations can be employed to predict WCP and SRE for Coanda-type intakes. It needs to be pointed out that the equations developed in this study have used laboratory data. It would be suggested to test these equations in field conditions.

With the advantage of reducing the number of variables that describe a system, the empirical equations derived from non-dimensional numbers reduce the number of experiments enabling correlations of physical phenomena to scalable systems. Noted that all the experiments are conducted using constant angled T-shape bars and a constant screen length of 60 cm. therefore, as a future study, at various discharge rates and varying angled T-shape bars, different screen lengths can be investigated, and accordingly the proposed empirical equations can be revised and improved.

REFERENCES

Hazar, O., and Elçi, S. (2020). Design of Coanda Intakes for Optimum Sediment Release Efficiencies. *KSCE Journal of Civil Engineering*. 25, 492-502 (2021). DOI: 10.1007/s12205-020-0760-4.

Howarth, J. Coanda hydro intake screen testing and evaluation. United Kingdom: N. p., 2001.

Huber, Dorothee. 2005 "BEDUIN Project (Better Design of Intakes)." Norwegian Water Resources.

Lauterjung, H.; Schmidt, G. (1989). Planning of water intake structures for irrigation or hydropower. A Publication of GTZ-Postharvest Project. In Deutsche Gesellschaft für Technische Zusammenarbeit (GTZ) GmbH; GTZ: Bonn, Germany.

LeChevallier M.W., Norton W.D. (1995) Giardia and Cryptosporidium in raw and finished water. J Am Water Works Assoc.1995;87(9):54–68.

May, Don. (2015). Sediment Exclusion from Water Systems Using a Coanda Effect Device. *International Journal of Hydraulic Engineering*, no. 4(2): 23-30. DOI: 10.5923/j.ijhe.20150402.01

McKinney DC, Lin M-D (1994) Groundwater optimization using genetic algorithms. *Water Resour. Res* 30(6):1897.

Raju KS, Kumar DN (2004) Irrigation planning using genetic algorithms. *Water Resur Manag* 18:163-176.

Strong, J. J., and Ott, R.F. (1998)" Intake Screens for Small Hydro Plants" Hydro Review, reprinted from Vol. VII, No. V, October 1988, HCL Publications 410 Archibald Street Kansas City, MO 64111 (816)931-1311.

Tayfur, G. (2012). *Soft Computing in Water Resources Engineering: Artificial neural network, fuzzy logic and genetic algorithm.* WIT Press, Southampton, United Kingdom.

Tayfur, G. (2017). Modern Optimization Methods in Water Resources. *Water Resour Manag* 31:3205-3233 DOI 10.1007/s11269-017-1694-6.

Tayfur G, Barbetta S, Moramarco T. (2009). Genetic algorithm-based discharge estimation at sites receiving lateral inflows. *J. Hydrol Eng* 14(5):463-474.

Wahl, T. (2001). Hydraulic Performance of Coanda-Effect Screens. *Journal of Hydraulic Engineering*. 127, no. 6: 480-488.

Wahl, T. 2003. Design guidance for Coanda-Effect screens. U.S. Depth. Of the Interior, Bureau of Reclamation, Technical Service Center, Research Report R-03-03. July 2003.

Wang QJ. (1991). The genetic algorithm and its application to calibrating conceptual rainfall-runoff models. *Water Resour. Res 27(9):2467.*

EXPERIMENTAL STUDY OF A HOMOGENEOUS DAM BREAK WITH A BREACH

Ebru Taşkaya

Civil Engineering Department, İzmir Kâtip Çelebi University

İzmir, Turkey

ebruutsky@gmail.com

Zehra Büyüker

Civil Engineering Department, İzmir Kâtip Çelebi University

İzmir, Turkey

zehra.buyuker@ikcu.edu.tr

Büşra Öztürk

Civil Engineering Department, İzmir Kâtip Çelebi University

İzmir, Turkey

busrraozturk@outlook.com

Gökçen Bombar

Civil Engineering Department, İzmir Kâtip Çelebi University

İzmir, Turkey

gokcen.bombar@ikcu.edu.tr

Gökmen Tayfur

Civil Engineering Department, Izmir Instıtute of Technology

İzmir, Turkey

gokmentayfur@iyte.edu.tr

ABSTRACT: Although dam failures are not a frequent occurrence, they can cause serious loss of life and property as a result of their failure. The large volume of water accumulating in the reservoir of the dam exceeds the dam body and reaches the downstream region uncontrollably, causing flooding. It is very important for the settlement areas in the downstream region to determine the progression of the flood wave formed by the dam break the downstream and the determination of the risky areas. In this study, the progress of the flood formed as a result of the homogeneous earth-fill dam failure and the movement of the sediment to be transported from the dam body with the flood wave downstream were experimentally investigated. A homogeneous earth-fill dam break was carried out by overtopping. A homogeneous earth-fill dam was constructed using a material with a median grain diameter of 0.441, compressed into 6 layers of 10 cm, and 60 cm. A breach was made in the middle of the dam crest level, 8 cm deep and 10 cm wide. During the experiments, the video was recorded with a camera. Water depth measurements were recorded from the ULS40-D device and metal rulers on the left wall of the channel. Sediment distribution at the end of the experiment is given by a contour map.

1. INTRODUCTION

Humans, animals, and plants need water to survive. Due to urbanization and the increase in the human population, they built dams in order to provide the water needs of the people more easily. Dams are needed and used for reasons such as mains drinking water, electricity generation, irrigation of agricultural areas, and meeting industrial water needs. It is built for the purpose of flood prevention in

order to control the excess water coming from the flood, especially in regions with abundant rainfall. The break of the dam can result in a huge loss of life and property. For this reason, being able to predict the movement of the flood wave that will occur as a result of dam failure before it occurs can increase the safety of the settlements in the downstream region and minimize the damage that may occur. The reasons for the break of dams; ınsufficient spillway, structural faults, earthquakes, overtopping, ground settlements in the dam body, leakage movements, filling of the reservoir due to heavy rains, and other reasons.

In the study published by Bozkuş (2004), it was stated that according to the report of the International Commission on Large Dams (ICOLD), 38% of dam failures were due to insufficient spillway capacity and 33% due to piping in the dam body. Costa et al. According to (1985), about 34% of dam failures are caused by overtopping, 30% by foundation defects, and 28% by piping. Overtopping is the way in which the water in the reservoir upstream of the dam is pass over the crest of the dam, causing erosion on the downstream surface of the dam. Tingsanchali and Chinnarasri (2001) conducted overtopping experiments on a homogeneous dam body in a channel and modeled the in one-dimensional form. Zhang et al. (2012) carried out overtopping dam break experiments on a homogeneous dam body from the laboratory channel. Güney et al. (2014) also investigated the flood wave formed as a result of the sudden break of the dam using the three-dimensional distorted model of the Ürkmez Dam. Haltaş et al. (2016) created flood maps for the downstream areas of the dam failure for the Porsuk Dam in Eskişehir and the Alibey Dam in Istanbul. In none of these studies, the sediment movement in the dam body as a result of dam failure was not investigated, and only the water flow part was studied experimentally and numerically.

In this experimental study, the distribution of the movement of sediment in the dam body along with the flood wave to the downstream region as a result of the failure of the dam was investigated.

2. EXPERIMENTAL SET-UP

In this study the experiments were performed in a reinforced concrete channel with 18 m in long, 2 m in wide and 0.88 m in deep, located in the hydraulic laboratory of Izmir Katip Celebi University. The water was supplied to the channel with a manual pump. The dam was constructed between x = -1 m and x= 1.02 m of the main channel with a width of 2 m, a length of 2.02 m, and a height of 0.6 m. The experiment, cube roughness elements 10 cm x 10 cm and 10 cm high concrete blocks were used as rigid roughness elements by arranging them in 5 rows in the configuration given in Figure 1.
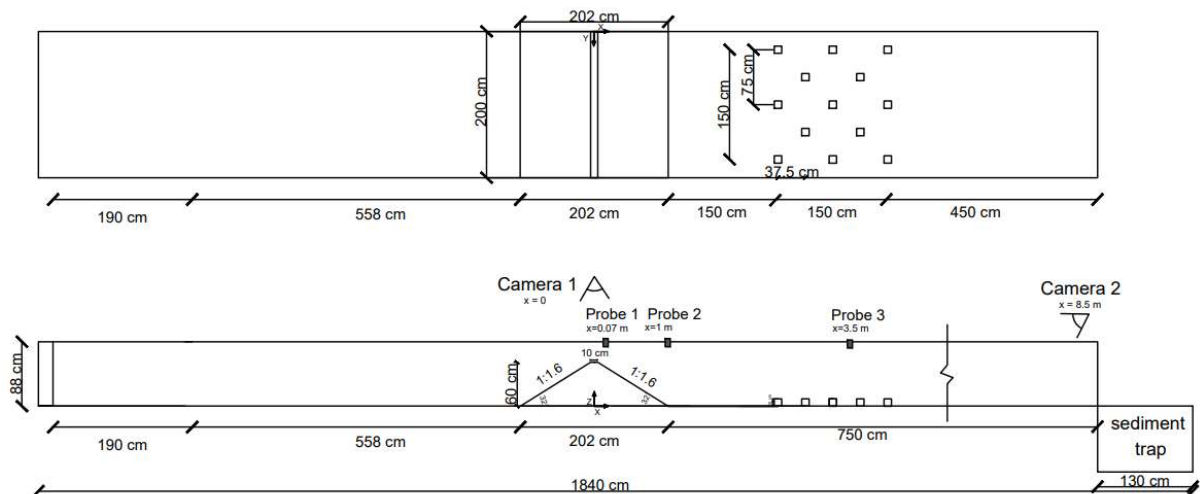
Figure 27. Channel cross-section

Since the dam type is homogeneous, with d_{50} = 0.441 mm sand was used in the construction of the dam. The size distribution curve is given in Figure 2. While the construction of the dam body the fill material is 1363 kg in the total using the sand.
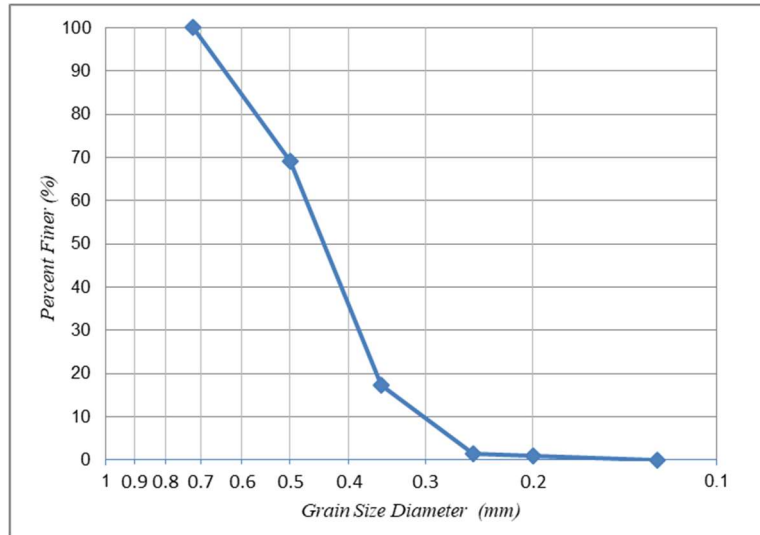
Figure 2. Grain size distribution

The homogeneous earth-fill dam body is constructed with six-layer (Figure 3.(c)). The first layer width is 2 m, a length of 2.02 m. After the placement process, the surface of the sand layer was smoothed (Figure 3.(a)). Following the placement process was completed, the 4.5 kg iron weight was dropped from 46 cm onto the 40 * 40 cm metallic plate 10 times (Figure 3.(b)). For the next five layers, the same procedure was followed. The dam body was built with a crest width of 10 cm by changing the base length of each floor. After the compression process is complete the upstream and downstream slopes were arranged at 32˚ with a spirit level.
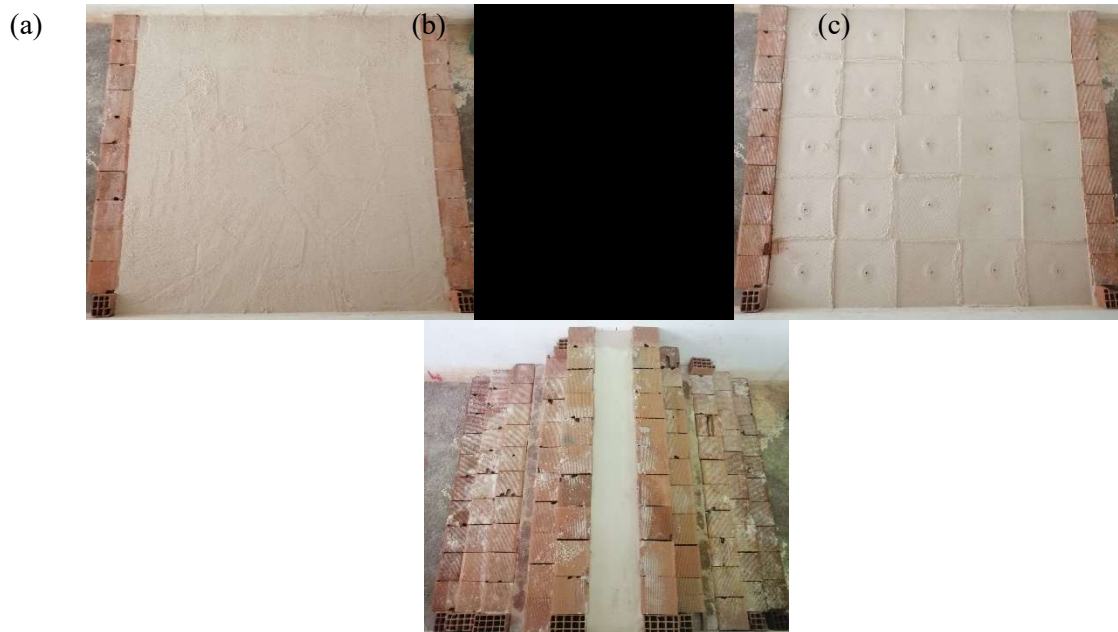
Figure 3. Dam body construction stages, (a) 1st layer uncompressed,(b) 1st layer compressed, and (c) dam body built 6 floors

At the beginning of the experiment process, the dam was covered with a plastic cover until the level of the water coming from the channel stabilized at approximately 45 cm as shown in Figure 4. After the water reached the desired level, the cover on the dam was removed, the pump was turned off. For dam failure, the waiting period was started for the dam to collapse. During the experiments video recordings were taken with 2 cameras. Camera 1 location is x = 0 m, camera 2 location is end of the channel, x = 8.5 m. Water depth measurements took 4 different points. The water depth was measured

with metal rulers on the left wall of the channel at 4 different points, x = -1.5 m, x = 3.5 m, x = 5 m, and x = 6.5 m, respectively. In addition, water depth measurements were made in the middle of the channel using the ULS40-D (Ultralab Level System) device with probes at 3 different points, one on the dam body (x = 0.07 m), the other two the downstream of the dam (x = 1 m and x = 3.5 m) taken.
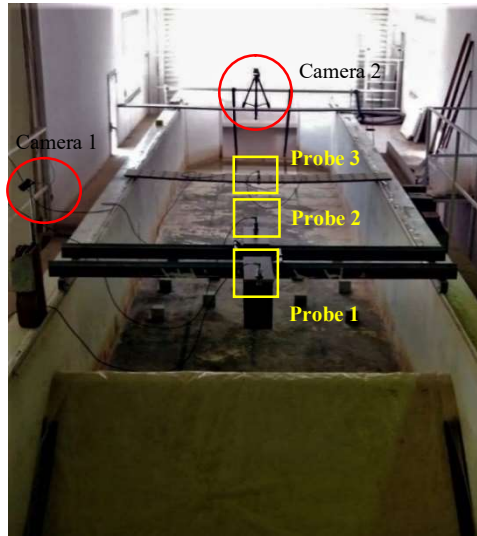
Figure 4. Final form of the channel

After the homogeneous earth-fill dam break, the measurement of the sediment propagation from the channel was made with using ULS40-D. In this measurement, the channel length is considered as the x-axis, the channel width as the y-axis, and the sediment depth as the z-axis. The measurement of the sediment thickness was made with 10 cm intervals on the x and y axes.

3. EXPERIMENTAL RESULTS

(1)   (2)
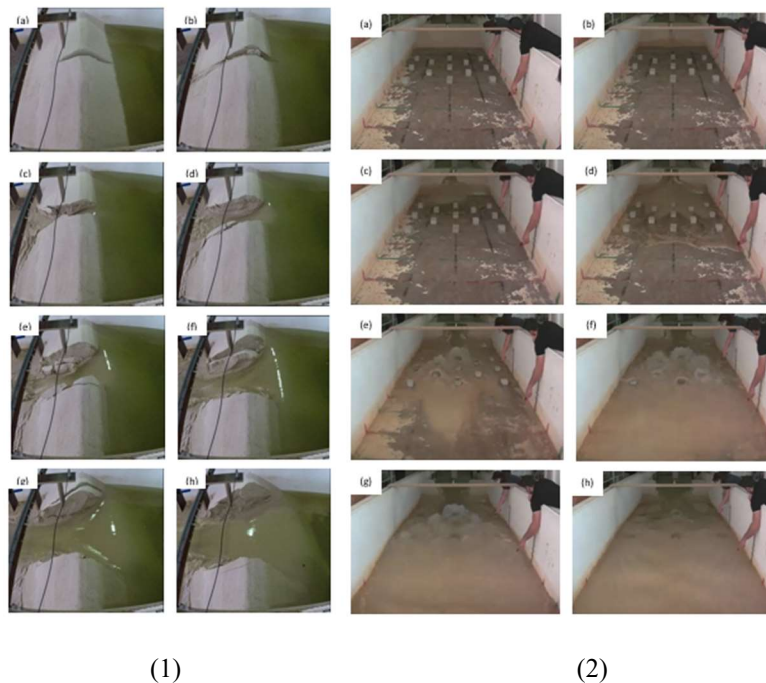
Figure 5. (1) Camera 1, (2) Camera 2, (a) 0, (b) 25 sec, (c) 70 sec, (d) 80 sec, (f) 90 sec, (e) 100 sec (g) 110 sec, (h) 140 sec.

As seen in Figure 5, the downstream of the homogeneous earth-fill dam body was eroded for 140 seconds, and sediment movement started because of the erosion middle of the dam body. The water level was increased up to 52.5 cm until it passed through the breach (Figure 5. (1),b). A breach occurred in the body of the dam and gradually expanded (Figure 5. c, d ,e , f). Sediment completely covered the channel within 100 seconds. The jumps occurred due to the cubes placed from 2.5 m of the canal (Figure 5. (2) e, f, g) and disappearing with the decrease of the water level. Figure 6 shows the sediment transport spread along the channel at the end of the experiment.
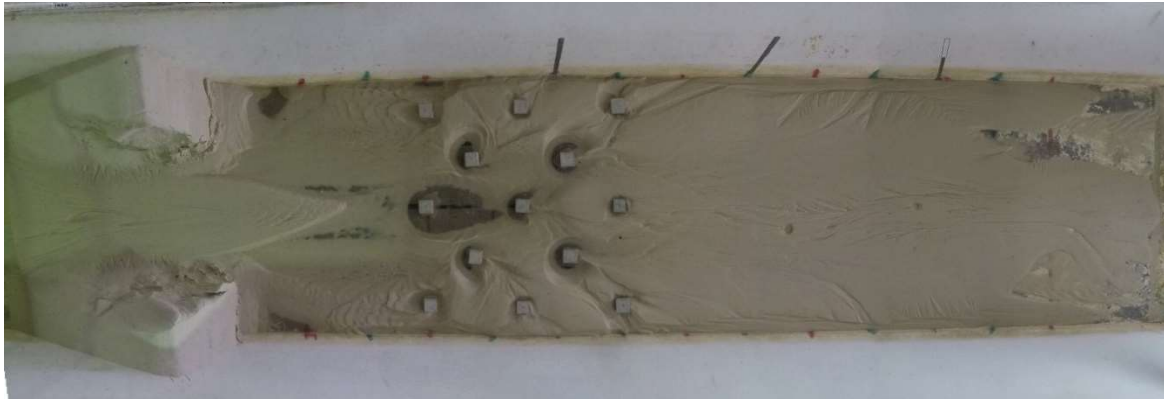
Figure 6. Top view of the channel at the end of the experiment

In Figure 7, the contour plot of the propagation from after the dam break dam body is given. The contour graph shows the sediment thickness (Z) of the channel between x= -1 m and x= 8.5 m in 2 different height ranges. The top graph shows the sediment distribution in the regions where the sediment thickness propagation along the channel is 0-100 mm, and the bottom graph shows the sediment thickness in the regions where the sediment thickness is 100-600 mm. The sediment in the dam body was transported along the x-axis between 50 cm and 150 cm on the y-axis. The sediment thickness of the channel is between 2.5 m and 4 m, thicker on the right and left walls, around 80 mm, and between 4 m and 7 m, it averages between 40 mm and 60 mm. It is observed that the sediment thickness is quite low at the points where jumps are seen in the cubes. It can be said that both the longitudinal and transverse profiles of the sediment distribution in the dam body and downstream region are uniform.
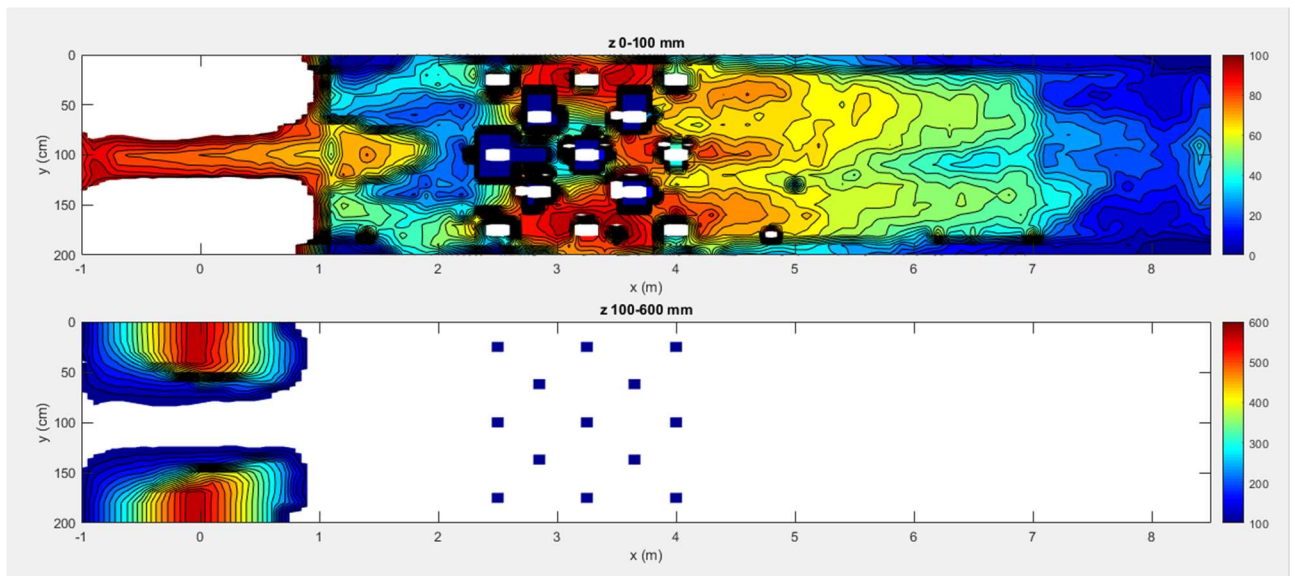
Figure 7. Contour graph
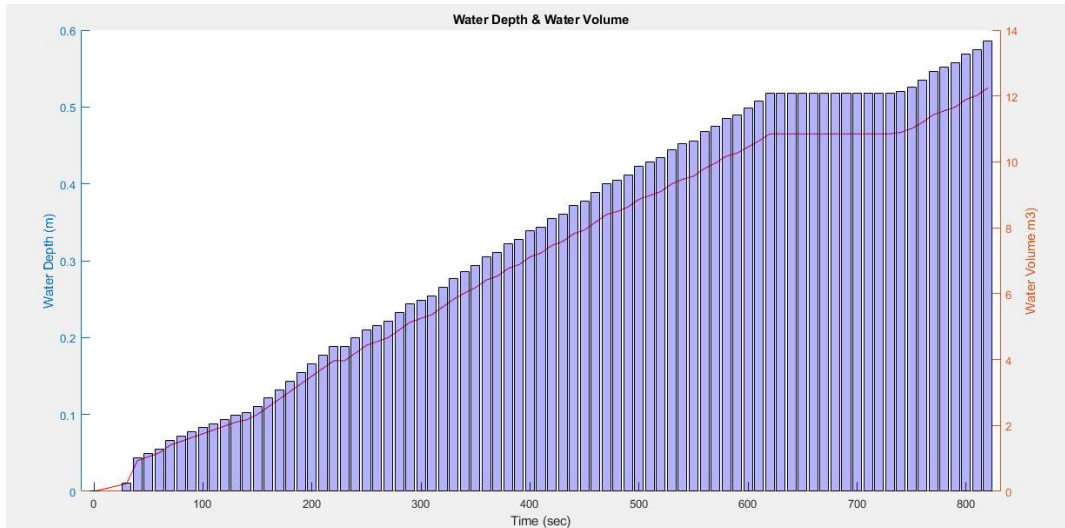
Figure 8. Upstream water depth and volume graph

Figure 8 shows a graph of the depth and volume of water accumulating in the reservoir downstream of the dam. The water depth downstream reached 52.5 cm, which was slowly filled for 820 seconds. While the water depth is 52.5 cm, the water volume upstream is 13.67 m^3.

Figure 9 shows the variation of water depth upstream and depth changes downstream. While the final water depth upstream was 9 cm, the final depths for x = 3.5 m, 5 m, and 6.5 m downstream were measured as 8 cm, 4.8 cm, and 1.8 cm, respectively. The maximum water depths due to hydraulic jump downstream were measured as 15 cm, 12 cm, and 14 cm for x = 3.5 m, 5 m, and 6.5 m, respectively.
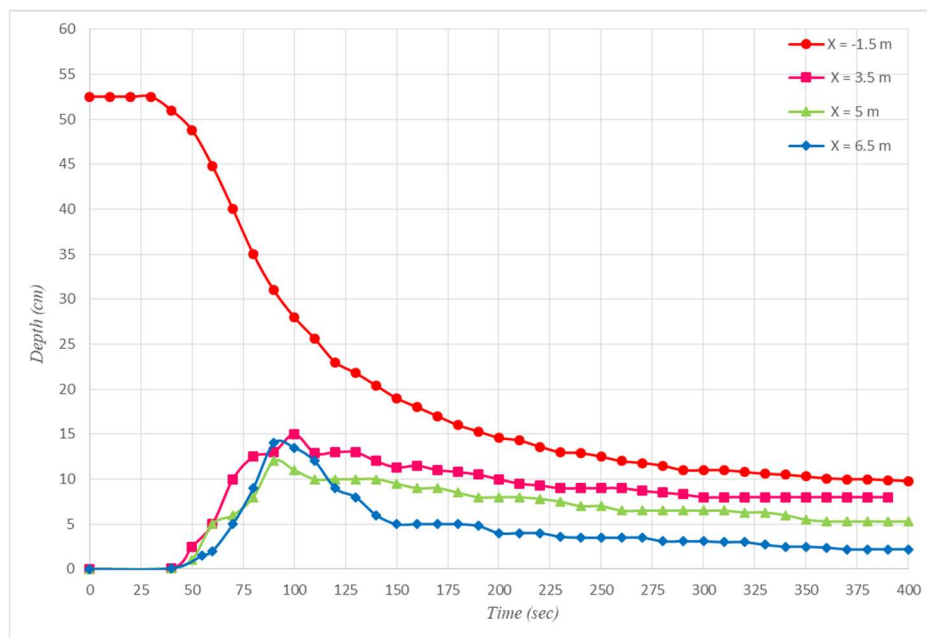
Figure 9. Water depth upstream and depths downstream

Figure 10, Figure 11, and Figure 12 show the depth-time graphs of the measurements taken with the help of Probes placed in the middle of the channel. When Probe 1 measurement is examined in Figure 10, it is seen that there is a decrease of 480 in the middle of the dam body. This decrease occurred between 50-100 seconds.
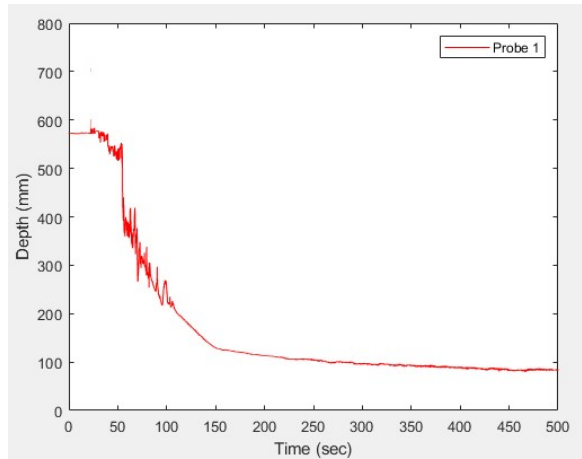
Figure 10. Depth-time graph obtained from the probe 1

Data from the probe 2 measurement point is shown in Figure 11. At this point, the depth variation is quite large. Maximum depth is 118 mm.
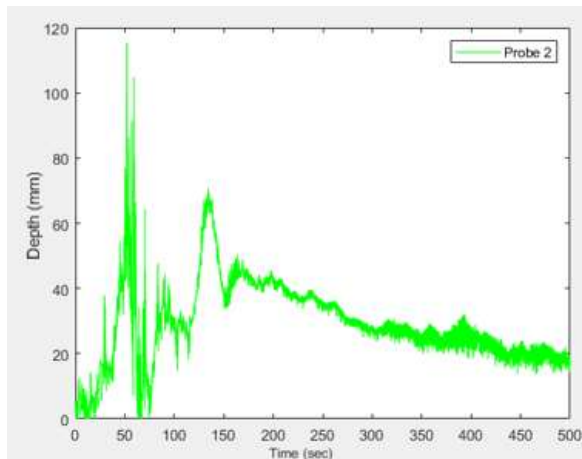
Figure 11. Depth-time graph obtained from the probe 2

Data from the probe 3 measurement point is shown in Figure 12. At this point, the depth increased from the first 100 seconds to 130 mm and then decreased to 60 mm.
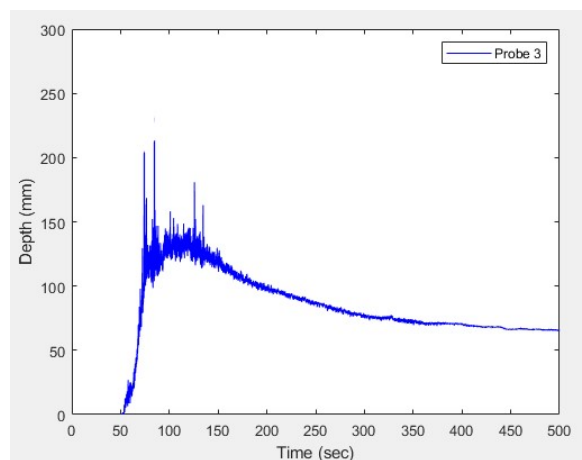
Figure 12. Depth-time graph obtained from the probe 3

4. CONCLUSIONS

This experimental study investigated the distribution of sediment in the dam body distributed to the rough downstream region of the homogeneous earth-fill dam, which breaks as a result of overtopping. The upstream of the dam was slowly filled with water for 820 seconds, and the dam was broken with a depth of 52.5 cm and a water volume of 13.67 m³. The experiment took 600 seconds. At the end of the experiment, the upstream water depth decreased by 82.9%. Depths to the left of the downstream channel are 15.2 % of the downstream water depth at x= 3.5 m, 9.1 % at x= 5 m, and 3.4 % at x= 6.5 m. According to the data obtained from the probes using the ULS40-D device according to the data obtained from the measurement in probe 1, the height of the dam body decreased by 82.8 %. The depth in probe 2 increased by a maximum of 21.5 % according to the upstream water depth, and the depth increased by 38.1 % according to the data of probe 3. At x = 6.5 m of the channel, the difference between the depth to the left of the channel and the maximum depth in the middle of the channel is 11.4 %. The sediment carried from the dam body propagation along with all downstream of the channel (8.5 m) and wide (2 m). 50 % of the dam width has propagated from the dam body to the downstream of the channel. The sediment propagation along the downstream channel is higher between 2.5 m and 5 m to the right and left of the channel.

REFERENCES

Bozkuş Z Afet yönetimi için yönetime için baraj yıkılma analizleri. Teknik Dergi,2004; 15(4), 3335-3350.

Costa, J. E., (1985). Floods from Dam Failures; Open File Report 85-560. US Geological Survey: Denver, CO, USA, 54

Guney, M. S.; Tayfur, G.; Bombar, G.; et al. (2014). 'Distorted Physical Model to Study Sudden Partial Dam Break Flows in an Urban Area.' JOURNAL OF HYDRAULIC ENGINEERING, Volume: 140 Issue: 11 Article Number: 05014006 Published: NOV 2014.

Haltas, Ismail; Elci, Sebnem; Tayfur, Gokmen Numerical Simulation of Flood Wave Propagation in Two Dimensions in Densely Populated Urban Areas due to Dam Break.' WATER RESOURCES MANAGEMENT Volume: 30 Issue: 15 Pages: 5699-5721 Published: DEC 2016

Tawatchaı Tıngsanchalı & Chaıyuth Chınnarasrı, 2001. Numerical modelling of dam failure due to flow Overtopping, Hydrological Sciences-Journal?des Sciences Hydrologiques, 46.

Zhang KQ, Liu FS, Sun L, Lin C. The theoretical research and finitet element analysis of toe weight on the earth and rockfill dam reinforcement. In: 2012 International conference on modern hydraulic engineering; 2012. p. 744–9.

14TH INTERNATIONAL CONFERENCE
ON HYDROSCIENCE & ENGINEERING

MAY 26-27, 2022
IZMİR-TURKEY

ICHE2022
IZMIR, TURKEY

TRANSITION PROCESSES OF SEDIMENT TRANSPORT MODES WITH STREAM GRADIENT CHANGES

Takashi Wada

Department of Social Systems and Civil Engineering, Graduate School of Engineering, Tottori University

Tottori, Japan

wada-t@tottori-u.ac.jp

Kazuki Kobayashi

Asahi Consultant Co., Ltd.

Tottori, Japan

k.kobayashi@asahic.co.jp

Hiroshi Miwa

Department of Social Systems and Civil Engineering, Graduate School of Engineering, Tottori University

Tottori, Japan

miwa-h@tottori-u.ac.jp

ABSTRACT: In a mountainous stream with a steep gradient, the sediment transport mode is a collective transportation, for example, a debris flow. The mode varies with the changes in stream gradients. However, few studies have investigated the transition processes of sediment transport modes. In this study, we investigated the transition processes of sediment transport modes on the debris flow composed of uniform-sized and mixed-sized gravels due to the changes in streambed gradients. For this purpose, we used the experimental flume with two variable gradients in the upstream and downstream parts. We measured the sediment transport velocities in the interior of the flow front at the gradient-changed point, and the flow front's depths at the upstream and downstream parts. We also sampled the flow front to measure the sediment transport concentration of the front at the downstream end of the flume. According to our experimental results, the transition sections of sediment transport modes are long with a high inflow rate because the transition progresses slowly due to the consumed momentum which is quite smaller than the whole debris flow momentum. In contrast, in the case with a low inflow rate, the transition is achieved with a shorter section because of the larger consumed momentum. When the inflow rates is constant, it was found that the transition is achieved with a shorter section as the debris flow material becomes coarser. For the debris flow composed of mixed-sized gravels, the transition section is short because the large debris flow momentum is consumed to transport the coarser particles concentrated at the flow front. Considering that the momentum is affected by the inflow rate and the particle size composition, the transition section of sediment transport modes due to changes in streambed gradients depends on the debris flow momentum.

1. INTRODUCTION

Sediment is transported from mountainous areas to seas through rivers and streams in a drainage basin. The sediment transport mode in most areas of a basin, i.e., a river with a gentle gradient, is an individual transportation. In contrast, in a mountainous stream with a steep gradient, the sediment transport mode is collective transportation, for example, a debris flow. This mode changes to the several stages during the downflow with the remarkable changes in the mountainous streambed gradients. The sediment transport mode on a streambed gradient of more than approximately 15° (in the case where the sediment concentration of the flow, C, is greater than 0.2, as reported by *Takahashi* (1982, 1987)) is a debris flow. For a gradient with less than approximately 15° (in the case where C is

less than 0.2), the weakening of the gravitational force in the flow direction makes it impossible to maintain the sediment distributed in the entire flow layer. Thus, the sediment transport mode changes to a two-layer flow, which forms a water flow in the upper part of the entire flow layer and a concentrated sediment flow in the lower part. *Hashimoto et al.* (1986) also suggested that the mode varied from a debris flow to a two-layer flow on a streambed gradient of less than approximately 14° based on their experimental results about the sediment transport modes on the several gradients. We call the sediment transport mode "a sediment sheet flow" or "an immature debris flow." As the streambed gradient decreases further, the sediment flow layer thickness decreases more, and the sediment transport mode changes to an individual transportation, that is, a bed load transport. Considering the above, the sediment transport mode is a sediment sheet flow or a bed load transport when a debris flow reaches to the downstream end of a mountain stream, which is at the top of an alluvial fan, because the gradient is often less than 15°. Therefore, to predict the damage caused by a debris flow on an alluvial fan more accurately, it is necessary to accurately determine the characteristics of the debris flow supplied to the fan from mountain streams based on the transition processes of sediment transport modes owing to the changes in streambed gradients.

Previous studies have clarified the sediment transport mechanisms in a debris flow and a sediment sheet flow on the flume with a constant gradient (e. g., *Takahashi, 1982, 1987; Hashimoto et al., 1986; Egashira et al., 1990*). On the other hands, several studies have clarified the sediment transport processes on the flume with continuously changing gradients (e. g., *Takahashi & Kuang, 1986; Ikeda et al., 2009*). However, these studies focused on only the process to generating a debris flow by a surface runoff on the streambed with steep gradients (more than 15°). Though *Takahama et al.* (2002) proposed a numerical model for the two-layer flow composed of a water flow in the upper part of the entire flow layer and a concentrated sediment flow in the lower part, based on the sediment transport mechanisms by *Egashira et al.* (1990), few researchers except them have attempted a numerical modeling for the transition processes of sediment transport modes. Thus, few studies have focused on the transition processes from a debris flow to a sediment sheet flow with changing gradients from more than 15° to less than 15°.

A debris flow is composed of various sized sediment particles, and these particles influence each other during the downflow, resulting in the occurrence of particle-size segregation in the flow interior. In particular, in a stony debris flow with many boulders, the boulders become concentrated toward the flow front during downflow in mountain streams as reported in many field studies (e.g., *Sharp et al., 1953; Okuda et al., 1977; Teramoto et al., 2002*) and experimental studies (e.g., *Hashimoto and Tsubaki, 1983; Miyamoto, 1986; Suwa, 1988; Takahashi et al., 1992; Iverson et al., 2010; Wada et al., 2015*). *Ashida et al.* (1978) conducted the flume experiments on the transport mechanisms of sediment mixtures on flume-bed gradients of 1° to 8°. They clarified that although the migration velocities of various sized particles in the flow interior are generally consistent, finer particles fall to the flow bottom; furthermore, it is difficult for finer particles to migrate because the coarser particles above block them from moving; thus, the coarsening of migrating particles becomes more pronounced. This indicates that the migrating particle-size segregation (coarsening of migrating particles) also occurs in the interior of the sediment sheet flow occurred on gradients of less than 15°. Thus, to predict the damage caused by a stony debris flow on an alluvial fan more accurately, it is also important to understand how the changes in streambed gradients affect the size segregation of migrating particles in the debris flow interior during downflow in mountain streams.

Based on the above background, this study focuses on the transition processes of sediment transport mode and the particle-size segregation for the sediment flows consisting of uniform-sized and mixed-sized gravels due to changes in streambed gradients from more than 15° to less than 15°. To investigate the processes, we conducted the flume experiments on sediment flows with uniform-sized and mixed-sized gravels, using an experimental flume consisting of two variable gradients in the upstream and downstream parts. Based on these experimental results, we determined the effect of changes in streambed gradients on the sediment transport mode and the size segregation of migrating particles.

2. MATERIALS AND METHODS

Figure 1 shows the experimental setup used in the study. We used the experimental flume consisting of two variable gradients in the upstream and downstream parts, with lengths of 150 cm long and widths of 10 cm, respectively, and a 50-cm-long fixed bed part for the rectification of supply water at the upstream end of the flume. We conducted the experiments under the uniform gradient conditions of 9° and 15°, and the changed gradient condition from 15° to 9°. We measured the sediment transport concentrations using a movable sediment sampler at the downstream end of the flume (P 0 in Figure 1), the flow front depth using ultrasonic water-level sensors (OMRON's E4C-DS30) at the points that were 100 and 200 cm upstream from the downstream end (P 100 and P 200 in Figure 1), and the sediment transport velocities in the interior of the flow front using a high-speed video camera (CASIO's EXILIM PRO EX-F1) at the point that was 150 cm upstream from the downstream end (the gradient-changed point, P 150 in Figure 1). The sediment with uniform-sized gravel consisted particles with diameters of 3.0 mm or 7.1 mm. In the gravel mixtures, 80% gravels had a diameter of 3.0 mm, and 20% gravels had a diameters of 7.1 mm. The mass density of the gravels (σ) was 2.650 g/cm^3, and the concentration in the static sediment bed (C_*) was 0.575, and the internal friction angle (ϕ) was 34.80°.

The experiments combined various conditions based on three key factors: the inflow rate of water supply at the upstream end of the flume, the particle size composition of debris flow materials, and the setting gradients in the upstream and downstream parts. Table 1 lists the experimental cases and their respective conditions. For all conditions of the particle size composition and setting gradients, the inflow rates of supplied water were set to 1,000 cm^3/s and 2,000 cm^3/s.

The experimental procedure is described as follows. After the materials were set with a thickness of 5 cm in the upstream and downstream parts of the flume (the total material volume including bulks: 15,000 cm^3), water was supplied by the two types of inflow rates as described above at the upstream end of the flume. As soon as starting the supply, the height measurement from the ultrasonic sensors to the materials under them was started. The debris flow depth was obtained by calculating the difference with the measured heights with no passage of a debris flow and during its passage. At this time, the signal of starting the supply was filmed within the view of the high-speed video camera that was set at the gradient-changed point (P 150). As the supplied water moved down on the flume, the water eroded the materials, and a debris flow was formed. When the debris flow arrived at the downstream end of the flume (P 0), the flow encountered the sampler moving at a constant speed in the transverse direction with respect to the flow direction. Since we focused on the debris flow front, which was considered to be affected by the gradient change, we obtained the materials in the frontal segment of the flow with the sampler. The sampler separated the debris flow front into the four boxes over the time intervals in the range of 1.0–2.0 s. These time intervals were measured by recording flowing of the material into boxes using a video camera. Measurements were performed to determine the temporal changes in the sediment transport concentration and the proportions of particle sizes of the flow front in each sample.
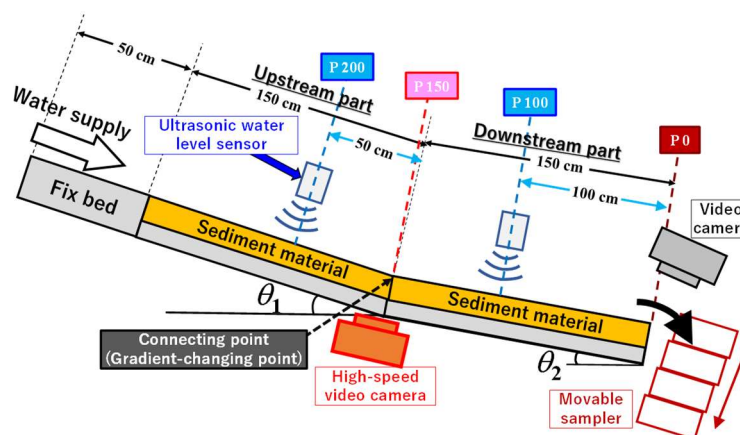
Figure 1. Experimental setup

Table 121. Experimental cases and conditions.

Case	Inflow rate (cm³/s)	Particle-size composition of debris flow material	Flume gradient (°) $\theta_1 \rightarrow \theta_2$
Case 1	2,000	Uniformed gravel with a diameter of 3.0 mm	9 → 9 (Gentle uniform gradient) 15 → 15 (Steep uniform gradient) 15 → 9 (Changed gradient)
Case 2	2,000	Mixed-sized gravel composed of 80% gravels; a diameters of 3.0 mm, 20% gravels; a diameters of 7.1 mm	9 → 9 (Gentle uniform gradient) 15 → 15 (Steep uniform gradient) 15 → 9 (Changed gradient)
Case 3	2,000	Uniformed gravel with a diameter of 7.1 mm	9 → 9 (Gentle uniform gradient) 15 → 15 (Steep uniform gradient) 15 → 9 (Changed gradient)
Case 4	1,000	Uniformed gravel with a diameter of 3.0 mm	9 → 9 (Gentle uniform gradient) 15 → 15 (Steep uniform gradient) 15 → 9 (Changed gradient)
Case 5	1,000	Mixed-sized gravel composed of 80% gravels; a diameters of 3.0 mm, 20% gravels; a diameters of 7.1 mm	9 → 9 (Gentle uniform gradient) 15 → 15 (Steep uniform gradient) 15 → 9 (Changed gradient)
Case 6	1,000	Uniformed gravel with a diameter of 7.1 mm	9 → 9 (Gentle uniform gradient) 15 → 15 (Steep uniform gradient) 15 → 9 (Changed gradient)

Based on these results, the sediment transport concentration of the flow front (C_s) was calculated using the following equations:

$$C_{Sn} = \frac{V_{Sn}}{V_{Wn} + V_{Sn}} \tag{1}$$

where n is the box number of the sampler ($n = 1$–4), V_{Sn} is the water volume obtained from the n-th box (cm³), and V_{Wn} is the sediment volume obtained from the n-th box (cm³). For the debris flow composed of mixed-sized gravels, V_S is the total volume of finer and coarser gravels. The average sediment transport concentration of the flow front ($\overline{C_S}$) is the average of the sediment transport concentrations of all boxes.

3. RESULTS AND DISCUSSION

By comparing the experimental results on the gentle (9°) and steep (15°) uniform gradients with those on the changed gradient (from 15° to 9°), we examined the transition processes of sediment transport modes and the particle-size segregation for the sediment flows consisting of uniform-sized and mixed-sized gravels owing to the changes in streambed gradients. The results to be compared were the sediment transport concentration of the flow front at P 0 and the flow depth of the flow front at P 100 and P 200, and the distribution of migration particle velocities in the interior of the flow front at P 150. The sediment transport modes at these observation points were investigated by examining which the results in the case of the changed gradient were closer to those in the case of a gentle or steep uniformed gradient.

1.1. Effect of changed gradient on sediment transport concentration of debris flow front

1.1.1. Validation of our experimental results on sediment transport concentration of debris flow front

Figure 2 shows the sediment transport concentration of the debris flow front (C_s) at P 0 for all cases. Figure 2 also shows the estimated C_s value for the uniform gradients of 9° and 15° using the experimental equation for a sediment sheet flow by *Mizuyama* (1980) (Equation 2). Note that because the applicable condition of Equation 2 is $0.05 < \tan \theta < 0.25$ ($\tan \theta$; the bed gradient), the estimated C_s values by Equation 2 for the gradient of 15° ($\tan 15° = 0.268$) are not appropriate. In our study, the
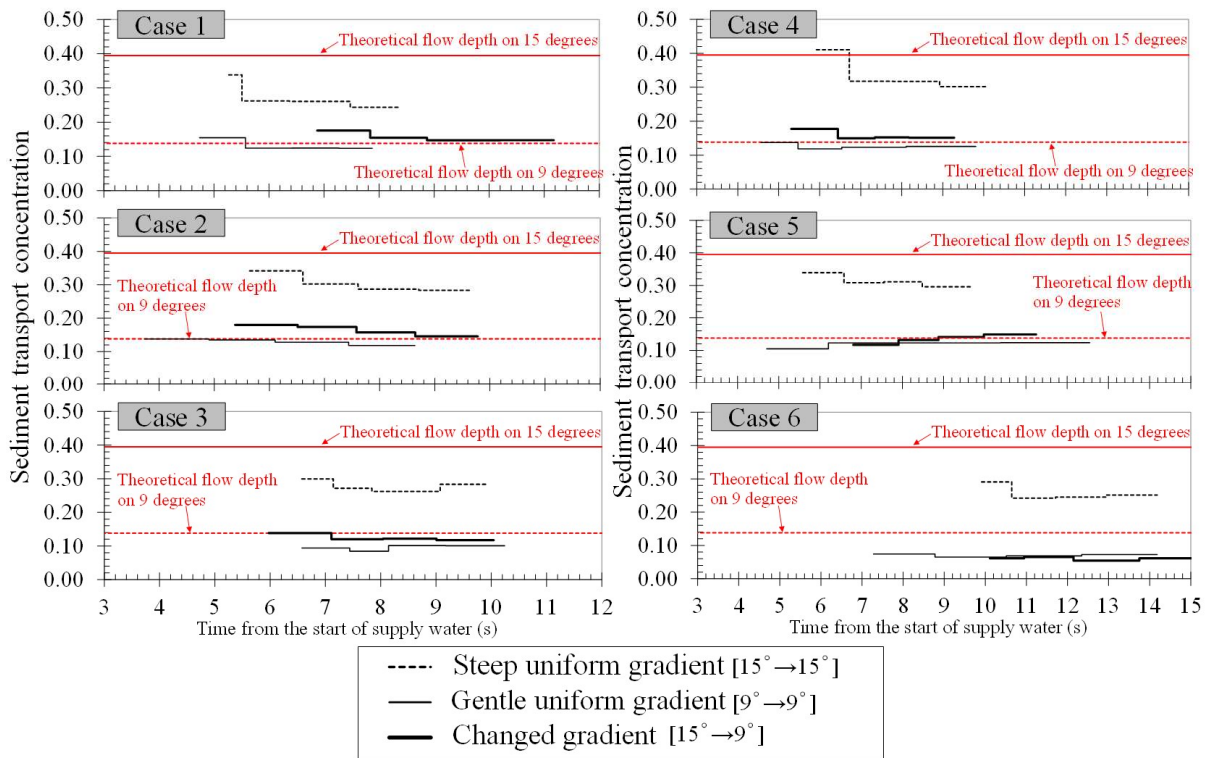
Figure 2. Sediment transport concentrations of the debris flow front for all cases, obtained by the sampler at P 0
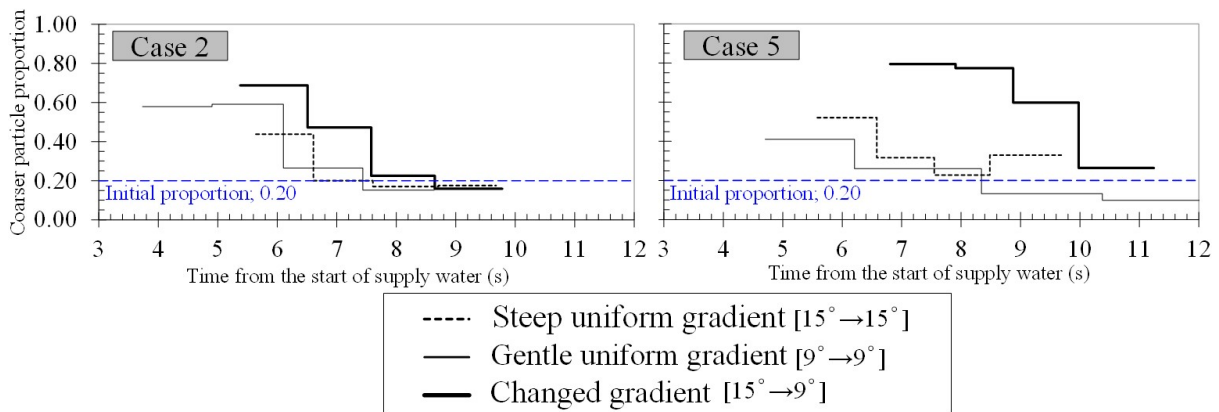
Figure 3. Coarser particle proportion of the debris flow fronts for Case 2 and 5, obtained by the sampler at P 0

value was used as a reference one.

$$C_s = \frac{q_s}{q} = 5.5(\tan\theta)^2 \tag{2}$$

where q_s is the sediment transport rate per a unit width, q is the debris flow rate (the total rate of sediment and water) per a unit width, and θ is the streambed gradient.

As shown in Figure 2, in all cases expect for Case 6, the experimental results and estimated C_s values for the uniform gradient of 9°, are in good agreement, suggesting that our experimental results are reasonable. In Case 6, where the ratio of flow depth to gravel diameter (h /d) is smaller, the experimental values are less than the estimated C_s value. A possible reason for this is that the number of the particle which could exist in the interior of the flow front was limited due to the large individual volume of the particle that composed the material (excluded volume effect), considering that h /d in our experiment is only 1/4th of the value obtained in *Mizuyama*'s experiment. The above results illustrated the validity of our experimental results on the C_s of the flow front. Therefore, the

effect of the changed gradient on the sediment transport mode and particle size segregation is discussed on the basis of these results in Section *3.1.2*.

Incidentally, the experimental values are less than the estimated C_s values for all cases with the uniform gradient of 15°. This may be attributed to the inadequate concentration at the debris flow front because of the shorter movable bed in our experiment than that of *Mizuyama*'s experiment.

1.1.2. *Effect of changed gradient on sediment transport concentration and particle-size segregation of debris flow front*

Figure 2 suggests that the experimental C_s values at P 0 on the changed gradient are similar to the estimated C_s values for a uniform gradient of 9° in most of the cases. This indicates that the transition to the sediment transport mode on the gradient of the downstream part (9°) is achieved at P 0, which is 150 cm downstream point from the gradient-changed point. According to the results, in all conditions for the particle size composition of materials and the inflow rates in our experiment, it is inferred that the transition of sediment transport mode occurs in the section from the gradient-changed point (P 150) to P 0. In the cases where the inflow rates were higher and the materials were finer in Cases 1 and 2, the experimental C_s values were slightly larger than the estimated values for the uniform gradient of 9°. This suggests that the transition to the mode on the gradient of the downstream part is not enough achieved at P 0 for these cases. Therefore, in the case where the inflow rate is higher or the material is finer, that is, the case of higher debris flow momentum, a longer flow distance is required to achieve the transition of sediment transport mode.

Figure 3 shows the proportions of coarser particle in the debris flow front at P 0 for the cases of debris flow materials composed of mixed-sized gravels (Cases 2 and 5). In Case 2, in which the inflow rate is higher, the proportion of coarser particle in the first box of the sampler on the changed gradient is closer to that on the uniform gradient of 9° than that on the uniform gradient of 15°. This suggests that the particle size segregation of the flow front was transited to that on the gradient of the downstream part (9°) in the section from P 150 to P 0 by the changed gradient. In Case 5, in which the inflow rate is lower, the proportion of coarser particle in the first box on the changed gradient is much larger than those on uniform gradients of 9° and 15°. This may be due to the falling of finer particles in the flow interior to the flow bottom owing to the reduction of apparent gravity force in the flow direction, caused by the gentle gradient on the downstream parts, as reported by *Ashida et al.* (1978); this effect may be more pronounced if the debris flow momentum is low. Thus, the concentration of coarser particles at the flow front in Case 5 is more pronounced than that in Case 2.

1.2. Effect of changed gradient on flow depth of debris flow front

1.2.1. *Validation of our experimental results on flow depth of debris flow front*

Figure 4 shows the flow depth of the debris flow front (*h*) at P 100 and P 200 for all cases. The measurement data shown in Figure 4 were limited to within the range of 3 s after the flow front reached at the observation points. The measurement data in this range was not affected by the riverbed erosion at these points. Figure 4 also shows the theoretical debris flow depth for the uniform gradients of 9° and 15°, obtained using the theoretical averaged velocity equation derived from the velocity distribution of a stony debris flow as proposed by *Takahashi* (1980) (Equation 3) and the continuity equation of the flow (Equation 4). Note that because Equation 3 applies to a steady-state stony debris flow where sediment particles are dispersed in the entire flow layer, the theoretical values obtained by Equation 3 for a sediment sheet flow on the gradient of 9° are not appropriate. In our study, the value was used as a reference one.

$$U_m = \frac{2}{5d} \left[\frac{g\sin\theta}{\alpha_i \sin\phi} \{C + (1-C)\} \left(\frac{\rho_m}{\sigma}\right) \right]^{1/2} \left\{ \left(\frac{C_*}{C}\right)^{1/3} - 1 \right\} h^{3/2} \tag{3}$$

$$q = U_m h \tag{4}$$
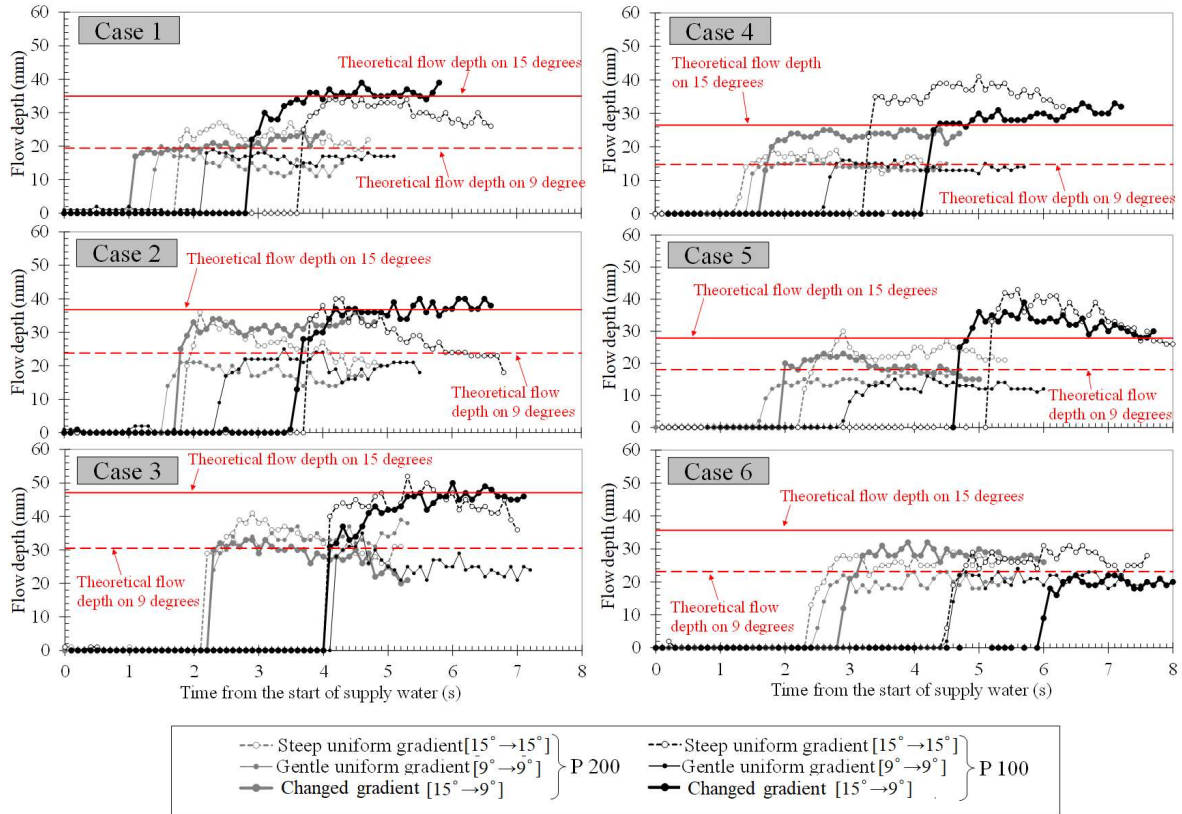
Figure 4. Flow depths of the debris flow front for all cases at P 100 and P 200

where U_m is the averaged velocity of a debris flow, d is the diameter of the material (the mean diameter of the materials in Cases 2 and 5), g is the gravitational acceleration, α_i is the coefficient (= 0.042), ρ_m is the mass density of interstitial fluid (= 1.0 g/cm³), and h is the debris flow depth. C is the equilibrium sediment concentration by Equation 5, which is derived from the equilibrium of the riverbed shear stress and the body forces of a debris flow on the riverbed in the dynamic equilibrium state of the flow (*Takahashi, 1980*).

$$C = \frac{\rho_m \tan\theta}{(\sigma - \rho_m)\left(\tan\phi - \tan\theta\right)} \tag{5}$$

As shown in Figure 4, for the uniform gradients of 9° and 15°in Cases 1 to 5, the experimental and theoretical flow depths at P 100 are in good agreement, suggesting that our experimental results are reasonable. In addition, these results suggest that the debris flows passing at P 100 were well developed and close to steady-state flows. On the other hands, the experimental flow depths at P 200 were smaller than the theoretical flow depths for the uniform gradient of 15°. This suggests that the debris flows passing at P 200 were not fully developed on the uniform gradient of 15°. In Case 6, where the ratio of flow depth to gravel diameter (h/d) is smaller, the experimental values are smaller than the theoretical value. A possible reason for this is the same as discussed in Section *3.1.1*, i.e., the number of the particle which could exist in the interior of the flow front was limited due to the large individual volume of the particle that composed the material (excluded volume effect). The above results illustrated the validity of our experimental results on the flow depth of the flow front. Therefore, the effect of the changed gradient on the sediment transport mode is discussed based on these results in Section *3.2.2*.

1.2.2. *Effect of changed gradient on flow depth of debris flow front*

Figure 4 suggests that the experimental flow depths of the debris flow front at P 100 on the changed gradient consist with the theoretical flow depths for the uniform gradient of 15° in most of the cases. This indicates that the transition to the sediment transport mode on the gradient of the downstream

part (9°) rarely occurs, and the mode on the gradient of the upstream part (15°) is preserved at P 100, which is 50 cm downstream point from the gradient-changed point. In Case 6, where the inflow rates are lower and the materials are coarser, the experimental flow depth at P 100 on the changed gradient is closer to the theoretical flow depth on the gradient of the downstream part (9°). This suggests that the transition to the mode on the gradient of the downstream part has already been achieved when the flow passes P 100. Therefore, in the case where the inflow rate is lower or the material is coarser, that is, the lower debris flow momentum, a shorter flow distance is required to achieve the transition of sediment transport mode. In the cases with the materials composed of mixed-sized gravels and (Case 5), the experimental flow depth at P 100 on the changed gradient is larger than the theoretical flow depth on the gradient of the upstream part (15°). This is because the flow front velocity decreased due to consuming of the debris flow momentum to transport the coarser particles significantly concentrated at the flow front as shown in Figure 3.

From the above discussion, it is considered that the transition section of sediment transport modes due to the changes in streambed gradients depends on the inflow rate and the particle size composition of the material. Considering that the debris flow momentum is affected by the inflow rate and the particle size composition, the length of transition section depends on the large/small relation with the consumed momentum and the whole debris flow momentum.

1.3. Effect of changed gradient on the distribution of migration particle velocities in the interior of debris flow front

1.3.1. Validation of our experimental results on the distribution of migration particle velocities in the interior of debris flow front

Figure 5 shows the distribution of migration particle velocities in the interior of the debris flow front at the gradient-changed point (P 150) for all cases. The migration velocities on the changed gradient are based on the axis along the flow direction on the gradient of the downstream part (9°) at P 150. The measurement data shown in Figure 5 was limited to within the range of 3 s after the flow front reached at the observation point. The measurement data in this range was not affected by the riverbed erosion at this point. Figure 5 also shows the theoretical velocity distribution for the uniform gradients of 9° and 15°, obtained using the equations that can be used for theoretical velocity distribution of both a stony debris flow and a sediment sheet flow as suggested by *Takahashi et al.* (1996). The internal friction angles (ϕ) for calculating the theoretical distribution were adjusted along the experimental results on the uniform gradients of 9° and 15°. Note that the distribution in the upper flow layer, in which the sediment concentration is less than 0.2–0.15, is not shown in the figure.

As shown in Figure 5, for the uniform gradients of 9° and 15° for all cases, although the dispersion of the experimental distributions is noticeable, the experimental and theoretical distributions are almost in agreement, suggesting that our experimental results are reasonable. In the cases of debris flow materials composed of mixed-sized gravels (Cases 2 and 5), the experimental distributions on the changed gradient are correspond to the theoretical distributions for 3.0-mm-diameter gravels, which constitute most of the material compositions. These results illustrated the validity of our experimental results on the distribution of migration particle velocities in the interior of the flow front. Therefore, the effect of the changed gradient on the sediment transport mode is discussed based on these results in Section *3.3.2*.

1.3.2. Effect of changed gradient on the distribution of migration particle velocities in the interior of debris flow front

Figure 5 suggests that the experimental distributions of migration particle velocities in the interior of debris flow front at the gradient-changed point (P 150) on the changed gradient are between the theoretical velocity distributions for the uniform gradients of 9° and 15° in for the cases of debris flow materials composed of uniform-sized gravels (Cases 1, 3, 4 and 6). Similarly, the average flow front's depths at P150 on the changed gradient are also between those on the uniform gradients of 9° and 15°. These results suggest that the transition to the sediment transport mode has already started to occur in the interior of the flow front at the gradient-changed point. In Case 6, where the inflow rates are lower

and the materials are coarser, the experimental distributions at P 150 on the changed gradient are closer
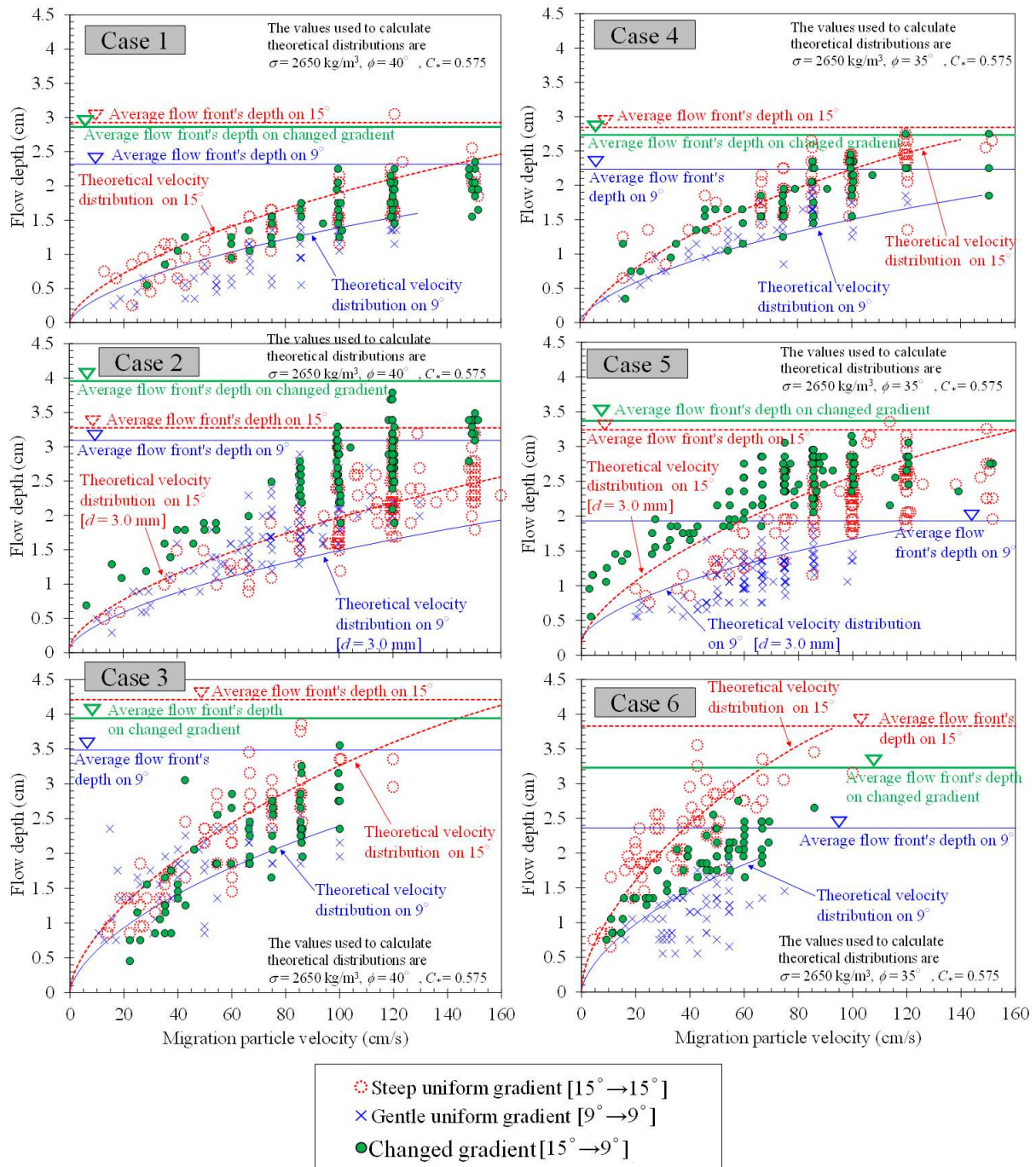
Figure 5. Distribution of migration particle velocities in the debris flow front's interior at the gradient-changed point (P 150) for all cases.

to the theoretical distribution on the gradient of the downstream part (9°). Considering that the inflow rate and the particle size composition affected the debris flow momentum, the transition to the mode on the gradient of the downstream part progresses more rapidly as the debris flow momentum decreases.

In the cases of debris flow materials composed of mixed-sized gravels (Cases 2 and 5), the experimental migration particle velocities at P 150 on the changed gradient are smaller than the theoretical velocities on the gradient of the upstream part (15°). In addition, the average flow front's depths at P 150 on the changed gradient in Cases 2 and 5 are higher than those on the gradient of the

upstream part (15°). This is because the flow front velocity decreased due to consuming of the debris flow momentum to transport the coarser particles significantly concentrated at the flow front as discussed in Section *3.2.2*. According to these results, in the cases of the debris flow materials composed of mixed-sized gravels, it is necessary to consider the effect of particle size distribution at the flow front on the transition processes of sediment transport mode due to changes in streambed gradients.

1.4. Estimation of transition sections of sediment transport modes due to changes of streambed gradients

Figure 6 shows the estimated transition sections of the sediment transport modes owing to changes in streambed gradients for all cases based on the estimated results of the modes at the observation points.

In Cases 1, 2 and 3, in which the inflow rates are higher, and the debris flow momenta are much larger than the consumed momentum due to the transition to the mode on the gradient of the downstream part (9°), because the transition sections of sediment transport modes are longer, the transitions are not sufficiently promoted, and the mode on the gradient of the upstream part (15°) is preserved when the debris flow passes P 100. After the flow passes P 100, the sediment transport mode gradually transits to the mode on the gradient of the downstream part during the downflow in the section from P 100 to P 0, and the transitions to the mode on the gradient of the downstream part are almost completed at P 0.

In Case 6, in which the debris flow momentum is the lowest among all the cases in our experiment, the transition of sediment transport mode is achieved with a shorter section, and then the transitions to the mode on the gradient of the downstream part (9°) are almost completed at P 100. On the other hands, in Case 4, in which the debris flow material is finer than that in Case 6, the transitions to the mode on the gradient of the downstream part (9°) are not completed at P 100 because of the smaller consumption of debris flow momentum to transport the material.

In Cases 2 and 5, where the materials consist of mixed-sized gravels, the coarser particles concentrate at the flow front during downflow. In Case 2, where the debris flow momentum is higher than that in Case 5, because the debris flow momentum is enough to be negligible the consumption to transport the coarser particles concentrated at the flow front, the transition section is longer than that in Case 5. Thus, the sediment transport mode on the gradient of the upstream part (15°) is preserved when the debris flows pass P 100 in Case 2. In Case 5, where the debris flow momentum is lower, the transitions to the mode on the gradient of downstream part (9°) progress more rapidly because of the larger consumption of debris flow momentum to transport the coarser particles concentrated at the flow front. Considering the above, the transition section of sediment transport modes due to changes in streambed gradients depends on the debris flow momentum, and the particle size segregation at the flow front affect to the transition process through the consumption of the debris flow momentum.
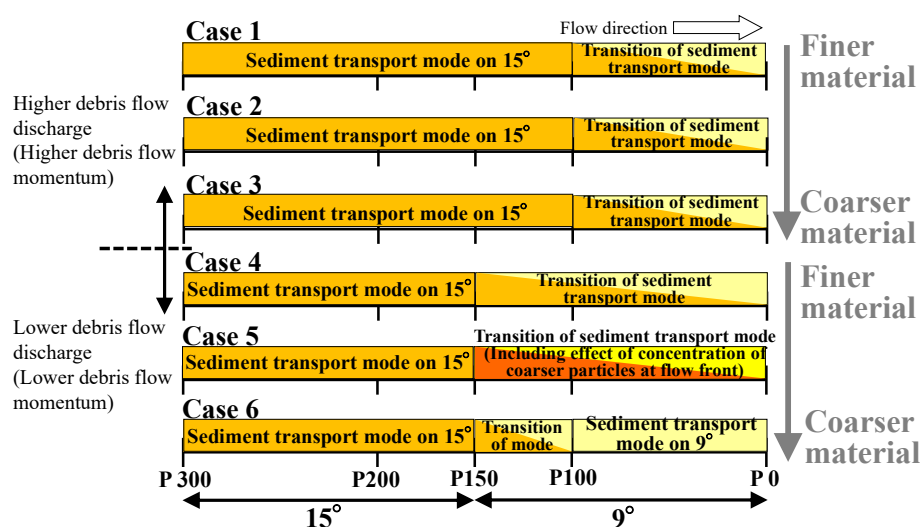
Figure 6. Estimated transition sections of sediment transport modes due to changes of streambed gradients

2. CONCLUSIONS

In this study, using an experimental flume with two variable gradients in the upstream and downstream parts, we investigated the transition processes of sediment transport modes on the debris flows consisting of uniform-sized and mixed-sized gravels due to the changes in streambed gradients. In addition, we also investigated the effect of changes in streambed gradients on the size distribution of migrating particles.

According to our experimental results, in the case with a higher inflow rate, the transition sections of sediment transport modes are longer because the consumed momentum to transport the material is less than the whole debris flow momentum. In contrast, in the case with a lower inflow rate, the transition of sediment transport mode is achieved with a shorter section because of the large consumption of the momentum. For the cases in which the inflow rates are the same, the transition of sediment transport mode is achieved with a short section if the debris flow has coarser particles. For the debris flow consisting of mixed-sized gravels, the transition section is shorter than that for the debris flow consisting of uniform-sized gravels because the debris flow momentum is consumed to transport the coarser particles concentrated at the flow front. Considering that the debris flow momentum is affected by the inflow rate and the particle size composition, the transition section due to changes in streambed gradients strongly depends on the debris flow momentum.

To investigate the validity of the above discussion, it is necessary to conduct flume experiments under the various conditions on the gradient change and the particle size composition of materials, as well as to measure the distribution of migration particle velocities in the flow's interior and flow depth at more observation points on the downstream part. Using these measurements, the transition processes should be investigated in more detail.

REFERENCES

Ashida, K., Takahashi, T. & Mizuyama, T. (1978). Study on bed load equations for mountain streams. *Journal of the Japan Society of Erosion Control Engineering*, *30*(4), 9–17 (in Japanese with English abstract).

Egashira, S., Ashida, K., Takahama, J. & Tanonaka, S. (1990). Sediment transport formula derived from an energy dissipation model of solid-fluid mixture, *Disaster Prevention Research Institute Annuals*, *Kyoto University*, *33*(B-2), 293-306 (in Japanese with English abstract).

Hashimoto, H. & Tsubaki, T. (1983). Reverse grading in debris flow, *Journal of the Japan Society of Civil Engineers*, *336*, 75–84 (in Japanese).

Hashimoto, H., Tsubaki, T. & Hirano, M. (1986). Sediment Gravity Flow on Relatively Gentle Slopes. *Annual Journal of Hydraulic Engineering*, *Japan Society of Civil Engineers*, 235–240 (in Japanese).

Ikeda, A., Mizuyama, T., Sugiura, N. & Hasegawa, Y. (2009). Study about deformation of stream bed deposit at initiation zone of debris flow. *Journal of the Japan Society of Erosion Control Engineering*, *62*(4), 46–51 (in Japanese with English abstract).

Iverson, R. M., Logan, M., LaHusen, R. G. & Berti, M. (2010). The perfect debris flow? Aggregated results from 28 large-scale experiments, *Journal of Geophysical Research*, *115*: F03005.

Miyamoto, K. (1986). Mechanics of grain flows in Newtonian fluid, *Ph.D. Thesis Ritsumeikan Univ.*, 73–99 (in Japanese).

Mizuyama, T. (1980). Sediment transport rate in the transition region between debris flow and bed load transport. *Journal of the Japan Society of Erosion Control Engineering*, *33*(1), 1-6 (in Japanese with English abstract).

Okuda, S., Suwa, H., Okunishi, K., Nakano, M. & Yokoyama, K. (1977). Synthetic observation on debris flow part. 3, Observation at valley Kamikamihorisawa of Mt.Yakedake in 1976, *Disaster Prevention Research Institute Annuals*, *Kyoto University*, *20*(B-1), 237-263 (in Japanese with English abstract).

Sharp, R. P. & Nobles, L. H. (1953). Mudflow of 1941 at Wrightwood, southern California, *Bulletin of the Geological Society of America*, *64*, 547–560.

Suwa, H. (1988). Focusing mechanism of large boulders to a debris–flow front, *Disaster Prevention Research Institute Annuals*, *Kyoto University*, *31*(B-1), 139–151 (in Japanese with English abstract).

Takahama, J., Fujita, Y., Kondo, Y., & Hachiya, K. (2002). A two layer simulation model unifying debris flow and sediment sheet flow. *Proceedings of International Congress INTERPRAEVENT 2002 in the Pacific Rim*, *1*, 113–124.

Takahashi, T (1980). Debris flow on prismatic open channel, *Journal of the Hydraulics Division, Proceedings of the American Society of Civil Engineer*, *106*(HY3), 381–396.

Takahashi, T (1982). Study on the deposition of debris flows (3); Erosion of debris fan, *Disaster Prevention Research Institute Annuals*, *Kyoto University*, *25*(B-2), 327–348 (in Japanese with English abstract).

Takahashi, T. & Kuang, S. (1986). Formation of debris flow on varied slope bed, *Disaster Prevention Research Institute Annuals*, *Kyoto University*, *29*(B-2), 345-349 (in Japanese with English abstract).

Takahashi, T (1987). High velocity flow in steep erodible channels. *Proceedings of 22nd IAHR Congress*, Lausanne, 42–53.

Takahashi, T., Nakagawa, H., Harada, T. & Yamashiki, Y. (1992). Routing debris flows with particle segregation, *Journal of Hydraulic Engineering*, *118*, 1490–1570.

Takahashi, T. Satofuka, Y. & Chishiro, K. (1996). Dynamical law of debris flows in inertial regime, *Disaster Prevention Research Institute Annuals*, *Kyoto University*, *39*(B-2), 333-346 (in Japanese with English abstract).

Teramoto, Y., Jitousono, T. & Shimoyama, E. (2002). Flow properties of the debris flow that occurred on September 11, 1999, in the Akamatsu-dani River Basin at Unzen Volcano, *Research Bulletin of Kagoshima Univ. Forest*, *30*, 19–25 (in Japanese with English abstract).

Wada T., Furuya T., Nakatani K., Mizuyama T. & Satofuka, Y. (2015). Experimental Study on the Concentration of Coarser Particles at the Frontal Segment of a Debris Flow, *International Journal of Erosion Control Engineering*, *8*(2), 20–30.

HBV-DE: A NEW DIFFERENTIAL EVOLUTION-BASED CALIBRATION APPROACH FOR THE HBV HYDROLOGICAL MODEL

Pinar Gokce Durgut [1]

Department of Civil Engineering, Pamukkale University

Denizli, Turkey

pgkargi@gmail.com

Tugba Altiparmak Ay

Department of Civil Engineering, Pamukkale University

Denizli, Turkey

taltiparmakay@gmail.com

M. Tamer Ayvaz [2]

Department of Civil Engineering, Pamukkale University

Denizli, Turkey

tayvaz@pau.edu.tr

ABSTRACT: Hydrological models can be classified as the physical, conceptual, and empirical models. Conceptual models are widely used due to their ease of implementation and their simplified form based on the laws of physics. However, since conceptual models have model parameters that cannot be measured in field physically, their calibration is needed. In this study, a differential evolution (DE) based calibration approach for the conceptual HBV (Hydrologiska Byråns Vattenbalansavdelning) hydrological model (HBV-DE) is proposed. The proposed HBV-DE approach integrates an externally developed DE optimization routine in MATLAB platform with the HBV-light model, which is one of the graphical user interfaces (GUI) of HBV model. The objective of the DE based optimization approach is to calibrate the parameters of HBV-light model by minimizing the discrepancies between the simulated and observed flow values at selected monitoring point over the basin. The applicability of the proposed HBV-DE approach is evaluated in Murat sub-basin of the Gediz River Basin (GRB) in Turkey. Identified results indicated that the proposed HBV-DE approach resulted with the similar or better calibration and verification performances than the built-in calibration approach of HBV-light.

1. INTRODUCTION

The amount of water in the world is limited. Nowadays, rapid population growth, unplanned urbanization, and unconscious water consumption adversely affect the water resources in terms of quantity and quality manners. For this reason, sustainable management of the water resources becomes an important task that should be considered by decision makers. Hydrological models are the key tools in management and operation of water resources systems at a basin scale. Note that hydrological models can be classified as physical, conceptual and empirical models (Devia ve diğ., 2015). In physical models, governing partial differential equations of the natural system including continuity and momentum equations are solved by means of the analytical or numerical solution approaches (Wheater ve diğ., 1993). These models provide detailed results regarding the flow processes over basin. However, they require spatially distributed input data (e.g., soil types, plant

---

[1] *PhD Scholar of the 100/2000 Program of the Turkish Council of Higher Education Institution (YÖK)*
[2] *Corresponding Author*

441

species, land use, etc.) which is their main drawback compared to the other modeling approaches. Therefore, their calibration is more difficult than the other models due to high computation cost (Kunstmann ve diğ., 2006). Empirical models can perform well in processing and predicting nonlinear hydrological processes (Zhang ve diğ., 2018). However, these data-driven models are heavily influenced by data availability, data preprocessing, and selection of input variables. Another disadvantage of data-driven models is the problem of overfitting which significantly reduces the generalization ability of the model. Furthermore, the noise in the data can negatively influence the prediction performance while processing new data in the models (Ghaith ve diğ., 2019). Conceptual models are based on the laws of physics in a simplified form and are widely used in the simulation of hydrological events. These models are used in studies such as water balance analysis, expansion and filling of stream flow records, forecasting, reservoir operation, water supply and watershed management (Jin et al., 2010; Liu et al., 2017). Even though parameters of a conceptual model have their physical interpretation, there is no possible way to measure them on field, and therefore, they need to be calibrated based on the flow observations (Romanowicz et al., 2013; Willems, 2000). Note that optimization approaches are mostly used in calibration of the hydrological models such that the objective is to determine the parameter values by minimizing the discrepancies between the observed and simulated flow values (Dakhlaoui et al., 2012).

In this study, a new calibration approach for the HBV (Hydrologiska Byråns Vattenbalansavdelning) conceptual hydrological model, developed by The Swedish Meteorological and Hydrological Institute (SMHI) (Bergström, 1976), is proposed by using the differential evolution (DE) optimization approach. For this purpose, an approach called HBV-DE is proposed. Note that HBV-DE integrates an external DE based optimization approach in MATLAB platform with the HBV-light model (Seibert & Vis, 2012), which is one of the developed graphical user interfaces (GUI) of the HBV hydrological model. The applicability of the proposed HBV-DE approach is evaluated on the Murat sub-basin of the Gediz River Basin (GRB) in Turkey. The identified results are also evaluated by solving the same problem by means of the genetic algorithm (GA) based optimization add-in (HBV-GA) which is available in HBV-light model. The identified results indicated the proposed HBV-DE approach resulted with the similar or better calibration-verification performances than those obtained by using the HBV-GA approach.

2. MODEL DEVELOPMENT

2.1. Differential Evolution Algorithm (DE)

DE, first proposed by (Storn & Price, 1997), is an evolutionary optimization algorithm which is based on the similar computational basis with the GA in terms of the genetic evolution processes. The main difference of DE and GA is that the binary coding is mostly used in GA whereas decimal coding is used in DE. Furthermore, each candidate solution in GA is subjected to the genetic evolution process if the associated probability of that process is satisfied. On the other hand, each candidate solution in DE is subjected to those processes without considering any probability. Compared to other heuristic optimization algorithms, DE is easy to employ and less prone to obtain local optimum solutions. Solution of an optimization problem with DE can be mathematically performed based on the following steps:

Let n_p be the number of population, n_d be the number of decision variables, x be the decision variables, i be the population index ($i = 1, 2, 3, \cdots, n_p$), j be the decision variables index ($j = 1, 2, 3, \cdots, n_d$), $x_j^{\max}$ and $x_j^{\min}$ be the upper and lower limits of the jth decision variables, respectively. Using these definitions, the initial value of the jth decision variable in the ith candidate solution at the generation $G = 0$ can be generated as follows.

$$x_{i,j}^{G=0} = x_j^{\min} + r(0,1) \times (x_j^{\max} - x_j^{\min}) \qquad (1)$$

where $r(0,1)$ represents a uniform random number within the range of (0,1). After this process, the mutation process is performed, and a new solution vector is obtained as follows:

$$v_j^G = x_{r_{1,j}} + F(x_{r_{2,j}} - x_{r_{3,j}}) \tag{2}$$

where F is the scale factor which controls the mutation process, r_1, r_2 , and r_3 are the randomly generated integers in the range of $[1, n_p]$ which are different from each other. After this process, the crossover operation is conducted to generate a new solution vector as follows:

$$u_j^G = \begin{cases} v_j^G & \text{if } r(0,1) \leq C_r \text{ or } j = j_{\text{rand}} \\ x_{i,j}^G & \text{otherwise} \end{cases} \tag{3}$$

where C_r is the crossover rate and j_{rand} is the randomly generated integer value in the range of $[1, n_d]$. After this process, the final value of x is selected based on the selection operator as follows:

$$x_{i,j}^{G+1} = \begin{cases} u_j^G & \text{if } f(u_j^G) \text{ is better than } f(x_{i,j}^G) \\ x_{i,j}^G & \text{otherwise} \end{cases} \tag{4}$$

It can be seen from Equation (4) that the final decision variable value is updated based on the objective function value and this condition guarantees to obtain the same or better objective function values through generations. Note that the computational procedure given between Equation (2) and (4) is repeated until satisfying the termination criterion of the optimization model.

2.2. Conceptual HBV Hydrological Model

The HBV (Bergström, 1976) is a conceptual hydrological model which simulates the flow process at the outlet of a watershed by using precipitation, temperature, and potential evaporation. The model consists of different modules representing snow, soil water and evaporation, groundwater, and channel routing (Figure 1). HBV model describes the continuity of flow using three storage reservoirs: a soil moisture zone, an upper zone storage (for sub-surface flow) and a lower zone storage (Driessen et al., 2010). General continuity equation can be given as follows:

$$P - E - Q = \frac{d}{dt}(SP + SM + UZ + LZ + lakes) \tag{5}$$

where P, E, and Q are the precipitation, evaporation, and discharge rate, respectively, SP is the snowpack storage, SM is the soil moisture storage, UZ and LZ are the upper and lower groundwater storages, and the $lakes$ is the lake storage. Note that some lumped and semi-distributed versions of the HBV model have been proposed in literature through some modifications. Also, some GUIs are also developed for building up the hydrological models without requirement any programming platforms. One of the developed GUIs is the HBV-light model (Seibert & Vis, 2012) which includes different modifications of standard HBV model. Among them, semi-distributed "Response Routine with Delay Model" is selected in this study (Figure 2). Note that the key difference of this model from the standard HBV is the the PART (portion of the recharge added to the soil upper zone) and DELAY (period of delay for water added to the soil lower zone) variables.

2.3. Study Area and Data Sets

The Gediz River Basin (GRB), located in the western part of Turkey, is one of the most important river basins in Turkey (Figure 3). It has a drainage area of 17500 km^2 and this value corresponds to approximately 2% of the country's total area. The main river branch of the basin is the Gediz river, which originates from Murat Mountain and reaches to Aegean Sea through 386 km long river branches (Temiz, 2009). As indicated previously, the applicability of the proposed approach is evaluated on a Murat sub-basin of the GRB. Note that Murat sub-basin is located in the upstream part of the Gediz River and has a drainage area of 3272.4 km^2.
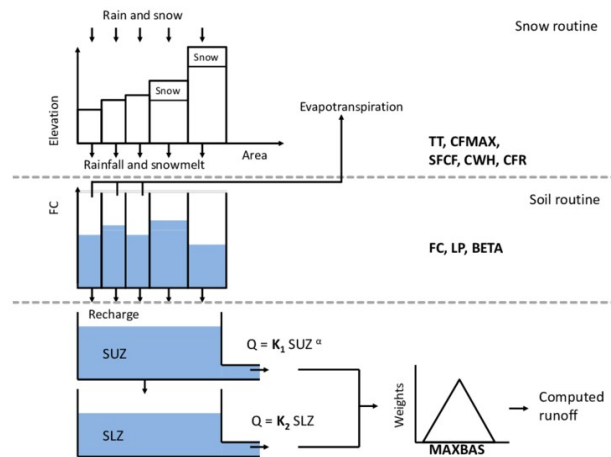
Figure 28. Standard HBV hydrologic model structure (Staudinger et al., 2015)
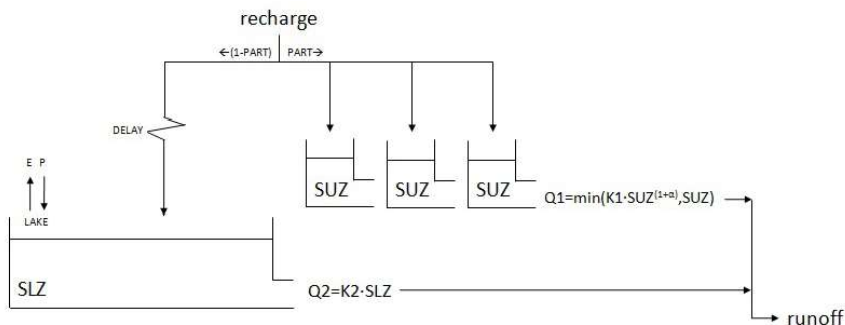
Figure 29. Response routine with delay model (Seibert, 2005)

It should be noted that there are various hydrological modeling approaches in the Murat sub-basin. Turan and Doğan (2015) calibrated daily GR4J and monthly GR2M conceptual models with different optimization techniques in three sub-basins including Murat sub-basin and compared their calibration performances. Turan and Yurdusev (2016) developed a hybrid approach by combining the GR2M monthly hydrological model with fuzzy systems in the Murat sub-basin. The fuzzy integration process is carried out through the replacement of the storage elements of conceptual model by fuzzy systems. Okkan et al. (2017) calibrated the three-parameter conceptual water balance model in the Murat sub-basin with Invasive Weed Algorithm and Differential Evolution Algorithm and compared their calibration performance. Okkan and Kırdemir (2019) developed a hybrid approach using a gradient-based algorithm and particle swarm optimization (PSO) algorithm and implemented a monthly dynamic water balance model (dynwbm) in the Murat sub-basin. Kumanlioglu and Fistikoglu (2019) developed a hybrid approach using the GR4J daily conceptual model and Artificial Neural Networks (ANN) and implemented it in seven sub-basins in the Gediz River Basin, including the Murat sub-basin. Okkan et al. (2021) developed a hybrid approach using monthly dynamic water balance model (dynwbm) and Machine Learning (ML) techniques and applied it to Murat sub-basin. Although these modeling efforts, there is not any HBV model application for this basin to the best of the authors' knowledge.

HBV model parameters are calibrated by using the flow measurements on the stream gage EIE 523-Acisu which is located at the outlet of the basin (Figure 3). For this purpose, the associated flow measurements between 2002 and 2006 are collected from the State Hydraulic Works (DSI) of Turkey. Among them, the data between 2003 and 2004 are used for model calibration and between 2005 and 2006 are used for model verification. The data for the water year of 2002 is used for the model warm-up to eliminate the effects of the initial parameter values. Note that HBV model requires three inputs for modeling the rainfall-runoff process: areal mean precipitation, areal mean temperature, and

evapotranspiration. The precipitation and temperature data are obtained from 17188-Uşak, 17750-Gediz, 17748-Simav and 17746-Demirci meteorological observation stations (Figure 3) and are converted into areal precipitation using Thiessen polygon approach. The calculated Thiessen polygon weights are given in Table 1. Evapotranspiration values are calculated using the Penman-Monteith method (Allen et al., 1998). The statistics of the flow and the meteorological data for the warm-up, calibration, and verification periods are given in Table 2.
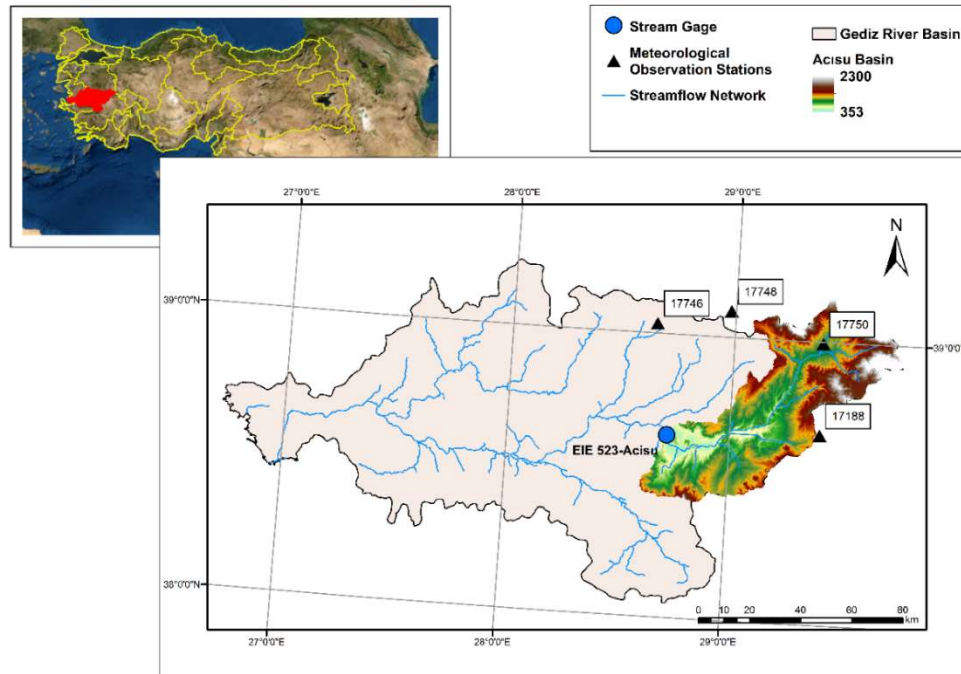
Figure 30. Location of the Murat sub-basin on GRB.

Table 22. Meteorological stations and the calculated Thiessen polygon weights.

Station No	Station Name	Thiessen Weight (%)
17188	Uşak	56.5
17746	Demirci	4.4
17748	Simav	8.2
17750	Gediz	30.9

Table 23. Statistics of the flow and meteorological data.

Period	Statistics	Discharge (m³/s)	Temperature (°C)	Statistics	Precipitation (mm)
Warmup (2002)	Mean	10.41	12.79	Total	784.64
	Maximum	96.90	28.30	Maximum	60.46
	Minimum	0.12	-5.92	Mean	2.15
Calibration (2003-2004)	Mean	7.54	12.68	Total	1087.39
	Maximum	118.00	27.97	Maximum	48.44
	Minimum	0.16	-10.17	Mean	1.49
Verification (2005-2006)	Mean	6.21	12.70	Total	1150.30
	Maximum	117.00	28.91	Maximum	34.80
	Minimum	0.13	-5.98	Mean	1.58

As indicated previously, semi-distributed version of the HBV model is used in this study. To simulate its semi-distributed nature, the basin area is divided into 10 different elevation zones using Digital

Elevation Model (DEM). Then, the mean elevation values together with the percent areas for each elevation zone are determined and entered to the HBV-light model (Figure 4).

	Mean Elevation (m)	Area (%)
Zone 1	449.40	100.00
Zone 2	642.20	93.33
Zone 3	835.00	68.70
Zone 4	1027.80	35.11
Zone 5	1220.60	18.03
Zone 6	1413.40	8.76
Zone 7	1606.20	3.75
Zone 8	1799.00	1.86
Zone 9	1991.80	1.02
Zone 10	2184.60	0.39
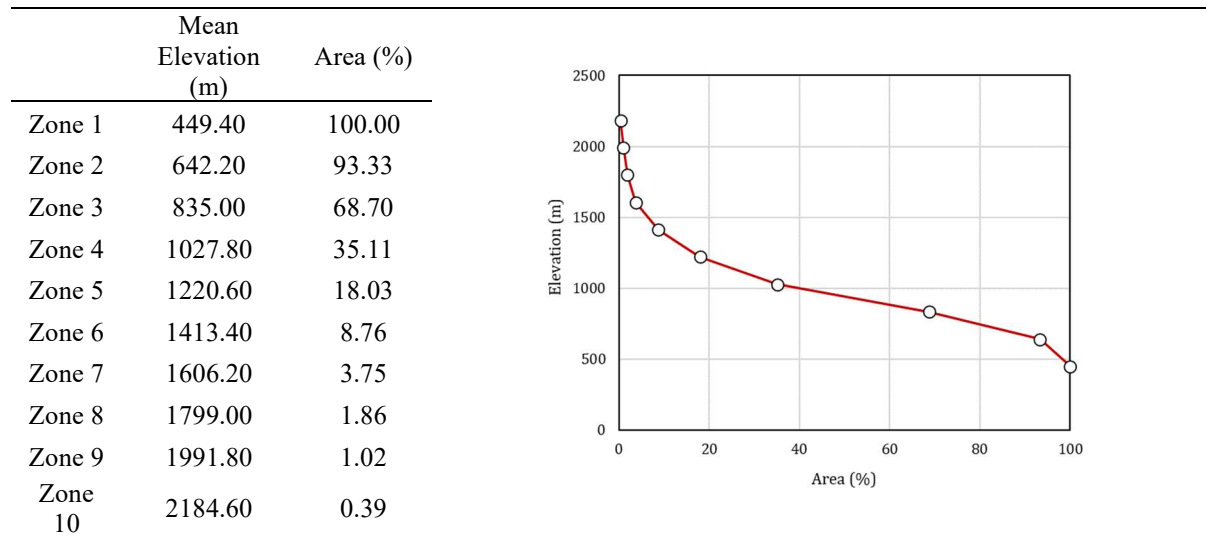
Figure 31. Hypsometric curve of Murat Basin

2.4. Problem Formulation

The problem of parameter calibration of HBV hydrological model is solved by using the proposed HBV-DE approach. In this solution sequence, DE determines the model parameters first, and pass this information to the HBV-light model by means of the associated XML files. Then, HBV-light simulates the rainfall-runoff process by using generated parameter set. After this process, discrepancies between the simulated and observed flow values at stream gage location are determined and parameter values are updated through genetic evolution processes in DE. Note that there are different error measures in literature to determine the discrepancies between the simulated and observed values. Among them, Nash-Sutcliffe (NS) model efficiency (Nash & Sutcliffe, 1970) is used as the objective function of the proposed HBV-DE approach. The NS measure can be defined mathematically as follows:

$$NS = 1 - \frac{\sum_{i=1}^{n_t}[Q_i^{obs} - Q_i^{sim}]^2}{\sum_{i=1}^{n_t}[Q_i^{obs} - \bar{Q}^{obs}]^2} \tag{6}$$

subject to

$$\tilde{x}_j^{\min} \leq \tilde{x}_j \leq \tilde{x}_j^{\max} \tag{7}$$

$$\tilde{x}_j \in \tilde{x} = [\tilde{x}_1, \tilde{x}_2, \cdots, \tilde{x}_{n_d}] \tag{8}$$

where n_t is the number of time steps in the simulation period, Q_i^{obs} and Q_i^{sim} are the observed and simulated flow values at i^{th} time period, and $\bar{Q}^{obs}$ is the mean of the observed flow values, $\tilde{x}_j$ is the jth model parameter of the HBV parameter set ($\tilde{x}$), and $\tilde{x}_j^{\min}$ and $\tilde{x}_j^{\max}$ are the lower and upper bounds of the jth model parameter. The value of NS is valid in the range of $(-\infty, 1]$ where the value of 1 means a perfect match between the simulated and observed values. In the current HBV-light version, there are 12 model parameters to be calibrated by means of the DE based optimization approach. Definition of each parameter and possible lower and upper limits are given in Table 3. As indicated previously, HBV-light also includes a built-in calibration routine that uses the Genetic Algorithm (GA) as the optimization approach (HBV-GA). Therefore, the identified results of the proposed approach are also compared by solving the same problem through HBV-GA by considering the same lower and upper bounds in Table 3.

Table 24. Parameter bounds for the HBV-light hydrological model and optimized values (Nonki et al., 2021; Seibert, 1997; Smith et al., 2014).

Parameter $(\tilde{x}_j)$	Description	Unit	Lower Limit $(\tilde{x}_j^{min})$	Upper Limit $(\tilde{x}_j^{max})$	Calibrated Value (HBV-DE)	Calibrated Value (HBV-GA)
TT	Threshold temperature	°C	-2.5	2.5	-2.489	-2.479
CFMAX	Degree-day Factor	mm d^{-1} °C^{-1}	1	6	4.638	3.624
SFCF	Snowfall correction factor	-	0.6	1.2	0.466	0.400
FC	Maximum soil moisture storage	mm	100	450	282.309	233.051
LP	Wilting point	-	0.2	1	0.683	0.651
BETA	Shape coefficient	-	1	5	3.335	3.593
Alpha	Non-linearity coefficient	-	0	1	0.816	0.589
K1	Recession coefficient 1	d^{-1}	0.01	0.2	0.055	0.096
K2	Recession coefficient 2	d^{-1}	0.00001	0.1	0.021	0.016
MAXBAS	Length of Triangular Weighting Function	d	1	2.5	2.010	1.712
PART	Portion of the recharge which is added to groundwater box 1	-	0	1	0.657	0.661
DELAY	Time period over which recharge is evenly distributed	d	0	50	0.114	16.551

3. RESULTS

3.1. HBV-GA Results

As indicated previously, HBV-GA consists of the calibration of the parameters of Murat sub-basin by using the built-in GA optimization add-in of the HBV light model. In this solution sequence, the calibration process was performed by conducting 50000 objective function executions. The population number was selected as $P = 100$. To eliminate the effect of the generated random numbers in GA, the problem has been solved 10 times. The results of these 10 solutions are given in Table 4. As can be seen, the best NS in the calibration period is obtained as 0.913 whereas the worst one is obtained as 0.910. For the verification period, the best and the worst NS values are obtained as 0.561 and 0.467, respectively. These solutions are obtained in average 432.70 generations. Among the identified results, 4th solution is considered as the best solution since the corresponding NS value in the verification period is maximum (0.561). For this solution, observed and predicted flow values are compared in Figure 5 for the calibration and verifications periods, respectively. The calibrated parameter values for the best solution are given in Table 3.

Table 25. The calculated NS values in calibration and verification stages and the final number of generations to reach these NS values in HBV-GA approach.

Model Runs	HBV-GA		
	Calibration	Verification	Number of Generations
1	0.913	0.476	430
2	0.911	0.539	432
3	0.913	0.467	435
4	0.909	0.561	432
5	0.911	0.511	433
6	0.913	0.489	434
7	0.911	0.509	434
8	0.911	0.489	428
9	0.910	0.533	436

10	0.912	0.485	433
Maximum	0.913	0.561	436
Minimum	0.909	0.467	428
Mean	0.911	0.506	432.700
St. Deviation	0.0011	0.0289	2.359
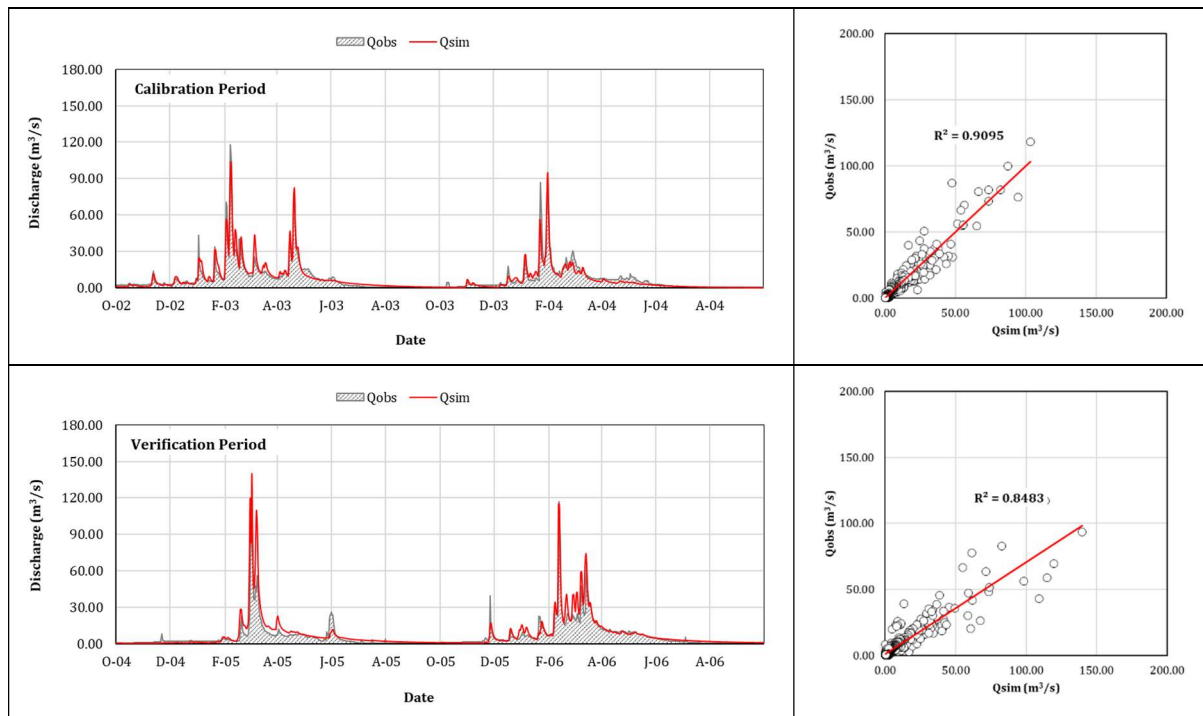
Figure 32. Comparison of the observed and predicted flows in the calibration and verification periods for HBV-GA

3.2. HBV-DE Results

Similar to the previous section, HBV-DE model consists of the integration of HBV-light model to DE based optimization approach. Unlike HBV-GA which uses the built-in GA optimization add-in, the optimization process is conducted externally in MATLAB platform in HBV-DE. In this context, HBV-light model is externally executed for each optimization cycle after generation of the associated XML files containing characteristics of the basin. To obtain comparable results, the calibration process is performed again by conducting 50000 objective function executions. The population number is again selected as $P = 100$ and the the problem is solved ten times to eliminate the effect of the random numbers. For these model executions, the final NS values, and the number of generations to reach these values are listed in Table 5. It can be seen that the maximum and minimum NS values for the calibration period are obtained as 0.913 and 0.855, respectively. For the verification period, these values are obtained as 0.745 and 0.431, respectively. These results are obtained in average generation numbers of 81.30. Among the identified results, 3rd solution is considered as the best solution since the corresponding NS value (0.745) of that solution is the maximum. For this solution, observed and predicted flow values are compared in Figure 6 for the calibration and verification periods, respectively. The calibrated parameter values for the best solution are again given in Table 3.

4. DISCUSSION AND CONCLUSIONS

In this study, the HBV-DE approach is presented to calibrate the HBV conceptual hydrological model. For this purpose, an external DE optimization routine is developed in MATLAB platform and directly integrated to the HBV-light model in an optimization framework. In this solution sequence, the DE based optimization model generates the associated parameter values and write them to the XML files of the HBV-light model. After this process, HBV-light is executed from the optimization

model and the corresponding model output is evaluated by DE. Since HBV-light also includes a built-in GA optimization add-in, the performance of the proposed approach is also evaluated by solving the same problem in similar optimization conditions. The performance of the proposed approach is evaluated on the Murat sub-basin of GRB for 10 different model executions in HBV-GA and HBV-DE approaches. The following outcomes can be drawn from the identified results of this study:
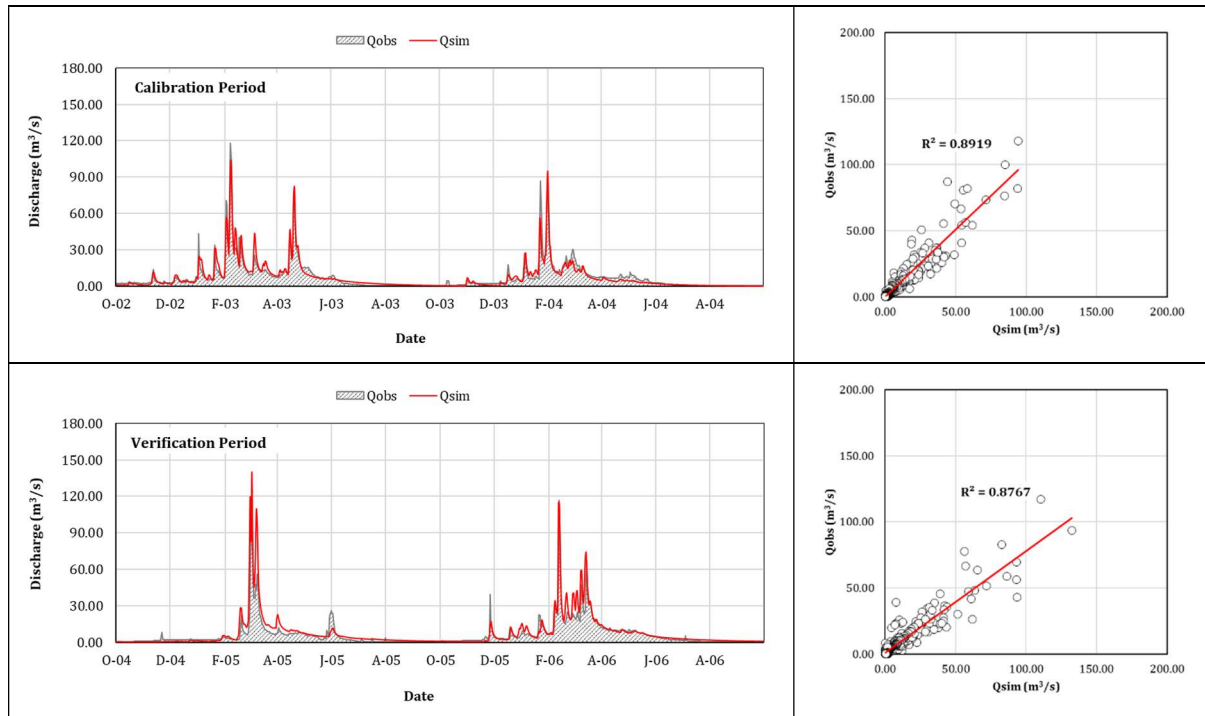
Figure 6. Comparison of the observed and predicted flows in the calibration and verification periods for HBV-DE

Table 5. The calculated NS values in calibration and verification stages and the final number of generations to reach these NS values in HBV-DE approach.

Model Runs	HBV-DE		
	Calibration	Verification	Number of Generations
1	0.877	0.704	61
2	0.855	0.672	17
3	0.891	0.745	70
4	0.857	0.688	32
5	0.865	0.683	17
6	0.86	0.688	26
7	0.881	0.681	12
8	0.867	0.728	58
9	0.856	0.72	20
10	0.913	0.431	500
Maximum	0.913	0.745	500
Minimum	0.855	0.431	12
Mean	0.872	0.674	81.300
St. Deviation	0.0177	0.084	148.590

As indicated previously, both HBV-GA and HBV-DE approaches are executed 10 times to eliminate the influence of the generated random numbers in the optimization process. When the identified results are evaluated in detail (Tables 4 and 5), it can be concluded that HBV-GA model has better calibration performance for almost all the solutions. However, the verification performance of HBV-GA is quite low compared to HBV-DE. For instance, while the maximum NS value for the calibration process in HBV-GA is 0.913, the corresponding NS of that solution is 0.489 in the verification period. The best NS value in HBV-GA for the verification period is 0.561 and this solution corresponds to the

calibration NS of 0.909. On the other hand, the best calibration NS in HBV-DE is 0.913 and this value corresponds to a verification NS of 0.431. However, when the verification performances are evaluated, it is seen that the best verification NS is obtained as 0.745 in HBV-DE and this solution corresponds to the calibration NS of 0.891.

One of the most important advantages of HBV-DE approach compared to HBV-GA is its requirement to the less computational efforts. This outcome can also be seen when the results in Tables 4 and 5 are compared. While HBV-GA required 432 generations, HBV-DE required only 70 generations to reach the final NS values for the selected solutions.

When the scatter plots (Figures 5 and 6) are evaluated for the selected solutions, it can be seen that the determination coefficients (R^2) of HBV-GA and HBV-DE for the calibration period are obtained as 0.9095 and 0.8919, respectively. These values correspond to the R^2 values in the verification period of 0.8483 and 0.8767, respectively.

REFERENCES

Allen, R. G., Pereira, L. S., Raes, D., & Smith, M. (1998). *Crop evapotranspiration-Guidelines for computing crop water requirements-FAO Irrigation and drainage paper 56.*

Bergström, S. (1976). *Development and application of a conceptual runoff model for Scandinavian catchments.* SMHI Norrköping, Report RH07.

Dakhlaoui, H., Bargaoui, Z., & Bárdossy, A. (2012). Toward a more efficient Calibration Schema for HBV rainfall–runoff model. *Journal of Hydrology*, *444–445*, 161–179. https://doi.org/10.1016/J.JHYDROL.2012.04.015

Devia, G. K., Ganasri, B. P., & Dwarakish, G. S. (2015). A Review on Hydrological Models. *Aquatic Procedia*, *4*, 1001–1007. https://doi.org/10.1016/J.AQPRO.2015.02.126

Driessen, T. L. A., Hurkmans, R. T. W. L., Terink, W., Hazenberg, P., Torfs, P. J. J. F., & Uijlenhoet, R. (2010). The hydrological response of the Ourthe catchment to climate change as modelled by the HBV model. *Hydrology and Earth System Sciences*, *14*, 651–665.

Ghaith, M., Siam, A., Li, Z., & El-Dakhakhni, W. (2019). Hybrid Hydrological Data-Driven Approach for Daily Streamflow Forecasting. *Journal of Hydrologic Engineering*, *25*(2), 04019063. https://doi.org/10.1061/(ASCE)HE.1943-5584.0001866

Jin, X., Xu, C. Y., Zhang, Q., & Singh, V. P. (2010). Parameter and modeling uncertainty simulated by GLUE and a formal Bayesian method for a conceptual hydrological model. *Journal of Hydrology*, *383*(3–4), 147–155. https://doi.org/10.1016/J.JHYDROL.2009.12.028

Kumanlioglu, A. A., & Fistikoglu, O. (2019). Performance Enhancement of a Conceptual Hydrological Model by Integrating Artificial Intelligence. *Journal of Hydrologic Engineering*, *24*(11), 04014039-1-04014039–9. https://doi.org/10.1061/(ASCE)HE.1943-5584.0001850

Kunstmann, H., Heckl, A., & Rimmer, A. (2006). Physically based distributed hydrological modelling of the Upper Jordan catchment and investigation of effective model equations. *Advances in Geosciences*, *9*, 123–130. https://doi.org/10.5194/ADGEO-9-123-2006

Liu, Z., Wang, Y., Xu, Z., & Duan, Q. (2017). Conceptual Hydrological Models. In *Handbook of Hydrometeorological Ensemble Forecasting* (pp. 1–23). Springer Berlin Heidelberg. https://doi.org/10.1007/978-3-642-40457-3_22-1

Nash, J. E., & Sutcliffe, J. V. (1970). River flow forecasting through conceptual models part I — A discussion of principles. *Journal of Hydrology*, *10*(3), 282–290. https://doi.org/10.1016/0022-1694(70)90255-6

Nonki, R. M., Lenouo, A., Tshimanga, R. M., Donfack, F. C., & Tchawoua, C. (2021). Performance assessment

and uncertainty prediction of a daily time-step HBV-Light rainfall-runoff model for the Upper Benue River Basin, Northern Cameroon. *Journal of Hydrology: Regional Studies*, *36*, 100849. https://doi.org/10.1016/J.EJRH.2021.100849

Okkan, U., Ersoy, Z. B., Kumanlioglu, A. A., & Fistikoglu, O. (2021). Embedding machine learning techniques into a conceptual model to improve monthly runoff simulation: A nested hybrid rainfall-runoff modeling. *Journal of Hydrology*, *598*. https://doi.org/10.1016/j.jhydrol.2021.126433

Okkan, U., & Kırdemir, U. (2019). Hibrit ve standart PSO algoritmalarının kontrol parametreleri için hassasiyet analizi: Bir yağış-akış modeli kalibrasyonu üzerinden uygulama. *SETSCI Conference Proceedings, 4 Th International Symposium on Innovative Approaches in Engineering and Natural Sciences, November 22-24, 2019*, *4*(6), 336–341. https://doi.org/10.36287/setsci.4.6.085

Okkan, U., Köse, O., Özsoy, M., & Uysal, H. (2017). Yabani ot ve diferansiyel evrim algoritmalarinin aylik kavramsal bir yağiş-akiş modeli kalibrasyonu üzerinden performanslarinin irdelenmesi. *DSİ Teknik Bülteni*, *124*.

Romanowicz, R. J., Osuch, M., & Grabowiecka, M. (2013). On the choice of calibration periods and objective functions: A practical guide to model parameter identification. *Acta Geophysica*, *61*(6), 1477–1503. https://doi.org/10.2478/S11600-013-0157-6

Seibert, J., & Vis, M. J. P. (2012). Teaching hydrological modeling with a user-friendly catchment-runoff-model software package. *Hydrology and Earth System Sciences*, *16*(9), 3315–3325. https://doi.org/10.5194/HESS-16-3315-2012

Seibert, Jan. (1997). Estimation of Parameter Uncertainty in the HBV ModelPaper presented at the Nordic Hydrological Conference (Akureyri, Iceland - August 1996). *Hydrology Research*, *28*(4–5), 247–262. https://doi.org/10.2166/NH.1998.15

Seibert, Jan. (2005). *HBV Light Version 2. User's Manual.* Department of Physical Geography and Quaternary Geology. https://www.scirp.org/(S(351jmbntvnsjt1aadkposzje))/reference/ReferencesPapers.aspx?ReferenceID=2014466

Smith, A., Freer, J., Bates, P., & Sampson, C. (2014). Comparing ensemble projections of flooding against flood estimation by continuous simulation. *Journal of Hydrology*, *511*, 205–219. https://doi.org/10.1016/J.JHYDROL.2014.01.045

Staudinger, M., Weiler, M., & Seibert, J. (2015). Quantifying sensitivity to droughts-an experimental modeling approach. *Hydrology and Earth System Sciences*, *19*(3), 1371–1384. https://doi.org/10.5194/HESS-19-1371-2015

Storn, R., & Price, K. (1997). Differential Evolution – A Simple and Efficient Heuristic for global Optimization over Continuous Spaces. *Journal of Global Optimization*, *11*(4), 341–359. https://doi.org/10.1023/A:1008202821328

Temiz, Ö. (2009). *Gediz havzası örneğinde, beklenen aylık toplam yağışların entropi yöntemiyle tayini*. Dokuz Eylül University, MS Thesis.

Turan, M. E., & Doğan, E. (2015). Kavramsal Hidrolojik Modellerin Farklı Optimizasyon Algoritmaları İle Kalibrasyonu. *CBÜ Fen Bilimleri Dergisi*, *11*(2), 265–277.

Turan, M. E., & Yurdusev, M. A. (2016). Fuzzy conceptual hydrological model for water flow prediction. *Water Resources Management*, *30*(2), 653–667. https://doi.org/10.1007/S11269-015-1183-8/FIGURES/13

Wheater, H., Jakeman, A., & Beven, K. (1993). Progress and directions in rainfall-runoff modelling. *Modelling Change in Environmental Systems*, 101–132. https://agris.fao.org/agris-search/search.do?recordID=GB9410004

Willems, P. (2000). *Probabilistic modeling of the emission receiving surface waters*. Faculty of Engineering, Katholieke Universiteit, Leuven, Belgium.

Zhang, Z., Zhang, Q., Singh, V. P., & Shi, P. (2018). River flow modelling: comparison of performance and evaluation of uncertainty using data-driven models and conceptual hydrological model. *Stochastic Environmental Research and Risk Assessment*, *32*(9), 2667–2682. https://doi.org/10.1007/S00477-018-1536-Y/FIGURES/13

14TH INTERNATIONAL CONFERENCE
ON HYDROSCIENCE & ENGINEERING

MAY 26-27, 2022
IZMİR-TURKEY

ICHE2022
IZMIR, TURKEY

ESTIMATION OF LEAKY-CONFINED AQUIFER PARAMETERS FROM PUMPING TEST DATA BY USING LEVENBERG-MARQUARDT ALGORITHM

Tugba Altiparmak Ay

Department of Civil Engineering, Pamukkale University

Denizli, Turkey

taltiparmakay@gmail.com

Pinar Gokce Durgut [3]

Department of Civil Engineering, Pamukkale University

Denizli, Turkey

pgkargi@gmail.com

M. Tamer Ayvaz [4]

Department of Civil Engineering, Pamukkale University

Denizli, Turkey

tayvaz@pau.edu.tr

ABSTRACT: Accurate estimation of aquifer parameters from pumping test data is a required step in development of the groundwater management models. The current literature includes various grapho-analytical curve matching approaches to determine aquifer parameters by considering different aquifer types (confined, leaky-confined, unconfined, etc.). Although these curve-matching approaches are very easy to employ, their accuracy is subjective based on the modeler's ability. In this context, the main objective of this study is to develop a Levenberg-Marquardt (LM) based optimization approach to determine the parameters of a leaky-confined aquifer from the results of the pumping tests. For this purpose, the process of the flow toward a pumping well in a leaky-confined aquifer system is modeled by means of the Hantush-Jacob Approach and directly integrated to the LM based optimization approach. The applicability of the proposed approach is evaluated by using the pumping test data of a leaky-confined sand-and-gravel aquifer system in Escambia County, Florida, US. The identified results indicated that the proposed LM based optimization approach provides better results than those obtained by using a different approach in literature.

1. INTRODUCTION

The rapid increasing of the world population, and consequently, more water requirements seriously threat sustainable use of the water resources. Although surface water resources are first affected from these negative impacts, groundwater resources are also exposed to pollution and the unconscious water consumption. Therefore, it is essential to develop management models for sustainable use of groundwater resources. Mathematical models, which are used to simulate groundwater head distributions for the considered pumping plans, are the key tools of these management models. These models require spatial distribution of the aquifer parameters which are usually obtained by interpolating the identified parameter values from the results of pumping tests. Note that these tests are conducted by continuously pumping groundwater from a well location and recording the

---

[3] *PhD Scholar of the 100/2000 Program of the Turkish Council of Higher Education Institution (YÖK)*
[4] *Corresponding Author*

corresponding drawdowns at monitoring locations. The current literature includes various analytical solution approaches to determine parameters of the aquifer systems from the results of pumping tests. These approaches differ depending on the types of the aquifer systems (confined, leaky-confined, unconfined, etc.). For instance, while flow toward a well in a confined system under transient flow condition is simulated by using the Theis approach, the same process is simulated on leaky-confined aquifers by means of the Hantush-Jacob approach. For the unconfined aquifers, the flow process is more complicated than the others and simulated by using the Neuman approach (Kresic, 2007). Note that some grapho-analytical solutions of these approaches are proposed to determine the aquifer parameters from results of the pumping tests. Although these approaches can be easily employed, accuracy of them is mostly dependent to the modeler's ability. Therefore, it is essential to determine aquifer parameters by integrating the analytical solutions with optimization approaches to eliminate subjective parameter estimation processes.

There exists a large body of literature that considers different deterministic and heuristic optimization approaches to solve aquifer parameter estimation problems (Samuel and Jha, 2003; Yeh et al. 2005; Sahin, 2017; Zheng et al., 2019; Ayvaz and Gurarslan, 2019; Tadj et al., 2021, etc.). The main idea behind of these approaches is to determine the aquifer parameters by minimizing the discrepancies between the simulated and observed drawdowns in piezometer locations. By considering the same idea, the main objective of this study is to propose an optimization approach to solve the aquifer parameter estimation problems in leaky-confined aquifer systems. In the simulation part of the proposed approach, the transient groundwater flow toward a pumping well in a leaky-confined aquifer is simulated by means of the Hantush-Jacob approach (Hantush and Jacob, 1955). This simulation part is then integrated to an optimization model where the Levenberg-Marquardt (LM) optimization approach is used. The applicability of the proposed approach is evaluated by using the pumping test data of the Escambia Aquifer in FL, USA. Identified results indicated that the proposed LM based optimization approach provides better results than those obtained by using a different approach.

2. MODEL DEVELOPMENT

In this section, the main structure of the proposed LM based optimization approach is presented. In this context, the mathematical structure of the Hantush-Jacob approach is defined first. Then, the main computational structure of the LM optimization approach is given. Finally, mathematical form of the optimization formulation is described.

2.1. Hantush-Jacob Approach

Unsteady groundwater flow toward a fully penetrating well in a leaky-confined aquifer without aquitard storage is given by the Hantush-Jacob approach as follows (Lohman, 1972):

$$s(r,t) = \frac{Q}{4\pi T}\left(2K_0(2v) - \int_{v^2/u}^{\infty} \frac{e^{(-x-v^2)/x}}{x}dx\right) \tag{1}$$

where r is the radial distance from pumping well, t is the time since pumping started, $s(r,t)$ is the drawdown at distance r and time t, Q is the pumping rate of the well, T is the transmissivity of the confined aquifer, $K_0(\cdot)$ is the modified Bessel function of the second time of the zero order, x is the variable of integration, u is the dimensionless Theis parameter which is given as follows:

$$u = \frac{r^2 S}{4Tt} \tag{2}$$

where S is the storage coefficient of the confined aquifer. Note that since confined aquifer is overlain by a semi confined layer (aquitard), the corresponding parameters of the aquitard should be defined. These parameters are given in the term of $\boldsymbol{v}$ as follows:

$$v = \frac{r}{2}\sqrt{\frac{K'}{b'T}} \tag{3}$$

where K' and b' are the vertical hydraulic conductivity and thickness of the confining layer, respectively. Note that solution of the equations given above is conducted by using different approaches. Among them, one of the well known solutions is the Walton grapho-analytical method, which is based on the type curves, to solve Hantush-Jacob approach in the following form (Kresic, 2007):

$$s(r,t) = \frac{Q}{4\pi T} W(u, r/B) \tag{4}$$

$$B = \sqrt{\frac{Tb'}{K'}} \tag{5}$$

where B is the leakage factor and $W(u, r/B)$ is the Hantush well function for the leaky-confined aquifer whose values are determined for the given values of u and r/B. Depending on these equations, the parameters of T, S, and K' can be determined by means of the optimization approach.

2.2. Levenberg-Marquardt Optimization Approach

Levenberg-Marquardt (LM) optimization approach is one of the most efficient optimization methods which uses the first and the second order gradient information of the Taylor series expansion. In its general form, LM can be defined as a mixed solution approach that integrates the steepest-descent and Gauss-Newton optimization methods. Mathematical solution of an optimization problem by using LM approach can be conducted based on the following solution sequence:

Let n be the number of decision variables; $x_k^{st} \in x^{st}$ be the kth decision variable at st^{th} solution step ($k = 1,2,3,\cdots,n$); ε_{tol} be the convergence criterion; μ_{st} be a scaling factor which is used to determine the search direction; $\nabla f(x^{st})$ be the gradient vector; $\nabla^2 f(x^{st})$ be the Hessian matrix; and $f(x^{st})$ be the objective function value which is calculated by using the vector of x^{st}. Depending on these definitions, search direction (p_{st}) of the optimization problem can be determined by solving the following linear system of equations:

$$[\nabla^2 f(x^{st}) + \mu_{st} \cdot I] \cdot p_{st} = \nabla f(x^{st}) \tag{6}$$

where I is the unit matrix with a dimension of $n \times n$. After determining the search direction of p_{st}, a step size of s_{st}, which guarantees the minimized function value, is determined by means of the univariate optimization approaches such as the line search, Newton-Raphson, or golden-section search, etc. After this process, the solution is updated by using the following equation:

$$x^{st+1} = x^{st} + s_{st} p_{st} \tag{7}$$

where x^{st+1} represents the decision variable vector in the next iteration. After this process, the objective function value of $f(x^{st+1})$ is calculated and the scaling factor of μ_{st} is updated by using the following equation:

$$\mu_{st+1} = \begin{cases} 2\mu_{st} & \text{if } f(x^{st+1}) \geq f(x^{st}) \\ \mu_{st}/2 & \text{if } f(x^{st+1}) \leq f(x^{st}) \end{cases} \tag{8}$$

It should be noted that a faster convergence is guaranteed when the value of μ_{st} is reduced and this process is possible if the new objective function value is better than the one in the previous iteration. If this condition is not satisfied, the value of μ_{st} is continuously increased until satisfying the minimized function value. After this process, all the identified values are used in Eq. (6) and the same solution sequence is followed until satisfying the following convergence criterion:

$$\left| \frac{f(x^{st+1}) - f(x^{st})}{f(x^{st+1})} \right| \leq \varepsilon_{tol} \tag{9}$$

2.3. Problem Formulation

The problem of aquifer parameter estimation for leaky-confined aquifer systems can be solved by using the proposed LM based optimization approach. As indicated previously, the objective of the LM optimization approach is to determine the parameters of T, S, and K' by minimizing the discrepancies between the simulated and observed drawdown values at selected monitoring locations and times. This problem can be mathematically stated as follows:

$$SSE(r) = \sum_{t=1}^{n_t} \big(s(r,t) - s'(r,t) \big)^2 \tag{10}$$

subject to

$$T_{\min} \leq T \leq T_{\max} \tag{11}$$

$$S_{\min} \leq S \leq S_{\max} \tag{12}$$

$$K'_{\min} \leq K' \leq K'_{\max} \tag{13}$$

where $SSE(r)$ is the objective function value, which is the sum of square errors, for a distance r from the pumping well location, n_t is the number of monitoring steps, $s(r,t)$ and $s'(r,t)$ are the simulated and observed drawdown values, respectively at distance r and monitoring step t, $T_{\min}$, $S_{\min}$, and $K'_{\min}$ are the lower; and $T_{\max}$, $S_{\max}$, and $K'_{\max}$ are the upper bounds of the decision variables of T, S, and K', respectively.

3. MODEL APPLICATION

3.1. Pumping Test Data

The applicability of the proposed approach is evaluated by using the pumping test data of the sand-and-gravel aquifer system in Escambia County, FL, USA. At 15th October 1986, a two-day constant discharge pumping test was conducted by Northest Florida Water Management District (NFWMD) in order to determine the hydrogeological parameters of the aquifer system. In this context, the water supply well of ECUA-#8 was pumped at an average pumping rate of 448 gal/min (1.6959 m³/min) and its corresponding drawdowns were recorded at 9 monitoring wells penetrating the main production zone of the aquifer system. The general hydrogeological cross-section of the aquifer system together with the pumping and monitoring well locations can be seen in Figure 1 (Richards and Murray, 2004).
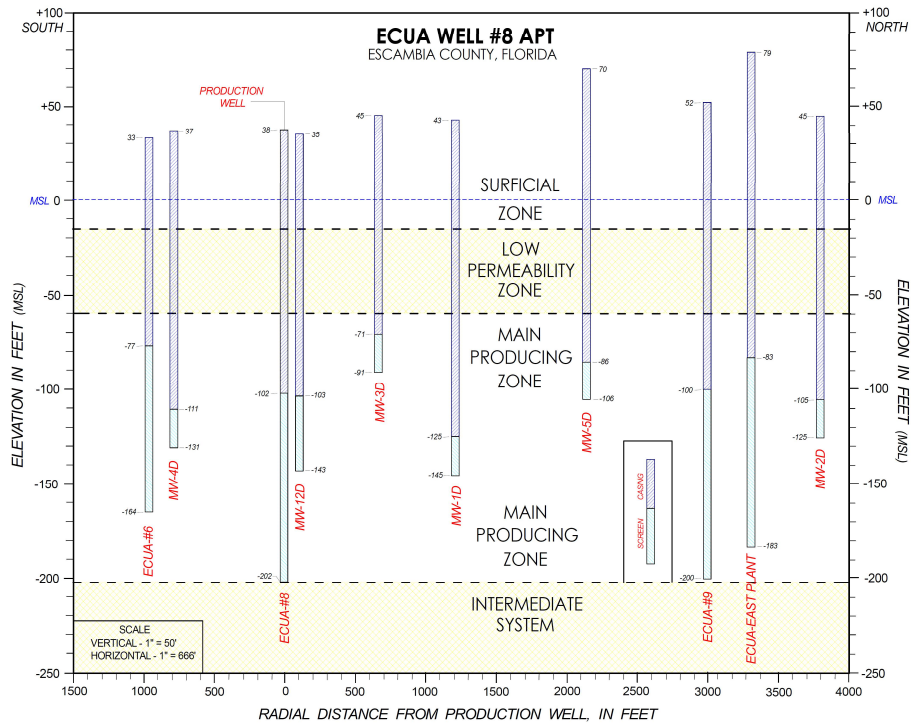
Figure 1. General hydrogeological cross-section of the aquifer system (Richards and Murray, 2004)

As can be seen from Figure 1, the aquifer system is subdivided into 3 district zones based on hydrogeological characteristics. The surficial part consists of the moderately well-sorted sand-and-gravel which produces unconfined flow conditions within this zone. Below this part, there is a low permeability zone consisting of poorly sorted clay and sand formations which behaves as a leaky-confined unit. The lowermost zone of the system consists of the moderate to well-sorted medium sand and this part is the most productive that is why all the wells have their screens in this unit. Below this unit, there is an intermediate system which behaves as the confining unit. As indicated previously, ECUA-#8 is the main withdrawal well in the test and the other wells are used as the monitoring wells where the effect of the pumping test is recorded. Radial distances of each monitoring wells from the ECUA-#8 are given in Table 1. By using this information, a two-day pumping test was conducted by NFWMD and corresponding drawdowns were collected. Figure 2 shows these drawdown records after completing the test.

Table 1. Radial distances of the monitoring wells from pumping well.

Monitoring Well	r (ft)	r (m)
MW-1D	1212	369
MW-2D	3800	1158
MW-3D	667	203
MW-4D	788	240
MW-5D	2133	650
MW-12D	104	32
ECUA-#6	968	295
ECUA-#9	2997	913
ECUA-East Plant	3300	1006
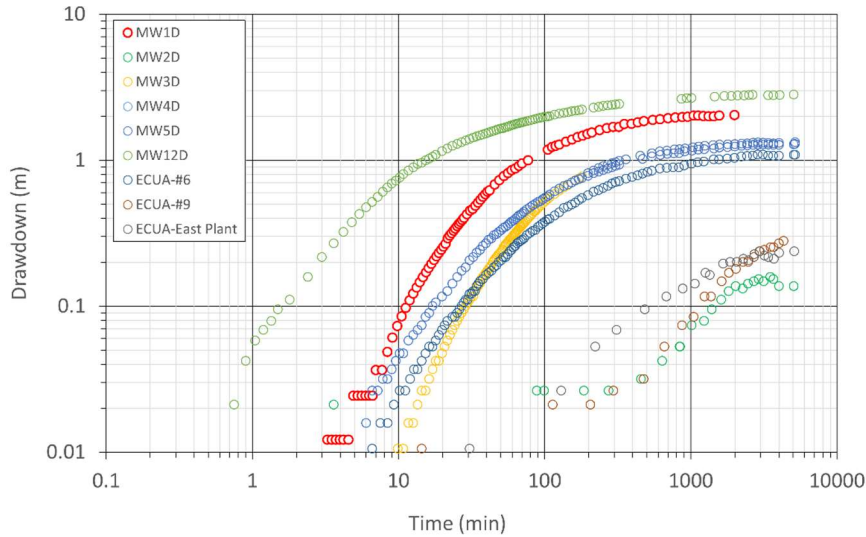
Figure 2. Aquifer's response to pumping in terms of drawdown observations

3.2. Results of the Proposed Approach

The proposed LM based optimization approach is applied to the pumping test data given in Figure 2 by considering the Hantush-Jacob approach. As indicated previously, the main objective of the proposed approach is to determine the T, S, and K' values by minimizing the objective function given in Equation (10). In this context, the optimization process is conducted by considering $\varepsilon_{tol} = 10^{-6}$, $\mu_{st} = 10^3$, and the parameter bounds given in Table 2.

Table 2. Bounds of the decision variables.

Parameters	Parameter Bounds	
	Lower	Upper
T	0	100
S	0.00001	0.01
K'	0.00001	0.01

By using these values, the proposed LM based optimization approach is executed for each monitoring test data. Table 3 shows the identified parameter values for each monitoring wells. Note that these parameter values were also calculated by NFWMD (Richards and Murray, 2004) by using the AquiferWin32 software package, developed by Environmental Simulations, Inc. Table 3 also includes the results of this software package for comparison purposes. As can be seen from Table 3, there are some slight differences among the identified T values for each monitoring well location such that the minimum and the maximum values are obtained for MW-5D (29.45 m²/h) and MW-2D (48.28 m²/h), respectively. The mean T value for all the monitoring wells is obtained as 34.50 m²/h. Note that the reason of these differences may be associated with the field conditions. As an example, in Hantush-Jacob approach, it is required that the pumping well and all the monitoring wells should fully penetrate the confined aquifer thickness. However, this requirement is not satisfied as seen in Figure 1 where only pumping well and ECUA-#9 fully penetrates the main production zone. Another important requirement is that the water level in the uppermost unconfined part should not change during the test. This requirement may not be satisfied due to the hydraulic gradients from unconfined to confined zone during pumping occurs. For the other parameters (S and K'), the proposed approach is resulted with the parameter values about same order of magnitudes. When the identified values are compared with the ones obtained by using the AquiferWin32 software, it is seen that the same trend is obtained with the identified T values. Note that Richards and Murray (2004) determined these parameter values by considering a constant leakage factor ($B = 2800 \; ft = 853 \; m$) depending on the relative homogeneity of the aquifer across the test site. Therefore, the same assumption is also

followed in the proposed approach to obtain the comparable results. However, this assumption is not required in the proposed approach and the value of leakage factor can also be used as a variable parameter. For each monitoring well location, the final objective function values (SSE) are listed in Table 4. Note that, Table 4 also includes a comparison in terms of Nash-Sutcliffe (NS) model efficiency vales which is a well-known error indicator in hydrological prediction studies.

Table 3. Comparison of the identified parameter values for each monitoring well location with AquiferWin32 software.

Well Name	Proposed Approach			AquiferWin32 (Richards and Murray, 2004)		
	$T \ [m^2/h]$	$S \ [-]$	$K' \ [m/h]$	$T \ [m^2/h]$	$S \ [-]$	$K' \ [m/h]$
MW-1D	33.58	4.28E-04	6.32E-04	33.68	3.90E-04	6.34E-04
MW-2D	48.28	8.58E-04	9.09E-04	42.19	9.40E-04	7.94E-04
MW-3D	33.78	4.45E-04	6.36E-04	33.68	4.20E-04	6.29E-04
MW-4D	31.54	3.96E-04	5.94E-04	31.74	3.50E-04	5.94E-04
MW-5D	29.45	3.97E-04	5.55E-04	29.03	4.20E-04	5.49E-04
MW-12D	33.35	7.64E-04	6.28E-04	34.06	5.60E-04	6.40E-04
ECUA-#6	32.35	4.58E-04	6.09E-04	32.13	4.00E-04	6.06E-04
ECUA-#9	33.70	1.37E-03	6.35E-04	33.29	1.33E-03	6.29E-04
ECUA-East Plant	40.10	6.05E-04	7.55E-04	39.87	5.70E-04	7.49E-04
Mean Value	34.50	6.40E-04	6.50E-04	33.73	6.01E-04	6.34E-04

Table 4. Comparison of the final SSE and NS values for each monitoring well location with AquiferWin32 software.

Well Name	Proposed Approach		AquiferWin32 (Richards and Murray, 2004)	
	SSE	NS	SSE[1]	NS[1]
MW-1D	8.95E-04	0.9961	2.16E-03	0.9905
MW-2D	1.80E-03	0.9338	4.10E-03	0.8492
MW-3D	2.06E-03	0.9932	4.20E-03	0.9861
MW-4D	2.78E-03	0.9903	5.16E-03	0.9820
MW-5D	3.93E-03	0.9776	4.49E-03	0.9744
MW-12D	2.83E-02	0.9242	1.16E-01	0.6889
ECUA-#6	3.53E-03	0.9881	9.52E-03	0.9680
ECUA-#9	8.59E-04	0.9928	1.17E-03	0.9902
ECUA-East Plant	2.02E-03	0.9569	2.26E-03	0.9519
Mean Value	5.52E-03	0.9745	1.84E-02	0.9287

[1] These values have been calculated by using the determined parameter values in Richards and Murray (2004) to the simulation part of the proposed approach.

As can be seen from Table 4, the final objective function values of the proposed approach are all better than those obtained by means of the AquiferWin32 software. This result can also be seen in the final NS values such that the minimum and maximum NS values are obtained as 0.9242 (MW-12D) and 0.9961 (MW-1D), respectively. Note that the final NS values at the same monitoring wells which are obtained by using the AquiferWin32 software are 0.6889 and 0.9905, respectively. For all the monitoring wells, while the proposed approach is resulted with the mean NS value of 0.9745, the AquiferWin32 resulted with the mean NS value of 0.9287. This result indicates the efficiency of the proposed LM based optimization approach.

4. CONCLUSIONS

In this study, an optimization approach is proposed to determine the hydrogeologic parameters of the leaky-confined aquifer systems from the results of pumping tests. In the proposed approach, the transient groundwater flow toward a pumping well in a leaky-confined aquifer system is analytically modeled by means of the Hantush-Jacob approach. This solution is then integrated to an optimization model where LM optimization algorithm is used. The objective of the LM based optimization approach is to determine the aquifer parameters by minimizing the discrepancies between the simulated and observed drawdown values at selected monitoring wells in the pumping test. This kind of a solution is useful in preventing the subjective curve-matching approaches to determine the aquifer parameters. The applicability of the proposed LM based optimization approach is evaluated by using a real pumping test data conducted in FL, USA. The identified results of this evaluation indicated that the proposed LM based optimization approach resulted with the better identification performances than those obtained by using a different approach in literature.

REFERENCES

Ayvaz, M. T., & Gurarslan, G. (2018). Identification of the Aquifer Parameters from Pumping Test Data by Using a Hybrid Optimization Approach. In: HIC 2018. *13th International Conference on Hydroinformatics* (G. La Loggia, G. Freni, V. Puleo & M. De Marchis, eds), EasyChair, pp. 147–154. https://doi.org/10.29007/11v5

Ayvaz, M. T., & Gurarslan, G. (2019). A hybrid optimization approach for parameter estimation of confined and leaky confined aquifers. *Water Supply*, 19(8), 2359–2366. https://doi.org/10.2166/ws.2019.117

Hantush, M.S., & Jacob, C.E. (1955). Non-steady radial flow in an infinite leaky aquifer. *Trans., Am. Geophys. Union*, Vol. 36, pp. 95-100. https://doi.org/10.1029/TR036i001p00095

Kresic, N. (1997). *Quantitative Solutions in Hydrogeology and Groundwater Modeling*, 1st edn. CRC Press, Boca Raton, FL, USA.

Lohman, S. W. (1972). *Ground-Water Hydraulics*: U.S. Geological Survey Professional Paper 708, 70 p.

Richards, C. J., & Murray, C. M. (2004). Results of the ECUA #8 Constant Rate Aquifer Test Sand-and-Gravel Aquifer, Escambia County, Florida, Northwest Florida Water Management District, USA.

Şahin, A. U. (2018). A Particle Swarm Optimization Assessment for the Determination of Non-Darcian Flow Parameters in a Confined Aquifer. *Water Resources Management*, 32(2), 751–767. https://doi.org/10.1007/s11269-017-1837-9

Samuel, M. P., & Jha, M. K. (2003). Estimation of Aquifer Parameters from Pumping Test Data by Genetic Algorithm Optimization Technique. *Journal of Irrigation and Drainage Engineering*, 129(5), 348–359. https://doi.org/10.1061/(asce)0733-9437(2003)129:5(348)

Storn. R., & Kenneth, P. (1997). Differential evolution–a simple and efficient heuristic for global optimization over continuous spaces. *Journal of global optimization*, 11.4: 341-359.

Tadj, W., Chettih, M., Mouattah, K. (2021). A new hybrid algorithm for estimating confined and leaky aquifers parameters from transient time-drawdown data. *Soft Computing*, 25(24), 15463–15476. https://doi.org/10.1007/s00500-021-06224-z

Yeh, H-D., Lin Y-C., Huang, Y-C. (2007). Parameter identification for leaky aquifers using global optimization methods. *Hydrological Processes*, 21:862–872. https://doi.org/10.1002/hyp.6274

Zheng, G., Ha, D., Loaiciga, H., Zhou, H., Zeng, C., Zhang, H. (2019). Correction: Estimation of the hydraulic parameters of leaky aquifers based on pumping tests and coupled simulation/optimization: verification using a layered aquifer in Tianjin, China. *Hydrogeology Journal*, 27(8), (3081-3095). https://doi.org/10.1007/s10040-019-02043-7

14TH INTERNATIONAL CONFERENCE
ON HYDROSCIENCE & ENGINEERING

MAY 26-27, 2022
IZMİR-TURKEY

ICHE2022
IZMIR, TURKEY

GRAVEL MOBILIZATION AND CHANNEL EVOLUTION DUE TO SAND-COVERING ON GRAVEL BEDS

Hiroshi Miwa

Department of Social Systems and Civil Engineering, Faculty of Engineering, Tottori University

Tottori-City, Tottori, Japan

miwa-h@tottori-u.ac.jp

Takashi Wada

Department of Social Systems and Civil Engineering, Faculty of Engineering, Tottori University

Tottori-City, Tottori, Japan

wada-t@tottori-u.ac.jp

Yuhei Ota

Engineering Department, Hiroshima Branch, Central Consultant Inc.

Hiroshima-City, Hiroshima, Japan

yota@central-con.co.jp

ABSTRACT: Gravel-bed formation in rivers downstream of dams may cause several problems, such as bed degradation and channel immobilization. Therefore, several studies and many public works have been conducted to restore these rivers. Gravel can be more easily removed when fine sediment (i.e., sand) is present in streambeds with gravel than in gravel beds without fine sediment. This phenomenon may indicate that sediment augmentation of gravel beds using fine sediment is a viable alternative for mobilizing coarse surface layers. In this study, we investigated the effects of sediment augmentation on gravel beds associated with sand-covering on gravel mobilization and channel evolution. Because a subsurface layer in an armored bed may contain not only gravel but also sand, we also experimentally examined the effect of sand in the subsurface layer on gravel mobilization. The results can be summarized as follows: (1) Gravel in rivers with armored beds can be relatively easily mobilized by supplying sand as cover. When exposed to the removal of coarse armor material, the fraction of sand in the subsurface layer in the bed can play a role in the reduction of the friction angle of the gravel. (2) Sand-covering promotes bed variation through gravel mobilization in gravel-bed rivers. The bed variation also developed into an area without sand-covering. Therefore, these phenomena may contribute to channel evolution. (3) The sand-covering on an armored overbank area causes widening of the low-flow channel and bed aggradation of the low-flow channel through gravel mobilization of its surface layer. Such results may depend on the thickness of the sand-covering, and a large value produces large results. The quantitative evaluation obtained in this study may be useful for designing river restoration schemes.

1. INTRODUCTION

Riverbeds downstream of dams typically degrade and coarsen and become essentially immobile (CALFED Science Program and Ecosystem Restoration Program Gravel Augmentation Panel, 2005), leading to a loss of spawning and rearing habitats. These issues are caused by the cutoff of the sediment supply to downstream rivers. To enable the conservation and restoration of riverine environments, sediment replenishment technology has been developed which involves the conveyance of sediments excavated and/or dredged from reservoirs and deposited in the river below the corresponding dam. The sediment placed downstream of the dam can then be mobilized by floodwater or dam releases. This technology has been implemented in several dams in Japan and the USA (Committee on Hydroscience and Hydraulic Engineering, 2008; CALFED Science Program and

461

Ecosystem Restoration Program, Gravel Augmentation Panel, 2005). Sediment flushed from the placement site can ameliorate the degradation and variation of the pool riffle sequence of the low-flow channel (Stillwater Science et al., 2008; Miwa & Parker, 2012). Due to the replenishment of sediments, sand supply to downstream rivers may influence physical and environmental aspects, such as bed variations and fish and plant habitats; therefore, systematic investigations are necessary to enable practical implementation and management of this technology.

Gravel can be more easily removed when fine sediment (i.e., sand) is present in streambeds composed of gravel than in gravel beds without fine sediment. This phenomenon can be applied to gravel mobilization in armored gravel-bed rivers by means of sand supply. The mechanisms of fine sediment for coarse gravel mobilization have been discussed by many researchers and engineers. Ikeda (1984) and Ikeda and Iseya (1988) found that the presence of sand in mixtures of sand and gravel might increase the mobility of gravel itself. Ikeda and Iseya (1988) indicated that this was due to increased fluid stresses on protruding grains and reduced friction angles. Wilcock (1998) and Wilcock and Kenworthy (2002) proposed to divide the sediment into two size fractions, sand (grain size $d_s < 2$ mm) and gravel ($d_g > 2$ mm), in flume experiments and field measurements, and demonstrated that the dimensionless reference shear stresses corresponding to the critical Shields stress for sand and gravel decreased sharply over a range of sand fractions in the mixtures. Wilcock and Crowe (2003) proposed an empirical relationship between the dimensionless reference shear stress for the mean grain size of the bed surface and the proportion of sand in the surface size distribution and presented a surface-based sediment transport model for sand and gravel mixtures using the empirical relationship and their hiding function. Miwa and Parker (2017) examined the effects of the sand fraction in sand and gravel mixtures on the critical Shields stress for gravel.

The results mentioned above can be used to design river restoration, such as sediment augmentation. These studies focused on the mobilization and mobility of sand and gravel in their mixture, but the effects on bed variation and channel evolution have not been investigated in detail. Because sediment augmentation techniques, such as the sediment replenishment, cannot easily control a target area for sediment supply, it may be difficult to provide an effective sediment supply to the target area for sand and gravel mobilization and mobility. A sand-covering method can supply sand to the target area in advance. Miwa and Yamada (2018) investigated the effects of sand supply on armored gravel beds associated with sand-covering on gravel mobilization and bed variation. They found that gravel mobility was improved by sand-covering, and bed variation was promoted through gravel mobilization. In particular, sand in the subsurface layer of the armored bed also contributed to gravel mobilization in the subsequent sedimentation process. In this study, we investigated the effects of sand-covering on gravel mobilization and channel evolution as well as the width and depth of a low-flow channel, using flume experiments as the next step. We also examined the effect of sand in the subsurface layer on gravel mobilization.

2. EXPERIMENTAL SETUP AND PROCEDURES

Experiments were conducted in a straight open channel 10 m long, 0.5 m wide and 0.6 m deep, as shown in Figure 1. A box was used to set a surface defining a mobile-bed zone of 2.7 m length, 0.5 m width and 0.04 m depth. A sedimentation box, which was divided into two parts in the transverse direction, was placed downstream, immediately below the mobile-bed box to capture the moving sediment. The upstream and downstream regions of the box were provided a fixed bed of uniform gravel. The grain size distributions of the sediments used in the experiments are shown in Figure 2. The sediment characteristics are listed in Table 1. In the table, d_s and d_g are the mean grain sizes of sand and gravel, respectively; d_m is the mean grain size of the mixture; d_{16} and d_{84} are grain sizes for which 16% and 84% of the sediment is finer, respectively; and σ_g is the geometric standard deviation ($= (d_{84}/d_{16})^{1/2}$). The specific gravities of sand and gravel are equal to 2.65. The mixture was made from gravel A and sand B under the condition $f_s = 0.2$, where f_s denotes the fraction of sand in the mixture, defined as

$$f_s = \frac{V_s}{V_g + V_s} \tag{1}$$

where V_s = volume of sand and V_g = volume of gravel.
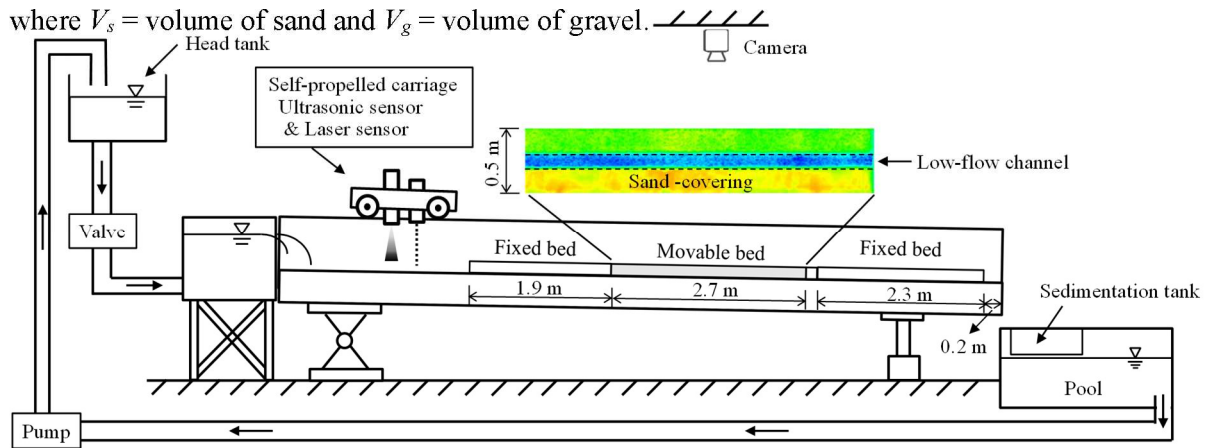
Figure 1. Schematic of the testing flume and experimental setup
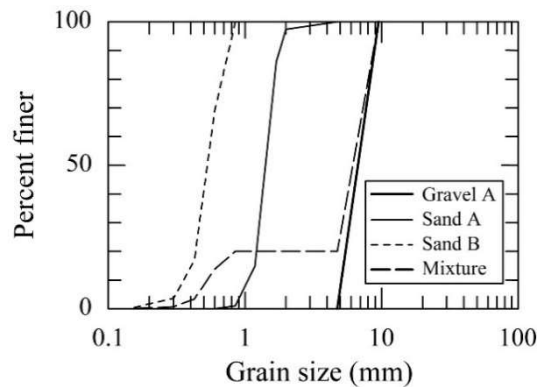
Figure 2. Grain size distributions of sediments used in experiments

Table 1. Characteristics of gravel, sand and mixtures used in experiments.

Sediment	d_s mm	d_g mm	d_m mm	d_{16} mm	d_{84} mm	σ_g
Gravel A		7.1		5.6	8.2	1.22
Sand A	1.4			1.1	1.6	1.19
Sand B	0.52			0.4	0.7	1.35
Mixture (f_s=0.2)			5.8	0.7	7.7	3.42

A riparian area and low-flow channel were created in the movable-bed zone in the channel, as shown in Figure 3. Symbols characterizing the dimensions of the riparian area and low-flow channel are also shown in the figure. Sand-covering was performed using sand A in the right riparian area. Three bed sediment compositions were used in the experiments. Figure 4 illustrates the sediment composition of the initial beds. Type 1 corresponded to a gravel bed using gravel A, and Type 2 corresponded to Type 1 with sand-covering. Type 3 corresponds to an armored bed with sand-covering. For Type 3, we prepared the amounts of sand and gravel, which were measured using Equation (1) as $f_s = 0.2$. The gravel grains were placed such that the thickness of these grains was one to two times their size, and the corresponding amount of sand was then added to the interstices among the placed gravel grains. This procedure was repeated until the surface elevation of the mixture was equal to the fixed-bed surface elevation. The armored bed was made by supplying a flow rate $Q_1 = 0.007$ m³s⁻¹ in the absence of sediment feed to the mobile bed composed of the mixture (Table 1). The experimental conditions are listed in Table 2. In the table, D/d_g is the ratio of the average thickness of the sand-covering layer (difference between the average bed elevations before and after sand-covering) to the mean gravel size, Q_2 = flow rate. A flow rate of 0.030 m³s⁻¹ corresponds to 300 m³s⁻¹ in a field at a scale of 1/40 by Reynolds' Law of Similarity. The threshold grain size for movement was over 20 cm under this condition.
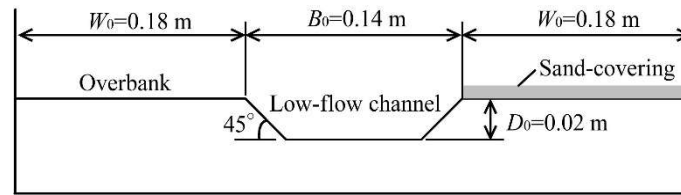
Figure 3. Cross-sectional profile and symbol definitions for flood plain (riparian areas and low-flow channel)

(a) Type A　　　　　　(b) Type B　　　　　　(c) Type C
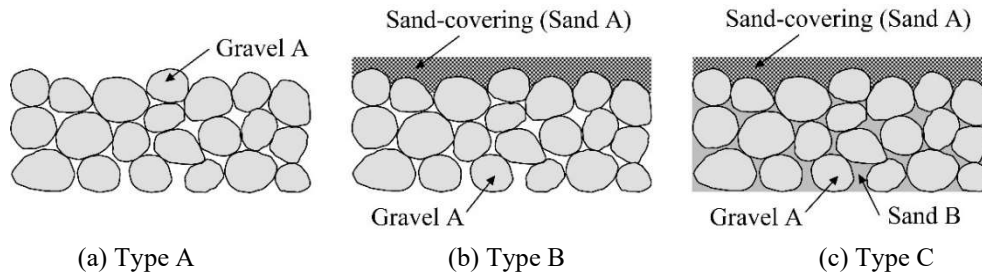
Figure 4. Bed sediment compositions of initial beds (side view)

In the experiments, sediments were set in the mobile-bed zone of the channel (Types A, B, or C). The bed was set to a longitudinal slope of 0.01. The longitudinal profiles of the bed surface elevation were measured using a laser sensor mounted on a self-propelled carriage. The profiles were obtained at intervals of 1 cm in the transverse direction of the channel before commencing each run. In each run, the am ou nt of gravel A entrained from the mobile bed and transported to the sedimentation box for approximately 60 s (120 s for the last run of each experiment) was measured under quasi-uniform flow conditions. In Type C, the amount of sand B entrained from the subsurface layer of the mobile bed and transported to the sedimentation box was measured. During each run, longitudinal profiles of the water surface were measured at transverse locations of $y = 13$ cm and 37 cm from the right bank of the channel with an ultrasonic sensor mounted on the self-propelled carriage. The longitudinal profiles of bed surface elevation were measured again after the flow was stopped. This procedure was repeated six times for each experiment. After each run, a plain view of the colored water flow of $Q_3 = 0.0002$ m^{3}s^{-1} in the low-flow channel was recorded by the camera above the channel. The entrainment observations of the experiments are presented in Table 2. In the table, h_m is the mean flow depth, which was calculated by averaging the difference in the average water surface elevation at $y = 13$ cm and 37 cm and the transverse averaged bed elevation at longitudinal intervals of 10 cm. I_e = energy slope, F_r = Froude number, u_* = shear velocity, and τ_{*g} = dimensionless bed shear stress for Gravel A. The minimum value of D/d_g was approximately 0.3-0.4 when the bed surface gravel was fully covered with sand A. The flow rate of 0.030 m^{3}s^{-1} corresponded to 300 m^{3}s^{-1} in the field at a scale of 1/40, and the threshold grain size of movement was approximately 27 cm under this condition.

Table 2. Experimental conditions and entrainment observations.

Case	Bed sediment condition	D/d_g	Q_2 m^{3}s^{-1}	h_m m	I_e	F_r	u_* m/s	τ_{*g}
A-1	Type A	0	0.030	0.083	0.0084	0.81	0.072	0.044
B-1	Type B	0.78	0.030	0.079	0.0072	0.87	0.065	0.037
C-1	Type C	0.79	0.030	0.079	0.0091	0.86	0.073	0.047
C-2	Type C	0.55	0.030	0.080	0.0093	0.84	0.074	0.048

3.　EXPERIMENTAL RESULTS AND DISCUSSION

3.1. Effects of Sand Supply by Means of Sand-Covering on Gravel Mobilization

Figure 5 shows the volumes of gravel A and sand B removed from the right half of the mobile-bed

zone during the experiment. Sand B is initially present in the subsurface layer of the armored bed. The volume of gravel A that was transported in the experiments for which sand A was placed on the mobile-bed zone via sand-covering (Cases B-1 and C-1) was larger than that for the experiment without sand-covering (Case A-1). These results indicate that the presence of sand on the gravel-bed surface activates gravel mobilization. In particular, the volume of gravel A removed in the experiment with the armored bed (Case C-1) was the largest among the three experiments. This may have been caused by the low friction angle of Gravel A engendered by the exposure of sand B, which was originally in the subsurface layer, to the flow after removing Gravel A from the surface layer. This result suggests that sand-covering is a viable alternative for mobilizing coarse gravel for the restoration of gravel-bed rivers downstream of dams. However, this must be discussed seriously because the initial covering of the bed with sand may negatively impact ecological systems.
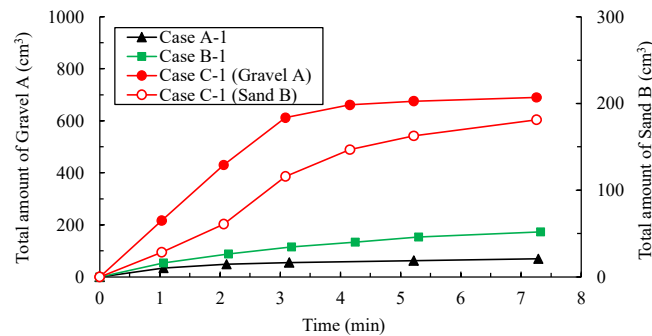
Figure 5. Temporal change of total volume of gravel and sand transported from mobile bed

Regarding aspects such as project costs and environmental issues of the sand-covering work, it is necessary to achieve the effect with the least amount of sand. In this section, we discuss the effects of the amount of sand-covering sand on gravel mobilization. Figure 6 shows the temporal variations in the amounts of gravel A and sand B removed from the mobile-bed area (Type C) for each thickness of the sand-covering layer, which is standardized by the size of gravel A. Figure 6(a) shows the total amount of gravel A and sand B. It was found that greater the thickness of the sand-covering, the greater the amount of mobilized gravel A. This tendency can be observed for mobilized sand B. Therefore, the total amount of gravel A is proportional to the thickness of the sand-covering layer in this study. However, Miwa and Yamada (2018) indicated that the mass of gravel runoff increased with increasing D/d_g; meanwhile, the efficiency of the sand-covering work was relatively reduced when the value of D/d_g exceeded about 0.6-0.7. They explained that this was because part of the sand-covering sand did not contribute to gravel mobilization. They also suggested that the efficiency of the sand-covering might be produced at $D/d_g = 0.3$-0.4. Although their experiments are not the same as ours, we must investigate the efficiency of gravel mobilization with reference to their approach. Figure 6(b) shows the ratios of the amounts of gravel A and sand B to the amount of sand A at each measurement time. The transport efficiency of gravel A (transportation volume of gravel A relative to the transportation volume of sand A) indicated a large value at an earlier stage when the sand-

| (a) Total amounts of gravel A and sand B | (b) Ratio of gravel A and sand B to sand A |
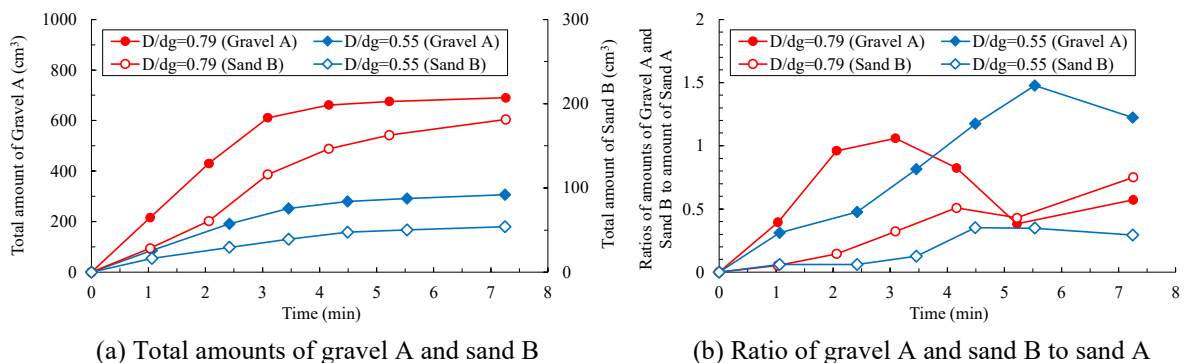
Figure 6. Temporal variations in amounts of gravel and sand removed from mobile-bed for each thickness of the sand-covering layer standardized by gravel size D/d_g (Type C)

covering layer thickness was large. This suggests that the bed variation progressed relatively fast in the case of a large amount of sand-covering sand. As for sand B, the transport efficiency is not always clear.

3.2. Effects of Sand Supply by Means of Sand-Covering on Channel Evolution

Because a sediment supply to the riverbed influences the physical environment of rivers, it is necessary to investigate bed variations and channel evolution. Figure 7 shows the bed topography of the initial and final stages of the experiment and transverse bed profiles at longitudinal phases x/L in the final stage of the experiment. In this figure, x denotes the distance from the upper edge of the mobile-bed zone, L denotes the length of the zone, y denotes the distance from the left edge of the channel, and B denotes the width of the channel. The datum line ($z = 0$) is the average initial bed elevation in the mobile-bed zone. Δz denotes the deviation of bed surface elevation from the datum line. In the figure, the transverse profile of the initial bed (solid line) shows the longitudinally-

(a) Case A-1 (no sand-covering)

(b) Case B-1 ($D/d_g = 0.78$)

(c) Case C-1 ($D/d_g = 0.79$)

(d) Case C-2 ($D/d_g = 0.55$)
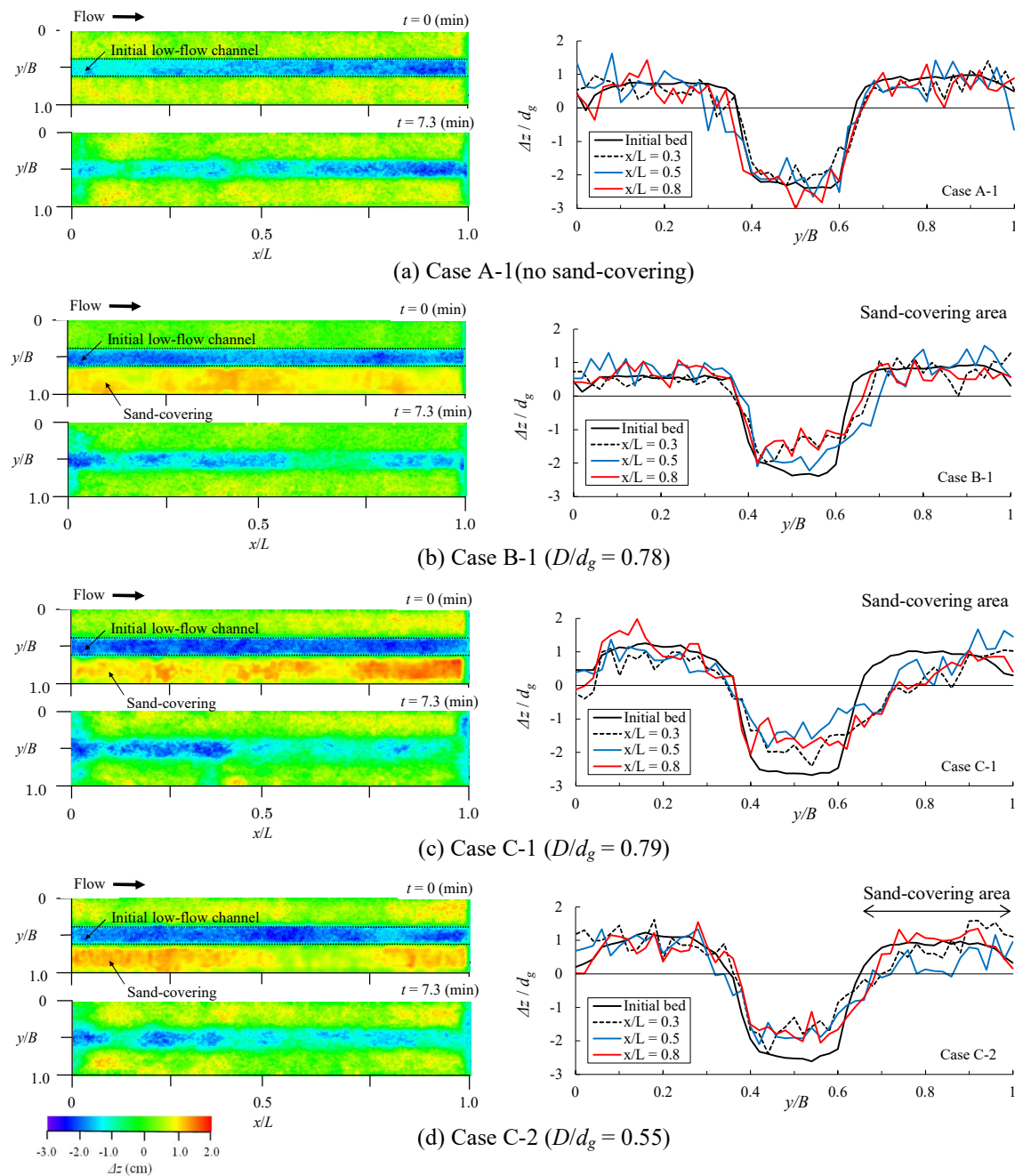
Figure 7. Bed topography (plain view) at the initial and final stages of experiment and transverse bed profiles at some longitudinal phases (x/L) in the final stage of the experiment

averaged bed elevation.

In Case A-1, the mobile bed hardly varied, and the transverse profile of the low-flow channel almost maintained its initial shape. Because the average dimensionless tractive force in this experiment was $\tau_* = 0.044$ (the dimensionless tractive force in the low-flow channel might be larger than that in the riparian area), which was less than the critical dimensionless tractive force $\tau_{*c} = 0.05$, the sediment transport was hardly observed in the experiment. Such a lower tractive force condition for gravel was common in all the experiments. On the other hand, bed variations could be found in the right overbank area and low-flow channel in other cases with sand-covering. In Case B-1, aggradation of the low-flow channel bed and degradation of the right overbank could be found in the mobile bed. Similar results were obtained for Case C-1. Although the thickness of the sand-covering was almost the same in Cases B-1 and C-1, the degradation area in Case C-1 was found to be larger than that in Case B-1 from their transverse profiles (Figures 7(b) and 7(c)). This difference may have been caused by sand B in the bed subsurface layer. The thickness of the sand-covering in Case C-2 was less than that in Case B-1. However, the degradation area in Case C-2 was the same and larger than that in Case B-1. This difference may also be caused by sand B. Therefore, sand B plays an important role not only in the sediment runoff shown in the previous chapter but also in bed variation. From these experimental results, we found that sand-covering promoted the erosion of the original bed, and part of the dredged sand and gravel accumulated in the low-flow channel bed. This phenomenon causes low-flow channel evolution. The difference between the transverse profiles of Cases C-1 and C-2 is influenced by the thickness of the sand-covering in the scope of the experiments. Therefore, the efficiency of sand-covering in the channel evolution also depends on its thickness.

The grain size distributions in the surface and subsurface layers of the right bank and the low-flow channel bed at $x/L = 0.75$ in the final stage of Case C-1 are shown in Figure 8. The thickness of each layer was almost the same as the grain size of gravel A. In the right overbank, the grain size distributions of both layers were almost the same as those of gravel A and mixture. On the other hand, in the low-flow channel bed, the main grain size in the surface layer was gravel A and that in the subsurface layer was sand A, which was the sand-covering material. These results indicate that the aggradation of the low-flow channel was caused by the accumulation of sand A, followed by the accumulation of gravel A, sand A, and sand B. It can be expected that the surface gravel of the overbank may be removed by the next sand-covering work.
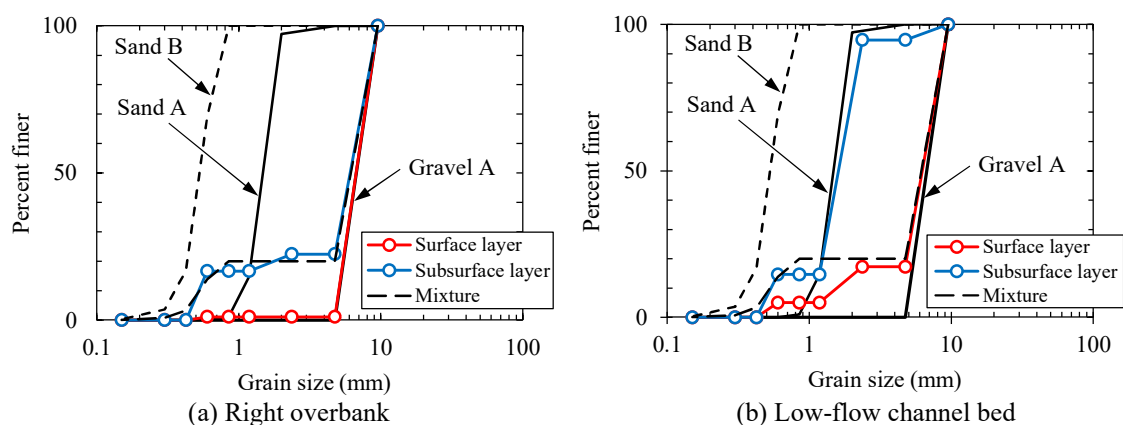
Figure 8. Grain size distributions in surface and subsurface layers of right overbank and low-flow channel bed at longitudinal phase $x/L = 0.75$ in the final stage of Case C-1

Figure 9 shows the temporal variations in the averaged degradation depth of both overbanks and in the averaged aggradation height of the low-flow channel bed in the range of $x/L = 0.2$-0.9. These values were standardized by the size d_g of Gravel A. The averaged degradation depths of the right bank in both cases were greater than those of the left bank in the experiments. The averaged degradation depth of the right overbank of Case C-1 and Case C-2 were approximately 0.7 and 0.3 times the size of Gravel A, respectively. These values show that the averaged degradation depths were less than the gravel size of the bed surface. However, the runoff of sand B from the subsurface layer

(Figure 6) indicated bed degradation until the subsurface layer. Therefore, sand-covering may contribute to bed variation through gravel mobilization. The average aggradation heights of Cases C-1 and C-2 were approximately 1 and 0.7 times the size of Gravel A, respectively. The difference in the aggradation rates between the two cases also depends on the thickness of the sand-covering.

(a) Case C-1 ($D/d_g = 0.79$) (b) Case C-2 ($D/d_g = 0.55$)
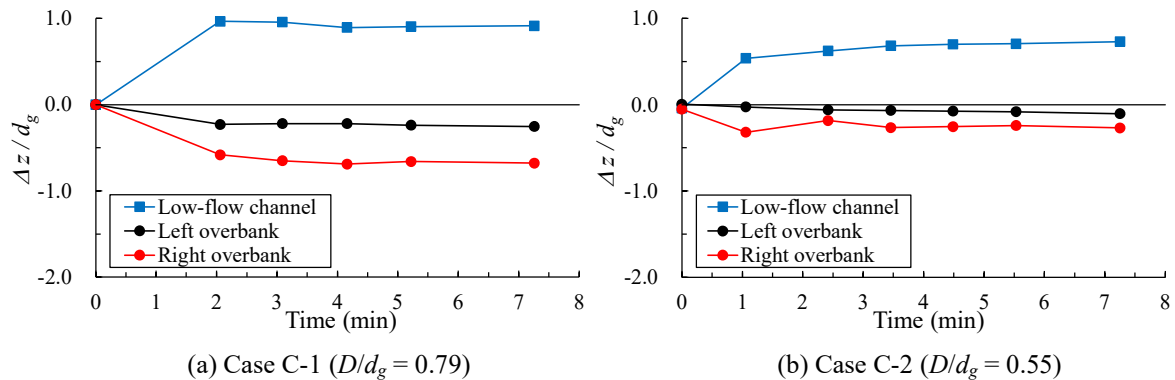
Figure 9. Temporal variations in averaged degradation depth of both overbanks and in averaged aggradation height of low-flow channel bed ($x/L = 0.2$-0.9)

Temporal variations in the low-flow channel of width W and depth D are shown in Figure 10. They were standardized based on their initial values. The definitions of the width and depth are presented in the figure. The width of the low-flow channel gradually increased with the erosion of the overbank area and expanded to approximately 1.6 times of the initial value in Case C-1 and 1.3 times of it in Case C-2. While the depths of the low-flow channel in both cases were reduced by the accumulation of sand and gravel, they were approximately 0.6 to 0.7 times of their initial value at their final stage. As described above, it was shown that sand-covering promoted low-flow channel evolution through gravel mobilization, and induced large-scale channel evolution when the thickness of the sand-covering was large.
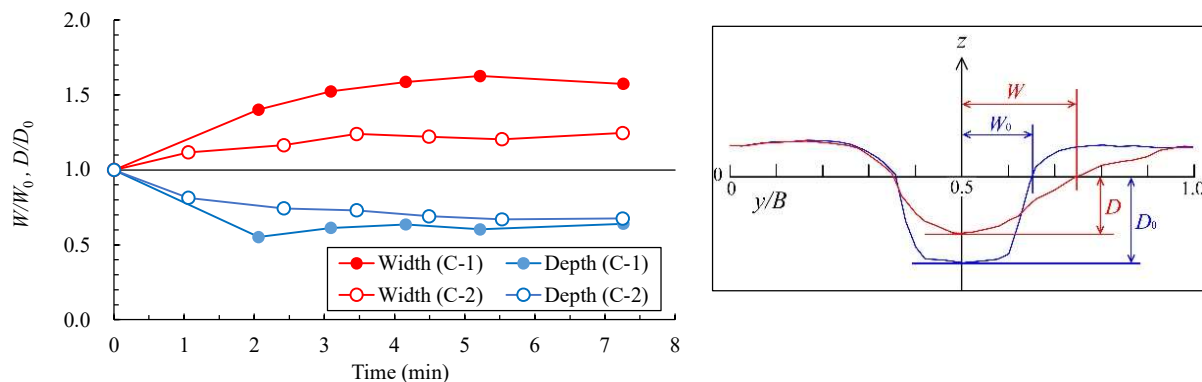
Figure 10. Temporal variations in low-flow channel width and depth along with their definitions

3.3. Consideration of the Application of Sand-Covering to Gravel-Bed Rivers

As mentioned above, sediment supply as a sand-covering to armored gravel beds caused bed erosion and progressed the channel evolution. The thickness of the sand-covering layer significantly affected these activities. The key points for conducting sand-covering of real rivers based on these results are discussed as follows:

(a) Applicable physical environment

Sand supply to gravel beds by sand-covering may cause not only the mobilization of surface gravel but also channel evolution. Therefore, sand-covering may be an effective method for armored gravel beds and channel immobilization. However, sand-covering is not always an effective countermeasure

of riverbed degradation because excessive mobilization of surface gravel can cause further riverbed degradation.

(b) Implementation period

In a river reach, sand-covering works, as discussed here, are conducted by releasing water from a dam or floodwater during the rainy season. In this study, the flow rate was determined by assuming a relatively large flood, such as the annual maximum river flow. Because sediment supply to the streamflow may influence the ecological environment of rivers, it is important to consider the spawning season of aquatic organisms.

(c) Target area

In the experiments, the low-flow channel evolution developed as channel widening and channel-bed aggrading caused by the erosion of the channel bank and deposition of sediment on the channel bed. Therefore, it is reasonable to assume that sand-covering may be conducted in an overbank area near the target channel. Although sand-covering far from the channel does not always directly contribute to the channel evolution, it will cause a disturbance in the surface sediments of gravel beds due to gravel mobilization.

(d) Amount of sand

It is important to determine the amount of sand in sand-covering works. A large sand-covering thickness caused a large amount of mobilized gravel and active channel evolution in this study. Miwa and Yamada (2018) reported similar results for gravel mobilization. However, considering the implementation costs and effects on the ecological environment, a large sand supply is not always desirable. The sand-only layer on the gravel-bed surface may not always directly affect the mobilization of surface gravel. Therefore, it will be effective that a sand-covering works using small amount of sand conduct multiple times. The effects of multiple sand-covering works on gravel mobilization and channel evolution will be investigated in future studies.

4. CONCLUSIONS

The sand supply to streambeds composed of gravel activates the mobilization of gravel. Sand-covering through the supply of sand, while still in the developmental stage, appears to be an effective method for removing gravel that has become an armored bed and may promote bed variations and channel evolutions. Although further investigations are necessary to evaluate the efficiency of sand-covering, the results of this study can be used in river restoration work. Here, we conducted experiments to investigate the effects of sand supply as a means of sand-covering gravel beds with low-flow channels on the mobilization of gravel and the evolution of the channel. The results are summarized as follows:

1 Gravel in streams with armored beds can be easily mobilized by supplying sand as a sand cover. The fraction of sand in the bed subsurface layer can also promote the mobilization of gravel in the subsurface layer. This may have been caused by the low friction angle of gravel engendered by the exposure of sand, which was originally in the subsurface layer, to the flow after removing gravel from the surface layer. The mass of gravel runoff increased with increasing thickness of the sand-covering layer.

2 Sand supply to the armored overbank area can contribute to bed variations and channel evolutions through gravel mobilization. The sand-covering promoted erosion of the original bed, and part of the dredged sand and gravel accumulated in the low-flow channel bed. This phenomenon causes low-flow channel evolution through the widening and shallowing of the channel by the degradation of the sand-covering area and aggradation of the low-flow channel bed. The efficiency of sand-covering the channel evolution also depends on its thickness.

3 As for the key points for conducting sand-covering in actual rivers, the concepts of an applicable physical environment, an implementation period, target areas, and amount of sand were presented based on the experimental results in this study.

REFERENCES

CALFED Science Program and Ecosystem Restoration Program Gravel Augmentation Panel (2005). Key uncertainties in gravel augmentation: geomorphological and biological research needs for effective river restoration.

Committee on Hydroscience and Hydraulic Engineering (2008). *Proceedings of the Symposium on Sediment Augmentation*, JSCE (in Japanese).

Ikeda H. (1984). Flume experiments on the causes of superior mobility of sediment mixtures. *Annual Report of the Institute of Geoscience* 10, University of Tsukuba, 53-56.

Ikeda, H., & Iseya, F. (1986). Thresholds in the mobility of sediment mixtures. Int. Geomorphology, Part 1, Gardiner V (ed). John Wiley and Sons: Chichester, 561-570.

Ikeda H, &Iseya F. (1988). Experimental study of heterogeneous sediment transport. *Environmental Research Center* Paper 12, University of Tsukuba, 1-50.

Miwa, H., & Parker, G. (2012). Numerical simulation of low-flow channel evolution due to sediment augmentation. *International Journal of Sediment Research*, 27(3), 351-361.

Miwa, H., & Parker, G. (2017). Effects of sand content on initial gravel motion in gravel-bed rivers. *Earth Surface Process and Landforms*, 42(9), 1355-1364.

Miwa, H., & Yamada, K. (2018). Gravel mobilization and channel evolution due to sand covering to gravel-beds. *Advances in River Engineering*, JSCE, 24, 89-94 (in Japanese with English abstract).

Stillwater Sciences, UC Berkeley, & SFSU. (2008). Physical modeling experiments to guide river restoration projects: Final report (Restoration Manuals). 1- Contract No. ERP-02D-P55. Prepared for CALFED Ecosystem Restoration Program, Sacramento.

Wilcock PR. (1988). Two-fraction model of initial sediment motion in gravel-bed rivers. *Science* 280-5362, 410-412.

Wilcock PR, & Crowe JC. (2003). Surface-based transport model for mixed-size sediment. *Journal of Hydraulic Engineering*, 129-2, 120-128.

Wilcock PR, & Kenworthy ST. (2002). A two-fraction model for the transport of sand/gravel mixtures. *Water Resources Research*, 38-10, 12-1-12-12.

WATERSHED HYDROLOGY AND MANAGEMENT

14TH INTERNATIONAL CONFERENCE
ON HYDROSCIENCE & ENGINEERING

MAY 26-27, 2022
IZMİR-TURKEY

ICHE2022
IZMIR, TURKEY

PREDICTION OF FLOOD SUSCEPTIBILITY USING FREQUENCY RATIO METHOD: A CASE STUDY OF FIFTH DISTRICT, EGYPT

Mohamed Wahba

Environmental Engineering Department, School of Energy Resources, Environment, Chemical and Petrochemical Engineering, Egypt-Japan University of Science and Technology, E-JUST, 21934

Alexandria, Egypt.

Civil Engineering Department, Faculty of Engineering, Mansoura University

Mansoura, Egypt.

H. Shokry Hassan

Environmental Engineering Department, School of Energy Resources, Environment, Chemical and Petrochemical Engineering, Egypt-Japan University of Science and Technology, E-JUST, 21934

Alexandria, Egypt.

Electronic Materials Researches Department, Advanced Technology and New Materials Research Institute, City of Scientific Researches and Technological Applications (SRTA-City), New Borg El-Arab City,

Alexandria, Egypt.

Wael M. Elsadek

Civil Engineering Department, Faculty of Engineering, South Valley University

Qena, Egypt.

Shinjiro Kanae

Department of Civil and Environmental Engineering, Tokyo Institute of Technology

Tokyo, Japan.

Mahmoud Sharaan

Environmental Engineering Department, School of Energy Resources, Environment, Chemical and Petrochemical Engineering, Egypt-Japan University of Science and Technology, E-JUST, 21934

Alexandria, Egypt.

Civil Engineering Department, Faculty of Engineering, Suez Canal University

Ismailia, Egypt.

ABSTRACT: Flash floods can be considered as one of the most deleterious impacts on the urban dwellings, particularly after the unprecedented changes in climate. Society, economy, and environment are largely affected by the negative consequences of floods. This study aims to predict the most susceptible area to flash floods in the region of Fifth District, New Cairo - Egypt. The studied area is constantly struck by flash floods which paralyzes the livelihood during the period of floods. Meanwhile, after surveying the studied district, 100 spots were considered as flooded points. 70% of them were randomly selected for training, whilst 30% were used for validation. In addition, five factors of the environmental parameters were considered in order to produce the flood hazard map (elevation, slope, land use, flow length, distance to streamlines). Furthermore, the weightage of each environmental parameter was obtained by Frequency Ratio (FR) method. The hazard map was categorized into 5 classes (Very Low, Low, Moderate, High, Very High). Moreover, nearly 10.85% of the entire area was classified as very high. Eventually, the results were validated by using AUC-ROC as the area under the curve was found to be 83.3% which can be acceptable. Furthermore, decision makers can use the obtained flood susceptible map to alleviate the effect of flash floods.

1.INTRODUCTION

Every year, various natural and man-made dangers including disasters such as flash floods, landslides, and earthquakes cause a high number of deaths and property damage throughout the world. (WHO 2003; Youssef et al. 2011; Tehrany et al. 2017; Du et al. 2013). Therefore, it is imperative to allocate the most prone regions to floods to construct protective measures. One of the widely employed methods is the frequency ratio (FR). It is an approach utilized to assess flood likelihood and produce flood vulnerability maps using geographic information system techniques (Youssef et al., 2015; Anucharn and Iamchuen, 2017; Samanta et al., 2018). Furthermore, The FR is a bivariate statistical analytic approach for determining the impact of each spatial factor's classes on flood occurrence (Lee et al. 2012).

In Egypt, a rainfall struck Egypt's northern region, killing at least 73 people, and injuring another 30 in October 2016 (Elnazer, Salman, and Asmoay, 2017; FloodList, 2016; IFRC, 2017). Furthermore, many flash floods ravaged New Cairo City between April 2018 and October 2019, prompting the evacuation of many dwellers, property destruction, considerable economic losses, and the deaths of seven people. (FloodList, 2018; FloodList, 2019; FloodList, 2020). In 2015, at least six and 25 individuals were killed in Alexandria and Beheria, respectively.

Moreover, in terms of generation of flood hazard map, frequency ratio (FR) resembles one of the most efficacious statistical approaches which is adopted broadly (Liao and Carin 2009). Furthermore, this method has been utilized in a plethora of different purposes such as landslide hazard mapping (Lee and Sambath 2006; Vijith and Madhu 2008), groundwater mapping (Oh et al. 2011; Naghibi et al. 2015), estimating the risk of forest fire (Pradhan et al. 2007).

Tehrany et al. (2013) contrasted the predictive accuracy of a decision tree-based technique to mapping flood vulnerability in Kelantan, Malaysia, with a combination of frequency ratio and logistic regression.

For the environmental parameters, many studies propose utilizing SAR imaging to anticipate flood-susceptible areas using remote sensing images. (Giustarini et al., 2011; Anusha & Bharathi, 2020; Elkhrachy, 2018; Li, Martinis, Plank, & Ludwig, 2018; GarcíaPintado et al., 2015; Hong Quang et al., 2020; Schlaffer, Matgen, Hollaus, & Wagner, 2015; Schumann, di Baldassarre, & Bates, 2009; Cao, Zhang, Wang, & Zhang, 2019; Shahabi et al., 2020; Twele, Cao, Plank, & Martinis, 2016).

Therefore, in order to minimize the negative effects of flooding, it is vital to locate flooded areas (Wahba et al. 2022). The target of this study is to generate the flood susceptibility map in the region of Fifth District-Egypt which is essential to find a commensurate resolution to flash floods.

2. STUDY AREA

Flash flood frequently strikes the Fifth District, one of the worst events occurred in April 2018. Figure (1) depicts sides of different flood events in various parts in Fifth District.

The Fifth District, with an area of nearly 160000 m^2, is located in the west of New Cairo City, Egypt. Figure (2) illustrates the New Cairo city including the location of the Fifth District. This region is considered to be one of Egypt's most gorgeous and wealthy areas. Even though it was just established lately, it is one of New Cairo's most populous districts. It's between 29 59' 30″N and 301'0″N and 3124'00″E and 3127'00″E. Moreover, The Fifth District has around 6500 structures; the value of these buildings is rated based on the type of building, as it may be categorized as residential, commercial, industrial, religious, and governmental buildings.

Figure 1. Sides of flash floods in Fifth District (a, b, c, d)
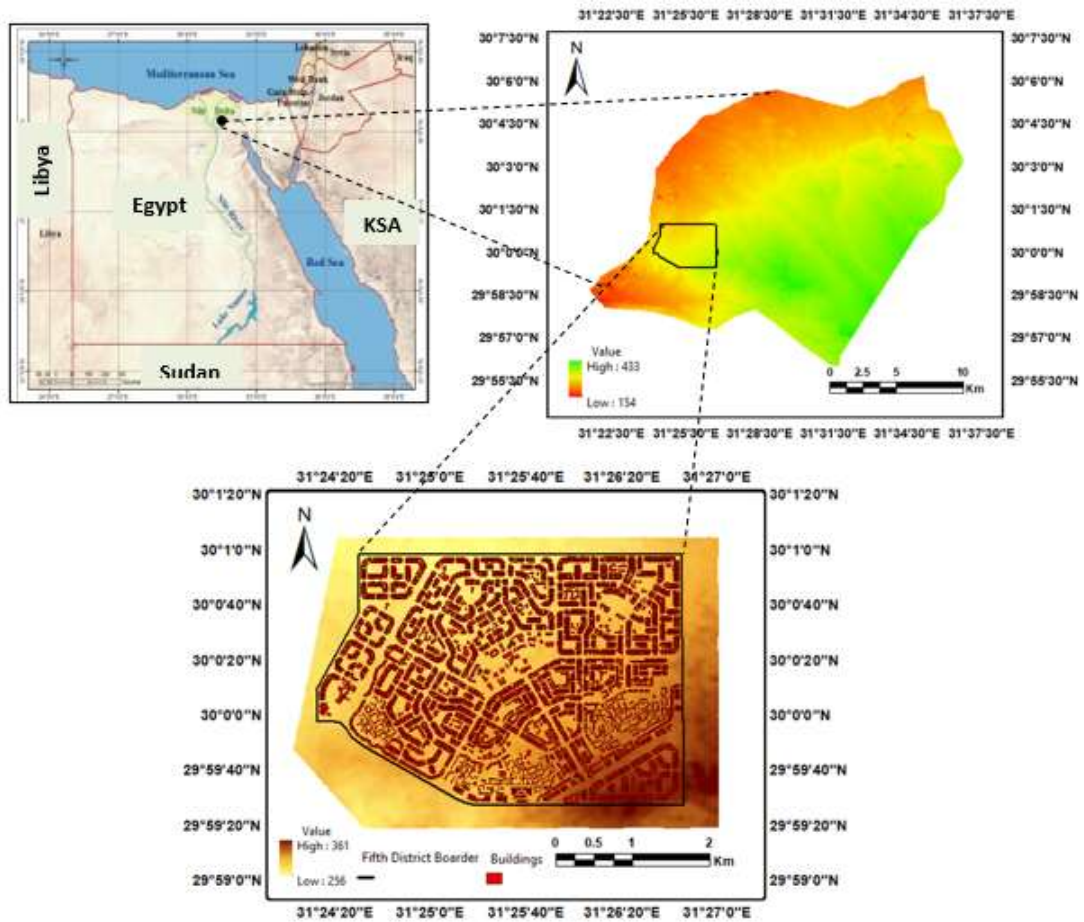
Figure 2. The location of the studied area

3. MATERIAL AND TOOLS

A 12.5m resolution digital elevation model (DEM) was employed and imported into ArcGIS, where a hydrological delineation was carried out to identify basins, flow direction, flow accumulation, flow length, distance to streams, and slope.

4. METHODOLOGY

The flood susceptibility map (FSM) was produced using the method of frequency ratio (FR). The methodological procedure is illustrated in Fig (3).
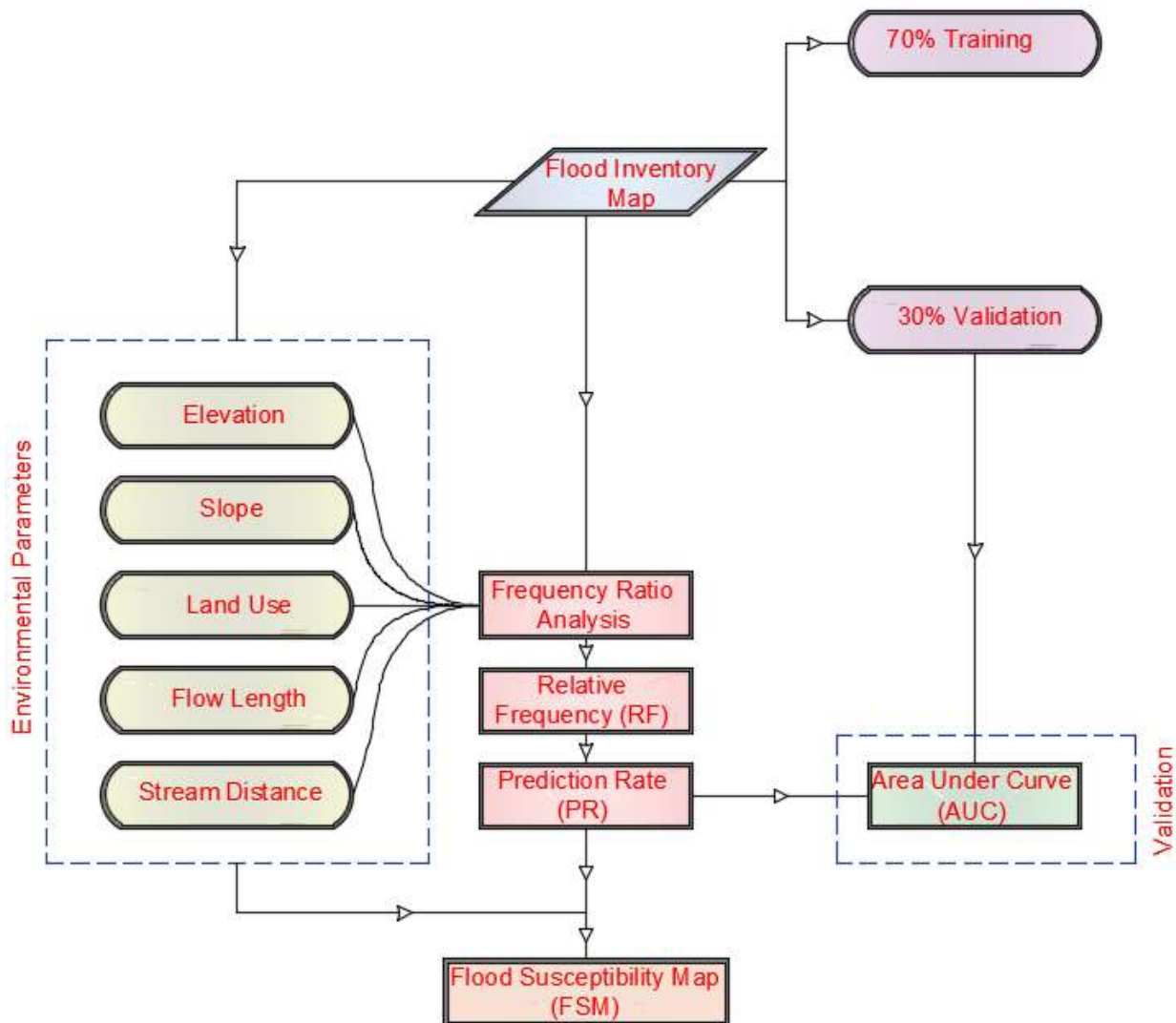
Figure 3. The methodological procedure

4.1. Flood Inventory Map (FIM)

The flood inventory map is imperative step to generate the flood susceptibility map. The optimum way to construct flood inventory maps is still up for dispute (Kia M.B, 2012). In terms of flood susceptibility, it is necessary to have scientifically validated previous flood occurrence data for accurately predicting flood risk (Manandhar 2010). Figure 4 illustrates the FIM with 100 flooded points divided into 70 points for training and 30 points for testing. The flooded points were selected according to the last devastating flood event in April 2018.
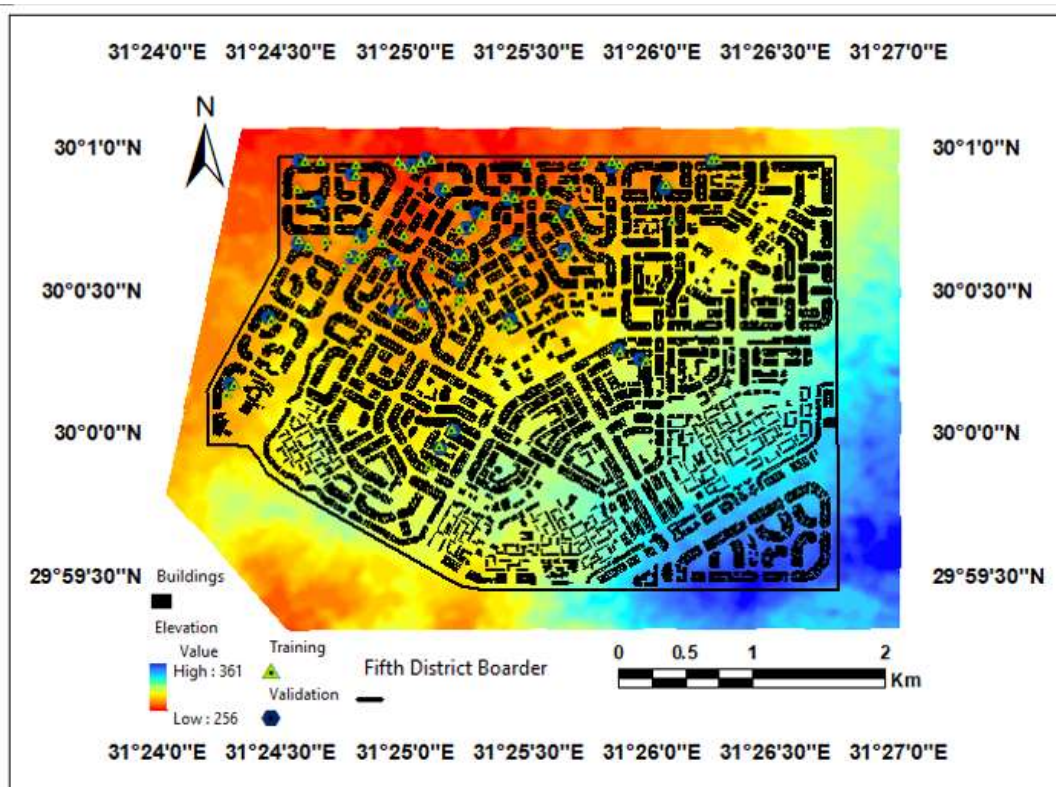
Figure 4. The flood inventory map

4.2. Environmental Parameters

Five environmental factors were utilized to establish the FSM (Elevation, Slope, Land use, Flow length, distance to streams). All the employed factors were classified into 4 categories as shown in Figure 5.
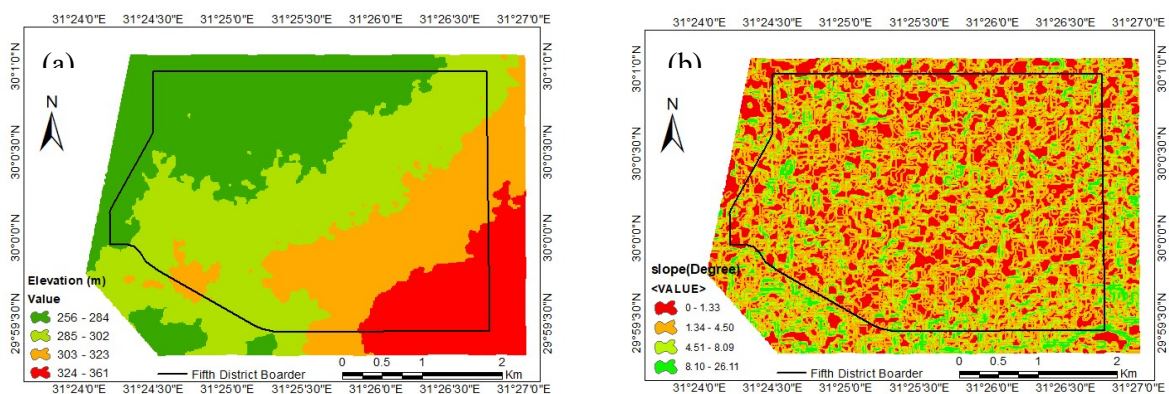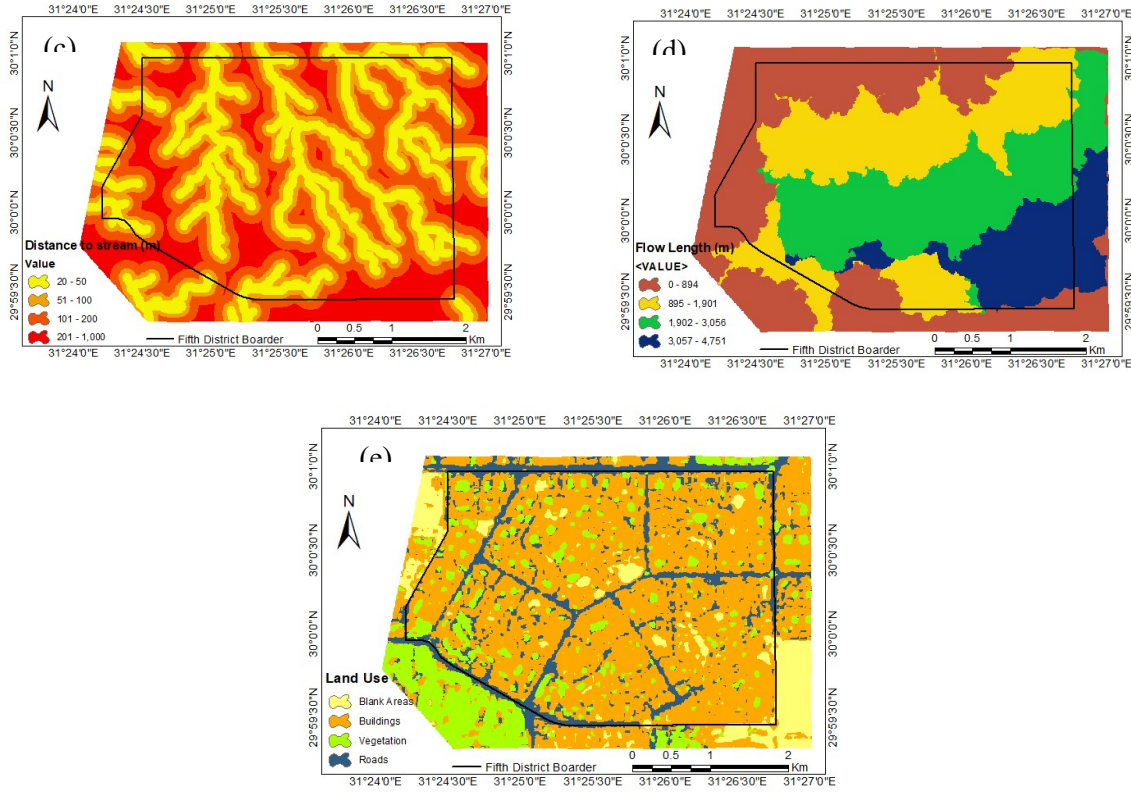
Figure 5. The environmental layers (a) Elevation, (b) Slope, (c) Distance to stream, (d) Flow length, (e) Land use

4.3. Frequency Ratio Method

It is essential to assess the flood susceptibility map in order to determine the flood-related parameters. Past flooding occurance and their causitive characteristics might be used to deduce the link between flood and the environmental factors that can induce flooding. The frequency ratio can be calculted via equation (1).

$$\lambda_{ij} = \frac{N_p\,(CX_i)/\sum_{i=1}^{m} CX_i}{N_p\,(X_j)/\sum_{j=1}^{n} N_p(X_j)} \tag{1}$$

Where, $N_p\,(CX_i)$ is the count of flooded points in class (i) in variable X, $N_p(X_j)$ is the count of pixels in variable X_j. m denotes the overall count of pixel in class of variable X_i, n describes the total number of environmental parameters in the studied area (Jaafari et al. 2014; Regmi et al. 2013). Subsequentially, the relative frequency is determined for each class by equation (2).

$$\eta_{ij} = \frac{\lambda_{ij}}{\sum \lambda_{ij}} \tag{2}$$

Moreover, the prediction ratio (PR) can be evaluated through equation (3) (Omar F. Althuwaynee et al. 2014).

$$PR = \frac{\eta_{max} - \eta_{min}}{(\eta_{max} - \eta_{min})_{min}} \tag{3}$$

The calculations of frequency ratio, relative frequency, prediction ratio for all the utilized environmental parameters is shown in table (1).

Table 1. Calculation of prediction ratio (PR).

Factor	Class	no. of total pixels	no. of flooded points	λ	η	max	min	max - min	PR
DEM (m)	256 - 284	44210	63	0.00143	0.912				
	285 - 302	50926	7	0.00014	0.088				
	303 - 323	30805	0	0.00000	0.000				
	324 - 361	19285	0	0.00000	0.000				
						0.912	0.000	0.912	4.006
	Class								
Slope (Degree)	0 - 1.33	39360	44	0.00112	0.733				
	1.34 - 4.50	66601	25	0.00038	0.246				
	4.51 - 8.09	30654	1	0.00003	0.021				
	8.10 - 26.11	7130	0	0.00000	0.000				
						0.733	0.000	0.733	3.218
	Class								
Land use	Blank Areas	11848	1	0.00844	0.042				
	Buildings	20863	16	0.07669	0.381				
	Vegetation	21217	16	0.07541	0.374				
	Roads	90620	37	0.04083	0.203				
						0.381	0.042	0.339	1.489
	Class								
Flow length (m)	0 - 894	51525	38	0.00074	0.469				
	895 - 1,901	38962	27	0.00069	0.441				
	1,902 - 3,056	35311	5	0.00014	0.090				
	3,057 - 4,751	19428	0	0.00000	0.000				
						0.469	0.000	0.469	2.061

Continue table (1) Calculation of prediction ratio (PR).

Factor	Class	no. of total pixels	no. of flooded points	λ	η	max	min	max - min	PR
Distance to stream(m)	20 - 50	38361	27	0.00070	0.371				
	51 - 100	33796	18	0.00053	0.281				
	101 - 200	46594	18	0.00039	0.204				
	201 - 1,000	25700	7	0.00027	0.144				
						0.371	0.144	0.228	1.000

5.RESULTS

5.1. Flood Susceptibility Map Generation

The prediction ratio was employed as weightage to produce the flood susceptibility map according to equation (4).

$$\text{FSI} = \sum_{j=1}^{n} E_j * PR_j \qquad (4)$$

Where, "FSI" is the flood susceptibility index, and "E" denotes the spatial parameter

Eventually the flood susceptibility map was generated and classified into five categories (very low, low, moderate, high, very high) as illustrated in figure 6.
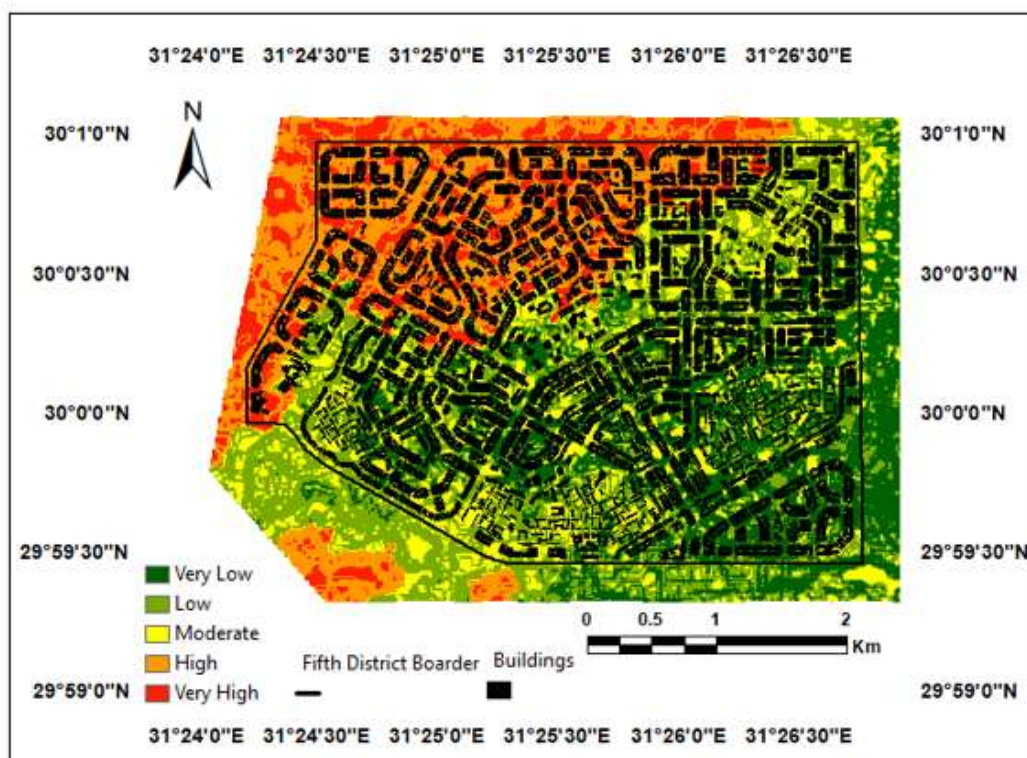
Figure 6. The flood susceptibilty map

The raster size of the flood susceptibility map was resembled in ArcMap to be 1m. Subsequentially, Figure 7 illustrates the ratio of every hazard category.
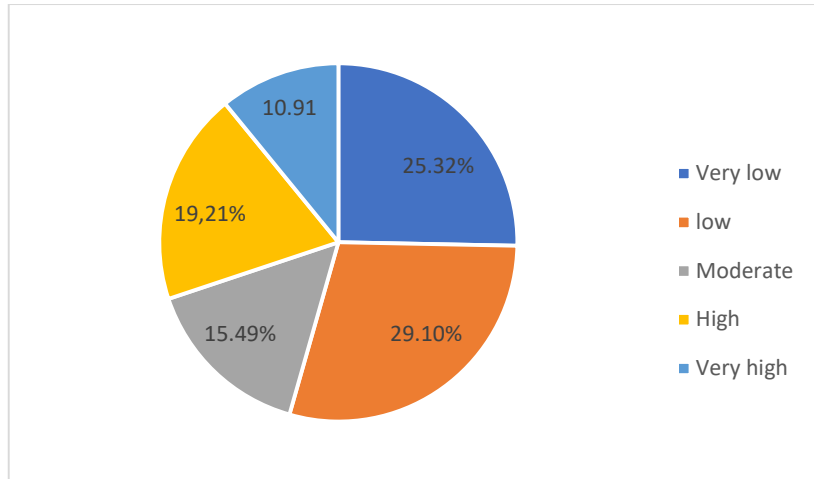
Figure 7. The proportion of each category

The map shows that nearly quarter of the study area has very slight effect of flash flood whereas less than fifth of the area is categorized as moderate in terms of hazard. However, approximately fifth of the studied area is high prone to floods, nearly 10% is considered as very high.

5.2. Validation Of the Integrated FSM

The area under the curve – receiver operator characteristics (AUC-ROC) was used to test the FSM, using the remaining 30% of the flooded points. The area under the curve was estimated as 83.3 % which gives an acceptable trust in the FSM. Fig. (8) sketches the AUC.
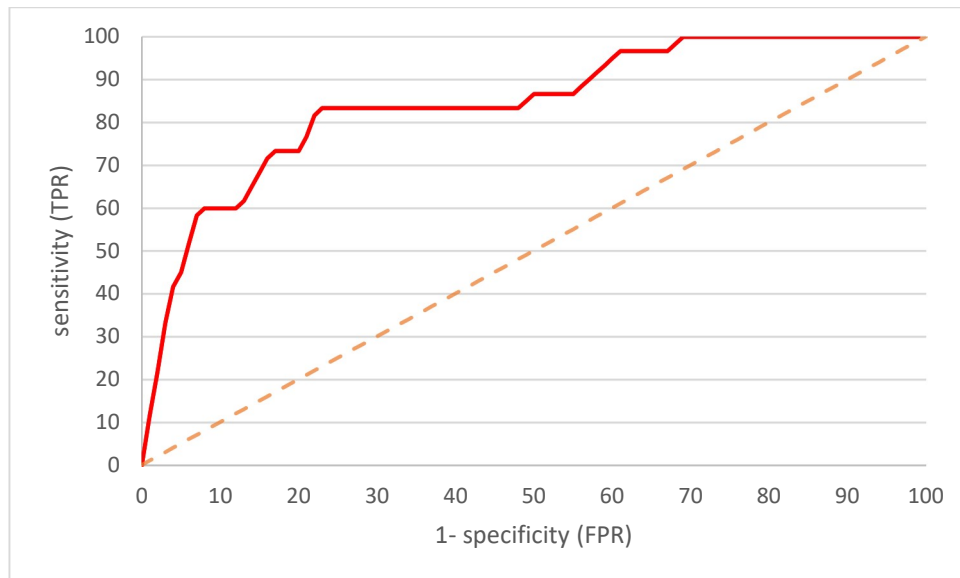
Figure 8. Receiver operating characteristics

The vertical axis represents the sensitivity or the true positive rate (TPR), whilst the horizontal axis describes (1- Specificity) or the false positive rate (FPR).

6.CONCLUSION

In this research, the frequency ratio method was employed to generate the flood susceptibility map. Five spatial parameters were utilized to predict the most prone areas to flash floods. Furthermore, 100 flooded points were arbitrarily classified as 70 % for training and 30 % for testing. Moreover, the FSM was produced using the weightages that were calculated via frequency method. In addition, the generated map was validated using AUC-ROC which gave area under the curve equal to 83.3%. The map showed that half of the study area is classified as "very low" and "low" while about 10%

resembles the most vulnerable area to floods. The FSM is paramount particularly for the decision makers to find mitigation measures for the most susceptible areas to floods.

ACKNOWLEDGMENT

REFERENCE

Al-Thuwaynee, Omar & Pradhan, Biswajeet & Park, Hyuck Jin & Lee, Jung-Hyun. (2014). A novel ensemble bivariate statistical evidential belief function with knowledge-based analytical hierarchy process and multivariate statistical logistic regression for landslide susceptibility mapping. Catena. 114. 21–36. 10.1016/j.catena.2013.10.011.

Anusha, N., & Bharathi, B. (2020). Flood detection and flood mapping using multi-temporal synthetic aperture radar and optical data. The Egyptian Journal of Remote Sensing and Space Science, 23, 207–219.

Cao, H., Zhang, H., Wang, C., & Zhang, B. (2019). Operational flood detection using Sentinel-1 SAR data over large areas. Water, 11, 786

Du J, Fang J, Xu W, Shi P (2013) Analysis of dry/wet conditions using the standardized precipitation index and its potential usefulness for drought/flood monitoring in Hunan Province China. Stoch Environ Res Risk Assess 27(2):377–387

Elkhrachy, I. (2018). Assessment and management flash flood in Najran Wady using GIS and remote sensing. Journal of the Indian Society of Remote Sensing, 46, 297–308.

Elnazer, A. A., Salman, S. A., & Asmoay, A. S. (2017). Flash flood hazard affected Ras Gharib city, Red Sea, Egypt: A proposed flash flood channel. Natural Hazards, 89, 1389–1400.

García-Pintado, J., Mason, D. C., Dance, S. L., Cloke, H. L., Neal, J. C., Freer, J., & Bates, P. D. (2015). Satellite-supported flood forecasting in river networks: A real case study. Journal of Hydrology, 523, 706–724.

Giustarini, L., Matgen, P., Hostache, R., Montanari, M., Plaza Guingla, D. A., Pauwels, V., … Hoffmann, L. (2011). Assimilating SAR-derived water level data into a hydraulic model: A case study. Hydrology and Earth System Sciences, 15, 2349–2365.

Hong Quang, N., Tuan, V. A., Le Hang, T. T., Manh Hung, N., Thi Dieu, D., Duc Anh, N., & Hackney, C. R. (2020). Hydrological/hydraulic modeling-based thresholding of multi SAR remote sensing data for flood monitoring in regions of the Vietnamese Lower Mekong River Basin. Water, 12, 71.

IFRC. 2017. Emergency Plan of Action Final Report, Egypt: Floods [Online]. Retrieved from https://reliefweb.int/sites/reliefweb. int/files/resources/MDREG013dfr.pdf.

Jaafari A, Najafi A, Pourghasemi HR, Rezaeian J, Sattarian A (2014) GIS-based frequency ratio and index of entropy models for landslide susceptibility assessment in the Caspian forest, northern Iran. Int J Environ Sci Technol 11(4):909–926.

Kia, M.B.; Pirasteh, S.; Pradhan, B.; Wan, N.A.S.; Moradi, A. An artificial neural network model for flood simulation using gis: Johor river basin, malaysia. Environ. Earth Sci. 2012, 67, 251–264.

Lee MJ, Kang JE, Jeon S (2012) Application of frequency ratio model and validation for predictive flooded area susceptibility mapping using GIS. In: Geoscience and Remote Sensing Symposium (IGARSS), 2012 IEEE International. IEEE, p 895–898

Li, Y., Martinis, S., Plank, S., & Ludwig, R. (2018). An automatic change detection approach for rapid flood mapping in Sentinel-1 SAR data. International Journal of Applied Earth Observation and Geoinformation, 73, 123–135.

Manandhar B (2010) Flood plain analysis and risk assessment of Lothar Khola, Nepal. Unpublished Ph.D. thesis, Tribhuvan University, Nepal

Regmi AD, Devkota KC, Yoshida K, Pradhan B, Pourghasemi HR, Kumamoto T, Akgun A (2013) Application of frequency ratio, statistical index, and weights-of-evidence models and their comparison in landslide susceptibility mapping in Central Nepal Himalaya. Arab J Geosci 7(2):725–742

Shahabi, H., Shirzadi, A., Ghaderi, K., Omidvar, E., Al-Ansari, N., Clague, J. J., … Bahrami, S. (2020). Flood detection and susceptibility mapping using Sentinel-1 remote sensing data and a machine learning approach: Hybrid intelligence of bagging ensemble based on K-nearest neighbor classifier. Remote Sensing, 12, 266.

Schlaffer, S., Matgen, P., Hollaus, M., & Wagner, W. (2015). Flood detection from multi-temporal SAR data using harmonic analysis and change detection. International Journal of Applied Earth Observation and Geoinformation, 38, 15–24.

Schumann, G., di Baldassarre, G., & Bates, P. D. (2009). The utility of spaceborne radar to render flood inundation maps based on multialgorithm ensembles. IEEE Transactions on Geoscience and Remote Sensing, 47, 2801–2807.

Tehrany MS, Shabani F, Jebur MN, Hong H, Chen W, Xie X (2017) GIS-based spatial prediction of flood prone areas using standalone frequency ratio, logistic regression, weight of evidence and their ensemble techniques. Geomat Nat Hazards Risk. https://doi.org/10.1080/19475705.2017.1362038

Twele, A., Cao, W., Plank, S., & Martinis, S. (2016). Sentinel- 1-based flood mapping: A fully automated processing chain. International Journal of Remote Sensing, 37, 2990–3004.

Wahba, M., Mahmoud, H., Elsadek, W.M., Kanae, S. and Hassan, H.S., 2022. Alleviation approach for flash flood risk reduction in urban dwellings: A case study of Fifth District, Egypt. Urban Climate, 42, p.101130.

WHO (2003) World Health Organization. Disaster data-key trends and statistics in world disasters report. WHO, Geneva, Switzerland. http://www.ifrc.org/PageFiles/89755/2003/43800-WDR2003_En.pdf. Accessed 5 Apr 2017

Youssef AM, Pradhan B, Hassan AM (2011) Flash flood risk estimation along the St. Katherine road, southern Sinai, Egypt using GIS based morphometry and satellite imagery. Environ Earth Sci 62:611–623

Liao X, Carin L (2009) Migratory logistic regression for learning concept drift between two data sets with application to UXO sensing. IEEE Trans Geosci Remote Sens 47:1454–1466

Lee S, Sambath T (2006) Landslide susceptibility mapping in the Damrei Romel area, Cambodia using frequency ratio and logistic regression models. Environ Geol 50(6):847–855

Vijith H, Madhu G (2008) Estimating potential landslide sites of an upland sub-watershed in Western Ghat's of Kerala (India) through frequency ratio and GIS. Environ Geol 55(7):1397–1405

Oh HJ, Kim YS, Choi JK, Park E, Lee S (2011) GIS mapping of regional probabilistic groundwater potential in the area of Pohang City, Korea. J Hydrol 399(3–4):158–172

Naghibi SA, Pourghasemi HR, Pourtaghi ZS, Rezaei A (2015) Groundwater qanat potential mapping using frequency ratio and Shannon's entropy models in the Moghan watershed, Iran. Earth Sci Inf 8(1):171–186

Pradhan B, Dini Hairi Bin Suliman M, Arshad Bin Awang M (2007) Forest fire susceptibility and risk mapping using remote sensing and geographical information systems (GIS). Disaster Prev Manag 16(3):344–352

Tehrany MS, Pradhan B, Jebur MN (2013) Spatial prediction of flood susceptible areas using rule based decision tree (DT) and a novel ensemble bivariate and multivariate statistical models in GIS. J Hydrol 504:69–79

A QUANTITATIVE COMPARISON OF GROUND-BASED, SATELLITE-BASED AND MODEL-BASED PRECIPITATION PRODUCTS OVER TURKEY

Onur Gungor Sahin[1], Behnam Khorrami[2], Orhan Gunduz[3]

1Department of International Water Resources, Izmir Institute of Technology, Izmir-Turkey

onursahin@iyte.edu.tr

2Department of Geographic Information Systems, Dokuz Eylul University, Izmir-Turkey

behnam.khorrami@ogr.deu.edu.tr

3Department of Environmental Engineering, Izmir Institute of Technology, Izmir-Turkey

orhangunduz@iyte.edu.tr

ABSTRACT: Precipitation data play a predominant role in the hydro-meteorological assessments such as climate change and drought analysis. The limited accessibility to continuous spatio-temporal data is a major challenge for better application of field-based observations of precipitation. With the recent advancements in remote sensing satellites as well as hydrological models, precipitation data is now obtainable from a number of missions with varying precision at large scales. Although remotely sensed and simulated variables have their own advantages, the different algorithms applied by each mission engender different precision levels, which necessitate validation against real observations to ensure the reliability of the remote sensing-based analysis. In this study, a total of seven remotely estimated precipitation dataset including two satellite-based (IMERG and TRMM) and five model-based (FLDAS, GLDAS, MERRA-2, ERA and CHELSA) products were compared with ground-based observations obtained from the main meteorological stations over Turkey. The remotely sensed data were validated against in-situ observations at monthly and annual time scales based on different evaluation indicators such as Correlation Coefficient (CC), Relative Bias (RB), Nash-Sutcliffe Efficiency (NSE), and Root Mean Squared Error (RMSE). The results revealed that, with the monthly CC value of 0.78, TRMM outperforms the remaining datasets in estimating the monthly precipitation. The results also indicate that IMERG (0.76), CHELSA (0.74) and ERA5 (0.72) are found to be the more precise when compared to FLDAS (0.39) MERRA-2 (0.38) and GLDAS (0.271). The validation results also showed insignificant correlation between the modelled values received from MERRA-2, FLDAS and GLDAS and the in-situ observations. Although TRMM turned out to be the best estimator of monthly and annual precipitation of Turkey, the climatology (mean monthly) evaluation suggests that CHELSA has the best performance with a CC value of 0.91. The climatology investigation also signifies good CC values for TRMM (0.90), IMERG (0.88) and ERA5 (0.87). Overall, this study introduces CHELSA model as the most promising remote sensing dataset of precipitation for Turkey, which can be applied either in environmental analysis and modeling or for gap-filling of the field-based precipitation data over the country.

Keywords: Precipitation, Remote Sensing, Reanalysis, Quantitative Analysis, Turkey

1. INTRODUCTION

Water resources are of remarkable importance for the human as well as wildlife. They play a determining role in terms of meeting the water requirements for different purposes such as drinking water, sanitation, irrigation, and industrial production. As one of the most important compartments of the hydrological water cycle, precipitation is used as the main input data in many hydrological assessment and modeling studies (Shef and Wood 2018). The water received from precipitation feeds surface and subsurface water resources, thus is vital for the sustainability of water resources. Having access to accurate spatio-temporal variations of precipitation is an essential part of water resource management (Ma et al., 2021). Better management of water resources requires uninterrupted and

precise data on the spatio-temporal characteristics of precipitation, which is further critical for the analysis of the extreme hydro-meteorological events such as floods and droughts. Unfortunately, such data are not always accessible on account of the limitations ascribed to the traditional data gathering techniques. With the advancements achieved in the field of remote sensing and data modeling missions, there is now an easy access to a wide range of environmental parameters worldwide, which eases better evaluation of different hydrological phenomena. Satellite- and model-based precipitation datasets are now widely used in a variety of studies due to the convenience of access, global coverage, economical affordability, and spatio-temporal continuity of the estimates they provide (Amjad et al., 2020).

Areal precipitation values can be achieved by means of different approaches that are categorized into three classes according to data source and data retrieval algorithms (Sun et al., 2018). These classes can be grouped as i) the geostatistical approach, ii) the satellite remote sensing approach and iii) the modeling approach. The geostatistical approach is based on the principle of generating interpolated surfaces through different interpolation techniques. The quality of the resulted surfaces is highly dependent upon quantity and quality of the point-wise observations as well as the accuracy of the selected interpolation technique. The satellite remote sensing approach provides direct and/or indirect measurements of precipitation (Shef and Wood 2018) such as microwave (MW) sensors that can sense rain clouds directly and provide accurate estimates of instantaneous precipitation rates as well as infrared (IR) sensors that have a high temporal resolution (30 min or one hour). In the modelling approach, on the other hand, the model data include vertical atmospheric information on different hydrometeorological variables such as temperature, humidity, water content and precipitation, where variables are produced by processing the data obtained from different sources (in situ or remote sensing) and processed using analysis/forecast systems and data assimilation techniques (Jiang et al., 2021).

Because of the spatio-temporal gaps seen in the field-based precipitation records, the point-wise precipitation data may not accurately represent the spatial distribution of precipitation over a given study area. The remotely sensed precipitation products can be used as an alternative approach f to minimize the limitations associated with the station-based ground observations (Macharia, J, Ngetich, F, and Shisanya, C, 2020). According to the literature, satellite- and model-based precipitation estimates have so far been extensively validated against ground-based observations all over the world (Derin and Yilmaz, 2014; Yang and Luo, 2014; Blacutt et al., 2015; Wehbe et al., 2017; Gao et al., 2018; Lu et al., 2018; Lu et al., 2019; Wang et al., 2019; Amjad et al., 2020; Macharia et al., 2020; Ma et al., 2021; Jiang et al., 2021).

The data offered by satellite and modeling remote sensing missions are accompanied by different levels of uncertainties, which can be linked to a number of influential parameters such as the differences of the utilized algorithms, uncertainties of the data processing practices, impacts of the weather and the geographic characteristics of the study area (Sun et al., 2018). Therefore, the accuracy assessment of these remotely sensed data is mandatory for a specific region of interest. Although accuracy validation of the remotely sensed precipitation data has been implemented in a variety of studies worldwide (Jiang et al., 2021), there is not enough study for Turkey, where geographic and climatic diversity bring about heterogeneous patterns of hydro-meteorological characteristics. To our knowledge, only a few studies of this kind have so far been implemented for Turkey (Bıyık et al., 2009; Derin and Yilmaz 2014; Amjad et al., 2020).

Bıyık et al. (2009) reported that 3 hourly TRMM precipitation data have errors and are not consistent for the area of interest. Derin and Yilmaz (2014) reported that there are major challenges in the satellite-based precipitation datasets in complex topography regions. These studies investigated remotely sensed data precipitation quality in the complex mountain regions and do not cover all of Turkey geographically. Amjad et al. (2020), on the other hand, compared two satellite-based (The Integrated Multi-Satellite Retrievals for GPM (IMERG) and The Tropical Rainfall Measurement Mission (TRMM)) and two model-based (ERA-Interim and ERA-Land) precipitation datasets with ground observation stations using different statistical methods for the years 2014-2018. They declared that the performances of satellite-based and model-based algorithms vary for regions but generally The IMERG data set produced the best correlation coefficient.

Overall, it can be said that there are not enough studies in the literature that include a broad range of remotely sensed precipitation datasets for the entire geography of Turkey. Based on this premise, this study aims to compare the quality of precipitation datasets obtained from seven different remotely sensed missions with ground stations.

2. METHODOLOGY

2.1. Description of the Study Area

Turkey is located at the intersection of Asia and Europe between 36-42 north latitudes and 26-45 east longitudes (Figure 1). With a total surface area of 78 million hectares, Turkey extends 1650 km from east to west, and 650 km from north to south. The geographic position of the country renders Turkey's regions to heterogeneity in terms of climatic situation (Khorrami and Gunduz 2021a). While the average annual precipitation of the country is 574 mm, it ranges from about 250 mm to 3000 mm from the central Anatolia, in the center, to the Black Sea region in the north of the country (Harmancioglu and Altinbilek 2020).
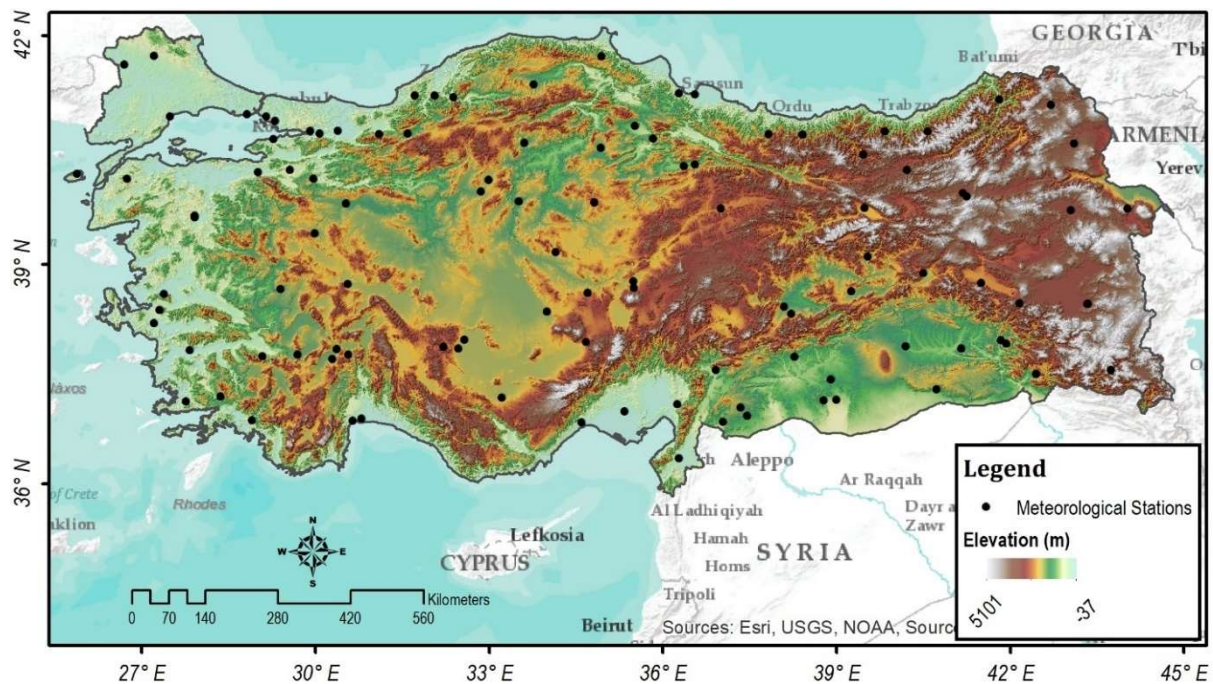
Figure 1. Illustration of the spatial distribution of the major meteorological stations over Turkey (after Khorrami and Gunduz 2021a)

2.2. DATA USED

Within the scope of the current study, remotely sensed and simulated precipitation values of Turkey were extracted from different space and modeling missions to come up with the best precipitation alternative for the country. To this end, seven datasets including two satellite-based (IMERG and TRMM) and five model-based (ERA-5, CHELSA, FLDAS, GLDAS and MERRA-2) products were used.

2.2.1. In-Situ (Ground-Based) Observations

The monthly records of precipitation over Turkey were received from the Turkish State Meteorological Service (TSMS), the official supervisor of the meteorological network of the country, for the study period from 2003 to 2016. Due to the restrictions in having access to all the available stations, the authors opted for only 107 major stations whose geographic location is given in Figure 1.

2.2.2. Satellite Estimates

- *The Tropical Rainfall Measurement Mission (TRMM)*

The Tropical Rainfall Measuring Mission (TRMM) Multi-Satellite Precipitation Analysis (TMPA) aims to provide the best possible spatial ($0.25° \times 0.25°$) and temporal (3-hr) estimate of global precipitation with modern satellite sensors between 1998-2019. The infrared (IR) precipitation estimates are generated using calibrated microwaves (MWs). MW is combined with IR and integrated with rain gauge data to produce the TRMM global precipitation dataset (Huffman et al., 2010).

- *The Integrated Multi-Satellite Retrievals for GPM (IMERG)*

Integrated Multi-satellite Retrievals for the Global Precipitation Measurement (GPM) Mission (IMERG) applies an algorithm that provides the multi-satellite precipitation estimates from various passive microwave sensors (Huffman et al., 2020). IMERG mission offers precipitation products in different temporal latencies such as the "Early", "Late", and the "Final" multi-satellite products, whose temporal latency values are 4 hours, 14 hours, and 3.5 months, respectively. In this study, the monthly estimates from the "Final" satellite-gauge product were used.

2.2.3. Model Estimates

- *Global Land Data Assimilation System (GLDAS)*

U.S. Naval Research Laboratory (NRL) and Goddard Space Flight Center (GSFC) produced near-real-time precipitation data for Global Land Data Assimilation System (GLDAS). NRL uses IR and microwave measurements to get precipitation fields with $0.25°$ spatial and 6 hours temporal resolution between 60°S to 60°N (Houser et al., 2004). This study uses monthly data that is produced by simulating 3 hours of data modeled by the Noah Model 3.6 in Land Information System (LIS) Version 7. The dataset includes precipitation values for 36 land surfaces from 2000 to the present (Beaudoing and Rodell 2020).

- *The Famine Early Warning Systems Network Land Data Assimilation System (FLDAS)*

Famine Early Warning Systems Network (FEWS NET) Land Data Assimilation System (FLDAS) integrates multi-model and multi-forcing estimations of hydroclimatic conditions such as soil moisture, evapotranspiration with the use of meteorological inputs such as temperature, rainfall and humidity (Khorrami and Gunduz 2021b). The FLDAS data covers several land surface parameters simulated from the Noah 3.6.1 in $0.1°$ spatial resolution and range from 1982 to present. The temporal resolution is monthly, and the spatial coverage is global 60S, 180W, 90N, 180E (McNally and NASA/GSFC/HSL 2018).

- *The Modern-Era Retrospective Analysis for Research and Applications (MERRA)*

Surface flux diagnostics data such as total precipitation, bias corrected total precipitation, surface air temperature etc. are available in the MERRA-2 model. The heights of the model surface layer (HLML) may change with time and location, range of ~60 meter above ground. Merra-2 bias corrected total precipitation values were taken from M2TMNXFLX v5.12.4, which is a time-averaged 2-dimensional monthly mean data collection in Modern-Era Retrospective analysis for Research and Applications version 2 (MERRA-2). The data covers $0.5° \times 0.625°$ resolution range from 1979 to present (GMAO 2015).

- *ERA5-Land*

ERA5-Land stands for the ECMWF Reanalysis 5th Generation dataset that is a global reanalysis model dataset offering spatio-temporal time series of the land variables over several decades with an improved spatial resolution compared to ERA5. It combines model data with observations to generate a complete and consistent dataset at a global scale based on the laws of physics.(Hersbach et al., 2020).

- *Climatologies At High Resolution for The Earth's Land Surface Areas (CHELSA)*

Climatologies at High Resolution for the Earth's Land Surface Areas (CHELSEA) is based on a mechanistic statistical downscaling of global reanalysis data or global circulation model output. It provides a 30 arc-second high-resolution dataset of global precipitation and temperature values (Khorrami and Gunduz 2021b). CHELSA uses reanalysis of ERA-Interim product with a bias correction (Karger et al., 2017).

The characteristics of the utilized data from different sources mentioned above are presented in Table 1. It is clearly seen from the table that the datasets used all have different resolutions spatially and temporarily (Table 1).

Table 26. Characteristics of the used dataset.

Precipitation Product	Data Type	Spatial Resolution	Temporal Range
IMERG (3IMERGM v06)	Satellite-based	$0.1° \times 0.1°$	2000-present
TRMM (TRMM_3B43 v7)	Satellite-based	$0.25° \times 0.25°$	1998-2019
FLDAS (NOAH01_C_GL_MA v001)	Model-based	$0.1° \times 0.1°$	1982-present
GLDAS (NOAH025_M v2.1)	Model-based	$0.25° \times 0.25°$	2000-present
MERRA-2 (M2TMNXFLX v5.12.4)	Model-based	$0.5° \times 0.625°$	1980-present
ERA5	Model-based	$0.25° \times 0.25°$	1979-present
CHELSA	Model-based	$0.008° \times 0.008°$	1979-2018

2.3. Validation

To investigate the precision of the remotely sensed and simulated precipitation over Turkey, point-wise evaluation approach was followed. The selection of the point precipitation values was carried out based on the nearest Euclidean distance (Jiang et al., 2021) from the field gages. From the used datasets, the closest point-values to the representative stations were picked out and paired with the corresponding station values. The primary statistics of the distance differences between selected datasets and ground stations can be seen in Table 2. Four commonly used statistical metrics including Correlation Coefficient (CC), Relative Bias (RB), Nash-Sutcliffe Efficiency (NSE) coefficient and Root Mean Squared Error (RMSE) were used to validate the used datasets. The statistical significance increases as CC increases. NSE value ranges from $-\infty$ to 1 with the optimal value of 1. RB and RMSE are reported in percentage (%) and mm/month, respectively, with the optimal values of 0 for both.

Table 2. Statistics of differences between the remote sensing data and ground stations in degrees.

Distance (°)	CHELSA	ERA5	FLDAS	GLDAS	IMERG	MERRA-2	TRMM
Minimum	0.006	0.002	0.006	0.018	0.006	0.042	0.018
Maximum	0.142	0.164	0.067	0.175	0.067	0.390	0.175
Mean	0.042	0.093	0.038	0.100	0.038	0.219	0.100
Standard Deviation	0.020	0.035	0.015	0.035	0.015	0.090	0.035

$$CC = \frac{\sum_{i=1}^{n}(r_i - \bar{r})(o_i - \bar{o})}{\sqrt{\sum_{i=1}^{n}(r_i - \bar{r})^2}\sqrt{\sum_{i=1}^{n}(o_i - \bar{o})^2}} \tag{1}$$

$$RB = \frac{\sum_{i=1}^{n}(r_i - o_i)}{\sum_{i=1}^{n}o_i} x100 \tag{2}$$

$$RMSE = \sqrt{\frac{1}{n}\sum_{i=1}^{n}(r_i - o_i)^2} \tag{3}$$

$$NSE = 1 - \frac{\sum_{i=1}^{n}(o_i - r_i)^2}{\sum_{i=1}^{n}(o_i - \bar{o})^2} \tag{4}$$

where n is the number of data-points for each station; r and o signify the remotely sensed and observed precipitation, respectively.

3. RESULTS AND DISCUSSION

Comparisons were made based on three different time scales including monthly, climatology (monthly averages) and annual time scales. The point-wise evaluation results are given in Tables 3 to 5 for monthly, climatology and annual time scales, respectively. According to the results, satellite-based estimates are better correlated with the in-situ data, which is in accordance with the findings of Amjad et al (2020). The results reveal that the model datasets of CHELSA, ERA5, FLDAS, MERRA-2 and GLDAS show monthly correlation values of 0.73, 0.71, 0.39, 0.38, 0.27, respectively. Satellite-based datasets of TRMM and IMERG, on the other hand, have mean CC values of 0.77 and 0.76, respectively. TRMM and IMERG produced almost the same correlation values. According to the results received by RB metric, CHELSA turned out to be the best with the lowest RB value of %2.65 Other datasets showed higher RBs as follow: GLDAS (%4.2), MERRA-2 (%8.9), FLDAS (%13.3), ERA5 (% 26.20), TRMM (%26.69) and IMERG (%27.43). On the other hand, RMSE values of CHELSA (26.53), IMERG (27.87) and TRMM (26.64) datasets are very close to each other. The RMSE value for ERA5 (33.03) is slightly worse than this trio. MERRA-2, FLDAS and GLDAS have more than 50 mm/month RMSE values. From the perspective of NSE, CHELSA, TRMM and IMERG yielded the best NSE values of 0.55, 0.41, and 0.37, respectively. The monthly evaluation metrics of all products are shown in the scatter plots given in Figure 2. MERRA-2, GLDAS and FLDAS precipitation datasets were not used for the comparison of climatology time scale as the evaluation metrics were statistically insignificant. In the climatology time scale, the analysis was only calculated for TRMM, IMERG, ERA5 and CHELSA.

Table 3: Evaluation metrics and performance of datasets for monthly comparison.

Dataset	Statistics	CC	RB	NSE	RMSE
TRMM	Minimum	0.14	-31.27	-3.84	11.26
	Maximum	0.96	129.65	0.93	63.26
	Mean	0.78	26.69	0.41	26.64
	Standard Deviation	0.17	29.60	0.73	11.62

IMERG	Minimum	0.13	-33.66	-4.84	10.62
	Maximum	0.96	146.79	0.92	89.12
	Mean	0.76	27.44	0.37	27.88
	Standard Deviation	0.18	29.65	0.77	12.84
GLDAS	Minimum	-0.17	-72.90	-18.30	15.90
	Maximum	0.76	238.70	0.50	169.10
	Mean	0.39	13.30	-1.30	56.00
	Standard Deviation	0.18	57.00	2.70	25.60
FLDAS	Minimum	-0.36	-61.70	-18.40	23.50
	Maximum	0.74	336.00	0.60	153.30
	Mean	0.28	8.90	-0.90	53.60
	Standard Deviation	0.25	55.80	2.20	22.80
MERRA-2	Minimum	-0.10	-72.10	-5.60	14.10
	Maximum	0.83	205.8	0.6	156.2
	Mean	0.38	4.2	-0.6	50.3
	Standard Deviation	0.20	45.9	1.1	20.5
CHELSA	Minimum	0.111	-34.375	-2.941	10.527
	Maximum	0.955	109.594	0.929	95.941
	Mean	0.736	2.657	0.553	26.535
	Standard Deviation	0.157	24.061	0.461	12.946
ERA5	Minimum	0.137	-27.859	-13.564	13.740
	Maximum	0.904	224.824	0.839	155.928
	Mean	0.715	26.206	0.116	33.034
	Standard Deviation	0.160	37.860	1.594	19.295
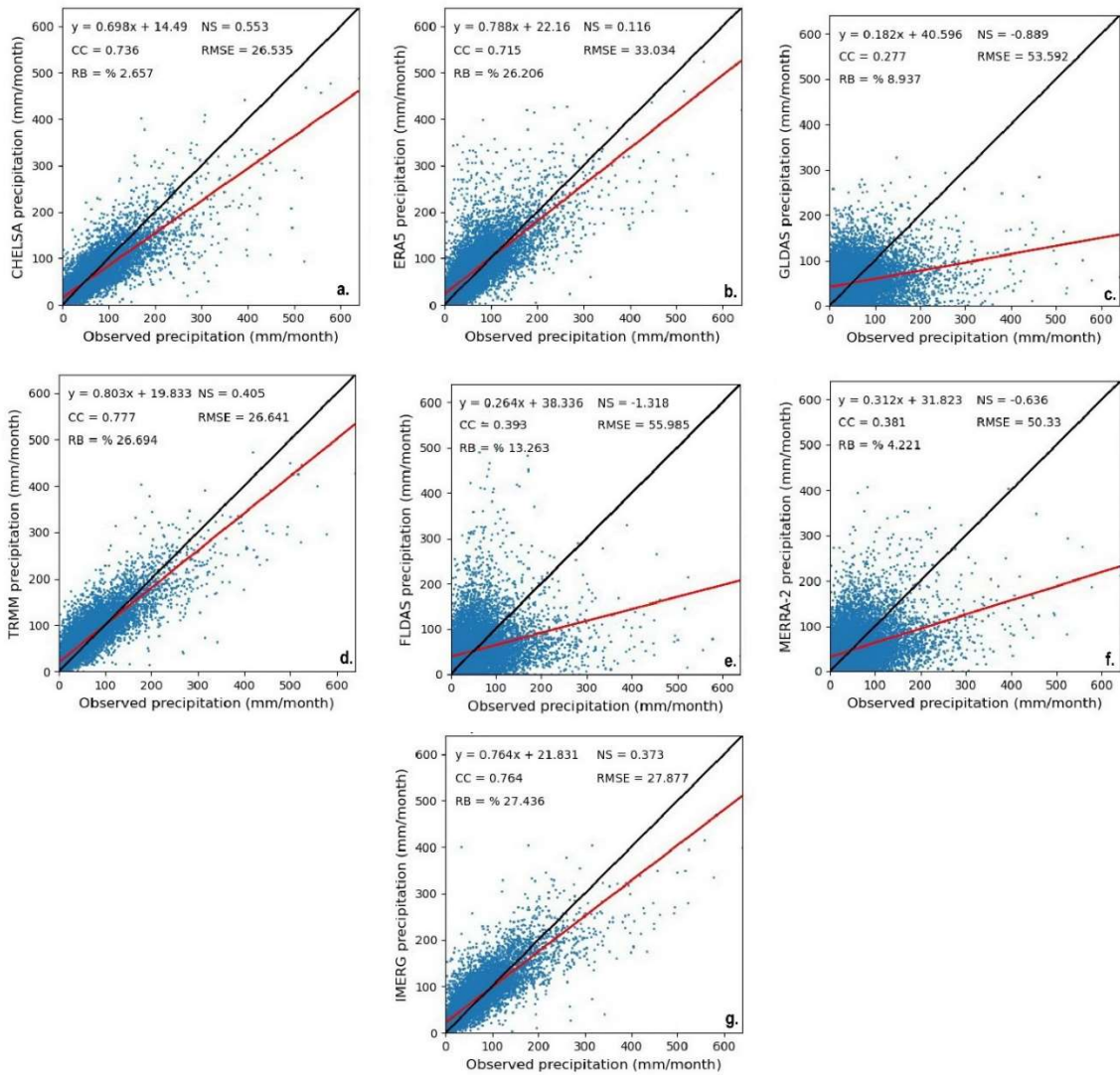
Figure 2. Scatter plots of the satellite-based and model-based precipitation datasets: CHELSA (a), ERA5 (b), GLDAS (c), TRMM (d), FLDAS (e), MERRA-2 (f), and IMERG (g)

The climatology results indicate that CHELSA gives the best correlation of 0.91. The climatology correlations for other datasets are as follows: TRMM (0.90), IMERG (0.87) and ERA5 (0.87). CHELSA gives the best NSE value of 0.58 at this time scale. The NSE for TRMM, ERA5 and IMERG are -0.08, -0.73 and -0.10, respectively. The negative NSE values signify the departure of the estimates from the optimal value. RB values, on the other hand, are calculated as follows: CHELSA (%0.75), ERA5 (%24.16), TRMM (%25.25) and IMERG (%25.61). Finally, the RMSE values at climatology time scale are CHELSA (9.72), TRMM (18.16), IMERG (18.93) and ERA5 (21.02).

At the annual scale, however, satellite-based TRMM and IMERG are better correlated with ground-based observations. All datasets produced meaningless NSE values (< 0) in the annual time scale. IMERG, TRMM and ERA produced approximately the same values of RB (29%). The annual RMSE values are as follows: CHELSA (136), TRMM (191), IMERG (198) and ERA5 (216) mm/year.

Table 4: Evaluation metrics and performance of datasets for climatology comparison.

Dataset	Statistics	CC	RB	NSE	RMSE
TRMM	Minimum	0.15	-31.27	-7.58	4.32
	Maximum	1.00	128.72	0.98	52.68
	Mean	0.90	25.26	-0.09	18.17
	Standard Deviation	0.15	30.26	1.58	10.51
IMERG	Minimum	-0.24	-33.66	-8.90	4.07
	Maximum	1.00	142.62	0.98	76.07
	Mean	0.88	25.61	-0.10	18.93
	Standard Deviation	0.21	29.99	1.57	11.17
CHELSA	Minimum	0.05	-35.53	-2.75	3.17
	Maximum	0.99	114.34	0.98	74.34
	Mean	0.91	0.74	0.58	13.79
	Standard Deviation	0.13	23.18	0.57	9.72
ERA5	Minimum	-0.61	-29.51	-66.15	5.45
	Maximum	0.99	224.82	0.97	147.38
	Mean	0.87	24.17	-0.74	21.03
	Standard Deviation	0.20	37.68	6.72	17.59

Table 5: Evaluation metrics and performance of datasets for yearly comparison.

Dataset	Statistics	CC	RB	NSE	RMSE
TRMM	Minimum	-0.064	-31.269	-309.191	52.613
	Maximum	0.977	129.645	0.896	624.674
	Mean	0.742	29.182	-8.416	191.262
	Standard Deviation	0.220	31.199	34.367	118.855

IMERG	Minimum	-0.092	-33.659	-217.614	38.755
	Maximum	0.969	146.790	0.919	813.749
	Mean	0.737	29.899	-8.374	197.737
	Standard Deviation	0.227	31.083	30.073	116.272
CHELSA	Minimum	-0.205	-34.375	-46.244	33.544
	Maximum	0.964	109.594	0.896	838.346
	Mean	0.684	4.668	-1.261	135.721
	Standard Deviation	0.232	25.419	5.477	104.816
ERA5	Minimum	-0.174	-27.737	-569.290	40.028
	Maximum	0.945	224.824	0.809	1680.648
	Mean	0.671	28.528	-15.905	216.375
	Standard Deviation	0.233	38.549	68.339	199.449

4. CONCLUSION AND RECOMMENDATIONS

In this study, seven remote sensing precipitation datasets were assessed using ground-based observations. Comparisons were made at monthly, climatology (monthly means) and annual time scales. Based on the results of this study, the following listed conclusions were achieved:

- The used datasets manifested different performances according to the used metrics. The satellite based TRMM and IMERG datasets give the highest monthly and annual correlation values, which are almost the same at all the used time scales. Therefore, this study reports no significant difference between TRMM and IMERG.
- Among the model datasets, CHELSA and ERA5 are distinguished from the FLDAS, MERRA-2 and GLDAS by statistically significant values. As a result, it was determined that in monthly precipitations FLDAS, GLDAS, and MERRA-2 precipitation products were not suitable over Turkey.
- Compared to ERA5, CHELSA produces better precipitation estimates at all-time scales and all metrics. It seems more meaningful to use CHELSA precipitation datasets instead of ERA5 for as model dataset. Considering all the evaluation metrics, it is found that CHELSA has significantly better performance than other satellite- and model-based precipitation datasets.
- Although remote sensing and simulation methods have certain uncertainties, they produce results that are quite compatible with in-situ stations over Turkey.

ACKNOWLEDGMENTS

REFERENCES

(GMAO), Global Modeling and Assimilation Office. 2015. Goddard Earth Sciences Data and Information Services Center (GES DISC) *MERRA-2 TavgM_2d_flx_Nx: 2d,Monthly Mean,Time-Averaged,Single-Level,Assimilation,Surface Flux Diagnostics V5.12.4*. Greenbelt, MD, USA. 10.5067/0JRLVL8YV2Y4.

Amjad, Muhammad, M Tugrul Yilmaz, Ismail Yucel, and Koray K Yilmaz. 2020. "Performance Evaluation of Satellite- and Model-Based Precipitation Products over Varying Climate and Complex Topography." *Journal of Hydrology* 584(February): 124707. https://doi.org/10.1016/j.jhydrol.2020.124707.

Beaudoing, H., and M. Rodell. 2020. *GLDAS Noah Land Surface Model L4 Monthly 0.25 x 0.25 Degree V2.1*. Greenbelt, Maryland, USA. https://disc.gsfc.nasa.gov/datasets/GLDAS_NOAH025_M_2.1/summary.

Bıyık, G. et al. 2009. "Assessment of Precipitation Forecast Accuracy over Eastern Black Sea Region Using WRF-ARW." *pcms* 11: Plinius11. https://ui.adsabs.harvard.edu/abs/2009pcms.confE.178B/abstract (November 7, 2021).

Blacutt, Luis A. et al. 2015. "Precipitation Comparison for the CFSR, MERRA, TRMM3B42 and Combined Scheme Datasets in Bolivia." *Atmospheric Research* 163: 117–31. http://dx.doi.org/10.1016/j.atmosres.2015.02.002.

Derin, Yagmur, and Koray K. Yilmaz. 2014. "Evaluation of Multiple Satellite-Based Precipitation Products over Complex Topography." *Journal of Hydrometeorology* 15(4): 1498–1516. https://link.springer.com/article/10.1007%2Fs00704-013-1072-0.

Gao, Feng et al. 2018. "Comparison of Two Long-Term and High-Resolution Satellite Precipitation Datasets in Xinjiang, China." *Atmospheric Research* 212(October 2017): 150–57. https://doi.org/10.1016/j.atmosres.2018.05.016.

Harmancioglu, N, and D Altinbilek. 2020. 2 Springer *Water Resources of Turkey*.

Hersbach, Hans et al. 2020. "The ERA5 Global Reanalysis." *Quarterly Journal of the Royal Meteorological Society* 146(730): 1999–2049.

Houser, P R et al. 2004. "THE GLOBAL LAND DATA ASSIMILATION SYSTEM." *Bulletin of the American Meteorological Society* (March).

Huffman, George J., Robert F. Adler, David T. Bolvin, and Eric J. Nelkin. 2010. "The TRMM Multi-Satellite Precipitation Analysis (TMPA)." *Satellite Rainfall Applications for Surface Hydrology*: 3–22. https://link.springer.com/chapter/10.1007/978-90-481-2915-7_1 (October 29, 2021).

Huffman, George J, David T Bolvin, Eric J Nelkin, and Jackson Tan. 2020. *Integrated Multi-SatellitE Retrievals for GPM (IMERG) Technical Documentation*.

Jiang, Qin et al. 2021. "Evaluation of the ERA5 Reanalysis Precipitation Dataset over Chinese Mainland." *Journal of Hydrology* 595(June 2020): 125660. https://doi.org/10.1016/j.jhydrol.2020.125660.

Karger, Dirk Nikolaus et al. 2017. "Climatologies at High Resolution for the Earth's Land Surface Areas." *Scientific Data* 4: 1–20.

Khorrami, Behnam, and Orhan Gunduz. 2021a. "An Enhanced Water Storage Deficit Index (EWSDI) for Drought Detection Using GRACE Gravity Estimates." *Journal of Hydrology* 603(PA): 126812. https://doi.org/10.1016/j.jhydrol.2021.126812.

———. 2021b. "Evaluation of the Temporal Variations of Groundwater Storage and Its Interactions with Climatic Variables Using GRACE Data and Hydrological Models: A Study from Turkey." *Hydrological Processes* 35(3): 1–13.

Lu, Jing et al. 2018. "Performance of the Standardized Precipitation Index Based on the TMPA and CMORPH Precipitation Products for Drought Monitoring in China." *IEEE Journal of Selected Topics in Applied Earth Observations and Remote Sensing* 11(5): 1387–96.

Lu, Xinyu et al. 2019. "Correcting GPM IMERG Precipitation Data over the Tianshan Mountains in China." *Journal of Hydrology* 575(April): 1239–52. https://doi.org/10.1016/j.jhydrol.2019.06.019.

Ma, Qian et al. 2021. "Performance Evaluation and Correction of Precipitation Data Using the 20- Year IMERG and TMPA Precipitation Products in Diverse Subregions of China." *Atmospheric Research* 249(June 2020).

Macharia, J, M., K. Ngetich, F, and A. Shisanya, C. 2020. "Comparison of Satellite Remote Sensing Derived Precipitation Estimates and Observed Data in Kenya." *Agricultural and Forest Meteorology* 284(April 2019): 107875. https://doi.org/10.1016/j.agrformet.2019.107875.

McNally, Amy, and NASA/GSFC/HSL. 2018. *FLDAS Noah Land Surface Model L4 Global Monthly 0.1 x 0.1 Degree (MERRA-2 and CHIRPS)*. Greenbelt, MD, USA.

Shef, J, and E F Wood. 2018. "Satellite Remote Sensing for Water Resources Management : Potential for Supporting Sustainable Development in Data-Poor Regions." *Water Resources Research*: 9724–58. https://doi.org/10.1029/2017WR022437.

Sun, Qiaohong et al. 2018. "A Review of Global Precipitation Data Sets: Data Sources, Estimation, and Intercomparisons." *Reviews of Geophysics* 56(1): 79–107.

Wang, Fei et al. 2019. "Drought Evaluation with CMORPH Satellite Precipitation Data in the Yellow River Basin by Using Gridded Standardized Precipitation Evapotranspiration Index." *Remote Sensing* 11(5): 1–19.

Wehbe, Youssef et al. 2017. "Assessment of the Consistency among Global Precipitation Products over the United Arab Emirates." *Journal of Hydrology: Regional Studies* 12(May): 122–35. https://doi.org/10.1016/j.ejrh.2017.05.002.

Yang, Yanfen, and Yi Luo. 2014. "Evaluating the Performance of Remote Sensing Precipitation Products CMORPH, PERSIANN, and TMPA, in the Arid Region of Northwest China." *Theoretical and Applied Climatology* 118(3): 429–45.

14TH INTERNATIONAL CONFERENCE
ON HYDROSCIENCE & ENGINEERING

MAY 26-27, 2022
IZMİR-TURKEY

ICHE2022
IZMIR, TURKEY

APPLICATION OF IMPROVED VISUALIZATION TO THE TREND ASSESSMENT OF PRECIPITATION IN THE EASTERN BLACK SEA BASIN, TURKEY

Mehmet Berkant Yıldız

Department of Civil Engineering, Bursa Uludağ University

Bursa, Turkey

mberkantyildiz@uludag.edu.tr

Murat Şan

Department of Civil Engineering, Gümüşhane University

Gümüşhane, Turkey

muratsan@gumushane.edu.tr

Murat Kankal

Department of Civil Engineering, Bursa Uludağ University

Bursa, Turkey

mkankal@uludag.edu.tr

Sinan Nacar

Department of Civil Engineering, Tokat Gaziosmanpaşa University

Tokat, Turkey

sinan.nacar@gop.edu.tr

ABSTRACT: Precipitation, which is the most important component of the hydrological cycle, is a variable whose amount and time cannot be determined precisely and therefore can significantly affect the ecosystem, water resources and humanity. Climate change, which has increased its impact in recent years, also has important effects on the precipitation regime, and therefore natural disasters such as floods and droughts occur more often. Therefore, it is extremely important to determine the trends of precipitation variable time series in regions where the effects of climate change are experienced intensely. The aim of this study is to determine the temporal trends of monthly total precipitation in the Eastern Black Sea Basin (EBSB), which receives the highest precipitation in Turkey. To achieve the aim, Improved visualization the innovative trend analysis (IITA), Mann–Kendall (MK) test, and innovative trend analysis with significant test (ITST) methods were used. The data set covering the period 1969-2020 belonging to eight stations in the EBSB was used in the trend analysis. As a result, an increasing trend was observed in all trend tests, especially at station 17034 at all confidence levels. The increase is higher for the stations located in the east of the basin compared to the others. The MK method also shows that it is more rigid in figuring out the trend by detecting less trends than the others. As a result of the IITA, there was an average increase of 74.8 mm (5.8%) in the low groups, while an average increase of 85.7 mm (7.9%) was seen in the high groups. So, trends in high groups increased more than low groups for the basin. Based on these results, it is thought that there will be an increase in the number and severity of floods in future periods in the basin.

KEY WORDS: Climate Change; Eastern Black Sea Basin, Innovative Trend Analysis, Mann-Kendall, Trend Analysis

1. INTRODUCTION

Observations and records from all continents and oceans show new behavior as hydrological cycle intensification, water availability, quality and services are affected by climate change (Şen 2020). So,

climate change has significant impacts on different human activities such as groundwater recharge, water supply, agricultural activities, hydroelectric power generation and irrigation practices (Şen 2012). For this reason, relevant institutions and organizations should examine the changes in hydro-meteorological data to give a preliminary idea about climate change.

Since precipitation is one of the main factors in the hydrological cycle, precipitation variations have a direct impact on agricultural productivity as well as the occurrence of droughts or floods (Abdi et al. 2017). Therefore, precipitation changes need to be investigated to plan and manage water resources and prepare proper plans to deal with drought and flood conditions (Sanikhani et al. 2018). One of the methods used to examine this variability is trend analysis.

Trend analyzes are grouped into parametric and non-parametric. In recent years, non-parametric methods have been preferred in hydrometeorology applications since these do not require any assumptions (Onyutha 2016). Among these methods, the Mann-Kendall (Mann 1945; Kendall 1975) test has a recommendation for the use of the world meteorological organization (Kumar et al. 2009), and it is frequently preferred in the literature for hydro-meteorological data. Because evaluating hydro-meteorological variables in different groups (low, medium, and high) allows us to take into account extreme events such as heatwave, flood and drought (Dabanlı et al. 2016; Elouissi et al. 2016), Innovative trend analysis (ITA) method, which also allows to visually examine data in low, medium and high groups, was proposed by Şen (2012) as an alternative to MK, which is used to examine monotonic trends. The statistical significance test of ITA (ITST) was also suggested by Şen (2017) to examine monotonic trends. Although the ITA method can be used to analyze trends in different groups, the issue of determining group boundaries is left to the user's preference. For the reason, Güçlü (2020) suggested improved visualization of ITA (IITA) for numerical determination of this distinction between groups and for alternative visual representation to classical ITA. However, when the literature is examined, there is no study examining the performance of these three methods together and using them in hydro-meteorological studies.

The aims of this study are to examine temporal trends on the monthly total precipitation series of eight meteorological stations in the Eastern Black Sea Basin (EBSB), which receives the most precipitation in Turkey and is frequently exposed to flood and landslide events (Görüm and Fidan 2021) and to compare the trend methods. For this purposes, MK and ITST methods were used to examine monotonic trends, while IITA method was used to examine trends in low and high groups. Before the trend analysis, the homogeneity control of the stations was performed with various the tests.

2. MATERIAL AND METHOD

2.1. Study Area

There are 25 hydrological basins in Turkey. The EBSB is found on the north-eastern coast of Turkey. The basin is geographically found between 40° 15'- 41° 34' north latitudes and 36° 43'- 41° 35' east longitudes and comprises the provinces Ordu, Giresun, Gümüşhane, Trabzon, and Rize, respectively, along the Black Sea coast (Figure 1). The climate characteristic of the northeast coastal region of Turkey is rainy and humid. The Black Sea coast receives the greatest amount of precipitation and is the only region of Turkey that receives precipitation throughout the year (Yüksek et al., 2013). The annual total precipitation average of the EBS basin is around 1330 mm, considering the 1981-2010 period data. This value is approximately 2300 mm at the stations located on the Black Sea coastline (TSMS, 2012).

In this study, the stations which are considered to represent the basin and have a measured data set of 52 years, including 1969-2020, were identified. Eight meteorological stations are available within the basin. The settlements of these stations within the basin are also shown on the Figure 1 and the basic statistics of the stations are given in Table 1. Monthly precipitation records for these stations are obtained from the Turkish State Meteorological Service in Turkey.
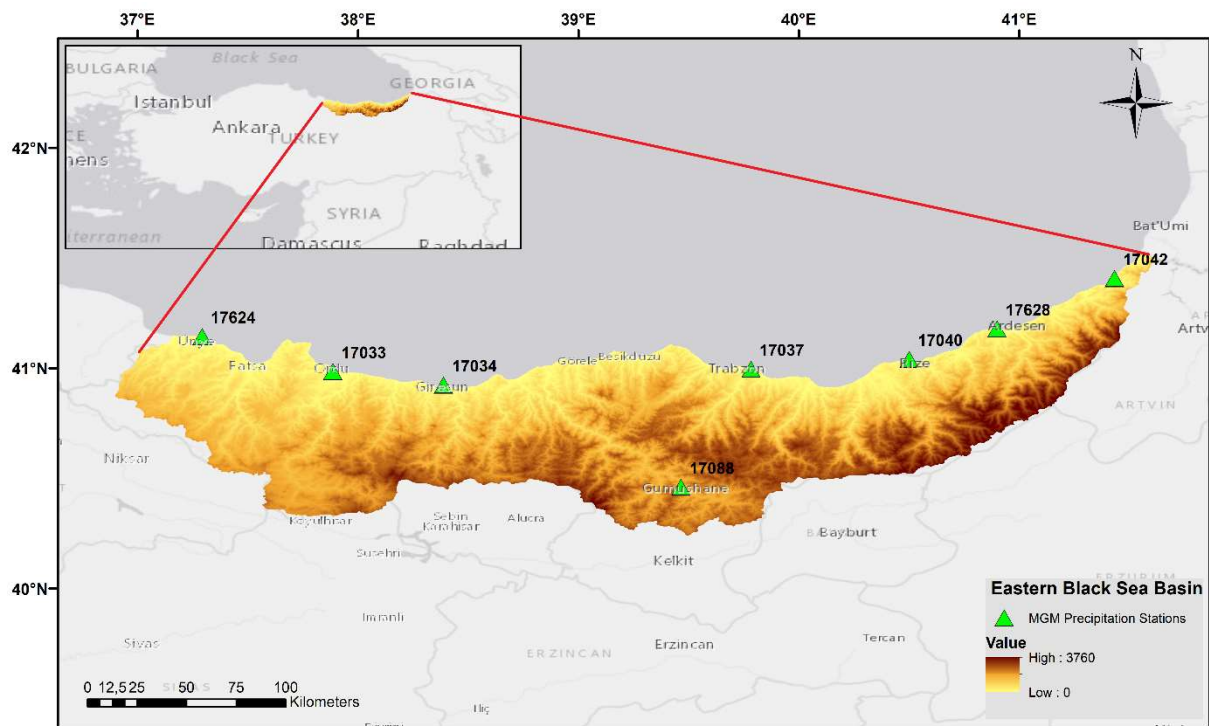
Figure 1. Meteorological stations in the basin and digital elevation model

Table 1. Locations and annual total precipitation statistics of meteorological stations.

Station	Name	Latitude (°)	Longitude (°)	Mean (mm)	Std. deviation (mm)
17033	Ordu	40.9838	37.8858	1042.93	125.16
17034	Giresun	40.9227	38.3878	1279.15	161.49
17040	Rize	41.0400	40.5013	2247.17	256.99
17042	Hopa	41.4065	41.4330	2284.08	337.01
17088	Gümüşhane	40.4598	39.4653	461.39	78.49
17624	Ünye	41.1430	37.2930	1172.67	168.38
17628	Pazar	41.1777	40.8993	2058.81	336.75
17037	Trabzon	40.9950	39.7830	805.63	107.74

2.2. Homogeneity Tests

In this study, the homogeneity is evaluated in two stages as suggested by Wijngaard et al. (2003) (Şan et al., 2021). To evaluate the homogeneity of the precipitation time series, the Pettitt (1979), Standard Normal Homogeneity Test (SNHT) (Alexandersson 1986), Buishand (1982) and Von-Neumann (1941) homogeneity tests were applied at the 5 % significance level (Meshram et al., 2017). Homogeneity is checked by testing the null hypothesis (H0). The H0 (H1) hypothesis shows that there is no change namely that the data are homogeneous (non-homogeneous). In the second stage, the test results are evaluated in three class as follows (Wijngaard et al. 2003; Şan et al., 2021):

Class 1: Useful (if at least three of the four methods accept H0),

Class 2: Doubtful (if two of the four methods accept H0),

Class 3: Suspect (if one of the four methods accepts H0 or not at all).

2.3. Trend Analysis

2.3.1. Mann-Kendall (MK) test

The MK test, which is frequently used in literature to examine monotonic trends, is calculated as follows:

$$S = \sum_{i=1}^{n-1} \sum_{j=i+1}^{n} sgn(x_j - x_i) \tag{1}$$

$$Var(S) = \frac{[n(n-1)(2n+5) - \sum_{i=1}^{p} t_i (t_i - 1)(2t_i + 5)]}{18} \tag{2}$$

$$Z = \begin{cases} \dfrac{S-1}{\sqrt{Var(S)}} & , \quad S > 0 \\[2ex] 0 & , \quad 0 \\[2ex] \dfrac{S+1}{\sqrt{Var(S)}} & , \quad S < 0 \end{cases} \tag{3}$$

where, S is test statistic, n is data length, x_i and x_j data value at times i and j, respectively, p is number of tied groups, t_i expresses how many times a data repeat. There is a trend if the absolute value of the Z value is greater than the standard z value corresponding to the chosen significance level. A positive(negative) S value shows the increasing(decreasing) direction of trend. For detailed information, studies Rao et al. (2003) and Yılmaz and Tosunoğlu (2019) can be examined.

2.3.2. Innovative trend significance test (ITST)

Şen (2017) proposed the ITST to quantitatively evaluate monotonic trends by suggesting a significance test for ITA (Şen 2012), which is a trend method that visually examines low, medium, and high group values. The implementation of the method is as follows: The hydrometeorological time series is divided into two equal parts. The average of the first part ($\bar{y}_1$) and the average of the second part ($\bar{y}_2$) are calculated. The slope is calculated as follows:

$$s = \frac{2(\bar{y}_2 - \bar{y}_1)}{n} \tag{4}$$

$$E(s) = \frac{2}{n}[E(\bar{y}_2) - E(\bar{y}_1)] \tag{5}$$

$$\sigma_s^2 = \frac{8}{n^2}[E(\bar{y}_2^2) - E(\bar{y}_2\bar{y}_1)] \tag{6}$$

$$\rho_{\bar{y}_2\bar{y}_1} = \frac{E(\bar{y}_2\bar{y}_1) - E(\bar{y}_2) - E(\bar{y}_1)}{\sigma_{\bar{y}_2}\sigma_{\bar{y}_1}} \tag{7}$$

$$\sigma_s^2 = \frac{8}{n^2}\frac{\sigma^2}{n}\left(1 - \rho_{\bar{y}_2\bar{y}_1}\right) \tag{8}$$

$$\sigma_s = \frac{2\sqrt{2}\,\sigma}{n\sqrt{n}}\sqrt{1 - \rho_{\bar{y}_2\bar{y}_1}} \tag{9}$$

where, n, $E(s)$, ρ, σ_s^2 and σ_s are the data length, the first-order moment of the slope, the cross-correlation coefficient between two mean values, the variance of trend slope, and standard deviation of the slope, respectively. There is an increasing (decreasing) trend when the slope exceeds the upper (lower) limit of the confidence interval (CL) and vice versa. CL is calculated as follows:

$$CL_{(1-\alpha)} = 0 \pm s_{cri}\sigma_s \qquad (10)$$

where, s_{cri} is the standard z value corresponding to the chosen significance level.

2.3.3. Improved visualization innovative trend analysis (IITA)

The Pettit test application has been suggested by Güçlü (2020) to make the grouping process in the ITA method objectively. Besides Güçlü (2020) proposed ITA's new visual representation method. In the method, the hydro-meteorological time series is divided into two equal parts and sorted in ascending manner. Both parts are placed on vertical axis in the coordinate system according to the data order. Then the difference of the two ordered parts is calculated and the difference series is placed on the vertical axis (Figure 2). If the difference series is located above (below) the horizontal axis, there is an increasing (decreasing) trend. By applying Pettit test to the difference series, the change point is obtained, and the low and high groups are objectively determined.
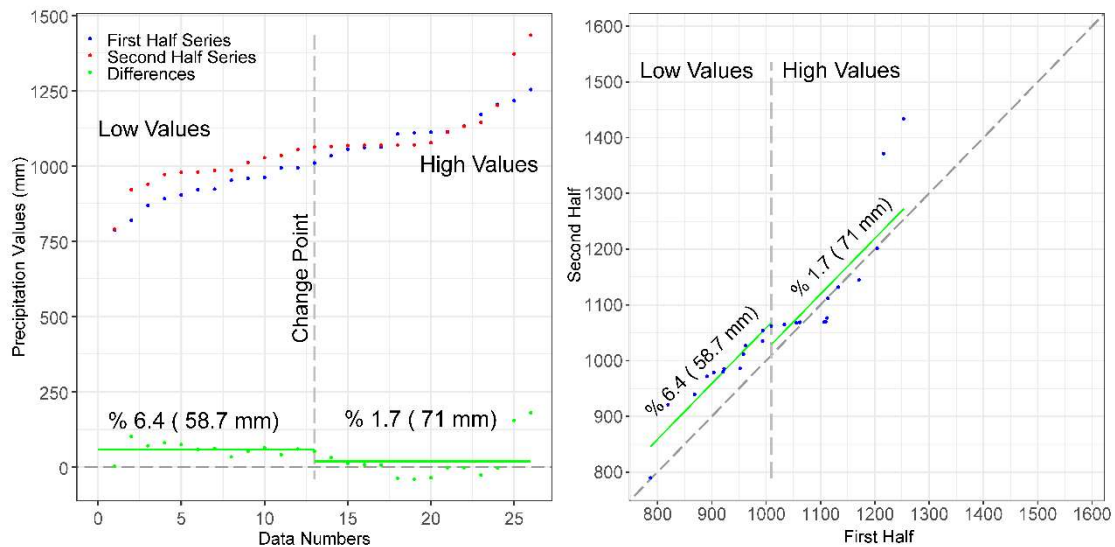
Figure 2. Representation of new (left) and classical (right) of ITA

3. RESULTS

3.1. Homogeneity test results

Homogeneity tests were applied on the annual total precipitation of eight stations at 95% confidence level. The station 17037 was determined as doubtful and excluded from the study, all the other stations were determined as useful class and homogeneous. The homogeneous stations were used to trend analysis.

3.2. MK results

The MK trend test was performed on the monthly total precipitation at the 99, 95, and 90% confidence intervals for homogeneous seven stations. The MK test results are given in Table 2. While there is an increasing monotonic trend at station 17034 at the 99% confidence level, it is no trend at the other stations. In addition to station 17034, stations 17042, 17624 and 17628 have an increasing monotonic trend at the 95% confidence level, but there is no trend at other stations. At the 90% confidence level, there is an increasing monotonic trend at all stations except for 17088 (Gümüşhane). That is, while there are increasing trends in the coastal areas, there is no trend in the interior (Figure 1).

Table 2. MK results.

Station No	Test Statistic	Z Value	Trends for the Confidence Interval		
			99%	95%	90%
17033	228	1.79	0	0	+
17034	396	3.12	+	+	+
17040	235	1.85	0	0	+
17042	307	2.41	0	+	+
17088	140	1.10	0	0	0
17624	300	2.36	0	+	+
17628	278	2.19	0	+	+

3.3. ITST results

The ITST was performed on the monthly total precipitation at the 99, 95, and 90% confidence intervals for homogeneous seven stations. The ITST results are given in Table 3. According to Table 3, there is a monotonic increasing trend at all confidence levels for all the stations. While the maximum trend slope (7.842) is seen at station 17628, the minimum trend slope (0.926) is seen at station 17088. The mean slope of the increasing trends at the stations of the basin was calculated as 4.124. The slope of the monotonic increasing trend at stations in the eastern parts of the basin is higher than in the western parts (Figure 1 and Table 3).

Table 3. ITST results.

Station No	Slope	Trends for the Confidence Interval								
		Lover Limit	Upper Limit	Trend (99%)	Lover Limit	Upper Limit	Trend (95%)	Lover Limit	Upper Limit	Trend (90%)
17033	1.488	-0.751	0.751	+	-0.572	0.572	+	-0.480	0.480	+
17034	3.356	-0.799	0.799	+	-0.608	0.608	+	-0.510	0.510	+
17040	5.841	-0.962	0.962	+	-0.732	0.732	+	-0.614	0.614	+
17042	5.809	-1.335	1.335	+	-1.016	1.016	+	-0.853	0.853	+
17088	0.926	-0.272	0.272	+	-0.207	0.207	+	-0.174	0.174	+
17624	3.606	-0.439	0.439	+	-0.334	0.334	+	-0.281	0.281	+
17628	7.842	-1.190	1.190	+	-0.905	0.905	+	-0.760	0.760	+

3.4. IITA results

The IITA method was applied to examine trends in different groups of precipitations. Petit test to separate groups was performed at 95% confidence level on the difference series. IITA representations are given in Figures 3, 4, and 5.

In Figures 3, 4 and 5, for the low group, the maximum increasing trend (10.1%) was observed at station 17624 and the minimum increasing trend (3.2%) was observed at station 17042. For the high group, the maximum increasing trend (11.9%) was seen at station 17628 and the minimum increasing trend (1.7%) was seen at station 17033. While there is a mean 5.8% increase trend in the low groups, there is a 7.8% increase trend in the high groups for the basin. When viewed holistically, there is a monotonic increasing trend as a mean of 6.8%.

To consider in general, there is an increasing trend in monthly total precipitation across the basin both for different groups and for monotonic trends. However, according to the studies (Partal and Kahya 2005; Eris and Agiralioglu 2012) covering the period 1960-2005, while no trend is observed in the basin in general, there is an increasing trend as the period is updated (Cengiz et al. 2020). In this study, as the data were updated, an increasing trend was seen similar to study Cengiz et al. (2020). However, according to the studies (Hırca et al. 2021; Akçay et al. 2021) examining the changes in precipitation, flow and temperature parameters within a year, there are trends in different directions within a year. However, according to studies examining the changes in precipitation, flow and temperature parameters within a year, there are trends in different directions within a year. This shows that while there is a general increase, the trend in the high group will increase more than the low

group, which will cause an increase in internal variability and complicate the management of water resources.
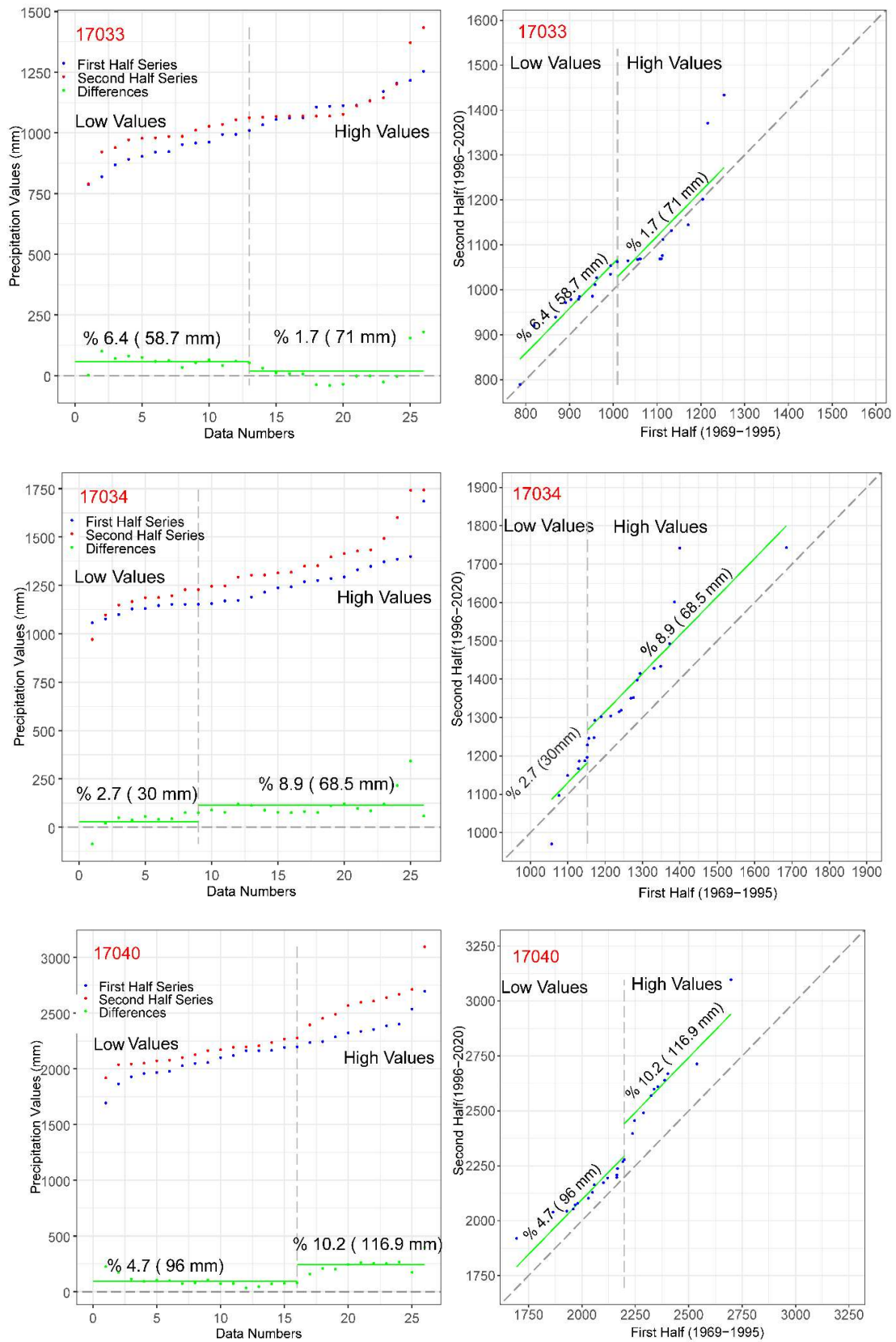
Figure 3. IITA representations for stations of 17033,17034 and 17040
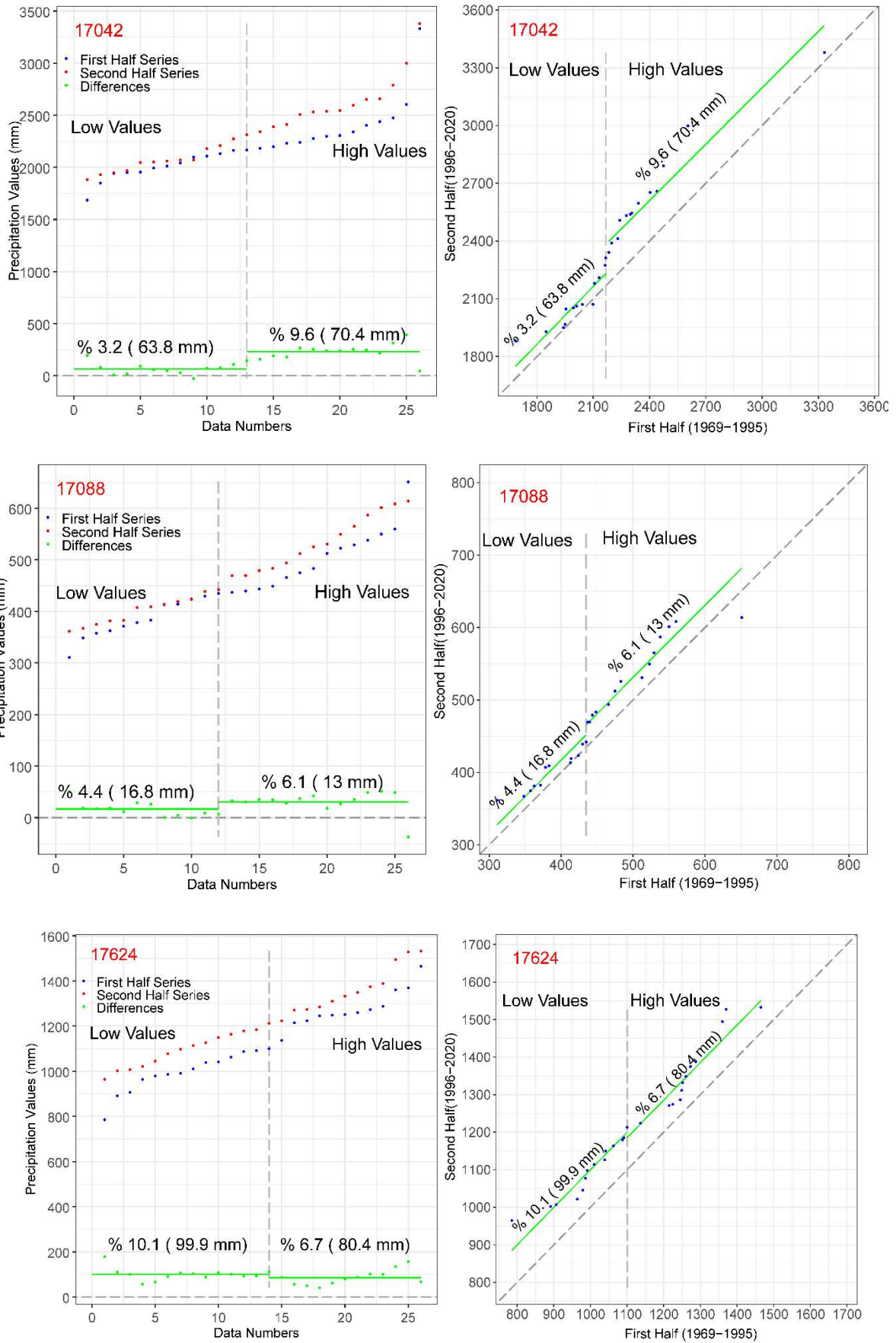
Figure 4. IITA representations for stations of 17042,17088 and 17624
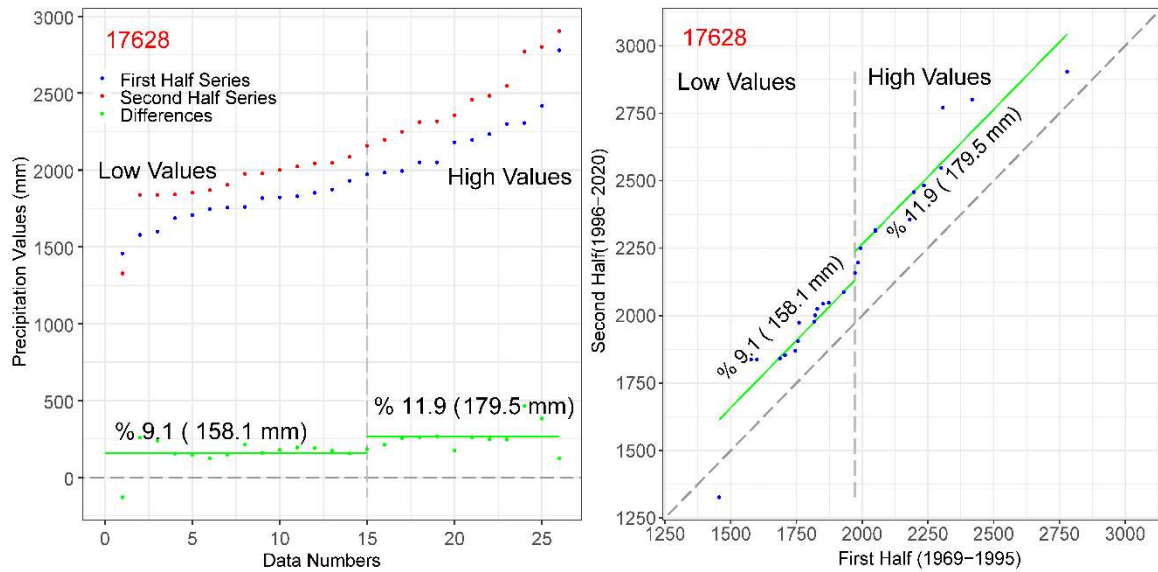
Figure 5. IITA representations for station of 17628

4. CONCLUSION

In this study, the trends of the monthly total precipitation data for the 1969-2020 period of the Eastern Black Sea Basin were investigated. For this purpose, in addition to the Mann Kendall (MK) method, which is frequently used in the literature, improved visualization the innovative trend analysis (IV_ITA) and innovative trend analysis with significant test (ITST) methods were used. Eight stations were selected to represent the basin, and homogeneity tests were performed before perform trend analysis. As a result of the homogeneity test, the station 16037 was not found to be homogeneous and was excluded from the study. According to the results obtained from the trend analysis, it has been determined that there is an increasing trend in all methods throughout the basin. In addition, an increasing trend was detected in all confidence (99, 95, and 90%) levels at station 17034. Although there is generally an increasing trend in the basin, the increasing in the high groups is higher than in the low group in IITA. This may worsen water resources and flood protection plans in the EBSB, which has a high flood frequency and high loss of life and property. In general, the MK is stricter in determining trend compared to the ITST and IITA methods. It was concluded that in addition to monotonic trend methods, i.e., MK and ITST, it is important to examine hydro-meteorological data by separating these into different groups to obtain more detailed information, because low and high values are of great importance for water resources management.

REFERENCES

Abdi, A., Hassanzadeh, Y., Talatahari, S., Fakheri-Fard, A., & Mirabbasi, R. (2017). Regional drought frequency analysis using L-moments and adjusted charged system search. *Journal of Hydroinformatics*, 19(3), 426-442.

Akçay, F., Kankal, M., & Şan, M. (2021). Innovative approaches to the trend assessment of streamflows in the eastern Black Sea basin, Turkey. *Hydrological Sciences Journal*, (just-accepted).

Alexandersson, H. (1986). A homogeneity test applied to precipitation data. *Journal of climatology*, 6(6), 661-675.

Buishand, T. A. (1982). Some methods for testing the homogeneity of rainfall records. *Journal of hydrology*, 58(1-2), 11-27.

Cengiz, T. M., Tabari, H., Onyutha, C., & Kisi, O. (2020). Combined use of graphical and statistical approaches for analyzing historical precipitation changes in the Black Sea region of Turkey. *Water*, 12(3), 705.

Dabanlı, İ., Şen, Z., Yeleğen, M. Ö., Şişman, E., Selek, B., & Güçlü, Y. S. (2016). Trend assessment by the innovative-Şen method. *Water resources management*, 30(14), 5193-5203.

Ebru, E., & Necati, A. (2012). Homogeneity and trend analysis of hydrometeorological data of the Eastern Black Sea Region, Turkey. *Journal of Water Resource and Protection*, 2012.

Elouissi, A., Şen, Z., & Habi, M. (2016). Algerian rainfall innovative trend analysis and its implications to Macta watershed. *Arabian Journal of Geosciences*, 9(4), 303.

Görüm, T., & Fidan, S. (2021). Spatiotemporal variations of fatal landslides in Turkey. *Landslides*, 18(5), 1691-1705.

Güçlü, Y. S. (2020). Improved visualization for trend analysis by comparing with classical Mann-Kendall test and ITA. *Journal of Hydrology*, 584, 124674.

Hırca, T., Eryılmaz Türkkan, G., & Niazkar, M. (2021). Applications of innovative polygonal trend analyses to precipitation series of Eastern Black Sea Basin, Turkey. *Theoretical and Applied Climatology*, 1-17.

Kendall MG (1975) Rank correlation methods. Griffin, London

Kumar, S., Merwade, V., Kam, J., & Thurner, K. (2009). Streamflow trends in Indiana: effects of long term persistence, precipitation and subsurface drains. *Journal of Hydrology*, 374(1-2), 171-183.

Mann, H. B. (1945). Nonparametric tests against trend. *Econometrica: Journal of the econometric society*, 245-259.

Meshram, S. G., Singh, V. P., & Meshram, C. (2017). Long-term trend and variability of precipitation in Chhattisgarh State, India. *Theoretical and Applied Climatology*, 129(3), 729-744.

Onyutha, C. (2016). Identification of sub-trends from hydro-meteorological series. *Stochastic Environmental Research and Risk Assessment*, 30(1), 189-205.

Partal, T., & Kahya, E. (2006). Trend analysis in Turkish precipitation data. *Hydrological Processes: An International Journal*, 20(9), 2011-2026.

Pettitt, A. N. (1979). A non-parametric approach to the change-point problem. *Journal of the Royal Statistical Society: Series C (Applied Statistics)*, 28(2), 126-135.

Rao, A. R., Hamed, K. H., & Chen, H. L. (2003). Nonstationarities in hydrologic and environmental time series (Vol. 45). *Springer Science & Business Media*.

Sanikhani, H., Kisi, O., Mirabbasi, R., & Meshram, S. G. (2018). Trend analysis of rainfall pattern over the Central India during 1901–2010. *Arabian Journal of Geosciences*, 11(15), 1-14.

Şen, Z. (2012). Innovative trend analysis methodology. *Journal of Hydrologic Engineering*, 17(9), 1042-1046.

Şen, Z. (2017). Innovative trend significance test and applications. *Theoretical and applied climatology*, 127(3-4), 939-947.

Şen, Z. (2020). Water structures and climate change impact: a review. *Water Resources Management*, 34(13), 4197-4216.

TSMS (2012). Turkish State Meteorology Service, Türkiye alansal yağış analizi 1981-2010 (Turkish), 1-96. https://www.mgm.gov.tr/FILES/genel/kitaplar/alansalyagisanalizi.pdf

Von Neumann, J. (1941). Distribution of the ratio of the mean square successive difference to the variance. *The Annals of Mathematical Statistics*, 12(4), 367-395.

Wijngaard, J. B., Klein Tank, A. M. G., & Können, G. P. (2003). Homogeneity of 20th century European daily temperature and precipitation series. *International Journal of Climatology: A Journal of the Royal Meteorological Society*, 23(6), 679-692.

Yilmaz, M., & Tosunoglu, F. (2019). Trend assessment of annual instantaneous maximum flows in Turkey. *Hydrological Sciences Journal*, 64(7), 820-834.

Yüksek Ö., Kankal M., Üçüncü O. (2013). Assessment of big floods in the Eastern Black Sea Basin of Turkey. *Environmental Monitoring and Assessment* 185:797–814.

14TH INTERNATIONAL CONFERENCE
ON HYDROSCIENCE & ENGINEERING

MAY 26-27, 2022
IZMİR-TURKEY

ICHE2022
IZMIR, TURKEY

ASSESSMENT OF REGIONAL DROUGHT TRENDS BY USING IMPROVED VISUALIZATION VERSION OF INNOVATIVE TREND ANALYSIS AND MANN KENDALL TEST

Mehmet Berkant Yıldız

Department of Civil Engineering, Bursa Uludağ University

Bursa, Turkey

mberkantyildiz@uludag.edu.tr

Sinan Nacar

Department of Civil Engineering, Tokat Gaziosmanpaşa University

Tokat, Turkey

sinan.nacar@gop.edu.tr

Murat Kankal

Department of Civil Engineering, Bursa Uludağ University

Bursa, Turkey

mkankal@uludag.edu.tr

Murat Şan

Department of Civil Engineering, Gümüşhane University

Gümüşhane, Turkey

muratsan@gumushane.edu.tr

ABSTRACT: Turkey's climatic characteristics show significant differences from region to region due to topography, geology, wind direction, and being surrounded by seas on three sides. Therefore, it is possible to reveal the sensitivity of a region to the effects of climate change by examining each region separately. Hydrological drought, which is one of the most obvious consequences of climate change, is an event that should be emphasized due to its negative effects on the environment, society, and livelihoods. Increasing temperatures with climate change are expected to increase the frequency and severity of extreme events such as drought, especially in Mediterranean climates. This study attempts to examine the drought severity, trend, and consequences applying the standardized precipitation index (SPI) indices in the Susurluk Basin (Turkey) considering the last 48 years period (1972-2019) along with 12 months' time scale. Improved visualization of the innovative trend analysis (IITA) and Mann–Kendall (MK) test methods were used to determine the trends of the SPI values. It was determined that the longest periods of extremely wet and extremely dry periods were experienced at Bursa (22 months) and Bandırma (15 months) stations and the longest wet and dry periods were observed at Keles (68 months) and Dursunbey (72 months) stations. According to the results of MK trend analysis performed for different confidence levels, increasing trends were observed across the basin (except Uludağ and Keles) for 50% and 85% confidence levels. At Uludağ and Keles stations, a decreasing trend was observed for similar confidence levels in many months of the year. According to the results of the IITA, it was observed that there was an increasing trend across the basin for drought and wet groups. In other words, the wetness has increased. It has been observed that drought increases especially in summer and autumn at Uludağ and Keles stations during wet periods. In the dry groups, it was determined that the drought increased in most of the stations in the winter and spring months. It is thought that the results obtained from this study will be useful in making decisions for drought management in the Susurluk Basin.

KEYWORDS: Climate Change; Susurluk Basin, Trend Analysis, Innovative Trend Analysis, Mann-Kendall

1. INTRODUCTION

During the last decades, a substantial emphasis has been devoted worldwide to extreme weather events, namely to droughts (Páscoa et al., 2021). As a result of these studies, researchers stated that drought is among the most destructive natural disasters. While drought affects livelihoods such as agriculture and animal husbandry, it also negatively affects natural resources such as water, ecological and biological diversity (Haroon et al., 2016; Liu et al., 2020; Kalisa et al., 2020).

Drought is a prolonged periodical incident of dryness and scarcity of water in different spheres (atmosphere, lithosphere, and hydrosphere) of the earth system which specifies as one of the most extreme climatic events (Bera et al., 2021). Regardless of geographical location, drought can be grouped under three classes. Firstly, the lack of rainfall results in a meteorological drought. It occurs when precipitation is well below its normal level during a long period. Secondly, hydrological drought occurs with insufficiency in water supply volume. However, agricultural drought is the third type. It takes place when the availability of soil moisture decreases for crops, which alters yields and endangers livestock (Wilhite and Glantz, 1985; Parente et al., 2019; Abdelmalek and Nouiri, 2020). Drought initially occurs as a result of below normal rainfall for extended periods often referred to as meteorological drought (Byakatonda et al., 2018).

In order to fight drought, the World Meteorological Organization (WMO) associated with the Global Water Partnership (GWP), had launched the Integrated Drought Management Program in 2013, which contributes to the Global Framework for Climate Services, including water, agriculture, food security, energy, and health. This program recommended the use of indices for efficient drought monitoring. Numerous indices are proposed in the literature (Abdelmalek and Nouiri, 2020). Drought indices allow the characterization of many facets of drought events, such as their spatial extension and intensity. In recent years, various methodologies have been developed for the assessment and classification of drought worldwide. Most of these methodologies use rainfall, air temperature, soil moisture, evapotranspiration (ET), and flow to calculate drought indices (Choi et al., 2013, Tigkas et al., 2013). These indices may give different results for the same region as they have different statistical methods and various data entry requirements (Sobral et al., 2019).

The Standardized Precipitation Index (SPI) (McKee et al., 1993) is the most used in the scientific literature and is recommended by the World Meteorological Organization (WMO) as the standard index (Sobral et al., 2019). According to the WMO, SPI is a recommended tool to show the calculated index probability in order to record the amount of rainfall, drought negative index value, and wet positive index value. It can also be used to forecast the condition of the climate condition monitoring on a range of time by insisting on some modeling approaches (Pramudya and Onishi, 2018).

The purposes of this study are to assess the hydrological drought conditions over the Susurluk Basin, Turkey by employing the SPI and detect the trends of hydrological drought by using the improved innovative trend analysis (IITA) (Güçlü, 2020) and Mann–Kendall (MK) test (Mann 1945; Kendall 1962) methods. The following section describes the data and methods, followed by the results and discussion with the main conclusions presented in the last section.

2. DATA AND METHODS

2.1. Study Area

Susurluk Basin is one of the most important basins of Turkey with its population, agricultural lands, industry, and tourism regions. The basin has a total precipitation area of 24,332 km². Important streams of the basin are Nilufer Stream, Mustafakemalpasa Stream, Simav Stream, and Koca Stream. The annual water potential of the basin is 6.08×10^9 m³. Flow in the basin generally comes from mountains and can be defined as a rainy period between November and February (Ceribasi et al., 2021). Uluabat and Manyas Lakes are located in this basin. Susurluk Basin is located in the south of the Marmara region and includes some of Bursa, Balıkesir, Kutahya, Bilecik, Canakkale, Manisa, and Izmir provinces (Ceribasi and Ceyhunlu, 2021).

In this study, the stations which are considered to represent the basin and have a measured data set of 48 years, including 1972-2019, were identified. Nine meteorological stations are available within the

basin. The settlements of these stations within the basin are also shown in Figure 1 and the basic statistics of the stations are given in Table 1. Monthly precipitation records for these stations are obtained from the Turkish State Meteorological Service in Turkey.
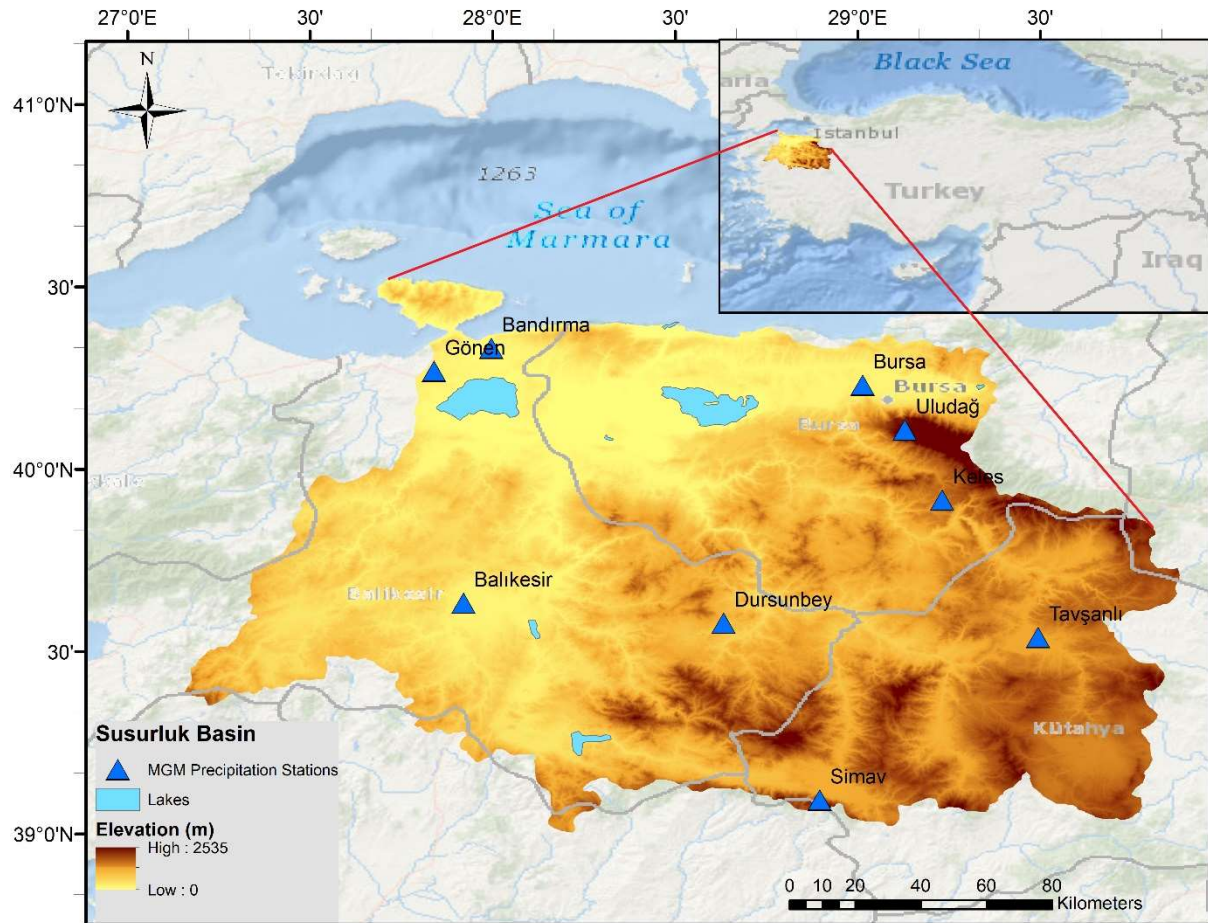
Figure 1. Meteorological stations in the Susurluk Basin and digital elevation model

Table 1. The basic statistics of annual total precipitation variable observed in meteorological stations.

Station Name	Bandırma	Balıkesir	Bursa	Dursunbey	Gönen	Keles	Simav	Tavşanlı	Uludağ
Maximum (mm)	1086.2	997.1	1328.6	824.0	1136.1	1189.2	1347.4	749.2	2132.2
Minimum (mm)	485.6	354.0	417.7	434.0	436.2	467.2	458.8	362.4	961.2
Mean (mm)	714.3	571.4	702.3	560.7	679.2	729.9	752.0	485.1	1459.4
Std. Deviation (mm)	155.8	120.2	143.1	88.1	131.5	130.6	197.3	81.9	239.8

2.2. Standardized Precipitation Index (SPI)

The SPI was designed to assess drought conditions based on suitable probability distribution of long-term precipitation (McKee et al., 1993). The SPI calculation, based on long-term precipitation data, is first adapted to a suitable cumulative probability distribution. It is then converted to standard normal probability via the random variable z, with the SPI value of mean zero (0) and variance one (1).(Eq. 1). In this study, the gamma distribution, which is commonly preferred for SPI, was taken into account. Since it is standardized, it can be used to describe and compare drought conditions in different areas.The index gives a good and reliable estimate of the magnitude, severity, and spatial extent of droughts. The periods when the SPI value falls below zero are considered as drought periods, while the periods when it rises above zero are considered as the end of the drought. In other

words, it is considered as wet periods. Unlike other drought indices, SPI is less cumbersome to use because it only requires a single input data series of long-term precipitation (Smakhtin and Hughes, 2004). Because it is based on normalized data, the SPI is spatially invariant and droughts can be assessed in different regions (Guttman, 1998). The index is calculated as follows:

$$SPI = \frac{x_i - \bar{x}}{\sigma} \qquad (1)$$

where, x_i is the precipitation of the selected period during the year i, x is the long term mean precipitation and σ is standard deviation for the selected period (Tirivarombo et al., 2018). The SPI classes are shown in Table 2 (Guttman, 1999).

Table 2. SPI classes.

	SPI classes		
	SPI	$\leq$ -2	Extremely dry
-2 <	SPI	$\leq$ -1.5	Moderately dry
-1.5 <	SPI	$\leq$ -1	Dry
-1 <	SPI	< 1	Neutral
1 $\leq$	SPI	< 1.5	Wet
1.5 $\leq$	SPI	< 2	Moderately wet
2 $\leq$	SPI		Extremely wet

2.3. Homogeneity tests

In this study, the homogeneity is evaluated in two stages as suggested by Wijngaard et al. (2003) (Şan et al., 2021). To evaluate the homogeneity of the precipitation time series, the Pettitt (1979), Standard Normal Homogeneity Test (SNHT) (Alexandersson 1986), Buishand (1982), and Von-Neumann (1941) homogeneity tests were applied at the 5 % significance level (Meshram et al., 2017). Homogeneity is checked by testing the null hypothesis (H0). The H0 (H1) hypothesis shows that there is no change (change), namely that the data are homogeneous (non-homogeneous). In the second stage, the test results are evaluated in three-class as follows (Wijngaard et al. 2003; Şan et al., 2021):

Class 1: Useful (if three or four out of the four methods accept H0),

Class 2: Doubtful (if three out of the four methods accept H0),

Class 3: Suspect (if one or zero out of the four methods accept H0).

2.4. Trend analysis

2.4.1. Mann Kendall (MK)

The MK test, which is frequently used in literature to examine monotonic trends, is calculated as follows:

$$S = \sum_{i=1}^{n-1} \sum_{j=i+1}^{n} sgn(x_j - x_i) \qquad (2)$$

$$Var(S) = \frac{[n(n-1)(2n+5) - \sum_{i=1}^{p} t_i(t_i-1)(2t_i+5)]}{18} \qquad (3)$$

$$Z = \begin{cases} \dfrac{S-1}{\sqrt{Var(S)}} & , \quad S > 0 \\[2mm] 0 & , \quad 0 \\[2mm] \dfrac{S+1}{\sqrt{Var(S)}} & , \quad S < 0 \end{cases} \qquad (4)$$

where S is test statistic, n is data length, x_i and x_j data value at times i and j, respectively, p is the number of tied groups, t_i expresses how many times a data repeat. There is a trend if the absolute value of the Z value is greater than the standard z value corresponding to the chosen significance level. A positive(negative) S value indicates the increasing(decreasing) direction of trend. For detailed information, studies Rao et al. (2003) and Yılmaz and Tosunoğlu (2019) can be examined.

2.4.2. *Improved innovative trend test (IITA)*

The Pettitt test application has been suggested by Güçlü (2020) to make objectively the grouping process in the ITA method. Besides Güçlü (2020) proposed ITA's new visual representation method. In the method, the hydro-meteorological time series is divided into two equal parts and sorted in ascending manner. Both parts are placed on the vertical axis in the coordinate system according to the data order. Then the difference of the two ordered parts is calculated and the difference series is placed on the vertical axis (Figure 2). If the difference series is located above (below) the horizontal axis, there is an increasing (decreasing) trend. By applying the Pettitt test to the difference series, the change point is obtained, and the low and high groups are objectively determined. Then, the amount of change is determined by calculating the group mean of the difference series.
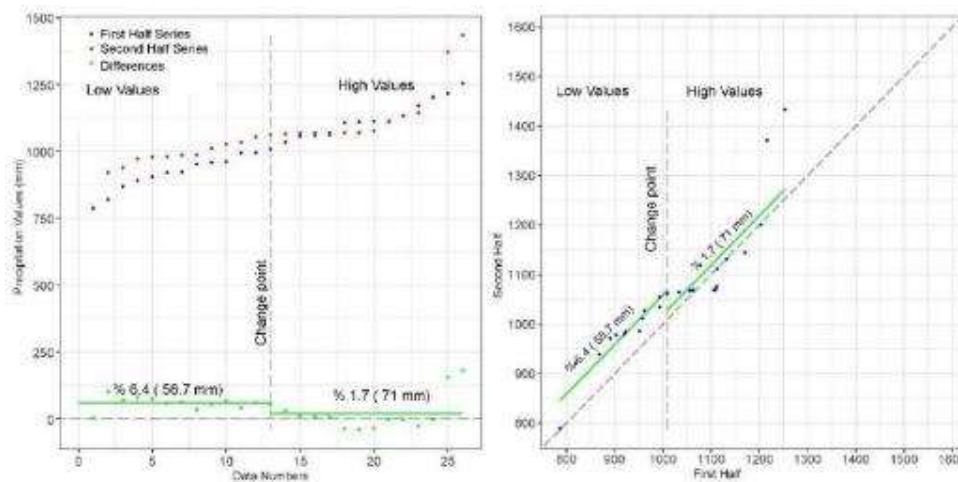
Figure 2. Representation of IITA (left) and classical (right) of ITA

3. RESULTS AND DISCUSSION

3.1. Homogeneity Results

Before calculating the SPI values of the Susurluk Basin meteorological stations and determining the trends of the SPI values, the homogeneity of the stations was tested. The homogeneity of the stations was determined at a 95% confidence level in two steps using the procedure recommended by Wijngaard et al. (2003) (Şan et al., 2021). Homogeneity tests were applied to nine stations in the basin with long-term data . As a result of homogeneity tests, it was determined that Balıkesir and Simav stations are in Class 3 (Suspect), and therefore these stations were not evaluated within the scope of the study.

3.2. Drought Analysis Results

The time series of the SPI values calculated for each station are given in Figure 3. When the time series are examined, it is seen that wetness and drought occur at almost the same time intervals in almost all stations throughout the basin. However, the magnitudes of the SPI values calculated for the determined time intervals differ from station to station. The longest wet period in Bandırma station started in 2009 and lasted until 2014. When the SPI graph of the station is examined, it is seen that there has not been a remarkable long drought period. In addition, the extremely dry (extremely wet) years for the Bandırma station were 1985 (1978) and 2007 (2010). Although there were humid periods (9 months) at intervals between 1972 and 1994 in Bursa station, the drought lasted longer in this period (67 months). Wetness has increased in Bursa station in the last period (2009-2016). In addition, the driest (wet) years at this station are 1985 (2010) and 1989 (2015). When the SPI graphs are evaluated for Dursunbey and Gönen stations, it is seen that the 1984-1997 period was a dry period for both stations. Although there is no clear wet period, the frequency of wet years has increased in recent years. Although some years were dry (wet) in the 1974-1982 (1983-2001) period at Keles station, the wetness is longer. The driest (wet) years at Keles station were 1985 (1982) and 2001 (2010). When the SPI graph of Uludag station is examined, it is seen that there is wetness in the 1971-1982 (except 1977) period, and drought in the 1985-1994 (except 1991) and 2016-2019 periods. In addition, it was seen that the driest year for Bursa station was 2017.
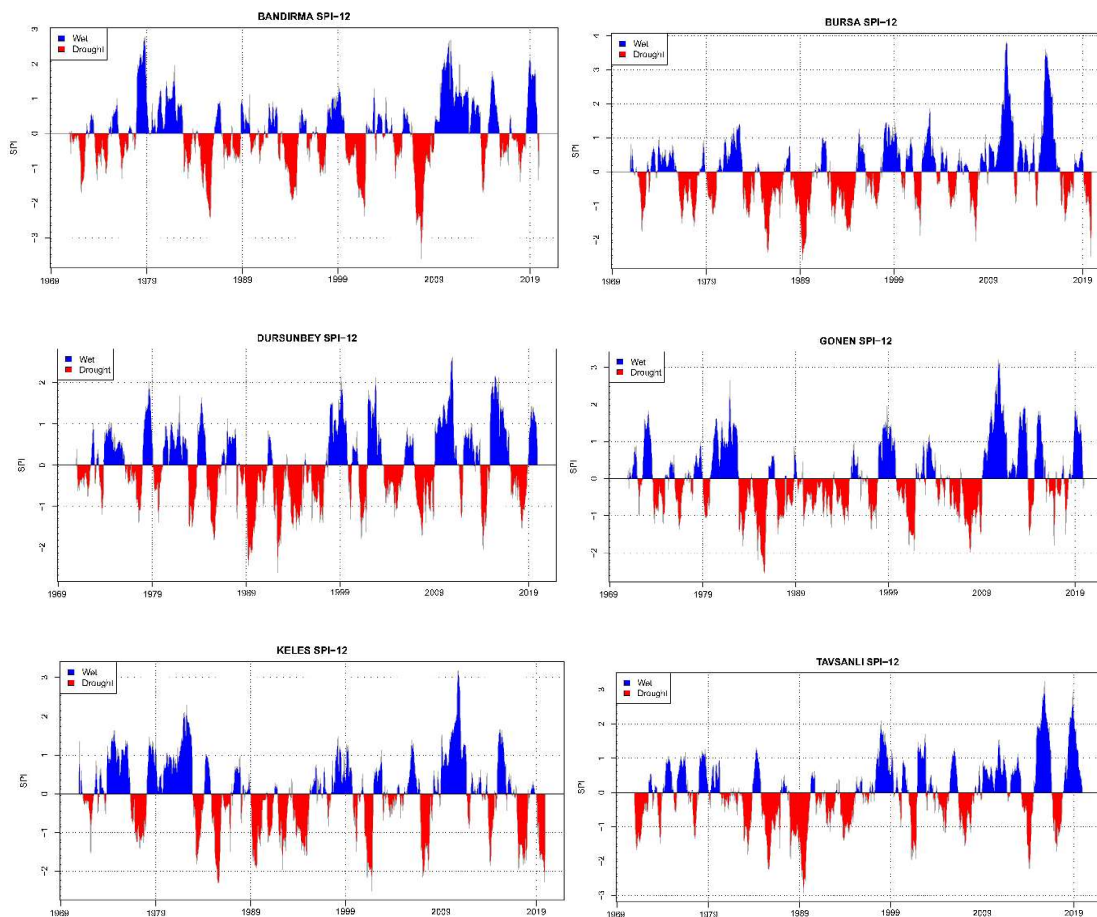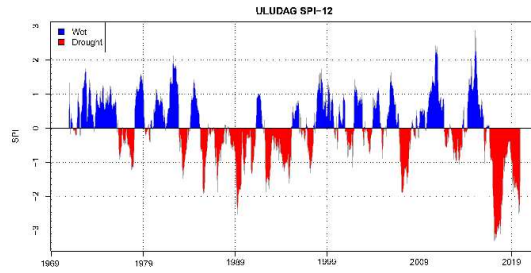
Figure 3. Drought index SPI for the time series of Susurluk Basin meteorological stations (1969–2019), at the time scale of 12 month

The number of months with dry and wet periods for each station in the basin is given in Figure 4 according to SPI classes. The neutral period is not indicated in this figure. When Figure 4 is examined, it has been determined that the longest periods of extremely wet and extremely dry SPI classes are 22 and 15 months at Bursa and Bandırma stations, respectively.
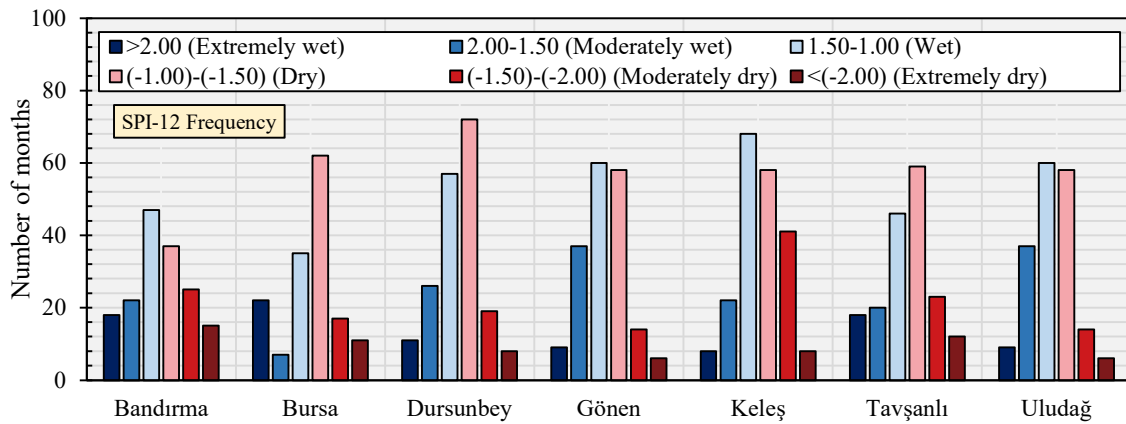
Figure 4. The number of months with dry and wet periods

3.3. Mann-Kendall Results

The MK trend test was performed on the SPI at the 99, 95, 90, 85, 75, and 50% confidence intervals for the seven stations in the basin. The MK analysis results are given in Table 2. Trends for different confidence levels are colored in the table and its legend is given in the last row of the table. No trend was observed at 95% and above confidence levels in all of the stations in the basin. When the trends at the 90% confidence level are examined, it is seen that there are only trends in Bursa and Uludağ stations. It has been determined that there is an increasing trend at Bursa station in January, August, and September. In addition, a decreasing trend was observed at Uludağ station only in February. It was determined that the decreasing trend at the 90% confidence level was only at Uludağ station in February. In other words, while the wetness increased for the mentioned three months at Bursa station, drought increased for Uludağ station in February. An increasing trend was observed in August for only 50% confidence level for Dursunbey station. In addition, a trend was determined at different confidence levels for all stations except Bandırma and Dursunbey stations in August and October.

Table 3. Mann-Kendall test results.

3.4. IITA Results

In the IITA, changes in groups are evaluated. For this, groups are determined by applying the Petitt test on the difference series. However, in this study, since the Petitt test found the change points close to zero, that is, in the neutral group, the zero value of the SPI was taken into account as the change point. The results of IITA are given in Table 4. The changes in the SPI values are presented in different color scales in the table. Value ranges of colors are given in the last row of the table. When Table 3 is analyzed for wet groups, it is seen that the trend has increased in all the other stations except Keles and Uludağ stations. It has been determined that there is a decreasing trend for 8 months for the Keles station and 6 months for the Uludağ station. When Table 3 is examined for dry groups, it is observed that the trends increase between 5-9 months for all stations. In other words, drought trend decreased during the group. It has been determined that the drought trend generally increases in the winter and early spring months. It is seen that there is an increasing trend in Bursa, Gönen, and Tavşanlı stations in all months. In other words, the drought trend has decreased in all months in these stations. The representation of Table 4 on the map is given in Figure 5.

Table 4. IITA results for the wet and dry group.

Figure 5. Distribution of trend change amounts in dry (left side) and wet (right side) groups on the basin

In Figure 5, the diameters of the rings indicate the magnitude of the change. In addition, the amount of increase and decrease are highlighted with different colors. The blue color represents the increase of SPI and the red color represents the decrease of SPI. A positive general increase is observed in both dry and wet groups in the basin. In other words, there is a general increasing trend in SPI values. Besides, the amount of increase in wet groups is higher than in dry groups (Figure 5).

4. CONCLUSION

This study aims to examine the severity of drought in the Susurluk Basin, Turkey with the help of a standardized precipitation index (SPI) and to determine the trends of SPI values. For this purpose, data for the period 1972-2019 for nine stations located in and around the basin were used. Before determining the SPI values of the stations and the trends of the SPI values, homogeneity tests were employed and seven stations that were determined to be homogeneous were used. In order to determine the trends of SPI values, the improved visualization version of innovative trend analysis (IITA) method, which is very new in the literature, and the classical Mann-Kendall (MK) test method, which is frequently used in trend analysis, were used. When the calculated SPI values are evaluated according to SPI classes, it is seen that all SPI classes are experienced at different time intervals in all stations in the basin. It was determined that the longest periods of extremely wet and extremely dry periods were experienced at Bursa (22 months) and Bandırma (15 months) stations, respectively. In addition, the longest wet and dry periods were observed at Keles (68) and Dursunbey (72) stations, respectively. When the MK trend analysis results for different confidence levels were examined, it was seen that there was no trend for 95% and above confidence levels. When the results obtained for the 90% confidence level were examined, it was seen that there was a trend only in Bursa and Uludağ stations. While an increasing trend was determined at Bursa station especially in the summer and

autumn months, a decreasing trend was observed for Uludağ station especially in February. According to IITA results, an increasing trend was determined for wet groups, except for Keles and Uludağ stations. There was a decreasing trend in 8 months for Keles station and 6 months for Uludağ station. For dry groups, it was observed that the drought trend decreased in all stations between the months of 5-9. The general increase in SPI values both in the dry and wet groups shows that the drought is in a decreasing trend as a general in the basin. When the MK method and IITA method were compared, it was seen that the MK method gave very limited information about the trends of SPI values. In the IITA method, the trends of SPI values were examined in two groups as dry and wet values, and more detailed information was obtained about the trends of drought and wetness.

REFERENCES

Abdelmalek, M. B., & Nouiri, I. (2020). Study of trends and mapping of drought events in Tunisia and their impacts on agricultural production. *Science of the Total Environment*, 734, 139311.

Alexandersson, H. (1986). A homogeneity test applied to precipitation data. *Journal of climatology*, 6(6), 661-675.

Bera, B., Shit, P. K., Sengupta, N., Saha, S., & Bhattacharjee, S. (2021). Trends and variability of drought in the extended part of Chhota Nagpur plateau (Singbhum Protocontinent), India applying SPI and SPEI indices. *Environmental Challenges*, 5, 100310.

Buishand, T. A. (1982). Some methods for testing the homogeneity of rainfall records. *Journal of hydrology*, 58(1-2), 11-27.

Byakatonda, J., Parida, B. P., Moalafhi, D. B., & Kenabatho, P. K. (2018). Analysis of long term drought severity characteristics and trends across semiarid Botswana using two drought indices. *Atmospheric Research*, 213, 492-508.

Ceribasi, G., & Ceyhunlu, A. I. (2021). Analysis of total monthly precipitation of Susurluk Basin in Turkey using innovative polygon trend analysis method. *Journal of Water and Climate Change*, 12(5), 1532-1543.

Ceribasi, G., Ceyhunlu, A. I., & Ahmed, N. (2021). Innovative trend pivot analysis method (ITPAM): a case study for precipitation data of Susurluk Basin in Turkey. *Acta Geophysica*, 1-16.

Choi, M., Jacobs, J. M., Anderson, M. C., & Bosch, D. D. (2013). Evaluation of drought indices via remotely sensed data with hydrological variables. *Journal of Hydrology*, 476, 265-273.

Güçlü, Y. S. (2020). Improved visualization for trend analysis by comparing with classical Mann-Kendall test and ITA. *Journal of Hydrology*, 584, 124674.

Güçlü, Y. S. (2020). Improved visualization for trend analysis by comparing with classical Mann-Kendall test and ITA. *Journal of Hydrology*, 584, 124674.

Guttman, N. B. (1998). Comparing the palmer drought index and the standardized precipitation index 1. JAWRA *Journal of the American Water Resources Association*, 34(1), 113-121.

Guttman, N. B. (1999). Accepting the standardized precipitation index: a calculation algorithm 1. JAWRA *Journal of the American Water Resources Association*, 35(2), 311-322.

Haroon, M. A., Zhang, J., & Yao, F. (2016). Drought monitoring and performance evaluation of MODIS-based drought severity index (DSI) over Pakistan. *Natural Hazards*, 84(2), 1349-1366.

Kalisa, W., Zhang, J., Igbawua, T., Ujoh, F., Ebohon, O. J., Namugize, J. N., & Yao, F. (2020). Spatio-temporal analysis of drought and return periods over the East African region using Standardized Precipitation Index from 1920 to 2016. *Agricultural Water Management*, 237, 106195.

Kendall MG (1975) Rank correlation methods. Griffin, London

Liu, Q., Zhang, S., Zhang, H., Bai, Y., & Zhang, J. (2020). Monitoring drought using composite drought indices based on remote sensing. *Science of The Total Environment*, 711, 134585.

Mann, H. B. (1945). Nonparametric tests against trend. *Econometrica: Journal of the econometric society*, 245-259.

McKee TB, Doesken NJ, Kleist J (1993) The relationship of drought frequency and duration to time scales. In: Preprints, 8th conference on applied climatology, Anaheim, CA, 17–22 January 1993, pp 179–184.

Meshram, S. G., Singh, V. P., & Meshram, C. (2017). Long-term trend and variability of precipitation in Chhattisgarh State, India. *Theoretical and Applied Climatology*, 129(3), 729-744.

Parente, J., Amraoui, M., Menezes, I., & Pereira, M. G. (2019). Drought in Portugal: Current regime, comparison of indices and impacts on extreme wildfires. *Science of the Total Environment*, 685, 150-173.

Páscoa, P., Russo, A., Gouveia, C. M., Soares, P. M., Cardoso, R. M., Careto, J. A., & Ribeiro, A. F. (2021). A high-resolution view of the recent drought trends over the Iberian Peninsula. *Weather and Climate Extremes*, 32, 100320.

Pettitt, A. N. (1979). A non-parametric approach to the change-point problem. *Journal of the Royal Statistical Society: Series C (Applied Statistics)*, 28(2), 126-135.

Pramudya, Y., & Onishi, T. (2018). Assessment of the standardized precipitation index (SPI) in Tegal City, Central Java, Indonesia. In IOP Conference Series: *Earth and Environmental Science*,129(1), 012019.

Rao, A. R., Hamed, K. H., & Chen, H. L. (2003). Nonstationarities in hydrologic and environmental time series (Vol. 45). *Springer Science & Business Media*.

Şan, M., Akçay, F., Linh, N. T. T., Kankal, M., & Pham, Q. B. (2021). Innovative and polygonal trend analyses applications for rainfall data in Vietnam. *Theoretical and Applied Climatology*, 144(3), 809-822.

Smakhtin, V. U., & Hughes, D. A. (2004). Review, automated estimation and analyses of drought indices in South Asia. *International Water Management Institute*, 1-24.

Sobral, B. S., de Oliveira-Junior, J. F., de Gois, G., Pereira-Júnior, E. R., de Bodas Terassi, P. M., Muniz-Júnior, J. G. R., ... & Zeri, M. (2019). Drought characterization for the state of Rio de Janeiro based on the annual SPI index: trends, statistical tests and its relation with ENSO. *Atmospheric Research*, 220, 141-154.

Tigkas, D., Vangelis, H., & Tsakiris, G. (2013). The RDI as a composite climatic index. *Eur Water*, 41, 17-22.

Tirivarombo, S., Osupile, D., & Eliasson, P. (2018). Drought monitoring and analysis: standardised precipitation evapotranspiration index (SPEI) and standardised precipitation index (SPI). *Physics and Chemistry of the Earth*, Parts A/B/C, 106, 1-10.

Von Neumann, J. (1941). Distribution of the ratio of the mean square successive difference to the variance. *The Annals of Mathematical Statistics*, 12(4), 367-395.

Wijngaard, J. B., Klein Tank, A. M. G., & Können, G. P. (2003). Homogeneity of 20th century European daily temperature and precipitation series. *International Journal of Climatology: A Journal of the Royal Meteorological Society*, 23(6), 679-692.

Wilhite, D. A., & Glantz, M. H. (1985). Understanding: the drought phenomenon: the role of definitions. *Water international*, 10(3), 111-120.

Yilmaz, M., & Tosunoglu, F. (2019). Trend assessment of annual instantaneous maximum flows in Turkey. *Hydrological Sciences Journal*, 64(7), 820-834.

14TH INTERNATIONAL CONFERENCE
ON HYDROSCIENCE & ENGINEERING

MAY 26-27, 2022
IZMİR-TURKEY

ICHE2022
IZMIR, TURKEY

EVALUATING THE POTENTIAL OF GRIDDED PRECIPITATION DATASETS FOR HYDROLOGICAL MODELING UNDER DIFFERENT CALIBRATION SCENARIOS

Hamed Hafizi

Civil Engineering, Eskisehir Technical University

Eskisehir, Turkey

Hydraulics and Hydraulic Structures, Kabul Polytechnic University

Kabul, Afghanistan

hamedhafizi@eskisehir.edu.tr

Ali Arda Sorman

Civil Engineering, Eskisehir Technical University

Eskisehir, Turkey

asorman@eskisehir.edu.tr

ABSTRACT: Precipitation is the most uncertain part of hydrologic cycle, and its accurate estimation requires a dense gauge network where their installation and maintenance are costly and more problematic over complex topography and remote regions. Moreover, precipitation with high spatial and temporal resolution is always recommended for streamflow prediction, which is limited for many catchments in Turkey. Hence, Gridded Precipitation Datasets (GPDs) from satellite and numerical weather prediction models or combining these sources can be an alternative to fill this shortcoming. This study aims to evaluate the consistency of four GPDs (MSWEPv2.8, CHIRPSv2.0, CFSR, and PDIR-Now) over time and space and assess their hydrological utility over a mountainous basin. The investigations are conducted at daily time step for five hydrologic years (October 2014–September 2019). Kling-Gupta Efficiency (KGE) and Hanssen-Kuiper (HK) skill score are utilized to compare GPDs with observed precipitation directly. Among selected GPDs, MSWEPv2.8 shows the highest performance (KGE; 0.36), and PDIR-Now presents the lowest (KGE; 0.02). Furthermore, the hydrological assessment is conducted with a conceptual hydrological model under different parameterization scenarios, in which the model parameters are calibrated by observed precipitation and each GPDs individually. The simulated streamflow by observed precipitation indicates the highest Nash-Sutcliffe Efficiency (NSE) value (0.84) compared to GPDs. For the calibration period, selected GPDs show high reproducibility when the model is calibrated by each GPD individually.

Keywords: Gridded Precipitation Datasets, Validation, Hydrological modeling, TUW, Turkey.

1. INTRODUCTION

Water resources management is one of the challenging tasks for hydrologists and decision-makers over data-scarce catchments (Behrangi et al., 2011). Further, remote sensing techniques have made an essential contribution to water resources management and development in recent decades (Hafizi and Kalkan, 2020). Additionally, the Passive Microwave (PMW) and Infrared (IR) satellite sensor information provide an indispensable opportunity for high spatio-temporal resolution precipitation estimates (Salmani-Dehaghi and Samani, 2021). Likewise, numerical weather prediction models are able to present Gridded Precipitation Datasets (GPDs) varies in spatial and temporal and could be an alternative for filling the data scarcity over highly elevated and remote regions (Jiang et al., 2021). Considering the input and technique utilized to retrieve the precipitation amount, Gridded Precipitation Datasets (GPDs) can be classified into four distinct groups: (a) utilizing rain gauges spatial information such as Global Precipitation Climatology Centre (GPCC) (Iizumi et al., 2017), (b)

employing PMW and IR satellite sensor information into their retrospective algorithms such as Precipitation Estimation from Remotely Sensed Information using Artificial Neural Networks-Dynamic Infrared Rain Rate near-real-time (PDIR-Now) (Nguyen et al., 2020), (c) those based on reanalysis data retrieved from numerical weather prediction model output such as Climate Forecast System Reanalysis (CFSR) (Saha et al., 2010), and (d) multi-source merging GPDs such as Multi-Source Weighted-Ensemble Precipitation (MSWEP) (Beck et al., 2019) and Climate Hazards group InfraRed Precipitation with Stations (CHIRPS) (Funk et al., 2015b).

In this context, hydrological models play a significant role in streamflow simulation and prediction while providing relevant information instead of simulating every realistic scenario to understand better the basin hydrologic characteristics (Nguyen et al., 2019; Singh, 2018).

Generally, two types of validation efforts are used by several authors whereby GPDs are evaluated either by direct comparison with gauge precipitation network (meteorological evaluation) or using them as a meteorological forcing in hydrologic models for streamflow prediction (hydrological evaluation) (Bitew and Gebremichael, 2011). Furthermore, the performance of some GPDs have been quantified by several authors over Turkey (Aksu and Akgül, 2020; Amjad et al., 2020; Derin and Yilmaz, 2014; Hafizi and Sorman, 2021; Saber and Yilmaz, 2018; Uysal et al., 2021; Uysal and Şorman, 2021).

The objective of this study is to assess the spatio-temporal consistency of four GPDs (MSWEPv2.8, CHIRPSv2.0, CFSR, and PDIR-Now) by direct comparison with observed precipitation, considering the seasonal variability of precipitation in daily time step, and hydrological utility under two different calibration scenarios for five hydrologic years from October 2014 to September 2019.

2. MATERIALS AND METHODS

2.1. Study Area

The Çukurkışla River Basin (Figure 1) is in the headwaters of Seyhan Basin located within the longitudes 36°02′ to 36°40′ E and latitudes 38°40′ to 38°01′ N. It has a drainage area of around 1510 km^2, with elevation ranging from 1312 m to 2952 m and the catchment is controlled by Göksu (E18A024) stream gauging station. The basin surface is covered by bare land (35.66 %), agricultural land (34.96 %), grassland (23.86 %), forest (5.09 %), urban area (0.33 %), and wetland (0.10 %). The topographic complexity, high altitude, and snow dominant characteristics of the basin are advantageous in validating GPDs and operating hydrologic models for areas under such difficult conditions.
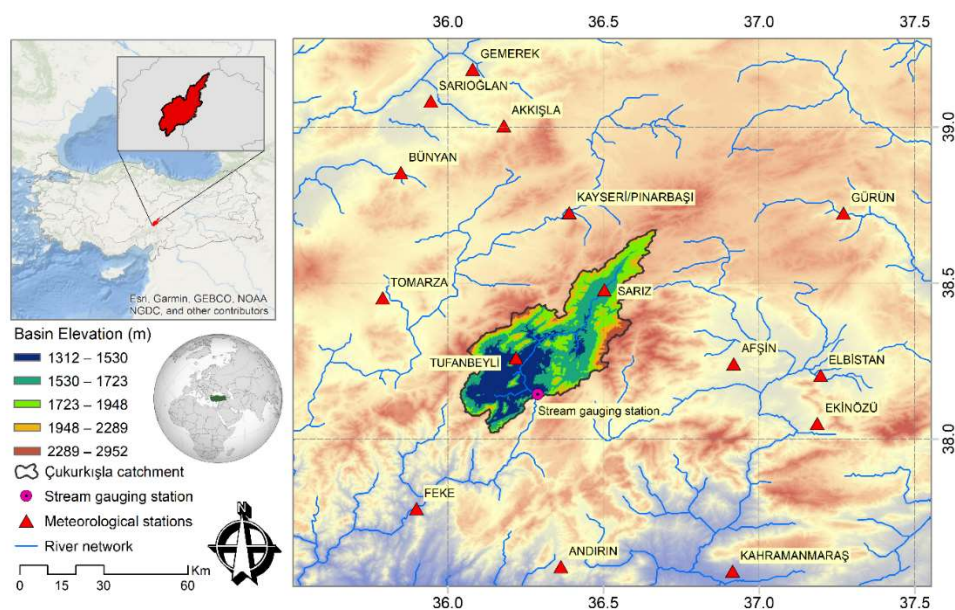
Figure 133. Geographical location, basin topography, and meteorological stations located around the study area

2.2. Data

In this context, four GPDs such as Multi-Source Weighted-Ensemble Precipitation (MSWEP) V2.8 (Beck et al., 2019), Climate Hazards group InfraRed Precipitation with Stations (CHIRPS) V2.0 (Funk et al., 2015a), The climate forecast system reanalysis (CFSR) (Saha et al., 2010), and Precipitation Estimation from Remotely Sensed Information using Artificial Neural Networks-Dynamic Infrared Rain Rate near-real-time (PDIR-Now) (Nguyen et al., 2020) were selected. Moreover, observed climate data from 15 stations are provided by the General Directorate of Meteorology (GDM), and the observed streamflow data at the outlet of basin is obtained from the General Directorate of Hydraulic Works (GDHW) in Turkey.

Table 1. Properties of selected GPDs. Abbreviations in the data source represent; G, Gauge; S, Satellite; and R, Reanalysis. Abbreviation in the spatial coverage represents; L, Land.

No	Dataset name	Data source(s)	Spatial resolution	Spatial coverage	Temporal resolution	Temporal coverage
1	MSWEPv2.8	G, S, R	0.10°	Global	3-hourly	1979–Present
2	CHIRPSv2.0	G, S, R	0.05°	L-50° N/S	Daily	1981–Present
3	CFSR	R	~ 0.31°	Global	Hourly	1979–Present
4	PDIR-Now	S	0.04°	60° N/S	Hourly	2000–Present

2.3. Evaluation Approach

In this study, the modified Kling-Gupta Efficiency (Kling et al., 2012) is utilized to evaluate the reliability of GPDs by direct comparison with observed precipitation. KGE is a relatively new performance metric combining Pearson correlation coefficient (r), the ratio of bias (β), and variability ratio (γ) components (Table 2). Furthermore, the Hanssen-Kuiper (HK) skill score is used to measure the detectability strength of GPDs by considering five precipitation intensity thresholds such as no-precipitation (less than 1 mm/day), light precipitation (1–5 mm/day), moderate precipitation (5–20 mm/day), heavy precipitation (20–40 mm/day) and violent precipitation (more than 40 mm/day) (Zambrano-Bigiarini et al., 2017).

Table 2. Statistical metrics used in the study (optimal value is unity for each of Indicators).

Indicators	Mathematical statements	Remarks
Kling-Gupta Efficiency and its components	$KGE=1-[(r-1)^2+(\beta-1)^2+(\gamma-1)^2]^{0.5}$ $r=\frac{1}{n}\sum_{1}^{n}(o_n-\mu_0)(s_n-\mu_s)/(\delta_o\times\delta_s),$ $\beta=\frac{\mu_s}{\mu_o},\qquad \gamma=(\delta_s\times\mu_o)/(\mu_s\times\delta_o)$	*R (Pearson correlation coefficient), β (the ratio of bias)* is the ratio of estimated and observed mean, *γ (Variability ratio)* is the ratio of estimated and observed coefficients of variation, *μ* and *δ* are the distribution mean and standard deviation where *s* and *o* indicate estimated and observed. *M (Miss)*; when the observed precipitation is not detected. *F (False)*; when the precipitation is detected but not observed, *H (Hit)*; when the observed precipitation is correctly detected, *CN (Correct Negative)*; a no precipitation event is detected. *n* is the sample size of th observed or calculated streamflow. Q_i^{ob} and Q_i^{sim} present the observed and simulated streamflow, $\overline{Q_t^{ob}}$ present the mean observed streamflow.
Hanssen-Kuiper	$HK=\frac{(H\times CN)-(F\times M)}{(H+M)\,(F+CN)}$	
Nash-Sutcliffe Efficiency	$NSE=1-\frac{\sum_{i=1}^{n}(Q_i^{sim}-Q_i^{ob})^2}{\sum_{i=1}^{n}(Q_i^{ob}-\overline{Q_i^{ob}})^2}$	

Moreover, for the hydrologic utility of GPDs, Nash-Sutcliffe Efficiency (NSE) and KGE statistical metrics are utilized. Overall, two scenarios are considered for streamflow simulation by GPDs; when the model parameters are calibrated by observed precipitation, the observed precipitation is replaced by each GPD (Scheme-1), and the model parameters are calibrated by each GPD individually. The conceptual TUW model (Parajka et al., 2007) is exploited for streamflow prediction, where its structure is similar to the HBV model. TUW model with 15 calibration parameters (Table 3) is able to simulate the runoff, snow and soil moisture, and the inputs are total daily precipitation (mm), mean

daily air temperature (°C) and daily potential evapotranspiration (mm). The PET is calculated using daily minimum and maximum near-surface air temperature (Hargreaves and Samani, 1985).

Table 3. TUW model parameter properties. Abbreviations in the process column represent; S, Snow; SM, Soil Moisture; and R, Runoff.

No	ID	Description	Units	Process	Range
1	SCF	Snow correction factor	-	S	0.9–1.5
2	DDF	Degree-day factor	mm/°C /day	S	0.0–5.0
3	Tr	Temperature threshold above which precip. is rain	°C	S	1.0–3.0
4	Ts	Temperature threshold below which precip. is snow	°C	S	−3.0–1.0
5	Tm	Temperature threshold above which melt starts	°C	S	−2.0–2.0
6	LPrat	Parameter related to the limit for potential evaporation	-	SM	0.0–1.0
7	FC	Field capacity	mm	SM	0.0–600
8	BETA	Non-linear parameter for runoff production	-	SM	0.0–20
9	cperc	Constant percolation rate	mm/day	SM	0.0–8.0
10	k0	Storage coefficient for very fast response	day	R	0.0–2.0
11	k1	Storage coefficient for fast response	day	R	2.0–30
12	k2	Storage coefficient for slow response	day	R	30–250
13	lsuz	Threshold storage state	mm	R	1.0–100
14	bmax	Maximum base at low flows	day	R	0.0–30
15	croute	Free scaling parameter	day^2/mm	R	0.0–50

3. RESULT AND DISCUSSION

3.1. Spatio-Temporal Evaluation of Daily Precipitation

Figure 2 displays the mean daily precipitation and bias at the station location derived from observed precipitation and selected GPDs for the entire period (2015–2019). Considering the observed precipitation, most stations record daily precipitation ranging from 1.0 to 1.5 mm. Moreover, the southwestern part stations show higher precipitation amounts, comparatively. Overall, MSWEPv2.8 and CHIRPSv2.0 present mean daily precipitation close to observed precipitation inside the basin, while CFSR and PDIR-Now exabit mean daily precipitation between 1.5 to 2.0 mm.
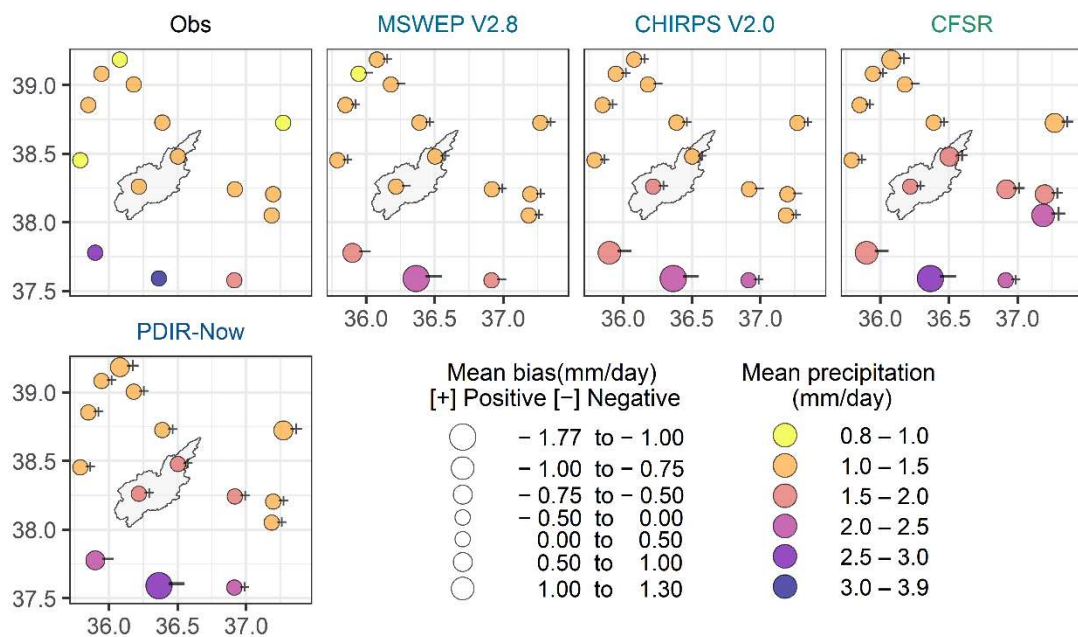
Figure 2. Mean daily precipitation at the station location derived from observed precipitation and four GPDs for the entire period. The title color presents the source(s) of GPDs: satellite (blue), reanalysis (green), reanalysis, ground, and satellite (steel blue).

Substantially, GPDs underestimate mean daily precipitation in the southwestern stations and show relatively low precipitation bias over the rest stations.

Figure 3 presents the mean daily precipitation and bias at the regional scale retrieved from observed precipitation and selected GPDs for the entire period and four seasons. In consideration of observed precipitation, the region experiences 1.4 mm mean daily precipitation for the entire period where high precipitation amount is measured during the winter and spring seasons (around 2 mm/day), and the region receives the lowest precipitation amount during the summer (0.51 mm/day) followed by autumn season (1 mm/day). All GPDs show the close precipitation pattern compared to observed for the entire period and four seasons. However, MSWEPv2.8 and CHIRPSv2.0 show less precipitation bias than the CFSR and PDIR-Now. MSEWPv2.8 consistently underestimates mean daily precipitation, but the bias is not exceeded to 0.18 mm/day. In the same way, CHIRPSv2.0 shows slightly higher precipitation estimates during the summer and autumn and underestimates precipitation during the spring and winter seasons. Among selected GPDs, CFSR shows the highest overestimation of mean daily precipitation (bias; 0.73 mm) during the winter season, followed by PDIR-Now (bias; 0.37 mm) through the autumn season.
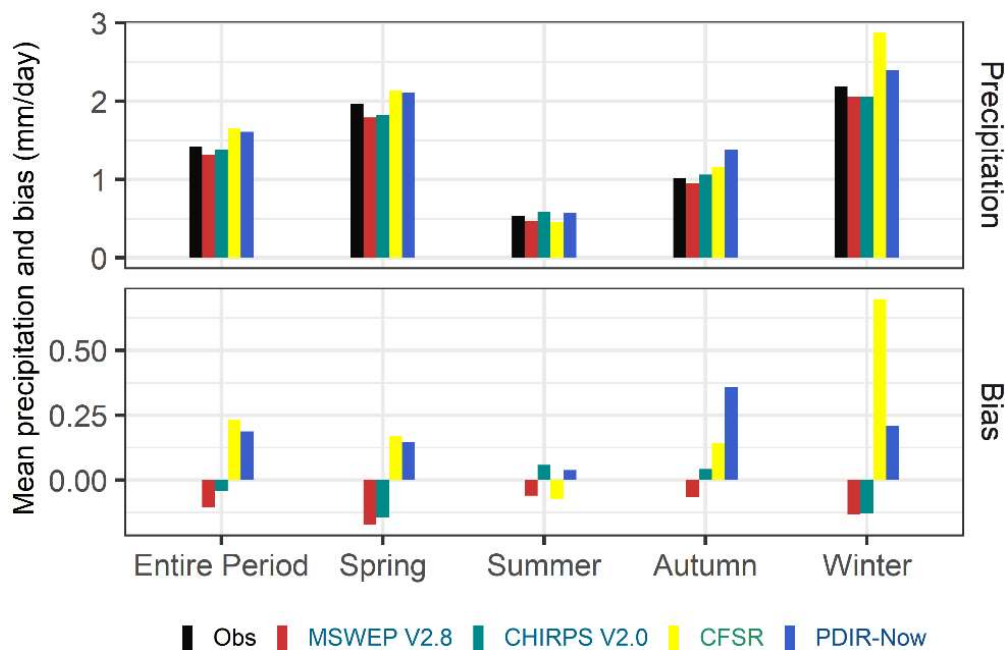
Figure 3. Mean daily precipitation at the regional scale is derived from observed precipitation and four GPDs for the entire period and four seasons. The legend color presents the source(s) of GPDs: satellite (blue), reanalysis (green), reanalysis, ground, and satellite (steel blue)

3.2. GPDs Reliability over Time and Space

Figure 4 maps the reliability of GPDs at the grid-cell level expressed in the form of Kling-Gupta Efficiency (KGE), along with its Pearson correlation coefficient (r), the ratio of bias (β), and variability ratio (γ) components for the entire period (2015–2019). MSWEPv2.8 shows the highest performance by demonstrating high KGE (0.30–0.40) and correlation (0.40–0.55) over many stations. Furthermore, MSWEPv2.8 underestimates both the ratio of bias (0.75–1.00) and variability ratio (0.70–0.80). In the same way, CFSR comes with the second-best performance. However, this dataset shows poor performance over some stations (KGE less than zero) and dispersion correlation, the ratio of bias, and variability ratio. Further, CFSR presents high performance in the southern parts (KGE; 0.30–0.50, r; 0.40–0.55). CHIRPSv2.0 shows higher performance in the eastern part stations (KGE; 0.00–0.20) than the western stations (KGE; 0.20–0.30), where it shows higher correlation in the southeastern (r; 0.20–0.40) station compared to northwestern stations (r; 0.10–0.20) with mostly 1.00 to 1.25 ratio of bias and 0.85 to 1.00 variability ratio appears for most stations. Finally, PDIR-Now shows the lowest performance (KGE; less than 0.20) among selected GPDs and presents weaker performance in the northwestern stations. Nevertheless, there are some discrepancies in the ratio of

bias and variability ratio. Looking at the performance of GPDs at the station location, MSWEPv2.8 exhibits promising performance followed by CFSR and CHIRPSv2.0, where PDIR-Now was not able to present reliable precipitation at the grid-cell level as the rest of the selected GPDs.
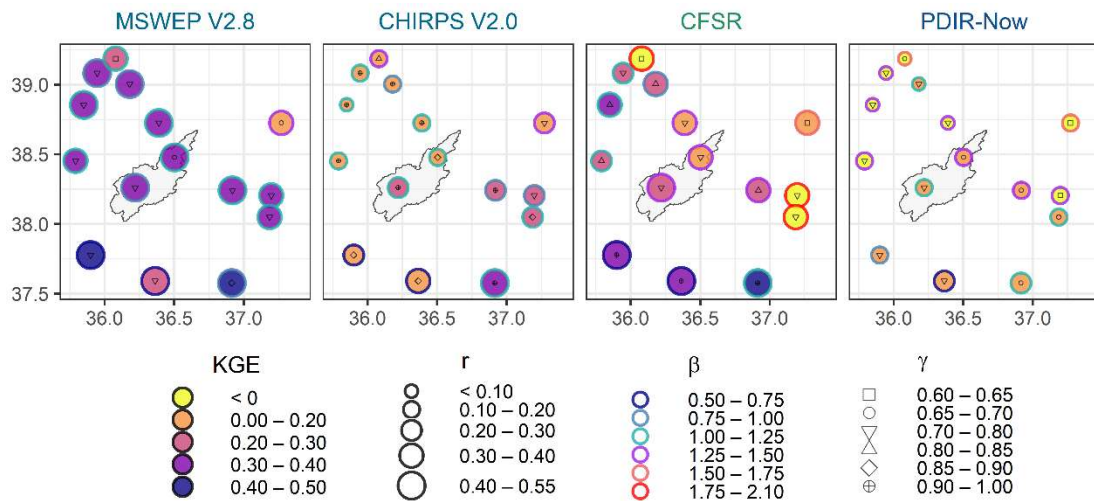
Figure 4. GPD reliability at the grid-cell level is expressed in the form of KGE and its three components for the entire period (2015–2019). The title color presents the source(s) of GPDs: satellite (blue), reanalysis (green), reanalysis, ground, and satellite (steel blue).

Figure 5 shows the consistency of GPDs at the regional scale expressed in the form of KGE and its three components (correlation, the ratio of bias, and variability ratio) for the entire period and all four seasons (spring, summer, autumn, and winter) at daily time step. All GPDs show low performance during the summer season. MSWEPv2.8 shows the highest performance considering the entire period (KGE; 0.36) and seasonal precipitation. CFSR shows the second-best performance for the entire period, and spring, summer, and autumn seasons, where this dataset shows weak performance during the winter season due to the highest bias that noticed for CFSR (bias; 1.65). Moreover, CHIRPSv2.0 demonstrated higher performance than CFSR during the winter season (KGE; 0.22). Finally, PDIR-Now figured out summer and autumn precipitation slightly better than the spring and winter seasons precipitation, and its performance is worst compared to other GPDs.
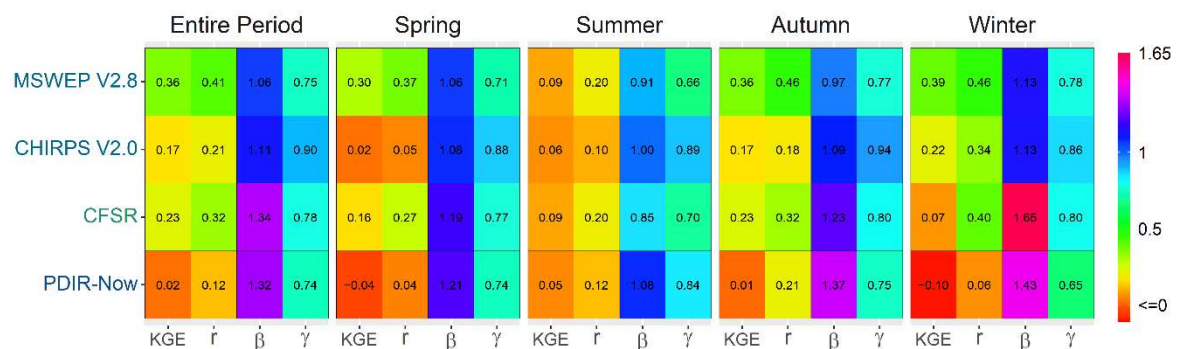
Figure 34. GPD reliability at the regional scale is expressed in the form of KGE and its three components for the entire period (2015–2019) and four seasons. The y axis color presents the source(s) of GPDs: satellite (blue), reanalysis (green), reanalysis, ground, and satellite (steel blue)

3.3. Evaluation of GPDs Detectability

Figure 6 presents the detectability strength of GPDs for five precipitation intensities at the regional scale expressed in the form of Hanssen-Kuiper (HK) skill score considers the entire period and seasonal precipitation. Overall, GPDs show high skill for precipitation events less than 1mm/day. GPDs show different detectability strengths for precipitation with specific intensity. MSWEPv2.8 exhibits higher detectability than the other GPDs. However, some GPDs such as CFSR and CHIRPSv2.0 outperform MSWEPv2.8 for heavy precipitation. CHIRPSv2.0 shows poor detectability

for light precipitation compared to selected GPDs. Moreover, GPDs show slightly higher detectability for moderate precipitation than ligth precipitation, where they show poor detectability for violent precipitation. The uneven detection ability of GPDs for different precipitation is partly due to the demanding classification criteria: five categories of precipitation intensities are utilized instead of the typical two classes (rain/no-rain), consistent with earlier studies concerned with GPDs validations (Hafizi and Sorman, 2022; Zambrano-Bigiarini et al., 2017).
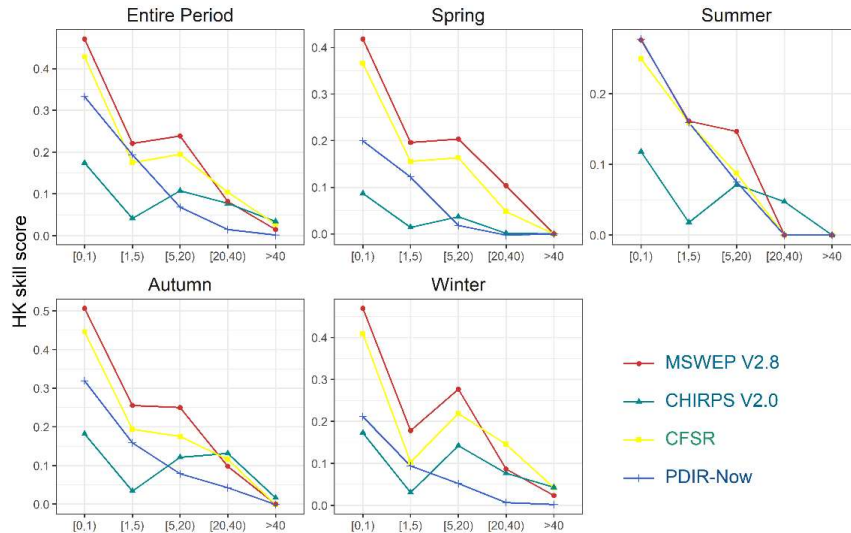
Figure 6. GPD detectability strength at the regional scale expressed in the form of Hanssen-Kuiper (HK) skill score for five different intensities considering the entire period and four seasons. The legend color presents the source(s) of GPDs: satellite (blue), reanalysis (green), reanalysis, ground, and satellite (steel blue)

3.4. Evaluation of GPDs Ability for Streamflow Simulation

The TUW was used for streamflow simulation at the Göksu (E18A024) stream gaging station located in the outlet of Çukurkışla River Basin. Figure 7 displays the hydrographs of observed and simulated streamflow for different precipitation inputs considering two-year calibration (2015–2016) and three-year validation (2017–2019). The model parameters are calibrated in two ways. Primarily, the model parameters are calibrated by observed precipitation then the observed precipitation is replaced by each GPD (Scheme-1). Afterward, the model parameters are calibrated by each GPDs individually (Scheme-2). Among GPDs, both CFSR and PDIR-Now show high degradation (overestimation) of daily streamflow.
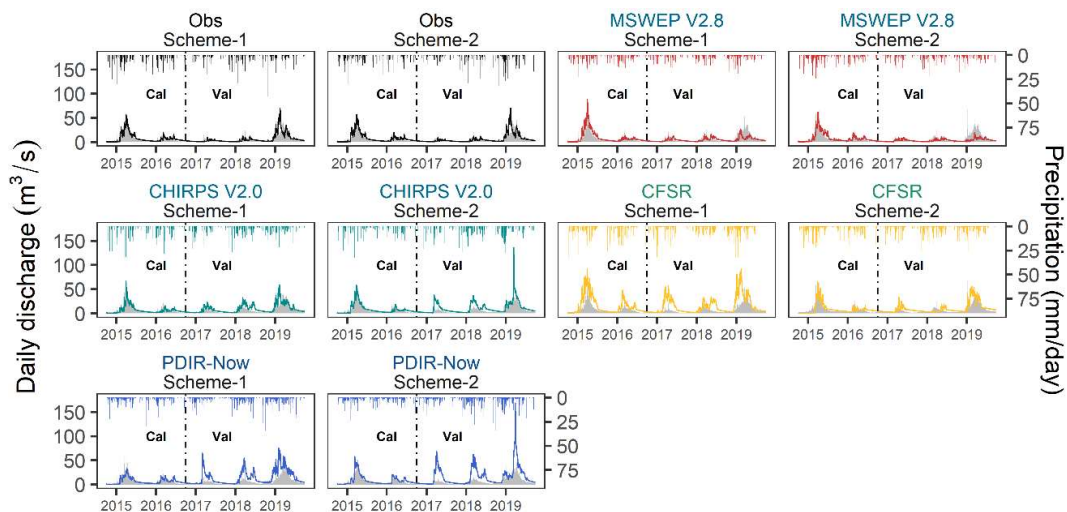
Figure 7. Streamflow simulation based on observed precipitation and selected GPDs for both calibration (Cal) and validation (Val) periods. The title color presents the source(s) of GPDs: satellite (blue), reanalysis (green), reanalysis, ground, and satellite (steel blue)

Figure 8 shows the result of statistical metrics computed between the observed and simulated daily streamflow for two schemes considering calibration, validation, and entire period time steps.

When the model is forced for streamflow simulation with observed precipitation, it shows pretty high ability of streamflow reproducibility for the calibration period (NSE; 0.84, KGE; 0.92) with almost no bias and variability ratio. For the validation period, simulated streamflow by observed precipitation shows lower ability (NSE; 0.38, KGE; 0.61) than the calibration period. The less efficient streamflow prediction for the validation period is partly due to the singularity of the 2019 hydrologic year, where the region received higher precipitation than the other years. In scheme-1, All GPDs (Except CFSR) show high streamflow reproducibility for the calibration period. CHIRPSv2.0 comes with the second-highest ability of streamflow simulation after observed precipitation for both calibration (KGE; 0.74) and validation (KGE; 0.56) periods. Moreover, PDIR-Now shows higher NSE (0.65) and lower KGE (0.68) than MSWEPv2.8 for the calibration period, presenting less streamflow prediction ability for the validation period. As a result, in scheme-1, CFSR presents streamflow simulation with high ratio of bias, and CHIRPSv2.0 shows the higher skill of streamflow reproducibility for both calibration and validation periods. Considering scheme-2, all GPDs show good streamflow reproducibility for the calibration period, whereas for the validation period, both CHIRPSv2.0 and MSWEPv2.8 show lower ability than scheme-1. Moreover, CFSR shows the highest KGE (0.57) and NSE (0.32) among selected GPDs in the validation period. On the other hand, PDIR-Now becomes worst in the validation period than scheme-1 and presents the highest ratio of bias (2.20) among GPDs.

Considering both schemes, multi-source merged GPDs (CHIRPSv2.0 and MSWEPv2.8) show reliable streamflow simulation than the satellite-based (PDIR-Now) and reanalysis (CFSR) GPDs in scheme-1. While in scheme-2, CFSR shows the highest performance for the validation period.
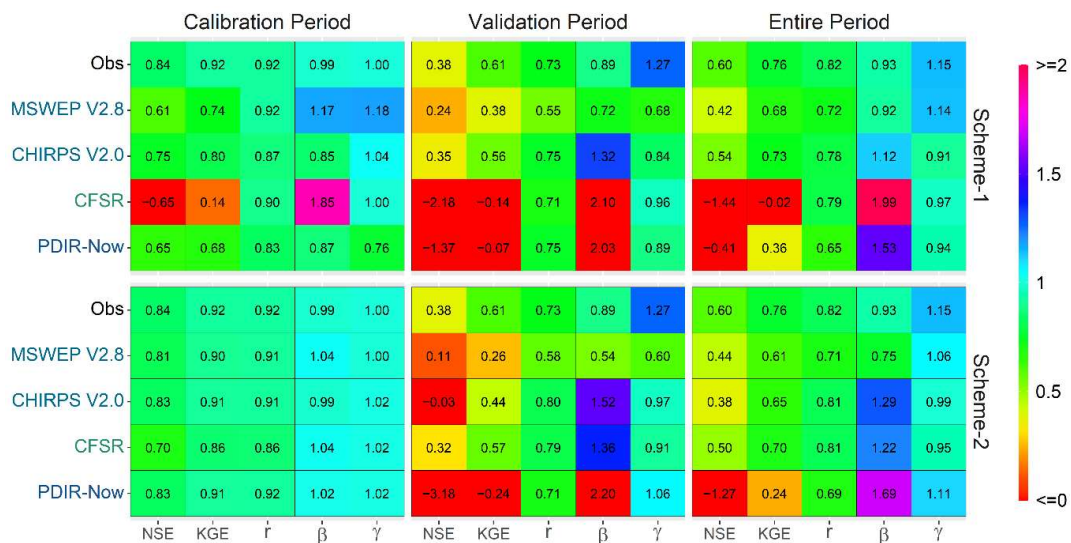
Figure 8. Statistical metrics computed between the observed and simulated daily streamflow forced by the observed precipitation (Scheme-1) and each GPDs individually (Scheme-2), respectively. The y axis color presents the source(s) of GPDs: satellite (blue), reanalysis (green), reanalysis, ground, and satellite (steel blue).

Figure 9 shows the TUW model calibrated parameters for observed precipitation and four GPDs. The green horizontal lines show the upper and lower bound of each parameter.

From the result, MSWEPv2.8 has the highest SCF value, where CFSR shows unusual K2 and Croute parameter values. Moreover, observed precipitation and four GPDs show lower cperc and bmax than these parameters' upper bound. In the same way, PDIR-Now presents the highest lsuz value among selected GPDs and observed precipitation.

Further uncertainties arising from meteorological forcing due to the existing bias in the GPDs, as noticed in section 3.2 and hydrological models, may indeed affect streamflow prediction. However, a comprehensive sensitivity/uncertainty analysis is not investigated within the scope of this study.
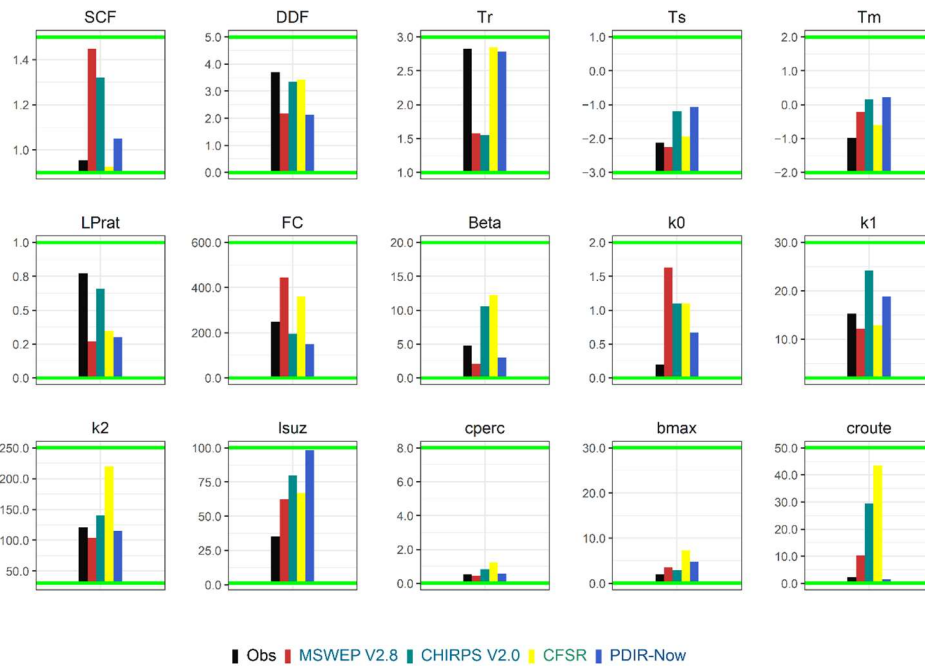
Figure 9.35 Optimum model parameters for observed precipitation and four GPDs. The legend color presents the source(s) of GPDs: satellite (blue), reanalysis (green), reanalysis, ground, and satellite (steel blue).

4. CONCLUSIONS

In this context, the spatio-temporal and hydrological utility of four GPDs (MSWEPv2.8, CHIRPSv2.0, CFSR, and PDIR-Now) are investigated over Çukurkışla River Basin considering five hydrologic years (October 2014 to September 2019). The reliability of GPDs are evaluated based on 15 precipitation gauges and one stream gauging station (E18A024). The KGE, including its three components (Pearson correlation coefficient, the ratio of bias, and variability ratio), NSE, and one categorical metric (Hanssen-Kuiper skill score), are selected for meteorological and hydrological evaluation. Essential conclusions are summarized below.

- Among selected GPDs, MSWEPv2.8 presents the highest reliability of precipitation estimates over time and space where CFSR comes with the second-best performance and outperforms CHIRPSv2.0 for the entire period, spring, summer, and autumn seasons, but this dataset shows poor performance for winter season precipitation (KGE; 0.07) than CHIRPSv2.0 (KGE; 0.22). PDIR-Now, the only satellite-based precipitation dataset, shows comparatively the worst performance.
- GPDs show high detectability for low-intensity precipitation, and their detectability strength decreases by increasing precipitation intensities. However, except for CHIRPSv2.0, all GPDs show higher detectability strength for heavy precipitation than moderate precipitation, and CHIRPSv2.0 shows an unclear pattern for different precipitation intensities.
- Overall, multi-source GPDs (MSWEPv2.8 and CHIRPSv2.0) show promising ability for streamflow prediction compared to a reanalysis (CFSR) and satellite-based (PDIR-Now) precipitation datasets in scheme-1.
- In a mountainous basin, CFSR shows higher performance (KGE; 0.23) in the direct comparison with observed data, while satellite-based precipitation (PDIR-Now) shows better streamflow prediction ability for the calibration period in scheme-2.
- All GPDs show high streamflow reproducibility for the calibration period when the model is calibrated by each GPD individually.

This study confirms the outperformance of MSWEPv2.8 over other GPDs considering the meteorological evaluations. Considering both schemes for the streamflow simulation, CHIRPsv2.0 and MSWEPv2.8 seem more reliable. Moreover, reanalysis (CFSR) and satellite-based (PDIR-Now) precipitation datasets show weak performance over snow dominant region in the winter season.

Future work will include more GPDs for direct precipitation comparison and hydrologic simulations over other basins of Turkey.

REFERENCES

Aksu, H., & Akgül, M. A. (2020). Performance evaluation of CHIRPS satellite precipitation estimates over Turkey. *Theoretical and Applied Climatology, 142*(1), 71-84. doi:10.1007/s00704-020-03301-5

Amjad, M., Yilmaz, M. T., Yucel, I., & Yilmaz, K. K. (2020). Performance evaluation of satellite-and model-based precipitation products over varying climate and complex topography. *Journal of Hydrology, 584*, 124707. doi:10.1016/j.jhydrol.2020.124707

Beck, H. E., Wood, E. F., Pan, M., Fisher, C. K., Miralles, D. G., Van Dijk, A. I., . . . Adler, R. F. (2019). MSWEP V2 global 3-hourly 0.1 precipitation: methodology and quantitative assessment. *Bulletin of the American Meteorological Society, 100*(3), 473-500. doi:10.1175/BAMS-D-17-0138.1

Behrangi, A., Khakbaz, B., Jaw, T. C., AghaKouchak, A., Hsu, K., & Sorooshian, S. (2011). Hydrologic evaluation of satellite precipitation products over a mid-size basin. *Journal of Hydrology, 397*(3-4), 225-237.

Bitew, M. M., & Gebremichael, M. (2011). Evaluation of satellite rainfall products through hydrologic simulation in a fully distributed hydrologic model. *Water Resources Research, 47*(6). doi:10.1029/2010WR009917

Derin, Y., & Yilmaz, K. K. (2014). Evaluation of Multiple Satellite-Based Precipitation Products over Complex Topography. *Journal of Hydrometeorology, 15*(4), 1498-1516. doi:10.1175/JHM-D-13-0191.1

Funk, C., Peterson, P., Landsfeld, M., Pedreros, D., Verdin, J., Shukla, S., . . . Hoell, A. (2015). The climate hazards infrared precipitation with stations—a new environmental record for monitoring extremes. *Scientific data, 2*(1), 1-21. doi:10.1038/sdata.2015.66

Funk, C., Verdin, A., Michaelsen, J., Peterson, P., Pedreros, D., & Husak, G. (2015). A global satellite-assisted precipitation climatology. *Earth System Science Data, 7*(2), 275.

Hafizi, H., & Kalkan, K. (2020). Evaluation of Object-Based Water Body Extraction Approaches Using Landsat-8 Imagery. *Journal of Aeronautics and Space Technologies, 13*(1), 81-89.

Hafizi, H., & Sorman, A. A. (2021). Assessment of Satellite and Reanalysis Precipitation Products for Rainfall–Runoff Modelling in a Mountainous Basin. *Environmental Sciences Proceedings, 8*(1), 25.

Hafizi, H., & Sorman, A. A. (2022). Assessment of 13 Gridded Precipitation Datasets for Hydrological Modeling in a Mountainous Basin. *Atmosphere, 13*(1), 143. doi:10.3390/atmos13010143

Hargreaves, G. H., & Samani, Z. A. (1985). Reference crop evapotranspiration from temperature. *Applied engineering in agriculture, 1*(2), 96-99. doi:10.13031/2013.26773

Iizumi, T., Takikawa, H., Hirabayashi, Y., Hanasaki, N., & Nishimori, M. (2017). Contributions of different bias-correction methods and reference meteorological forcing data sets to uncertainty in projected temperature and precipitation extremes. *Journal of Geophysical Research: Atmospheres, 122*(15), 7800-7819.

Jiang, Y., Yang, K., Shao, C., Zhou, X., Zhao, L., Chen, Y., & Wu, H. (2021). A downscaling approach for constructing high-resolution precipitation dataset over the Tibetan Plateau from ERA5 reanalysis. *Atmospheric Research, 256*, 105574.

Kling, H., Fuchs, M., & Paulin, M. (2012). Runoff conditions in the upper Danube basin under an ensemble of climate change scenarios. *Journal of Hydrology, 424*, 264-277. doi:10.1016/j.jhydrol.2012.01.011

Nguyen, H. H., Recknagel, F., Meyer, W., Frizenschaf, J., Ying, H., & Gibbs, M. S. (2019). Comparison of the alternative models SOURCE and SWAT for predicting catchment streamflow, sediment and nutrient loads under the effect of land use changes. *Science of The Total Environment, 662*, 254-265. doi:10.1016/j.scitotenv.2019.01.286

Nguyen, P., Ombadi, M., Gorooh, V. A., Shearer, E. J., Sadeghi, M., Sorooshian, S., . . . Ralph, M. F. (2020). PERSIANN Dynamic Infrared–Rain Rate (PDIR-Now): A Near-Real-Time, Quasi-Global Satellite Precipitation Dataset. *Journal of Hydrometeorology, 21*(12), 2893-2906. doi:10.1175/JHM-D-20-0177.1

Parajka, J., Merz, R., & Blöschl, G. (2007). Uncertainty and multiple objective calibration in regional water balance modelling: case study in 320 Austrian catchments. *Hydrological Processes: An International Journal, 21*(4), 435-446. doi:10.1002/hyp.6253

Saber, M., & Yilmaz, K. K. (2018). Evaluation and bias correction of satellite-based rainfall estimates for modelling flash floods over the Mediterranean region: application to Karpuz River Basin, Turkey. *Water, 10*(5), 657. doi:10.3390/w10050657

Saha, S., Moorthi, S., Pan, H.-L., Wu, X., Wang, J., Nadiga, S., . . . Behringer, D. (2010). The NCEP climate forecast system reanalysis. *Bulletin of the American Meteorological Society, 91*(8), 1015-1058. doi:10.1175/2010BAMS3001.1

Salmani-Dehaghi, N., & Samani, N. (2021). Development of bias-correction PERSIANN-CDR models for the simulation and completion of precipitation time series. *Atmospheric Environment, 246*, 117981.

Singh, V. P. (2018). Hydrologic modeling: progress and future directions. *Geoscience Letters, 5*(1), 1-18. doi:10.1186/s40562-018-0113-z

Uysal, G., Hafizi, H., & Sorman, A. A. (2021). *Spatial and temporal evaluation of multiple gridded precipitation datasets over complex topography and variable climate of Turkey.* Paper presented at the EGU General Assembly Conference Abstracts.

Uysal, G., & Şorman, A. Ü. (2021). Evaluation of PERSIANN family remote sensing precipitation products for snowmelt runoff estimation in a mountainous basin. *Hydrological Sciences Journal*, 1-18.

Zambrano-Bigiarini, M., Nauditt, A., Birkel, C., Verbist, K., & Ribbe, L. (2017). Temporal and spatial evaluation of satellite-based rainfall estimates across the complex topographical and climatic gradients of Chile. *Hydrology and Earth System Sciences, 21*(2), 1295. doi:10.5194/hess-21-1295-2017

MULTI-OBJECTIVE HYDROLOGIC MODEL CALIBRATION FOR RUNOFF FORECASTING

Y. Oğulcan Doğan

Department of Civil Eng., Eskişehir Technical University, Eskişehir, Turkey

Eskişehir, Turkey

fbogulcan06@gmail.com

A. Arda Şorman

Department of Civil Eng., Eskişehir Technical University, Eskişehir, Turkey

Eskişehir, Turkey

asorman@eskisehir.edu.tr

Aynur Şensoy

Department of Civil Eng., Eskişehir Technical University, Eskişehir, Turkey

Eskişehir, Turkey

asensoy@eskisehir.edu.tr

ABSTRACT: The increase in global temperatures negatively affects the ever-increasing world population, revealing the importance of the science of hydrology. Efficient planning, drought, and flood control are critical in managing water resources. For this reason, it is important to monitor the amount of snow accumulated in the high parts of the Çoruh Basin, which hosts the important dams such as Yusufeli and Deriner, and to make the necessary runoff forecasts. Since most of the flow is formed by snowmelt in the spring and early summer months, various surface analyses were carried out and the region's snow potential was determined using satellite snow products. A hydrological modeling study was carried out with HBV and the model was calibrated with multi- objective functions for 2003-2015 water years. A multi-objective hydrological modeling study was tested with the Monte Carlo method using snow-covered area values obtained from satellite images together with runoff data. The results indicate better model performance and increased accuracy in snow states. As a final result, ensemble runoff forecasts are generated with the best model parameters using day ahead numerical weather prediction data for a selected snowmelt period.

1. INTRODUCTION

Climate changes with global warming and the rapidly developing world population affect water resources in many ways. In this context, the necessity of the science of hydrology emerges. Hydrological modeling studies, especially in the snowy areas, will benefit the flow estimates and contribute to the increase in the efficiency of natural water resources. The optimum operation of the dams and the flood control depend on these flow estimates. Turkey's average altitude is 1140 m and mountainous areas increase from west to east. These topographically rugged regions make it challenging to collect hydro-meteorological data. These situations reveal the importance of snow modeling in the region.

The aim of the study is multi-objective hydrological modeling and flow estimation with data obtained from satellite images in a basin with high snow potential in our country. The upstream part of the Çoruh Basin, where a significant amount of energy production is provided in Turkey, has been chosen as the study area. With this study, the modeling of the precipitation-runoff relationship in a high-altitude basin fed mainly with snow is realized. Additionally, multi-objective modeling is used with the snow-covered area data obtained from the satellite images due to insufficient ground measurement

data. Therefore, the seasonal snow potential of the basin is determined using 500 m resolution MODIS satellite products. HBV model, which is a conceptual hydrological model to determine the precipitation-runoff relationship of the basin, is chosen. The success of the flow estimation with the multi-purpose calibrated model is assessed. For this purpose, flow forecasting studies were carried out using lead day numerical weather forecast data. The study achievements provide an exemplary decision support system by contributing to the more efficient and safe operation of the large dams on the basin and the important water structures planned in the future.

2. STUDY AREA AND DATA

2.1. Study Area

The Çoruh River originates from the western slopes of the Mescit Mountains at an altitude of 3255 m, passes through Bayburt, Erzurum and Artvin then exits the borders of Turkey. The river has a total length of 431 km with its tributaries, only 20 km of which is within the boundaries of Georgia. Çoruh Basin is one of Turkey's 25 hydrological basins with a total precipitation area of 22,100 km^2, and it is the one with the highest slope among these basins. The Çoruh River, which has an annual average flow volume of 6.3 billion m^3, provides high hydroelectricity potential. Erosion and avalanche problems pose an important issue for the region. In addition, since it is in the category of transboundary waters, it is important to measure and control river water. The study basin is located between 40º 02′ – 40º 24′ N latitudes and 40º 12′ – 41º 10′ E longitudes, and at its outlet is the E23A004 Çoruh-Bayburt stream gaging station (AGI) operated by the State Hydraulic Works (DSI) (Figure 1).
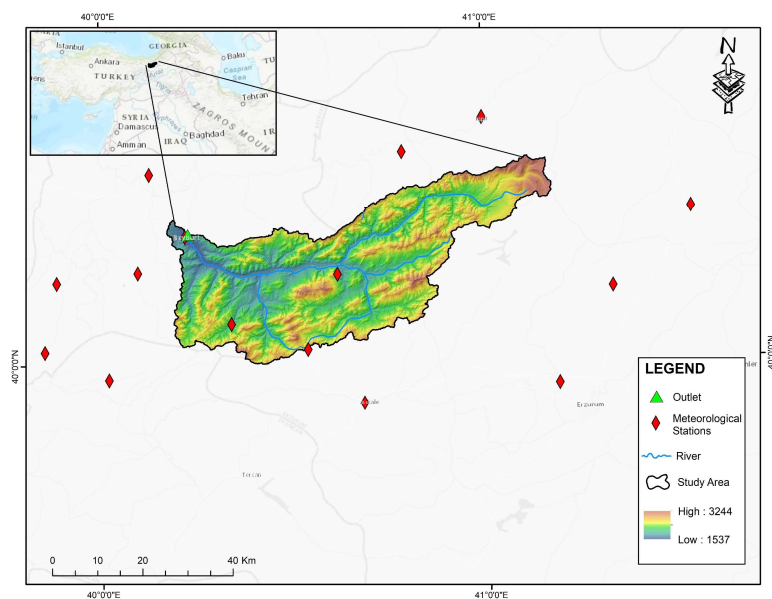
Figure 1. Location, topography and observation network of the basin

2.2. Satellite Data Analysis

Manual or automatic snow measurements in mountainous terrain can only represent the measured point and its immediate vicinity. The most effective way to monitor near real-time snow cover change on an extensive spatial basis is to use satellite images. Especially the area covered by snow accumulating in winter months and the changes in the melting snow during spring and early summer months in different locations and elevations can easily be monitored using satellite images. Due to the reflective properties of snow, snow cover monitoring with current remote sensing methods is best done in the visible (VIS) and near infrared (NIR) regions of the electromagnetic spectrum (Hall et al., 2002). On the other hand, the cloud situation mainly affects the snow cover monitored with optical imagers. MODIS and IMS satellite images are used in this study to track snow-covered area. An example of data is provided in Figure 2.
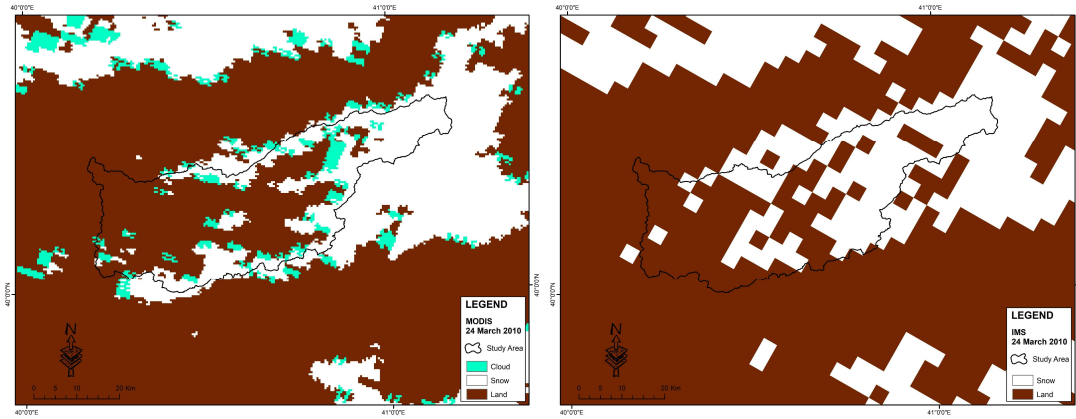
Figure 2. Snow cover images for 24 March 2010 a)MODIS b)IMS

3. METHODOLOGY AND RESULTS

Modeling the precipitation-runoff relationship in a hydrological basin is a complex process. In this study, the HBV model, one of the conceptual hydrological models, expresses the precipitation-flow relationship with the observed data through simple mathematical equations. The HBV (Hydrologiska Byrans Vattenbalansavdelning) model was developed in 1972 due to the need for flow prediction and flood warning into the reservoir. Today, it is used in many different versions (Bergström et al, 2002; Bergström and Lindström, 2015). The HBV model used in this study is the memorLight version with a graphic interface and automatic calibration option developed by Seibert and Vis (2012).

Since the HBV-Light model is a conceptual model, it is necessary to modify the parameters provided by the model so that the outputs produced are consistent with the values measured in the field. The calibration for the model parameters is done with the data measured during specific periods of application. Various automatic calibration methods have been developed, the methods presented in this study are Genetic Algorithm and Powell (GAP) Optimization method and Monte Carlo (MC) methods, which produce the best model parameters and random model parameter sets compatible with normal distribution, respectively. The performance metrics used in the multi-objective calibration is given in Equation 1-3.

$$\text{NSE} \qquad 1 - \frac{\sum (Q_{obs} - Q_{Mod})^2}{\sum (Q_{obs} - \overline{Q_{obs}})^2} \qquad (1)$$

$$\text{SCA\_RMSE} \qquad 1 - \sqrt{\frac{1}{n} (SCA_{Mod} - SCA_{obs})^2} \qquad (2)$$

$$\text{MARE} \qquad 1 - \frac{1}{n} \sum \frac{|Q_{obs} - Q_{Mod}|}{Q_{obs}} \qquad (3)$$

Evaluation of model performance was made with single and multiple criteria obtained from different objective functions. The MC method, which produces random model parameter sets compatible with the normal distribution, was used in the study performed with the objective functions specified and their different combinations.

In the hydrological modeling phase with the multi-criteria structure; the goal is to obtain the best 100 parameter sets with successful performance for 100,000 MC simulations in the overall ranking according to the criteria of high and low flow and snow-covered area. For this purpose, it is aimed to obtain parameter sets with the most successful performance in terms of basin representation according to the objective functions specified in the calibration period including the 2003-2009 water years. The best performance is obtained for the combination of all objectives (NSE; SCA-RMSE; MARE) with an overall ranking of 0.94. Then combination of high flows and snow cover (NSE; SCA-RMSE)

provides 0.91 and low flows and snow cover (SCA-RMSE; MARE) provides 0.80 over all combinations.

A day lead time runoff forecast analysis was also analyzed for the main melting period of 2015 water year. Numerical Weather Prediction data for daily total precipitation and average temperature, together with the best model parameter data set obtained with multi-calibration and MC simulation to forecast a day lead time runoff value. The average of daily runoff forecasts (best parameter set) are given with observed discharges in Figure 3.
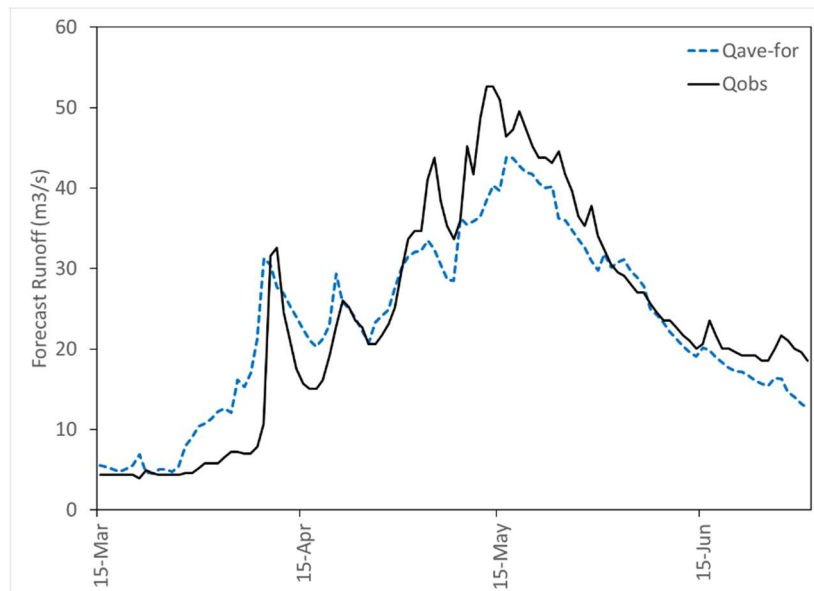
Figure 3. A lead day runoff forecast with forecast data

4. CONCLUSIONS

Two different calibration methods are utilized through the Light version of the HBV model. GAP method produces the best parameter set representing the basin. With this method, the NSE success value obtained for the calibration period is found to be 0.84. A multi-criteria calibration study was carried out by considering the compatibility between low, high flows and the daily snow-covered areas used as an additional data set. MC (Monte Carlo) simulation, which produces random model parameter sets, is used in this part of the study. The performance criteria depending on different objective functions (NSE, SCA and MARE) were selected and their combinations used with equal weights. According to the results obtained, when the calibration is performed with a multi-criteria combination, the overall success increases in both calibration and validation studies. Multi-calibration data sets are used for daily runoff forecasting and provided NSE of 0.85 for the average of ensemble forecasts.

REFERENCES

Bergström, S., Lindström, G. & Petterson, A. (2002). Multi-variable parameter estimation to increase confidence in hydrological modeling. *Hydrological Processes, 16*(2), 413-421.

Bergström, S., & Lindström, G. (2015). Interpretation of runoff processes in hydrological modelling experience from the HBV approach. *Hydrological Processes, 29*(16), 3535-3545.

Hall, D. K., Riggs, G. A., Salomonson, V. V., DiGirolamo, N. E., & Bayr, K. J. (2002). MODIS snow cover products. *Remote Sensing of Environment, 83*(1), 181-194.

Seibert, J., & Vis, M. (2012). Teaching hydrological modeling with a user-friendly catchment runoff model software package. *Hydrol. Earth Syst. Sci, 16*(9), 3315-3325.

A SHALLOW ARTIFICIAL NEURAL NETWORK MODEL FOR RAINFALL DISAGGREGATION

First Author: Hüsamettin Tayşi

Department of Civil Engineering, Gebze Technical University

Gebze, Kocaeli, Turkey

h.taysi@gtu.edu.tr

Second Author: Burak Aydoğan

Department of Civil Engineering, Gebze Technical University

Gebze, Kocaeli, Turkey

baydogan@gtu.edu.tr

ABSTRACT: Nowadays, urban floods are endangering urban life due to increasing climate change impact. With the impact of climate change, extreme rainfalls are getting higher and causing floods. Especially, short-duration rainfall accounts for flash floods. Therefore, considering short-duration rainfall plays a vital role in the assessment of floods. In this sense, Intensity-Duration-Frequency (IDF) curves can be generated using short-duration rainfall to be used as an efficient tool to demonstrate possible floods. However, measuring short-duration rainfall (5-, 10-, 15-, and 30-min) is not always straightforward due to some economical and spatial limitations. In this study, an Artificial Neural Network (ANN) disaggregation model was employed to generate short-duration rainfall from 1-, 6-, 12-, and 24-h rainfall. Afterward, these rainfalls were compared with the results of a stochastic disaggregation model HYETOS. The results have shown that the ANN model gives much better performance in estimating annual maximum rainfalls compared to the stochastic model. Annual 30-min maximum rainfalls were predicted better with coefficient of determination value of 0.903 and NSE 0.89.

Keywords: ANN, Disaggregation, IDF Curves, Rainfall, Stochastic model

1. INTRODUCTION

Flash floods, which occurred due to heavy short-duration rainfalls have destructive impacts on human life, cities, bridges, drainages, and agriculture facilities. Flash floods are the most common flood type in many countries. Moreover, climate change induces growth in the occurrence of flash floods since short-duration rainfalls are getting intensified. Impermeable surfaces in urban areas contribute the flash floods and hence, drainages are becoming insufficient against these kinds of floods (Hosseinzadehtalaeia et. al 2020). To fight against floods, it is necessary to control short-duration rainfalls and drainage systems. Rainfall Intensity-Duration-Frequency (IDF) curves provide an assessment of floods, and they can be generated using short-duration rainfalls to demonstrate flash flood effects. These curves give possible maximum rainfall for specific durations. Hence, IDF curves help engineers to be cautious about possible flood risks (Sarhadi & Soulis 2017). However, short-duration rainfalls are not always straightforward to measure due to some limitations of money and locations. To obtain these rainfalls, a process called "disaggregation" can be beneficial to employ. With the help of the disaggregation process, short-duration rainfall (5-, 10-, 15-, and 30-min) can be generated using rainfalls higher than 1-h (1-, 6-, 12-, and 24-h).

In this study, Artificial Neural Network (ANN) was employed to generate annual short-duration maximum rainfalls. Afterward, outputs were compared with observed annual maximum rainfalls. Moreover, another output obtained by (Taysi & Ozger 2021) using the HYETOS disaggregation

model (Koutsoyiannis & Onof, 2001) was compared with the ANN model and with observed maximum rainfalls.

2. STUDY AREA

A meteorological station from Istanbul was selected as the study area. The station is situated on the European side of Istanbul and is called the Florya station (Figure 1). Istanbul has the highest population in Turkey and is located in the Marmara region. The average rainfall per year is 817.4 mm and the wettest month is December with 122.6 mm rainfall (TSMS 2020). The station is operated by the Turkish State Meteorological State (TSMS) and required data were provided by TSMS.
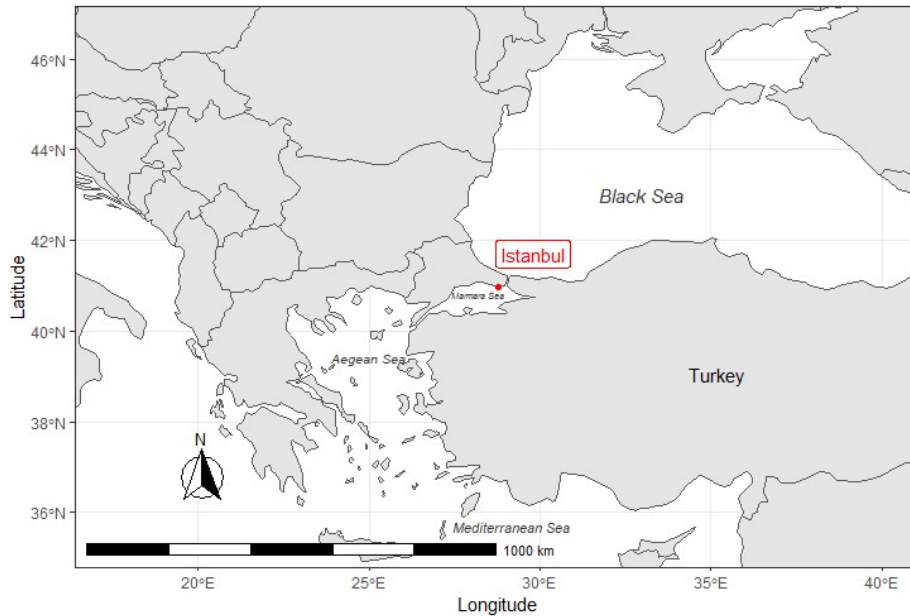
Figure 1. Florya meteorological station (Taysi & Ozger 2021)

Table 1 gives detailed information about Florya station, where W is wind, T is temperature, M is moisture, R is rainfall, ST is soil temperature and P is pressure. Data are collected from Automatic Meteorological Observation Station (AMOS) and daily climate (DC) stations (Taysi & Ozger 2021).

Table 1. Properties of Florya meteorological station.

Stations	Station Number	Coordinates	Sensors	Observation Type	Elevation (m)
Florya	17636	40°58'32.9"N 28°47'11.4"E	W, T, M, R, ST, P	AMOS-DC	37m

3. DATA

TSMS is a meteorological service that provides all kinds of meteorological data. In this study, maximum values for the 5-, 10-, 15-, 30-min rainfalls for 70 years, and IDF curves generated under observed rainfalls were provided by TSMS. Figure 2 illustrates the IDF curve for the Florya station and Table 2 gives statistical rainfall values of the station.

Table 227. Rainfall statistics of Florya station.

Statistics	January	February	March	April	May	June
Mean (mm)	77.16	73.14	55.6	40.91	28.04	32.24
Min (mm)	0	0	0.2	0	0.4	0.2
Max (mm)	158.4	164.4	117.2	115.2	77	127.6
Standard Deviation (mm)	50.49	52.54	32.75	33.35	21.87	33.69
	July	August	September	October	November	December
Mean (mm)	19.69	14.31	35.68	63.78	53.51	60.37
Min (mm)	0	0	0	0.2	0	0
Max (mm)	65.4	72	135.6	238	122.8	136.4
Standard Deviation (mm)	23.19	21.08	44.5	62.8	38.07	52.97
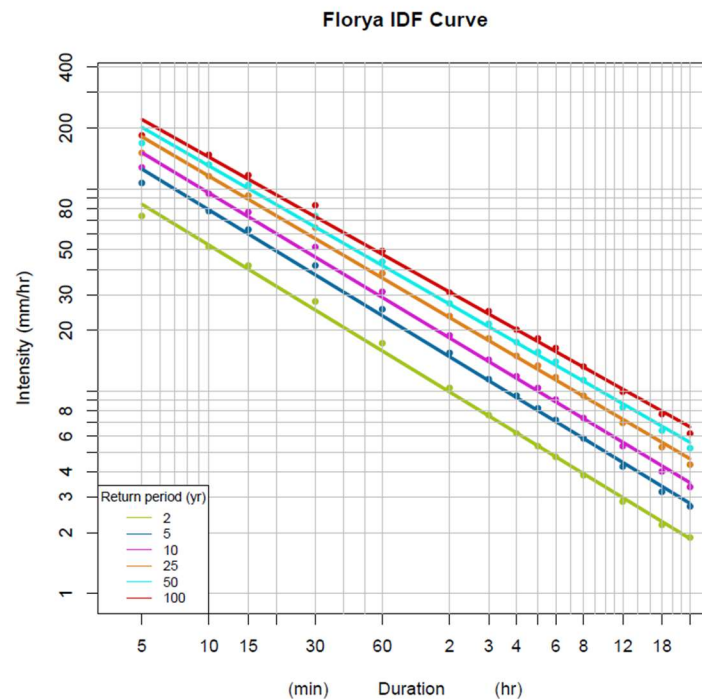
Figure 2. Rainfall IDF curve generated using TSMS observed maximum rainfalls

4. METHODOLOGY

4.1. ANN Disaggregation Model

ANN is a learning-based model which uses inputs and target outputs to train itself. Parameters are adjusted until reach meaningful outputs (Mirhosseini et al. 2014). ANNs can be used for hydrological studies (Halff et al. 1993; Smith and Eli 1995; Minns and Hall 1996; Burian et al. 2001), and disaggregation of precipitations (Burian et al. 2000).

In this study, a two-layer feed-forward model with a sigmoid transfer function was applied to predict sub-hourly (5-, 10-, 15-, and 30-min) rainfalls. The Lavenberg-Marquardt backpropagation algorithm was used to develop the model. The model includes three different layers: input, hidden, and output layers. 1-, 6-, 12- and 24-h annual maximum rainfalls were used as inputs for the prediction of each rainfall durations 5-, 10-, 15-, and 30-min. Target maximum rainfalls for each sub-hourly duration were selected as outputs. In total, 70 annual maximum rainfall values were selected. For each rainfall duration, 8 hidden neurons were assigned. For training, 70% of observed data were assigned, while 15% of the data were assigned for validation and test separately. Figure 3 demonstrates the ANN architecture to predict sub-hourly maximum rainfalls.
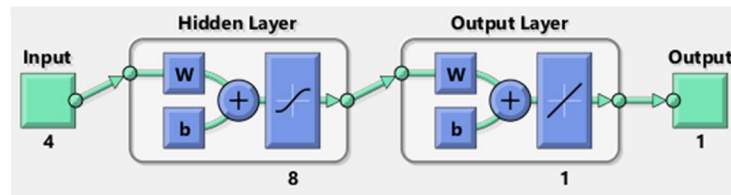
Figure 336. ANN architecture

5. RESULTS AND DISCUSSIONS

The performance evaluation of ANN and stochastic disaggregation models HYETOS are made by comparing outputs from disaggregation processes with the observed annual maximum 5-, 10-, 15-, and 30-min rainfalls. In total, 70 years annual maximum rainfalls were used for ANN model, while 78 annual maximum rainfalls were applied for HYETOS. To evaluate the performance of disaggregation models, different statistics and plots were used. Root mean square error (RMSE), Nash-Sutcliffe (NSE) (Nash & Sutcliffe 1970), coefficient of determination (R^2), and mean absolute error (MAE) were used to test variation between disaggregated and observed annual maximum rainfalls. RMSE measures the estimation error. NSE is an efficient measure to reveal the matching level between observed and simulated. The optimal value for the NSE is 1, which indicates a perfect fit. The relationship between two selected variables can be observed via R^2. This value ranges between 0 and 1, where 1 indicates a strong positive relationship. MAE gives the error between observed and predicted. Table 3 shows the performance measures between ANN and observed, HYETOS, and observed. Furthermore, annual maximum rainfalls obtained from ANN and stochastic disaggregation were compared with observed rainfalls using a scatter diagram for each duration in Figure 4-5. All measures indicate that the ANN model shows considerably better performance compared to the HYETOS model. NSE values for each duration are higher than 0.63 for ANN, whilst they are negative for HYETOS. Moreover, All R^2 values are close to 1 in ANN, on the other hand, HYETOS outputs have negative values. If error measures RMSE and MAE are considered, it is clear that ANN models have fewer values, which is the desired result. Even though rainfalls are predicted well by ANN, the best prediction performed by ANN was for 30-min maximum rainfall with an R^2 value of 0.903 and an NSE value of 0.89. ANN model has the weakest performance in the prediction of 5-min maximum rainfalls. In addition to statistical measures, scatter diagrams also demonstrate the prediction performances of each duration for each model. It is obvious that maximum rainfall values obtained by ANN stand near to best fit line, whilst they spread far away from the line in the HYETOS model.

On the other hand, overfitting possibility of the model should be considered. If the performance of the model is well for training data set, but being insufficient to capture different results for test sets, the model is more likely overfitting. When the model overfits data sets, it learns the desired output instead of learning general mechanicsm (de Andrade et al., 2020). Hence, as an example, performance of the model on training and test data sets for 30-min duration rainfall were evaluated in Figure 6 to measure the overfitting. Although model performs well for both of them, test data has a stronger performance in terms of R^2 comparing to training. This result provest that the model does not show an overfitting.

Table 3. Performance criteria of ANN and HYETOS models compared to observed data.

Model & Duration	R^2	RMSE	MAE	NSE
ANN 5-min	0.656	1.79	1.37	0.63
HYETOS 5-min	0.006	6.23	4.87	-2.73
ANN 10-min	0.689	2.46	1.91	0.70
HYETOS 10-min	0.012	9.34	7.73	-2.68
ANN 15-min	0.792	2.6	2.03	0.77
HYETOS 15-min	0.008	12.40	10.71	-2.85
ANN 30-min	0.903	2.38	1.62	0.89
HYETOS 30-min	0.004	16.44	15.08	-1.55
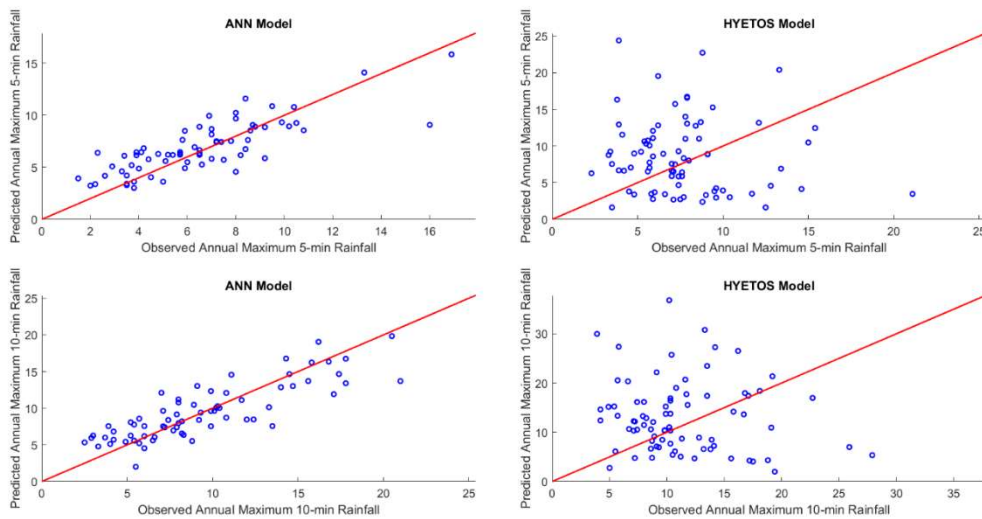
Figure 437. Scatter plots of observed and predicted maximum rainfalls for 5-min and 10-min durations for each model
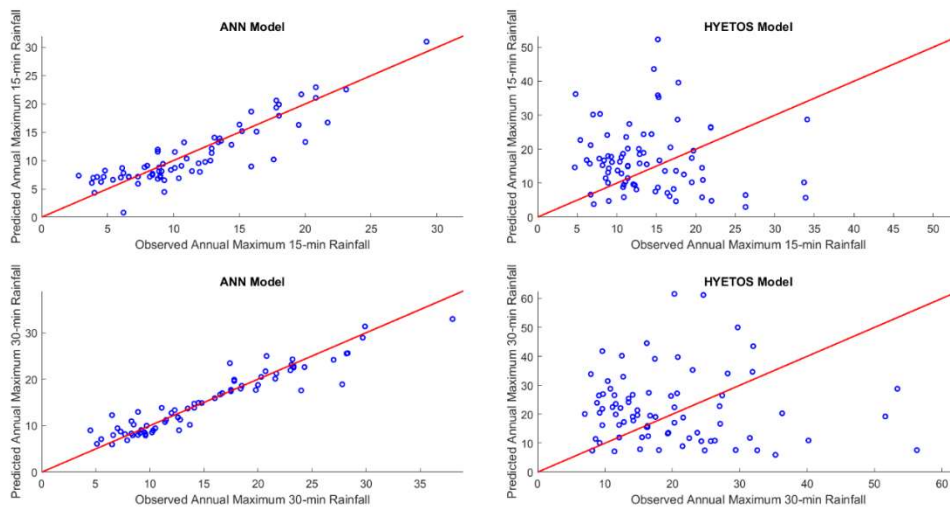
Figure 5. Scatter plots of observed and predicted maximum rainfalls for 15-min and 30-min durations for each model
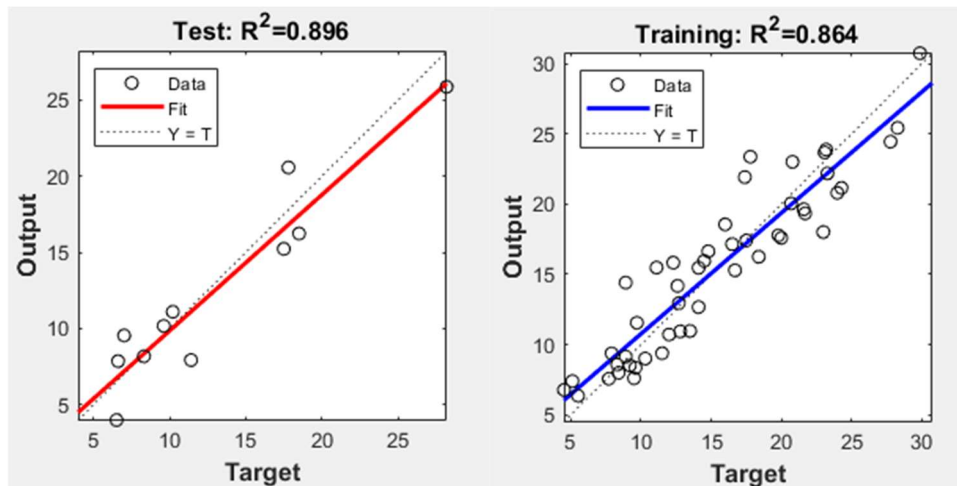
Figure 6.38 Performance of the model on test and training data sets for 30-min duration

6. CONCLUSIONS

Rainfall IDF curves are prominent tools to assess flash floods using short-duration rainfalls. Hence, these curves are employed to design drainage systems in urban areas. Even though obtaining short-duration rainfalls is necessary, it can be challenging due to limitations. On the other hand, meteorological stations can generally provide rainfalls for 1-h and 24-h. This study employs the ANN disaggregation model to generate short-duration rainfalls from inputs 1-, 6-, 12-, and 24-h rainfalls. As a result of the model, 5-, 10-, 15-, and 30-min maximum rainfalls were estimated. The performance of both models was evaluated with NSE, R^2, MAE, RMSE, and scatter plots by comparing with observed data. For each performance measure, results demonstrate that ANN performed much better compared to HYETOS in terms of each performance measure. In conclusion, this study proves that ANN is a highly effective model to generate sub-hourly maximum rainfalls via disaggregation processes. Therefore, it is advisable to use it in hydrological and water resources studies.

REFERENCES

Burian, B. S. J., Member, A., Durrans, S. R., Pimmel, R. L., & Wai, C. N. (2000). *R d u a n n. 5*(JULY), 299–307.

Burian, S. J., Durrans, S. R., Nix, S. J., & Pitt, R. E. (2001). Training artificial neural networks to perform rainfall disaggregation. Journal of Hydrologic Engineering, 6(1), 43–51.

de Andrade, B. M., de Gois, J. S., Xavier, V. L., & Luna, A. S. 2020 . Comparison of the performance of multiclass classifiers in chemical data: Addressing the problem of overfitting with the permutation test. Chemometrics and Intelligent Laboratory Systems, 201, 104013.

Halff, A. H., Halff, H. M., & Azmoodeh, M. (1993). Predicting runoff from rainfall using neural networks. *Engineering Hydrology*, 760–765.

Hosseinzadehtalaei, P., Tabari, H., & Willems, P. (2020). Climate change impact on short-duration extreme precipitation and intensity–duration–frequency curves over Europe. *Journal of Hydrology*, *590*, 125249.

Koutsoyiannis, D., & Onof, C. (2001). Rainfall disaggregation using adjusting procedures on a Poisson cluster model. *Journal of Hydrology*, *246*(1–4), 109–122. https://doi.org/10.1016/S0022-1694(01)00363-8

Minns, A. W., & Hall, M. J. (1996). Artificial neural networks as rainfall-runoff models. *Hydrological Sciences Journal*, *41*(3), 399–417.

Mirhosseini, G., Srivastava, P., & Fang, X. (2014). Developing Rainfall Intensity-Duration-Frequency Curves for Alabama under Future Climate Scenarios Using Artificial Neural Networks. *Journal of Hydrologic Engineering*, *19*(11), 04014022. https://doi.org/10.1061/(asce)he.1943-5584.0000962

Nash, J. E., & Sutcliffe, J. V. (1970). River flow forecasting through conceptual models part I—A discussion of

principles. *Journal of Hydrology*, *10*(3), 282–290.

Sarhadi, A., & Soulis, E. D. (2017). Time-varying extreme rainfall intensity-duration-frequency curves in a changing climate. *Geophysical Research Letters*, *44*(5), 2454–2463.

Smith, J., & Eli, R. N. (1995). Neural-network models of rainfall-runoff process. *Journal of Water Resources Planning and Management*, *121*(6), 499–508.

Taysi, H., & Ozger, M. (2021). Disaggregation of future GCMs to generate IDF curves for the assessment of urban floods. *JOURNAL OF WATER AND CLIMATE CHANGE*. https://doi.org/10.2166/wcc.2021.241

Turkish State Meteorological Service. (2020). *"Resmi İstatistikler (İl ve İlçelerimize Ait İstatistiki Veriler)."* https://web.archive.org/web/20180422234324/https:/mgm.gov.tr/veridegerlendirme/il-ve-ilceler-istatistik.aspx?k=A&m=ISTANBUL

14TH INTERNATIONAL CONFERENCE
ON HYDROSCIENCE & ENGINEERING

MAY 26-27, 2022
IZMİR-TURKEY

ICHE2022
IZMIR, TURKEY

PERFORMANCE OF DIFFERENT LOSS METHODS IN SNOWMELT RUNOFF MODELING

H. Soykan Civelek

Department of Civil Eng., Eskişehir Technical University,

Eskişehir, Turkey

hscivelek@eskisehir.edu.tr

Gökçen Uysal

Department of Civil Eng., Eskişehir Technical University, Eskişehir, Turkey

Eskişehir, Turkey

gokcenuysal@eskisehir.edu.tr

Talha Orhan

Department of Civil Eng., Eskişehir Technical University, Eskişehir, Turkey

Eskişehir, Turkey

talhaorhan@eskisehir.edu.tr

Aynur Şensoy

Department of Civil Eng., Eskişehir Technical University, Eskişehir, Turkey

Eskişehir, Turkey

asensoy@eskisehir.edu.tr

ABSTRACT: In the field of water resources, both for the use and management of water; in order to achieve different purposes such as flood, drought, climate change, reservoir management, etc., hydrological model applications including rainfall runoff relationship are carried out. Although model types are categorized in different ways, conceptual model approaches where data needs can be met rather easily are seen as the most used model type in hydrology. In these model applications, precipitation loss calculations can be carried out with various methods. In this study, a continuous hydrological model is applied for snowmelt runoff prediction for the Upper Euphrates Basin. The program HEC-HMS is selected for model simulations and two different precipitation loss methods are used as Deficit-Constant and Soil Moisture Accounting in comparison. In each application, loss function parameters are calibrated individually and then validation is done. Different model performance metrics are used in the analysis as NSE and P-Bias for comparison. The loss methods provided very similar model performance and runoff results for the pilot basin in a snow dominated region.

1. INTRODUCTION

Hydrological models are essential tools for efficient water resource management which necessitates accurate estimation of basin runoff. The HEC-HMS (Hydrologic Engineering Center's Hydraulic Modeling System) (SAUCE, 2020) is a reliable, freely available model having a wide use in hydrological applications on rainfall-runoff modeling for flood frequency analysis, flood management, hydraulic structure design and operation, assessment of climate change impact (Yener et.al., 2007; Chu and Steinman, 2009; Halwatura and Najim, 2013; Zema et.al., 2017)

One of the basic advantages of HEC-HMS is its ability to offer different methods for loss, transformation, baseflow, routing, etc. calculations. This different loss and baseflow estimation methods available in HEC-HMS have their own pros and cons. Infiltration as an important phenomenon in flood or drought formation has been modeled by loss methods such as SCS CN,

Green and Ampt, Initial Constant, Deficit and Constant, Soil Moisture Accounting methods. Certain loss methods are limited only to event-based while others can simulate event and continuous hydrological processes. Unlike event based, continuous hydrologic models consider watershed soil moisture balance over a long-term period and are suitable for simulating daily stream flow. Appropriate selection of these methods requires knowledge on the catchment, purpose of hydrologic application.

Karasu watershed in Euphrates river basin of Turkey was selected as the project area. Daily total rainfall and average temperature data, daily stream flow data of EIE2154 gauging station were used for the basin during 1974-2011. Deficit-Constant and Soil Moisture Accounting (SMA) methods have been compared in continuous runoff simulation HEC-HMS. The performances of loss methods were compared based on the ability to simulate discharge time series.

2. STUDY AREA

The Euphrates River, the longest in southwest Asia (2700 km), is formed by the union of two major tributaries: the Karasu which rises in the highlands of eastern Turkey north of Erzurum and the Murat which issues from the north of Lake Van (Figure 1). The Euphrates-Tigres basin is largely fed from snow precipitation over the uplands of northern and eastern Turkey. About two thirds of the precipitation occur in winter and may remain on the form of snow for half of the year. The concentration of discharge during spring causes not only extensive flooding, inundating large areas, but also the loss of much needed water required for irrigation and power generation purposes during the summer season (Altınbilek, 2004). The Karasu Basin, a sub-basin of the Euphrates River, is chosen as a pilot basin for the application of the snowmelt models. The total catchment area is 2817,5 km^2 and the elevation ranges between 1640 m and 3112 m a.s.l. (Table 1.).
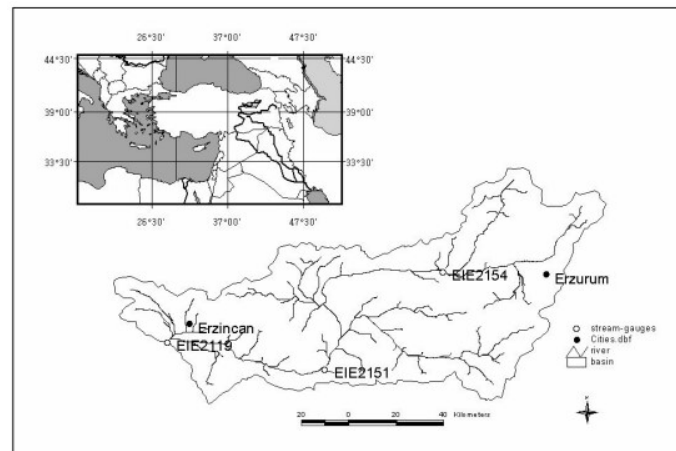
Figure 39. Location and topography of the basin

Table 1. Topographic properties of the catchment.

Elevation Range (m)	Area (km2)	Area (%)	Slope (%)
1640-1900	900.2	32.0	3.0
1900-2200	746.9	26.5	11.3
2200-2500	698.2	24.8	15.1
2500-2800	369.4	13.1	16.0
2800-3112	102.8	3.6	13.7
1640-3112	2817.5	100	10.3

3. METHODOLOGY

HEC-HMS provides options for loss calculations, only three of them selected in the analysis for comparison and explanations are given below with more details in USACE (2020). The model application also includes snow component since the pilot area is a snow dominated basin. Temperature index method is used to calculate snowmelt. The basin is sub divided into elevation zones to account for the change in temperature with altitude. The baseflow calculation method is selected as linear reservoir to make the model run compatible with continuous model application. Snow component and baseflow parameters are also calibrated. The model parameters are optimized with Particle Swarm Optimization.

3.1. Deficit and Constant (DC) Method

The deficit and constant loss method help to create continuous hydrological loss calculations and simplifies the complicated rainfall-runoff process with one soil layer. The model only concerns about computing infiltration during storm events and evapotranspiration between storm events. Precipitations leach in the soil during storms and evapotranspiration withdraws water from the layer between storm events. Precipitation that exceeds the capacity of the soil layer becomes surface runoff.

3.2. Soil Moisture Accounting (SMA) Loss Method

The soil moisture accounting (SMA) is one of the loss methods that interests with the changes in moisture content along the different soil layers of the continuous hydrological models Bennett (1998). SMA serves to produce water behavior in soil surface, soil profile which is divided into two zones as tension and upper zone storage, and groundwater layers. Additional surface and canopy method can be integrated. This loss method is able to produce surface runoff, groundwater flow and deep percolation over the basin. The volume of infiltration during a time interval is a function of the volume of water available for infiltration, the state (fraction of capacity) of the soil profile, and the maximum infiltration rate specified by the model user (USACE, 2020). For each time step in the analysis the potential infiltration volume is calculated by SMA model, when the water available for infiltration exceeds potential infiltration volume the excess contributes to surface interception storage.

The model performance is measure with NSE and P-Bias metrics as given in Equation 1-2.

$$NSE = 1 - \frac{\sum_{t=1}^{T} (Q_O^t - Q_S^t)^2}{\sum_{t=1}^{T} (Q_O^t - \bar{Q}_O)^2} \tag{1}$$

$$P - Bias = \frac{\sum_{t=1}^{T}(Q_S^t - Q_O^t)}{\sum_{t=1}^{T} Q_O^t} \tag{2}$$

where Q_O^t and Q_S^t are observed and simulated discharges at time instance, t. $\bar{Q}_O$ and $\bar{Q}_S$ are the mean of observed and simulated discharges, respectively. T stands for the total duration defined as daily time steps.

4. RESULTS

The model applied for calibration (1974-2000 water years) and validation periods (2001-2011). The model results are shown in Figure 2 in terms of modeled and observed discharges. Table 2 shows the model performance results which indicate very similar NSE and P-Bias values. In terms of infiltration 0.76 mm/day and 0.67 mm/day are found for SMA and DC, respectively. Unit hydrograph, snow component and baseflow parameters are taken as same for two different loss method applications.
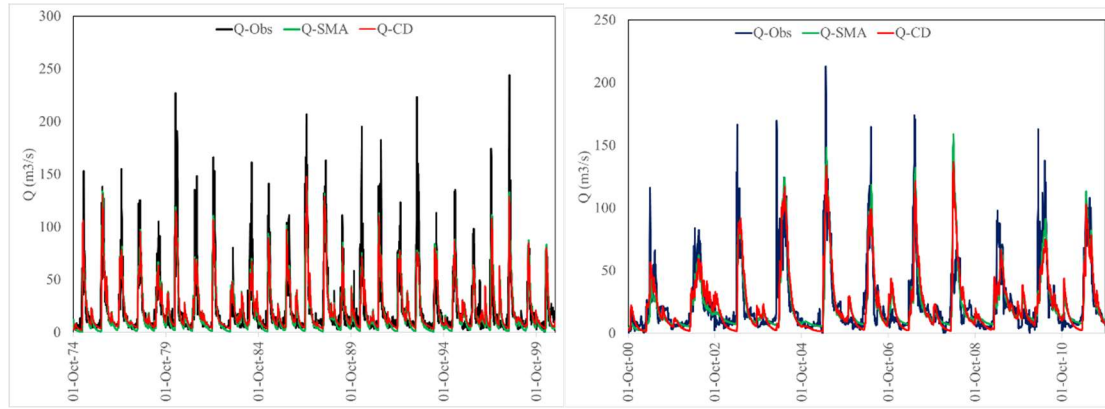
Figure 2. Runoff comparison for a) calibration b) validation

Table 2. Performance analysis for SMA and DC methods.

Period	SMA-NSE	DC-NSE	SMA-P-Bias (%)	DC-P-Bias (%)
Cal (1974-2000)	0.703	0.682	0.44	0.01
Val (2001-2011)	0.606	0.601	-0.09	2.51

5. CONCLUSIONS

HEC-HMS model is applied for Karasu Basin to examine the effect of loss methods. A continuous model run is carried for calibration (1974-2000) and validation (2001-2011) periods. Soil Moisture Accounting and Deficit and Constant methods are selected for loss calculations. SMA requires 14 model parameters and DC necessities only 4 parameters. The model is applied for a snow dominated basin with the same snow parameters. The model performance results indicate quite similar values in terms of NSE and P Bias when the model parameters are kept constant for other hydrological processes (transform, baseflow and snow component parameters). It highlights the advantage of the DC method with few parameters. On the other hand, when all the parameters (loss, transform, baseflow and snow component parameters) are automatically optimized for each model application with two different loss methods, SMA model performance is relatively higher compared to that of DC method. Baseflow values are increasing and direct runoff decreases in DC application, even though it provides total runoff values similar to that of SMA model application. Such studies are valuable for practitioners to make decisions more easily for their hydrological model implementations.

REFERENCES

Chu, X., & Steinman, A. (2009). Event and continuous hydrologic modeling with HEC-HMS. *Journal of Irrigation and Drainage Engineering*, 135(1), 119-124.

Halwatura, D., & Najim, M. M. M. (2013). Application of the HEC-HMS model for runoff simulation in a tropical catchment. *Environmental modelling & software*, 46, 155-162.

USACE (2020) U.S. Army Corps of Engineers, Hydrologic Engineering Center. 2000. *HEC-HMS Hydrologic Modeling System,* Technical Reference Manual, CPD-74B. Hydrologic Engineering Center, Davis, CA.

Yener, M. K., Sorman, A. U., Sorman, A. A., Sensoy, A., & Gezgin, T. (2007). Modeling studies with HEC-HMS and runoff scenarios in Yuvacik Basin, Turkiye. *Int. Congr. River Basin Manage*, 4(2007), 621-634.

Zema, D. A., Labate, A., Martino, D., & Zimbone, S. M. (2017). Comparing different infiltration methods of the HEC-HMS model: the case study of the Mésima Torrent (Southern Italy). *Land Degradation & Development*, 28(1), 294-308.

14TH INTERNATIONAL CONFERENCE
ON HYDROSCIENCE & ENGINEERING

MAY 26-27, 2022
IZMİR-TURKEY

ICHE2022
IZMIR, TURKEY

SIMULATION OF WATER RESOURCES OF TAHTALI-SEFERIHISAR SUB-BASIN BASED ON A WEAP MODEL

Sait Mutlu Karahan

Department of Civil Engineering, Izmir Institute of Technology

İzmir, TURKEY

saitkarahan@iyte.edu.tr

Şebnem Elçi

Department of Civil Engineering, Izmir Institute of Technology

İzmir, TURKEY

sebnemelci@iyte.edu.tr

ABSTRACT: Water managers have been confronted with complicated and tough problems due to population growth, industrialization, urbanization, pollution and changing rainfall and temperature regimes as a result of climate change. Therefore, it is becoming more and more important to distribute available water resources in a fair and balanced way among the users. Hence, the extensive evaluation of water budgets and the preparation of advanced water management plans based on these assessments have become compulsory. In this study, different simulated scenarios have been implemented to predict the future water needs of the Tahtalı-Seferihisar Sub-Basin via numerical modelling. The Water Evaluation and Planning (WEAP) model is utilized for this purpose. Management alternatives under various circumstances of water scarcity and capacity are evaluated through seven different water management scenarios: (1) Reference Scenario; (2) Best Case Scenario; (3) Worst Case Scenario, (4) Report Consumption Scenario, (5) Return Flow Scenario, (6) Population Extrapolation Scenario, and (7) Various Forecast Scenario. The results of the study showed that, the Tahtalı-Seferihisar Sub-Basin's water resources are sensitive for the next generations. Therefore, implementing appropriate water resources management is critical for the sustainable use of water resources.

1. STUDY SITE

The study site is selected as Tahtalı-Seferihisar Sub-Basin, which is the sub-basin of Küçük Menderes Basin and is located between 37° 58' and 38° 23' north latitudes and 26° 40' and 27° 22' east longitudes. Basin has an area of approximately 12.5 hectares and it is located within the borders of İzmir province and is placed in the southwest of the city. Since the sub-basin is located in the Aegean Region, the Mediterranean Climate prevailing in the region is observed. Typical features of this type of climate are hot and dry summers and mild and rainy winters. While the annual average precipitation in the basin is 731.1 mm, the annual average temperature is between 12.4 °C and 17.7 °C. The hottest months are July and August, while the coldest months are January and February (T.R. Ministry of Forestry and Water Affairs, 2016).

2. THE WATER EVALUATION AND PLANNING (WEAP) MODEL

The WEAP model is an easy-to-use and integrated program for calculating the sustainability of water resources, replicating today's supply and demand points (History and Credits: WEAP21). On the basis of WEAP, it calculates the water balance of the study area in the future years, using the relationships between the supply and demand points. The study area to be calculated can be a single agricultural area or it can be transboundary basins in the program (Stockholm Environment Institute, 2016).

The purpose of the WEAP program is to seek answers to the questions of whether the water needs of the agricultural areas can be met under different scenarios, as well as the question of what percentage of the water needs of the city can be met in the future.

2.1. Input Data of WEAP

The vector layer obtained from the State Hydraulic Works (DSI) of Tahtalı-Seferihisar Sub-Basin is redefined via QGIS and is added to the schematic view of WEAP. The generated hydrogeological, vegetation and lithology maps are also separated into different layers and are analyzed in QGIS. After the completion of the maps, supply and demand points are created on the model, and the relations between these points were established.

For streams, the monthly average flow data obtained from the State Hydraulic Works (DSI) are converted into daily flow data, and for groundwater resources, the initial storage capacity values are taken as equal to the water needs of the agricultural areas from which they supply irrigation water.

For the agricultural areas, which are among the demand points, the irrigation water requirement of each product grown in that agricultural area is calculated separately and added to the WEAP program. For the drinking water demand points, different population projection methods are used for various scenarios and are transferred to the program to calculate the future water needs

After the supply and demand points are completed, transmission links are defined in the program in order to establish the relationship between these points and WEAP uses to solve these relationships with linear programming.

With the addition of transmission links to the program, the schematic view of Tahtalı- Seferihisar Sub-Basin is completed and is shown in Figure 2. Water scarcity and capacity are evaluated through seven different water management scenarios: (1) Reference Scenario; (2) Best Case Scenario; (3) Worst Case Scenario, (4) Report Consumption Scenario, (5) Return Flow Scenario, (6) Population Extrapolation Scenario, and (7) Various Forecast Scenario as presented in Table 1. Total recharge values presented here are obtained from the Turkish Ministry of Forestry and Water Affairs (2016). Of these various water management scenarios, results of the three scenarios (Reference, Best and Worst Cases) will be presented and discussed here.
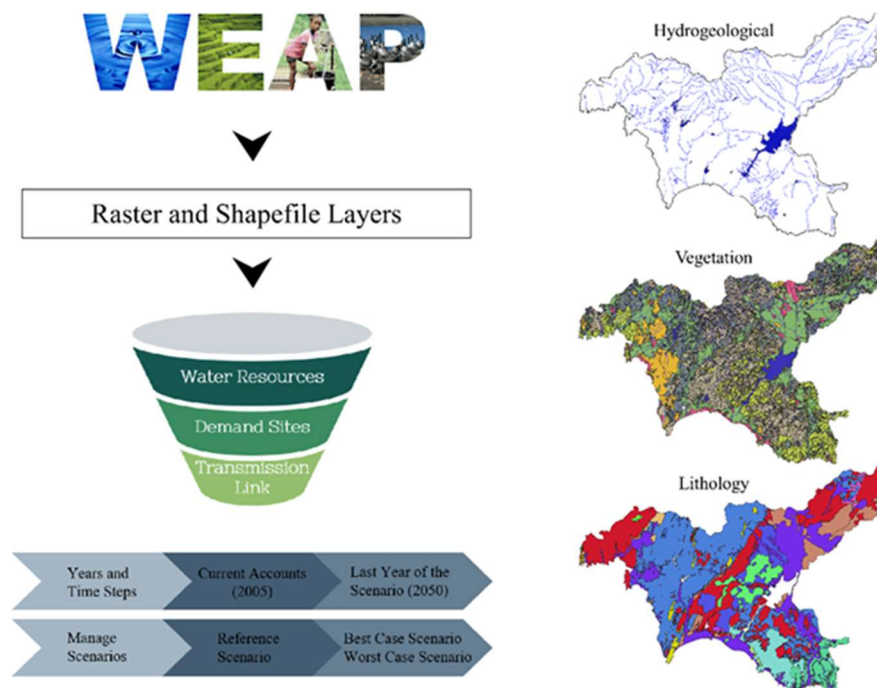
Figure 1. Summary of the methods and hydrogeological, vegetation and lithology maps generated to be used in the WEAP model
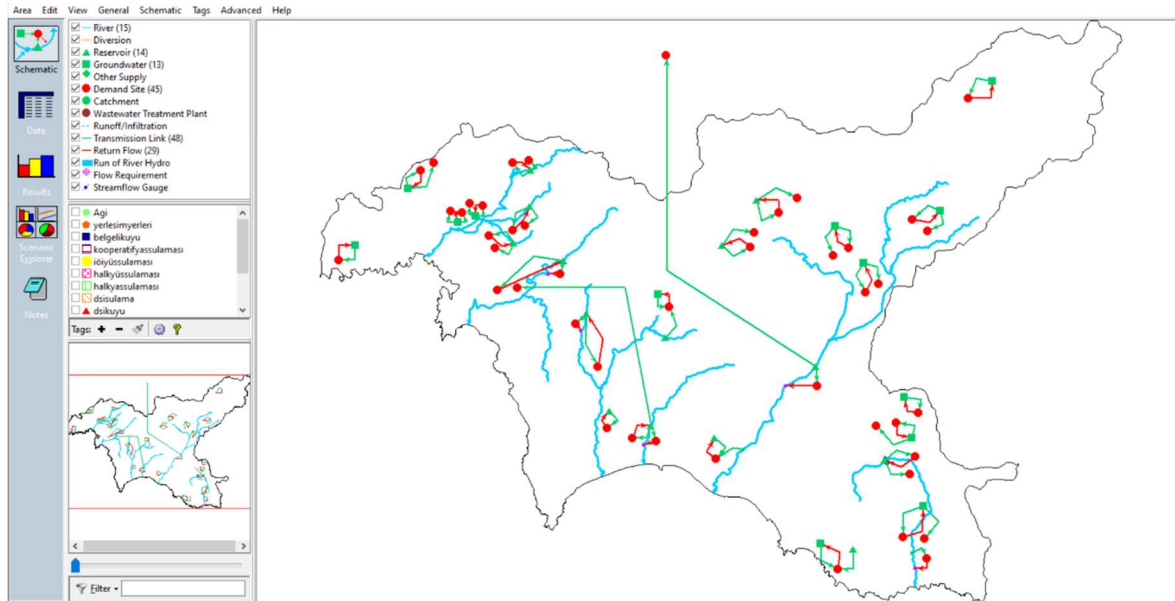
Figure 2. Schematic View of Tahtalı-Seferihisar Sub-Basin
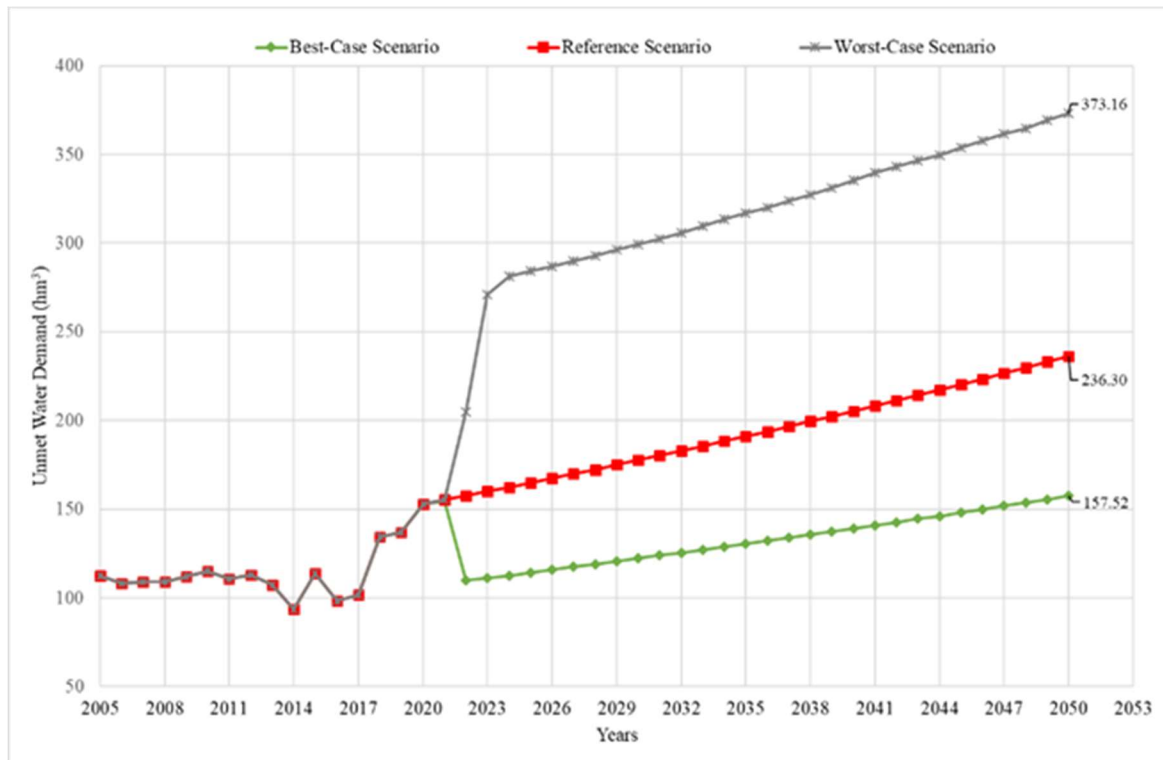
Figure 3. Unmet Amount of Water Demand for All Demand Sites (hm³)

The scenario where unmet water demand is expected to be the highest is the Worst Case Scenario, since all environmental conditions (flow rates decreased by 20%, net evaporation values increased by 20%) are considered as worst case in this scenario. The reason for the increase in the amount of unmet water demand in all three scenarios is the significant population growth in the study area. As a consequence of the increasing population, the water consumption that is calculated by per capita increases over the years. The amount of unmet water demand in the Worst Case Scenario is found to be more than twice the amount of unmet water demand in the Best Case Scenario.

Table 1. Summary of the Scenarios used in the study.

	Reference Scenario	Report Consumption Scenario	Best Case Scenario	Worst Case Scenario	Return Flow Scenario	Population Extrapolation Scenario	Various Forecast Scenario
Average flow rates	✓	✓	ARIMA flow rates	80% average flow rates	✓	✓	Average flow rate and Three Forecasting Method
Average Net Evaporation Values	✓	✓	80% of Average Net Evaporation	120% of Average Net Evaporation	✓	✓	✓
Initial Storage Capacity = Irrigation Water Needs	✓	✓	✓	✓	✓	✓	✓
Natural Recharge Values = Irrigation Water Needs	✓	Total Recharge Value: 87.5 hm³	Total Recharge Value: 115 hm³	Total Recharge Value: 34 hm³	✓	✓	✓
The Turkish Bank of Provinces Method	✓	✓	The Average Growth Rate Method	✓	✓	Four Different Population Projections	✓
Irrigation Water Needs	✓	✓	80% of Irrigation Water Needs	120% of Irrigation Water Needs	✓	✓	✓
Water Consumption per Capita	✓	✓	80% of Water Consumption per Capita	120% of Water Consumption per Capita	✓	✓	✓
Return Flow	x	x	x	x	20% of Irrigation Water Needs	x	x

3. CONCLUSION

As can be inferred from Figure 3, the water resources in the basin will be insufficient and the amount of unmet water demand will increase in all possible scenarios. Population growth is the main reason for the increase in the amount of unmet water demand. Even in the Best Case Scenario, where the best conditions are applied, the increase in the amount of unmet water demand is due to this situation.

While the amount of unmet water demand in the Worst Case Scenario is 373.2 hm³ in 2050, this value becomes 236.3 hm³ in the Reference Scenario for the same year. The unmet water demand difference between these two scenarios is approximately 137 million m³ and it is almost equal to unmet water demand in Best Case Scenario. It is an indication of that unmet water demand can be decreased significantly if water is used efficiently.

REFERENCES

History and Credits: WEAP21. (n.d.). Retrieved from WEAP21: https://www.weap21.org/index.asp?action=219

Stockholm Environment Institute. (2016). *Water Evaluation And Planning System Tutorial.* Stockholm Environment Institute.

T.R. Ministry of Agriculture and Forestry, General Directorate of Water Management. (2019). *Sektörel Su Tahsisi Eylem Planı ve Genelgesi (2020-2025).* Ankara: T.R. Ministry of Agriculture and Forestry.

T.R. Ministry of Forestry and Water Affairs, G. D. (2016). *Küçük Menderes Havzası Master Planı.* Ankara.

14TH INTERNATIONAL CONFERENCE
ON HYDROSCIENCE & ENGINEERING

MAY 26-27, 2022
IZMİR-TURKEY

ICHE2022
IZMIR, TURKEY

DATA-DRIVEN WATER QUALITY ASSESSMENT OF INLAND WATERBODIES USING SATELLITE SPECTRAL DATA: A CONCEPTUAL FRAMEWORK

Osama H. Heba

Civil Engineering Dept., Izmir Institute of Technology

Urla, Izmir, Turkey

osamaheba@iyte.edu.tr

Şebnem Elçi

Civil Engineering Dept., Izmir Institute of Technology

Urla, Izmir, Turkey

sebnemelci@iyte.edu.tr

ABSTRACT: This article advocates the exploitation of satellite spectral data in the scope of inland water quality assessment in lieu of in-situ monitoring. It also lays down a general framework that takes advantage of state of the art technology, especially in the field of remote sensing and data science, in the hope of achieving more economically viable solutions while maintaining acceptable levels of accuracy. As the following paragraphs emphasize, there is a great need for such an approach as well as great potential and practicality.

1. INTRODUCTION

Not only providing a crucial habitat for fauna and flora, inland waters are also a primary source for many anthropogenic activities. As a result, the highest levels of monitoring is an imperative practice to prevent any water quality degradation that could disturb our socio-ecological system that depends on such valuable resources (Kupssinskü et al., 2020; Saberioon, Brom, Nedbal, Souček, & Císař, 2020). This is particularly true taking into account the rapid population growth and the over-utilization of those waterbodies or their surroundings, which poses an ever-growing challenge to such preservation attempts(Batur & Maktav, 2019; Modiegi, Rampedi, & Tesfamichael, 2020). From these concerns, a broad definition of water quality can be established as the biological, chemical, and physical characteristics of water that fulfill the requirement of the different purposes water might be needed for. These can include direct consumption by humans, irrigation, maintaining healthy fisheries, or even generating hydropower. As a means of quantifying that, various parameters are usually measured; such as, concentrations of Chlorophyll-a (Chl-a), turbidity, sediment load, dissolved oxygen, nutrients, temperature, and salinity, etc., based on which different authorities can characterize the condition of the source of interest according to their own standards or benchmarks (Greb, Dekker, Binding, & Stuart, 2018; Sagan et al., 2020).

As the importance of water quality monitoring is globally recognized, few common practices are already pursued by the different parties that share such a concern. Although very accurate, field testing or sampling for lab analyses is expensive, time-consuming and demanding of highly skilled personnel. Moreover, it usually lacks the insight of spatio-temporal variation as it is performed on only some selected sampling points within a very limited period (Kupssinsku et al., 2019; Modiegi et al., 2020). Some more capable authorities might deploy a network of sensors across waterbodies within their jurisdiction that provides continuous water quality data in near real-time; however, it remains economically questionable to have an extensive network that covers all waterbodies within a nation. In addition, the spatial coverage remains suboptimal as such stations reduce two-dimensional surfaces to few points of data (Batur & Maktav, 2019; Peterson, Sagan, & Sloan, 2020).

Another paradigm of water quality monitoring, which has been gaining increasing attractiveness, is the utilization of spectral characteristics of water and the components in it that might affect its quality to evaluate its condition. This is particularly advantageous as such practice can be carried on with the assistance of airborne or space-borne platforms, allowing covering vast spatial extents and more frequent measurements, which eliminates some of the main disadvantages of traditional methods of monitoring. The fact that many of water quality parameters are impacted by Optically Active Components (OAC) – chromophoric substances- means that their presence in water alter the expected reflection/absorption characteristics expected from pure water. For example, clear water absorbs red and near-infrared radiation resulting in undetectable reflectance signal at that electromagnetic spectrum; however, the presence of Chlorophyll-a (Chl-a) causes pigmentation that is particularly detectable within that spectral range, which suggests the feasibility of utilizing optical sensors with thermal capabilities for monitoring this parameter. This aspect is not exclusive to the stated example as other OAC parameters; such as Suspended Solids (SS), and Colored dissolved organic matter (CDOM) have their own signature optical properties that can be used for the purpose of their detection (Kupssinsku et al., 2019; Pahlevan et al., 2020; Sagan et al., 2020).

Recognizing the potential of exploiting the optical characteristic of water and its component, many satellites where either released for that dedicated purpose, or received attention afterward of having data of useful information for water quality monitoring. In all references to Earth Observatories (EO) in this article, if not specified otherwise, the authors are referring to the optical data produced by a certain satellite as in most cases there are other sensors mounted on such platforms. Sentinel-3 Ocean and Land Color Instrument (OLCI) is one of those dedicate satellites for water quality monitoring of large waterbodies. It is deemed as a more specialized predecessor for the more general application satellites; such as, Moderate Resolution Imaging Spectroradiometer (MODIS), Medium Resolution Imaging Spectrometer (MERIS), Visible Infrared Imaging Radiometer Suite (VIIRS)(Binding, Pizzolato, & Zeng, 2021; Wang et al., 2021). Landsat on the other hand provides the most extended time series (nearly 50 years) with relatively high spatial resolutions (30 m) in some of its captured bands for continental part of the planet. Sentinel-2 multispectral imager (MSI), another land-focused satellite-based instrument, provides even better spatial resolution (down to 10 m) plus a higher temporal resolution that reach 5 day of revisit period -depending on location. This provides exceptional dataset in term of quality and quantity that could improve owner perspective on inland water remote sensing (Kupssinskü et al., 2020; Saberioon et al., 2020).

The literature on this scope bears very interesting outcomes with reports implying varying degrees of successes depending on the instrument of choice and the parameters selected for investigation. (Guo, Zou, Jiang, Tang, & Zhang, 2017) attempted to infer sea surface salinity and turbidity of Yellow Rive plume using surface reflectance products from MODIS and the Geostationary Ocean Color Imager (GOCI) satellites in combination with some observations from hydrographic surveys. The results suggest that both data sources enabled achieving substantially detailed quantification of plume specially the inter- and intraday variation of salinity and turbidity dynamics. Another work of (Fassoni-Andrade & Paiva, 2019) was focused in estimating surface suspended solids in the Amazon using reflectance data from MODIS as a proxy to study large scale temporal dynamics. The study also show an adequate overall accuracy, yet it proposes trying the same methodology on Sentinel-2 data as its higher spatial resolution provides new opportunity of achieving a more detailed local studies. (Binding et al., 2021) presents a functioning algal bloom monitoring service that derives its information from the spectral data produced by Sentinel-3 and MERIS. A full automation of bloom indices in operational capacity is showcased for multiple lakes, which allows a near-real-time reports through a user friendly web platform. Landsat-8 (OLI) data was assessed against in-situ spectral measurement in estimating Chl-a, and r a promising agreement is reported. The article emphasized on how using satellite data enables getting a better spatial distribution of the parameter of interest, it also promotes the exploration of producing a time-series for temporal analysis. This aspect was attempted by (Wang et al., 2021)using Landsat-5~8 (TM,ETM+,OLI) and MODIS, yet to estimate Total Suspended Matter (TSM) in lake Hulun in China. Temporal patterns between 1986-2003 were identified for TSM and this evidence was used to support the authors claim on the effectiveness of using such insight in decision making in water quality related issues. In (Pahlevan et al., 2020), a machine learning algorithm; namely, Mixture Density Network (MDN), was trained on both Sentinel-

2 (MSI) and Sentinel-3 (OLCI) to developed a single model that works across both data sources to retrieve Chl-a estimations. The model worked equally well using either input. However, the article emphasized the impact of the type of atmospheric correction applied on the overall performance of the model suggesting that it could cause a 30% loss in the performance of the model. The model is claimed to provide most accurate estimated from images processed via three different atmospheric correction processors, namely the SeaWiFS Data Analysis System (SeaDAS), POLYMER, and ACOLITE. (Batur & Maktav, 2019), on the other hand compared different machine learning models on three satellites' reflectance data, Göktürk-2, Landsat-8 (OLI), and Sentinel-2 (MSI). The article attempted estimating various water quality parameters; such as, Chl-a, total Suspended Solids (TSS), Dissolved Oxygen (DO), etc. in Gala lake in Turkey. Data from satellites with higher spectral resolution, Sentinel-2 and Landsat-8, showed better correlation between the reflectance data and the parameters of interest; however, the higher temporal resolution of Göktürk-2 also proved advantageous in providing better coverage for the region under study. It was also noted that seasonality introduces undesirable variability in the imagery data; hence, developing models for each season separately was advised.

As the work related to the application of EO data in water quality assessment is still in its infancy. This article aims to contribute to the maturity of the knowledge and techniques applied in such scope by exploring yet different data-driven methods on satellite reflectance data. The instrument of choice is MSI installed on Sentinel-2 satellite for the advantages to be highlighted in the following paragraphs. The water quality parameters to be investigated are Chl-a and turbidity. In the next section, a framework that outlines the main procedures to be followed in the current work is briefly discussed.

2. MATERIAL AND METHODS

2.1. Space-Borne Sourced Spectral Data

As implied by the literature, Sentinel-2 MSI dataset stands out as a very promising source for the intended scope of work. Hence, this subsection gives a brief description on the product of interest as well as the platform and the sensors that contribute in producing it.

Sentinel-2 is a two-satellite mission with a wide-swath, high-resolution, multi-spectral imagery supporting Copernicus land monitoring studies. The sun synchronous twin orbit the planet having a $180°$ phase enabling a high revisit frequency that reaches 5 days at the equator. The MSI mounted on these EO's samples 13 spectral bands: four bands at 10 meters, six bands at 20 meters and three bands at 60 meters spatial resolution. In terms of spatial coverage, this mission covers all continental land surfaces (including inland waters) between latitudes 56° south and 82.8° north, plus all coastal waters up to 20 km from the shore and more. Having a dataset of such spatio-temporal and spectral resolution openly available is an invaluable source for geo-information at local, regional, national and international scales. The elementary level of Sentinel-2 MSI products are granules of a fixed size. The granule size is dependent on the product level. For this particular work, Sentinel-2 Level-2A is being considered as it comes already preprocessed for atmospheric correction, resulting of what is called Bottom of Atmosphere (BoA) reflectance images. Those images come in 100-by-100 km tiles in UTM/WGS84 projection (ESA, 2015).

Sentinel-2 dataset can be retrieved from multiple cloud storages; however, Google Earth Engine (GEE) service not only gives access to the data of interest, but also allows leveraging the computational power at the server side by providing different algorithms and functions that can be applied to the data before downloading it. These functionalities can be applied either through the coding platform provided by Google, which uses Javascript programing language, or through an Application Programming Interface (API) that links to Python programing language with the assistance of some libraries, which the authors are opting for. There is also a good documentation for both the dataset and the tools that are available on GEE. The date range availability is also stated in the dataset documentation as 28/03/2017, this is due to fact that the constellation was not at its full coverage at launch time, 23/06/2015. The naming convention is also important to understand, as it is not similar to that from the original provider. An example of the naming convention for Sentinel-2

data retrieved from GEE is "20190307T155111_20190307T200107_ T18SUG", where the first block represents the timestamp of capturing the image, the second block time of generating the data in its current form, and the last block is a 6-character string of unique granule identifier indicating its UTM grid reference (Gorelick et al., 2017). There are also some band related essential information that are summarized in Table .

To have a clear perspective, Figure shows different ways of displaying part of imagery captured on 2019/03/07 for tile T18SUG by the MSI instrument on board of Sentinel-2. The left side of the figure shows composite images –made of multiple bands-, while the right side shows how one-band data looks like. (B:4-3-2) labeled sub-figure is what normal eyes are expected to see in nature; hence, named true color composite. On the other hand, in (B:8A-3-2) replacing the red band with infra-red allows more defined waterbody boundary at the cost of details inside the waterbody itself. These observations are more evident in the single band imagery at the right side where the bands B2 and B8A are displayed individually. Such discrepancies in captured information highlight the ability MSI sensor has in identify water related characteristics that could be of a great value in water quality assessment.

Table 1. Sentinel-2MSI L-2A bands details.

Name	Description	Resolution	Wavelength	Scale
B1	Aerosols	60 meters	443.9nm (S2A) / 442.3nm (S2B)	0.0001
B2	Blue	10 meters	496.6nm (S2A) / 492.1nm (S2B)	0.0001
B3	Green	10 meters	560nm (S2A) / 559nm (S2B)	0.0001
B4	Red	10 meters	664.5nm (S2A) / 665nm (S2B)	0.0001
B5	Red Edge 1	20 meters	703.9nm (S2A) / 703.8nm (S2B)	0.0001
B6	Red Edge 2	20 meters	740.2nm (S2A) / 739.1nm (S2B)	0.0001
B7	Red Edge 3	20 meters	782.5nm (S2A) / 779.7nm (S2B)	0.0001
B8	NIR	10 meters	835.1nm (S2A) / 833nm (S2B)	0.0001
B8A	Red Edge 4	20 meters	864.8nm (S2A) / 864nm (S2B)	0.0001
B9	Water vapor	60 meters	945nm (S2A) / 943.2nm (S2B)	0.0001
B11	SWIR 1	20 meters	1613.7nm (S2A) / 1610.4nm (S2B)	0.0001
B12	SWIR 2	20 meters	2202.4nm (S2A) / 2185.7nm (S2B)	0.0001
AOT	Aerosol Optical Thickness	10 meters		0.001

WVP	Water Vapor Pressure. The height the water would occupy if the vapor were condensed into liquid and spread evenly across the column.	10 meters	0.001
SCL	Scene Classification Map (The "No Data" value of 0 is masked out)	20 meters	0
TCI_R	True Color Image, Red channel	10 meters	0
TCI_G	True Color Image, Green channel	10 meters	0
TCI_B	True Color Image, Blue channel	10 meters	0
MSK_CLDPRB	Cloud Probability Map (missing in some products)	20 meters	0
MSK_SNWPRB	Snow Probability Map (missing in some products)	10 meters	0
QA10	Always empty	10 meters	0
QA20	Always empty	20 meters	0
QA60	Cloud mask	60 meters	0
QA60 Bitmask	Bit 10: Opaque clouds		

0: No opaque clouds

1: Opaque clouds present

Bit 11: Cirrus clouds

0: No cirrus clouds

1: Cirrus clouds present

Source : GEE, product identifier: COPERNICUS/S2_SR/20190307T155111_20190307T200107_T18SUG
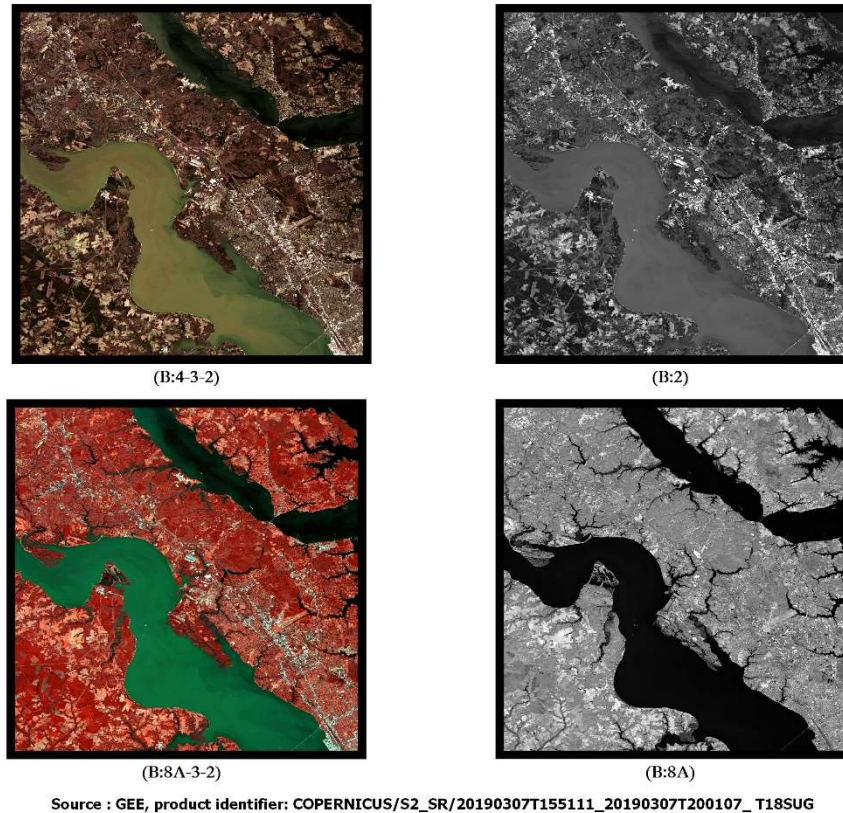
Figure 1. Sentinel-2-L2A imagery set, composite and single-band illustrations

2.2. Ground Observation Data

Before reaching the point of total reliance on spectral data for water quality assessment, readings for the investigated parameters using traditional methods are needed for model fitting purposes. These can be either sourced from national databases or collected in a scientific surveying campaign to provide the needed data for validation. The former option, if available, is preferable as it reduces the cost of the study and is likely to provide a better temporal coverage for the studied area. The latter can be more customized to meet the specific study requirements; however, it should be properly timed to match the satellite's schedule of passing over the region of interest. In both cases, synchronization between the space-borne data and the ground date is critical for the validity of the analysis; however, other environmental factors could have a very detrimental effect on the quality of collected data. Cloud, for instance, can obscure vision between the satellite sensors and the ground as most of the sensed wavelengths by the MSI instrument cannot penetrate cloud. That being said, an extensive inspection and cleaning of the data is required to ensure consistent input for the developed model.

2.3. Data Quality and Cleaning

It is unarguably the case that a low quality input shall only result in low quality model. This issue becomes more evident when sourcing data that are generated without prior consideration of the newly intended application. Hence, a rigorous inspection and good sense of judgment from the analyst side is required; especially in processes that are to be automated.

To highlight some of these issues, Figure illustrates some of the challenges that are expected to be encountered using satellite imagery data. All sub-figures are for the same location of Beydağ reservoir in Türkiye, yet at different times; to the left, (a), is an unobstructed view to the location of interest. This is also true for imagery (b); however, the lake boundary shrunk significantly, which raises two issues. The dynamic change of the lake boundary needs to be considered otherwise some sampled data will include readings for land rather than water. Moreover, the severe drop in water level

introduces the possibility of interference in reflectance readings from the lakebed in very shallow depths. SCL band , refer to Table , can be used as a guide for filtering entries as it contains a classification of the imagery based on various algorithms on the imagery bands (ESA, n.d.). Also, producing separate models for different seasons can be a solution to reduce the variability caused by possible interference of the bottom of the lake at draught seasons. Figure (c) on the other hand presents barely visible land features for the same location as both cloud and its overcast are either blocking the view or the sun light resulting in a very dark scene. Luckily, SCL band can help filter these unwanted entries too; in addition to the band MSK_CLDPRB, which gives the probability of a pixel in the imagery being a cloud.

Similarly, ground observations are prone to contain some quality issues, which are specific to the way how the data is collected or to the phenomenon measured. Generally speaking, it is expected to encounter missing readings and outliers. In both cases we need to investigate the cause behind these issues as there is no one-solution fit-all action that can be prescribed. Missing data can be filled with the average of the measured parameter, filled with zeros in some cases, or might require removing the entire entries with missing values, which is especially true if the dependent variable is missing compared to some other auxiliary variables. If the observations have a time series nature, that could also help fill missing data with more advanced, and expectedly more accurate, values. Outliers on the other hand are more interesting because they might be telling some certain information. If the analyst concluded that they are still valid readings, it might be a good idea to study the impact on their inclusion and exclusion from the data driven model. However, if they were deemed invalid, they ought to be removed or treated as missing data.
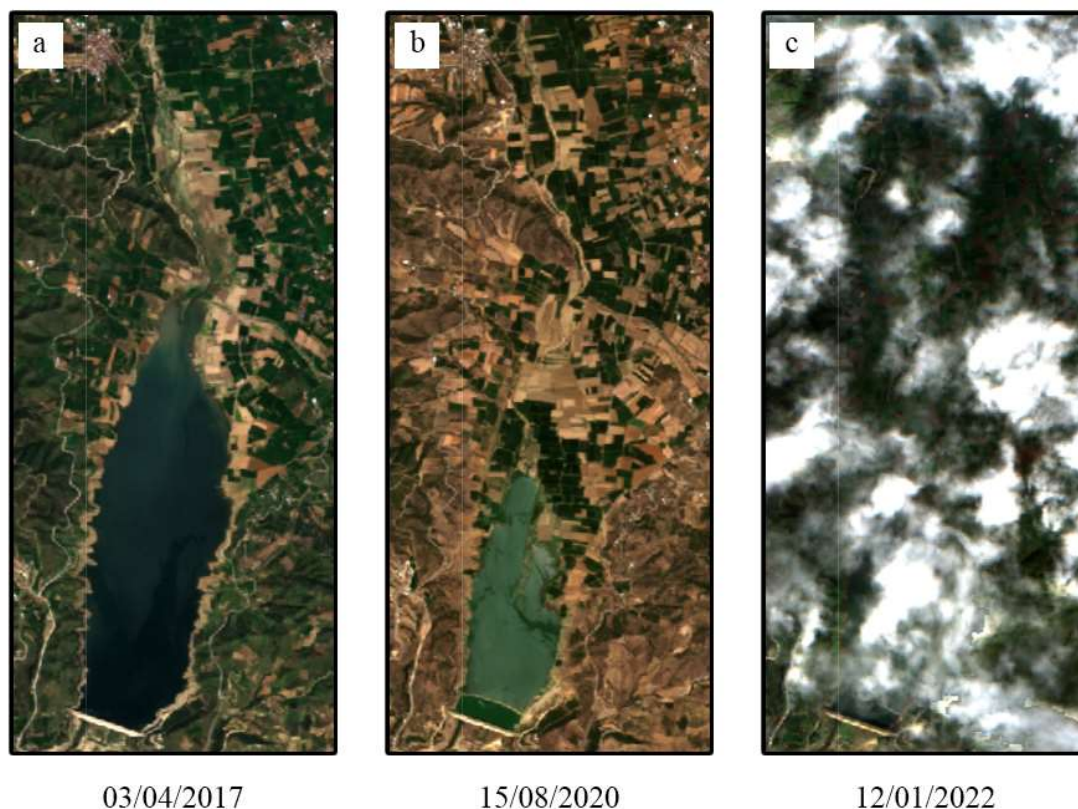
Figure 2. Sentinel-2 imagery for Beydağ reservoir at three different time points; (a) ideally clear view with the waterbody at its almost full extent, (b) clear view but the area suffers a severe draught, (c) view obscured by cloud and its overcast

2.4. Data Analysis and Prediction

Advancement in data science technologies has put in our hands a massive selection of tools and computation capabilities. As mentioned before, GEE gives access to a catalogue of valuable remote sensing data; in addition to over 1500 analysis tools that can be used on the data before retrieving it (Gorelick et al., 2017). It has been also possible to run Python code online in many online platforms, one of which is Google Colaboratory (GC). This enables more consistency than working on a regular Personal Computer (PC) as the analysis environment can be maintained fixed throughout the study with less risk of losing the initial configuration. Using GC has also the advantage of providing some advanced hardware capabilities that enable the use of some of the most common machine learning libraries; Keras and Tensorflow (Martín Abadi, Ashish Agarwal, Paul Barham, Eugene Brevdo et al., 2015). Anyway, Python still contains many powerful libraries that can also be run directly on a PC. Scikit-Learn, is one of the most common statistical libraries that could be used for a variety of models; such as, Linear Regression (LR), Support Vector Regression (SVR), and Random Forest Regression (RFR). The same library provides other tools like those for correlation and dimensionality reduction (Pedregosa et al., 2011). The chart in Figure highlights the general pathway intended to be followed in investigating the potential of utilizing Sentinel-2 reflectance data in assessing Chl-a concentration and turbidity in inland waterbodies.
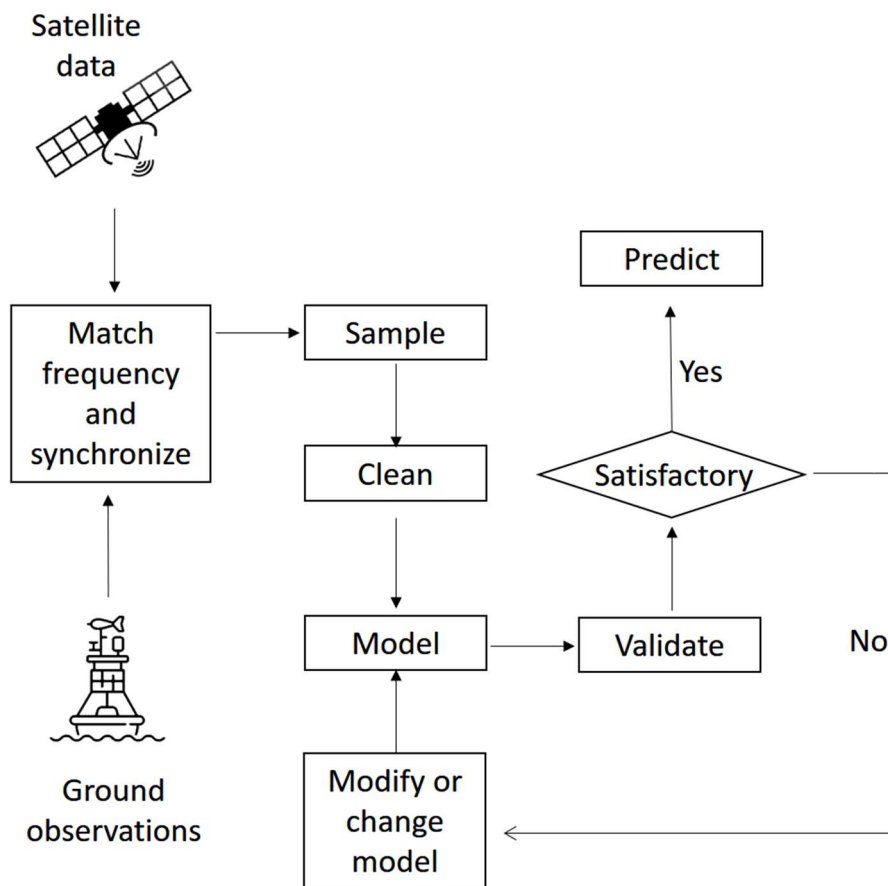
Figure 3. Framework for water quality assessment using spectral EO data

3. SUMMARY AND FINAL REMARKS

In this article, a proposition of utilizing satellite spectral data for water quality assessment is promoted. The discussion starts with addressing the shortcomings of traditional methods, and by shedding the light on the rapidly improving satellite data as well as data-driven methods. Then, a brief overview of the trends of utilizing satellite data is highlighted from the literature. Finally, some specific datasets and tools are proposed with a general framework as a starting point for investigating Chl-a and turbidity in inland waterbodies.

REFERENCES

Batur, E., & Maktav, D. (2019). Assessment of Surface Water Quality by Using Satellite Images Fusion Based on PCA Method in the Lake Gala, Turkey. *IEEE Transactions on Geoscience and Remote Sensing*, *57*(5), 2983–2989. https://doi.org/10.1109/TGRS.2018.2879024

Binding, C. E., Pizzolato, L., & Zeng, C. (2021). EOLakeWatch; delivering a comprehensive suite of remote sensing algal bloom indices for enhanced monitoring of Canadian eutrophic lakes. *Ecological Indicators*, *121*, 106999. https://doi.org/10.1016/j.ecolind.2020.106999

ESA. (n.d.). Level-2A Algorithm Overview. Retrieved January 19, 2022, from https://sentinels.copernicus.eu/web/sentinel/technical-guides/sentinel-2-msi/level-2a/algorithm

ESA. (2015). *Sentinel-2, User Handbook*. Retrieved from https://sentinels.copernicus.eu/web/sentinel/user-guides/document-library/-/asset_publisher/xlslt4309D5h/content/sentinel-2-user-handbook

Fassoni-Andrade, A. C., & Paiva, R. C. D. de. (2019). Mapping spatial-temporal sediment dynamics of river-floodplains in the Amazon. *Remote Sensing of Environment*, *221*(October 2018), 94–107. https://doi.org/10.1016/j.rse.2018.10.038

Gorelick, N., Hancher, M., Dixon, M., Ilyushchenko, S., Thau, D., & Moore, R. (2017). Google Earth Engine: Planetary-scale geospatial analysis for everyone. *Remote Sensing of Environment*, *202*, 18–27. https://doi.org/https://doi.org/10.1016/j.rse.2017.06.031

Greb, S., Dekker, A., Binding, C., & Stuart, V. (Eds.). (2018). *Earth Observations in Support of Global Water Quality Monitoring*. Dartmouth, Canada: International Ocean-Colour Coordinating Group (IOCCG). Retrieved from http://ioccg.org/wp-content/uploads/2018/09/ioccg_report_17-wq-rr.pdf

Guo, K., Zou, T., Jiang, D., Tang, C., & Zhang, H. (2017). Variability of Yellow River turbid plume detected with satellite remote sensing during water-sediment regulation. *Continental Shelf Research*, *135*(May 2016), 74–85. https://doi.org/10.1016/j.csr.2017.01.017

Kupssinsku, L. S., Guimaraes, T. T., De Freitas, R., De Souza, E. M., Rossa, P., Marques, A., … Mauad, F. F. (2019). Prediction of chlorophyll-a and suspended solids through remote sensing and artificial neural networks. *Proceedings of the International Conference on Sensing Technology, ICST*, *2019-Decem*, 4–9. https://doi.org/10.1109/ICST46873.2019.9047682

Kupssinskü, L. S., Guimarães, T. T., De Souza, E. M., Zanotta, D. C., Veronez, M. R., Gonzaga, L., & Mauad, F. F. (2020). A method for chlorophyll-a and suspended solids prediction through remote sensing and machine learning. *Sensors (Switzerland)*, *20*(7). https://doi.org/10.3390/s20072125

Martín Abadi, Ashish Agarwal, Paul Barham, Eugene Brevdo, Zhifeng Chen, Craig Citro, Greg S. Corrado, Andy Davis, Jeffrey Dean, Matthieu Devin, Sanjay Ghemawat, Ian Goodfellow, Andrew Harp, Geoffrey Irving, Michael Isard, Rafal Jozefowicz, Yangqing Jia, Lukasz Kaiser, Manjunath Kudlur, Josh Levenberg, Dan Mané, Mike Schuster, Rajat Monga, Sherry Moore, Derek Murray, Chris Olah, Jonathon Shlens, … Yuan Yu, and X. Z. (2015). TensorFlow: Large-Scale Machine Learning on Heterogeneous Systems. Retrieved from https://www.tensorflow.org/

Modiegi, M., Rampedi, I. T., & Tesfamichael, S. G. (2020). Comparison of multi-source satellite data for quantifying water quality parameters in a mining environment. *Journal of Hydrology*, *591*(June), 125322. https://doi.org/10.1016/j.jhydrol.2020.125322

Pahlevan, N., Smith, B., Schalles, J., Binding, C., Cao, Z., Ma, R., … Stumpf, R. (2020). Seamless retrievals of chlorophyll-a from Sentinel-2 (MSI) and Sentinel-3 (OLCI) in inland and coastal waters: A machine-learning approach. *Remote Sensing of Environment*, *240*(December 2019), 111604. https://doi.org/10.1016/j.rse.2019.111604

Pedregosa, F., Varoquaux, G., Gramfort, A., Michel, V., Thirion, B., Grisel, O., … Duchesnay, E. (2011).

Scikit-learn: Machine Learning in {P}ython. *Journal of Machine Learning Research*, *12*, 2825–2830.

Peterson, K. T., Sagan, V., & Sloan, J. J. (2020). Deep learning-based water quality estimation and anomaly detection using Landsat-8/Sentinel-2 virtual constellation and cloud computing. *GIScience and Remote Sensing*, *57*(4), 510–525. https://doi.org/10.1080/15481603.2020.1738061

Saberioon, M., Brom, J., Nedbal, V., Souček, P., & Císař, P. (2020). Chlorophyll-a and total suspended solids retrieval and mapping using Sentinel-2A and machine learning for inland waters. *Ecological Indicators*, *113*(July 2019). https://doi.org/10.1016/j.ecolind.2020.106236

Sagan, V., Peterson, K. T., Maimaitijiang, M., Sidike, P., Sloan, J., Greeling, B. A., … Adams, C. (2020). Monitoring inland water quality using remote sensing: potential and limitations of spectral indices, bio-optical simulations, machine learning, and cloud computing. *Earth-Science Reviews*, *205*(April), 103187. https://doi.org/10.1016/j.earscirev.2020.103187

Wang, Q., Song, K., Wen, Z., Shang, Y., Li, S., Fang, C., … Liu, G. (2021). Long-term remote sensing of total suspended matter using Landsat series sensors in Hulun Lake, China. *International Journal of Remote Sensing*, *42*(4), 1379–1397. https://doi.org/10.1080/01431161.2020.1829154

DROUGHT INDICES AND INTENSITY-DURATION-FREQUENCY CURVES FOR KUCUK MENDERES RIVER BASIN

Yonca Cavus

Beykent University, Department of Civil Engineering, Istanbul, Turkey

yoncacavus@beykent.edu.tr

Istanbul Technical University, Graduate School, Istanbul, Turkey

cavus17@itu.edu.tr

University of Freiburg, Environmental Hydrological Systems, Freiburg, Germany

yonca.cavus@hydrology.uni-freiburg.de

Halil Ibrahim Burgan

Akdeniz University, Department of Civil Engineering, Antalya, Turkey

burgan@akdeniz.edu.tr

Hafzullah Aksoy

Istanbul Technical University, Department of Civil Engineering, Istanbul, Turkey

haksoy@itu.edu.tr

Hakan Aksu

Samsun University, Department of Meteorological Engineering, Samsun, Turkey

hakan.aksu@samsun.edu.tr

Bulent Selek

Ministry of Agriculture and Forestry, Ankara, Turkey

bulent.selek@tarimorman.gov.tr

Ebru Eris

Ege University, Department of Civil Engineering, Izmir, Turkey

ebru.eris@ege.edu.tr

Hulya Boyacioglu

Dokuz Eylul University, Department of Environmental Engineering, Izmir, Turkey

hulya.boyacioglu@deu.edu.tr

ABSTRACT: Kucuk Menderes River basin in the western part of Turkey has a great importance for different sectors. Higher demand of water together with less availability in the river basin makes it necessary to plan and manage water resources in a more efficient and productive manner. In this study, a drought analysis is performed using precipitation and streamflow data from the Kucuk Menderes river basin. Drought analysis of the river basin is performed in this study by using the Standardized Precipitation Index (SPI), Standardized Precipitation Evapotranspiration Index (SPEI) and Streamflow Drought Index (SDI). The SPI and SPEI are calculated at time scales changing from 1 month up to 24 months. SDI is based on four time-scales as the accumulation of 3, 6, 9 and 12 months all starting from the beginning of October to the end of December of the same year, March, June, and September of the next year, respectively. Five meteorological and five streamflow gauging stations with ten years of length at minimum are used. Data analysis shows that the Kucuk Menderes River Basin has experienced extreme droughts in the past. Preliminary results based on the SPI, SPEI and SDI indices match with the observed droughts to validate the drought indices. Drought risk and drought severity are

561

obtained to demonstrate the areal extension of the drought in the river basin. It is seen from the preliminary analysis that drought risk decreases with the drought severity. The drought intensity-duration-frequency curves which could be quite important for any future drought-linked projection are also produced in this study. They are made available at each meteorological station for each drought index and for each time scale.

1. INTRODUCTION

Drought is defined as the lack of precipitation from normal condition that could occur slowly in time, and its impact may continue for a long time. Monitoring and predicting drought are real challenges since droughts are becoming more common and severe due to the impacts of climate change and variability (Alexander et al., 2009; Easterling et al., 2000; Aksoy et al., 2018). Therefore, a complicated natural drought is best characterized by using meteorological and hydrological variables, and indicators. Such variables or indicators are used to derive a drought index. A great number of drought indices have been developed in recent decades. A drought index comes to mind, first, to evaluate the impact of drought and drought characteristics which are the severity, intensity, magnitude, and duration (Mishra and Singh, 2010).

The drought indices, among many, include Palmer drought severity index (PDSI; Palmer, 1965); deciles (DI; Gibbs and Maher, 1967); crop moisture index (CMI; Palmer, 1968), surface water supply index (SWSI; Shafer and Dezman, 1982), standardized precipitation index (SPI; McKee et al., 1993), normalized difference vegetation index (NDVI; Kogan, 1995), vegetation condition index (VCI; Liu and Kogan, 1996), effective drought index (EDI; Byun and Wilhite, 1999), reconnaissance drought index (RDI; Tsakiris and Vangelis, 2005), soil moisture deficit index (SMDI), evapotranspiration deficit index (ETDI; Narasimhan and Srinivasan, 2005), standardized runoff index (SRI; Shukla and Wood, 2008), streamflow drought index (SDI; Nalbantis and Tsakiris 2009), standardized precipitation evapotranspiration index (SPEI; Vicente-Serrano et al., 2010), standardized groundwater index (SGI; Bloomfield and Marchant, 2013). Indices usually have a straightforward use due to their simplicity; those given especially for agricultural drought are however not that simple. For example, ETDI has a complex calculation procedure because of multiple inputs required; SMDI is complicated due to weekly calculations at different soil depths; soil water storage (SWS) is a difficult index to calculate owing to variations in both soil and crop types (WMO and GWP, 2016). The agricultural drought indices are limited owing to the large quantities of inputs required.

The indices can be used for short, medium and long-term projections. When particular examples among the drought indices are analysed, it is seen that the fundamental concept behind most of the indices is linked to the concept of SPI. For instance; Nalbantis and Tsakiris (2009) proposed SDI for characterizing the severity of hydrological droughts based on an analogy to SPI. Instead of precipitation data in SPI, streamflow data are used in SDI for overlapping periods of 3, 6, 9 and 12 months within each hydrological year. Khallili et al. (2011) used SPI and RDI, both being meteorological drought index and applied in different climatological zones. SPI is based on precipitation only while RDI utilizes the ratio of precipitation over potential evapotranspiration. Drought characteristics of the 3, 6, and 12 month-SPI and RDI time series were developed to examine Markov chain in using for the drought analysis. Both indices have shown similar behaviour; both followed the first order Markov chain dependency although climatological variability might have created some minor differences. Khattak et al. (2019) investigated the characteristics of the hydrological drought by using streamflow data of major rivers of the Indus River basin in Pakistan. The severities of drought were determined by SDI. A drought starting from 1999 to end in 2002 was observed for all stations which is considered to be the worst drought in the history of Pakistan. As a result, it was determined that all stations experienced a drought from moderate to severe in terms of severity in the common period starting in 1998 and terminating in 2002. Stahl (2001) developed the regional deficiency index to characterize hydrological droughts. The regional deficiency index uses daily flow data and removes the influence of streamflow seasonality on droughts. Nevertheless, the index does not indicate the magnitude of a drought–it only quantifies the duration from a binary time series–and it quantifies drought severity by the surface affected. This makes comparisons of hydrological droughts at different stations impossible.

The purpose of this study is to perform drought analysis using precipitation and streamflow data from the Kucuk Menderes river basin in the western part of Turkey. SPI, SPEI and SDI are used for the drought analysis. SPI and SPEI are calculated at 1, 3, 6, 9, 12 and 24 months-time scales while SDI is calculated on four time-scales as the accumulation of 3, 6, 9 and 12 months all starting from the beginning of October to the end of December of the same year, March, June, and September of the next year, respectively. The drought intensity-duration-frequency (IDF) curves which could be quite important for any future drought-linked projection are also produced in this study. Also the drought risk is provided in graphs and the drought severity in maps. The drought risk graphs and severity maps provide a comprehensive characterisation of the drought. This is followed by the results and discussion section, where spatial distribution of drought hazard, vulnerability and risk in western parts of Turkey has been discussed. This paper finally discusses future development directions of modelling approaches for the drought practice.

2. STUDY AREA AND DATA

Turkey is divided into 25 hydrological basins (Figure 1) with different topographical characteristics as well as meteorological conditions. Monthly precipitation and streamflow data from Kucuk Menderes River Basin are used in this study. Kucuk Menderes River Basin is located in the Aegean region, the western part of Turkey, with a drainage area of 6,963 km^2.
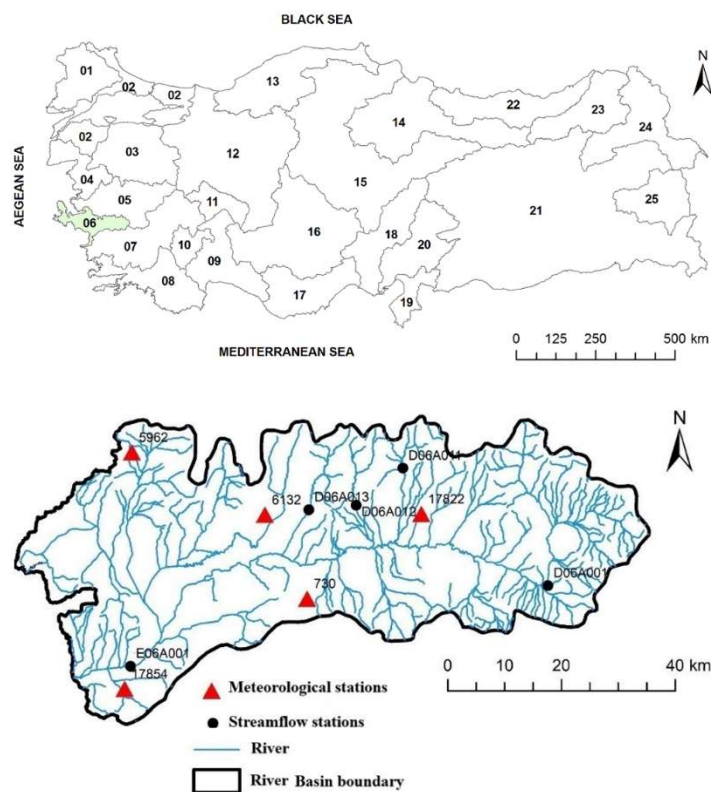
Figure 1. Location of Kucuk Menderes River Basin in Turkey, and layout of the meteorological and streamflow gauging stations

The long-term average of annual precipitation in the basin is 727 mm, the annual runoff is 17,16 m^3/s. Land in the basin is used for agriculture followed by forests and semi-natural areas. The agricultural area covers about 41% of the basin of which 52% is irrigated agriculture whereas the rest is used for dry agriculture. The relatively urbanized basin has also some wetlands and reservoirs. The basin exhibits the characteristics of the Mediterranean climate; thus, the summer season is hot and dry while the winter season is warm and rainy.

As for the data, monthly precipitation for 5 meteorological stations were obtained from State Meteorological Service (MGM with its Turkish acronym) while monthly streamflow data were obtained from the State Hydraulic Works of Turkey (DSI with its Turkish acronym) for Kucuk

Menderes River Basin. The meteorological and streamflow data are listed in Tables 1 and 2, respectively, in which the code and name of stations are given together with the observation period of each station. Statistical characteristics calculated from the monthly precipitation and streamflow time series of each station are given in Tables 1 and 2. They are the minimum, maximum, mean, standard deviation, coefficient of variation (C_v), coefficient of skewness (C_s), kurtosis, and lag-one autocorrelation coefficient (r_1). Also, the altitude and area are given for streamflow gauging stations. Data quantity and quality are important issues in hydrological and meteorological applications. Thus, in this study, any station with 10 years of observation at minimum is considered for the analysis. Gaps in the data are filled unless the gap is longer than 12 consecutive months. That is, if a gap longer than 12 months exists in the time series, it is not considered for the analysis. Layout of the meteorological and hydrometric stations in the Kucuk Menderes River Basin is shown in Figure 1 from which it is seen that the stations are scattered over the basin almost homogeneously.

Table 1. Characteristics of meteorological stations in Kucuk Menderes River Basin.

Station Code	Station name	Observation period	Number rainy months (%)	Mean (mm)	Min (mm)	Max (mm)	St. Dev. (mm)	C_v	C_s	C_k	r_1
730	Tire	1960-1994	15.24	63.59	0.00	428.2	75.16	1.18	1.75	3.63	0.41
5962	Dağkızılca	1985-1996	13.89	57.23	0.00	407.8	69.90	1.22	1.90	4.83	0.28
6132	Bayındır	1966-1984	11.84	55.29	0.00	347.6	60.95	1.10	1.47	2.46	0.47
17822	Ödemiş	1960-2018	22.88	43.86	0.00	333.7	53.35	1.22	1.67	3.36	0.45
17854	Selçuk	1964-2018	28.48	50.17	0.00	326.5	66.43	1.32	1.66	2.58	0.46

Table 2. Characteristics of gauging streamflow stations in Kucuk Menderes River Basin.

Station Code	Observation period	No-runoff months (%)	Mean (m³/s)	Min (m³/s)	Max (m³/s)	St. Dev. (m³/s)	C_v	C_s	C_k	r_1	Drainage Area (km²)	Elev. (m)
D06A001	1986-1999	17.95	1.32	0.00	10.22	1.83	1.39	2.08	5.27	0.56	445	171
D06A011	1990-2014	2.43	0.32	0.00	3.65	0.48	1.53	2.59	9.87	0.61	37	220
D06A012	1985-2002	23.53	0.23	0.00	5.03	0.47	2.00	6.15	56.00	0.45	73.4	130
D06A013	1979-1990	1.52	0.68	0.00	6.80	0.94	1.38	3.59	17.40	0.49	83	130
E06A001	1960-2008	11.63	9.33	0.00	144.1	17.50	1.88	3.38	14.49	0.61	3255.2	4

3. METHODOLOGY

3.1. Standardized Precipitation Index (SPI)

With the help of SPI, dry and wet periods of monthly precipitation can be identified. SPI is obtained simply as the standard normal variable transformed from the gamma distribution by

$$SPI_{ij} = \frac{x_{ij} - \mu_j}{\sigma_j} \tag{1}$$

where x_{ij} is the precipitation (in mm) in month j (j = 1, 2, 3, ……, 12) of year i (i = 1, 2, …, n); μ_j and σ_j, are the average and standard deviation of precipitation (in mm) in month j, respectively. The SPI values are calculated for different time scales such as k = 1, 3, 6, 9, 12, 24 months. These arbitrarily selected time scales are used to represent the three types of drought; meteorological, agricultural and hydrological. It can be assumed that 1- and 3-month time scales are used for meteorological drought; 6- and 9-month time scales are for agricultural drought; and 12- and 24-month time scales are for hydrological drought.

Table 3. Drought categorization based on SPI, SPEI and SDI values.

Drought Category	SPI, SPEI, SDI
Mild	-1.0 < SPI, SPEI, SDI < 0.0
Moderate	− 1.5 < SPI, SPEI, SDI ≤ −1.0
Severe	−2.0 < SPI, SPEI, SDI ≤ −1.5
Extreme	SPI, SPEI, SDI ≤ −2.0

3.2. Standardized Precipitation Evapotranspiration Index (SPEI)

Standardized precipitation evapotranspiration index (SPEI) is based on precipitation and potential evapotranspiration data. This represents a basic climatic water balance (Thornwaite 1948) that is calculated at different time scales to obtain the SPEI. The simplest approach to calculate PET is given by Thornthwaite (1948), which requires the monthly-mean temperature data only. Following this method, the monthly PET (in mm) is obtained by

$$PET = 16K\left(\frac{10T}{I}\right)^m \tag{2}$$

where K is a correction coefficient depending on the latitude, T is the monthly-mean temperature (ºC), I is the heat index, which is calculated as the sum of 12 monthly index values, and m is a coefficient given as a third order polynomial depending on the heat index. With a given value of PET, the difference between precipitation (P) and PET is calculated using

$$D_i = P_i - PET_i \tag{3}$$

which provides a simple measure of the water surplus or deficit for month i. The calculated D values are aggregated at different time scales, following the same procedure as that for the SPI. The log-logistic distribution adapted very well to the D values for all-time series after the frequency analysis is applied using L-moments. The classical approximation of Abramowitz and Stegun (1965) between the cumulative distribution function and SPEI,

$$SPEI = W - \frac{C_0 + C_1 W + C_2 W^2}{1 + d_1 W + d_2 W^2 + d_3 W^3} \tag{4}$$

is obtained. Here, W is the probability of exceeding a determined D value (Pr)

$$Pr = 1 - F(x) \tag{5}$$

where

$$W = \sqrt{-2\ln(Pr)} \qquad P \leq 0.5 \tag{6}$$

is calculated. If Pr > 0.5, then Pr is replaced by 1-Pr and the sign of the resultant SPEI is reversed. The constant are $C_0 = 2.515517$, $C_1 = 0.802853$, $C_2 = 0.010328$, $d_1 = 1.432788$, $d_2 = 0.189269$, $d_3 = 0.001308$ (Vicente-Serrano et al., 2010). Drought is categorised depending on the values of SPEI as given in Table 3. The SPEI calculation is detailed by Vicente-Serrano et al. (2010).

3.3. Streamflow Drought Index (SDI)

Streamflow drought index (SDI) was developed by Nalbantis and Tsakiris (2009). It is assumed that a time series of monthly streamflow volumes Q_{ij} is available where i denotes the hydrological year and j the month within the hydrological year (j = 1 for October and j = 12 for September of the next year). Using the streamflow time series,

$$V_{ik} = \sum_{j=1}^{3k} Q_{ij} \qquad i = 1, 2, \dots, N \qquad j = 1, 2, \dots, 12 \quad k = 1, 2, 3, 4 \tag{7}$$

is calculated where V_{ik} is the cumulative streamflow volume for the i-th hydrological year and the k-th reference period, k = 1 for October-December, k = 2 for October-March, k = 3 for October-June and k = 4 for October-September. It is seen that October-September for k = 4 represents the annual total streamflow. Based on the cumulative streamflow volumes V_{ik}, SDI is defined for each reference period k of the i-th hydrological year as

$$SDI_{ik} = \frac{V_{ik} - \overline{V_k}}{S_k} \quad i = 1, 2, \dots, N \quad k = 1, 2, 3, 4 \tag{8}$$

where $\overline{V_k}$ and S_k are, respectively, the mean and the standard deviation of cumulative streamflow volumes of reference period k. The approximation followed in SPI is used; e.g., the distribution is transformed into normal distribution from its non-normal distribution. Drought is categorised depending on the values of SPEI as given in Table 3.

3.4. Dimensionless Precipitation Anomaly Index (DPAI)

Difference (anomaly) between precipitation in a year and the mean precipitation for one particular meteorological station is incomparable due to its dimension. Therefore, the precipitation difference (anomaly) calculated for each station is made dimensionless by dividing the anomaly with the mean of precipitation (P_{mean}) so that a comparable index is obtained. The so-called Dimensionless Precipitation Anomaly Index (DPAI) (Eris et al., 2020) is defined as

$$DPAI(\%) = \frac{P - P_{mean}}{P_{mean}} 100 \tag{11}$$

DPAI can be evaluated as an index similar to the Percentage of Normal Precipitation Index (PNPI) which has a common use in literature and defined as

$$PNPI(\%) = \frac{P}{P_{ort}} 100 \tag{12}$$

DPAI and PNPI are linked by

$$DPAI(\%) = PNPI(\%) - 100 \tag{13}$$

Although there is no significant difference compared to PNPI, DPAI provides an easier way to determine dry and wet periods, because it gets positive and negative values, the former indicates a wet period while the latter shows a dry period.

Table 4 illustrates how the drought is categorized based on DPAI adapted from PNPI, and Table 5 shows the PNPI and DPAI values calculated for each meteorological station. Dry periods are determined at least for one year (between 1960-2018) for all meteorological stations. In this context, it can be said that the longest dry period between 1960 and 2018 was observed from 1985 to 1994, although drought category is close to normal; however, it is slightly dry in 1989 and it is moderately dry in 1992.

Table 4. Drought categorization based on PNPI and DPAI.

Drought category	PNPI (%)	DPAI (%)
No drought	PNPI > 100	DPAI > 0
Normal	80 < PNPI < 100	-20 < DPAI < 0
Mild	70 < PNPI > 80	-30 < DPAI < -20
Moderate	55 < PNPI < 70	-45 < DPAI < -30
Severe	40 < PNPI < 55	-60 < DPAI < -45
Extreme	PNPI < 40	DPAI < -60

3.5. Frequency Analysis

Frequency analysis is performed to characterize the drought and to determine the best-fit probability distribution function. Frequency analysis are applied on the drought severity. In the frequency analysis of drought, the 2- and 3-parameter Gamma (G2, G3), the Generalized Extreme Value (GEV), the 2- and 3-parameter log-normal (LN2, LN3), Log-Pearson Type 3 (LP3) and the 2- and 3-parameter Weibull (W2, W3) probability distribution functions are often used in the literature. For the sake of consistency with the literature, the above probability distribution functions were considered for the frequency analysis of drought in this study.

For months, when no drought is observed in some particular years, the frequency analysis is applied on the non-zero values only to distinguish zero values from the non-zero values; because, the frequency analysis would otherwise not be meaningful. Any process that is composed of zero and non-zero values is called a censored or intermittent process. The total probability theorem is available to use for such processes to examine them in two parts; the zero- and non-zero parts. According to the total probability theorem (Haan, 1977)

$$P(S \geq s) = P(S \geq s | S = 0)P(S = 0) + P(S \geq s | S \neq 0)P(S \neq 0) \tag{14}$$

is used. Here,

$$P(S \geq s \mid S = 0) = 0$$

(15)

Therefore,

$$P(S \geq s) = P(S \geq s \mid S \neq 0)P(S \neq 0)$$

(16)

is obtained.

$P(S \neq 0)$ is the rate of years with non-zero values in the SPI_k (k = 1, 3, 6, 9, 12, 24-month) time series Equation (16) can also be written in terms of the cumulative probability distribution as

$$1 - F(s) = (1 - p)[1 - F^*(s)]$$

(17)

In Equation (17), p is the probability of zero values. $F(s)$ is the cumulative probability distribution function of all S including zeros which is expressed as $P(S \leq s \mid S \geq 0)$ and $F^*(x)$ is the cumulative probability distribution function of the non-zero values of S which is expressed as $P(S \leq s \mid S \neq 0)$. The rate of the non-zero values, $1 - p$ in Equation (17), can be expressed in terms of the probability as

$$1 - p = P(S \neq 0)$$

(18)

The magnitude of an event with return period T can be predicted by solving Equation (17) for $F^*(s)$ and then by using the inverse transformation of $F^*(s)$ to get the value of S. From Equation (17)

$$F^*(s) = \frac{F(s) - p}{1 - p}$$

(19)

can be written. Considering that the return period of a given severity for a particular drought duration can be predicted by

$$F(s) = 1 - \frac{1}{T}$$

(20)

Equation (20) turns into

$$F^*(s) = \frac{1 - \frac{1}{T} - p}{1 - p}$$

(21)

Table 5. Percent of Normal Precipitation index (PNPI, left panel) - Dimensionless Precipitation Anomaly Index (DPAI, right panel) for meteorological stations in Kucuk Menderes River Basin at annual time scale.

YIL	PNPI (%) 730	5962	6132	17822	17854	ORT (%)	DPAI(%) 730	5962	6132	17822	17854	ORT (%)
1960	113.4			125.0		119.2	13.4			25.0		19.2
1961	80.5			99.2		89.8	-19.5			-0.8		-10.2
1962	157.8			165.2		161.5	57.8			65.2		61.5
1963	121.9			121.7		121.8	21.9			21.7		21.8
1964	86.0			94.4	102.0	94.1	-14.0			-5.6	2.0	-5.9
1965	141.8			137.6	141.9	140.4	41.8			37.6	41.9	40.4
1966	154.6		105.2	126.6	138.6	131.2	54.6		5.2	26.6	38.6	31.2
1967	74.2		72.0	83.0	96.1	81.3	-25.8		-28.0	-17.0	-3.9	-18.7
1968	87.9		101.8	122.9	110.1	105.7	-12.1		1.8	22.9	10.1	5.7
1969	101.5		99.8	98.4	100.0	99.9	1.5		-0.2	-1.6	0.0	-0.1
1970	91.6		105.5	89.9	104.1	97.8	-8.4		5.5	-10.1	4.1	-2.2
1971	80.5		111.1	120.3	134.7	111.7	-19.5		11.1	20.3	34.7	11.7
1972	69.4	54.5		64.1	87.1	68.8	-30.6	-45.5		-35.9	-12.9	-31.2
1973	91.5		72.5	77.9	75.0	79.2	-8.5		-27.5	-22.1	-25.0	-20.8
1974	114.5		107.0	110.6	122.2	113.6	14.5		7.0	10.6	22.2	13.6
1975	121.9		98.1	116.0	117.8	113.4	21.9		-1.9	16.0	17.8	13.4
1976	90.7		90.7	92.5	82.0	89.0	-9.3		-9.3	-7.5	-18.0	-11.0
1977	74.2		95.0	83.6	101.5	88.5	-25.8		-5.0	-16.4	1.5	-11.5
1978	134.1		138.0	147.9	134.2	138.6	34.1		38.0	47.9	34.2	38.6
1979	103.0		111.0	110.2	104.9	107.3	3.0		11.0	10.2	4.9	7.3
1980	126.3		107.8	122.3	103.3	114.9	26.3		7.8	22.3	3.3	14.9
1981	170.6		139.4	147.5	154.7	153.1	70.6		39.4	47.5	54.7	53.1
1982	106.3		88.9	83.0	94.7	93.2	6.3		-11.1	-17.0	-5.3	-6.8
1983	99.6		96.9	104.1	101.2	100.4	-0.4		-3.1	4.1	1.2	0.4
1984	88.8		104.8	90.9	118.2	100.7	-11.2		4.8	-9.1	18.2	0.7
1985	76.9	103.9		84.9	72.0	84.4	-23.1	3.9		-15.1	-28.0	-15.6
1986	86.8	118.9		86.1	83.4	93.8	-13.2	18.9		-13.9	-16.6	-6.2
1987	98.2	105.8		94.5	81.3	94.9	-1.8	5.8		-5.5	-18.7	-5.1
1988	98.0	111.2		88.9	92.1	97.5	-2.0	11.2		-11.1	-7.9	-2.5
1989	65.6	70.6		70.8	59.9	66.7	-34.4	-29.4		-29.2	-40.1	-33.3
1990	77.9	103.5		81.7	74.9	84.5	-22.1	3.5		-18.3	-25.1	-15.5
1991	78.6	78.1		62.7	67.7	71.8	-21.4	-21.9		-37.3	-32.3	-28.2
1992	50.7	61.5		63.3	49.9	56.4	-49.3	-38.5		-36.7	-50.1	-43.6
1993	79.4	102.2		88.3	85.5	88.9	-20.6	2.2		-11.7	-14.5	-11.1
1994	105.3	94.7		87.6	98.2	96.4	5.3	-5.3		-12.4	-1.8	-3.6
1995		139.6		93.0	100.2	110.9		39.6		-7.0	0.2	10.9
1996		110.0		101.5	109.8	107.1		10.0		1.5	9.8	7.1
1997				102.3	95.5	98.9				2.3	-4.5	-1.1
1998				117.7	125.7	121.7				17.7	25.7	21.7
1999				81.0	109.0	95.0				-19.0	9.0	-5.0
2000				81.7	78.5	80.1				-18.3	-21.5	-19.9
2001				110.9	124.7	117.8				10.9	24.7	17.8
2002				111.0	103.2	107.1				11.0	3.2	7.1
2003				111.5	108.6	110.0				11.5	8.6	10.0
2004				73.7	89.0	81.4				-26.3	-11.0	-18.6
2005				94.8	119.5	107.1				-5.2	19.5	7.1
2006				93.5	74.1	83.8				-6.5	-25.9	-16.2
2007				85.8	79.5	82.7				-14.2	-20.5	-17.3
2008				67.7	65.3	66.5				-32.3	-34.7	-33.5
2009				129.7	131.6	130.6				29.7	31.6	30.6
2010				108.8	115.1	111.9				8.8	15.1	11.9
2011				104.7	88.7	96.7				4.7	-11.3	-3.3
2012				121.9	114.5	118.2				21.9	14.5	18.2
2013				109.8	103.2	106.5				9.8	3.2	6.5
2014				95.4	115.5	105.4				-4.6	15.5	5.4
2015				85.8	99.2	92.5				-14.2	-0.8	-7.5
2016				88.9	81.2	85.0				-11.1	-18.8	-15.0
2017				89.9	90.4	90.2				-10.1	-9.6	-9.8
2018				95.3	89.4	92.3				-4.7	-10.6	-7.7
MIN	50.7	61.5	54.5	62.7	49.9	56.4	-49.3	-38.5	-45.5	-37.3	-50.1	-43.6

4. RESULTS

4.1 Observed Dry Periods

SPI and SPEI time series at k = 1, 3, 6, 9, 12 and 24-month time scales between 1960 and 2016 for station 17822 are given in Figures 2 and 3. It is possible to detect dry periods from SPI and SPEI time series. Using the drought category lines marked on the time series, it is possible to understand the drought category in any dry period. The drought severity can be read from the SPI_k values which indicate the severity of the drought. According to SPI and SPEI, the main drought episodes occurred in 1972, 1992, and 1994. Minor differences appear between the SPI and the SPEI time series independent from the time scale. The drought analysis similar to that done by SPI and SPEI is made with SDI for which the time series is obtained at k = 1, 2, 3, and 4-time scales as given in Figure 4 for streamflow gauging station E06A001.

According to the results, dry periods determined by the SDI overlap the observed dry periods. It is seen that SDI based on the streamflow data is a meaningful index for Kucuk Menderes River Basin as well as SPI and SPEI based on precipitation data.
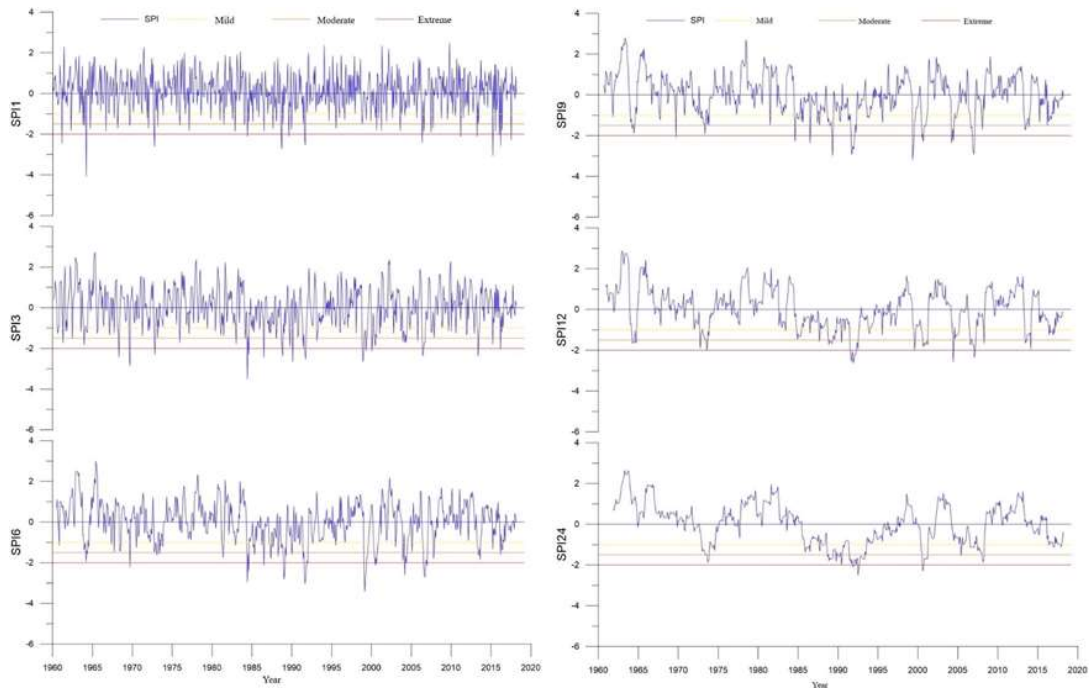
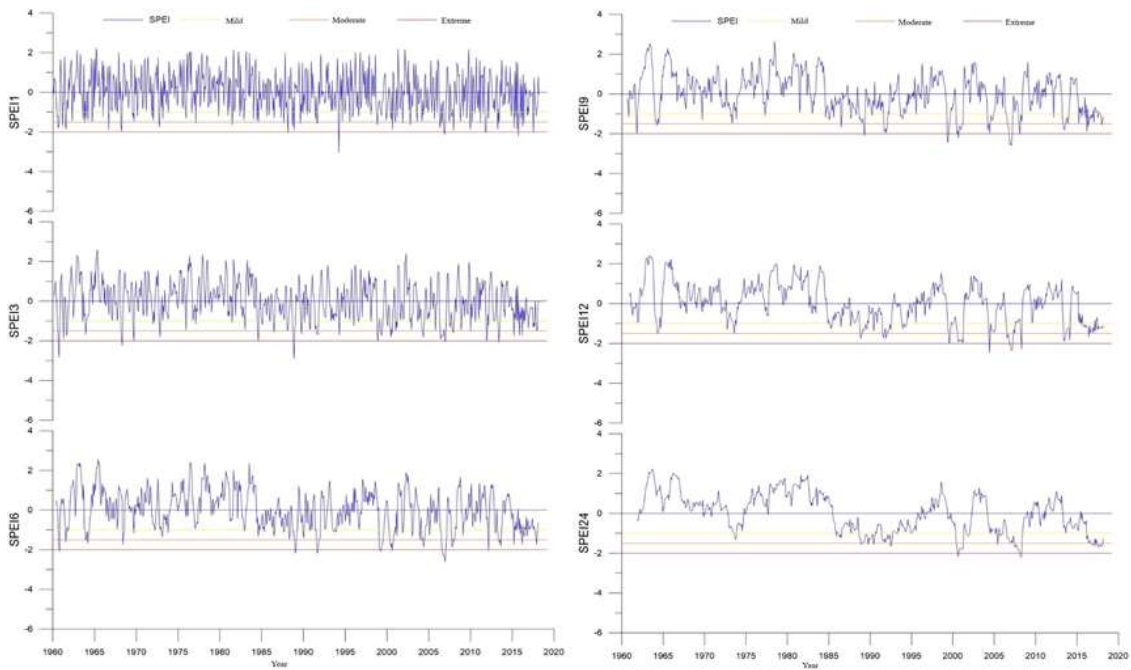Figure 2. SPI1, SPI3, SPI6, SPI9, SPI12 and SPI24 time series for station 17822

Figure 3. SPEI1, SPEI3, SPEI6, SPEI9, SPEI12, and SPEI24 time series for station 17822

4.2 Drought Risk Graphs

Drought risk graphs were obtained by using the time series of SPI_k (k = 1, 3, 6, 9, 12, and 24-months) for five meteorological stations in Kucuk Menderes River Basin. Drought risk is defined as the likelihood that a specific drought category is observed. It was calculated in this study as follows: The SPI and SPEI time series were detected to count each drought falling into drought categories as in Table 3, and the frequency of each drought category in the observation period was calculated. The frequency is equal to the observation probability (the risk) of the relevant drought category based on the observation period. Calculated probabilities are given in Figures 5-6 for SPI_k and $SPEI_k$ (k = 1, 3, 6, 9, 12, and 24-months) time scales, respectively. It is seen that mild drought mostly dominates. The frequency of the mild drought is higher than other drought categories because, as stated in Table 3,

mild drought has been defined to have a wider range than other drought categories. SPI for the mild drought ranges in -1.00 < SPI < 0, while the moderate and severe droughts are between -1.50 < SPI ≤ -1.00 and -2.00 < SPI ≤ -1.50, respectively. As for the extreme drought, there is an open-end range SPI ≤ -2. The probability of extreme drought is much lower than the central values due to the open-end range with low likelihood of occurrence.
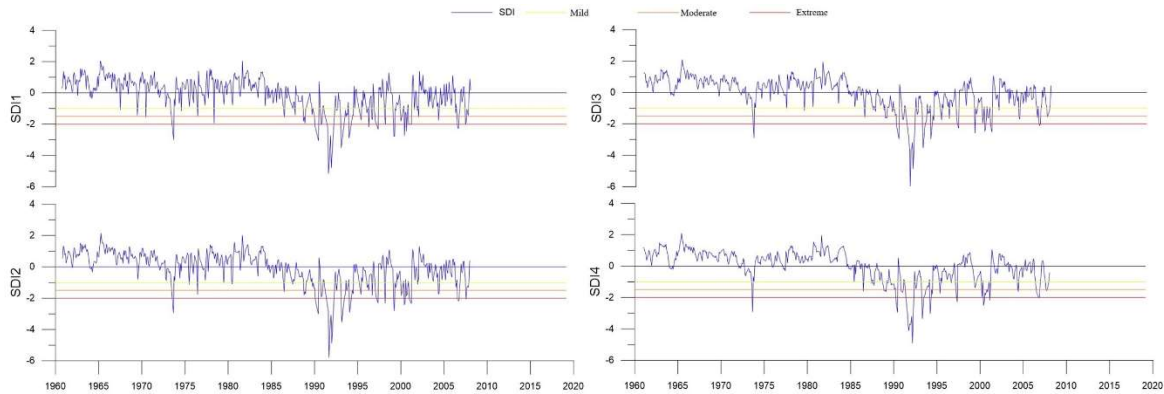

Figure 4. SDI1, SDI2, SDI3 and SDI4 time series for gauging station E06A001

It is obviously seen that mild drought at each time-scale is the most observed drought category for the five meteorological stations in the Kucuk Menderes River Basin (Figures 6-7). The drought intensity decreases as the drought intensity increases. This result can be accepted as a rule that applies to all stations with a few exceptions depending, probably, on short data records. The average drought risk graph was obtained from five stations in the river basin by taking the average of SPI values. It reveals the general validity of the rule that the drought risk always decreases at all-time scales as the drought intensity increases without exception.

4.3 Drought Intensity-Duration-Frequency Curves

Frequency analysis is generally performed to characterize the severity, intensity, duration and return period of the point-scale or regional drought. In hydrology, it determines extreme values that play an important role in water resources development projects and gives the information about drought features of the relevant region. It has, therefore, been performed frequently in research and applications about drought. In this study, the most severe drought in any year is called the critical drought of the year. When drought is not observed in a year, no critical drought has been assigned to this particular year. In other words, a zero value is assigned to the time series of drought severity for years with no drought. The total probability theorem is used for the frequency analysis of intermittent time series (which has zero and non-zero values) in the literature (Haan, 1977). Frequency analysis of critical drought time series with ten values at minimum is performed.
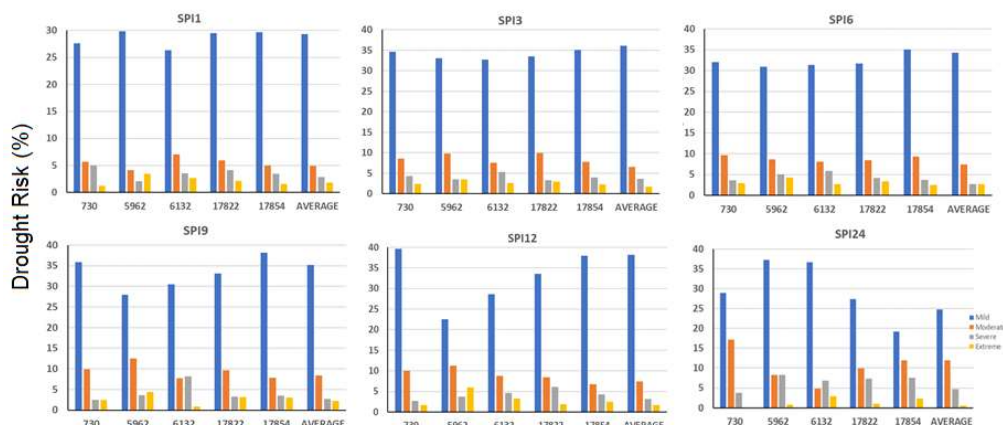

Figure 5. Probabilities of each drought category (drought risk) using SPI for 5 meteorological stations and their average in Kucuk Menderes River Basin
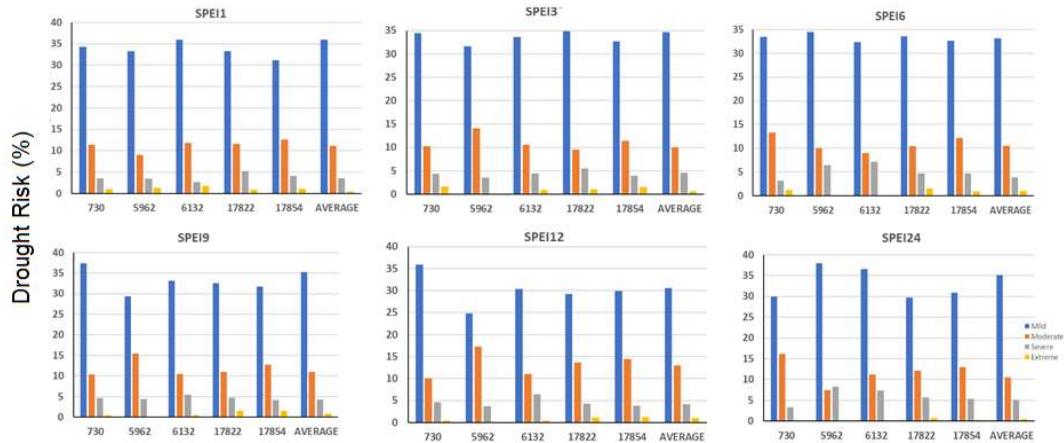
Figure 6. Probabilities of each drought category (drought risk) using SPEI for 5 meteorological stations and their average in Kucuk Menderes River Basin

Aksoy et al (2018) used the 2- and 3-parameter Weibull (W2, W3), General Extreme Value (GEV), 2- and 3-parameter Gamma (Pearson Type III) (G2, G3) and 2- and 3-parameter Log-Normal (LN2, LN3) for the drought severity as potential probability distribution functions. When the best-fit probability distribution function is determined for each time scale, drought severity and intensity of any return period can be calculated. Drought intensity-duration-frequency curves (IDF) are then obtained with repeating this process for all time scales, drought duration and return period.

IDF curves were obtained for 1, 3, 6, 9, 12 and 24-month time scales for each meteorological station by using the SPI and SPEI time series (Figures 7-8). It is seen from the IDF curves that drought intensity decreases with increasing drought duration. Drought IDF curves are useful tools to determine the drought intensity at certain duration and return period. They are similar to the precipitation intensity-duration-frequency curves used in hydrology for the design. At the same time, it provides information about precipitation deficit. Therefore, it is possible to consider drought IDF curves an important and useful result of this study. Instead of SPI or SPEI-based drought IDF curves, drought SDF or IDF curves based on precipitation deficit can be alternatively proposed as developed by Cavus (2019) and Cavus and Aksoy (2019, 2020) for Seyhan River Basin in Turkey. The precipitation deficit based IDF curve were shown to be of great importance for the physical understanding of drought including its practical use.
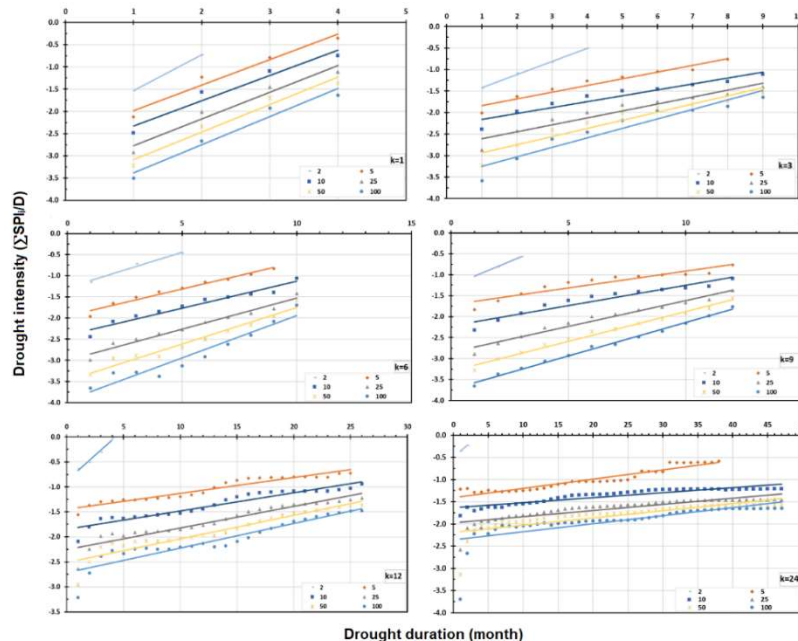

Figure 7. Drought intensity-duration-frequency curves of hydrometric station 17822 based on SPI
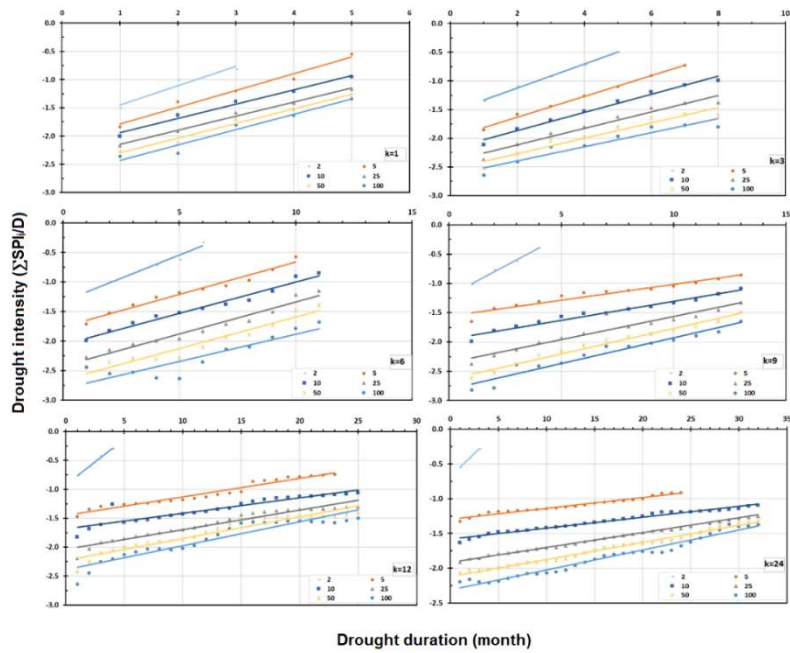
Figure 8. Drought intensity-duration-frequency curves of hydrometric station 17822 based on SPEI

5. CONCLUSION

In this study, it has been carried out to investigate the extent and impact of droughts in Kucuk Menderes River Basin. SPI, SPEI and SDI are used to detect the drought and wet periods. Also, Dimensionless Precipitation Anomaly Index (DPAI) is introduced as a new drought index which gives novelty to this study. Applications using precipitation and streamflow data and comparison with current indices are good enough to show the drought intensity. The DPAI is used to assess the drought, and frequency analysis is applied to characterize the drought. Drought intensity-duration-frequency (IDF) curves and drought risk graphs are provided. As the assessment of risk is one of the main aspects of drought mitigation and planning, it is hoped that the drought risk graphs will assist in guiding the operational responses for the drought practice.

REFERENCES

Abramowitz, M., & Stegun, A. (1965). *Handbook of Mathematical Formulas, Graphs, and Mathematical Tables*, Dover Publications. Inc.: New York

Aksoy, H., Cetin, M., Onoz, B., Yuce, M.I., Eris, E., Selek, B, Aksu, H., Burgan, H.I., Esit, M., Orta, S., Cavus, Y. (2018). Hidrolojik havzalarda düşük akımlar ve kuraklık analizi. (Rapor No. TUJJB-TUMEHAP-2015-01). ISTANBUL: TUJJB Sonuç Raporu, 2018

Alexander, L. V., Tapper, N., Zhang, X., Fowler, H.J., Tebaldi, C., Lynch, A. (2009). Climate extremes: progress and future directions, *International Journal of Climatology*, Vol. 29, pp.317-319.

Bloomfield, J.P. & Marchant, B.P. (2013). Analysis of groundwater drought building on the standardised precipitation index approach. *Hydrology and Earth System Sciences*, 17, 4769–4787.

Byun, H.R. & Wilhite, D.A. (1999). Objective quantification of drought severity and duration. American Meteorological Society. *Journal of Climate*, 12, 2747-2756.

Çavuş, Y. (2019). Critical drought severity-duration-frequency curves based on precipitation deficit. İTÜ Fen Bilimleri Enstitüsü, Master thesis, 199.

Cavus, Y., & Aksoy, H. (2019). Spatial drought characterization for Seyhan River basin in the Mediterranean region of Turkey. *Water*, 11, 1331.

Cavus, Y., & Aksoy, H. (2020). Critical drought severity/intensity-duration-frequency curves based on precipitation deficit, *Journal of Hydrology,* 584, 124312.

Easterling D.R., Meehl, G.A., Parmesan, C., Changnon, S.A., Karl, T.R., Mearns, L.O. (2000). Climate extremes: observations, modelling, and impacts. *Sciences Compass*, 289, 2068-2075.

Eris, E., Cavus, Y., Aksoy, H., Burgan, H.I., Aksu, H., Boyacioglu (2020). Spatiotemporal analysis of meteorological drought over Kucuk Menderes River Basin in the Aegean Region of Turkey. *Theoretical and Applied Climatology,* 142, 1515-1530.

Gibbs, W. J., & Maher, J.V. (1967). Rainfall deciles as drought indicators. *Bureau of Meteorology Bull.48.* Commonwealth of Australia, Melbourne, Australia.

Haan, C.T. (1977). *Statistical methods in Hydrology,* Iowa State University Press.

Khalili, D., Farnoud, T., Jamshidi, H., Kamgar-Haghighi, A.A., Zand-Parsa, S. (2011). Comparability analyses of the SPI and RDI meteorological indices in different climatic zones. *Water Resources Management*, 25, 1737-1757.

Khattak, M.S., Khan, A., Khan, M.A., Ahmad, W., Rehman, S., Sharif, M., Ahmad, S. (2019). Investigation of characteristics of hydrological drought in Indus basin. Sarhad *Journal of Agriculture*, 35, 48-56.

Kogan, F.N. (1995). Application of vegetation index and brightness temperature for drought detection. *Advances in Space Research Journal-Elsevier,* 15, 11, 91.

Liu W.T., & Kogan F.N. (1996). Monitoring regional drought using the vegetation condition index. *International Journal of Remote Sensing,* 17(14), 2761-2782.

Mishra A.K, & Singh V.P. (2010). A review of drought concepts. *Journal of Hydrology,* 391 (1-2), 202-216**.**

McKee, T.B., & Doesken, N.J., Kleist, J. (1993). The relationship of drought frequency and duration to time scales. *Eighth Conference on Applied Climatology*, American Meteorological Society, Jan17-23, 1993, Anaheim CA.

Nalbantis, I. & Tsakiris, G. (2009). Assessment of hydrological drought revisited. *Water Resource Management*, 23, 881-897.

Narasimhan, B., & Srinivasan, R. (2005). Development and evaluation of soil moisture deficit index (SMDI) and evapotranspiration deficit index (ETDI) for agricultural drought monitoring. *Agricultural Forestry Meteorological,* 133, 69-88.

Palmer, W.C. (1965). Meteorological drought. *US Department of Commerce. Weather Bureau, Research Paper* No. 45, p. 58.

Palmer, W.C. (1968). Keeping track of crop moisture conditions, nationwide: the new crop moisture index. *Weather-wise,* 21(4), 156-161.

Shafer, B.A., & Dezman, L.E. (1982). Development of a surface water supply index (SWSI) to assess the severity of drought conditions in snowpack runoff areas. In: Preprints, *Western Snow Conference,* Reno, NV, Colorado State University, 164-175.

Shukla, S. & Wood, A.W. (2008). Use of a standardized runoff index for characterizing hydrologic drought. *Geophysical Research Letters*, 35, L02405.

Stalh, K. (2001). Hydrological drought: A study across Europe. Institut für Hydrologie der Universität.

Thornthwaite, C.W. (1948). An approach toward a rational classification of climate. *American Geographical Society*, Stable URL: https://www.jstor.org/stable/210739.

Tsakiris, G. & Vangelis, H. (2005). Establishing a drought index incorporating evapotranspiration. *European Water*, 9/10, 3-11.

Vicente-Serrano, S.M., Begueria, S., Moreno, J.I.L. (2010). A multiscalar drought index sensitive to global warming: the standardized precipitation evapotranspiration index. *Journal of Climate,* 23, 1696-1718.

World Meteorological Organization (WMO) & Global Water Partnership (GWP) (2016). *Handbook of drought indicators and indices* (M. Svoboda and B.A. Fuchs). Integrated Drought Management Programme (IDMP), Integrated Drought Management Tools and Guidelines Series 2, Geneva.

CRITICAL DROUGHT INTENSITY-DURATION-FREQUENCY CURVES AND SPATIAL DISTRIBUTION OF PRECIPITATION DEFICIT

Yonca Cavus

Beykent University, Department of Civil Engineering, Istanbul, Turkey

yoncacavus@beykent.edu.tr

Istanbul Technical University, Graduate School, Istanbul, Turkey

cavus17@itu.edu.tr

University of Freiburg, Environmental Hydrological Systems, Freiburg, Germany

yonca.cavus@hydrology.uni-freiburg.de

Hafzullah Aksoy

Istanbul Technical University, Department of Civil Engineering, Istanbul, Turkey

haksoy@itu.edu.tr

ABSTRACT: Drought causes scarcity and lack of water in river basins and affects seriously the majority of population in many ways such as economic, social and environmental. Drought plays a significant role in the risk management of water resources systems to sustain sectoral development. Drought analysis in this study is two-fold; (i) station-based, (ii) spatial characterization. For the former, the standardized precipitation index (SPI) is used for Adana meteorological station while, for the latter, SPI is calculated at the 12-month time scale for 19 meteorological stations scattered over the Seyhan River basin. From the SPI time series dry and wet periods are determined. Droughts with different durations are extracted from the dry periods. For each duration, drought with the largest severity in each year is defined as the critical drought. Frequency analysis is applied on the critical drought severity by using the total probability theorem. From the probability distribution function, the intensity-duration-frequency (IDF) curves are plotted in terms of precipitation deficit which is a physically measurable variable. For the station-based analysis, drought IDF curves are plotted. For the spatial characterization of drought, precipitation deficit is calculated and mapped over the Seyhan River basin for 1, 3, 6 and 12 month-drought durations and 2-100 year-return periods at the 12-month time scale. Spatial characterization suggests that the river basin experiences quite mild and severe droughts. While the coastal part of the river basin is vulnerable to droughts at all return periods and drought durations, the northern part of the basin would be expected to be less affected by the drought.

1. INTRODUCTION

Drought is a stochastic natural event which emerges from remarkable deficiency in precipitation. It has an impact on large number of sectors since water is the source of life. The fact that the lack of water affects different sectors makes it harder to point one certain definition for the drought. A certain definition does not exist for the drought because of the complicated stochastic nature of hydrometeorological variables and water demand in different regions around the world (Mishra and Singh, 2010) and the variability in the climate of the region under investigation. Drought hydrology has been receiving much attention due to the increase in water demand. As a result, many studies have so far been performed on the drought (Heim, 2002; Mishra and Singh, 2010;2011; Zargar, et al., 2011; Hao and Singh, 2015; Eslamian et al., 2017)

Drought typically has probabilistic characteristics which are severity, duration, intensity, frequency and interarrival time (Mishra and Singh, 2011; Dracup et al., 1980; Rossi et al., 1992; Loaiciga and Leipnik, 1996). In the literature, there have been limitless studies on the drought characterization (Dalezios et al., 2001; Tsakiris and Vangelis, 2005; Eris and Aksoy, 2008; Nalbantis and Tsakiris,

2009; Vicente-Serrano et al., 2010; Santos et al., 2011; Tigkas et al., 2015). The total probability theorem was used for the frequency analysis of drought severity to derive precipitation deficit from the drought Severity-Duration-Frequency (SDF) curves developed in different hydrological basins in Turkey (Aksoy et al., 2018a, b). One of the most recent studies on drought in Turkey, Cavus (2019) and Cavus and Aksoy (2019; 2020) developed a methodology based on precipitation deficit, precipitation threshold and critical precipitation concepts, all newly introduced. Also used is a regression equation established between the SPI and the corresponding precipitation. As the outputs of the methodology, drought SDF and intensity-duration-frequency (IDF) curves were plotted with which it is possible to determine the severity and intensity of a drought with a given duration and return period.

A meteorological station is used when the point-scale temporal analysis of drought is concerned. On the other hand, spatial analysis of drought is as important as its temporal analysis. Because, it could be common for one point in an area to suffer dry conditions, whilst surrounding points in the same area experience normal or even humid conditions. Thus, information related to not only one certain station but also to neighboring stations are needed in making decision for drought mitigation or preparedness at basin scale. Spatial analysis is performed using data from all available meteorological stations in the basin. This provides spatial drought characterization that utilizes the severity, intensity, duration and return period. It can be presented in the form of spatial patterns of drought intensity contours for a given drought duration and return period. Spatial variability of drought events in the literature have been approached from different perspectives (Turkes, 1996; Komuscu, 2001; Bonaccorso et al., 2003; Loukas and Vasiliades, 2009; Bin et al., 2011).

The aim of this study is to provide drought IDF curves and maps to characterize the drought variability based on precipitation deficit by using the SPI for the Seyhan River basin in the Eastern Mediterranean region of Turkey. In the IDF maps, intensity contours based on precipitation deficit are plotted for a given drought duration and return period. The maps are given in this study for drought durations of 1, 3, 6 and 12 months and return periods of 2, 5, 10, 25, 50, and 100 years at 12 month-time scale. They are expected to provide useful information to use in drought management plans taking actions against drought such that it becomes less destructive and does not create irreversible effects on the economy, society and ecology.

2. STUDY AREA AND DATA

The Seyhan River Basin is located in the southern part of Turkey. The drainage area of the basin is 20731 km^2. The average annual total precipitation is 624 mm in the coastal part of the basin; it increases to approximately 1000 mm in higher elevations in the north. The annual mean flow at the outlet of the basin to the Mediterranean Sea is 211.07 m^3/s. The most important river in the basin is the Seyhan River, which gives its name to the basin. It is formed by the confluence of Zamanti and Goksu rivers and flows into the Mediterranean Sea. It has a length of 560 km as one of the largest rivers in Turkey (SYGM, 2016; 2017).

The climate in the Seyhan River basin is strongly influenced by the topography. The northern part of the basin is characterized by a mountainous steep, harsh topography while lowlands prevail in the southern part of the basin. The basin extends from the Mediterranean coast to the Central Anatolia and shows three different characteristics in terms of climate. The northern part of the basin exhibits the characteristics of the Central Anatolian climate; thus, it is colder than the southern part of the basin; the highest precipitation is observed at highlands in this part of the basin. In the coastal parts of the Çukurova plain and the surrounding areas, the summer season is hot and dry while the winter is warm and rainy. That part of the basin between the coastal zone in the south and the Tarsus mountains in the north has a semi-arid Mediterranean climate with dry and hot summers and rainy and warm winters.

Monthly precipitation data were obtained from 19 meteorological stations operated by the State Meteorological Service (MGM) and from the General Directorate of State Hydraulic Works (DSI). The meteorological stations are listed in Table 1 in which the number and name of the stations are given together with the observation period of each station and the total number of missing data filled

(in months). Statistical characteristics calculated from the monthly precipitation time series of each meteorological station are also given in Table 1. They are the minimum, maximum and mean values of monthly precipitation data in each meteorological station.

3. METHODOLOGY

3.1. Standardized Precipitation Index (SPI)

SPI was developed by McKee et al. (1993) to define and observe the drought. SPI calculated by using only monthly precipitation data, dry periods can be identified as well as wet periods. SPI is calculated for various time scales of 1, 3, 6, 9, 12, 24, 48 months.

Typically, precipitation does not have a normal probability distribution for the accumulation periods shorter than 12 months, but the non-normality can be overcome by a transformation. It is presumed that precipitation has gamma probability distribution function which is transformed into the standard normal distribution with zero mean and unit variance by

$$SPI_{ij} = \frac{x_{ij} - \mu_j}{\sigma_j} \qquad (1)$$

and defined as SPI where x_{ij} is the precipitation (in mm) in month j (j = 1, 2, 3, ……, 12) of year i (i = 1, 2, …, n); μ_j and σ_j, are the average and standard deviation of precipitation (in mm) in month j, respectively. The SPI values are calculated similarly for different time scales such as k = 1, 3, 6, 9, 12, 24 months. These arbitrarily selected time scales are used to represent the three types of drought; meteorological, agricultural and hydrological (McKee et al., 1993).

Table 1. Statistical characteristics of meteorological stations in the Seyhan River basin.

Code	Station name	Latitude	Longitude	Altitude (m)	Data Source	Observation period	Missing data (month)	No-rainy months (%)	Mean (mm)	Min (mm)	Max (mm)
6204	Tufanbeyli	38.2600	36.2195	1415	MGM	1998-2012	3	6.67	545	312	706
6560	Saimbeyli	37.9811	36.0853	1050	MGM	1986-1995	4	4.17	923	625	1233
6893	Çamardı	37.8358	34.9975	1603	MGM	1969-1982	1	7.74	412	316	546
6902	Feke	37.7764	35.9000	583	MGM	1970-1993	1	4.86	910	598	1352
17351	Adana Bölge	37.0041	35.3443	23	MGM	1960-2016	0	11.40	663	317	1265
17802	Kayseri Pınarbaşı	38.7251	36.3904	1542	MGM	1963-2009	5	4.08	423	267	597
17837	Tomarza	38.4522	35.7912	1402	MGM	1965-2010	8	4.53	408	269	585
17840	Sarız	38.4781	36.5035	1599	MGM	1968-2011	0	5.30	524	354	748
17906	Ulukışla	37.5480	34.4867	1453	MGM	1962-2011	11	6.33	322	182	428
17934	Pozantı	37.4758	34.9022	1080	MGM	1963-1992	24	6.11	719	380	1299
17936	Karaisalı	37.2505	35.0628	240	MGM	1965-2011	0	4.61	881	437	1451
17981	Karataş	36.5683	35.3894	22	MGM	1963-2011	5	15.31	777	366	1365
D18M003	Uzunpınar	38.9710	36.8990	1740	DSI	1959-2005	11	7.45	303	161	493
D18M004	Seyhan Baraj	37.7000	35.0830	55	DSI	1974-2015	4	14.48	657	314	1117
D18M011	Kazancık	39.0670	36.7330	1585	DSI	1965-2003	8	7.69	274	176	433
D18M012	Hasan Çavuşlar	37.8330	35.5830	1400	DSI	1990-2005	0	3.65	1006	713	1539
D18M013	Kamışlı	37.5670	34.9500	1225	DSI	1963-2002	2	9.17	628	328	1123
D18M018	Gıcak	37.5670	35.2000	975	DSI	1988-2006	0	10.53	843	520	1173
D18M019	Çeralan	38.1000	36.0000	1600	DSI	1991-2005	4	6.67	970	622	1342

3.2. Frequency Analysis

Frequency analysis is performed to characterize the drought and to determine the best-fit probability distribution function. In the frequency analysis of drought, the 2- and 3-parameter Gamma (G2, G3), the Generalized Extreme Value (GEV), the 2- and 3-parameter log-normal (LN2, LN3), Log-Pearson Type 3 (LP3) and the 2- and 3-parameter Weibull (W2, W3) probability distribution functions are often used (Heim, 2002; Mishra and Singh, 2010; 2011). Frequency analysis was applied on the severity of drought in this study. For the sake of consistency with the literature, the above probability distribution functions were considered for the frequency analysis of drought.

In some months, it is highly likely that no drought is observed. For the months, when no drought is observed, drought severity is zero. Frequency analysis is applied on non-zero values only to distinguish zero values from the non-zero values; thus, months with no drought is eliminated from the frequency analysis. Any process that is composed of zero and non-zero values is called a censored or intermittent process. The total probability theorem is available to use for such processes to examine them in two parts; the zero- and non-zero parts. According to the total probability theorem (Haan, 1977).

$$P(S \geq s) = P(S \geq s|S = 0)P(S = 0) + P(S \geq s|S \neq 0)P(S \neq 0) \tag{2}$$

is used. Here,

$$P(S \geq s \,|\, S = 0) = 0 \tag{3}$$

Therefore,

$$P(S \geq s) = P(S \geq s|S \neq 0)P(S \neq 0) \tag{4}$$

is obtained.

$P(S \neq 0)$ is the rate of years with non-zero values in the SPI_k (k = 1, 3, 6, 9, 12, 24 months) time series. Equation (4) can also be written in terms of the cumulative probability distribution as

$$1 - F(s) = (1 - p)[1 - F^*(s)] \tag{5}$$

In Equation (5), p is the probability of zero values. $F(s)$ is the cumulative probability distribution function of all S including zeros which is expressed as $P(S \leq s|S \geq 0)$ and $F^*(s)$ is the cumulative probability distribution function of the non-zero values of S which is expressed as $P(S \leq s|S \neq 0)$. The rate of the non-zero values, $1 - p$ in Equation (5), can be expressed in terms of the probability as

$$1 - p = P(S \neq 0) \tag{6}$$

The magnitude of an event with return period T can be predicted by solving Equation (5) for $F^*(s)$ and then by using the inverse transformation of $F^*(s)$ to get the value of S. From Equation (5)

$$\frac{1 - F(s)}{1 - p} = 1 - F^*(s) \tag{7}$$

and

$$F^*(s) = \frac{F(s) - p}{1 - p} \tag{8}$$

can be written. Considering that the return period of a given severity for a particular drought duration can be predicted by

$$F(s) = 1 - \frac{1}{T} \tag{9}$$

Equation (8) turns into

$$F^*(s) = \frac{1 - \frac{1}{T} - p}{1 - p} \tag{10}$$

3.3. Basic Concepts and Definitions

The cluster of consecutive negative values of SPI refers to as the dry period which has length (L) (Figure 1) to begin in a month with a negative SPI and to continue until a positive SPI value is obtained in the time series. Droughts are determined from the dry periods after which their characteristics such as the duration, severity, intensity and return period are calculated. Duration (D) of a drought in a dry period with length L changes as $0 < D \leq L$. Any drought with a duration shorter than the length of the dry period is called *within-period drought* while drought that extends

over the dry period is defined as *singular drought* (Cavus and Aksoy, 2020). The sum of negative SPI values for a D-month long drought

$$S = \sum_{i=1}^{D} |SPI_i| \tag{11}$$

is called *drought severity*. The *drought intensity* is obtained by dividing *drought severity* to *drought duration* as

$$I = S/D \tag{12}$$

Cavus and Aksoy (2020) accounted only one drought per a year, which is the most severe in terms of the drought severity over the drought duration and called it *critical drought*. It is likely that no drought is observed in some years as years with no negative run of SPI have no dry period and thus no drought. The critical drought severity does not exist for a year with no drought; therefore, a zero value is assigned to the critical drought severity of such years.
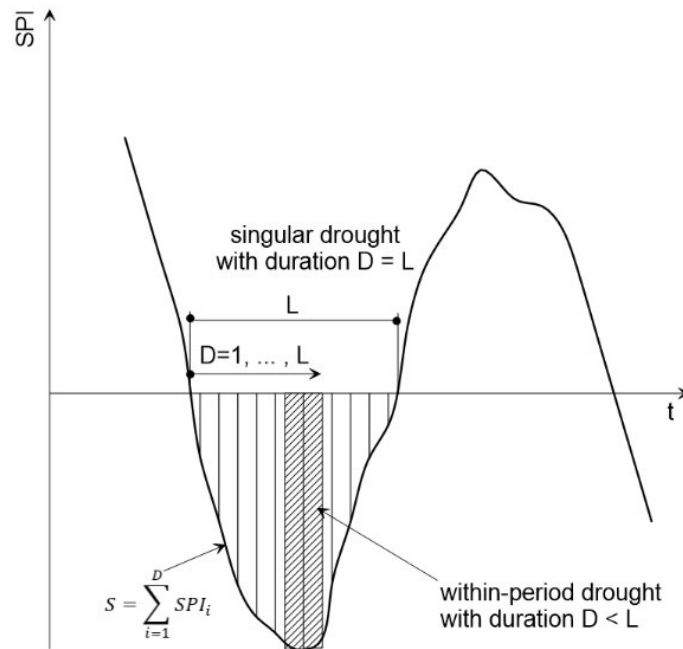

Figure 1. Dry period length (L), drought duration (D), drought severity (S), within-period drought and singular drought in the dry period (Cavus and Aksoy, 2019, 2020)

3.4 Precipitation Deficit

Instead of using drought indices to develop SDF curves as in previous studies (Dalezios et al., 2001), precipitation deficit is calculated in this study. This approach allows to derive tangible information for precipitation required to overcome the drought (Cetin et al., 2018), and to better understand the drought event so that it can be easily identified by end-users such as farmers and decision-makers.

As a part of the methodology in this study, the relationship between the precipitation and SPI is detected by regression analysis. In the drought analysis, when the drought duration (D month) and return period (T years) increase, precipitation is expected to decrease, and therefore, precipitation deficit is expected to increase. Any function to be applied on the relationship between precipitation and the corresponding SPI should satisfy this physical expectation. Some types of functions such as the second and the third order polynomials were omitted as they might produce negative values of precipitation deficit, which has no sense. As a result, it was seen that the logistic function could be

appropriate to choose among the functions tested due to the above expectation of the physical realization. The logistic regression equation was fitted to the relation between precipitation and the corresponding SPI values in the form of

$$f(x) = \frac{a}{1 + be^{-cx}}$$ (13)

in which a, b and c are parameters to be estimated using data scatter.

Referring to Figure 2 precipitation threshold (P_{TH}) were taken as precipitation at SPI = 0 for all time scales. Regression equation can be used to calculate the precipitation threshold value and critical precipitation in the most severe droughts for each drought duration. For time scales k = 1, 3, 6 and 9 months, relation between precipitation and SPI changes from month to month. That is, a particular function should be used for each month of the year. However, one curve exists for time scales of 12 and 24 months.
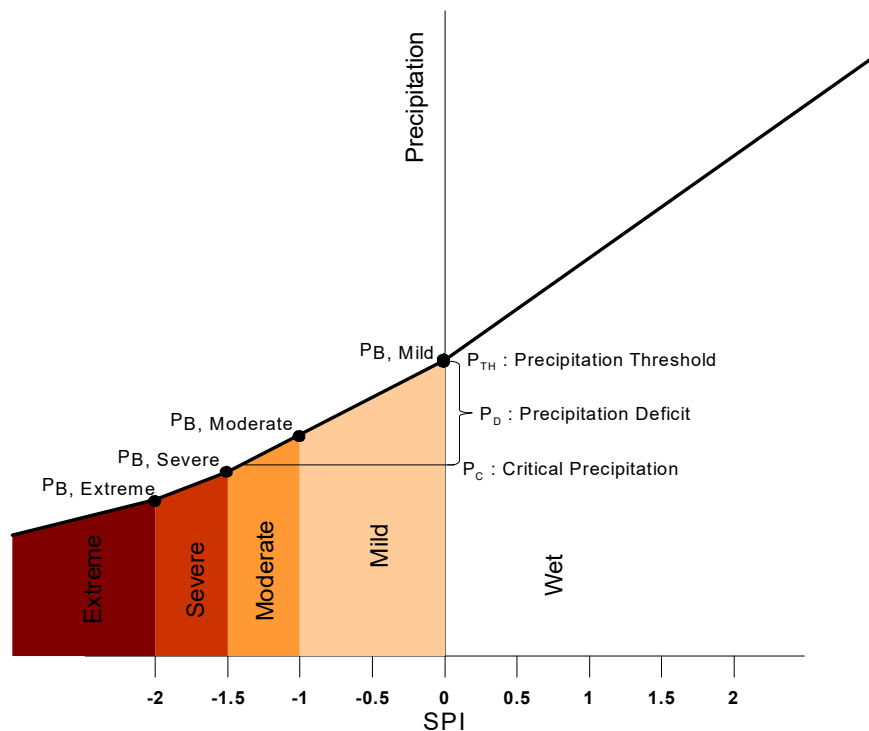

Figure 2. Definition of precipitation threshold, boundary precipitation and critical precipitation

Precipitation at the boundary of drought classes ($P_{B,Extreme}$, $P_{B,Severe}$, $P_{B,Moderate}$, $P_{B,Mild}$) are shown in Figure 2. Also shown is the critical precipitation (P_c) which is expected to occur under a critical drought. The difference between the precipitation threshold and the critical precipitation is defined as the precipitation deficit and calculated by

$$P_D = P_{TH} - Pc$$ (14)

for each drought of a given duration and return period.

4. INTENSITY-DURATION-FREQUENCY (IDF) CURVES

In this study, drought occurrence was investigated for each of 19 meteorological stations in the Seyhan River basin in the Mediterranean region of Turkey based on precipitation deficit at different month-time scale. Critical drought severity was calculated from the SPI values which were first implemented by frequency analysis after which critical drought severities were calculated for return periods 2, 5, 10, 25, 50 and 100 years. From the critical drought severity, precipitation deficits were calculated for different drought durations (D = 1 month up to 48-month long droughts) and 2, 5, 10, 25, 50 and 100-year return periods, and 1, 3, 6, 9, 12 and 24-month time scales. The drought intensity values were also calculated as the ratio of the severity of the drought to its duration (Equation 12).

The IDF curves based on the intensity of precipitation deficit for SPI_1, SPI_6 and SPI_{12} were given in Figures 3-5 as examples. With increase in drought duration, the intensity decreases; it increases however slightly with increasing return period although it converges to the same curve for return periods other than 2 years. Because, the difference between the intensity becomes quickly negligible with increase in the drought duration. The likelihood of very severe droughts decreases with increasing drought duration, thus droughts become milder when they persist. This is a general result which is valid for all months in the year and more obvious in long drought durations. Also, comparison of the intensity at $k = 1$ and 6 months indicates an increase in the intensity as the time scale increases. The intensity of precipitation deficit decreases in summer while it increases in winter due to the seasonality in the precipitation.
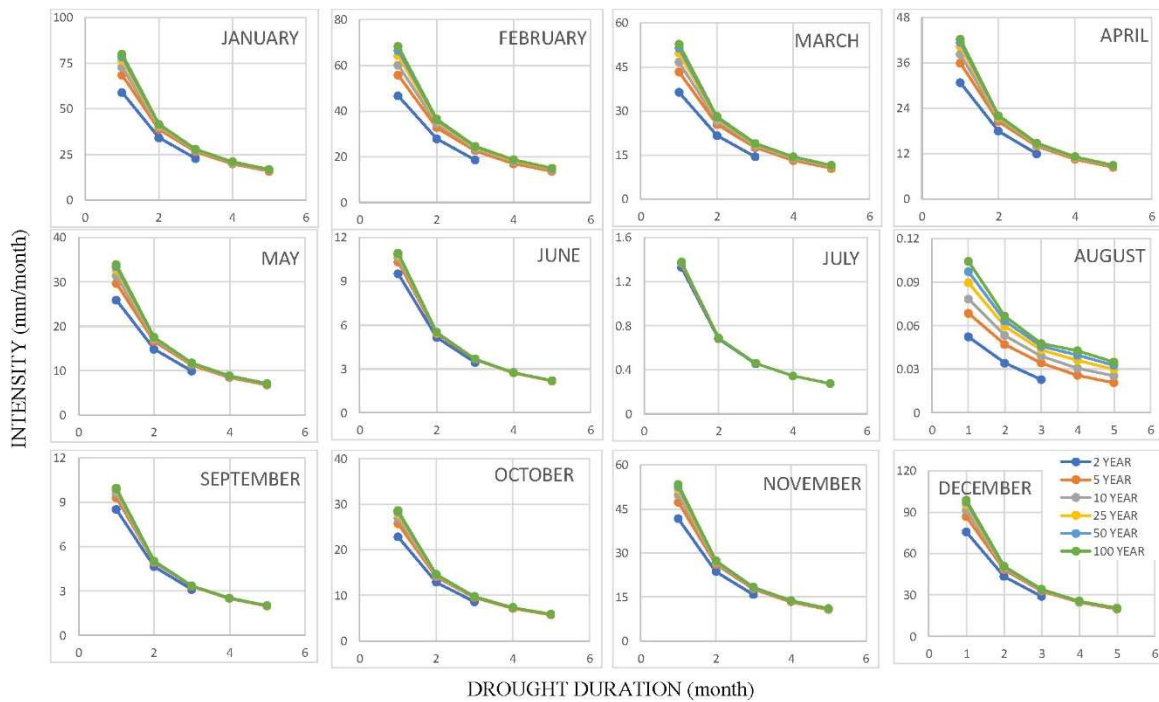

Figure 3. Critical drought IDF curves based on precipitation deficit for SPI_1
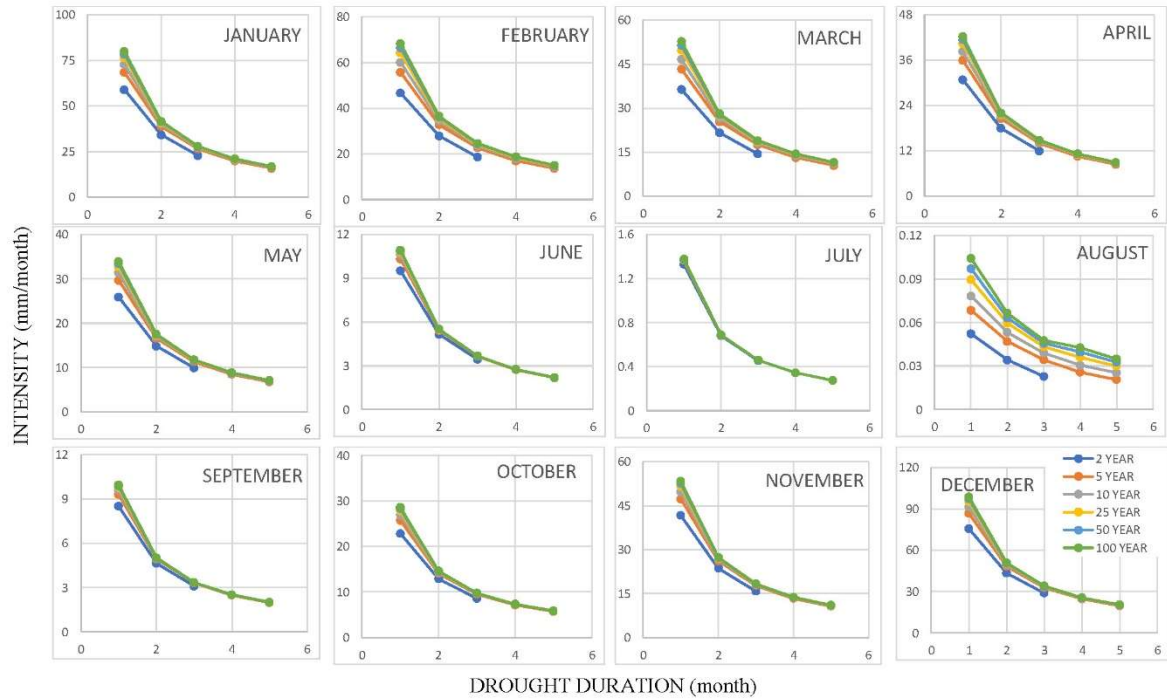
Figure 4. Critical drought IDF curves based on precipitation deficit for SPI_6
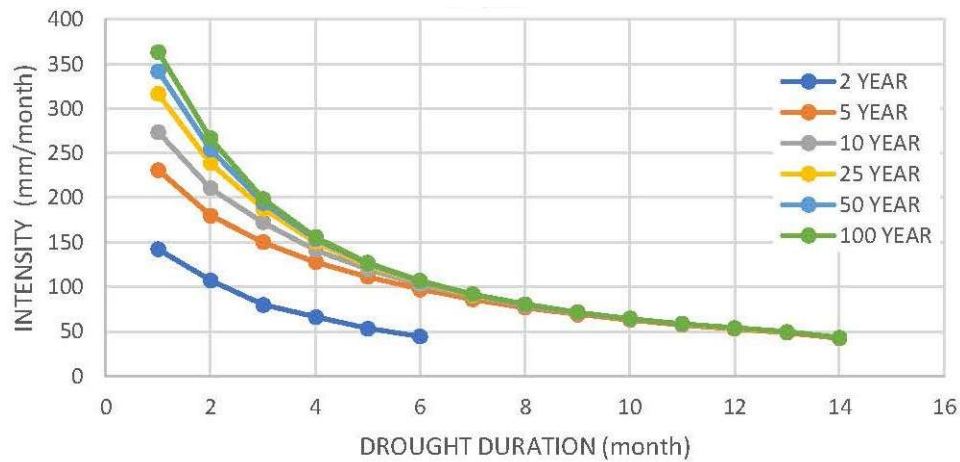

Figure 5. Critical drought IDF curves based on precipitation deficit for SPI_{12}

5. SPATIAL MAPPING

Spatial drought characteristics of the Seyhan River basin were investigated based on precipitation deficit by considering 19 meteorological stations. Precipitation deficit was mapped using the kriging interpolation technique to show the spatial distribution of precipitation deficit based on SPI_{12} (Figure 6). Values of precipitation deficits corresponding to the T year-return period and D month-drought duration for SPI_{12} used in Figure 6 were tabulated in Table 2.
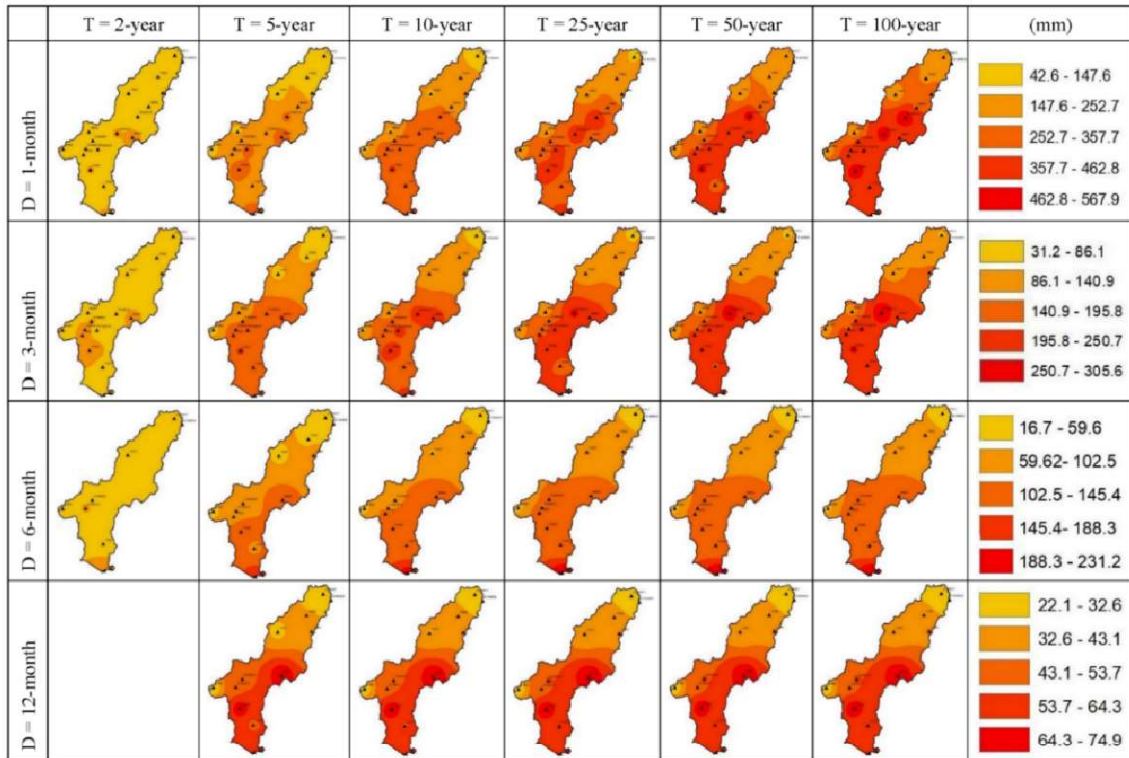
Figure 6. Precipitation deficit maps for droughts of 1, 3, 6 and 12 month-durations and T = 2, 5, 10, 25, 50 and 100 year-return periods over the Seyhan River Basin

The spatial distribution of D = 1 month-drought duration indicates that more severe precipitation deficits tend to occur in the coastal parts of the basin for all return periods while the north-eastern part of the basin is prone to lower precipitation deficit at the same return periods. In other words, majority of precipitation deficit that occurred in the coastal part were severe in D = 1 month-drought duration. As the return period increases from 2 years to 100 years, almost no difference is observed at the drought intensity, rather there is a shift in the drought severity towards the northern part of the basin. The drought intensity becomes lower with moving to the north. The intensity of precipitation deficit exhibits a more variable behaviour over the basin when the return period increases. Large areas have been affected from severe droughts at the 1 month-drought duration.

At the D = 3 month-drought duration, much more severe droughts are typically observed at the coastal part of the basin. Especially, the northern part of the Seyhan River basin exhibits lower precipitation deficit. Nevertheless, as the return period increases, more severe droughts shift from south towards the northerly centre of the basin. Except for the northern part, most of the basin has severe droughts for all return periods. Another result shows that the coastal part of the basin experiences severe drought at all return periods while the northern part of the basin is characterized with milder drought at the same return periods.

At the D = 6 month-drought duration, on the other hand, no severe drought is extended over the basin, rather severe precipitation deficit is observed in a few locations. For the 2 year-return period at the same drought duration, severe precipitation deficits are typical not only in the coastal part of the basin but also in the interior parts. Also, as the return period increases, drought intensity becomes milder particularly along the Mediterranean coast and in some locations in the north. Droughts with short return periods such as 2 years were not calculated for longer drought durations. Because, long-duration droughts are observed less frequently compared to short-duration droughts. This is what happened for D = 12 month-drought duration and T = 2 year-return period (Figure 6) which is interpreted as follows: The least severe drought of 12 month-duration is more severe than the 2 year-return period droughts. In other words, once a 12 month-drought is observed, it is as severe as a drought with a return period longer than 2 years. The drought characterization based on precipitation deficit completely changes at longer drought durations and return periods. The river basin experiences severe prolonged droughts, which means at k = 12 month-time scale the coastal part will suffer from severe hydrological drought. It shows also that the coastal parts of the basin are more likely to be affected from hydrological drought with a consequence of loss in water resources.

6. CONCLUSION

This study was assessed as a framework of methodologies for the temporal and spatial analysis of drought characteristics by utilizing frequency analysis in Seyhan River basin in the eastern part of the Mediterranean region of Turkey. It could be common for one point in the basin to suffer from the drought, whilst surrounding points in the same basin experience normal or even humid conditions. This reminds the importance of spatial analysis over the basin instead of the point-scale temporal analysis made in each meteorological station in the basin. Results of the spatial drought analysis indicate that the Seyhan River basin experiences mild and severe droughts in term of precipitation deficit. The spatial distribution would alter greatly with increasing return period and drought duration. While the coastal part of the basin is vulnerable to droughts at all return periods and drought durations, the northern part of the basin would be expected to be less affected by the drought. Also, as the drought duration and return period increase, drought severity based on precipitation deficit is expected to decrease. The SDF/IDF curves are developed based on precipitation deficit to provide a comprehensive characterization of the drought. The precipitation deficit is calculated from the SPI which is a technical tool and thus difficult to be understood by end-users and decision-makers. Precipitation deficit is however more useful and meaningful, and physically more understandable. With the use of IDF curves, it is expected that the destructive and irreversible effects of meteorological, agricultural and hydrological droughts can be realized with physically measurable variables rather than the more technical drought indices such as SPI. When using the SPI, information on the drought phenomenon is hidden. It requires technical and analytical backgrounds to extract the final information in the form of physical variables such as precipitation as in this study. With the use of precipitation, a direct and physically meaningful information is provided to the end-users who are familiar with monthly, seasonal or annual precipitation after their experience in the field. Such direct information on precipitation deficit allow making advance planning and taking measures against drought. Thus, the IDF curves based on precipitation deficit are important tools to mitigate the consequences of drought.

Table 2. Precipitation deficit (in mm) corresponding to 2, 5, 10, 25, 50 and 100-year return periods at k = 12-month time scale.

Station no	D = 1 month						D = 3 months						D = 6 months						D = 12 months					
Return period	2	5	10	25	50	100	2	5	10	25	50	100	2	5	10	25	50	100	2	5	10	25	50	100
6204	50.4	152.7	214.8	281.1	321.0	353.5																		
6560																								
6893	81.3	108.7	123.0	138.6	148.7	158.1	65.3	79.3	86.1	93.3	97.8	101.8												
6902	174.3	280.5	320.4	354.2	371.5	384.3	96.4	199.7	218.4	230.4	235.4	238.6		131.3	137.6	141.1	142.5	143.4		73.4	74.4	74.7	74.8	74.9
17351	142.0	230.9	273.7	316.4	342.1	363.7	79.9	150.2	172.4	187.7	194.3	198.6		96.9	102.4	105.3	106.2	106.7		52.6	53.4	53.6	53.6	53.7
17802	42.6	113.4	156.4	199.8	224.6	243.7	31.4	81.4	99.4	114.8	122.5	127.9	44.1	56.2	63.8	67.8	69.0	69.5		32.7	34.4	34.8	34.9	34.9
17837	66.6	113.9	136.9	158.7	170.8	180.4	48.1	76.9	90.7	103.8	111.0	116.5	34.0	52.5	58.8	63.3	65.1	66.1		29.9	32.3	33.2	33.4	33.5
17840	69.7	136.4	170.9	207.8	231.4	252.2	38.6	94.3	113.4	130.4	139.6	146.7		66.6	75.4	81.3	83.7	85.2		40.2	42.3	43.2	43.5	43.6
17906	42.7	96.5	125.2	151.9	165.9	176.4	32.0	66.1	78.4	88.1	92.7	95.9	22.1	45.9	49.7	51.5	52.1	52.4		25.6	26.3	26.4	26.5	26.5
17934	146.1	242.9	294.1	348.3	382.5	412.4	98.4	154.5	178.1	199.0	209.8	217.5		98.9	107.6	113.7	115.7	116.6						
17936	150.8	296.0	374.1	452.4	498.3	535.5	105.8	204.3	228.8	246.5	254.7	260.4		129.6	136.4	140.0	141.2	141.9		70.5	71.3	71.5	71.5	71.6
17981	149.7	270.4	325.1	377.9	408.8	434.0	80.4	179.0	201.9	218.4	226.0	231.2	80.4	179.0	201.9	218.4	226.0	231.2		62.3	62.9	63.1	63.1	63.1
D18M003	57.9	109.1	134.8	159.3	173.0	183.9	45.7	72.1	80.9	87.7	90.8	93.0	31.0	45.3	47.6	48.6	48.9	49.1		24.3	24.5	24.6	24.6	24.6
D18M004	129.2	208.8	254.0	305.7	340.6	372.8	89.4	141.5	161.9	180.1	189.7	196.8	58.9	95.0	100.8	104.3	105.7	106.5		52.2	53.4	53.8	53.9	54.0
D18M011	43.0	85.6	108.3	130.9	143.9	154.3	31.2	60.7	69.8	76.9	80.3	82.8	16.7	39.6	42.8	44.4	44.8	45.0		22.1	22.5	22.6	22.6	22.6
D18M012	152.6	247.5	312.4	396.4	459.6	521.3	70.3	165.4	216.2	264.3	288.9	305.6												

REFERENCES

Aksoy, H., Cetin, Onoz, B., Yuce, M.I., Eris, E., Selek, B., Aksu, H., Burgan, H.I., Esit, M., Orta, S., Cavus, Y. (2018a). Hidrolojik havzalarda düşük akımlar ve kuraklık analizi. (Rapor No. TUJJB-TUMEHAP-2015-01). ISTANBUL: TUJJB Sonuç Raporu, 2018.

Aksoy, H., Onoz, B., Cetin, M., Yuce, M.I., Eris, E., Selek, B., Aksu, H., Burgan, H.I., Esit, M., Orta, S., Cavus, Y. (2018b). SPI-based drought severity-duration-frequency analysis. *13th International Congress on Advances in Civil Engineering,* 12-14 September 2018, Izmır/ Turkey.

Bonaccorso, B., Bordi, I., Cancelliere, A., Rossi, G., Sutera, A. (2003). Spatial variability of drought: an analysis of the SPI in Sicily. *Water Resources Management,* 17, 273-296.

Bin, H., Aifeng. L., Jianjun, W. U., Lin, Zhao, Ming, L. (2011). Drought hazard assessment and spatial characteristics analysis in Chine. *Journal of Geographical Sciences*, 21(2), 235-249.

Çavuş, Y. (2019). Critical drought severity-duration-frequency curves based on precipitation deficit. Istanbul Technical University, Graduate School of Science, Engineering and Technology, M.Sc. Thesis, June 2019, 199.

Cavus Y, Aksoy H (2019) Spatial drought characterization for Seyhan River basin in the Mediterranean region of Turkey. *Water*, 2019, 11, 1331.

Cavus, Y., & Aksoy, H. (2020). Critical drought severity/intensity-duration-frequency curves based on precipitation deficit, *Journal of Hydrology*, 584, 123312.

Cetin, M., Aksoy, H., Onoz, B., M., Yuce, M.I., Eris, E., Selek, B., Aksu, H., Burgan, H.I., Esit, M., Cavus, Y., Orta, S. (2018) Deriving accumulated precipitation deficits from drought severity duration-frequency curves: a case study in Adana province, Turkey. *1st International, 14th National Congress on Agricultural Structures and Irrigation,* 26-28 September 2018 Antalya.

Dalezios, N.R., Loukas, A., Vasiliades, L., Liakopoulos, E. (2001). Severity-duration-frequency analysis of droughts and wet periods in Greece. *Hydrological Sciences Journal*, 45(5).

Dracup, J.A., Lee, K.S., Paulson, E.G. (1980). On the statistical characteristics of drought events. *Water Resources Research*. Vol. 16, No. 2, Pages 289-296, April 1980.

Eslamian, S., Ostad-Ali-Askari, K., Singh, V.P., Dalezios, N.R., Ghane, M., Yihdego, Y., Matouq, M., (2017). A review of drought indices. I*nternational Journal of Constructive Research in Civil Engineering*, 3(4), 48-66.

Eris, E., Aksoy, H. (2008). Persistency in wet and dry periods in Goztepe meteorological station in Istanbul, Turkey. *AMHY-FRIEND International Workshop on Hydrological Extremes, Analyses and images of hydrological extremes in Mediterranean environments. Cosenza, Italy*, pp.93-99.

Haan, C.T. (1977). *Statistical methods in Hydrology,* Iowa State University Press.

Hao, Z., Singh, V.P. (2015). Drought characterization from a multivariate perspective: A review. *Journal of Hydrology,* 527, 668-678.

Heim, R. (2002). A review of twentieth-century drought indices used in the United States, *Bulletin of the American Meteorological Society*, 83(8), 1149-1165.

Komuscu, A.U. (2001). An analysis of recent drought conditions in Turkey in relation to circulation patterns. Drought Network News, Summer–Fall 2001, University of Nebraska Lincoln. *Drought-National Drought Mitigation Center*.

Loaiciga, H.A., Leipnik R.B. (1996). Stochastic renewal model of Iow-fow streamflow sequences. *Stochastic Hydrology and Hydraulics,* 10, 65-85 Springer-Verlag.

Loukas, A., Vasiliades, L. (2009). Probabilistic analysis of drought spatiotemporal characteristics in Thessaly region, Greece. *Natural Hazards and Earth System Sciences,* 4, 719–731.

McKee, T.B., Doesken, N.J., Kleist, J. (1993). The relationship of drought frequency and duration to time scales. Eighth Conference on Applied Climatology, *American Meteorological Society*, Jan17-23, 1993, Anaheim CA.

Mishra, A.K, & Singh V.P. (2010). A review of drought concepts. *Journal of Hydrology*, 391 (1-2), 202-216.

Mishra, A.K., & Singh, V.P. (2011). Drought modeling - A review. *Journal of Hydrology*, 403(1-2), 157-175

Nalbantis, I., & Tsakiris, G. (2009). Assessment of hydrological drought revisited. *Water Resource Management*, 23, 881-897.

Rossi, G., Benedini, M., Tsakiris, G., Giakoumakis, S. (1992). On regional drought estimation and analysis. *Water Resources Management*, 6(4), 249-277.

Santos, J., Portela, M., Pulido-Calvo, I. (2011). Regional frequency analysis of droughts in portugal. *Water Resources Management*, 25, 3537-3558.

Su Yönetimi Genel Müdürlüğü (2016). Seyhan Havzası Sektörel Su Tahsis Planı Hazırlanması Projesi. (Impact of Climate Change on Water Resources Project). (in Turkish). Ankara.

Su Yönetimi Genel Müdürlüğü (2017). İklim Değişikliğinin Su Kaynaklarına Etkisi Projesi, Proje Nihai Raporu, Ek 20-Seyhan Havzası. (Impact of Climate Change on Water Resources Project). (in Turkish). Ankara.

Tigkas, D., Vangelis, H., Tsakiris, G. (2015). The drought indices calculator (DrinC). *Earth Science Informatics*, 8, 697–709.

Tsakiris, G., Vangelis, H. (2005). Establishing a drought index incorporating evapotranspiration. *European Water*, 9/10, 3-11.

Turkes, M. (1996). Spatial and temporal analysis of annual rainfall variations in Turkey. *International Journal of Climatology,* 16, 1057-1076.

Vicente-Serrano, S.M., Begueria, S., Moreno, J.I.L. (2010). A multiscalar drought index sensitive to global warming: the standardized precipitation evapotranspiration index. *Journal of Climate*, 23, 696-1718.

Zargar, A., Sadiq, R., Naser, B., Khan, F.I. (2011). A review of drought indices. *Environmental Reviews,* 19, 333-349.

URBAN FLOODING AND DRAINAGE

14TH INTERNATIONAL CONFERENCE
ON HYDROSCIENCE & ENGINEERING
MAY 26-27, 2022
IZMİR-TURKEY

ICHE2022
IZMIR, TURKEY

FLOOD HAZARD ANALYSIS DUE TO OVERTOPPING OF DALAMAN AKKOPRU DAM: A CASE STUDY

First Author: Kutay Yilmaz

Alter International Engineering and Consultancy Co.

Ankara, Turkey

ktyylmz@gmail.com

Second Author: Yunus Oruç

Alter International Engineering and Consultancy Co.

Ankara, Turkey

yns.orucc@gmail.com

Third Author: Yakup Darama

Civil Engineering Department, Atilim University

Ankara, Turkey

yakup.darama@atilim.edu.tr

Forth Author: Abiddin Berhan Melek

Civil Engineering Department, Middle East Technical University

Ankara, Turkey

berhan@metu.edu.tr

Fifth Author: Çağla Irmak Ünal

Alter International Engineering and Consultancy Co.

Ankara, Turkey

cagla.irmak.unal@outlook.com

ABSTRACT: A study was made to determine the hypothetical failure of the Dalaman Akköprü Dam by overtopping failure mechanisms. For this purpose, a 2D Hydraulic Model was constructed using HEC-RAS to determine the propagation of flood due to the failure of the dam body for this case. Froehlich equations were used to predict breaching parameters of the Akköprü Dam. After the calibration of the hydraulic model, the hydraulic model was run to determine the possible flooding of Ortaca, Dalaman, and Köyceğiz towns. Analysis of the results obtained from the modeling in the case of overtopping failure of the Akköprü Dam showed that the peak flood reaches to Ortaca and Dalaman towns in 2 hr 20 min 2 hr 50 min respectively and the significant portion of the study area highly populated, is located in the H6 hazard zone. Due to the high risk of H6 and H5 Type hazard class, structural failure may occur, city centers should be evacuated within 2 hours.

Keywords: Dam Breach, Flood, Overtopping, Hydraulic Modelling, Flood Mitigation Measures

1. INTRODUCTION

Dams are constructed to serve various purposes, such as supplying municipal and irrigation water, generating hydroelectric power, and flood protection. In contrast to these valuable benefits, flooding events caused by dam failure results in considerable property damage and loss of human life in the towns located downstream of the dam. Even though dam failures are rare events, they may conclude

591

with catastrophic floods that cause huge damages like loss of lives or economic assets; thus, engineers, decision-makers, and researchers have paid considerable attention due to changes in the regimes and intensity of the precipitation produced flash floods.

Flash flood hazards have been one of the most dangerous and frequent global-wide natural hazards resulting in loss of lives, livestock, and economic assets (Slater & Villarini, 2016, Alfier et al., 2017, Kreibich et al., 2017, Zhai et al., 2020). Some of the most popular dam failures in the past are the Buffalo Creek Coal–Waste dam near Saunders and the Teton Dam in Idaho, the Kelly Barnes Lake dam near Toccoa, and the Laurel Run R-Servitors dam near Johnston. At the Laurel dam, a heavy rainstorm caused heavy flooding in many areas near Johnston. Flooding in the valley caused severe property damage, and more than 40 lives were lost (Rashid, 1999 and Arthur, 1977). The dam's failure resulted in the sudden release of about 550,000 m^3 of water, whose effects on the flow rates and stages along the valley downstream of the reservoir were significant (Rashid, 1999). 300 million m^3 of water was discharged during the failure of the Teton Dam in Idaho in 1976 in the USA. The casualties during this event were 11 people dead, 200 homeless, 560000 acres of flooded agricultural area and 13000 cattle lost, which constituted 2 billion dollars damage (Daher, 2001). Li et al. (2006) indicated that 3462 dam failures occurred in China between 1954 and 2004. Ingles (1984) reported that 56 dam failures were recorded in Australia between 1857 and 1983, doubling every 25 years. According to Australian records, 26 % of the dam failures were due to piping, and 20 % were overtopping. The study conducted by Zhang et al. (2009) on the historical dam break events database consisting of more than 1600 dam failures, excluding the ones in China, showed that approximately 66.2 % of the all-failure cases occurred in earthen dams and while %41 of these failures caused by overtopping, 42 % of them were due to piping. In addition, according to FEMA (2013), the studies on the dam failures between 1975-2011 showed that most of the failures occur in earth-fill dams, and 71 % of the failures were due to overtopping while 14 % of the failures were due to piping. After these events, several studies were made for the safety of dams (ICOLD, 2007) and numerical modeling studies were performed to determine inundation and flood hazard maps in the case of failure of the dams. (Arila and Nair, 2015).

Floods are categorized as river floods, storm surges, urban floods and flash floods. The most devastating form of floods is accepted as flash floods. This type of flood is the driving force for a dam breach due to heavy precipitation and may occur due to a dam breach. The main characteristics of flash floods are the rapid occurrence and causing high water velocities on the surface. Hence, a flash flood due to a dam breach threatens the downstream settlements; thus, the living beings, structures downstream of a dam may be destroyed due to flash floods. Such big disasters also have social effects on the people living in the region. For example, the failure of a series of dams due to extreme storms in Henan Province of China caused approximately 26000 deaths, and 5.4 million people were affected by that catastrophic event (Graham, 1999; Ru and Niu,2001).

The main failure mechanisms of dams are overtopping, piping and slides. The main reason for the overtopping is the inadequate capacity of the spillways due to underestimated flood discharges (Zhang et al., 2015, Zhang et al., 2009). It is the most common mode of failure within embankment dams. The second failure mechanism, which is piping or hydraulic fracturing, results from a crack in the core and propagation of this crack with the hydraulic pressure (Wang and Zhu 2007). The slides occurred downstream, and upstream of a dam and liquefaction due to earthquakes are less predominant reasons for a dam failure.

The simulation takes a critical role in observing the threats under a dam breach incident and the flash floods. According to the simulation results, crucial parameters like dissemination of the flood in the basin, flow depths, flow velocities can be obtained. These parameters state the destructive force of a flood. Thus the hazardous region of the basin can be determined, early warning systems can be installed, and mitigation plans can be prepared. Early warning systems can decrease fatalities drastically. The study conducted by Costa (1995) indicated that if there is no warning system, fatalities may increase by 19-fold. The General Directorate of State Hydraulic Works started an extensive study on dam breaches for the dams under operation in Turkey.

Firstly, a set of breach parameters should be determined for the simulations. Researchers propose different sets of parameters using the historical dam failure data. The proper one was selected and used to define the breaching dimensions. For the solution, 1D, 2D or 1D/2D modeling can be used. Past studies for the dam breach simulation mostly use 1D models (Yanmaz et al., 2001; Macchione, 2008; Natale & Petaccia, 2008); (Froehlich, 2008)). Qi & Altinakar (2011) stated that two-dimensional studies are generally more appropriate for highly unsteady dam-break floods on wide and flat terrains by considering the rapidly varied flow, which may lead to severe stability and accuracy problems in a 1D analysis. Xiong (2011) identified dam break analysis in model and theory by combining case studies with mechanics. Predicting breach parameters and peak outflow were essential points for the dam break phenomenon and estimation of potential damages. As a result of the analysis, downstream regions relatively close to the dam body were more affected by dam break.

This study aims to reveal a methodology to determine possible flood risks due to dam breaching and develop mitigation measures for the case of the Dalaman Akköprü Dam breach and resulting flood event. 2D simulations were conducted on HEC-RAS for the most common failure modes, which is overtopping with proper breach parameters, and flood hazard maps were constructed to show the devastating effect of the flash flood in Dalaman Basin due to the failure of the Akköprü Dam. The proposed methodology is applied to one of Turkey's most popular tourist destinations on the Western Mediterranean coast, and the case study area can be seen in Figure 1.
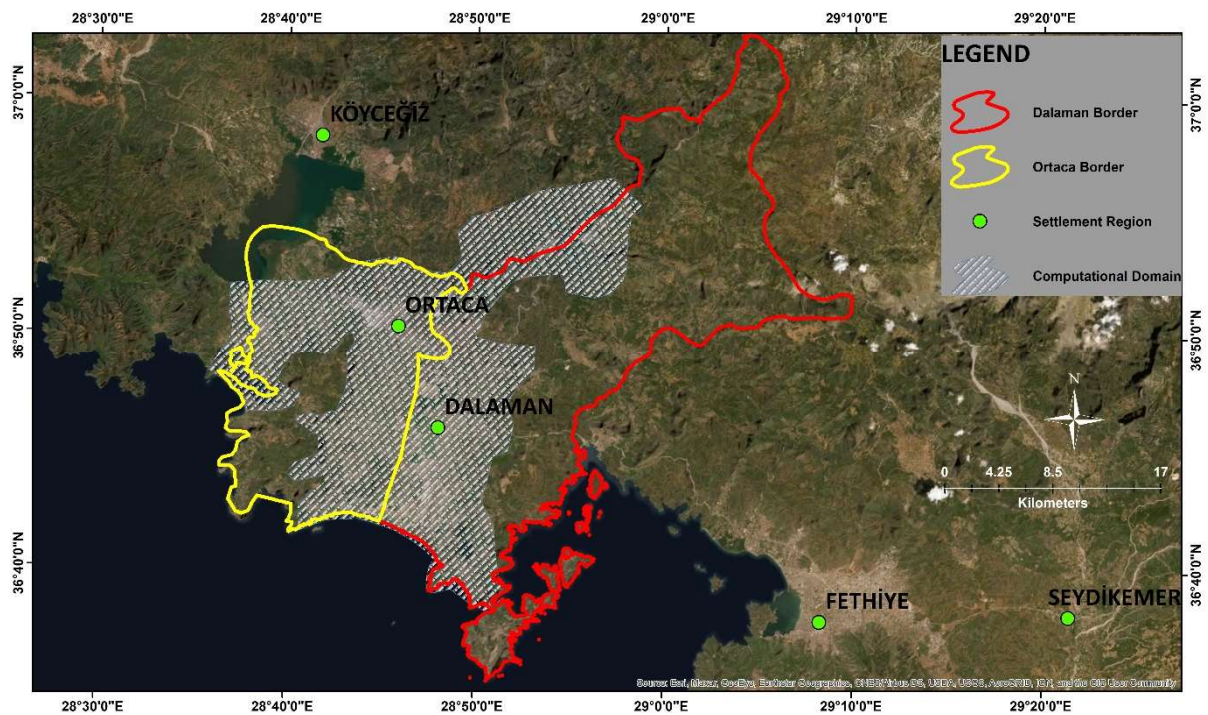

Figure 1. Study Area (Dalaman & Ortaca City Centers) and Computational Domain

2. METHODOLOGY

A hydraulic model was implemented to determine potential hazards downstream of a failed dam. For this reason, the Akköprü Dam, located on the southwestern coast of Turkey, is selected for the study. Necessary data of project area such as digital elevation model (DEM) and dam characteristics were provided by State Hydraulic Works of Turkey (DSI). After obtaining the necessary data, dam breach parameters were calculated by implementing the prediction method developed by Froehlich (2008) for the failure mode of overtopping. Consequently, a hydraulic model was conducted, velocity and water-depth data were obtained, and hazard mapping studies were carried out by implementing GIS works. Potential flood hazards and consequent early warning systems to mitigate potential threats were discussed.

2.1 Dam Characteristics

Dalaman Akköprü Dam is a homogeneous earth-fill dam with specific characteristics (Elevation-Storage-Area Curve) presented in Figure 2. The dam is the largest dam within the Aegean Region, and construction of the dam was started in 1996. Moreover, construction works were completed in 2011. It is located on Dalaman Creek and close to the centers of Dalaman, Ortaca and Köyceğiz towns. It can be seen from Figure 3 that the volume of water stored in the reservoir of the Akköprü dam is 385.26 hm^3 at the normal water surface elevation. In the case of failure of the dam body, at least this volume of water could create catastrophic damages located downstream of the dam.
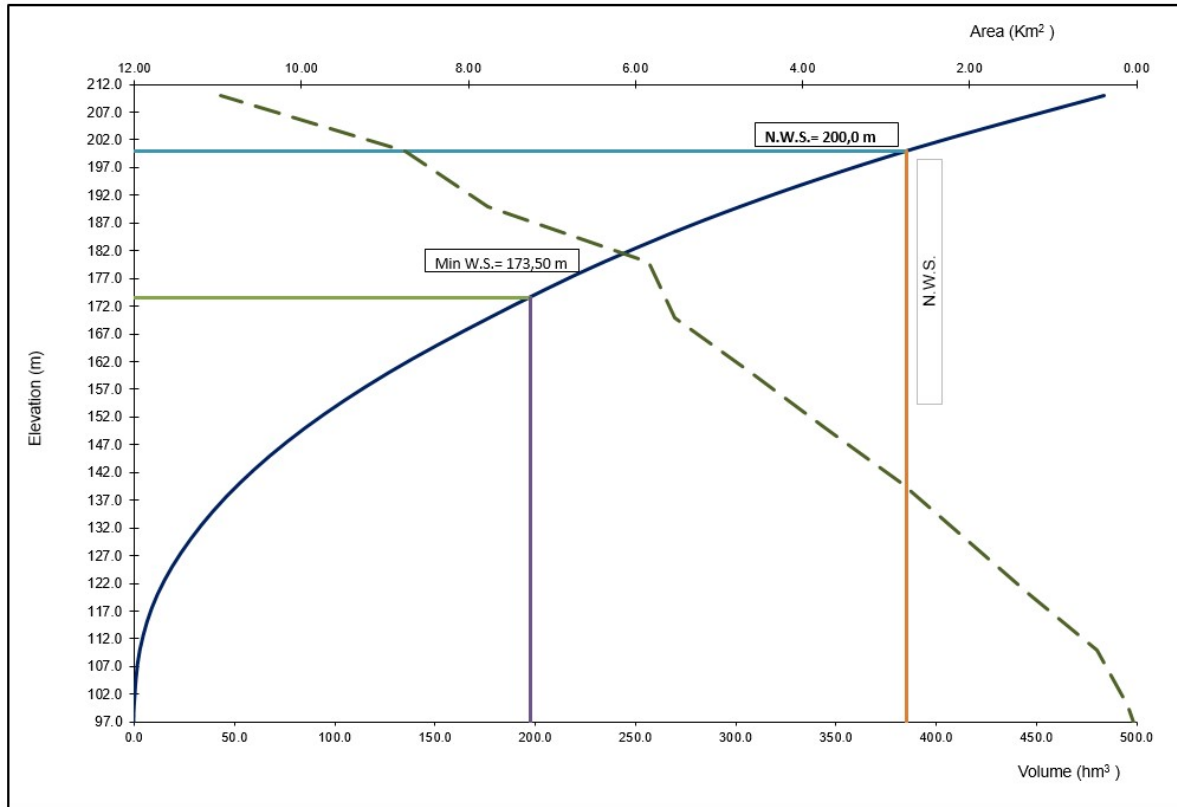
Figure 2. Elevation-Storage-Area Curve of the Dalaman Akköprü Dam

2.2 Failure Mechanisms & Calculation of Breach Parameters

Earth fill dams are the most vulnerable dam type to fail, and almost all of these failures are due to piping and overtopping (Limin Zhang et al., 2009). There are several sets of equations to predict breach parameters of a dam. The most recent ones are developed by the studies of Froehlich (1995), Von Thun Gillette & David R. (1990), and Xu & Zhang (2009). A survey by Kostecki and Banasiak shows that Froehlich's (2008) equations predict peak discharge within a 3 % confidence interval. Therefore, the equations of Froehlich (2008) were used to determine the breaching parameters for this study. Froehlich firstly developed his equations by considering 63 embankment dams, including earth fill, core wall and rockfill ones, to estimate breach parameters (Froehlich, 1995). The study was extended by himself later with the addition of 74 embankment dam data (Froehlich, 2008). The current equations of Froehlich, which were used to define the breaching parameters for the numerical solution of this study, is presented below;

$$B_{ave} = 0.27 K_0 V_w^{0.32} h_b^{0.04} \tag{1}$$

$$t_f = 63.2 \sqrt{\frac{V_w}{g h_b^2}}_w \quad \text{for easily erodible} \tag{2}$$

where; B_{ave} is the average breach width (in meters), K_0 is the failure mode constant (1.3 for overtopping and 1.0 for piping), V_w is the reservoir volume at the time of failure (in cubic meters), h_b is the height of the final breach (in meters), g is the gravitational acceleration (in meters per second squared), and t_f is the time of breach formation (in seconds).

2.3 Determination of Surface Roughness

The computational area was classified according to land use data of CORINE 2018, as shown in Fig 3. The surface roughness coefficients of the specific land cover were implemented according to the study by Papaioannou et al. (2018).
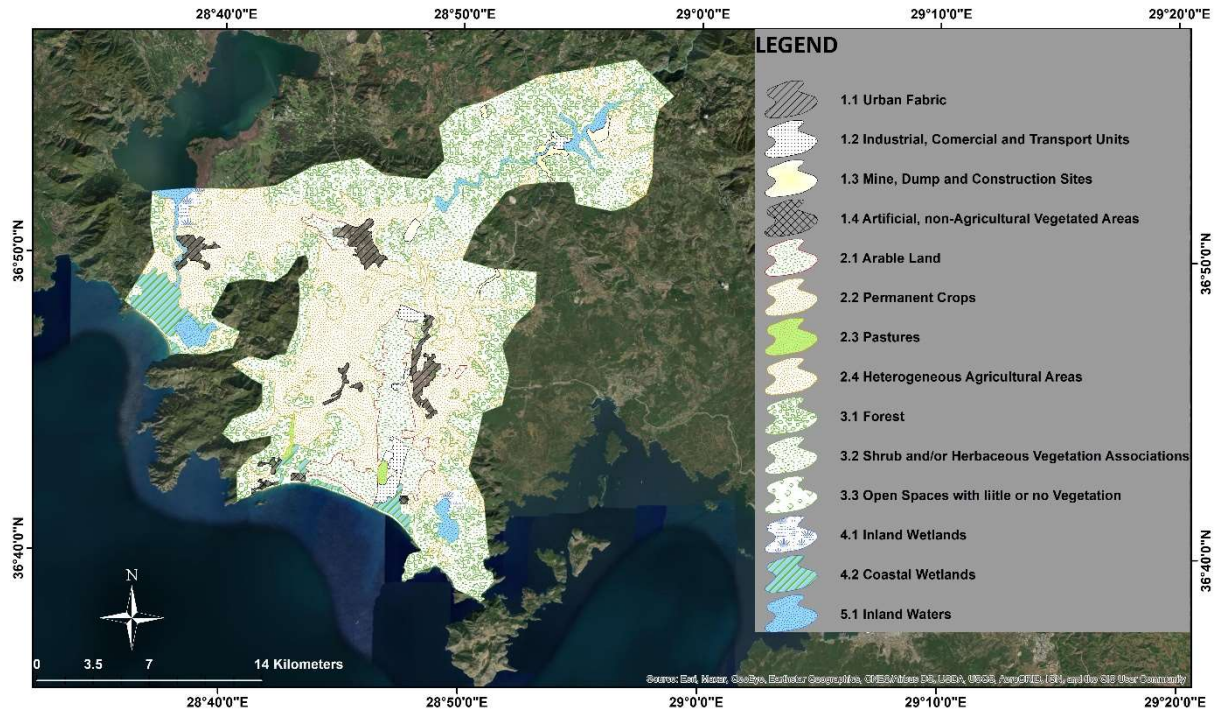
Figure 3. Study Area (Dalaman & Ortaca City Centers) and Computational Domain

Table 1 shows the study area's average surface roughness values implemented into the hydraulic model. The values in Table 1 were determined using the study of Papaioannou et al. (2018) based on the CORINE 2018 land cover data.

Table 1. Variation of Surface Roughness with respect to Land Cover for the Computational Domain.

Regions	Surface Roughness values Used in HEC-RAS
Residential	0.013
Commercial and services	0.013
Industrial	0.013
Transportation, communication, utilities	0.025
Cropland and pasture	0.030
Orchards, groves, vineyards, nurseries, and ornamental horticultural	0.080

Confined feeding operations	0.035
Other agricultural land	0.045
Herbaceous rangeland	0.100
Shrub and brush rangeland	0.040
Mixed rangeland	0.025
Deciduous forest land	0.040
Evergreen forest land	0.040
Streams and canals	0.050

2.4 Hydraulic Model

2D hydraulic modeling of the Dalaman Akköprü Dam for failure mode of overtopping was carried out using HEC-RAS, widely accepted and used software for solving hydraulic engineering problems.

Digital elevation model (DEM) of the area shown in Figure 4 with a 1 m of resolution implemented into HEC-RAS. The software solves shallow water equations, which are incompressible Reynolds averaged Navier-Stokes equations. Several preliminary runs determined the computational domain to determine possible inundated areas. At first, it was predicted that only Dalaman town Center could be affected by the breaching incident. However, prior runs show that Ortaca town center could be affected as much as Dalaman town center did. Therefore, the computational domain and DEM were extended by considering the results of preliminary runs.
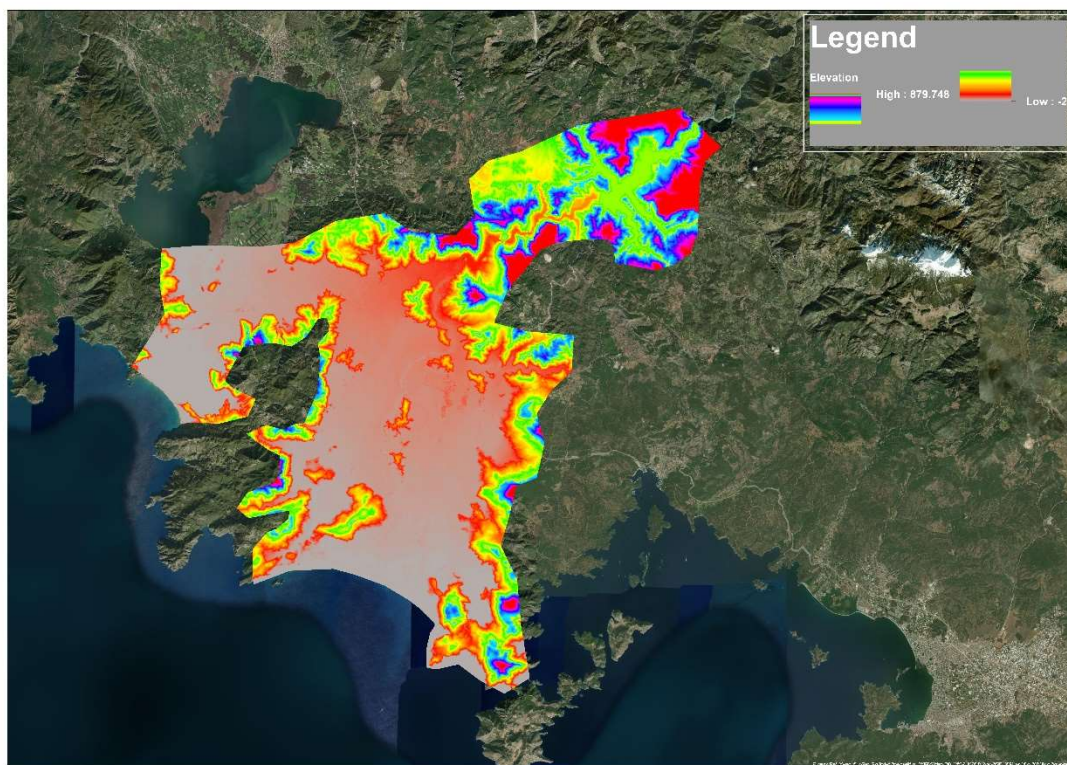

Figure 4. Digital Elevation Model of the study area and Computational Domain

After determining the computational domain covering Dalaman and Ortaca town centers and a small portion of Köyceğiz province, the computational domain was covered with non-uniform unstructured

meshes to solve surface flow. Moreover, buildings within the domain were digitized and implemented into the software. The main idea behind the process is to implement finer meshes around buildings to obtain a more precise solution. To get a more precise solution, facilities were specially treated by implementing finer meshes.

The solution was provided by a 2D numerical model for the failure mode of overtopping. The breach geometry is presented in Figure 5.
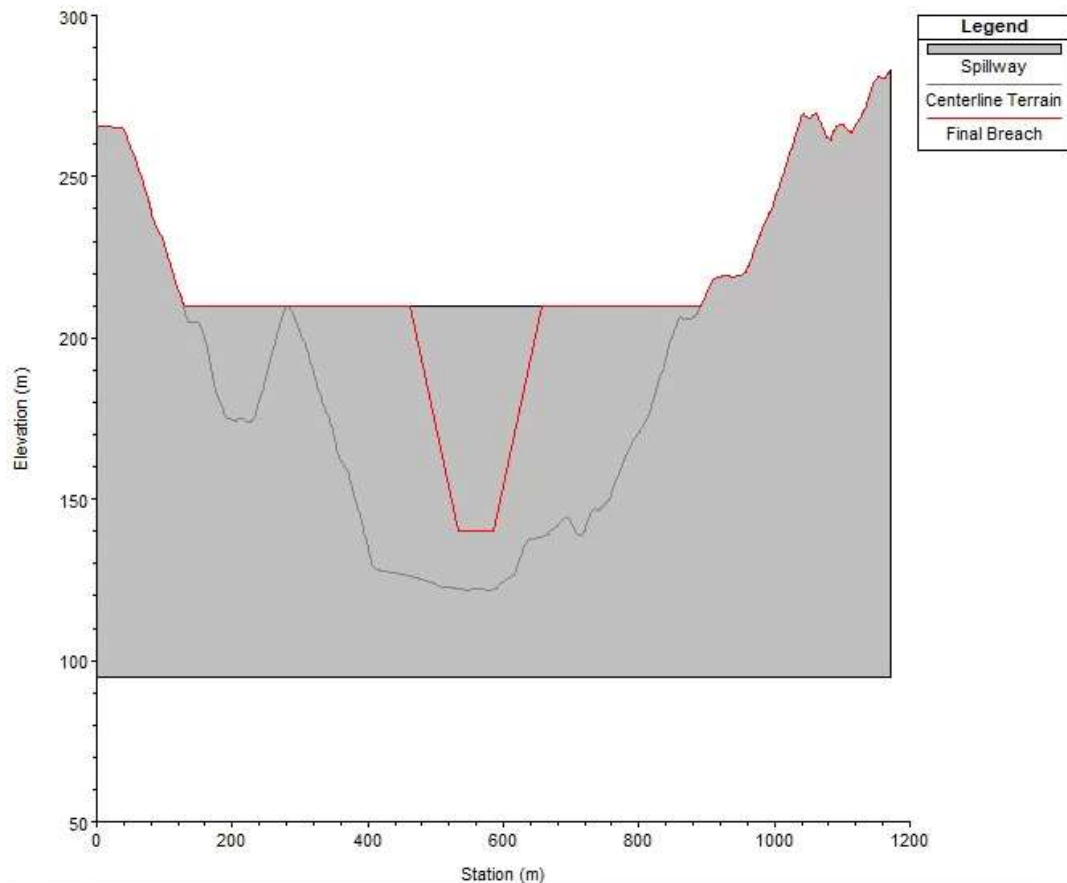

Figure 5. Breach Geometry

Throughout the simulation processes, input boundary conditions are provided by the dam breach process, while outlet boundary conditions were implemented to avoid the accumulation of excess water within the computational domain, which is the primary source of unstable hydraulic modeling and unreliable results.

2.5 Calibration of Hydraulic Model

It is often considered that the main calibration parameter of 1D and 2D hydraulic modeling is roughness values. Due to a lack of flood inundation records, calibration of the 2D hydraulic model could not be achieved. Nevertheless, determination of roughness with respect to land cover provides an excellent insight to present actual physical conditions. Calibration of the 1D hydraulic model was performed by considering records of two measurement stations.

Rating curves for each station were constructed by examining flow records of DSI (DSI, 2021). The rating curves of each station are presented in Figure 6.
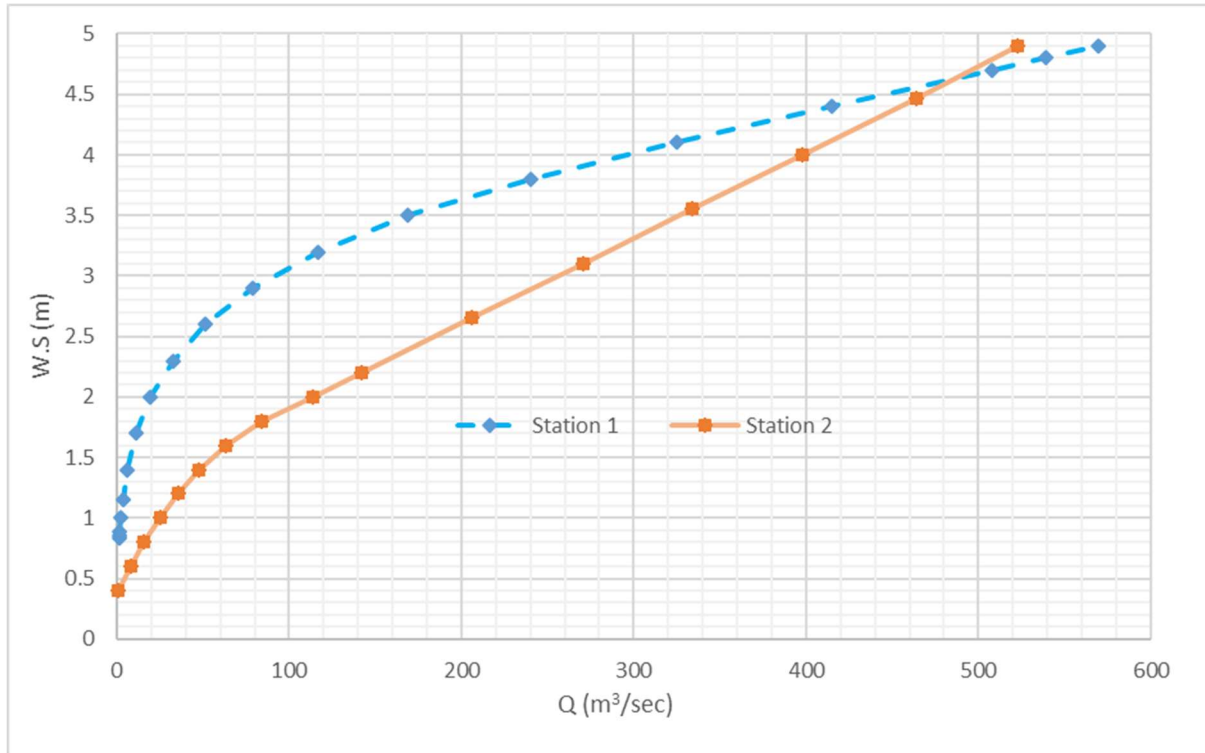
Figure 6. Rating Curve for Station 1 and Station 2

The equations representing discharge-water surface (W.S.) relation were obtained for Station 1 and Station 2 with correlation coefficients of 0.9721 and 0.9776, respectively. 1D hydraulic model calibration achieved by obtaining discharge and W. S. values. As a result of the trial-error procedure, the riverbed roughness coefficient is determined as 0.021. It should be noted that discharges of 200 m^3/sec or higher were neglected throughout the calibration because a quick inspection of the discharge-W.S. curve suggests limited data within the discharge range of 200 m^3/sec or higher.

2.6. Flood Hazard Analysis

Quantification of flood hazards is often conducted by considering depth and velocity. Although there are several methods in literature to quantify flood hazard with depth and velocity, direct multiplication of depth and velocity is taken into consideration as recommended by the Australian Disaster Resilience Handbook. In addition, the output of the hydraulic model provides spatially distributed depth and velocity data, which allows the construction of spatially distributed hazard mapping. Moreover, the Australian Disaster Resilience Handbook (Smith, Davey & Cox,2014) determined flood hazard and vulnerability thresholds, and a summary of that is presented in Table 2.

Table 2. Hazard Curves Vulnerability Threshold & Classification Limits (Smith, Davey & Cpx,2014).

Hazard Vulnerability Classification	Description	Classification Limit (m^2/s)
H1	Generally safe for vehicles, people and building	$D*V \leq 0.3$
H2	Unsafe for small vehicles	$D*V \leq 0.6$
H3	Unsafe for vehicles, children and the elderly	$D*V \leq 0.6$
H4	Unsafe for vehicles and people	$D*V \leq 1$
H5	Unsafe for vehicles and people. All buildings vulnerable to structural damage.	$D*V \leq 4$
H6	Unsafe for vehicles and people. All building vulnerable to failure	$D*V \leq 4$

In the Akköprü Dam break analysis, the first wave of the water reaches Ortaca City in 2 hours and 20 minutes for overtopping case after starting from the dam break. That means quite a percentage of people at risk within this city could be evacuated within that warning time. As per the model results, the water reaches Dalaman after 2 hours and 50 minutes and 3 hours and 10 minutes, respectively. This city will have more time for evacuation regarding Ortaca town. Unfortunately, all of the residential areas within these two cities will be covered by water with quite a high degree of risk, so evacuation within the town is not an option in that case.

3. RESULTS AND DISCUSSION

This study evaluated probable flood hazards due to dam breaks according to the overtopping mode of failure for the Dalaman Akköprü Dam. In the case of overtopping, a large portion of the Dalaman and Ortaca city centers were inundated. In Figure 6, flood hazard classification of the inundated area is demonstrated for the overtopping mode.
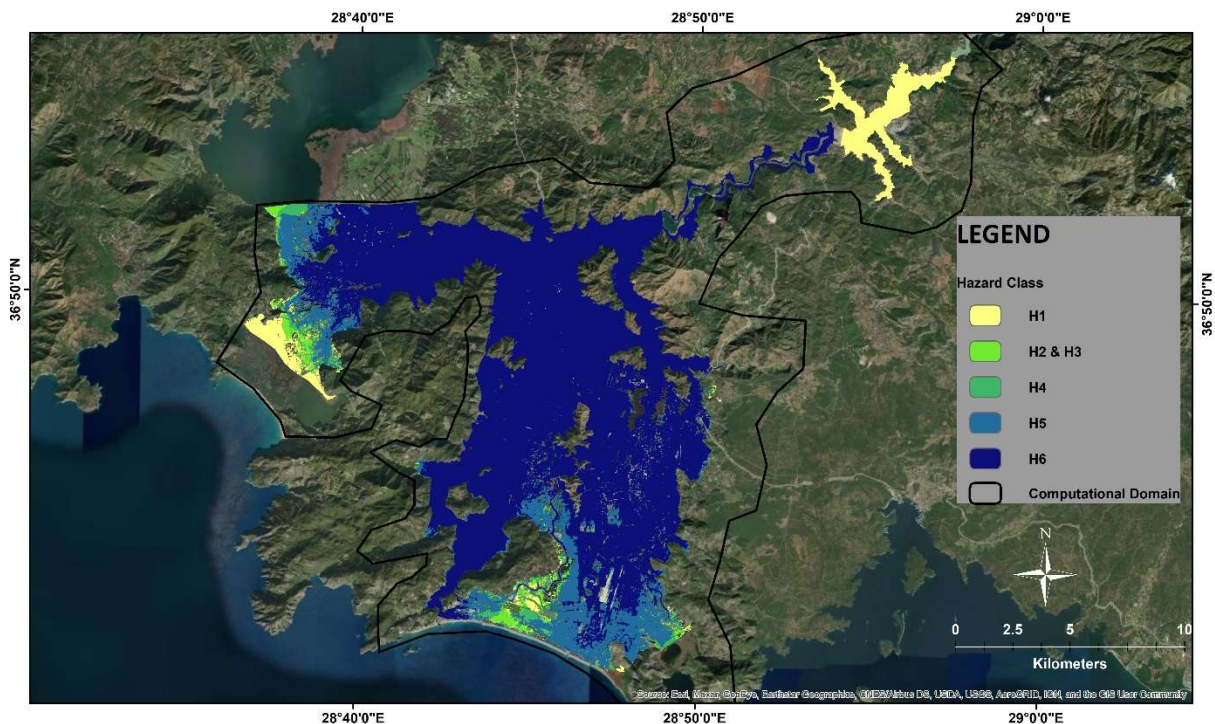

Figure 7. Spatially Varied Hazard Mapping of the Inundated Area for the Case of Overtopping

As shown in Figure 7, most of the inundated area is classified as H6 hazard class, while other hazard classes of H1 – H5 were observed in coastal regions. However, densely populated areas are more prone to H6 type hazards, unsafe for people, vehicles, and buildings. Therefore, the roads, buildings, and Dalaman Airport are at a high risk of failure in case of potential flood inundation. In addition, it can be stated that flow physics can change in case of a structural failure. However, this situation would not affect the destructiveness of the dam break event. In addition, the determination of evacuation plans is not convenient for the larger or higher structures within residential areas at the city centers due to the H6 Type hazard class. The hydraulic model results suggest that the average flood arrival time for the city centers of Ortaca and Dalaman is about 2 hours and 20 minutes and 2 hours and 50 minutes, respectively, for overtopping mode of failure. Therefore, city centers should be evacuated within 2 hours to prevent loss of life and property.

Thus, it should be noted that an evacuation plan should be implemented for the worst-case scenario by taking into account the H6 class hazard zone. With the preparation of emergency action plans by the authorities in charge of public safety, probable damage and losses can be prevented in a potential flood on this scale.

4. CONCLUSIONS

Although dam breach incidents are considered rare events, their results are catastrophic. This study evaluates the potential breach of Dalaman Akköprü Dam and potential hazards due to the hypothetical incident of overtopping failure case. The relatively quick release of water from the reservoir in overtopping results in mainly H6 type flood hazard which is a potential cause of failed buildings, roads etc. Flood peak reaches the residential areas within 2 hr 20 minutes to 2 hr 50 minutes. Therefore, instead of determining evacuation routes to higher buildings, evacuation of Ortaca and Dalaman town centers is considered. Moreover, due to the high risk of H6 and H5 Type hazard class, potential structural failure of high risk of a building during the event city centers should be evacuated within 2 hours. It is also investigated that possible structural measures to reduce the hazard of flooding downstream of the Dalaman Akköprü Dam were not feasible due to the region's topography. Thus it was not considered. Determining potential hazard and mitigation measures is essential for dam breach incidents because, once a breach occurs, there would be catastrophic events, including loss of lives depending on the topography and storage volume of a dam. Therefore, it is essential to evaluate potential hazards due to dam breach, especially for earth-fill dams.

The dam break phenomenon is considered a rare event; however, it has great risks considering catastrophic consequences. In this study, the potential hazard of the possible collapse of Dalaman Akköprü Dam was evaluated for the overtopping mode of failure.

The potential hazard is relatively high for overtopping failures as water is quickly released from the reservoir. In addition, as a result of the models examined in this study, overtopping failures cause H6 type flood hazards, which can pose severe dangers to the downstream region.

Flood wave reaches the residential areas within 2 hrs. 20 minutes to 2 hrs. 50 minutes in case of overtopping, which is considered a worst-case scenario.

Therefore, instead of determining evacuation routes to higher buildings, evacuation of Ortaca and Dalaman city centers is considered. In addition, due to the high risk of structural failure at flood inundation areas, which is in the H6 and H5 Type hazard class, city centers should be evacuated within 2 hours.

Furthermore, due to the topographic condition of the region, it was investigated whether possible structural measures to reduce the flood risk downstream of Dalaman Akköprü Dam could be applied as a result of related studies, and were not taken into account due to the unfeasible result.

It should be noted that the determination of potential hazards and mitigation measures is crucial to eliminate the potential risks of a dam failure. Therefore, evacuation action plans should be prepared by taking required measures to prevent loss of life and property.

REFERENCES

Akım Gözlem Yıllıkları. Devlet Su İşleri Genel Müdürlüğü. (n.d.). Retrieved December 5, 2021, from https://www.dsi.gov.tr/Sayfa/Detay/744

Alfier, L., Bisselink, B., Dottori, F., Naumann, G., Roo, A. de, Salamon, P., Wyser, K., Luc, & Feyen. (2017). Supplementary Global projections of river flood risk in a warmer world. Earth's Future, 5, 171–182. https://doi.org/10.1002/2016EF000485 Australian Institute for Disaster Resilience. (2013). Flood Hazard Guideline 7-3.

Arila G. and T..Nair. (2015) "Dam Break Analysis using Boss Dam Break," International Conference on Water Resources," Coastal and Ocean Engineering ICWRCOE. Elsevier Aquatic Procedia: Four (2015)853-860.

Arthur, G., (1977) "Teton Dam Failure," pp.61-71 in. "The Elevation of Dam Safety Engineering Foundation Conference Proceeding," Asilomar, Nov.28 – Dec. 3 1979). American Society of Civil Engineers, New York, 523p, 1977.

Daher A.H, "Hypothetical Failure of Sencherib Dam,(2001)" Master's Thesis, University of Baghdad, Iraq.

FEMA. (2013). Federal Guidelines for Inundation Mapping of Flood Risks Associated with Dam Incidents and Failures.

Foster, M., Fell, R., & Spannagle, M. (2000). The statistics of embankment dam failures and accidents. Canadian Geotechnical Journal, 37(5), 1000–1024. https://doi.org/10.1139/t00-030

Froehlich, D. C. (1995). PEAK OUTFLOW FROM BREACHED EMBANKMENT DAM. Journal of Water Resources Planning and Management, 121(1), 90–97.

Froehlich, D. C. (2008). Embankment Dam Breach Parameters and Their Uncertainties. Journal of Hydraulic Engineering, 134(12), 1708–1721. https://doi.org/https://doi.org/10.1061/(ASCE)0733-9429(2008)134:12(1708)

Graham, W. (1999). A Procedure for Estimating Loss of Life Caused by Dam Failure. Sedimentation & River Hydraulics, September, 43.

ICOLD International Committee on Large Dams "Dams and Floods Guidelines and Case History," Paris, Bulletin 125, 2007.

Ingles, O. G. (1984). A short study of dam failures in Australia, 1857-1983. Civil Engineering Systems, 1(4), 190–194. https://doi.org/10.1080/02630258408970342

Kreibich, H., Baldassarre, G. Di, Vorogushyn, S., Aerts, J. C. J. H., Apel, H., Aronica, G. T., Arnbjerg-Nielsen, K., Bouwer, L. M., Bubeck, P., Caloiero, T., Chinh, D. T., Cortès, M., Gain, A. K., Giampá, V., Kuhlicke, C., Kundzewicz, Z. W., Llasat, M. C., Mård, J., Matczak, P., … Merz, B. (2017). Adaptation to flood risk Results of international paired flood event studies.pdf. Earth's Future, 5, 953–965. https://doi.org/10.1002/2017EF000606

Kostecki, S. and Banasiak, R.: The catastrophe of the Niedów dam – the dam break causes, development and consequences, Nat. Hazards Earth Syst. Sci.

Macchione, F. (2008). Model for Predicting Floods due to Earthen Dam Breaching. I: Formulation and Evaluation. Journal of Hydraulic Engineering, 134(12), 1688–1696. https://doi.org/10.1061/(ASCE)0733-9429(2008)134

Natale, L., & Petaccia, G. (2008). Simulation of 2008 Pellice River Flood. Information Systems, May 2014, 1–6.

Papaioannou, G., Efstratiadis, A., Vasiliades, L., Loukas, A., Papalexiou, S. M., Koukouvinos, A., Tsoukalas, I., & Kossieris, P. (2018). An operational method for Flood Directive implementation in ungauged urban areas. Hydrology, 5(2), 1–23. https://doi.org/10.3390/hydrology5020024

Rashid M.A., "Transient Simulation and Hypothetical Model for AL-ADHAIM Dam–Break," PhD. Thesis. University of Technology, Baghdad, Iraq, 1999.

Qi, H., & Altinakar, M. (2011). A GIS-based decision support system for integrated flood management under uncertainty with two dimensional numerical simulations. Environmental Modelling and Software, 26, 817–821. https://doi.org/10.1016/j.envsoft.2010.11.006

Slater, L. J., & Villarini, G. (2016). Recent trends in U.S. flood risk. Geophysical Research Letters, 43(24), 12,428-12,436. https://doi.org/10.1002/2016GL071199

Smith, G. P., Davey, E. K., & Cox, R. (2014). Flood Hazard.

US Army Corps of Engineers. (2014). Using HEC-RAS for Dam Break Studies. https://www.scopus.com/inward/record.uri?eid=2-s2.0-84876361807&partnerID=40&md5=dfcbf4adad65f78943b9945d7689f84d

Von Thun Gillette, David R., J. L. (1990). Guidance on breach parameters. [U.S. Dept. of the Interior, Bureau of Reclamation].

Wahl, T. L. (1998). Prediction of Embankment Dam Breach Parameters - A Literature Review and Needs Assessment, Dam Safety Research Report. In Water Resources Research Laboratory: Vol. DSO-98-004 (Issue July). http://www.usbr.gov/pmts/hydraulics_lab/pubs/DSO/DSO-98-004.pdf

Xiong, Y. (2011). A Dam Break Analysis Using HEC-RAS. Journal of Water Resource and Protection, 03, 370–379. https://doi.org/10.4236/jwarp.2011.36047

Xu, Y., & Zhang, L. M. (2009). Breaching Parameters for Earth and Rockfill Dams. Journal of Geotechnical and Geoenvironmental Engineering, 135(12), 1957–1970. https://doi.org/10.1061/(ASCE)gt.1943-5606.0000162

Yanmaz, A. M., G, S., & V, O. (2001). A method for optimum layout design of concrete gravity dams. In Int J Korea Water Resources Assoc (Issue Water Eng Res).

Zhai, R., Tao, F., Lall, U., Fu, B., Elliott, J., & Jägermeyr, J. (2020). Larger Drought and Flood Hazards and Adverse Impacts on Population and Economic Productivity Under 2.0 than 1.5°C Warming. Earth's Future, 8(7). https://doi.org/10.1029/2019EF001398

Zhang, L, Peng, M., Chang, D. S., & Xu, Y. (2015). Dam Failure Mechanisms and Risk Assessment. https://doi.org/10.1002/9781118558522

Zhang, Limin, Xu, Y., & Jia, J. S. (2009). Analysis of earth dam failures: A database approach. Georisk, 3(3), 184–189. https://doi.org/10.1080/17499510902831759

14TH INTERNATIONAL CONFERENCE
ON HYDROSCIENCE & ENGINEERING

MAY 26-27, 2022
IZMİR-TURKEY

ICHE2022
IZMIR, TURKEY

IDENTIFICATION OF A PRACTICAL METHOD AND A SET OF MORPHOMETRIC PARAMETERS FOR FLASH FLOOD POTENTIAL PRIORITIZATION

Mahmoud M. Mansour

Department of Environmental Engineering, School of Energy Resources, Environment, Chemical and Petrochemical Engineering, Egypt-Japan University of Science and Technology, Alexandria, Egypt

Department of Civil Engineering, Faculty of Engineering, Menoufia University, Menoufia, Egypt

mahmoud.monir@ejust.edu.eg

Mahmoud Nasr

Department of Environmental Engineering, School of Energy Resources, Environment, Chemical and Petrochemical Engineering, Egypt-Japan University of Science and Technology, Alexandria, Egypt

Department of Sanitary Engineering, Faculty of Engineering, Alexandria University, Alexandria, Egypt

mahmoud.nasr@ejust.edu.eg

Manabu Fujii

Department of Civil and Environmental Engineering, School of Environment and Society, Tokyo Institute of Technology, Tokyo, Japan

fujii.m.ah@m.titech.ac.jp

Chihiro Yoshimura

Department of Civil and Environmental Engineering, School of Environment and Society, Tokyo Institute of Technology, Tokyo, Japan

yoshimura.c.aa@m.titech.ac.jp

Mona G. Ibrahim

Department of Environmental Engineering, School of Energy Resources, Environment, Chemical and Petrochemical Engineering, Egypt-Japan University of Science and Technology, Alexandria, Egypt

Department of Environmental Health, High Institute of Public Health, Alexandria University, Alexandria, Egypt

mona.gamal@ejust.edu.eg

ABSTRACT: Flash floods cause losses to sustainable development spheres (environment, society, and economy). Because of the shortage of hydrological and meteorological records, basin prioritization using topographical and morphological features provides a feasible tool for flash flood hazard prediction. Nevertheless, several attempts using varied groups of morphometric parameters were lacking validation and reliability evidence. This study aims to investigate the accuracy of an identified approach and conventional methods considering two morphometric parameter sets using historical data. Therefore, Remote Sensing (RS) and Geographic Information Systems (GIS) were incorporated to estimate the main morphometric parameters of basin geometry, drainage network and texture and relief characteristics. Then, three approaches (El-Shamy, Compound Parameter (CP) and Analytical Hierarchy Process (AHP)) were employed through two groups of morphometric parameters to determine flash flood-based basin priority. The collected data of flash flood past events was adopted to appraise the efficiency of the considered methods and the significance of morphometric parameter groups. Drainage network and texture-based methods (El-Shamy and CP) attained low success rates ($< 25\%$) and minimal coefficient of determination ($R^2 \leq 0.2$), while basin geometry and relief-based approaches (CP and AHP) witnessed high success rates exceeding 55% and significant R^2 more than 0.7. AHP was the most

reliable method, so its results were employed to present the flash flood-based basin prioritization map, which revealed that 6 basins covering about 60% of the study area had the highest flash flood priority, for guiding further consequent mitigation and sustainable management strategies.

1. INTRODUCTION

Flash floods are considered serious hydrological phenomena, because of their rapid and unforeseen attributes and threats to properties, humans, the environment, infrastructure, and development, (Helmi & Zohny, 2020). Although precipitation quantity and intensity are significant elements in flash flood occurrence, topography, underlying lithology, drainage network, and basin features are all interconnected factors that determine flash flood severity and basin prioritization for implementing management strategy, (Youssef, Pradhan, & Hassan, 2011). To evaluate and manage severe climatic events such as flash floods, a watershed is a common unit, (Bogale, 2021). Basin geometry and relief attributes, in addition to drainage network and texture characteristics, are the primary groups of morphometric characterization, (Helmi & Zohny, 2020). Flash flood hazard-based basin prioritization can be implemented in ungauged basins utilizing morphometric parameters-based techniques as follows: El-Shamy approach, which relies solely on three drainage network and texture parameters, and Compound Parameter (CP), which allows any combination of morphometric factors to be included, (Mansour, Ibrahim, Fuji, & Nasr, 2022a). However, there are reliability shortages and uncertainty about the previous results due to a lack of robust validation processes with field data gaps which have been covered in this study.

The Suez Gulf area of the Sinai Peninsula witnessed severe rainfall and flash flood episodes, (Dadamouny & Schnittler, 2016). Many people were displaced, some homes were damaged, and highway pieces were swept away as a result of these occurrences. Flash floods caused several fatalities, livestock and animal deaths and uprooted diverse trees, (Eliwa, Murata, & Ozawa, 2015). Due to the region's climate and complex physiography, a flash flood is considered a serious and recurring incident. As a result, understanding flash flood triggers to guarantee adequate and successful management for long-term development requires flash flood potential-based basin prioritization for identifying flood-prone locations, (Nasir, Iqbal, & Ahmad, 2020). Therefore, the study's goal is to find a credible approach and significant morphometric parameters for determining the prioritization of basins regarding flash flood hazards. In addition to the previously stated methods, another proposed approach incorporates the AHP, (Helmi & Zohny, 2020). These are the most practical and widely used geospatial approaches with various principles, (Prabhakaran & Raj, 2018). These methods employ a variety of morphometric criteria to measure flash flood hazard priority at the basin level. However, the previous results were compatibly lacking as field observations and flash flood data are rarely compared and checked with them. Therefore, the following are the precise goals of the study:

- Assess flash flood hazard priority for the Suez Gulf region utilizing El-Shamy, CP, and AHP methods.
- Compare their dependability and present applicable worldwide flash flood hazard assessment method.
- Present the basin prioritization map as a base for flash flood alleviation and sustainable management.

2. STUDY AREA

The Sinai Peninsula lies in Egypt's northeastern corner, the Asiatic part of the country. The Arabian-Nubian massif, which consists of magmatic and metamorphous rocks, underlies the South Sinai region. Several formed valleys with steep slopes cut through this massif. A small number of drainage channels are flat concave, but the majority are steep, with exposed rock floors and dried waterfalls obstructing their longitudinal profiles, (Youssef, Pradhan, & Hassan, 2011). The area of study, which is estimated at 13,000 km^2, lies in the southwestern Sinai Peninsula, adjacent to the Suez Gulf (Figure 1). Drainage in this horst block is towards the Gulf of Suez. This region is a favoured destination for

thousands of tourists annually due to its existing historical, cultural, and religious monuments, deluxe resorts and charming beaches and coral reefs. This region has a mild to cold winter and a hot dry summer. Meteorological data for the study area were retrieved from the existing 3 stations (Ras Sudr, Saint Catherine and El-Tor stations) over the period from 1995 to 2014, presented by (Dadamouny & Schnittler, 2016). The minimum and maximum temperatures were -6 and 45°C. Relative humidity ranged from 20% to 58%. The total precipitation per year varied from 1 to 94.5 mm. The largest amount of daily precipitation ever recorded in the study region was 86.3 mm. However, the study area has an almost uniform average total and highest daily precipitation, suggesting insignificant factors for spatial flash flood potential. Recently, the frequency of flash floods has increased, especially in the autumn and spring, and led to considerable destruction of the existing infrastructures, cities, villages and vital facilities, (Eliwa, Murata, & Ozawa, 2015).

3. MATERIAL AND METHOD

In this study, various sorts of data were freely obtained from (https://earthexplorer.usgs.gov/) to be further utilized, which included Digital Elevation Model (DEM) and true colour imagery (band 1, 2 and 3), derived from Shuttle Radar Topography Mission (SRTM) data and Landsat 7 Enhanced Thematic Mapper Plus (ETM+) data, respectively, with 30 m spatial resolution. The latter data was utilized to realize the surface form of the considered region and to validate the drainage course derived from the DEM (Figure 1a). The Arc Hydro tools of ArcGIS 10.4.1 were utilized to well understand the watershed and drainage system in the studied area. The DEM preprocessing was performed by filling the sinks before creating the basins and drainage networks. ArcGIS facilitated retrieving crucial attributes and values and creating the required maps.

Data source: https://earthexplorer.usgs.gov/
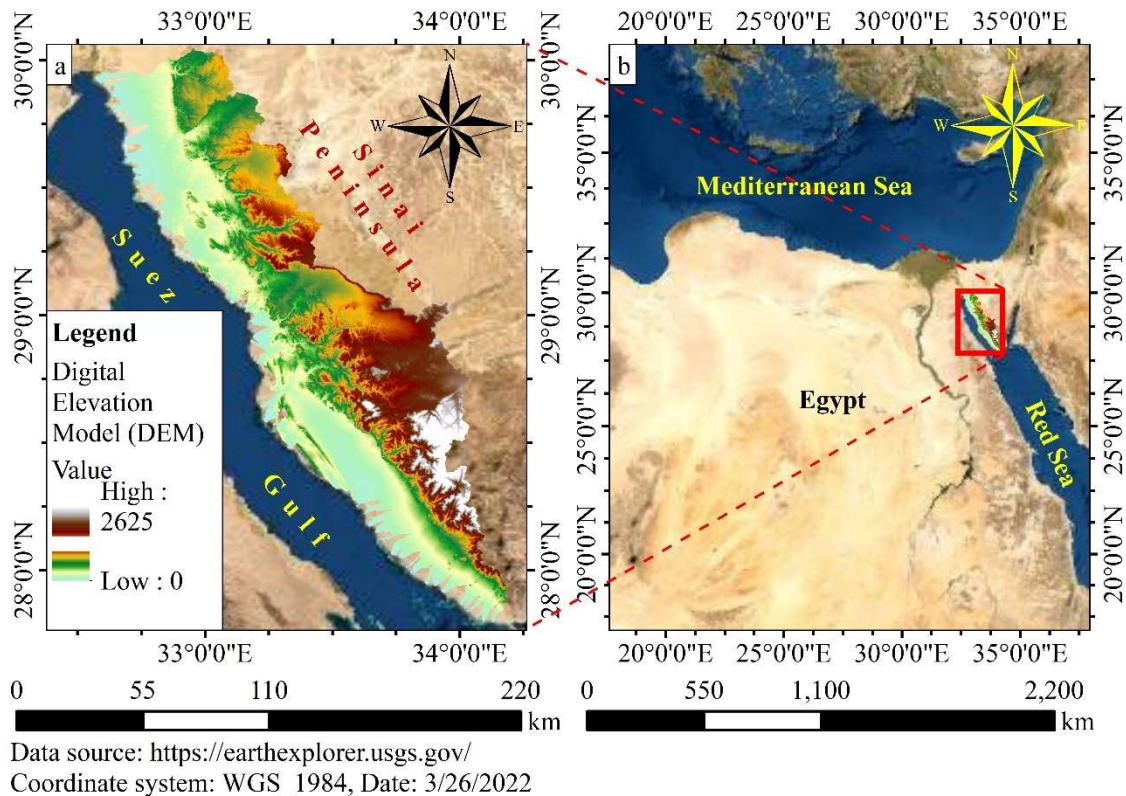Coordinate system: WGS_1984, Date: 3/26/2022

Figure 1. (a) Digital Elevation Model (DEM) of Suez Gulf basin and (b) Study area location

Flash flood events cause damage ranging from slight inundation (20 cm in depth) to destructive events with environmental, human and economic losses. The frequently occurring events in the study area were collected over the period from 1979 to 2020, including the spatial distribution of affected basins from published articles and books, dissertations, available reports and newspapers, (Youssef, Pradhan, & Hassan, 2011; Eliwa, Murata, & Ozawa, 2015; Gabr & El Bastawesy, 2015). Collected

events were filtered to ensure temporal consistency by omitting periods with incomplete reports. Then, affected basins were descendingly sorted regarding the recurrence and quantity of the considered events and categorized to five flash flood hazard degrees (FFHDs), viz, very high, high, moderate, low and very low, respectively, ((EXCIMAP), 2007; Mansour M. M., Ibrahim, Fuji, & Nasr, 2022b).

3.1. Morphometric Parameters Estimation

Basin attributes, namely, length, area, min/max elevations, land slope, stream order and stream length, were generated and retrieved by ArcGIS. Then, these parameters were exported to Microsoft Excel for subsequent calculations of other influential morphometric parameters, viz, mean bifurcation ratio, stream frequency, drainage density, elongation ratio and relief. Table 1 gives the main parameters, which belong to the three categories of morphometric characteristics, units and, where appropriate, the formulae used to calculate them. Basin geometry, or areal properties, illustrates the plan dimensions of the basin. The basin area (A) includes a region that collects rainfall and delivers it to a particular outlet, which is a significant hydrological feature; it governs runoff quantity resulting from rainfall events, (Schumm, 1956). The quotient of the circle diameter having the same area as the basin and the basin length is defined as the elongation ratio (R_e), (Schumm, 1956). R_e is a crucial property of the basin that expresses the plan shape of the basin. Low values of R_e indicate an elongated shape, while R_e near unity implies a near-circular basin.

Table 1. Morphometric parameters equations for estimating the corresponding values of the Suez Gulf basins.

No.	Morphometric parameter	Formula	Unit	References
Basin Geometry				
1	Basin area (A)	GIS software analysis	km²	(Schumm, 1956)
2	Elongation ratio (R_e)	$R_e = \left(2\sqrt{(A_b/\pi)}\right)/L_b$; where L_b = basin length	Dimensionless	(Schumm, 1956)
Drainage Network and Texture				
3	Drainage density (D)	$D = \sum L_u/A_b$; where L_u = stream length of order 'u'	km/km²	(Horton, 1945)
4	Stream frequency (F)	$F = \sum N_u/A_b$; where N_u = number of streams of order 'u'	1/km²	(Horton, 1945)
5	Mean bifurcation ratio (R_b)	$R_b = \sum\left(N_u/N_{(u+1)}\right)/(S-1)$; where $N_{(u+1)}$ = Number of streams of next higher order 'u+1' and S = basin's stream order	Dimensionless	(Strahler A. N., 1953)
Relief				
6	Relief (R)	R= Highest elevation - Lowest elevation	m	Schumm (1956)
7	Mean basin slope (S_m)	GIS software Analysis using DEM	Degree	(Prabhakaran & Raj, 2018)

Drainage network and texture attributes describe the interconnected stream network in a basin. It is highly influenced by the user-defined stream threshold, which was set to be 0.2 km², (Mejía & Moglen, 2010). Each stream segment was assigned a certain order, following (Strahler, 1964). Drainage density (D) is the total length of the drainage network with all orders per basin area, (Horton, 1945). It is an estimate of channels closeness and indicates the balance between the resistance of rocks and surface soils and the erosive flow power. The primary morphometric parameters affecting drainage density are relative relief and slope gradient. (Magesh, Chandrasekar, & Soundranayagam, 2011). Stream frequency (F) is the number of drainage network channels per unit area of the drainage basin, (Horton, 1945). It may be independent of the D as it just considers the number of streams, not lengths. A bifurcation ratio is defined as the number of channels of a certain order divided by the number of the next higher-order channels. It is an estimate of the ramification trend in the drainage network (Schumm, 1956). For a basin, the average bifurcation ratio implies the divergence degree of the drainage network. The mean bifurcation ratio (R_b) is fundamental for linking

a watershed's hydrological response under various topological and climatic circumstances. and a useful measure to define a flash flood-prone area by deciphering the runoff behavior, (Horton, 1945). Relief Characteristics are quantitative measurements of the land surface vertical alignment describing the landscape change. Relief (R) equals the vertical range between the highest point and outlet elevations in the basin. It is crucial to comprehend the denudational features and erosional properties of the terrain that are generated due to active eroding and weathering mainly induced by rainfall-runoff episodes (Magesh, Chandrasekar, & Soundranayagam, 2011). The mean basin slope (S_m) is the equivalent value of the entire basin's land surface slope. It is a key morphometric characteristic that influences hydrological response, particularly the volume and velocity of surface runoff, as well as the time it takes for runoff to reach the stream segment. Higher S_m results in faster runoff and less groundwater recharge, which implies the high potential of surface runoff, (Youssef, Pradhan, & Hassan, 2011). Flash floods are more probable in basins with increased R and S_m.

3.2. El-Shamy Approach

(El-Shamy, 1992, April) presented an approach for evaluating the prioritization of basins or subbasins for flash flooding or groundwater recharge potential. It is based on three morphometric parameters and two relationships: R_b versus D and R_b versus F. R_b is on the x-axis with a normal scale, while D and F are on the y-axis with a logarithmic scale (Figure 3). The domain for both relationships is divided into three zones: B, C and A. Zone B indicates an increased likelihood of flash flooding and a decreased likelihood of groundwater recharge, whereas zone A indicates the opposite. Meanwhile, zone C represents the intermediate possible conditions. For the overall assessment, the higher hazard degree should be considered.

3.3. Data Normalization

Normalization aims to create shifted or scaled copies of values measured on multiple scales to a defined scale (from 1 to 5) by "Equation 1", (Han, Kamber, & Pei, 2012). As a result, normalized values of morphometric parameters can be compared without the impact of certain gross factors.

$$Y(i) = a + \frac{x(i) - x_{min}(i)}{x_{max}(i) - x_{min}(i)}(b - a) \qquad (1)$$

where $x(i)$, $x_{min}(i)$, $x_{max}(i)$ and $Y(i)$ are original, minimum original, maximum original and normalized values, respectively, while a and b are minimum and maximum values or the required range.

3.4. Compound Parameter

To estimate the integrated effect of morphometric characteristics on the hydrological responses and flash flooding potential at the basin scale. A Compound Parameter (Cp) could be calculated for different sets of morphometric parameters to depict flash flood susceptibility. This approach relies on scientific knowledge of the phenomena and related parameters to drive a quantitative estimation. It is widely utilized to investigate topographic conditions among comparative components such as basins (Youssef, Pradhan, & Hassan, 2011). In the present study, Cp was determined for all basins using two sets of morphometric parameters. The first set (DT) included the normalized drainage network and texture parameters (D, F and R_b), while the second set (AR) involved areal properties and relief characteristics parameters (A, R_e, R and S_m) using "Equations 2-3". Then, basins were categorized into the five hazard degrees mentioned.

$$CP - DT = \frac{Y(D) + Y(F) + Y(R_b)}{3} \qquad (2)$$

$$CP - AR = \frac{Y(A) + Y(R_e) + Y(R) + Y(s_m)}{4} \qquad (3)$$

Where $Cp - DT$ is the compound parameter of drainage network and texture parameters and $Cp - AR$ is the compound parameter of areal properties and relief characteristics parameters.

3.5. Analytical Hierarchy Process

(Saaty, 1980) first proposed the analytic hierarchy process (AHP) as a decision analysis method that solves complex problems more simply and flexibly. The problem is broken down into an objective

and a set of criteria. Thus, this technique is employed for prioritization of the considered basins (alternatives) to assess the flash flood potentials using areal properties and relief characteristics parameters. The AHP-AR method consisted of assigning relative weight to each parameter and its sub-classes, checking weight consistency, aggregating equivalent values for each basin, and similarly classifying them.

4. RESULTS AND DISCUSSION

Basin prioritization techniques have been utilized to identify the features and extent of flash flood hazards in the Suez Gulf region. To assess flash flood-based prioritization for fifty-six basins in the Suez Gulf region (Figure 2a), morphometric parameters were utilized. Thereafter, three different methods were proposed: (a) El-Shamy approach, (b) CP, and (c) AHP. Figure 2a shows the map of the Suez Gulf basins' boundary and the cities' locations. Basins with larger areas are in the middle region, while elongated low area basins lie in the southern part. All cities are located near the outlet of some basins, except Saint Catherine, which is found upstream of the Feran basin. A significant match was observed for the obtained basins' boundary compared to (Helmi & Zohny, 2020). Figure 2b shows the drainage network for each basin, describing the order of each stream. The order of the mainstream in each basin ranges from 3 to 7. The 7th order stream was observed at El-Aawag and Wardan basins, while 7 basins had the 6th order stream. The delineated drainage networks were validated by matching them with the observed ephemeral streams in the true colour satellite imagery, indicating a high resemblance of the field conditions.

Data source: https://earthexplorer.usgs.gov/
Coordinate system: WGS_1984, Date: 3/26/2022
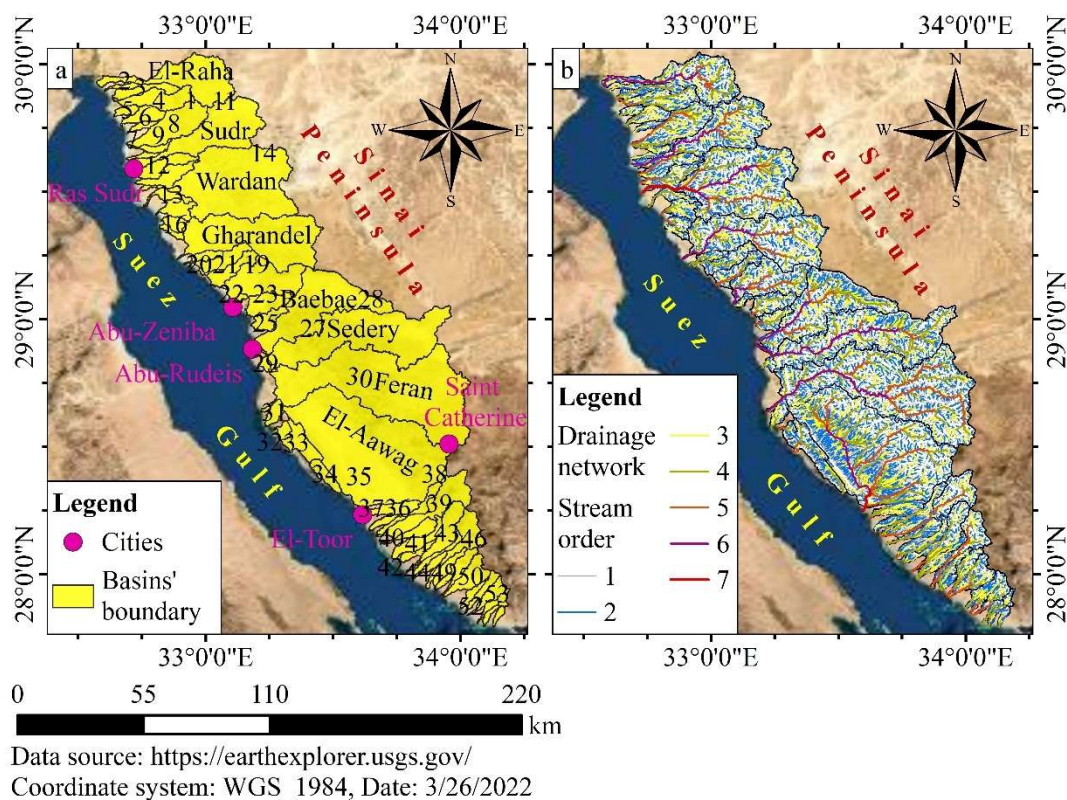
Figure 2. a) Boundary of Suez Gulf basins and the cities' locations; and b) Drainage network and stream order classification of Suez Gulf basins

Table 2 shows the minimum, average and maximum estimated values of the considered morphometric parameters. The area of the Suez Gulf basins was 12441 km². A range from 17.9 km² to 1906.6 km² of El-Aawag basin. According to (Horton, 1945), 21 basins, or 86.65% of the total area, were classified by size into the large basin category (>100 km²). The moderate basins (25-100 km²) account for 27 and cover 12% of the study area, while the small basins are 8, representing only around 1.32%. A constitutes a governing parameter in determining the peak flow discharge of a basin because it

controls the collected portion of rainfall and determines the peak discharge of flash floods, (Mimikou, 1984). So, a large-sized basin almost produces a high peak discharge and runoff volume.

R_e ranges from 0.28 for basins 38 (Sely) and 44 (Rout) to 0.9 of El-Aawag basin. The basins can be classified by values of the R_e into five categories: more elongated (< 0.5), elongated (0.5-0.7), less elongated (0.7-0.8), oval (0.8-0.9) and circular (> 0.90), (Strahler, 1964). Therefore, a higher number of elongated basins could be inferred due to the decreased average value of R_e (0.48). R_e is crucial for determining the hydrology of a basin and estimating the hazard of flash flooding. Peak discharge for an elongated basin would be lower than that of a circular basin having the same area within a longer concentration period. In a circular basin, the drainage network is more similarly formed, and branch flows simultaneously reach the mainstream, (Bogale, 2021). As a result, a larger amount of runoff is transferred to the outlet at the same time and at a faster rate (high peak flow and short duration). The driving impact of thrusting and faulting causes variation in the basins' R_e. Thus, the Suez Gulf basins reflect a wide range of elongation degrees, resulting in varied hydrological response patterns.

Table 2. Minimum, average and maximum values of morphometric parameters for the Suez Gulf basins.

Morphometric parameter	A (km^2)	R_e	D (Km^{-1})	F (Km^{-2})	R_b	R_f (m)	S_m (°)
Minimum	17.9	0.28	1.74	1.43	2.83	104	1.35
Average	222.1	0.48	2.15	1.80	4.10	896	6.71
Maximum	1906.6	0.90	2.88	2.39	6.63	2620	17.95

D varies from 1.74 km^{-1} for basin 46 (El-Mhash) to 2.88 km^{-1} for basin 56, with an average of 2.15 km^{-1} (Table 2). The increased D values are ascribed to the bare ground of the study area; arid and semi-arid areas have greater D than humid areas with similar topography due to flash floods and rare vegetation (Strahler, 1964). Both peak flow and lag time might be affected by D, as increased flash flood peaks are associated with increased D, (Bogale, 2021). High D is potential where basin relief is high, implying high runoff, while low D almost exists where basin relief is low and reflects erosion-resistant fractured hard rocks, indicating high infiltration and groundwater recharge, (Strahler, 1964). So, El-Mhash basin provides better conditions for groundwater replenishment. F may be directly related to lithological characteristics, (Horton, 1945).

F varies a little, ranging from 1.43 streams/km^2 for basin 2 (Mabaoq) to 2.39 streams/km^2 for basin 32. Based on the calculated F, the basins were categorized as follows: low (< 1.75 streams/km^2), moderate (1.75–2.05 streams/km^2) and high stream frequency (> 2.05 streams/km^2). F is proportional to the level of dissection and runoff. A higher F indicates greater surface runoff, increased land surface slopes, an impervious subsurface with scattered plants, and greater relief, (Soni, 2017; Prabhakaran & Raj, 2018). This suggests that watersheds with decreased F such as basins 38 and 43 (Aman) are likely to witness a lower degree of dissection and lower runoff. To appraise the correlation between D and F for Suez gulf basins, linear regression shows an inverse relationship between the two parameters but with a low R^2 (0.11) dissimilar to (Magesh, Chandrasekar, & Soundranayagam, 2011) that is ascribed to the spatial geological and structural differences.

Bifurcation ratios show significant variation among various orders in each basin. These differences rely on the local physiography and geomorphological conditions of the watershed, (Strahler, 1964). R_b ranges from 2.83 for basin 32 to 6.63 for basin 37. As 90% of R_b values are within the range of 2 to 5, many well-developed drainage patterns and maturely dissected basins are implied, (Horton, 1945; Strahler, 1964). The decreased R_b is connected to basins that are fatter or more rolling and have witnessed less distortion of drainage patterns or structural disturbances (Strahler, 1964; Bogale, 2021). A higher R_b value is ascribed to a significant variation in stream frequencies across subsequent orders and implies a mature topography, shorter lag time, greater peak discharge and higher flash flood potential (Bogale, 2021).

The total R of the Suez Gulf basins is 2625 m. This high value generally indicates greater surface runoff and lower infiltration conditions. R ranges from 104 m (basin 5) to 2620 m (Feran basin). R is

low (< 900 m) in 37 basins such as El-Raha and Sudr basins; high (> 1800 m) in 6 basins (El-Aawag and Feran basins) and moderate (900–1800 m) in the rest 13 basins. R is directly proportional to the potential energy, denudation rate and discharge rate of a watershed; The high value of R implies that the water flow is gravity-driven, with limited infiltration and heavy runoff, suggesting a high potential of flash flood occurrence in those basins, (Magesh, Chandrasekar, & Soundranayagam, 2011).

The highest land surface slope of the study area is slightly more than 73°, which is slightly higher than the 70° obtained by (Magesh, Chandrasekar, & Soundranayagam, 2011). S_m ranges from 1.35° for basin 10 to 17.95° for basin 39 (Abu-Jurf) with an average value of 6.7°. The net runoff volume and duration of concentration are often affected by the slope of the land. Runoff volumes and peaks are smaller in basins with decreased slopes. In these basins, the velocities of overland flows are lower and longer periods are available for water infiltration, thus less surface runoff reaches the streams for basins 2, 3 (Abu-Remt), 6 (Marbae) and 16 (Seaeda). A steep slope, observed in the southeastern study area, suggests greater velocity and quicker removal of runoff potential in the basin. Hence, quicker times of concentration may be evident in Feran, El-Aawag, Sely, Abu-Jurf, Aman and El-Mhash basins.

4.1. El-Shamy Output

Figure 3a-b and Table 5 show the flash flood basin prioritization of the Suez Gulf basins using El-Shamy approach. Figure 3a illustrates the priority of the Suez Gulf basins according to the R_b and D relationship. It was discovered that 7 Basins (12.5% of the total sub-basins) with relatively low R_b (<3.6) and high D (>2.33) had high flash flood potential, whereas 20 basins (35.7 %) with D less than 2.50 and R_b greater than 4.13 had high groundwater recharge conditions, combating seawater intrusion instead of costly physical barriers, (Mansour, Ellayn, Helal, Rashwan, & Sobieh, 2018; Allam, Helal, & Mansour, 2019). The remaining 29 basins (51.8% of total basins) are assigned moderate flash flood potential. Similarly, the relationship between R_b and F for basin prioritization in Figure 3b implies that 23 basins (41.1% of the total basins) with F ranging from 1.42 to 2.08 and R_b ranging from 4.1 to 6.3 had low flash flood priority, while 33 basins (85.9% of total basins) with F up to 2.4 and R_b lower than 4.06 had moderate flash flood potential and none of the basins had high flash flood potential. The overall classification, considering the higher hazard, exactly matched the classification of R_b and D.
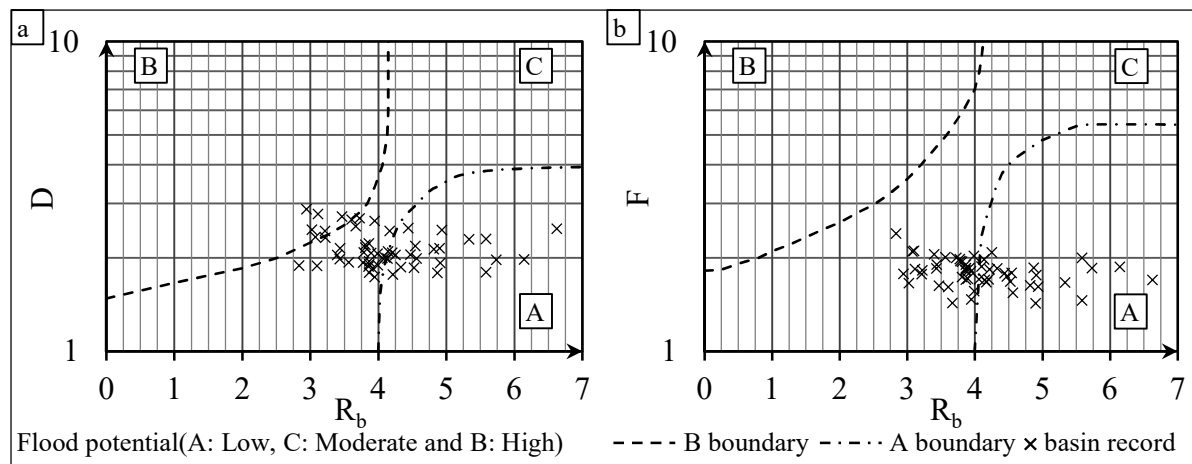

Figure 3. Flash flood potential of the Suez gulf basins using El-Shamy approach a) R_b vs D and b) R_b vs F

4.2. Analytical Hierarchy Process Results

Table 3 shows the pair-wise comparison matrix of the considered factors and their weights. Mean basin slope was assigned the highest weight and elongation ratio had the lowest weight, resembling their effect on flash flooding potential. The consistency index (CI) for this condition was 0.021 (< 0.1), suggesting reliable parameter weights. Moreover, Table 4 shows the sub-class weights of S_m. Higher weights were given to lower sub-classes because most of the values belonged to them, depicting the positive skewness distribution of these records. CI counted for 0.085 in this case,

implying suitability. For the rest of the parameters, equal weights were favoured for sub-classes as they seemed to have a balanced effect.

Table 3. Pair-wise comparison matrix of considered factors and parameters weight.

Factor	Mean basin slope	Basin area	Relief	Elongation ratio	Parameter weight
Mean basin slope	1	2	3	7	0.487
Basin area	0.5	1	1	6	0.254
Relief	0.333333333	1	1	4	0.205
Elongation ratio	0.142857143	0.166666667	0.25	1	0.054

Table 4. Sub-classes weight of mean basin slope parameter.

Mean basin slope sub class	1.35 - 4.67°	4.67 - 7.99°	7.99 - 11.31°	11.31 - 14.63°	14.63 - 17.95°
weight	0.29	0.26	0.20	0.14	0.10

4.3. Assessment of the Proposed Methods

Table 5 shows the flash flood hazard degree (FFHD) of past events and the estimated basin prioritization allocation and success rate of the examined methods. Feran basin was a very high hazard basin because it witnessed the most serious flash flood events regarding count and intensity, while basins 9,10,12,13,15, 20 (Abu-Mugrat basin), 36 and 37 were almost never exposed to runoff events, suggesting very low hazard basins, (Youssef, Pradhan, & Hassan, 2011; Eliwa, Murata, & Ozawa, 2015). Similarly, the rest of the considered basins were comparatively assigned appropriate flash flood hazard degrees.

Average success rates for El-Shamy and CP-DT were 22.4% and 6.66%, respectively. Moreover, the approximation for El-Shamy due to having only three categories might exaggerate its success rate, indicting the weak abilities of drainage network and texture parameters-based methods. Meanwhile, the other two methods relying on areal properties and relief characteristics showed higher prediction ability with a high success rate, complying with reported results (Nasir, Iqbal, & Ahmad, 2020). The average success rate for AHP-AR, which consisted of sophisticated procedures, controversially decreased to 57.5% compared to 80% for CP-AR because of a shortage in the assessing technique. Although the success rate was a straightforward feasible mean and gave reasonable results for evaluating predictors, it depended on discrete records and a single target, overlooking wrong predictions' effects on the comprehensive performance. To overcome this issue, the linear regression technique was employed to test the proposed methods' results (Figure 4a).

Table 5. FFHD past events and estimated hazard priority allocation and success rate of the investigated methods.

Hazard priority	Past events (count)	El-Shamy (success rate)	CP-DT (success rate)	CP-AR (success rate)	AHP-AR (success rate)
Very low	9, 10, 12, 13, 15, 20, 36 and 37 (8)	2, 3, 6, 7, 8, 10, 18, 19, 20, 21, 24, 28, 30, 31, 34, 37, 38, 39, 40 and 47 (5/11, 45.5%)	1, 4, 14, 16, 19, 25, 35, 38, 39, 43 and 46 (0/8, 0.0%)	2, 3, 5, 6, 7, 9, 10, 12, 13, 15, 16, 17, 18, 20, 36, 37, 40, 42, 44, 45, 47, 48, 51, 54 and 56 (8/8, 100.0%)	2, 3, 5, 6, 7, 9, 10, 13, 15, 37, 42, 45, 48 and 54 (5/8, 62.5%)
Low	21, 22 and 24 (3)		2, 3, 5, 6, 8, 9, 11, 12, 13, 15, 17, 22, 23, 26, 27, 28, 30, 42, 45, 49, 52, 53, 54	1, 4, 8, 11, 21, 22, 23, 24, 25, 26, 29, 31, 32, 34, 41, 49, 50, 52, 53 and 55	4, 12, 16, 17, 18, 20, 21, 22, 24, 25, 26, 36, 40, 41, 44, 47, 51 and 56 (3/3,

		and 55 (1/3, 33.3%)		(3/3, 100.0%)	100.0%)
Moderate	14, 27 and 28 (3)	1, 4, 5, 9, 11, 12, 13, 14, 15, 16, 17, 22, 23, 25, 26, 27, 32, 33, 35, 42, 43, 44, 45, 46, 49, 50, 51, 53 and 55 (2/3, 66.7%)	7, 10, 20, 24, 29, 31, 32, 33, 34, 36, 40, 41, 44, 50 and 56 (0/3, 0.0%)	14, 19, 27, 28, 33, 38, 43 and 46 (3/3, 100.0%)	1, 8, 11, 23, 29, 31, 32, 33, 34, 38, 39, 43, 46, 49, 50, 52, 53 and 55 (0/3, 0.0%)
High	11, 19, 23 and 35 (4)	29, 36, 41, 48, 52, 54 and 56 (0, 0.0%)	18, 21, 47, 48 and 51 (0/4, 0.0%)	39 (0/4, 0.0%)	14, 19, 27 and 28 (1/4, 25.0%)
Very high	30 (1)	37 (0/1, 0.0%)		30 and 35 (1/1, 100.0%)	30 and 35 (1/1, 100.0%)
Average success rate		22.44 %	6.66 %	80.0 %	57.5 %

Figure 4a illustrates the correlation between the FFHD of the past events and the predicted hazard degree of the investigated methods. The R^2s for El-Shamy and CP-DT were very low, indicating unreliable methods for basin prioritization as implied by (Nasir, Iqbal, & Ahmad, 2020). AHP-AR and CP-AR showed strong correlations to historical data with high convergent values of R^2 of 0.82 and 0.74, respectively, indicating the projected superiority of the AHP-AR method and suggesting appropriate efficiency of flash flood hazard evaluation for similar arid worldwide regions. The results of linear regression outweigh the success rate as it thoroughly measures the distributed results of these methods. So, the results of AHP-AR were employed to present the flash flood hazard-based basin prioritization map for the entire basins in the area (Figure 4b).

4.4. Flash Flood Hazard Map and Sustainable Management Strategy

Figure 4b shows the flash flood hazard-based basin prioritization map of the study area using AHP-AR methods. Six basins with high and very high priorities or hazard degrees cover the middle part, representing around 60% of the total area of the region. They are characterized by high A, R, S_m and R_e (less elongated or oval shapes). The rest of the categories contain many basins ranging from 14 to 18. The latter basins are mainly located in the northern and southern portions of the study area. Basins with very low and low hazard priorities are characterized by relatively small basin areas and highly elongated shapes. As such, Feran and El-Aawag basins have the highest hazard degree or priority. They have precedence over the rest of the basins in implementing a comprehensive management strategy and promoting Sustainable Development Goals (SDGs). Integrated non-structural and structural measures are crucial to safeguard the environment, touristic places, local communities, cities and infrastructures, meeting SDG 15 "Life on Land", SDG 8 "Decent work and economic growth" and SDG 11 "Sustainable cities and communities" and provide clean water for human activities, achieving SGD 6 "Clean Water and Sanitation", (https://sdgs.un.org/goals/). Non-structural countermeasures involve early warning practices and land use planning, while structural measures encompass escape channels, sediment traps, surface and recharge lake diversion dikes and detention and retention dams, (Mansour, Ibrahim, Fuji, & Nasr, 2022b). As the hazard degree reduces, so do the number and capacity of required measures.
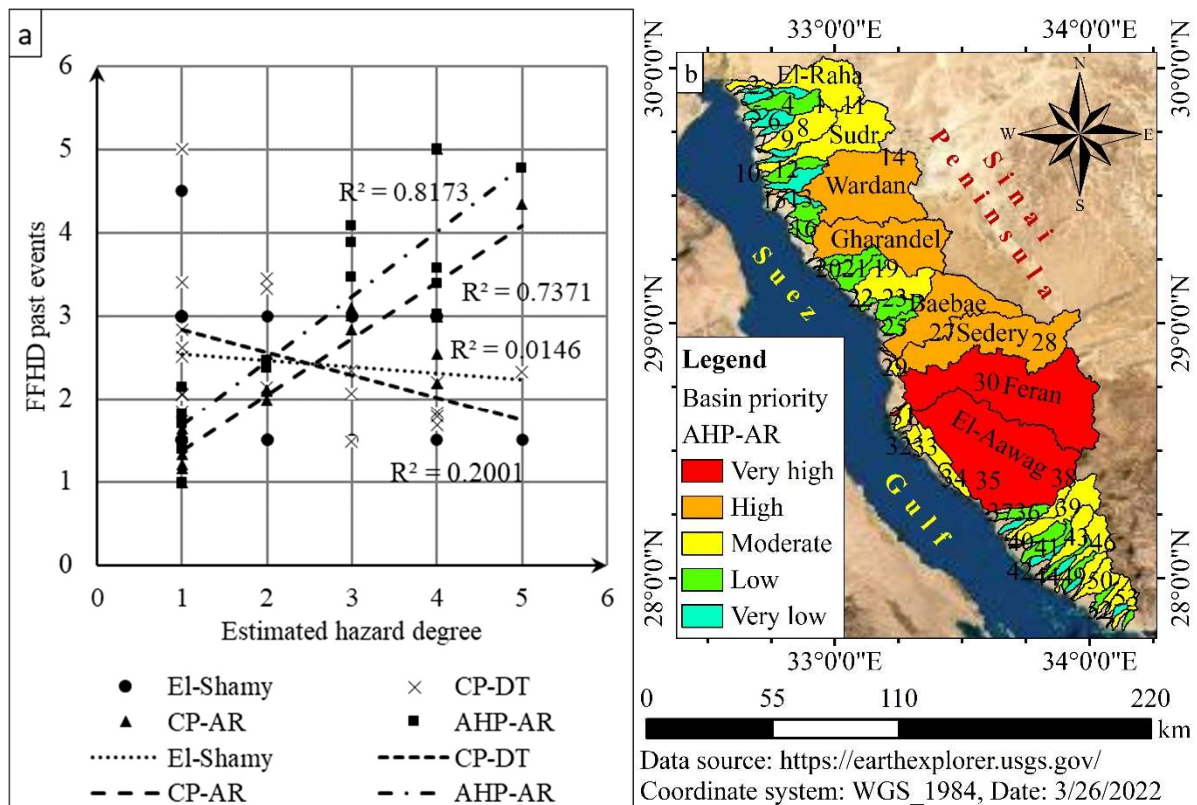
Figure 4. a) Correlation between calculated hazard degree of the investigated methods and FFHD of past events and b) flash flood hazard-based basin prioritization map of the AHP-AR method

5. CONCLUSIONS

The results of the study show that employing remote sensing data in a GIS environment to measure hydrological response at the basin scale is valuable. The procedures of study implied that data resolution has a significant impact on the methodology's reliability and applicability. Although the current study used a 30-m resolution STRM for drainage network delineation, which might be termed "coarse-resolution", the alignment of ephemeral streams in the true-color satellite image indicates uniformity. However, including fine resolution, data could improve the precision of the results. The present research adopted GIS and RS using morphometric parameters for flash flood hazard assessment of the Suez Gulf basin in the Sinai Peninsula, Egypt. An evident variation was found in the most considered morphometric parameters of the 56 basins. Morphometric parameters based-methods include El-Shamy approach, CP-DT, CP-AR and AHP-AR were employed for basin prioritization. Validation using historical data through success rate and linear regression revealed that areal properties and relief characteristics parameters, as well as the AHP technique, provide a more accurate and reliable prediction for hydrological response than drainage network and texture parameters. El-Shamy and CP-DT showed a below 25% average success rate and a max R^2 of 0.2, suggesting inaccurate prediction methods. Meanwhile, CP-AR and AHP-AR exceeded 0.50 and 0.75 for the average success rate and R^2. Another study's output is the spatial flash flood priority map, developed by the most accurate investigated method (AHP), grading the basins in the studied region that are prone to flash floods. The AHP-AR method indicated that El-Aawag, Feran, Sedery, Baebae, Gharandel and Wardan basins (60% of the total area) had the highest flash flood susceptibility. Similarly, 18 basins had moderate flash flood priority, while 30 basins had the lowest flash flood potential. The maps and data provided are intended to aid in decision-making through comprehending the spatial hazard of flash floods in the studied region. The findings of the study are expected to prompt the implementation of appropriate management measures to mitigate the potential consequences of future flash floods in the study area and comply with global goals or SDGs.

REFERENCES

(EXCIMAP), E. e. (2007). Handbook on good practices for flood mapping in Europe. Copenhagen, Denmark: European Environment Agency.

Allam, A., Helal, E., & Mansour, M. (2019). Retarding contaminant migration through porous media using inclined barrier walls. Journal of Hydrology and Hydromechanics, 67(4), 339–348.

Bogale, A. (2021). Morphometric analysis of a drainage basin using geographical information system in Gilgel Abay watershed, Lake Tana Basin, upper Blue Nile Basin, Ethiopia. Applied Water Science, 11, 122.

Dadamouny, M. A., & Schnittler, M. (2016). Trends of climate with rapid change in Sinai, Egypt. Journal of Water and Climate Change, 7(2), 393–414.

Eliwa, H. A., Murata, M., & Ozawa, H. (2015). Post Aswan High Dam flash floods in Egypt : causes, consequences and mitigation strategies. Bulletin of Center for Collaboration in Community Naruto University of Education, 29(2), 173–186.

El-Shamy, I. (1992, April). New approach for hydrological assessment of hydrographic basins of recent recharge and flooding possibilities. In proceeding of the 10th Symposium Quaternary and Development, Mansoura, Egypt, p. 15.

Gabr, S., & El Bastawesy, M. (2015). Estimating the flash flood quantitative parameters affecting the oil-fields infrastructures in Ras Sudr, Sinai, Egypt, during the January 2010 event. Egyptian Journal of Remote Sensing and Space Science, 18(2), 137–149.

Han, J., Kamber, M., & Pei, J. (2012). Data Preprocessing. In J. Han, M. Kamber, & J. Pei (Eds.), Data Mining (Third Edition ed., pp. 83–124). Elsevier.

Helmi, A. M., & Zohny, O. (2020). Flash flood risk assessment in Egypt. In A. M. Negm (Ed.), Flash floods in Egypt (pp. 253–312). Cham: Springer.

Horton, R. E. (1945). Erosional development of streams and their drainage basins; hydrophysical approach to quantitative morphology. Geological Society of America Bulletin, 56(3), 275–370.

Magesh, N. S., Chandrasekar, N., & Soundranayagam, J. P. (2011). Morphometric evaluation of Papanasam and Manimuthar watersheds, parts of Western Ghats, Tirunelveli district, Tamil Nadu, India: a GIS approach. Environmental Earth Sciences, 64, 373–381.

Mansour, M. M., Ellayn, A. F., Helal, E., Rashwan, I. M., & Sobieh, M. F. (2018). Delaying solute transport through the soil using unequal double sheet piles with a surface floor. Ain Shams Engineering Journal, 9(4), 3399–3409.

Mansour, M. M., Ibrahim, M. G., Fujii, M., & Nasr, M. (Forthcoming 2022a). Recent applications of flash flood hazard assessment techniques: case studies from Egypt and Saudi Arabia. Materials Science Forum.

Mansour, M. M., Ibrahim, M. G., Fujii, M., & Nasr, M. (2022b). Sustainable development goals (SDGs) associated with flash flood hazard mapping and management measures through morphometric evaluation. Geocarto International. https://doi.org/10.1080/10106049.2022.2046868

Mejía, A. I. and Moglen, G. E. (2010), Impact of the spatial distribution of imperviousness on the hydrologic response of an urbanizing basin. Hydrological Processes, 24(23), 3359-3373.

Mimikou, M. (1984). Regional relationships between basin size and runoff characteristics. Hydrological Sciences Journal, 29(1), 63–73.

Nasir, M. J., Iqbal, J., & Ahmad, W. (2020). Flash flood risk modeling of swat river sub-watershed: a comparative analysis of morphometric ranking approach and El-Shamy approach. Arabian Journal of Geosciences, 13(1082).

Prabhakaran, A., & Raj, N. J. (2018). Drainage morphometric analysis for assessing form and processes of the watersheds of Pachamalai hills and its adjoinings, Central Tamil Nadu, India. Applied Water Science, 7(31).

Saaty, T. L. (1980). The analytic hierarchy process : planning, priority setting, resource allocation. New York: McGraw-Hill.

Schumm, S. A. (1956). Evolution of drainage systems and slopes in badlands at Perth Amboy, New Jersey. Bulletin of the Geological Society of America.

Soni, S. (2017). Assessment of morphometric characteristics of Chakrar watershed in Madhya Pradesh India using geospatial technique. Applied Water Science, 7, 2089–2102.

Strahler. (1964). Quantitative geomorphology of drainage basins and channel networks. In V. Chow, Handbook of Applied Hydrology (pp. 439–476). New York: McGraw-Hill.

Strahler, A. N. (1953). Revision of Hortons' quantitative factors in erosional terrain. Transactions, American Geophysical Union, 34, 345–365.

Youssef, A. M., Pradhan, B., & Hassan, A. M. (2011). Flash flood risk estimation along the St. Katherine road, southern Sinai, Egypt using GIS based morphometry and satellite imagery. Environmental Earth Sciences, 62(3), 611–623.

14TH INTERNATIONAL CONFERENCE
ON HYDROSCIENCE & ENGINEERING

MAY 26-27, 2022
IZMİR-TURKEY

ICHE2022
IZMIR, TURKEY

HYDRODYNAMIC MODELLING OF THE URBAN FLOODING IN BOZKURT DISTRICT, KASTAMONU, TURKEY ON AUGUST 11, 2021

Hayri BAYCAN

Civil Engineering Department, Istanbul University - Cerrahpasa

Istanbul, Turkey

hayri.baycan@ogr.iuc.edu.tr

Ceyhun GÖK

Civil Engineering Department, Istanbul University - Cerrahpasa

Istanbul, Turkey

ceyhun.gok@ogr.iuc.edu.tr

Uğur BOYRAZ

Civil Engineering Department, Istanbul University – Cerrahpasa

Istanbul, Turkey

uboyraz@iuc.edu.tr

ABSTRACT: Flood is one of the most common disasters that may occur due to a heavy rainfall event or failures of dams and channels. Rapid and intensive urbanization increases the surface runoff. Flood control systems require more complicated solutions to control the excessive volume of runoff. As a result, the hazards caused by floods are inevitable. The northern part of Turkey is severely affected by heavy rains due to the climate of the Black Sea region. In this region, many small villages and towns are located around the rivers and the banks are occupied by buildings. The urbanization on the floodplain causes loss of life and property after a sudden urban flood. One of the latest catastrophic events in the Black Sea region happened in Bozkurt, Kastamonu on August 11, 2021. An average of 276 mm of rain had fallen in 24 hours and the Ezine stream was flooded. In this study, a flood model was built by using US Environmental Protection Agency's Storm Water Management Model (EPA SWMM) to determine the effects of this catastrophic flood. The flood depth, the hydrographs, and the water velocity were calculated using the EPA SWMM model. The results were compared with the site observations. It has been concluded that the flood hazards are mostly caused by urbanized floodplains in the Bozkurt district. Also, it is determined that the capacity of the Ezine stream channel should be improved. The urbanized areas are still in danger because of the region's climate, the insufficient stream channel capacity, and the occupied banks. The relevant precautions should be taken immediately for the study area.

1. INTRODUCTION

It is crucial to create flood hazard and risk maps, and prepare flood management plans for the urbanized areas on the floodplain. The applications are needed to reduce flood risk and hazards in these areas. Some factors such as climate change, rapid urbanization, etc. may change the current situation and therefore, the flood management plans may need to be improved (Konrad, 2003). The hydrodynamic modeling of a watershed is essential to determine the flood risk and predict the hazards depending on the flood disaster. EPA SWMM is commonly used in urban flood modeling and planning (Jiang et al., 2015). Although the flood models created in SWMM are generally used to model urban floods (Gülbaz et al., 2019; Gülbaz and Kazezyılmaz-Alhan, 2013), it is also used to model larger-scale basins (Rai et al., 2017). In this study, the Bozkurt district, which is urbanized on the banks of the Ezine Stream and located in Kastamonu, Turkey, was modeled to simulate the catastrophic flood event on August 11, 2021. EPA SWMM was used for modeling the region and

simulating the flood. The hydrographs, the flow depths, and the flow velocity were obtained as outputs. The results were validated by the photographs and videos that were captured during and after the flood.

2. MATERIALS AND METHODS

2.1. Ezine Stream Basin and Bozkurt District

The Ezine Stream basin has a drainage area of 375 km^2 approximately. It is located between 33°−34° east longitudes and 41°−42° north latitudes. The basin is mountainous, and forests cover the mountains generally. The Ezine Stream begins from Devrekani district of Kastamonu province, passes through Küre mountains and Bozkurt district respectively, then reaches the sea from Abana district. Bozkurt is a district of Kastamonu in the Western Black Sea Region. The district is located 2 km south of the Black Sea coast and 95 km north of the city center. The Ezine Stream is restored around the Bozkurt district for flood control. The cross-section of the improved stream is rectangular. The width of the stream is 32 m and the depth is 2.5 m. The total length of the channel is 3.7 km. Bozkurt district is urbanized on the banks of the Ezine stream and it is located close to the outlet of the basin. Therefore, the flood risk is very high for this region.

2.2. Storm Water Management Modelling

SWMM is a dynamic simulation program improved by Environmental Protection Agency. The program consists of hydraulics, hydrology, and water quality modules. SWMM models the rainfall-runoff relationship and is often used for urban areas, sewer systems, and drainage systems. It is also capable of simulating flood, groundwater flow, and LID controls (Rossman, 2010). While calculating surface runoff; precipitation and upstream flow contribute to the inflow, infiltration and evaporation contribute to the outflow. The program uses the Manning equation to determine the flow rate, depth, and velocity. SWMM also includes different options for hydraulic routing such as steady flow, kinematic wave method, and dynamic wave method. Infiltration may be integrated into the models via one of the following methods: Horton, Modified Horton, Green Ampt, Modified Horton, and Curve Number.

2.3. Model Development

The rainfall-runoff model of the Ezine Stream Basin requires the parameters such as topographical maps, cross-sections of the river, slope and width values of sub-basins, and soil characteristics of the study area. Most of the data needed for the hydrodynamic model and the information about the basin were provided by using the Quantum Geographical Systems (QGIS). The soil maps and information were provided from the Food and Agriculture Organization of the United Nations (FAO). The precipitation data were also obtained from the Turkish State Meteorological Service (MGM) and the hyetograph was calculated (Figure 1).

The Ezine Stream Basin was delineated by using the dem data obtained from QGIS. The delineated watershed boundaries were imported into the EPA SWMM. The watershed was divided into 29 subcatchments. Then, the stream sections were defined in the model by using 34 conduits, and cross-sections of the channels were assigned to the model through the data obtained from the QGIS program. The Manning's roughness coefficients for both overland flow and open channels, the parameters required for the Green Ampt infiltration method, and the soil properties are determined based on the literature (McCuen et al. 1996; ASCE, 1982; Rawls et al. 1983; EEA, 2021). The kinematic wave method was chosen as the routing method, and the model was run under the precipitation data of the August 10-12 storm.

3. RESULTS

In Figure 1, the hyetograph of the storm and the hydrograph obtained from the model are presented. The hydrograph is in line with the hyetograph characteristics and has two peak values. The maximum flow rate obtained at the upstream point of Bozkurt was calculated as 320 m^3/s on August 10, and 1670 m^3/s on August 11. As a result of the rainfall dropped on August 10, the soil was fully saturated. Therefore, the rainfall dropped on August 11 completely turned into the surface runoff. Because of

the excessive runoff volume, the Ezine Stream flooded, and the urban areas were damaged seriously. The channel depth of the Ezine Stream is 2.5 m. The model results showed that the water depth reached this level at the 24th hour of the analysis (August 11, 00:00). The capacity of the channel was sufficient to carry the flow observed at that time. However, on August 11, around ten o'clock, the water height exceeded this level. The maximum runoff was observed around 15:30 with a rate of 1670 m^3/s. At these hours, the flood depth rose to 7 m at the entrance of Bozkurt district center and 5 m at the exit point (Figure 2). The flood depth decreased towards the exit point of the city due to the spreading of the flood. The results of the developed model were compared with the photographs and videos captured during and after the flood. According to the model, the flood depth in the urban area was calculated as 4.5 m around the upstream side of the river and 2.5 m around the downstream side. The site observations show that the water height in the city center is compatible with the calculations. A building was photographed after the flood and the watermark on the building indicates that the flood depth reached approximately 3.5-4 m (Figure 3 (b)). Therefore, it is concluded that the water depths obtained from the model are in good agreement with the observations. The flood spread width was obtained as 240 m when the maximum flood depth was observed. This result also matched well with the site observations (Figure 3 (a)). Finally, the velocity of the water was calculated as 6.5 m/s approximately in Bozkurt City Center which is also compatible with the videos of the flood event.
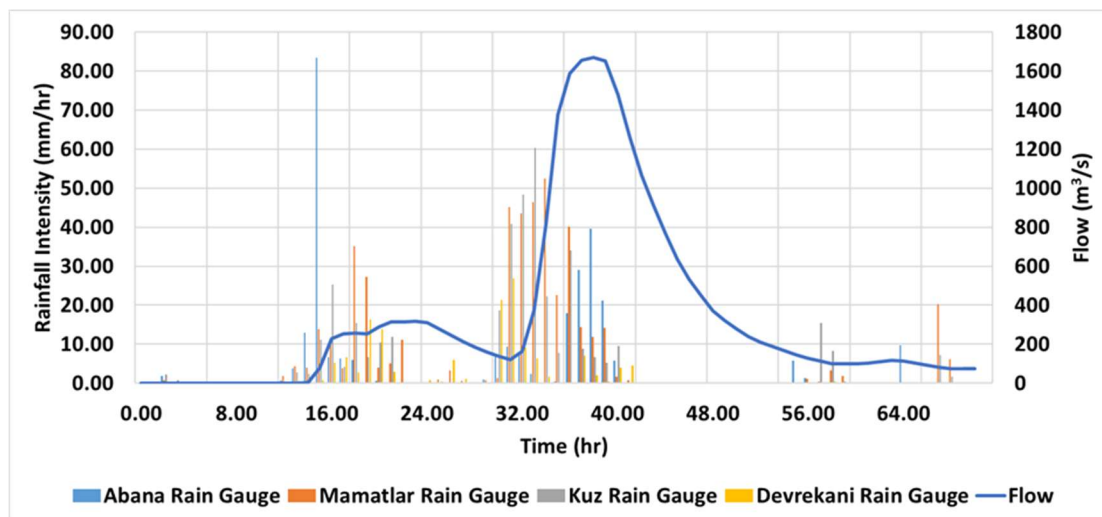
Figure 1. Precipitation data obtained from the 4 rain gauges placed in the watershed and the hydrograph of the exit point of the Bozkurt district on August 10-12, 2021
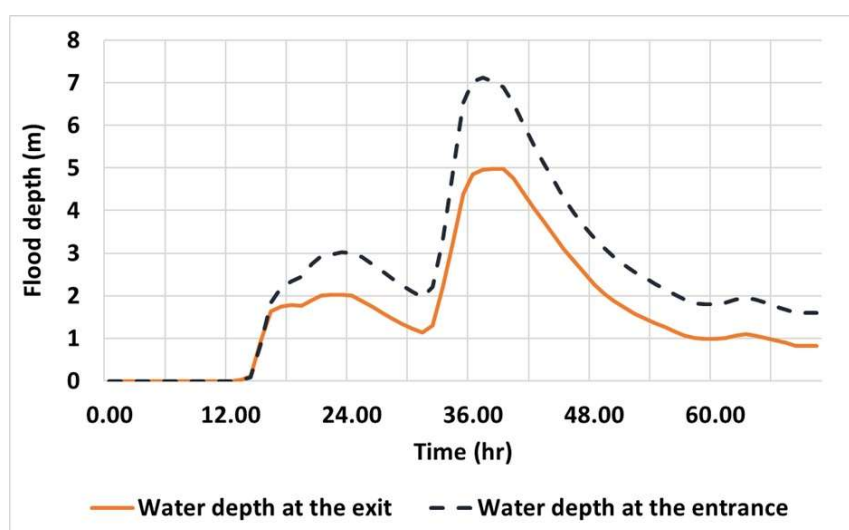
Figure 2. The flood depths obtained at the entrance and exit points of the city center

4. CONCLUSIONS

In this study, a hydrodynamic model of the Ezine Stream Basin in Kastamonu, Turkey was developed by using EPA SWMM. The flood event on August 11, 2021, was simulated. The flood depths and the peak flow rates were obtained at the upstream and downstream points of the Bozkurt district. The outputs obtained from the model were compared with the site observations. According to the results, the following conclusions are obtained:

- The rainfall dropped on August 10-11 was very heavy. The duration of the rainfall was long enough to saturate the soil and it was inevitable to have a huge volume of excess runoff.
- The main cause of the damage was the urbanization of the Bozkurt district on the floodplain.
- The river channel capacity was insufficient to carry this excessive volume of runoff. The movement of the wooden logs also decreased the capacity and affected the flow distribution. The damaged weirs around the upstream part of the stream were another important cause of flooding.
- Since the region is prone to heavy rainfall, necessary precautions should be taken immediately for the study area. The outputs of this work will be useful for predicting the hazards of the flood planning future improvements on flood mitigation, and future research about the study area.
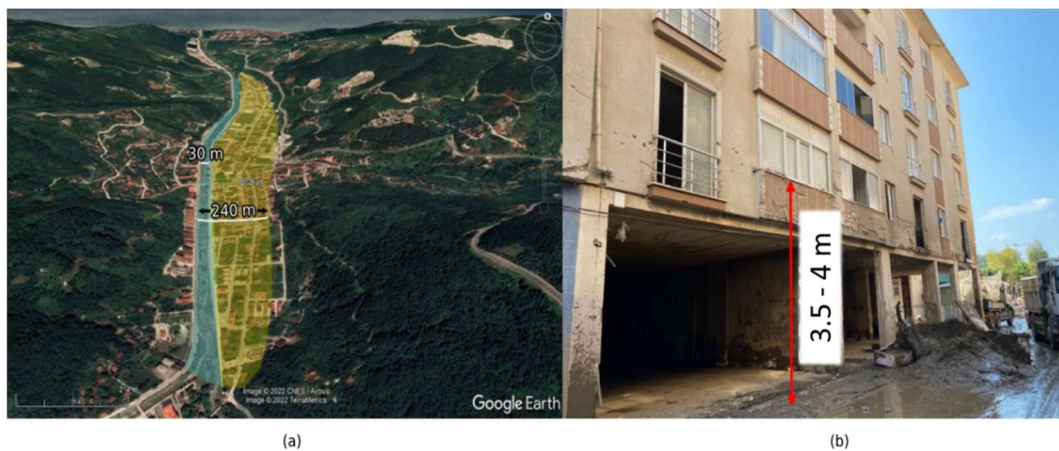
Figure 3. (a) Channel width and the flood spread width (Retrieved from Google Earth, Data SIO, NOAA, U.S. Navy, NGA, GEBCO, © 2022 Basarsoft, Image CNES/Airbus Image © 2022 TerraMetrics, Image © 2022 Maxar Technologies) and (b) Watermark on a building after the flood event

REFERENCES

ASCE (1982) "Gravity Sanitary Sewer Design and Construction," ASCE Manual of Practice No. 60, New York, NY. [Preprint].

Environmental European Agency (EEA) (2021) Soil moisture deficit, https://www.eea.europa.eu/ims/soil-moisture-deficit.

Google earth V 7.3.4.8248. (June, 2021). Bozkurt District, Kastamonu, Turkey. 41°57'27.83"N, 34° 1'7.94"E, Eye alt 1.19 km. SIO, NOAA, U.S. Navy, NGA, GEBCO. TerraMetrics 2022, DigitalGlobe 2022. http://www.earth.google.com [March 24, 2022].

Gülbaz, S. and Kazezyılmaz-Alhan, C.M. (2013) "Calibrated Hydrodynamic Model for Sazlıdere Watershed in Istanbul and Investigation of Urbanization Effects," *Journal of Hydrologic Engineering*, 18(1), pp. 75–84. doi:10.1061/(ASCE)HE.1943-5584.0000600

Gülbaz, S. et al. (2019) "Flood Modeling of Ayamama River Watershed in Istanbul, Turkey," *Journal of Hydrologic Engineering,* 24(1), p. 05018026. doi:10.1061/(ASCE)HE.1943-5584.0001730.

Jiang, L., Chen, Y. and Wang, H. (2015) "Urban flood simulation based on the SWMM model," Proceedings of the International Association of Hydrological Sciences, 368, pp. 186–191. doi:10.5194/piahs-368-186-2015.

Konrad C.P. (2003) "Effects of Urban Development on Floods", https://pubs.usgs.gov/fs/fs07603/.

McCuen, R. et al. (1996) "Hydrology," FHWA-SA-96-067, *Federal Highway Administration*, Washington, DC.

Rai, P.K., Chahar, B.R. and Dhanya, C.T. (2017) "GIS-based SWMM model for simulating the catchment response to flood events," *Hydrology Research,* 48(2), pp. 384–394. doi:10.2166/nh.2016.260.

Rawls, W.J., Brakensiek, D.L. and Miller, N. (1983) "Green-ampt Infiltration Parameters from Soils Data," *Journal of Hydraulic Engineering*, 109(1), pp. 62–70. doi:10.1061/(ASCE)0733-9429(1983)109:1(62).

Rossman, L. A. 2010. Storm water management model, user's manual, version 5. EPA/600/R-05/040. Cincinnati: Water Supply and Water Resources Division, National Risk Management Research Laboratory, USEPA.

FLOOD MODELING OF EZINE AND AYANCIK STREAM WATERSHEDS IN WESTERN BLACK SEA BASIN, TURKEY

Hayri BAYCAN

Civil Engineering Department, Istanbul University–Cerrahpasa,

Istanbul, Turkey

hayri.baycan@ogr.iuc.edu.tr

Miraç Nur CİNER

Civil Engineering Department, Istanbul University–Cerrahpasa,

Istanbul, Turkey

miracnur.ciner@ogr.iuc.edu.tr

Ceyhun GÖK

Civil Engineering Department, Istanbul University–Cerrahpasa,

Istanbul, Turkey

ceyhun.gok@ogr.iuc.edu.tr

İsmail Bilal PEKER

Civil Engineering Department, Istanbul University–Cerrahpasa,

Istanbul, Turkey

pekerbilal@iuc.edu.tr

Sezar GÜLBAZ

Civil Engineering Department, Istanbul University–Cerrahpasa,

Istanbul, Turkey

sezarg@iuc.edu.tr

ABSTRACT: Uncontrolled urbanization and inadequate infrastructure result in frequent flooding. Flood disaster affects life negatively and cause loss of life and property. Flood model development has crucial importance to mitigate flood hazard and to prevent loss of life. Especially, it is necessary to model the streams passing through urban areas and to generate flood inundation maps. Moreover, existing flood inundation map should be updated by considering land use change in urban areas. Engineering structures such as bridges, culverts or retaining walls should be reconstructed utilizing the flood maps, if they are not enough to carry maximum flowrate in the stream. In addition, the current settlement areas having flood risk near the streams should be moved to safer areas with the guidance of the flood maps. In this study, the flood disaster occurred on August 11, 2021 in Ezine (in Kastamonu Province) and Ayancık (in Sinop Province) Streams are examined. For this purpose, firstly, the hydrologic-hydraulic models for each stream watershed are constituted by using Hydrologic Engineering Center-Hydrologic Modeling System (HEC-HMS) and Hydrologic Engineering Center-River Analysis System (HEC-RAS), respectively. Then, the flood inundation maps are presented via Watershed Modeling System (WMS). The model flood depths are compared with the images and videos taken during the flood event to validate the models. Finally, the reasons that cause the flood disaster in Bozkurt and Ayancık Districts and the precautions to mitigate the flood risk are discussed.

1. INTRODUCTION

Flood, which is the most common natural disaster in the world, deeply affects many countries on a global scale and constitutes one-third of the total economic losses caused by natural disasters (De Moel and Aerts, 2011). The most common reason of flooding is heavy and prolonged precipitation. Floods can also occur because of strong flows from snowmelt or clogging of drainage channels. Floods affect approximately 178 million people worldwide each year and in financial terms, cause the greatest economic damage after earthquakes, storms, and drought (Kundzewicz et al. 2014). In our country, life, property and economy are significantly affected by the flood disaster. The Turkish Disaster Database reported 1076 flood events that caused 795 deaths and economic losses of US$ 800 million in the period 1960-2014 (Koç et al., 2021; Koç and Thieken, 2018). In Ayamama flood that took place in Istanbul between 8-12 September 2009, 32 people lost their lives, 3816 houses and 1490 workplaces were damaged (Kömüşçü et al. 2011). More than 2 million people were affected by the flood disasters that occurred in the Western Black Sea Region in 1998 alone, more than 30 lives were lost, and 478 houses were completely submerged. All these historical records indicate that studies to prevent or reduce flood-related damages and losses are of great importance both in our country and in the world. It is vital to prepare flood maps for the establishment of early warning systems and the construction of flood protection facilities. In this context, geographic information systems (such as QGIS or WMS) and hydrological-hydraulic modeling software (such as HEC-HMS and HEC-RAS) are robust tools. There are some studies that these type of softwares are employed to obtain flood inundation maps in the literature (Taş et al. 2016; Gülbaz, 2019; Bakırcı and Gülbaz, 2019).

The aim of the present study is to reveal the flood disasters that occurred on August 11, 2021 in the Ezine and Ayancık Streams by hydrologic-hydraulic modelling. HEC-HMS and HEC-RAS software are employed for hydrological and hydraulic modeling, respectively. Also, WMS software is used to process data and present spatial results more effectively. Thus, the flood inundation maps are obtained for the considered region. The results of this study will be useful for envision the possible adverse effects of the future flood events and determining flood management in the Ezine and Ayancık Stream Watersheds.

2. MATERIALS AND METHOD

2.1. Study Area

Ezine and Ayancık Stream Watersheds are in the Western Black Sea Basin, which is one of these 25 watersheds in Turkey. These watersheds are selected as the study area based on the flood event to be investigated. The location of the study area is shown in Figure 1. Bozkurt is located between $42^o\ 00'$ $00"-41^o\ 40'\ 00"$ north latitudes and $33^o\ 45'\ 00"-34^o\ 10'\ 00"$ east longitudes. Ezine Stream flows through the Bozkurt district of Kastamonu Province, which has a watershed area of 375 km^2 and reaches the Black Sea downstream. The stream flows in south-north direction and there are high density residential and commercial areas located on the east and west shores of the Ezine Stream. Ayancık is a district of Sinop Province, located between $42^o\ 00'\ 00"-41^o\ 45'\ 00"$ north latitudes and $34^o\ 20'\ 00"-34^o$ $45'\ 00"$ east longitudes. It has a watershed area of 675 km^2 and reaches the downstream of the Black Sea. The stream flows through the center of the Ayancık and there is the residential area on the east and west of the Ayancık Stream at the downstream part of the watershed. Elevations range from the sea level to 1993 m for Ezine and from the sea level to 1845 m for Ayancık.
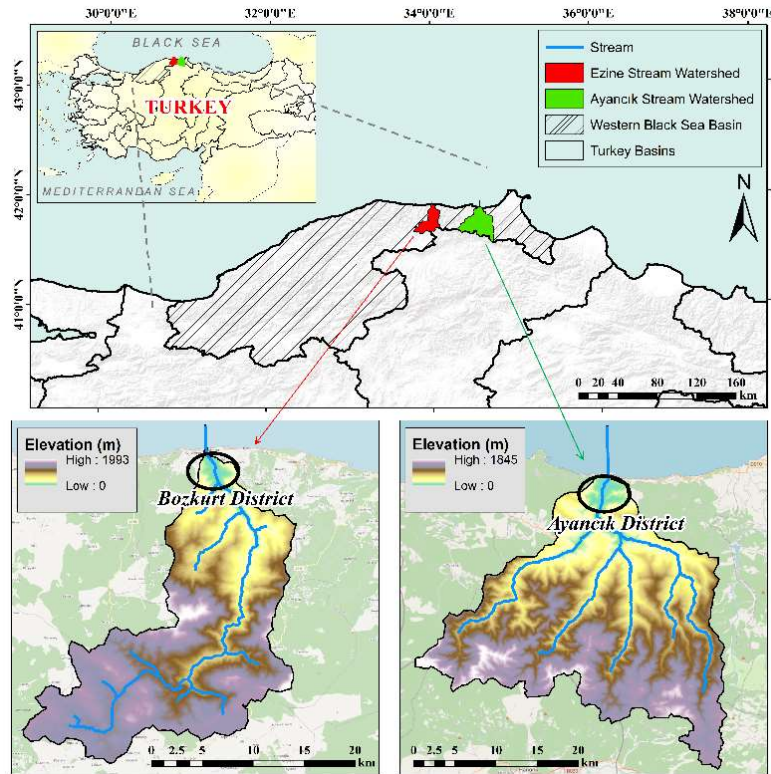
Figure 1. Location of the Ezine (Bozkurt) and Ayancık Stream Watersheds

2.2. Model Setup

In this study, Ezine and Ayancık Stream Watersheds are modeled by applying WMS, HEC-HMS and HEC-RAS programs together. HEC-HMS and HEC-RAS can be integrated with WMS. Firstly, digital elevation model (DEM), land use and soil maps are obtained by using the web-enabled resources of WMS. Then, the rain gauges are designated and defined into the Ezine and Ayancık Stream Watershed models. The gauge stations are Abana, Mamatlar, Kuz Village and Devrekani for the Ezine Stream Watershed and Ayancık, Akören, and Çangal for Ayancık Stream Watershed. The rainfall data recorded during the storm event between 9-12 August at 7 rain gauge stations are obtained from the Turkish State Meteorological Service (TSMS). In the next step of the modeling, the data obtained from WMS are exported to the HEC-HMS. Soil Conservation Service (SCS) Curve Number (CN) model and kinematic wave for flow routing in channel are selected for the hydrological model. Subsequently, channel cross sections are assigned by WMS and exported to HEC-RAS. Then, the flow rate obtained from the HEC-HMS is entered into the HEC-RAS. The results of the HEC-RAS hydraulic model are transferred to WMS for visualization of flood inundation maps.

3. RESULTS

When the causes of flood events are examined, first of all heavy rainfall can be mentioned in the region. Hence, the amount of precipitation data recorded rain gauges in the region is above the precipitation value with a greater return period than a 100-year. Bozkurt and Ayancık are located at the downstream point of the watersheds and have been exposed to the peak runoff. For this reason, the channels in the regions could not carry the flow to the surface flow. In addition, due to the landslides that took place in the regions, the sediment is transported and caused the blockage of bridges and culverts. Clogging of the bridges causes the backwater effect and the water accumulated behind the bridges overflows from the stream bed towards the residential areas located on the floodplain of the stream.

In this study, the flood event that occurred in Bozkurt and Ayancık Districts is simulated, and flood inundation map is presented. The maximum flow rates on the outlet points of the watersheds are calculated by the HEC-HMS. Maximum flow rates in the watersheds are calculated as 1026 m³/s and

1603 m^3/s for the Ezine and Ayancık Stream Watersheds, respectively. Flood inundation maps are obtained through the HEC-RAS as a hydraulic model generated with the results of the heavy rainfall that occurred on August 9-12, 2021. Flood inundation maps are shown in the Figure 2 and Figure 3 for Ezine and Ayancık Stream Watershed, respectively. Flood depth and extended area are shown in the model.
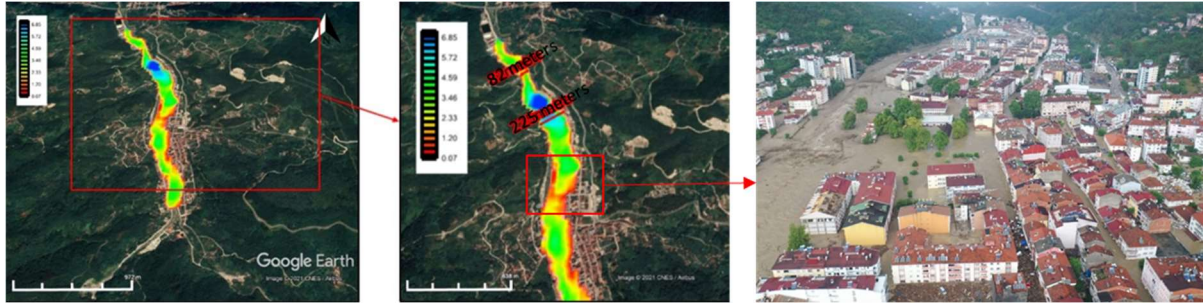
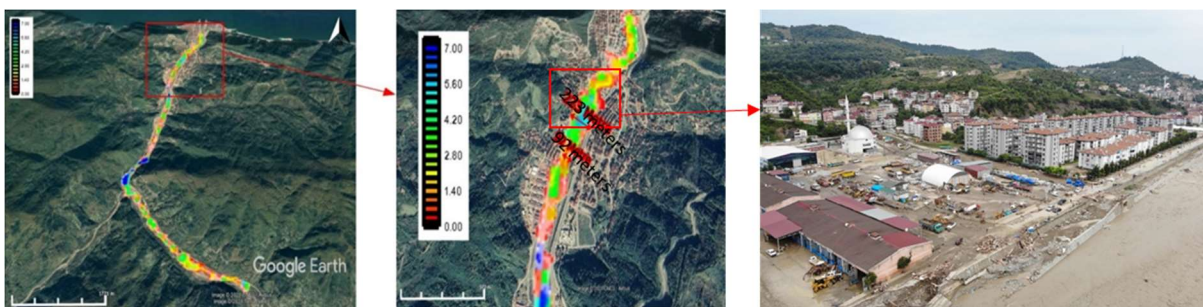Figure 2. Flood inundation map for Ezine Stream (Bozkurt) and photograph for Bozkurt District (URL 1)

Figure 3. Flood inundation map for Ayancık Stream and photograph for Ayancık District (URL 2)

4. CONCLUSIONS

In this study, hydrological and hydraulic models of Bozkurt and Ayancık Districts are developed and flood inundation maps are generated. Peak flow rates, flood depth, and flood extent are obtained by using the WMS, HEC-HMS and HEC-RAS programs. It is concluded that the obtained flood inundation maps are consistent with the observations made in the flood region. Flood inundation maps in the regions under extreme flood risk has an importance to take precautions in case of a possible flood disaster. Also, the flood inundation maps of these regions are obtained in order to give input for potential precautions and interpretations. The following recommendations are summarized to reduce the flood damages based on the lessons learned from the flood:

- The reclamation studies should be practiced utilizing with the flood inundation maps.
- The engineering design guidelines of the structures including bridges, culverts, revetments, and embankments located close to the floodplain should be prepared by taking into account the flood inundation map.
- Best management practices (BMP) such as detention ponds and retention basin should be taken into account to reduce the peak flood flow.
- Permeable sediment trap should be used to decrease amount of sediment occurring during floods.
- The hydraulic dimensions of current bridges and culverts in residential areas and in regions have heavy rainfall should be examined. They should be redesigned by taking into account the 500-year flood flow.
- The current stream sections of Ezine and Ayancık are not large enough to route water generated over the watershed downstream under extreme storm events and significant flooding occurs. The stream section should be increased by taking into account the 500-year flood flow.
- Within the scope of all this, flood early warning system (EWS) in the regions under extreme flood risk, flood risk notification and evacuation planning should be provided.

REFERENCES

Bakırcı, M. and Gülbaz, S. (2019). "Calibrated Hydrological Model for Alibeyköy Watershed in Istanbul by Using WMS and HEC-HMS", *9th International Symposium on Atmospheric Sciences ATMOS 2019*, İstanbul, Turkey, 1-8.

De Moel, H. and Aerts, J. C. J. H. (2011). "Effect of Uncertainty in Land Use, Damage Models and Inundation Depth on Flood Damage Estimates", *Natural Hazards*, 58(1), 407-25.

Gülbaz, S. (2019). "Developing Flood Extent Map by using Numerical Models and Determination of Areas under Flood Risk: Türkköse Stream Case", *Journal of Natural Hazards and Environment*, 5(2), 335-349.

Jha, A.K., Bloch, B. and Lamond, J. (2012). "Cities and Flooding: A Guide to Integrated Urban Flood Risk Management for 21st Century". World Bank Publications. USA/ Washington, D.C.

Koç, G., Natho, S., Thieken, A.H., (2021). "Estimating direct economic impacts of severe flood events in Turkey (2015-2020)." *International Journal of Disaster Risk Reduction*, 58, Article Number102222.

Koç, G., Thieken, A.H., (2018). "The relevance of flood hazards and impacts in Turkey: What can be learned from different disaster loss databases?." Natural Hazards, 91(1), 375–408.

Kömüşçü, A.Ü., Çelik S. and Ceylan A. (2011). "Rainfall analysis of the flood event that occurred in Marmara Region on 8-12 September 2009", *Journal of Geographical Sciences*, 9(2), 209-220.

Kundzewicz Z.W., Kanae S., Seneviratne S.I., Handmer J., Nicholls N., Peduzzi P., Mechler R., Bouwer L.M., Arnell N., Mach K., Muir-Wood R., Brakenridge G.R., Kron W., Benito G., Honda Y., Takahashi K. and Sherstyukov B. (2014). "Flood Risk and Climate Change: Global and Regional Perspectives", *Hydrological Sciences Journal*, 59(1), 1-28.

Taş, E., İçağa, Y. and Zorluer, İ., (2016). "Constitution of Flood Inundation Maps and Flood Damage Analysis: A Case Study of Akarcay Afyon Subbasin", *Afyon Kocatepe University Journal of Science and Engineering Sciences*, 16(3), 711-721.

[URL 1] Ihlas News Agency (IHA), Retrieved December 4, 2021 from https://www.iha.com.tr/haber-sel-felaketinin-vurdugu-bozkurtta-catilarda-kurtarilmayi-bekleyenler-var-962748/

[URL 2] Ihlas News Agency (IHA), Retrieved December 4, 2021 from https://www.iha.com.tr/haber-ayancikta-selin-yikimi-buyuk-oldu-963093/

14TH INTERNATIONAL CONFERENCE
ON HYDROSCIENCE & ENGINEERING

MAY 26-27, 2022
IZMİR-TURKEY

ICHE2022
IZMIR, TURKEY

VARIABILITY OF PRECIPITATION UNDER THE EXPECTED CHANGE IN CLIMATE USING CMIP5 PROJECTIONS OVER ENTIRE TURKEY

M. Tugrul Yilmaz

Civil Engineering Department, Middle East Technical University

Ankara, Turkey

tuyilmaz@metu.edu.tr

N. Erhan Ersoy

Civil Engineering Department, Middle East Technical University

Ankara, Turkey

ersoy.erhan@metu.edu.tr

Ismail Yucel

Civil Engineering Department, Middle East Technical University

Ankara, Turkey

iyucel@metu.edu.tr

ABSTRACT: In this study high number of ensemble members obtained from CORDEX climate projections are used to investigate the trend and the variability in the long term mean of precipitation. Total of 56 GCM-RCM couples obtained from the CORDEX simulations over EURO-11 domain are obtained and later 14 couples are eliminated following the accuracy assessments performed using ground station-based observations. The study region is selected as Turkey, while the statistics are calculated for entire Turkey as well as 25 basins separately. Historical simulations are corrected for their means between 1970 and 2005 using ERA5-Land product. The trends of ERA5-Land simulations are dominantly negative over 25 basins, while only 10 basins are negative for the historical RCM trends. On average, historical ERA5-Land precipitation show a decline at -1.62mm/year rate, while the RCM trends between 2020 and 2060 is -1.62 mm/year and between 2060 and 2100 is -2.17 mm/year. This implies the second half of the future projections show steeper decline in the precipitation trends and water resources will be further stressed over Turkey at a rate that has not been observed before.

1. INTRODUCTION

Precipitation is one of the most important variables that directly impact the availability of water resources and agricultural production. Accordingly, estimation of the variability of the state of future precipitation is critical for many applications. There are many Global Circulation Models (GCM) and Regional Climate Models (RCM) that provide projections of precipitation for future climate. While these models are primarily used to infer about the future conditions, some of these models may provide wildly different estimates of the precipitation for the same future period and region.

Part of the difference between the estimates of these GCM/RCM models and the real observations are due to systematic differences between the simulations and the observations, where such systematic differences can be partly removed via post-processing methodologies. On the other hand, remaining systematic errors and/or in particular the random errors are not easy to remove, hence they are of great interest for many applications that use the predictions of these models. Accordingly, models should be evaluated prior to any analysis that use such products.

In addition to the variability in the accuracy of different GCM/RCM projections, the variability in the mean state and the trend of the precipitation simulations are also of great interest for many

applications, in particular the ones that utilize processes driven through the climate projections of precipitation. For example, streamflow estimates are directly linked with the amount of precipitation that falls on land and the agricultural productivity of plants are directly related with soil moisture which is driven by the precipitation. Accordingly, estimation of the change in the mean and the trend components of the precipitation products are necessary for many hydrological and agricultural applications that require precipitation as input forcing data.

Estimates of the future climate are available through many model simulations that are generated by different research centers. International Coordinated Regional Climate Downscaling Experiment (CORDEX) (Climate Information, 2021) initiative is a framework to produce improved regional climate simulations with the support by the World Climate Research Program (WRCP). Regional CORDEX simulations are performed over 14 different domains, where different GCM outputs are utilized to force RCM simulations over each domain. As a result, high number of different projections obtained from various GCM-RCM couples are available over each domain. For example, over EURO11 domain around 56 different dynamically downscaled projections are available.

These RCM simulations performed as part of CORDEX utilized WCRP Coupled Model Intercomparison Project Phase 5 (*CMIP5*) outputs, while similar simulations are not available for latest CMIP6 outputs. Even though GCM simulations obtained from these CMIP5 and CMIP6 outputs yield valuable results about the future conditions of precipitation, temperature, etc., these models cannot resolve many details (e.g., land-water contrast, orography) particularly over regions with complex topography, hence higher resolution RCM results are often necessary for many applications.

Being one of the hot climate spots on earth, Mediterranean region is expected to face higher rates of climate change, in particular the states of temperature and precipitation. Being one of the Mediterranean countries, Turkey is expected to face significant changes in temperature and precipitation. Many studies utilized climate projections obtained over Turkey in variety of different studies.

Among all the CMIP experiments, the latest one (i.e., CMIP6) is the most relevant for the most climate change related studies. However, there is only one study investigated the performance of different CMIP6 GCM simulations over Turkey (Bagcaci et al., 2021). This study has performed a comprehensive analysis and compared the accuracy of monthly precipitation and near-surface temperature outputs of 36 CMIP5 and 33 CMIP6 models. On the other hand, many studies require higher resolution simulations, namely RCM outputs. Given RCM simulations utilizing CMIP6 outputs are not available yet, studies requiring higher spatial resolution projections over Turkey currently rely on CMIP5 output-based RCM simulations.

So far, there are two institutions run climate models and generated RCM projections utilizing GCM simulations of CMIP5 outputs focusing over Turkey only. The simulations performed by Turkish State Meteorological Service (2016) utilized only 3 GCM models (HadGEM2-ES, MPI-ESM-MR, and GFDL-ESM2M) and a single RCM (RegCM4.3.4) with a total of 3 ensemble members. Similarly, the simulations performed by Directorate of Water Management (2016) also utilized only 3 GCM models (HadGEM2-ES, MPI-ESM-MR, and CNRM-5.1) and a single RCM (RegCM4.3) with a total of 3 ensemble members. Accordingly, the number of ensemble members is limited to 3 in the climate change related studies using these datasets (Demircan 2016; Oruc et al. 2020).

Regional CORDEX simulations offer an excellent source of high resolution CMIP5-based RCM outputs over Turkey. Among the studies utilized CORDEX-based datasets, Öztürk et al. (2018) used 2 ensemble members, Cetinkaya (2020) used 8 ensemble members, Poyraz (2018) and Aziz (2018) used 12 ensemble members, and Dino and Akgul (2019) and Mesta et al. (2022) used 14 ensemble members in their studies. While the number of available ensemble members (i.e., GCM-RCM couples) available at CORDEX repository were limited 5-6 years ago, now this number has increased to 56 over EURO-11 domain. On the other hand, a comprehensive study that investigated projections of precipitation over Turkey with high number of ensemble members is missing so far.

In this study, all available 56 GCM-RCM couples over CORDEX EURO-11 domain are utilized to investigate the projections of precipitation over Turkey for the first time. Below section 2 describes

the datasets and the methodology, section 3 presents the results and section 4 offers discussions and conclusions.

2. METHODOLOGY

2.1. Climate Projections (RCM – GCM)

CORDEX simulations over EURO-11 domain for the pessimistic RCP8.5 emission scenario at 0.11° spatial resolution are used in this study. Daily precipitation datasets for 56 GCM-RCM model couples (Table 1) over EUR-11 domain (Figure 1) are downloaded from CORDEX official web page (https://cordex.org/data-access/). Historical datasets are obtained between 1970 and 2005 and future projections are obtained between 2005 and 2100. The number of available RCM ensemble member decrease considerably before 1970, therefore to maximize the number of available ensemble members the historical period is selected to start from 1970.
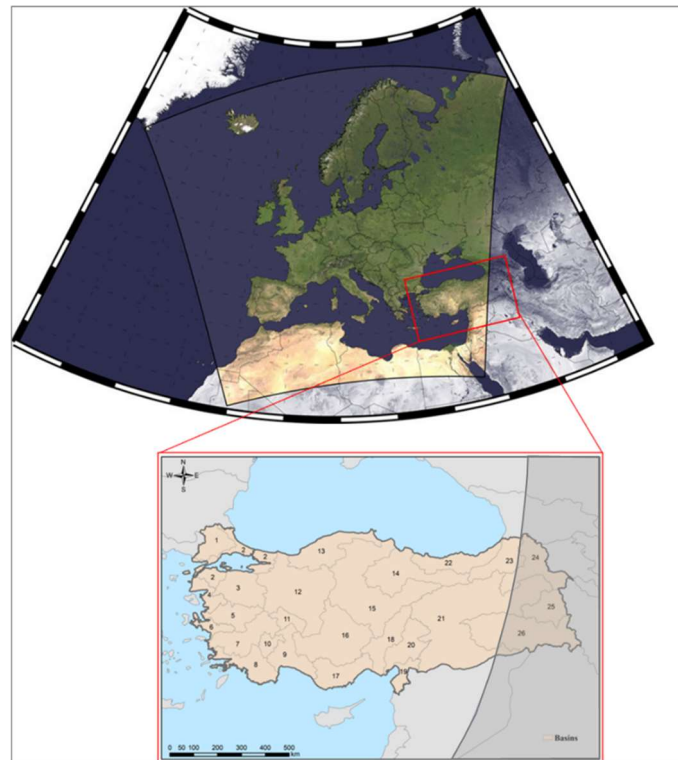
Figure 40. Study Area and The Border of EUR-11 Domain

Figure 41. Distribution of MGM Stations used in ranking of RCM

Table 1. GCM-RCM Couples.

ID	USED	GCM	RCM
1	1	CCCma-CanESM2	CLMcom-CCLM4-8-17
2	1	CCCma-CanESM2	GERICS-REMO2015
3	1	CNRM-CERFACS-CNRM-CM5	CLMcom-CCLM4-8-17
4	0	CNRM-CERFACS-CNRM-CM5	CLMcom-ETH-COSMO-crCLIM-v1-1
5	0	CNRM-CERFACS-CNRM-CM5	CNRM-ALADIN53
6	1	CNRM-CERFACS-CNRM-CM5	CNRM-ALADIN63
7	1	CNRM-CERFACS-CNRM-CM5	DMI-HIRHAM5
8	0	CNRM-CERFACS-CNRM-CM5	GERICS-REMO2015
9	0	CNRM-CERFACS-CNRM-CM5	ICTP-RegCM4-6
10	1	CNRM-CERFACS-CNRM-CM5	IPSL-WRF381P
11	1	CNRM-CERFACS-CNRM-CM5	KNMI-RACMO22E
12	0	CNRM-CERFACS-CNRM-CM5	MOHC-HadREM3-GA7-05
13	1	CNRM-CERFACS-CNRM-CM5	RMIB-Ugent-ALARO-0
14	1	CNRM-CERFACS-CNRM-CM5	SMHI-RCA4
15	1	ICHEC-EC-EARTH	CLMcom-ETH-COSMO-crCLIM-v1-1
16	1	ICHEC-EC-EARTH	DMI-HIRHAM5
17	1	ICHEC-EC-EARTH	KNMI-RACMO22E
18	1	ICHEC-EC-EARTH	SMHI-RCA4
19	1	IPSL-IPSL-CM5A-MR	DMI-HIRHAM5
20	1	IPSL-IPSL-CM5A-MR	GERICS-REMO2015
21	1	IPSL-IPSL-CM5A-MR	IPSL-WRF381P
22	1	IPSL-IPSL-CM5A-MR	KNMI-RACMO22E
23	1	IPSL-IPSL-CM5A-MR	SMHI-RCA4
24	1	MIROC-MIROC5	CLMcom-CCLM4-8-17
25	1	MIROC-MIROC5	GERICS-REMO2015
26	0	MOHC-HadGEM2-ES	CLMcom-CCLM4-8-17
27	0	MOHC-HadGEM2-ES	CLMcom-ETH-COSMO-crCLIM-v1-1
28	1	MOHC-HadGEM2-ES	CNRM-ALADIN63
29	0	MOHC-HadGEM2-ES	DMI-HIRHAM5
30	0	MOHC-HadGEM2-ES	GERICS-REMO2015
31	0	MOHC-HadGEM2-ES	ICTP-RegCM4-6
32	1	MOHC-HadGEM2-ES	IPSL-WRF381P
33	0	MOHC-HadGEM2-ES	KNMI-RACMO22E
34	0	MOHC-HadGEM2-ES	MOHC-HadREM3-GA7-05
35	0	MOHC-HadGEM2-ES	SMHI-RCA4
36	0	MOHC-HadGEM2-ES	UHOH-WRF361H
37	1	MPI-M-MPI-ESM-LR	CLMcom-CCLM4-8-17
38	1	MPI-M-MPI-ESM-LR	CLMcom-ETH-COSMO-crCLIM-v1-1
39	1	MPI-M-MPI-ESM-LR	CNRM-ALADIN63
40	1	MPI-M-MPI-ESM-LR	DMI-HIRHAM5
41	1	MPI-M-MPI-ESM-LR	ICTP-RegCM4-6

42	1	MPI-M-MPI-ESM-LR	IPSL-WRF381P
43	1	MPI-M-MPI-ESM-LR	KNMI-RACMO22E
44	1	MPI-M-MPI-ESM-LR	MOHC-HadREM3-GA7-05
45	1	MPI-M-MPI-ESM-LR	MPI-CSC-REMO2009
46	1	MPI-M-MPI-ESM-LR	SMHI-RCA4
47	1	MPI-M-MPI-ESM-LR	UHOH-WRF361H
48	1	NCC-NorESM1-M	CLMcom-ETH-COSMO-crCLIM-v1-1
49	1	NCC-NorESM1-M	CNRM-ALADIN63
50	1	NCC-NorESM1-M	DMI-HIRHAM5
51	1	NCC-NorESM1-M	GERICS-REMO2015
52	1	NCC-NorESM1-M	ICTP-RegCM4-6
53	1	NCC-NorESM1-M	IPSL-WRF381P
54	1	NCC-NorESM1-M	KNMI-RACMO22E
55	1	NCC-NorESM1-M	MOHC-HadREM3-GA7-05
56	1	NCC-NorESM1-M	SMHI-RCA4

The daily datasets are initially accumulated to monthly sums before their use in the study, accordingly, all analyses in this study uses these monthly sums. All the analysis are performed over entire Turkey and 26 different basins defined as Turkish State Hydraulics (i.e., total 27 different regions). Although EUR-11 domain does not cover some part of Turkey (Van Gölü, Dicle and Aras Basins), some couples still have data on those basins. Accordingly, these basins (i.e., Dicle, Aras, and Van Basins) still contain some data even though they seem to be located outside of the EUR-11 domain.

Even though CORDEX offers corrected precipitation data, the number of GCM-RCM couples for such datasets is very low. Accordingly, non-corrected pr values are obtained from CORDEX and later these non-corrected datasets are later corrected using ERA5-Land datasets.

Obtained raw RCM datasets are pre-processed before they are used in drought index calculations. Namely, raw datasets are 1) ranked for their accuracy so that poorest performing models are eliminated from the analyses, 2) interpolated to have consistent grid geolocation information with ERA5-Land datasets, 3) bias correction is made for each model at each pixel and month separately, 4) gridded precipitation datasets are converted to basin average estimates.

Initially, raw RCM datasets (total for 56 different GCM-RCM couples) are obtained over Turkey, where the study domain is selected to be between 25E and 45E, and 35N and 43N. Then the number of RCM model datasets are reduced from 56 to 42 based on their accuracy in the historical period (1970-2005). Given there is a mismatch between the nature of RCM and observation datasets (spatially continuous gridded vs point dataset), one of them should be converted to the others space. This could be performed either by selecting the grids that contain the observing stations (i.e., conversion of the model space to the space of stations), or averaging the station-based observations that fall inside the model grid. The latter methodology cannot be implemented as the number of stations is too few compared against the total number of grids. Also, following the Figure 10 of the study of Amjad et al., (2020), there is no difference between the selection of these methods as long as the ranking of the models is concerned. Accordingly, the first methodology is selected here such that the RCM values are obtained from the grids that contain the stations. This data extraction results in total of 374 time series (i.e., total 374 station-based time series are available) for each RCM between 1970 and 2005.

2.2. Calculated Statistics

Once the relevant datasets are retrieved for both the observations and the RCM datasets, Pearson correlation is calculated between the station-based observations and RCM values to rank the 56 model historical datasets between 1970 and 2005:

$$CORR_{(b,r,s)} = \frac{\sum_{t=1}^{432}(x_{(b,r,s,t)} - \mu x_{(b,r,s)})(y_{(b,r,s,t)} - \mu y_{(b,r,s)})}{\sqrt{\sum_{t=1}^{432}(x_{(b,r,s,t)} - \mu x_{(b,r,s)})^2}\sqrt{\sum_{t=1}^{432}(y_{(b,r,s,t)} - \mu y_{(b,r,s)})^2}} \qquad (1)$$

where b is number of basins, r is RCM number, s is station number, t refers to month, and CORR refers to correlation coefficient. CORR values are calculated over 27 regions (26 basins + entire Turkey), (b), 56 RCM couples (r), and 374 stations (s) using 432 monthly time series between 1970 and 2005 (i.e., 12 months/year * 36 years = 432 months total).

Utilizing the correlations calculated above, the number of RCM datasets used in this study is reduced from 56 to 42. There is no unique way to decide about the number of poorest performing models to be eliminated. In this study, the threshold 25% is arbitrarily selected (i.e., eliminating 50% of the datasets would result in removal of too many datasets, where 10% is seemed to be not sufficient).

There is a difference between the spatial resolutions of the raw RCM datasets and ERA5-Land datasets. Once the poorest performing models are eliminated from the analyses, RCM datasets are interpolated to have the same geolocation as ERA5-Land datasets using nearest neighborhood interpolation method. Accordingly, RCM datasets are resampled to have 0.10° spatial resolution (in horizontal space) from their raw 0.11° resolution. The nearest neighbor interpolation technique is selected because of its simplicity and widely usage. As a result, all RCM and ERA5-Land datasets are obtained at 0.10° over the study domain (25E-45E and 35N-43N), with a total of 81 pixels in the N-S direction and 201 pixels in the E-W direction.

Next, pixel-by-pixel bias correction was made separately for each RCM model using ERA5-Land dataset, where a separate correction factor was calculated for each month:

$$CORRfac_{(r,x,y,m)} = \overline{RCM\_H_{(r,x,y,m,y1:y2)}} \ / \ \overline{ERA5Land_{(x,y,m,y1:y2)}} \qquad (2)$$

$$RCM\_H\_correct_{(r,x,y,m,y1:y2)} = RCM\_H_{(r,x,y,m,y1:y2)} * CORRfac_{(r,x,y,m)} \qquad (3)$$

$$RCM\_F\_correct_{(r,x,y,m,y)} = RCM\_F_{(r,x,y,m,y)} * CORRfac_{(r,x,y,m)} \qquad (4)$$

where r refers to the RCM model, x refers to the grid number from the western border of the study area (25.0E), y refers to the grid number from the northern border of the study area (43.0E), m refers to month, y refers to year, $y1$ and $y2$ refer to the beginning and ending years of historical RCM datasets respectively (i.e., 1970 and 2005), RCM_H and RCM_F are the RCM precipitation datasets for the historical (1970-2005) and the future (2006-2100) periods, $RCM\_H\_correct$ and $RCM\_F\_correct$ are the corrected historical and future monthly precipitation data, overbar is an averaging operator (e.g., $\overline{w}$ is the average of w).

Above calculated gridded $RCM\_H\_correct$ and $RCM\_F\_correct$ datasets are averaged over each basin and over ensembles so that an ensemble mean estimate is obtained over each basin:

$$RCM\_H\_ens_{(b,m,y1:y2)} = \overline{RCM\_H\_correct_{(r,x,y,m,y1:y2)}} \qquad (5)$$

$$RCM\_F\_ens_{(b,m,y1:y2)} = \overline{RCM\_F\_correct_{(r,x,y,m,y1:y2)}} \qquad (6)$$

where RCM_H_ens and RCM_F_ens are the monthly historical and future RCM values estimated from the gridded products ($RCM\_H\_correct$ and $RCM\_F\_correct$) over each basin (total 27). Here the gridded precipitation data is converted into average precipitation estimates over each basin by simply taking the average of the values of the grids that fall inside the borders of the basins (basin borders are given in Figure 1). These monthly time series are used to calculate the statistics [mean (mm/year) and trend (mm/year)] for the precipitation estimates over each basin. To investigate the variability in the mean and the trend values, the statistics are calculated for the three historical periods (1970-2005, 2020-2060, and 2061-2100).

3. RESULTS

Ranking precipitation products and eliminating the 25% poorest performing models is the first step implemented in this study based on the calculated correlations against observations obtained from 374 ground stations. Some of the RCM datasets derived from CNRM and HadGEM2 GCM models are eliminated, while RCM datasets derived from other GCMs are not eliminated. The model datasets that are utilized in this study are marked as 1 and not used are marked as 0 in Table 1 (i.e., the column "USED"). Results show the couple with the highest correlation among the models is the downscaled version of the Met Office Hadley Center (MOHC) HadGEM2-ES global climate model with Institut Pierre-Simon Laplace (IPSL) - WRF381P RCM.

Once the correlation ranking based dataset elimination phase is complete, remaining 42 RCM gridded datasets are corrected using ERA5-Land dataset. After correcting the precipitation, data the temporal variability of RCM datasets has decreased (Figures 3 and 4). The 130-year average precipitation data of the ensemble member in non-corrected data is 745.8 mm. After correcting, this value was observed as 677.0 mm.
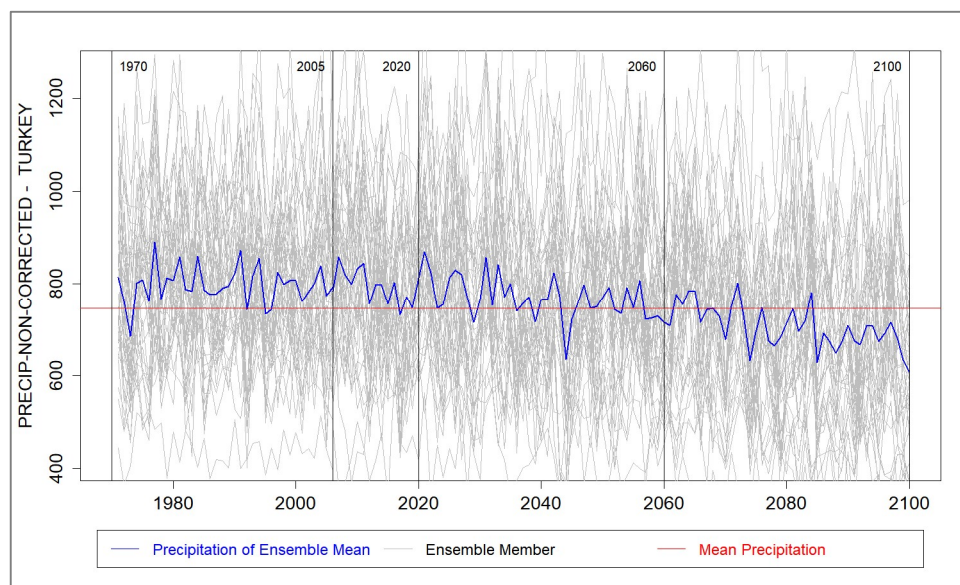
Figure 42. Ensemble precipitation of 42 non-corrected (gray) and ensemble mean (blue) RCM time series
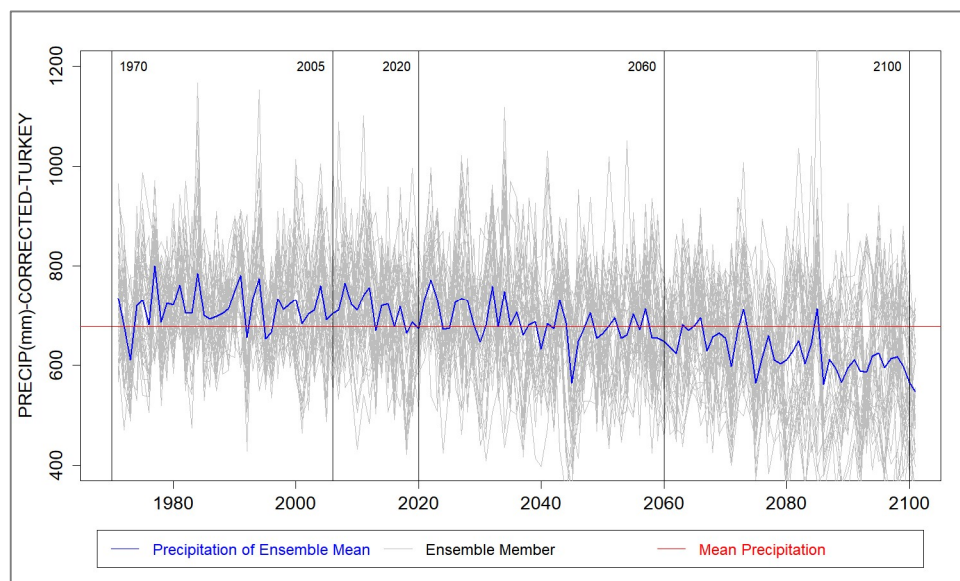
Figure 43. Similar to Figure 3, but corrected precipitation time series

After the bias correction step, the trendline equations and the mean precipitation lines of reference periods of Turkey are given in Figure 5. The basin specific details of the trendline (slope and intercept) are provided in Table 2. These results show that average precipitation over Turkey decreases from 714mm (between 1970 and 2005) to 624mm (between 2060 and 2100) according to the RCP8.5 scenarios. Average observation-based mean precipitation over entire Turkey between 1991 and 2020 is estimated as 571mm by Turkish State Meteorological Service (MGM, 2022). Here, the RCM precipitation values are corrected to ERA5-Land climatology, for this reason mean precipitation values estimated from RCM ensemble mean over entire Turkey is found as the same as ERA5-Land mean of 714mm between 1970 and 2005. Even though ERA5-Land annual mean precipitation estimate is higher than observations, this precipitation product has much better performance than other precipitation products (Amjad et al., 2020).

Forecasted precipitation shows that the expected decrease in precipitation within is around 13% between the historical (1970-2005) and future (2060-2100) periods. When analyzed on a basin-based basis, it is seen that the precipitation trend became more negative in all basins in the future, in particular during the second investigated future period (2060-2100). Looking at the basic trendlines, it is seen that the basin with the highest slope (i.e., highest decrease in precipitation per year) is Antalya Basin (-4.26mm/year) and lowest slope is in Coruh Basin (-1.21mm/year) during the second future period. When the first (2020-2060) and the second (2060-2100) future periods are compared, the rate of precipitation decline has increased, implying all basins will lose precipitation source at an increasing rate. Overall, there is a negative trend in precipitation over almost all the basins, perhaps this is as a result of the decrease in the winter precipitation which dominates the annual sums.
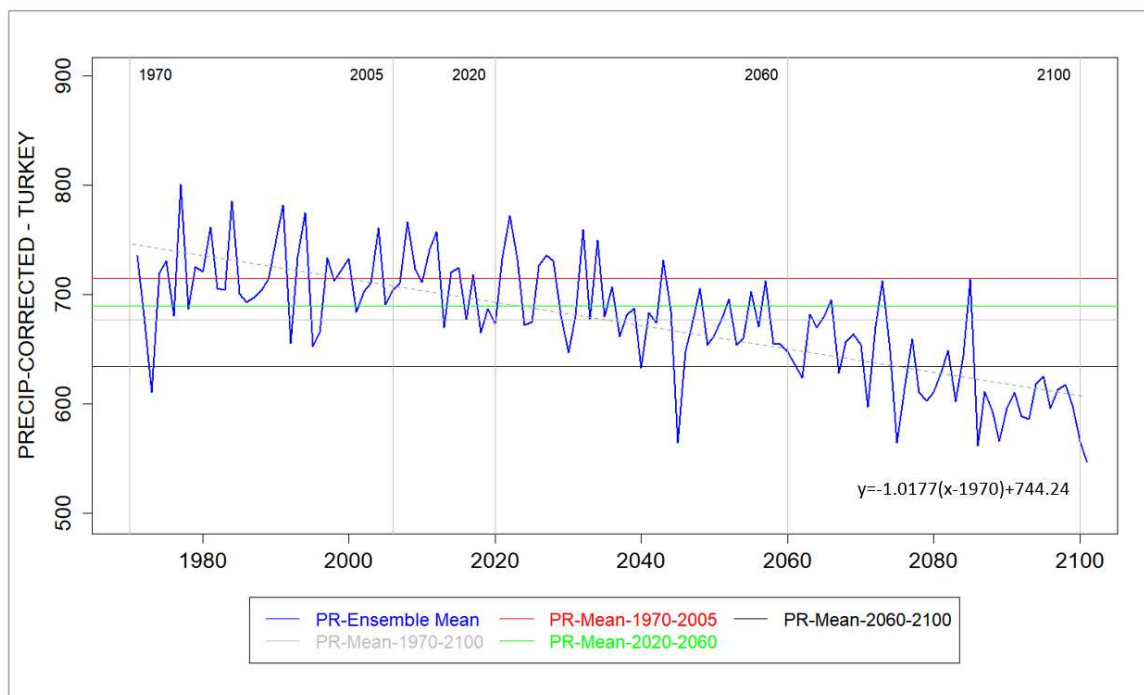
Figure 44. Annual Corrected Precipitation Projection of Ensemble Mean y-axis represents precipitation in mm, x-axis represents years. Each precipitation mean lines are given to visualize climatological differences between the reference years. All the lines are plotted all the way through the margins of graph to be able see the decreasing trend better, even though they are calculated for their relevant time period (e.g., red line is calculated as the mean of precipitation between 1970 and 2005)

Table 2. Estimated precipitation trendlines' parameters of ensemble mean [β=Slope, α=Intercept, μ=Mean precipitation (mm/year)]

Basins	ERA (1970-2005)			RCM (1970-2005)			RCM (2020-2060)			RCM (2061-2100)		
	β	α	μ	β	α	μ	β	α	μ	β	α	μ
Doğu Akdeniz	-2.75	752	703	-0.76	717	720	-2.48	815	624	-3.35	908	549
Seyhan	-1.40	774	750	-0.29	755	764	-1.99	847	694	-2.80	940	640
Asi	-1.82	735	703	-1.20	724	724	-2.66	851	644	-2.90	890	582
Konya Havzası	-1.92	446	413	0.01	412	421	-0.88	456	386	-1.22	489	359
Batı Akdeniz	-1.95	773	739	-0.80	753	758	-2.73	865	658	-4.01	1001	581
Burdur	-1.29	513	490	0.18	487	499	-1.36	554	446	-1.90	608	406
Antalya	-2.65	902	855	-0.46	863	875	-2.62	970	764	-4.26	1135	679
Küçük Menderes	-3.25	776	719	-0.14	721	733	-1.60	799	671	-3.28	978	624
Ceyhan	-0.78	764	751	-0.77	764	769	-2.52	890	696	-2.84	942	639
Büyük Menderes	-2.01	603	568	-0.15	570	579	-1.59	644	518	-2.38	726	471
Akarçay	-0.87	475	459	0.11	457	467	-1.04	510	429	-1.47	556	399
Gediz	-2.84	599	549	-0.05	550	559	-1.15	603	512	-2.09	700	475
Kuzey Ege	-4.25	802	728	0.18	724	737	-1.33	794	691	-2.58	935	655
Marmara	-2.94	792	740	0.47	732	749	-1.19	821	724	-1.51	865	705
Fırat	-0.86	671	656	-0.57	666	673	-1.94	775	625	-2.15	818	589
Susurluk	-3.18	725	669	0.37	663	678	-1.19	731	637	-1.78	796	605
Sakarya	-1.66	562	532	0.29	527	540	-0.89	580	508	-1.28	618	483
Yeşilırmak	-1.35	762	738	0.59	728	749	-1.20	807	717	-1.40	841	692
Doğu Karadeniz	-1.01	1540	1522	1.81	1491	1534	-2.37	1656	1487	-1.48	1610	1451
Çoruh	0.53	957	967	0.09	965	975	-1.60	1057	948	-1.21	1060	926
Kızılırmak	-1.65	586	557	0.37	551	567	-0.91	607	536	-1.29	649	512
Meriç-Ergene	-1.98	640	606	0.37	599	612	-0.83	658	590	-1.24	705	573
Batı Karadeniz	-2.77	1046	998	1.14	978	1008	-1.36	1084	977	-1.54	1115	953
Turkey	-1.79	746	714	0.08	713	714	-1.62	798	684	-2.17	864	624

4. CONCLUSIONS

The effects of climate change are becoming more noticeable with each passing day. With the policies and agreements developed on a global scale, the negative effects of drought on sectors such as agriculture, drinking water, industry and ecosystem are tried to be minimized. In determining these policies, climatic studies are of great importance. For this reason, the outputs of climatic projects, which have a very important role in our analysis and analysis of the effects of climate change both globally and regionally should be studied well.

In this study, expected precipitation rates over entire Turkey were estimated by using model couples under the EUR-11 domain, which has the highest resolution data of CORDEX. These periods are

presented on a basis basis and as 36 years of historical time (1970-2005) and 2 future periods of 40 years (2020-2060 and 2061-2100). In the analysis made with 56 model couples in total, the correlations of the station data and these couples were examined. The 14 worst model pairs including in which some of have negative correlations were eliminated. After correlation ranking based elimination, all RCM datasets are bias corrected using ERA-5 Land data.

When the precipitation trends and trendline equations are examined, the precipitation trend was positive between 1970 and 2005 at 0.08 mm/year rate. Overall, the trend equation has changed its sign and become negative between 2020 and 2100. The rate of decrease in precipitation increases for the period 2061 – 2100 compared to the period 2020 – 2060. On average the precipitation over Turkey will decrease at 1.62 mm/year between 2020 and 2060, while this declining rate will increase to 2.17 mm/year between 2061 and 2100. This implies the water resources over Turkey will be further stressed during the second period compared to historical period.

Overall, the results found differ from the earlier studies that the rate of precipitation decline is found as 1.90mm/year in this study (between 2020 and 2100) and 0.22mm/year in the study of MGM (2022b), where both studies have used the same pessimistic scenario (i.e., RCP8.5) and the same CMIP experiment (i.e., CMIP5). This inconsistency is perhaps related to the results that HADGEM – RegCM couple is eliminated in this study after the correlation ranking analyses while this model is one of the 3 models that are used in the study of MGM (2022b).

The results obtained in this study can be improved with the CMIP6 experiment datasets, which have increased sensitivity to the temperature and are expected to have higher accuracy than CMIP5 experiment results. Yet, such a study would require higher resolution RCM datasets to be available that are currently unavailable.

ACKNOWLEDGEMENT

REFERENCES

Amjad, M., Yilmaz, M. T., Yilmaz, K., Yucel, I. (2020). Performance evaluation of satellite- and model-based precipitation products over varying climate and complex topography. Journal of Hydrology, 584, 124707. https://doi.org/10.1016/j.jhydrol.2020.124707

Aziz, R. (2018). *Impacts of Climate Nonstationarities on Hydroclimatological Variables in Turkey* (Issue August). Middle East Technical University.

Bağçaci, S. Ç., Yucel, I., Duzenli, E., & Yilmaz, M. T. (2021). Intercomparison of the expected change in the temperature and the precipitation retrieved from CMIP6 and CMIP5 climate projections: A Mediterranean hot spot case, Turkey. *Atmospheric Research*, *256*. https://doi.org/10.1016/j.atmosres.2021.105576

Demircan, Mesut, et al. (2016), Türkiye İçin İklim Değişikliği Projeksiyonları. TMMOB Harita ve Kadastro Mühendisleri Odası, 16. Türkiye Harita Bilimsel ve Teknik Kurultayı, 3-6 Mayıs 2017, Ankara.

Dino, I. G., & Akgül, C. M., 2019. Impact of climate change on the existing residential building stock in Turkey: An analysis on energy use, greenhouse gas emissions and occupant comfort. Renewable Energy. 141, 828-846. doi:10.1016/j.renene.2019.03.150.

Directorate of Water Management. (2018). *Kuraklık Yönetim Planları*. https://www.tarimorman.gov.tr/SYGM/Sayfalar/Detay.aspx?SayfaId=61

Einstein, H. A., & Krone, R. B. (1962). Experiments to determine modes of cohesive sediment transport in salt water. *Journal of Geophysical Research*, *67*(4), 1451-1461.

Çetinkaya, İ. (2020). Assessment of changes in climate indices of the Mediterranean climate region of Turkey. MS thesis. Middle East Technical University.

Mesta, B., Sasaki, H., Nakaegawa, T., Kentel E. (2022). Changes in precipitation climatology for the Eastern Mediterranean using CORDEX RCMs, NHRCM and MRI-AGCM. Atmospheric Research, 2022, 106140.

MGM, Turkish State Meteorological Institute (2022a). https://mgm.gov.tr/veridegerlendirme/yillik-toplam-yagis-verileri.aspx (last checked on 15th of March 2022)

MGM, Turkish State Meteorological Institute (2022b). https://www.mgm.gov.tr/iklim/iklim-degisikligi.aspx?s=projeksiyonlar (last checked on 15th of March 2022)

Oruc, S., Yucel, I., & Yilmaz, A. (2020). Investigation of The Effect of Climate Change on Stormwater Networks: Capital Ankara Case. *Turkish Journal of Water Science and Management*, *4*(1), 109–133. https://doi.org/10.31807/tjwsm.623511

Ozturk, T., Turp, M. T., Türkeş, M., & Kurnaz, M. L. (2018). Future projections of temperature and precipitation climatology for CORDEX-MENA domain using RegCM4.4. Atmospheric Research, 206, 87-107.

Poyraz, A. Y. (2018). *Drought Analysis Using Cordex Simulations Over the Mediterranean Climate Regions of Turkey* (Issue April). http://etd.lib.metu.edu.tr/upload/12622080/index.pdf

PERFORMANCE EVALUATION OF THE EUROPEAN FLOOD AWARENESS SYSTEM OVER ANTALYA BASIN, TURKEY

Koray K. Yilmaz

Department of Geological Engineering, Middle East Technical University

Ankara, Turkey

yilmazk@metu.edu.tr

Robert F. Adler

Earth System Science Interdisciplinary Center (ESSIC), University of Maryland

College Park, Maryland, USA

radler@umd.edu

ABSTRACT: Floods and droughts are frequent natural disasters that are threatening lives, property, irrigated lands and food security. Turkey is situated in the Mediterranean Region - which is one of the regions that is expected to be most affected by climate change. It is hence expected that the effects of floods and droughts will be felt more in the future due to intensification of the water cycle extremes coupled with rapid population growth and urbanization. A reliable hydrological prediction system is accepted as the most effective method for mitigating flood and drought impacts. Despite its importance, the use of hydrological prediction systems in Turkey is still in its infancy. In this project LISFLOOD model - a spatially distributed, semi-physical hydrologic model which forms the core of the European Flood Awareness System (EFAS), the official operational hydrological forecast system of the European Union – was evaluated in Antalya Basin located in the Mediterranean region. The performance of the LISFLOOD model driven by the EFAS system to simulate the observed hydrographs as well as floods and droughts has been investigated. The results indicated that the EFAS system cannot adequately capture the flow variability across the watersheds. Therefore, model calibration and data assimilation techniques are needed to increase the performance of the EFAS system in Turkey.

1. INTRODUCTION

The Mediterranean region, where Turkey is located in, is one of the two regions in the world that will be most affected by climate change, and a significant increase is expected in water cycle extremes (floods and droughts) as well as increase in hot and dry periods (Giorgi, 2006). It is therefore expected that the effects of floods and droughts will be felt more in the future and will be further accelerated by rapid population growth and urbanization. For example, recent flood disaster that occurred after heavy rains in the Bozkurt district of Kastamonu on 11 August 2021 caused significant loss of life and extensive damage. It is accepted that the most effective method in mitigating the effects of floods and droughts is a reliable hydrological forecasting system. With hydrological forecasting systems, it is ensured that floods/droughts are predicted before they occur and necessary precautions are taken. Reliable hydrological forecasts are also an indispensable element in the effective management of various water-related sectors – for example, flood forecasting, drought risk analysis, agriculture, hydroelectric power plant operation and water supply. Among the main factors affecting the reliability of hydrological forecasting systems are the accuracy of hydrometeorological data, the effectiveness of the methods used to correct observation errors, the capacity of the hydrological model to represent basin hydrological processes, the initial conditions of the forecast, and the accuracy of future meteorological forecasts (Lavers et al. 2020).

European Flood Awareness System (EFAS) is the official operational hydrological forecast system of the European Union. LISFLOOD model - a spatially distributed, semi-physical hydrologic model

forms the core of the EFAS system (Thielen et al., 2009; Bartholmes et al., 2009). In a recent upgrade (2018) to the EFAS system, the geographical limits of the system have been extended to include Turkey. It is therefore important to test the performance of the EFAS system over Turkey.

2. STUDY AREA, DATASETS AND HYDROLOGICAL MODEL

2.1. Study Area

Study area is selected as the Antalya Basin situated in southern Turkey, located in the Mediterranean region (Figure 1). The climate in Antalya Basin is classified as Mediterranean Climate characterized by mild winters and hot and dry summers.
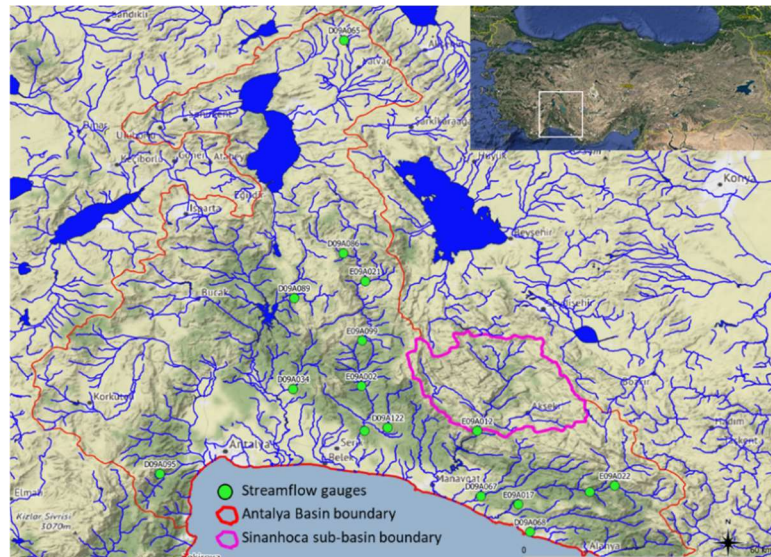
Figure 1. Map showing the Antalya Basin and streamflow gauges used in this study

2.2. Datasets

Streamflow gauging stations for the Antalya Basin were obtained from the General Directorate of State Hydraulic Works (DSİ). A total of 16 gauging stations (Figure 1, Table 1) having long-term daily streamflow observations without gaps have been selected for performance evaluation of the hydrological model. Daily streamflow observations cover the period 2002-2015.

Table 1. Streamflow gauging stations used in this study.

Gauge ID	Area (km^2)	Elev (m)	Easting	Northing
D09A034	238.6	62	30.9422	37.1317
D09A065	103.48	1198	31.1269	38.3942
D09A067	303.2	100	31.6228	36.7439
D09A068	336.32	16	31.8000	36.6139
D09A086	349	1000	31.1236	37.6231
D09A089	313.9	320	30.9455	37.4606
D09A095	164	160	30.4594	36.8244
D09A101	2330	20	31.1997	36.9800
D09A122	144.84	80	31.2847	36.9917
E09A002	1942.4	116	31.1886	37.1417
E09A012	625.6	245	31.6086	36.9794
E09A017	875.5	28	31.7585	36.7135

E09A021	1005.5	738	31.2025	37.5217
E09A022	396.3	382	32.1072	36.7814
E09A024	611	250	32.0167	36.7592
E09A099	1538.4	435	31.1914	37.3061

2.3. Hydrological Model

LISFLOOD hydrological model is the core of the European Flood Awareness System (EFAS) and is used in operational flood forecasting over the European Union (Thielen et al., 2009; Bartholmes et al., 2009). In a recent upgrade (2018) to the EFAS system, the geographical limits of the system have been extended to include Turkey. Moreover, the products of the EFAS system are available freely from the Copernicus Emergency Management Service with a one-month lag. The LISFLOOD hydrological model is an open-source model supported by the Joint Research Center of the EU. Therefore, due to its availability, flexibility and open-source nature, evaluation of the performance of the LISFLOOD and EFAS over Turkey is critical to point towards potential improvements in monitoring and forecasting of floods and droughts in Turkey. Historical simulations of the EFAS Version 3.0 is used in this study.

LISFLOOD is a spatially distributed hydrological rainfall-runoff-routing model that is run at 5km spatial scale over Europe and the extended model domain, including Turkey. EFAS Version 3.0 is run at the daily time scale. The meteorological forcing of the LISFLOOD model consists of daily precipitation, daily potential evapotranspiration, and the average daily temperature. These forcing datasets are embedded in the EFAS system. The model consists of a vegetation layer, three layers for the unsaturated zone, one fast responding and one slow responding linear groundwater reservoir and a channel network for discharge routing (Figure 2). The kinematic wave equation is used for discharge routing using an hourly time step for both surface runoff to the channel network and routing within the channel network.
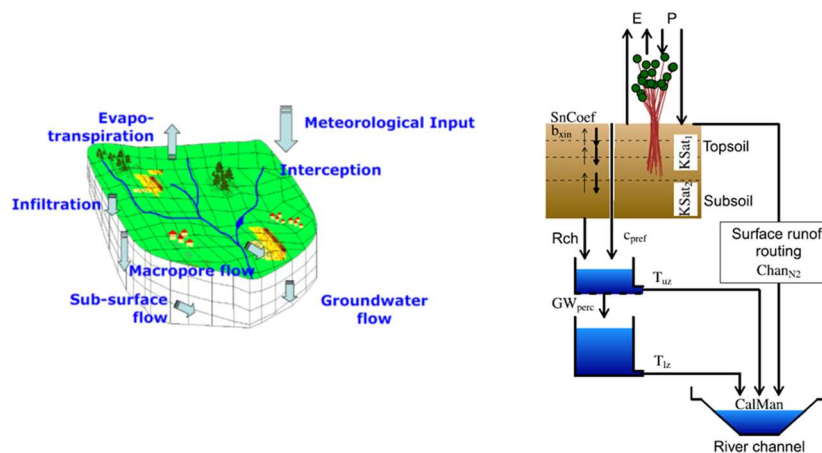
Figure 2. LISFLOOD model components. Precipitation (P), evaporation (E) and model parameters: snowmelt coefficient (SnCoef), Xinanjiang shape parameter (bxin), saturated conductivity of the topsoil (KSat1), saturated conductivity of the subsoil (KSat2), empirical shape parameter preferential macropores flow (cpref), recharge from the unsaturated zone to the groundwater (Rch), maximum percolation rate from upper to lower groundwater (GWprec), reservoir constant upper groundwater (Tuz), reservoir constant lower groundwater (Tlz), surface runoff roughness coefficient (ChanN2), and Channel Manning's roughness coefficient (CalMan)

3. METHODOLOGY

3.1. Performance Metrics

In the hydrologic model performance evaluation process, the footsteps of the diagnostic model evaluation strategy (Yilmaz et al., 2008) has been employed. In this strategy, multiple hydrologically relevant signature measures have been formulated. The advantage of the diagnostic approach is that it uses hydrologically appropriate functions rather than commonly used statistical functions (e.g mean

square error) that are insensitive to the causes of model failure. In this study, signature measures were extracted from the flow duration curve (Figure 3) and comprised of High flow index (HFI, flow value corresponding to 1% exceedance probability), Median flow index (MFI, flow value corresponding to 50% exceedance probability), Low flow index (LFI, flow value corresponding to 85% exceedance probability) and the slope of the flow duration curve (SLP, the difference between flow values corresponding to 70% and 30% exceedance probabilities). These measures were calculated using the log-transformed flow values observed at the stream gauging station and LISFLOOD simulation. Note that while high flow index is important to test the model performance in detecting floods, low flow index is important for drought analysis.
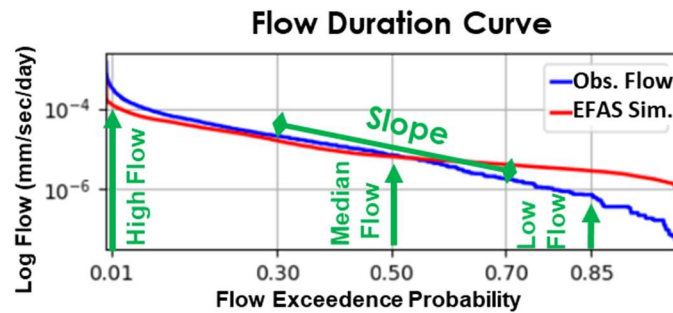
Figure 3. Sample flow duration curve depicting signature measures

In addition to the signature measures above that are obtained from the flow duration curve, a modified version of the Kling-Gupta efficiency criteria (KGE) (Gupta et al., 2009; Kling et al., 2012) and its components were also used in the evaluation process:

$$KGE = 1 - \sqrt{(r-1)^2 + (\gamma - 1)^2 + (\beta - 1)^2} \qquad (1)$$

$$\beta = \frac{\mu_s}{\mu_o} \qquad (2)$$

$$\gamma = \frac{\sigma_s / \mu_s}{\sigma_o / \mu_o} \qquad (3)$$

where r is the Pearson correlation coefficient between simulated (s) and observed (o) flows, β is the bias ratio, γ is the variability ratio, μ the mean flow, and σ the flow standard deviation. The KGE and its three decomposed components (correlation, bias ratio, and variability ratio) are all dimensionless with an optimum value of 1. Note that, KGE components measure flow variability, flow bias and flow correlation (sensitive to flow timing) between LISFLOOD simulated flows and observed flows.

3.2. Analysis of Historical Floods and Droughts

Historical floods and droughts were investigated in Sinanhoca watershed (Figure 1, Table 1, Station ID: E09A012). Daily LISFLOOD streamflow simulations driven by the EFAS forcing datasets were used. The observed and simulated hydrographs were plotted together with the high flow event threshold to visually compare the high flow events. High flow event threshold was selected as the 1% exceedance probability of observed flows during 2002-2015 water years and shown on observed and simulated hydrographs.

Standardized Drought Analysis Toolbox (SDAT) developed by Farahmand and AghaKouchak (2015) has been used to analyze historical hydrological droughts. SDAT offers a generalized framework for deriving nonparametric univariate and multivariate standardized indices. The SDAT methodology standardizes the marginal probability of drought-related variables (e.g., precipitation, streamflow, soil

moisture, relative humidity) using the empirical distribution function of the data. Thus, the approach does not require an assumption on representativeness of a parametric distribution function for describing drought-related variables. For this reason, SDAT framework have been selected to investigate Standardized Streamflow Index for analysis of hydrological droughts.   In this standardized form, the degree of drought is classified as follows: 0> Mild Drought> -1, -1> Moderate Drought> -1.5, -1.5 > Severe Drought > -2, -2> Extreme Drought.

4.   RESULTS

4.1. Performance Metrics over the Antalya Basin

The performance of the EFAS system over 16 streamflow stations in Antalya basin (Figure 4) was evaluated using daily historical simulations and daily flow observations over 2006-2015 period. It can be seen that the EFAS system showed good performance (0.5 > KGE > 0.75) for 4 stations and showed poor performance (0.25 > KGE) for 5 stations out of 16 stations. Note that the LISFLOOD model in the EFAS system has not yet been calibrated, therefore good performance over 4 out of 16 stations is expected. Figure 5 summarizes the EFAS system performance for 16 watersheds as violin plots. It can be seen from Figure 5a that the EFAS system resulted in a wide range of KGE components. The flow bias is generally less than 1 indicating underestimation of flows by the EFAS system. Flow correlation is generally below 0.75 indicating mismatch of timing of flows. Figure 5b shows the distribution of flow signatures obtained from flow observations (green half) and EFAS system simulations (orange half). It can be noticed from this figure that the EFAS system simulations resulted in narrow distribution of signatures compared to observations indicating that the simulations are unable to capture the flow variability across the watersheds.
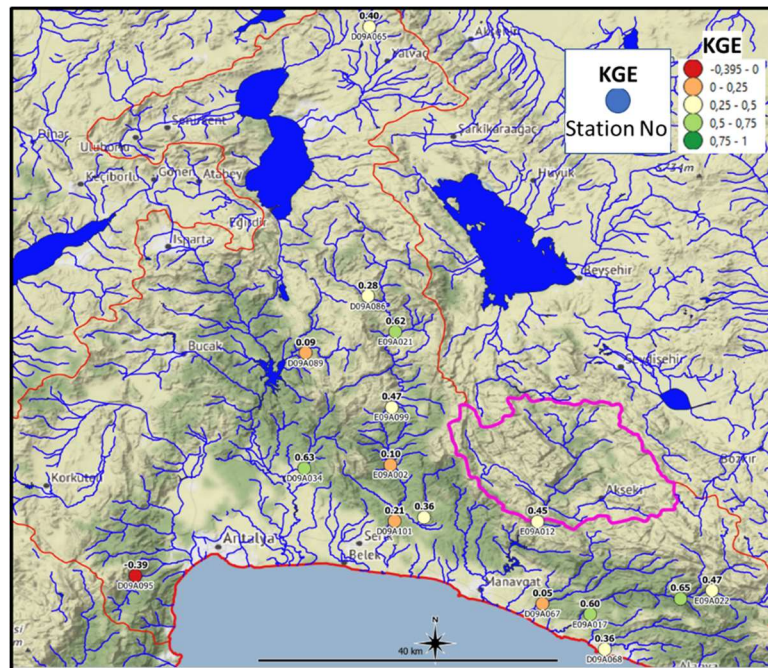
Figure 4. Map showing the performance of the EFAS system for the study streamflow stations in Antalya basin
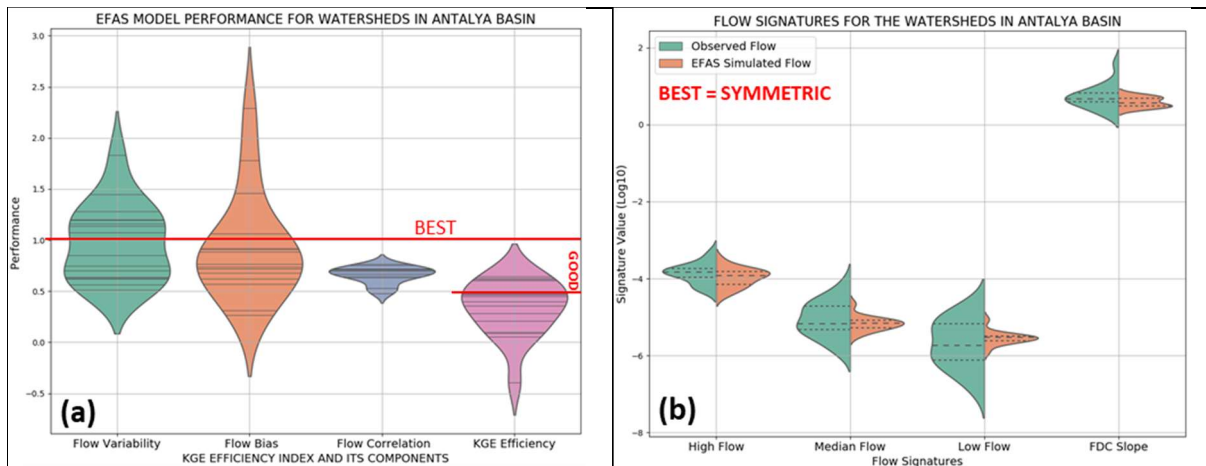
Figure 5. EFAS System performance over 16 watersheds in Antalya basin summarized as violin plots (a) KGE efficiency index and its components, (b) flow signatures

4.2. Detection of Floods and Droughts over Sinanhoca Watershed

Analysis of historical flood and drought events were performed using daily streamflow observations at Sinanhoca streamflow gauging station (Station No: E09A012) for the October 2001-October 2015 water year period. Figure 6 shows the hydrographs of observed flows and LISFLOOD simulated flows driven by EFAS system, respectively. The red horizontal line in these hydrographs is drawn as a reference and represents the high flow threshold for observed flows that is equal to 1% observed flow exceedance value. It can be seen that LISFLOOD model driven by EFAS system underestimates observed flow values and generally misses high flow events, see for example events during water years 2002-2006, 2008, 2009, 2012 and 2014. Also, a number of false events are evident, see for example, 2010, 2011 and 2012. High flow events in 2007, 2011 and 2013 were detected by the LISFLOOD model driven by EFAS system. Note also that the EFAS system cannot capture the recession part of the hydrograph events, thus indicating that improvement is needed in groundwater component of the model.
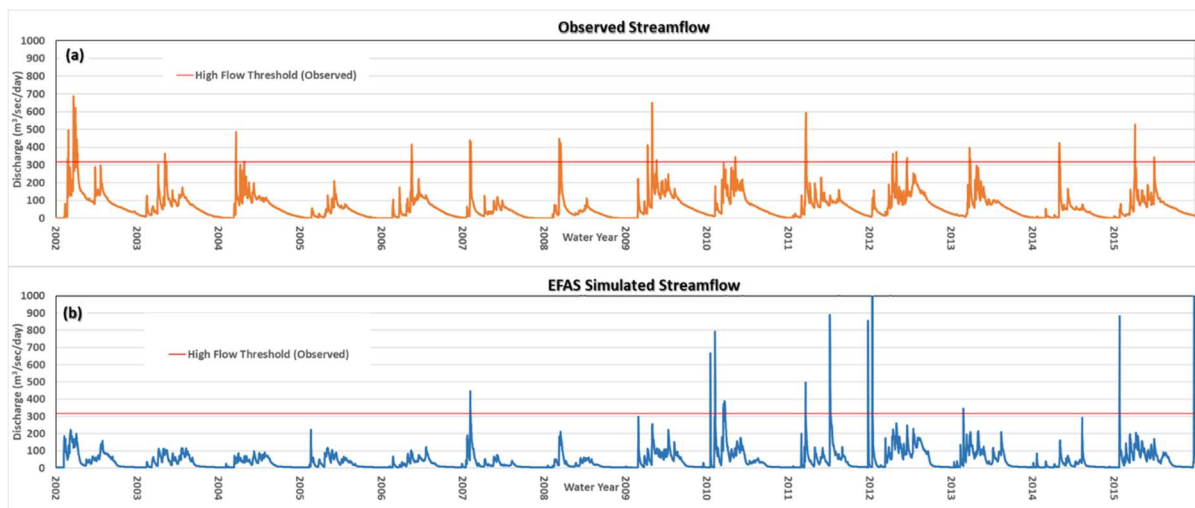
Figure 6. Daily hydrographs for Sinanhoca watershed (a) observed flows, (b) EFAS simulated flows.

12-month Standardized Streamflow Index (SSI) values are shown in Figure 7. Three severe drought periods are evident from SSI-12 values obtained from observed flows, specifically, years between 2005-2006, 2008-2009 and the year 2014. Two of the three severe hydrological drought periods were successfully captured by the LISFLOOD simulated flows driven by EFAS system, while one of the periods were classified as moderate hydrological drought period.
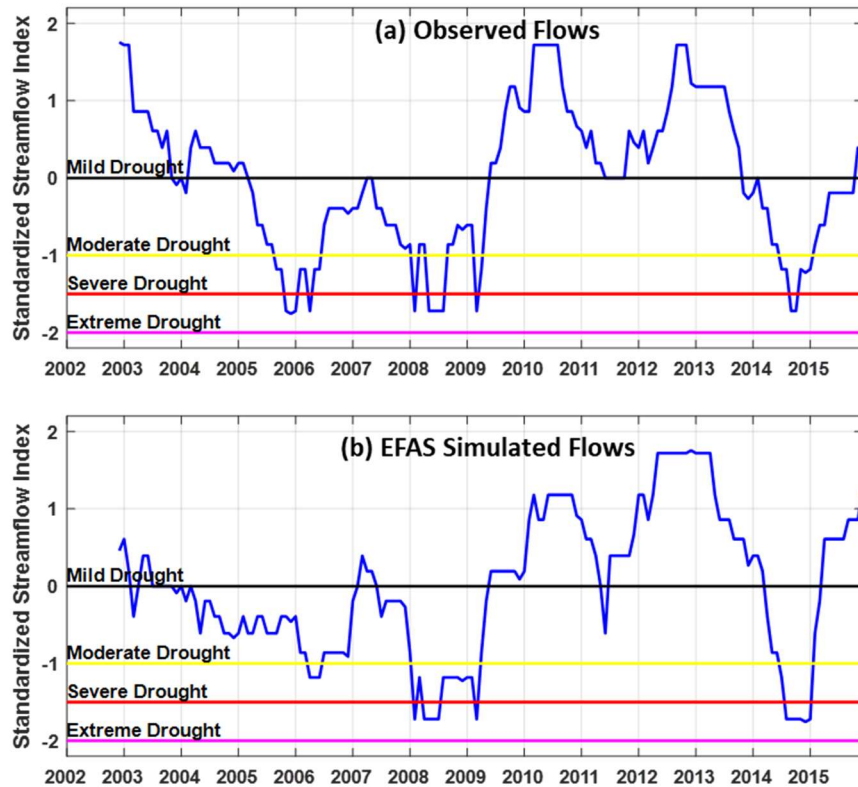
Figure 7. 12-month Standardized Streamflow Index (SSI-12) values for Sinanhoca watershed (a) observed flows, (b) EFAS simulated flows

5. CONCLUSIONS

The performance of the European Flood Awareness System was evaluated by the daily streamflow observations in 16 watersheds in Antalya basin, Turkey. The analysis indicated that the system cannot adequately capture the flow variability across the watersheds, which is possibly due to the fact that the LISFLOOD model in the EFAS system has not yet been calibrated over Turkey. Therefore, a suggestion for future work is to apply effective and efficient model calibration schemes for calibration of the LISFLOOD model over different hydroclimatic regions in Turkey. Moreover, data assimilation, for example soil moisture, is expected to improve the performance of the system in the forecast mode. The LISFLOOD model driven by EFAS system generally missed the high flow events, moreover, simulated also a number of false flow events. Two out of three severe drought periods were successfully captured by the model. Incorporation of local rain gauge measurements as input to the hydrological model could be a future direction of research.

REFERENCES

Giorgi, F. (2006). Climate change hot-spots, *Geophys. Res. Lett.,* 33, L08707, doi:10.1029/2006GL025734

Lavers, D.A., Ramos, M.-H., Magnusson, L., Pechlivanidis, I., Klein, B., Prudhomme, C., Arnal, L., Crochemore, L., Van Den Hurk, B., Weerts, A.H., Harrigan, S., Cloke, H.L., Richardson, D.S., Pappenberger, F. (2020). A Vision for Hydrological Prediction. *Atmosphere*, 11, 237.

Thielen, J., J. Bartholmes, M. Ramos, and A. de Roo (2009), The European flood alert system—Part 1: Concept and development, *Hydrol. Earth Syst. Sci.*, 13(2), 125–140, doi:10.5194/hess-13-125-2009.

Bartholmes, J. C., J. Thielen, M. H. Ramos, and S. Gentilini (2009), The European flood alert system EFAS—Part 2: Statistical skill assessment of probabilistic and deterministic operational forecasts, *Hydrol. Earth Syst. Sci.*, 13(2), 141–153, doi:10.5194/hess-13-141-2009.

Yilmaz, K. K., H. V. Gupta, and T. Wagener, (2008) A process-based diagnostic approach to model evaluation: Application to the NWS distributed hydrologic model, *Water Resour. Res.,* 44, W09417.

Gupta H.V., Kling H., Yilmaz K.K., Martinez G.F., (2009) Decomposition of the mean squared error and NSE performance criteria: Implications for improving hydrological modeling, *J. of Hydrol.*, 377(1-2), pp. 80-91.

Kling, H., Fuchs, M., Paulin, M., (2012) Runoff conditions in the upper Danube basin under an ensemble of climate change scenarios. *J. Hydrol.* 424–425,264–277, http://dx.doi.org/10.1016/j.jhydrol.2012.01.011.

Farahmand A., AghaKouchak A., 2015, A Generalized Framework for Deriving Nonparametric Standardized Drought Indicators, *Advances in Water Resources*, 76, 140-145, doi: 10.1016/j.advwatres.2014.11.012

ADVANCES IN LABORATORY MEASUREMENTS AND INSTRUMENTATION

A WAVE CONTROL SYSTEM FOR IRREGULAR AND REGULAR WAVE GENERATION

Bassem Nouioui

The Graduate School of Natural and Applied Sciences Dokuz Eylül University

Tinaztepe Campus Buca Izmir 35160 Turkey

bassem.nouioui@ogr.deu.edu.tr

Muhammed Ikbal Tortumluoğlu

The Graduate School of Natural and Applied Sciences Dokuz Eylül University

Tinaztepe Campus Buca Izmir 35160 Turkey

muhammedikbal.tortumluoglu@deu.edu.tr

Mustafa Doğan

Faculty of Engineering Civil Engineering Departement Dokuz Eylül University

Tinaztepe Campus Buca Izmir 35160 Turkey

mustafa.dogan@deu.edu.tr

Yalçın Arisoy

Faculty of Engineering Civil Engineering Departement Dokuz Eylül University

Tinaztepe Campus Buca Izmir 35160 Turkey

yalcin.arisoy@deu.edu.tr

ABSTRACT:The paper describes the design and execution of a wave maker system in the Dokuz Eylül University Hydraulic Laboratory flume to perform hydraulic model tests. The system consists of a servo motor and a piston type paddle with the capacity to produce all forms of regular and irregular gravity waves. In this paper, we will focus on generating irregular waves for given significant wave heights and peak frequencies using JONSWAP spectrum, also the control software used to generate the wave types and its parameters was described. Finally, the testing method and the obtained results from the experiments on the wave flume were provided.

1. INTRODUCTION

Hydraulic model tests are used to study coastal issues and to solve various problems related to the planning, design and construction of coastal infrastructure. Today, hydraulic model tests with irregular waves are generally preferred. For this reason, all laboratories are trying to have equipment to produce irregular waves for such tests.

During physical modeling process in a wave flume, the random wave simulation is performed to reproduce a specified goal wave energy density spectrum. For a given significant wave height and peak period pair, the simulation approach allows for direct simulation of wave particle kinematics at any position in a given water depth. Spanos (1983) and Hudspeth and Chen (1979) provide two alternatives for simulating random waves from a given one-dimensional spectrum.

Wave generation techniques in physical models are proposed by Goda (2000, Chapter 7), Huges (1993, chapter 7), Dean and Dalrymple (1984, chapter 6), and Biésel and Suquet (1951) who theorized the basis for the modern wave generation in hydraulics laboratories.

651

It is extremely difficult to have a wave channel with an irregular wave generator due to the high initial investment cost. Achieving this through imports from Europe or the United States is not possible for some developing countries. The system has been created to generate all forms of regular and irregular gravity waves, with the domestic capabilities without using expensive equipment.

2. EXPERIMENT SETUP

The studies were performed in Dokuz Eylül University Hydraulic Laboratory wave flume that is 23.4 m long, 1.0 m wide, and 1.2 m deep. One side of the flume is covered with thick glass to make visual observations during the experiments (Figure 1). To achieve the appropriate wave qualities, a piston-type wave generator is employed to move the water in the flume. The wave generator is situated the beginning of the flume, and two passive wave absorbers are utilized to avoid wave reflection.

Waves propagate backwards on the piston-paddle due to the presence of water on both sides, causing splashes of water that pose a danger of damaging the motor when the created and reflected waves collide. The first absorber is a steel cage packed with absorbent material is placed at the back of the generator to absorb wave energy, while the second absorber is rocks of varying size with slope of 1:7 is installed at the end of the flume.

The experiments were conducted at a constant water depth of d=0.55 m. A servo motor controls the piston, which can create both regular and random waves. The variability of the water surface with time was plotted using three vertical wave probes positioned at the selected measuring points (i.e. P1, P2, and P3 are set at distance of 6 m ,13 m ,and 16 m respectively from the offshore side) attached to ULS with precision of 1.0 mm and 0.2 s.

(a) Profile (not to scale)

(b) Plan (not to scale)
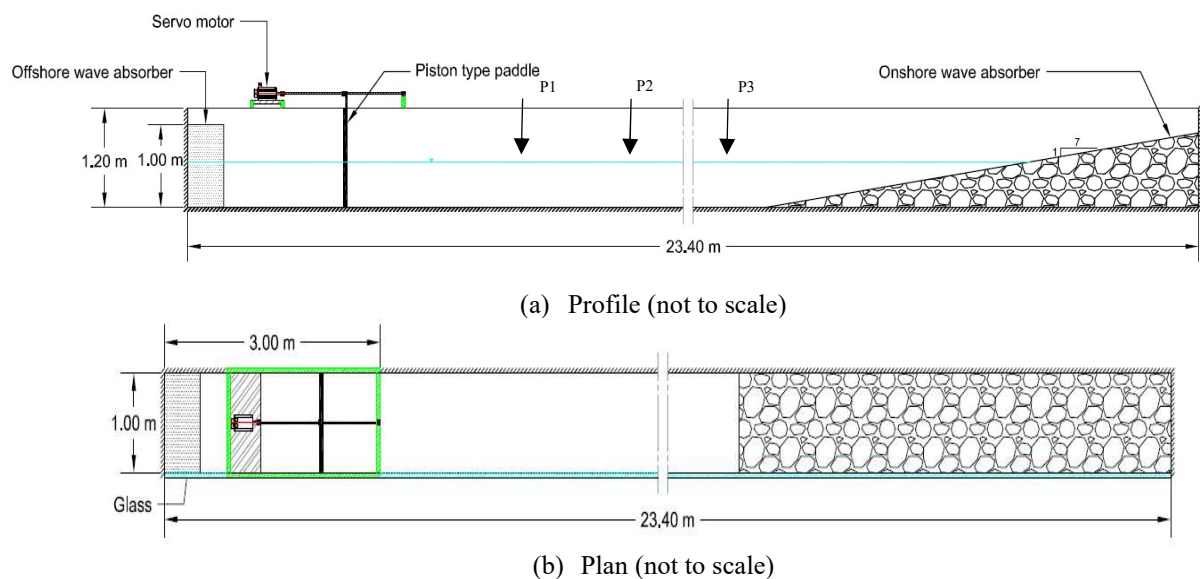
Figure 1. Wave flume sketch with piston-type wave maker

3. WAVE MAKER SETUP

3.1. Mechanical Construction

The wave generator is an AC servo motor attached to a ball screw shaft that supports a piston-type wave generator that was installed at the beginning of the wave flume to generate waves (Figure 2 and Figure 3) controlled by Programmable Logic controller PLC. The servo motor's rotations are transformed into linear motion, which moves the wave paddle back and forth in the wave flume.
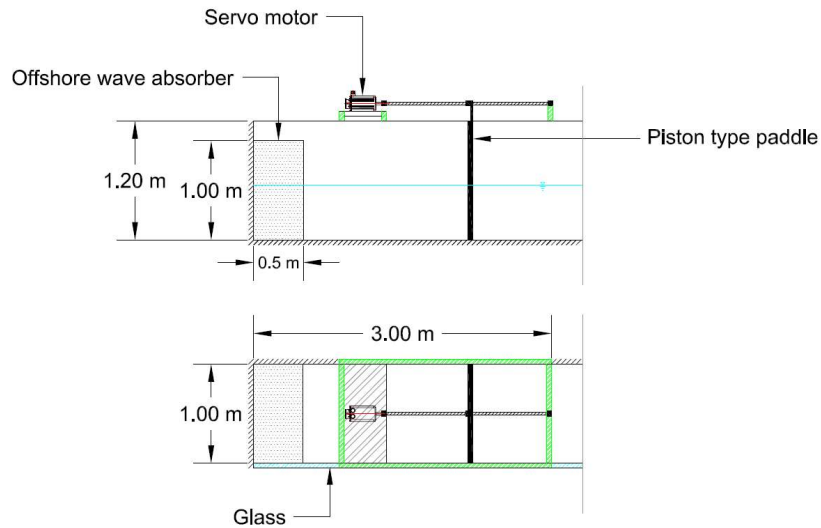
Figure 2. Side and top view of the piston-type wave maker section design (Not to scale)
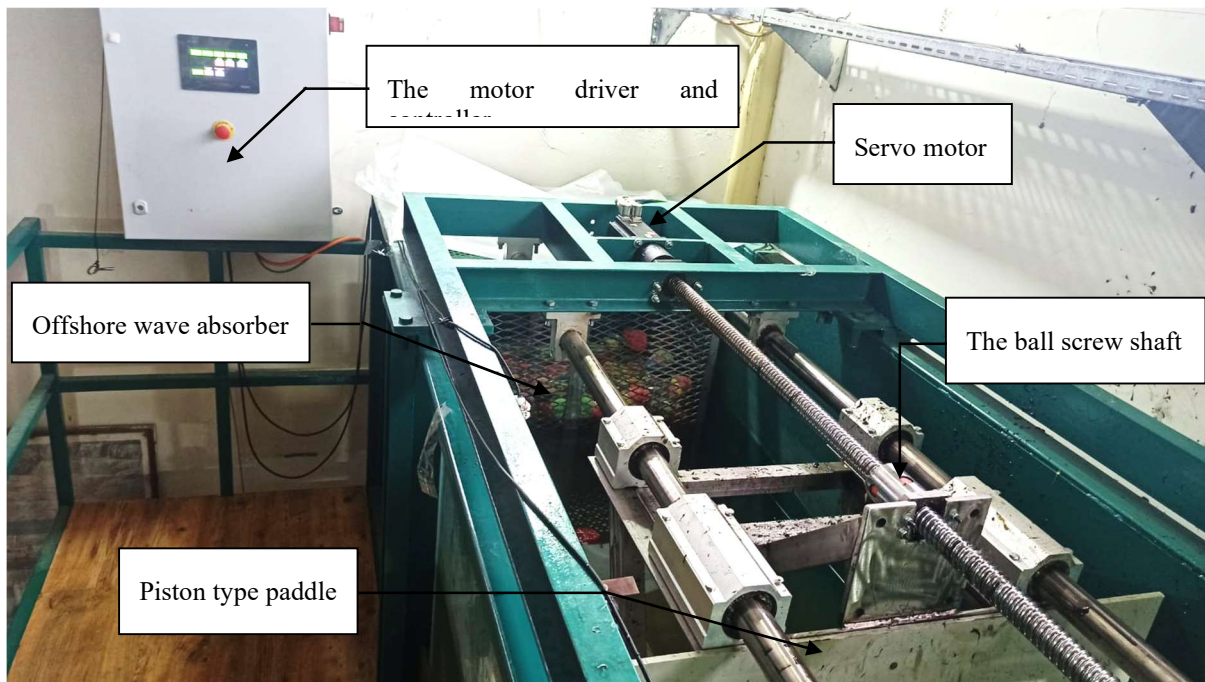
Figure 3. View of the piston-type wave generator showing the servo motor and ball screw shaft with the motor driver and controller

3.2. The Control Software

A user application (Figure 4) written in Python code which is loaded on a PC controls the wave maker. The graphs displaying the paddle movement and surface elevation signals, as well as the spectrum, depending on the type of experiment set.

Figure 4. User interface of the control software

4. GENERATION OF WAVES

4.1. Regular Waves

The development of regular waves is always a fundamental function of a wave-maker and important in the generation of other waves. The wave maker setup allows for all kinds of regular waves to be generated (Stokes, cnoidal, and solitary waves).

Waveform generation for Stokes (sinusoidal) waves is based on the Biesel equations for piston-type wave maker (eq.1).

$$e_0 = \frac{4\ sinh^2}{2k_0 h + \sinh(2k_0 h)} \tag{1}$$

e_0 for piston-type paddle transfer function, k_0 the wave number , and h the water depth .

4.2. Irregular Waves

The waveform is calculated corresponding to the target JONSWAP spectrum function (eq.2), using the random phase method.

$$S(f) = \beta_J H_{\frac{1}{3}}^2 T_p^{-4} f^{-5}\ exp\left[-1{,}25\left(T_p f\right)^{-4}\right] \gamma^{exp\left[-\frac{\left(T_p f - 1\right)^2}{2\sigma^2}\right]} \tag{2}$$

Where $H_{1/3}$ is the significant height, f is the frequency , T_p the peak period , f_p the peak frequency, and γ is the peak enhancement factor varied from 1 to 7 with a mean value of $\gamma=3.3$.

$$\sigma=0{,}07\ for\ f\leq fp \qquad \sigma=0{,}09\ for\ f>fp$$

$$f_p = 1/T_p$$

$$\beta_J = \frac{0.0624}{0.230 + 0.0336\gamma - 0.185(1.9 + \gamma)^{-1}}[1.094 - 0.01915ln\gamma]$$

$$T_p \cong T_{\frac{1}{3}}/[1 - 0.132(\gamma + 0.2)^{-0.559}]$$

Where $T_{1/3}$ is the significant period,

In the Random Phase Method, the wave profile is expressed as

$$\eta(t) = \sum_{n=1}^{N} a(n) \, cos[2\pi f(n)t + \varepsilon(n)] \tag{3}$$

The amplitude a should be computed as

$$a(f_n) = \sqrt{2S(f_n)\Delta f}$$

$$\varepsilon(f_n) = 2\pi r_N$$

Where the phase angle ε is arbitrary since r_N is a random number between zero and one.

4.3. Wave Board Displacement Time Series

The target spectrum of the wave paddle motion $S_{paddle}(f)$ is calculated for the target wave spectrum $S(f)$. After that the wave paddle motion (Figure 5) is achieved using Random Phase Method , but by utilizing the same randomly generated phases for the irregular waves. Figure 5 shows a plot of the paddle displacement over the number of data points, which equals to the time of the experiment divided by the sampling rate Δt in seconds.

$$S_{paddle}(f) = S(f)/e_0^2 \tag{4}$$
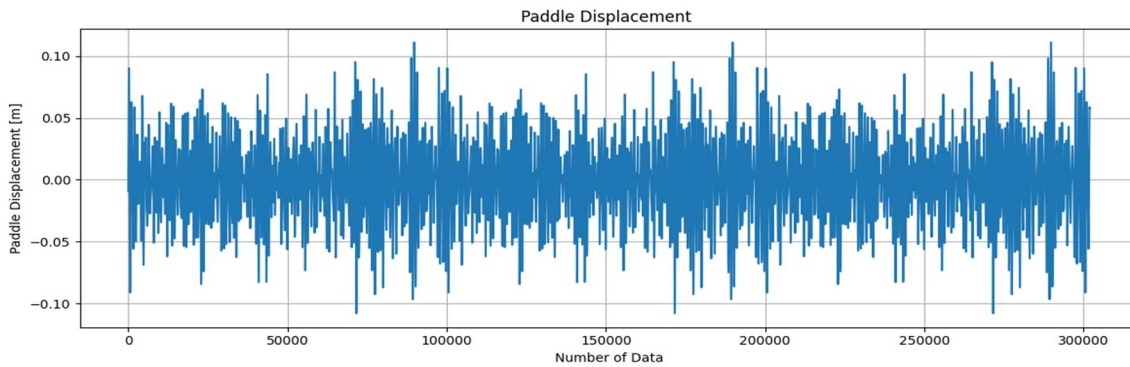
Figure 5. example of the paddle control signal (H_s=0,144 m, T_s=1,56 s, duration=600 s, and Δt=0,002 s).

5. EXPERIMENT SET AND RESULTS

The irregular waves (IRW) have been generated after specifying the target JONSWAP spectrum, the significant wave heights H_s(0.13 to 0.25 m), of peak periods T_s (1.56 to 3.6 s) are selected. The spectrum is discretized to N=351 samples. The durations of the experiments are set to 1 hour. Water

depth at the paddles of the wave maker is 0.55 m. Experiments set and results are summarized in Table 1.

Table 1.Experiments set.

Experiment	Target waves		Measured waves	
	Hs(m)	Ts(s)	Hs(m)	Ts(s)
IRW_01	0.250	2.00	0.2348	1.929
IRW_02	0.220	2.30	0.2220	2.297
IRW_03	0.200	2.70	0.2023	2.733
IRW_04	0.170	3.10	0.1687	3.050
IRW_05	0.130	3.60	0.1331	3.650
IRW_06	0.144	1.56	0.1363	1.561

The wave gauge P2 attached to the ULS are used to obtain the surface elevation of the experiments, which is then used to calculate the wave characteristics using the zero up crossing method. (H_s denotes significant wave height which corresponds to the mean value of 1/3th of all individual wave heights in the zero-up crossing method). Figure 6 compares the JONSWAP spectrum of the generated wave (measured Hs, and Ts) at the wave gauge P2 to the desired spectrum (Target Hs, and Ts). The figures show a good match between the control signal and the measured data. Table 2 shows the ratios of the variations between the measured and target wave properties, which were found to be within accepted limits of around 6%.
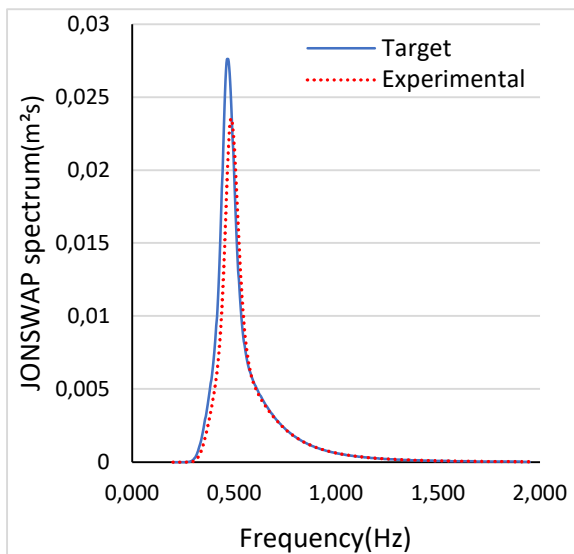
(a). IRW_01
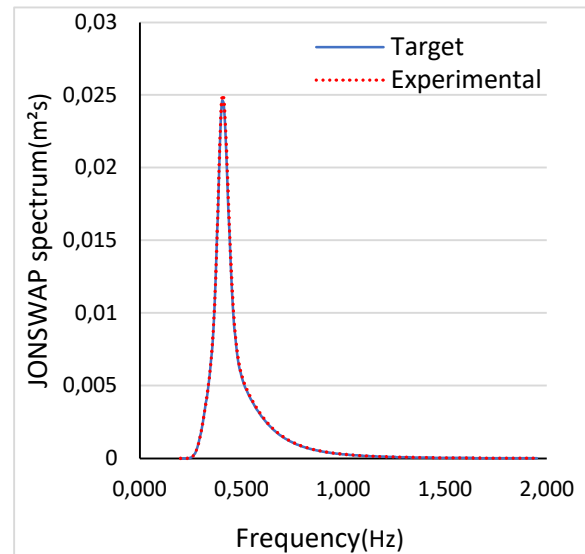
(b). IRW_02
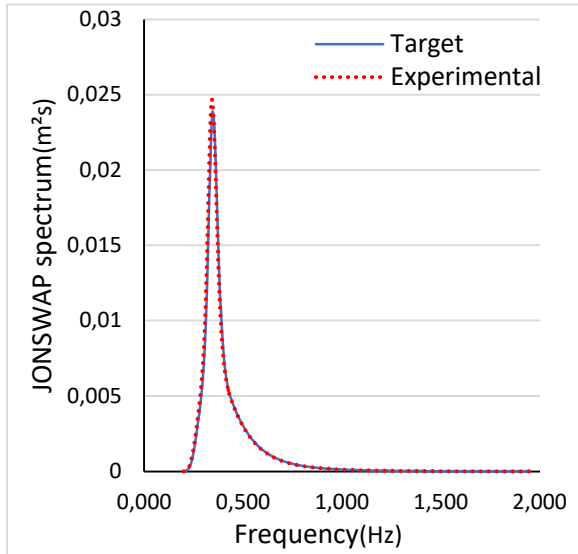
(c). IRW_03
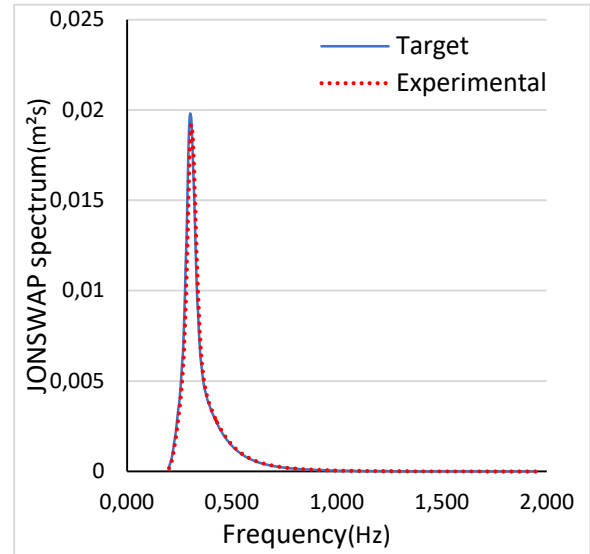
(d). IRW_04
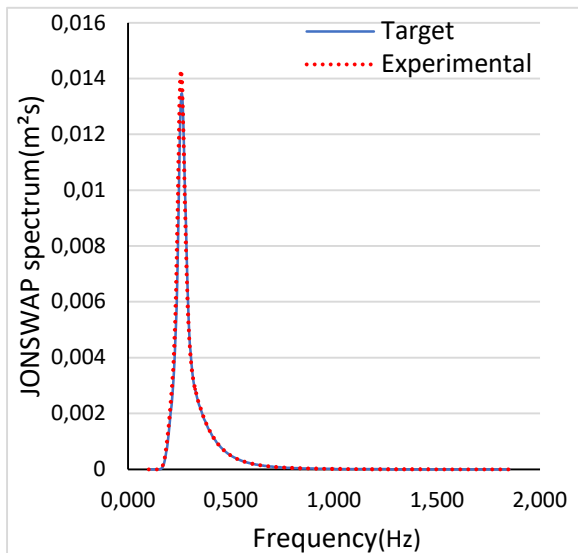
(e). IRW_05
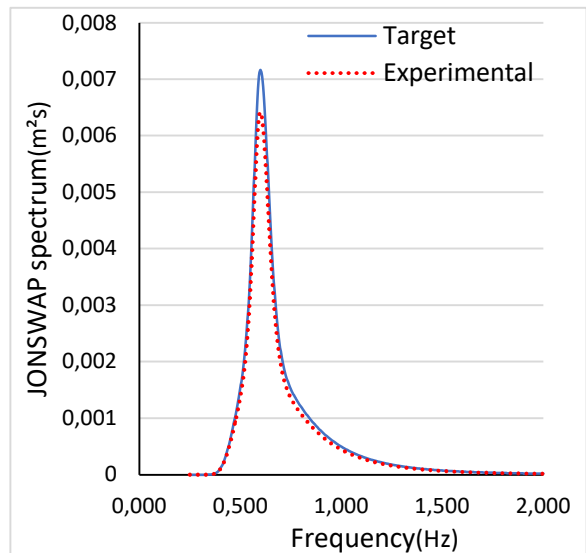
(f). IRW_06

Figure 6. JONSWAP spectrum of target and measured wave elevation in the wave flume.

Table 2. Experiments error ratios.

	Error ratios			
Experiment	*fp* (Hz)	S(f)	Hs(m)	Ts(s)
IRW_01	3.68%	14.68%	6.08%	3.55%
IRW_02	0.13%	1.56%	0.91%	0.13%
IRW_03	1.20%	3.27%	1.15%	1.22%
IRW_04	1.63%	3.08%	0.76%	1.61%
IRW_05	1.36%	6.08%	2.38%	1.39%
IRW_06	0.06%	14.52%	5.35%	0.06%

6. CONCLUSION

The results revealed that the measured wave parameters were extremely close to the target characteristics, notice that the major two deviations of the measured JONSWAP spectrum of the obtained wave forms to the target spectrums are 14,68% for IRW_01 (Hs = 0.25 m, Ts = 2.0 s) and 14.52% for IRW_06 (Hs = 0.144 m, Ts = 1.56 s). The wave reflections in the flumes can increase the ratio of variations between the target and the measured spectra, especially for wave periods of less than or equal to 2 seconds.

The goal of future work in this project is to introduce a unique shape of passive wave absorption mechanism in the wave flume. Also, improvements in waveform calculation, control algorithms, and wave generating precision will be the focus of future work.

REFERENCES

Biesel, F., & Suquet, F. (1951). Les appareils générateurs de houle en laboratoire. *Houille Blanche*, *4*, 475–496. https://doi.org/10.1051/lhb/1951049.

Dean, R. G., & Dalrymple, R. A. (1984). *Water wave mechanics for engineers and scientists.* https://doi.org/10.1029/eo066i024p00490-06.

Frigaard, P., & Andersen, T. L. (2010). Technical Background Material for the Wave Generation Software AwaSys 5. *DCE Technical Reports, No. 64*, 114.

Funke, E.,& Mansard, E. (1993). *Laboratory Wave Generation.*333–457. https://doi.org/10.1142/9789812795939_0007.

Guillouzouic, B. (2014). Collation of Wave Simulation Methods. *MARINET Report*, 1–85.

Hudspeth, R. T., and Chen, M. C. (1979). "Digital Simulation of Nonlinear Random Waves," *ASCE Jour.*

Waterw., Port, Coastal and Ocean Engr., Vol 105, pp 67-85.Hughes, Steven A. 1993. *Physical Models and Laboratory Techniques in Coastal Engineering. Advanced Series*

on Ocean Engineering. Vol. Volume 7. WORLD SCIENTIFIC. https://doi.org/doi:10.1142/2154.

Isaacson, B. M. (1992). *MEASUREMENT OF REGULAR WAVE REFLECTION. 117*(6), 553–569.

Khalilabadi, M. R., & Bidokhti, A. A. (2012). *Design and Construction of an Optimum Wave Flume M.R. 5*(3), 99–103.

Mišković, I., Eškinja, Z., & Horvat, K. (2008). Wavemaker control system for irregular developed sea waves generation. *2008 Mediterranean Conference on Control and Automation - Conference Proceedings, MED'08*, 791–794. https://doi.org/10.1109/MED.2008.4602205.

Schäffer, H. A. (1996). Second-order wavemaker theory for irregular waves. *Ocean Engineering*, *23*(1), 47–88. https://doi.org/10.1016/0029-8018(95)00013-B.

Schäffer, H. A., & Steenberg, C. M. (2003). Second-order wavemaker theory for multidirectional waves. *Ocean Engineering*, *30*(10), 1203–1231. https://doi.org/10.1016/S0029-8018(02)00100-2.

Spanos, P. D. (1983). "ARMA Algorithms for Ocean Wave Modeling," *ASME Jour. Energy Resources Tech.*Vol

105, pp 300-309.

Y.goda. (2000). *Random seas and design of maritime structure*. https://doi.org/10.1142/3587.

INVESTIGATION OF THE FLOW CHARACTERISTICS OF LABYRINTH SPILLWAYS BY EXPERMENTAL AND MATHEMATİCAL MODELLING METHODS

Ezgi Ispir

Necmettin Erbakan University

Konya, Turkey

ezgi.ozturk@windowslive.com

Serife Yurdagul Kumcu

Necmettin Erbakan University

Konya, Turkey

yurdagulkumcu@gmail.com

ABSTRACT: Spillways are structures that have an important place in the project cost of a dam and have important functions related to the security of the dam. The labyrinth spillway concept involves reducing the reservoir water level by increasing the effective length of the spillway crest with various forms applied on the plate, increasing the discharge that can be discharged at a certain lake level or passing a constant stream with smaller crest water loads. These weirs can also be considered as alternatives that provide advantages within the topographic boundaries. In addition, easier construction and more reliable operating conditions compared to classical controlled spillways are other advantages. Many experiments have been conducted in the laboratory to investigate the hydraulic properties of labyrinth spillways. In each experiment, the flow discharges passing over the weirs and the corresponding water heads were measured. At the same time, these experimental studies were also tested in the FLOW-3D software program and the results of the experimental and mathematical studies were compared with each other and presented in the form of graphs. As a result of the studies, it was observed that the flow rate increased as the length of the weir increased with the same water height and the results obtained with the use of FLOW-3D software were similar to those of experimental studies.

1. INTRODUCTION

Spillways are dam safety structures that play a very important role in a dam construction due to construction and cost. Studies conducted so far have revealed that 1/3 of the damages in dams are due to insufficient spillway capacity. When the project hydrology is examined in some existing water structures, the need to increase the PMF (possible maximum flood) flow rate arises. If the dam spillway is not capable of passing this determined flow rate, a solution to increase the flood storage capacity is sought. Dams in the USA are made by using advanced hydrological methods by examining whether there is a danger of water penetration or not (DSI TAKK Department, 1993). In the same study, it is stated that the most important reason for the damage to dams is not having sufficient spillway capacity.

The discharge of large flood flows entering the reservoir is possible by increasing the length of the spillway or by increasing the project water load on the spillway. In recent years, labyrinth type spillways have been an effective method to increase the discharge capacity of spillways. Labyrinth spillways are a type of spillway that provides a much longer spillway length in plan than linear spillways with a certain spillway width, and they take their name from their geometry. Total crest lengths are generally three to five times the length of the standard spillway. The discharge capacity is approximately twice the discharge capacity of the linear or standard spillway (Tullis et al., 1995).

This increase in crest length enables labyrinth spillways to increase the discharge flow or pass a fixed flow through lower water heights and reduce the reservoir water level. These weirs are particularly advantageous for areas where the topography limits the width of the spillway. In addition, labyrinth spillways are preferred because of their easy construction and being more reliable than traditional spillways.

Labyrinth spillways are preferred in order to increase the discharge capacity at a certain crest level and without changing the width where the spillway will be placed. Because labyrinth spillways aim to increase the storage capacity of the reservoir without decreasing the discharge capacity by raising the level of the weir.

There are also a few less important variables such as length, l, labyrinth width, w, weir height P, labyrinth angle, α, number of meshes, N, and wall thickness, t, and weir shape, which should be considered in labyrinth spillway design. In Figure 1, a plan and section view of a labyrinth spillway is given.

w = Weir width

P = Weir height
h = Flow height

l = weir length

t = Weir thickness

N= Number of eyes

α =Weir angle
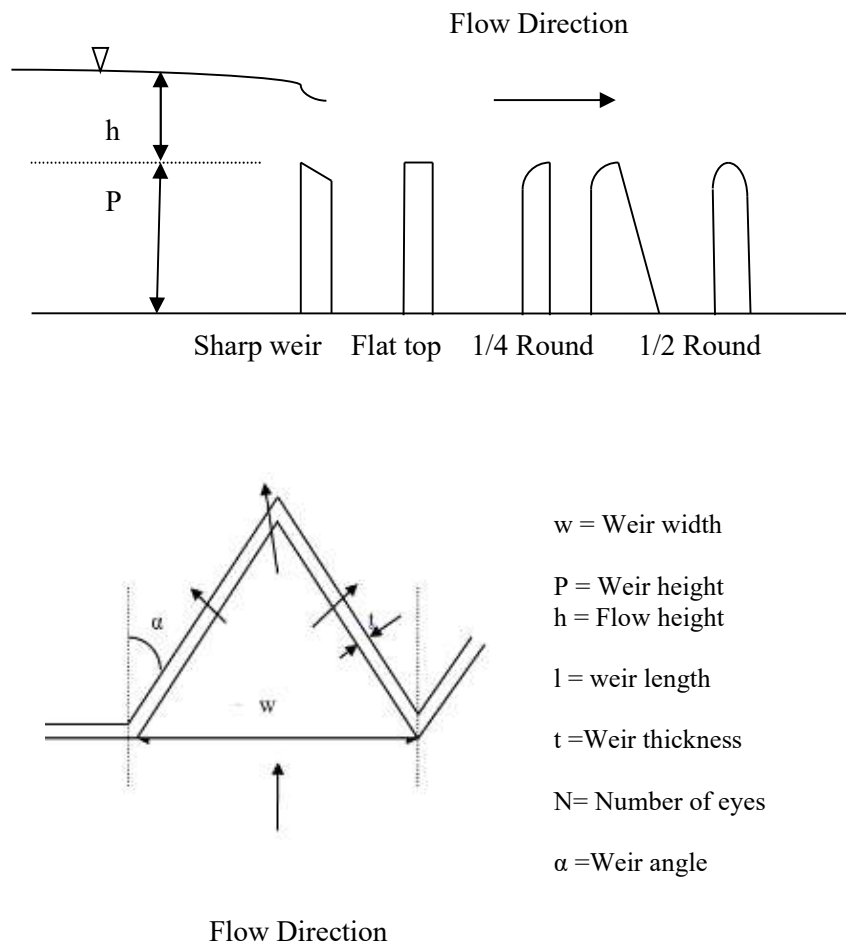
Figure 1. Typical triangular labyrinth-spillway model

Labyrinth spillways can discharge current more safely compared to traditional spillways. The labyrinth design also increases the capacity and flood discharge of an existing operating dam. This design is one of the most effective solutions, especially in areas where height and topography are limited.

The main factors determining the performance of the labyrinth spillway are the maximum flow rate and the water load passing over the weir. It is known that it is easier to design and construct the structure for labyrinth spillways with wall heights up to 1m, but more analysis is needed for larger labyrinths.

In this study, the hydraulic characteristics of labyrinth weirs with a triangular plan view were analyzed experimentally at various lengths in the laboratory.

In the laboratory, h-Q graphs were drawn against the measured values in different geometric shapes and at three different weir heights between Q = 10-100 l / s flow rate, P = 15cm, P = 22.5 cm and P = 30 cm. Experimental studies were carried out in a commercial software program, FLOW-3D, and the results were compared.

The first comprehensive study of the hydraulic performance of labyrinth spillways was done by Hay and Taylor (1971).

Taylor determined the flow as Q_o for a sharp cross-section linear weir with the same channel width, and Q for the labyrinth weir flow and showed the results in terms of the magnitude of the Q / Q_o ratio. In Figure 2. for h / P values ranging from 0 to 0.5, the Q / Qo sizes corresponding to the sizes L / Lo = 3, 4, 5, 6, 7 and 8 are drawn. Where L is the length of the channel used, Lo is the width of the channel. On this curve, it is seen that Q / Qo ratio and L / Lo ratio increase in direct proportion.
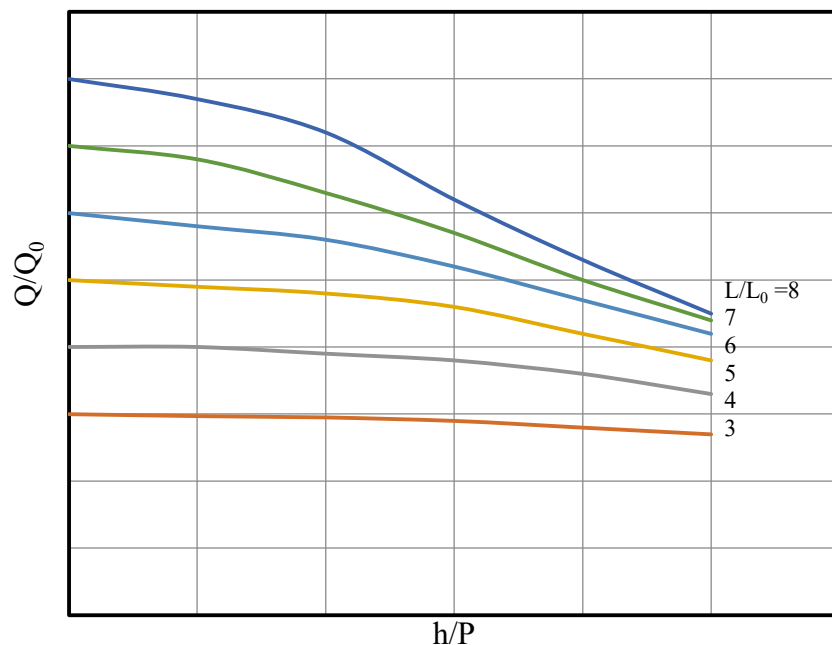
Figure 2. Hay and Taylor design curves (Hay and Taylor, 1971)

A model study was made for the UTE dam built in the USA in 1982 (USBR, 1982). The United States Rehabilitation Bureau has requested the United State of Bureau of Reclamation (USBR) to increase the capacity of the reservoir by adding a new labyrinth spillway structure on top of the spillway structure by developing a more economical alternative. A model study has been made using Froude analogy and the project design flow rate is drawn in dimensionless proportions as Q / Q_o and Q / Q_o plots are drawn against the design's H / P. Figure 3 shows the total flow head load H and the sluice height is given as P.
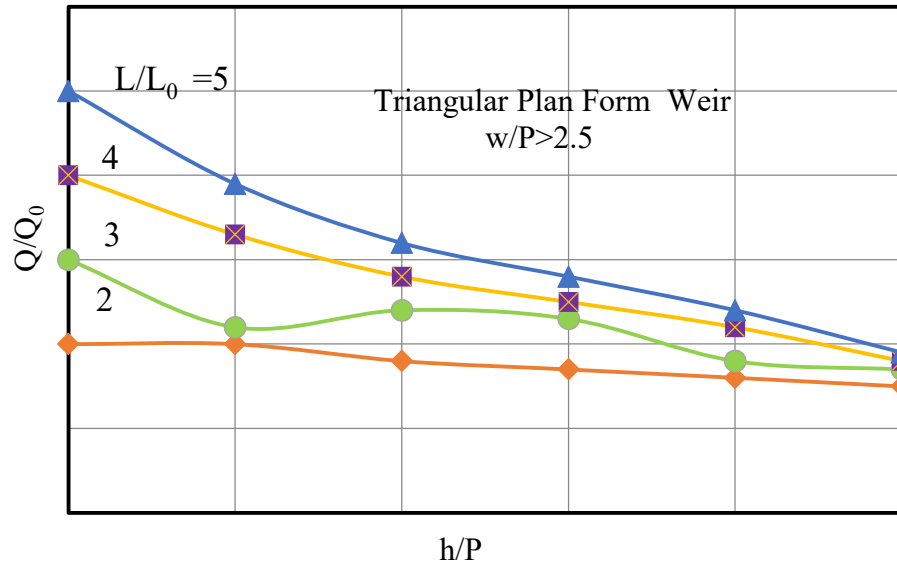
Figure 3. USBR Design Curves

$$Q = \frac{2}{3} C_d L \sqrt{2g} H^{1,5} \tag{1}$$

Here;

C_d	:	Dimensional flow coefficient
g	:	Gravitational acceleration
L	:	Weir Length
H	:	Total Water Height

As the H/P value increases for the labyrinth weir, the Cd coefficient decreases. To increase the efficiency of the labyrinth spillway, it is necessary to limit the H/P' coefficient. For the maximum flow over the spillway, the H/P value should be less than 0.9.
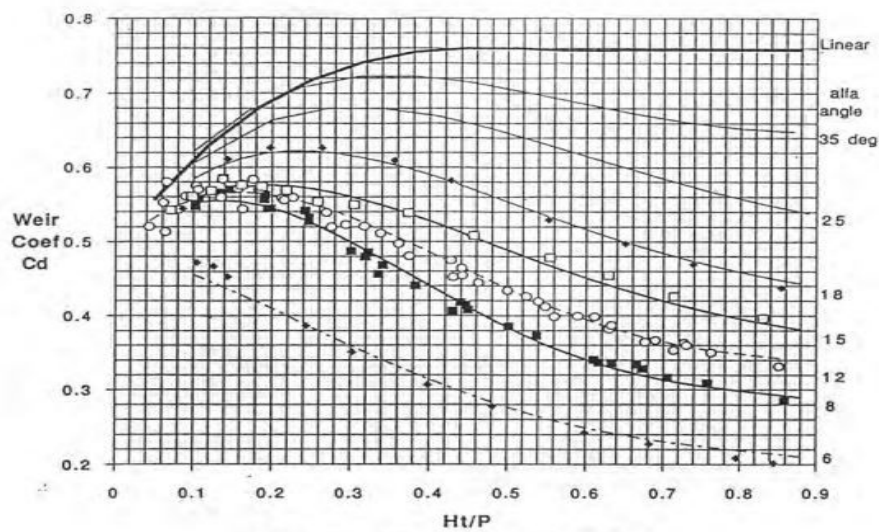
Figure 4. Weir coefficient for labyrinth spillways (Tullis et al., 1995)
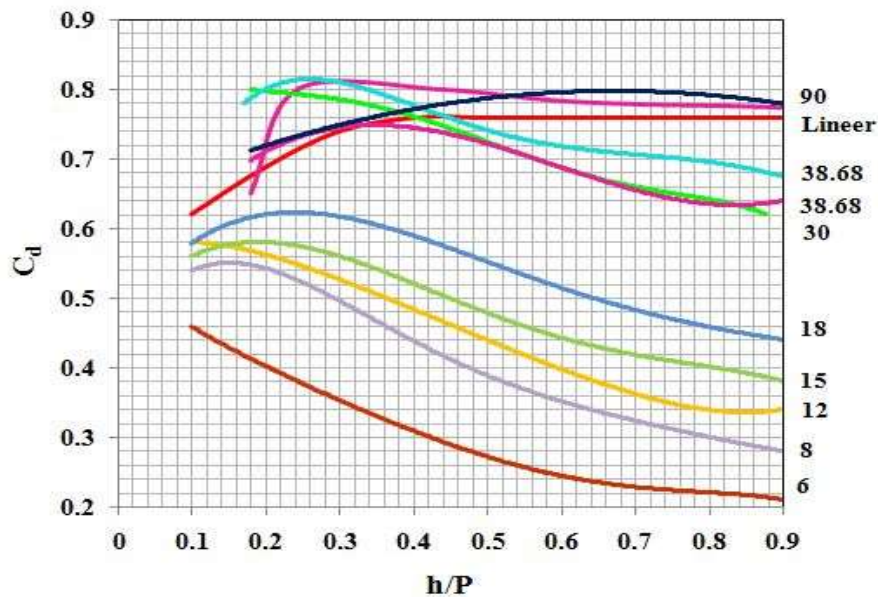
Figure 5. Literature comparison based on experimental results for labyrinth spillways

Yıldız and Kaş, (1997) and Kumcu, (1997) stated that labyrinth spillways are the type of spillway providing much longer crest length in the plan than linear spillways, that these spillways are three or five times the crest length of standard spillways; They stated that their discharge capacity was nearly twice the capacity of standard weirs.

2. METHODOLOGY

2.1. Experimental Study

The experiments were carried out in a rectangular section open channel of 7 m in length, 0.50 m in width and 0.70 m in depth. At the last part of the channel whose sidewalls and base are concrete, weir used in experiments and made of fiberglass are placed. The shapes and other relevant parameters of the models used are Figures 6. and Table 1. is also given. The tested model a is perpendicular to the flow, the length of the weir is equal to the width of the channel, L = 50 cm long, and the angles they make with the horizontal are = 90 °. In the tested b model, L = 80 cm and α angle is 38.68 °. Weir model is preferred straight with an angle. In the tested c series, L = 80 cm and angle is 38.68 °. Weir model is triangular single-eyed. In the tested d series, weir model is triangular single chamber, L = 100 cm and weir angle α angle is 30 °. In the last series, the tested e series, that is, the triangular four-cavity weir model was preferred and L = 100 cm Weir angle α = 30 °. In the figures, plan views are given for a, b, c and d series.

a-series - straight
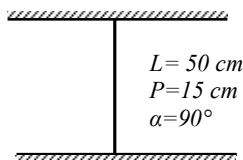
a) a1
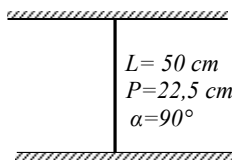
b) a2
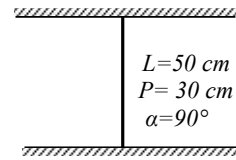
c) a3

a) Linear weir plan view

b-series - cross straight
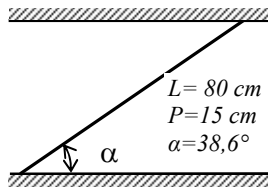
a) b1
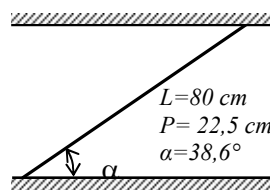
b) b2
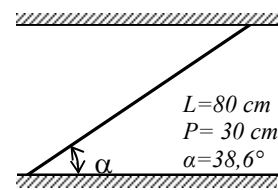
c) b3

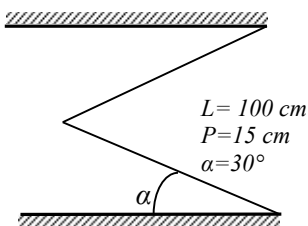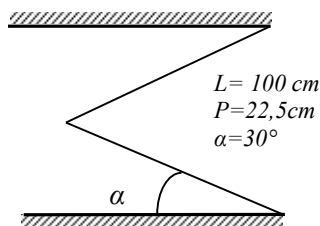b) Angled straight weir plan view

c-series-triangle
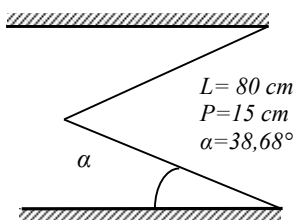
a) c1
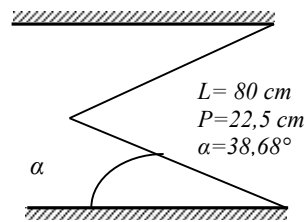
b) c2
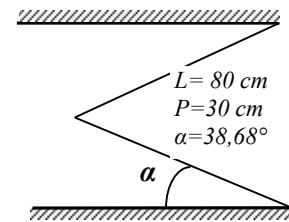
c) c3

c) Triangular labyrinth weir plan view for L = 80 cm
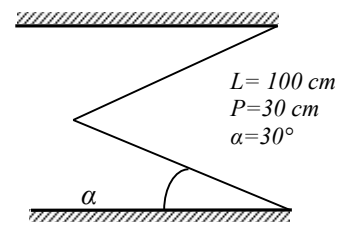
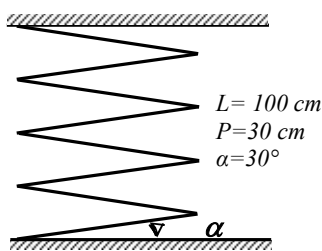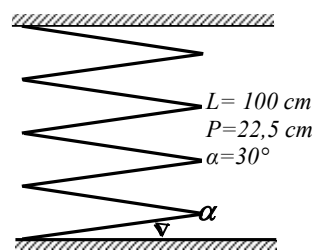d-series- triangle

a) c1

b) c2

c) c3

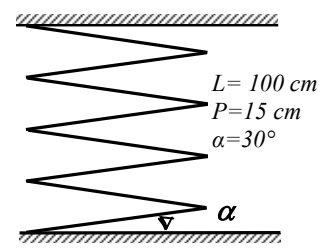d) Triangular labyrinth weir plan view for L = 100 cm

e-series – triangle

a) e1

b) e2

c) e3

e) Plan view of 4 compartment triangular labyrinth weir for L = 100 cm

Figure 6. Plan view of tested labyrinth weirs

Table 1. Features of the tested weir models.

Model type	Channel width (W) cm	Weir height (P) cm	Weir length (L) cm	Weir angle (α)	Plan view of weir
a1	50	15	50	90°	
a2	50	22,5	50	90°	
a3	50	30	50	90°	
b1	50	15	80	38,68°	
b2	50	22,5	80	38,68°	
b3	50	30	80	38,68°	
c1	50	15	80	38,64°	
c2	50	22,5	80	38,64°	
c3	50	30	80	38,64°	
d1	50	15	100	30°	
d2	50	22,5	100	30°	
d3	50	30	100	30°	
e1	50	15	100	30 °	
e2	50	22,5	100	30°	
e3	50	30	100	30°	

In each experiment, the flow rate delivered from the upstream, Q and the corresponding water height h were measured. The experiments were repeated according to limnimeter zero for flow rates between Q=10-100 l/s separately for each series.

The results found were compared with the FLOW-3D mathematical results. Images of the experimental study can be seen in Photo 1.
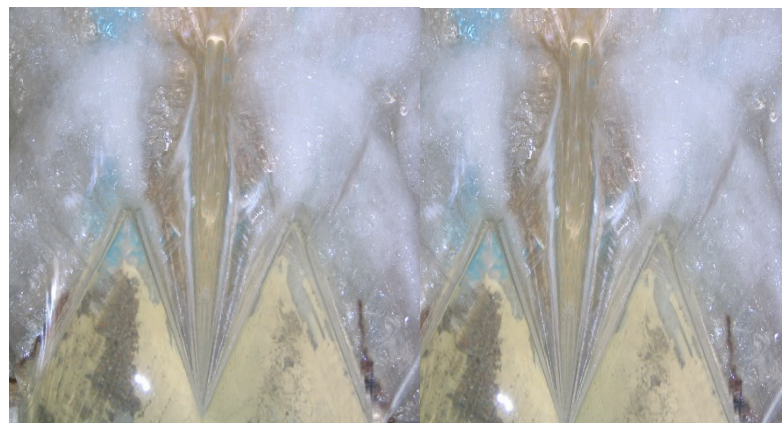

Photo 1. Photographs of the experimental study
(Top view of 4-span triangular labyrinth spillway flow conditions)

2.2. FLOW 3D and Mathematical Modeling

Within the scope of this study, the model types used in the experimental study were tested with the FLOW-3D mathematical method method and the results were compared with the experimental study. In the FLOW-3D mathematical modeling part of this study, taking into account the sensitivity of the measurement points, the mesh cell structure of the model is composed of three parts.

- The reservoir part where the flow is given to the channel: In order to ensure the uniformity of the flow conditions, the flow in the reservoir part is slowly filled from the bottom from a point source.
- Main channel: The section that is long enough for the flow to flow uniformly, where the flow passes by increasing the flow rate.
- Weir placement compartment: The section where the linear and labyrinth spillway is located, affecting the flow through the channel.

The program, which was run by making a precise modeling in this way, took an average of three days for each modeling, since the network cell structure affected the model run time. Sample pictures obtained from this model are given in Figure 7.
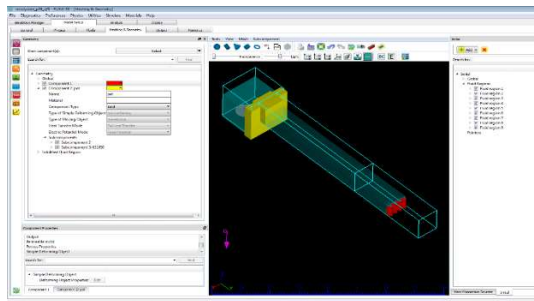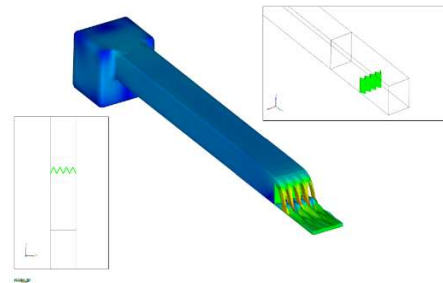

Figure 7. Model setup for labyrinth weir

Figure 8. Labyrinth weir plan view

The same experiments were tested again under experimental working conditions with the Flow-3D Model setup. Both linear spillway shape and 4-span labyrinth spillway shape were tested by increasing 10 lt / sec between Q = 10 - 100 lt / s. The labyrinth spillway features used:

    P: Weir height =30 cm
    L: Weir length = 100 cm
    N: Number of openings = 4 pieces.
    After running any current condition with FLOW-3D, current profiles of each study were taken in order to obtain the desired current profiles.

3. RESULTS AND DISCUSSION

In the studies conducted within the scope of this study, the effect of linear and labyrinth spillway models on spillway capacity was investigated. The water heights corresponding to the flow rates are given in Table 2., belonging to the upstream side obtained from the experimental and FLOW-3D mathematical model studies, belonging to the upstream where the flow is uniform and does not change anymore.

The results of the experimental study and the study with FLOW-3D, respectively. Figure 9. a) and 9.b). It is given graphically in. The use of the labyrinth spillway shape instead of the linear spillway shape has increased the capacity of the spillway due to the increase in the spillway.

For example, when h = 10 cm, the spillway discharge capacity is Q = 30 lt / s in the linear weir, while for the labyrinth spillway Q = 40 lt / s. As a result, labyrinth spillways will be able to discharge the same discharge capacity from upstream to downstream in a more secure way than linear spillways at lower flow heights. This situation is similar to the studies conducted with FLOW-3D.
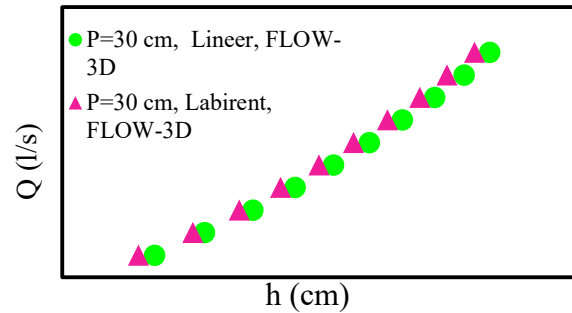
Table 2. Uniform current rate-flow heights

P: 30 cm,

L_{lineer}=50 cm, $L_{labirent}$=100 cm

Q (lt/sn)	Water depth (cm)			
	Experimental		FLOW-3D	
	Linear	Labyrint	Linear	Labyrint
10	3.90	2.65	4.48	3.70
20	6.80	5.35	6.9	6.35
30	9.15	7.70	9.24	8.59
40	11.15	9.75	11.29	10.60
50	13.15	11.50	13.16	12.46
60	14.9	13.20	14.9	14.14
70	16.55	14.80	16.5	15.78
80	18.00	16.20	18.06	17.35
90	19.40	17.50	19.49	18.67
100	20.65	18.90	20.73	20.00
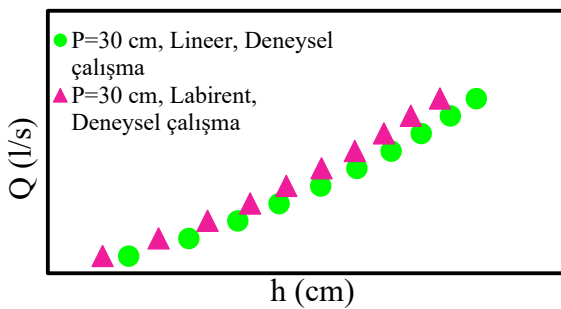
a) Experimental study   b) Working with FLOW-3D

Figure 9. Effect of linear and labyrinth spillway shape on flow capacity

The measurement results obtained by the FLOW-3D mathematical model study were compared with the results obtained from the experimental study. Therefore, the results obtained for both linear and labyrinth studies were compared with each other. As can be seen from Figure 10 a), the experimental and Flow-3D study results for linear spillways almost overlap on the graph. So the results are very close to each other. In the studies conducted for the labyrinth spillway, the results seem close to each other, albeit with a slight difference.
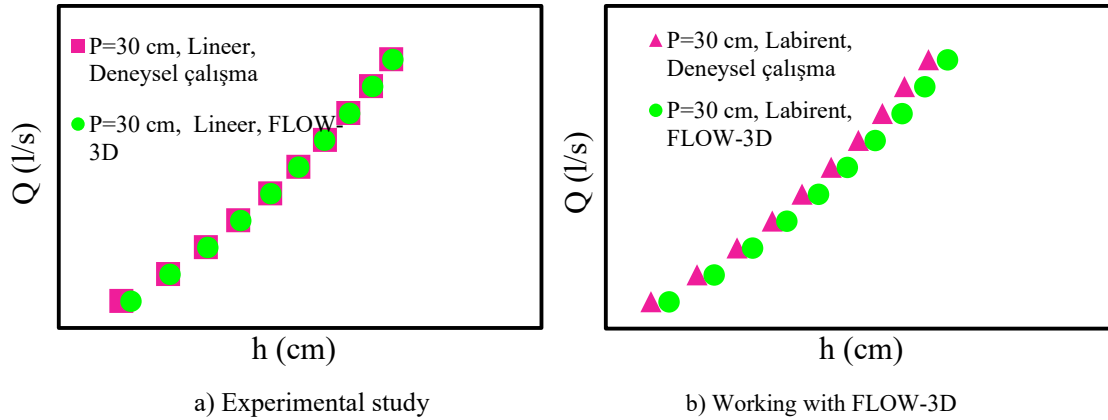
a) Experimental study   b) Working with FLOW-3D

Figure 10. Effect of linear and labyrinth spillway shape on flow capacity

4. CONCLUSIONS

A series of experiments were conducted to investigate the effects of labyrinth spillways on the flow capacity and the similarities and differences between the experimental study in hydraulic calculations and the results of FLOW-3D mathematical calculations, and the same test conditions were studied with the mathematical model. The results were compared with each other. The results obtained according to the studies carried out are as follows: When L=80 cm and L=50 cm linear weirs are compared, the discharged flow increases by 24% as the spillway length increases for a given flow height. When L=100 cm and L=80 cm labyrinth spillways are compared with each other, the spillway length increases, while the discharge capacity is 17% for the same spillway flow height.

For a given spillway length, the Cd coefficient increases as the spillway height decreases. For a constant h/L value in L=50 cm linear spillway test experiments; If the height of the spillway P=15 cm and the spillway heights of P=22.5 and P=30 cm are compared, the increase in the Cd coefficients is 3% and 8%, respectively. For L=80 cm linear spillway, the results are 2% and 7%, respectively, under the same conditions. If P=15 cm spillway height and P=22.5 and P=30 cm spillway heights are compared in labyrinth spillways with L=80 cm, N=1 openings, the increase in Cd coefficients is 5.7% and 10%, respectively. In labyrinth spillways with L=80 cm and N=4 openings, these increases are 4.4% and 9%. Despite the decrease in the spillway height, the increase in Cd coefficients is higher in labyrinth spillways.

In increases. If the labyrinth and linear spillways of the same height and length are compared with each other, the Cd values for all tested h/L ratios are approximately 15% greater in the labyrinth spillway. linear and labyrinth spillways, the Cd coefficient decreases as the weir length.

While experimental study results and FLOW-3D results have almost the same values for linear spillway, they show slightly close values for labyrinth spillway. Experimental studies are thought to give more reliable results, but it should be kept in mind that experimental studies cannot always be performed, considering laboratory facilities, time, labor and construction costs.

REFERENCES

Amanian, N., (1987). '' Performance and design of labyrinth spillways '' MSc thesis Utah State University, Logan, Utah.

Aydın, M. C. (2012). ''CFD simulation of free-surface flow over triangular bayrinth side weir. '' Advances in Engineering Software, Vol. 45, No. 1, pp. 159-166, DOI: 10.1016/j.advengsoft.2011.09.006.

Aydın, M. C. and Emiroğlu, M.E. (2013). ''Determination of capacity of labyrinth side weir by CFD.'' Flow Measurement and Instrumentation, Vol. 29, pp. 1-8, DOI: 10.1016/j.flowmeasinst.2012.09.008.

Azamathulla, H. (2014). ''Discussion of ''Orifice spillway aerator: Hydraulic design'' by V. V. Bhosekar, V. Jothiprakash, and P. B. Deolalikar.'' *Journal of Hydraulic Engineering,* Vol. 141, No. 1, 07014016-1, DOI: 10.1061/(ASCE)HY.1943-7900.0000932.

Azamathulla, H. M. and Ahmad, Z. (2013). ''Estimation of critical velocity for slurry transport through pipeline using adaptive neurofuzzy interference system and gene –expression programming.'' *Journal of Pipeline Systems Engineering and Practice,* Vol. 4, No. 2, pp. 131-137, DOI: 10.1061/(ASCE)PS.1949-1204.0000123.

Azamathulla, H. and Ahmad, Z. (2014). ''Closure to ''Estimation of critical velocity for slurry transport through pipeline using adaptive neuro-fuzzy interference system and gene-expression programming.'' by H. Md. Azamathulla and Z. Ahmad. ''*Journal of Ppipeline Systems Engineering and Practice*, DOI: 10.1061/(ASCE)PS. 1949- 1204.0000192 (In pres).

Azamathulla, H. M., Deo, M. C., and Deolalikar, P. B. (2008). ''Alternative neural Networks to estimate the scour below spillways. '' *Advances in Engineering Software,* Vol. 39, No. 8, pp. 689-698, DOI: 10.1016/j.advengsoft.2007.07.004.

Barati, R. (2011). ''Parameter estimation of nonlinear Muskingum models using Nelder- Mead simplex algorithm.'' *Journal of Hydrologic Engineering*, Vol. 16, No. 11, pp. 946-954, DOI: 10.1061/(ASCE)HE.1943-5584.0000379.

Barati, R. (2013). ''Aplication of Excel solver for parameter estimation of the nonlinear Muskingum models.'' *KSCE Journal of Civil Engineering*, Vol. 17, No. 5, pp. 1139-1148, DOI: 10.1007/s12205-013-0037-2.

Bilhan, O., Emiroğlu, M. E., and Kişi, O. (2011). ''Use of artificial neural Networks for prediction of discharge coefficient of triangular labyrinth side weir in curved channels.'' *Advances in Engineering Software*, Vol. 42, No. 4, pp. 208-214, DOI: 10.1016/j.advengsoft.2011.02.006.

Blanc P. and Lempeiere F. (2001) '' Labyrinth spillways have a promising future'' Reprinted from Hydropower and Dams Issue Four, 2001

Blanc P. and Lempeiere F. (2003) '' The Piano Keys Weir: a new cost effective solution for spillways'' Reprinted from Hydropower and Dams Issue Four, 2003

Cassidy, JJ., Gardner, C,A., and Peacock R.T. (1985) '' Boardman labyrinth crest '' J,Hydr, Engrg. ASCE 11 (3).

Crookston, B. M. (2010). *Labyrinth weirs*, PhD Thesis, Utah State University.

Crookston, B. M. and Tullis, B. P. (2012). ''Labyrinth weirs: Nappe interference and local submergence. '' *Journal of Irrigation and Drainage Engineering*, Vol. 138, No. 8, pp. 757-765, DOI: 10.1061/(ASCE)IR.1943-4774..0000466.

Crookston, B. M. and Tullis, B. P. (2013). '' Hydraulic design and analysis of labyrinth weirs. I: Discharge relationships.'' *Journal of Irrigation and Drainage Engineering*, Vol. 139, No. 5, pp. 363-370, DOI:10.1061/(ASCE)IR.1943-4774.0000558.

Dabling, M. R., Tullis, B. P., and Crookston, B. M. (2013). ''Staged labyrinth weir hydraulics. '' *Journal of Irrigation and Drainage Engineering*, Vol. 139, No. 11, pp. 955-960, DOI: 10.1061/(ASCE)IR.1943-4774.0000558.

Darvas, L. A. (1971) "Discussion on performance and design of labyrinth weirs" Journal of Hydraulic Division, A.S.C.E. p. 1246-1251.

Emiroğlu, M. E. and Kişi, O. (2013). ''Prediction of discharge coefficient for trapezoidal labyrinth side weir using a neuro-fuzzy approach.'' *Water Resources Management*, Vol. 27, No. 5, pp. 1473-1488, DOI: 10.1007/s11269-012-0249-0.

Emiroğlu, M. E., Cihan Aydin, M., and Kaya, N. (2014). ''Discharge characteristics of a trapezoidal labyrinth side weir with one and two cycles in subcritical flow.'' *Journal of Irrigation and Drainage Engineering*, Vol. 140, No. 5, 04014007-04014007-13, DOI: 10.1061/(ASCE)IR. 1943-4774.0000709.

Emiroğlu, M. E., Kişi, O., and Bilhan , O. (2010). ''Predicting discharge capacity of triangular labyrinth side weir located on a straight channel by using an adaptive neuro- fuzzy tecnique. '' *Advances in Engineering Software*, Vol. 41, No. 2, pp. 154-160, DOI:10.1016/j.advengsoft.2009.09.006.

Emiroğlu, M, E, (2010). ''Estimating Flow Characteristics of Different Weir Types and Optimum Dimensions of Downstream Receiving Pool'' Journal of Hydrology and Hydromechanics.

Falvey, H.T. (2003). ''Hydraulic Design of Labyrinth Weirs.'' *ASCE Press Pub., Virginia, USA.*

Emiroğlu, M. E., Bilhan, O., and Kişi, O. (2011). ''Neural Networks for estimation of discharge capacity of triangular labyrinth side-weir located on a straight channel. '' *Expert Systems with Applications*, Vol. 38, No. 1, pp. 867-874, DOI: 10.1016/Jj.eswa.2010.07.058.

SIMULTANEOUS LATERAL FLOW OVER WEIRS AND UNDER GATES (H-WEIRS)

First Author: Veysi KARTAL

Department of Civil Engineering, Engineering Faculty, Firat University

Elazıg, Turkey

E-mail Address: vkartal@firat.edu.tr

Second Author: M. Emin EMIROGLU

Department of Civil Engineering, Engineering Faculty, Firat University

Elazıg, Turkey

E-mail Address: memiroglu@firat.edu.tr

ABSTRACT: Combined weir-gate structure is an important structure to control and regulate the flow and measure discharge in the Hydraulic Engineering. The use of combined weir-gate is common for frontal flow in hydraulic structures. The lateral flow is complicated since flow conditions change along section. The present study investigates experimentally the lateral flow passing through combined weir-gate consists of rectangular sharp crested weir and rectangular side sluice gate installed in straight channel. In this study, a series of experiments was carried out in order to examine the hydraulic characteristics of side weir-gate structures according to dimensional analysis and experimental data. The results show that the discharge capacity of combined weir-gate is larger than that of the classical rectangular side weirs and rectangular side sluice gates. Finally, the empirically-obtained equations for discharge capacity of side weir-gate structures are compatible with the experimental data.

Key words: Hydraulic, lateral flow, combined weir-gate, discharge

1. INTRODUCTION

Discharge estimation or measurement in the open channels is one of the most important topics in the Hydraulic Engineering. Sediment deposition in the lateral intake region can be reduced by using combined weir-gate structure. Weirs and sluice gates have been used separately for many years as both a control and flow measurement structures in open channel flows. There are many studies in the literature about weirs and gates that operate separately from each other.

The lateral flow is discharged through structure placed parallel to the main flow direction (Fig. 1). Since the water is discharged out of the channel along the side weir, the discharge of the channel decreases along the x- direction. The specific energy (E) of the flow in the channel along the side weir is assumed to be constant ($E_1 \cong E_2$) in the studies of lateral flows (De Marchi, 1934; Domínguez, 1935) . Several studies were carried out to determine the hydraulic characteristics of the flow over the side weirs. (Borghei et al. 1999; Emiroglu et al., 2011; Bagheri et al., 2014). Emiroglu and Ikinciogulları (2016) used Domínguez Approach to determine discharge coefficient of classical rectangular side weir. Borghei et al. (1999) found that the effect of channel slope in subcritical flow regime is very small. They stated that the constant specific energy assumption in the channel across the side weir for subcritical flow is acceptable and they proposed an equation considering the dimensionless parameters of F_1 (upstream Froude number), the ratio of crest height to flow depth (p/y_1) and the ratio of weir length to main channel width (b_w/B). In addition to above dimensionless parameters, Emiroglu et al. (2011) also considered the ratio of weir length to flow depth (b_w/y_1). In particular, Emiroglu et al. (2010, 2014) found that the discharge capacities of the labyrinth side weirs

are higher than classical weirs. The flow through a side sluice gate is a typical case of spatially varied flow with decreasing discharge. Panda (1981), Ojha and Subbaiah (1997), Ghodsian (2003) and Esmailzadeh et al. (2015) studied the discharge coefficient of the side sluice gates. Panda (1981) and Ghodsian (2003) used the De Marchi approach for the discharge coefficient of side sluice gates. The weirs and sluice gates have advantages as well as disadvantages. The accumulation of sediment and floating materials from the bed in weirs and gates over time reduces the efficiency of the structure and also causes measurement errors and operational maintenance difficulties. So, many researchers try to develop and present methods for overcoming these problems. These problems can be overcome the use of combined weir-gate. Combined weir-gate structure has the advantages of both weir and gate. This useful structure can control the water flow, measure the flow rate pass through the combined weir-gate, avoiding the sedimentation behind the weir by passing the sediment through the gate. Ahmed (1985) pioneered to study the combination of rectangular weir with a rectangular gate. Ahmed (1985) tried to find a discharge coefficient for this combined structure. Then, Alhamid et al. (1997) showed that the combined structure has high efficiency and it can pass more suspended and bed loads sediment. Ferro (2000) presented an equation for estimating discharge for flow over and under the broad rectangular gate based on the dimensional analyses. Negm et al. (2002) experimentally evaluated the combined rectangular weir-gate structure for various conditions such as different geometry, different bed slope of channel and etc.; and finally, they represented an equation for all geometry and hydraulic conditions. Altan-Sakarya et al. (2005) investigated the combined weir-gate measuring the discharge of it. Samani and Mazaheri (2009) presented a physically based approach to estimate the discharge of weir-gates structure in frontal flow. Altan-Sakarya and Kokpınar (2013) studied combined weir-gate as well as weir. Salehi and Azimi (2019) reported that weir-gate structures with both sharp-crested weirs and weirs of finite crest length design can be used as a flow distributor in frontal flow. Altan-Sakarya et al. (2020) investigated combined weir gate and presented numerical results in addition to experiments. The studies given above related to weir-gates were conducted for frontal flows not lateral flows. However, Ghodsian et al. (2020) carried out an experimental study to determine the discharge coefficient of a side-combined structure in curved channels. The approach Froude number F_1, the ratio of approach flow depth to gate opening y_1/a, the ratio of gate height to gate opening d/a were considered. Equations proposed by researchers for rectangular side weir and sluice gates are given in Table 1.

Table 1. Equations proposed by researchers for rectangular side weir and sluice gate.

Eq. Number	Discharge coefficient equations	The authors	Type of side structure
Eq. (1)	$C_{dw} = 0.265 F_1^{-0.404} \left(\dfrac{h_1}{b_w}\right)^{-0.115} \left(\dfrac{h_1}{p}\right)^{0.134} \left(\dfrac{b_w}{B}\right)^{-0.086}$	Bagheri et al. (2014)	Classical Rectangular weir
Eq. (2)	$C_{dg} = 0.611 \left(\dfrac{y_1 - a}{y_1 + a}\right)^{0.216} (1 + 0.558 F_1^{0.1526})^{0.46}$	Ghodsian (2003)	Rectangular side sluice gate

The combined side weir-gate was used for lateral flow in a straight channel (see Fig. 1). There is a lack of information about combined side weir-gate in straight channels. Thus, investigation of the flow characteristics of weir-gates for lateral flow will contribute to literature and hydraulic designers. In the current study; the combined weir-gate was studied experimentally in order to analyze flow characteristics of combined weir-gate for lateral flow. The present study aims to determine the effect of parameters affecting the discharge of combined side weir-gate, predict the discharge of the combined side weir-gate and suggest equations for hydraulic design of combined side weir-gate structure.
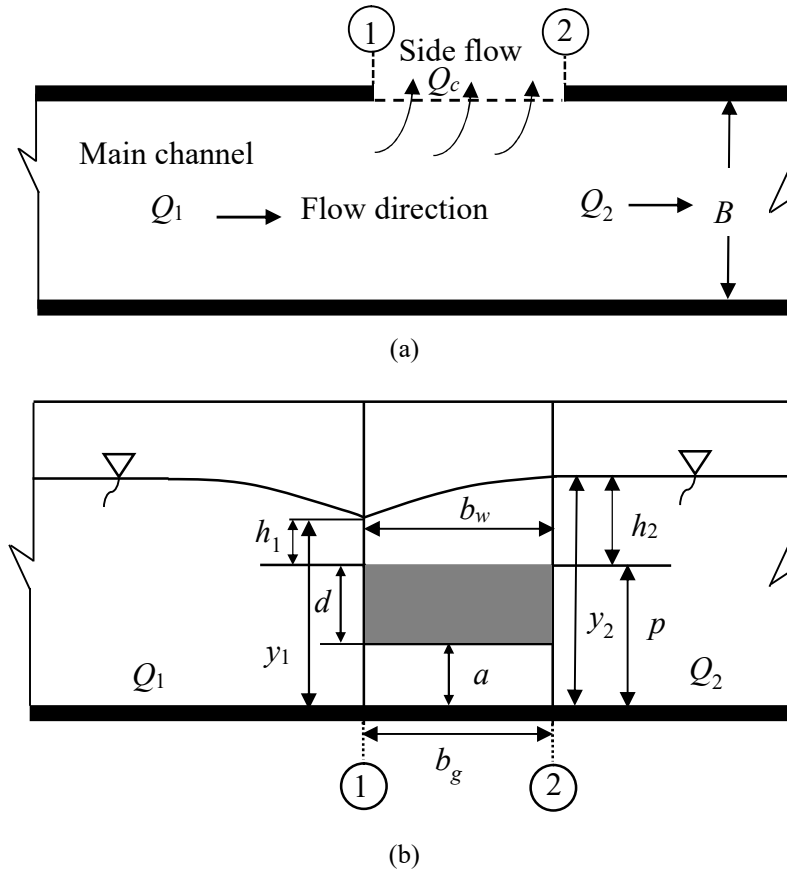
(a)

(b)

Figure 1. Sketch of side flow in a rectangular channel: (a) plan view, (b) frontal view of side combined weir-gate

2. THEORETICAL BACKGROUND

The dynamic equation of spatially varied flow for overflow over a weir is (Chow, 1959)

$$\frac{dy}{dx} = \frac{S_0 - S_f - \left(\frac{\alpha Q}{gA^2}\right)\left(\frac{dQ}{dx}\right)}{1 - \left(\frac{\alpha Q^2 B}{gA^3}\right)} \tag{3}$$

in which; x = distance along the side weir from upstream to downstream (m); S_0 = slope of main channel (-); S_f = slope of friction (-); α = kinetic energy correction coefficient (-); Q= discharge of main channel (m³/s); dQ/dx = unit discharge (m³/s/m); g = acceleration due to gravity (m/s²); A = cross-sectional area of flow (m²); ve B= width of main channel (m). The discharge at any section is (Chow, 1959)

$$Q = By\sqrt{2g(E - y)} \tag{4}$$

where E is the specific energy (m)

Unit discharge of side sluice gate was given by Ojha and Subbaiah (1997)

$$\frac{dQ}{dx} = -aC_{dg}\sqrt{2gy} \tag{5}$$

The conservation principles of the energy and continuity can lead to the theoretical base of the free flow over weir and under the gate as two parts of the hydraulic flow measurements structure. Theoretically if no energy is lost, well-known equations for evaluating the discharge over the weirs and under the sluice gates can be presented as in Eqs. (6) and (7), respectively. Figure 1 shows the definition sketch for the flow with the geometric parameters. The discharge of combined side weir-gate, Q_c

$$Q_c=Q_1-Q_2 \tag{6}$$

$$Q_c = Q_g+Q_w \tag{7}$$

in which Q_1 is the discharge of the main channel, Q_2 is the discharge at the downstream of the side structure. Using the energy conservation equation, the general discharge equations of a side sluice gate (Panda, 1981; Ghodsian, 2003) and a side weir (Bagheri et al., 2014) are, respectively:

$$Q_w = C_{dw}\frac{4}{15}b_w\sqrt{2g}\left(\frac{h_2^{2.5} - h_1^{2.5}}{h_2 - h_1}\right) \tag{8}$$

$$Q_g = C_{dg}ab_g\sqrt{2gy_1} \tag{9}$$

$$Q_c = C_{dw}\frac{4}{15}b_w\sqrt{2g}\left(\frac{h_2^{2.5} - h_1^{2.5}}{h_2 - h_1}\right) + C_{dg}ab_g\sqrt{2gy_1} \tag{10}$$

C_{dw} and C_{dg} are discharge coefficient of side weir and sluice gate, respectively. b_g is the length of side sluice gate (m); a is the opening of side sluice gate (m), h is piezometric height over the weir (m), and b_w is the weir length (m). Subscripts 1 and 2 refer to upstream and downstream sections, respectively.

2.1. Dimensional Analysis

The parameters affecting discharge capacity of combined side weir-gate were written in Eq. (11)

$$\Phi(Q_c, a, b, B, h, d, S_o, y_1, \mu, \sigma, g, \rho) = 0 \tag{11}$$

where B is the width of the main channel (m); Since length of weir and sluice gate was equal to each other ($b_g = b_w=b$), b was taken into consideration (b (m)) in the study. d (m) is the distance from the top of the sluice gate to the crest ($d=p-a$). y_1 is the upstream flow depth of the main channel (m); σ is the surface tension (kg/s^2); μ is the dynamic viscosity of water (kg/m s); and ρ is the mass density of water (kg/m^3); g is the gravitational acceleration (m/s^2)

By choosing ρ, g, and a as repeated variables, the following dimensionless functional relationship can be derived according to the Buckingham Π-theorem:

$$\Phi\left(\frac{\frac{Q_c}{b}}{\sqrt{g}\,a^{1.5}}, \frac{y_1}{a}, \frac{b}{B}, \frac{b}{a}, \frac{h}{b}, \frac{d}{a}, \text{Re}, \text{F}_1, \text{We}, S_o\right) = 0 \tag{12}$$

in which F_1, Re, and We are Froude number, Reynolds number, and Weber number at the upstream section of combined side weir-gate, respectively. The slope of main channel (S_0) can be disregarded (Borghei et al. 1999). Neglecting the effect of viscosity and surface tension ($\text{Re} > 200{,}000$ and $\text{We}>40$) according to Negm et al. (2002), Eq. (12) becomes:

$$\Phi\left(\frac{\frac{Q_c}{b}}{\sqrt{g}\,a^{1.5}}, \frac{y_1}{a}, \frac{b}{B}, \frac{b}{a}, \frac{h}{b}, \frac{d}{a}, F_1\right) = 0 \tag{13}$$

If necessary arrangements are made:

$$\frac{\frac{Q_c}{b}}{\sqrt{g}\,a^{1.5}} = f_1\left(\frac{y_1}{a}, \frac{b}{B}, \frac{b}{a}, \frac{h}{b}, \frac{d}{a}, F_1\right) \tag{14}$$

3. METHODOLOGY

The experimental study was carried out at the Hydraulic Laboratory of the Firat University, Turkey. Experiments were conducted in a rectangular channel (see Fig. 2). The main channel walls were made of Plexiglas and supported by steel frames. The width, height and length of the main channel are 0.4 m, 0.5 m, and 12.5 m, respectively. An evacuation channel with 1.20 m width, 0.40 m height with angle of $\alpha = 90°$ to the main channel was set at the outer bank of the channel. It is below 0.61 m from the base of main channel. Several rectangular side weir-gates with different geometries (i.e.; $a = 0.02$, 0.03 m, and 0.04; $b_w = b_g = 0.04$, 0.06, 0.08 m); $p = 0.06$, 0.09, and 0.12 m) were used to investigate for the combined side weir-gate flow. The slope of the main channel is constant (i.e., $S_0 = 0.11\%$). The combined weir-gate structures were placed at the entrance of the evacuation channel (see Fig. 1a). The piezometric heads over the weir were taken higher than 0.03 m in all experiments. There is a water tank at the end of the main channel for recirculating by pump. In this study, the discharge of main channel was between 0.010 and 0.046 m³/s and was measured by the electromagnetic flowmeter (Krohne, ±0.01 L/s accuracy) installed on the supply line. A calibrated sharp-crested triangular weir at the end of evacuation channel was used to measure the downstream discharge (Q_c). The flow depth was adjusted in via a control gate at the end of the main channel. Flow depths were measured by using a digital limnimeter (Mitutoyo, ±0.1 mm accuracy) set in the gauge car at three points (upstream, centerline and downstream) for both center and bank of side structures. Flow depths were measured after about 10-15 minutes from the beginning of experiments until the steady state flow conditions were occurred. The experiments were conducted under free flow condition in the evacuation channel. The main channel flow was always in subcritical conditions ($F_1 < 1$) for all experiments tested.
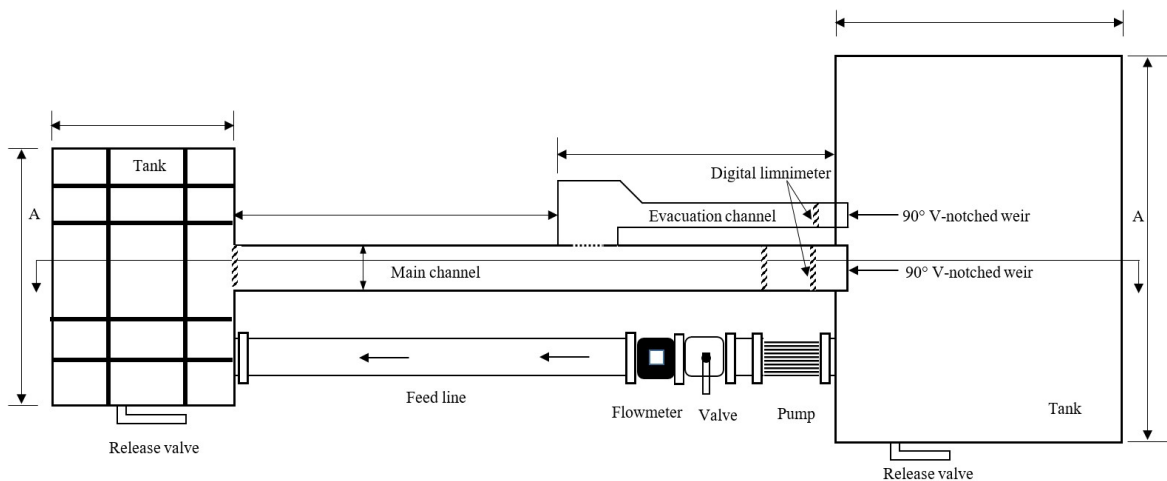
(a) plan
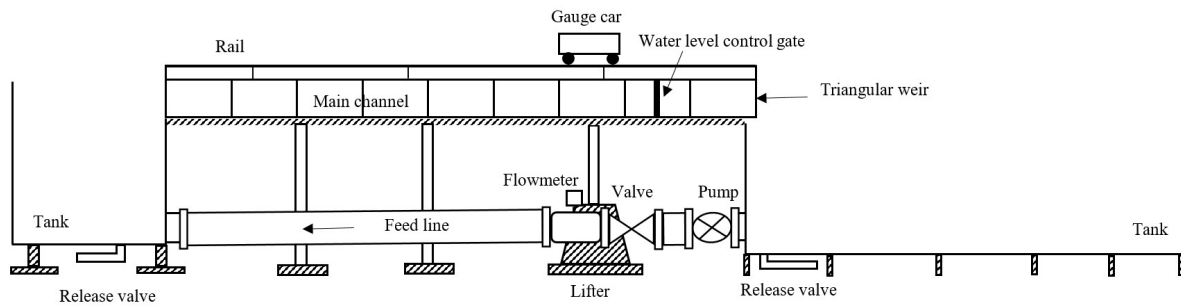
(b) A-A cross section

Figure 2. Experimental setup: (a) plan, (b) A-A cross section

4. RESULTS AND DISCUSSIONS

4.1 Constancy of Energy

The specific energy was calculated using the measured upstream and downstream flow depths and velocity heads ($E_i = h_i + \frac{V_i^2}{2g}$). Where i=1 represents the upstream of weir-gate structure and i=2 represents the downstream end of weir-gate structure. The variation of specific energy at upstream and downstream of side weir-gate is given in Fig. 3. The average difference between E_1 and E_2 is about 1.46%. Borghei et al. (1999) estimated a 3.7% value for conventional rectangular side weir.
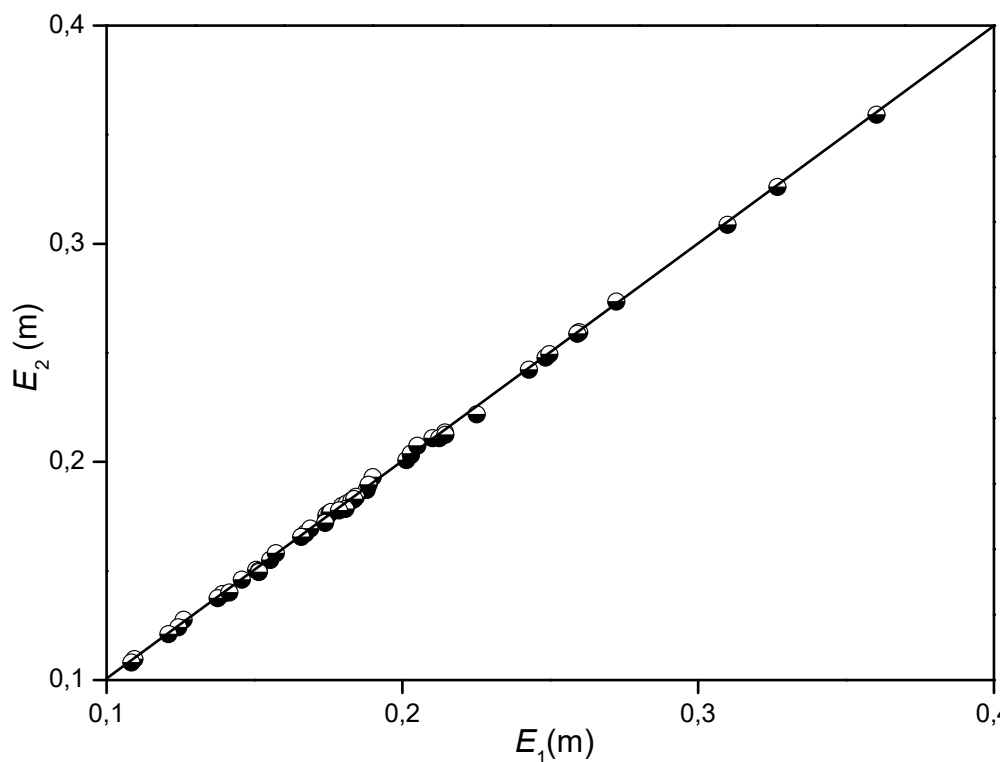
Figure 3. The variation of specific energy at upstream and downstream of side weir-gate

4.2 Flow Characteristics of Combined Side Weir-Gate

The findings for the combined side weir-gate are discussed in the following sentences. The water surface profile along the centerline of combined side weir-gate is given in Fig. 4. As seen in Fig. 4, water surface changes along the side structure. The water surface fluctuates with the increase of

upstream Froude number. There are large differences between in the upstream and downstream flow depths at the side of structure for high Froude numbers.
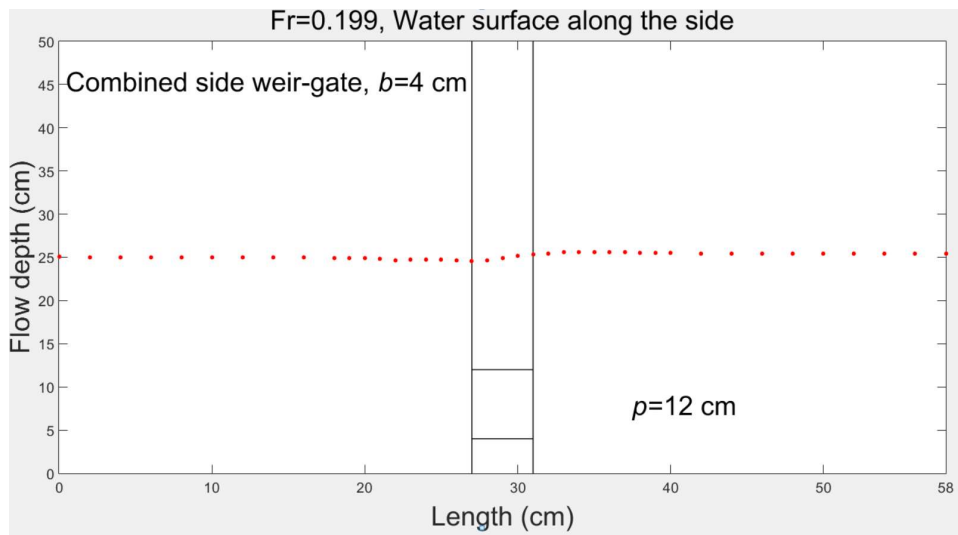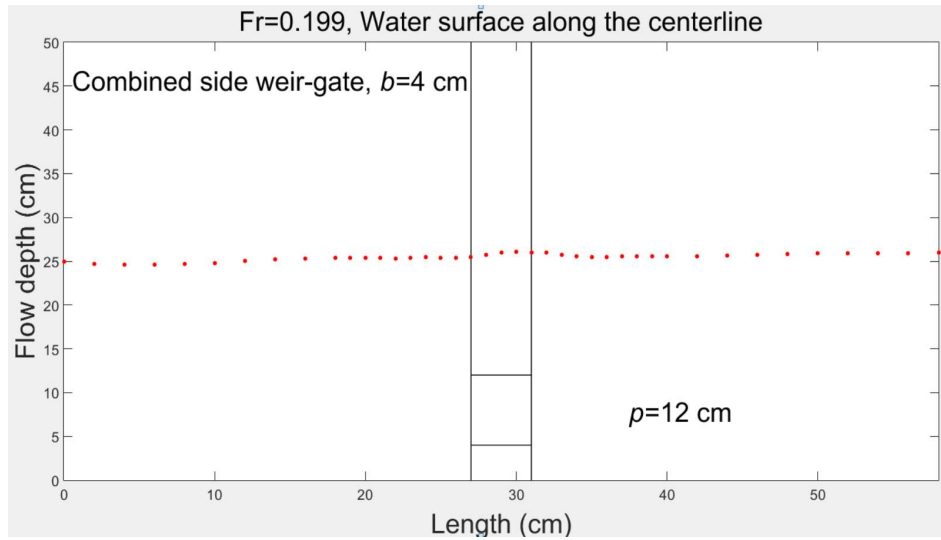

(a)

(b)

Figure 4. The variation of water surface profile of combined weir-gate: (a) along the centerline, (b) along the side.

The variation of $\frac{Q_c/b}{\sqrt{g}\,a^{1.5}}$ with a/y_1 under different conditions is given in Fig. 5. It is clear that the $\frac{Q_c/b}{\sqrt{g}\,a^{1.5}}$ of side weir-gate decreases with the increase of a/y_1 as seen in Fig. 5.
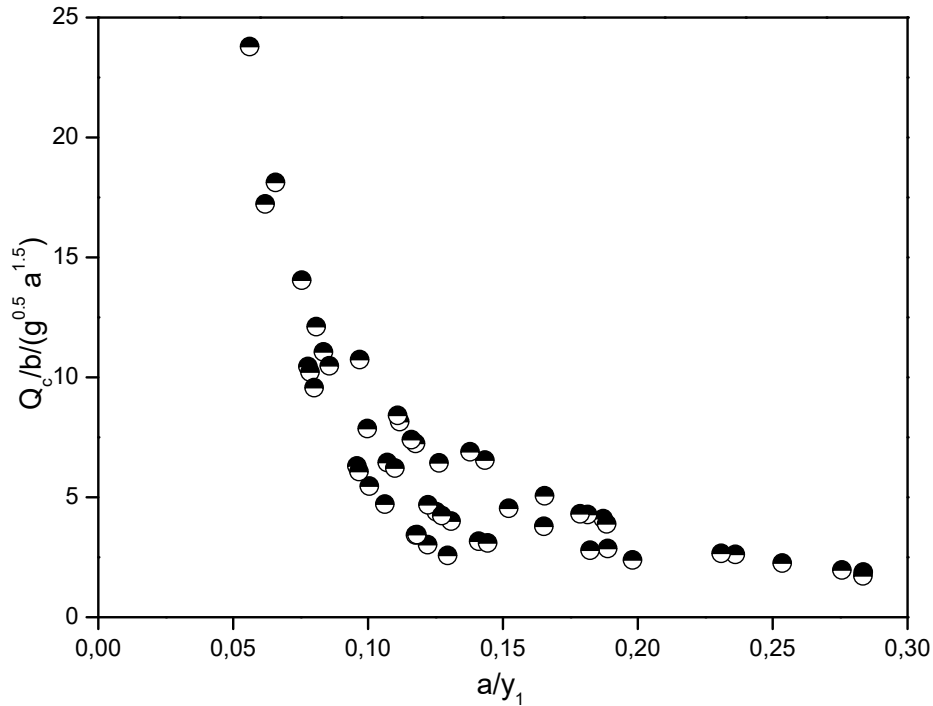
Figure 5. The variation of $\frac{Q_c/b}{\sqrt{g}\,a^{1.5}}$ with a/y_1 under different conditions

4.3 Flow Characteristics of Combined Side Weir-Gate

An equation for combined side weir-gate were proposed according to results obtained from the experiments. Equation (15) was proposed to predict $\frac{Q_c/b}{\sqrt{g}\,a^{1.5}}$ parameter of combined weir-gate in lateral flows. On the basis of the dimensional analysis of combined side weir-gates and by using the least squares error, the following equation was obtained to predict the $\frac{Q_c/b}{\sqrt{g}\,a^{1.5}}$ ($R^2=0.99$):

$$\frac{Q_c/b}{\sqrt{g}\,a^{1.5}} = 0.48 F_1^{-0.11} \left(\frac{a}{y_1}\right)^{-0.62} \left(\frac{b}{B}\right)^{-0.15} \left(\frac{d}{a}\right)^{-0.13} \left(\frac{b}{a}\right)^{0.284} \tag{15}$$

On the basis of the dimensional analysis of side weir and sluice gates and by using the least squares error, the comparison of the measured and predicted values of $\frac{Q_c/b}{\sqrt{g}\,a^{1.5}c}$ from the obtained equation (Eq. (15) is given in Fig. 6. As seen in Fig. 6, The predicted and observed values of $\frac{Q_c/b}{\sqrt{g}\,a^{1.5}}$ are compatible with each other ($R^2=0.99$)
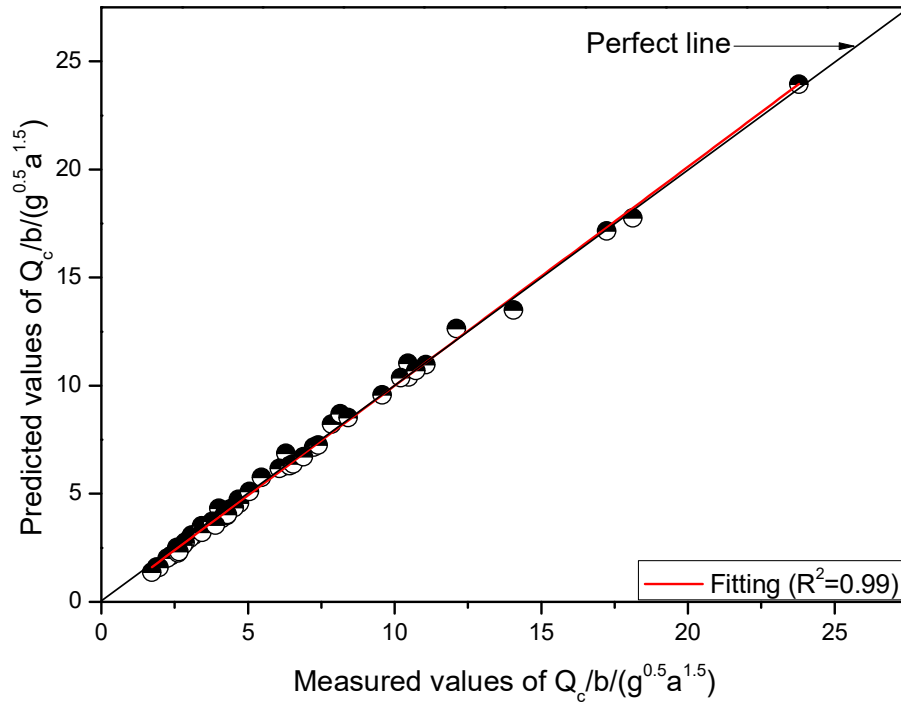
Figure 6. The comparison of the measured and predicted values of $\frac{Q_c/b}{\sqrt{g}\ a^{1.5}}c$ from Eq. (15)

The comparison of the discharge capacity of combined weir-gate with that of side sluice gate and weir was shown in Fig. 7. The discharge capacity of side sluice gate using C_{dg} proposed by Ghodsian (2003) (Eq. 2) and weir using C_{dw} suggested by Bagheri et al. (2014) (Eq. 1) was plotted in addition to present study. As seen in Fig. 7, the discharge capacity of all side structures decreased with the increase of the Froude numbers. Higher flow rates were obtained for smaller Froude numbers. In particular, the flow rate of side sluice gate increases in a limited number with the increase in flow depth, while there are noticeable increases in weir and combined weir-gate.
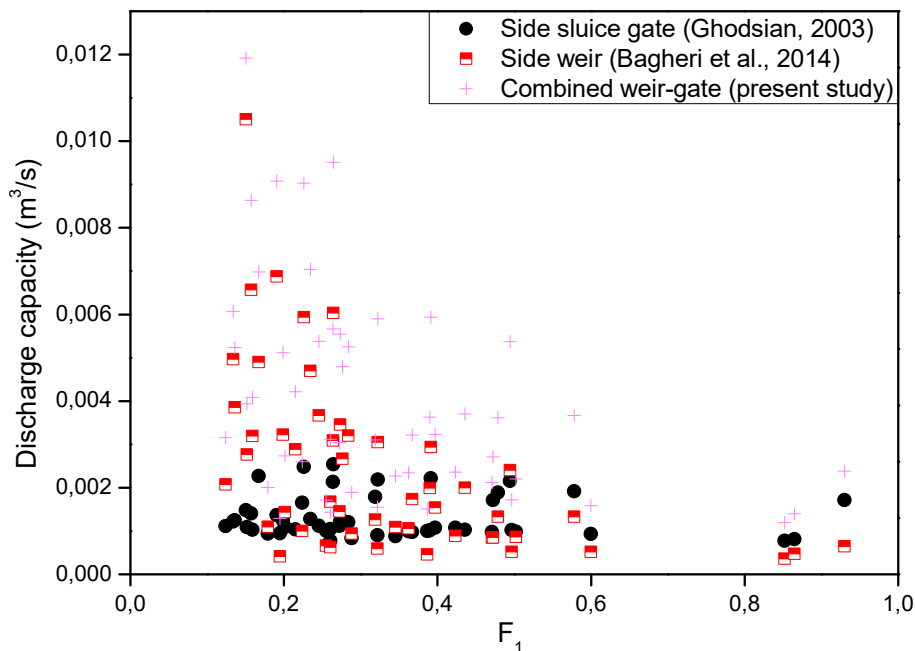

Figure 7. The comparison of discharge capacity of present study with side weir (obtained from Eq. (1) and side sluice gate (obtained from Eq. (2))

In addition, it was observed the flow fluctuates with the increase of upstream Froude number and jet there is small deviation between side weir and sluice gate jet trajectory in small Froude numbers, but these deviations increased as Froude number increased. The side flow discharged over weir and under the sluice gate always contact with each other under the crest heights and small Froude numbers but this didn't occur for large crest height and high Froude numbers. The weir flow broke the energy of the sluice gate flow. The flow over side weir broke flow under the sluice gate in small Froude numbers.

5. CONCLUSIONS

This study presents experimental results of flow through combined side weir-gate. An empirical equation is suggested for combined side weir-gate. The findings from the study was summarized below.

- The parameter $\frac{Q_c/b}{\sqrt{g}\,a^{1.5}}$ of combined side weir-gate is a function of approach Froude number, a/y_1, d/a, b/a, h/b and b/B.
- The discharge capacity of combined side weir-gate decreases with the increase of upstream Froude number.
- The flow fluctuates with the increase of upstream Froude number and jet there is small deviation between side weir and sluice gate jet trajectory in small Froude numbers, but these deviations increased as Froude number increased.
- The flow over side weir broke flow under the sluice gate in small Froude numbers.

Notations

a	Opening of side sluice gate (m)
B	Width of main channel (m)
b	Length of side structure (m)
C_d	Discharge coefficient (-)
d	Distance from the top of the sluice gate to the crest (m)
E	Specific energy (m)
F	Froude number (-)
g	Acceleration due to gravity (m/s^2)
h	Piezometric head over the weir (m)
p	Crest height (m)
Q	Discharge (m^3/s)
Re	Reynolds number (-)
S_0	Slope of main channel (-)
S_f	Slope of friction (-)
V	Flow velocity (m/s)
We	Weber number (-)
x	Distance along the side structure (m)
y	Flow depth (m)
α	Kinetic energy coefficient (-)
μ	Dynamic viscosity (kg/m s)
ρ	Mass density of water (kg/m^3)
σ	Surface tension (N/m)

Subscripts

c	Combined Side-Weir-Gate
g	Side Sluice Gate
m	Measured
w	Side Weir
p	Predicted
1	Upstream Section Of Lateral Structure
2	Downstream Section Of Lateral Structure

REFERENCES

Ahmed FH. Characteristics of discharge of the combined flow through sluice gates and over weirs J Engineering and Technology, Iraq,1985; 3(2): 49-63 (in Arabic).

Alhamid AA, Negm AAM, Al-Brahim AM. Discharge equation for proposed self-cleaning device. J King Saud University-Engineering Sciences 1997; 9(1): 13-23.

Altan-Sakarya B, Ozaydin V, Kokpinar MA. Birlesik çalısan savak ve kapaklarda debi ölçümü. II. Ulusal Su Mühendisligi Sempozyumu. 2005; 245–253. (in Turkish)

Altan-Sakarya AB, Kokpinar MA. Computation of discharge for simultaneous flow over weirs and below gates (H-weirs). Flow Measur Instrum 2013; 29: 32-38.

Altan-Sakarya AB, Kokpinar MA, Duru A. Numerical modelling of contracted sharp-crested weirs and combined weir and gate systems. Irrig Drain 2020; 69(4), 854-864.

Bagheri S, Kabiri-Samani AR, Heidarpour M. Discharge coefficient of rectangular sharp-crested side weirs Part II: Domínguez's method. Flow Measur Instrum 2014; 35:116-121

Borghei SM, Jalili MR, Ghodsian M. Discharge coefficient for sharp-crested side weir in subcritical flow. J Hydraul Eng ASCE 1999; 125(10): 1051-1056.

Chow VT. Open channel hydraulics. New York; McGraw-Hill: 1959.

De Marchi G. Essay on the performance of lateral weirs. L' Energia Electtrica, Milan 1934;11(11):849–60 [in Italian].

Domínguez FJ. Hidráulica. 1st ed., Nascimento editor, Santiago, Chile; 1935; Domínguez FJ. 6th ed. Editorial Universitaria, Santiago, Chile; 1999 (in Spanish).

Emiroglu ME, Kaya N, Agaccioglu H. Discharge capacity of labyrinth side weir located on a straight channel. J Irrig Drain Eng ASCE 2010; 136(1):37-46.

Emiroglu ME, Agaccioglu H, Kaya N. Discharging capacity of rectangular side weirs in straight open channels. Flow Measur Instrume 2011; 22(4): 319-330.

Emiroglu ME, Aydin MC, Kaya N. Discharge characteristics of a trapezoidal labyrinth side weir with one and two cycles in subcritical flow. J Irrig Drain Eng ASCE 2014; 140(5): 04014007.

Emiroglu ME, Ikinciogullari E. Determination of discharge capacity of rectangular side weirs using Schmidt approach. Flow Measur Instrum 2016; 50: 158-168.

Esmailzadeh M, Heidarpour M, Eslamian SS. Flow characteristics of a sharp-crested side sluice gate. J Irrig Drain Eng ASCE 2015; 141(7): 06014007.

Ferro V. Simultaneous flow over and under a gate. J Irrig Drain Eng ASCE 2000; 126(3): 190-193.

Ghodsian M. Flow through side sluice gate. J Irrig Drain Eng ASCE 2003;129(6): 458-463.

Ghodsian M, Feyzollahi F, Ghodsian M. Flow through side-combined structure in a channel bend under subcritical flow regime. ISH J Hydraul Eng 2020: 1-9.

Negm AAM, Al-Brahim AM, Alhamid AA. Combined-free flow over weirs and below gates. J Hydraul Res 2002; 40(3): 359-365.

Ojha CSP, Subbaiah D. Analysis of flow through lateral slot. J Irrig Drain Eng ASCE 1997; 123(5): 402-405.

Panda S. Characteristics of side sluice flow (ME Thesis). Univ. of Roorkee, Roorkee, India: 1981.Salehi S, Azimi AH. Discharge characteristics of weir-orifice and weir-gate structures. J Irrig Drain Eng ASCE 2019; 145(11): 04019025.

Samani JM, Mazaheri M. Combined flow over weir and under gate. J Hydraul Eng ASCE 2009; 135(3): 224-227.

FRICTIONAL PRESSURE LOSSES IN SEDIMENT TRANSPORTING CLOSED CONDUITS

Pelin İlker

Civil Engineering Department, Izmir Katip Celebi University

Izmir, Cigli, Turkey

pelin.ilker@ikcu.edu.tr

Prof. Dr. Mehmet Sorgun

Civil Engineering Department, Izmir Katip Celebi University

Izmir, Cigli, Turkey

mehmet.sorgun@ikcu.edu.tr

ABSTRACT: One of the key areas of interest in hydraulic engineering is the efficient sediment transport through pipelines. Sediment transport is influenced by shear stress acting on the sediment particles. Considering shear stress and pressure drop are directly related, precise pressure drop prediction is essential for transporting sediment particles with water. For calculating frictional pressure losses, the friction factor is a critical component. It is intended that by doing so, the friction factor, and accordingly, the frictional pressure loss can be predicted. To that end, statistical technique is used and a friction factor equation is developed in this study. In this regard, the main variables impacting friction factor are determined by employing dimensional analysis.

1. INTRODUCTION

One of the most important concerns in hydraulic engineering is the proper transportation of sediment through pipes. Many researchers have been working on this subject both experimentally and using a wide variety of numerical approaches over the years.

Two-phase flow occurs, according to Zandi and Govatos [1], when solid particles are coarse and have a high density, and the mean velocity of flow allows for partial separation of the solid particles from the fluid. The rheological properties of the fluid are relatively unaffected by these coarse solid particles. The solid and liquid phases behave differently. The particles move because they are suspended. The suspended load was analyzed by Rijn [2], as the depth-integration of the product of the local concentration and flow velocity. A new expression was presented that defines the reference concentration as a function of local flow parameters and sediment properties, as well as the parameters that drive suspended load transfer were examined. To verify the accuracy of the expression, the total bed material load was compared between predicted and experimental values.

A large scale experimental study was conducted by Tomren et al. [3] with high fluid velocities. They stated that the higher velocities are more efficient for the proper sediment transport. They also observed that the high viscous fluids showed better performance than the low viscous ones.

An extensive experimental study was carried out and a sediment transport model for high angle wellbores including horizontal wells was developed by Larsen et al. [4] They presented empirical correlations and they observed that the model worked well when compared the experimental data with the model predictions.

For determining the settling velocity of individual natural sediment particles, an explicit and simple formula was established by Cheng [5]. The formula works for a variety of flow regimes. The

proposed formula exhibits a good level of prediction accuracy when compared to available experimental data.

Kokpinar and Gogus established a novel empirical correlation to determine sediment transport critical flow velocity in horizontal pipelines [6]. When compared to experimental data, the accuracy of the empirical correlation was found to be satisfactory. The empirical equation may be applied reliably for non-cohesive, uniform, and non-uniform coarse particles, according to the researchers.

Sumer et al. [7] conducted an experimental investigation on the impact of an external turbulence field on the movement of bed load sediment in an open channel. The current findings would help improve their prediction capability for sediment transport estimations in conjunction with scour around maritime infrastructure such as pipelines, piles, pile-supported platforms, and subsea structures, as well as bed form shape projections, according to the researchers.

Various models and correlations for threshold velocities in horizontal conveying systems, such as incipient motion, pickup from a layer of particle, pickup from a deposit, boundary saltation, and minimum pressure velocities, were summarized and compared in the thorough work of Rabinovich and Kalman [8]. Furthermore, it was demonstrated that for short conveyance systems, there is no need to offer a fluid velocity greater than the saltation velocity, and that it can be substantially lower. The entire saltation length, which must be equal to or greater than the system length, can be used to determine an accurate fluid velocity value.

Rice et al. [9] thoroughly investigated the difference between the critical deposition velocity at low solids volume fractions and that at zero volume fractions. Based on experimental results and data from the literature, a new method for identifying the critical velocity was presented, and equations for the appropriate particle Reynolds number were produced.

The influence of carrier fluid viscosity on single-phase particle transport in a horizontal pipe was explored experimentally by Najmi et al [10]. The effect of particle size, particle concentration, and particle shape was investigated using two different particle kinds. Experiments revealed that increasing particle size and particle concentration in the studied regions increased critical velocity. Two sets of tests in laminar and turbulent flow were conducted to investigate the effect of viscosity. The viscosity effect on particle movement was shown to be dependent on the liquid flow regime. In laminar flow, as viscosity rises, critical velocity falls, whereas in turbulent flow, as viscosity rises, critical velocity rises.

Zorgani et al. [11] performed an experimental research on sand particle behavior and sand transport velocity for varied fluid viscosities. The sand minimum transport condition was found to be controlled by fluid viscosity, and the sand/liquid flow regimes at different transport conditions were discovered to be distinct. Because of the lack of turbulence energy, sand movement is mostly via shear force with high viscosity, and no sand dunes have been recorded. Furthermore, as the sand concentration increased, no change in the sand flow regime was observed. They stated that, the correlations from past researches were unable to predict measured sand movement velocities. Therefore, to better account for fluid viscosity, a new correlation would be required.

Shirazi and Frigaard [12] provided a steady-state three-layer mechanistic model for solid-liquid flow to predict pressure loss, critical velocity, and concentration profiles. They also developed a formula for turbulent solids diffusivity correlation. The convenient results were obtained when the projected data derived from the steady-state model and the proposed correlation were compared to the experimental data accessible in the literature.

Azamathulla and Ahmad [13] investigated the critical velocity as a design parameter in sediment transport systems to prevent the obstruction of the pipeline by using Gene- expression programming (GEP) and Adaptive neuro-fuzzy inference system (ANFIS) techniques and the GEP and ANFIS results were compared with the empirical data available in the literature. They inferred that the models gave better results than those obtained from the formula in the literature. They also developed a formula with the GEP model for the prediction of the critical velocity. They obtained considerable results when compared with the existing data.

Another investigation was carried out using supervised machine learning methods by Singh et al. [14] To determine pressure losses, data-driven statistical learning models were used, and the results were compared to those from experiments and empirical formulas from previous works. The statistical supervised learning method was shown to be effective and relevant to actual drilling operations.

2. THEORY

The flow of fluid in the space between two pipes is known as an annular flow. Flow and heat transport difficulties in annuli, both concentric and eccentric, have aroused researchers' interest for many years. As a result, proper annular flow analysis is critical. The gap between two cylinders, one inside the other, is known as the annulus. The following is the definition of eccentricity:

$$e = \frac{\delta}{(r_o - r_i)} \tag{1}$$

where δ is offset distance between the center of inner and outer pipes, r_i is outer radius of inner pipe r_o is inner radius of outer pipe. For concentric annuli, e=0, while for a fully eccentric annuli, e=1 [15,16]. Figure 1 illustrates the annular geometries.
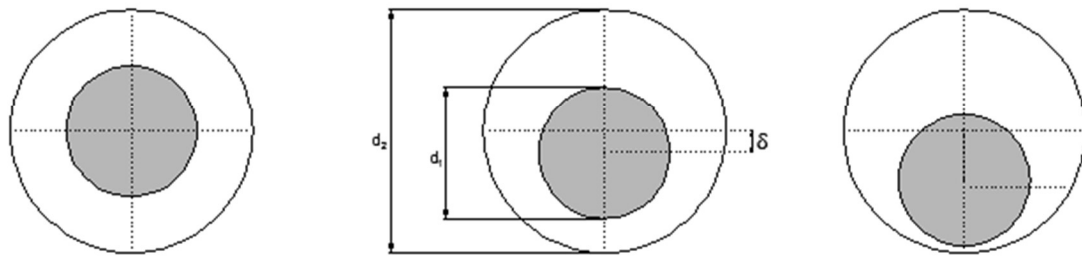

Figure 1. Representative Concentric, Partially Eccentric and Fully Eccentric Annulus [16]

Experimental studies for the sediment transport in the annulus were conducted by Sorgun [17]. In this study, experimental data from the work of Sorgun are used and major variables affecting friction factor are determined as:

$$f = funf(v, \rho, \mu, D_h \, \Omega, g, \theta, Sc) \tag{2}$$

where v is the fluid velocity (L/T), ρ is the fluid density (M/L³), μ is the dynamic viscosity (M/LT), Ω is the inner pipe rotation speed (1/T), Do is the outer pipe diameter (L), Di is the inner pipe diameter (L), Dh = Do – Di (hydraulic diameter), S_c is the sediment concentration, g is gravitational acceleration (L/T²), and θ is hole inclination.

Dimensional analysis has been conducted by using Buckingham-Pi theorem and following dimensionless π parameters are found:

$$\pi_1 = \rho v D / \mu \tag{3}$$

$$\pi_2 = (v^2)/gD \tag{4}$$

$$\pi_3 = S_c \tag{5}$$

$$\pi_4 = \theta \tag{6}$$

$$\pi_5 = (\Omega \, D)/v \tag{7}$$

3. RESULTS AND DISCUSSION

Darcy friction factor can be written as

$$f = func\ (\pi_1, \pi_2, \pi_3, \pi_4, \pi_5) \tag{8}$$

Relation between friction factor and dimensionless groups are presented in Figure 2-6. As seen from Fig.2 and Fig.3, as the Reynolds Number and Froude Number increase, friction factor decreases. Therefore, while the Re number increases, the effect of Reynolds number approaches zero, and the other parameters become significant. However, if Fig. 4-6 are analyzed, no significant relation between the dimensionless groups π_3, π_4, π_5 and friction factor are observed.
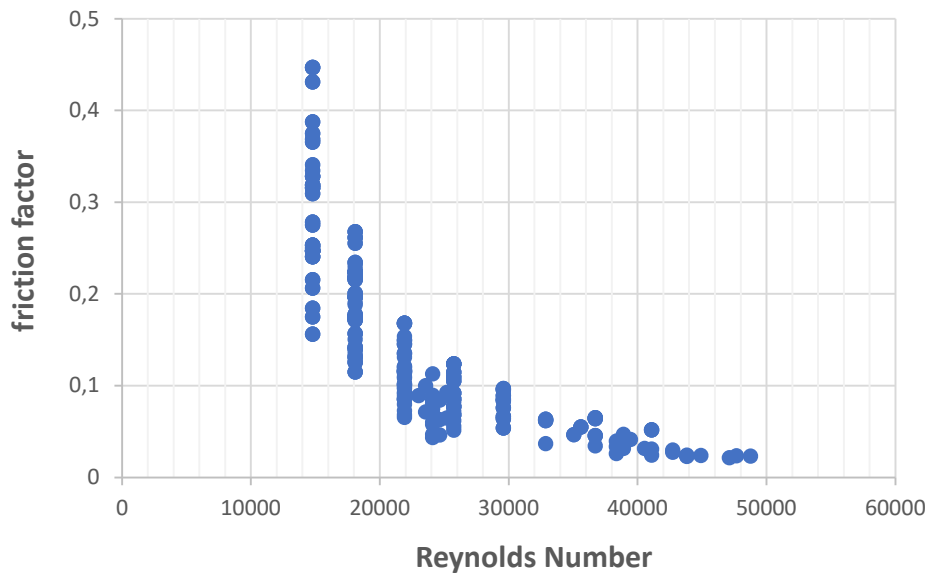
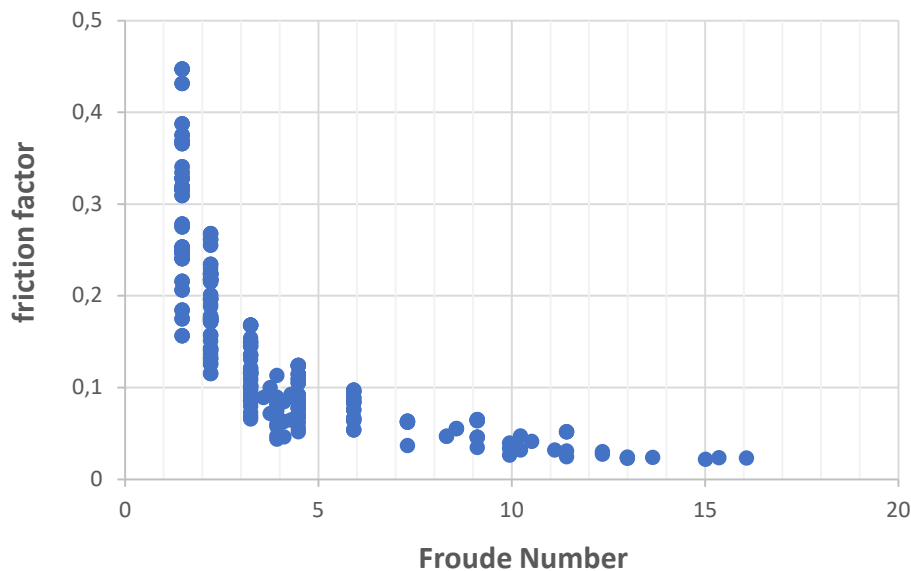Figure 2. Relation between friction factor and Reynolds Number

Figure 3. Relation between friction factor and Froude Number
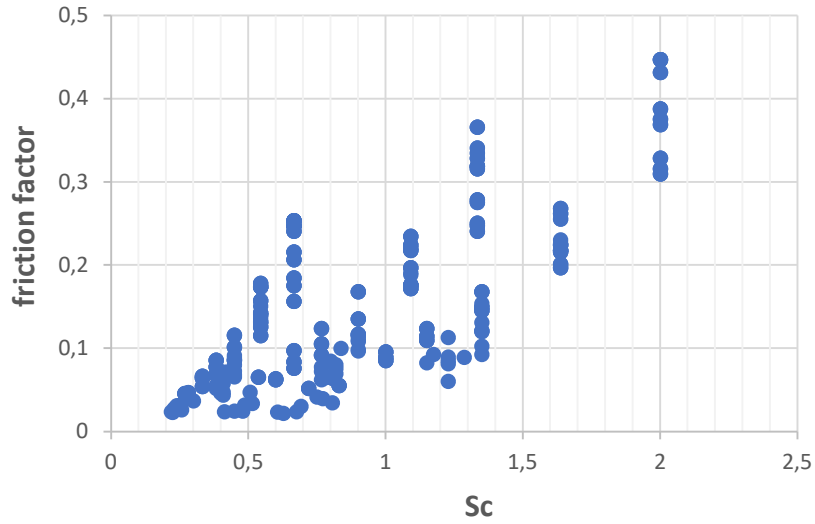
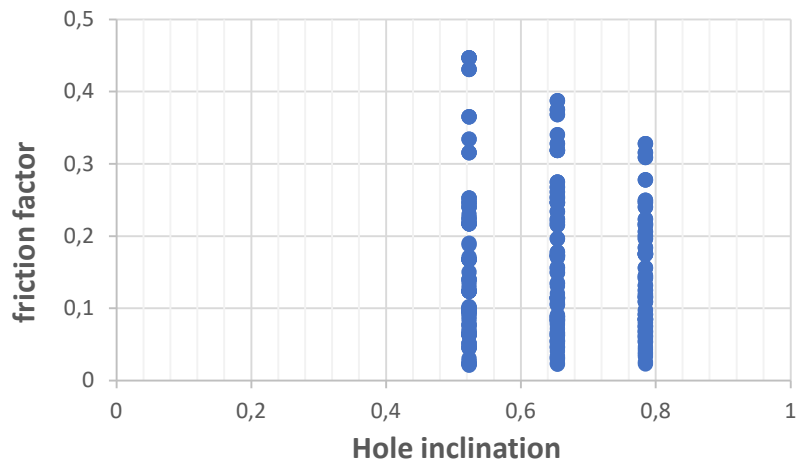Figure 4. Relation between friction factor and Sediment Concentration

Figure 5. Relation between friction factor and Hole Inclination
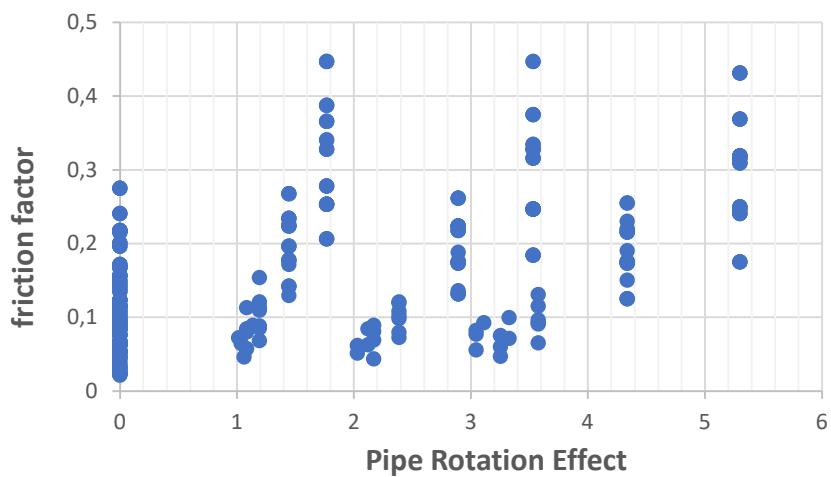

Figure 6. Relation between friction factor and Pipe Rotation Effect

In the light of the relationships between the dimensionless groups and friction factor, the following friction factor formula is developed as:

$$f = \left(\frac{\text{Re}}{10000}\right)^{a_1} + Fr^{a_2} + a_3 * S_c + a_4 * \theta + a_5 * (\Omega\,D)/v \tag{9}$$

Using the experimental data, the constants of Equation 9 are determined using statistical method. Table 1 shows

coefficients of the formula.

Table 1. Coefficients of the formula.

No (n)	a_n
1	-34.7
2	-0.00312
3	0.104
4	0.0392
5	0.00272

Using Equation 9, a performance analysis are carried out in Fig. 7 and Table 2. In Table 2, RMSE stands for Root Mean Square Error; AAE means Average Absolute Error and AAPE is used for Average Absolute Percent Error. Proposed equation has developed with 96% level of confident and 0.87 R^2 value.
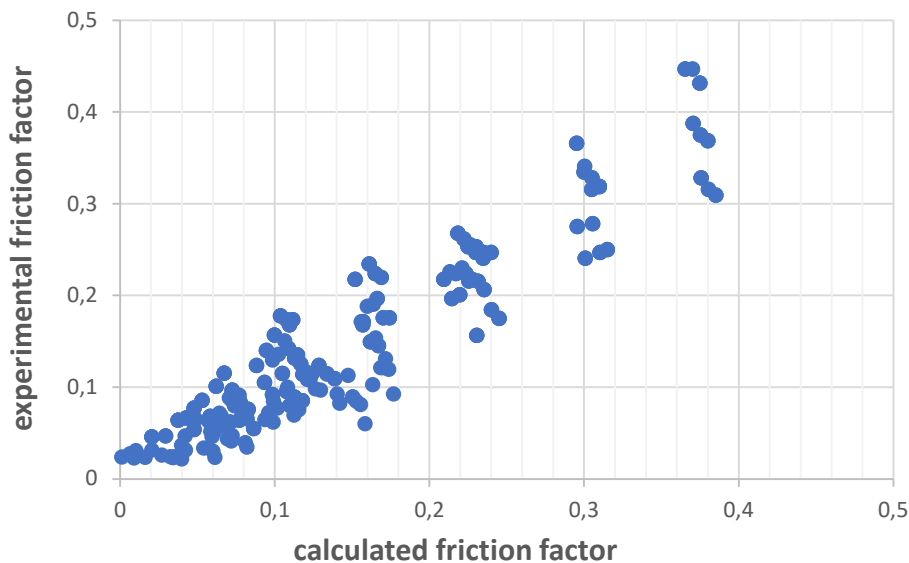

Figure 7. Relation between calculated and experimental friction factor

Table 2. Performance of developed friction factor equation.

R^2	RMSE	AAE	AAPE
0.87	0.300	0.03268	16.34

4. CONCLUSIONS

In this study, statistical methods are used to predict the friction factor of sediment transport in closed conduits using experimental data. Dimensional analysis is performed to identify the major variables that affect friction factor. Five dimensionless groups were defined after applying the Buckingham-Pi theorem,

including Reynolds number (π_1), Froude number (π_2), sediment concentration (π_3), hole inclination (π_4) and inner pipe rotation effect (π_5).

The root-mean-square-error (RMSE) and R-squared (R^2) metrics are used to evaluate the statistical formulas' performance. The proposed formula gives satisfactory results in comparison to the experimental data.

REFERENCES

Zandi, I., & Govatos, G. (1967). Heterogeneous flow of solids in pipelines. *Journal of the Hydraulics Division*, *93*(3), 145-159.

Rijn, L. C. V. (1984). Sediment transport, part II: suspended load transport. Journal of hydraulic engineering, 110(11), 1613-1641.

Tomren, P. H., Iyoho, A. W., & Azar, J. J. (1986). Experimental study of cuttings transport in directional wells. SPE Drilling Engineering, 1(01), 43-56.

Larsen, T. I., Pilehvari, A. A., & Azar, J. J. (1997). Development of a new cuttings-transport model for high-angle wellbores including horizontal wells. SPE Drilling & Completion, 12(02), 129-136.

Cheng, N. S. (1997). Simplified settling velocity formula for sediment particle. Journal of hydraulic engineering, 123(2), 149-152.

Kökpınar, M. A., & Göğüş, M. (2001). Critical flow velocity in slurry transporting horizontal pipelines. Journal of Hydraulic engineering, 127(9), 763-771.

Sumer, B. M., Chua, L. H., Cheng, N. S., & Fredsøe, J. (2003). Influence of turbulence on bed load sediment transport. Journal of Hydraulic Engineering, 129(8), 585-596.

Rabinovich, E., & Kalman, H. (2011). Threshold velocities of particle-fluid flows in horizontal pipes and ducts: literature review.

Rice, H. P., Fairweather, M., Peakall, J., Hunter, T. N., Mahmoud, B., & Biggs, S. R. (2015). Constraints on the functional form of the critical deposition velocity in solid–liquid pipe flow at low solid volume fractions. Chemical Engineering Science, 126, 759-770.

Najmi, K., Shirazi, S. A., Cremaschi, S., & McLaury, B. (2013, July). A generalized model for predicting critical deposition velocity for particle entrained in horizontal liquid and gas pipe flows. In Fluids Engineering Division Summer Meeting (Vol. 55560, p. V01CT20A006). American Society of Mechanical Engineers.

Zorgani, E., Al-Awadi, H., Yan, W., Al-Lababid, S., Yeung, H., & Fairhurst, C. P. (2018). Viscosity effects on sand flow regimes and transport velocity in horizontal pipelines. Experimental Thermal and Fluid Science, 92, 89-96.

Shirazi, A. S., & Frigaard, I. A. (2019). A three layer model for solids transport in pipes. Chemical Engineering Science, 205, 374-390.

Azamathulla, H. M., & Ahmad, Z. (2013). Estimation of critical velocity for slurry transport through pipeline using adaptive neuro-fuzzy interference system and gene-expression programming. Journal of Pipeline Systems Engineering and Practice, 4(2), 131-137.

Singh, K., Miska, S., Ozbayoglu, E., & Alp Aydin, B. (2018, October). Using supervised machine learning algorithms to predict pressure drop in narrow annulus. In SPE/AAPG Eastern Regional Meeting. OnePetro.

Whittaker, A. (1985). Theory and application of drilling fluid hydraulics.

Dosunmu, I. T., & Shah, S. N. (2015). Friction pressure prediction for annular flow of power law fluids. Chemical Engineering Communications, 202(10), 1380-1388.

Sorgun, M. (2010). Modeling of Newtonian fluids and cuttings transport analysis in high inclination wellbores with pipe rotation.